Measurement of Polarization Observables in π^0 and $\pi^0\pi^0$ Photoproduction from Protons and Neutrons at MAMI and ELSA

Inauguraldissertation

zur
Erlangung der Würde eines Doktors der Philosophie
vorgelegt der
Philosophisch-Naturwissenschaftlichen Fakultät
der Universität Basel

von

Manuel Dieterle

aus Biel-Benken, BL

Basel, 2015

Genehmigt von der Philosophisch-Naturwissenschaftlichen Fakultät
auf Antrag von

Prof. Dr. Bernd Krusche
Prof. Dr. Volker Metag

Basel, 8. Dezember 2015

Prof. Dr. Jörg Schibler
Dekan

Abstract

A detailed understanding of the nucleon and its excitation spectrum is inevitable for the investigation of the underlying strong interaction in the non-perturbative regime. Unfortunately, it is still poorly understood and the agreement between predicted and experimentally observed excited states is still unsatisfactory. For most quantum numbers, many more states are predicted than were experimentally identified. This is known as the problem of *missing resonances*. It is still unknown whether these discrepancies between theoretical predictions and experiment result from an inappropriate consideration of the internal degrees of freedom of the nucleon in the models or from experimental bias in the measurements. In the past, mostly pion-induced reactions were used to investigate the excitation spectrum of the nucleon. However, such experiments are only sensitive to excited states that couple significantly to $N\pi$, while other states would remain undiscovered. On the other hand, higher excited nucleons might decay via a cascade of intermediate states and with the emission of multiple mesons thereof, such that these states are only accessible using multiple meson production.

In the last few years, several new developments from the theory side in the non-perturbative regime have led to very promising results and are accompanied with a lot of experimental efforts using meson photoproduction, which include measurements of sequential decays via intermediate nucleon resonances. However, the measurements are complicated by the huge amount of broad and overlapping resonances, such that the identification of the individual contributions requires an elaborate partial wave analysis of the measured spectrum. Depending on the meson of interest, the situation can though be simplified. For example, in η photoproduction (as the η meson has isospin zero), contributions from isospin 3/2 (Δ) resonances are excluded and only isospin 1/2 (N^*) resonances can contribute to the nucleon excitation spectrum. On the other hand, single π^0 photoproduction is complicated by contributions from Δ resonances, but eliminates a lot of background contributions, since photons only couple weakly to neutral mesons. Investigations of $\pi^0\pi^0$ or $\eta\pi^0$ share the mentioned properties, but in addition allow for the investigation of higher lying resonances, R, by a cascade of decays via intermediate resonances, $R^{'}$, and the subsequent emission of meson m_1 and meson m_2: $\gamma N \to R \to R^{'} m_1 \to N m_1 m_2$.

Experiments on neutrons are especially important, as a distinct isospin decomposition of pion photoproduction requires the measurement on the neutron, which is only feasible with quasi-free neutrons bound in the deuteron. Due to the complication of the reaction and the non-trivial detection of neutrons, such data is so far sparse. In the last years, numerous developments on the experimental side rendered experiments with the coincident neutron detection possible and the availability of deuterated butanol targets even allows for the measurement of observables from polarized neutrons.

In this work, single and double π^0 photoproduction from unpolarized and polarized neutrons bound inside the deuteron was studied throughout the second and third resonance region of the nucleon. The experiments were carried out within the A2 and CBELSA/TAPS Collaborations at the electron accelerator facilities MAMI in Mainz, Germany, and ELSA in Bonn, Germany. Data was taken with circularly polarized tagged photon beams, unpolarized liquid deuterium targets, and longitudinally polarized deuterated butanol targets. The experimental setups mainly comprised of the electromagnetic calorimeters Crystal Ball and TAPS at A2 and Crystal Barrel and MiniTAPS at CBELSA/TAPS, which both almost cover the full solid angle.
The present data revealed significant differences in the production mechanisms of single and double π^0 photoproduction from protons and neutrons. Furthermore, it was found that significant nuclear effects result in a suppression of the single (double) π^0 photoproduction cross section for quasi-free protons of 35% (15%) with respect to the free proton. This indicates that a direct deduction of the results for the free neutron from those of the quasi-free neutron is not possible. Influences from nuclear Fermi motion have been removed by a complete reconstruction of the final state. A correction for the effects from nuclear final state interaction has been established by a comparison of the cross section from quasi-free protons to the results from free protons and was used to estimate the results on the free neutron. Thereby, the correction is based on the assumption that the nuclear effects are similar for protons and neutrons.
For the first time, results for the unpolarized and helicity dependent differential and total cross sections for single and double π^0 photoproduction from free and quasi-free nucleons have been extracted with high statistical quality. The results are compared to the latest available predictions from reaction models and partial-wave analyses that are based on data from other isospin channels. The impact of the present results from single π^0 photoproduction from the free neutron will be demonstrated by the results of a new analysis in the framework of the Bonn-Gatchina coupled-channel partial-wave analysis, which included the present data. A detailed investigation of the contributions from sequential decays to double π^0 photoproduction discloses the different nature of the corresponding cross section on the proton and the neutron.
The first time measurements of unpolarized and polarized observables in single and double π^0 photoproduction from the neutron provide substantial input for the partial-wave analyses and will put stringent limits on the resonance contributions to the excitation spectrum of the nucleon.

Acknowledgments

This work would not have been possible without the help and support of many people. I would like to express my gratitude for all the unforgettable moments and experiences.

At first I would like to thank Prof. Dr. Bernd Krusche for giving me the opportunity to participate in his research group and to do a Ph.D. in this fascinating field. I highly appreciate the impressive support and confidence during the last years. Thanks for all the valuable discussions we shared and for the helpful advice in intricate situations. I enjoyed these interesting and intensive years very much and will always remember this time with pleasure. I would also like to thank Prof. Dr. Volker Metag for his support and for serving as my co-referee.

I hold Irakli Keshelashvili, *my brother from another mother*, in high regard. Thanks for the priceless transfer of knowledge and his patience, support and encouragement in good and bad times. Special thanks to Lilian Witthauer, without whom this work would not have come that far. I am grateful for the unique time and the efficient collaboration and am sorry for the tough moments in between.

Thanks to Dominik Werthmüller for all the computational support and for sharing his experiences with me. Thanks to Natalie Walford for the crazy and funny last year and the high speed corrections of my thesis. Thanks to all the former and present group members I. Jaeglé, F. Pheron, Y. Maghrbi, R. Trojer, T. Rostomyan, M. Oberle, A. Käser, T. Strub, S. Garni, S. Lutterer, F. Müller, M. Günther, and S. Abt. I will never forget the professional collaboration and the incredible moments in and outside of the department. Many thanks to all the members of the A2 and CBELSA/TAPS collaborations for the support, teamwork, and exchange of knowledge before, during and after the experiments and meetings.

Thanks to D. Biesinger for the great moments, discussions and the emergency provisions.

Cordial thanks to my family and all my close friends. I deeply appreciate their patience and unquestioning support during the tough times of my Ph.D.

Contents

1 Introduction

1.1 The Structure of Matter

Until the beginning of the 20th century, it was controversial whether matter is a continuum of infinite substructure or is rather made of finite sized building blocks, that can not be further decomposed into smaller substructures. Such particles initially were denoted *atoms* (from Greek *átomos*, the indivisible) and it was the chemist John Dalton who around 1800 first established the term within science [1]. He represented the opinion that all elements consist of the same type of particles, the atoms, which are responsible for the various forms and reactivities of the known elements and molecules. These atoms were thought of as the fundamental particles of matter, until Antoine Henri Becquerel in 1896 and later Marie and Pierre Curie in 1898 discovered radioactivity [2]. They showed that atoms have a substructure and consist of an atomic shell of electrons and an atomic nucleus, which itself consists of protons and neutrons. Thereupon, electrons, protons, and neutrons were considered as *elementary particles*.

After the discovery of cosmic radiation and the first experiments with particle accelerators, pions, kaons, muons, positrons, and other particles followed. In the 1950s, the particles were subdivided into particles that are held together by the strong force (*hadrons*), and others, which do not undergo strong interactions (*leptons*). Nowadays, leptons are still considered elementary particles, but in the 1970s hadrons were further decomposed into quarks [4]. The interaction among the different elementary particles is based on the *fundamental forces of physics*: the *gravitational*, the *electromagnetic*, the *weak*, and the *strong* force. These four fundamental types of interactions are responsible for all physical processes, independent of space and time. The gravitational (described by the law of gravity) and electromagnetic (described by quantum electrodynamics, QED) force act over an infinite distance and are responsible for most of the every day phenomena. In contrast, the weak force (described by quantum flavordynamics, QFD) and strong forces (described by quantum chromodynamics, QCD) are short ranged and irrelevant for distances larger than roughly the size of an atomic nucleus. Even though they are not directly noticeable, their effect is crucial. The strong interaction holds the quarks, and by that the hadrons,

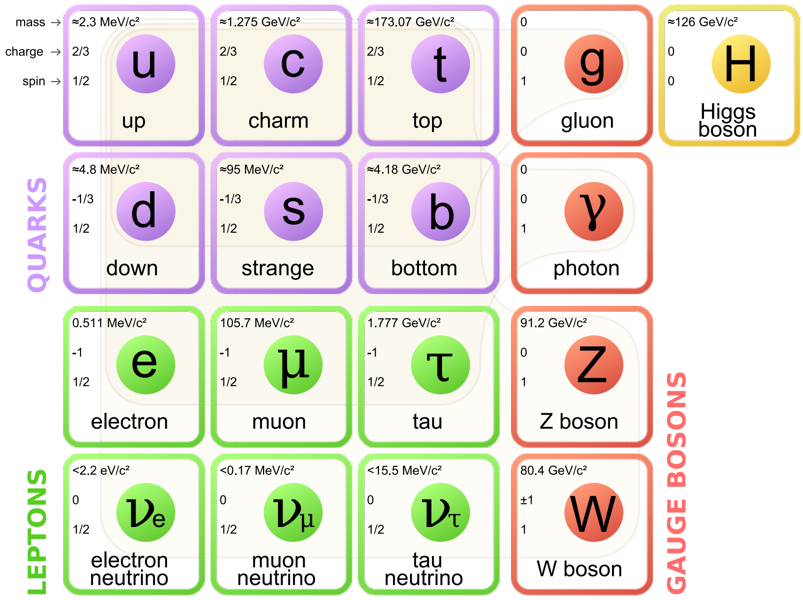

Figure 1.1: Chart of the elementary particles according to the standard model of physics. The elementary particles are subdivided into two main groups: the fundamental fermions (half-integer spin particles: quarks, antiquarks, leptons, and antileptons) and the fundamental bosons (integer-spin particles: gauge bosons and the Higgs boson). Figure taken from [3].

such as protons and neutrons, together. It is thus responsible for the existence of stable nuclei and the existence of matter in general. The weak interaction is responsible for the radioactive decay of subatomic particles and plays an essential role in nuclear fusion, such as the fusion of hydrogen to helium, the relevant process for the generation of light in the sun. The electromagnetic, weak and strong force are modeled as discretized quantum fields and are mediated by elementary particles, the *gauge bosons* (γ, Z^0, $W^{\pm}$, and gluons). The description of gravity as a quantum field is still outstanding and hypothesizes another elementary particle, the *graviton* [5]. Additionally, the standard model requires the lately discovered *Higgs-boson* to break the electroweak symmetry, which is necessary in order to give mass to the Z^0 and $W^{\pm}$ bosons. The *Standard Model* is the quantum field theory that describes all different kind of interactions (besides gravity, for which a quantum field theoretical description was not yet achieved) and classifies the elementary particles. It is summarized in Figure 1.1.

1.1.1 The Structure of the Nucleon

Nucleons, i.e. protons and neutrons, are the building blocks of atomic nuclei. The properties of the atomic nuclei and the elements thereof strongly depend on the structure of the nucleons. As previously mentioned, protons and neutrons were initially interpreted as elementary particles before it was discovered that they exhibit an internal substructure. First evidence of an internal structure of the nucleon was

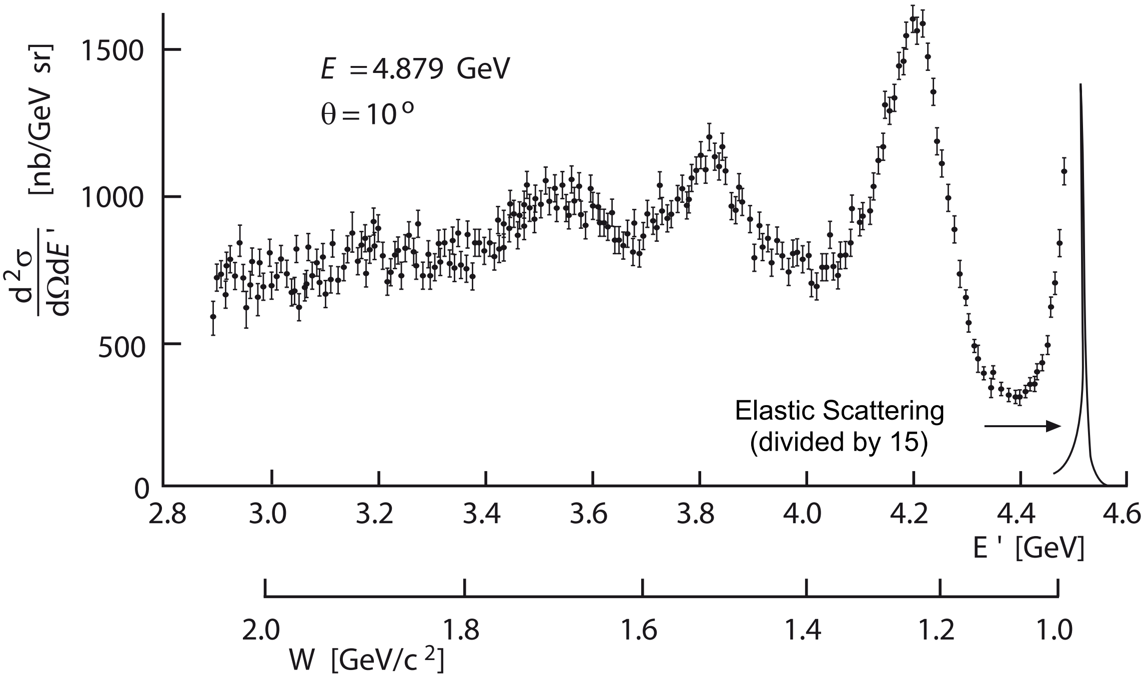

Figure 1.2: Spectrum of the scattered electrons in electron-proton scattering at an electron beam energy of $E = 4.9$ GeV and for scattering angles of $\theta = 10°$. Figure adapted from [6].

already found in 1933, when R. Frisch and O. Stern [7] measured the magnetic moment of the nucleons. The magnetic moment of the proton was expected to correspond to that of a charged, pointlike spin-1/2 particle, such as the electron, i.e. $\mu_N = e\hbar/(2m_pc)$, denoted as the *nuclear magneton*, where $\hbar$ is the reduced Planck constant, m_p is the mass of the proton, and c is the speed of light. Furthermore, the magnetic moment of the neutron was expected to be zero. In contradiction to expectations, an anomalous large magnetic moment of the proton and a nonzero magnetic moment of the neutron with a different sign compared to that of the proton, were observed. The present values of $\mu_p = 2.792 \cdot \mu_N$ and $\mu_n = -1.913\mu_N$ [8] confirm the observations and prove that the nucleon does have a structure.

In 1964, Gell-Mann postulated quarks as the building blocks of the hadrons [4], since he found evidence of a possible substructure of the nucleons while arranging the different particles due to their properties. He proposed baryons to be composed of three quarks and mesons of a quark-antiquark pair. In 1968, scattering experiments with electrons on nucleons at DESY[1] [10] revealed further evidence for the internal structure of the nucleon. In the energy range of $W = 1.0 - 2.0$ GeV, the scattering cross section (see Figure 1.2) exhibits distinct maxima, which correspond to the excited states of the nucleon. At higher energies, i.e. $W \gtrsim 2.5$ GeV, no distinct resonances are visible anymore, since in this energy range, scattering occurs not on the nucleon as a whole, but on its constituents, the postulated quarks.

[1]DESY: Deutsches Elektronen-Synchrotron in Hamburg, Germany

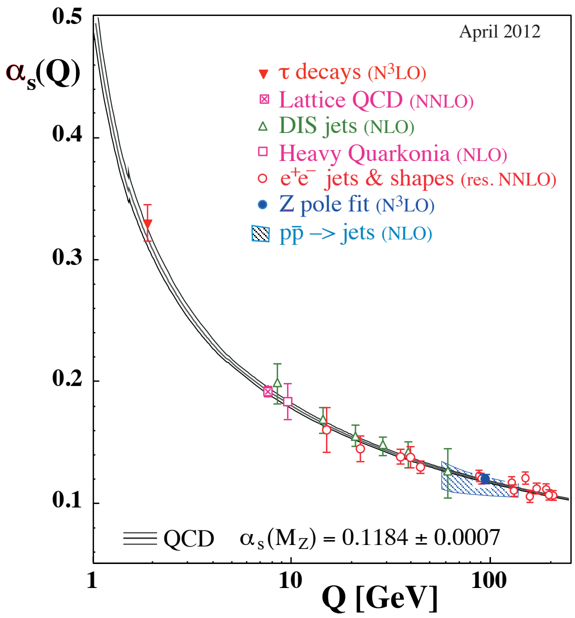

Figure 1.3: Overview of the measurements of the strong coupling constant α_s as a function of the respective energy scale Q. The curves are the QCD predictions for the combined world average of α_s. Figure taken from [9].

The interactions among quarks are described by the gauge theory of the strong interaction, quantum chromodynamics (QCD). Contrary to quantum electrodynamics (QED), which describes the interaction among electrically charged particles with photons, the force carriers of QCD are the gluons and the analog to the electric charge are the three color charges: red, blue, and green. The gluons carry a color charge itself and hence can interact with each other. For this reason, the coupling constant of the strong interaction α_s increases with decreasing momentum transfer Q^2 (large distances). This is the opposite behavior of the electromagnetic coupling constant α_{em}, which as a result of the screening due to the vacuum polarization, increases with increasing Q^2 (small distances). The dependence of α_s is illustrated in Figure 1.3 and shows the two main features of the strong interaction: First, large values of the strong coupling constant correspond to large distances. This phenomenon is referred to as *confinement* of quarks and denotes that free quarks are non-existent. The potential energy between two quarks increases linearly with the distance until the energy is sufficient to produce another quark-antiquark pair. As a consequence, only color neutral particles can be observed in nature. Secondly, small distances correspond to small coupling constants, which is referred to as *asymptotic freedom* of quarks. This means that quarks, which are bound in a hadron, behave as free particles. This characteristic behaviour is responsible for the stable nuclei and matter as a whole.

The theoretical description of the hadrons, and by that of the nucleons, is complicated by the size of the strong coupling constant. Depending on the energy range

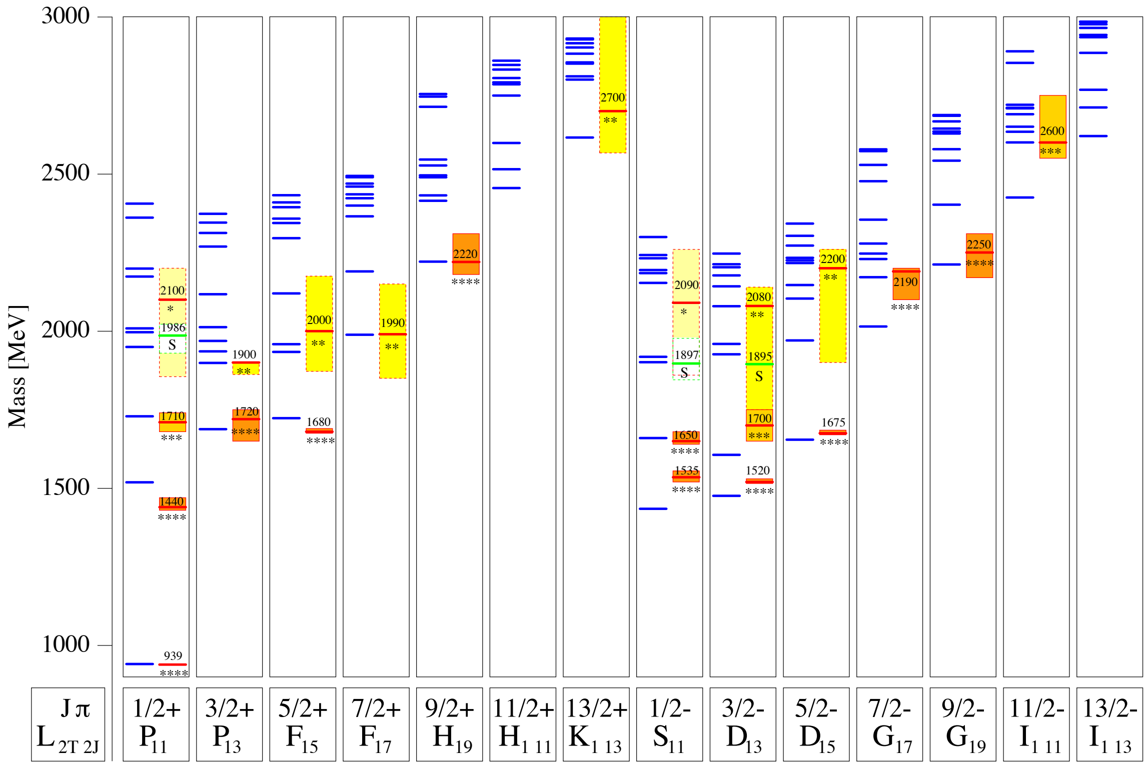

Figure 1.4: Overview of the positive and negative parity nucleon resonance spectrum predicted by Löring et al. [11] compared to the experimentally observed resonances. The results from the model calculations are shown as blue lines and the experimentally observed resonances are indicated with by the yellow to red bars. The size of the bars corresponds to the experimentally determined position and the color of the bar denotes the uncertainty of the resonance. The darker the color, the more reliable is the resonance. The status of the resonance is also indicated by stars, where one star denotes *evidence of existence is poor* and four stars denote *existence is certain, and properties are at least fairly well explored.* Figure taken from [12].

of interest, the equations of the theoretical description from the standard model in general can not be solved exactly, such that the solution has to be achieved by a perturbative consideration of the problem. Thereby, the size of the coupling constant is relevant for the necessary number of orders that have to be considered in the perturbative series. Small coupling constants, i.e. $\alpha \ll 1$, result in fast convergence and exact results, which works satisfactorily for QED calculations, where $\alpha_{em} \approx 1/137$. However, for QCD at the rather low energies, sufficient precision of the results can only be achieved by the consideration of higher order terms in the calculation, which is not feasible at present due to the computationally intensive calculations. Instead, one makes use of chiral perturbation theory, which is based on hadronic rather than gluonic degrees of freedom. At present, both approaches still fail on the energy scale of the nucleon, especially for the description of the higher lying excited states. Therefore, the description relies on lattice gauge calculations or phenomenological quark models. Whereas the former shows promising results but is still in a very early stage, the latter has no general agreement about the effective degrees of freedom or how to properly account for the quark-quark interactions. For this reason, the models results are all of comparable quality. Additionally, even the models with the fewest effective degrees of freedom predict a larger number of states than are experimentally confirmed. An example for such a model which achieves rather satisfactory results is the model from Löring et al. [11]. The model is based on the three-fermion Bethe-Salpeter equation, which describes the bound states of a system consisting of three fermions and is able to account for the main features of the light baryon spectrum up to excited nucleon states with spin $J = 13/2$ by means of seven degrees of freedom only. The results are shown in Figure 1.4 (solid blue lines) and show an overall remarkable agreement with the experimentally observed states (colored bars). Especially at low energies, the number and the position in general is in reasonable agreement with the observations, except for the well-known Roper resonance ($N(1440)1/2^+$) and the $N(1535)1/2^-$, which exhibit significant differences. With higher energies, disagreement between the position and numbering of the excited states increases and is often referred to as the *problem of missing resonances*. It is still unknown, whether this significant discrepancy is due to a wrong consideration of the effective degrees of freedom, the modeling of the interactions among the quarks, or if its simply due to experimental bias. Since most of the well established nucleon resonances were observed in elastic pion scattering from the nucleon, resonances that couple only weakly to $N\pi$ states would be suppressed and hence not observed. For this reason, investigation of the excitation spectrum of the nucleon via photon-induced reactions drew a lot of attention and nowadays are among the most promising programs in the search for the missing resonances.

1.1.2 The Excited States of the Nucleon

As mentioned in Section 1.1.1, besides the prominent maximum (see Figure 1.2), which is related to elastic scattering, the cross section of electron-proton scattering exhibits distinct maxima at low scattering energies. These maxima correspond to the excited states of the nucleon and are called *nucleon resonances*. The mass of the resonance at an incident photon energy of roughly 4.2 GeV is $W = 1232$ MeV and is denoted as the $\Delta(1232)3/2^+$ resonance. Thereby the notation stands for $R(m_R)J^P$, where R is the resonance (resonances with isospin $I = 1/2$ are referred to as N^*- and resonances with $I = 3/2$ as Δ-resonances), m_R is its mass in the center of mass (cm) frame in units MeV/c^2, J is its total angular momentum, and P is its parity. The width of this resonance is roughly $\Gamma_\Delta \approx 120$ MeV and is only slightly larger than the typical width of nucleon resonances of $\Gamma \approx 100$ MeV. According to Heisenberg's uncertainty principle, $\tau \cdot \Gamma \approx \hbar$, the resonances have a very short lifetime of $\tau_\Delta \approx \hbar/\Gamma = 5.5 \cdot 10^{-24}s$, due to the rather large width, which corresponds to the timescale of the strong interaction [6]. The nucleon resonances then dominantly decay to the nucleon ground state via the emission of mesons. The number and type of the emitted meson(s) thereby depends on the intrinsic properties (mass, charge)

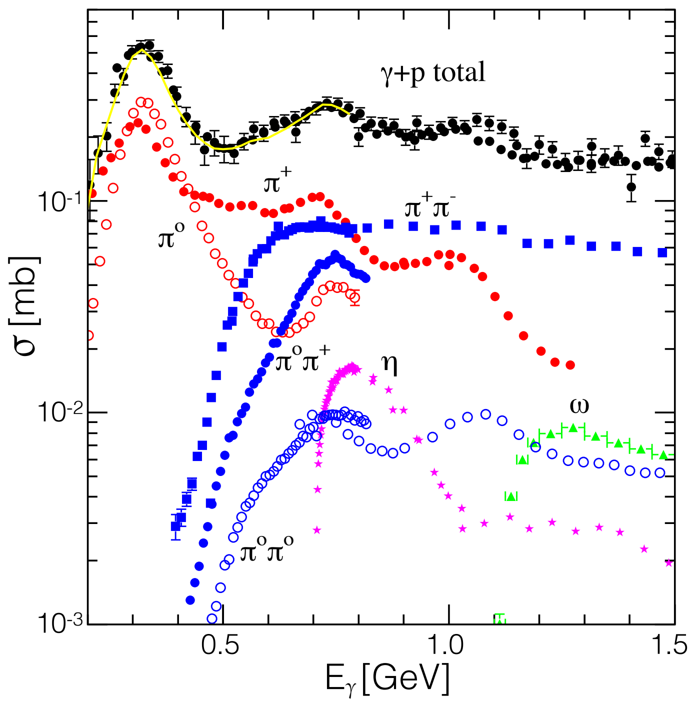

Figure 1.5: Total photoabsorption cross section from the free proton (black circles) and the individual contributions from different single and double meson final states (colored symbols). Figure taken from [13].

and the quantum numbers (spin, parity) of the individual resonance.

Besides inelastic electron scattering, nucleon resonances can also be produced by pion scattering or by photon-induced reactions. An example of the latter is shown in Figure 1.5. It shows the total photoabsorption cross section from the free proton (solid black circles) and the individual contributions from the different single and double meson final states (colored symbols). At incident photon energies of $E_\gamma \approx 340$ MeV, the dominant contribution from the $\Delta(1232)3/2^+$ resonance that was already seen in the electron-proton scattering spectrum (see Figure 1.2), is clearly visible. This region denotes the first resonance region of the nucleon excitation spectrum. At higher energies, two smaller but well defined maxima can be observed, which correspond to the second and third resonance region. The cross section for each specific meson photoproduction reaction has its characteristic shape, which depends on the production threshold and the contributing resonances, interferences among them, non-resonant background contributions, and possible nuclear effects (meson-meson, meson-nucleon and nucleon-nucleon final state interaction effects).

Even though different resonances contribute to the individual cross sections, their identification, as well as the extraction of their intrinsic properties, is difficult, since the resonances are broad and overlapping. Figure 1.6 illustrates the different resonance contributions for single π^0 photoproduction (left-hand side) and η photo-

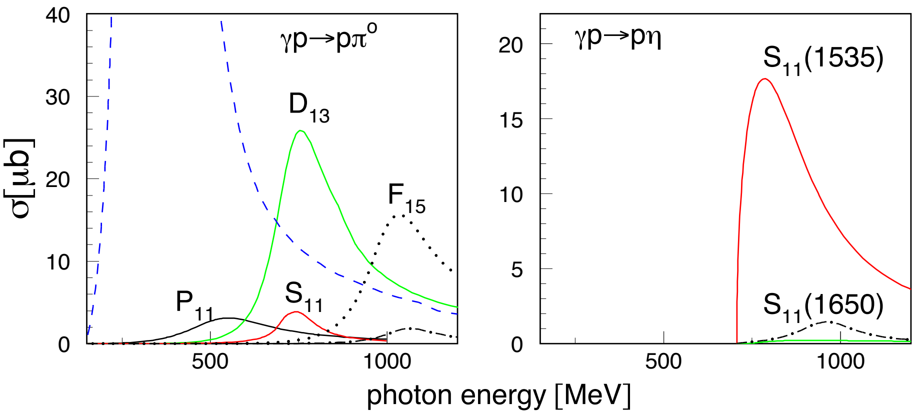

Figure 1.6: Schematic overview of the different resonance contributions (colored lines) to $\gamma p \to \pi^0 p$ (left-hand side) and $\gamma p \to \eta p$ (right-hand side) in the first and second resonance region. Figure taken from [14].

production (right-hand side) from the free proton in the first and second resonance region. It demonstrates that a careful choice of the final state allows for the investigation of specific resonances. The resonances are labeled with the corresponding partial wave:

$$L_{2I2J}(W) \ , \tag{1.1}$$

where L denotes the angular momentum of the nucleon-meson system, W is the mass in MeV/c^2, I is the isospin, and J is the total angular momentum of the excited state. As seen in the left-hand side of Figure 1.6, single π^0 is ideally suited for the extraction of the properties of the $\Delta(1232)3/2^+$ resonance (dashed blue line), since it dominates the spectrum at these low energies and contributions from other resonances are sparse. On the other hand, the extraction of the properties of the $N(1535)1/2^-$ excited state of the nucleon (solid red line labeled as the S_{11} partial wave) from the same reaction is not feasible and requires elaborate model analyses, since the resonance contributes only weakly to the excitation spectrum and is strongly overlapped by the other resonances. In contrast, the η photoproduction cross section is completely dominated by contributions from the $N(1535)1/2^-$, such that its investigation with this reaction is straightforward. Furthermore, compared to the π^0 meson which has isospin $I = 1$, the η meson has isospin $I = 0$ and can only originate from decays with $\Delta I = 0$. As a consequence, only N^* resonances contribute to the nucleon excitation spectrum, such that the η photoproduction cross section is free of contributions from Δ resonances, which simplifies the interpretation.

The investigation of higher lying excited states is complicated by the presence of decays via intermediate excited states, which is accompanied by the emission of multiple mesons. Such states can therefore be explored by double or triple meson photoproduction. Thereby the probability of decays via intermediate states increases with the nucleon excitation energies. Nevertheless, already low lying excited states have significant decay branching ratios to intermediate states, as shown in Figure 1.7.

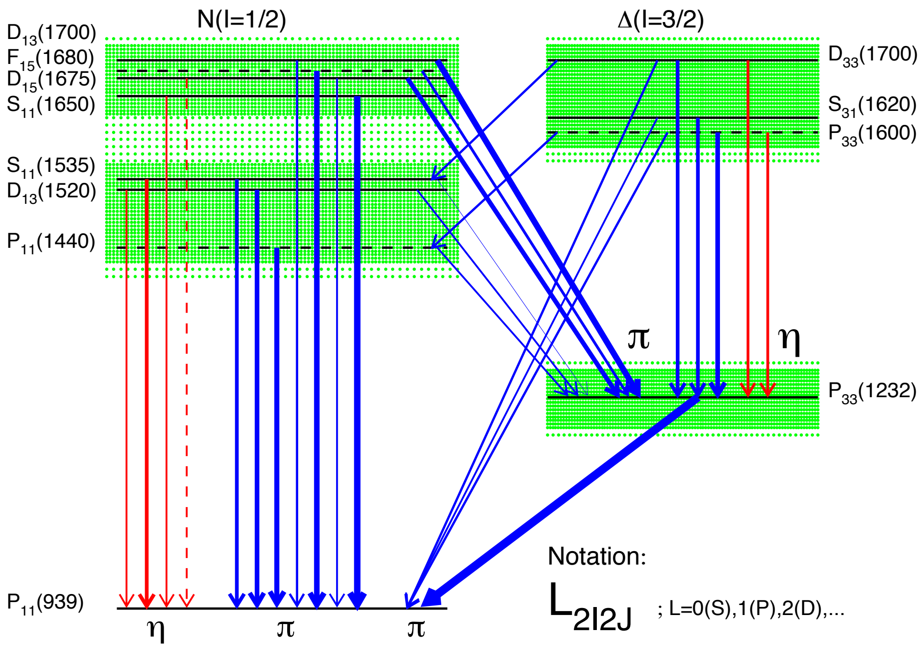

Figure 1.7: Low energy excitation scheme of the nucleon. Left column: isospin $I = 3/2$ Δ-resonances. Right column: isospin $I = 1/2$ N^*-resonances. Arrows: typical decays. The width corresponds roughly to the decay branching ratio. Blue: π^0 decays. Red: η decays. Figure taken from [14].

In summary, meson photoproduction is ideally suited to study the excitation spectrum of the nucleon. The measurement of different final states allows for the investigation of specific resonances and multiple meson photoproduction gains access to the higher lying excited states of the nucleon. However, differential cross section data often does not sufficiently constrain the model descriptions, such that the measurement of single and double polarization observables is necessary for an unambiguous identification of the different resonance contributions, which is essential for the understanding of the excitation spectrum of the nucleon.

1.2 Meson Photoproduction

The problem of the missing resonances gave rise to a world wide experimental program for the investigation of the nucleon excitation spectrum with meson photoproduction. The relevant processes are illustrated in Figure 1.8 for the example of single π^0 photoproduction, whereas the figure on the left-hand side is valid for any pseudoscalar meson[2]. The general process is the following: a photon with total angular momentum $\vec{L}_\gamma$ and parity P_γ couples electromagnetically to the nucleon with spin $\vec{J}_N$ and parity P_N to produce a resonance with spin $\vec{J}_{N^*}$ and parity P_{N^*}. The resonance then decays by strong interaction to the nucleon ground state via the emission of

[2]In principle, also for vector mesons, but since they have spin 1, the notation would have to be changed from L_m^P to J_m^P.

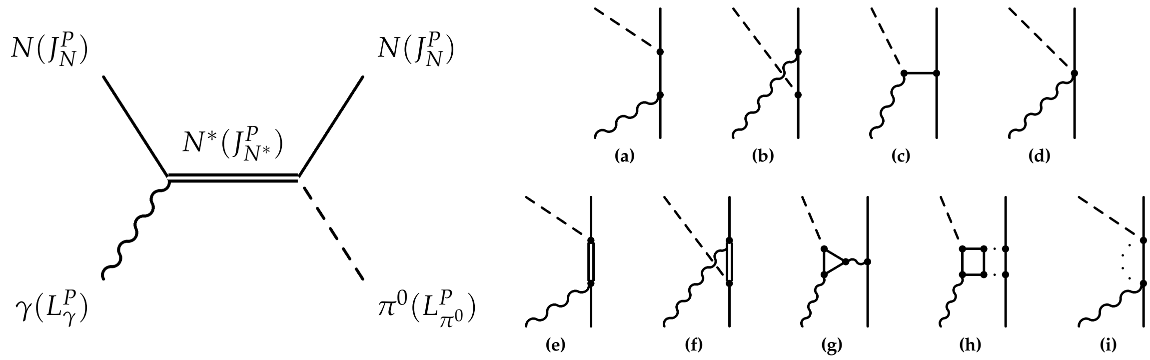

Figure 1.8: Left-hand side: Feynman diagram for π^0 photoproduction via excitation of nucleon resonances. Right-hand side: Feynman diagrams contributing to pion photoproduction. (a)-(d) Born terms. (a) Direct term. (b) Crossed nucleon pole. (c) Pion pole. (d) Kroll-Ruderman term. (e),(f) Isobar excitations. (g) Triangle anomaly (photon pole, vector meson exchange). (h) Square anomaly. (i) Rescattering terms.

a pseudoscalar meson m with spin 0, relative orbital angular momentum L_m, and parity P_m.

Photoproduction experiments have several advantages: on the one hand they might be sensitive to resonances that are not visible in pion scattering experiments and hence could solve the missing resonance problem. On the other hand, in addition to the dominant hadronic decay modes, they provide access to the informative electromagnetic transition amplitudes. Nevertheless, there are also a few drawbacks: the electromagnetic cross sections are significantly smaller than hadronic ones and the reaction mechanism is accompanied by substantial non-resonant background contributions, such as nucleon Born terms or vector meson exchange, as shown on the right-hand side of Figure 1.8. For this reason, photoproduction of neutral mesons is of special interest, since they do not couple directly to photons, such that non-resonant background contributions as pion-poles and Kroll-Ruderman terms are suppressed. This again emphasizes the importance of the measurements of multiple final states. On the one hand it ensures that no bias from the coupling of the excited nucleon states to specific decay channels is present. On the other hand it allows for a more quantitative extraction of the individual resonances, as specific reactions are better suited for the extraction of certain resonances than others or are differently influenced by non-resonant background contributions.

1.2.1 Kinematics of the Reaction

Single meson[3] photoproduction from a free nucleus can be described by the following reaction:

$$\gamma(k) + N(p_i) \rightarrow m(q) + N(p_f) \ , \tag{1.2}$$

where a photon, γ, with four-momentum k impinges onto a free target nucleon, N, with initial state four-momentum p_i, and final state momentum p_f, to produce a meson, m, with four-momentum q. For a scattering process involving two initial and two final state particles, the kinematics are fully determined by use of the three Lorentz-invariant *Mandelstam variables* s, t, and u. They are defined as:

$$\begin{aligned} s &= (k + p_i)^2 &&= (q + p_f)^2 \\ u &= (k - p_f)^2 &&= (q - p_i)^2 \\ t &= (q - k)^2 &&= (p_i - p_f)^2 \ , \end{aligned} \tag{1.3}$$

under the constrain that the sum of the variables is equal to the squared masses of the participating particles, i.e. $s + t + u = 2m_N^2 + m_m^2 + k^2$. From the Mandelstam variable s, the center of mass energy $W = \sqrt{s}$ is given by

$$W = \sqrt{s} = \sqrt{(k + p_i)^2} = \sqrt{2E_\gamma m_N + m_N^2} \ , \tag{1.4}$$

and a resonance in the hadronic final state at a mass W occurs at an incident photon energy of

$$E_\gamma = \frac{W^2 - m_N^2}{2m_N} \ . \tag{1.5}$$

Photoproduction of mesons from nuclei is mainly characterized by three types of final states: the *coherent*, *incoherent*, and *quasi-free* (breakup) reaction. In the following, they will be briefly described for the example of single π^0 photoproduction from the deuteron.

Coherent Photoproduction

In the coherent reaction, the incident photon (wiggly line) interacts with the target nucleus, A, to produce a π^0 meson. Thereby, the nucleus in the final state remains intact and in the ground state. The process is illustrated in Figure 1.9.

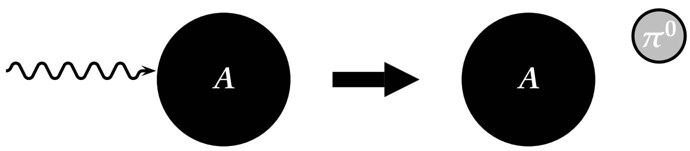

Figure 1.9: Schematic diagram of the coherent photoproduction process.

[3] This also applies for multiple meson photoproduction, if the final state mesons are combined to a quasi-meson.

Since the center of mass energy of the reaction has to be large enough to produce the π^0 and the recoil deuteron, i.e. $W \geq m_{\pi^0} + m_d$, the threshold for coherent π^0 photoproduction can be determined from Equation (1.5):

$$E_\gamma^{\text{thresh,coherent}} = m_{\pi^0} + \frac{m_{\pi^0}^2}{2m_d} \approx 139.83 \text{ MeV} \ . \tag{1.6}$$

However, in the energy range of interest, i.e. above incident photon energies of 400 MeV, the coherent reaction cross section for single (and double) π^0 photoproduction is negligible and thus will not be considered in this work.

Incoherent Photoproduction

Incoherent photoproduction corresponds to the process where the final state nucleus, A, remains intact, but is in a excited state, A'. It then usually decays to the ground state by the emission of γ-radiation. The process is illustrated in Figure 1.10.

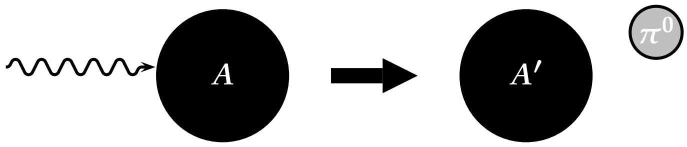

Figure 1.10: Schematic diagram of the incoherent photoproduction process.

This reaction allows for additional identification criteria, such as spin- and isospin filters, by selecting the final state quantum numbers. However, due to the small cross sections, these reactions are still unexplored. Furthermore, since the deuteron has no excited state and hence only exists in its ground state, the incoherent process results in a breakup of the nucleus. As a consequence, for the reaction on the deuteron this process is identical to the quasi-free process.

Quasi-Free Photoproduction

The quasi-free photoproduction is described by the *participant-spectator model*, in which the incident photon only interacts with one nucleon, the participant. The remaining nucleon, the spectator, is assumed not to be part of the reaction. The scattered participant is then knocked out of the target nucleus, as illustrated in Figure 1.11.

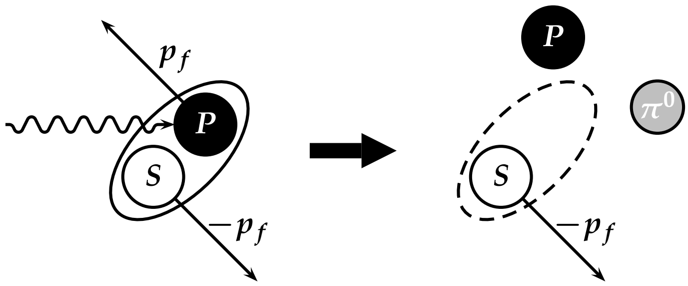

Figure 1.11: Schematic diagram of the quasi-free photoproduction process.

Compared to free nucleon targets, the participant in quasi-free kinematics is not at rest, but exhibits a Fermi momentum according to the probability distribution of the corresponding nucleus (see Figure 3.9 for a few examples). As a consequence, the threshold of quasi-free π^0 photoproduction is not a well-defined value and depends on the Fermi momentum of the participant nucleon. However, the production threshold can be approximated by the coherent threshold increased by the amount of the binding energy E_{bind} of the nucleus ($E_{\text{bind}} \approx 2.225$ MeV for the deuteron):

$$E_\gamma^{\text{thresh,quasi-free}} = E_\gamma^{\text{thresh,coherent}} + E_{\text{bind}} \approx 142.06 \text{ MeV} . \tag{1.7}$$

1.2.2 Multipole Decomposition

The process of photoproduction of π^0-mesons via the intermediate excitation of nucleon resonances is shown on the left-hand side of Figure 1.8. The determination of the multipole amplitudes requires an angular momentum decomposition of both the initial and final state. The photon in the initial state has an orbital momentum $\vec{l'}$ relative to the target nucleon and carries spin $\vec{s}_\gamma$ ($s_\gamma = 1$) with helicity λ ($\lambda = \pm 1$ for real (transverse) photons and $\lambda = 0, \pm 1$ for virtual (longitudinal or transverse) photons). Hence its total angular momentum is given by $\vec{L}_\gamma = \vec{l'} + \vec{s}_\gamma$. The photon wave function can be characterized by vector spherical harmonics [15]:

$$\vec{Y}_{l'LM} = \sum_\mu \langle 1 l' \lambda \mu \mid LM \rangle \vec{e}_\lambda Y_{l'\mu}(\Omega) , \tag{1.8}$$

where L determines the multipolarity of the transition. Transverse helicities ($\lambda = \pm 1$) lead to electric (EL) and magnetic (ML) multipole transitions, whereas longitudinal helicities lead to longitudinal or, equivalently, Coulomb (scalar) transitions (CL). However, only real photons are of interest for photoproduction, such that CL terms do not contribute. The photon then couples electromagnetically to the nucleon with spin $J_N = \frac{1}{2}$ and parity $P_N = +1$ to produce a resonance with spin J_{N^*} and parity P_{N^*}. The electric (EL) and magnetic (ML) multipoles with angular momentum L have parity

$$P_\gamma = \begin{cases} (-1)^L & \text{(EL)} \\ (-1)^{L+1} & \text{(ML)} \end{cases} . \tag{1.9}$$

The total spin and the parity of the initial state has to be equal to the total spin and the parity of the intermediate resonance, such that the following selection rules apply:

$$\begin{aligned} |L_\gamma - J_N| = |L_\gamma - \tfrac{1}{2}| \leq J_{N^*} \leq |L_\gamma + \tfrac{1}{2}| = |L_\gamma + J_N| \\ P_\gamma \cdot P_N = P_\gamma \stackrel{!}{=} P_{N^*} . \end{aligned} \tag{1.10}$$

The resonance then decays by the strong interaction to the nucleon ground state via emission of the π^0 meson with spin 0, parity $P_{\pi^0} = -1$ and relative orbital angular momentum L_{π^0}. The total spin and the parity of the excited state have to be equal to those of the final state, which, equivalently to Equation (1.10), yields:

$$\begin{aligned} |L_{\pi^0} - J_N| = |L_{\pi^0} - \tfrac{1}{2}| \leq J_{N^*} \leq |L_{\pi^0} + \tfrac{1}{2}| = |L_{\pi^0} + J_N| \\ P_N \cdot P_{\pi^0} \cdot (-1)^{L_{\pi^0}} = (-1)^{L_{\pi^0}+1} \stackrel{!}{=} P_{N^*} \ . \end{aligned} \tag{1.11}$$

The comparison of the conditions from Equations (1.10) and (1.11) yields:

$$\begin{aligned} J_{N^*} &= |L_\gamma \pm \tfrac{1}{2}| = |L_{\pi^0} \pm \tfrac{1}{2}| \\ P_{N^*} &= P_\gamma = (-1)^{L_{\pi^0}+1} \ , \end{aligned} \tag{1.12}$$

where the two conditions $\pm$ are independent from each other. Finally, conservation of angular momentum and parity from Equations (1.9) and (1.12) restricts the possibilities for the electric and magnetic multipoles to:

$$\begin{aligned} EL: &\quad L = L_{\pi^0} \pm 1 \\ ML: &\quad L = L_{\pi^0} \ . \end{aligned} \tag{1.13}$$

Thereby, conservation of angular momentum does not allow monopole radiation ($L = 0$). Examples for the lowest order multipoles for photoproduction of pseudo-scalar mesons are given in Table 1.1.

L	photon M-Pole	IS (L_γ^P, J_N^P)	ImS State $J_{N^*}^P$	FS $(J_N^P, L_{\pi^0}^P)$	M-Pole	$(k^*/q^*)d\sigma/d\Omega$
1	$E1$	$(1^-, \frac{1}{2}^+)$	$\frac{1}{2}^-$	$(\frac{1}{2}^+, 0^-)$	E_{0+}	$\|E_{0+}\|^2$
			$\frac{3}{2}^-$	$(\frac{1}{2}^+, 2^-)$	E_{2-}	$\frac{1}{2}\|E_{2-}\|^2(5-3x^2)$
	$M1$	$(1^+, \frac{1}{2}^+)$	$\frac{1}{2}^+$	$(\frac{1}{2}^+, 1^+)$	M_{1-}	$\|M_{1-}\|^2$
			$\frac{3}{2}^+$	$(\frac{1}{2}^+, 1^+)$	M_{1+}	$\frac{1}{2}\|M_{1+}\|^2(5-3x^2)$
2	$E2$	$(2^+, \frac{1}{2}^+)$	$\frac{3}{2}^+$	$(\frac{1}{2}^+, 1^+)$	E_{1+}	$\frac{9}{2}\|E_{1+}\|^2(1+x^2)$
			$\frac{5}{2}^+$	$(\frac{1}{2}^+, 3^+)$	E_{3-}	$\frac{9}{2}\|E_{3-}\|^2(1+6x^2-5x^4)$
	$M2$	$(2^-, \frac{1}{2}^+)$	$\frac{3}{2}^-$	$(\frac{1}{2}^+, 2^-)$	M_{2-}	$\frac{9}{2}\|M_{2-}\|^2(1+x^2)$
			$\frac{5}{2}^-$	$(\frac{1}{2}^+, 2^-)$	M_{2+}	$\frac{9}{2}\|M_{2+}\|^2(1+6x^2-5x^4)$

Table 1.1: Lowest order multipole amplitudes for photoproduction of pseudo-scalar mesons. IS: initial state. ImS: intermediate state. FS: final state. M-Pole: multipole. The last column indicates the differential cross section in the center of momentum frame in terms of the CGLN-amplitudes, decomposed into multipole amplitudes, according to Equation (1.17), where $x = \cos\theta^*$.

For example, the $\Delta(1232)$ resonance with $J^P_{N^*} = \frac{3}{2}^+$ can be excited by $M1$ and $E2$ radiation. Its multipoles are denoted by M_{1+} and E_{1+}, respectively. The first index characterizes the orbital momentum of the meson ($l = L_{\pi^0} = 1$), the second one (+) indicates that the spin of the nucleon has to be added to l to yield the total angular momentum J_{N^*} of the intermediate state. In contrast to resonances with $J_{N^*} = \frac{1}{2}$, which can only be excited by one multipole (E_{0+} for negative parity states and M_{1-} for positive parity states), resonances with $J > \frac{1}{2}$ can be excited by one electric *and* one magnetic multipole. As also visible in the last column of Table 1.1, a pair of multipoles (E_{l+}, $M_{(l+1)-}$ and E_{l-}, $M_{(l-1)+}$) always have the same angular distribution, which is known as the *Minami ambiguity*.

1.2.3 CGLN Amplitudes

The general structure of the transition current for the production of a pion on a nucleon is ruled by Lorentz invariance. The hadron current operator J^μ, which has to be a pseudo-four-vector in order to ensure the negative parity of the pion, can be written as [16]:

$$\boldsymbol{J}_\mu = \left(A\tilde{\gamma}_\mu + B\tilde{P}_\mu + Ck_\mu\right)\gamma_5 + \left(D\tilde{\gamma}_\mu + E\tilde{P}_\mu + Fk_\mu\right)\gamma_5 \not{q} \ , \tag{1.14}$$

where $\tilde{a}^\mu = a^\mu - (a \cdot q/q^2)q^\mu$ is the explicitly gauge-invariant (transverse) vector representation of the four independent four-vectors (γ^μ, q^μ, k^μ and $p^\mu = \frac{1}{2}(p_i^\mu + p_f^\mu)$) of the kinematics, and A-F are the invariant amplitudes that depend on the three independent scalar quantities s, t, and Q^2. By evaluating Equation (1.14) between two-component Dirac spinors, one can give an equivalent form of Equation (1.14) in terms of Pauli matrices $\boldsymbol{\sigma}$ and the unit vectors $\hat{\boldsymbol{k}} = \hat{\boldsymbol{k}}_{CM}$ and $\hat{\boldsymbol{q}} = \hat{\boldsymbol{q}}_{CM}$ of the independent momenta in the center of mass system. This defines the structure functions F_i, also referred to as the CGLN-amplitudes [17]:

$$\begin{aligned} \boldsymbol{J} = \frac{4\pi W}{m}\big(& i\tilde{\boldsymbol{\sigma}}F_1 + (\boldsymbol{\sigma}\cdot\hat{\boldsymbol{k}})(\boldsymbol{\sigma}\times\hat{\boldsymbol{q}})F_2 + i\tilde{\boldsymbol{k}}(\boldsymbol{\sigma}\cdot\hat{\boldsymbol{q}})F_3 \\ & + i\tilde{\boldsymbol{k}}(\boldsymbol{\sigma}\cdot\hat{\boldsymbol{k}})F_4 + i\hat{\boldsymbol{q}}(\boldsymbol{\sigma}\cdot\hat{\boldsymbol{q}})F_5 + i\hat{\boldsymbol{q}}(\boldsymbol{\sigma}\cdot\hat{\boldsymbol{k}})F_6\big) \end{aligned} \tag{1.15}$$

$$\rho = \frac{4\pi W}{m}\big(i(\boldsymbol{\sigma}\cdot\hat{\boldsymbol{k}})F_7 + i(\boldsymbol{\sigma}\cdot\hat{\boldsymbol{q}})F_8\big) = \frac{\boldsymbol{q}\cdot\boldsymbol{J}}{\omega} \ ,$$

where $\tilde{\boldsymbol{\sigma}} = \boldsymbol{\sigma} - (\boldsymbol{\sigma}\cdot\hat{\boldsymbol{q}})\hat{\boldsymbol{q}}$ and $\tilde{\boldsymbol{k}} = \boldsymbol{k} - (\boldsymbol{k}\cdot\hat{\boldsymbol{q}})\hat{\boldsymbol{q}}$. These structure functions depend on three independent variables: the square of the four-momentum transfer Q^2 and on two of the Mandelstam variables (s, t, or alternatively the threshold laboratory energy ω_{Lab} and θ_π^{CM}). The structure functions F_1, F_2, F_3, and F_4 describe the transverse current, F_5 and F_6 describe the longitudinal component [16].
Gauge invariance assumes that the charge can be replaced by the longitudinal current or vice versa. The coincidence cross section for electroproduction can be expressed by the six structure functions $F_1, ..., F_6$ describing the transition current, whereas in the case of photoproduction only the four invariants $(F_1, ..., F_4)$ contribute. Hence,

in the following, the longitudinal components F_5 and F_6 will no longer be considered. Then, the differential cross section in the center of mass frame for an unpolarized target and an unpolarized photon beam can be written as [18]:

$$\begin{aligned}\frac{k^*}{q^*}\frac{d\sigma}{d\Omega} = &\left[|F_1|^2 + |F_2|^2 + \frac{1}{2}|F_3|^2 + \frac{1}{2}|F_4|^2 + Re(F_1F_3^*)\right] \\ &+ [Re(F_3F_4^*) - 2Re(F_1F_2^*)]\cos\theta^* \\ &- \left[\frac{1}{2}|F_3|^2 + \frac{1}{2}|F_4|^2 + Re(F_1F_4^*) + Re(F_2F_3^*)\right]\cos^2\theta^* \\ &- [Re(F_3F_4^*)]\cos^3\theta^* \ ,\end{aligned} \tag{1.16}$$

where q^* and k^* are the meson and photon cm momenta and θ^* is the polar angle of the meson in the cm system. Due to the strong interaction in the πN system, these structure functions have complex values. Thus, in general, there are six absolute values and five relative phases (four absolute values and three relative phases in case of photoproduction) which have to be determined in each kinematical situation. Because the number of independent structure functions depends on the spin degrees of freedom of the interacting particles, a complete determination of the structure functions requires additional measurements from the four $\mathcal{S}$-type experiments (the differential cross section $d\sigma/d\Omega$, the photon beam asymmetry Σ, the target asymmetry T, and the recoil nucleon polarization P) and in addition from the double-polarization experiments (out of the three groups: $\mathcal{BT}$ (beam-target), $\mathcal{BR}$ (beam-recoil), and $\mathcal{TR}$ (target-recoil)). The question of how many observables from which sets allow for a unique determination of the amplitudes, which would result in the *complete experiment*, is not trivial and will be discussed in Section 1.3.2. However, in general, it is not possible to do such an ideal experiment. As a result, the analysis of meson photoproduction depends on reaction models. Nevertheless, concerning the analysis close to production threshold, where only a few partial waves contribute, useful information can already be obtained by measuring the differential cross sections.

The structure functions F_i (see Equation (1.15)) can be decomposed into a multipole series in the form of derivatives of the Legendre polynomials $P_l = P_l(\cos(\Theta^*))$ [16]:

$$\begin{aligned}F_1(W,\theta^*) &= \sum_{l\geq 0}\{(lM_{l+} + E_{l+})P'_{l+1} + [(l+1)M_{l-} + E_{l-}]P'_{l-1}\} \\ F_2(W,\theta^*) &= \sum_{l\geq 1}\big[(l+1)M_{l+} + lM_{l-}\big]P'_l \\ F_3(W,\theta^*) &= \sum_{l\geq 1}\big[(E_{l+} - M_{l+})P''_{l+1} + (E_{l-} + M_{l-})P''_{l-1}\big] \\ F_4(W,\theta^*) &= \sum_{l\geq 2}(M_{l+} - E_{l+} - M_{l-} - E_{l-})P''_l \ .\end{aligned} \tag{1.17}$$

This points out the importance of the CGLN-amplitudes. As the angular distributions reflect the quantum numbers of the nucleon resonance, the CGLN amplitudes directly relate the measured angular distributions to the parity and angular momentum of the resonance. However, the extraction of the multipole amplitudes is not unique, since (due to the Minami ambiguity) the results exhibit a certain symmetry. This is visible in Table 1.1 where for example the excitation of the $\Delta(1232)3/2^+$ resonance with the M_{1+} multipole exhibits the typical $(5-3\cos\theta^*)$ shape of the differential cross section, but the same characteristic distribution would also result from a state with opposite parity and the excitation with a E_{2-} multipole. This ambiguity is obvious, as the differential cross sections depend on the combination of the spin of the resonance and the order of the multipole and not on the combination of the parities of the resonance and the multipole. The extraction of distinct resonance properties therefore requires the measurement of polarization observables.

1.2.4 Helicity Amplitudes

A different approach for the description of the transition matrix element can be realized with the information about the initial and final state helicity. It is convenient to work with helicity amplitudes, as the helicity of hadrons is conserved in the limit where quark masses or off-shell effects can be neglected. They are defined in the center of mass system when the initial and final spins are quantized along the directions of the incident photon momentum and the final pion momentum as depicted in Figure 1.12.

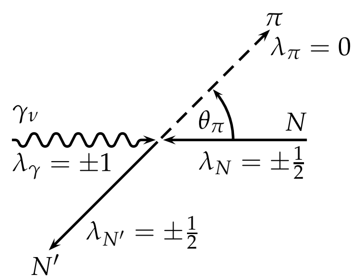

Figure 1.12: Helicities in single-pion photoproduction on a nucleon.

This results for the initial and final nucleon helicity in the values $\lambda_{N,N'} = \pm\frac{1}{2}$. As previously mentioned, the photon can be transverse ($\lambda_\gamma = \pm 1$) or longitudinal ($\lambda_\gamma = 0$). The total helicity of the initial state is then $\lambda = \lambda_\gamma - \lambda_N = \pm\frac{1}{2}, \pm\frac{3}{2}$. Since the pion has no spin, the final state helicity is $\lambda' = \lambda_\pi - \lambda_{N'} = -\lambda_{N'}$. The $2 \times 2 \times 3 = 12$ helicity amplitudes $A_{\lambda,\lambda'} = \langle \lambda_{N'} \mid J_{\lambda_\gamma} \mid \lambda_N \rangle$ are not independent, since the helicity amplitudes with $\lambda_\gamma = +1$ can be related to those with $\lambda_\gamma = -1$ by parity symmetry. Thus, there are 6 independent (complex) matrix elements remaining [15]:

$$\begin{aligned} H_i &= \langle \lambda_{N'} \mid J_{\lambda_\gamma} \mid \lambda_N \rangle \\ &= \big\{ \langle -\tfrac{1}{2} \mid J_{+1} \mid -\tfrac{1}{2} \rangle, \langle -\tfrac{1}{2} \mid J_{+1} \mid +\tfrac{1}{2} \rangle, \langle +\tfrac{1}{2} \mid J_{+1} \mid -\tfrac{1}{2} \rangle, \\ &\quad \langle +\tfrac{1}{2} \mid J_{+1} \mid +\tfrac{1}{2} \rangle, \langle +\tfrac{1}{2} \mid J_0 \mid +\tfrac{1}{2} \rangle, \langle -\tfrac{1}{2} \mid J_0 \mid +\tfrac{1}{2} \rangle \big\} \ , \end{aligned} \tag{1.18}$$

where the first four amplitudes apply for transverse and the latter two for longitudinal photons. By combining the helicities of the incoming nucleon and of the photon, the helicity of the excited state can be determined. The first and third term correspond to an overall helicity of $\lambda = \frac{1}{2}$ and the second and fourth term to helicity $\lambda = \frac{3}{2}$. The two longitudinal contributions have helicity $\lambda = \frac{1}{2}$, but they do not contribute to the photoproduction with real photons and will be omitted.

Using the following notation for the remaining four matrix elements:

$$\begin{aligned} H_1 &= H_{+1/2,+3/2} = +H_{-1/2,-3/2} \quad H_2 &= H_{+1/2,+1/2} = -H_{-1/2,-1/2} \\ H_3 &= H_{-1/2,+3/2} = -H_{+1/2,-3/2} \quad H_4 &= H_{+1/2,-1/2} = +H_{-1/2,+1/2} \;, \end{aligned} \tag{1.19}$$

the helicity amplitudes can be expanded in terms of derivatives of Legendre polynomials $P_l = P_l(\cos\theta^*)$ [18]:

$$\begin{aligned} H_1(\theta^*,\phi) &= \frac{1}{\sqrt{2}} e^{i\phi} \sin(\theta^*) \cos(\theta^*/2) \sum_{l\geq 1} \left(B_{l+} - B_{(l+1)-}\right) \left(P_l'' - P_{l+1}''\right) \\ H_2(\theta^*,\phi) &= \sqrt{2} \cos(\theta^*/2) \sum_{l\geq 0} \left(A_{l+} - A_{(l+1)-}\right) \left(P_l' - P_{l+1}'\right) \\ H_3(\theta^*,\phi) &= \frac{1}{\sqrt{2}} e^{2i\phi} \sin(\theta^*) \sin(\theta^*/2) \sum_{l\geq 1} \left(B_{l+} + B_{(l+1)-}\right) \left(P_l'' + P_{l+1}''\right) \\ H_4(\theta^*,\phi) &= \sqrt{2} e^{i\phi} \sin(\theta^*/2) \sum_{l\geq 0} \left(A_{l+} + A_{(l+1)-}\right) \left(P_l' + P_{l+1}'\right) \;, \end{aligned} \tag{1.20}$$

where the transverse partial wave helicity elements $A_{l\pm}$ and $B_{l\pm}$ correspond to transitions with nucleon-meson relative orbital angular momentum l, final state total angular momentum $J = l \pm \frac{1}{2}$, and γN initial state helicity $\frac{1}{2}$ for $A_{l\pm}$ and $\frac{3}{2}$ for $B_{l\pm}$. The relation between the helicity amplitudes and the CGLN amplitudes can be found in Ref. [18]. The helicity elements from the partial wave expansion are linear combinations of the electromagnetic multipoles [15]:

$$\begin{aligned} A_{l+} &= \frac{1}{2}\left[(l+2)E_{l+} + lM_{l+}\right] \\ B_{l+} &= E_{l+} - M_{l+} \\ A_{(l+1)-} &= \frac{1}{2}\left[-lE_{(l+1)-} + (l+2)M_{(l+1)-}\right] \\ B_{(l+1)-} &= E_{(l+1)-} + M_{(l+1)-} \;, \end{aligned} \tag{1.21}$$

which points out the advantage of the helicity amplitudes. Due to their connection to the electromagnetic couplings of the resonances $A_{1/2}$ and $A_{3/2}$ via:

$$\begin{aligned} A_{1/2} &= \sqrt{2\pi\alpha/k^*}\langle N^*, J_z = +1/2|J_{em}|N, S_z = -1/2\rangle \\ A_{3/2} &= \sqrt{2\pi\alpha/k^*}\langle N^*, J_z = +3/2|J_{em}|N, S_z = +1/2\rangle \;, \end{aligned} \tag{1.22}$$

the electromagnetic multipoles can be brought into relation with the electromagnetic couplings, according to [19]:

$$A_{1/2} = \mp(1/C_{Nm})\sqrt{(2J+1)\pi\frac{q^*}{k^*}\frac{M_R}{m_N}\frac{\Gamma_R^2}{\Gamma_m}}\ \mathrm{Im}\left\{A_{l\pm}(W=M_R)\right\} \tag{1.23}$$

$$A_{3/2} = \pm(1/C_{Nm})\sqrt{(2J+1)\pi\frac{q^*}{k^*}\frac{M_R}{m_N}\frac{\Gamma_R^2}{\Gamma_m}}\sqrt{(2J-1)(2J+3)/16}\ \mathrm{Im}\left\{B_{l\pm}(W=M_R)\right\}\ ,$$

where a Breit-Wigner shape was assumed for the resonances, J, M_R, and Γ_R are the total angular momentum, the mass and the width of the resonance, respectively, Γ_m is the partial width of the decay channel, and C_{Nm} is the Clebsch-Gordan coefficient for the decay of the resonance into the relevant $N\pi$ state. Equation (1.23) shows that for spin $J = 1/2$, the term $(2J-1)$ in Equation (1.23) vanishes. As a consequence, resonances with spin $J = 1/2$ have only a $A_{1/2}$ electromagnetic coupling, whereas resonances with $J \geq 3/2$ have $A_{1/2}$ and $A_{3/2}$ couplings.

1.2.5 Isospin Amplitudes

A very important aspect of meson photoproduction, the treatment of isospin, was not yet considered in the discussion. For photoproduction of mesons via the excitation of nucleon resonances, as depicted in Figure 1.8, the isospin is violated at the electromagnetic vertex and conserved at the hadronic vertex, such that the electromagnetic current contains isoscalar ($\Delta I = 0$) and isovector ($\Delta I = 0, \pm 1$) components. As a consequence, each multipole amplitude has to be reconstructed from the different isospin contributions.

The transition amplitude A for pion production in isospin space can be decomposed in terms of the Pauli isospin matrices $\tau_0 \equiv \tau_3$ and $\tau_\pm = \frac{1}{2}(\tau_1 \pm i\tau_2)$. The initial state is described by the target nucleon with isospin $I = \frac{1}{2}$. The nucleon couples to the electromagnetic current, which behaves like an isoscalar ($\Delta I = 0$) plus the third component of an isovector ($\Delta I = 0, \pm 1$), i.e. $J_\mu = J_\mu^S + J_\mu^V \tau_0$. In the final state, the pion is an isovector particle and is described by the field $\boldsymbol{\phi}$, where $\phi_\pm = \frac{1}{\sqrt{2}}(\phi_1 \pm i\phi_2)$ creates a $\pi^\pm$ and ϕ_0 creates a π^0. By assuming that isospin is conserved in the hadronic system, the interaction in isospin space has the form $\boldsymbol{\tau}\cdot\boldsymbol{\phi} = \tau_0\phi_0 + \sqrt{2}(\tau_+\phi_- + \tau_-\phi_+)$. One can then arrange the isospin content of the interaction of the nucleon with the photon and pion in a symmetrical form, to produce three independent combinations [15, 16]:

$$\begin{aligned} I^{(+)} &= \frac{1}{2}(\tau_\alpha\tau_0 + \tau_0\tau_\alpha) = \delta_{\alpha 0} \\ I^{(-)} &= \frac{1}{2}(\tau_\alpha\tau_0 - \tau_0\tau_\alpha) = -\alpha\tau_\alpha \\ I^{(0)} &= \tau_\alpha\ , \end{aligned} \tag{1.24}$$

where $\alpha = 0, \pm$ is the isospin index of the pion ($\alpha = \pm$ for the charged pions $\pi^\pm$, $\alpha = 0$ for the neutral pion π^0). In turn, one defines three isospin amplitudes $A^{(+)}$, $A^{(-)}$, and $A^{(0)}$ as follows: [15]

$$A = A^{(+)}\delta_{\alpha 0} + A^{(-)}(-\alpha)\tau_\alpha + A^{(0)}\tau_\alpha\ . \tag{1.25}$$

From this, the physical amplitudes are given by:

$$\begin{aligned}A(\gamma p \to n\pi^+) &= \sqrt{2}(A^{(0)} + A^{(-)})\\ A(\gamma n \to p\pi^-) &= \sqrt{2}(A^{(0)} - A^{(-)})\\ A(\gamma p \to p\pi^0) &= A^{(0)} + A^{(+)}\\ A(\gamma n \to n\pi^0) &= -A^{(0)} + A^{(+)} \ .\end{aligned} \tag{1.26}$$

The initial nucleon state is an eigenstate χ_μ of the total isospin with $I = \frac{1}{2}$ and third component $I_3 = \mu = \pm\frac{1}{2}$, while the final πN system has isospin eigenstates with $I = \frac{1}{2}, \frac{3}{2}$:

$$\mid I, I_3\rangle = \sum_{\mu,\nu} \langle \tfrac{1}{2} 1 \mu\nu \mid I I_3\rangle \chi_\mu \phi_\nu \ . \tag{1.27}$$

From Equation (1.27), the corresponding isospin states are given in Table 1.2:

I	I_3	Eigenstate
$\frac{1}{2}$	$+\frac{1}{2}$	$\frac{1}{\sqrt{3}} \mid p\pi^0\rangle - \frac{\sqrt{2}}{\sqrt{3}} \mid n\pi^+\rangle$
	$-\frac{1}{2}$	$\frac{\sqrt{2}}{\sqrt{3}} \mid p\pi^-\rangle - \frac{1}{\sqrt{3}} \mid n\pi^0\rangle$
$\frac{3}{2}$	$+\frac{3}{2}$	$\mid p\pi^+\rangle$
	$+\frac{1}{2}$	$\frac{\sqrt{2}}{\sqrt{3}} \mid p\pi^0\rangle + \frac{1}{\sqrt{3}} \mid n\pi^+\rangle$
	$-\frac{1}{2}$	$\frac{1}{\sqrt{3}} \mid p\pi^-\rangle + \frac{\sqrt{2}}{\sqrt{3}} \mid n\pi^0\rangle$
	$-\frac{3}{2}$	$\mid n\pi^-\rangle$

Table 1.2: Isospin states of the πN system.

The isoscalar amplitude $A^{(0)}$ always results in a final state with isospin $I = \frac{1}{2}$. The isovector transition amplitudes $A^{(\pm)}$ can be expressed in terms of the amplitudes $A^{(2I)}$, where $I = \frac{1}{2}, \frac{3}{2}$ indicates the final isospin states, as:

$$\begin{aligned}A^{(1)} &= A^{(+)} + 2A^{(-)}\\ A^{(3)} &= A^{(+)} - A^{(-)} \ .\end{aligned} \tag{1.28}$$

Then the multipole amplitudes of the four possible photoproduction reactions (Equation (1.26)) can be expressed in terms of these isospin amplitudes as:

$$\begin{aligned}A(\gamma p \to n\pi^+) &= \sqrt{2}(A^{(0)} + \tfrac{1}{3}A^{(1)} - \tfrac{1}{3}A^{(3)})\\ A(\gamma p \to p\pi^0) &= A^{(0)} + \tfrac{1}{3}A^{(1)} + \tfrac{2}{3}A^{(3)}\\ A(\gamma n \to p\pi^-) &= \sqrt{2}(A^{(0)} - \tfrac{1}{3}A^{(1)} + \tfrac{1}{3}A^{(3)})\\ A(\gamma n \to n\pi^0) &= -A^{(0)} + \tfrac{1}{3}A^{(1)} + \tfrac{2}{3}A^{(3)} \ .\end{aligned} \tag{1.29}$$

In literature, the isospin amplitudes (Equation (1.29)) are often expressed in terms of the three independent matrix elements: *isoscalar* $A^{IS} = \langle \frac{1}{2}, \pm\frac{1}{2}|\hat{S}|\frac{1}{2}, \pm\frac{1}{2}\rangle$, *isovector* $A^{IV} = \langle \frac{1}{2}, \pm\frac{1}{2}|\hat{V}|\frac{1}{2}, \pm\frac{1}{2}\rangle$, and *isospin changing* $A^{V3} = \langle \frac{3}{2}, \pm\frac{1}{2}|\hat{V}|\frac{3}{2}, \pm\frac{1}{2}\rangle$, in the notation $\langle I_f, I_{f3}|\hat{A}|I_i, I_{i3}\rangle$ [20]:

$$\begin{aligned} A(\gamma p \to n\pi^+) &= -\sqrt{\frac{1}{3}}A^{V3} + \sqrt{\frac{2}{3}}(A^{IV} - A^{IS}) \\ A(\gamma p \to p\pi^0) &= +\sqrt{\frac{2}{3}}A^{V3} + \sqrt{\frac{1}{3}}(A^{IV} - A^{IS}) \\ A(\gamma n \to p\pi^-) &= +\sqrt{\frac{1}{3}}A^{V3} - \sqrt{\frac{2}{3}}(A^{IV} + A^{IS}) \\ A(\gamma n \to n\pi^0) &= +\sqrt{\frac{2}{3}}A^{V3} + \sqrt{\frac{1}{3}}(A^{IV} + A^{IS}) \ , \end{aligned} \tag{1.30}$$

where $A^0 = -\sqrt{1/3} \cdot A^{IS}$, $A^1 = \sqrt{3} \cdot A^{IV}$ and $A^3 = \sqrt{3/2} \cdot A^{V3}$ were used.

The treatment of isospin shows up to be a complication of meson photoproduction. Photoproduction from isovector mesons, such as the π^0 meson, depends on all three isospin amplitudes. However, the situation is different for N^*- and Δ-states, which follows directly from Equation (1.30). Δ-resonances only involve the isospin changing amplitudes A^{V3}, which results in an identical contribution for protons and neutrons. On the other hand, N^* resonances depend on isoscalar A^{IS} and A^{IV} amplitudes, such that the electromagnetic couplings for protons and neutrons in general are different. In contrast, for isoscalar mesons, such as the η meson, only the A^{IS} and A^{IV} amplitudes contribute. Nevertheless, the characterization of the photoproduction amplitudes for both reactions requires measurements off the neutron, which follows from Equation (1.29) or (1.30). This means that one has to rely on meson photoproduction from light nuclei, which in addition introduces uncertainties due to nuclear effects, such as Fermi motion, rescattering processes, and final state interactions (FSI). The cross section on the neutron then has to be extracted from the measurement of photoproduction from bound nucleons in quasi-free kinematics (see Section 1.2.1). In this case, the meson is produced on the participant nucleon, which is knocked out of the nucleus afterwards, whereas the other nucleons act as spectators. This singles out the deuteron as a remarkably important target nucleus. Due to its small binding energy and the relatively well understood nuclear structure the investigation of the nuclear effects is less complicated as it is the case with more complex nuclei.

1.3 Single and Double Polarization Observables

As discussed in Section 1.2, profound knowledge about the nucleon excitation spectrum is essential for the understanding of the underlying strong interaction. However, theoretical predictions for the excitation spectrum are not straightforward, since the relevant energy range of a few GeV is too low for a sufficiently accurate perturbative treatment of QCD and too high for reliable predictions from lattice gauge calculations or chiral perturbative approaches. Therefore, one has to rely on phenomenological approaches from quark models. As a consequence, the results of the different methods are not consistent among each other and also in very poor agreement with the experimental observations, which is known as the problem of missing resonances. It is not known whether the discrepancy is due to wrong considerations in the models or rather due to experimental bias in the data. Whereas there are several promising developments from the theory side, a lot of experimental effort using photon-induced meson production aims for the discovery of the missing resonances. However, the nucleon resonances are broad and overlapping, such that the extraction of the corresponding quantum numbers is not straightforward. The differential cross sections are related to four CGLN amplitudes, which can be expressed in Cartesian (F_i), spherical or helicity (H_i), or transversity (b_i, not discussed, see e.g. Ref. [21] for information) representations from which the electromagnetic multipoles can be extracted under the proper consideration of the isospin amplitudes. Nevertheless, a multipole decomposition of the differential cross sections, especially for energies above the reaction threshold, does not yield unambiguous results, such that the measurement of more observables, i.e. single and double polarization observables, is necessary.

1.3.1 The General Cross Section

In contrast to experiments with unpolarized beam and target from which the unpolarized cross section σ_0 can be extracted, experiments with polarized beam and/or target allow for the additional extraction of single and double polarization observables. As briefly mentioned in Section 1.2.3, these can be divided into groups of single polarization observables ($\mathcal{S}$-type experiments) or double polarization observables ($\mathcal{BT}$- (beam-target), $\mathcal{BR}$- (beam-recoil) and $\mathcal{TR}$- (target-recoil) type experiments).

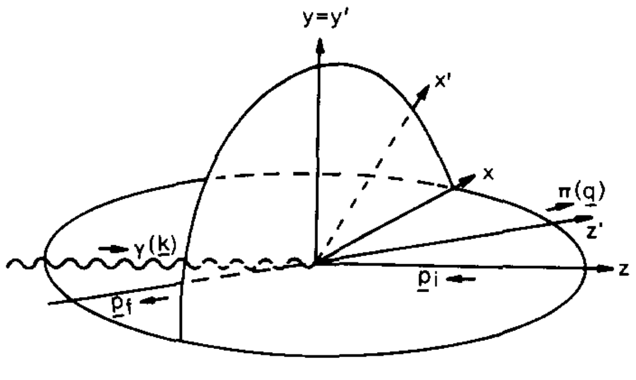

Figure 1.13: The coordinate system used for the definition of the polarization observables from Equation (1.35). The axis are defined with respect to the momentum of the incoming photon $\vec{k}$ and the momentum of the outgoing meson $\vec{q}$: $\vec{x} = \vec{y} \times \vec{z}$, $\vec{x}' = \vec{y} \times \vec{z}'$, $\vec{y} = \vec{k} \times \vec{q}/|\vec{k} \times \vec{q}|$, $\vec{y}' = \vec{y}$, $\vec{z} = \vec{k}/|\vec{k}|$, $\vec{z}' = \vec{q}/|\vec{q}|$.

Whereas photon beams are either circularly or linearly polarized (elliptically polarized photons have contributions of both), the target and the recoil nucleon can be polarized in any of the three orthogonal directions (x, y, or z). Therefore, in addition to the unpolarized cross section and the three single polarization observables, 18 different double polarization observables can be measured, from which, due to symmetry reasons in the xy-direction, only 12 are relevant. The 16 possible observables (labeled in red) are presented in Table 1.3. However, the single polarization observables can also be measured with double-polarization (labeled in green) and the double polarization observables with triple polarization (labeled in blue).

The most general form of the cross section, including all 32 observables, is given in Equation (1.35) [22]. Thereby the observables $\hat{A}$ denote profile functions and not observables (i.e. not the observable itself, but the product of observable and cross section $\hat{A} = A \cdot d\sigma_0$), since this form is most simply determined by the CGLN amplitudes. $\vec{P}^T$ and $\vec{P}^R$ denote the target and recoil polarization vector according to the coordinate system introduced in Figure 1.13, $\vec{P}_c^\gamma$ ($\vec{P}_L^\gamma$) is the polarization vector of the circularly (linearly) polarized photon, and ϕ is the angle of the transverse polarization with respect to the reaction plane.
The experiments that have been carried out in this work used a circularly polarized photon beam of polarization P_c^γ and a longitudinally polarized target of polarization P_z^T (the direction of polarization is the direction of the beam, i.e. the z-direction) with the aim to extract the double polarization observable E. As the recoil polarization was not measured and the amount of linear beam and transverse target polarization is assumed to be negligible, the expression for the general cross section in this case is reduced to

$$d\sigma(P_c^\gamma, P_z^T) = \frac{1}{2} d\sigma_0 \left[1 - E p_c^\gamma p_z^T\right] \ . \tag{1.31}$$

The double polarization observable E is defined as the asymmetry between the helicity dependent cross sections $\sigma_{1/2}$ and $\sigma_{3/2}$:

$$E = \frac{\sigma_{1/2} - \sigma_{3/2}}{\sigma_{1/2} + \sigma_{3/2}} \tag{1.32}$$

where the index 1/2 denotes the antiparallel, and 3/2 the parallel configuration of photon and nucleon spin. In order to determine the properties of the contributing nucleon resonances, the corresponding amplitudes have to be extracted from the double polarization observable E. For this purpose, the double polarization observable E can be expressed in terms of the CGLN amplitudes as follows [22]:

$$\hat{E} = +\mathrm{Re}\left\{F_1^* F_1 + F_2^* F_2 - 2\cos\theta^* F_1^* F_2 + \sin^2\theta^* (F_2^* F_3 + F_1^* F_4)\right\} \rho_0 \ , \tag{1.33}$$

and in terms of the helicity amplitudes H_i according to [23]:

$$\hat{E} = \frac{1}{2}\left\{|H_2|^2 + |H_4|^2 - |H_1|^2 - |H_3|^2\right\} \rho_0 \ , \tag{1.34}$$

where $\rho_0 = q/k$ is the phase space factor.

Beam (P^γ)		Target (P^T)			Recoil (P^R)			Target (P^T) + Recoil (P^R)								
					x'	y'	z'	x'	x'	x'	y'	y'	y'	z'	z'	z'
		x	y	z				x	y	z	x	y	z	x	y	z
unpol.	$d\sigma_0$		$\hat{T}$			$\hat{P}$		$\hat{T}_{x'}$		$\hat{L}_{x'}$		$\hat{\Sigma}$		$\hat{T}_{z'}$		$\hat{L}_{z'}$
$P_L^\gamma \sin(2\phi_\gamma)$		$\hat{H}$		$\hat{G}$	$\hat{O}_{x'}$		$\hat{O}_{z'}$		$\hat{C}_{z'}$		$\hat{E}$		$\hat{F}$		$-\hat{C}_{x'}$	
$P_L^\gamma \cos(2\phi_\gamma)$	$-\hat{\Sigma}$		$-\hat{P}$			$-\hat{T}$		$-\hat{L}_{z'}$		$\hat{T}_{z'}$		$-d\sigma_0$		$\hat{L}_{x'}$		$-\hat{T}_{x'}$
P_γ^c		$\hat{F}$		$-\hat{E}$	$\hat{C}_{x'}$		$\hat{C}_{z'}$		$-\hat{O}_{z'}$		$\hat{G}$		$-\hat{H}$		$\hat{O}_{x'}$	

Table 1.3: Polarization observables in pseudoscalar meson photoproduction. All observables occurs twice in the table. Red: observables of leading polarization dependence in the general cross section (see Equation (1.35)). Green: nominal *single polarization* observables that can also be measured with double polarization. Blue: unpolarized cross section and 12 nominal *double polarization* observables that can also be measured with triple polarization.

$$
\begin{aligned}
d\sigma^{B,T,R}(\vec{P}_\gamma, \vec{P}_T, \vec{P}_R) = \frac{1}{2} \Big\{ & d\sigma_0 \left[1 - P_L^\gamma P_y^T P_{y'}^R \cos(2\phi_\gamma)\right] \\
& + \hat{\Sigma} \left[-P_L^\gamma \cos(2\phi_\gamma) + P_y^T P_{y'}^R\right] \\
& + \hat{T} \left[P_y^T - P_L^\gamma P_{y'}^R \cos(2\phi_\gamma)\right] \\
& + \hat{P} \left[P_{y'}^R - P_L^\gamma P_y^T \cos(2\phi_\gamma)\right] \\
& + \hat{E} \left[-P_c^\gamma P_z^T + P_L^\gamma P_x^T P_{y'}^R \sin(2\phi_\gamma)\right] \\
& + \hat{G} \left[P_L^\gamma P_z^T \sin(2\phi_\gamma) + P_c^\gamma P_x^T P_{y'}^R\right] \\
& + \hat{F} \left[P_c^\gamma P_x^T + P_L^\gamma P_z^T P_{y'}^R \sin(2\phi_\gamma)\right] \\
& + \hat{H} \left[P_L^\gamma P_x^T \sin(2\phi_\gamma) - P_c^\gamma P_z^T P_{y'}^R\right] \\
& + \hat{C}_{x'} \left[P_c^\gamma P_{x'}^R - P_L^\gamma P_y^T P_{z'}^R \sin(2\phi_\gamma)\right] \\
& + \hat{C}_{z'} \left[P_c^\gamma P_{z'}^R + P_L^\gamma P_y^T P_{x'}^R \sin(2\phi_\gamma)\right] \\
& + \hat{O}_{x'} \left[P_L^\gamma P_{x'}^R \sin(2\phi_\gamma) + P_c^\gamma P_y^T P_{z'}^R\right] \\
& + \hat{O}_{z'} \left[P_L^\gamma P_{z'}^R \sin(2\phi_\gamma) - P_c^\gamma P_y^T P_{x'}^R\right] \\
& + \hat{L}_{x'} \left[P_z^T P_{x'}^R + P_L^\gamma P_x^T P_{z'}^R \cos(2\phi_\gamma)\right] \\
& + \hat{L}_{z'} \left[P_z^T P_{z'}^R + P_L^\gamma P_x^T P_{x'}^R \cos(2\phi_\gamma)\right] \\
& + \hat{T}_{x'} \left[P_x^T P_{x'}^R - P_L^\gamma P_z^T P_{z'}^R \cos(2\phi_\gamma)\right] \\
& + \hat{T}_{z'} \left[P_x^T P_{z'}^R - P_L^\gamma P_z^T P_{x'}^R \cos(2\phi_\gamma)\right] \Big\}
\end{aligned}
\tag{1.35}
$$

1.3.2 The Complete Experiment

From Equation (1.35), it can be seen that the general cross section depends on 16 observables, of which one is the unpolarized cross section, three are single polarization observables, and 12 are double polarization observables. However, the cross section in this way is overdetermined and as mentioned in Section 1.2.3, knowledge of the four complex functions F_i and three of the four phases (the overall phase is arbitrary) is sufficient for an unambiguous determination of the cross section. Therefore, seven independent real values as a function of two kinematical variables (W and θ^* for example) have to be measured. The question of which set of observables allows for an unambiguous determination of the amplitudes (*the complete experiment*) is not trivial and was, and is still considered controversial.
In 1975 Barker, Donnachie, and Storrow [21] showed that the four $\mathcal{S}$-type experiments and five double polarization observables (at least one of each $\mathcal{BT}, \mathcal{BR}, \mathcal{TR}$-type) allow for an unambiguous determination of all amplitudes. This is referred to as the *BDS-rule* and implies that in total nine of 16 observables have to be measured. In 1996, Keaton and Workman [24] stated that the BDS-rule is not sufficient for a distinct extraction of the amplitudes, as certain combinations of double polarization observables do not eliminate all discrete ambiguities. However, Chiang and Tabakin [25] showed in 1997 that in addition to the four $\mathcal{S}$-type experiments, knowledge of already four carefully chosen double polarization observables are sufficient for an unambiguous identification of the amplitudes. As a consequence, the complete experiment requires the measurement of at least eight observables. Very recently, Wunderlich and coworkers [26] showed that a complete measurement in a truncated partial-wave analysis (TPWA) with maximum angular momentum $l_{\max} = 4$ is possible with only five measurements, i.e. the four $\mathcal{S}$-type and the double polarization observable F, G or any other from the recoil observable groups $\mathcal{BR} and \mathcal{TR}$.
However, depending on the incident photon energy and especially at threshold, where only a few partial waves contribute, the knowledge of a few observables may already provide sufficient information for the extraction of the resonance contributions.

1.4 Previous Results on Single and Double π^0 Photoproduction

Among the different final states in photoproduction experiments, single and double π^0 always played a special role. Single pion photoproduction was widely used to study the properties of the first excited state of the nucleon, the $\Delta(1232)3/2^+$ resonance. The Δ-resonance is the best known excited state of the nucleon and has been studied with many different reactions on the free proton and on bound nucleons. Thereby neutral pion photoproduction has the advantage that non-resonant background terms (Kroll-Ruderman and pion pole terms, see diagrams (c) and (d) in Figure 1.8) are suppressed, since the photon couples only weakly to neutral mesons. This is especially beneficial, as only the Δ-resonance contributes significantly to the first resonance region of the nucleon excitation spectrum.

In the higher energy range of the nucleon, more and more higher lying excited states contribute to the nucleon excitation spectrum. These states decay via intermediate resonances and the subsequent emission of mesons to the ground state and hence can only be measured in multiple meson photoproduction. Even though the reaction cross section of double π^0 photoproduction in the second and third resonance region is smaller than for the mixed-charge and double-charge pion pairs, it is still sizable. Furthermore, as for single π^0 photoproduction, the non-resonant background in the neutral channel is suppressed. In addition, in contrast to the other isospin channels, the production of ρ-mesons does not contribute to the final state, as the ρ^0-meson only decays into $\pi^+\pi^-$ and not into $\pi^0\pi^0$. This makes the $\pi^0\pi^0$ ideally suited for the investigation of sequential decays of s-channel resonances.

In contrast to the reactions on the proton, data on the neutron is sparse. This work presents the first time measurement of unpolarized and helicity dependent differential and total cross sections from single and double π^0 photoproduction from the neutron.
In the following sections, the results of the single and double polarization observables from previous works measurements of single and double π^0 photoproduction will be briefly summarized.

1.4.1 Status of Single π^0 Photoproduction

Most of the previous experiments for single π^0 photoproduction focused on the extraction of angular distributions for the reaction on the free proton [27–33] and abundant data is available for the full angular range from threshold up to photon energies of $E_\gamma = 3$ GeV. In the last years, the first results from the single polarization observable Σ [28, 34] and the double polarization observables G [34] (linearly polarized beam, longitudinally polarized target), E [35] (circularly polarized beam, longitudinally polarized target) and $C_{x'}$ [36] (circularly polarized beam, recoil nucleon polarization) were reported.
The results are summarized in Figure 1.14 and are compared to the predictions from the MAID, SAID, and BnGa partial wave analyses. Overall, the models are in good agreement with the data, but significant differences between the different solutions are visible. On the first sight this is astonishing, as all models predict the same total cross section, as illustrated in the upper right insert of Figure 1.15. This points out the significant impact of the data on the theoretical models and demonstrates that the knowledge of several observables is necessary for an appropriate extraction of the resonance properties. The polarization data confirmed the dominant contribution of the $N(1535)1/2^-$ and the $N(1520)3/2^-$ resonances in the second resonance region and of the $N(1680)5/2^+$ resonance in the third resonance region. However, different strengths of the $N(1440)1/2^+$, the $N(1535)1/2^-$, and the $N(1520)3/2^-$ resonances (all rated with four stars in the RPP [37]) and a significant contribution of the $N(1700)3/2^-$ were reported.

As discussed in Section 1.2.5, the isospin decomposition of pion photoproduction

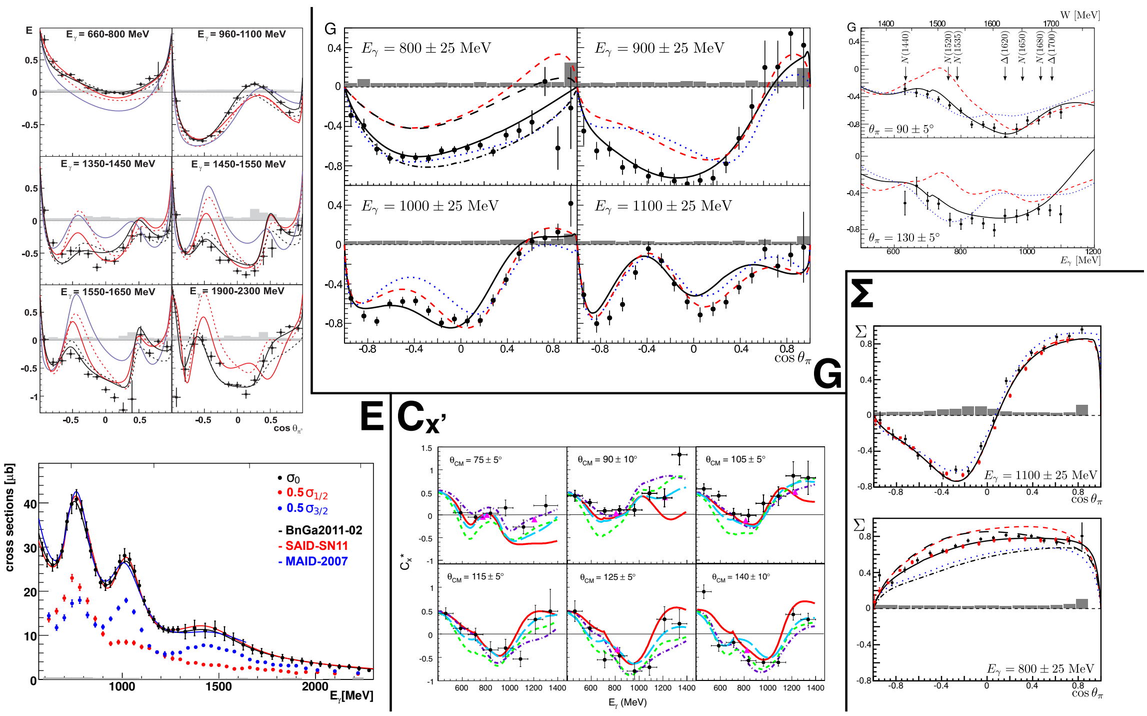

Figure 1.14: Previous measured polarization observables for single π^0 photoproduction from the free proton [34–36]. Observable Σ: black dots: [34]. Red dots: [28]. Solid (black curve): BnGa [38]. Dashed (red): SAID [39]. Long-dashed (black): BnGa with E_{0+} and E_{2-} from SAID. Dotted (blue): MAID [40]. Observable G: notation as for Σ. Observable E: Solid black: refit of BnGa [38]. Dashed black: BnGa [38]. Solid blue: MAID [40]. Solid red: SAID CM12 [39]. Dashed red: SAID SN12 [41]. Observable $C_{x'}$: black circles: [36]. Magenta triangles: [42]. Long-dashed (cyan): SAID CM12 [39]. Short-dashed (green): [41]. Solid red line: BnGa [38]. Dash-dotted violet: MAID [40].

requires additional measurements of the reaction on the neutron. Due to the absence of free neutron targets, this has to be realized with quasi-free neutrons bound in light nuclei, mostly the deuteron. However, this is accompanied by two complications: in contrast to protons, the detection efficiency and energy resolution of neutrons are rather low. Furthermore, the results are affected by nuclear effects, such as Fermi motion, re-scattering, and FSI, which has to be properly considered in the interpretation of the results. As a consequence, the different formalisms and results are strongly model dependent. This is illustrated by the bottom insert in Figure 1.15. It shows the available differential cross section data for single pion photoproduction from the nucleon from the four different isospin channels (see Equation (1.30)). Whereas abundant data is available for the reactions on the proton ($\gamma p \to p\pi^0$ or $\gamma p \to n\pi^+$), fewer results for the $n\pi^+$ final state and only a few scattered points for the $n\pi^0$ final state have been measured. This is a direct consequence of the difficulties that arise from experiments that involve neutrons. In contrast to $\gamma n \to n\pi^0$, the final state of $\gamma n \to p\pi^-$ does not rely on the detection of any neutral particles and

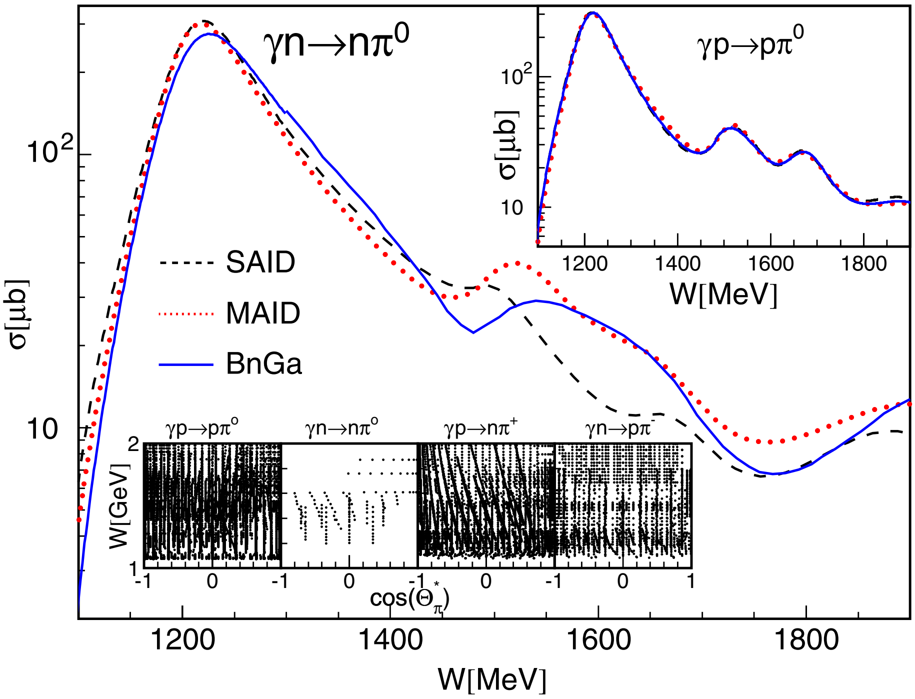

Figure 1.15: Predicted total cross sections for single π^0 photoproduction from protons (upper right insert) and neutrons (main plot). Shown are the solutions from MAID [40], SAID [39], and BnGa (neutron: [38], proton: [43]). Insert at bottom: previously available database [39]. Each point represents one measurement at W and $\cos(\theta^*_{\pi^0})$.

hence is less problematic. The few data points from $\gamma n \rightarrow n\pi^0$ were measured in the 1970s [44, 45] and are of poor quality, since the background from $2\pi^0$ photoproduction could not be eliminated. The only reasonable data from this reaction results from the measurement of the beam asymmetry at GRAAL in 2009 [46], but angular distributions were not determined.
However, theoretically, the measurement of three of the four isospin channels is sufficient for a complete determination of the isospin structure of the amplitudes (see Equation (1.30)) and it could be assumed that the measurement of the neutral channel $\gamma n \rightarrow n\pi^0$ is redundant. In reality, knowledge of the $n\pi^0$ final state is essential, as the measurement of the charged channels do not only contain contributions from resonances, but also from the previously mentioned non-resonant background. Therefore, the results from these channels are affected by contributions from background terms, e.g. Kroll-Ruderman, pion-poles, diffractive t-channel, and others, that all have to be properly considered in the analysis and contribute differently to the individual isospin channels.

The importance of the neutral $n\pi^0$ final state is illustrated in Figure 1.16 on the example of pion photoproduction in the Δ-resonance region (no data for the $n\pi^0$ channel is available). Shown are the total cross sections for the four different isospin channels. As previously mentioned, only the $\Delta(1232)3/2^+$ resonance contributes

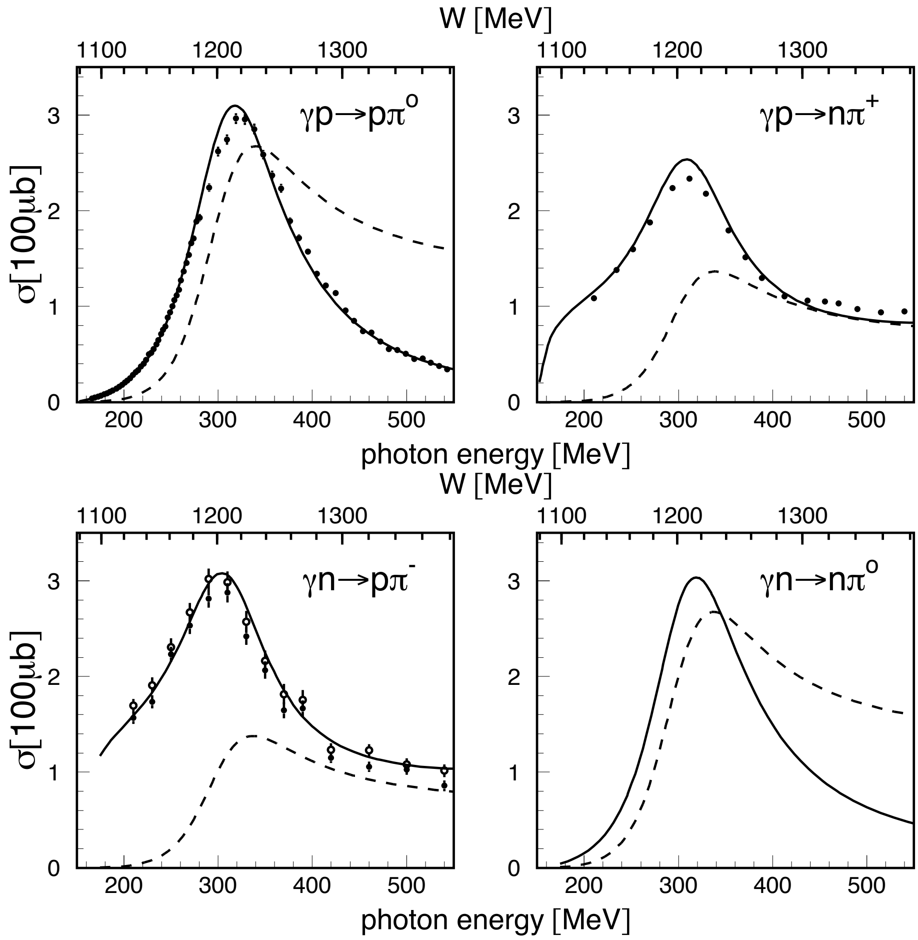

Figure 1.16: Total cross sections for single π^0 photoproduction for the four different isospin channels. Top left: $\gamma p \to p\pi^0$. Top right: $\gamma p \to n\pi^+$. Bottom left: $\gamma n \to p\pi^-$. Bottom right: $\gamma n \to n\pi^0$. Solid line: MAID [40]. Dashed line: MAID [40], only $\Delta(1232)3/2^+$ resonance.

significantly to the nucleon excitation spectrum in this energy range. If contributions from the non-resonant background are neglected, only the isospin changing matrix element A^{V3} contributes to the isospin amplitudes in Equation (1.30), and the cross sections are related by:

$$\sigma(\gamma p \to p\pi^0) = \sigma(\gamma n \to n\pi^0) = 2\sigma(\gamma p \to n\pi^+) = 2\sigma(\gamma n \to p\pi^-) \ . \tag{1.36}$$

However, this is only fulfilled by the dashed model curves (MAID [40], only contributions from the $\Delta(1232)3/2^+$ resonance). Due to the presence of the non-resonant background, which is mainly present in the charged channels, the measured data show a completely different behavior. Therefore, already in this rather simple case where only one resonance contributes, additional information from the $n\pi^0$ final state is essential for an appropriate extraction of the resonance properties. For higher energies where several (and also N^*) resonances contribute, knowledge of the reaction $\gamma n \to n\pi^0$ is inevitable.

1.4.2 Status of Double π^0 Photoproduction

Double π^0 photoproduction from the free proton from threshold up to the second resonance region was intensively studied with the DAPHNE [47, 48], TAPS [49–51], and Crystal Ball/TAPS [52–54] detectors at MAMI. The latter setup was also used for measurements up to the third energy region [55, 56], for which additional results were obtained from the GRAAL experiment [57] and with the Crystal Barrel/TAPS detectors at ELSA [51, 58–61]. Total cross sections and invariant mass distributions were used to extract the resonance contributions from the different sequential decays via intermediate N^*- and Δ^*-resonances.

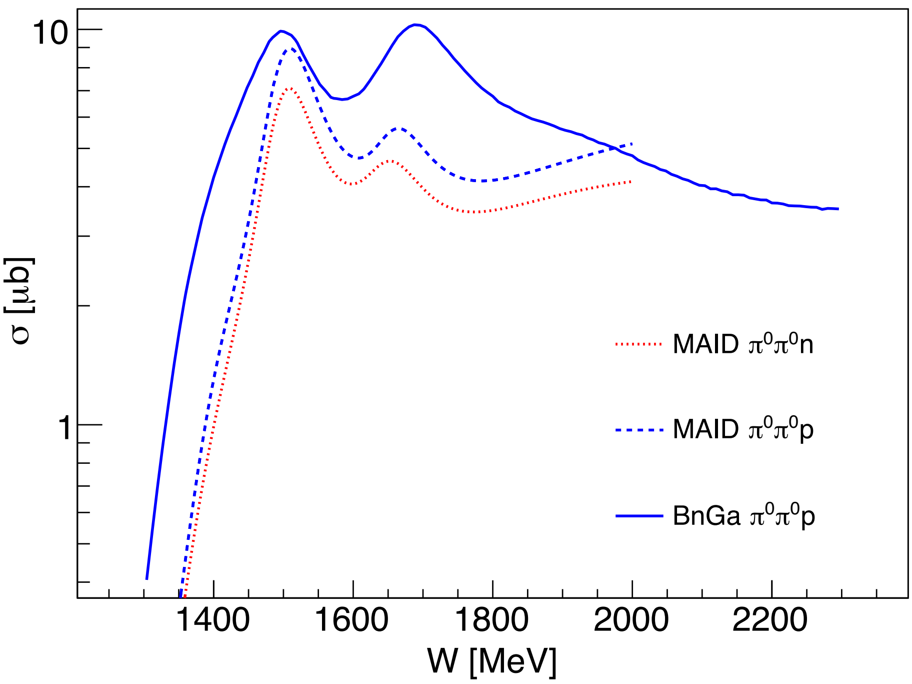

Figure 1.17: Predicted total cross sections for double π^0 photoproduction from protons and neutrons. Shown are the solutions from MAID [62] and BnGa (only proton: [43]).

The total cross section exhibits the typical double-hump structure, which correspond to the second and third resonance region of the proton, as can be seen by the solution from the BnGa coupled-channel partial wave analysis [43] (solid blue line) in Figure 1.17. The solution from this model currently achieves the best agreement with the most recent results, which is not surprising, since the result is obtained from a fit of the model to all of the available data. The comparison with the other model predictions from the MAID [62] solution demonstrates the huge demand for additional observables. Significant discrepancies between the two calculations are visible, which indicates that substantial contributions are missing in this model, mostly in the third resonance region. However, analyses in the frameworks of other models [63–66] also revealed discrepancies, even close to threshold, where only a few resonances con-

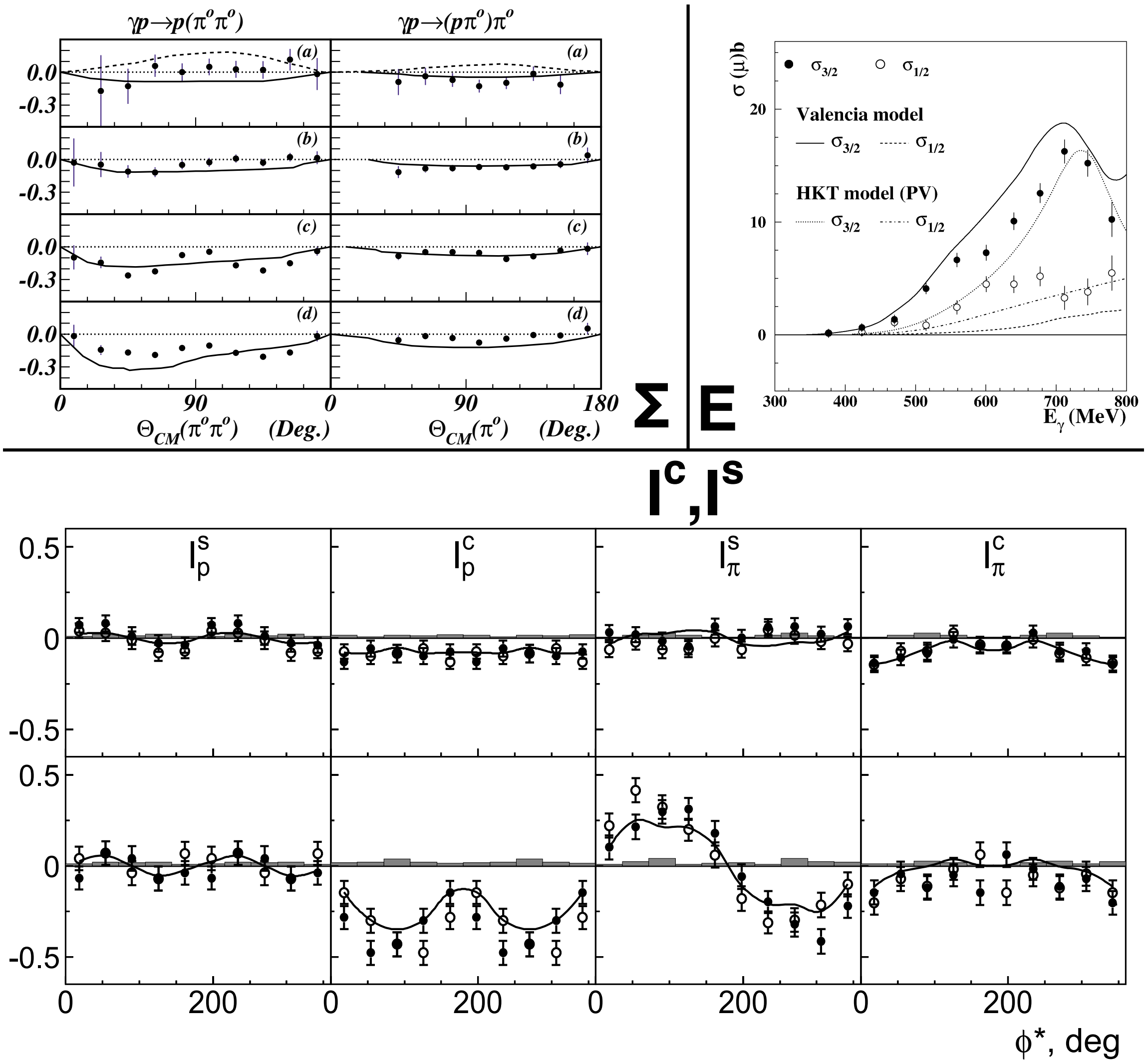

Figure 1.18: Previous measured polarization observables for double π^0 photoproduction from the free proton [48, 57, 60]. Observable *Sigma* [57]: solid lines: Laget model [63]. Dashed lines: Valencia model [64–66]. Observable E [48]: shown are the helicity dependent cross sections $\sigma_{1/2}$ (open circles) and $\sigma_{3/2}$ (filled circles). Solid and dashed lines: Valencia model [64–66]. Dotted and dashed-dotted lines: HKT model (PV) [67]. Observables I^s and I^c [60]: upper row: results for the $\Delta(1232)3/2^+$ region. Lower row: results for the $N(1520)3/2^-$ region. Open circles: mirror points of solid circles. Solid lines: BnGa PWA fit.

tribute. The main difference between the different calculations are the contributions of the sequential decays via intermediate resonances. Whereas the model by Murphy and Laget [63] (compared to the total cross section and beam asymmetry Σ (see top left figure in Figure 1.18) from the GRAAL data in Ref. [57]) assumes significant contributions from the decay of the Roper resonance $N(1440)1/2^- \rightarrow N\sigma$ (where $N\sigma$ corresponds to the $N(\pi^0\pi^0)_S$ state with the two pions in a relative s-wave), the

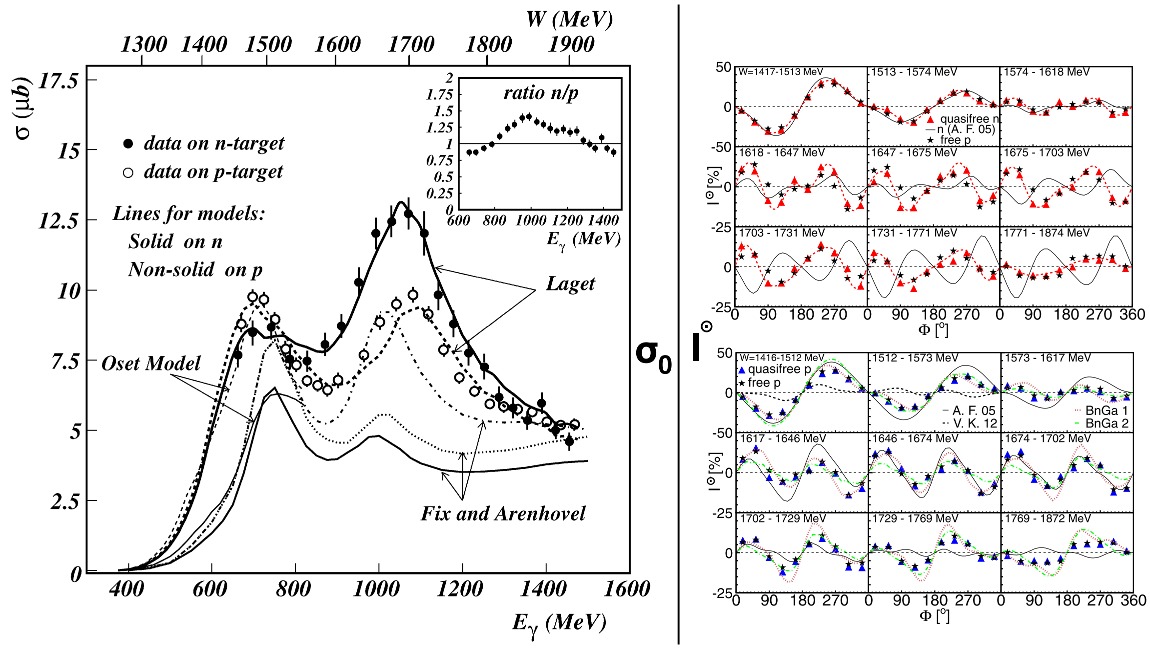

Figure 1.19: Previous measured observables for double π^0 photoproduction from quasi-free protons and neutrons [56, 68]. Unpolarized cross sections σ_0 [68]: model curves: notations are given in the figure (Laget model [63], Oset model [64, 65], Fix and Arenhövel [62]). The dashed-dotted curve from Fix and Arenhövel corresponds to the dotted curve with an inverse sign of the $F_{15}\pi\Delta$ coupling. Observable $I^{\odot}$: notations are given in the figure. Model curves from: A.F. 05 [62], V.K. 12 [55], BnGa 1/2 [38].

MAID [62] and Valencia model [64–66] proposed a significant contribution from the decay of the $N(1520)3/2^-$ resonance via an intermediate $\Delta(1232)3/2^+\pi^0$ state. In 2003, the measurement of the helicity dependent cross sections $\sigma_{1/2}$ and $\sigma_{3/2}$ (see top right figure in Figure 1.18) excluded a possible dominance of the $N\sigma$ state, since $\sigma_{1/2}$ is much smaller in the second resonance region.

Another discrepancy between the models was the almost complete absence of contributions of the $\Delta(1700)3/2^-$ resonance in the second region, from which in contrast a substantial contribution was predicted by the BnGa result [51, 59]. They observed a strong interference of this resonance with the $N(1520)3/2^-$ state. In 2012, Kashevarov et al. [55] obtained significant contributions from resonances with spin $J = 3/2$ for energies below the excitation of the $N(1520)3/2^-$ resonance. This is still controversial, but could result either from contributions of the $\Delta(1700)3/2^-$ or from rescattering effects, which is not accounted for in most of the other calculations. Recent results from CBELSA/TAPS extended the discussion to energies up to the third [59] and fourth [58, 60, 61] resonance region and first results for the polarization observables I^s and I^c were obtained with linearly polarized photon beams (see bottom figure in Figure 1.18). These new results were used for an explicit re-analysis with the BnGa model [61]. They reported dominant decays into the $p\pi^0\pi^0$ final state via intermediate $\Delta(1232)3/2^+\pi^0$, $N(1440)1/2^+\pi^0$, $N(1520)3/2^-\pi^0$ and $N(1680)5/2^+\pi^0$ states as well as contributions from the light unflavored f_i mesons, i.e. $pf_0(500)$, $pf_0(980)$, and $pf_2(1270)$.

As discussed for single π^0 photoproduction in Section 1.4.1, the investigation of the isospin degree of freedom requires the measurement on the neutron. At present, cross sections are only available from two inclusive measurements at MAMI [69, 70] and from one exclusive measurement at GRAAL [68]. In addition, recent MAMI data was used for the extraction of the beam helicity asymmetry $I^{\odot}$ [56]. The GRAAL results for the cross sections for the proton and neutron are shown on the left-hand side and the beam helicity asymmetry on the right-hand side of Figure 1.19. GRAAL reported similar neutron and proton cross sections in the second resonance region followed by a sudden excess of the neutron result with respect to the proton in the third resonance region. This is in agreement with the expectations from the relevant resonance contributions in this energy range ($N(1680)5/2^+$ for the proton and $N(1675)5/2^-$ for the neutron), but is in contradiction with the obtained results for the beam helicity asymmetry, which are almost identical for the proton and neutron. The MAID predictions do not support such a similar behavior of the beam helicity asymmetry, but on the other side achieve only poor agreement with the measured cross sections.
Even though only few polarization observables have been measured so far and most of them on the free proton, the results achieved significant improvement of the models. However, the identification of the large number of contributing N^* and $\Delta(1232)$ resonances with the present observables is limited and thus requires the measurement of polarization observables and the reaction on the neutron.

1.5 Partial Wave Analysis and Reaction Models

For an interpretation of the results obtained in this work, they will be compared to the most recent model calculations from the MAID isobar model [40] (single π^0 photoproduction), the MAID unitary isobar model [62] (double π^0 photoproduction), the SAID partial wave analysis [39] (only single π^0 photoproduction), and the Bonn-Gatchina coupled-channel partial-wave analysis [38, 43] (single and double π^0 photoproduction). From the latter, only a prediction for double π^0 from the proton is available and the solution for single π^0 photoproduction from the neutron is not available in the latest calculation [43]. The results of the models for single π^0 photoproduction are shown in Figure 1.15 (main plot: neutron, top right insert: proton) and those for double π^0 photoproduction in Figure 1.17.
The following sections summarize the basic principles of the different models.

1.5.1 SAID

The SAID (*Scattering Analysis Interactive Dial-in*) partial wave analysis [39, 41, 71] is based at George Washington University and is developed by the CNS Data Analysis

Center [72] at the George Washington University, Washington DC, USA. It maintains a database which contains the world data on πN, πd, KN, and NN scattering, as well as π-, K-, η, and η'-photoproduction data and provides multipole results from PWA of the data. Since the database contains only single meson photoproduction, predictions for double π^0 photoproduction are not available. Predictions for single π^0 photoproduction are available from production threshold throughout the first, second, and third resonance region up to $E_\gamma \approx 2.7$ GeV and contains information on unpolarized and polarized observables. The observables are defined in terms of both helicity and transversity amplitudes (see Section 1.2.4 and 1.3) as defined in by Barker, Donnachie, and Storrow [21].

The initial results for meson photoproduction (solution SP06 [71]) mainly result from a coupled-channel partial wave analysis of πN and ηN data. Later on, pion photoproduction data (the largest influence on the solution was due to the addition of the GRAAL data for the beam asymmetry Σ for $\vec{\gamma}n \to \pi^- p$ and for $\vec{\gamma}n \to \pi^0 n$) was included in the analysis (solution SN11 [41]). In addition, a different approach in the calculation was developed using the Chew-Mandelstam parametrization described in [71] (solution CM12 [39]) and was applied to the same database used for the SN11 solution. The latest solution, i.e. CM12, corresponds to the version used for the comparison of the present data. This version uses fewer parameters than the earlier versions for the determination of the scattering and reaction amplitudes and was mainly developed to achieve a unified description of single π photoproduction data together with that of the π and η hadroproduction and their fit, according to the authors, achieves a better χ^2 than the other available parametrizations or models. The obtained photo-decay couplings of the CM12 solution in general are in agreement with the SN11 solution and the PDG values. The largest differences are seen in the $N(1535)1/2^-$ and $N(1720)3/2^+$ resonances.

1.5.2 MAID

The MAID model [73] has been developed at the Johannes Gutenberg University in Mainz, Germany and provides several models for meson and multiple meson photo- and electroproduction. The unitary isobar model for pion photo- and electroproduction on the nucleon [40, 74] provides predictions for single π^0 photoproduction from protons and neutrons and the isobar model for two-pion photoproduction on the nucleon [62] provides predictions for double π^0 photoproduction from protons and neutrons.

The MAID Unitary Isobar Model

The unitary isobar model [40, 74] has been developed with the aim to analyze the world data on pion photo- and electroproduction. The model consists of a common background and several resonance terms. Whereas the background is unitarized according to the K-matrix formalism, the 13 four-star rated resonances with masses below 2 GeV are described by unitarized Breit-Wigner forms. It provides results for the transverse and longitudinal helicity amplitudes for the four-star resonances below

2 GeV, which were obtained by a single-energy and global fit of the world database of photo- and electroproduction data. According to the authors, the solution provides confident results for the helicity couplings for the $\Delta(1232)3/2^+$, $N(1440)1/2^+$, $N(1535)1/2^-$, $N(1520)3/2^-$, and $N(1680)5/2^+$ resonances. Due to the lack of results for polarization observables, the predictions of higher resonances are less confident.

The MAID Isobar Model

The predictions from the MAID Isobar Model [62] are based on an effective Lagrangian approach for the elementary operator including resonance and Born terms. The model parameters have been fixed by resonance decay widths and multipole analyses of data from single pion photoproduction. For the proton, the model achieves satisfactory agreement with the mixed-charged and charged channels, but significantly underestimates the neutral channel, mainly at threshold. For the predictions of the reaction on the neutron, the reaction on the deuteron is evaluated with the same operator in the impulse approximation. Additionally, the model accounts for effects from nucleon-nucleon rescattering in the final state, but neglects those from pion-nucleon and pion-pion rescattering.

1.5.3 Bonn-Gatchina

The Bonn-Gatchina (BnGa) model [75] has been developed in collaboration of the Rheinische Friedrich-Wilhelms-Universität in Bonn, Germany, and the Petersburg Nuclear Physics Institute in Gatchina, Russia. The model is a coupled-channel reaction model (with background terms) and simultaneously fits the world baryon spectroscopy data, including πN scattering and single and multiple meson photoproduction. At present, the latest model, i.e. BnGa14-02 [43], is only available for the reactions on the proton and for single π^0 photoproduction. Therefore, for the comparison of the single π^0 data from the neutron, the BnGa11-02 solution was used, whereas for single and double π^0 photoproduction from the proton, the BnGa14-02 solution was considered.
In the analysis, the partial waves at low energies are described by the K-matrix approach and resonances of masses above 2.2 GeV are described by relativistic multi-channel Breit-Wigner amplitudes [76]. For the non-resonant contributions, reggeized t- and u-channel amplitudes are added to the resonant part. The difference between the individual solutions is mainly the data to which the model was fitted. The latest model (BnGa14-02) includes recent results for the polarization observables Σ, I^c, and I_s from $\eta\pi^0$ photoproduction from the free proton [43].

1.6 Final State Interaction Effects

The extraction of the results on the free neutron relies on measurement on light nuclei. Due to the small binding energy and its simple and relatively well known nuclear structure, the deuteron is mostly used as target. However, the results are affected by nuclear effects, such as Fermi motion or final state interaction effects. Whereas the former can be eliminated by a complete kinematical reconstruction of the final state, the latter can be investigated by a comparison of the reaction cross section on the quasi-free protons bound in the deuteron to the result from the free proton. The findings can then be applied to the quasi-free neutron result in order to obtain an estimate for the results on the free neutron. However, this assumes that the effects are similar for protons and neutrons, which in general does not have to be the case. Even though first theoretical calculations of such effects exist for the reaction $\gamma d \to \pi^- pp$ [77] and are on the way for the reaction $\gamma d \to \pi^0 pn$ [78–82], they are still in an early state. The main statement of the calculations is that the FSI effects for the reaction on the proton and the neutron are in general not equal, but for single π^0 photoproduction there are certain cases where they have to be identical. In addition, for a large energy and meson polar angle range, the effects are expected to be very similar, which justifies the above mentioned estimation of the free neutron cross section to a certain extent. In the following, the final state interaction effects will be briefly discussed by means of the underlying theoretical model [82].

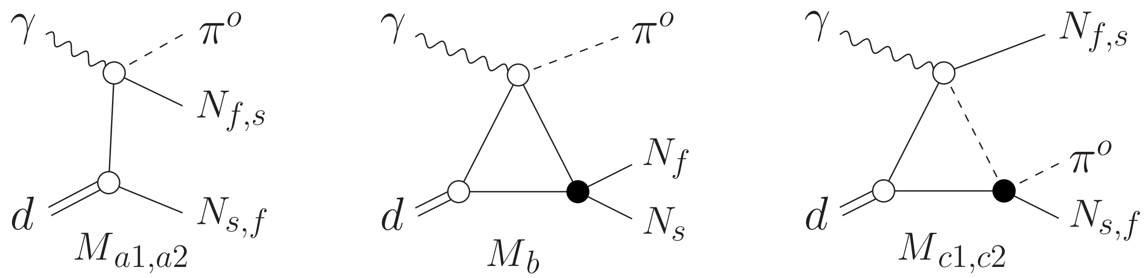

Figure 1.20: Feynman diagrams for the reaction $\gamma d\pi^0 pn$. M_{a1}, M_{a2}: impulse-approximation. M_b: NN-FSI. M_{c1}, M_{c2}: πN-FSI. N_f: fast final-state nucleon. N_s: slow final-state nucleon. Figure taken from [82].

In π^0 photoproduction from the deuteron, the elementary γN reaction can occur on the proton or on the neutron of the deuteron. The calculation is based on the consideration of the two nucleons in quasi-free kinematics (see Section 1.2.1). Thereby the participant nucleon on which the reaction occurred receives a much larger momentum $\vec{q}_f$ as the spectator nucleon $\vec{q}_s$, i.e. $\vec{q}_f \ggg \vec{q}_s$, and is referred to as the *fast* nucleon and the spectator as *slow* nucleon. The amplitude $M_{\gamma d}$ of the reaction $\gamma d \to \pi^0 pn$ can be written as:

$$M_{\gamma d} = M_{a1} + M_{a2} + M_b + M_{c1} + M_{c2} \ , \tag{1.37}$$

where the individual amplitudes are illustrated in Figure 1.20. The total amplitude $M_{\gamma d}$ contains the impulse approximation (IA) [83] terms M_{a1}, M_{a2} and the FSI terms M_b, M_{c1}, M_{c2}, where M_b denotes the nucleon-nucleon (NN) rescattering and M_{c1}, M_{c2} correspond to the pion-nucleon (πN) rescattering amplitudes.
Since the πN-FSI effects were shown to be small and even negligible at energies above 200 MeV [79–81], the πN-amplitudes can be omitted from the further discussion. The

total amplitude is then given by:

$$M_{\gamma d} = M_{a1} + \Delta \ , \qquad \Delta = M_{a2} + M_b \ . \tag{1.38}$$

Correction factors for the quasi-free results were then obtained from the model by the ratio of the free to quasi free cross sections:

$$R_p = \frac{d\sigma^{(p)}(\gamma d)}{d\Omega} \Big/ \frac{d\sigma(\gamma d)}{d\Omega} \ , \qquad R_n = \frac{d\sigma^{(n)}(\gamma d)}{d\Omega} \Big/ \frac{d\sigma(\gamma d)}{d\Omega} \ , \tag{1.39}$$

where $d\Omega$ is the solid angle and $d\sigma^{(p)/(n)}(\gamma d)$ is calculated from the main IA diagram M_{a1} and $d\sigma(\gamma d)$ from the full amplitude $M_{\gamma d}$, as defined in Equation (1.38). The results for the correction factor for the quasi-free proton and the quasi-free neutron are compared to each other in Figure 1.21.

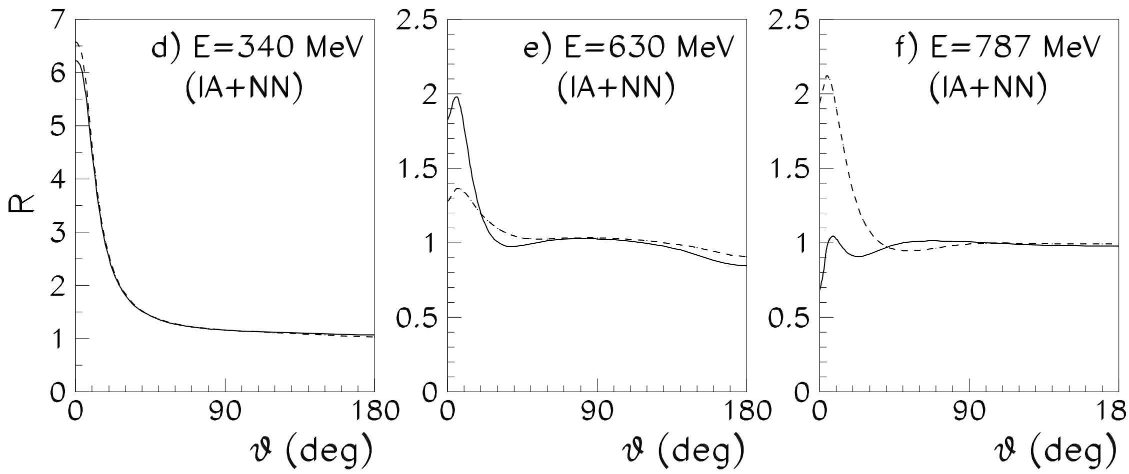

Figure 1.21: Comparison of the correction factor for the quasi-free proton R_p (solid curves) and the quasi-free neutron R_n (dashed curve). Except for small meson cm polar angles θ^*, the correction factors are almost identical. Figure taken from [82].

It can be seen that the FSI effects affect both results at small meson cm polar angles θ^*, which corresponds to pions that are emitted at forward angles, whereas at larger angles, both effects are negligible and $R_p = R_n \approx 1$.

2 Experimental Setup

The development of electron accelerator facilities drastically increased in the late 1960's when nuclear and medium energy particle physics research was strongly depending on suitable machines for coincidence experiments. The three most successful types of electron accelerators that were developed and are the most common accelerators today are: the *recirculated superconduction linac*, the *stretcher ring*, and the *race track microtron*. The most famous example for a facility using a recirculated superconduction linac is CEBAF ("*Continuous Electron Beam Accelerator Facility*") at the Thomas Jefferson National Accelerator Facility (Jefferson Lab) [84] in Newport News, USA. The world's largest racetrack microtron can be found at MAMI [85] at the Institute of Nuclear Physics in Mainz, Germany. ELSA, at the Institute of Physics in Bonn, Germany [86], makes use of the stretcher ring scheme. All three accelerators are mainly used for hadron physics experiments, probing the nucleus of the atom.

The following chapter introduces the two electron accelerator facilities MAMI (from German "*Mainzer Mikrotron*") in Mainz and ELSA (from German "*Elektronen Stretcher Anlage*") in Bonn where the experiments that form the basis of this work have been carried out. At both facilities, the principles of the experimental setup is very similar: the electron beam is extracted and directed into the experimental area where it hits a thin radiator foil to produce a photon beam via the bremsstrahlung process. The photon beam then impinges onto a target material, which is surrounded by the different detector components used to track and detect the reaction products. The main detector components consist of two electromagnetic calorimeters: one surrounds the target and another one is arranged as a forward wall (behind the latter in the direction of the beam). Charged particles are distinguished from neutral particles by using different kinds of plastic scintillators.

The first sections introduce the MAMI accelerator (Section 2.1), the setup (Section 2.2) and detector readout (Section 2.3) of the A2 experiment, followed by the ELSA accelerator (Section 2.4), the setup (Section 2.5) and the detector readout (Section 2.6) of the CBELSA/TAPS experiment. Then the principles and techniques of polarized beams (Section 2.7) and targets (Section 2.8) will be explained and finally, an overview of the different beamtimes (Section 2.9) is given.

2.1 The Electron Accelerator Facility MAMI

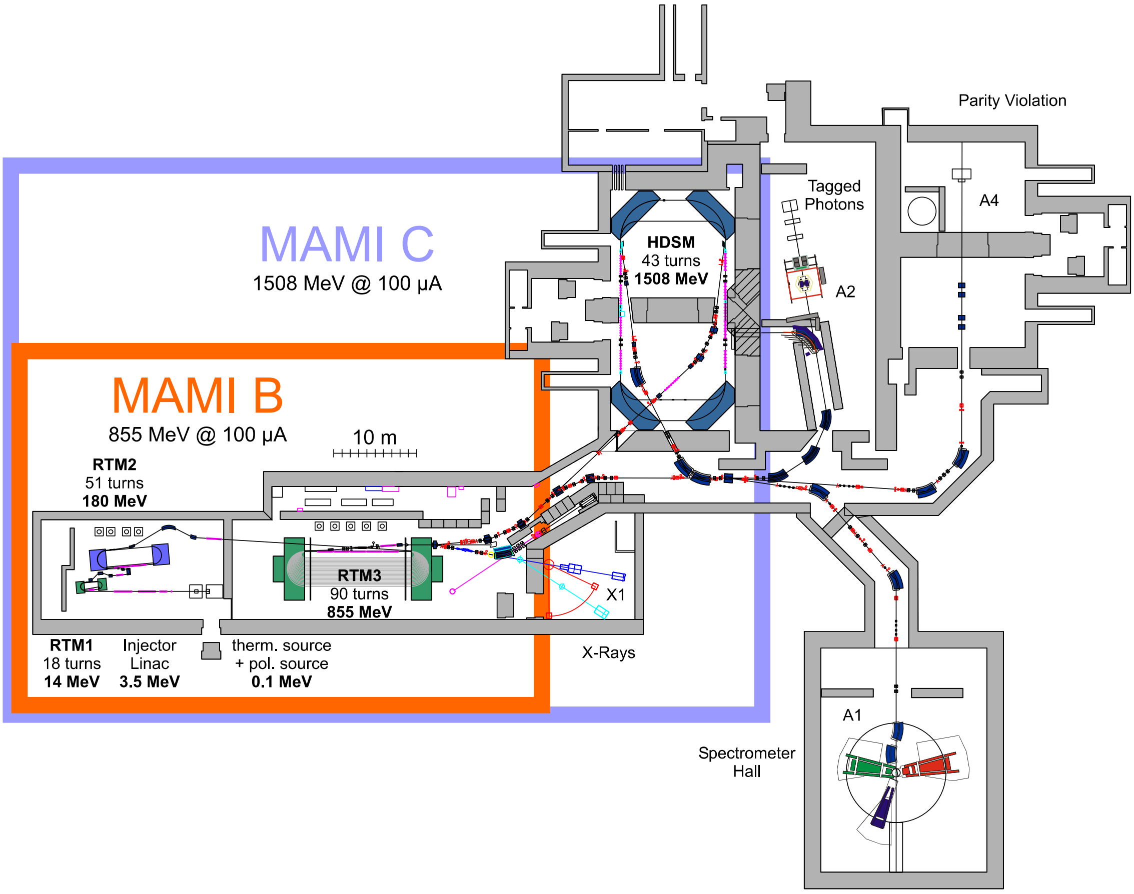

Figure 2.1: Floor plan of the MAMI electron accelerator facility. It shows the unpolarized and polarized electron sources and the pre-accelerating linac stages (bottom left), the cascade of racetrack microtrons (RTM1-3) the harmonic double-sided microtron (HDSM) and the different experimental halls (right-hand side). The former accelerator, MAMI-B, comprised of the RTM cascade (red framed area), the present accelerator comprises of the RTM cascade and the HDSM (violet framed area). Figure taken from [87].

The MAMI electron facility [85, 88–95] accelerates electrons via a cascade of three racetrack microtrons (RTM) and an additional harmonic double-sided microtron (HDSM) up to relativistic electron beam energies of nearly 1.6 GeV. It provides polarized electron beams with 80 % degree of polarization and a beam current of more than 20 μA and unpolarized electron beams up to 100 μA. The continuous wave acceleration results in a continuous electron current, a beam width of less than 0.1 mm, and an energy uncertainty of less than 13 keV. In addition, a complex control mechanism confines the beam position to be within 200 μm [85].

2.1.1 The Electron Gun and Injector Linac

In its first ten years of operation, the electrons of the beam have been produced by thermal emission at the cathode inside the electron gun. Before being injected into the first race track microtron, the electrons have been pre-accelerated to 2.1 MeV with a Van De Graaff accelerator [88]. With this thermal source, an unpolarized electron beam up to 100 μA current was achieved.
In the late 80's, it was decided to replace the Van de Graaff pre-accelerator by a more reliable and simple continuous wave radio frequency linac. Besides providing improved beam stability, it also guarantees the space and the high vacuum that was necessary for the implementation of a polarized electron source [96]. The polarized electron source is based on the photoelectron emission of III-V-semiconductors. In this case the cathode is a strained layer GaAsP crystal, which is irradiated by a titanium sapphire laser resulting in a polarized electron beam of a maximum current of 20 μA and a degree of polarization of up to 80 %. Figure 2.2 shows a schematic of the polarized electron source at MAMI.

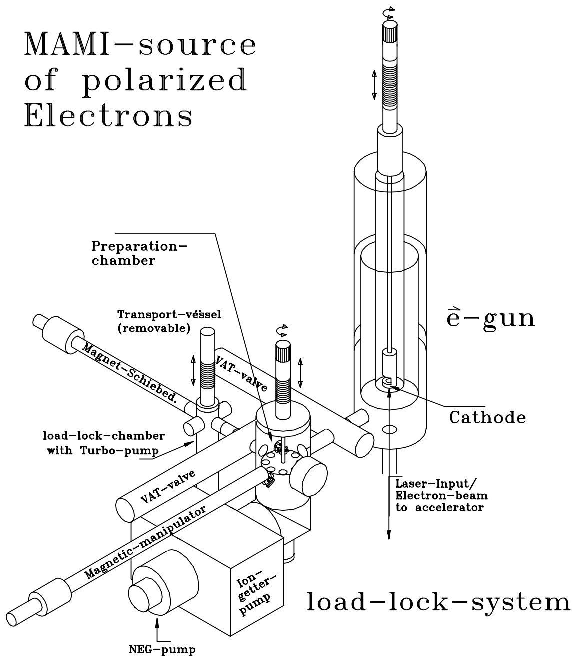

Figure 2.2: Polarized electron source at MAMI. Figure taken from [97].

2.1.2 The Racetrack Microtron Cascade

The energy gain ΔT of a charged particle being accelerated with a linear accelerator of length L, shunt impedance r, and total radio frequency power P is given by [98]:

$$\Delta T^2 = r \cdot L \cdot P \ . \tag{2.1}$$

Accelerating particles in the amount of energy ΔT of several 100 MeV is only possible in pulsed mode, as the shunt impedance r in normal conducting linear accelerators is on the order of 50 $M\Omega/m$. This results in an extremely high product $L \cdot P$, which is not practicable at all. This problem can be avoided by letting the particle recirculating the linac several times. A number of $n = 30$ cycles in a linac already saves three orders of magnitude in the product $L \cdot P$, such that Equation (2.1) becomes

$$T^2 = \left(n \cdot \Delta T^2\right) = r \cdot L \cdot P \cdot n^2 \ . \tag{2.2}$$

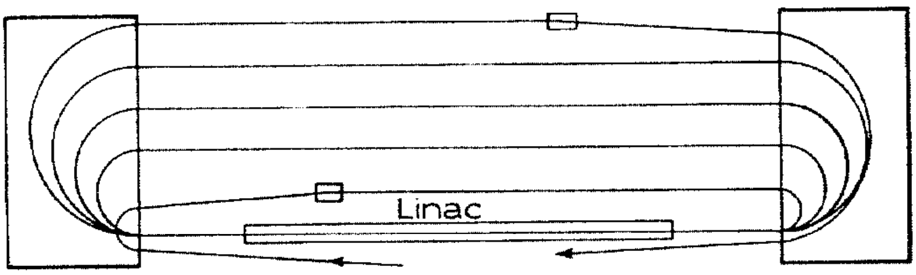

Figure 2.3: Schematic drawing of a race track microtron. Figure taken from [98].

A common way to realize this idea of recirculating particles in a linac is the racetrack microtron, as shown in Figure 2.3. From one passage through the linac to another, the path length has to be increased by a multiple of the wavelength in order to fulfill the resonance condition between the energy gain per mass and the magnetic flux density in the bending magnets. Empirically, the energy of the initial beam entering the RTM should not be much smaller than one tenth of the output energy. On the other hand, the output energy is limited by increasing synchrotron radiation emission to about 1 GeV.
At MAMI, the injection energy problem is circumvented by the cascade of three RTMs as shown in Figure 2.4. From stage to stage, the magnetic flux density has to be increased in order to allow for the resonant energy gain per turn and a constant growing orbit length.

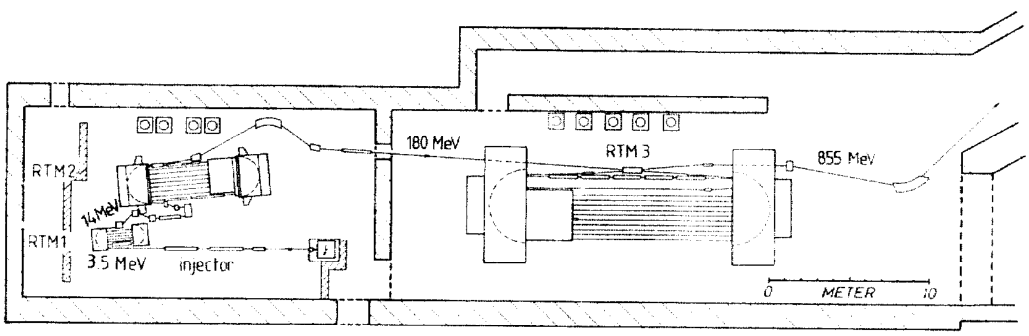

Figure 2.4: Schematic drawing of the RTM cascade at MAMI. The two first RTM stages have been used at MAMI-A and the full RTM cascade at MAMI-B. Figure taken from [98].

2.1.3 The Harmonic Double Sided Microtron

To provide a beam of higher electron energy, a fourth accelerator stage was planned. A fourth RTM would have not been feasible due to the immense weight of the magnets and the emittance growth due to synchrotron radiation. A solution was found by using four light magnets (instead of two heavy bending magnets) forming a Double Sided Microtron (DSM). In order to avoid defocussing and to improve the stability, one of the two linacs is driven by the fundamental frequency, the other one at the first harmonic frequency. Compared to a RTM, it delivers twice the beam energy for the same total weight of the magnets. This so-called Harmonic Double Sided Microtron (HDSM) was successfully commissioned at the end of 2006 and provides an electron beam of 1508 MeV maximum energy. After two additional upgrades of the magnetic field maps, the maximum beam energy was increased from 1508 MeV to 1558 MeV to finally 1604 MeV. The HDSM is shown in Figure 2.5.

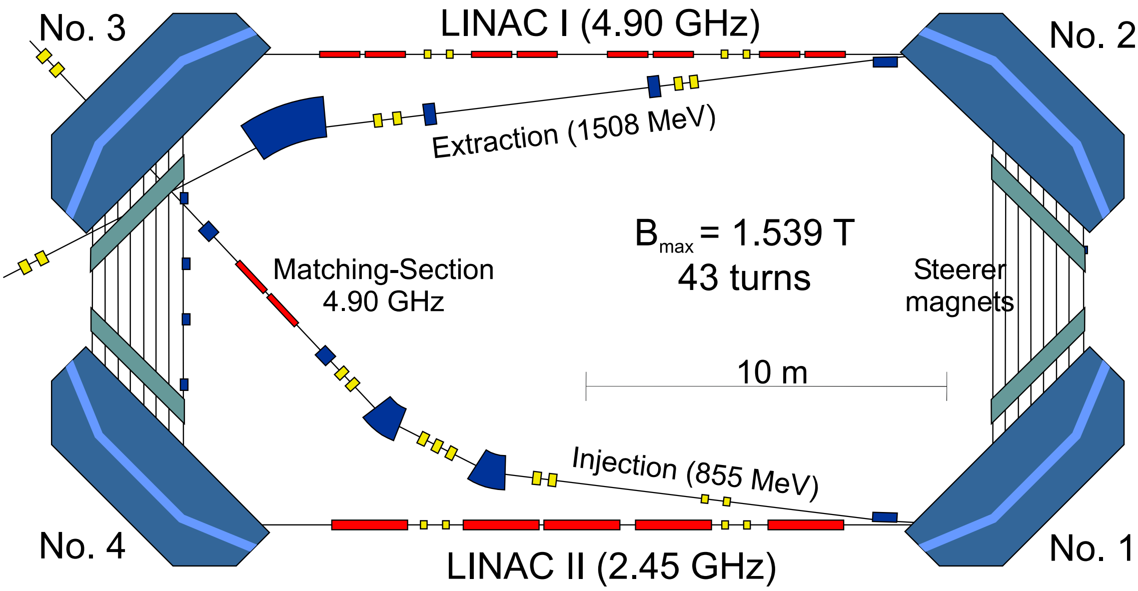

Figure 2.5: Schematic drawing of the HDSM at MAMI. Figure taken from [87].

The beam is then extracted and can be guided into one of four experimental halls, as seen in the MAMI floor plan in Figure 2.1. The different halls focus on electron scattering experiments (A1), photoproduction experiments (A2), parity violation experiments (A4) and x-ray radiation experiments (X1). An overview of the different acceleration stages is given in Table 2.1.

	unit	injector	RTM1	RTM2	RTM3	HDSM
inj. energy	MeV	0.611	3.97	14.86	180	855
extr. energy	MeV	3.97	14.86	180	855	1508
energy gain / turn	MeV	3.36	0.599	3.24	7.5	13.66-16.58
# turns	a.u.	-	18	51	90	43
power cons.	kW	92	92	220	650	1500
r.f. freq.	GHz	2.4495	2.4495	2.4495	2.4495	2.4495/4.8990
magn. flux dens.	T	-	0.1026	0.5550	1.2842	0.95-1.53

Table 2.1: Overview of the different acceleration stages at MAMI-C. Note: The present values will slightly differ from those given in this table as the magnetic flux density was altered in order to achieve the maximum energy of 1604 MeV. Values taken from [99].

2.2 The A2 Experimental Setup

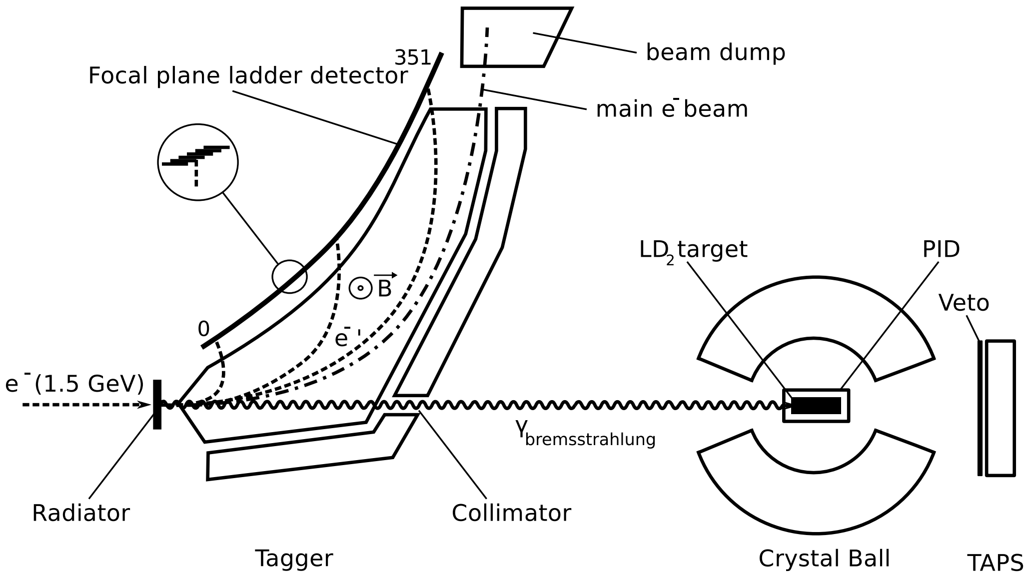

Figure 2.6: Schematic illustration of the A2 experimental setup at MAMI. The electron beam (dashed horizontal line at the bottom left) impinges on the radiator and produces a beam of bremsstrahlung photons (wiggly horizontal line). The electron beam is deflected by the dipole magnet. Electrons that interacted with the radiator are deflected onto the focal plane detector, the other electrons are annihilated in the beam dump. The photon beam impinges on the target, which is surrounded by the detector system, that mainly comprises of the Crystal Ball detector with the Particle Identification Detector (PID) and of the TAPS detector with the vetos. Figure taken from [100].

As the A2 Collaboration performs experiments with real photons, the electron beam has to be converted into a photon beam. This is realized by directing the electron beam onto a radiator. Electrons scattering in the Coulomb field of the radiator nucleons produce real photons via the bremsstrahlung process. The bremsstrahlung cross section has the following energy and angular dependence [101]:

$$\begin{aligned}
\frac{d\sigma}{dE_\gamma} &\propto \frac{1}{E_\gamma} \ , \\
\frac{d\sigma}{d\theta_\gamma} &\propto \frac{\theta_\gamma}{\left(\theta_\gamma^2 + \theta_c^2\right)^2} \ , \\
\theta_c = \sqrt{< \theta_\gamma^2 >} &\propto \frac{m_{e^-}}{E_{e^-}} \ ,
\end{aligned} \tag{2.3}$$

where E_γ, θ_γ are the energy and emission angle of the photon and θ_c is the characteristic angle (corresponding to the opening angle of the bremsstrahlung cone) within half of the photons are emitted. At MAMI energies, the fraction of the electron mass m_{e^-} and the electron energy E_{e^-} goes to zero and hence most of the bremsstrahlung photons are emitted in the forward direction.

2.2.1 The Glasgow Photon Tagging Spectrometer

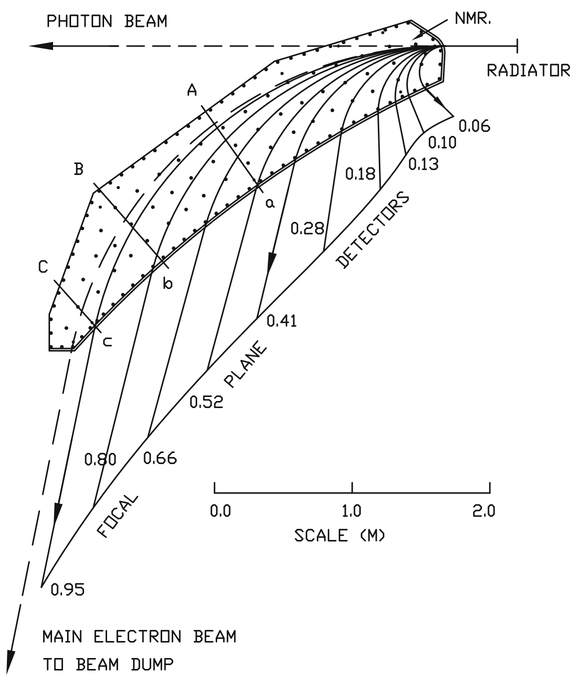

Figure 2.7: Schematic illustration of the Glasgow Photon Tagging Spectrometer. Figure taken from [102].

The Glasgow photon tagging spectrometer consists of the main focal-plane detector [103] covering 5-93 % of the full MAMI-C energy[1], a focal-plane microscope

[1]As the latest MAMI-C upgrade provides electron energies up to 1.6 GeV, an additional tagging system, the endpoint-tagger, was developed to cover energies above 1.4 GeV.

to improve the resolution over part of the energy range (not used in this work), and a large dipole magnet.

According to the small cross section (see Equation (2.3)), not all of the beam electrons lose their energy via bremsstrahlung. Hence, the remaining electron beam has to be deflected into the electron beam dump by using a large dipole magnet that produces an average magnetic field of ~ 1.96 T at a current of 440 A. The other electrons lost some of their energy by the emission of the bremsstrahlung photons and therefore, are stronger deflected. Depending on their momentum, they hit a detector element that corresponds to a certain electron energy. The 353 detector elements are EJ-200[2] plastic scintillators of long attenuation length and fast timing and are read out with Hamamatsu R1635 photomultiplier tubes (PMTs). The scintillators overlap by slightly more than half of their width, such that an electron hit is defined by coincident hits between two neighboring elements. This results in 352 effective channels which are 2 mm in thickness, 80 mm long and have a decreasing width from 32 to 9 mm such that each detector covers more or less a constant energy range. This results in an energy width of ~ 4 MeV and an overlap region of about 0.4 MeV. Figure 2.7 shows the principle of the tagging system.
In the bremsstrahlung process, only a negligible amount of the energy of the incoming electron E_0 is transferred to the nuclei inside the radiator. Therefore, the energy loss of the electron, i.e. the energy of the outgoing photon, E_γ is fully determined by measuring the energy of the scattered electron E_{e^-} with the Glasgow tagger:

$$E_\gamma = E_0 - E_{e^-} \ . \tag{2.4}$$

Due to the bremsstrahlung process, the photon beam is divergent and has to be collimated. For this purpose, a lead collimator (see Figure 2.8) with an opening diameter of a few millimeter is placed between the radiator and the target cell, which leads to a beam spot diameter of about one centimeter on the target cell.

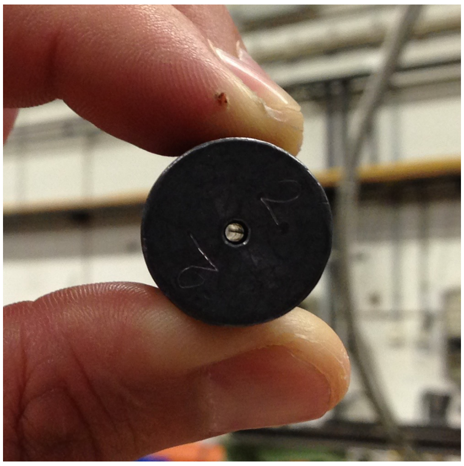

Figure 2.8: 2 mm lead collimator used for the deuterated Butanol beamtimes.

[2]see Table A.1 for more physical properties.

2.2.2 The Crystal Ball Detector

The Crystal Ball is a spherically shaped calorimeter based on the geometry of a icosahedron[3] [104, 105]. Each of the twenty triangular shaped faces is split into four smaller equilateral triangles (see left illustration in Figure 2.9). In each of these triangles, nine triangular shaped thallium doped sodium iodide (NaI(Tl)) crystals are mounted. As the Crystal Ball surrounds the target and also the beamline, 12 crystals in the backward and 12 crystals in the forward direction are spared, reducing the acceptance by 6.7 % and yielding a total amount of 672 crystals. For optical isolation, each crystal is wrapped in reflecting paper and then in aluminized mylar foil (see right part of Figure 2.9). Due to the complicated geometry, 11 crystals had to be

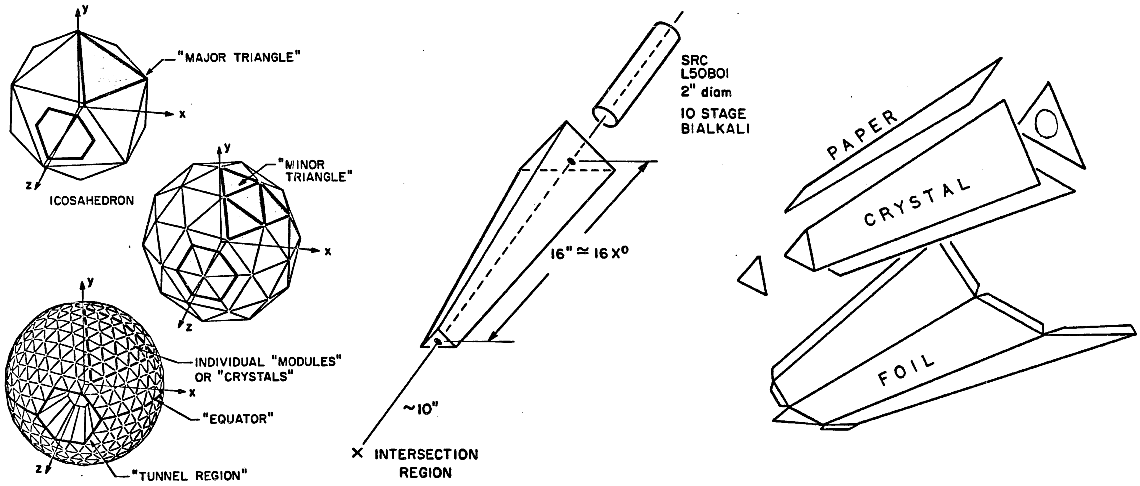

Figure 2.9: Schematic illustration of the Crystal Ball and its components. Left-hand side: Decomposition of the Crystal Ball geometry. Middle: Example crystal geometry. Right-hand side: Wrapping material. Figures taken from [104].

manufactured in a different shape to ensure a seamless arrangement. Nevertheless, every crystal is a truncated triangular shaped pyramid of 16 " length (40.64 cm, see middle illustration of Figure 2.9) corresponding to 15.7 radiation lengths (see Table A.1 for more characteristic properties of NaI(Tl)). The inner radius of the Crystal Ball is 10 " (25.4 cm) and the outer radius 26 " (66.04 cm). Each crystal is connected to a SRC L50 B01 PMT of 5.1 cm in diameter, which is separated from the crystal by a glass window and a 5 cm air gap. To sustain mobility and maintenance, the detector is split up into two hemispheres and the upper one can be lifted. The inner surfaces of the two hemispheres are completed by two 0.76 mm thick steel plates (corresponding to 0.09 radiation lengths) and are separated by an air gap of about 5 mm. In order to protect the delicate hygroscopic crystals from moisture and dust, both hemispheres are evacuated. Additionally, the vacuum also stabilizes the heavy detector components.
The full detector covers 93 % of the solid angle, i.e. polar angles in the range

[3] a polyhedron, i.e. a three dimensional solid with 20 polygonal faces

$20° < \theta < 160°$, and nearly full azimuthal range in ϕ, except for the region of the gap between the two hemispheres.

2.2.3 The Particle Identification Detector

The Particle Identification Detector (PID) is a cylindrical shaped detector inside of the Crystal Ball detector, surrounding the target and the beamline and covering the full solid angle of the Crystal Ball. Together with the multi-wire proportional chambers (MWPC), which have not been used in any analysis of this work, it is part of the inner detector system of the Crystal Ball and is used to identify and discriminate among charged particles. This is done by plotting the deposited energy of the charged particle versus its cluster energy in the Crystal Ball (see Section 6.5.3). In addition it serves as a veto detector for the identification of neutral particles.

The PID is made of 24 EJ-204 plastic scintillators of 50 cm in length and 4 mm

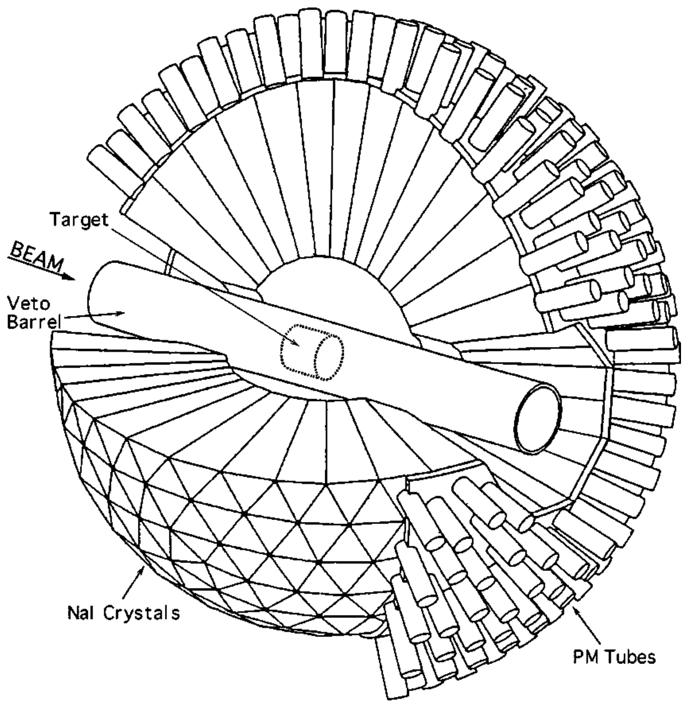

Figure 2.10: Schematic illustration of the PID (Veto Barrel) inside the Crystal Ball. Figure taken from [105].

in thickness, each covering 15° of the azimuthal angle ϕ. They are arranged in a cylindrical barrel with an inner diameter of 11.65 cm and an outer diameter of 12.45 cm. In order to provide optimal contact, the cross section of the PID elements has an asymmetric trapezoidal shape. For optical isolation, they are wrapped in an aluminium foil and a layer of black Tedlar[4]. Every PID element is connected via lucite light guides to a Hamamatsu H3164-10 PMT in the upstream direction. See Table A.1 for some of the characteristic properties of the EJ-204 plastic scintillators.

[4]A fine film of polyvinyl fluoride (PVF).

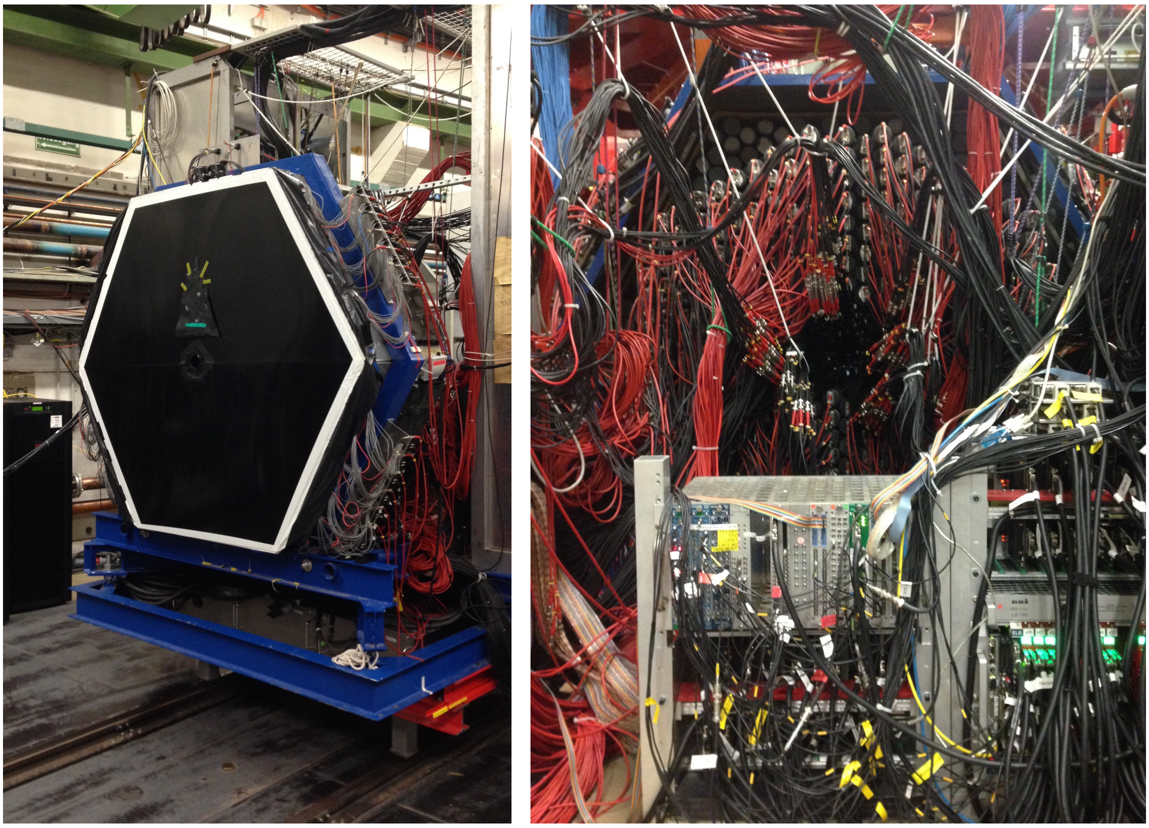

Figure 2.11: Photographs of the TAPS detector from the front (left) and from the back (right).

2.2.4 The Two Arm Photon Spectrometer Detector

The Two Arm Photon Spectrometer (TAPS) [106–108] was in fact only a two arm photon spectrometer in its earlier times and was later rearranged as a hexagonal forward wall at a distance of 1.5 m from the target center in beam direction.

It covers the full azimuthal range in ϕ and polar angles from about $5° < \theta < 20°$. Until 2007, it consisted of 384 barium fluoride (BaF_2) crystals that are ideally suited for the detection of low and high energy single photons. The BaF_2 crystals have a diameter of 5.9 cm and a length of 22.5 cm. Every crystal is equipped with a 2.5 cm long cylindrical endcap of 5.4 cm in diameter. In total, one crystal has a length of 25.0 cm, which corresponds to 12.3 radiation lengths. BaF_2 crystals have the special property of having several scintillation emission bands. Due to the high light yield, the slow component (decay time of 630 ns) provides a high energy resolution. In contrast, the fast component (decay time of 60 to 80 ps) provides a high time resolution. The good time resolution together with the sufficiently large distance to the target allows for time of flight measurements that can be used to discriminate between different types of particles (see Section 6.5.1). This is also possible by separating the detected signals from the short and the long component, with the so-called pulse-shape analysis (PSA, see Section 6.5.2). Optical isolation of the crystals is realized with eight layers of 38 μm thick reflecting Teflon foil and an additional 15 μm thick

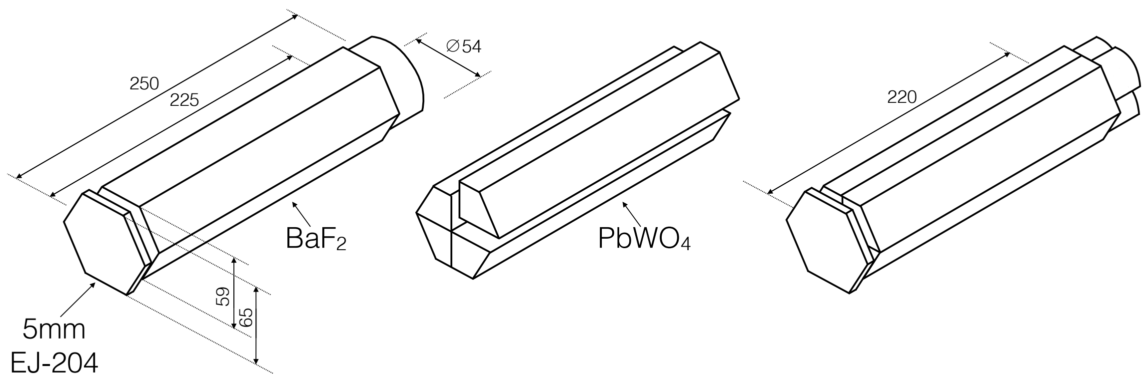

Figure 2.12: TAPS crystal geometries. The dimensions are given in mm. Left-hand side: BaF_2 crystal with veto. Middle: Decomposition of a BaF_2 crystal into four $PbWO_4$ crystals. Right-hand side: PWO_4 block with veto. Figure adapted from [108].

aluminium foil. Hamamatsu R2059-01 PMTs are connected to the endcaps to collect the light output. Table A.1 summarizes the most important physical properties of the BaF_2 crystals.

In 2008, each crystal of the two inner rings (18 crystals in total) was exchanged with four lead tungstate ($PbWO_4$) crystals (72 crystals in total), which have a shorter decay time than the BaF_2 crystals and are better suited for the high rates in the forward direction. To ease the integration procedure, the geometry of four lead tungstate crystals was chosen to match the shape of one barium fluoride crystal, as illustrated in Figure 2.12. The length of the $PbWO_4$ crystals is 20 cm, corresponding to 22.5 radiation lengths. They are isolated with 70 μm thick reflecting VME 2000 foil and one layer of 20 μm thick aluminium foil and are connected to a Photonis XP 1911 PMT. Table A.1 lists some of the physical properties of the $PbWO_4$ crystals.

2.2.5 The Veto Detectors

A 5 mm thick EJ-204 plastic scintillator of hexagonal shape is mounted in front of every BaF_2 and group of four $PbWO_4$ crystals. The front of the veto is enclosed in a black foil for optical isolation and can be seen in the left-hand figure of Figure 2.11. In every veto, a wavelength shifting fiber forms a loop to collect the light and is read out by a Hamamatsu H6568 16-channel multi-anode PMT. Unfortunately, not all of the light can be collected by the fibers and their rather strong curvature does not conserve total reflection. This results in a loss of light and hence, a bad energy resolution. However, to a certain degree they can still be used to differentiate between charged particles by plotting the deposited energy in the veto detector versus the energy deposited in TAPS (see Section 6.5.3).

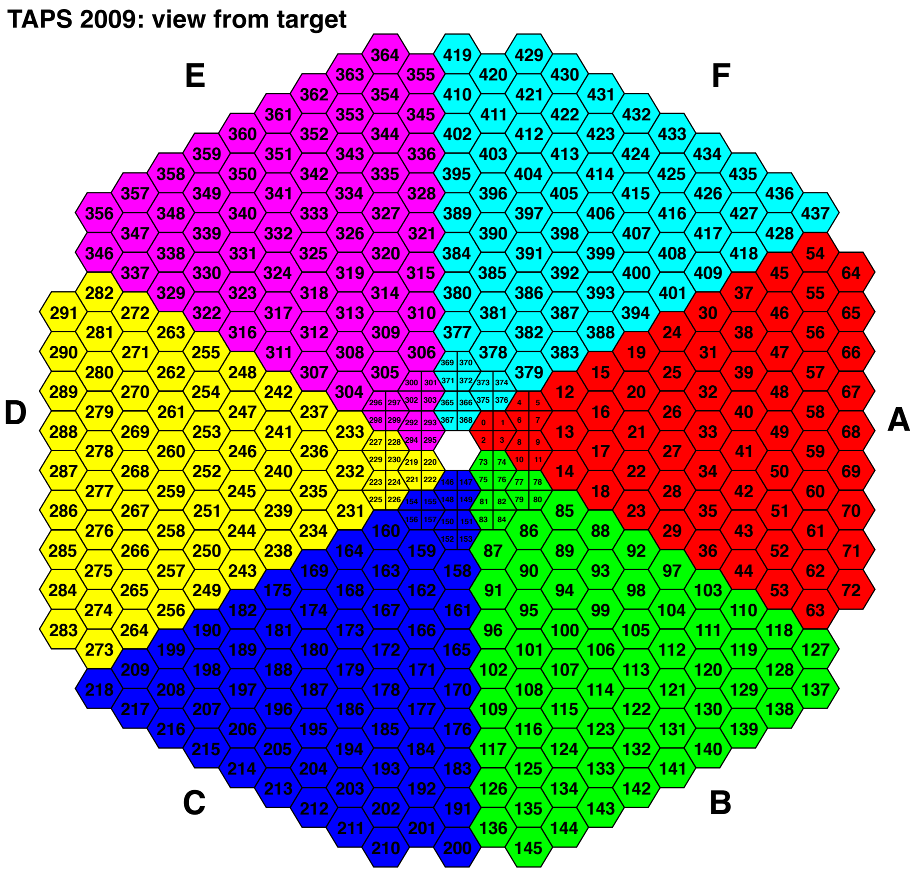

Figure 2.13: Layout and crystal numbering of the TAPS detector showing the nine outer BaF_2 rings and the two inner $PbWO_4$ rings. The six different colored sections, referred to as sectors, show the logical groups of crystals used for the trigger. Figure taken from [100].

2.2.6 The Lead Glass Detector

The lead glass detector is a Cherenkov detector with a response behavior for photons of nearly 100%. It plays an important role in the determination of the tagging efficiency measurement (see Section 6.10), which is inevitable for the absolute normalization of cross sections and asymmetries. It is a block with edge lengths of a sufficiently large dimension[5], i.e. 20 cm, and is made entirely of lead glass. For the measurement with the lead glass detector, the standard experiment has to be paused and the detector is moved into the beam line behind all the detectors, but in front of the P2 ionization chamber (see Section 2.2.7). Photons that impinge on the detector convert by pair production into an electron-positron pair. Via the subsequent bremsstrahlung process, a cascade of charged particles is produced. These particles emit Cherenkov light that is detected by a PMT. For its optical isolation the lead glass is wrapped in a layer of mylar foil and an additional black lightproof synthetic foil.

[5]note: a usual beam diameter is on the order of 2 cm at the location of the lead glass detector

2.2.7 The P2 Ionization Chamber

The P2 ionization chamber is located in the photon beam in front of the photon absorber. With a diameter of about 29 cm, it is able to detect the full beam, even if it is out of alignment. It consists of a series of parallel metallic plates, which are surrounded by air. Photons impinging on the plates generate electromagnetic showers that ionize the air in between the plates. At a voltage of about 40 V, it collects the charges and produces a current that is permanently measured. This allows for the constant survey of the relative photon flux (see Section 6.10).

2.3 Data Acquisition at the A2 Experiment

During the experiment, the PMTs of all the different detectors collect signals of the particles that interacted with the detector material. These analog signals are then digitized by the different electronic components via either timing information, using a time to digital converter (TDC), energy information using an analog to digital converter (ADC), or with a counter, referred to as a scaler. The trigger system decides when and which event has to be recorded or rejected. The data acquisition system finally collects all the informations and stores them to a data storage medium from which they can then be used for the offline analysis. The following paragraphs briefly summarize the readout of the detector components, the trigger system will be discussed afterwards.

2.3.1 Readout of the Detector Components

Table 2.2 gives an overview of the available readout devices for the individual detector components used for the A2 experiments at MAMI in this work. A complete list of all components can for example be found in [109]. In the following the readout of the first and second level trigger related detectors will be discussed.

Detector	Device
Glasgow Tagger	TDC, Scaler
Crystal Ball (NaI(Tl)-crystals	TDC, ADC
PID	TDC, ADC
TAPS (BaF_2-crystals)	TDC, ADC
TAPS ($PbWO_4$-crystals)	TDC, ADC
TAPS (Veto)	TDC, ADC
Lead glass	TDC, ADC

Table 2.2: Overview of the available readout devices for the individual detector components used at the A2 experiments at MAMI.

Glasgow Photon Tagging Spectrometer

For the standard data analysis, only the timing and the number of the electron hits in the individual tagger scintillators are recorded. The energy information is only used for the calibration of the detectors and is not written to the data stream.
A discriminator checks if the signal is above a predetermined value (by calibration). If so, the signal is sent to a CATCH[6] multi-hit TDC where the time informations of the hits within the actual event are recorded. An additional FASTBUS scaler unit counts the number of the received signals.

Crystal Ball Detector

A dedicated readout of the Crystal Ball is of great importance. As it covers most of the solid angle, any loss of information would strongly influence the results. On the other side, reading out all the information can drastically slow down the entire system. However, as the readout is fast enough, this can be bypassed by including the Crystal Ball in a first level trigger. In this way, by using the sum of the deposited energy (Crystal Ball energy sum trigger, see Section 6.6.2), it is possible to decide[7] whether an individual event is accepted or rejected.
An active splitter collects all the signals of the 672 NaI(Tl) crystals. The analog sum of these signals is used for the Crystal Ball energy sum trigger. One part of the signal is delayed by 300 ns and sent to sampling ADCs where the signals are integrated. The other part is sent to a dual-threshold discriminator, consisting of two leading-edge discriminators, LED1 and LED2. LED1 checks if the signal exceeds a low threshold and if fulfilled, it sends the signals to the CATCH TDCs. The outputs of the high threshold LED2 are used for the multiplicity trigger.

Particle Identification Detector

For particle identification, time and energy information of the PID are required. Since the PID is not a part of the experimental trigger the readout is simple. The detected signals are amplified, split, and sent to ADCs for the signal integration and to CATCH TDCs for the time measurement.

TAPS Detector

The readout for the BaF_2 and $PbWO_4$ crystals is identical. Constant fraction discriminators (CFDs) check all channels to see if the signal is above the noise level (which corresponds to a threshold of about 3 MeV). Time to amplitude converters (TAC) are used for the time measurement, charge to amplitude converters (QAC) for the energy integration, and ADCs for the digitalization of the signals. In order to include TAPS in the multiplicity trigger, a low and high LED threshold are used.

[6] COMPASS Accumulate, Transfer and Control Hardware
[7] by means of a threshold value

Veto Detector

The Veto Detector readout is very similar to the TAPS readout. The time measurement with TDCs and energy integration with ADCs is initialized by a leading edge discriminator.

2.3.2 Trigger System before October 2012

In October 2012, the old trigger system, which was based on CAMAC[8] and NIM[9] electronics, was replaced by a much faster, more simple and less error-prone FPGA logic [109, 110]. As the unpolarized data on liquid hydrogen and deuterium used for this work were taken with the old trigger system in 2007 and 2009 (see Tables 2.5 and 2.6 for detailed information), it will be briefly summarized in the following paragraphs. More detailed information can be found in [100].

An idealized data acquisition would be capable of writing all information of all events at any time. In reality, the readout of the individual detector components, as well as the digitalization of the data, takes a certain amount of time. During this time, no further information can be recorded, which is referred to as the deadtime. For this reason it is essential to avoid occupying the system when it is not needed. The trigger system is used to reduce the event rate and to lower the dead time according to the needs of the experiment. Hence, for every experiment the best possible trigger conditions that yield the highest rate of desired events at the lowest dead time has to be determined.

The trigger system consists of a first and a second level trigger. Based on the bare signals, the first level trigger allows for a very fast decision that the most general trigger requirements are fulfilled. If not, the event is immediately rejected. If yes, the second level trigger checks further requirements such as multiplicities.

In two of three liquid deuterium beamtimes (December 2007 and February 2009), the first level trigger considered only the Crystal Ball energy sum by comparing the analog sum of all Crystal Ball signals with a discriminator threshold. The value of the threshold was set according to the needs of the experiment. As all three beamtimes were designed for photoproduction of η-mesons, a rather high threshold corresponding to about 300 MeV was set. This threshold suppresses the high rate of events from single π^0, with which the acquisition would have been occupied and many η events would not have been recorded.

The second level trigger is based on the multiplicity trigger, i.e. on the number of detected particles. At this point, the number of particles that generated the individual signals is unknown and has to be estimated. In the Crystal Ball, this is realized by building logical groups of 16 neighbouring channels. If the sum of all signals exceeds the LED2 threshold of 10-30 MeV (depending on the beamtime), the multiplicity is

[8]CAMAC: Computer Automated Measurement and Control; a standard bus and modular-crate electronics standard.

[9]NIM: Nuclear Instrumentation Module; defines mechanical and electrical specifications for electronics modules.

increased by an integer number. Hits in TAPS contribute in the same way to the multiplicity if the signal of at least one crystal in one of six sectors (see sections of different color in Figure 2.13) is above the LED1 threshold of 35-45 MeV. As these criteria are only a rough estimate, the multiplicity trigger has to be chosen very carefully.
As listed in Tables 2.5 and 2.6, the multiplicity trigger of the beamtimes in December 2007 and May 2009 was set to M2+, and in the February 2009 beamtime to M3+. This means that the multiplicity has to be at least two (M2+) or three (M3+) in order to fulfill the trigger condition. In addition, events where the multiplicity condition was fulfilled by the multiplicity of the TAPS detector alone were rejected. The reason for this multiplicity setting is that the goal of the beamtime was the measurement of photoproduction of η mesons that decay either into two photons or via three pions into six photons. In order to have enough statistics for the decay into two photons, a multiplicity of at least two is required. The multiplicity of three in the second beamtime was chosen in order to improve the statistics for the decay into six photons. For this work, this had the consequence that single π^0 photoproduction could only be measured with two of the three beamtimes. However, for the May 2009 beamtime the TAPS M2 condition was added to the first level trigger. This allows for the detection of π^0 mesons going in the forward direction, whose two decay photons produce two clusters in TAPS and would not exceed the Crystal Ball energy sum threshold. However, for this work, in order to ensure comparability between the three beamtimes, events that fulfil this condition were not (yet) considered.
The rather high Crystal Ball energy sum threshold of 300 MeV, which is far above the quasi-free π^0 production threshold of roughly 140 MeV, lowers the statistics at low energies and requires a dedicated consideration in the analysis (see Section 6.6.2). The production threshold of double π^0 photoproduction from quasi-free nucleons of roughly 290 MeV is just below the Crystal Ball energy threshold and affects the data to a lower extent.

2.3.3 Trigger System since October 2012

One year before the first of three beamtimes on a polarized deuterated butanol target used for this work, the trigger system was upgraded with the aim to speed up the data acquisition. The successful replacement of the old trigger electronics with a new FPGA logic effectively led to a four times faster data acquisition. In addition, the number of readout CPUs was doubled and the readout strategy was optimized. The upgrade began in October 2012 and was done in several steps until the end of 2014. However, until the first deuterated butanol beamtime, the new electronics were successfully tested. More detailed information about the new trigger system can be found in [109].
The multiplicity trigger condition for the deuterated butanol beamtimes was fixed by the reaction channels of interest. As the goal of these experiments was the measurement of the double polarization observable E in η, and $2\pi^0$ photoproduction with either two ($\eta \rightarrow 2\gamma$), four ($2\pi^0 \rightarrow 4\gamma$) or six photons ($\eta \rightarrow 6\gamma$) in the final state, the

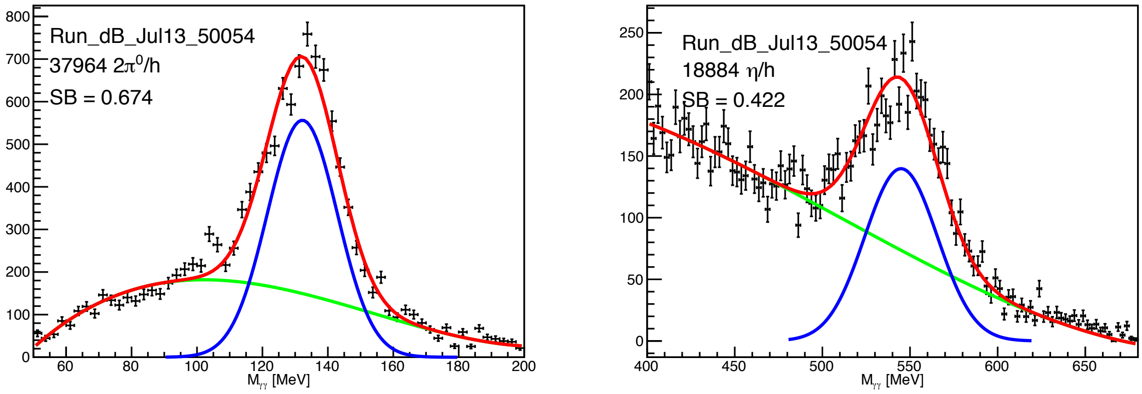

Figure 2.14: Representative result of the count rate measurement of the July 2013 beamtime with the final trigger settings at a current of 8.1 nA. Left-hand side: measured number of $2\pi^0$ events per hour. Right-hand side: measured number of $\eta \to 2\gamma$ events per hour. The reactions were measured inclusively (without the requirement of the detection of the recoil nucleon). The number of events per hour and the signal to background ratio (SB) are indicated in each figure. Black crosses: data with statistical errors. Solid curves: fit results. Blue: Gaussian for the signal. Green: polynomial for the background. Red: sum of Gaussian and polynomial.

multiplicity condition at least had to be two. Otherwise the decay of the η meson into two photons could not be measured.
The decision about the threshold of the CB energy sum trigger evolved during the count rate measurement on the first day of the July 2013 beamtime. Using a preliminary analysis and a preliminary calibration, the number of η and $2\pi^0$ mesons per hour were counted. According to the measured count rate, a beam current of 8.1 nA, a multiplicity condition of M2+ (not to be fulfilled by the TAPS detector alone) and a Crystal Ball energy sum threshold of $\sim$ 250 MeV resulted in the highest production rate and the most stable data acquisition. A representative example of the count rate investigation is shown in Figure 2.14. For the February 2014 and March 2015 beamtimes, the experimental trigger conditions were resumed, but due to the ongoing data acquisition upgrade, the beam current had to be adapted. The beam current could be increased accordingly during the different beamtimes due to the faster data acquisition and handling of higher rates. Figure 2.15 shows the result of the count rate measurement from the March 2015 beamtime under the trigger conditions from the July 2013 beamtime, but with a current of 10 nA instead of 8.1 nA. The higher production rate resulting from the final upgrade of the data acquisition is clearly visible.

The same trigger was applied to the carbon beamtime in order to allow for the best possible estimation of the unpolarized background in the deuterated butanol data.
The applied trigger conditions were a CB energy sum threshold of 250 MeV on the first level and a multiplicity of at least two on the second level. Events with

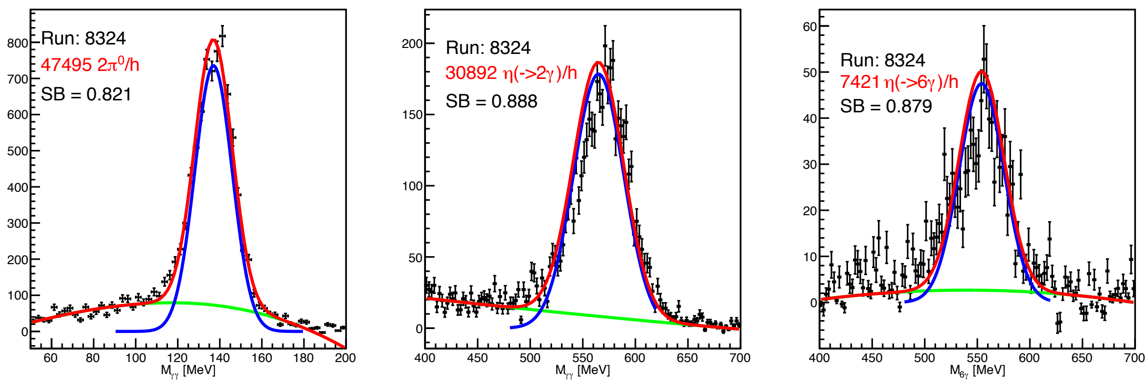

Figure 2.15: Representative result of the count rate measurement of the March 2015 beamtime with the same trigger settings as in July 2013 but at a current of 10 nA. Left-hand side: measured number of $2\pi^0$ events per hour. Middle: measured number of $\eta \rightarrow 2\gamma$ events per hour. Right-hand side: measured number of $\eta \rightarrow 6\gamma$ events per hour. The reactions were measured inclusively (without the requirement of the detection of the recoil nucleon). The number of events per hour and the signal to background ratio (SB) are indicated in each figure. Black crosses: data with statistical errors. Solid curves: fit results. Blue: Gaussian for the signal. Green: polynomial for the background. Red: sum of Gaussian and polynomial.

multiplicity two from TAPS alone were not accepted.

2.4 The Electron Accelerator Facility ELSA

The ELSA electron accelerator facility [111–115] produces an electron beam of relativistic energies up to 3.5 GeV. Unpolarized or polarized electrons are accelerated in the 2.5 GeV synchrotron to energies of up to 1.6 GeV and are then injected into the storage ring where they reach their final energy before they are extracted to the experimental areas. Electron beams of up to 80 % polarization and currents of up to 100 nA, depending on the operational mode of the accelerator, can be achieved.

2.4.1 The Electron Gun and the Injector Linac

In 1953, the construction of the first accelerator at the University of Bonn, a 500 MeV synchrotron, started and came into operation in 1958. As in the early times at MAMI, the electrons were produced by thermal emission at the cathode of the electron gun and were then pre-accelerated by a van de Graaff accelerator to a beam energy of 3 MeV, before being injected into the synchrotron. After five years of successful operation and experiments, a new and more powerful 2.5 GeV synchrotron was developed and launched in 1967. The van de Graaff accelerator was then replaced by a linear accelerator, which delivers a pulsed 25 MeV beam with a current of 250 mA and an energy spread of $\pm$ 0.5 % [115]. In the meantime, two linear accelerators

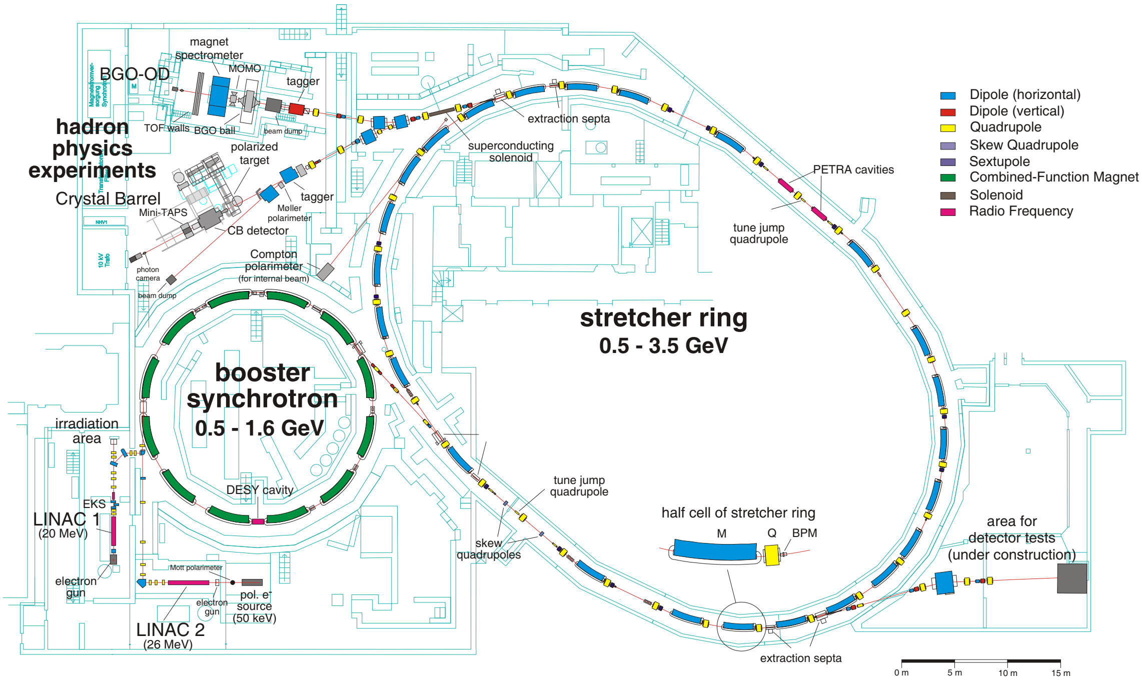

Figure 2.16: Floorplan of the Electron Stretcher Facility ELSA in Bonn, Germany. It shows the polarized and unpolarized electron sources with the pre-accelerator linacs (bottom left), the injector (booster) synchrotron (middle left), the storage ring (right) and the hadron physics experimental sites (top left). Figure taken from [86].

serve as injectors. Polarized electrons are pre-accelerated to energies of 26 MeV with LINAC 2 and unpolarized electrons to energies of 20 MeV with LINAC 1 (see bottom left of Figure 2.16).

2.4.2 The 2.5 GeV Synchrotron

The 2.5 GeV Synchrotron is a synchrotron with 50 Hz repetition rate. It has a radius of 7.65 m and accelerates electrons to a maximum energy of 2.3 GeV at a maximum magnetic field of 1.003 T. It consists of 12 combined function bending magnets that are based on a $O/2$-FD-$O/2$ lattice[10] [111]. As the orbit of a synchrotron is constant, the magnetic field has to be increased in order to achieve an acceleration. Hence, the 25 MeV electrons are injected at a field of about 0.01 T. Two cylindrical radio frequency cavity resonators then perform the acceleration. The maximum circulating beam intensity is about $15{\cdot}10^{12}$ electrons/s, of which about 60 % can be ejected with spill times of up to 1 ms.

[10] O: *nothing*, F: *focussing*, D: *defocussing*, numbers stand for unit lengths, i.e. $O/2$-FD-$O/2$ = half a unit no magnet, then one unit of a focussing magnet, one of a defocussing magnet and again half a unit no magnet. See Figure 2.16 for a better understanding.

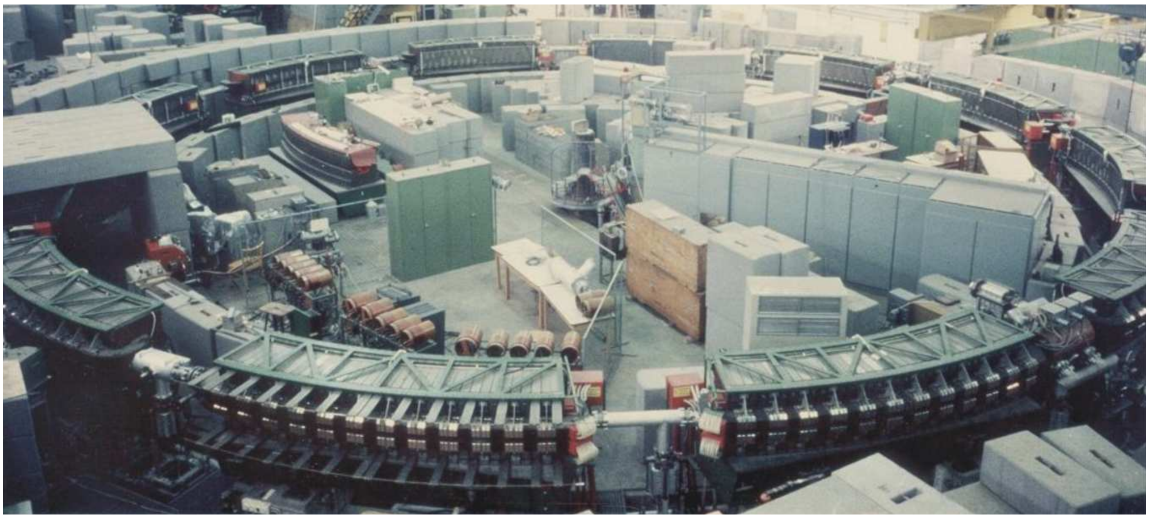

Figure 2.17: The 2.5 GeV synchrotron at ELSA in Bonn. Figure taken from [115].

2.4.3 The 3.5 GeV ELSA Stretcher Ring

The ELSA stretcher ring was commissioned in 1988 in order to solve the limits that came from the low duty factor of the pulsed synchrotron of roughly 5 %. The ELSA stretcher ring is located in a separate tunnel system and the synchrotron is used to inject the electron beam with an energy of 1.6 GeV into the stretcher ring. The electron stretcher is a separated function machine based on the standard *FODO*[11] type, which has the advantage of lower radiation losses as it is indispensable for storage rings.
ELSA can either be operated in the *stretcher mode*, the *post accelerator mode*, or in the *storage mode*:

stretcher mode: single pulses from the synchrotron are injected at the maximum rate of 50 Hz. An external beam of constant intensity is achieved, but the energy is limited to the maximum synchrotron energy of 1.6 GeV.

post accelerator mode: several pulses of the synchrotron are injected and the accumulated beam is post accelerated to the maximum possible energy of 3.5 GeV. This mode is limited by the dipole magnet power supply and the radio frequency generated acceleration voltage.

storage mode: a large number of pulses from the synchrotron are injected and stored for several hours (1-2 hours at standard operation settings of 2.3 GeV and 50 mA). In this mode, ELSA is used as a synchrotron radiation source.

For the data extracted in this work, the accelerator was operated in the post accelerator mode at a maximum electron beam energy of 2.35 GeV.

[11]FODO: one unit of a focussing magnet, one unit of no magnet, one unit of a defocussing magnet, one unit of no magnet

2.5 The CBELSA/TAPS Experimental Setup

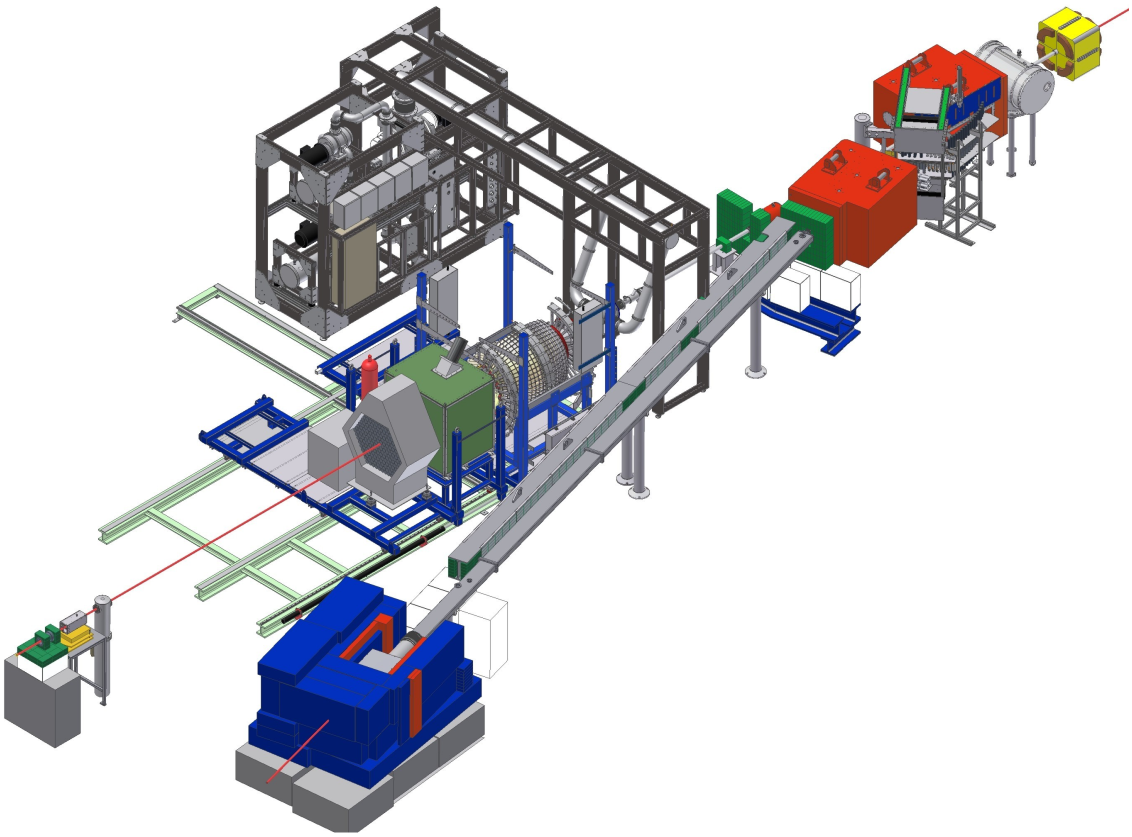

Figure 2.18: Schematic illustration of the CBELSA/TAPS experimental setup. The electron beam (red line, upper right) impinges on the radiator in the tagging spectrometer (red block, upper right) and produces a beam of bremsstrahlung photons. The electrons that did not interact with the radiator are deflected into the beam dump (blue block, bottom left). The photon beam impinges onto the target which is surrounded by the detector system, which mainly comprises of the Crystal Barrel detector (central calorimeter), the Cherenkov detector (green block in the center) and the MiniTAPS detector (gray, hexagonal block next to the Cherenkov detector). Figure taken from [86].

The CBELSA/TAPS experiment is located in the synchrotron hall of the Physical Institute in Bonn (see upper left part of Figure 2.16, labeled with "Crystal Barrel"). As the A2 experiment at MAMI, it is designed for photoproduction experiments in order to investigate the structure of the nucleon. Hence, the main principle and components of the setup are identical. Real photons are produced by bremsstrahlung of the electron beam on a thin radiator foil and then impinge on the target. The scattered electrons are detected in the focal plane of a tagging spectrometer and the remaining electron beam is deflected into a beam dump. The unpolarized or polarized target is surrounded by a calorimeter covering a large amount of the solid angle, a second calorimeter acts as forward wall, and plastic scintillator components serve as charged particle identification detectors. For all the experiments used in this work, except for the one using the hydrogen target, a Cherenkov detector was placed as charged particle veto between the main calorimeter and the forward wall. In contrast to the experiment at MAMI, this was necessary due to the high amount of electromagnetic background in the forward direction. At MAMI this background is reliably suppressed to a great extent by the Crystal Ball energy sum threshold, which is part of the first level trigger.

2.5.1 The Photon Tagging Spectrometer

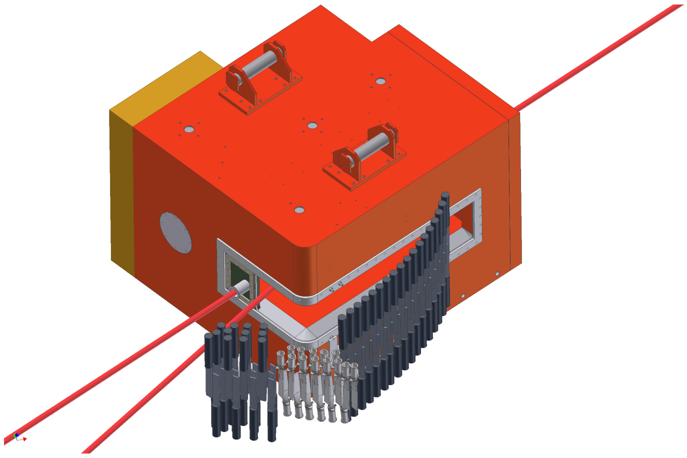

Figure 2.19: Schematic illustration of the photon tagging spectrometer at the CBELSA/TAPS experiment at ELSA. Figure taken from [116].

The photon tagging spectrometer [117] at the CBELSA/TAPS experiment at ELSA is similar to the Glasgow photon tagging spectrometer of the A2 experiment. The main difference is that at CBELSA/TAPS, in addition to plastic scintillators, scintillating fibers are used in order to increase the energy resolution at low photon energies.
The tagging spectrometer mainly consists of 96 EJ-204 and NE-104[12] partly overlapping plastic scintillator bars that are connected to Hamamatsu R13P8HA PMTs. These tagger bars covers 2.1 % to 82.5 % of the full beam energy range and have a relative energy resolution of 0.1 % - 6 %. In order to ensure a constant energy resolution, the width of the bars varies from 1.4 cm at the location of high electron energies to 5 cm at low electron energies. An additional improvement due to the poor energy resolution at high electron energies is the installation of 480 scintillating fibers[13], 2 mm in diameter and 6 cm in length, in the range of 16.6 % - 87 % of the electron beam energy. They have an energy resolution of 0.1 % - 0.4 % and are

[12] plastic scintillators from an older tagging spectrometer implemented in the present one
[13] of material Kuaray SCSF-78MJ

grouped to modules of 16 fibers arranged in two layers. Every module is read out by a 16-channel Hamamatsu H6568 PMT. The electrons are deflected in the 2 T magnetic field of a dipole magnet, which is operated at 1500 A. Table A.1 summarizes the physical properties of the scintillators used in the tagging spectrometer.

2.5.2 The Crystal Barrel Detector

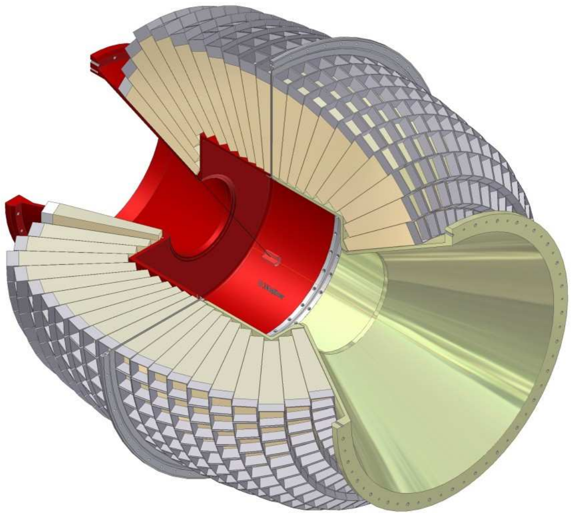

Figure 2.20: Schematic illustration of the Crystal Barrel calorimeter at the CBELSA/TAPS experiment at ELSA. Figure taken from [118].

The Crystal Barrel [119] is a calorimeter made of 1230 thallium doped caesium iodide (CsI(Tl)) crystals, each 30 cm length, corresponding to 16.1 radiation lengths (see Table A.1 for more physical properties of the CsI(Tl) crystals). Compared to the NaI(Tl) crystals used in the Crystal Ball detector at the A2 experiment, the CsI(Tl) crystals have the advantage that they have a shorter radiation length, are less hygroscopic, and are easier to handle. On the other side, the caesium iodide crystals have a longer decay time and a smaller light output [120].
The crystals are arranged in 21 rings, forming a barrel that surrounds the target (see Figure 2.20). Each ring covers 6° in polar angle θ and consists of 60 crystals of 6° in azimuthal angle ϕ. The last ring in backward direction consists only of 30 crystals, each covering 12° in azimuthal angle. Hence, the full calorimeter covers polar angles from $30° < \theta < 156°$ and the full azimuthal range. The crystals are read out by Hamamatsu S2575 PIN photodiodes. For its protection from humidity and mechanical damage, every crystal is wrapped in a 100 μm titanium envelope. An additional kapton foil serves as electric isolation.

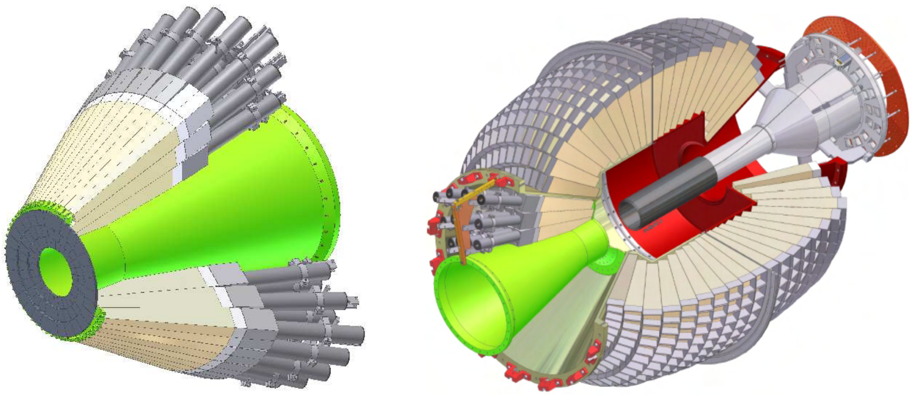

Figure 2.21: Schematic illustration of the Forward Cone (left) and when installed inside the Crystal Barrel detector (right). Figures taken from [118, 121].

2.5.3 The Forward Cone Detector

The Forward Cone[14] detector [121, 122] was designed as an extension of the Crystal Barrel detector in order to increase the angular coverage of the trigger in the forward direction. It is installed in the front-side opening of the Crystal Barrel detector (see Figure 2.21) and is made of 90 of the original crystals of the Crystal Barrel. The crystals are arranged in three rings and are, due to their holding structure, not precisely aligned with the target center, but shifted by 3 cm in forward direction. It covers polar angles from $11.2° < \theta < 27.5°$.

The Forward Cone detector is of special importance, since the rate in the forward direction is very high. Due to the high rate, it is inevitable to have detectors at forward angles that can be included in the first level trigger. For this reason, the readout device of the caesium iodide crystals of the Forward Cone detector has been changed from photodiodes to Hamamatsu H6568Mod4 PMTs. Additionally, 180 Bicron BC-408 plastic scintillators are mounted in front of the crystals and allow for the identification of charged particles. The plastic scintillators are installed in two layers resulting in a polar and azimuthal resolution of 6°. The plastic scintillators are read out by the same type of PMTs that are used for the readout of the crystals.

2.5.4 The Inner Detector

Inside the Crystal Barrel detector, the target is surrounded by the Inner detector [123] that serves as charged particle identification detector. It is made of three layers of in total 513 scintillating Bicron BCF-12 fibers of 2 mm diameter (see Figure 2.22). The center of the detector is shifted by 5.1 cm with respect to the target center. The outer layer consists of 191 fibers and has a radius of 6.45 cm, the middle layer of 165 fibers and radius 6.13 cm, and the inner layer of 157 fibers and a radius of 5.81 cm. The outer layer is arranged in the beam direction, the middle layer is rotated

[14] also called Forward Plug

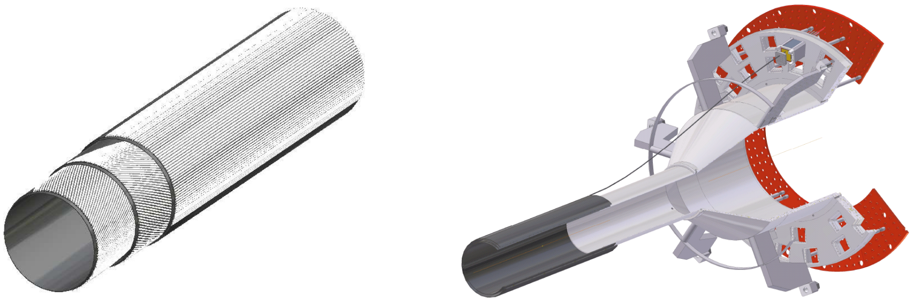

Figure 2.22: Schematic illustration of the Inner Detector (right) and of its three layers of fibers (left). Figures taken from [118].

by 25.7°, and the inner by -24.5° with respect to the outer layer. With this setup, an interaction point of a particle with the detector can be determined distinctly even if only two of three fibers received a signal. The sensitive region of every fiber ranges over 40 cm. The whole detector covers a polar region from $23.1° < \theta < 166.0°$. In the backward direction, the fibers are connected to lightguides, which transport the signals to 16-channel Hamamatsu H6568 PMTs.

2.5.5 The MiniTAPS and Veto Detectors

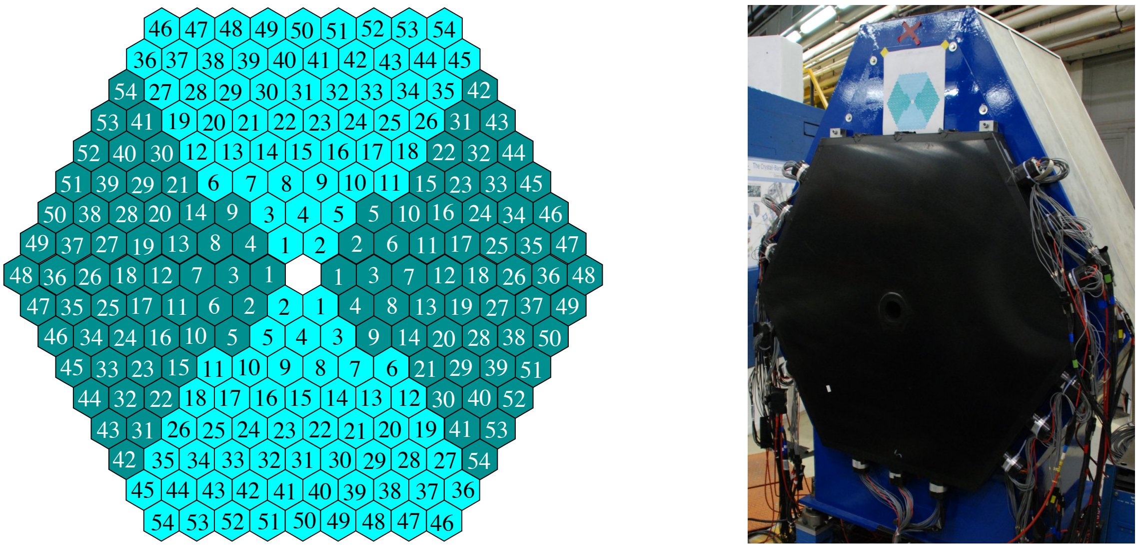

Figure 2.23: Photograph of the MiniTAPS detector (right) and its crystal layout (left). The four different colored sections, referred to as sectors, show the logical groups of crystals used for the trigger. Figure adapted from [124], photograph taken from [118].

The MiniTAPS detector at the CBELSA/TAPS experiment at ELSA (see Figure 2.23) is a small version of the TAPS detector at MAMI. Due to the usage of the Gas Cherenkov Detector (see Section 2.5.6) which is located between the Crystal Barrel detector and MiniTAPS (see Figure 2.24), its distance of 2.1 m to the target center is somewhat larger as at the A2 setup (1.5 m). It consists of 216 BaF_2 crystals of the same dimension and of the identical readout as for the TAPS detector at MAMI. The crystals are also arranged as a hexagonal forward wall. Due to the smaller size of MiniTAPS compared to TAPS at MAMI, it only covers polar angles in the range $1° < \theta < 12°$. The veto detectors are identical to the ones used at MAMI as well. Further information is found in Sections 2.2.4 and 2.2.5.

2.5.6 The Gas Cherenkov Detector

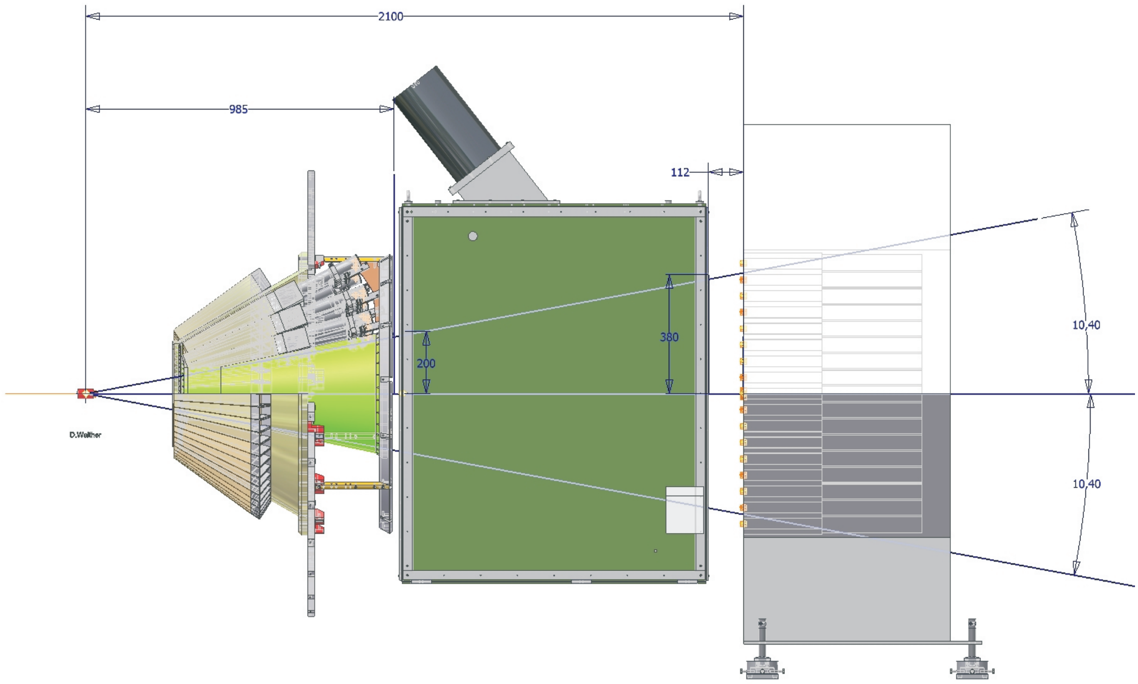

Figure 2.24: The Gas Cherenkov Detector at its place of installation between the Forward Cone Detector and the MiniTAPS Detector. Figure taken from [125].

The Gas Cherenkov Detector is a Cherenkov detector used as threshold detector. Therefore it is only of interest if a particle emitted Cherenkov light or not. Due to its high relativistic momentum, a large amount of the electromagnetic background is emitted at small angles in the forward direction. The first level trigger at the CBELSA/TAPS experiment, to which mainly detectors in the forward direction (Forward Cone and MiniTAPS detector) contribute, would primarily respond to signals from the electromagnetic background. With the choice of a suitable threshold, the electromagnetic background can be identified, rejected, and the fraction of hadronic events increased.

The detector is 100 cm long, has a width and height of 120 cm, and is filled with gaseous carbon dioxide (CO_2). A 3 mm thick and elliptic shaped acrylic glass plate is mounted inside the detector. It's surface is coated with a 200 nm layer of aluminium and a 250 nm thick protection layer of magnesium fluoride (MgF_2) and serves as a mirror. The dimensions and shapes are chosen such that all the Cherenkov light is reflected to one Hamamatsu R1584-03SEL PMT, which is mounted on top of the Cherenkov detector to detect the Cherenkov light emitted by the charged particles.

2.5.7 The Gamma Intensity and Flux Monitor

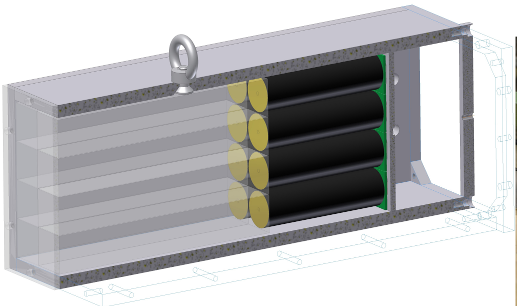

(a) GIM

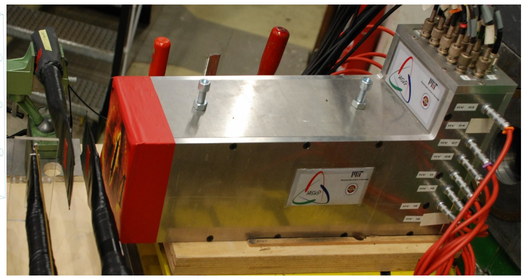

(b) FluMo

Figure 2.25: (a) The Gamma Intensity Monitor (GIM). (b) The Flux Monitor (FluMo). Figure taken from [118].

The Gamma Intensity Monitor (GIM, see Figure 2.25a) is the last detector and is located immediately in front of the beam absorber. It is used to detect the photons that did not interact with the target and thus allows for the determination of the photon flux (see Section 6.10.2). Therefore its efficiency of detecting photons should be as high as possible. The dominating interaction process at energies above 10 MeV is pair production with a cross section proportional to the square of the atomic number Z^2. For this reason, the GIM consists of 16 lead fluoride (PbF_2) crystals that are read out by Photonix XP2900 PMTs. It is worth mentioning that lead fluoride is not a scintillator and therefore, the PMTs do not detect scintillation but Cherenkov light. An additional advantage of the lead fluoride crystals is their very short decay times. Hence, saturation does not occur until rates of 4.2 MHz. However, the electronics are the limiting factor of the setting, not the crystals. Due to the deadtime of the discriminators, saturation already occurs at lower rates [118].

To ensure an exact flux determination at high rates, as present during standard data taking, another detector, the Flux Monitor (FluMo, see Figure 2.25b) [126] is used. In contrast to the GIM, the FluMo does not detect every photon, but a known fraction. The FluMo consists of a thin conversion target in which the incoming photons convert to an electron positron pair. These electrons, as well as the scattered Compton electrons, are then detected in coincidence by two plastic scintillators. An additional plastic scintillator serves as veto detector to reduce background events and is mounted in front of the FluMo.

Detector	Device
Tagging Spectrometer (bars)	TDC, ADC, Scaler
Tagging Spectrometer (fibers)	TDC, Scaler
Crystal Barrel (CsI(Tl)-crystals)	ADC
Forward Cone	TDC, ADC
Inner Detector	TDC
TAPS (BaF_2-crystals)	TDC, ADC
TAPS (Veto)	TDC, ADC
Cherenkov	TDC, ADC
Gamma Intensity Monitor	TDC, ADC
Flux Monitor	TDC, ADC

Table 2.3: Overview of the different devices that are used to readout the individual detector components used for this work at the CBELSA/TAPS experiment at ELSA.

2.6 Data Acquisition at the CBELSA/TAPS Experiment

2.6.1 Readout of the Detector Components

Table 2.3 summarizes the devices that are available for the readout of the individual detector components used for the CBELSA/TAPS experiments at ELSA in this work. The readout of the detectors that contribute to the trigger system are discussed in the following paragraphs.

The Tagging Spectrometer

A passive splitter splits the analog signals from the tagger bars into two components. One of them is sent to a LED that is used to start the time measurement by the CATCH TDC and to check for coincidence between two adjacent bars. A scaler counts the coincidences. The other analog signal is led to an ADC in order to get the energy information.
Coincidence or energy information of the tagger fibers are not used, as they are not part of the trigger. The analog signal of the PMT is sent to a discriminator and then to a CATCH TDC to start the time measurement and the scaler.

The Crystal Barrel Detector

The crystal readout was realized with Hamamatsu S2575 PIN photodiodes that are connected to the backside of the crystal by wavelength shifters. As the photodiode does not have any intrinsic gain, a charge sensitive preamplifier with a rise time of 10-15 μs and a decay time of more than 100 μs was used. A pulse shaper transforms the signal into a 6 μs long pulse that is then digitized by an ADC. Due to the enormously long rise time of the pulses, a time measurement with discriminators is not reasonable and hence the calorimeter could not be included in the first level trigger. Instead, the multiplicity of the hits in the calorimeter (above a threshold of 15-20 MeV) is determined by a Fast Cluster Encoder (FACE) [127] and is used in a second level trigger. With this information, events of no interest can be rejected and the deadtime can be reduced from 1 ms to less than 1 μs.

The Forward Cone Detector

The signals of the photomultipliers of the Forward Cone are led to LED modules with adjustable threshold values. If the signal of a PMT is above the corresponding threshold of $\sim$ 30MeV, the signal is sent to start the CATCH TDCs. The analog signals of the photomultiplier tubes is digitized by charge sensitive FASTBUS-ADC's. As they are placed 50 m apart in a different experimental hall, the signals first need to be prepared by using drivers and shapers [128]. As the Forward Cone is included in the first level trigger, the number of detected particles has to be estimated from the number of signals received by the PMTs. This is realized by mapping the hit distribution of the crystals to pregenerated distributions, where every defined distribution corresponds to a certain multiplicity. The Cluster Finder algorithm [122] performs this mapping within 70 ns and then sends the corresponding multiplicity to the trigger system.

The Inner Detector

The PMT signals of the 513 lightguides of the Inner Detector are led to discriminators, which check whether the signal is above a certain threshold (corresponding to electronic noise) and then generates a digital signal of suitable length, which is sent to the CATCH TDCs. For every layer, an additional window discriminator checks if the sum of the discriminator signals of the layer is above a certain threshold, corresponding to a certain number of hits. The logical signals of those three discriminators is then sent to the trigger system. The hits of two of the three layers can then be used for the trigger signal.

The MiniTAPS and Veto Detectors

The readout and digitalization of the MiniTAPS and veto detectors are identical to the A2 standard, more information may be found in Section 2.3.1.

The Gas Cherenkov Detector

The readout of the Gas Cherenkov Detector is integrated into the readout of the Forward Cone (see Section 2.6.1) and also available in the common data acquisition. The amplified signal of the PMT is led to a discriminator, which sends a logical signal to the trigger system and starts the CATCH TDC. In order to reject events from electromagnetic background as soon as they have been noticed by the PMT, the Cherenkov Detector is included in the first level trigger where the signal contributes as veto decision. If the first level trigger receives a signal from the Cherenkov Detector, the event will be rejected. Therefore, it is important that the Cherenkov signal is the first signal in the trigger and that it lasts long enough in order to cover all the successive signals.

2.6.2 Trigger System

At the CBELSA/TAPS experiment at ELSA, the detectors that can contribute to the first level trigger are the tagger, the Inner Detector, the Forward Cone Detector, and the Cherenkov Detector. As the readout of the photodiodes of the caesium iodide crystals of the Crystal Barrel detector is too slow (see Section 2.6.1), it is only part of the second level trigger. Furthermore, only the estimate of the hit multiplicity as determined from the FACE goes into the second level trigger decision. Hence, the complete trigger system depends on multiplicities of the different detectors, i.e. on the number of detected particles. Constraints on the type of detected particle can only be made by considering information about the charge, either with the requirement of a hit in the Cherenkov or a hit in the Inner Detector.

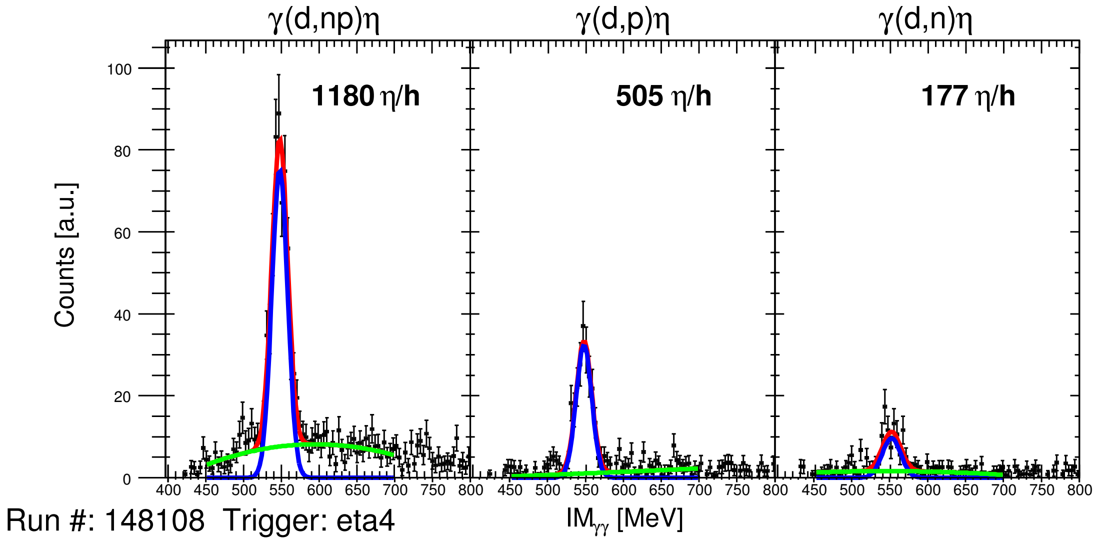

Figure 2.26: Representative result of the count rate measurement of the January 2011 beamtime with the final trigger settings at a current of 0.6 nA. Left-hand side: measured number of inclusive η events per hour. Middle: measured number of exclusive $\eta \rightarrow 6\gamma$ events on the proton per hour. Right-hand side: measured number of exclusive $\eta \rightarrow 6\gamma$ events on the neutron per hour. The reactions were measured inclusively (without the requirement of the detection of the recoil nucleon). The number of events per hour and the signal to background ratio (SB) are indicated in each figure. Black crosses: data with statistical errors. Solid curves: fit results. Blue: Gaussian for the signal. Green: polynomial for the background. Red: sum of Gaussian and polynomial.

As at MAMI, the trigger for the experiments at the CBELSA/TAPS experiment had to be optimized for η and $2\pi^0$ photoproduction (the latter reaction channel has only been considered for the trigger decision of the experiment with the polarized target) from polarized protons and neutrons. The experiments on the unpolarized liquid hydrogen and deuterium targets were carried out in the framework of another work. For analysis purposes, a trigger was chosen that only depends on the detection of photons. For this reason, it was clear that the Inner Detector, which only detects charged particles, should not contribute to the trigger. As a consequence, the full trigger comprises decisions on the multiplicity. Information about energy, i.e. the sum of the deposited energies in the Crystal Barrel, can not be included.

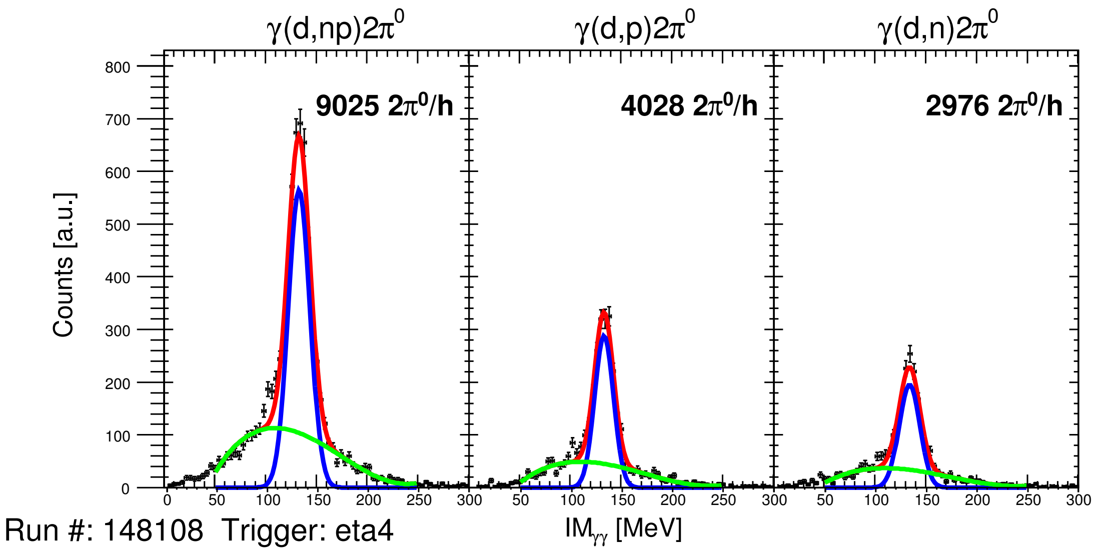

Figure 2.27: Representative result of the count rate measurement of January 2011 beamtime with the final trigger settings at a current of 0.6 nA. Left-hand side: measured number of inclusive $2\pi^0$ events per hour. Middle: measured number of exclusive $2\pi^0$ events on the proton per hour. Right-hand side: measured number of exclusive $2\pi^0$ events on the neutron per hour. The reactions were measured inclusively (without the requirement of the detection of the recoil nucleon). The number of events per hour and the signal to background ratio (SB) is indicated in each figure. Black crosses: data with statistical errors. Solid curves: fit results. Blue: gaussian for the signal. Green: polynomial for the background. Red: sum of Gaussian and polynomial.

Under these conditions, the ideal trigger conditions for the reactions with quasi-free production thresholds of about 290 MeV ($2\pi^0$) and 630 MeV (η) and the detection of two, four or six photons was not easy to find. Due to the electromagnetic background it was rather clear for the experiments with a polarized target, that the η decay into two photons had to be omitted in order to preserve a reasonable rate. Furthermore, as the polarized target has to be maintained with a holding coil, the magnetic field fans out the electromagnetic showers of the beam in the forward direction and yields a very high rate in the MiniTAPS detector. To avoid that in the forward direction, mainly the electromagnetic background contributes to the trigger, the Cherenkov Detector had to be used as a veto and the LED thresholds of the

trig42c		eta3	
1st level	FACE	1st level	FACE
Inner & Tagger & !C	≥ 2	Taps1 & Tagger & !C	≥ 2
CF1 & Tagger & !C	≥ 1	CF2 & Tagger & Taps1 & !C	bypass
CF2 & Tagger & !C	bypass	CF1 & Tagger & Taps1 & !C	≥ 1
CF1 & Taps1 & Tagger & !C	bypass	CF2 & Tagger & !C	≥ 1
Taps1 & Tagger & !C	≥ 1	CF1 & Tagger & !C	≥ 2
Taps3 & Tagger & !C	bypass	Taps3 & Tagger & !C	≥ 1
		Taps3 & Tagger & CF1 & !C	bypass
		Taps3 & Tagger & CF2 & !C	bypass

eta4	
1st level	FACE
Taps1 & Tagger & !C	≥ 3
CF2 & Tagger & Taps1 & !C	≥ 1
CF1 & Tagger & Taps1 & !C	≥ 2
CF2 & Tagger & !C	≥ 2
CF1 & Tagger & !C	≥ 3
Taps3 & Tagger & !C	≥ 2
Taps3 & Tagger & CF1 & !C	≥ 1
Taps3 & Tagger & CF2 & !C	bypass

Table 2.4: Trigger settings used for the beamtimes at ELSA. !C = no hit in the Cherenkov detector, CF1(CF2) = multiplicity 1(2) in the Forward Cone detector, Taps1(Taps3) = multiplicity 1(2) in the MiniTAPS detector. The eta3nc/eta4nc trigger correspond to eta3/eta4 without the !C condition, the eta4ns trigger to the eta4 trigger without the tagger condition and the trig42nc trigger to the trig42c without the inner condition.

two most inner MiniTAPS rings were increased to suppress the high rate. The fanning out of the electromagnetic showers also occurs at the A2 experiment at MAMI. However, the trigger at MAMI does not primarily depend on the forward direction. With the first level trigger decision on the energy sum in the Crystal Ball detector, the electromagnetic background could be drastically suppressed.
An additional modification had to be done, since the tagger contributes to the first level trigger. During the analysis of the data, it is important to know which tagger electron radiated the bremsstrahlung photon that initiated the reaction in the target. As there are, in addition to the prompt electron, a lot of random background hits, these background hits have to be properly subtracted. With the tagger in the trigger, these random tagger hits are affected and hence the background can not be reliably subtracted. For this reason, the tagger was taken out of the trigger decision. However, for the beamtimes of the unpolarized targets, this was not utilized, but no significant difference was observed in the analysis.
The trigger decision for the experiment on the unpolarized hydrogen target was a multiplicity two trigger combined with the Cherenkov detector (no hit condition)

(referred to as "trig42c", see Table 2.4 for the complete trigger list), as this beamtime was primarily designed for single π^0 photoproduction from the free proton. For the liquid deuterium beamtime, several triggers were tested (eta3, eta3nc, eta4, eta4nc, see Table 2.4), but mainly eta3 and eta3nc, corresponding to a multiplicity three trigger with and without the Cherenkov detector (no hit condition), respectively, have been used. For the experiment on deuterated butanol the count rate measurement showed that the best setting was achieved with the Cherenkov detector (no hit condition) on the first level and multiplicity 4 on first and second level combined (eta4ns). A representative result of the count rate measurements is shown for $\eta \rightarrow 6\gamma$ in Figure 2.26 and for $2\pi^0$ in Figure 2.27. A complete list of the trigger settings is given in Table 2.4.

2.7 Polarized Photon Beams

Photon beams can either be linearly or circularly polarized. Linearly polarized photon beams can be produced via coherent bremsstrahlung of unpolarized electrons on a diamond radiator. Circularly polarized photon beams are obtained by the helicity transfer of longitudinally polarized electrons to the radiated bremsstrahlung photons when scattering on a radiator foil. As this work only used circularly polarized photons, background information about linearly polarized photon beams will be omitted. Details can be found in [129].

2.7.1 Circularly Polarized Photon Beams

Circularly polarized photon beams can be achieved by using polarized electron sources, as previously mentioned in Sections 2.1.1 and 2.4.1. A longitudinally polarized electron beam is produced by photoelectron emission on a superlattice photocathode. Whereas at MAMI, the photocathode is a III-V semiconductor of type InGaP/GaAsP [96, 130], at ELSA a Be-InGaAs/Be-AlGaAs crystal [115, 131] is used. The light source used for this photoelectron emission process is a linearly polarized Ti:Sapphire laser, operated at the optimal wavelength of $\sim$830 nm. This process is enhanced by ensuring a negative electron affinity through the additional coverage of the semiconductor surface with a submonolayer of caesium and oxygen. Using a $\lambda/2$ plate, the orientation of the plane of linear polarization of the laser light can be adjusted, and a Pockels cell acts as a $\lambda/4$ plate and transforms the polarization of the laser light from linear to circular. The spin orientation of the electron beam depends on the helicity of the laser light, which is switched from positive to negative at a frequency of about 0.5 Hz. This is important as it guarantees that instrumental asymmetries in the experiment cancel out.

During the acceleration of the polarized beam, the longitudinally oriented spins of the electrons, originally pointing in the beam direction, have to be rotated to point perpendicular to the accelerator plane, in order to avoid depolarization. After the extraction of the beam, a spin rotator is used to rotate the spin back into its original

position. As this process does not necessarily have to be reversible, the Møller measurement, as discussed in Section 2.7.2, is used to determine the remaining degree of longitudinal polarization.
By conservation of spin angular momentum [132], the longitudinally polarized electron beam transfers its helicity to the bremsstrahlung photon, when it is deflected in the Coulomb field of the nuclei in the radiator foil. Forward (or backward) longitudinally polarized electrons produce right (left) circularly polarized photons. What is important for the experimental side is how the polarization from the longitudinally polarized electrons is transferred to the circularly polarized photons. According to the mathematical description of this problem from Olsen and Maximon [133], the polarization transfer is given by

$$P_\gamma = P_{e^-} \cdot \frac{4x - x^2}{4 - 4x + 3x^2} \ , \tag{2.5}$$

where x is the ratio of the energy of the bremsstrahlung photon E_γ and the electron beam energy E_{e^-}, i.e. $x = E_\gamma / E_{e^-}$, and P_{e^-} is the degree of longitudinal polarization of the electron beam. Therefore, with the electron beam energy and electron polarization (see Section 2.7.2) known, the degree of circular polarization of a photon of energy E_γ can be directly calculated. The dependency of the helicity transfer on the ratio of the bremsstrahlung photon and the beam electron is shown in Figure 2.28.

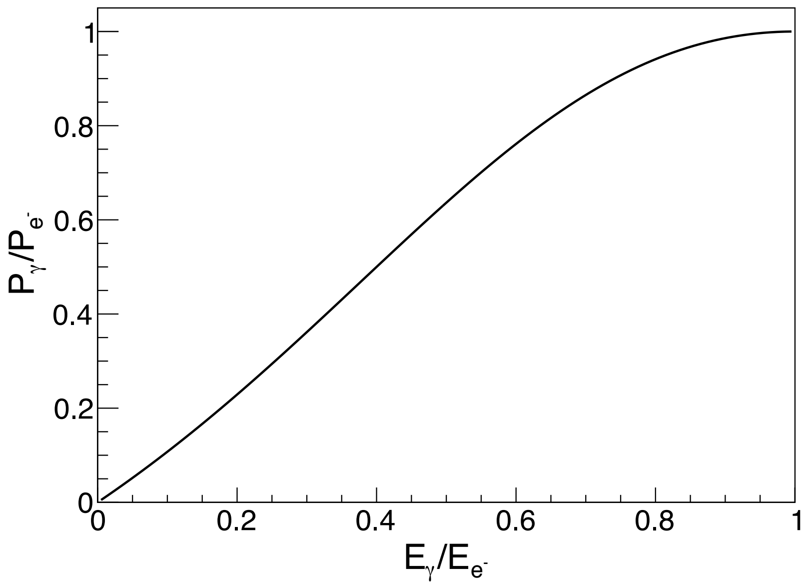

Figure 2.28: Helicity transfer as a function of the energy ratio of beam electron and radiated photon according to Equation (2.5).

2.7.2 The Measurement of the Longitudinal Electron Polarization

Electrons, as leptons, are spin 1/2 particles. From Quantum Mechanics it is known that its z-component, characterized by the quantum number m, can only be in ei-

ther the $m = +1$ or the $m = -1$ state. Furthermore, only the probability that the electron spin is in one of the two states can be measured. If a beam of electrons is *polarized*, it means that it contains a net excess of electrons in one of the two states. The degree of polarization can be determined by observing a reasonable number of electrons that were scattered by a spin-dependent interaction, such as Coulomb scattering from heavy nuclei (Mott scattering[15]), scattering from polarized electrons (Møller scattering[16]), or scattering from polarized photons (Compton scattering).
Due to the continuous acceleration of the electron beam at MAMI, the Mott measurement (right after the electron source) and the Møller measurement (at the end of the beamline) are in good agreement. Due to the better statistical and systematical quality of the Mott measurement, only those results have been used in this work. At ELSA, for energies above 1.32 GeV, due to the fast ramping speed and high periodicity of the accelerating fields, partial depolarization is observed while transferring the beam from the Booster synchrotron to the stretcher ring. Even though this effect can be reduced by applying certain dynamic and harmonic corrections to the accelerator settings, a reliable polarization can only be determined by means of a Møller measurement after the extraction of the beam.

The Mott Measurement at MAMI

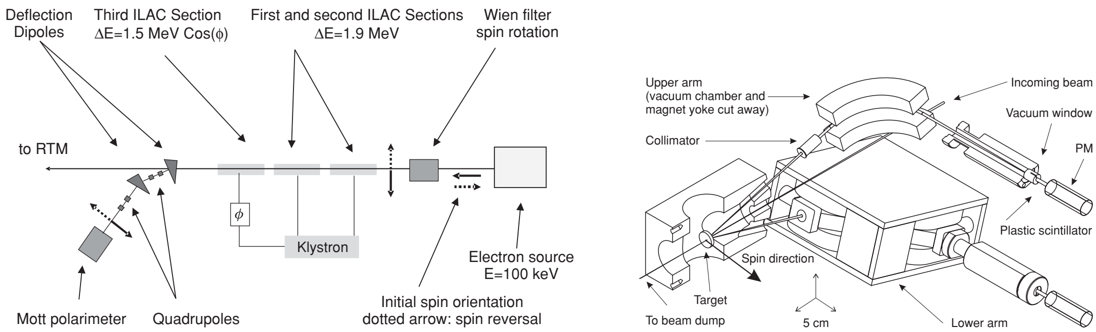

(a) Location of the Mott polarimeter at the MAMI beamline

(b) Illustration of the Mott polarimeter

Figure 2.29: (a) Schematic illustration of the location of the Mott polarimeter at the A2 experiment at MAMI. (b) Schematic layout of the Mott polarimeter. The housing of the upper magnet is removed for a better visibility of the electron trajectory. Figures taken from [134].

The Mott polarimeter (see Figure 2.29) used for the Mott measurement is located behind the injector linac, described in Section 2.1.1 and operates in the energy range between 1.0 and 3.5 MeV and currents of up to 1 μA. As the beam has to be guided into the Mott polarimeter, the measurement, which takes less than one hour, can not be performed during data taking.

[15]Scattering of a pointlike spin-1/2 particle on a pointlike spinless charged particle
[16]Scattering of a pointlike spin-1/2 particle on a pointlike charged spin-1/2 particle

As the Mott cross section is spin-dependent, Mott scattering is an ideal way to separate electrons of the two possible spin states. Depending on the spin, electrons that scatter in the Coulomb field of a heavy nucleus, e.g gold, will either scatter in one or the other direction. The degree of polarization of the beam can then be determined by measuring the asymmetry between the two states.
The Mott polarimeter consists of a series of thin gold foils as the target and two identical detectors placed in a vertical plane at a fixed scattering angle of $\theta = \pm 164°$. It is common to repeat the measurement for all foil thicknesses and then to extrapolate to zero thickness. Thin foils are important in order to minimize multiple scattering. For the Mott measurement, it is necessary that the polarization vector of the electron is perpendicular to the scattering plane, so a Wien filter is used to rotate the vector into the transverse plane [134]. However, a rotation of the vector by an angle of ϕ_{Wien} reduces the measured asymmetry by a factor $A = A_{exp} \sin(\phi_{Wien})$ and has to be accounted for in the calculation of the beam polarization (see Section 6.11).

During the measurement, the countrate in the two detectors (referred to as detectors "1 "and "2") is measured once per second and per direction of the beam polarization (initial transverse polarization: "+", reversed polarization: "-"). This ensures that systematic uncertainties from the two detector arms or foil inhomogeneities cancel out. The measured asymmetry A_{exp} can then be calculated from two successive measurements as follows:

$$A_{\text{exp}} = \frac{1-\sqrt{Q}}{1+\sqrt{Q}} \qquad \text{and} \qquad Q = \frac{1-\sqrt{\frac{R_1^+ R_2^-}{R_1^- R_2^+}}}{1+\sqrt{\frac{R_1^+ R_2^-}{R_1^- R_2^+}}}\ , \tag{2.6}$$

where R_i^j denotes the elastic count rate measured in detector i with the electron beam polarized in direction j. The degree of polarization is then given by the ratio of the measured asymmetry and the analyzing power[17] S_0, which can be calculated theoretically. In order to adapt the theoretically determined analyzing power one in addition has to apply a correction factor depending on the effects of multiple scattering in the target, yielding the effective analyzing power S_{eff}. The degree of longitudinal electron polarization $P_{e^-}^{\text{long}}$ (which corresponds to the measured transversal polarization) is directly proportional to the measured asymmetry and is given by

$$P_{e^-}^{\text{long}} = \frac{A_{\text{exp}}}{S_{\text{eff}}} \tag{2.7}$$

As mentioned in the beginning of this section, the Mott measurement is carried out at very low beam energies below 5 MeV and at very high beam currents of $\sim$1 μA, but has to be applied to the settings used during the experiment, i.e. to energies of 1.5 GeV and low currents of a few nA. It is expected that the degree of polarization of the beam is independent of the beam current. However, at higher beam energies

[17]The analyzing power is called Sherman function and depends on the scattering angle θ, the beam energy E_{e^-} and on the atomic number Z of the material

the polarization vector starts to exhibit a nonzero vertical component. To account for this vertical component, an additional correction factor, depending on the beam energy, has to be applied.

The Møller Measurement

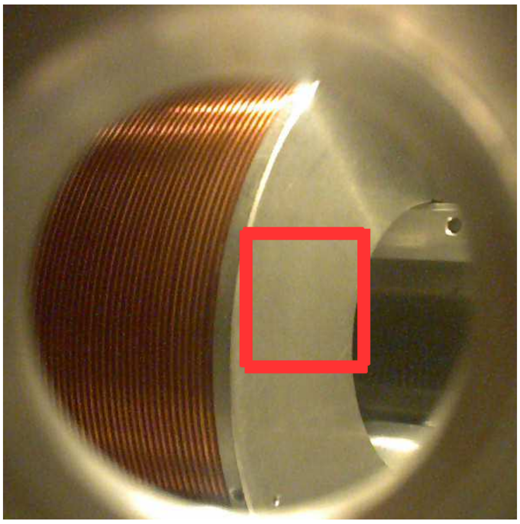

(a) Møller coil

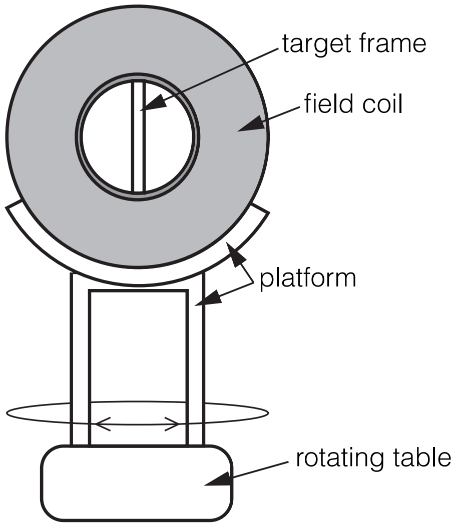

(b) Moeller setup

Figure 2.30: (a) Photograph of the Møller coil at MAMI in beam direction. (b) Schematic illustration of the Møller setup. The setup at the CBELSA/TAPS experiment at ELSA is equivalent. Photograph taken from [135], figure taken from [136].

In the Møller polarimeter [136–138], the polarized electron beam scatters from polarized electrons in the Møller target. The target consists of a 10 μm thick ferromagnetic foil made of Vacoflux, which is tilted by an angle of 20° (25°) at ELSA (MAMI) compared to the beam direction. The target is surrounded by a coil that is used to polarize the target material (in direction of the foil plane) at a magnetic field of ~10 mT. Since only a very small fraction of the target electrons are polarized, the Møller cross section is very low. For this reason, the Møller target can directly be used as a radiator and the beam polarization can be measured online during data taking.
Similarly to the Mott measurement, the asymmetry in the countrate has to be determined in order to determine the beam polarization. At MAMI, the two scattered Møller electrons are detected in the Glasgow photon tagging spectrometer (see Section 2.2.1). At ELSA, an individual Møller detector, consisting of four lead glass detectors, is used. The scattered Møller electrons are then identified with the time and energy information of the detectors. As the helicity of the beam electrons is periodically flipped (see Section 2.7.1), the two possible spin configurations (beam and target electron parallel ($\uparrow\uparrow$) or anti-parallel ($\uparrow\downarrow$)) have to be summed up and the

asymmetry $A = (N^{\uparrow\downarrow} - N^{\uparrow\uparrow})/(N^{\uparrow\downarrow} + N^{\uparrow\uparrow})$ can be calculated. Using the polarization of the Møller target P_T, the angle of the Møller foil α, and the analyzing power a_{zz}, that can be calculated theoretically, the degree of longitudinal beam polarization is given by:

$$P_{e-}^{\text{long}} = \frac{1}{a_{zz} \cdot P_T} \frac{A}{\cos(\alpha)} \ . \tag{2.8}$$

2.8 Unpolarized and Polarized Targets

For the unpolarized data at MAMI and ELSA, a liquid hydrogen (LH_2) and deuterium (LD_2) target [139] and for the polarized data, the Frozen Spin Target, were used. In the next sections, the setup, procedure, and materials of the different targets will be discussed.

2.8.1 The Cryogenic Target

Figure 2.31: Liquid Hydrogen/Deuterium target cell used at the A2 experiment at MAMI. Photograph taken from [139].

At MAMI and ELSA the setup, the materials and the procedure are almost identical. Thus, in the following sections, the cryogenic target will only be explained for the example of the one used at MAMI. The necessary parameters of the target used in Bonn are summarized in Section 2.9.
The cryogenic target consists of five components that form a closed system: the target cell, which is placed in the center of the experimental setup, the gas liquefier, the liquid hydrogen/deuterium supply line, the storage tank of the gas, and the gas compressor. Under running conditions, the target cell is cooled down to approximately 20 K so that about 25 % of the gas is liquified. The temperature and pressure is maintained and is automatically regulated by adding cold liquid or by evaporating the liquid by addition of heat. The cylindrical cell has a diameter of 4 cm and is made of a 125 μm thick Kapton foil (see Figure 2.31). The length can be varied from 3.02±0.03 cm to 4.72±0.05 cm or 10.0±0.1 cm by using different adapters for the beam entrance window of the target. For a better thermal isolation, the target cell is wrapped in eight layers of superisolation foil, each made of 8 μm mylar and 2

μm aluminium and then positioned in a 1 mm thick carbon-fiber reinforced vacuum tube at a vacuum of $3{\cdot}10^{-7}$ mbar.

2.8.2 The Frozen Spin Target

In contrast to unpolarized targets, measurements on polarized nuclei require a much more elaborate target system. In general, every polarized target system follows the same scheme. At first, the yet unpolarized target material has to be cooled down to temperatures below 1 K. It is then placed inside a homogeneous high magnetic field and is exposed to microwave radiation in order to align the spins of the nucleons in the desired direction. Finally, a nuclear magnetic resonance (NMR) measurement allows the determination of the degree of polarization.
Immense improvements concerning cryogenics and magnet technology have been achieved within the last decades, which results in better and more stable conditions and hence, to higher degrees of polarization, as well as longer relaxation times. In the following paragraphs the dedicated components and steps of the polarized target systems used at MAMI [140] and ELSA [141] for the experiments in this work, will be discussed.

Target Material

For the measurement on polarized protons and neutrons, a suitable target has to be chosen. In general, there are two different types of polarized solid state targets: hydrogen rich alcohols (butanol and propandiol) or ammonia and lithium hydrate [142–147]. A suitable target material should not only have the ability to have maximum polarization, it should also have short polarization buildup times, a high hydrogen content, a high relative content of polarizable nucleons (dilution factor), resistance against radiation damage, and reproducible manufacturing. In addition, the dependence of its relaxation time on the temperature and the magnetic field, as well as the absence of polarizable background nuclei, are also important [141, 148].
Using the areal target density n_t, the target polarization P_t, and the dilution factor f, the quality of an external polarized solid state target can be expressed by the figure of merit (FOM) as follows [149]:

$$\mathrm{FOM}_{ext} = n_t \cdot P_t^2 \cdot f^2 \ . \tag{2.9}$$

For measurements on polarized neutrons, usually hydrogen rich materials are chosen and the hydrogen atoms are being replaced by deuterons, e.g. deuterated butanol (C_4D_9OD) lithium deuteride (^{6}LiD), or nitrogen trideuteride (ND_3). Technically, ^{6}LiD provides the highest number of polarizable nucleons, since the lithium nucleus can be considered as an α particle with two additional weakly bound nucleons [152]. As for the deuteron, the spins of the two valence nucleons are essentially parallel and hence, responsible for the polarizability of the lithium nucleus. However, for experiments at medium energies, as the case for photoproduction experiments, the residing nuclear binding effects may contaminate the experimental data. For this reason, organic materials such as alcohols or diols are preferred, although they

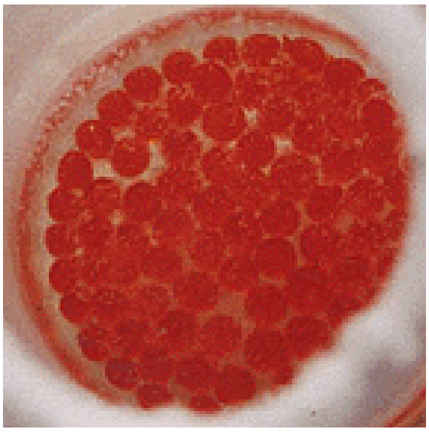

(a) deuterated butanol beads.

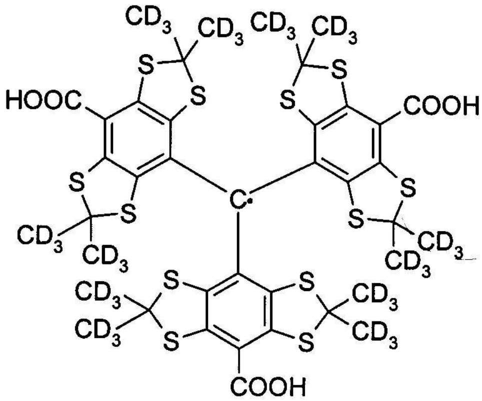

(b) trityl radical *Finland D36.*

Figure 2.32: (a) Photograph of the deuterated butanol target material. (b) Chemical formula of the trityl radical used for the doping of the deuterated butanol target material. Photograph taken from [150], figure taken from [151].

are rather prone to radiation damage and the polarizability of the deuterons in the deuterated materials is limited. Whereas the polarization of the protons in butanol (C_4H_9OH) can reach up to 90 % at a magnetic field of 2.5 T, the maximum polarization of undoped deuterated butanol will not exceed 30-40 % under the same conditions.
At thermal equilibrium, the polarization[18] P of a spin system with spin I and magnetic moment μ under an external magnetic field B and at a temperature T, is given by the *Brillouin Funktion* $\mathscr{B}_I$:

$$P = \frac{< I_z >}{I} = \frac{N(I) - N(-I)}{\sum_{m=-I}^{m=+I} N(m)} = \mathscr{B}_I \left(\frac{\mu B}{2 k_B T} \right) , \tag{2.10}$$

where k_B denotes the Boltzmann constant. Equation (2.10) implies that the maximum polarization is achieved by the largest possible ratio of magnetic energy μB and thermal energy $k_B T$. As the magnetic moment of electrons is about three orders of magnitude higher than the one for protons, almost complete polarization for an electron spin system can already be achieved with a field of a few Tesla and a temperature of about one Kelvin. Under the same conditions, the polarization of a nuclear spin system is less than 1 %.

The improvements in cryogenics and magnet technology over the past years already lead to a rather advantageous ratio, but after all its the method of dynamic nuclear polarization (DNP) [153] that rendered deuteron polarizations in deuterated butanol of more than 60 % possible. At appropriate magnetic fields and temperatures, this technique makes use of microwave induced excitations of coupled electron-nucleus Zeeman transitions to transfer the high electron polarization to the nuclei[19].

[18] in principle, as defined in the following, the polarization is a vector quantity.
[19] a detailed description of the DNP mechanism can be found in [153]

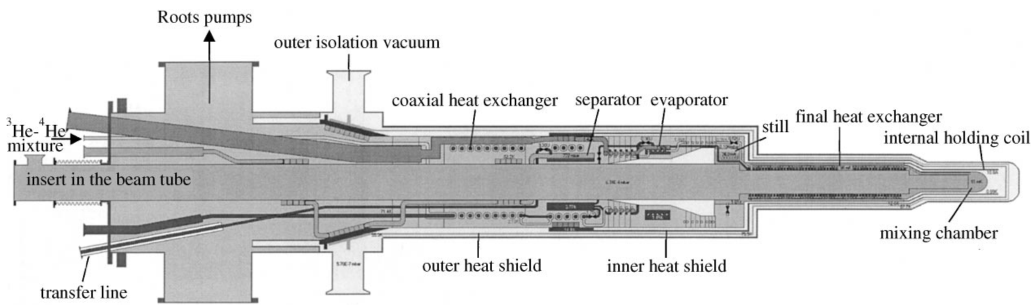

Figure 2.33: Schematic illustration of the ^{3}He/^{4}He dilution refrigerator of the Frozen Spin Target used for the experiments with the deuterated butanol targets at the A2 and CBELSA/TAPS experiments at MAMI and ELSA. Figure taken from [141].

However, this procedure requires the presence of paramagnetic centers in the vicinity of the nuclear spin that otherwise is of a diamagnetic nature. This is achieved by implanting unpaired electrons into the material by either chemical doping or by ionizing radiation. In the case of butanol or deuterated butanol, it was shown that doping with the trityl-radical[20] yields the most desirable results [154].

Deuterium as Neutron Target

The deuteron consists of a proton and a neutron that are bound with a binding energy of 2.225 MeV. While the sum of the magnetic moments of the proton and neutron is $\mu_p + \mu_n = 0.88\mu_k$[21], the magnetic moment of the deuteron is only $\mu_d = 0.857\mu_k$ [151]. Due to this, the spin of the deuteron $S_d = 1$ is not simply given by the addition of the spins of the proton and neutron and neither applies to its magnetic moment. However, the admixture of a state with nonzero orbital angular momentum $L > 0$ can explain this situation. Due to parity conservation, the admixture of a state with $L = 1$, i.e. $^3P_1$, to the ground state is forbidden. The admixture of a state with $L = 2$, i.e. $^3D_1$, is allowed and is shown to solve the puzzle, though it results in a non-spherically symmetric wave function of the deuteron, which affects its magnetic moment. This has to be accounted for when using polarized deuteron targets for experiments on polarized nucleons. Quantum mechanical calculations yield an admixture of the *d*-wave state of 7.35 % [151]. Due to different sources, calculations and experiences, in this work an admixture of $c_{d-wave} = 9\%$ was considered [155]. In order to derive the nucleon polarization P_N from the deuteron polarization, the measured target polarization P_T has to be corrected as follows:

$$P_N = \frac{(100 - c_{d-wave})}{100} \cdot P_T \; . \tag{2.11}$$

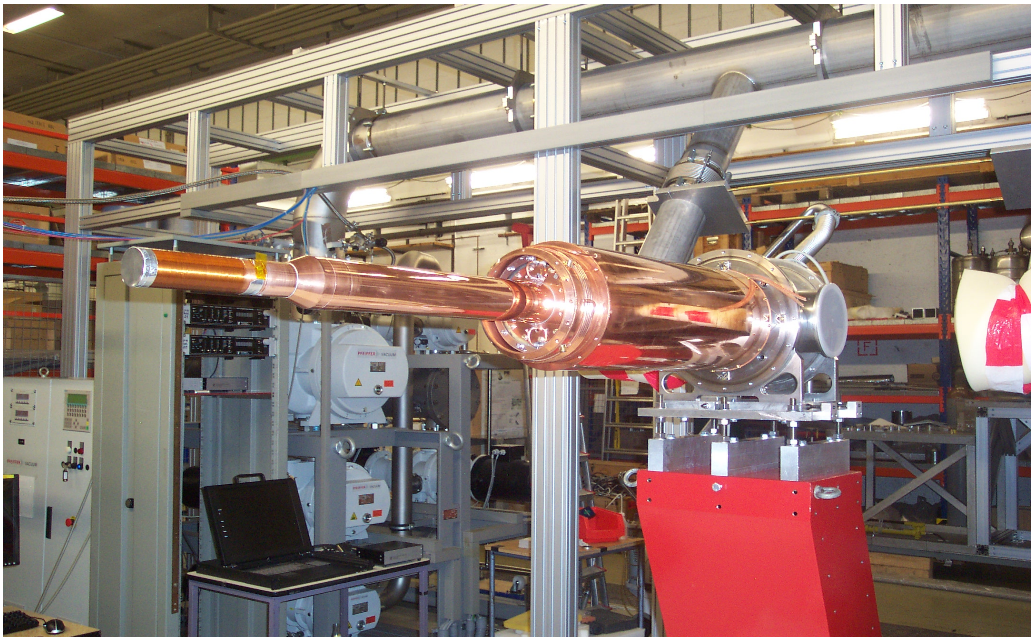

Figure 2.34: Photograph of the dilution refrigerator of the A2 experiment at MAMI. The longitudinal holding coil is mounted on its end (left-hand side of the cryostat). Photograph taken from [156].

The ^{3}He/^{4}He Dilution Refrigerator

As discussed in Section 2.8.2 and resulting from Equation (2.10), the temperature of the target material should be as low as possible in order to allow for a maximum polarization. In former times, the procedure was rather simple: the cryostat was filled with liquid helium, cooled down for four to six hours and then the target was polarized. With the remaining helium reservoir, data taking was possible for about six to twelve hours before the cryostat had to be warmed up, refilled, cooled down, and repolarized. This procedure was very inefficient and a lot of helium was wasted without reaching temperatures below 1 K. Hence, the DNP method was not practicable and relaxation times were short. A lot of developments and improvements finally led to the technique of cooling with the ^{3}He/^{4}He dilution refrigerator [141, 157], which is used in both experiments at MAMI and ELSA.

The ^{3}He/^{4}He dilution refrigerator has a total length of more than 2 m and a diameter of roughly 10 mm in the target area to about 20 cm in the back part. It is installed horizontally along the beam axis. In order to achieve a symmetric distribution of the materials and to minimize influences to the experiment, the cryogenic components are mounted at backward angles and are arranged symmetrically around the beam tube that is the central part of the refrigerator. Several heat shields and isolation vacuums prevent the system from heating up by the thermal heat load from the thermal radiation.

[20] common abbreviation for triphenylmethyl
[21] $\mu_k = e\hbar/2/m_p$ is the nuclear magneton

The main principle of this refrigerator is based on the separation of the liquid and gaseous phases of the $^3He/^4He$ mixture. Below the critical temperature of 0.88 K the mixture spontaneously forms a ^3He-poor phase (dilution phase) and a ^3He-rich phase (concentrated phase). At sufficiently low temperatures, the diluted phase never contains less than 6.6 % ^3He (and 93 % ^4He) while the concentrated phase is nearly entirely made of ^3He. In the mixing chambers (in the target region) the two phases are in thermal equilibrium and are only separated by the phase boundary. The pumping of ^3He from the diluted to the concentrated phase disturbs the thermal equilibrium and lowers the fraction of ^3He in the diluted phase. If the amount of ^3He in the diluted phase falls below the critical fraction of 6.6 %, ^3He from the concentrated phase transfers spontaneously to the dilution phase. This process corresponds to an evaporation of the liquid. The energy that is necessary for the evaporation process is taken from the system, i.e. it is cooled. Theoretically arbitrarily low temperatures can be achieved, as the amount of ^3He falls never below the critical fraction [149]. However, due to the finite temperature of the surrounding materials, the temperature transfer to the target limits the minimum temperature to a few millikelvin such that at CBELSA/TAPS temperatures of 60 mK were reached. At A2, due to the newer cryostat, even lower temperatures of 25 mK are possible.
A cylindrical basket made of teflon[22] contains the target material and is mounted at the end of an insert. Microwave guides, needed for the DNP process, and NMR guides, used for the measurement of the degree of polarization, are also connected to this part. A schematic illustration of the dilution refrigerator is shown in Figure 2.33.

The Polarizing Magnet and the Internal Holding Coil

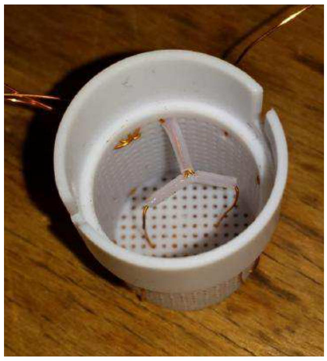

Figure 2.35: NMR coils as used for the measurement of the deuteron polarization. Left-hand side: surface coil (anti-Helmholtz configuration) used for the normal NMR measurements. Right-hand side: in-beam coil, used for the investigation of the polarization inhomogeneities of the experiments within the A2 collaboration. Photographs taken from [158].

The target material is polarized by moving the cryostat into the bore of a super-

[22] common name for PTFE: polytetrafluorethylen

conducting solenoid at a magnetic field of 2.5 T. In this polarization mode, the target is completely enclosed by the magnet in order to provide enough field homogeneity, as required for the DNP method. Due to the size of the magnet, data taking is not possible during the polarization mode. For this reason, it has to be switched to the frozen-spin mode by removing the magnet from the cryostat and placing the target in the isocenter of the detector system for data taking. For an easier, reproducible and faster procedure, the polarizing magnet and the detectors are mounted on a railway system.
Without the superconducting polarization magnet, the nucleon polarization would, depending on the relaxation time, vanish quite fast. To circumvent this problem, a superconducting internal holding coil[23] is installed inside the refrigerator. A temperature of 1.2 K and a field of 0.6 T are sufficient to maintain the nucleon polarization sufficiently high. Figure 2.34 shows a picture of the cryostat and the longitudinal holding coil.

2.8.3 The Measurement of the Target Polarization

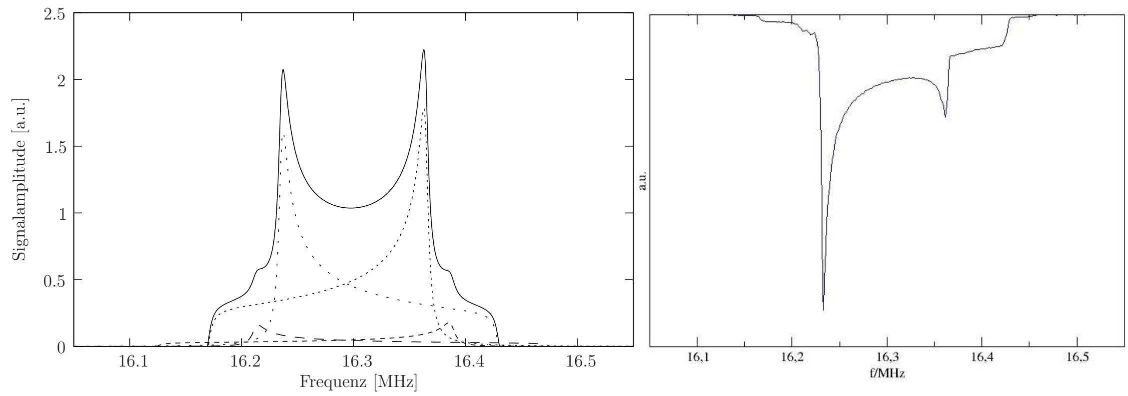

(a) low polarization

(b) high polarization

Figure 2.36: Example NMR signals of deuterated butanol. Left-hand side: long dashed lines: small contribution of the oxygen-deuteron binding. Short dashed lines: dominating contribution from the carbon-deuteron binding. Solid line: sum of all four contributions. Right-hand side: envelope at a high degree of target polarization of $P_T = 81.5\%$ at a magnetic field of 2.5 T. The left (right) peak corresponds to the m=-1(0) to m=0(1) transition. Figures taken from [151].

The degree of polarization of the target material is determined using NMR. For this purpose a coil with only a few windings is attached to the target material basket (see left-hand side of Figure 2.35). The coil is part of a serial RCL resonant circuit that is driven at a resonance frequency ω close to the nuclear larmor frequency. This induces spin transitions of a few nuclei in the target material which slightly reduces

[23]a holding coil for longitudinal polarization and a saddle coil for transverse polarization exist.

the target polarization. This change in the magnetization of the target affects the inductance and hence the impedance of the coil. This change can be measured and related to the degree of polarization P via the magnetic susceptibility χ [151]:

$$P = k \cdot \int_{\Delta\omega} \chi''(\omega) d\omega \ , \tag{2.12}$$

where the factor k depends on the properties of the nucleon system and of the apparatus. The frequency range $\Delta\omega$, that has to be scanned around the nuclear larmor frequency, depends on the width of the signal to be detected. For deuterons, the typical width of the signal is about 260 kHz, and $\Delta\omega$ is chosen to be on the order of 500 kHz. In an external magnetic field, deuterons, as spin-1 particles, exhibit three equidistant Zeeman levels of quantum number $m = -1, 0, 1$. The transitions from level 0 to 1 should therefore occur at the same resonance frequency as the transition from -1 to 0. However, for deuterons chemically bound inside butanol, this does not hold. In deuterated butanol, the chemical bindings give rise to electric field gradients that affect the quadrupole moment of the deuterons. This results in an energy change of the individual spin states and hence to two NMR lines in the spectrum of deuterated butanol, as illustrated in Figure 2.36. For a polarized target, the two spin states are unequally occupied. Therefore with a higher degree of polarization, the NMR signal becomes more asymmetric, as depicted in Figure 2.36b. The degree of target polarization can then be derived from the NMR signal in two ways: either with the TE[24]-method, which is based on Equation (2.12), or by determination of the asymmetry of the signal.

[24]TE: thermal equilibrium

2.9 Beamtime Overview

The following tables summarize the analyzed liquid hydrogen, liquid deuterium, deuterated butanol and carbon beamtimes and the most relevant settings which have been used for the experiments at MAMI and ELSA.

2.9.1 Liquid Hydrogen Data

The settings for the liquid hydrogen beamtimes at MAMI and ELSA are summarized in Table 2.5.

	ELSA	MAMI
Parameter	Nov. 2008	Apr. 2009
beamtime duration [h]	220	240
electron beam energy [MeV]	2350	1558
electron beam current [nA]	0.19	10
tagged photon energy range [MeV]	360 - 2290	410 - 1401
collimator diameter [mm]	4	4
radiator material	Møller	10 μm Cu
target material	LH_2	LH_2
target length [cm]	5.262	10.0 ± 0.1
target radius [cm]	3.0	4.0
beamspot radius on target [cm]	1.2	1.3
CB energy sum threshold [MeV]	-	360
multiplicity trigger	M2+	M3+
Cherenkov	yes	no

Table 2.5: Overview of the analyzed liquid hydrogen beamtimes from the A2 and CBELSA/TAPS experiments.

2.9.2 Liquid Deuterium Data

Table 2.6 gives an overview of the most relevant experimental settings of the liquid deuterium beamtimes from MAMI and ELSA.

	ELSA	MAMI		
Parameter	Dec. 2008	Dec. 2007	Feb. 2009	May 2009
beamtime duration [h]	45/120	140	141	190
electron beam energy [MeV]	2350	1508	1508	1558
electron beam current [nA]	0.32	10	5	4.5
tagged photon energy range [MeV]	410 - 2290	410 - 1401	413 - 1401	423 - 1447
collimator diameter [mm]	4 / 7	4	4	4
radiator material	Møller	10 μm Cu	10 μm Cu	Møller
target material	LD_2	LD_2	LD_2	LD_2
target length [cm]	5.258	4.72 ± 0.05	4.72 ± 0.05	3.02 ± 0.03
target radius [cm]	3.0	4.0	4.0	4.0
beamspot radius on target [cm]	1.2	1.3	1.3	1.3
CB energy sum trheshold [MeV]	-	300	300	300
multiplicity trigger	M3+	M2+	M3+	M2+
Cherenkov	yes / no	no	no	no

Table 2.6: Overview of the analyzed liquid deuterium beamtimes from the A2 and CBELSA/TAPS experiments.

2.9.3 Carbon Data

An overview of the most important experimental settings from the carbon beamtimes at MAMI and ELSA is given in Table 2.7.

	ELSA	MAMI
Parameter	Nov. 2011	Feb. 2014
beamtime duration [h]	115	55
electron beam energy [MeV]	2350	1558
electron beam current [nA]	0.7	9
tagged photon energy range [MeV]	500 - 2290	395 - 1448
collimator diameter [mm]	4	2
radiator material	Møller	Møller
target material	^{12}C	^{12}C
target length [cm]	1.88	2.0 ± 0.05
target radius [cm]	2.0	2.0
beamspot radius on target [cm]	1.2	0.9
CB energy sum threshold [MeV]	-	250
multiplicity trigger	M4+	M2+
Cherenkov	yes	no

Table 2.7: Overview of the analyzed carbon beamtimes from the A2 and CBELSA/TAPS experiments.

2.9.4 Deuterated Butanol Data

The main experimental settings used for the experiments with a deuterated butanol target are summarized in Table 2.8.

	ELSA		MAMI			
Parameter	Jan. 2011	Jun. 2011	Jul. 2013	Feb. 2014	Mar. 2015	Mar. 2015
beamtime duration [h]	190	115	145	80	27	48
average target polarization [%]	+63/-56	63	62	-55	-57	55
target pol. scale factor	1	1	1.5	1.5	1.40958	1.16764
average electron polarization [%]	60	62	85	83	84	84
helicity asymmetry factor	1	1	0.00447465	-0.0022007	-0.000032	0.000032
electron beam energy [MeV]	2350	2350	1558	1558	1558	1558
electron beam current [nA]	0.7	0.7	8.3	9.0-10.0	10	10
tagged photon energies [MeV]	500 - 2290	500 - 2290	395 - 1448	395 - 1448	395 - 1448	395 - 1448
collimator diameter [mm]	4	4	2	2	2	2
radiator material	Møller	Møller	Møller	Møller	Møller	Møller
target material	C_4D_9OD	C_4D_9OD	C_4D_9OD	C_4D_9OD	C_4D_9OD	C_4D_9OD
target length [cm]	1.88	1.88	2.0 ± 0.05	2.0 ± 0.05	2.0 ± 0.05	2.0 ± 0.05
target radius [cm]	2.0	2.0	2.0	2.0	2.0	2.0
beamspot radius on target [cm]	1.2	1.2	0.9	0.9	0.9	0.9
CB energy sum threshold [MeV]	-	-	250	250	250	250
multiplicity trigger	M4+	M4+	M2+	M2+	M2+	M2+
Cherenkov	yes	yes	no	no	no	no

Table 2.8: Overview of the analyzed deuterated Butanol beamtimes from the A2 and CBELSA/TAPS experiments.

3 Software

This chapter presents the strategy and developments of the parallel analysis of data from the A2 and CBELSA/TAPS experiments that have been used within this work. Analyzing data of two different, but similar experiments requires an elaborate organization concerning the different software packages that are used. This is not only important in order to save time, but especially important in order to avoid systematic errors. For this reason, a very important step of this work was the preparation of the software structure to be used for the data analysis of the experimental datasets from the two experiments at MAMI and ELSA.

All the used software packages and frameworks are based on `ROOT` [159–161] from CERN [162], which is mainly written in `C++` and hence is well integrable in other frameworks. In the A2-Collaboration at MAMI, the framework `AcquRoot` [163] is used for the data acquisition, data analysis, and the generation of Monte Carlo (MC) events that are used for the simulation with `Geant4` im combination with the `A2` package [164]. In contrast, the CBELSA/TAPS-Collaboration uses `ExPlORA` [165, 166] for the data acquisition and data analysis and `CBGEANT` [167] for the event generation and the subsequent simulation with `Geant3.21`.

3.1 Structure of the Parallel Analyses at the A2 and CBELSA/TAPS Collaborations

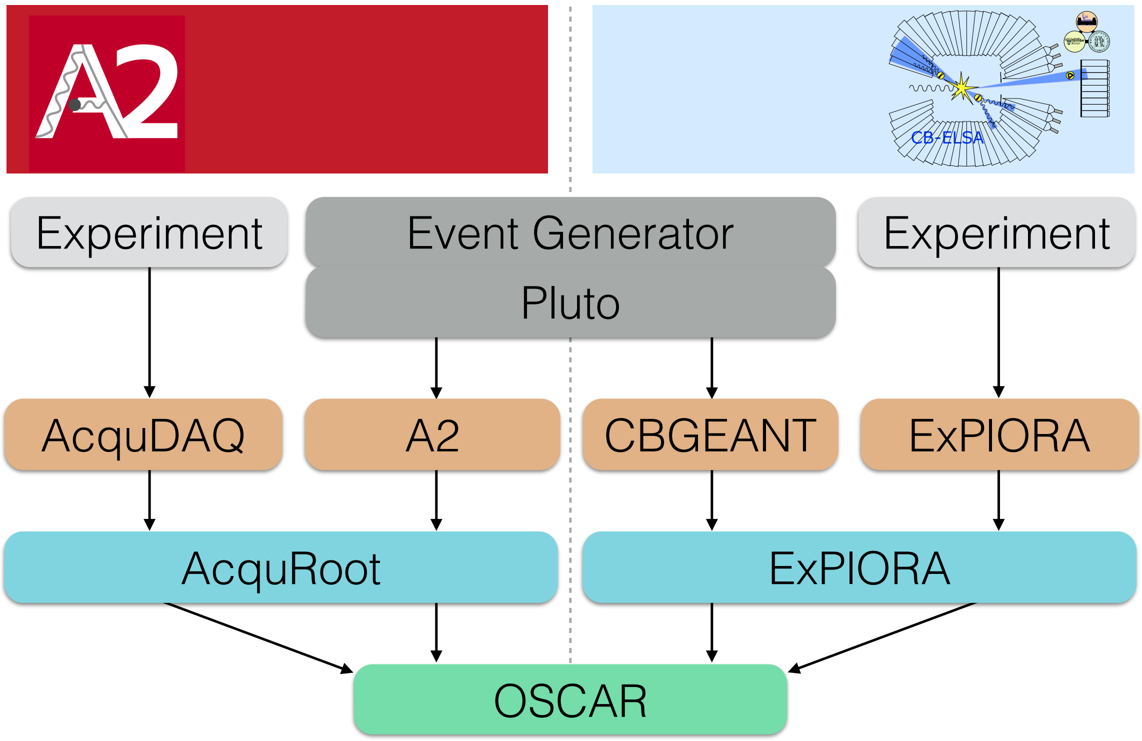

Figure 3.1: Structure of the analysis and simulation procedure developed for the parallel analysis of experimental data at the A2 and CBELSA/TAPS Collaboration. Grey: source of real or generated events. Orange: data acquisition or simulation. Blue: pre-analysis. Green: post-analysis. The light gray, orange, and blue categories are separate for the two collaborations. The dark gray, and green categories are combined for the two collaborations and were developed for the parallel analysis within this work.

In general, the procedure of a data analysis is the following: events from either a real experiment or from a Monte Carlo event generator pass through the detectors of the experimental setup and produce signals in the individual detector components. A dedicated data acquisition software records the detector information and stores them to digital files. These data files can then be analyzed with a data analyzing software in order to extract the physical information of interest.
The scheme of the developed parallel analysis is shown in Figure 3.1. There were two stages of the analysis, where an interface has been integrated within this work.

The first interface concerns the Monte Carlo simulation, i.e. the generation of events. Simulations based on Monte Carlo are used to imitate the reaction and detectors response as it occurs during a real experiment. Based on the generation of a certain number of events of the reaction of interest, the simulation then models

the detector response. This offers the advantage that besides the response of the detector components, also its origin, i.e. the particles that went into the detector and induced the signals in the detectors, is known. This allows for the determination of the acceptance and also the efficiency of the individual components, which can be used to correct the results of the real data.
Each experiment has its own implementation of the experimental setup and may also use a different toolkit for the simulation of the particles through the virtual detectors. A representative, and as realistic as possible, virtual setup of the experiment requires the proper implementation of the geometry of all detector components. Whereas the virtual setup of the A2 experiment "`A2`" is based on the `Geant 4` simulation toolkit [168, 169], the CBELSA/TAPS setup "`CBGEANT`" uses Geant3.21 [170]. The development of the individual virtual setup was tested extensively and all requirements that are necessary for the analysis of the output files from the simulation are implemented in the analysis software. Hence, it is not recommended to change anything in this structure.
The simulation toolkits need an event generator as input that contains all the four vectors of the participating particles of every event and then simulates their passage through the materials of the defined detector components. This event generator is the base of the simulation and, as it defines the origin of the reaction, immediately influences the outcome of the simulation. In order to reduce systematic uncertainties and to ensure that the identical reaction is investigated in the simulations of the two different experiments, it was reasonable to make it possible to use the same event generator as input for both simulations. With its flexibility and completeness, `Pluto` [171, 172] was soon established as the event generator of choice, but its output had to be adapted to be compatible as an input for both simulation toolkits.

The second interface was based on the analysis of either experimental or simulated data. At the time when the experiments within the CBELSA/TAPS Collaboration at ELSA have been carried out, a simplified analysis procedure for the A2 data already existed. This procedure is based on the *pre*-analysis of the experimental or simulated data with `AcquRoot` and the *post*-analysis of the data with `OSCAR` [100]. The pre-analysis with `AcquRoot` is used to presort the data, i.e. to perform a general event selection based on the number of neutral and charged particles of interest. The post-analysis with OSCAR then takes care of the post-processing of the data. As most of the detector dependent analysis steps are part of the pre-analysis and the post-analysis primarily contains general physics investigations, this two-step analysis offers the ideal base for a parallel analysis of the same reaction of two different experiments. For this reason, an interface was also incorporated into `ExPlORA` in order to presort the experimental or simulated data [173] in a similar way as for the A2 data. With this technique, the presorted data from the A2 and the CBELSA/TAPS experiment can be post-analyzed with an almost identical analysis and systematic uncertainties from inconsistencies between the two can be avoided.

The following sections present the different softwares that have been used and/or developed as part of this work. In the first two sections, the independent software frameworks used within each collaboration, i.e. `AcquRoot`, `A2 Geant4`, and `CaLib` for the A2 analysis and `ExPlORA` and `CBGEANT` for the CBELSA/TAPS analysis, will be presented. The third and last section introduces `Pluto` and `OSCAR`, the two frameworks that have been used in a combined way for both analyses.

3.2 Software used within the A2 Collaboration

The following sections present the different software packages that were used for the handling and the analysis of A2 data. For the data acquisition and the presort of the raw data, the `C++`-based analysis framework `AcquRoot` (see Section 3.2.1) was used. The simulation of the reactions, used for kinematical investigations and the determination of the detection efficiencies, was carried out by means of the virtual experimental setup from the `A2` package (see Section 3.2.2) in combination with the `GEANT4` toolkit from Cern. The calibration of the raw data was performed with the `C++`-based calibration library `CaLib` (see Section 3.2.3).

3.2.1 AcquRoot

`AcquRoot` is a software package written in `C++` and is used for the data acquisition, analysis, and MC event generation within the A2 Collaboration [174]. It is based on the software toolkit `ROOT` from CERN and consists of `AcquDAQ`[1] (data acquisition), `AcquRoot` (data analysis), and `AcquMC` (MC event generator). As mentioned in Section 3.1, for a better control of systematics and a better compatibility, `Pluto` was used for the generation of the MC events instead of `AcquMC`.
The data acquisition toolkits, `AcquDAQ` for the experimental and `A2` for the simulated data, both generate binary output files that then can be decoded and analyzed within the `AcquRoot` framework. `AcquRoot` contains classes for all the available detectors that inherit from certain base classes, which contain the common features and physical properties. Individual settings such as distances, angles, and calibration values of the different detectors are manageable with configuration files in the ASCII[2] format. Individual concepts and physics can be easily incorporated into the framework that then provides an easily accessible and powerful toolkit.
In this work, `AcquRoot` was only used for the calibration (see Section 3.2.3) and to presort the experimental and simulated A2 data. The presorted data was then analyzed with `OSCAR` (see Section 3.4.2) in order to extract the information and results of interest.

[1] AcquDAQ is the follower of `ACQU` which has been used for the acquisition of the unpolarized data.

[2] ASCII: American Standard Code for Information Interchange; a 7-bit character-encoding scheme

3.2.2 A2 Geant4 Simulation

The `A2` simulation is based on `Geant4` (GEometry ANd Tracking 4) and was the package used for the MC simulations of the A2 data in this work. It contains the geometry and the material composition of the detector components of the experiment of the A2 collaboration, as depicted in Figure 3.2.

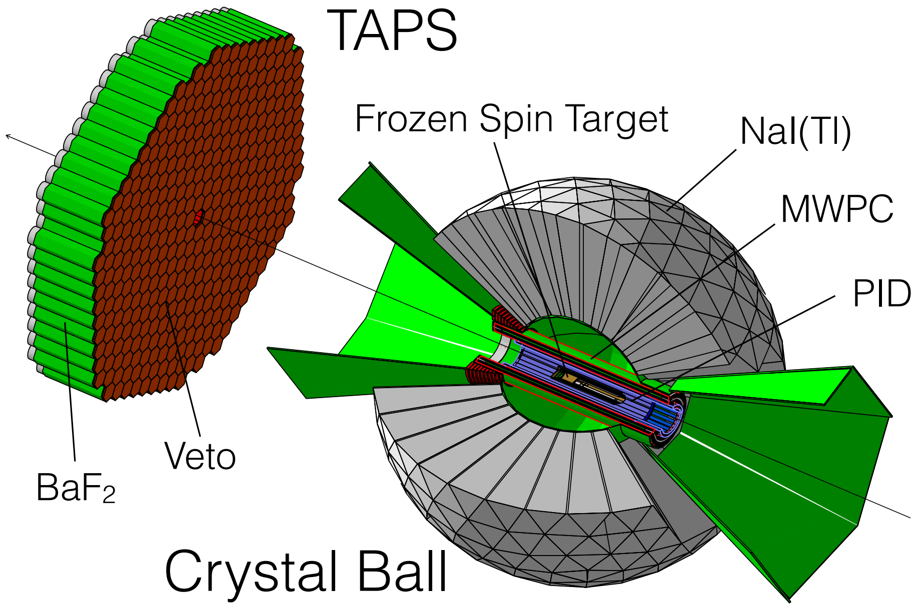

Figure 3.2: The A2 experimental setup at MAMI as defined in the A2 Geant4 package visualized with DAWN (Drawer for Academic WritiNgs). It shows the two main calorimeters, the Crystal Ball and TAPS and the detectors that are used to discriminate between neutral and charged particles, i.e. the Particle Identification Detector (PID), the Multi-Wire Proportional Chambers (MWPC), and the vetos. The container of the Frozen Spin Target is as well visible in the center of the Crystal Ball detector.

`Geant4` is based on `C++` and is used to simulate the interactions of particles with different kind of materials over a wide energy range, from 250 eV up to the TeV range. It contains electromagnetic, hadronic, and optical processes and different kinds of long-living particles, materials, and elements.

The `A2 Geant4` package can be handled very easily by adjusting two configuration files. One contains hardware parameters that might have to be adjusted between different beamtimes and allow for a flexible adjustment of the setup, such as the type of target and its material, detectors to be used, and the arrangement of them. The other configuration file is responsible for the physics processes and contains information about the physics models that have to be used for the particle interactions or which of the generated particles should be tracked by the simulation. Depending on the version of `Geant4`, up to 30 physics models for different purposes are available. Table 3.1 gives an overview of the naming convention of some of the most common

Abbreviation	Name	energy range
QGS	Quark Gluon String model	20 GeV - 50 TeV
CHIPS	CHiral Invariant Phase Space	
FTF	FriTioF model	> 5 GeV
LHEP	Low and High Energy Parametrization	
BIC	BInary Cascade model	< 10 GeV
BERT	BERTini cascade model	< 10 GeV
HP	High Precision neutron model	< 20 MeV
EMV	standard EM package Variation	

Table 3.1: Name convention of some of the common physics lists available in Geant4. Models with no indicated applicable energy range have no general limitation or can only be used in addition to another list. Informations taken from [175, 176].

physics models available [175, 176].

Physics Models

`QGSP` is the primary physics list based on the quark gluon string model for high energy interactions of pions, kaons, nucleons, and nuclei. It accurately models the excitation and subsequent de-excitation of nuclei. `QGSP-BERT` is based on `QGSP`, but uses the *Bertini* cascade for modeling primarily pions, kaons, and nucleons below ~ 10 GeV. The high precision neutron package `HP` ensures that the neutron transport from 20 MeV down to thermal energies is modeled in a realistic way. The additional option `EMV` uses tuned parameters in order to yield a better cpu performance with a marginal loss of precision. `QGSC` is similar to the `QGSP` model, but applies the `CHIPS` modeling to the nuclear de-excitation, which improves nuclear de-excitation and results in a somewhat higher amount of low energy secondary protons and neutrons.

In this work, the `Geant4` version 9.5 (patch-02) was used together with the physics model `QGSP-BERT-HP`. In Figures 3.3, 3.4 and 3.5 several medium energy physics models have been tested and compared with the results from the experimental data by means of π^0 photoproduction from the deuteron. As the models mainly differ by the way they describe the interaction of particles with matter, the relevant quality criteria was found in the resulting cluster size of nucleons in the detectors. Whereas the simulated cluster size of protons is almost independent of the physics model, the most realistic cluster size of neutrons was achieved with the model `QGSP-BERT-HP`, even though three other models yield results of similar quality. This indicates that if only protons have to be considered, the simulation does not strongly depend on the physics lists. However, if neutrons are involved, as in this work, the proper physics model is of great importance and can severely influence the result.

Figure 3.3 shows the results of the simulations with four of the different `QGSC` models compared to the spectra from the analysis of the data, after all kinematic cuts, i.e. where the identification of the reaction is of the highest quality. Whereas for the

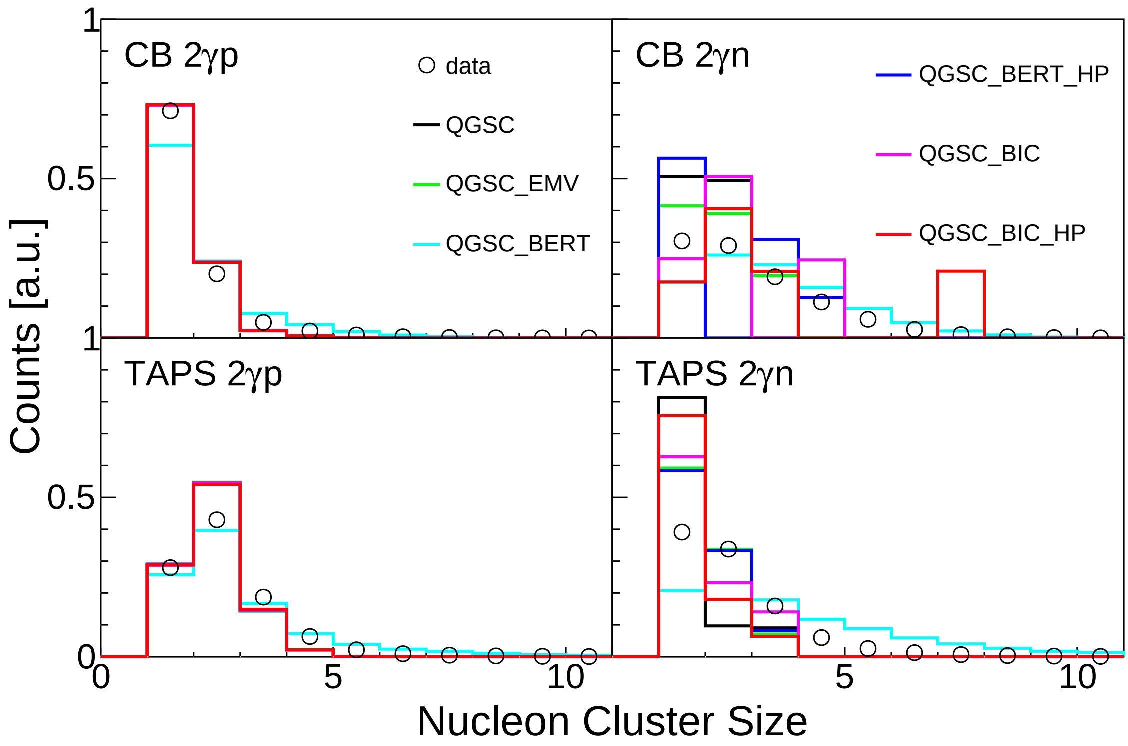

Figure 3.3: Investigation of the behavior of the different QGSC physics lists. Shown are nucleon cluster sizes in the Crystal Ball detector (top) and in the TAPS detector (bottom) for photoproduction of π^0-mesons from protons (left) and neutrons (right). The results from the simulations with the different physics models are shown as colored histograms (see legend in the figure for the notation). The results from the data (May 2009 beamtime) are shown as open black circles.

proton, the results of the simulation are in rather good agreement with the data, the simulation for the neutron yields mostly too small cluster sizes. This is a direct consequence of the `CHIPS` modeling which as previously mentioned produces an enhanced amount of low energy recoil particles. However, in combination with the Bertini cascade (`QGSC_BERT`) model, the results are satisfactory, making this model the only candidate from the `CHIPS` list.

The situation is already much better if the `QGSP` model is used instead of the `QGSC` model. As Figure 3.4 shows, any of the compared models yields rather good results, except for `QGSP_EMV` model. In Figure 3.5, the best candidate of the `QGSC` models is compared with the three best candidates of the `QGSP` models. Overall, the two best candidates are the `QGSP` and the `QGSP_BERT_HP` model, from which the latter shows the best agreement for the cluster size of neutrons in TAPS and hence on average is the favorite candidate. However, due to the negligible differences, both models would yield similar and sufficient results.

The `Geant4` simulation needs an event generator as an input, for which every event

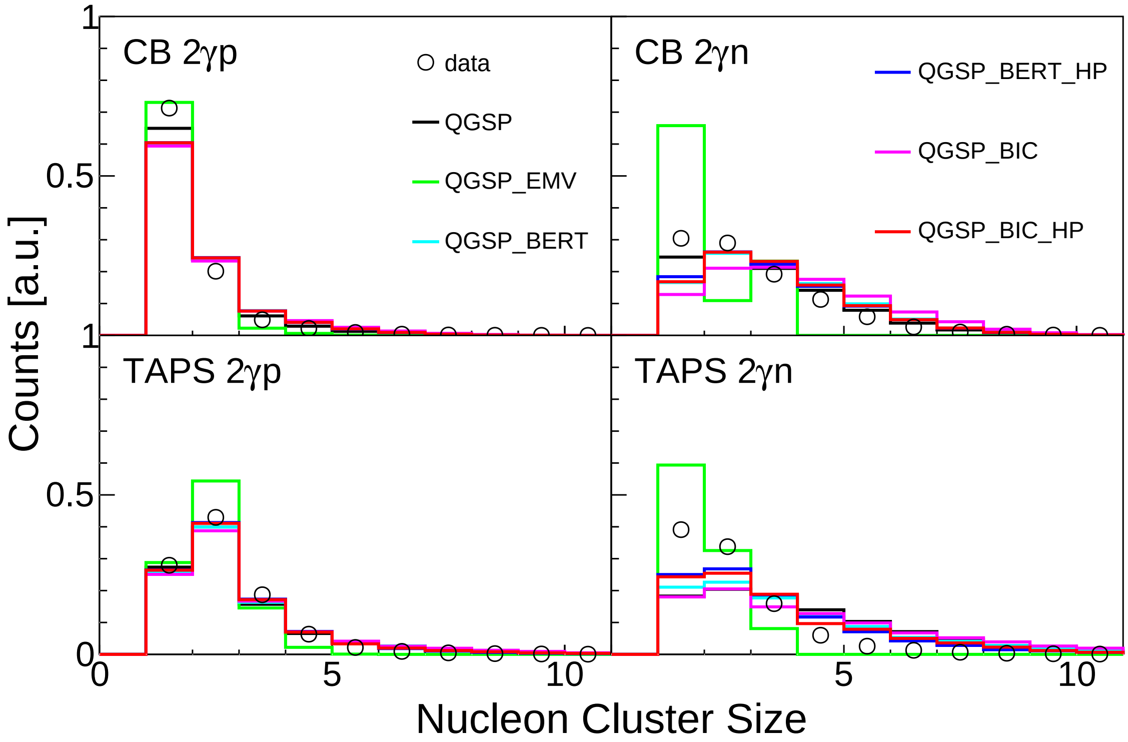

Figure 3.4: Investigation of the behavior of the different QGSP physics lists. Shown are nucleon cluster sizes in the Crystal Ball detector (top) and in the TAPS detector (bottom) for photoproduction of π^0-mesons from protons (left) and neutrons (right). The results from the simulations with the different physics models are shown as colored histograms (see legend in the figure for the notation). The results from the data (May 2009 beamtime) are shown as open black circles.

contains the vertices and four momenta of the particles that have to be tracked in the simulation. For this work, Pluto (see Section 3.4.1) was chosen as the event generator of choice. The `Geant4` simulation then simulates the interactions of the particles with the different materials and components. As the detector components are defined as sensitive volumes, the deposited energy and the time information can be determined and are written to the output file, which can then be analyzed with `AcquRoot`.

In contrast to real data, in the simulation it is known which particles of which energy have been produced in the target and hence, how much energy should be detected and at which angle. This advantage allows for the determination of detection efficiencies of the different detector components or of the reaction itself and is necessary for the absolute normalization of cross sections.

Magnetic Field Map

During the experiment with the polarized deuterated butanol target, the deuteron polarization was supported by a magnetic field of the holding coil (see Section 2.8.2)

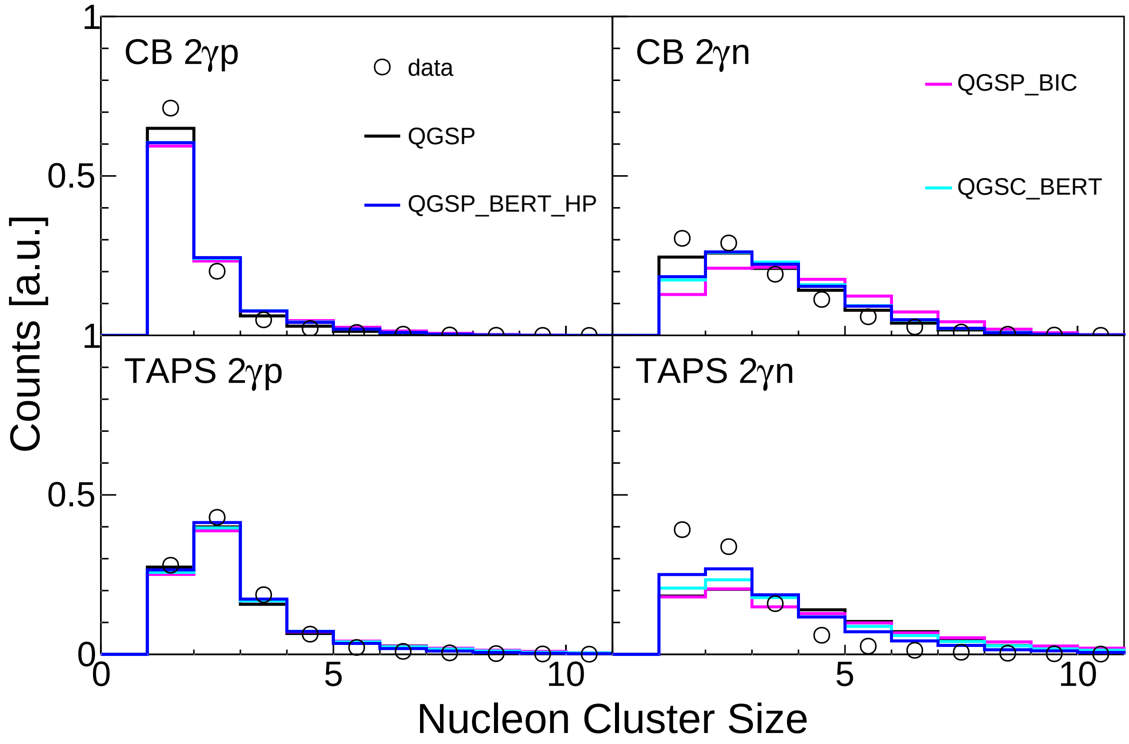

Figure 3.5: Investigation of the behavior of the most well-suited physics lists. Shown are nucleon cluster sizes in the Crystal Ball detector (top) and in the TAPS detector (bottom) for photoproduction of π^0-mesons from protons (left) and neutrons (right). The results from the simulations with the different physics models are shown as colored histograms (see legend in the figure for the notation). The results from the data (May 2009 beamtime) are shown as open black circles.

which produced a magnetic field of about 0.6 T in or against the z-direction, depending on the direction of the polarization. As the magnetic field does not only maintain the polarization, but also affects the flightpath of charged particles (especially those perpendicular to the magnetic field, i.e. perpendicular to the z-axis), it was important to include the magnetic field in the simulation. For this purpose, a field map of the magnetic field with the NMR corrected fields was calculated with a simulation [177]. As the magnetic field is axially symmetric around the the z-axis and mirror symmetric around the target center, only one fourth of the cross section field map was provided (upper left quadrant of the positive field map in Figure 3.6). For the usage in the simulation, this quadrant first had to be rotated around the z-axis and then mirrored at the target center without flipping the direction of the field. The vector components of the field vector were then provided for the three-dimensional volume within the holding coil in millimeter precision. For the magnetic field in the opposite direction, the same field with opposite direction of the field vectors was generated. A cross section of the result for the magnetic field in z-direction (positive, referred to as “pos”) and against the z-direction (negative, referred to as “neg”) used

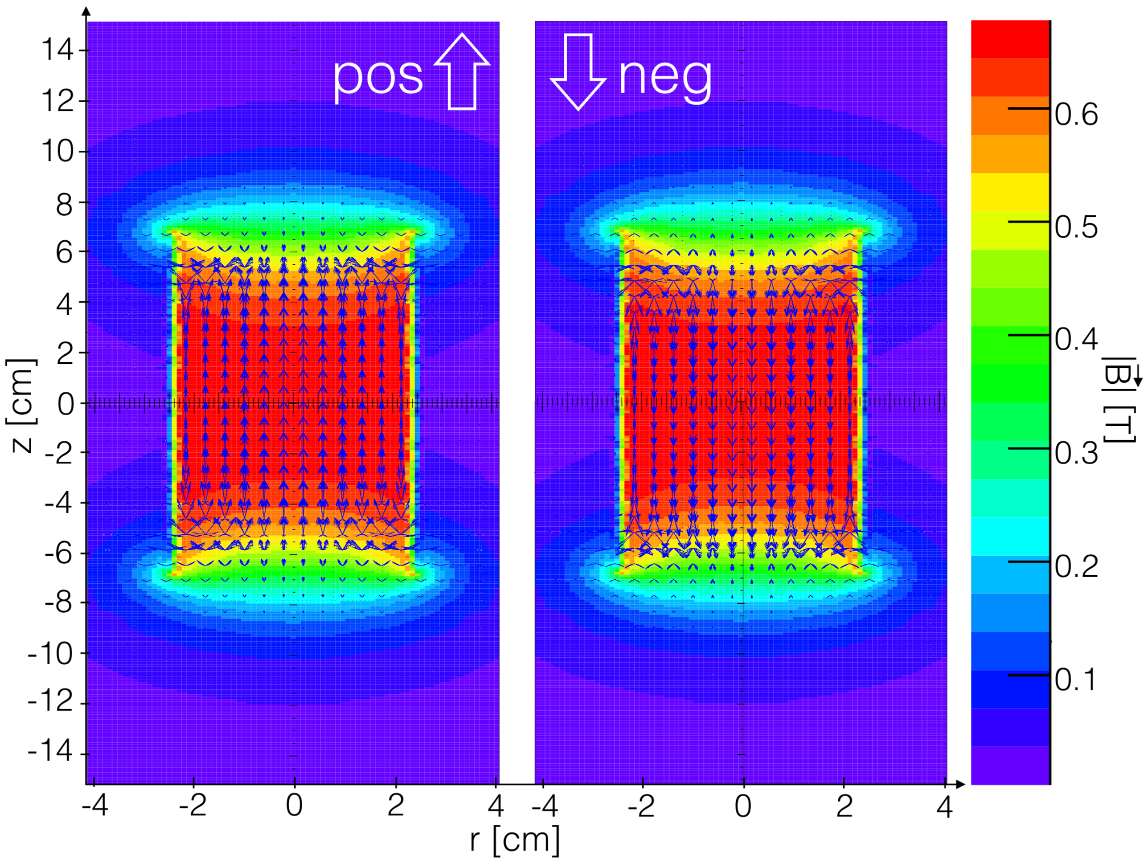

Figure 3.6: Magnetic field maps of the internal holding coil used for the simulation of A2 data with the longitudinally polarized target. Left-hand side: magnetic field in z-direction (pos). Right-hand side: magnetic field in -z-direction (neg). Size and direction of the arrows indicate the absolute value and direction of the z-component. Colors indicate the absolute value of the magnetic field.

in the simulation is illustrated in Figure 3.6.

3.2.3 CaLib

`CaLib` (Calibration Library) is a `ROOT`-based collection of classes which was initiated by Dr. Irakli Keshelashvili[3] within the A2 collaboration in order to improve, speed up, and simplify the calibration process of experimental data of A2 experiments. Within this work, part of the base classes and the interface to a `SQL`[4] database have been developed. The basic version of `CaLib` was later revised by Dr. Dominik Werthmüller[5] and now is the main tool for the calibration of experimental data within the A2 collaboration at MAMI.

[3] i.keshelashvili@fz-juelich.de
[4] SQL: Structured Query Language
[5] dominik.werthmueller@glasgow.ac.uk

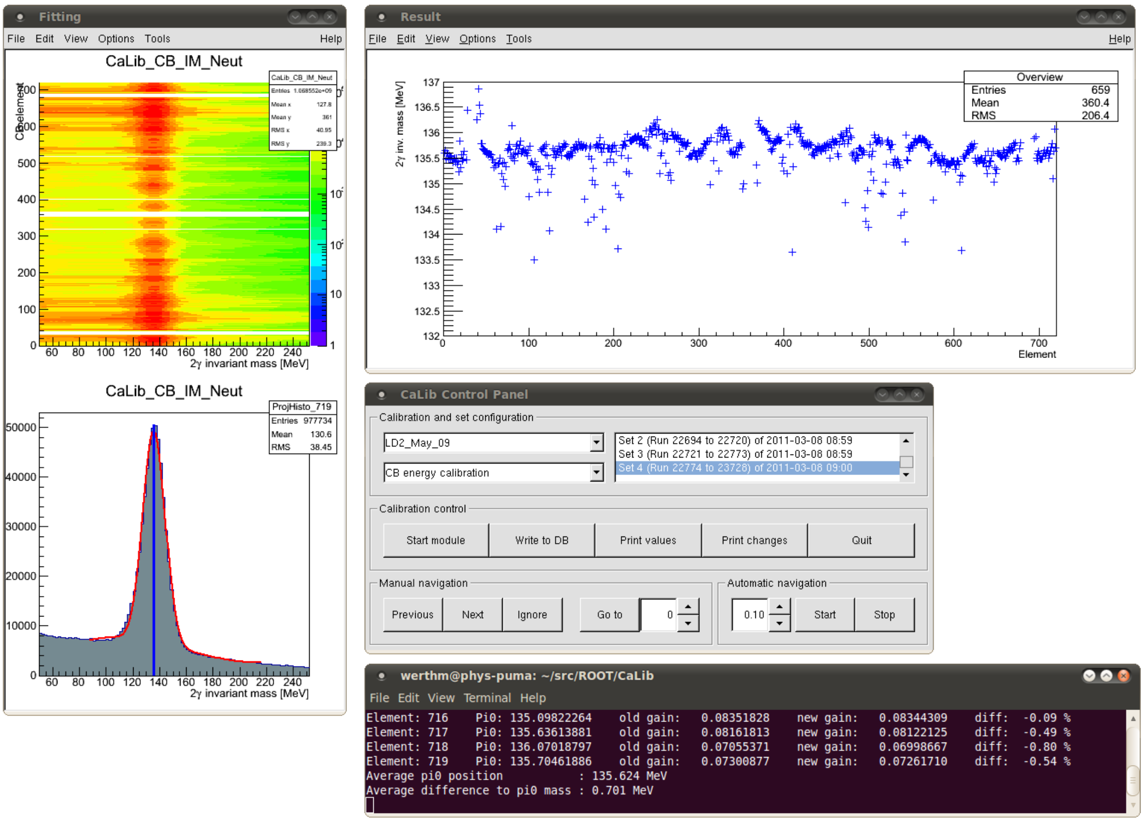

Figure 3.7: Snapshot of the graphical user interface (GUI) of the CaLib software during the energy calibration of the NaI(Tl) crystals. Shown is the control panel (middle), the command prompt (bottom), crystal number versus $\gamma\gamma$ invariant mass (top left) with a spectrum of one crystal (bottom left) as well as the calibration quality status (top right). Taken from [100].

The behavior of the different detector components during an experiment depend on the actual conditions, e.g. temperature, humidity, supply voltage, as well as the chosen settings, e.g. threshold values. As a consequence, equivalent detector components do not show the same behavior and response to identical signals. In order to correctly convert the electronic signals into physical quantities, each experimental data has to be calibrated. Such a calibration has to be done for each of the different detectors in regard to timing and energy information. Only an appropriate calibration allows for an analysis that is based on time coincidence and deposited energy of the detected particles. For this reason, time and energy calibrations for the different detector modules have to be carried out and poorly performing components have to be fixed or excluded from the analysis. The calibration with the `CaLib` library is based on a run by run extraction of characteristic quantities, e.g. peak position of the $\gamma\gamma$ invariant mass and coincidence of detected photons, and results in a time dependent overview of the detector information. The outcome is visualized by the

help of a GUI[6] (see Figure 3.7), which allows for the navigation through the different calibration steps and processes and for checking the calibration quality.
The procedure of all calibrations is based on the same principle. The start calibration values of a given detector are read from the configuration files used for the analysis with `AcquRoot` and are filled into the `SQL` database. The data is then analyzed with the corresponding calibration analysis in order to produce the histograms that contain the necessary information. According to the experimental variations, runs belonging to a period of stable detector behavior can be grouped into calibration sets. For each calibration set, the histograms of all the corresponding runs are summed up and serve as input for `CaLib`, which then performs a calibration iteration of all individual detector elements. The resulting new configuration parameters are then written to the database and can be used for the subsequent calibration analysis. Depending on the type of calibration, the procedure can be iteratively repeated until the desired quality of calibration is reached.

3.3 Software used within the CBELSA/TAPS Collaboration

This section presents the different software packages that were used for the handling and analysis of data from CBELSA/TAPS experiments. `ExPlORA` is used for the analysis, calibration and the presort of the raw data. The simulations are performed with the virtual experimental setup `CBGEANT` in combination with the `Geant3.21` toolkit from Cern.

3.3.1 Explora

`ExPlORA` (Extended Pluggable Objectoriented Root Analysis) [165, 166] is the basis for the analysis of data from the CBELSA/TAPS experiment at ELSA. It is based on `ROOT` and has the main objective to constrain the programmable part of the data analysis into the physically essential extent. This is realized by means of a plugin concept, which allows to simply add individual parts without the need to modify the main core. The analysis can then easily be controlled with corresponding `xml`[7] files. As the strategy of this work was to analyze the CBELSA/TAPS data in the same way as the A2 data, `ExPlORA` was used to create a presort of the CBELSA/TAPS data of the same structure as the presort of the `A2` data. The presorted data was then analyzed with an equivalent analysis in `OSCAR` (see Section 3.4.2).

3.3.2 CBGEANT Geant3 Simulation

The `CBGEANT` [178] simulation contains the virtual setup of the CBELSA/TAPS experiment at ELSA, as illustrated in Figure 3.8. In contrast to the `A2` package, it

[6]GUI: Graphical User Interface
[7]Xml: Extensible Markup Language

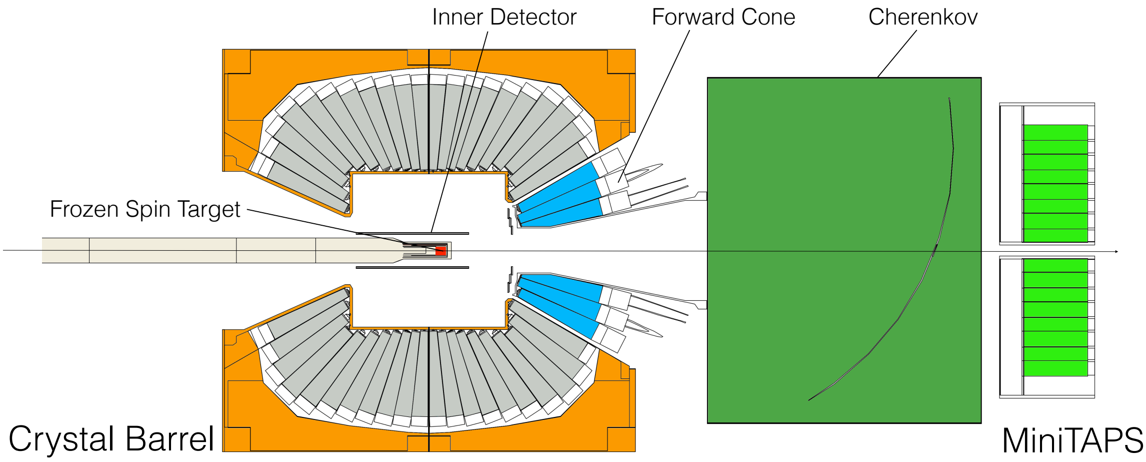

Figure 3.8: Cross section of the CBELSA/TAPS setup at ELSA in beam direction as defined in the CBGEANT Geant3.21 package visualized with PAW (Physics Analysis Workstation). It shows the Crystal Barrel detector with the Forward Cone and the Inner Detector, and the MiniTAPS detector as the forward wall. In between the Crystal Barrel detector and MiniTAPS is the Cherenkov detector that is used as a veto detector for the electromagnetic background in the forward direction. From the left, the Frozen Spin Target is moved inside the Crystal Barrel detector.

is based on `Geant3.21`, the predecessor of `Geant4` and is written in `FORTRAN`. All necessary parameters for the simulation, i.e. models and detectors, have to be adjusted in one configuration file. However, all detector geometries are hard-coded in the `CBGEANT` code and need recompilation in case of applying changes.

Physics Models

As for the `Geant4` simulation, the proper physics model had to be set up first in order to ensure that the interaction of the particles with the detector materials matches the experimental situation. By default, `Geant3.21` uses the `GHEISHA` and `FLUKA` models for the modeling of the different hadronic interactions. The `GHEISHA` model reproduces the shape of the average electromagnetic showers and the energy resolution of standard calorimeters. `FLUKA` is a standalone code that calculates single hadronic interactions in more detail by means of fragmentation models. However, it does not provide any information about low energetic neutrons. Due to this fact, the appropriate physics model that had to be used for the simulations with `Geant3` in this work is `CALOR89` [179]. This model accurately describes hadronic interactions down to 1 MeV for charged pions and nucleons and down to the thermal region for neutrons (corresponding to `QGSP_BERT_HP` used in `Geant4`). For energies above 10 GeV the `FLUKA` model is used. The `CALOR` interface for the usage with `Geant3.21` is called `GCALOR`. It mainly contains the high energy transport code (HETC) for high energetic hadrons up to 10 - 15 GeV, the `FLUKA` code for hadrons above the

HETC limit[8], the MICAP (Monte Carlo Ionization Chamber Analysis Package) point cross section code for neutrons below 20 MeV, and EGS 4 (Electron Gamma Shower, version 4) for electrons, positrons, and photons.

Magnetic Field Map

As for the A2 Geant4 simulation, the magnetic field of the polarized deuterated butanol target had to be included in the simulation. However, in contrast to the A2 package, the longitudinal magnetic field in CBGEANT was not calculated by using a field map, but by using a magnetic field of at most 0.6 T in or versus the direction of the beam (z-axis). The field was implemented such that it is homogeneous within the region of the holding coil.

3.4 Software used within both Collaborations

As mentioned in Section 3.1, the parallel analysis of A2 and CBELSA/TAPS data required an elaborate strategy in order to reduce systematic uncertainties and to sustain comparability between the results. For this purpose the software packages of the individual collaborations (presented in the previous sections) were only used to presort the raw data (from either experiment or simulation) by means of a primary event selection. All presorts were then analyzed with OSCAR in order to extract the results. Additionally the generation of the events for both simulations were carried out with 'Pluto'.

3.4.1 Pluto

Pluto is a Monte Carlo simulation framework for heavy ion and hadronic physics reactions. It is written in C++ and uses ROOT only. It was originally designed as an experimentalist's tool within the HADES[9] collaboration [180], providing an easily accessible platform for simulations from within an analysis. It includes detailed models for resonance and Dalitz decays, resonance spectral functions including mass-dependent widths, anisotropic angular distributions, and many versatile features such as manipulating particles or reaction channels or adding filters to the kinematical conditions. The output can either directly be analyzed or used as input for the simulations with GEANT.
The simple handling of Pluto and its powerful skills and tools made it already from the beginning of this work the event generator of choice. However, it was not designed for beams of bremsstrahlung photons with an energy spectrum rather than a single specific energy and also not for reactions on nucleons inside a nucleus. Therefore, two major things had to be solved in the beginning of this work: the implementation

[8]As in this work the energies of the hadrons are well below 10 GeV the 'FLUKA' code will not be employed in the simulation

[9]HADES: High Acceptance DiElectron Spectrometer

of the Fermi distributions of different nuclei and the ability of having a beam of a well defined energy spectrum rather than a fixed value.

Adaption to Photoproduction from Quasi Free Nucleons

The bremsstrahlung problem was solved by modifying an already existing class, `PBeamSmearing`, which mainly was used to smear the angular distribution of the beam particles. By implementing a smearing of the beam momentum by means of a user defined function, a beam of particles with a defined distributed energy can be easily created. The distribution of the energy can be defined by a function, e.g. a constant function for a true phase space behavior or an inverse function in energy for a bremsstrahlung spectrum.

For the implementation of the Fermi distributions of different nuclei, the available parametrizations of the Fermi distributions (see Table 3.2) of ^{2}H [181], ^{3}He [182], ^{4}He [182], ^{7}Li [183], ^{12}C [184], and ^{40}Ca [185], as illustrated in Figure 3.9, have been implemented. The Fermi momentum distribution of ^{12}C or ^{40}Ca can also be used for heavier nuclei since for higher atomic numbers, the Fermi distribution is almost identical (see the nearly non-existent difference between the cyan colored ^{40}Ca and the magenta colored ^{12}C distributions in Figure 3.9).

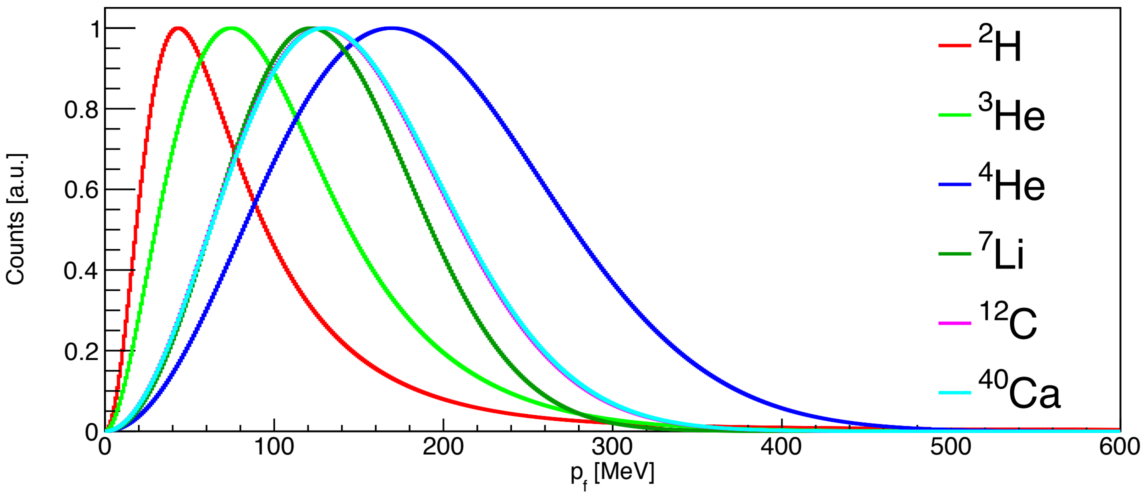

Figure 3.9: Normalized Fermi momentum distributions of ^{2}H, ^{3}He, ^{4}He, ^{7}Li, ^{12}C and ^{40}Ca according to the individual parametrizations from Table 3.2. Notations are given in the figure.

Nucleus	Probability Density
^{2}H	$\frac{x^2}{\hbar^2}\left[\frac{2}{\pi}\left(\sum_{j=1}^{13}\frac{C_j}{x^2/\hbar^2+m_j^2}\right)+\frac{2}{\pi}\left(\sum_{j=1}^{13}\frac{D_j}{x^2/\hbar^2+m_j^2}\right)\right]$
^{3}He	$0.001\cdot\frac{4d}{\pi}a^{3/2}\frac{25x^2}{10^6}\left[\exp\left(-a\frac{25x^2}{10^6}\right)+c\cdot\exp\left(-b\sqrt{\frac{25x^2}{10^6}}\right)\right]$
^{4}He	$\frac{x^2}{b\hbar^2}\exp\left(-\frac{x^2}{a\hbar^2}\right)$
^{7}Li	$0.001\cdot ax^2\left(1+bx\right)\exp\left(-\frac{x^2}{c^2}\right)$
^{12}C	$0.001\cdot\frac{4}{\sqrt{\pi}}a^{3/2}\frac{25x^2}{10^6}\left[\exp\left(-a\frac{25x^2}{10^6}\right)+c\cdot\exp\left(-b\sqrt{\frac{25x^2}{10^6}}\right)\right]$
^{40}Ca	$0.001\cdot\frac{4}{\sqrt{\pi}}a^{3/2}\frac{25x^2}{10^6}\left[\exp\left(-a\frac{25x^2}{10^6}\right)+c\cdot\exp\left(-b\sqrt{\frac{25x^2}{10^6}}\right)\right]$

Table 3.2: Parametrization of the Fermi momentum distributions for ^{2}H, ^{3}He, ^{4}He, ^{7}Li, ^{12}C, and ^{40}Ca. The parameters for ^{2}H have to be calculated using Equations (3.1) and (3.2) together with the parameters from Table 3.3. The parameters for the parametrization of the other nuclei are given in Table 3.4.

The mass parameters, m_j, for the parametrization of the deuteron wave function [181] are given by

$$m_j = 0.23162461 + (j-1)\cdot m_0 \qquad \text{with} \qquad m_0 = 1\ \text{fm}^{-1} \tag{3.1}$$

and the coefficients C_j and D_j are listed in Table 3.3. The last coefficient of C_j and the three last coefficients of D_j have to be calculated via:

$$\begin{aligned} C_n &= -\sum_{j=1}^{n-1} C_j \\ D_{n-2} &= \frac{m_{n-2}^2}{(m_n^2-m_{n-2}^2)(m_{n-1}^2-m_{n-2}^2)} \\ &\quad\times\left(-m_{n-1}^2 m_n^2\sum_{j=1}^{n-3}\frac{D_j}{m_j^2}+(m_{n-1}^2+m_n^2)\sum_{j=1}^{n-3}D_j-\sum_{j=1}^{n-3}D_j m_j^2\right)\ . \end{aligned} \tag{3.2}$$

C_j [fm$^{-1/2}$]	D_j [fm$^{-1/2}$]
$0.88688076 \cdot 10^0$	$0.23135193 \cdot 10^{-1}$
$-0.34717093 \cdot 10^0$	$-0.85604572 \cdot 10^0$
$-0.30502380 \cdot 10^1$	$0.56068193 \cdot 10^1$
$0.56207766 \cdot 10^2$	$-0.69462922 \cdot 10^2$
$-0.74957334 \cdot 10^3$	$0.41631118 \cdot 10^3$
$0.53365279 \cdot 10^4$	$-0.12546621 \cdot 10^4$
$-0.22706863 \cdot 10^5$	$0.12387830 \cdot 10^4$
$0.60434469 \cdot 10^5$	$0.33739172 \cdot 10^4$
$-0.10292058 \cdot 10^6$	$-0.13041151 \cdot 10^5$
$0.11223357 \cdot 10^6$	$0.19512524 \cdot 10^5$
$-0.75925226 \cdot 10^5$	0.0
$0.29059715 \cdot 10^5$	0.0
0.0	0.0

Table 3.3: Coefficients of the parametrized deuteron wave function components [181]. The last coefficient for C_j and the last three coefficients D_j have to be computed from Equation (3.2).

Nucleus	a	b	c	d
^{3}He	7.09078	5.38753	9.90202	0.779408
^{4}He	0.7352	0.05511	–	–
^{7}Li	$1.2 \cdot 10^{-4}$	$6.87 \cdot 10^{-3}$	110	–
^{12}C	1/0.416	1/0.23	0.04	–
^{40}Ca	1/0.42	1/0.23	0.04	–

Table 3.4: Parameters for the parametrized wave functions of the nuclei ^{3}He, ^{4}He, ^{7}Li, ^{12}C, and ^{40}Ca.

According to the Fermi distribution of the corresponding nucleus, a Fermi momentum of an absolute value p_f and of a random unit vector $\vec{u} = (u_x, u_y, u_z)$ was then assigned to the four momenta of the spectator $\mathbb{P}_{\text{spec}}$ and participant nucleon $\mathbb{P}_{\text{part}}$ as follows

$$\mathbb{P}_{\text{part}} = \left(-p_f^x, -p_f^y, -p_f^z, \sqrt{m_{\text{part}}^2 + p_f^2}\right) \qquad \mathbb{P}_{\text{spec}} = \left(p_f^x, p_f^y, p_f^z, \sqrt{m_{\text{spec}}^2 + p_f^2}\right) \quad (3.3)$$

In order to check the implementation of the Fermi momentum distributions, the result of the reaction $\gamma p(n) \to \eta p(n)$ has been compared to those from two other common event generators, `TGenPhaseSpace` (from `ROOT`) and `gdecay` (from `FORTRAN`). The resulting four momenta of the recoil nucleon are shown in Figure 3.10 and are in good agreement.

The implementation of the Fermi momentum distributions, as well as the bremsstrahlung extension, have been successfully incorporated into `Pluto` and are available for the community in the official `Pluto` release [186].

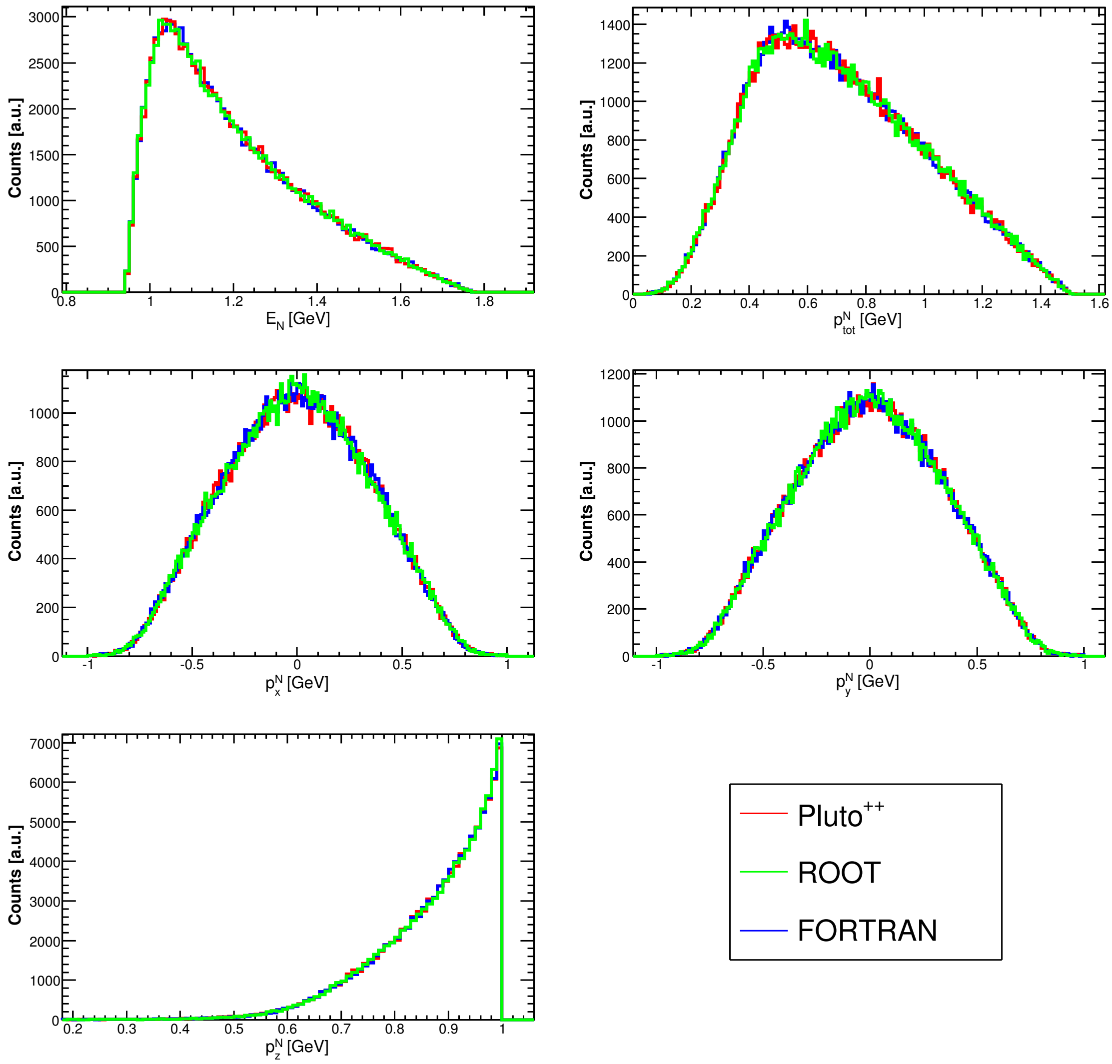

Figure 3.10: Distributions of the four momentum components of the recoil neutron obtained for the reaction $\gamma p(n) \to \eta p(n)$ from three different event generators. Green histogram: ROOT. Blue histogram: FORTRAN. Red histogram: Pluto. Shown are the energy of the neutron (top left), the absolute value of the momentum (top right), the x-component of the momentum (middle left), the y-component of the momentum (middle right), and the z-component of the momentum (bottom left).

Interface to Geant3 and Geant4

`Geant3` and `Geant4` need `.hbook` and `.root` event generator input files of a special format. For the conversion from `Pluto` to `Geant4` the `OSCAR` routine `pluto2mkin` was used, which simply generates leafs of the components of the four momentum vector labeled in the `Geant4` convention for every particle.
For the convertor from `Pluto` to `Geant3`, the `Pluto` output had to be extended in a way that the same event generator file can be used for the `A2` and `CBGEANT`

simulations. The main difficulty in this case was that, in contrast to Geant4, Geant3 usually does not generate all the events before passing them to the simulation, but rather step by step generates one event, passes it directly to the simulation, and then generates the next one. For this reason, in addition to the standard Pluto output file, the output class was modified to write the identical content in addition to a binary output file. A special FORTRAN routine, READ_PLUTO, which can read the binary file event by event, was written and added to the CBGEANT library. Another routine, PLUTO, creates the reaction tree with the particle hierarchy. This ensures that the simulation receives exactly the information and structure of the contributing particles that is needed.

3.4.2 OSCAR

OSCAR [100] (OSCAR Simplifies Coding and Analyzing with ROOT) is a ROOT-based library that contains a collection of physics classes that are mostly independent of the experiment from which the data stems. It provides a lot of additional functions to the ROOT library, as well as specific physics related classes. It presents the main software for the user specific analysis and was used for the analysis of the presorted data from the A2 as well as the CBELSA/TAPS-experiments. Due to its flexibility, the almost identical analysis was used for the analysis of the presorted data from the two different experiments, which immediately eliminates an important source of systematic errors.

4 Particle Reconstruction

This chapter presents the different steps that were necessary in order to reconstruct the detected particles from the measured electronic signals of the different detector components. This represents the basis of the analysis of the data and involves many elaborate procedures, used to assign the measured raw information to the particles that generated the detected signals. The main principle of the reconstruction of any particle from the collection of detected signals is to find out which of the measured information originates from the same particle. This is realized by means of the clustering. Based on the size and timing of the signals and on the distance of the involved crystals, algorithms create groups of crystals, the clusters, that share information from the same particle.

Section 4.1 will discuss the reconstruction of the different particles at A2. This involves the reconstruction of the bremsstrahlung photons that triggered the reaction and the reconstruction of the reaction products that deposited their energy in the calorimeters from the experimental setup. Subsequently Section 4.2 presents the methods used for the reconstruction of the particles at CBELSA/TAPS

4.1 Reconstruction of Particles at A2

For the analysis of the experimental A2 data, it is necessary to identify the energy and time information of the incoming beam photon as well as the energy, time, and position information of the final state particles that have been detected with the experimental setup. The information of the incoming photon beam is reconstructed from the deflected electrons in the Glasgow photon spectrometer (Section 2.2.1), the reaction products are determined by using the energy and time information of the clusters in the Crystal Ball (Section 2.2.2) and TAPS (Section 2.2.4) detectors. The information about their charge is obtained by requiring individual coincidence requirements with the charged particle detectors PID (Section 2.2.3) and Veto (Section 2.2.5).

4.1.1 Reconstruction of the Photon Beam

The electrons that lost part of their energy from the bremsstrahlung process will be deflected by the tagger dipole magnet towards the focal plane detector that consists of 353 overlapping detector elements. As described in Section 2.2.1, only coincident hits between two neighboring elements are defined as an electron hit, which results in 352 logical channels. Every hit in the 352 channels has a corresponding time value, which was recorded by multihit TDCs. The energy of the detected electron corresponds to a characteristic energy of each element that first has to be determined by an energy calibration of the tagger, as described in Section 5.2.11.
As explained in more detail in Section 2.2.1, the energy of the bremsstrahlung photon, E_γ, is then given by the difference of the measured electron energy, E_{e^-}, and the electron beam E_0:

$$E_\gamma = E_0 - E_{e^-} \ . \tag{4.1}$$

For the analysis, the number of electron hits and corresponding times are associated with a corresponding photon beam of energy E_γ according to equation 4.1. Up to three multiple tagger hits per channel and event have been taken into consideration in the analysis.

4.1.2 Reconstruction of Particles in the Crystal Ball Detector

Different types of particles exhibit different interactions with the detector materials and hence, deposit their energy in various neighboring detector elements. The group of detector elements over which a particle deposited its energy is called a cluster. In order to exclude background signals from electronic noise, only signals above a threshold of about 2 MeV are considered.
An iterative algorithm is then used to assign the detector elements to the cluster. At first, the element with the maximum detected energy is defined as the cluster center and the time information of this element is assigned to the cluster hit. The energy and position information of the cluster hit are then determined by the algorithm that identifies the elements, which as well collected energy from the same electromagnetic

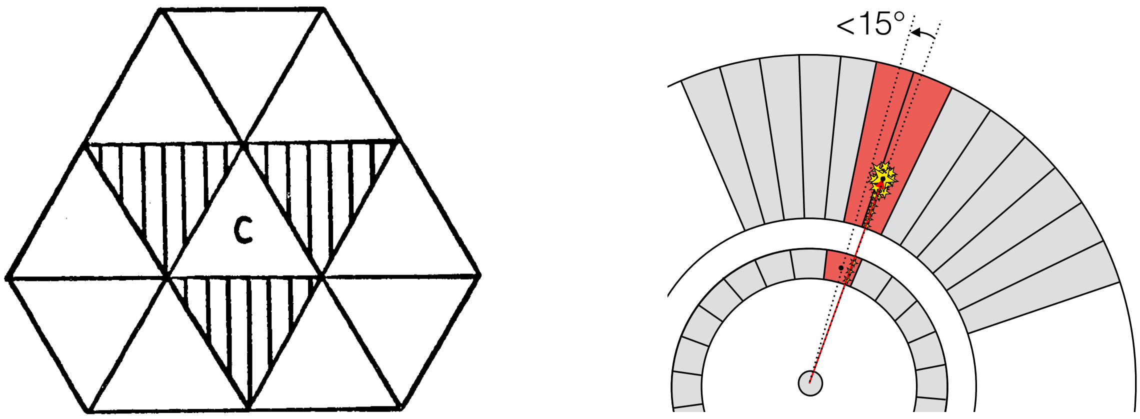

Figure 4.1: Schematic illustration of the particle reconstruction with the Crystal Ball detector and the PID. Left-hand side: thirteen nearest neighboring crystal configuration, i.e. central crystal (C) with its 12 nearest neighbors. Right-hand side: coincidence requirement for charged particles between a hit in the PID and a hit in the Crystal Ball detector.

shower. In total 13 neighboring elements are considered, since in general 98% of the deposited energy is not spread over more than 13 elements with a resolution of $\sigma_E = 0.028 \cdot E^{3/4}$ [104]. Such a 13 crystal configuration is illustrated on the left-hand side of Figure 4.1. Every element that received a signal above the threshold value is added to the cluster and excluded from the algorithm in order not to contribute to more than one cluster per event. The total cluster energy E_{cluster} is then given by the sum over the energies E_i of the n elements that have been found by the algorithm:

$$E_{\text{cluster}} = \sum_{i=1}^{n} E_i \ . \tag{4.2}$$

If the cluster energy E_{cluster} is below a cluster threshold of 20 MeV, the cluster is rejected in order to avoid split-offs being identified as particles. If not, the impact position vector of the particle $\vec{r}_{\text{cluster}}$ is determined by the weighted arithmetic mean, using the center of mass coordinate $\vec{r}_i$ (with respect to its origin in the target center) of each element and the square root of the individual energy E_i as weights:

$$\vec{r}_{\text{cluster}} = \frac{\sum_{i=1}^{n} \sqrt{E_i} \cdot \vec{r}_i}{\sum_{i=1}^{n} \sqrt{E_i}} \ . \tag{4.3}$$

For the remaining detector elements the algorithm is repeated until no detector element that received a signal above the threshold remains. Every determined cluster then corresponds to a particle of energy E_{cluster} and position vector $\vec{r}_i$.
In order to know if the particle corresponding to the cluster was neutral or charged, coincidences with hits in the PID are considered. From all of the PID hits, the one with the minimal difference in azimuthal angle, ϕ_{PID}, is compared with the azimuthal angle of the cluster ϕ_{Cluster}. According to the number of PID elements (24) and the finite distribution of the reaction vertex, a coincidence between a hit in the PID and

the Crystal Ball was assigned if the difference is smaller than 15°. The situation is illustrated in the right-hand side of Figure 4.1.

4.1.3 Reconstruction of Particles in TAPS

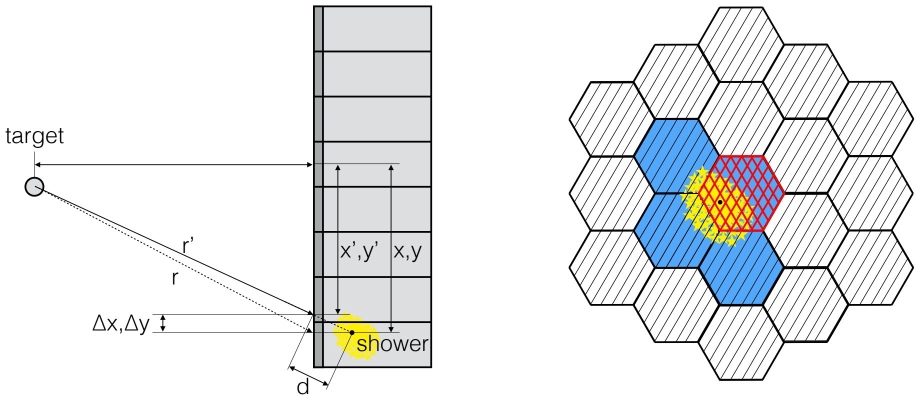

Figure 4.2: Schematic illustration of the particle reconstruction with TAPS and the Veto detectors. Left-hand side: illustration of the correction of the impact position. Right-hand side: coincidence requirement for charged particles between a hit in the Veto detectors and a hit in TAPS.

The identification of the crystals that contain information of a detected particle in TAPS is similar to the one in the Crystal Ball, as explained in Section 4.1.2. First, the element with the maximum deposited energy above a threshold value between 3 and 5 MeV is assigned to the center and time reference of the cluster. In contrast to the Crystal Ball cluster algorithm, all neighboring crystals in TAPS are considered. All neighboring crystals that received a signal above the threshold are added to the cluster. As for the Crystal Ball, the energy of the cluster is determined by the sum of all individual crystal energies, as given in Equation (4.2). However, the determination of the center of mass coordinates of the cluster is different. Contrary to the NaI(Tl) crystals of the Crystal Ball, the BaF_2 crystals of TAPS do not point in the direction of the target center, as shown in the left-hand side of Figure 4.2. Depending on the energy of the particle, the center of mass of the cluster is not on the surface, but at a certain depth in the crystal. The center of mass coordinates of the cluster (x,y) have to be corrected for the penetration depth d of the shower. The true impact position $(x'$,$y')$ is then given by [187, 188]:

$$\begin{aligned} x' &= x - x \cdot \left(\frac{r}{d} + 1\right)^{-1} \\ y' &= y - y \cdot \left(\frac{r}{d} + 1\right)^{-1} \\ d &= X_0 \cdot \left(\log\left\{\frac{E_{\text{cluster}}}{E_C}\right\} + 1.2\right) \quad , \end{aligned} \tag{4.4}$$

where $X_0 = 2.05$ cm is the radiation length, $E_C = 12.78$ MeV is the critical energy of BaF_2, and r is the *wrong* distance from the target to the cluster center of mass. The cluster coordinates $\vec{r}_{\text{cluster}}$ are given by logarithmic weighting with weights W_i according to [189]:

$$\vec{r}_{\text{cluster}} = \frac{\sum_{i=1}^{n} W_i \cdot \vec{r}_i}{\sum_{i=1}^{n} W_i} \quad \text{and} \quad W_i = \max\left\{0, W_0 + \log\left(\frac{E_i}{\sum_{i=1}^{n} E_i}\right)\right\} \ , \tag{4.5}$$

where $W_0 = 5$ is a free parameter and was determined by simulations [107]. The energy and position vector is then assigned to the detected particle. In addition, it is marked as charged if a coincidence with a veto detector was detected. For this, as illustrated in Figure 4.2, not only the veto element in front of the corresponding central TAPS crystal is checked, but also the vetos in front of all crystals that were assigned to the cluster. This is especially important for particles that are detected in the outer TAPS rings, since with increasing distance to the TAPS center, the impact offset (Δx, Δy) (see Figure 4.2) is larger.

4.2 Reconstruction of Particles at CBELSA/TAPS

The reconstruction of the particles at CBELSA/TAPS is similar as at A2. The reaction products are reconstructed over the energy and time information of the Crystal Barrel (Section 2.5.2), Forward Cone (Section 2.5.3), and MiniTAPS (Section 2.5.5) detectors and the information about charge by using the Inner detector (Section 2.5.4) or Veto detectors (sections 2.5.3, 2.5.5). The main difference is the reconstruction of the photon beam with the tagging spectrometer (Section 2.5.1). In contrast to A2, the tagger at CBELSA/TAPS consists of two different detectors, the bars and fibers, which require a combined reconstruction analysis.

4.2.1 Reconstruction of the Photon Beam

The energy and time information of the photon beam has to be reconstructed from the electrons that were detected by the scintillating bars and fibers of the tagger. As the bars and fibers are partly overlapping, it is necessary to combine their information in order to achieve proper identification of the deflected electron. While the time information of the photons is given by the signals measured by the bars and fibers, the energy is directly given by the deflection angle of the detected electron in the magnetic field of the tagger magnet. For a given electron beam energy, individual polynomials for the bars and fibers have been determined, which directly map a hit in a detector element to a corresponding electron energy. If the impact point in the tagger has been covered by the scintillating fibers, the energy information is extracted from their polynomials or otherwise those from the tagger bars are taken. The photon energy is also given by the beam energy, E_0, and the energy of the detected electron, E_{e^-}, that is given by the average energy from the polynomials of the coincident hits:

$$E_\gamma = E_0 - E_{e^-} \ . \tag{4.6}$$

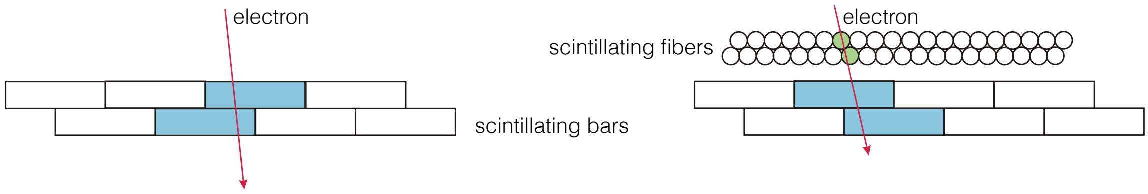

Figure 4.3: Illustration of the coincidence requirements in the tagger bars (left) and between the tagger bars and the scintillating fibers (right). Figure adapted from [190].

In order to correlate a photon from the beam with a detected electron, the individual timing signals of the tagger elements have to be investigated. This is achieved by coincidence requirements among the neighboring fibers and bars individually and afterwards, additionally among adjacent bars and fibers. Hits in the bars are considered coincident if they occur within 12 ns, in the fibers within 7 ns, and in the region of the overlap within 4 ns. This ensures that random tagger hits from electronic noise or cosmic radiation are suppressed. Furthermore, covering a certain region of the tagger with bars and fibers yields a higher energy resolution. The situation is illustrated in Figure 4.3

4.2.2 Reconstruction of Particles in the Crystal Barrel and Forward Cone Detector

In principle the cluster reconstruction in the Crystal Barrel detector is equivalent to that of the Crystal Ball detector, as explained in Section 4.1.2, except for the number of neighboring crystals that may contribute to the cluster. The procedure is as follows: every crystal with a measured energy above the threshold of 2 MeV is considered in the clustering algorithm. The crystal with the maximum deposited energy is set as the cluster center. In the case where one particle deposited its energy irregularly in the crystals, besides the main maximum, a second cluster (called a split-off) can occur. To avoid such misleading contributions, the central crystal of the cluster must have an energy above 20 MeV. The energy of the reconstructed particle is then given by the sum of the energies of the central crystal and its neighbors according to Equation (4.2). In the case of two individual but overlapping clusters, the energies are summed up weighted by the corresponding Molière radius [191]. The reconstructed cluster energy is then corrected for shower losses due to particles that do not fully deposit their energy in the crystals. This correction function has been determined by Monte Carlo simulations and allows for a correction depending on the impact point of the particle in the detector [192]. As for the Crystal Ball detector, the position vector $\vec{r}_{\text{cluster}}$ is reconstructed by the weighted arithmetic mean of the position vectors from the n crystals that were assigned to the cluster. But in this case the vectors are weighted with the logarithm of the individual energy ratios E_i/E_{cluster}

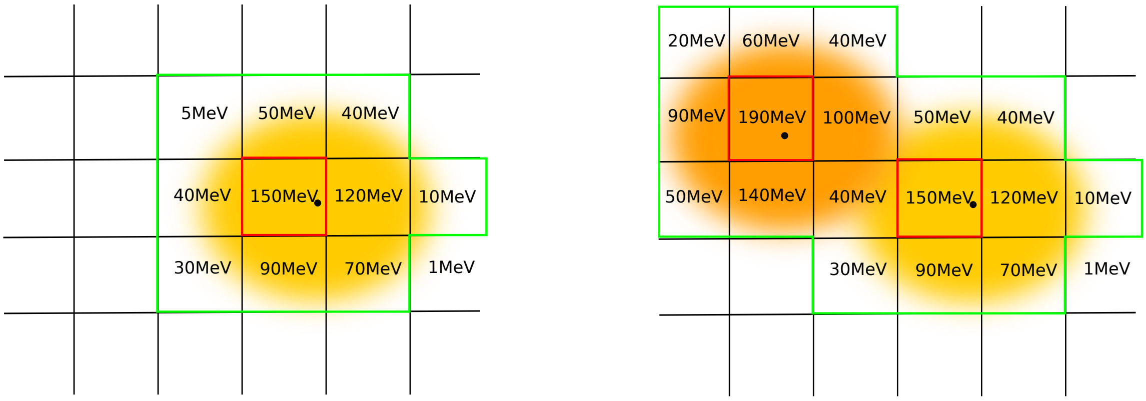

Figure 4.4: Illustration of the cluster reconstruction in the Crystal Barrel and Forward Cone detectors. Black: schematic representation of the crystal arrangement. Red: central crystals. Green: contributing crystals. Yellow: electromagnetic shower in the calorimeter. Left-hand side: cluster from an electromagnetic shower created by one incident particle. Right-hand side: cluster from two overlapping electromagnetic showers from two incident particles. Figure adapted from [190].

and an additional cut off parameter $P = 4.25$ [193]:

$$\vec{r}_{\text{cluster}} = \frac{\sum_{i=1}^{n}\left(P + \ln\left(\frac{E_i}{E_{\text{cluster}}}\right)\right)\cdot\vec{r}_i}{\sum_{i=1}^{n}\left(P + \ln\left(\frac{E_i}{E_{\text{cluster}}}\right)\right)} \qquad \text{where} \qquad \frac{E_i}{E_{\text{cluster}}} \geq \exp(-P) \tag{4.7}$$

The inner detector which surrounds the target inside the Crystal Barrel detector provides the information about the charge of the identified clusters. As described in Section 2.5.4, it consists of three layers of scintillating fibers which are rotated by roughly $\pm$ 25 $^\circ$ with respect to each other. This allows for the unambiguous determination of the crossing point of a particle from a hit in at least two of the three layers. Thus, in the first step, the cluster reconstruction is performed for each layer individually. Figure 4.5 illustrates the clustering process. For every layer, the fibers that received a signal are grouped into spatial clusters. Each spatial cluster is then subdivided into smaller clusters if the time difference between neighboring fibers is more than 14 ns. Spatial clusters that (due to the timing) have been divided into two or more sub-clusters are finally separated from each other. In the next step, the clusters of the individual layers are combined with each other in order to determine the penetration point. For this, every fiber is parametrized by an equation such that the intersection of two fibers, corresponding to a certain azimuthal angle ϕ and polar angle θ, can be determined analytically. Depending on the number of layers that successfully yield an intersection point, the cluster is marked as charged with a quality factor of 1 (all three layers) or 2/3 (two of three layers). By comparing the azimuthal angle ϕ and polar angle θ of the cluster in the Crystal Ball detector with those from the Inner detector, the cluster is marked as charged when the difference in ϕ is smaller than 12° and smaller than 30° in θ, as determined from the upper two

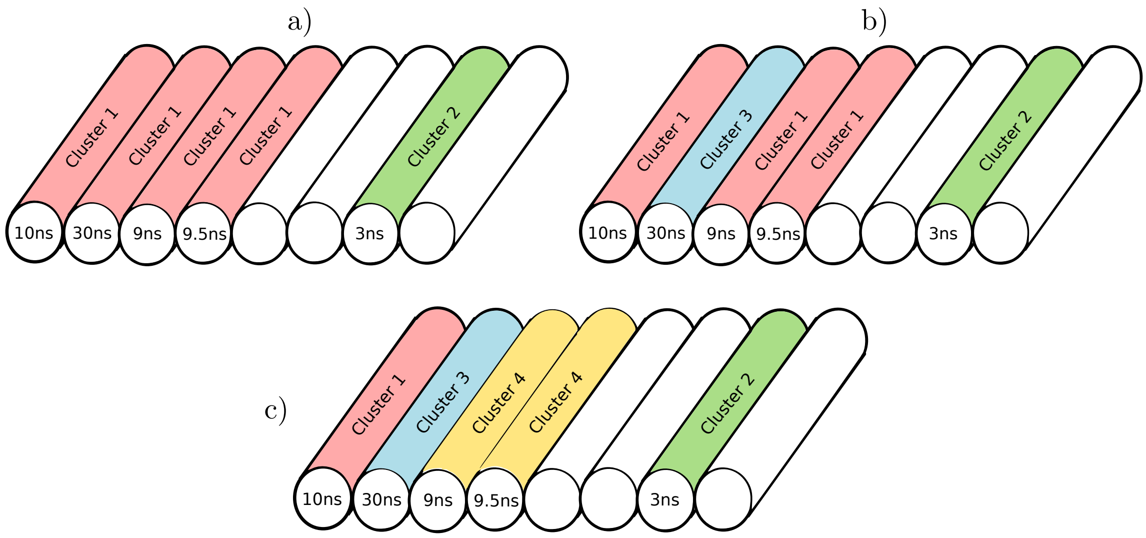

Figure 4.5: Illustration of the cluster reconstruction in the Inner detector. a) Initial spatial clustering of the fibers of an individual layer. b) Additional clustering based on the timing of the fibers within each cluster. c) Subsequent and final spatial re-clustering. Figure taken from [190].

spectra in Figure 4.6.

4.2.3 Reconstruction of Particles in the Forward Cone Detector

As already mentioned in sections 2.5.2 and 2.5.3, the Forward Cone detector consists of the same crystals as the Crystal Barrel detector. Hence, the clustering algorithm for particles in the Forward Cone detector is identical to the one described for the Crystal Barrel in Section 4.2.2
It is then checked to see if the charge sensitive scintillator plates have been fired. As mentioned in Section 2.5.3, these plastic scintillators are arranged in two layers that are shifted by 6°. In this configuration, the full angular range of the detector is covered by two plates and a cluster is only marked as charged if both plates have been fired within 20 ns. If the angular difference between the cluster in the Forward Cone and the coincident hit in the Veto detector is smaller than 14 ° in ϕ and 15 ° in θ, the hit is marked as charged. This criterium is illustrated in the bottom spectra of Figure 4.6.

4.2.4 Reconstruction of Particles in MiniTAPS

For the cluster reconstruction in the MiniTAPS detector, the energy threshold of a contributing crystal has to exceed 13 MeV and the minimal cluster energy is 25 MeV. In addition, as the two most inner rings are close to the photon beam, a slightly higher crystal threshold of 17 MeV was chosen in order to avoid contributions from interactions of the photon beam. The cluster algorithm is equivalent to the one

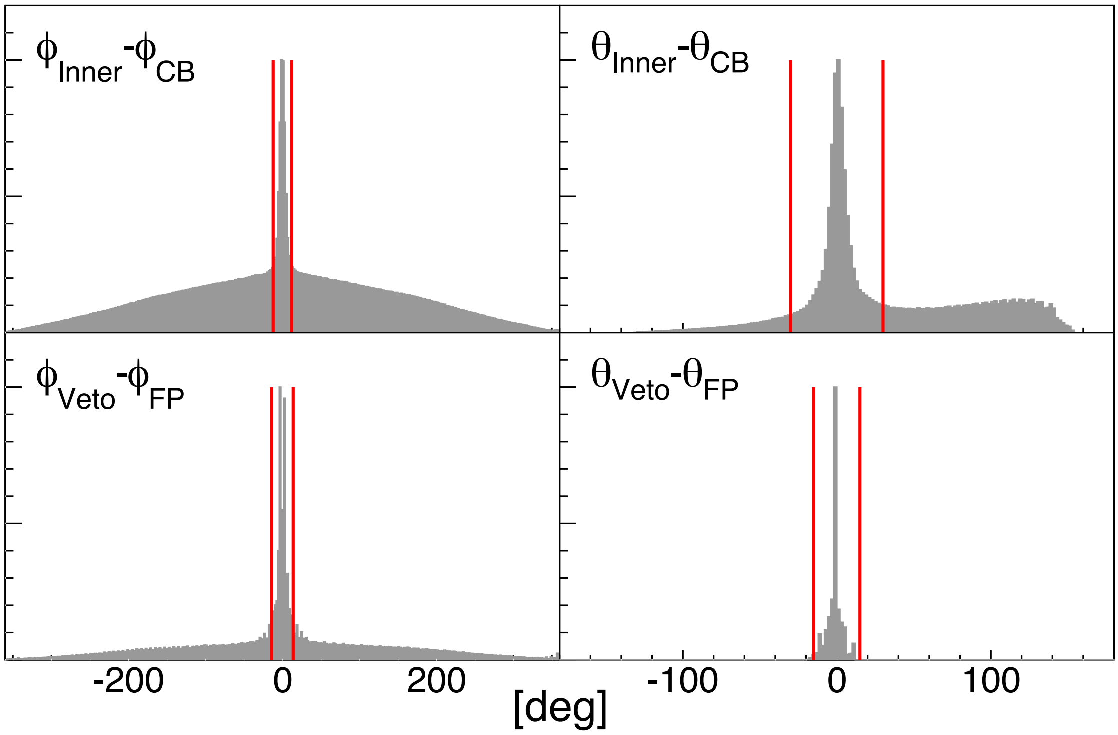

Figure 4.6: Illustration of the coincidence requirements for the identification of charged particles in the Crystal Barrel detector and the Forward Cone detector. The identification is based on the difference between the azimuthal angle ϕ and polar angle θ of the clusters from the Crystal Barrel detector (CB) and the Inner Detector (Inner), and from the Forward Cone (FP) and Veto Detectors (Veto).

for the Inner detector. First, spatial clusters are formed which then are regrouped depending on a time coincidence of 5 ns. The resulting groups then form the final clusters that are marked as charged with the same condition used for the TAPS detector at A2, i.e. if one of the vetos in front of any cluster crystal was fired.
As described in Section 4.1.3, the position vector of the cluster in the MiniTAPS detector has to be corrected for the penetration depth of the electromagnetic shower. Even though the same correction (Equation (4.4)) could be applied[1], an improved correction based on Monte Carlo simulation was developed, resulting in a better angular homogeneity. The correction is based on an initial linear correction (similar to the old method) and an additional correction of the energy due to shower losses. More details about the correction are given in [194].

[1]However, due to the geometrical difference between TAPS and MiniTAPS the summand in the formula for the penetration depth has to be changed from 1.2 to 2. [194]

5 Calibrations

The calibration of the experimental data is an important step and strongly affects the precision and resolution of the different analysis steps and thereby the results. The A2 data for this work includes a beamtime of liquid hydrogen (April 2009), three beamtimes of liquid deuterium (December 2007, February 2009 and May 2009), three beamtimes of deuterated butanol (July 2013, February 2014 and March 2015) and a beamtime of a carbon foam target (February 2014). The CBELSA/TAPS data for this work includes a beamtime of liquid hydrogen (November 2008) and liquid deuterium (December 2008), two beamtimes of deuterated butanol (January and June 2011) and one of a carbon foam target (November 2011). All beamtimes were calibrated after the beamtime concluded but since it would have exceeded the time frame, not all of the calibrations were done as part of this work. Furthermore, the data from the unpolarized targets (liquid hydrogen and deuterium) at A2 and CBELSA/TAPS was already taken in advance and thus, their calibration was part of a different work. In the A2 collaboration, the calibration software `CaLib` (as introduced in Section 3.2.3) allows for a completely single-handed data calibration within a reasonable time and hence, most often is carried out by one person alone. In contrast, at CBELSA/TAPS, every calibration step is distributed among the local group members [195] and hence, was carried out outside of this work. However, their standard calibration procedure does not include the energy calibration of the short gate component of the BaF_2 crystals of the MiniTAPS detector. In order to be able to do a pulse shape analysis (PSA, see Sections 5.2.6 and 6.4.1), the short gate information was additionally calibrated single-handedly.

The following sections introduce the main principles and techniques of the different calibration procedures of the A2 and CBELSA/TAPS data and presents an overview of the resulting calibration quality.

5.1 Calibration Principle

The measurement of time and energy information with electronic devices always requires an elaborate calibration of the individual components. While energies are usually measured by an accumulated charge in a QDC (Charged to Digital Converter), times are measured with TDCs. It is necessary to determine the correct conversion of the raw electronic signals into the corresponding physical quantity, which is the goal of the calibration procedure. Based on the linear response of the electronic devices, the conversion is similar for both cases.
In this way, the conversion from a TDC channel c to the physical time t is given by

$$t = g \cdot (c - o) \ , \tag{5.1}$$

where g is the proportional constant called the *gain*, which depends on the intrinsic behavior of the device and o is an offset that can be chosen according to the aim of the calibration. In general, it is chosen such that the coincidence time between any two elements is zero.
Concerning the readout of the PMTs with QDCs, in first approximation the dependence of the accumulated on the deposited energy is also linear, resulting in a similar conversion from charge to energy:

$$E_{\text{dep}} = g \cdot (c - p) \ , \tag{5.2}$$

where c corresponds to the digital channel of the QDC, p to the position of the pedestal, and g to the gain. The pedestal indicates the channel that corresponds to zero charge, i.e. zero energy. This intrinsic characteristic is individual for every device and is an anchor for the conversion. The gain is the proportionality constant and is a measure for the correlation of charge and energy. Using energy calibrations, the pedestal and gain of every individual detector component can be determined in a way that depending on the quality of the calibration, every device yields the same values for identical signals. By the above definitions, the unit of the gains are [ns/channel], respectively [MeV/channel], that of the offset and pedestal is [channel].

5.2 Calibration of the A2 Data

As previously mentioned, the four beamtimes on unpolarized targets were already calibrated in advance [100]. In this work, preliminary and raw calibrations have been carried out right before the data taking of the deuterated butanol beamtimes. This was important in order to provide a sufficiently accurate online analysis for the rate estimation, which was used to optimize the experimental conditions and settings. Furthermore it allows for the production of preliminary results that includes the rates and show the quality of the data. After the beamtime, the final calibrations were carried out by Dr. Lilian Witthauer [173].
In the following sections, the main principles and steps of the energy and time calibrations of the different detector components of the A2 experiment will be presented,

specifically for the May 2009 beamtime, a liquid deuterium beamtime, used in this work.

5.2.1 Crystal Ball Energy Calibration

Covering about 94% of the solid angle, the Crystal Ball detector is the main part of the detector system. Furthermore, the ability of using the sum of deposited energies, i.e. the Crystal Ball energy sum (see Section 6.6.2), in the first level trigger makes it a very powerful component of the experimental setup. Hence, it is necessary to have high quality calibrations, not only for the analysis, but also already during data taking. For this reason, the calibration procedure is divided into several parts, of which one, the low energy calibration, already takes place before the experiment. This mainly ensures that the relative behavior of the many detector components of the Crystal Ball is equal and that the information of the sum of deposited energy that is used for the trigger decision is sufficiently accurate.

Low Energy Calibration

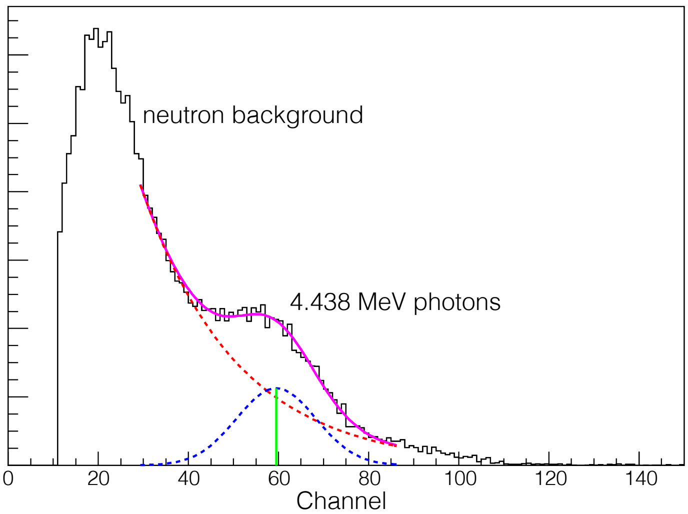

Figure 5.1: Measured signal of an individual NaI(Tl) crystal of the Crystal Ball detector obtained from the measurement with a ^{241}Am/^{9}Be source. Dashed blue curve: Gaussian fit of the 4.438 MeV photon peak. Solid green line: position of the 4.438 MeV photon peak. Dashed red curve: exponential fit of the neutron background. Solid magenta line: sum of signal and background fit. Figure adapted from [196].

The low energy calibration is a hardware calibration and is realized by using a neutron source ^{241}Am/^{9}Be. ^{241}Am is a long-living nucleus that decays by the emission of α particles that are captured by the ^{9}Be nucleus, which then becomes an excited ^{13}C* state. This excited nucleus then dominantly decays to an excited carbon ^{12}C* state by the emission of neutrons and to the ^{12}C ground state under the subsequent γ emission. These monoenergetic photons of energy 4.438 MeV are then used for the calibration of the readout of the NaI(Tl) crystals. The gains of all individual PMTs were regulated such that the 4.438 MeV photon peak in the raw ADC spectrum was located at the same position for all detector elements [196].

High Energy Calibration

The typical energies of the decay photons in an experiment are much higher than those used for the low energy calibration. A direct application of the calibration to such conditions, in general, can not be expected and therefore has to be verified, or if necessary, has to be extended. An efficient and rather straightforward method for this purpose is a calibration with real data where the kinematics are well defined, such as is the case of single π^0 photoproduction from free protons inside a hydrogen target. The π^0 decays into two photons of a broad energy range and are ideally suited for the calibration. Furthermore, the kinematics of the reaction are overdetermined such that the energy and the angles of the two decay photons can be calculated and compared with the measured values [196]. This method was initially carried out in addition to the calibration with the ^{241}Am/^{9}Be source at the time when the Crystal Ball detector arrived at MAMI and the PMTs had to be recalibrated. Both results were compared to each other and the gain of the PMTs was readjusted for those channels where the difference between the two calibrations was larger than 20%. Adjustments of the hardware components are not usually done frequently, unless the detector components were changed or moved. However it is important to monitor the calibration and detector responses for every beamtime. For this reason, every beamtime data is calibrated individually and serves as a fine tuning of the hardware settings.

The situation is different for data from beamtimes that used a nuclear target, e.g. liquid deuterium. Due to the Fermi motion of the nuclei inside the nucleus, the kinematics are not overdetermined anymore and a direct calibration, as mentioned in the beginning of this section, is not possible. Instead, an iterative approach is used that is based on the calibration of the individual detector elements against each other. In the data used in this work, this is realized by measuring the invariant mass of the two decay photons from single π^0. For every NaI(Tl) crystal, the $\gamma\gamma$ invariant mass $m_{\gamma\gamma,i}$ is determined when one of the photons was detected in this particular element i and the other photon in any other crystal o, by:

$$m_{\gamma\gamma,i} = \sqrt{2E_{\gamma,i}E_{\gamma,o}(1-\cos(\psi_{\gamma,io}))}\ , \tag{5.3}$$

where $E_{\gamma,i}$ denotes the reconstructed photon energy from the cluster with central element i and $\psi_{\gamma,io}$ is the opening angle between the two photon clusters with central element i and j. By comparing the measured invariant mass $m_{\gamma\gamma,i}$ with the theoretical value of the pion, $m_{\pi^0} = 134.976$ MeV, the conversion gain for crystal i can be

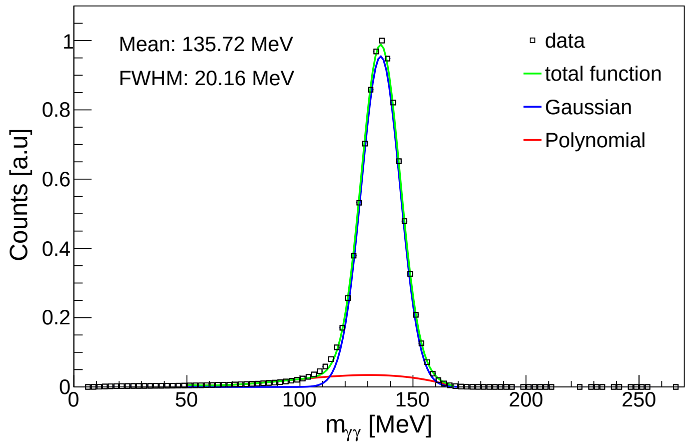

Figure 5.2: Invariant $\gamma\gamma$ mass spectrum of two photons detected in the Crystal Ball detector with the final calibration values used in the analysis. The spectrum was extracted in the analysis of single π^0 photoproduction from quasi-free protons after having applied all kinematic cuts. Shown is the integrated spectrum over all beam photon energies. Black squares: measured distribution from the May 2009 beamtime. Red line: polynomial of third order for the fit of the background. Blue line: Gaussian function for the fit of the signal. Green line: sum of polynomial and Gaussian functions.

determined and applied to the next calibration step[1]. As the invariant mass depends on the energies of the two photons and those depend on the conversion gain, every change in gain of one element affects the calibration of the other crystals. Using a sufficient number of iterations[2], the deviations of the invariant mass values can be minimized and converges to the theoretical value. The quality of the energy resolution obtained with this calibration procedure is presented in Figure 5.2 on the example for π^0 photoproduction from quasi-free protons.

Quadratic Energy Correction

The high energy calibration reliably adjusts the individual gains such that the invariant mass of the two photons peaks at the theoretical mass of the π^0. However, it assumes that the measured raw energies are correct, which is not the case. Due to the detector thresholds, as well as shower losses (especially at the border of the detector elements and the edges of the Crystal Ball detector), the uncalibrated energies are smaller and should not add exactly to the pion mass. Hence, the calibration results in an overcorrection, which is mainly prominent for higher photon energies as the relative fraction of energy loss is smaller. As a consequence, decay photons of higher energy, as produced in the decay of the η meson, receive a too high energy.

[1] Note, that due to the readout with sampling ADCs the pedestal is directly subtracted and hence does not have to be determined by the calibration.

[2] up to 15 iterations were performed for the energy calibration of CB of the May 2009 beamtime.

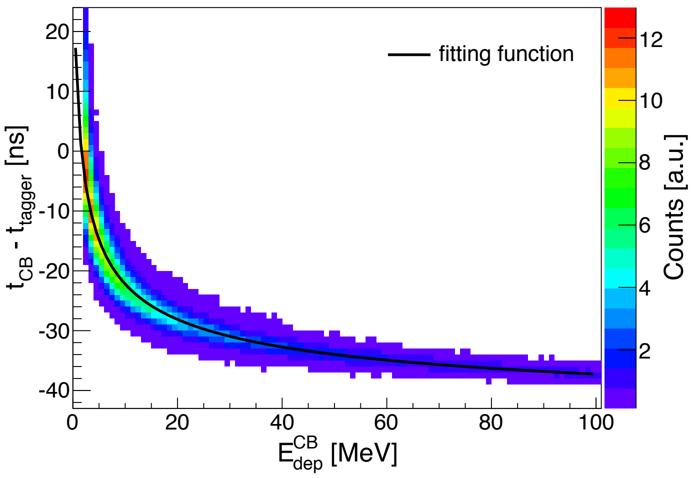

Figure 5.3: Illustration of the time walk effect of the NaI(Tl) crystals in the Crystal Ball detector. The solid black line corresponds to the fit function that was used for the correction of this effect. Figure taken from [100].

This effect is compensated by a quadratic energy correction:

$$E' = a \cdot E + b \cdot E^2 \ , \tag{5.4}$$

where E is the uncorrected photon energy and a and b are the parameters to be determined. The correction is carried out for every detector element such that the π^0 and η meson peak in the $\gamma\gamma$ invariant mass are located at their correct theoretical value.

5.2.2 Crystal Ball Time Calibration

The time calibration of the Crystal Ball detector requires more effort, as the rise time of the NaI(Tl) crystal signals is rather slow. As a consequence, the time at which a signal exceeds the LED threshold depends on the signals amplitude and on the deposited energy. This effect is called time walk and is illustrated in Figure 5.3. The calibration according to Equation (5.1) is performed in three steps. Only the offset had to be determined by the calibration as the gain of the CATCH TDCs was fixed to 117 ps/channel.

First, for every cluster in the Crystal Ball, the time difference between the contributing elements was calculated depending on the central element of the cluster. For every element, the mean value of the distribution was determined by a fit with a Gaussian and then used to calculate the new offset. Only a few iterations are necessary in order to align the mean time differences at zero.

The resolution of the CB time can be improved with the correction of the time walk effect. The correction is determined by fitting the measured time dependent on the deposited energy in the corresponding crystal with a four parameter power law, as shown in Figure 5.3. For every detector element, according to the deposited energy,

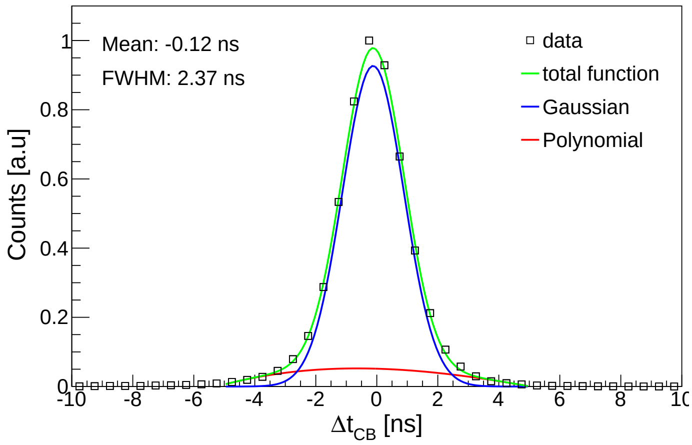

Figure 5.4: Time coincidence spectrum of clusters in the Crystal Ball detector. Black squares: measured distribution from the May 2009 beamtime. Red line: polynomial of third order for the fit of the background. Blue line: Gaussian function for the fit of the signal. Green line: sum of polynomial and Gaussian functions.

the time is then shifted to zero by the value of the fit result.
As the time walk correction affects the time, improper fits yield in a misalignment of the relative timing that has to be corrected by repeating the first step. The quality of the time calibration is presented in Figure 5.4.

5.2.3 Crystal Ball LED2 Threshold Calibration

As discussed in Section 2.3.1, the high LED threshold (LED2) is used for the multiplicity trigger condition. Unfortunately, the information, about which element contributed to the multiplicity by exceeding the threshold, is not written to the data stream. Hence, the energy threshold has to be reconstructed as follows: For each of the 45 discriminator blocks containing signals from 16 neighboring NaI(Tl) crystals, the element with the maximum deposited energy was determined. The procedure had to be repeated for the 6 logical segments from TAPS, as it was allowed to contribute to the total multiplicity as well. Then, depending on the multiplicity condition, the two or three elements that had the highest amount of deposited energy of all blocks, were expected to have contributed to the multiplicity condition and contain the information for the LED high calibration. For these elements, an energy spectrum is created (see left-hand side of Figure 5.5), from which the LED high threshold can be determined by fitting the derivative of the histogram with a Gaussian (see right-hand side of Figure 5.5).

5.2.4 PID Angle Calibration

The PID only provides information about the azimuthal angle, ϕ, and not about the polar angle, θ. Since ϕ is used for the identification of charged particles in the Crystal

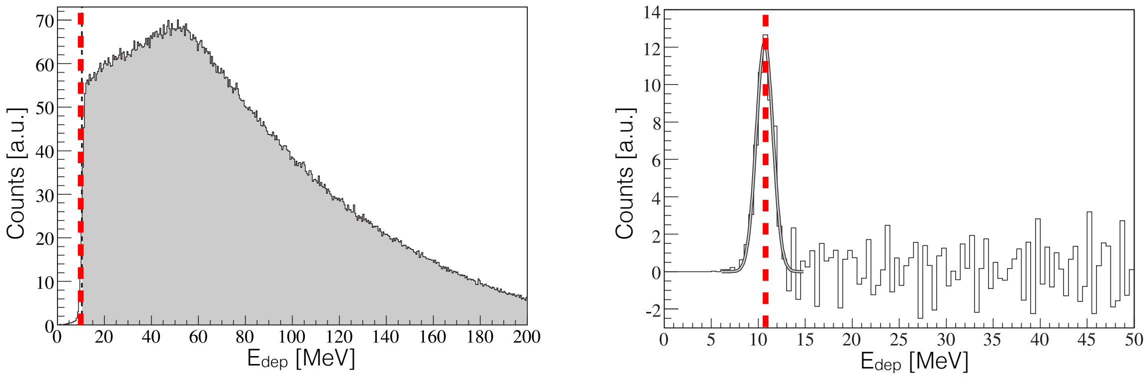

Figure 5.5: Determination of the CB LED2 threshold on the example of one NaI(Tl) crystal. Left-hand side: deposited energy spectrum. Right-hand side: derivative of the deposited energy fitted with a Gaussian. Dashed red line: mean value of the Gaussian that corresponds to the LED2 threshold. Figure adapted from [197].

Ball detector, a comparison of the azimuthal angle of the hit in the PID and the hit in Crystal Ball can provide accurate knowledge of the orientation of the PID. For this reason, the azimuthal correlation between both detectors was determined by an offline calibration. For this, events with exactly one hit in the Crystal Ball detector and one hit in the PID were selected and the measured ϕ angle of the hit in the Crystal Ball detector was plotted as function of the PID element. This distribution was then fit with a linear function in order to extract the corresponding azimuthal angles of all PID elements.

5.2.5 PID Energy Calibration

The energy information of the PID is only qualitatively needed in the analysis. For the discrimination of neutral and charged particles it is sufficient to know whether the corresponding PID element registered a signal above the threshold. However, for the identification of the charged particles it is necessary to have access to the energy information, although knowledge of the relative deposited energies of the different particles is sufficient. For this reason, the main principle of the energy calibration of the PID is to match the detector response to that from the simulation, i.e. to find the pedestals and gains such that a simulated proton deposits the same amount of energy in the PID as it does in the real data.
For the calibration, it is necessary to know the amount of energy that a proton of a certain energy deposits in the PID. Whereas the energy of the proton can be measured with the Crystal Ball detector, since it was already calibrated at this stage, from the PID only the raw ADC information is available. However, by using simulations with protons, the deposited energy in a PID element is known and is then used to determine the proper pedestal and gain of the data.

5.2.6 TAPS Energy Calibration

The TAPS detector is arranged as a forward wall and has to cope with very high rates. A sufficiently precise calibration of the hardware components of the detector is mandatory. Usually it is done before and after every experiment in order to monitor the stability and for setting the proper thresholds to accept or reject the desired events. The calibration procedure is very similar to the one of the Crystal Ball, as explained in Section 5.2.1 and will only be briefly summarized.

Low Energy Calibration

The horizontal alignment of the TAPS crystals allows for the calibration of the detector elements with cosmic radiation as the cosmic radiation passes equally through all crystals. In this way, the detector elements can be calibrated at any time without the need for any radioactive sources or a particle beam. For every detector element, the gain is then calculated with Equation (5.2) by using the position of the pedestal and of the cosmic peak. The situation is illustrated in Figure 5.6.

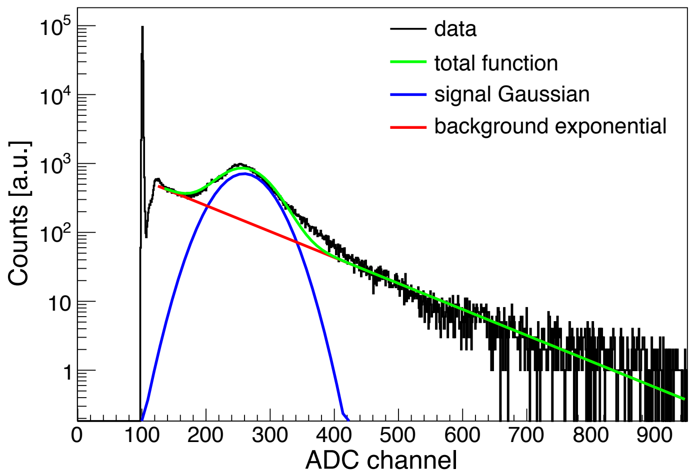

Figure 5.6: Typical BaF_2 energy calibration spectrum using cosmic radiation. Solid black histogram: raw ADC signal showing the pedestal at about channel 100 and the cosmic peak on background around channel 250. Red line: exponential fit of the background. Blue line: Gaussian fit of the 37.7 MeV cosmic peak. Green line: sum of exponential and Gaussian functions. Figure taken from [100].

High Energy Calibration

For every individual detector element, the position of the pedestal can be directly determined from the raw ADC spectra that were obtained during data taking. The gains were determined by the same method as used for the Crystal Ball. However, as the two decay photons from the pion only rarely go into TAPS, the statistics are too poor to do the calibration with the TAPS crystals only. As a consequence, the

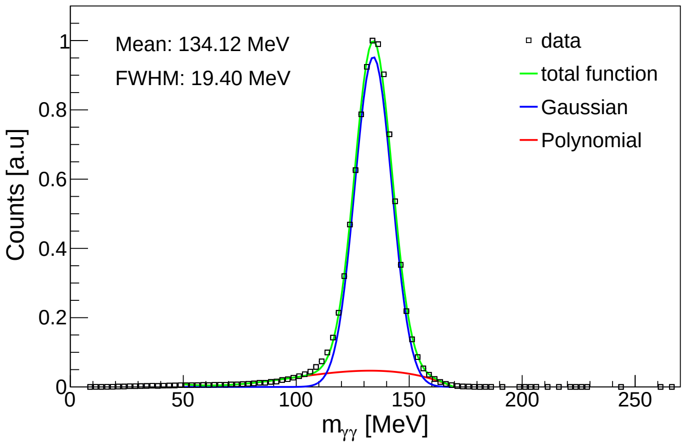

Figure 5.7: Invariant $\gamma\gamma$ mass spectrum of one photon detected in the Crystal Ball detector and one detected in TAPS with the final calibration values used in the analysis. The spectrum was extracted in the analysis of single π^0 photoproduction from quasi-free protons after having applied all kinematic cuts. Shown is the integrated spectrum over all photon beam energies. Black squares: measured distribution from the May 2009 beamtime. Red line: polynomial of third order for the fit of the background. Blue line: Gaussian function for the fit of the signal. Green line: sum of polynomial and Gaussian functions.

calibration has to be done with only one photon in TAPS and the other one in the Crystal Ball detector, making the TAPS energy calibration dependent on the Crystal Ball energy calibration. A representative spectrum of the invariant mass resulting from one photon in TAPS and one in the Crystal Ball detector is illustrated in Figure 5.7

Short Gate Calibration

As previously mentioned in Section 2.2.4, the BaF_2 have two well separable scintillation components that, in the readout, are integrated over a short and a long time interval. The standard energy calibration of the BaF_2 crystals corresponds to the energy calibration of the long component. However, proper knowledge of both components allows for a investigation of the correlation between the two energy yields, referred to as the pulse shape analysis (PSA), as illustrated in Figure 5.8. For the identification of particles, instead of the energy yields, the PSA radius r_{PSA} and PSA angle ϕ_{PSA}, as seen in the left-hand side of Figure 5.8 are suitable. They are defined as:

$$\begin{aligned} \phi_{\mathrm{PSA}} &= \arctan\left(\frac{E_S}{E_L}\right) \\ r_{\mathrm{PSA}} &= \sqrt{E_S^2 + E_L^2}\ , \end{aligned} \tag{5.5}$$

where E_S denotes the short gate energy, and E_L the long gate energy. As for photons, the ratio of the short to the long component is larger than for massive particles such as protons or neutrons. The energy yield is different and allows for a separation of

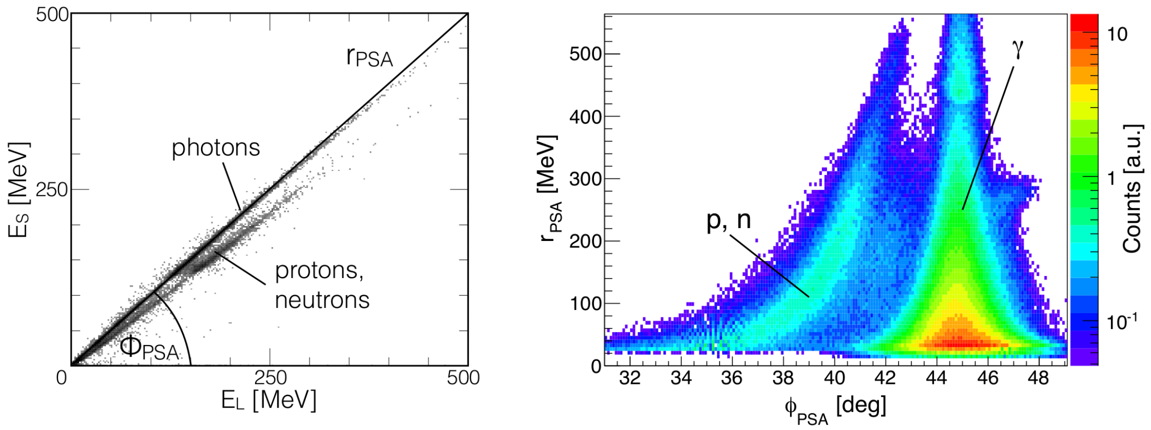

Figure 5.8: Typical pulse shape analysis (PSA) spectra of a BaF_2 crystal from the TAPS detector. Left-hand side: short gate energy as function of the long gate energy. Right-hand side: PSA radius r_{PSA} as function of the PSA angle ϕ_{PSA}. Data from the May 2009 beamtime. Photons are located at PSA angles of $\phi_{PSA} = 45\,°$ for all PSA radii r_{PSA} whereas for nucleons the PSA angle increases with increasing PSA radius. Left-hand side figure adapted from [188], right-hand side figure taken from [100].

these (see left-hand side of Figure 5.8).
In the calibration process, the gain and pedestal of the short gate readout are chosen such that the energy yield for photons is identical for both components, i.e. $E_S = E_L$, corresponding to PSA angles of $\phi_{PSA} = 45°$, as shown on the right-hand side of Figure 5.8.

Quadratic Energy Correction

The same procedure for the quadratic energy correction as for the Crystal Ball (see Section 5.2.1) was applied to the TAPS detector. Thereby one decay photon from the π^0 and η meson, respectively, was requested in the Crystal Ball detector and one in TAPS.

5.2.7 TAPS Time Calibration

The distance between the target and TAPS detector is about 1.5 m. Due to the high intrinsic time resolution of the BaF_2 crystals, the TAPS detector is ideally suited for time of flight measurements, which can be used for the identification of various particles (see Section 6.5.1). This is especially important as the energy resolution of the Veto detectors is not sufficient for a quantitative, but only a qualitative, discrimination among different particles. In order to maximize the time resolution, the TDC's were calibrated precisely. A time walk correction for the BaF_2 crystals was not necessary since the crystals have a very fast rise time and the time measurement is initialized by CFDs[3].

[3] CFD: Constant Fraction Discriminator

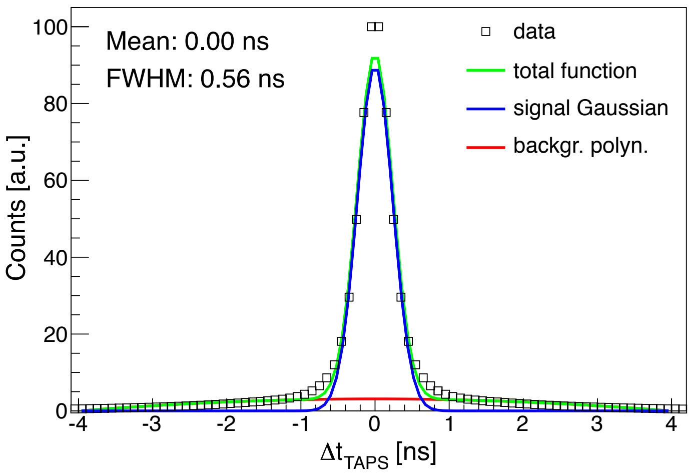

Figure 5.9: Time coincidence spectrum of clusters in TAPS. Black squares: measured distribution from the May 2009 beamtime. Red line: polynomial of third order for the fit of the background. Blue line: Gaussian function for the fit of the signal. Green line: sum of polynomial and Gaussian functions. Figure taken from [100].

The conversion gains of the TDCs were determined experimentally before the experiment. For this, the stop signal of the time measurement of the BaF_2 crystals is delayed with a series of cables of an exact known delay. Cosmics measurements were carried out with and without the subsequent adding of the delay cables. From the difference of the known delays plotted versus the difference of the pedestal positions, the conversion gain is given by the slope of the linear fit function.
The determination of the TDC offsets is done equivalently as for the Crystal Ball. The quality of the calibration is shown in Figure 5.9 for the example of the May 2009 beamtime.

5.2.8 TAPS LED Threshold Calibration

As for the Crystal Ball detector, the TAPS LED thresholds are used for the multiplicity trigger. However, in contrast to the Crystal Ball detector, the LED pattern of TAPS is available from the data stream and can directly be used for the determination of the LED thresholds. For a given detector element, the energy spectrum that contains all hits is divided by the same spectrum, but with the requirement of a coincident LED hit (see left-hand side of Figure 5.10). As was observed for the Crystal Ball detector, the spectrum shows a sudden steep rise at a certain value of deposited energy that corresponds to the LED threshold. For all elements the threshold was then determined by fitting the derivative with a Gaussian (see right-hand side of Figure 5.10).

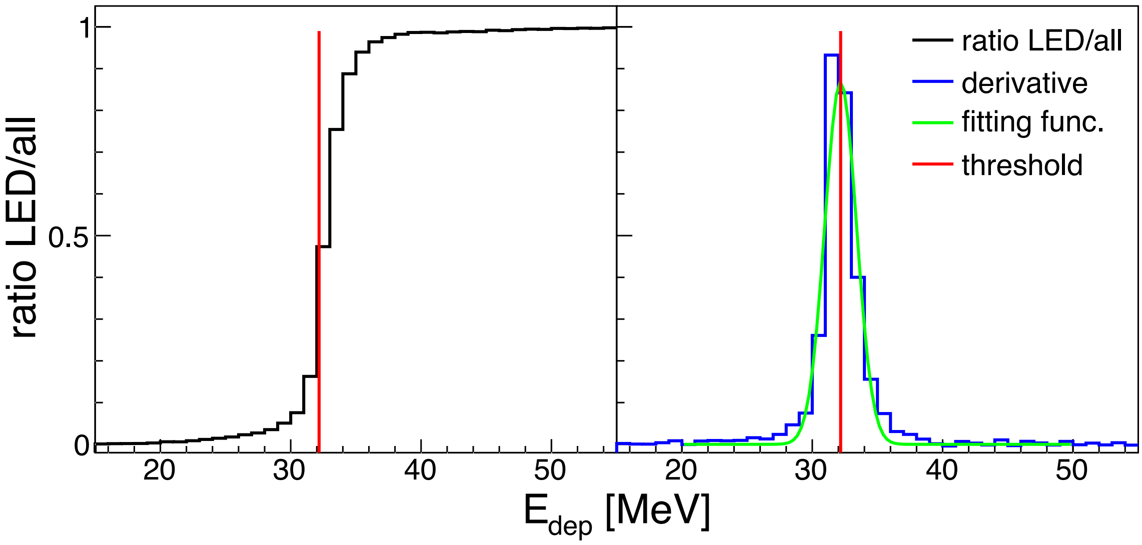

Figure 5.10: Determination of the TAPS LED threshold for the example of one BaF_2 crystal. Left-hand side: ratio of the energy spectrum with all hits and the spectrum with additional LED coincidence (black histogram). Right-hand side: derivative of the deposited energy (blue histogram) fitted with a Gaussian (solid green line). Solid red line: mean value of the Gaussian that corresponds to the LED threshold. Figure taken from [100].

5.2.9 TAPS CFD and Veto LED Threshold Calibration

The TAPS CFD (see Section 2.3.1) and Veto LED thresholds (Section 2.3.1) are calibrated with the same method as discussed above for the TAPS LED thresholds.

5.2.10 Veto Energy Calibration

In contrast to the BaF_2, the Vetos can not be calibrated using cosmic radiation as they are vertically aligned in front of the TAPS wall. Therefore, the calibration is carried out using experimental data. The raw ADC spectra were used to determine the positions of the pedestals. The conversion gain was, similarly to the calibration of the PID, determined from a comparison of the energy deposit in the data and simulation.

5.2.11 Tagger Energy Calibration

The quality and resolution of the energy information of the tagger is directly related to those of the photon beam. The energy resolution is given by the design of the tagger, i.e. the number, size, and overlapping of the scintillator bars. The quality depends on the knowledge of the magnetic field that deflects electrons onto the detectors, as well as on the electron beam energy. As both quantities depend on the experimental requirements and can vary between beamtimes, the energy calibration of the tagger has to be done individually for each beamtime. However, as the beam

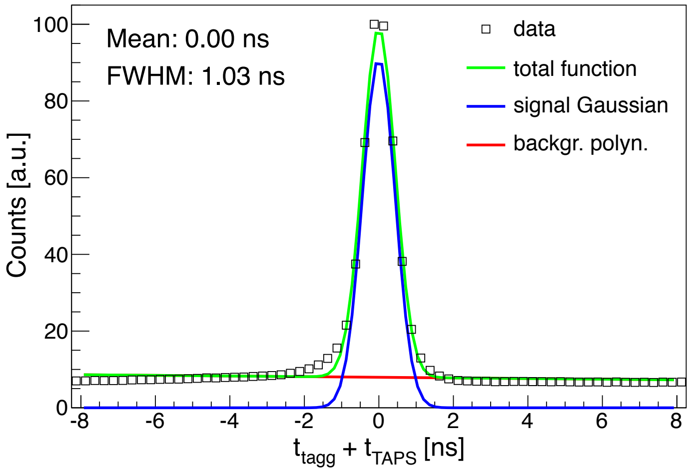

Figure 5.11: Time coincidence spectrum between clusters in TAPS and hits in the tagger. Black squares: measured distribution from the May 2009 beamtime. Red line: polynomial of third order for the fit of the background. Blue line: Gaussian function for the fit of the signal. Green line: sum of polynomial and Gaussian functions. Figure taken from [100].

energy is usually very stable and the magnetic field is monitored during the beamtime, one calibration is sufficient and can be used for the entire beamtime.
The calibration is based on the knowledge of the electron beam energy and elaborate measurements of the magnetic field [102]. In principle, this is sufficient for the determination of the electrons that hit the center of each tagger channel. However, an additional measurement with different magnetic fields and with a low intensity electron beam of different energies was carried out. A linear relationship was then used to allocate the electron energies to the tagger channels and to calculate the mean electron energy and the energy range of every individual element.

5.2.12 Tagger Time Calibration

As for the Crystal Ball, the time in the tagger is measured with CATCH TDCs with fixed conversion gains. Thus, only the offset had to be calibrated. The TAPS detector was taken as reference for the offset, as it has the best time resolution and it was already calibrated.
The time difference between the hits in the tagger and in TAPS dependent on the corresponding tagger channel was used to determine the position of the coincidence peak and by this the offset. Figure 5.11 shows the quality of the calibration.

5.3 Calibration of the CBELSA/TAPS Data

The calibration principle of the different detector components of the CBELSA/TAPS experiment is almost identical to that used in A2 except for a few exceptions that will be pointed out in the following sections. The energy and time calibrations are also based on the linear relation of electronical channel and physical quantity, as given by Equations (5.1) and (5.2), even though the gain and offset at CBELSA/TAPS in the definition of Equation (5.1) are decoupled in contrast to the definition at A2 [190]. The relation is defined as:

$$t = o + (g \cdot c) \; . \tag{5.6}$$

However, this only affects the values and not the interpretation or procedure of the calibration.

5.3.1 Time Calibrations

The time calibration of the individual detectors is first based on a rough calibration, which is used to shift all the prompt peaks of the TDC spectra to zero. However, the result is limited by the time resolution of the trigger signal and is optimized in the subsequent fine tuning of the calibration. By considering time differences instead of single time signals, the influence from the reference trigger signal can be removed. Hence, a reference detector has to be used for the fine tuning of the calibration. In the CBELSA/TAPS experiment the tagger is usually chosen as the reference detector and had to be calibrated first. For this, the time information of the Cherenkov detector was used as reference signal as it has only one channel and a high time resolution. For MiniTAPS, the only detector for which the time measurement is not done with CATCH TDC's, in addition to the offsets also gains had to be determined. Additional time walk corrections (see Section 5.2.2) were only performed for the CsI(Tl) crystals of the Forward Cone detector. For the Crystal Barrel detector, it was not possible since the correction needs time and energy information. For MiniTAPS, the correction is nonessential as previously discussed for the TAPS detector at A2 (see Section 5.2.7). The timing of the Inner detector was calibrated in the same way as for the other detectors. However, time information of the Inner detector was not used in this work since it was only assigned to charged particles, which for this analysis were not considered in the trigger and hence, did not have to meet the coincidence requirement.

5.3.2 Energy Calibrations

The high energy calibration of the detectors is also done iteratively. The peak of the $\gamma\gamma$ invariant mass spectrum is matched to the theoretical mass of the π^0 meson (see Section 5.2.1 for an example). Whereas the rough low energy calibration of MiniTAPS is also done with cosmic radiation, the initial calibration of the Crystal Barrel detector is different from that used for the Crystal Ball detector. At A2 the initial calibration of the Crystal Ball detector is based on a low energy calibration with the radioactive ^{241}Am/^{9}Be source, while at CBELSA/TAPS, a lightpulser system is used that feeds every crystal of the Crystal Barrel with light signals of different intensities, covering the full range of the ADCs [198]. In order to have an optimal energy

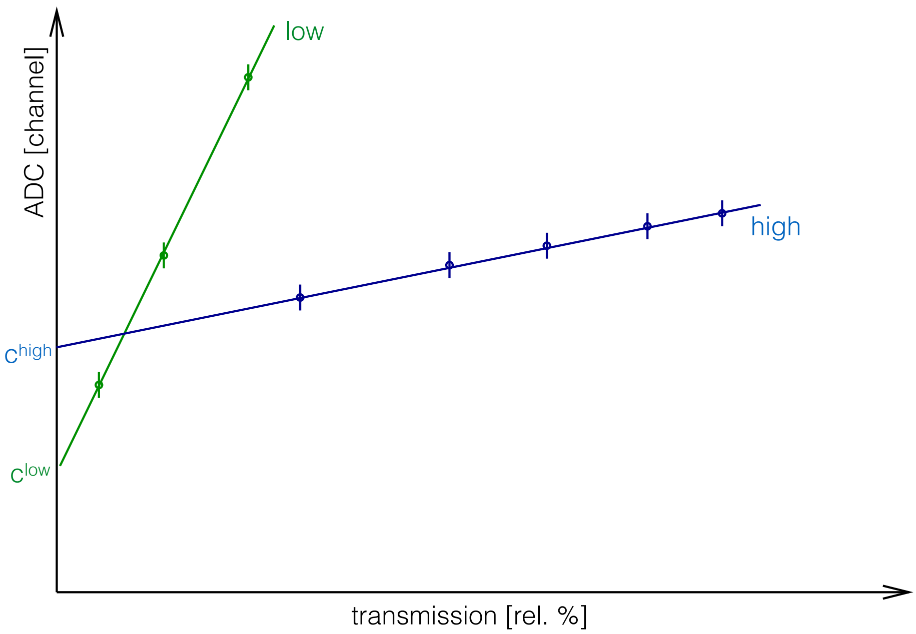

Figure 5.12: Showcase of a lightpulser measurement for the rough calibration of the Crystal Barrel detector. Shown is the ADC value versus the transmission. The intersection of the two lines with the y-axis determine the individual pedestals. The reduction factor is given from the ratio of the different slopes. Figure taken from [198].

resolution in the Crystal Barrel detector, ADCs with two different energy ranges are used. Therefore the conversion contains two equations with four unknowns, i.e. two pedestals $\mathrm{p}^{\mathrm{low}}$, $\mathrm{p}^{\mathrm{high}}$ one conversion gain g and a reduction factor between low and high range g_{R}, which are related to the deposited energies $E_{\mathrm{dep}}^{\mathrm{low}}$ and $E_{\mathrm{dep}}^{\mathrm{high}}$ according to Equation (5.2):

$$\begin{aligned} E_{\mathrm{dep}}^{\mathrm{low}} &= g \cdot \left(c^{\mathrm{low}} - p^{\mathrm{low}}\right) \\ E_{\mathrm{dep}}^{\mathrm{high}} &= g \cdot \left(c^{\mathrm{high}} - p^{\mathrm{high}}\right) \cdot g_{\mathrm{R}} \ . \end{aligned} \tag{5.7}$$

For all crystals, a gain of $g = 0.033$ MeV/channel was used and the pedestals and the reduction factor were determined from the lightpulser measurement. The lightpulser is a type of flash lamp that emits light signals of similar shape as the spectrum of the CsI(Tl) crystals. Using lightguides, the light pulses are fed into the wavelength shifters of the individual crystals. Using six different filters, the intensity of the light pulse can be changed. With this setup, the signals correspond to the dynamic range of the Crystal Barrel detector. As the characteristics of the lightpulser are well known and cover the full range of the ADC, the three parameters can be fully determined from the measurement, as shown in Figure 5.12.

5.4 Calibration of the A2 and CBGEANT Simulations

The calibration of the simulation is necessary since the simulation is used to compare or correct the experimental data. However, this depends on how accurate the setup was described in the simulation. Due to the complex geometry and material composition of the detectors, this is not self-evident and in general not within reach. Furthermore, the response of the individual detectors and the interactions of the particles with the detector matter are based on calculations and do not have to match reality.

5.4.1 Energy Calibration of the A2 Simulation

In general, time information does not have to be calibrated for the simulation, as coincidence is always given in the simulation. Hence, the calibration of the simulation involved only the energy calibration of the Crystal Ball and TAPS detectors and the thresholds were set to those determined from the real data. For this reason, the high energy and quadratic energy calibration for the CB detector and TAPS have been carried out in the same way as described for the data (see Sections 5.2.1, 5.2.6).

As in this work data from several beamtimes using different settings and target lengths were analyzed, it was important to adapt the behavior of the simulation to that of the experiment. For this reason, the energy and angular resolutions of the Crystal Ball and TAPS detectors have been determined for every individual simulation.

5.4.2 Energy Resolutions in the Simulations

In order to achieve the same energy resolution in the simulation as in the data, the deposited energies in the simulation were smeared according to an experimentally determined parametrization of the energy resolution for the Crystal Ball [199], Crystal Barrel detector [119, 200], MiniTAPS, and TAPS. TAPS and MiniTAPS have the same energy resolution [199]:

$$\frac{\Delta E}{E} = \frac{2\%}{(E[\mathrm{GeV}])^{0.36}} \qquad \text{(Crystal Ball)}\ , \tag{5.8}$$

$$\frac{\Delta E}{E} = 1.8\% + \frac{0.8\%}{(E[\mathrm{GeV}])^{0.5}} \qquad \text{(TAPS)}\ , \tag{5.9}$$

$$\frac{\Delta E}{E} = \frac{2.8\%}{(E[\mathrm{GeV}])^{0.25}} \qquad \text{(Crystal Barrel)}\ , \tag{5.10}$$

$$\frac{\Delta E}{E} = 1.8\% + \frac{0.8\%}{(E[\mathrm{GeV}])^{0.5}} \qquad \text{(MiniTAPS)}\ . \tag{5.11}$$

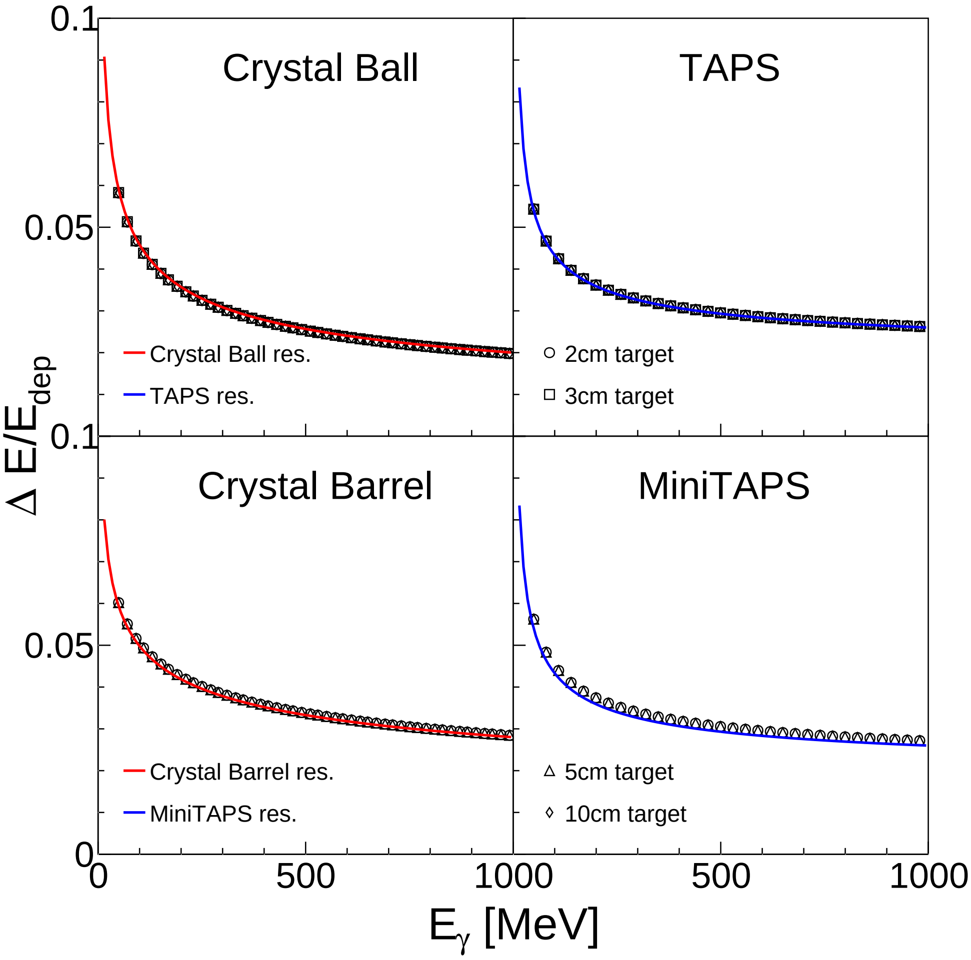

Figure 5.13: Energy resolution for photons in the Crystal Ball and TAPS detector (top row) at A2 and Crystal Barrel and MiniTAPS at CBELSA/TAPS (bottom row). Open symbols: parametrized resolution for different target lengths (see legend). Solid red line: resolution parametrization for the Crystal Ball/Crystal Barrel detector (Equation (5.8)). Solid blue line: resolution parametrization for MiniTAPS/TAPS (Equation (5.9)).

For this purpose, isotropically distributed photons of energies up to 1 GeV were simulated. The deposited energy and the resolution were determined by fitting an experimental response function to the measured spectra [107]. The energy of the simulation was smeared such that it fits the corresponding parametrization from equations (5.8)-(5.11). However, as the parametrizations were determined experimentally and hence their precision obviously exceeds that obtained from the simulation, the smearing procedure was only used to achieve a preferably similar resolution. The energy resolution that was used in the analyses using different target lengths hence was in all case given by that of the parametrizations, as illustrated in Figure 5.13. Effects from the different target lengths hence can not be observed in that Figure. Detailed information about the influence of the target length on the energy resolution can be found in [100, 173].

5.4.3 Angular Resolutions in the Simulations

The angular resolutions in the Crystal Ball and TAPS detector were determined with the same simulation of isotropically distributed photons of energies up to 1 GeV. The difference between the generated and the measured photon azimuthal and polar angles was calculated in dependence of the polar angle for every simulation of a different experimental setup. A dependence on the energy was not taken into consideration. The results for the resolution of the azimuthal angle, ϕ, and polar angle, θ, for the Crystal Ball detector are presented in Figure 5.14 and for TAPS in Figure 5.15. The influence of the target length on the resolution of the polar angle, θ, for the detection in the Crystal Ball and Crystal Barrel detector is clearly visible. With longer targets, the difference of the flightpath of a particle along and perpendicular to the target increases and results in a poor resolution. Due to the similar target diameters, the influence of the target length on the resolution of the azimuthal angle, ϕ, is negligible in both the Crystal Ball and the Crystal Barrel detector and only somewhat larger in MiniTAPS and TAPS. In MiniTAPS and TAPS, the resolution does not really depend on the target length, but for TAPS the effect of the $PbWO_4$ crystals in the two most inner rings is visible in the top right figure in Figure 5.15. As the $PbWO_4$ crystals were not used in any of the beamtimes, the resolution suddenly decreases at smaller polar angles.

5.5 Calibration Quality

A summary of the overall resolutions after the final calibration is presented in Table 5.1. Shown is the energy resolution on the example of the $\gamma\gamma$ invariant mass and the different detector time resolutions. The values were determined in the analysis of single and double π^0 photoproduction from the proton in the July 2013 beamtime at A2 and in the analysis of double π^0 photoproduction from the proton in the January 2011 beamtime at CBELSA/TAPS.

<table>
<tr><th colspan="3">A2</th><th colspan="2">CBELSA/TAPS</th></tr>
<tr><th>Type</th><th>Quantity</th><th>ΔE or Δt</th><th>Quantity</th><th>ΔE or Δt</th></tr>
<tr><td>Energy</td><td>π^0 in $m_{\gamma\gamma}$
$2\pi^0$ in $m_{\gamma\gamma}$</td><td>21 MeV
20 MeV</td><td>$2\pi^0$ in $m_{\gamma\gamma}$</td><td>19 MeV</td></tr>
<tr><td>Time</td><td>CB-CB
CB-TAPS
TAPS-TAPS
Tagger-CB
Tagger-TAPS</td><td>3.53 ns
1.97 ns
0.54 ns
2.07 ns
0.91 ns</td><td>FP-FP
FP-TAPS
TAPS-TAPS
Tagger-FP
Tagger-TAPS</td><td>2.35 ns
1.72 ns
0.73 ns
1.61 ns
0.86 ns</td></tr>
</table>

Table 5.1: Overview of the average energy and time resolutions (FWHM) of the A2 (left) and CBELSA/TAPS (right) experiments. Values obtained from the π^0 and $2\pi^0$ analyses of the deuterated butanol data.

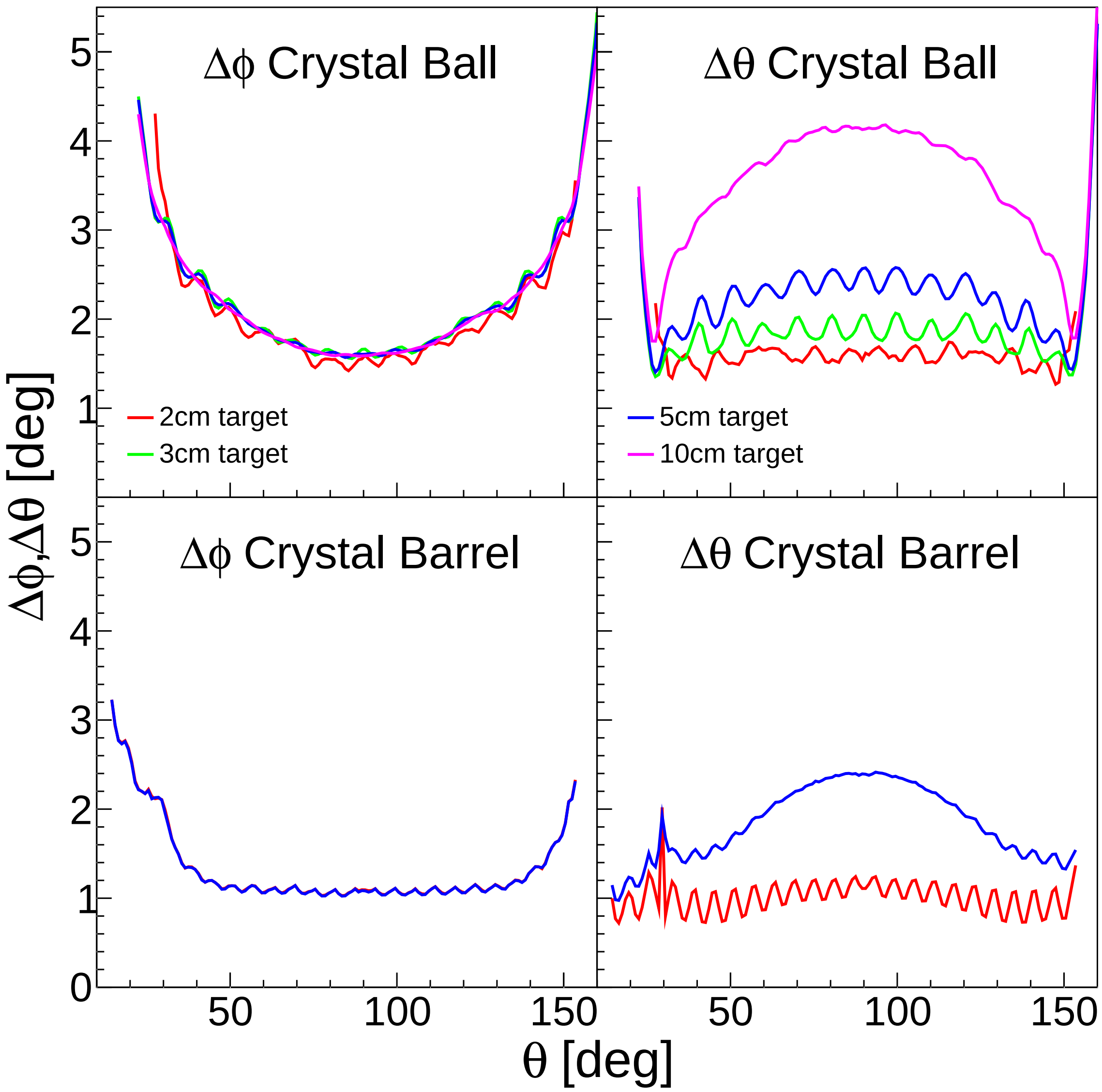

Figure 5.14: Simulated angular resolution of photons in the Crystal Ball detector (top row) and the Crystal Barrel detector (bottom row). Left-hand side: resolution of azimuthal angle ϕ. Right-hand side: resolution of polar angle θ. Solid red line: resolution for a 2 cm target. Solid green line: resolution for a 3 cm target. Solid blue line: resolution for a 5 cm target. Solid magenta line: resolution for a 10 cm target.

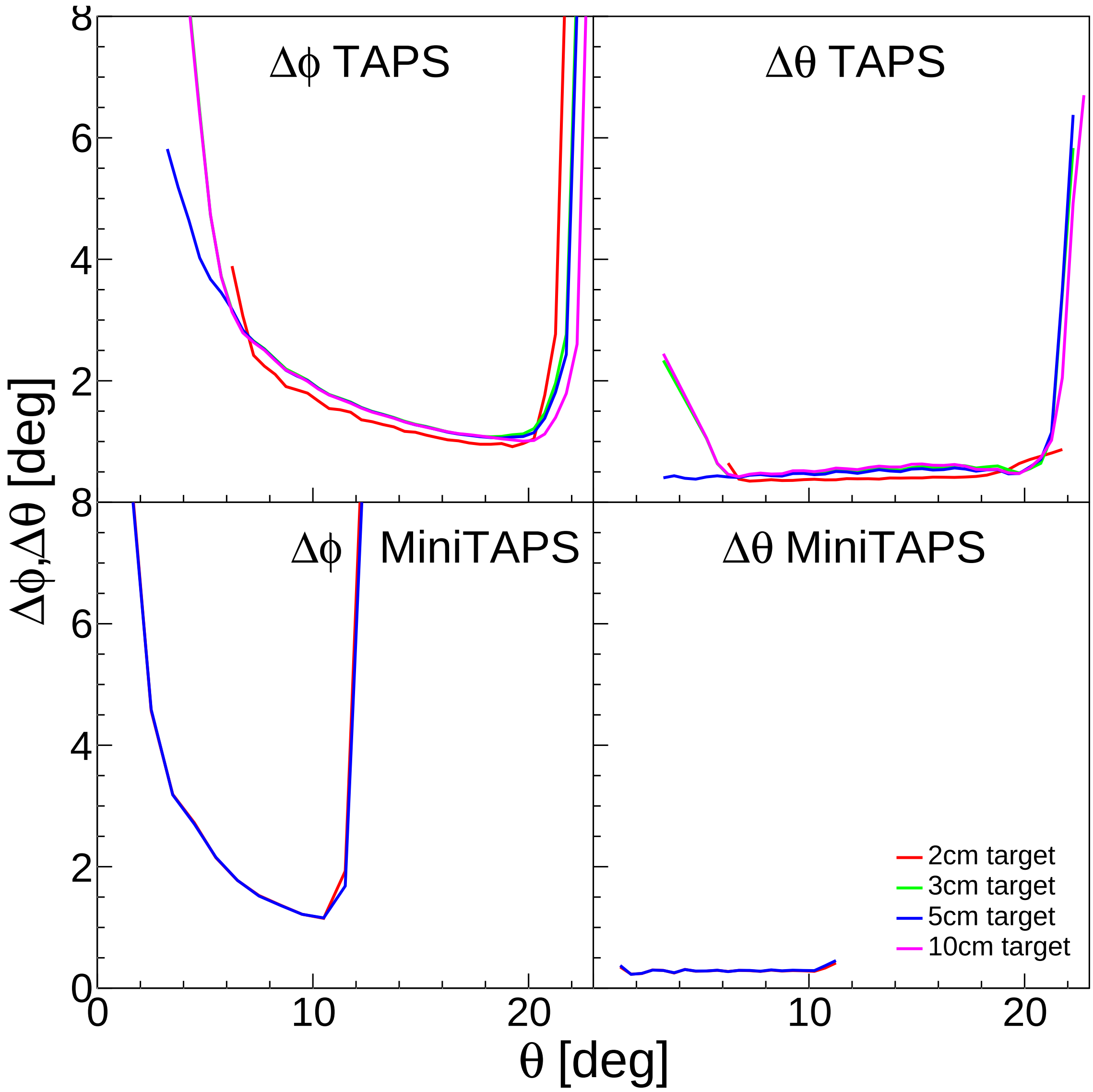

Figure 5.15: Simulated angular resolution of photons in the TAPS detector (top row) and MiniTAPS (bottom row). Left-hand side: resolution of azimuthal angle ϕ. Right-hand side: resolution of polar angle θ. Solid red line: resolution for a 2 cm target. Solid green line: resolution for a 3 cm target. Solid blue line: resolution for a 5 cm target. Solid magenta line: resolution for a 10 cm target.

6 Data Analysis

After the calibration of all detector components has been performed and a proper reconstruction of the particles was done, the data can be analyzed for the quantities of interest in specific physical reactions. This chapter presents the different steps and methods to extract the differential mass distributions and differential and total cross sections of unpolarized hydrogen and deuterium data as well as the extraction of the differential and total helicity dependent cross sections and the double polarization observable E of polarized deuterated butanol data.

Within this work, two experiments at ELSA and three experiments at MAMI (see Table 2.8) were carried out using a polarized deuterated butanol target. At both accelerators, an additional experiment with the identical setup, but with a different target material, i.e. carbon foam instead of deuterated butanol, were performed (see Table 2.7) in order to allow for the determination of the unpolarized background reactions on the unpolarized nuclei of the deuterated butanol. The experiments on liquid hydrogen and deuterium stem from previous works, but these data were used for the extraction of the unpolarized results.
As the main goal of the experiments with the deuterated butanol and carbon target was to determine the helicity dependent cross sections and the double polarization observable E of η (see doctoral thesis of Lilian Witthauer [173]) and double π^0 photoproduction from quasi-free protons and neutrons (this work), the trigger was optimized to the rates of these two reactions. However, since the energy sum of the Crystal Ball detector at A2 is a part of the first level trigger, it was possible to use a multiplicity two trigger in order to allow for the measurement of the $\eta \to 2\gamma$ and $\pi^0 \to 2\gamma$ decays, which was not possible at the CBELSA/TAPS experiment. Since the Crystal Barrel detector was not part of the first level trigger, only the detector components in the forward direction (where due to the electromagnetic background the highest rates occur) contributed to the trigger. With a lower multiplicity condition the required production rates would not have been possible. For this reason, only results for double π^0 photoproduction (and not single for π^0) could be extracted from the CBELSA/TAPS experiment, whereas the A2 data allowed to determine additional results for single π^0 photoproduction.

The data from the experiments on the unpolarized liquid hydrogen and deuterium targets were on the one hand used for a high statistics measurement of differential and total cross sections on the quasi-free proton and neutron, respectively. On the other hand, it provided additional possibilities for the extraction of the double polarization observable E as well as the helicity dependent cross sections, which improved the investigation of systematic errors.

In this work, the following reactions were analyzed for the extraction of the results (an initial state nucleon in brackets denotes the spectator nucleon, a final state nucleon in brackets denotes that its coincident detection was not required):

Analyzed reactions from the A2 data

$\gamma N(N) \to \pi^0(N)$	quasi-free inclusive π^0 photoproduction from the deuteron
$\gamma p(n) \to \pi^0 p$	quasi-free exclusive π^0 photoproduction from the proton
$\gamma n(p) \to \pi^0 n$	quasi-free exclusive π^0 photoproduction from the neutron
$\gamma p \to \pi^0\pi^0(p)$	inclusive $\pi^0\pi^0$ photoproduction from the free proton
$\gamma p \to \pi^0\pi^0 p$	exclusive $\pi^0\pi^0$ photoproduction from the free proton
$\gamma N(N) \to \pi^0\pi^0(N)$	quasi-free inclusive $\pi^0\pi^0$ photoproduction from the deuteron
$\gamma p(n) \to \pi^0\pi^0 p$	quasi-free exclusive $\pi^0\pi^0$ photoproduction from the proton
$\gamma n(p) \to \pi^0\pi^0 n$	quasi-free exclusive $\pi^0\pi^0$ photoproduction from the neutron

Analyzed reactions from the CBELSA/TAPS data

$\gamma p \to \pi^0\pi^0(p)$	inclusive $\pi^0\pi^0$ photoproduction from the free proton
$\gamma p \to \pi^0\pi^0 p$	exclusive $\pi^0\pi^0$ photoproduction from the free proton
$\gamma N(N) \to \pi^0\pi^0(N)$	quasi-free inclusive $\pi^0\pi^0$ photoproduction from the deuteron
$\gamma p(n) \to \pi^0\pi^0 p$	quasi-free exclusive $\pi^0\pi^0$ photoproduction from the proton
$\gamma n(p) \to \pi^0\pi^0 n$	quasi-free exclusive $\pi^0\pi^0$ photoproduction from the neutron

The main analysis principle is identical for all of the reactions mentioned above. The main difference is given between the inclusive and exclusive analyses, of which the latter requires the detection of recoil nucleons, which is more difficult and requires additional analysis steps. Another difference is given between the analyses of data from free protons (liquid hydrogen data) and quasi-free nucleons (all other data). Nucleons bound in nuclei exhibit Fermi motion (according to a certain momentum probability distribution, see Figure 3.9 for a few example distributions), which drastically affects the kinematics and also the resolution of the results. Additionally, it complicates the extraction of the results as a function of the final state invariant mass W, which will be discussed in Section 6.7.

The analysis strategy is based on the reconstructed clusters in the individual detectors. In the beginning, the clusters are assigned to neutral or charged particle candidates. According to the number of neutral and charged particles that participate in the reaction of interest, in a first analysis step, the presort analysis, the events with the corresponding clusters are selected and the remaining events are rejected. First candidates for the π^0 or $\pi^0\pi^0$ mesons and the recoil neutrons (if required) are reconstructed out of the neutral clusters (see Section 6.1), whereas the charged cluster is assigned to the proton. These particle candidates will then be tested and confined with several primarily kinematics related cuts (see Section 6.4). Thereby, it is important to point out that for the identification of the neutral and charged particles, only logical information of the charged particle identification detectors have been used, i.e. if the detector has seen a charged particle or not and not any information about time of flight or deposited energies. Such information was only used at the final stage before the extraction of the results in order to check the quality of the identification (see Section 6.5). In contrast to an analysis that is based on the usage of all possible detector information from the beginning, this in fact might result in a worse efficiency of the particle reconstruction, but it is less prone to inconsistencies between simulation and data. Reproducibility of simulation and data is one of the main fundaments of a reliable analysis with the aim of absolute normalization. Therefore the main challenge of the simulation is the realistic modeling of the detection of nucleons, which depends on the correct implementation of the detector geometries and materials, but also on the physics models that are used. This mainly affects the exclusive analyses that rely on the coincident detection of the recoil nucleon. In contrast to the modeling of nucleon interactions, the modeling of the photon interactions in the simulation is much more solid. Therefore, the identification of the particles in the analysis primarily relies on the latter, i.e. the reconstruction of the intermediate state meson(s) and by that, on the detection of photons.

Section 6.1 is dedicated to the method and quality of the π^0 and $\pi^0\pi^0$ meson reconstruction. In Section 6.2, the coincidence requirements between the detectors and the participating particles will be explained and Section 6.3 presents the subtraction of random background hits in the tagging spectrometer. The identification of the reaction by using different cuts on kinematics and other characteristics will be discussed in Section 6.4 and the quality of the particle identification will be investigated in Section 6.5. The next sections will introduce the application of the software trigger (Section 6.6), the reconstruction of the final state invariant mass W (Section 6.7), the determination of the detection efficiencies (Section 6.8), the correction of the gap between the Crystal Ball and TAPS detectors at A2 (Section 6.9), the calculation of the photon flux (Section 6.10), and the determination of the polarization values (Section 6.11). The last sections present the estimation of the cross section on the free neutron (Section 6.12), the different methods that have been used for extraction of cross sections, mass distributions and the polarization observable E (Section 6.13), the empty target subtraction (Section 6.14), the determination of the systematic uncertainties (Sections 6.15 and 6.16) of the experiment and analysis and finally the merging of datasets (Section 6.17).

6.1 Identification of the π^0 and $\pi^0\pi^0$ Mesons

After the reconstruction of the neutral and charged clusters, the first step of the analysis is to assign the available clusters to the particles of the reaction. In principle, considering the rather large Molière radius of the NaI(Tl) crystals of the Crystal Ball detector (4.105 cm [201]), the slightly shorter Molière radius of the CsI(Tl) crystals of the Crystal Barrel and Forward Cone detector (3.531 cm [201]), and the again shorter Molière radius of the BaF_2 crystals of the TAPS and MiniTAPS detectors (3.117 cm [201]), one could suggest that a discrimination between photons and neutrons is possible by regarding the size of the individual clusters. Figure 6.1 shows the typical cluster sizes for the different cluster types of single π^0 photoproduction (upper row) and double π^0 photoproduction (lower row) in the Crystal Ball and Crystal Barrel[1] detectors (left column) and in the TAPS and MiniTAPS detectors (right column). The cluster sizes from the Crystal Barrel and MiniTAPS detectors were only determined for double π^0 photoproduction and are only shown in the lower row. The difference of the cluster sizes is the largest in the Crystal Ball detector from A2 whose NaI(Tl) crystals have the largest Molière radius. The Crystal Barrel with the CsI(Tl) crystals have a smaller Molière radius and exhibit slightly smaller differences in cluster size. The Molière radius of the BaF_2 crystals is already too small for achieving reasonably large cluster size differences for the individual types of particles. Due to the large overlap of the individual distributions, even for the Crystal Ball, where the largest differences were observed, a discrimination of the particles (especially between photons and neutrons) over the size of the clusters in the detectors is not feasible. However, the differences of the cluster sizes of the different particles are sufficient for a cross check of the particle identification, since it is clearly visible that protons have the smallest and most well-defined cluster sizes. Neutrons have larger, but still well-defined cluster sizes and photons, depending on their energy, have rather extended clusters.
For this reason, the most suited identification method for the discrimination among neutral particles is the χ^2 test. This is a statistical hypothesis test that is based on an assumption that gives a measure, the χ^2 value, for the reliability of the considered sample. In this analysis, the hypothesis is that the detected photons of the sample originate from one or two π^0 of the nominal pion mass. Reliable samples result in small, improbable results in large χ^2 values. Details about the mathematical background of the χ^2 test can be found in the appendix, in Section B.1.

Table 6.1 summarizes the number of cluster types that were required for the different analyses of single and double π^0 photoproduction off free protons and quasi-free nucleons. Whereas these events were selected, those with a different number of clusters were rejected. Only one charged cluster was required in any of the analyzed

[1] combined with the Forward Cone detector

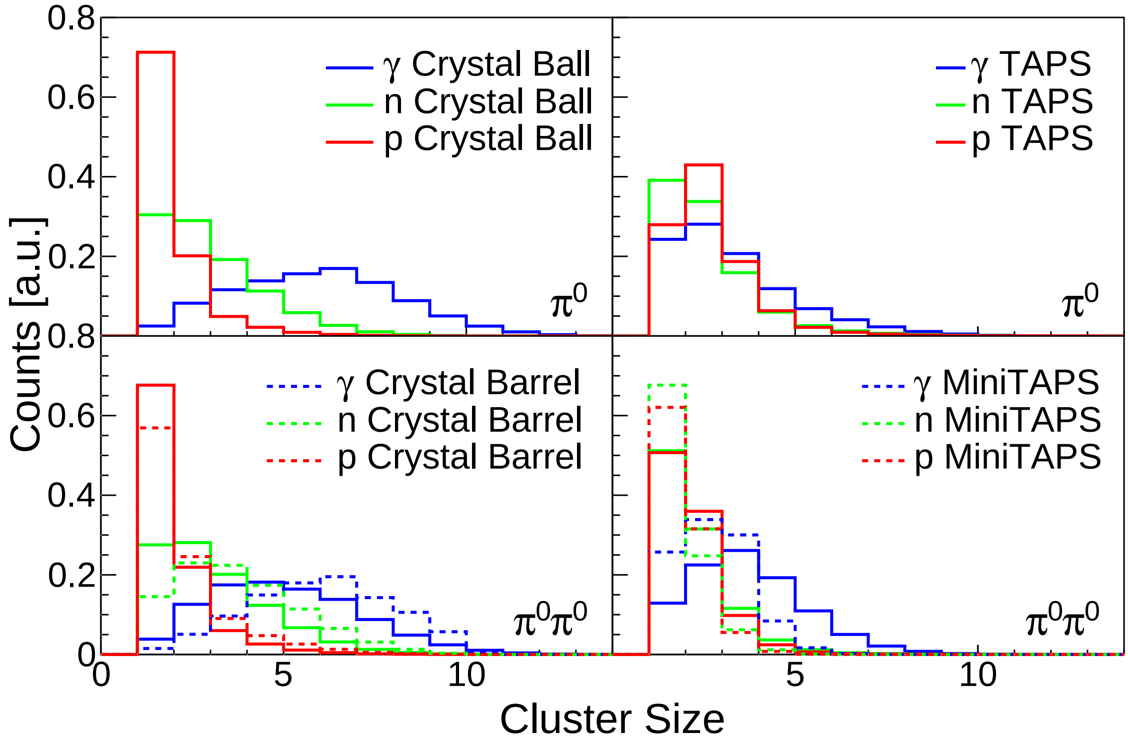

Figure 6.1: Cluster sizes for photons (blue), neutrons (green) and protons (red) as obtained from single π^0 (upper row, only A2 data) and double π^0 (lower row) photoproduction from quasi-free protons and neutrons in the Crystal Ball detector and TAPS from A2 (solid lines) and in the Crystal Barrel detector and MiniTAPS from CBELSA/TAPS (dashed lines).

reaction channels. Whereas this cluster was thus simply assigned to a proton candidate, the neutral clusters that originate from the photons from the pion decay or from the neutron had to be identified first. For quasi-free single π^0 photoproduction from the proton or when the recoil nucleon was not detected in coincidence (quasi-free inclusive reaction), the identification was straightforward. In these cases, the two neutral clusters were directly assigned to the two photon candidates. In the other cases, where it had to be distinguished among the different neutral clusters, a χ^2 test was performed (see Section B.1 for a detailed mathematical background). The χ^2 value for the reconstruction of one or two π^0 mesons out of three to five neutral clusters according to Equation (B.6) is given by:

$$(\chi^2)_k^{ij} = \sum_{i=1}^{k} \left(\frac{m_{\gamma_i\gamma_j} - m_{\pi^0}}{\Delta m_{\gamma_i\gamma_j}} \right)^2 \begin{cases} k=1, & i,j=1,2,3, \qquad\qquad i \neq j \quad | \quad \pi^0 \\ k=2, & i,j=1,2,3,4,(5), \quad i \neq j \quad | \quad \pi^0\pi^0 \end{cases}, \tag{6.1}$$

where $m_{\pi^0} = 134.98766$ MeV is the nominal mass of the π^0 meson [202] and $m_{\gamma_i\gamma_j}$ is the invariant mass of the considered photon pair. $\Delta m_{\gamma_i\gamma_j}$ is the corresponding error of the invariant mass $m_{\gamma_i\gamma_j} = \sqrt{2E_{\gamma_i}E_{\gamma_j} \cdot (1 - \cos\phi_{\gamma_i\gamma_j})}$. As the invariant mass depends on the energies of the two photons E_{γ_1} and E_{γ_2} and their opening angle $\phi_{\gamma_1\gamma_2}$, the error depends on the errors of the azimuthal and polar angle, as well as

<table>
<tr><th rowspan="2">Reaction channel</th><th colspan="2">Required clusters</th><th rowspan="2">χ^2 test necessary</th></tr>
<tr><th>Neutral</th><th>Charged</th></tr>
<tr><td rowspan="3">$\gamma N(N) \to \pi^0(N) \to 2\gamma(N)$</td><td>2</td><td>0</td><td>no</td></tr>
<tr><td>2</td><td>1</td><td>no</td></tr>
<tr><td>3</td><td>0</td><td>yes</td></tr>
<tr><td>$\gamma p(n) \to \pi^0 p \to 2\gamma p$</td><td>2</td><td>1</td><td>no</td></tr>
<tr><td>$\gamma n(p) \to \pi^0 n \to 2\gamma n$</td><td>3</td><td>0</td><td>yes</td></tr>
<tr><td rowspan="2">$\gamma p \to \pi^0\pi^0(p) \to 4\gamma(p)$</td><td>4</td><td>0</td><td>yes</td></tr>
<tr><td>4</td><td>1</td><td>yes</td></tr>
<tr><td>$\gamma p \to \pi^0\pi^0 p \to 4\gamma p$</td><td>4</td><td>1</td><td>yes</td></tr>
<tr><td rowspan="3">$\gamma N(N) \to \pi^0\pi^0(N) \to 4\gamma(N)$</td><td>4</td><td>0</td><td>yes</td></tr>
<tr><td>4</td><td>1</td><td>yes</td></tr>
<tr><td>5</td><td>0</td><td>yes</td></tr>
<tr><td>$\gamma p(n) \to \pi^0\pi^0 p \to 4\gamma p$</td><td>4</td><td>1</td><td>yes</td></tr>
<tr><td>$\gamma n(p) \to \pi^0\pi^0 n \to 4\gamma n$</td><td>5</td><td>0</td><td>yes</td></tr>
</table>

Table 6.1: Overview of the number of required clusters for the individual reaction channels. If multiple conditions are given for a certain reaction, they are connected via a logical "OR". Note: an initial state nucleon in brackets denotes the spectator nucleon, a final state nucleon in brackets denotes, that its coincident detection is not required.

of the deposited energy of the photons, as given in the appendix, in Section B.2. Therefore, they had to be accurately determined for the individual calorimeters, i.e. Crystal Ball and TAPS at A2 and Crystal Barrel, Forward Cone detector and Mini TAPS at CBELSA/TAPS (see Sections 5.4.1 and 5.4.3 for the results).
The photon pair(s) with the lowest χ^2 value is (are) the most confident combination and hence most probably originate from the decay of the meson(s). The energy and angular information of these photons are then assigned to the meson candidate and the remaining neutral particle is selected as neutron candidate.

The quality of the identification of the π^0 and $\pi^0\pi^0$ mesons can be investigated by the corresponding χ^2 distribution, as obtained from the χ^2 test. Additional considerations of the associated confidence intervals give evidence about the reliability of the identification. The following sections discuss the results of the individual χ^2 tests of the identification of the π^0 and $\pi^0\pi^0$ mesons at A2, as well as those of the $\pi^0\pi^0$ mesons at CBELSA/TAPS.

6.1.1 π^0 Identification Quality at A2

The assignment of the neutral and charged clusters to the contributing photons, neutrons, and protons of single π^0 photoproduction from the deuteron is in most of the cases straightforward. For the case of quasi-free exclusive photoproduction from the proton, two photons and a proton have to be reconstructed from two neutral

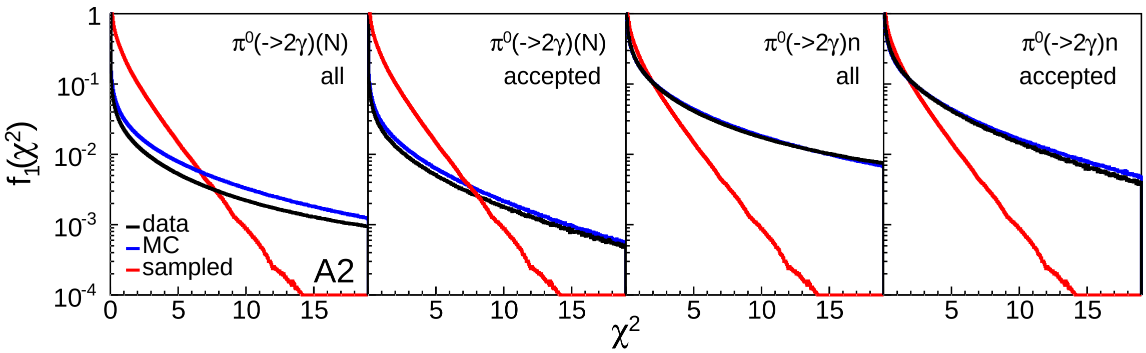

Figure 6.2: Normalized χ^2 distributions from the reconstruction of the π^0 meson out of two photons for single π^0 photoproduction from the deuteron from the A2 data. Left two figures: quasi-free inclusive $\gamma N \to \pi^0(N)$ reaction from the deuteron. Right two figures: quasi-free exclusive reaction $\gamma n(p) \to \pi^0 n(p)$ from the neutron. Shown are for both groups of figures the distributions of all events (labeled as "all") and after all cuts were applied (labeled as "accepted"). Black histogram: experimental data. Blue histogram: simulated data. Red histogram: sampled χ^2 distribution $f_1(\chi^2)$.

and one charged cluster, where only one possibility exists. Thus, this case does not need any discussion concerning the identification of the π^0 in the following sections. The same applies if the recoil nucleon was not detected in coincidence, as it is the case for the quasi-free inclusive reaction. In this case, only the two photons have to be identified from two neutral clusters, which is trivial. Hence, only when the two decay photons have to be detected in coincidence with the recoil neutron is a combinatorial χ^2 test necessary. This is the case for the quasi-free exclusive reaction on the neutron, as well as in one of the three contributions to the quasi-free inclusive measurement (see Table 6.1 for the different contributions). Even though this is the only contribution to the quasi-free inclusive measurement (and thus the results from the χ^2 test should in principle correspond to those of the exclusive reaction on the neutron), this analysis is slightly different from the quasi-free exclusive analyses, since kinematical cuts that depend on the recoil nucleon can not be applied.

The results of the χ^2 test for single π^0 photoproduction according to Equation (6.1) are shown in Figure 6.2 and the corresponding confidence levels are shown in Figure 6.3. Shown are the χ^2 distributions and confidence levels for the quasi-free inclusive reaction (two left-hand side figures) and for the quasi-free exclusive reaction on the neutron (two right-hand side figures) as obtained from the analysis of the experimental data, as well as of the simulation. The distributions are given for all initial events of three neutral clusters (labeled as *all*), as well as for the final events after all cuts were applied (labeled as *accepted*), as discussed in Section 6.4. Additionally, the distributions are compared to the expected distributions $f_1(\chi^2)$, $W_1(\chi^2)$, that were sampled according to Equations (B.4) and (B.7) with $k = 1$ as degree of freedom.
If the reconstructed invariant masses, $m_{\gamma\gamma}$, are truly independent and normally dis-

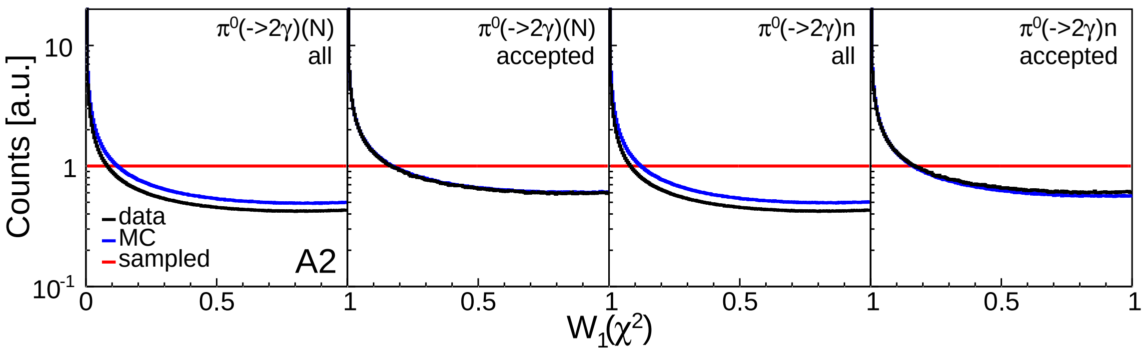

Figure 6.3: Normalized confidence level distributions of the reconstruction of the π^0 meson out of two photons for single π^0 photoproduction from the deuteron from the A2 data. Left two figures: quasi-free inclusive $\gamma N \to \pi^0(N)$ reaction from the deuteron. Right two figures: quasi-free exclusive reaction $\gamma n(p) \to \pi^0 n(p)$ from the neutron. Shown are for both groups of figures the distributions of all events (labeled as "all") and after all cuts were applied (labeled as "accepted"). Black histogram: experimental data. Blue histogram: simulated data. Red histogram: sampled confidence level distribution $W_1(\chi^2)$.

tributed random variables and the errors $\Delta m_{\gamma\gamma}$ are realistically estimated, the obtained χ^2 distribution should correspond to the theoretical distribution from Equation (B.4) with one degree of freedom, i.e. $k = 1$, as illustrated by the red curves in Figure B.1. This theoretical formalism was used to generate a sampled distribution and is compared to the measured yield in Figure 6.2. Although the y-axis is shown logarithmically, which visibly strengthens the difference, the agreement between reconstructed and sampled distributions is rather poor in all cases. This is most probably due to the fact that the measured invariant mass is not normally distributed. The spectra are clearly asymmetric and exhibit a low energy tail, which is due to the resolution of the detector components (see Figure 5.2 or 5.7 for a visualization of this characteristic). Another explanation may be found in the estimation of the errors of the invariant mass $\Delta m_{\gamma\gamma}$. The χ^2 values obtained from the test are clearly higher than those of the sampled distribution, which indicates that the errors are underestimated. This indeed might be the case since the correlation between energy and angles was neglected. The assumption is supported by the corresponding confidence level distributions $W(\chi^2)$ (see Figure 6.3). As discussed in Section B.1, the confidence level represents the possibility that a random value x^2 of the same distribution is greater than or equal to the χ^2 value. Thus, large values of χ^2 correspond to small values of $W(\chi^2)$ and vice versa and the ideal confidence level for distributions of any number of degrees of freedom should be flat. However, the measured confidence level exhibits a strong increase at lower values, corresponding to too high values of χ^2. Indeed, by comparing the χ^2 distributions of all and the accepted events, it can be seen that contributions from background reactions, as present in the distribution of all events, correspond to large χ^2 values. Applying the cuts drastically lowers the average χ^2 value, but a certain amount of the events with large χ^2 values was not removed in the analysis. However, this is not a big issue, as the most important requirement is the conformity of data and simulation. Whereas the differences of the simulation and data are rather large in the distributions of all events, an almost perfect agreement between the two is achieved when the events passed all the cuts. This is especially important, since the simulation only contains events from the desired reaction, whereas the experimental data involves all reactions that fulfill the required conditions. Therefore, the good agreement between the χ^2 and confidence level distributions shows that the event selection in the analysis of the experimental and simulated data is equivalent. Based on these quality checks, the identification of the π^0 meson seems to be well under control and is equivalently reproduced by the simulation.

6.1.2 $\pi^0\pi^0$ Identification Quality at A2

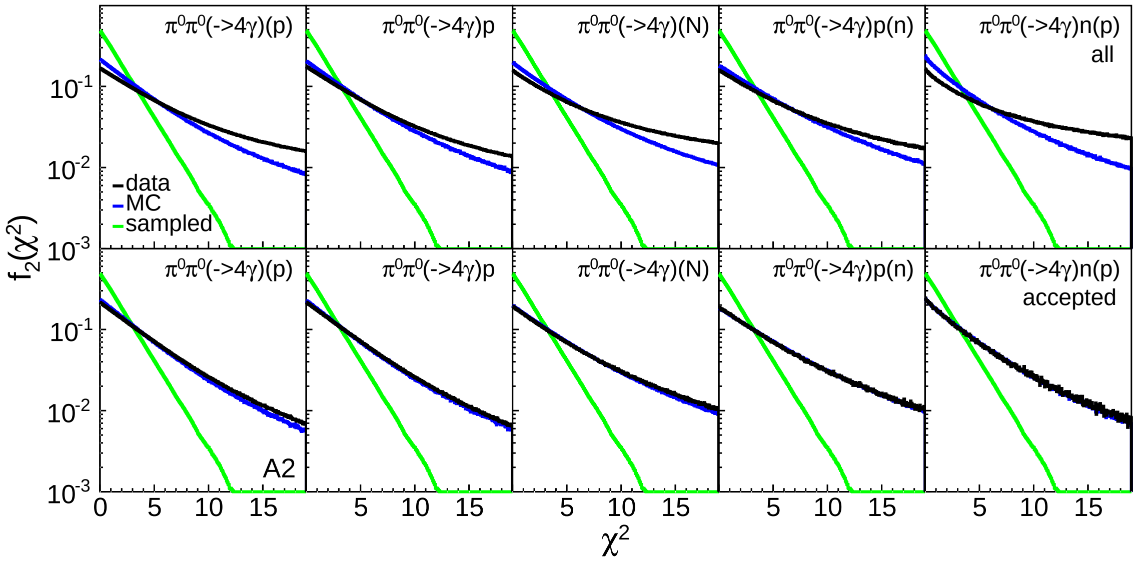

Figure 6.4: Normalized χ^2 distributions of the reconstruction of the two π^0 mesons out of four photons for double π^0 photoproduction from the A2 data. Upper row: all events. Lower row: accepted events. First column from left: inclusive reaction $\gamma p \to \pi^0\pi^0(p)$ from the free proton. Second column from left: exclusive reaction $\gamma p \to \pi^0\pi^0 p$ from the free proton. Middle column: quasi-free inclusive reaction $\gamma N \to \pi^0\pi^0(N)$ from the deuteron. Second column from right: quasi-free exclusive reaction $\gamma p(n) \to \pi^0\pi^0 p(n)$ from the proton. First column from right: quasi-free exclusive reaction $\gamma n(p) \to \pi^0\pi^0 n(p)$ from the neutron. Black histogram: experimental data. Blue histogram: simulated data. Green histogram: sampled χ^2 distribution $f_2(\chi^2)$.

Compared to single π^0, the identification of the two π^0 mesons is more delicate. On the one hand, more combinations are possible[2] to form two photon pairs out

[2]For single π^0 one pair has to be formed out of three clusters, yielding three possible combinations. For double π^0 two pairs out of four or five clusters are required, yielding three or 15 possibilities.

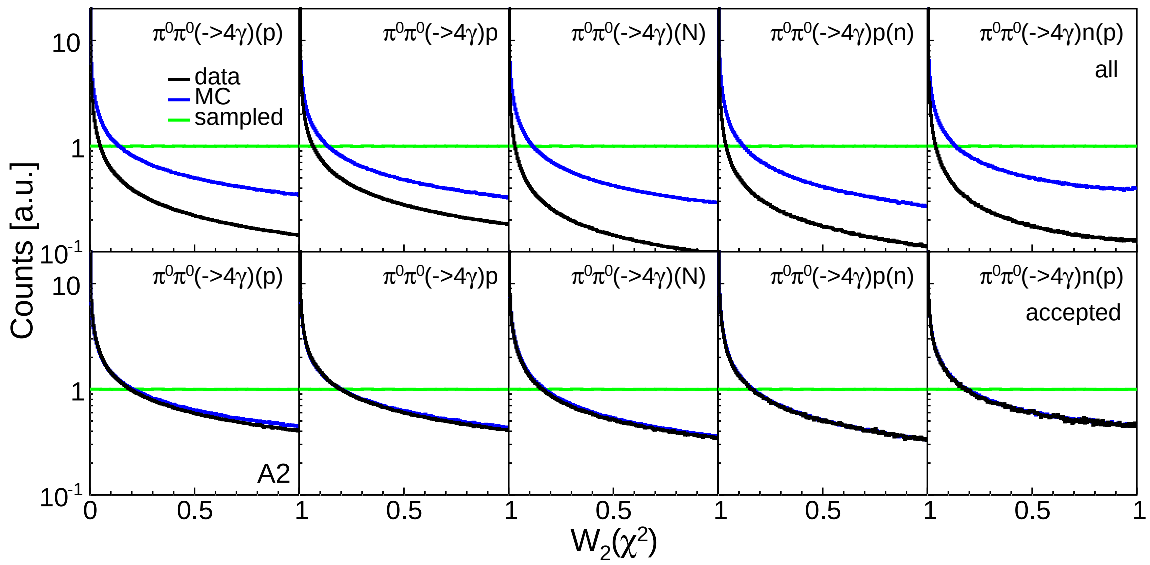

Figure 6.5: Normalized confidence level distributions of the reconstruction of the two π^0 mesons out of four photons for double π^0 photoproduction from the A2 data. Upper row: all events. Lower row: accepted events. First column from left: inclusive reaction $\gamma p \to \pi^0\pi^0(p)$ from the free proton. Second column from left: exclusive reaction $\gamma p \to \pi^0\pi^0 p$ from the free proton. Middle column: quasi-free inclusive reaction $\gamma N \to \pi^0\pi^0(N)$ from the deuteron. Second column from right: quasi-free exclusive reaction $\gamma p(n) \to \pi^0\pi^0 p(n)$ from the proton. First column from right: quasi-free exclusive reaction $\gamma n(p) \to \pi^0\pi^0 n(p)$ from the neutron. Black histogram: experimental data. Blue histogram: simulated data. Green histogram: sampled confidence level distribution $W_2(\chi^2)$.

of four or five neutral clusters than to form one pair out of three clusters. On the other hand the identification of the two π^0 mesons is complicated by combinatorial background, i.e. when a wrong combination of photons exhibit the lowest χ^2 and hence are erroneously accepted for the analysis. These events may originate from the desired reaction, but the wrong combination does not possess the correct physical information and these events should be rejected. The main difficulty with this problem is that, as these events exhibited the best χ^2, this also means that they most likely fulfill the general kinematic relations and will pass the different cuts such that they end up in the selection for the results. Therefore, special attention concerning the identification of the π^0 pair is required in the analysis, which will be discussed in Section 6.5.

Photoproduction of $\pi^0\pi^0$ was investigated on the free proton (using a liquid hydrogen target) and on quasi-free nucleons (using a liquid deuterium or deuterated butanol target). In all three cases, the mesons were detected once in coincidence with the recoil nucleon (exclusive reaction) and once without this requirement (inclusive and quasi-free inclusive reactions). For this reason, four neutral clusters had to be considered in the inclusive analysis. In the exclusive analysis, an additional fifth clus-

ter had to be taken into account for the in coincidence detected recoil neutron. For all cases, the two π^0 were identified using the χ^2 test and, if available, the remaining neutral cluster was assigned to the neutron candidate. The test was performed in the same way as for single π^0, but for $2\pi^0$ photoproduction two terms (one for each pion) contribute to the χ^2 value (see Equation (6.1)). The resulting χ^2 distributions are shown in Figure 6.4 and the corresponding confidence level distributions in Figure 6.5. The upper row shows the initial distribution of all available events of the corresponding requirement and the lower row shows the distribution of those events that passed all different analysis cuts. The results for the analysis of the free proton data are shown in the two most left-hand sided Figures and the three right-hand sided Figures correspond to the analysis of the quasi-free data.
Compared to the distributions from single π^0 photoproduction, it can immediately be seen that the discrepancies between the initial distributions from the experimental, simulated, and sampled data are much larger. In contrast to single π^0, the ideal distributions were sampled as well with the same mathematical description from Equation (B.4), but in this case with one additional degree of freedom, i.e. $k = 2$. The large differences between data and simulation again demonstrate the large contamination of the data with background that is primarily due to contributions from competing reactions as all events with four or five neutral clusters contribute to the distributions. Any reaction with the same or a larger number of final state particles can contribute either directly or when, due to detector inefficiencies, particles were not detected. The largest difference is observed for the quasi-free inclusive reaction, which is evident, as it contains events with two pions and a coincident recoil nucleon but also events where the recoil nucleon was lost. In contrast, the smallest initial difference can be seen in the exclusive reaction on the free proton. This is also evident, since in this case only the two pions have to be identified. The difference between the measured and the sampled distributions has the same origin as discussed for single π^0 photoproduction and will be omitted from further discussions.
Considering the distributions in the lower row of Figure 6.4, i.e. at the final stage when only those events remain that passed all cuts, the situation has already improved. Nearly perfect agreement between the distributions of the experimental data and simulation are visible. Again this indicates that the most important requirement of conformity of simulation and data was met. The corresponding confidence level distributions (Figure 6.5) confirm the above discussion: the initial distributions of the data exhibit much higher χ^2 values compared to the simulation and even higher values compared to the sampled distributions. The confidence levels after all cuts demonstrates that background events from competing reactions are eliminated and that remaining combinatorial background is equivalently present in data and simulation.

6.1.3 $\pi^0\pi^0$ Identification Quality at CBELSA/TAPS

The starting position and the methods used for the identification of the two neutral pions in the analysis of the CBELSA/TAPS data is identical to the analysis of the A2 data, which was discussed in the Section 6.1.2. From four or five neutral clusters,

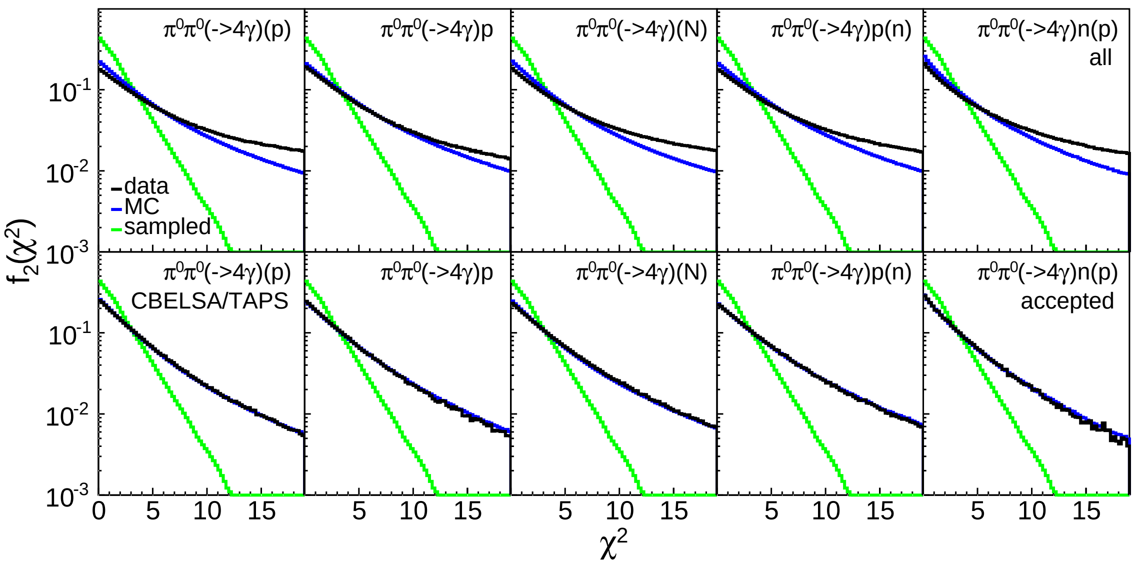

Figure 6.6: Normalized χ^2 distributions of the reconstruction of the two π^0 mesons out of four photons for double π^0 photoproduction from the CBELSA/TAPS data. Upper row: all events. Lower row: accepted events. First column from left: inclusive reaction $\gamma p \to \pi^0\pi^0(p)$ from the free proton. Second column from left: exclusive reaction $\gamma p \to \pi^0\pi^0 p$ from the free proton. Middle column: quasi-free inclusive reaction $\gamma N \to \pi^0\pi^0(N)$ from the deuteron. Second column from right: quasi-free exclusive reaction $\gamma p(n) \to \pi^0\pi^0 p(n)$ from the proton. First column from right: quasi-free exclusive reaction $\gamma n(p) \to \pi^0\pi^0 n(p)$ from the neutron. Black histogram: experimental data. Blue histogram: simulated data. Green histogram: sampled χ^2 distribution $f_2(\chi^2)$.

the photon pairs that stem from the pion decays were identified using the χ^2 test. In the case of five neutral clusters, the remaining fifth cluster was assigned to the neutron candidate. The resulting χ^2 distribution are shown in Figure 6.6 and the corresponding confidence level distributions in Figure 6.7. The obtained distributions for all events show large discrepancies compared to the sampled distributions (green histogram) but in this case show slightly smaller deviations among each other. When those events that do not fulfill the analysis cuts were rejected, the agreement improves significantly. Again, the agreement between data and simulation is excellent throughout all analyzed reactions as affirmed by the confidence level distributions (see Figure 6.7). Overall, it seems that the quality of the identification of the π^0 pair even exceeds the quality of the identification as shown in the A2 data. The quality of the identification of the pion pairs of both analyses will be investigated and discussed in more detail in Section 6.1.4.

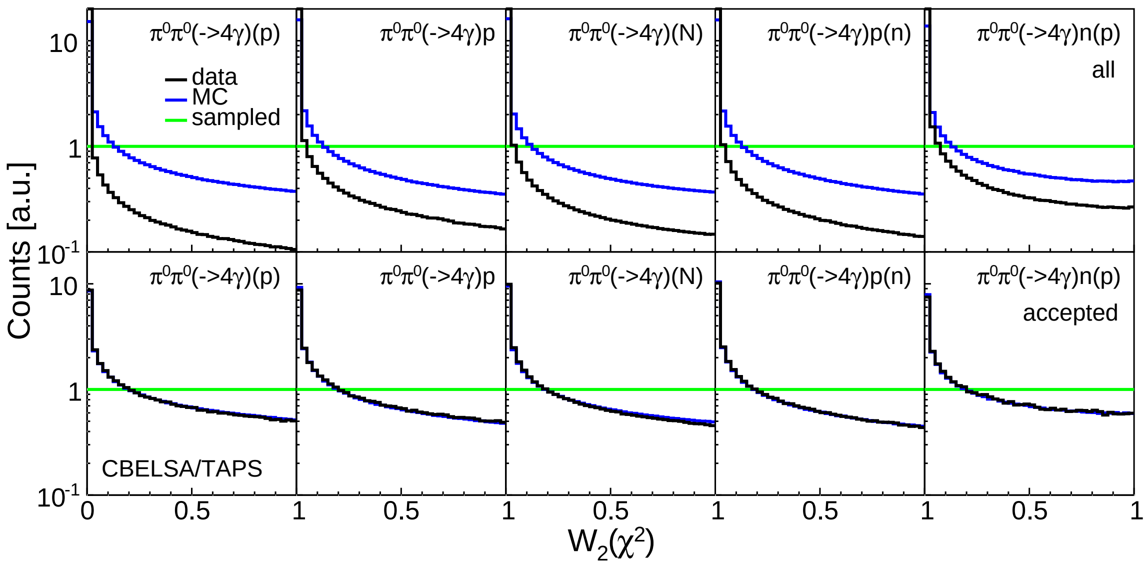

Figure 6.7: Normalized confidence level distributions of the reconstruction of the two π^0 mesons out of four photons for double π^0 photoproduction from the CBELSA/TAPS data. Upper row: all events. Lower row: accepted events. First column from left: inclusive reaction $\gamma p \rightarrow \pi^0\pi^0(p)$ from the free proton. Second column from left: exclusive reaction $\gamma p \rightarrow \pi^0\pi^0 p$ from the free proton. Middle column: quasi-free inclusive reaction $\gamma N \rightarrow \pi^0\pi^0(N)$ from the deuteron. Second column from right: quasi-free exclusive reaction $\gamma p(n) \rightarrow \pi^0\pi^0 p(n)$ from the proton. First column from right: quasi-free exclusive reaction $\gamma n(p) \rightarrow \pi^0\pi^0 n(p)$ from the neutron. Black histogram: experimental data. Blue histogram: simulated data. Green histogram: sampled confidence level distribution $W_2(\chi^2)$.

6.1.4 Identification Quality at A2 and CBELSA / TAPS

Figure 6.8a shows the χ^2 distributions of the $\pi^0\pi^0$ identification of the A2 and CBELSA/TAPS analysis for double pion photoproduction off the free proton after all cuts have been applied. The corresponding confidence levels are shown in Figure 6.9a. It can be seen that besides the small differences that will be discussed below, the identification of the π^0 pairs is of high quality in the analysis of the A2 and CBELSA/TAPS data. However, as already noticed in Section 6.1.3, the direct comparison of both distributions clearly shows that the quality of the identification in the CBELSA/TAPS data is slightly better, i.e. yields smaller χ^2 values. This is also confirmed by the corresponding confidence level distributions, that are flatter in the case of CBELSA/TAPS, which indicates that the average χ^2 is lower and the identification is more reliable. However, the most important criterium is the agreement between data and simulation, which for A2 and CBELSA/TAPS is excellent.

The two datasets can moreover be better compared by using a probability plot, the quantile-quantile plot. A q-q plot compares two distributions by plotting the

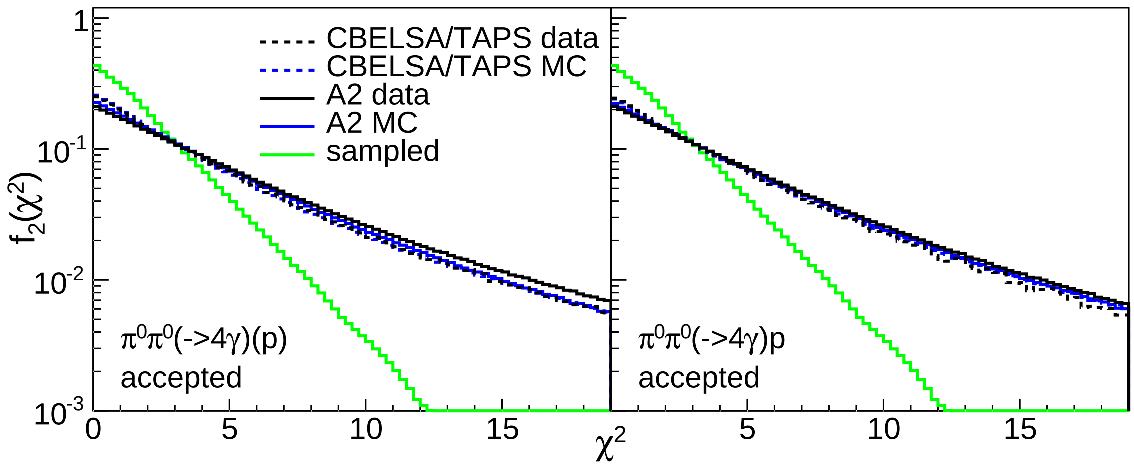

(a) $f_2(\chi^2)$ from the A2 and CBELSA/TAPS data

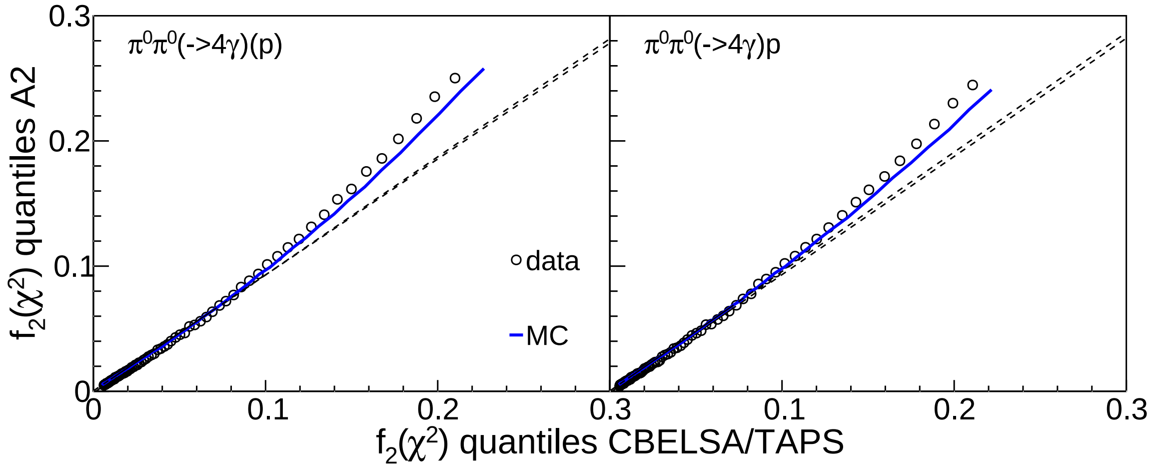

(b) $f_2(\chi^2)$ q-q plot

Figure 6.8: (a) Normalized χ^2 distributions. (b) $f_2(\chi^2)$ quantile-quantile plots of the reconstruction of the two π^0 mesons out of four photons for $2\pi^0$ photoproduction from free protons. Data from A2 and CBELSA/TAPS after all cuts were applied. Notations are given in the figure. The dashed lines in the q-q plot connect the $x_{0.25}$ and $x_{0.75}$ quantiles of data and simulation.

quantiles of one distribution against those of the other. Quantiles x_q correspond to the inverse function of the cumulative distribution function (see Equation (B.3) in Section B.1) and can be interpreted as a function of the probability q. For example, the 25% quantile $x_{0.25}$ represents the value at which the cumulative distribution function has the value 0.25 and the 75% quantile $x_{0.75}$, where the CDF has the value 0.75 and so on. Therefore, the quantile x_q gives the probability q that a sample value that follows the distribution lies below that value. Such a quantile-quantile plot for the final χ^2 distribution of the A2 and CBELSA/TAPS data is presented in Figure 6.8b and for the final confidence levels in Figure 6.9b. In both figures, the quantiles of the A2 dataset are plotted against those of the CBELSA/TAPS data. Shown are

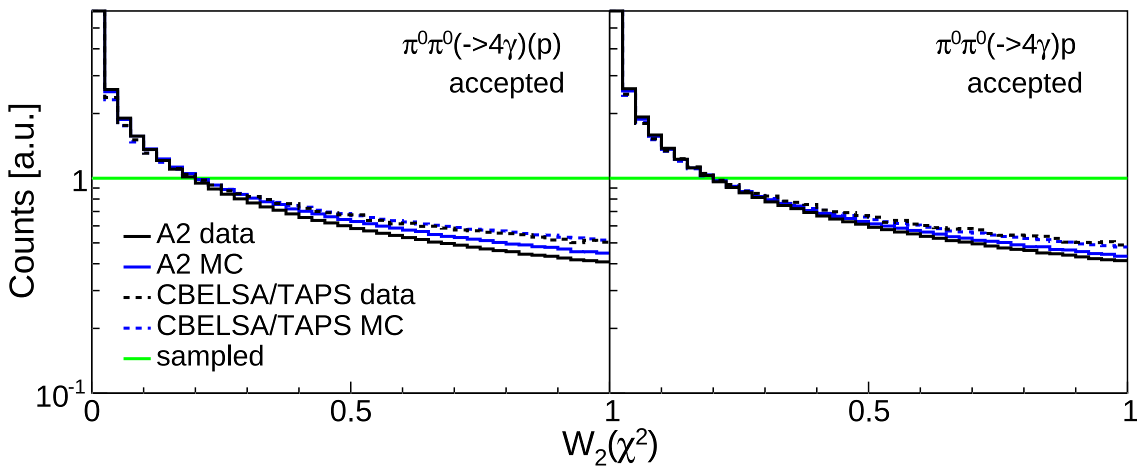

(a) $W_2(\chi^2)$ from the A2 and CBELSA/TAPS data

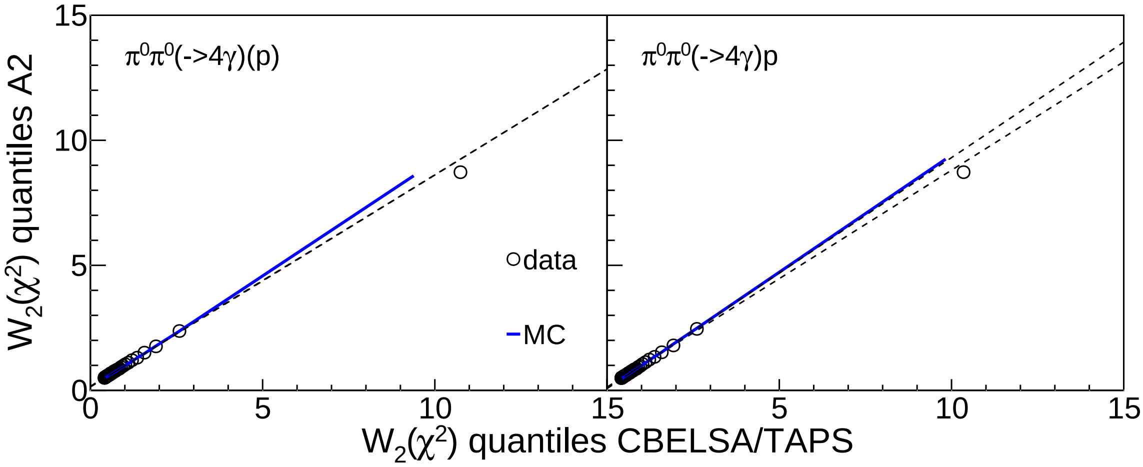

(b) $W_2(\chi^2)$ q-q plot

Figure 6.9: (a) Normalized confidence level distributions. (b) $W_2(\chi^2)$ quantile-quantile plots of the reconstruction of the two π^0 mesons out of four photons for $2\pi^0$ photoproduction from free protons. Data from A2 and CBELSA/TAPS after all cuts were applied. Notations are given in the figure. The dashed lines in the q-q plot connect the $x_{0.25}$ and $x_{0.75}$ quantiles of data and simulation.

the results for the data (open black circles) and the simulation (solid blue line). The dashed line connects the $x_{0.25}$ and $x_{0.75}$ quantiles and thus represents a robust linear fit, which is not sensitive to the extreme values of the datasets. If both datasets come from the same distribution, the points should all fall on a 45° line with respect to the x- and y-axis. If they originate from the same distribution function, but of different parameters, they still fall on a line but not at 45°.
The q-q plots of the χ^2 distributions (Figure 6.8b) show that the χ^2 distributions of both datasets are rather equal, but it confirms that the average χ^2 value is lower for the identification of the mesons in the CBELSA/TAPS data. For the exclusive

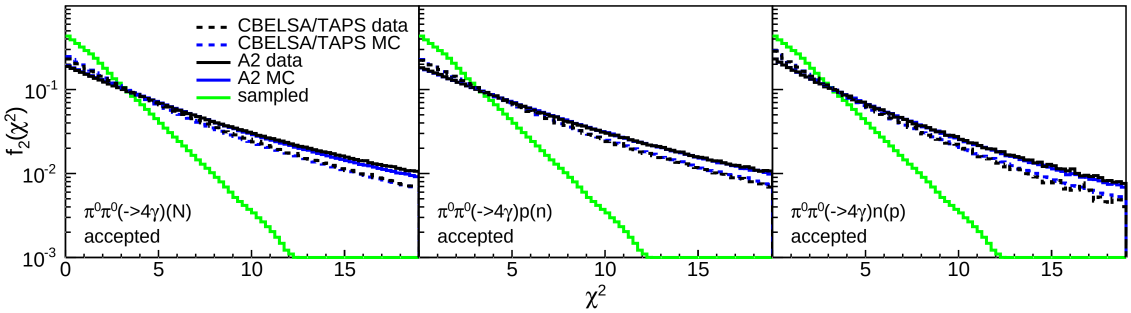

(a) $f_2(\chi^2)$ from the A2 and CBELSA/TAPS data

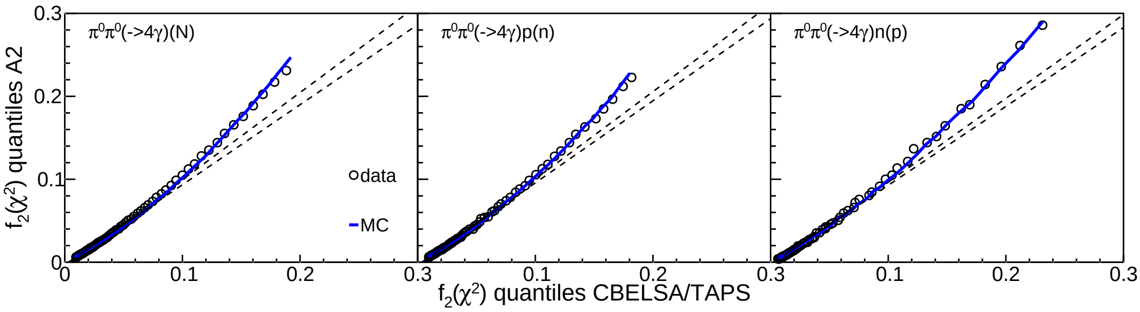

(b) $f_2(\chi^2)$ q-q plot

Figure 6.10: (a) Normalized χ^2 distributions. (b) $f_2(\chi^2)$ quantile-quantile plots of the reconstruction of the two π^0 mesons out of four photons for $2\pi^0$ photoproduction from the deuteron. Data from A2 and CBELSA/TAPS after all cuts were applied. Notations are given in the figure. The dashed lines in the q-q plot connect the $x_{0.25}$ and $x_{0.75}$ quantiles of data and simulation.

reaction on the free proton the difference is smaller, but of the same trend. However, in general the identification is equally good. This is even more emphasized by the q-q plots of the confidence level distributions shown in Figure 6.9b. The points of data and simulation lie almost perfectly on the dashed line, which indicates that the quality of the identification at A2 and CBELSA/TAPS is equal for at least 75 % of the events.

Possible reasons for the difference of the quality of the identification of the pion pairs from A2 and CBELSA/TAPS might be the different method of the identification of the charged particles, i.e. the veto condition that is imposed on the neutral particles. Whereas at forward angles, the identification with the TAPS (A2) and MiniTAPS (CBELSA/TAPS) detectors are nearly identical, this does not hold for the main calorimeters, the Crystal Ball (A2) and Crystal Barrel (CBELSA/TAPS) detectors. As discussed in Sections 4.1 and 4.2, the charge characteristic of the individual particles in the Crystal Ball is determined with the help of the particle identification detector (PID) and in the Crystal Barrel detector with the Inner detector. The angular resolution of the Inner detector is much better than that of the PID. Whereas the Inner detector allows for the identification of charged particles (and hence for the veto condition for neutral particles) in both azimuthal and polar angles with high resolution, the identification with the PID is only possible in the azimuthal angle.

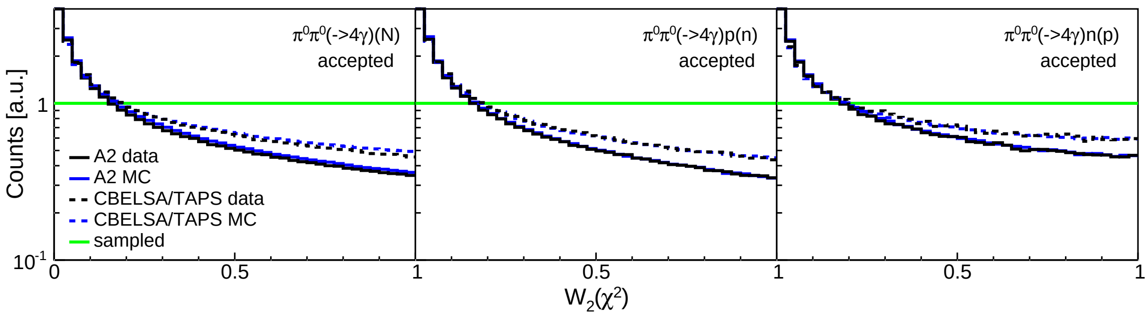

(a) $W_2(\chi^2)$ from the A2 and CBELSA/TAPS data

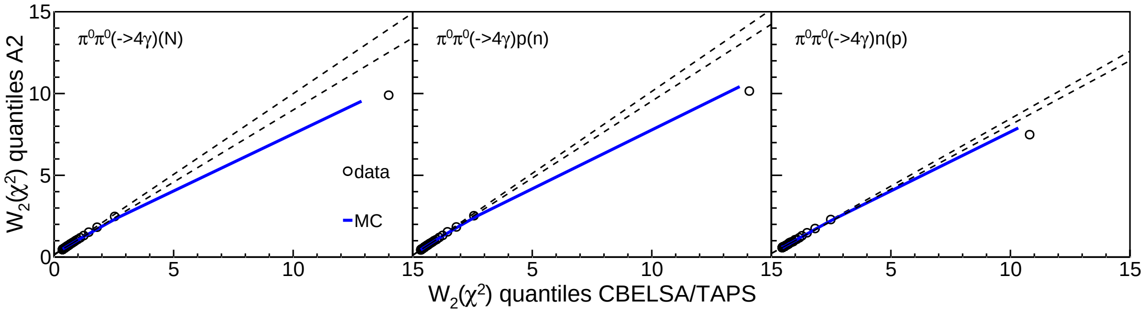

(b) $W_2(\chi^2)$ q-q plot

Figure 6.11: (a) Normalized confidence level distributions. (b) $W_2(\chi^2)$ quantile-quantile plots of the reconstruction of the two π^0 mesons out of four photons for $2\pi^0$ photoproduction from the deuteron. Data from A2 and CBELSA/TAPS after all cuts were applied. Notations are given in the figure. The dashed lines in the q-q plot connect the $x_{0.25}$ and $x_{0.75}$ quantiles of data and simulation.

Hence, when using the PID, there is a nonzero probability that a neutral particle is marked as charged, or vice versa, because the coincidence was only checked with the azimuthal angle. This could result in events where particles are misidentified, which results in an unreliable identification and large χ^2 values.
As the estimation of the energy and angular errors was carried out identically for both experimental setups and only affects photons, an influence on the difference between the two datasets from this part is unlikely and rather expected to be of the same quality for both cases.
The situation for the quasi-free reactions on the deuteron is similar. The results are shown in Figures 6.10 and 6.11. The χ^2 distributions are in good agreement but tend towards higher values in the A2 data. Therefore, it is also reflected in the distribution of the confidence levels, which though, to a high percentage, are in excellent agreement. However, the behavior is the same for the simulation, which again indicates that the identification is systematically under control in both analyses.

6.1.5 Identification Quality with Polarized Data

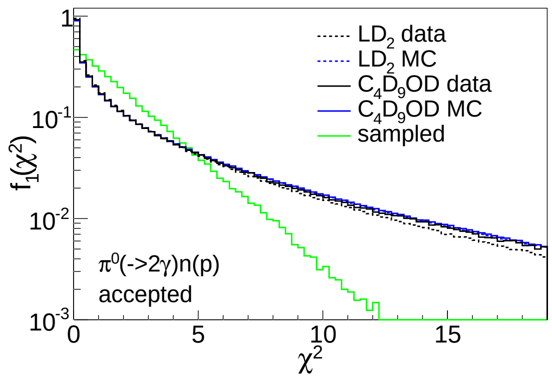

(a) $f_1(\chi^2)$ from the LD_2 and C_4D_9OD data from A2

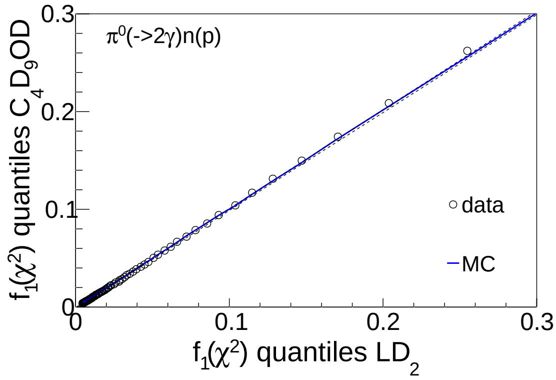

(b) $f_1(\chi^2)$ q-q plot

Figure 6.12: (a) Normalized χ^2 distributions. (b) $f_1(\chi^2)$ quantile-quantile plots of the reconstruction of the π^0 meson out of two photons for π^0 photoproduction. Data from liquid deuterium and deuterated butanol from A2 after all cuts were applied. Notations are given in the figure. The dashed lines in the q-q plot connect the $x_{0.25}$ and $x_{0.75}$ quantiles of data and simulation.

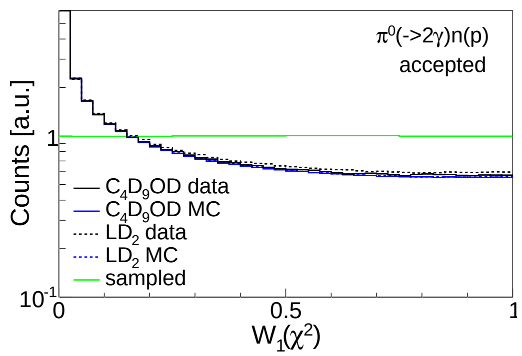

(a) $W_1(\chi^2)$ from the LD_2 and C_4D_9OD data from A2

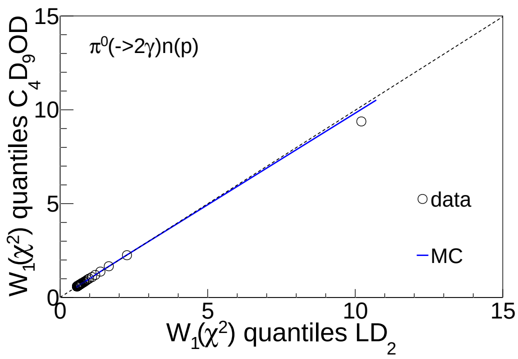

(b) $W_1(\chi^2)$ q-q plot

Figure 6.13: (a) Normalized confidence level distributions. (b) $W_1(\chi^2)$ quantile-quantile plots of the reconstruction of the π^0 meson out of two photons for π^0 photoproduction. Data from liquid deuterium and deuterated butanol from A2 after all cuts were applied. Notations are given in the figure. The dashed lines in the q-q plot connect the $x_{0.25}$ and $x_{0.75}$ quantiles of data and simulation.

The last section about the identification of the π^0 mesons is dedicated to the reconstruction and quality of the mesons in the analysis of the polarized deuterated butanol data. Besides the polarized deuterons, this target comprises unpolarized carbon and oxygen nuclei. Therefore, many reactions occur on the unpolarized nuclei

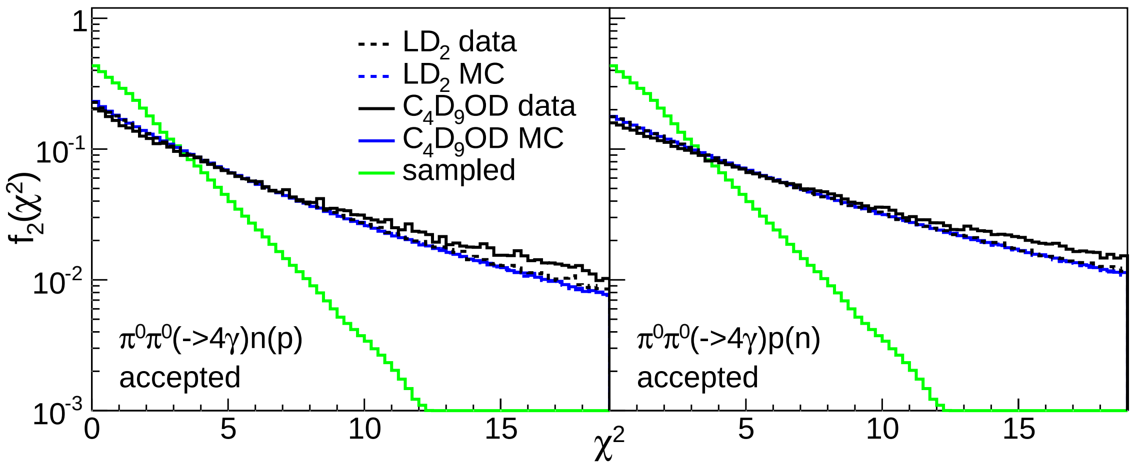

(a) $f_2(\chi^2)$ from the LD_2 and C_4D_9OD data from A2

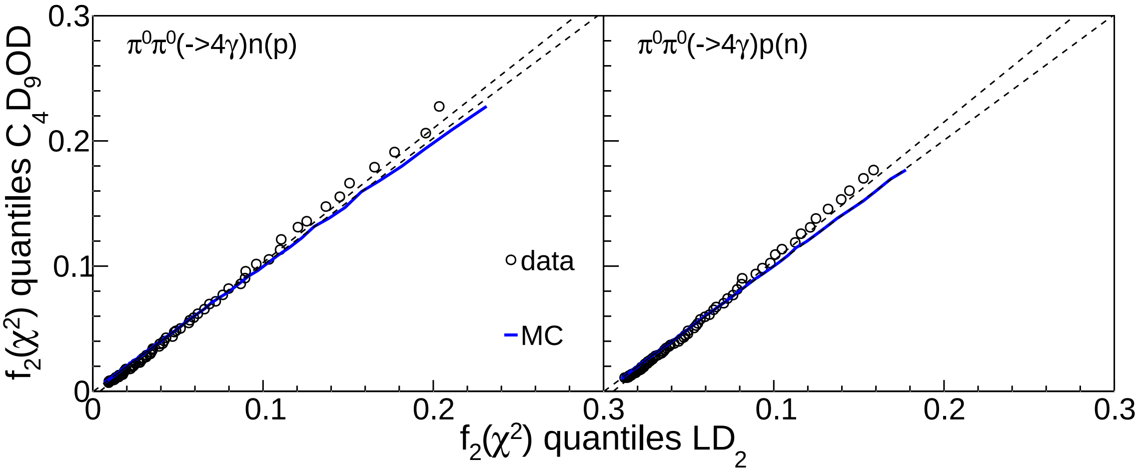

(b) $f_2(\chi^2)$ q-q plot

Figure 6.14: (a) Normalized χ^2 distributions. (b) $f_2(\chi^2)$ quantile-quantile plots of the reconstruction of the two π^0 mesons out of four photons for $2\pi^0$ photoproduction. Data from liquid deuterium and deuterated butanol from A2 after all cuts were applied. Notations are given in the figure. The dashed lines in the q-q plot connect the $x_{0.25}$ and $x_{0.75}$ quantiles of data and simulation.

that contaminate the sample. These additional degrees of freedom severely complicate the identification and reconstruction of the pions and recoil nucleons. Therefore, it can be expected that the quality of the identification is poor compared to hydrogen or deuterium data.

The main goal of the analysis of the polarized data is to isolate the events that contain particles from reactions on the polarized deuterons. Events from reactions on unpolarized nuclei have to be rejected or eventually estimated and subtracted by a carbon background measurement (see Section 6.13.4). Hence, the comparability of the results with those from liquid deuterium is very important for the analysis of polarized data. For this reason, the χ^2 and confidence level distributions from the

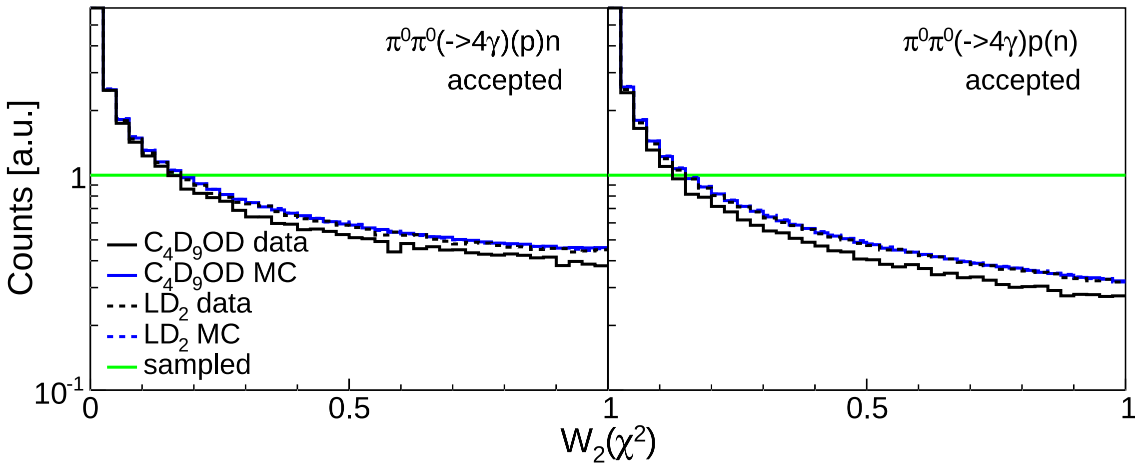

(a) $W_2(\chi^2)$ from the LD_2 and C_4D_9OD data from A2

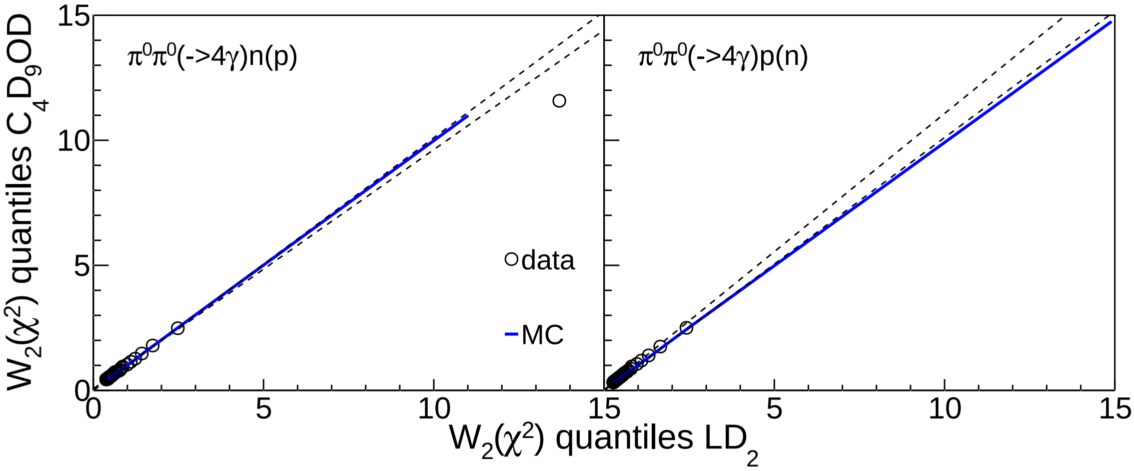

(b) $W_2(\chi^2)$ q-q plot

Figure 6.15: (a) Normalized confidence level distributions. (b) $W_2(\chi^2)$ quantile-quantile plots of the reconstruction of the two π^0 mesons out of four photons for $2\pi^0$ photoproduction. Data from liquid deuterium and deuterated butanol from A2 after all cuts were applied. Notations are given in the figure. The dashed lines in the q-q plot connect the $x_{0.25}$ and $x_{0.75}$ quantiles of data and simulation.

analysis of liquid deuterium data were directly compared to those from the analysis of the deuterated butanol data.

The comparison of the χ^2 distributions and the corresponding q-q plots of the single π^0 analysis of A2 data are shown in Figure 6.12 and the confidence level distributions and the q-q plots are shown in Figure 6.13. The χ^2 and confidence level show an incredible agreement between the identification quality of the two different datasets and between data and simulation. This demonstrates the high quality identification of the π^0 in the liquid deuterium data. The analysis cuts that have been

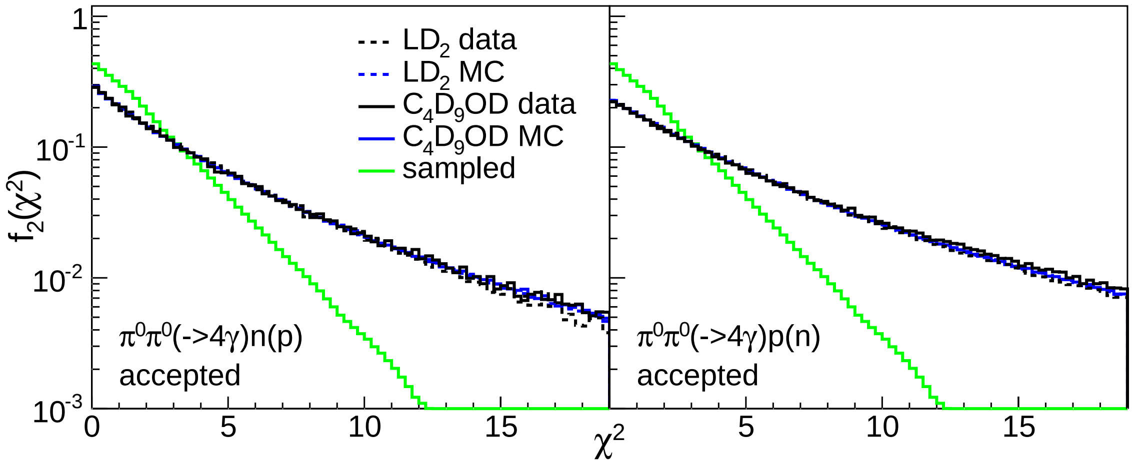

(a) $f_2(\chi^2)$ from the LD_2 and C_4D_9OD data from CBELSA/TAPS

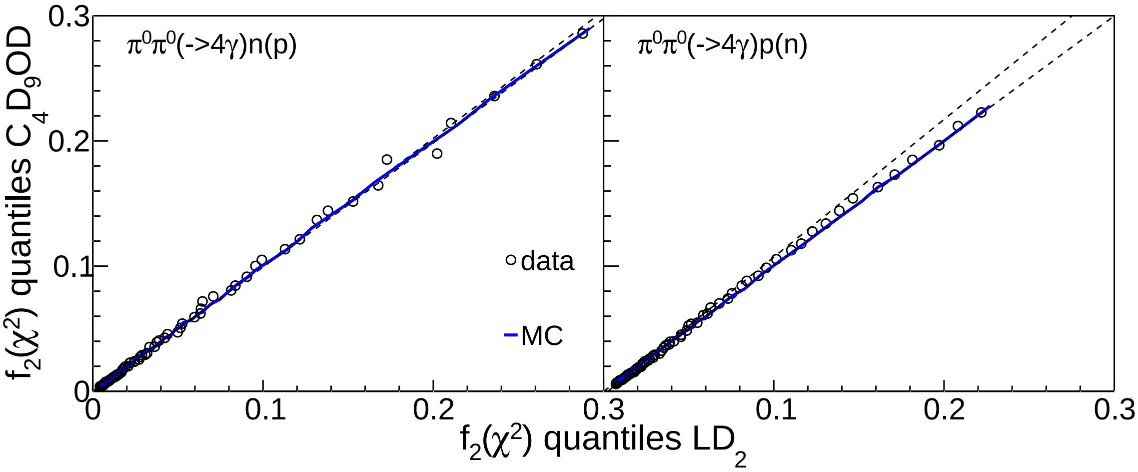

(b) $f_2(\chi^2)$ q-q plot

Figure 6.16: (a) Normalized χ^2 distributions. (b) $f_2(\chi^2)$ quantile-quantile plots of the reconstruction of the two π^0 mesons out of four photons for $2\pi^0$ photoproduction. Data from liquid deuterium and deuterated butanol from CBELSA/TAPS after all cuts were applied. Notations are given in the figure. The dashed lines in the q-q plot connect the $x_{0.25}$ and $x_{0.75}$ quantiles of data and simulation.

established in the liquid deuterium analysis have also been used for the analysis of the polarized data. Hence an agreement on this level is only possible if the analysis and identification methods are reliable.

The corresponding comparison of the distributions of the $\pi^0\pi^0$ analysis of the A2 data is shown in Figures 6.14 and 6.15 and the CBELSA/TAPS data in Figures 6.16 and 6.17. Overall, good agreement between the different datasets and between data and simulation can be observed for both the A2 and CBELSA/TAPS data. For the CBELSA/TAPS analyses, the agreement between liquid deuterium and deuterated

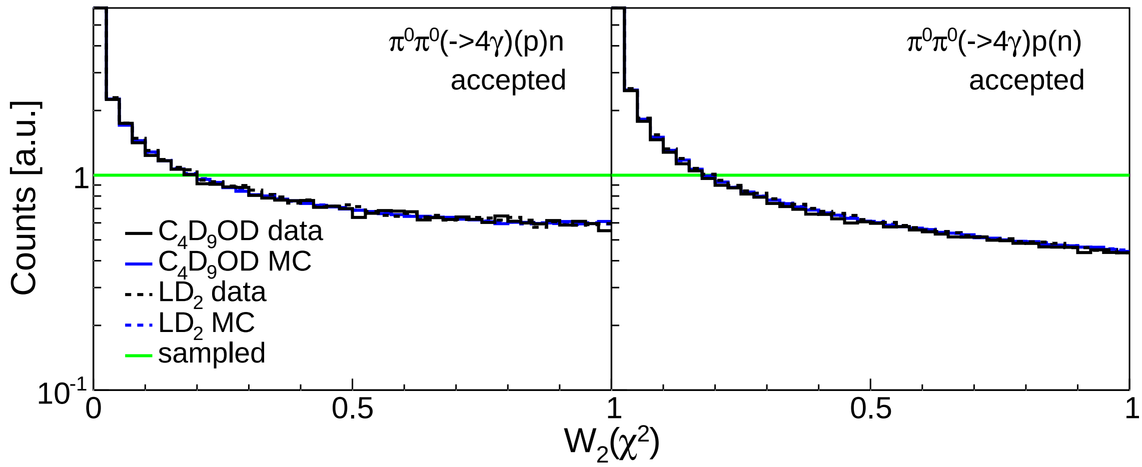

(a) $W_2(\chi^2)$ from the LD_2 and C_4D_9OD data from CBELSA/TAPS

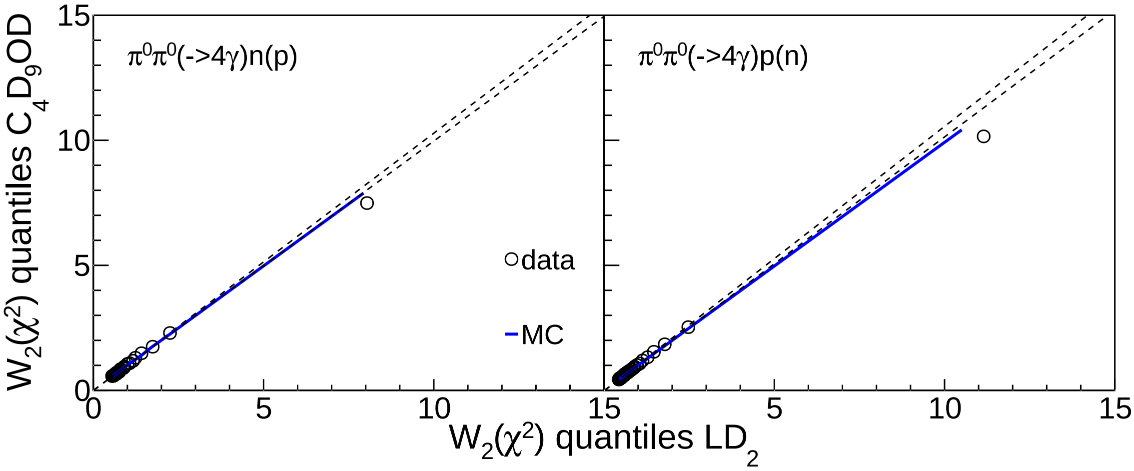

(b) $W_2(\chi^2)$ q-q plot

Figure 6.17: (a) Normalized confidence level distributions. (b) $W_2(\chi^2)$ quantile-quantile plots of the reconstruction of the two π^0 mesons out of four photons for $2\pi^0$ photoproduction. Data from liquid deuterium and deuterated butanol from CBELSA/TAPS after all cuts were applied. Notations are given in the figure. The dashed lines in the q-q plot connect the $x_{0.25}$ and $x_{0.75}$ quantiles of data and simulation.

butanol data and between simulation and data is excellent, all four χ^2 and confidence level distributions are highly superimposable, and the q-q plots of both quantities show an almost perfect correlation. The largest discrepancy can be found in the identification of the pion pair from the deuterated butanol data at A2. Whereas the yields from the simulations on both targets, as well as that from the liquid deuterium data are identical, that from the polarized data is slightly off and exhibits larger χ^2 values. Most probably it comes from reactions on the unpolarized carbon and oxygen background, which are not present in the liquid deuterium data and the simulations. However, the corresponding q-q plots show that the discrepancy is very small and not of a systematic problem.

In summary, for all reaction channels of data from A2 and CBELSA/TAPS, the χ^2 and confidence level distributions show a very good agreement between data and simulation. This is the most important criterion as it indicates that the selection of the events, as well as the identification of the π^0 pairs, are equivalent with high precision. The difference to the sampled distributions is mostly due to the underestimation of the invariant mass errors. The small difference between the identification quality of the A2 and CBELSA/TAPS analyses probably stem from the particle identification with the PID in the A2 analysis. The identification with the PID is more error-prone and hence should yield higher χ^2 values and a lower confidence level. However, both differences do not pose a systematic problem, as their influence on the event selection is negligible. Cuts on the confidence level were attempted but did not show a significant change of the results and were omitted for this reason. The comparison of the identification quality in the analysis of liquid deuterium with deuterated butanol data showed no systematic discrepancy and demonstrates that the analysis methods established in the analysis of the unpolarized data can be applied to the polarized data.

The coordinates and deposited energies of the clusters were then used to create the four momentum of the corresponding particle. The clusters from the best combinations were assigned to the photons of the associated pion and the remaining neutral cluster, if available, to the neutron candidate. In the case of a charged cluster, it was directly assigned to the proton candidate. An additional energy correction[3] [188], described by

$$E'_{\gamma_{i,j}} = \frac{m_{\pi^0}}{m_{\gamma_i \gamma_j}} E_{\gamma_{i,j}} \ , \tag{6.2}$$

where m_{π^0} is the nominal π^0 mass, $E_{\gamma_{i,j}}$ is the energy and $m_{\gamma_i\gamma_j}$ the invariant mass of each photon pair. It was shown that this correction improves the energy resolution of the photons. However, it is only exact for equivalent photons, i.e. photons of the same energy, which is generally not the case. This effect was investigated, but no significant change of the results was observed.

6.2 Photon Time Coincidence Criteria

From the selected events an additional condition on the time coincidence of the detected photons is required in order to ensure that the photons originate from the same reaction. For this purpose, the time difference of all detected photons of the corresponding detectors was considered. Only those events were accepted, for which the difference is within a certain window around the prompt peak, the others were rejected. The window was intentionally chosen as conservative since the background is negligible. Figures 6.18 for A2 and 6.19 for CBELSA/TAPS show typical spectra

[3]The correction is based on a kinematic fit of the energies whereas the angular resolutions are neglected. This simplification is only valid as long as the angular resolution is much better than the energy resolution.

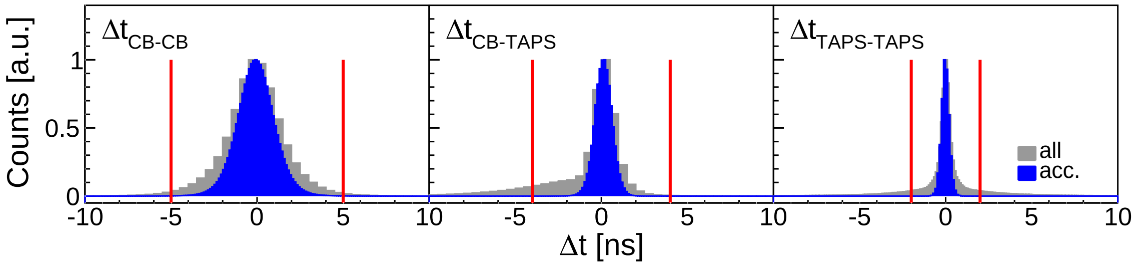

Figure 6.18: Time coincidence of the detected photons in the detectors of the A2 setup. Left-hand side: Crystal Ball - Crystal Ball. Middle: Crystal Ball - TAPS. Right-hand side: TAPS - TAPS. Gray histogram: all events. Blue histogram: accepted events. Data from the April 2009 beamtime.

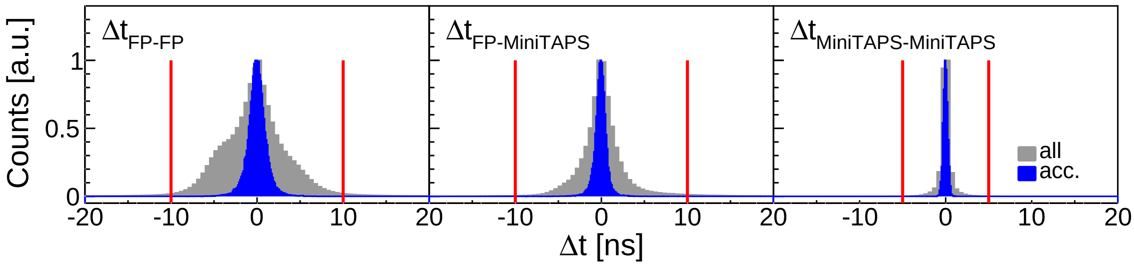

Figure 6.19: Time coincidence of the detected photons in the detectors of the CBELSA/TAPS setup. Left-hand side: Forward Cone - Forward Cone. Middle: Forward Cone - MiniTAPS. Right-hand side: MiniTAPS - MiniTAPS. Gray histogram: all events. Blue histogram: accepted events. Data from the November 2008 beamtime.

and the required coincidence conditions (red lines) on the example of the liquid hydrogen data.

Shown are the spectra of all allowed events (gray) as well as those of the events that passed all analysis cuts (blue). The effect of the analysis cuts to the time coincidence is clearly visible, especially for the spectra from the analysis of the CBELSA/TAPS data where the Forward Cone detector contributes. Since in the Forward Cone detector only those particles that fired both veto layers are marked as charged (which for the electromagnetic background might not be the case), the initial photon selection (gray area) is contaminated by charged particles. As soon as all kinematic cuts are applied (blue area) and such misidentified particles are removed, the spectra are symmetric and reasonably narrow.

6.3 Subtraction of Random Tagger Hits

The coincidence requirement explained in Section 6.2 ensures that the final state photons originate from the same time window, i.e. from the same reaction. To know

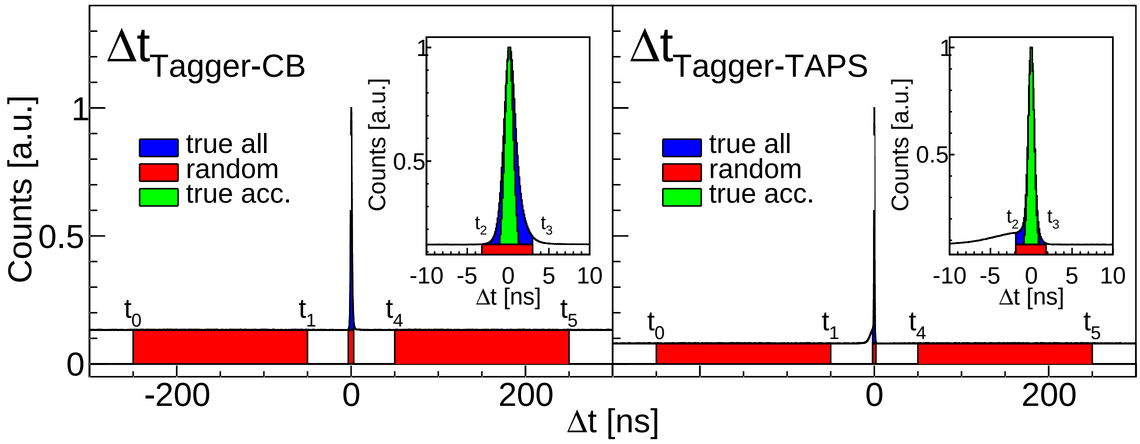

Figure 6.20: Time coincidence of the tagged electrons and the detected photons in the detectors of the A2 setup. Left-hand side: Tagger - Crystal Ball. Right-hand side: Tagger - TAPS. Main window: full spectrum. Upper right inset: prompt region. Blue histogram: true events in the prompt time window. Red histograms: random tagger events in the background and prompt time windows. Green histogram: true and accepted events in the prompt time window. Data from the April 2009 beamtime.

at which incident photon energy the reaction took place, the corresponding beam photon, and hence the proper tagger electron, has to be identified. During the time window of an event, all electrons that hit the tagger are registered, but only one of them produced the bremsstrahlung photon. This specific electron has to be tagged in order to know the energy of the incident beam photon. The number of detected electrons per event depends on the intensity of the electron beam. With the comparable high electron beam current of ∼10 nA at A2, up to 35 electrons per event are be recorded. In contrast, at CBELSA/TAPS, where the beam current was below 1 nA, only up to 10 electrons per event are registered. This can be seen on the height of the background in Figures 6.20 for A2 and 6.21 for CBELSA/TAPS.
Due to the rather high number of detected electrons and the finite time resolution of the detectors, random background electrons can not be distinguished from the true electron by means of a time coincidence requirement between the electrons and detected photons. Instead, a time window for the true electron has to be specified within which the contributions from random electrons has to be estimated and properly subtracted. This is realized by a so-called sideband subtraction [203].

The sideband subtraction is based on the assumption of the time coincidence between the true electron in the tagger and the signals of the detected photons in the calorimeters. Such spectra are illustrated for the A2 analysis in Figure 6.20 and for the CBELSA/TAPS analysis in Figure 6.21. Shown is the time coincidence between the time of all hits in the tagging spectrometer and the detected photons in the calorimeters for the $\gamma p \to \pi^0\pi^0 p$ analysis for all possible events (full histogram in the main window) and for the events that passed all analysis cuts (green histogram in the upper right inset). The time difference is given by the difference of the time of an

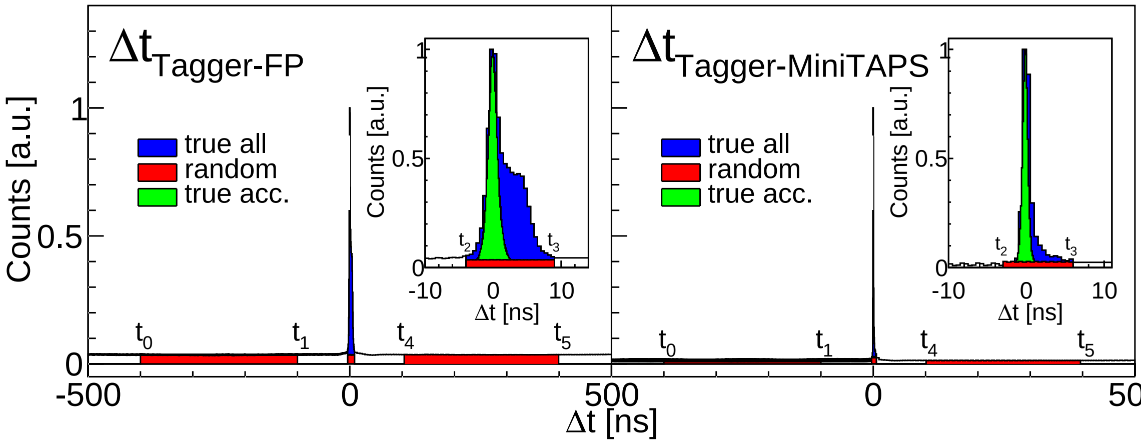

Figure 6.21: Time coincidence of the tagged electrons and the detected photons in the detectors of the CBELSA/TAPS setup. Left-hand side: Tagger - Forward Cone. Right-hand side: Tagger - MiniTAPS. Main window: full spectrum. Upper right inset: prompt region. Blue histogram: true events in the prompt time window. Red histograms: random tagger events in the background and prompt time windows. Green histogram: true and accepted events in the prompt time window. Data from the November 2008 beamtime.

individual tagger hit to the time average of all calorimeter hits. Because of the better time resolution of TAPS and MiniTAPS (see the width of the prompt peak in Figures 6.20, 6.21), their time information was used as reference if possible. The prompt peak from the coincident events, as well as the flat background from the random tagger hits, is clearly visible in all spectra. In addition, the influence of the different electron beam intensity is visible. In the spectra from the CBELSA/TAPS analysis, which stem from experiments at rather low electron beam currents of below 1 nA, the height of the background is much lower than in the spectra of the analysis of the A2 data at electron beam currents of 10 nA. In addition, as previously discussed in Section 6.2, the time difference between the Forward Cone detector and MiniTAPS of the CBELSA/TAPS analysis exhibits contributions from misidentified charged particles that broaden the prompt peak (see blue area in the insert of the left-hand side of Figure 6.21). Nevertheless, the application of all analysis cuts (green area) reliably removes such contributions. Another interesting feature is visible in the time difference spectrum of the tagger and the MiniTAPS detector from CBELSA/TAPS. On the left side of the peak, a periodic structure with a period of 2 ns is visible. This comes from the beam characteristics at ELSA, since the electrons are accelerated by a 500 MHz alternating field, which results in a time difference of the electron bunches of 2 ns. It is also slightly visible in the spectrum of the tagger and Forward Cone detector, but due to the poor time resolution of the Forward Cone, the structure is almost smeared out. At MAMI the beam is much more continuous and hence the time resolution is not sufficient for dissolving the structure.

In order to subtract the random background below the prompt peak, different time windows were selected that contain the prompt peak on top of the background contribution (time window $[t_2, t_3]$ in Figures 6.20, 6.21), as well as regions of pure background (time windows $[t_0, t_1]$ and $[t_4, t_5]$ in Figures 6.20, 6.21). Background contributions in the time window are marked as red and prompt events as blue. If the background hits are completely random, their contributions to any time interval in the spectrum should be equal. Therefore, the events from the two background windows can be used to statistically subtract the background contribution inside the prompt window. This is realized by weighting events within the prompt window with $w_{\text{prompt}} = 1$ and those within one of the background windows with:

$$w_{\text{random}} = \frac{(t_3 - t_2)}{(t_1 - t_0) + (t_5 - t_4)} \ . \tag{6.3}$$

The number of true tagger hits N_{true} and its statistical error ΔN_{true} are then given by:

$$\begin{aligned} N_{\text{true}} &= N_{\text{prompt}} + \sum_{i=1}^{N_{\text{random}}} w_{\text{random}} = N_{\text{prompt}} + w_{\text{random}} \cdot N_{\text{random}} \\ \Delta N_{\text{true}} &= \sqrt{N_{\text{prompt}} + w_{\text{random}}^2 \cdot N_{\text{random}}} \ , \end{aligned} \tag{6.4}$$

where N_{prompt} is the number of hits in the prompt window and N_{random} is the number of hits in the background window. From the definition of the background weight w_{random} in Equation (6.3), it follows that using large background windows results in a smaller statistical error. For this reason, rather large windows were chosen, as shown in Figures 6.20 and 6.21.
In the simulation, for each event exactly one hit exists in the tagger. Therefore, a sideband subtraction is not necessary and for all events, $w_{\text{prompt}} = w_{\text{random}} = 1$ applies.

6.4 Analysis Cuts

At this stage in the analysis, the events that contain the correct number of neutral and charged particles were selected, charged clusters were assigned to protons, the different neutral clusters were combined to the π^0 meson or to the $\pi^0\pi^0$ pair and, if available, the remaining neutral cluster to the neutron (see Section 6.1). Using coincidence cuts (see Section 6.2), the proper correlation between the detected particles was ensured. The electron that radiated the bremsstrahlung photon (that triggered the reaction) was identified by means of a statistical sideband subtraction (see Section 6.3). Therefore, the present sample of events contains mostly particles of the same reaction and of the general properties as required for the reaction of interest. However, the actual sample is not already clean, but contains all kind of particles of any reaction that might fulfill the selection criteria. For example, as the charged particle identification detectors (PID and Veto detectors at A2, Inner detector and Veto detectors at CBELSA/TAPS) exhibit a certain detection inefficiency, charged particles might have been wrongly identified as a neutral particle. In the same manner, neutral particles can be marked as charged if a certain threshold value was not set properly, a detector component did not work properly, or simply because of accidentally coincidental signals. On the other hand, reactions of the same selection criteria or reactions that initially have different criteria, might end up in the sample when one or several particles were missed by the detectors. Therefore, it is important to note at that point, that the particles that have been identified up to now are only considered to be particle candidates. The subsequent analysis steps that will be described in the following are necessary to remove the candidate flag.

Analysis	Simulated Reaction	Threshold
$\gamma p(n) \to \pi^0 p(n)$	$\gamma p(n) \to \pi^0 p(n)$	142.06 MeV*
	$\gamma p(n) \to \pi^0\pi^0 p(n)$	291.60 MeV*
	$\gamma n(p) \to \pi^0\pi^- p(n)$	296.87 MeV*
	$\gamma p(n) \to \pi^0\pi^+\pi^- p(n)$	462.06 MeV*
	$\gamma p(n) \to \eta(\to 2\gamma) p(n)$	629.57 MeV*
$\gamma n(p) \to \pi^0 n(p)$	$\gamma n(p) \to \pi^0 n(p)$	142.06 MeV*
	$\gamma n(p) \to \pi^0\pi^0 n(p)$	291.60 MeV*
	$\gamma p(n) \to \pi^0\pi^+ n(p)$	296.87 MeV*
	$\gamma p(n) \to \Delta^0(1232)\pi^+ \to \pi^0\pi^+ n(p)$	296.87 MeV**
	$\gamma p(n) \to \Delta^+(1232)\pi^0 \to \pi^0\pi^+ n(p)$	296.87 MeV**
	$\gamma n(p) \to \pi^0\pi^+\pi^- n(p)$	462.06 MeV*
	$\gamma n(p) \to \eta(\to 2\gamma) n(p)$	629.57 MeV*
$\gamma p \to \pi^0\pi^0 p$	$\gamma p \to \pi^0\pi^0 p$	308.79 MeV
	$\gamma p \to \Delta^0(1232)\pi^0 \to \pi^0\pi^0 p$	308.79 MeV**
	$\gamma p \to N(1520)\pi^0 \to \pi^0\pi^0 p$	308.79 MeV**
	$\gamma p \to \eta(\to 2\gamma)\pi^0 p$	930.60 MeV
	$\gamma p \to \eta(\to 6\gamma) p$	707.16 MeV
$\gamma p(n) \to \pi^0\pi^0 p(n)$	$\gamma p(n) \to \pi^0\pi^0 p(n)$	291.60 MeV*
	$\gamma p(n) \to \Delta^0(1232)\pi^0 \to \pi^0\pi^0 p(n)$	291.60 MeV**
	$\gamma p(n) \to N(1520)\pi^0 \to \pi^0\pi^0 p(n)$	291.60 MeV**
	$\gamma p(n) \to \eta(\to 2\gamma)\pi^0 p(n)$	808.80 MeV*
	$\gamma p(n) \to \eta(\to 6\gamma) p(n)$	629.57 MeV*
$\gamma n(p) \to \pi^0\pi^0 n(p)$	$\gamma n(p) \to \pi^0\pi^0 n(p)$	291.60 MeV*
	$\gamma n(p) \to \Delta^0(1232)\pi^0 \to \pi^0\pi^0 n(p)$	291.60 MeV**
	$\gamma n(p) \to N(1520)\pi^0 \to \pi^0\pi^0 n(p)$	291.60 MeV**
	$\gamma n(p) \to \eta(\to 2\gamma)\pi^0 n(p)$	808.80 MeV*
	$\gamma n(p) \to \eta(\to 6\gamma) n(p)$	629.57 MeV*

Table 6.2: Overview of the simulated reactions used for the different analyses. (*) Quasi-free production thresholds were approximated by the coherent threshold plus the binding energy per nucleus ($E_b \approx 2.225$ MeV for the deuteron). (**) Production thresholds for sequential decays depend on the width of the intermediate resonance and an exact threshold value is not reasonable. For this reason the quasi-free threshold is indicated.

In order to reject such events from the sample, a combination of additional conditions on the selected events were required. Such conditions involve criteria that are based on the kinematics of the reaction, as well as on the information of the several detector components. Conditions of the latter case were tried to keep at a minimum, as they strongly depend on the detector performance and also sometimes are difficult to model with simulation. The identification was focussed on the understanding of the kinematics of the reaction, i.e. by rather excluding wrong background events than selecting correct ones. This method might require a more extensive analysis and more elaborate selection criteria, but avoids the above mentioned complications. Finally, the information of the detector components that could have been used for the selection of the events were used to check the quality of the definite sample (see Section 6.5).
The development of the cuts on the reaction kinematics were mostly determined by a comparison of a certain physical quantity from simulation with that from the data. Thereby, one takes advantage of the fact that the simulation only contains the reaction of interest and with a given experimental setup it is known which particle should have deposited which amount of energy in which detector element. By comparing the distribution of a certain spectrum of the simulation with that obtained from the data, one can draw conclusions about what limits should be held. As the kinematics are different for every kind of reaction, the distributions of different reactions will certainly not be identical, but rather overlap to a certain degree or in the ideal case, are separable from each other. The proper condition allows to either minimize the contributions from background events or totally exclude them from the sample.
For the comparison of the kinematics of the reaction of interest with those from competing reactions, distributions from the data as well as from the simulated reaction of interest and of background reactions were carried out. For this purpose, it was necessary to first identify which reactions may contribute to the sample in the examined energy range. Table 6.2 summarizes the reactions that have been simulated for the different analyses. As the type of reaction is independent of the simulation, the same reactions were generated for the analysis of the A2 and the CBELSA/TAPS data. For this purpose, $20 \cdot 10^6$ to $100 \cdot 10^6$ events of each reaction have been generated with `PLUTO` (see Section 3.4.1) and then either passed through the `A2 GEANT4` (see Section 3.2.2) or the `CBGEANT Geant3.21` simulation (see Section 3.3.2). The output was then analyzed with the same analysis used for the analysis of the data (see Sections 3.1, 3.2.1, 3.3.1 and 3.4.2).

In the following sections, the different analysis cuts are discussed that have been used to ensure a proper identification of the particles and of the reaction. At first, the different cuts are described for the example of the analysis of single π^0 photoproduction from quasi-free protons and neutrons using liquid deuterium data (December 2007 beamtime). Subsequently, its adaption to the analysis of polarized deuterated butanol data will be described. In the next sections, the procedure of the analysis of double π^0 photoproduction from free protons, quasi-free nucleons and as well polarized nucleons will be discussed. However, since a lot of the different analysis steps were identical, their discussion will be kept short and only the applied cuts will be presented. In the end, the quality of the reaction and particle identification will be presented.

6.4.1 Single π^0 Analysis on quasi-free Nucleons

The main difficulty in the analysis of single π^0 photoproduction from quasi-free protons and neutrons are the many different competing reaction channels that end up in the selected events. As the neutral pion is the lightest meson, its production threshold of $\sim$ 142 MeV is not only very low, but also well below the lowest tagged photon energy of $\sim$ 400 MeV. Hence, at the first available energy, background reactions such as photoproduction of $\pi^0\pi^0$ (threshold $\sim$ 292 MeV) and $\pi^0\pi^\pm$ (threshold $\sim$ 297 MeV) mesons already contribute to the event selection. At slightly higher energies of $\sim$ 462 MeV and $\sim$ 630 MeV also contributions from photoproduction of $\pi^0\pi^+\pi^-$ and $\eta(\rightarrow 2\gamma)$ contaminate the sample. Depending on the final state of each competing reaction, the chance of contributing to the event sample is different and depends on the type of available particles. Contamination with events from $2\pi^0$ photoproduction may occur, if two neutral particles or one neutral and one charged particle are not detected. Additional possibilities arise if a charged particle is detected as neutral or vice versa. The chance that this reaction contributes is rather small. In contrast, the chance that the final state $\pi^0\pi^\pm$ contributes is much higher, as it is already sufficient that the charged pion is not detected, which is not too unlikely. The same applies for photoproduction of $\pi^0\pi^+\pi^-$ with the difference that both charged pions must not be detected. The decay of the η into two photons immediately meets the selection requirement, but can be easily rejected by a condition of the invariant mass of the two photons, as the η mass is roughly four times higher than the mass of the π^0. However, in case of combinatorial disorder, the reaction might survive the invariant mass cut. This immediately points out the criticality of the other reactions. They all comprise neutral pions and as soon as they end up in the data sample, they can not be rejected by means of the invariant mass of the two photons and hence, need further conditions on the coplanarity or missing mass of the reaction.

The last difficulty that discriminates single π^0 photoproduction from other reactions is also due to the light mass of the pion. The energy that is available for the production of the final state particles depends on the incident photon energy and the mass and momentum of the target nucleon. The heavier the sum of the masses of the final state particles, the more energy is required by the incident photon. Every additional energy of the photon beam is available as kinetic energy for the reaction products. As the mass of the final state particles in single π^0 photoproduction is lower than for the other reactions, the recoil nucleon on average receives more kinetic energy. At the available incident photon energies, this indeed results in a challenge. The kinetic energy of the proton is especially high when it goes into TAPS, which is the case when the pion has only few kinetic energy, i.e. at backward angles in the center of mass of the proton-pion system. This is illustrated in Figure 6.22 for the angular regions, when the proton goes in forward direction ($\cos(\theta^*_{\pi^0}) < -0.6$), and for the regions when it goes in backward direction ($\cos(\theta^*_{\pi^0}) > -0.6$).

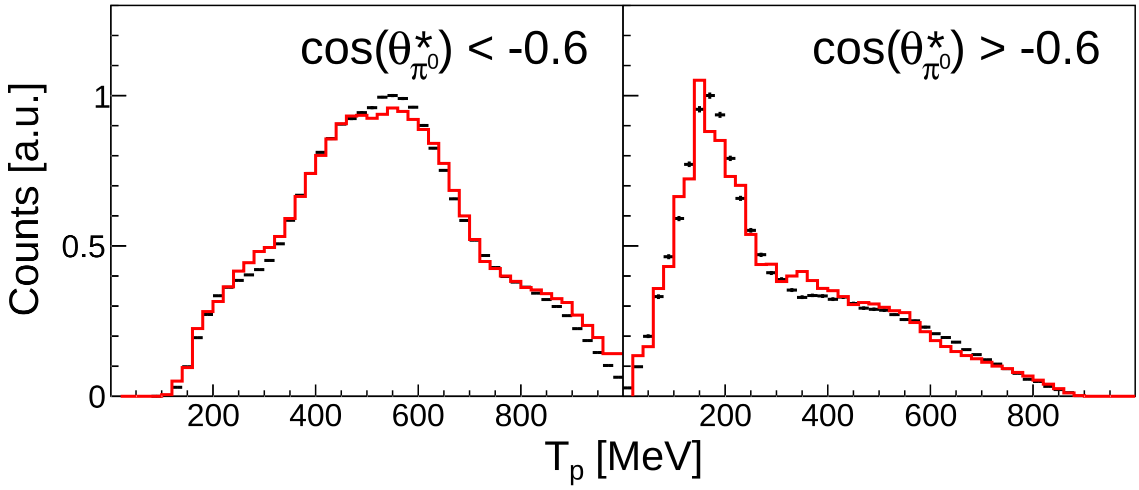

Figure 6.22: Distribution of the kinetic energy of the recoil proton for single π^0 photoproduction off quasi-free protons from the A2 data. Shown are forward and backward angles of the π^0-meson in the center of mass frame of the $\pi^0 p$-system. Black crosses: data. Red histogram: simulation. Left-hand side: $\cos(\theta^*_{\pi^0}) < -0.6$. Right-hand side: $\cos(\theta^*_{\pi^0}) > -0.6$.

The rather high kinetic energy of the recoil nucleons results in them not being stopped within the detector, i.e. they punch-through. This yields in a wrong energy reconstruction as the nucleons will not deposit all of their energy in the detectors. In addition, the amount of deposited energy of all nucleons with a higher energy (than necessary to punch-through the detectors) is identical, which makes their identification via their energy useless. Furthermore, these punch-through protons might even not deposit enough energy in the veto detectors and can be misidentified as neutrons. The problem of protons that are misidentified as neutrons has to be investigated to ensure a clean separation of the reaction on the proton and on the neutron and will be examined in more detail in the subsequent sections. Nevertheless, the energy can be reconstructed by a kinematical calculation (see Section B.3), as used for the reconstruction of the invariant mass W of the final state, which will be discussed in Section 6.7.

In the following sections, the different analysis cuts will be discussed in the chronological order they were determined and applied. As a consequence, all events that contribute to the spectra shown in this section have passed all cuts and requirements from the previous sections. This implies that the events of the first spectrum, the PSA, already fulfilled the time coincidence requirement of the individual detectors and the random background hits in the tagger have been subtracted.

Pulse Shape Analysis (PSA)

The first condition was made on the scintillation properties of the BaF_2 crystals of the TAPS detector by means of the Pulse Shape Analysis (PSA). As the information

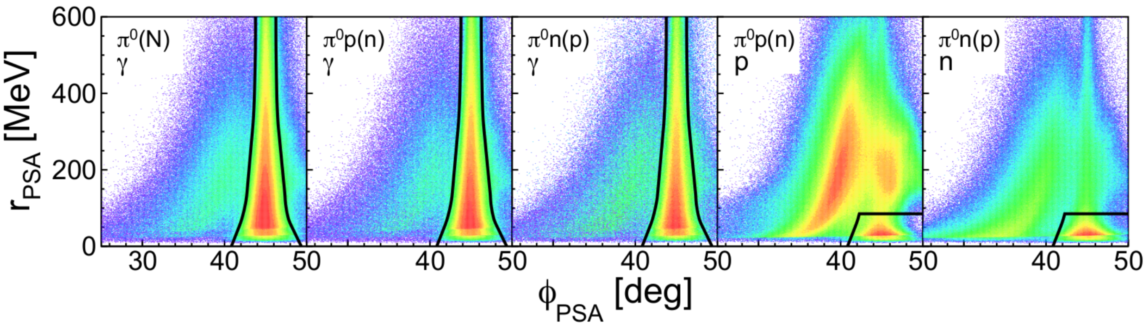

Figure 6.23: PSA spectra for single π^0 photoproduction from the deuteron from the A2 data. No cut was applied to the data. Columns: analysis channels (see labels). Solid black lines: cut positions.

about the short gate component of the BaF_2 crystals is not available in the simulation, this condition can only by applied to the data. Therefore, this cut is delicate and should only be applied carefully. The resulting PSA spectra for the photons and nucleons of the three investigated reactions are shown in Figure 6.23.

As mentioned in Sections 2.2.4 and 5.2.6, the energy information of the short gate of the BaF_2 crystals of TAPS has been calibrated such that that photons are located at PSA angles of $\phi_{PSA} = 45°$ for all PSA radii r_{PSA}. For massive particles such as protons and neutrons, the PSA angle increases with an increasing PSA radius. However, their PSA angles will not exceed 45° which allows for a proper distinction from photons. Protons usually exhibit a much better defined band structure than neutrons. Due to their charge, they always deposit roughly the same amount of energy at a given proton energy. An exception is given for the protons when they punch-through the crystals, as mentioned in Section 6.4.1 and is often the case in π^0 photoproduction because of their comparatively high kinetic energy (see left-hand side of Figure 6.22). This is especially problematic as in such cases the protons are not distinguishable from photons anymore because their PSA band structure crosses that of the photon. This can be seen when the PSA spectra obtained after all cuts were applied are divided into the same two angular regions, as shown in Figure 6.24. In the upper left figure the proton band exhibits a circular structure at PSA angles of about $\phi_{PSA} = 45°$, which stems from the punch-through protons. As a consequence, some of the protons were misidentified as neutrons, which is visible in the upper right figure of Figure 6.24, where a small aggregation of events is visible at the same position as observed in the proton spectrum. In the remaining angular range the spectra do not exhibit any structures of punch-through particles.
Nevertheless, as the nucleon bands overlap with the photon band, the PSA spectrum is not suited for solving this issue. Any cut on the punch-through region would also involve photons and can cause loss of events. Instead, the problem can be considered using the time of flight technique, which will be discussed in Section 6.5.1.

Due to the overlap of the proton and photon bands, a simple and conservative

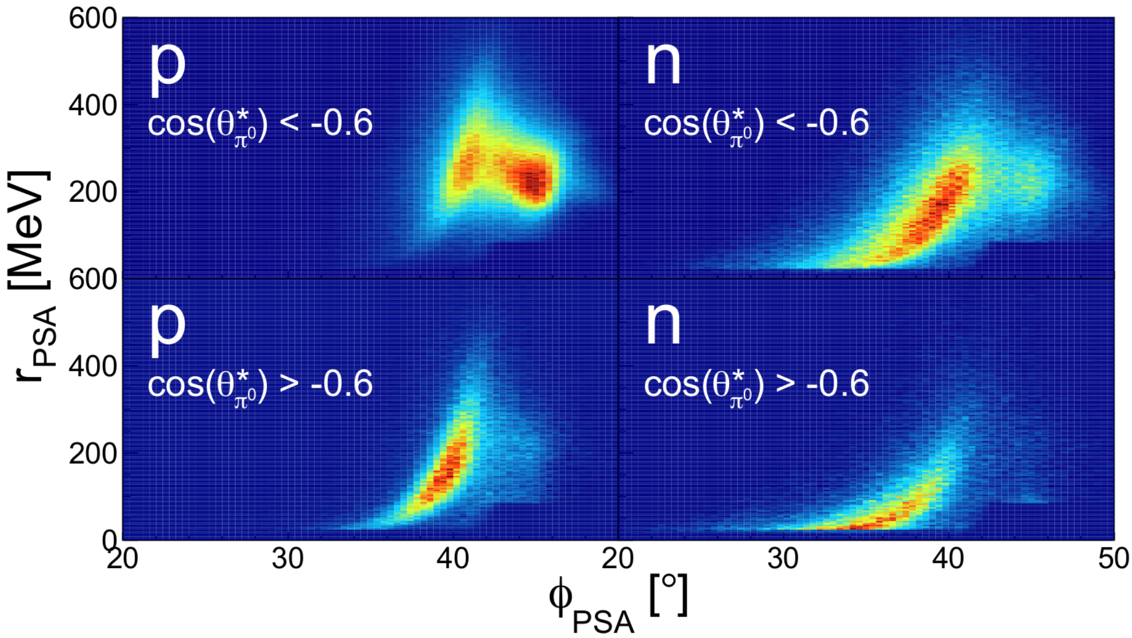

Figure 6.24: Illustration of the punch-through protons by means of nucleon PSA spectra from π^0 photoproduction from the deuteron from the A2 data. All cuts were applied to the data. Left column: protons. Right column: neutrons. Upper row: angular region of high kinetic energy recoil protons ($\cos(\theta^*_{\pi^0}) < -0.6$). Lower row: remaining angular region ($\cos(\theta^*_{\pi^0}) > -0.6$). Punch-through protons exceed PSA angles of $\phi_{\mathrm{PSA}} = 45°$ (upper left figure). A contamination of misidentified protons is visible in the neutron PSA (upper right figure).

cut on the nucleon PSA was applied. Only the events at the lowest PSA radii, where photons contaminate the sample, were rejected by means of an exclusion zone as illustrated in the two most right-hand side figures of Figure 6.23. For the identification of the photons, the photon band was fit for different slices of PSA radii with a Gaussian in order to determine a $\pm 3\sigma$ exclusion zone, as illustrated with solid black lines in Figure 6.23.

Invariant Mass Analysis

The invariant mass of a particle is a quantity of its total energy and momentum, which is the same in all reference frames that are related by Lorentz transformations. If a neutral pion with four momentum $\mathbb{P}_{\pi^0}$ decays into two photons γ_1 and γ_2, of four momenta $\mathbb{P}_{\gamma_1}$ and $\mathbb{P}_{\gamma_2}$, its invariant mass m_{π^0} is given by

$$\begin{aligned} m_{\pi^0} = m_{\gamma\gamma} = \sqrt{\mathbb{P}_{\pi^0}^2} &= \sqrt{(\mathbb{P}_{\gamma_1} + \mathbb{P}_{\gamma_2})^2} \\ &= \sqrt{\underbrace{\mathbb{P}_{\gamma_1}^2}_{=0} + \underbrace{\mathbb{P}_{\gamma_2}^2}_{=0} + 2\mathbb{P}_{\gamma_1}\mathbb{P}_{\gamma_2}} \\ &= \sqrt{2 \cdot (E_{\gamma_1}E_{\gamma 2} - \vec{p}_{\gamma_1}\vec{p}_{\gamma_2} \cdot \cos(\phi_{\gamma_1\gamma_2})))} \\ &= \sqrt{2E_{\gamma_1}E_{\gamma_2}(1 - \cos(\phi_{\gamma_1\gamma_2}))} \end{aligned} , \tag{6.5}$$

where E_{γ_i} is the energy and $\phi_{\gamma_1\gamma_2}$ the opening angle of the photons.

Since only neutral pions were considered in this work, the invariant mass of the detected photons serves as the ideal tool to identify the contributing mesons and to reject competing background reactions. For this reason, at this stage loose invariant mass cuts were determined in order to already eliminate unessential events and allowing for a better determination of the subsequent analysis cuts.

The invariant mass spectra of the two photons that are from the pion decay, as identified with the χ^2 test, are shown in Figure 6.32. Shown are the spectra from the data analysis for all previous cuts, i.e. detector time coincidence, random tagger background subtraction, and pulse shape analysis cuts. Selected energy and angular bins are presented for the quasi-free exclusive reaction from the proton (open blue upward triangles) and the neutron (open red downward triangles). Note that the histograms were renormalized and that those in the first column are scaled further down in order to have enough space for the legend.

In order to determine the cut positions (vertical solid black lines), the spectra from the corresponding analysis were fit with the same spectra from the simulated target reaction and all considered background reactions, as shown in Table 6.2. The spectra show a clear peak at the mass of the neutral pion, $m_{\pi^0} = 134.9766$ [37]. The sum of the line shapes of the simulations (black histogram) is in excellent agreement with the yield of all energy and angular bins from the data. This indicates that the most important competing reactions were successfully considered. Even though the invariant mass spectra, as shown in Figure 6.32, are from a very early stage of the analysis, not a lot of background (dotted magenta line) is visible. This is due to the fact that most of the competing reactions involve true π^0, which as a matter of fact exhibit the proper invariant mass. Therefore, they exhibit the same line shape as the signal and do not have to be considered for the fit. Events from $\eta \to 2\gamma$ are a part of the sample, but their invariant mass is well outside the region shown in the spectra and will be removed by this cut.

The line shape of the fit result for the target reaction was then fit with a Gaussian in order to determine the mean value and the width, σ, of the true signal contribution. Cut positions of $\pm 3\sigma$ were determined by means of 75 energy and 20 angular bins.

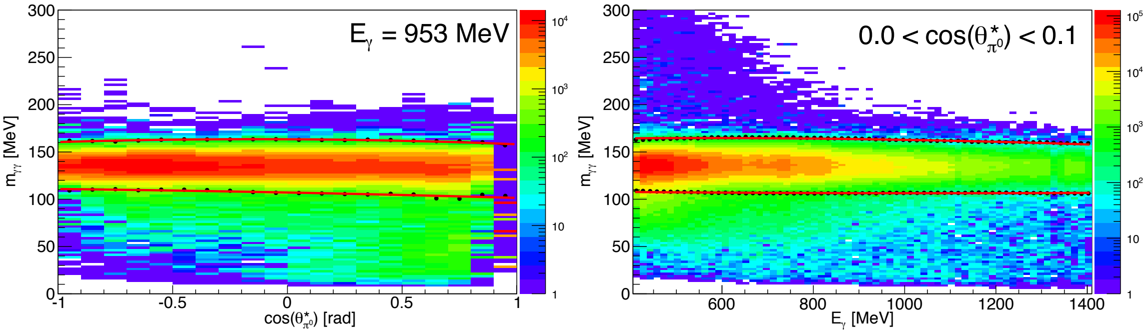

Figure 6.25: Illustration of the invariant mass cut for single π^0 photoproduction from the deuteron from A2 data. Example result from the exclusive reaction on the quasi-free proton. Only the PSA cut was applied to the data. Left-hand side: invariant mass as function of $\cos(\theta^*_{\pi^0})$ for one energy bin ($E_\gamma = 953$ MeV). Right-hand side: invariant mass as function of E_γ for one angular bin ($0.0 < \cos(\theta^*_{\pi^0}) < 0.1$). Black circles: cut positions obtained from the fit. Red lines: fit of the cut positions as applied in the analysis.

The size of the cut was intentionally chosen to be of this size since $\pm 3\sigma$ already contains 99 % of all true events. Hence, a minimum number of signal, but a maximum number of background events are rejected. For every angular bin, the cut position was then fit with a polynomial function as a function of the photon beam energy in order to obtain a continuous smooth cut position. This is illustrated in Figure 6.25 for one angular bin as a function of the incident photon beam energy (right-hand side) and for one energy bin as a function of the polar angle of the pion in the center of mass system (left-hand side).

Coplanarity Analysis

The second condition that was required on the event sample in the analysis is the meson-nucleon coplanarity, which is illustrated in Figure 6.26. If two particles, referred to as 1 and 2, are produced by a incident beam particle γ, due to momentum conservation, all three momentum vectors lie in the same plane, i.e. are coplanar. As there is no transversal momentum component in the initial state, the condition only depends on the azimuthal angle and is fulfilled if the difference of the azimuthal angles of particles 1 and 2 is 180°. For symmetric reasons in the analysis, the difference of the angles is determined according to:

$$\Delta\phi_{12} = \begin{cases} \phi_1 - \phi_2 & \text{if } \phi_1 - \phi_2 \geq 0 \\ 360° - |\phi_1 - \phi_2| & \text{if } \phi_1 - \phi_2 < 0 \end{cases} . \tag{6.6}$$

However, the transversal component is only nonzero if the target nucleon is at rest, e.g. for the reaction on the free proton. In deuterium, the nucleons are not at rest, but exhibit Fermi motion of an arbitrary direction and with a magnitude that is given by a probability density function (see Figure 3.9). This nonzero transversal component results in statistical smearing and a loss of the resolution of the coplanarity condition.

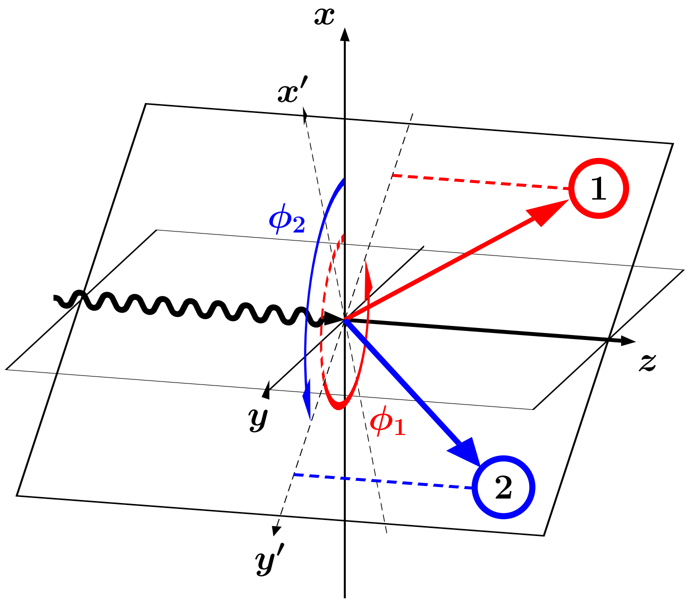

Figure 6.26: Illustration of the coplanarity analysis. Wiggly line: incoming photon. Red (blue) arrows: final state particles 1 (2). The difference of the two azimuthal angles of the nucleon and meson $\Delta\phi$ is always 180°.

Besides the effect on the resolution, this has no further consequence as it affects not only the signal but also all background contributions.

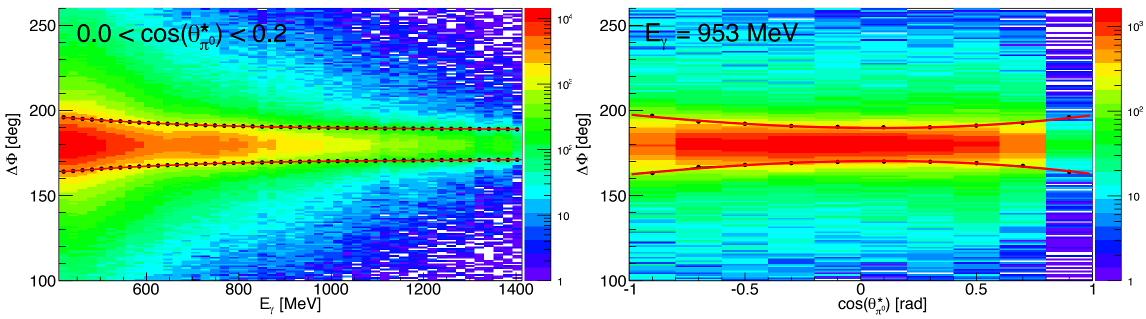

Figure 6.27: Illustration of the coplanarity cut for single π^0 photoproduction from the deuteron from A2 data. Example result from the exclusive reaction on the quasi-free proton. The PSA and invariant mass cuts were applied to the data. Left-hand side: coplanarity as function of $\cos(\theta^*_{\pi^0})$ for one energy bin ($E_\gamma = 953$ MeV). Right-hand side: coplanarity as function of E_γ for one angular bin ($0.0 < \cos(\theta^*_{\pi^0}) < 0.2$). Black circles: cut positions obtained from the fit. Red lines: fit of the cut positions as applied in the analysis.

For the determination of the cuts on the coplanarity of the pion nucleon system, the difference in the azimuthal angle of the pion and the recoil nucleon was fit with the simulated signal and background contributions for 55 energy and 10 angular bins in the same way as explained in the invariant mass analysis. The resulting

coplanarity spectra for five angular bins and for five energy bins are shown in Figure 6.33. Again, the events that contribute to the spectra have passed all precedent cuts, i.e. detector time coincidence, random tagger background subtraction as well as the lastly described invariant mass cut.
Again the sum of the simulated line shapes is in good agreement with the data. Cut positions of $\pm 1.5\sigma$ have been determined from each individual fit and were then fit with a polynomial function for every angular bin as a function of the energy. An example for an energy and angular dependent cut is given in Figure 6.27. The size of the cut was chosen rather narrow as it was found that in this way, the separation from background and signal in the missing mass analysis (see Section 6.4.1) is more sufficient.

Missing Mass Analysis

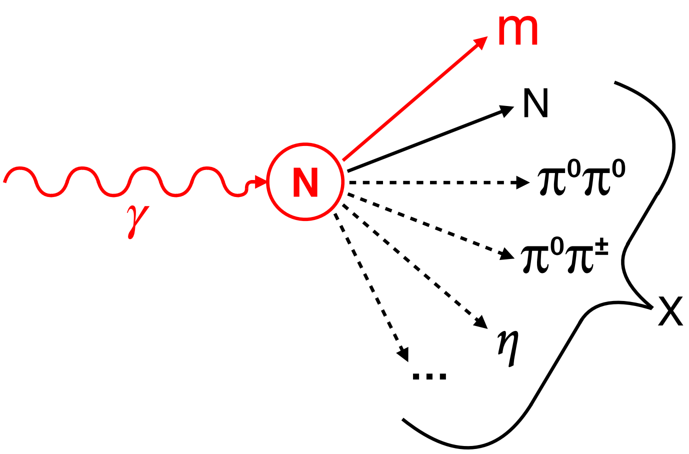

Figure 6.28: Illustration of the missing mass analysis. Wiggly line: incoming photon. Red arrow/particle: measured meson. Black arrows/particles: particles that are treated as *missing* particles, among which the solid black arrow indicates the recoil nucleon and the dashed arrows the possible background contributions.

The most powerful and most kinematically dependent method to reject events from undesired reactions is the missing mass analysis. It is based on the reliable detection and reconstruction of the meson, which is in general justified, as it mainly decays to photons that can be confidentially detected. In addition, proper knowledge of the initial state, i.e. the incoming photon beam and the target nucleon, is required. These three quantities are the most well detected among the participating particles. The fact that the target nucleon exhibits a certain Fermi momentum, that besides its probability density is unknown, has thereby only an influence on the resolution of the missing mass and poses no further problem.

The main idea of the missing mass is that the mass balance of every reaction depends on its final state particles. When the final state meson is detected, the only remaining unknown particle is the recoil nucleon. In this kind of analysis, its information, although measured, are ignored. Instead it is treated as the *missing* particle, and its invariant mass is denoted as the *missing mass*. Using the known four momenta of the incoming photon $\mathbb{P}_\gamma$, the target nucleon $\mathbb{P}_{N_{IS}}$, and the detected meson $\mathbb{P}_m$, the invariant mass of the final state nucleon $m_{N_{FS}}$, i.e. the missing mass m_X, is given by:

$$\begin{aligned} m_{N_{FS}} \stackrel{!}{=} m_X &= \sqrt{\mathbb{P}_\gamma + \mathbb{P}_{N_{IS}} - \mathbb{P}_m} \\ &= \sqrt{(E_\gamma + E_{N_{IS}} - E_m)^2 - (\vec{p}_\gamma + \vec{p}_{N_{IS}} - \vec{p}_m \ ,)} \end{aligned} \tag{6.7}$$

or for a nucleon at rest

$$m_X = \sqrt{(E_\gamma + m_N - E_m)^2 - (\vec{p}_\gamma - \vec{p}_m)} \ . \tag{6.8}$$

The principle of the missing mass analysis is shown in Figure 6.28. The red labeled

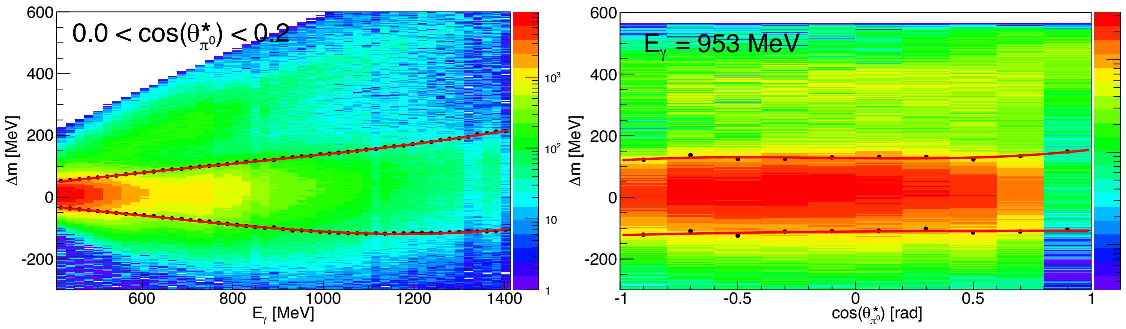

Figure 6.29: Illustration of the missing mass cut for single π^0 photoproduction from the deuteron from A2 data. Example result from the exclusive reaction on the quasi-free proton. The PSA, invariant mass, and coplanarity cuts were applied to the data. Left-hand side: missing mass as function of $\cos(\theta^*_{\pi^0})$ for one energy bin ($E_\gamma = 953$ MeV). Right-hand side: missing mass as function of E_γ for one angular bin ($0.0 < \cos(\theta^*_{\pi^0}) < 0.2$). Black circles: cut positions obtained from the fit. Red lines: fit of the cut positions as applied in the analysis.

particles are used for the calculation of the missing mass m_X. Depending on the number and type of the other (black labeled) particles, the missing mass is either equal to the nucleon mass, i.e. if the desired reaction occurred, or higher than the nucleon mass, if any additional particles contribute. In this analysis, the nucleon mass m_N is directly subtracted from the missing mass m_X such that the correct events exhibit a missing mass of zero:

$$\Delta M = m_X - m_N \ . \tag{6.9}$$

The missing mass spectra from the analysis of single π^0 photoproduction from quasi-free protons and neutrons are shown in Figure 6.34 for the same energy and angular bins as for the coplanarity analysis. The cut positions have been determined in the same way and were as well chosen to be of the size $\pm1.5\sigma$. Wider cuts would increase the signal rate, but in the same way would start to strongly contaminate the sample with background. The cut positions again were fit with a polynomial function in order to smoothen the cut as a function of energy. The situation is shown in Figure 6.29.

Time of Flight Cut

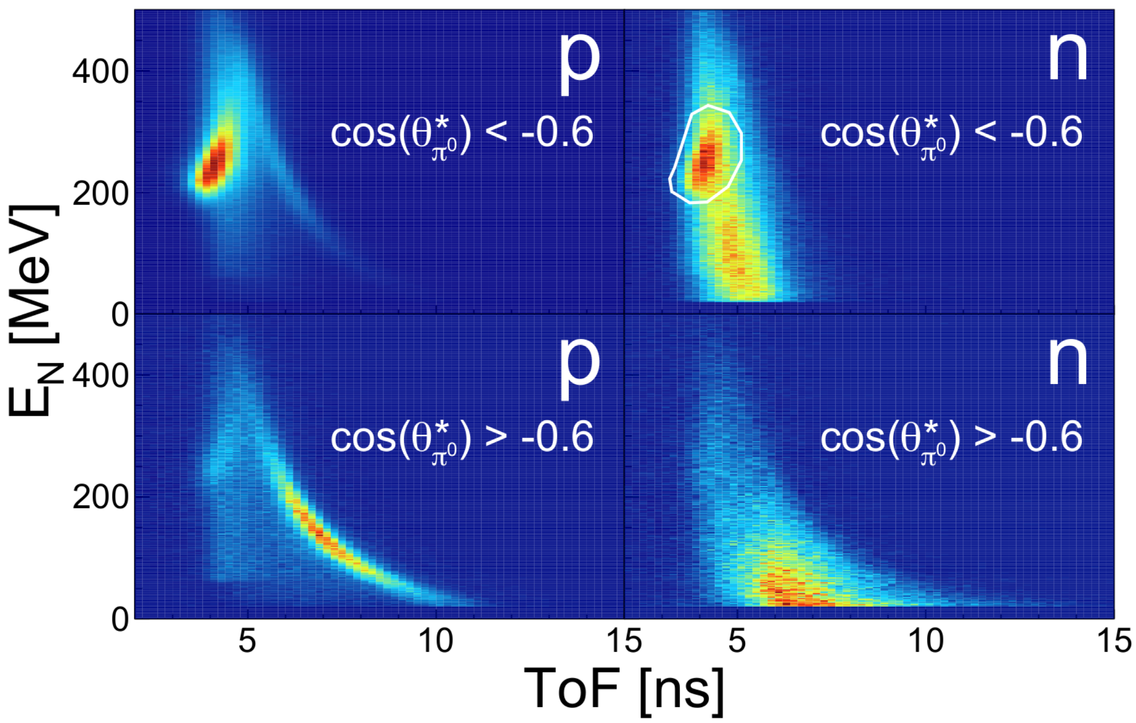

Figure 6.30: Identification of the punch-through protons by means of deposited energy versus time of flight (TOF) spectra from π^0 photoproduction from the deuteron from the A2 data. All cuts were applied to the data. Left column: protons. Right column: neutrons. Upper row: angular region of high kinetic energy recoil protons ($\cos(\theta^*_{\pi^0}) < -0.6$). Lower row: remaining angular region ($\cos(\theta^*_{\pi^0}) > -0.6$). Protons of high kinetic energy may punch through the detector and always deposit roughly the same amount of energy in the detector. This results in the typical circular accumulation of events in the TOF spectrum of the proton (upper left figure). If the deposited energy of the protons does not exceed the threshold requirement of the crystal, they may be misidentified as neutrons (accumulated events within the white border in upper right figure). White region: cut on neutron TOF.

As already discussed in Sections 2.2.4 and 5.2.7, the sufficiently large distance of the TAPS detector from the target of ~ 1.5 m, as well as the excellent time resolution of the BaF_2 crystals, allow for the discrimination of particles that are detected in TAPS with the time of flight technique (see Section 6.5.1). As mentioned in the beginning of this section, it is advisable to use such techniques only for the verification of the quality of the particle identification. However, it was observed that protons in the very forward direction generally have high enough kinetic energy to punch-through the detector and only deposit a minimum fraction of their energy. As a consequence, their energy reconstruction fails and a certain fraction is even misidentified as neutrons. This behavior was already discussed in the pulse shape analysis (see Figure 6.24), but an intervention at this stage was not possible, since the punch-through protons could not be distinguished from photons.

In contrast, it was found that the time of flight property of the TAPS detector is

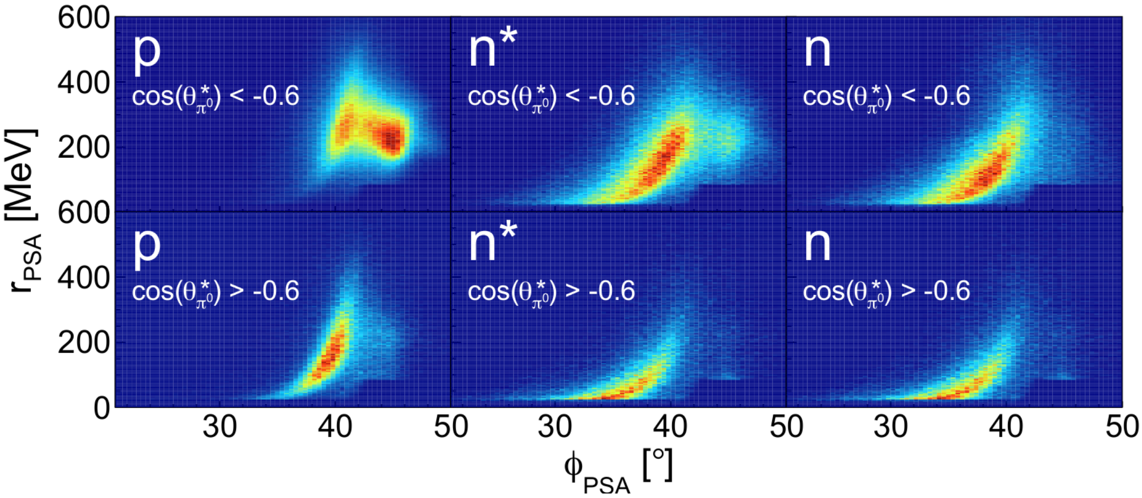

Figure 6.31: Influence of the cut on the neutron TOF onto the neutron PSA. In order to reject events, where high energy protons were misidentified as neutrons, a cut on the neutron TOF was applied (indicated by the white border in the upper right figure of Figure 6.30). Left column: final proton PSA. Middle column: final neutron PSA, without the cut on the neutron TOF. Right column: final neutron PSA, including the cut on the neutron TOF. The contamination from protons was eliminated. Upper row: angular region of high kinetic energy recoil protons ($\cos(\theta^*_{\pi^0}) < -0.6$). Lower row: remaining angular region ($\cos(\theta^*_{\pi^0}) > -0.6$).

ideally suited to solve this challenge. The TOF spectrum for π^0 photoproduction from quasi-free protons and neutrons is shown in Figure 6.30. Shown are the deposited energy versus time of flight spectra for protons (left column) and neutrons (right column) divided in very forward direction (upper row) and the remaining angular range (lower row). The punch-through property of the protons at very forward angles is more visible than observed in the PSA. It is clearly visible in the upper left figure that almost all protons at forward direction punch-through the detector and always deposit the same amount of energy at the same time of flight value resulting in the circular punch through region. Protons at other angles (bottom left figure) exhibit the typical proton band structure. In contrast to the typical proton band, neutrons are located in a rather uncorrelated wide region. Here the punch-through

protons that were misidentified as neutrons can easily be identified in the neutron spectrum. On top of the uncorrelated neutron area in the upper right figure, a clear accumulation of punch-through protons can be recognized exhibiting the same TOF and deposited energies, as encircled with a solid white line.
This border was then used as the last cut in the analysis by means of an anti cut for neutrons. Events where the neutron fell into the white marked region were rejected. In this way, all misidentified protons were reliably removed from the neutron sample, but with them also true neutrons were rejected within this region. This cut might affect the kinematics, but this is rather unlikely as neutrons do not have a well-defined correlation between energy and time of flight. However, this was checked by having another look at the pulse shape spectrum of the neutrons after the cut was applied. If the cut affects the kinematics, it should be visible in the pulse shape analysis. The result is shown in Figure 6.31. The initial PSA spectra without the TOF cut, i.e. identical to Figure 6.24, are given by the two left-hand side columns. After the cut, the punch-through protons that were identified as neutrons (see the upper middle figure) have disappeared (see the upper right figure). A typical and clean neutron spectrum is visible. Further investigations of the events within the cut region showed that only about 1.5% of all protons were identified as neutrons and only 4.4% of all neutrons were contaminated by protons.

Summary

Table 6.3 summarizes the cuts that were applied to the initial sample of events for the analysis of single π^0 photoproduction from the deuteron. The quasi-free inclusive analysis was not discussed in detail as it comprises the same analysis steps with the exception of the condition on the meson-nucleon coplanarity, which requires the detection of the recoil nucleon.

Analysis cut	Analysis		
	qf. inclusive	exclusive p.	exclusive n.
pulse shape analysis	$\pm 3\sigma$ / nucleon exclusion zone		
$\gamma\gamma$ invariant mass	$\pm 3\sigma$		
π^0-N coplanarity	-	$\pm 1.5\sigma$	
missing mass	$\pm 1.5\sigma$		
ΔE vs. TOF	-	-	exclusion zone

Table 6.3: Overview of the applied cuts for single π^0 photoproduction from the deuteron from the A2 data.

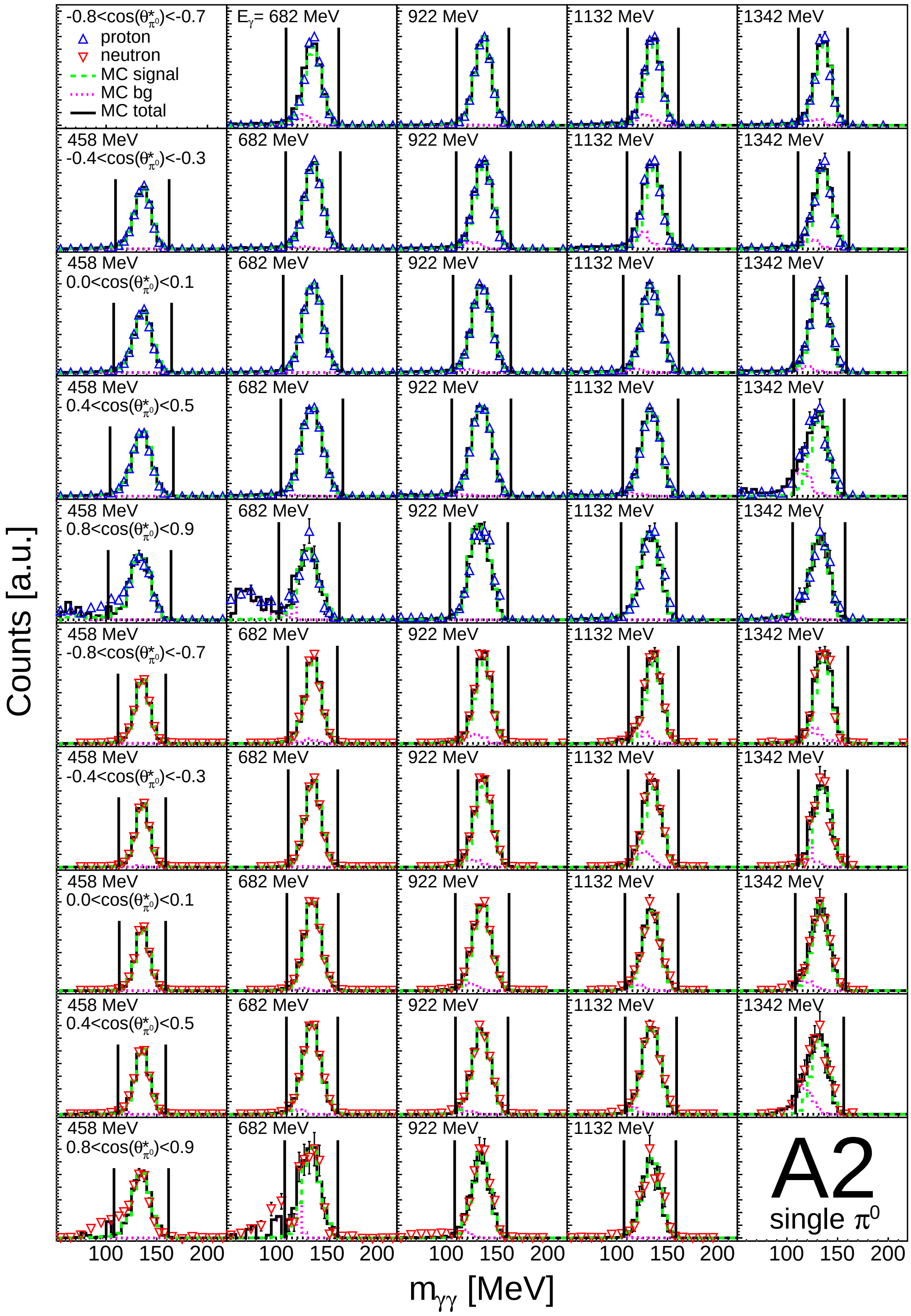

Figure 6.32: Invariant mass spectra for single π^0 photoproduction from quasi-free protons (upper half) and neutrons (lower half) from the A2 data. Shown are five selected energy and angular bins. Only the PSA cut was applied to the data. Notations are given in the figure and the vertical black lines indicate the $\pm 3\sigma$ cut positions.

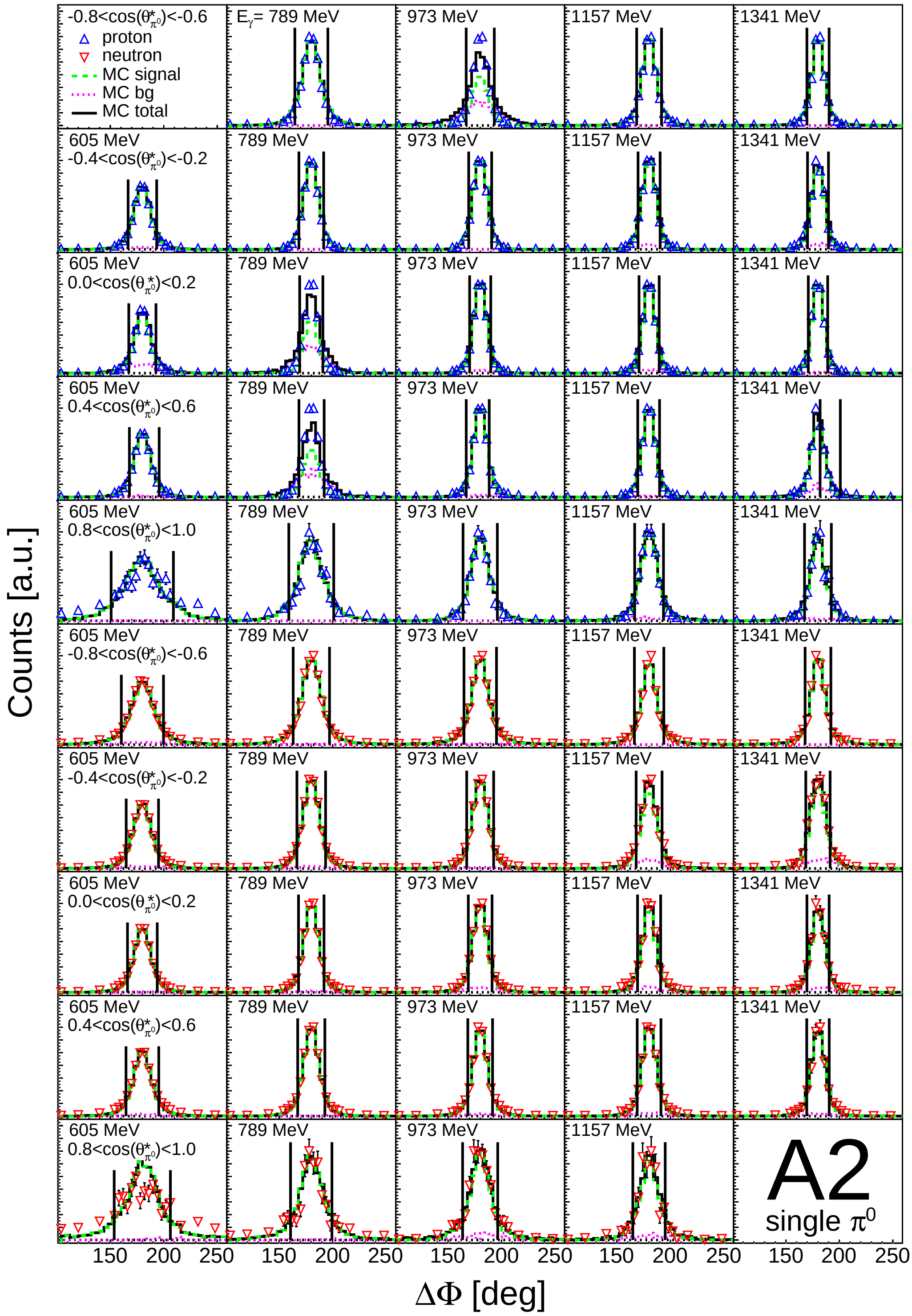

Figure 6.33: Coplanarity spectra for single π^0 photoproduction from quasi-free protons (upper half) and neutrons (lower half) from the A2 data. Shown are five selected energy and angular bins. The PSA and invariant mass cuts were applied to the data. Notations are given in the figure and the vertical black lines indicate the $\pm 1.5\sigma$ cut positions.

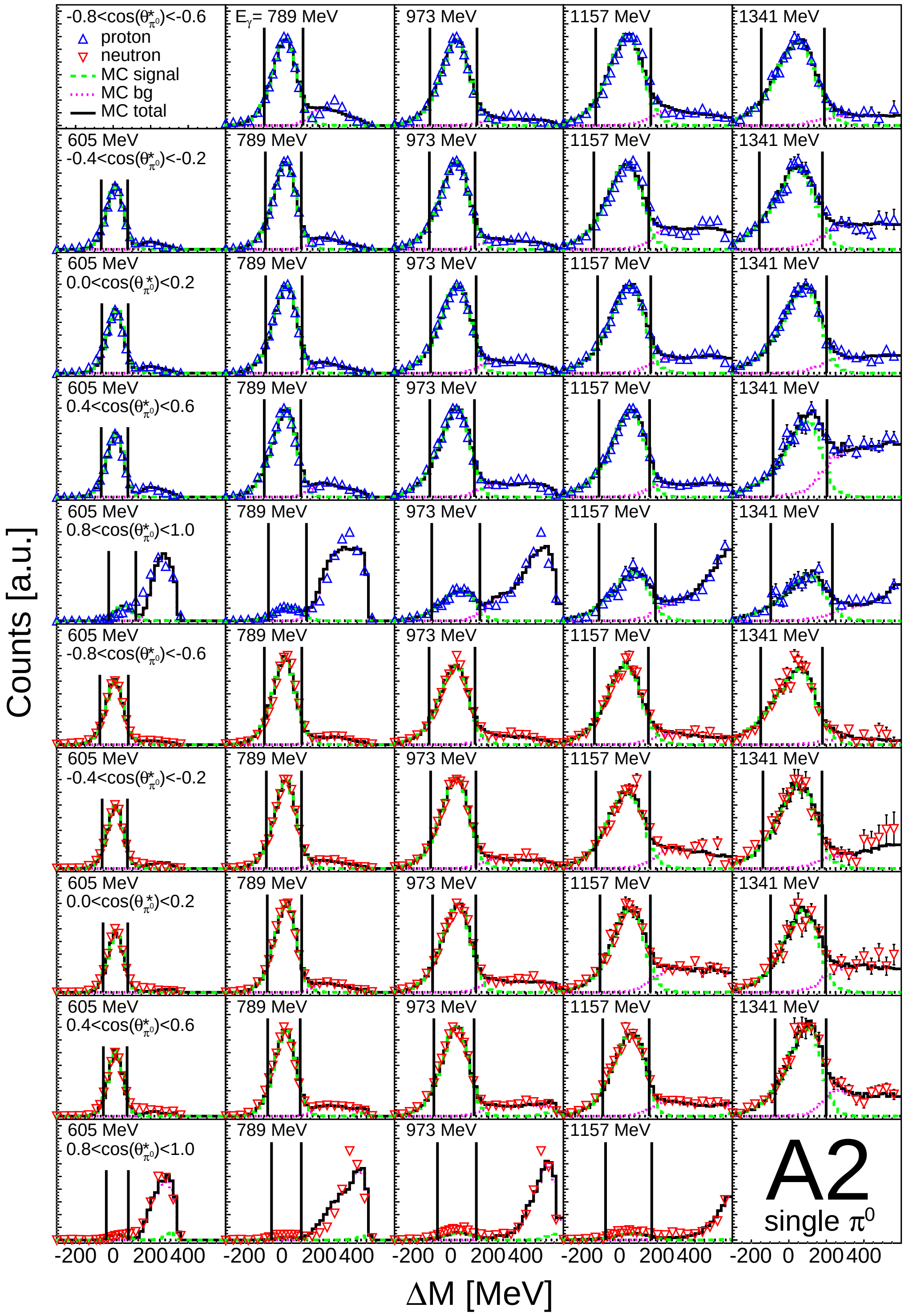

Figure 6.34: Missing mass spectra for single π^0 photoproduction from quasi-free protons (upper half) and neutrons (lower half) from the A2 data. Shown are five selected energy and angular bins. The PSA, invariant mass, and coplanarity cuts were applied to the data . Notations are given in the figure and the vertical black lines indicate the $\pm 1.5\sigma$ cut positions.

6.4.2 Single π^0 Analysis on Polarized Nucleons

For the analysis of single π^0 photoproduction from polarized nucleons inside the deuterated butanol target, the understanding of the reaction on the unpolarized nucleons in the deuterium target is necessary. The goal of the analysis is to select the events that occurred on the nucleons of the polarized deuterons and not on the nucleons of the unpolarized carbon and oxygen nuclei. Therefore, the analysis is based on the assumption that the identification of the reaction is identical to that of the deuterium target. The analysis of the reaction on quasi-free nucleons in deuterium was carried out in detail, as discussed in Section 6.4.1 and is well understood and reliable, as will be presented in Section 6.5. Therefore, the event selection and reconstruction was carried out in the same way as for the deuterium data. The cut positions were not redone or adapted, but directly taken from the deuterium analysis. This provides a sample of the same quality from which events from competing reactions were successfully removed. However, although it will contain mainly real single π^0 events from quasi-free protons and neutrons, they will not only originate from the polarized nucleons, but also from the unpolarized carbon and oxygen nuclei. Such contributions have to be estimated and subsequently subtracted in order to obtain a pure sample of reactions from polarized nucleons only. For this reason, the carbon data was analyzed with the same analysis and then properly subtracted (see Section 6.13.4).

Even though the experiment with the deuterated butanol and carbon targets were planned and carried out to optimally fit to those of liquid deuterium, a few differences remain. The most obvious difference is the presence of the magnetic field of the holding coil in the deuterated butanol experiment, which was not present in the liquid deuterium and carbon beamtimes. As magnetic fields influence charged particles, this obviously as well affects the data. However, simulations with and without magnetic field showed that the influence is negligible. To be on the safe side, the simulations used for the detection efficiencies were carried out under the presence of the magnetic field (see Section 3.2.2).
Another difference is the unavoidable discrepancy between the detector thresholds and trigger settings used in the different experiments. Even if they were intended to be identical, certain differences are present due to the electronic fluctuations and hardware or software upgrades. Nevertheless, the settings had to be changed, as the usage of a magnetic field fans out the electromagnetic background in the forward direction of the beam. In order to suppress the high rates in the TAPS detector, the thresholds of the most inner rings had to be increased and the trigger settings were adjusted to the maximum production rates (see Section 2.3.3). Therefore, in order to have comparable analyses, the deuterium, carbon and deuterated butanol data were analyzed with the strongest common trigger and threshold settings of the different beamtimes, which resulted in a good agreement between them.

A further variation is related to the different target materials used for the experiments. Whereas the lengths of the target cells of the liquid deuterium targets range

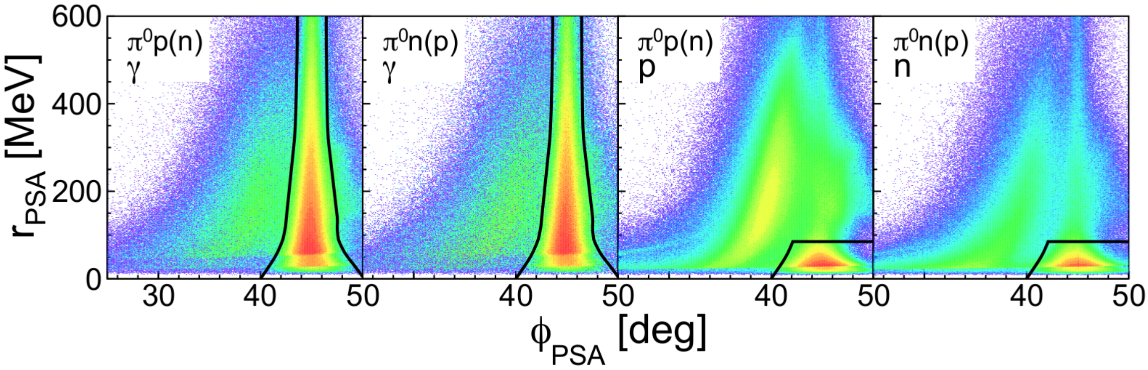

Figure 6.35: PSA spectra for single π^0 photoproduction from the deuterated butanol from the A2 data. No cut was applied to the data. Columns: analysis channels (see labels). Solid black lines: cut positions.

from 3 to 5 cm (see Section 2.8.1), the deuterated butanol target has a length of 2 cm. However, the length of the target cell directly affects the energy and angular resolution of the experiment, since the particles will undergo more interactions with the target material, and the interaction vertex (and therefore all angles) are less well defined, in the case of a longer cell. The different energy and angular resolutions on one side might change the detection efficiency and on the other side might also impede the comparison of spectra from different beamtimes. Even though a slight difference of the resolutions was observed, the effect was kept at a minimum by using the liquid deuterium beamtime from May 2009, which used the shortest target length of 3 cm. Therefore, the effect is negligible.

The last noticeable difference lies between the deuterated butanol and the carbon beamtime. As previously mentioned, the experiments were in principle identical, with the exception that the deuterated butanol material was replaced with a carbon foam. Other experimental settings from the beam quality to the applied thresholds were unaltered, as the experiments were carried out during the same beamtime and hence under the same conditions. However, the deuterated butanol target was cooled down with a mixture of ^{3}He/^{4}He, which was not feasible with the carbon foam target. The carbon beamtime is only directly applicable for the estimation and subtraction of the contributions from the reactions on unpolarized nucleons inside the carbon and oxygen nuclei and may not reproduce the contributions from reactions on the helium nuclei. This is a possible explanation of the small difference that was observed in the subtraction process, as will be discussed in Section 6.13.4, but does not have a systematic effect on the results.

Only the quasi-free exclusive reaction on the proton and neutron were analyzed using the deuterated butanol and carbon data. The quasi-free inclusive analysis primarily serves as an important check of the nucleon detection and identification, which was successfully investigated using the deuterium data and was omitted in this analysis. As previously mentioned, the event selection and reconstruction of the particles was done in the same way as for the analysis of the deuterium data, and the same analysis cuts were performed.

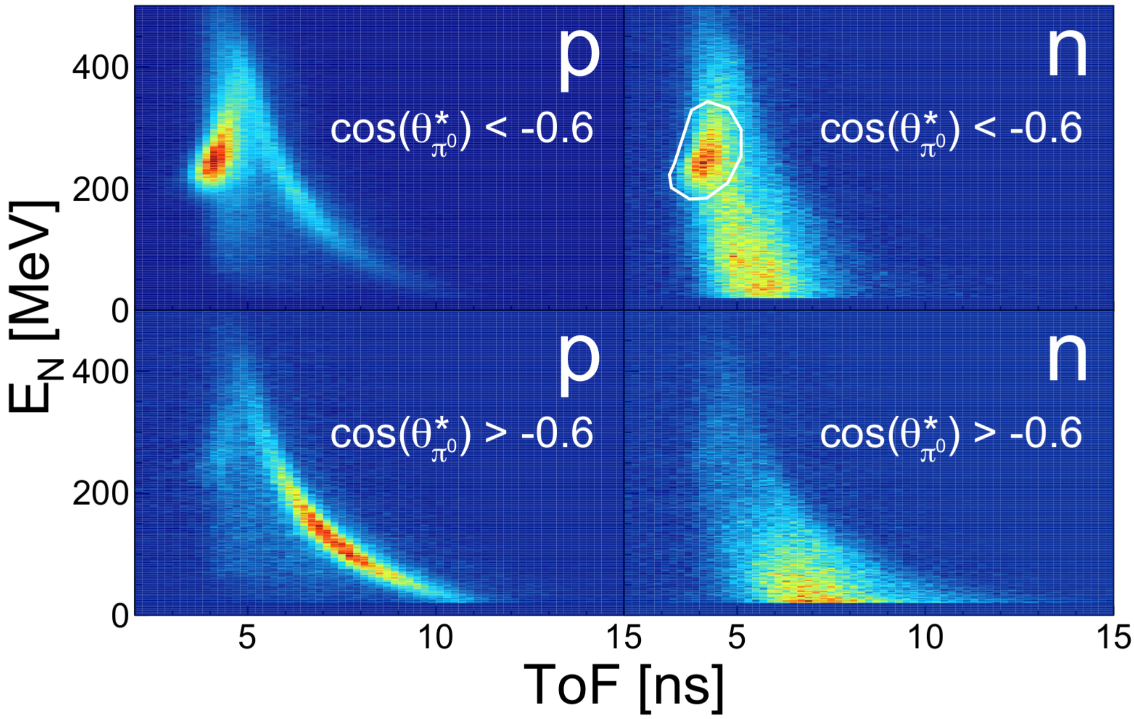

Figure 6.36: Identification of the punch-through protons by means of deposited energy versus time of flight (TOF) spectra from π^0 photoproduction from the deuterated butanol from the A2 data. All cuts were applied to the data. Left column: protons. Right column: neutrons. Upper row: angular region of high kinetic energy recoil protons ($\cos(\theta^*_{\pi^0}) < -0.6$). Lower row: remaining angular region ($\cos(\theta^*_{\pi^0}) > -0.6$). White region: cut on neutron TOF.

As the different spectra of the analysis of the deuterated butanol data will be discussed in detail in Section 6.13.4, in the following section only the cut positions as determined from the deuterium data will be shown in comparison with the corresponding spectra of the deuterated butanol data. The PSA cuts are shown in Figure 6.35, the invariant mass cuts in Figure 6.37, the coplanarity cuts in Figure 6.38, the missing mass cuts in Figure 6.39, and the cut on the deposited energy versus the time of flight of the neutron in Figure 6.36. Thereby it should be noted that only the spectra from the deuterium data are shown in chronological order, i.e. the events that contribute to an individual spectrum only fulfilled the previous analysis cuts. For a better comparison, the spectra from the deuterated butanol data are shown at their final stage, i.e. when all cuts were applied.

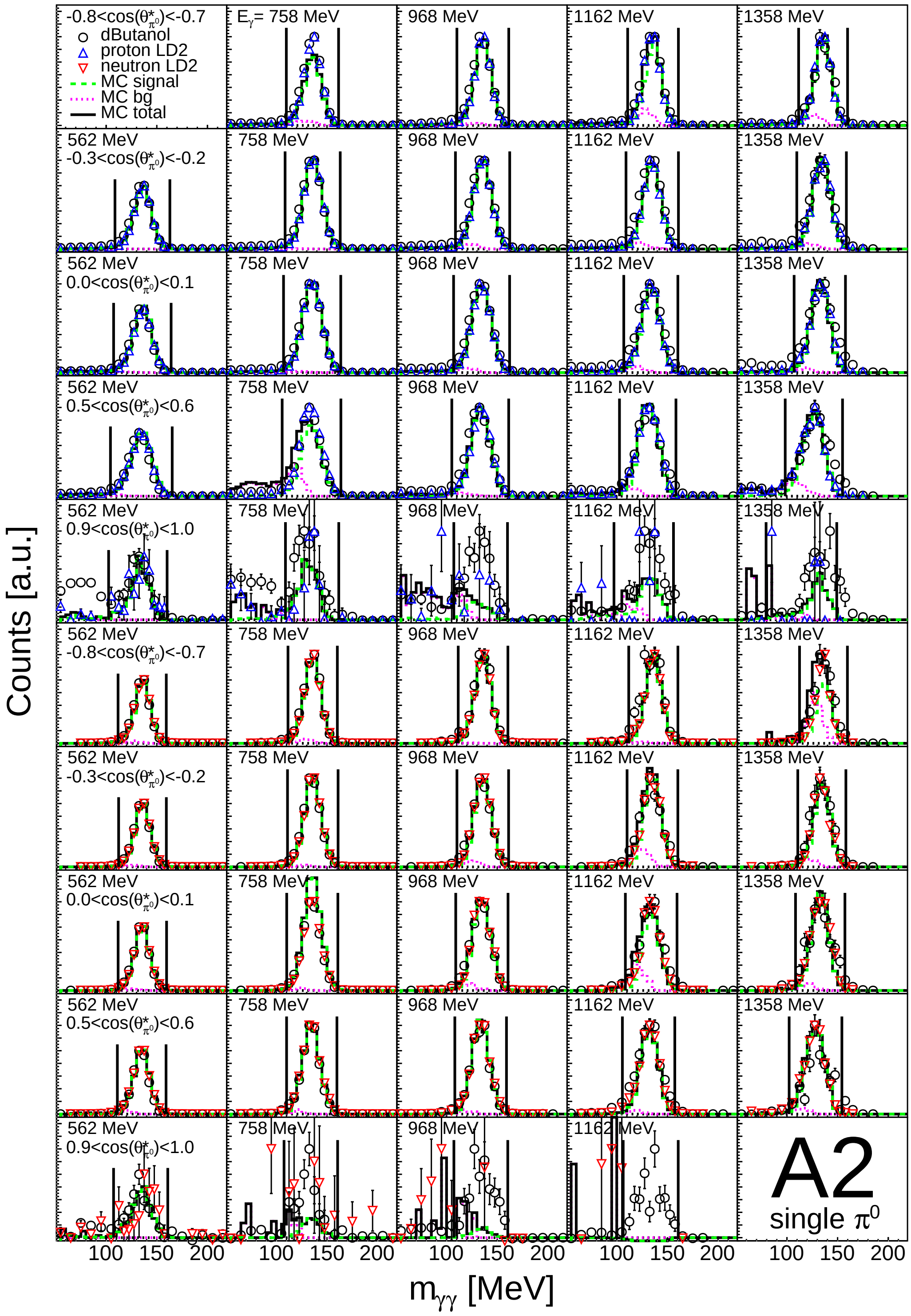

Figure 6.37: Invariant mass spectra for single π^0 photoproduction from deuterated butanol (black circles) compared to those from liquid deuterium (proton: blue triangles, upper half. Neutron: red triangles, lower half). Results from the A2 data. Shown are five selected energy and angular bins. Only the PSA cut was applied to the deuterium data. All cuts were applied to the deuterated butanol data. Notations are given in the figure and the vertical black lines indicate the $\pm 3\sigma$ cut positions.

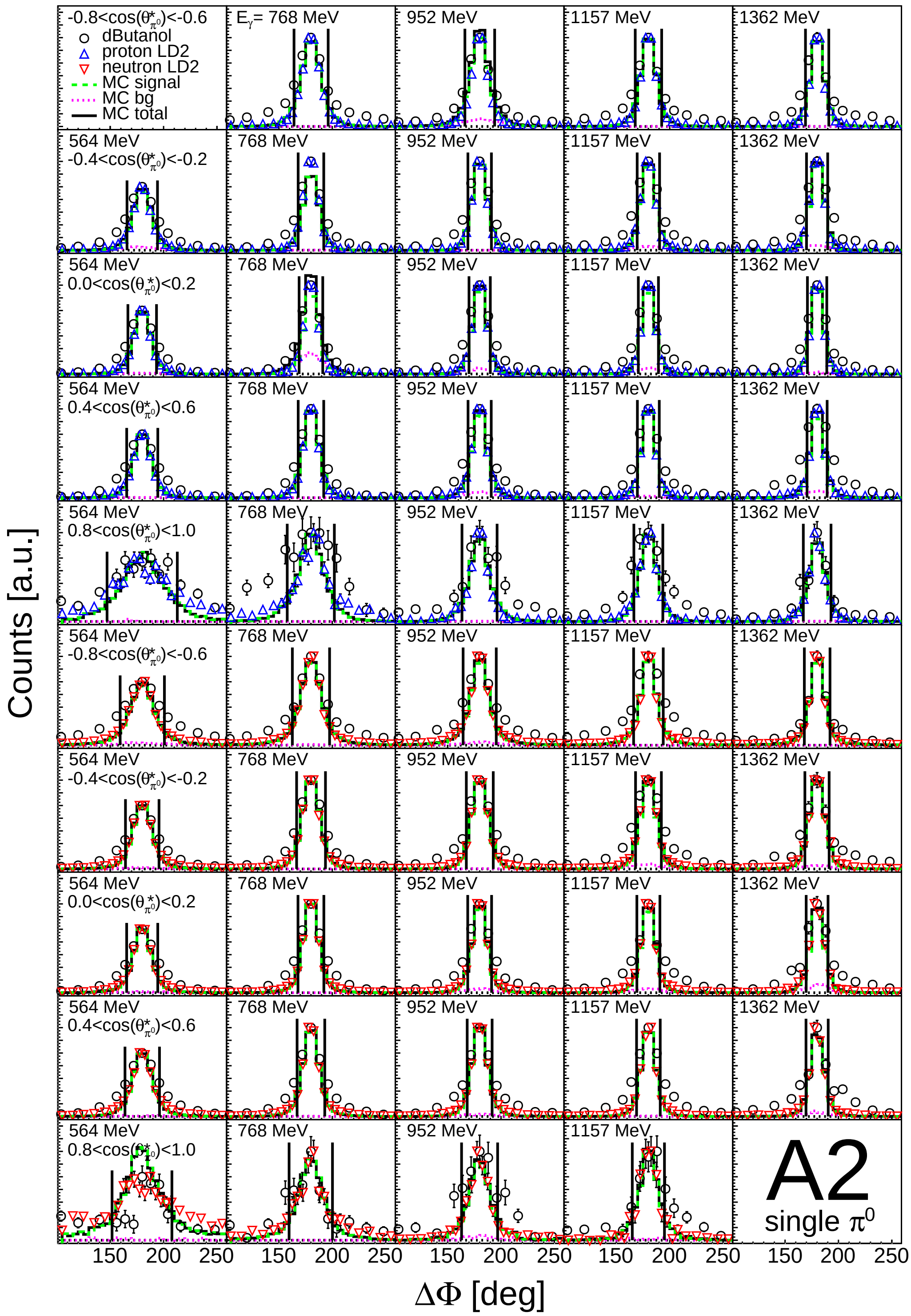

Figure 6.38: Coplanarity spectra for single π^0 photoproduction from deuterated butanol (black circles) compared to those from liquid deuterium (proton: blue triangles, upper half. Neutron: red triangles, lower half). Results from the A2 data. Shown are five selected energy and angular bins. The PSA and invariant mass cuts were applied to the deuterium data. All cuts were applied to the deuterated butanol data. Notations are given in the figure and the vertical black lines indicate the $\pm 1.5\sigma$ cut positions.

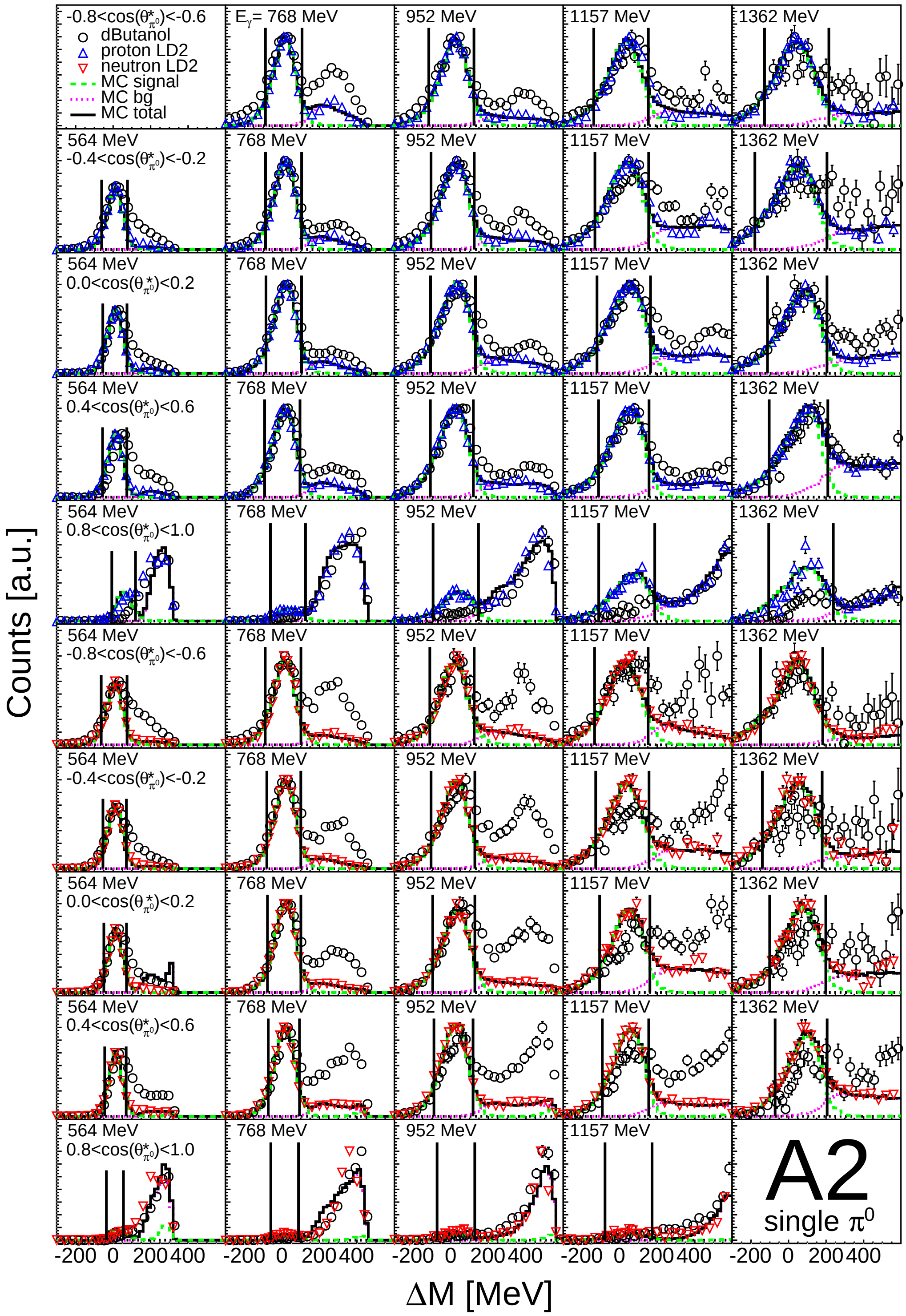

Figure 6.39: Missing mass spectra for single π^0 photoproduction from deuterated butanol (black circles) compared to those from liquid deuterium (proton: blue triangles, upper half. Neutron: red triangles, lower half). Results from the A2 data. Shown are five selected energy and angular bins. The PSA, invariant mass, and coplanarity cuts were applied to the deuterium data. All cuts were applied to the deuterated butanol data. Notations are given in the figure and the vertical black lines indicate the $\pm 1.5\sigma$ cut positions.

6.4.3 Double π^0 Analysis on the Free Proton

Double π^0 photoproduction was in a first step analyzed on the free proton, i.e. on liquid hydrogen data. This on one side serves as analysis cross check, since the cross section on the free proton is already well known in the energy range of interest. On the other side, it was necessary to have the information of the reaction of the free proton for the estimation of the free neutron cross section, which will be discussed in Section 6.12.

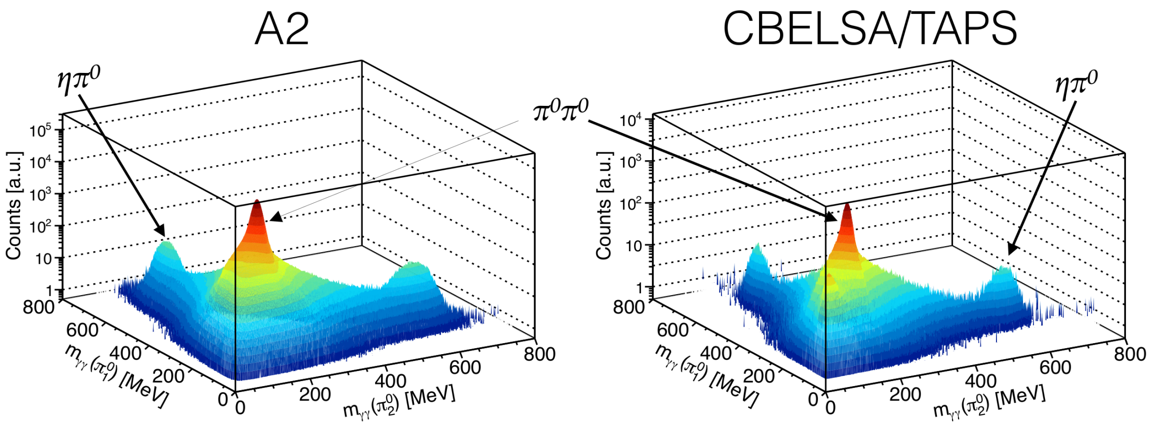

Figure 6.40: Spectra of the invariant mass π^0_1 versus invariant mass π^0_2 of $\pi^0\pi^0$ photoproduction from free protons. No cut was applied to the data. Left-hand side: A2 data. Right-hand side: CBELSA/TAPS data.

Compared to single π^0 photoproduction, double $\pi^0\pi^0$ has the advantage of a higher required multiplicity, which is four particles in the inclusive case or five particles in the exclusive case. This immediately reduces the number of possible competing reactions. In contrast, finding the two photon pairs out of the four neutral hits that originate from the pion decay is rather challenging. As the four neutral clusters have to be grouped to the same type of particle that in addition has a very small mass, the chance that the smallest χ^2 value was obtained with a wrong combination is not negligible. The combinatorial background is what makes this analysis different from single π^0 photoproduction and this background should be understood in order to produce reliable results. In order to ensure that the combinatorial background is under control, a side-band subtraction in the invariant mass analysis was performed for both data and simulation, as some of the combinatorial background comes from true $\pi^0\pi^0$ events and hence are also present in the simulation. However, within statistical errors the results were identical to those from an analysis without the side-band subtraction indicating that the different analysis cuts removed those events from the sample successfully.

In order to avoid correlations in the statistical uncertainty, the two pions were randomized for each event, i.e. it was randomly chosen which is the first pion and which is the second pion. The invariant mass spectrum of one photon pair versus the other (as resulting from the χ^2 test and after the cuts on the detector time coincidence and the random tagger background subtraction were applied) are presented in Fig-

ure 6.40. The figure shows the prominent peak from $\pi^0\pi^0$ photoproduction, which sits on top of a small background of either combinatorial or competing origin from primarily $\eta\pi^0$ photoproduction, as indicated by the two small shoulders.
$\pi^0\pi^0$ photoproduction from the free proton was analyzed inclusively, i.e. without the condition on the coincident detection of the recoil proton, as well as exclusively, where the detection of the recoil proton is required. This does not only allow for an estimation of the systematic uncertainties of the recoil proton detection, but also for a better comparison with already published results, as they mostly stem from analyses which did not require a coincident detection of the recoil proton. Additionally, the comparison of the inclusive and exclusive measurements is necessary for the determination of the proton detection efficiency correction, which is applied to the quasi-free analysis of liquid deuterium data (see Section 6.8.3). The neutron detection efficiency correction thereby was determined as well and using the same liquid hydrogen data, but using the reaction $\gamma p \to \pi^0\pi^+ n$, whose description of the analysis will be omitted. Further details of this analysis can be found for example in Ref. [100].

Analysis of A2 Data

As for the analysis of single π^0 photoproduction, the particle candidates in the analysis of $2\pi^0$ photoproduction at first have to fulfill the PSA requirements. Whereas the PSA spectrum of protons in single π^0 photoproduction was complicated by the overlap of the proton and photon bands due to the high kinetic energy of the recoil protons, for double π^0 photoproduction this was not observed. Furthermore, a loss of protons due to punch-through would immediately show up as a discrepancy between the inclusive and exclusive results and since it does not it is well understood. Nevertheless, only a conservative cut was applied due to the previously mentioned absence of PSA information in the simulation. The cuts on the pulse shape analysis information of the photons and protons are shown in Figure 6.41. Only small contamination of nucleons in the photon spectra are visible with a weak trend to higher contamination in the inclusive spectrum. This is due to the fact that the additional requirement of the recoil proton excludes certain contributions. In the proton PSA spectrum, few contamination from photons and mostly electrons are visible. Whereas the electrons (accumulation of events at PSA angles of 45° and at low PSA radii) are well separated from the protons, the photons are not. Thus, the requirement of photons was chosen to be a $\pm 3\sigma$ zone around PSA angles of $\phi_{PSA} = 45°$ and for protons two moderate exclusion zones were defined.

In the following sections, an initial invariant mass cut on the two individual $\gamma\gamma$ invariant mass spectra from both pions was determined by fitting the contributions from the simulated signal and background reactions (see Table 6.2) to the yield of the data. Figure 6.42 shows the resulting fits and cut positions for one of the two pions for selected energy and angular bins. As the pions were randomized and the spectra are identical within statistical fluctuations, the second spectra were omitted. It is

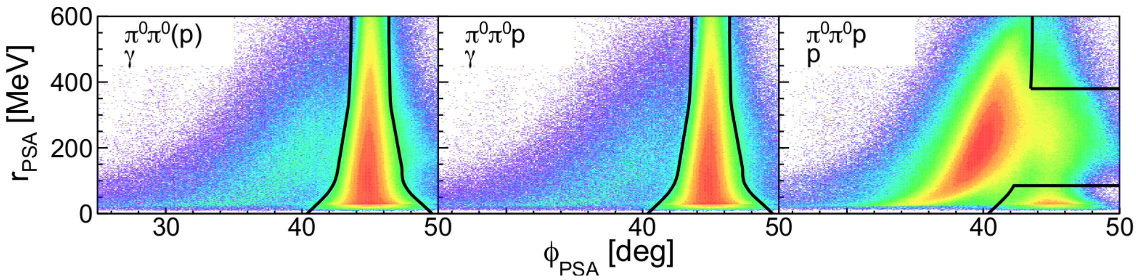

Figure 6.41: PSA spectra for double π^0 photoproduction from the free proton from the A2 data. No cut was applied to the data. Columns: analysis channels (see labels). Solid black lines: cut positions.

clearly visible that even though no further cut than the previous ones were applied to the invariant mass, the sum of the simulated lineshapes (black histogram) is in good agreement with the line shape of the data. The fit result of the background (mainly from $\eta(\rightarrow 2\gamma)\pi^0$) describes the background shape in the data with high precision. Disagreement only occurs at very forward angles of the pion in the pion-nucleon center of mass at low energies. The interpretation of this discrepancy is not straightforward, but is likely due to split offs of a reaction of lower multiplicity, such as radiative pion photoproduction, which is already present at such low energies. As it is not visible in the coplanarity and missing mass spectra, it either does not originate from a neglected background contribution or it was already removed by the invariant mass cut. Nevertheless, it only showed up at this stage and is negligible. As there is a slight energy and angular dependence of the width of the invariant mass peak, the cut positions were determined by energy and angular dependent cuts. The cut condition on the invariant mass of each pion was chosen to be $\pm 3\sigma$.

All events that passed the invariant mass cut of the two pions were used to investigate the meson nucleon coplanarity. As previously discussed in Section 6.4.1, the coplanarity requirement of the reaction can be verified by comparing the difference in azimuthal angles of the meson and nucleon. However, as this is only valid for a two-body decay and in this reaction three outgoing particles exist, the two pions were combined to one quasi-meson and its azimuthal angle was compared to that of the recoil proton. This strongly depends on the assumption that all three particles originate from roughly the same vertex, which is fulfilled within the experimental resolution. The resulting distributions of the combined meson nucleon system are shown in Figure 6.43. Although the binning was chosen somewhat too coarse the good agreement between data and simulations is clearly visible. The disadvantageous binning only has a visual consequence, as it was rebinned for the visualization of the results and hence after the determination of the cut positions. Due to the rather strong dependence on energy and center of mass polar angle, the cuts were determined individually for all energy and angular bins. In order to reduce the background contributions, a rather strong cut of $\pm 1.5\sigma$ was chosen.

The last condition on the kinematics of the reaction was the missing mass analysis.

The result is shown for the same selection of energy and angular bins in Figure 6.44. Again, the agreement between simulation and data indicate the correct consideration of the background reactions. The latter thereby are only weakly present in the spectra but exhibit a rather flat and broad structure that range as far as the peak of the signal. Therefore an additional rather strict cut of $\pm 1.5\sigma$ was determined in order to reject a maximum of the background while keeping the signal rate reasonably high.

Summary

The different cuts of the analysis are summarized in Table 6.4. The inclusive analysis was not discussed as it is based on the same analysis steps, but without the condition of the meson-nucleon coplanarity.

Analysis cut	Analysis	
	inclusive	exclusive
pulse shape analysis	$\pm 3\sigma$ / nucleon exclusion zones	
$\gamma\gamma$ invariant mass	$\pm 3\sigma$	
$\pi^0\pi^0$-p coplanarity	-	$\pm 1.5\sigma$
missing mass	$\pm 1.5\sigma$	

Table 6.4: Overview of the applied cuts for double π^0 photoproduction from the free proton from the A2 data.

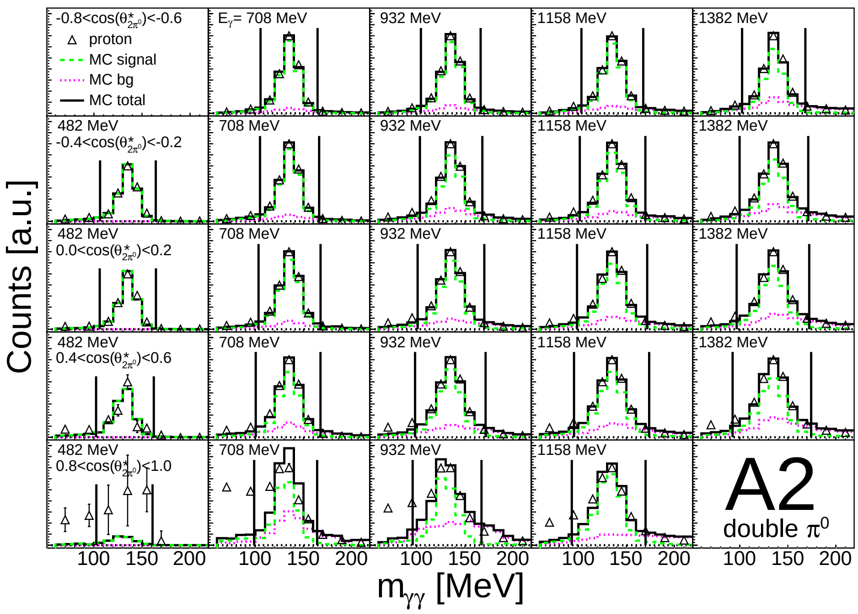

Figure 6.42: Invariant mass spectra for double π^0 photoproduction from free protons from the A2 data. Shown are five selected energy and angular bins. Only the PSA cut was applied to the data. Notations are given in the figure and the vertical black lines indicate the $\pm 3\sigma$ cut positions.

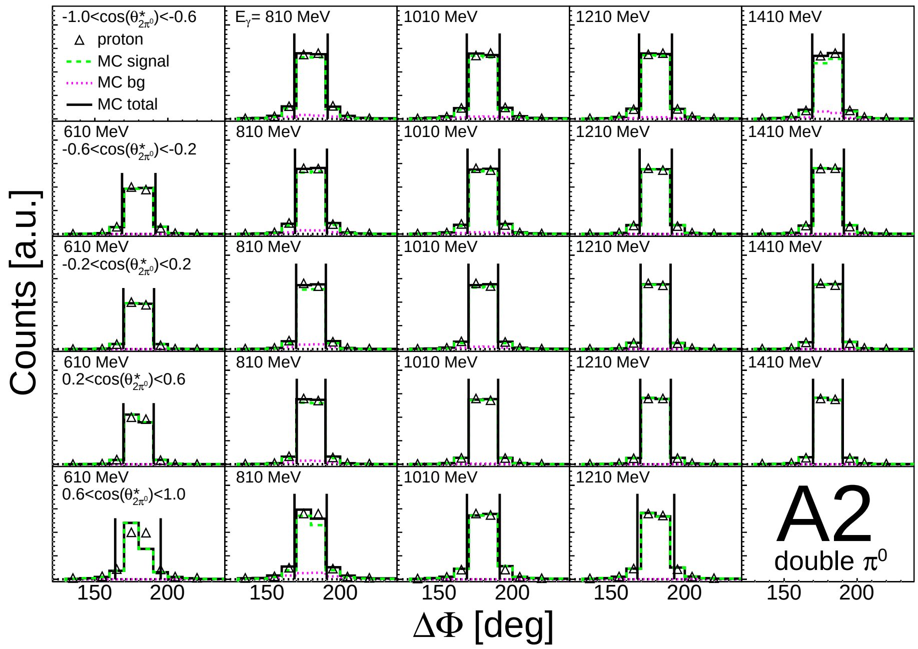

Figure 6.43: Coplanarity spectra for double π^0 photoproduction from free protons from the A2 data. Shown are five selected energy and angular bins. The PSA and invariant mass cuts were applied to the data. Notations are given in the figure and the vertical black lines indicate the $\pm1.5\sigma$ cut positions.

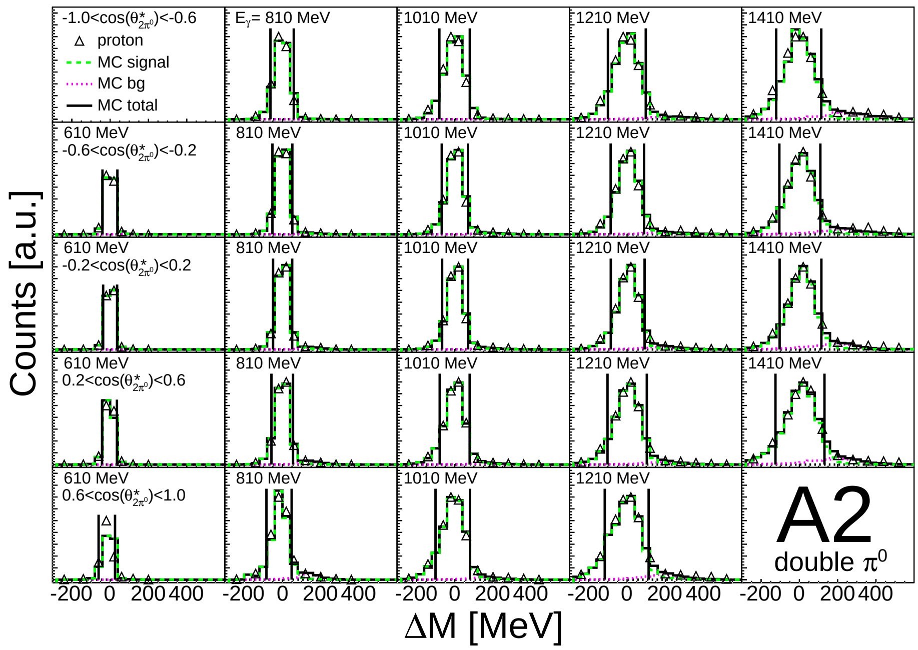

Figure 6.44: Missing mass spectra for double π^0 photoproduction from free protons from the A2 data. Shown are five selected energy and angular bins. The PSA, invariant mass, and coplanarity cuts were applied to the data. Notations are given in the figure and the vertical black lines indicate the $\pm1.5\sigma$ cut positions.

Analysis of CBELSA/TAPS Data

The analysis of double π^0 photoproduction from free protons of the CBELSA/TAPS liquid hydrogen data is equivalent to that discussed in Section 6.4.3 from the A2 data. The same reactions were simulated (see Table 6.2) and the same analysis cuts were applied. This directly shows the advantage of the combined analysis of A2 and CBELSA/TAPS data. The presort analysis using `ExPlORA` was carried out equivalently using the same techniques and methods as for the presort of the A2 data with `AcquRoot`, but adapted to the experimental settings and detectors of the CBELSA/TAPS experiment. In both presorts of the data, the particle reconstruction and subsequently the χ^2 test and the detector time coincident requirements as well, were carried out. For programming reasons, for the A2 data the PSA cut was applied in the presort, at CBELSA/TAPS it was done as first step of the post analysis with `OSCAR`. Therefore, it has no effect on the physics and as well not on the analysis. As soon as both datasets are presorted, they contain the same type of event candidates with, apart from a few additional experimental characteristics, the same information and can directly be analyzed in the same way. This is a very informative method and immediately gives an important estimate of the systematic uncertainties of the analysis procedure.

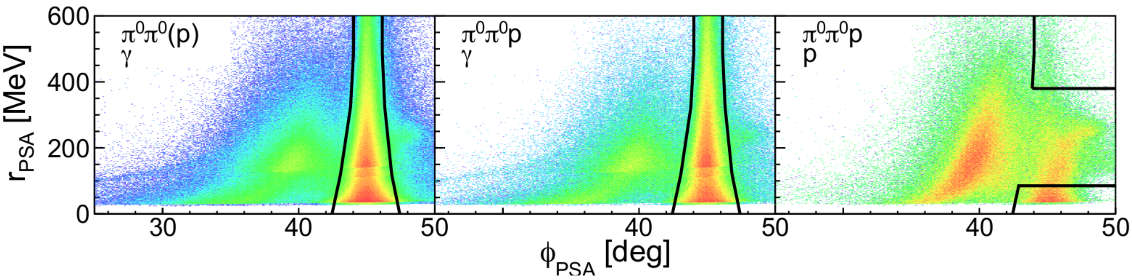

Figure 6.45: PSA spectra for double π^0 photoproduction from the free proton from the CBELSA/TAPS data. No cut was applied to the data. Columns: analysis channels (see labels). Solid black lines: cut positions.

Figure 6.45 illustrates the PSA spectra of the photons (left and middle columns) and protons (right column) from the inclusive analysis (only photons, i.e. left figure) and the exclusive analysis (photons and protons, middle and right figure). The quality of the individual PSA spectra is almost identical to that from the A2 analysis (Figure 6.41). The photon spectra are minimally contaminated with nucleons. In contrast to A2, the proton PSA spectrum at the initial stage of this analysis shows more contamination from photons. This is most likely due to the higher beam energy and that the incident photons might deposit enough energy in the TAPS veto detectors in order to be recognized as charged particle. It will be shown later (in Section 6.5.5), that the further analysis steps successfully remove this background contribution.

The second condition, the initial cut on the invariant mass of the two photons of each pion, is shown in Figure 6.46. Besides the slightly higher energy resolution at

CBELSA/TAPS (see Table 5.1), the spectra are of equivalent quality to those of the A2 analysis (Figure 6.42) and the line shape of the data is well reproduced by the sum of the simulated contributions. The discrepancy between data and simulation at very forward angle bins and at lower photon energies is visible as well, although the lowest shown energy bin is already of a higher energy than in the A2 spectra. As mentioned in the A2 analysis, with increasing energy, this difference vanishes, which confirms the assumption of possible contributions from split offs from radiative π^0 photoproduction. The cuts were as well determined dependent on the incident photon beam energy and the polar angle of the combined pion in the pion-nucleon center of mass system. Events with an invariant mass outside a $\pm 3\sigma$ region were rejected. The coplanarity spectra, as well as the $\pm 1.5\sigma$ cut positions, are shown in Figure 6.47 and the missing mass analysis and the determined $\pm 1.5\sigma$ cuts are shown in Figure 6.48. The agreement of all spectra from the data and the sum of the simulated contributions is overall very good and shows a reliable determination of the cut positions.

Summary

Table 6.5 summarizes the cuts that were applied to the initial sample of events for the analysis of double π^0 photoproduction from free protons from the CBELSA/TAPS data. As for the A2 analysis the inclusive analysis was not discussed. The size of the analysis cuts was determined independently from the A2 analysis but it was found that the same size for all spectra was reasonable for the rejection of the background as well as for not losing too much signal contributions.

Analysis cut	Analysis	
	inclusive	exclusive
pulse shape analysis	$\pm 3\sigma$ / nucleon exclusion zones	
$\gamma\gamma$ invariant mass	$\pm 3\sigma$	
$\pi^0\pi^0$-p coplanarity	-	$\pm 1.5\sigma$
missing mass	$\pm 1.5\sigma$	

Table 6.5: Overview of the applied cuts for double π^0 photoproduction from the free proton from the CBELSA/TAPS data.

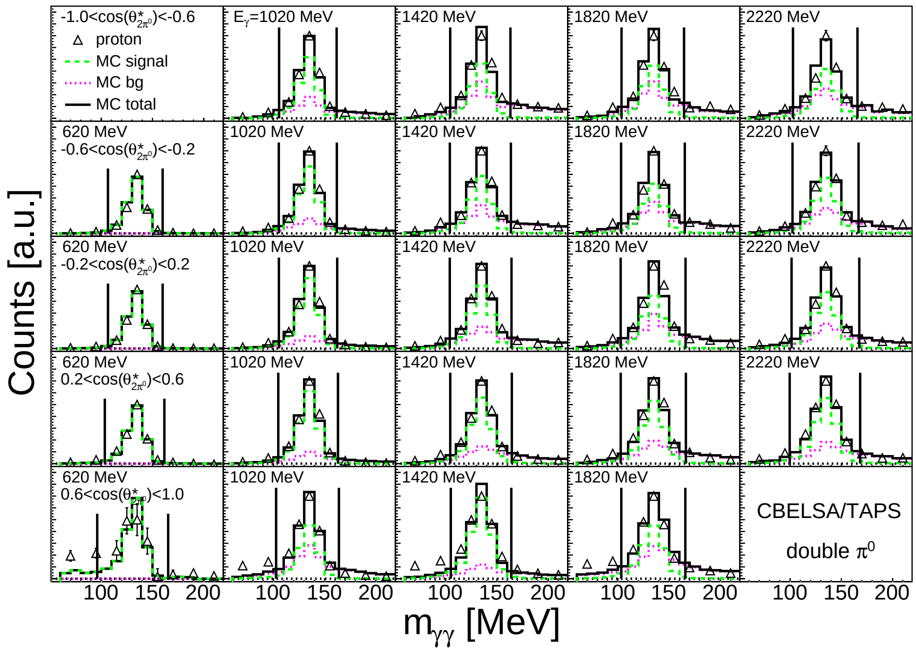

Figure 6.46: Invariant mass spectra for double π^0 photoproduction from free protons from the CBELSA/TAPS data. Shown are five selected energy and angular bins. Only the PSA cut was applied to the data. Notations are given in the figure and the vertical black lines indicate the $\pm 3\sigma$ cut positions.

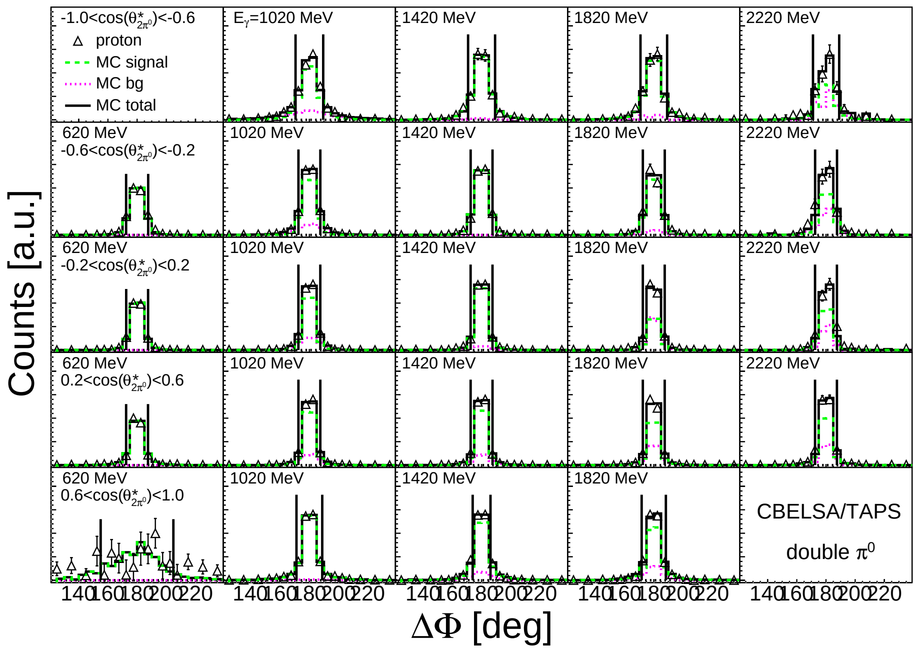

Figure 6.47: Coplanarity spectra for double π^0 photoproduction from free protons from the CBELSA/TAPS data. Shown are five selected energy and angular bins. The PSA and invariant mass cuts were applied to the data. Notations are given in the figure and the vertical black lines indicate the $\pm 1.5\sigma$ cut positions.

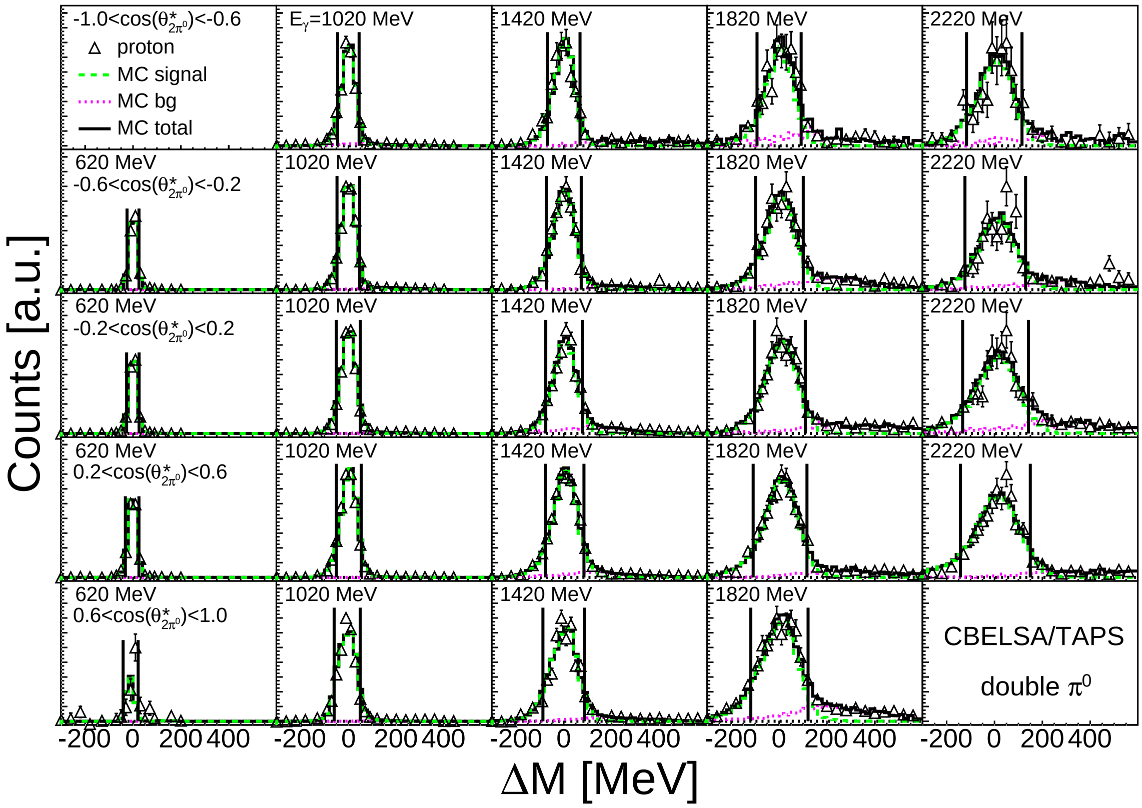

Figure 6.48: Missing mass spectra for double π^0 photoproduction from free protons from the CBELSA/TAPS data. Shown are five selected energy and angular bins. The PSA, invariant mass and coplanarity cuts were applied to the data. Notations are given in the figure and the vertical black lines indicate the $\pm 1.5\sigma$ cut positions.

6.4.4 Double π^0 Analysis on quasi-free Nucleons

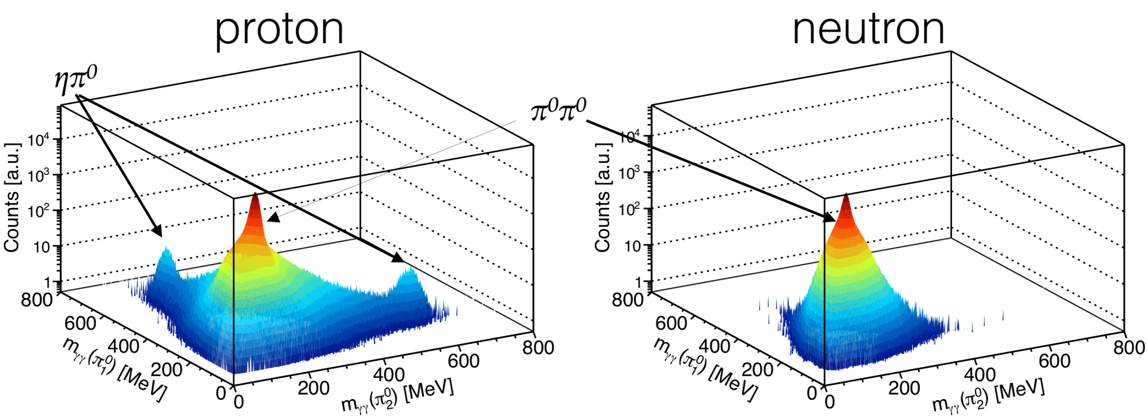

(a) Results from the A2 data

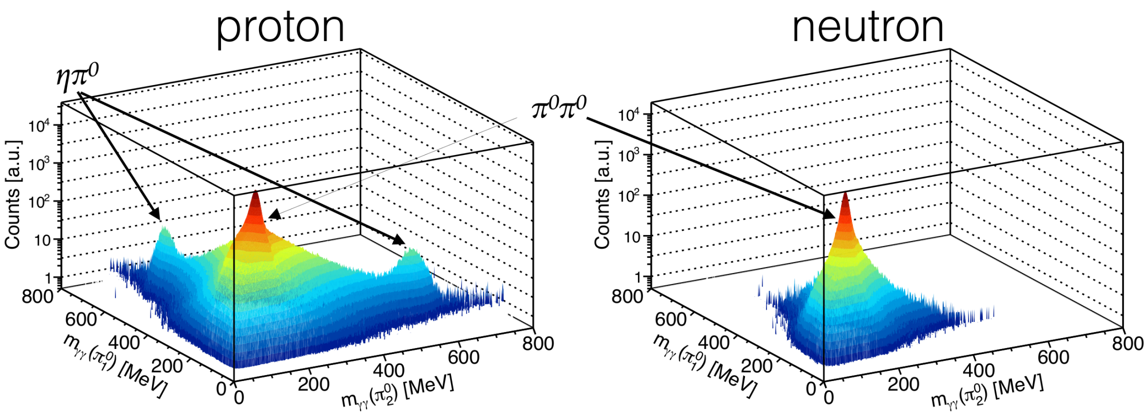

(b) Results from the CBELSA/TAPS data

Figure 6.49: Spectrum of the invariant mass π_1^0 versus invariant mass π_2^0 of $\pi^0\pi^0$ photoproduction from quasi-free protons and neutrons. No cut was applied to the data. (a) A2 data. (b) CBELSA/TAPS data. Left-hand side: proton. Right-hand side: neutron.

The analysis of double π^0 photoproduction from quasi-free protons and neutrons follows the exact structure of the analysis from the free proton. The main difference is given in the χ^2 test, which for the case of the exclusive production from the neutron includes an additional fifth neutral cluster. There are 15 different possibilities to form two pions from four photons out of five neutral clusters compared to three possibilities from four neutral clusters, which makes it more difficult to find the correct combination. However, the additional neutral cluster is an additional degree of freedom, i.e. an extra possibility for the search after the lowest χ^2 value. As already encountered in the χ^2 distribution and its confidence level (Figures 6.4 - 6.7), the identification of the reaction on the neutron yields slightly smaller χ^2 values and flatter confidence level distributions. It seems that, depending on the energy and especially for the cases where the event comes from $\eta\pi^0$, the wrong combination that includes the neutron instead of a photon yields smaller χ^2 values in a χ^2 test for

two pions. The consequence can be seen in the invariant mass spectrum as shown in Figure 6.49. Whereas the invariant mass spectrum of the two photon pairs from the proton exhibits the typical $\eta\pi^0$ shoulders, they are almost completely missing in that from the neutron, but instead, these events broaden the $\pi^0\pi^0$ peak. Nevertheless these events were removed by the analysis cuts since they were easily identified and they exhibit false kinematics.
The invariant mass spectra from the A2 data are very similar to those from the CBELSA/TAPS data. The width of the neutron $\pi^0\pi^0$ peak is somewhat smaller at CBELSA/TAPS, which is likely due to the higher beam energy. At higher beam energies, the recoil neutron increasingly obtains more kinetic energy and does not end up in the best combination. The width of the peak in the proton spectra are of similar width, but at CBELSA/TAPS it sits on a larger background. This results from the higher beam energy, since at higher photon energies more background reactions are present, which contribute to the spectrum.

Analysis of A2 Data

As for the other analyses, the first condition is made on the PSA of the photons and nucleons. The corresponding spectra and the applied cuts are shown in Figure 6.50. Shown are the PSA spectra for photons and nucleons of the quasi-free inclusive and the two exclusive reactions. The $\pm 3\sigma$ condition for the photons and the small exclusion zone for the nucleons are indicated by the solid black lines. Small contamination of photons with nucleons are visible as well as clear photon traces in the nucleon spectra. As already encountered in the analysis on the free proton, the kinetic energy of the recoil nucleons is not sufficient for punch-through. Therefore, the nucleon and photon traces do not overlap and are well separable.

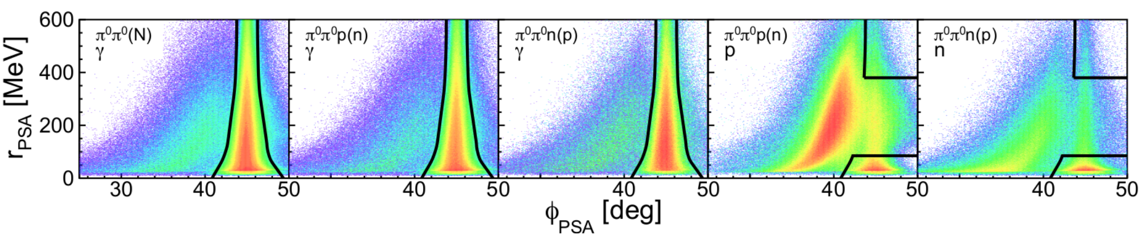

Figure 6.50: PSA spectra for double π^0 photoproduction from the deuteron from the A2 data. No cut was applied to the data. Columns: analysis channels (see labels). Solid black lines: cut positions.

The invariant mass spectra for the reaction on the proton and the neutron are shown in Figure 6.51. They were fit with the simulated background contributions (see Table 6.2) and the $\pm 3\sigma$ cut positions were determined. The simulation is in good agreement with the data except at low energies in the forward angles, as already encountered in the analysis of the free proton (see Figure 6.42).
The coplanarity and missing mass spectra are shown in Figures 6.52 and 6.53. The

agreement between data and simulation is very good. Whereas the coplanarity spectra are almost identical for the proton and neutron, clear differences can be observed in the missing mass spectra of the two. In particular at very forward angles at the energy of 810 MeV a distinct shoulder at positive missing mass values arises, which is reproduced by the simulation. This difference is due to $\eta \rightarrow 6\gamma$ photoproduction, which contributes stronger to the reaction on the neutron than on the proton.

Summary

Table 6.6 summarizes the cuts that were applied to the initial sample of events for the analysis of double π^0 photoproduction from the A2 deuteron data. The quasi-free inclusive analysis was not discussed in detail as it comprises the same analysis steps with the exception of the condition on the meson-nucleon coplanarity, which requires the detection of the recoil nucleon.

Analysis cut	Analysis		
	qf. inclusive	exclusive p.	exclusive n.
pulse shape analysis	$\pm 3\sigma$ / nucleon exclusion zone		
$\gamma\gamma$ invariant mass	$\pm 3\sigma$		
$\pi^0\pi^0$-N coplanarity	-	$\pm 1.5\sigma$	
missing mass	$\pm 1.5\sigma$		

Table 6.6: Overview of the applied cuts for double π^0 photoproduction from quasi-free nucleons from the A2 data.

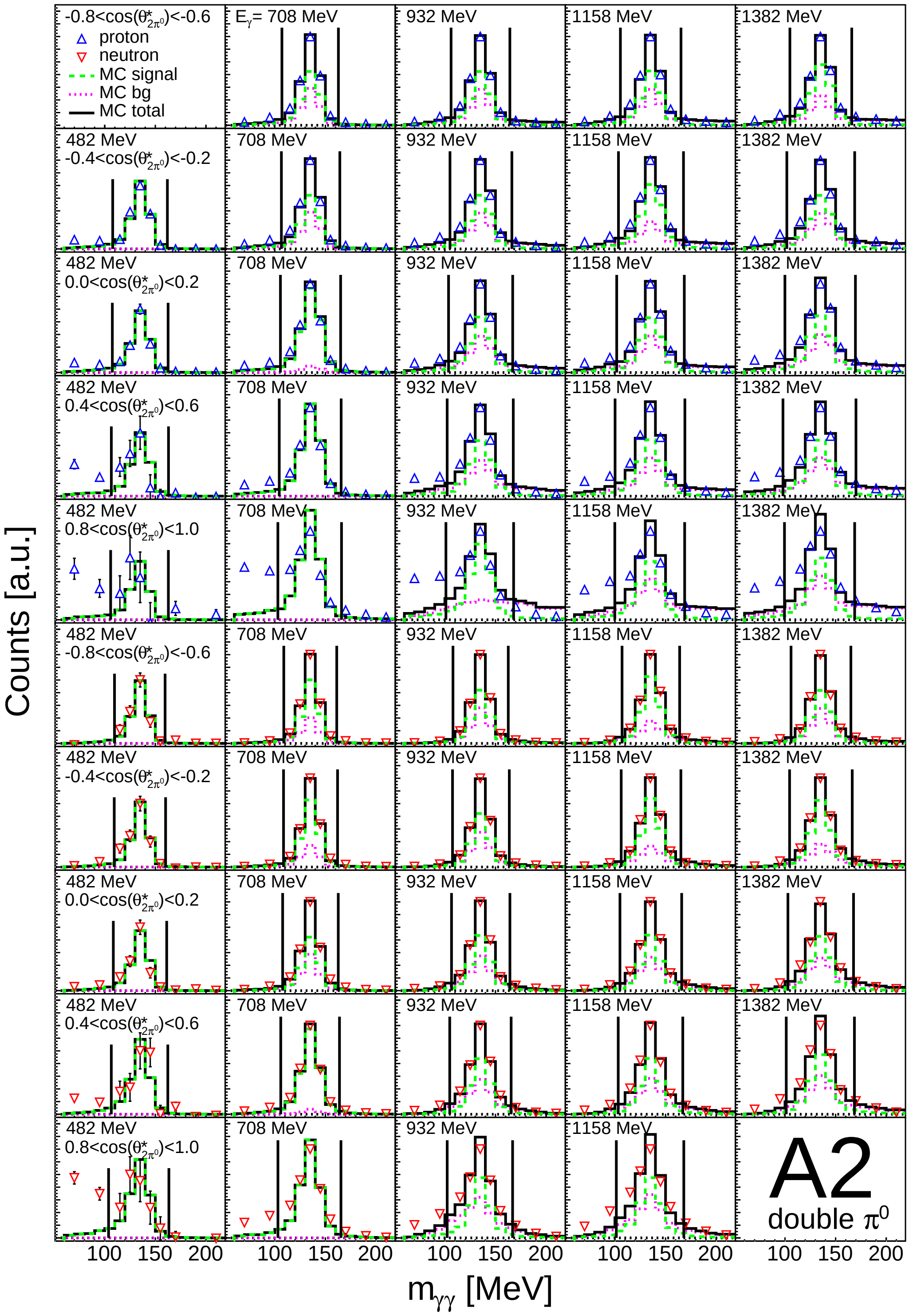

Figure 6.51: Invariant mass spectra for double π^0 photoproduction from quasi-free protons (upper half) and neutrons (lower half) from the A2 data. Shown are five selected energy and angular bins. Only the PSA cut was applied to the data. Notations are given in the figure and the vertical black lines indicate the $\pm 3\sigma$ cut positions.

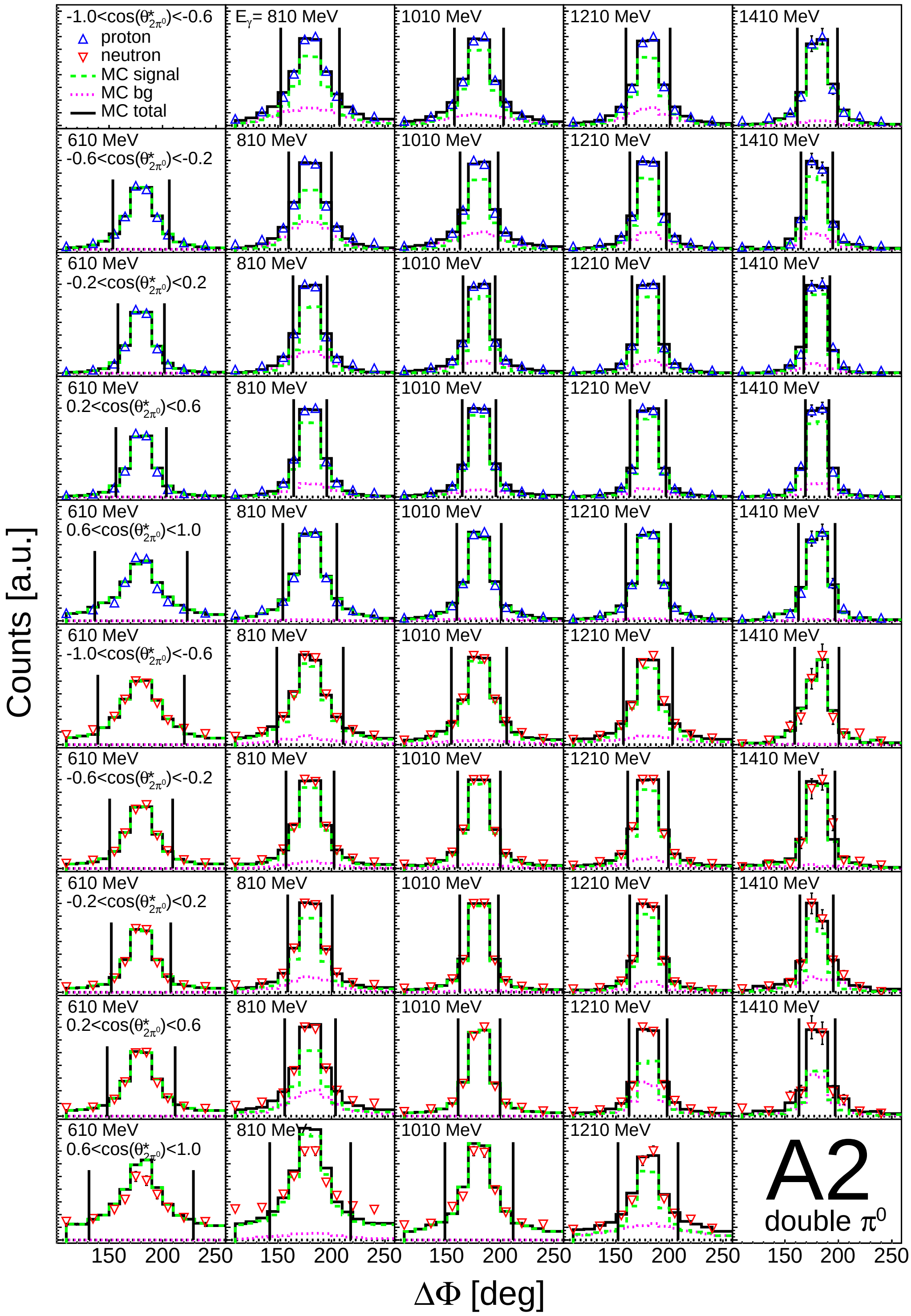

Figure 6.52: Coplanarity spectra for double π^0 photoproduction from quasi-free protons (upper half) and neutrons (lower half) from the A2 data. Shown are five selected energy and angular bins. The PSA and invariant mass cuts were applied to the data. Notations are given in the figure and the vertical black lines indicate the $\pm 1.5\sigma$ cut positions.

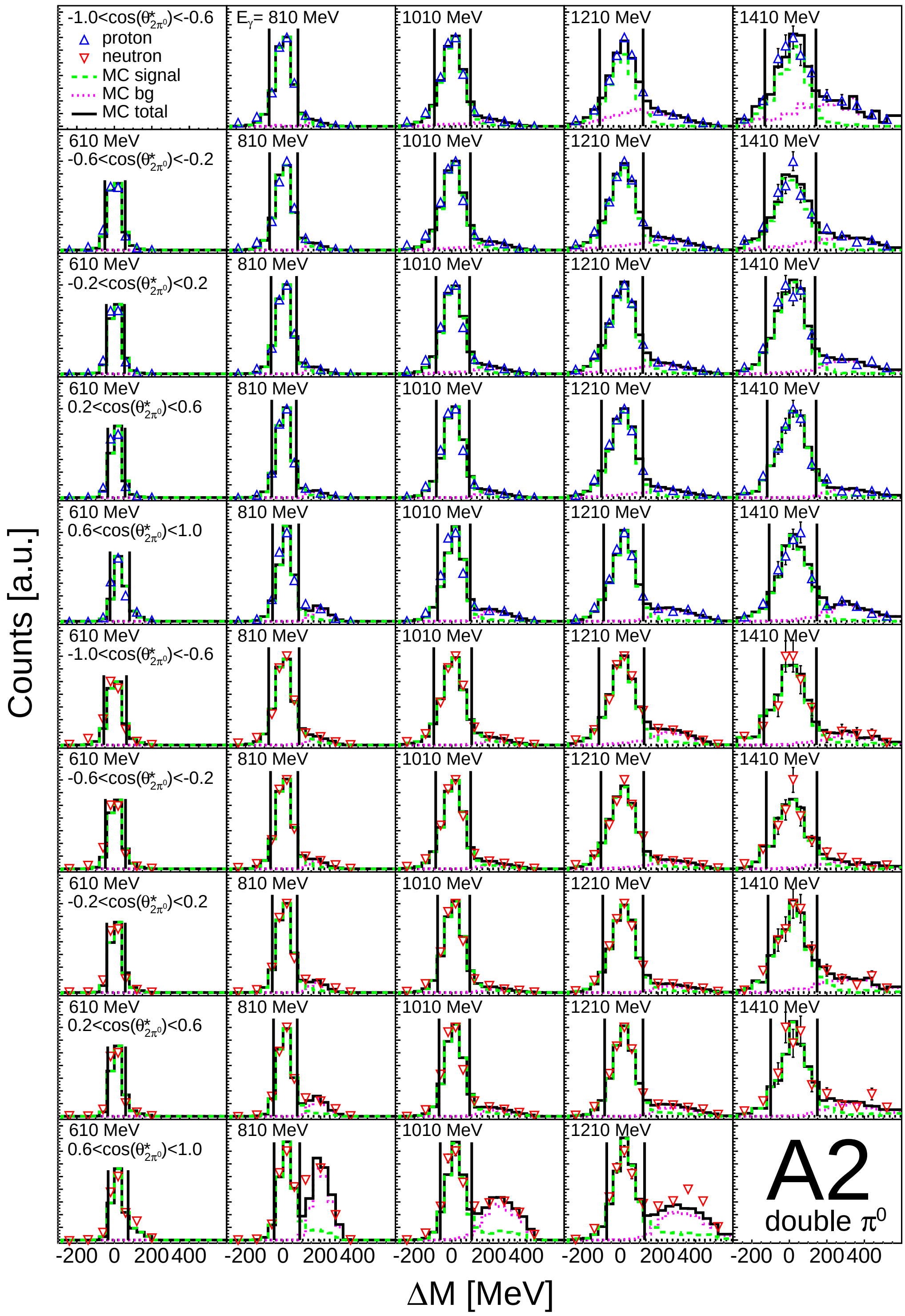

Figure 6.53: Missing mass spectra for double π^0 photoproduction from quasi-free protons (upper half) and neutrons (lower half) from the A2 data. Shown are five selected energy and angular bins. The PSA, invariant mass and coplanarity cuts were applied to the data. Notations are given in the figure and the vertical black lines indicate the $\pm 1.5\sigma$ cut positions.

Analysis of CBELSA/TAPS Data

The CBELSA/TAPS analysis of $\pi^0\pi^0$ photoproduction from quasi-free protons and neutrons is identical to that of A2 data as previously discussed in Section 6.4.4. The PSA cuts are shown in Figure 6.54, the invariant mass cuts in Figure 6.55, the coplanarity spectra in Figure 6.56, and the missing mass spectra in Figure 6.57.

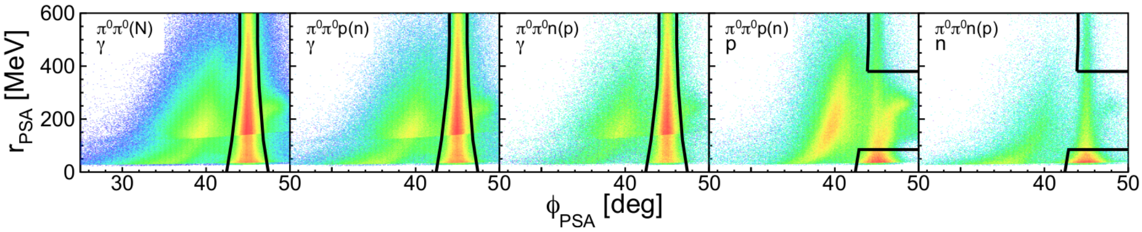

Figure 6.54: PSA spectra for double π^0 photoproduction from the deuteron from the CBELSA/TAPS data. No cut was applied to the data. Columns: analysis channels (see labels). Solid black lines: cut positions.

Differences from the A2 data are, for example, present in the PSA spectra (Figure 6.54), where in this analysis the initial event sample shows a much higher contamination of photons with nucleons and vice versa. As already observed in the PSA spectra in the analysis from free protons in Section 6.4.3, this is mostly due to the higher photon beam energy, but the corresponding events will be removed to a large extent by the analysis cuts. A further difference is visible in the invariant mass spectra (Figure 6.55), where at low energies in the forward angles the agreement between data and simulation is much better compared to the corresponding results from A2 (Figure 6.51). Even though the first energy bin shown in the invariant mass spectrum from CBELSA/TAPS (Figure 6.55) is about 200 MeV higher than the lowest energy bin shown in the corresponding spectra from A2 (Figure 6.51), at lower energies the agreement is also better at CBELSA/TAPS. This could confirm the radiative pion photoproduction split off theory, since the possibility of the identification of split offs depends strongly on the clustering method which is not identical at CBELSA/TAPS and A2 (see Sections 4.1 and 4.2).
The coplanarity (Figure 6.56) and missing mass spectra (Figure 6.57) are reproduced well by the simulation and also agree with the results from the A2 analysis.

Summary

Table 6.7 summarizes the cuts that were applied to the initial sample of events for the analysis of double π^0 photoproduction from the CBELSA/TAPS deuteron data. The quasi-free inclusive analysis was not discussed in detail as it comprises the same analysis steps with the exception of the condition on the meson-nucleon coplanarity, which requires the detection of the recoil nucleon.

Analysis cut	Analysis		
	qf. inclusive	exclusive p.	exclusive n.
pulse shape analysis	$\pm 3\sigma$ / nucleon exclusion zone		
$\gamma\gamma$ invariant mass	$\pm 3\sigma$		
$\pi^0\pi^0$-N coplanarity	-	$\pm 1.5\sigma$	
missing mass	$\pm 1.5\sigma$		

Table 6.7: Overview of the applied cuts for double π^0 photoproduction from quasi-free nucleons from the CBELSA/TAPS data.

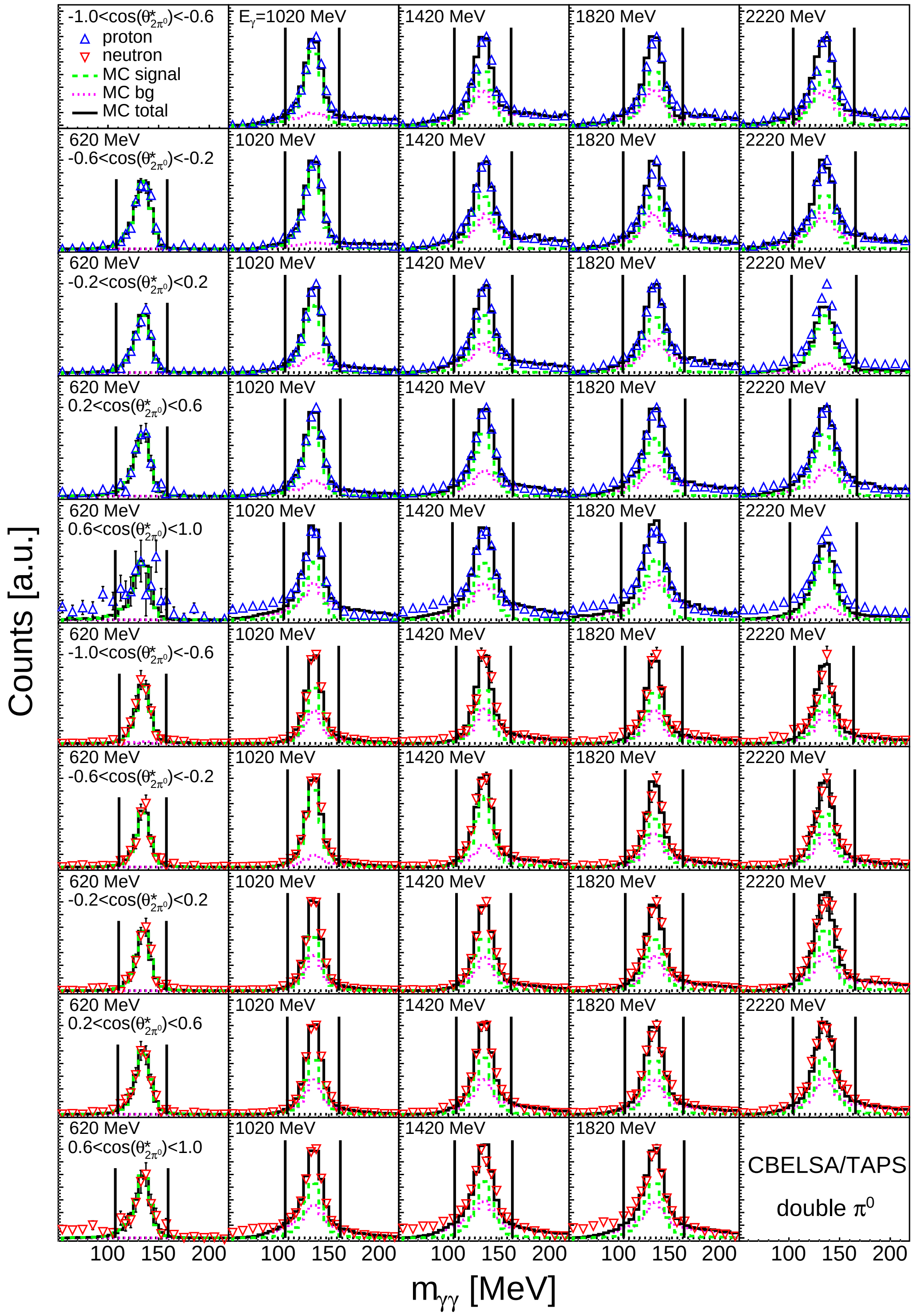

Figure 6.55: Invariant mass spectra for double π^0 photoproduction from quasi-free protons (upper half) and neutrons (lower half) from the CBELSA/TAPS data. Shown are five selected energy and angular bins. Only the PSA cut was applied to the data. Notations are given in the figure and the vertical black lines indicate the $\pm 3\sigma$ cut positions.

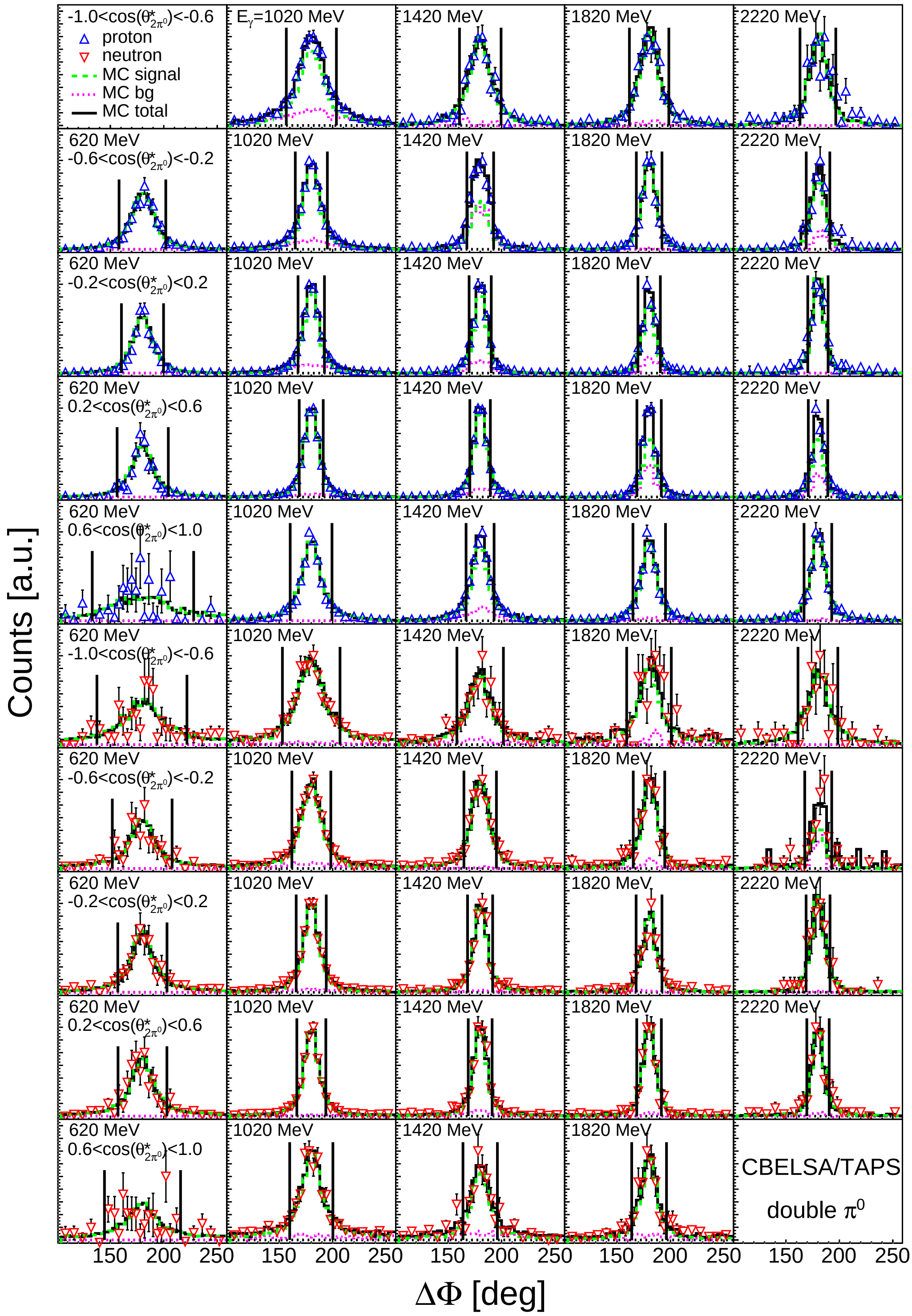

Figure 6.56: Coplanarity spectra for double π^0 photoproduction from quasi-free protons (upper half) and neutrons (lower half) from the CBELSA/TAPS data. Shown are five selected energy and angular bins. The PSA and invariant mass cuts were applied to the data. Notations are given in the figure and the vertical black lines indicate the $\pm 1.5\sigma$ cut positions.

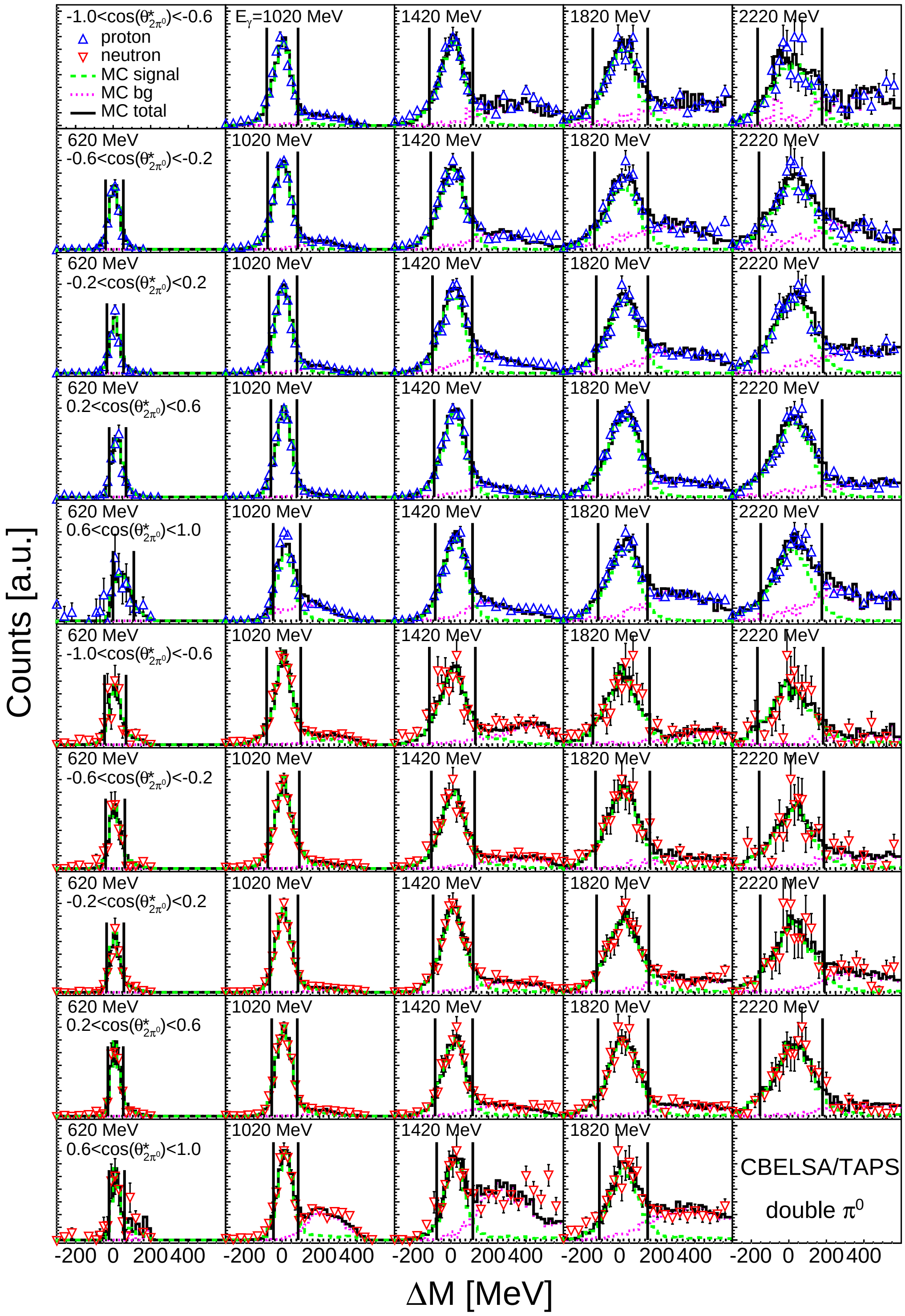

Figure 6.57: Missing mass spectra for double π^0 photoproduction from quasi-free protons (upper half) and neutrons (lower half) from the CBELSA/TAPS data. Shown are five selected energy and angular bins. The PSA, invariant mass, and coplanarity cuts were applied to the data. Notations are given in the figure and the vertical black lines indicate the $\pm 1.5\sigma$ cut positions.

6.4.5 Double π^0 Analysis on Polarized Nucleons

For the $\pi^0\pi^0$ analysis of the deuterated butanol data, an elaborate and carefully processed analysis of the unpolarized deuterium data, as explained in the previous Section 6.4.4, is required. Exact cross sections of the reaction on unpolarized nuclei are used for the normalization of the asymmetries and the missing mass spectra are fundamental of the understanding of the contribution from reactions on the unpolarized carbon and oxygen nuclei that are later subtracted. The quality of the identification and reconstruction of the reaction on the deuterated butanol data hence strongly depends on the quality of the analysis of the deuterium data. For this reason, as already discussed in the single π^0 analysis of the same data (see Section 6.4.2), besides the basic identification and reconstruction of the initial particles (clustering, χ^2 test and detector coincidence cuts), the identical analyses and also cuts of the unpolarized analysis were applied to the polarized data.

Analysis of A2 Data

The analysis of the polarized data is identical to that of liquid deuterium, as described in Section 6.4.4. The cuts on the PSA of the photons and nucleons are shown in Figure 6.58. The influence of the invariant mass cuts from the deuterium analysis on the polarized data are shown in Figure 6.60, those of the coplanarity cut in Figure 6.61 and of the missing mass in Figure 6.62. The deuterated butanol spectra are shown at their final stage, i.e. after all the analysis cuts were applied. The spectra of the liquid deuterium data are shown chronologically and contain all events that fulfilled the previous analysis conditions.

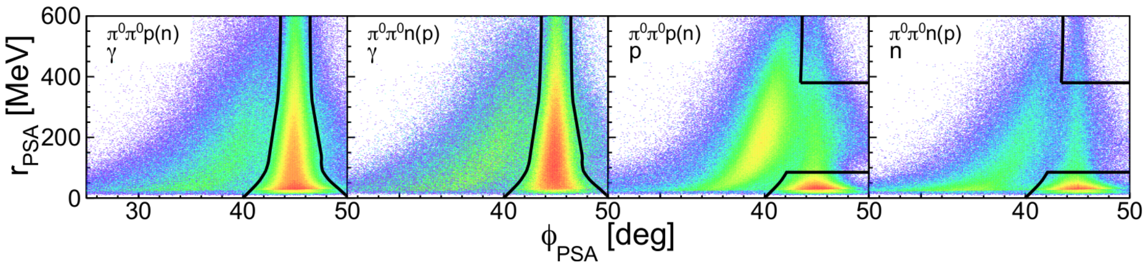

Figure 6.58: PSA spectra for double π^0 photoproduction from the deuterated butanol from the A2 data. No cut was applied to the data. Columns: analysis channels (see labels). Solid black lines: cut positions.

Analysis of CBELSA/TAPS Data

As for the A2 data, the analysis of the deuterated butanol data from CBELSA/TAPS was carried out identically to that from the liquid deuterium data, as discussed in Section 6.4.4. The PSA spectra and the corresponding cuts are shown in Figure 6.59, the invariant mass spectra in Figure 6.63, the coplanarity spectra in Figure 6.64, and the missing mass spectra in Figure 6.65.

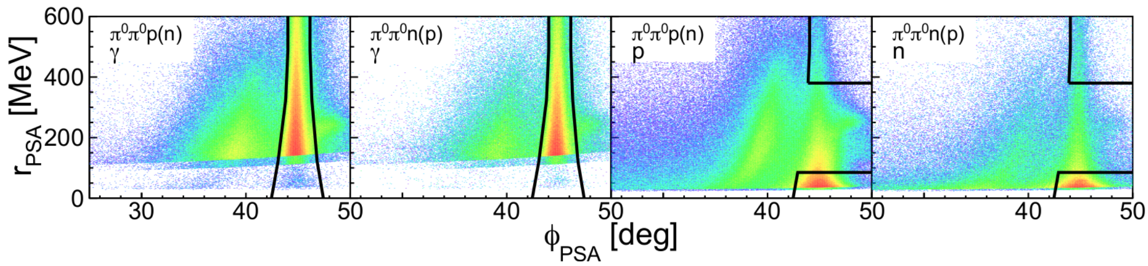

Figure 6.59: PSA spectra for double π^0 photoproduction from the deuterated butanol from the CBELSA/TAPS data. No cut was applied to the data. Columns: analysis channels (see labels). Solid black lines: cut positions.

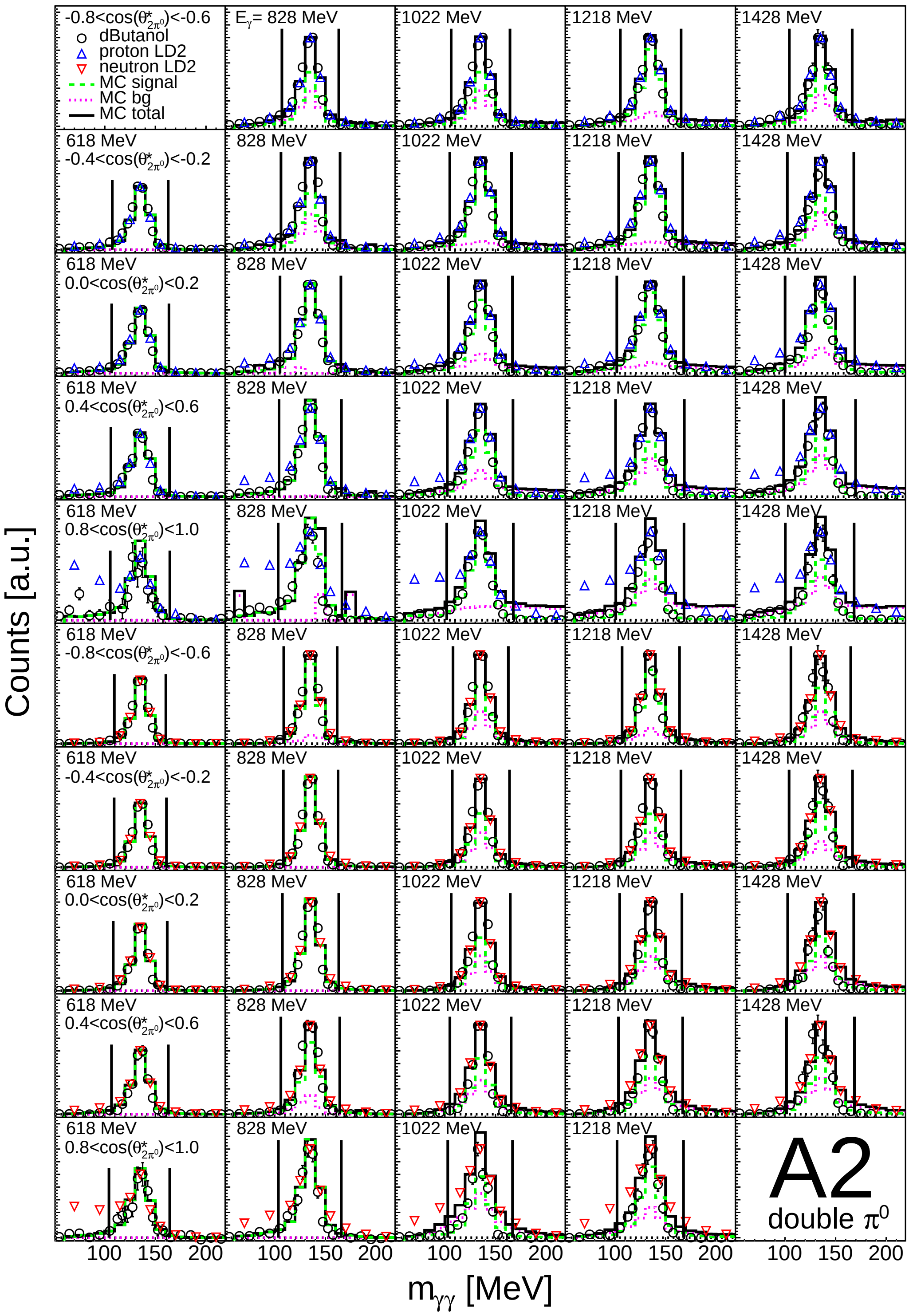

Figure 6.60: Invariant mass spectra for double π^0 photoproduction from deuterated butanol (black circles) compared to those from liquid deuterium (proton: blue triangles, upper half. Neutron: red triangles, lower half). Results from the A2 data. Shown are five selected energy and angular bins. Only the PSA cut was applied to the deuterium data. All cuts were applied to the deuterated butanol data. Notations are given in the figure and the vertical black lines indicate the $\pm 3\sigma$ cut positions.

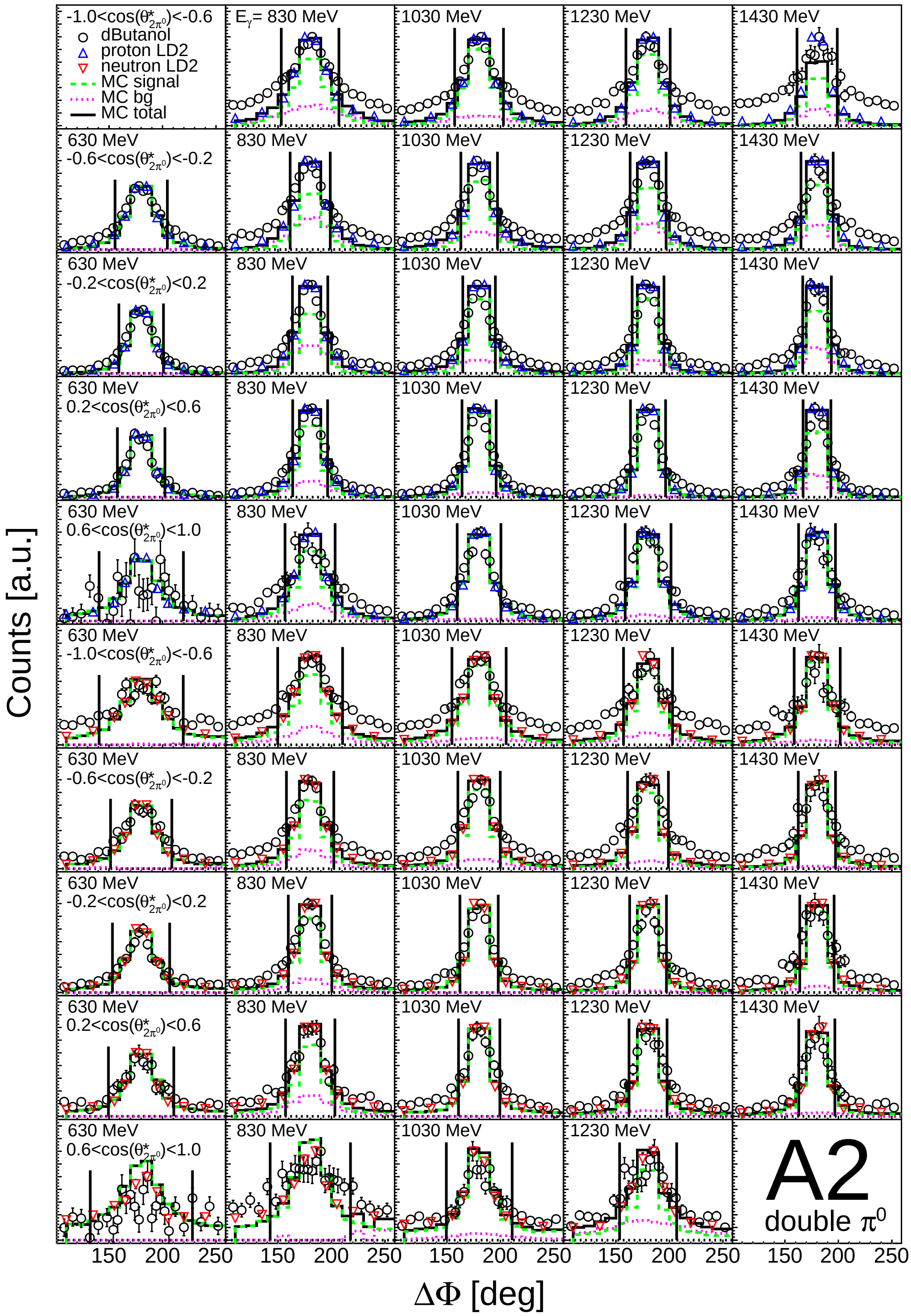

Figure 6.61: Coplanarity spectra for double π^0 photoproduction from deuterated butanol (black circles) compared to those from liquid deuterium (proton: blue triangles, upper half. Neutron: red triangles, lower half). Results from the A2 data. Shown are five selected energy and angular bins. The PSA and invariant mass cuts were applied to the deuterium data. All cuts were applied to the deuterated butanol data. Notations are given in the figure and the vertical black lines indicate the $\pm 1.5\sigma$ cut positions.

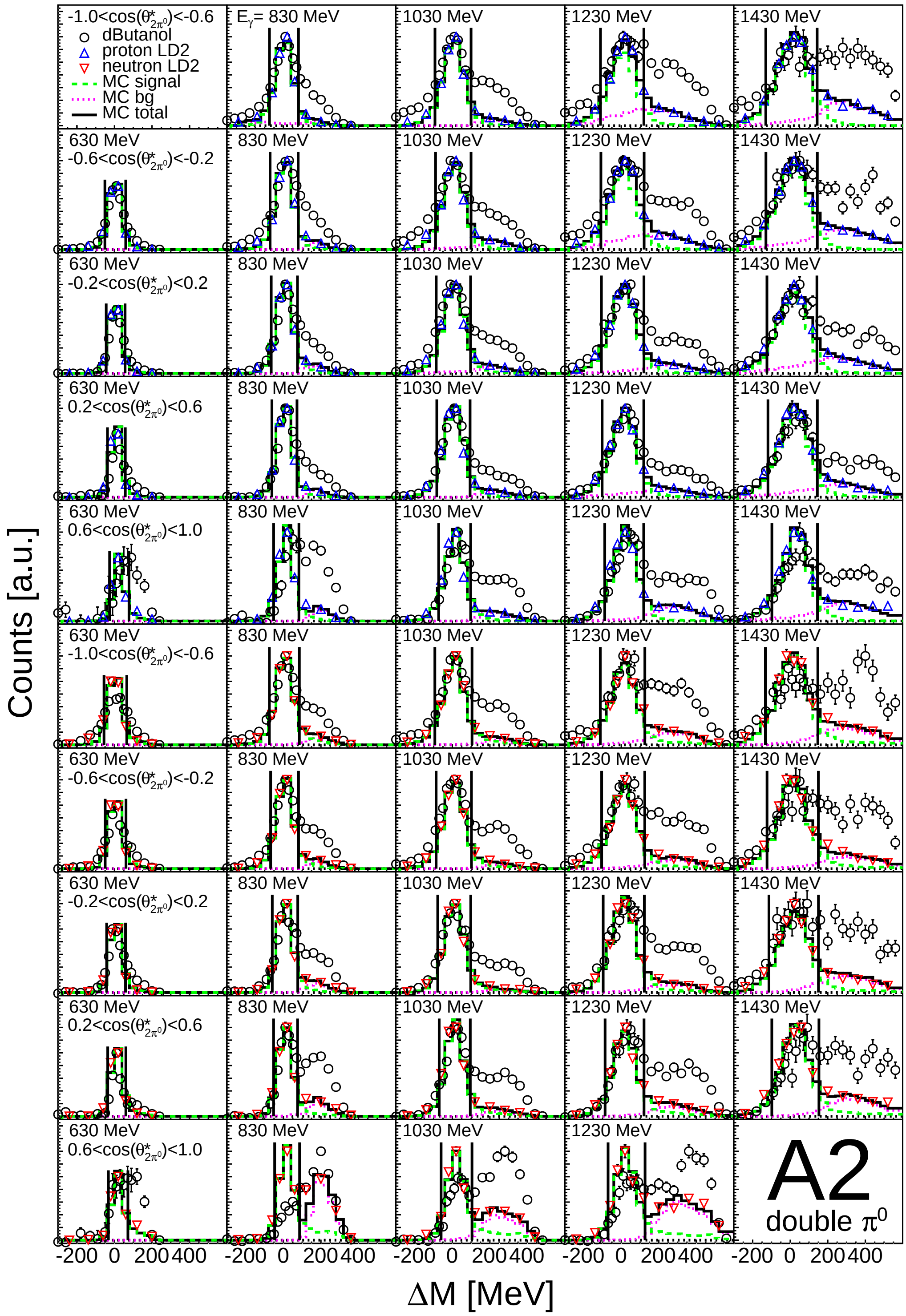

Figure 6.62: Missing mass spectra for double π^0 photoproduction from deuterated butanol (black circles) compared to those from liquid deuterium (proton: blue triangles, upper half. Neutron: red triangles, lower half). Results from the A2 data. Shown are five selected energy and angular bins. The PSA, invariant mass, and coplanarity cuts were applied to the deuterium data. All cuts were applied to the deuterated butanol data. Notations are given in the figure and the vertical black lines indicate the $\pm 1.5\sigma$ cut positions.

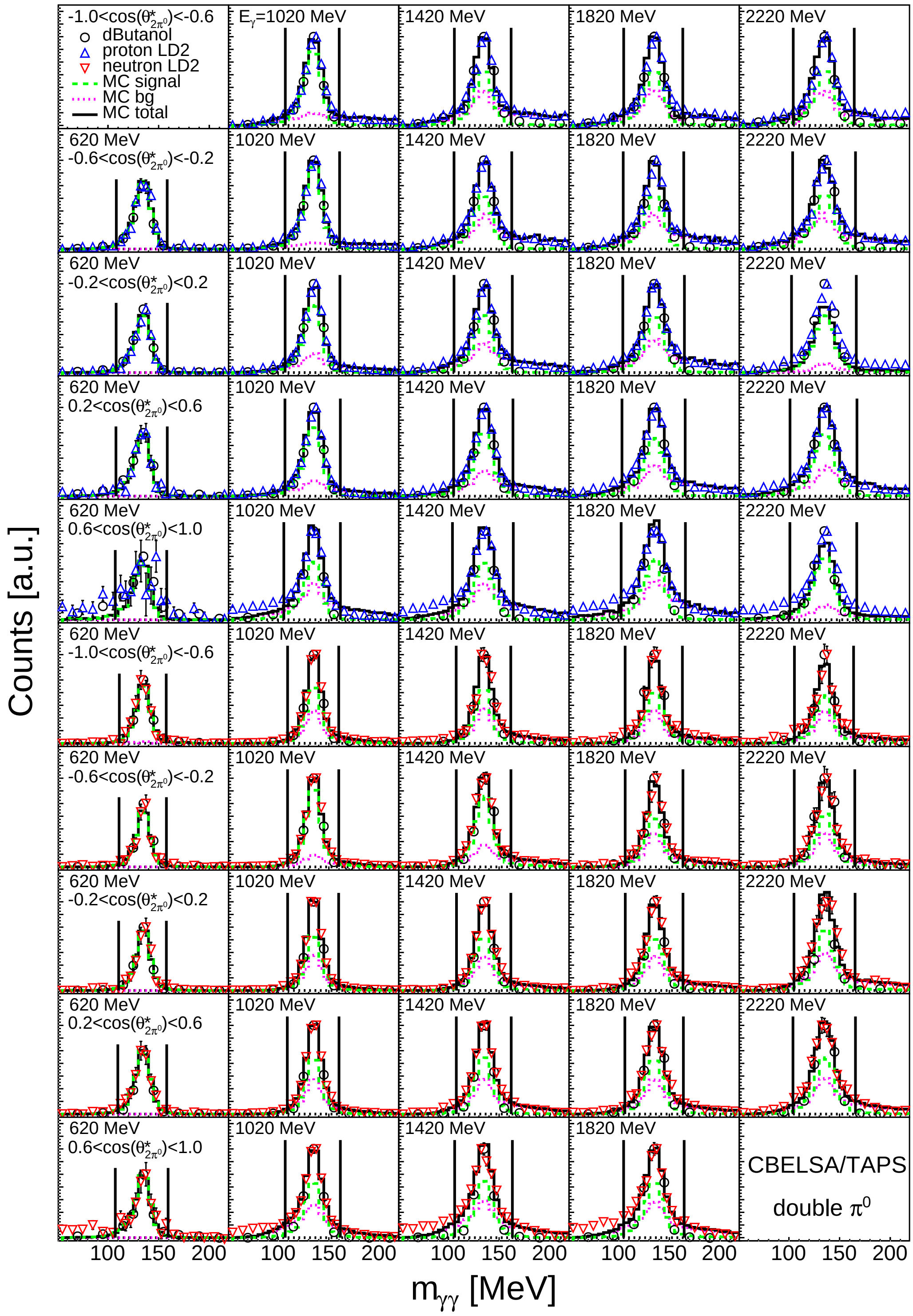

Figure 6.63: Invariant mass spectra for double π^0 photoproduction from deuterated butanol (black circles) compared to those from liquid deuterium (proton: blue triangles, upper half. Neutron: red triangles, lower half). Results from the CBELSA/TAPS data. Shown are five selected energy and angular bins. Only the PSA cut was applied to the deuterium data. All cuts were applied to the deuterated butanol data. Notations are given in the figure and the vertical black lines indicate the $\pm 3\sigma$ cut positions.

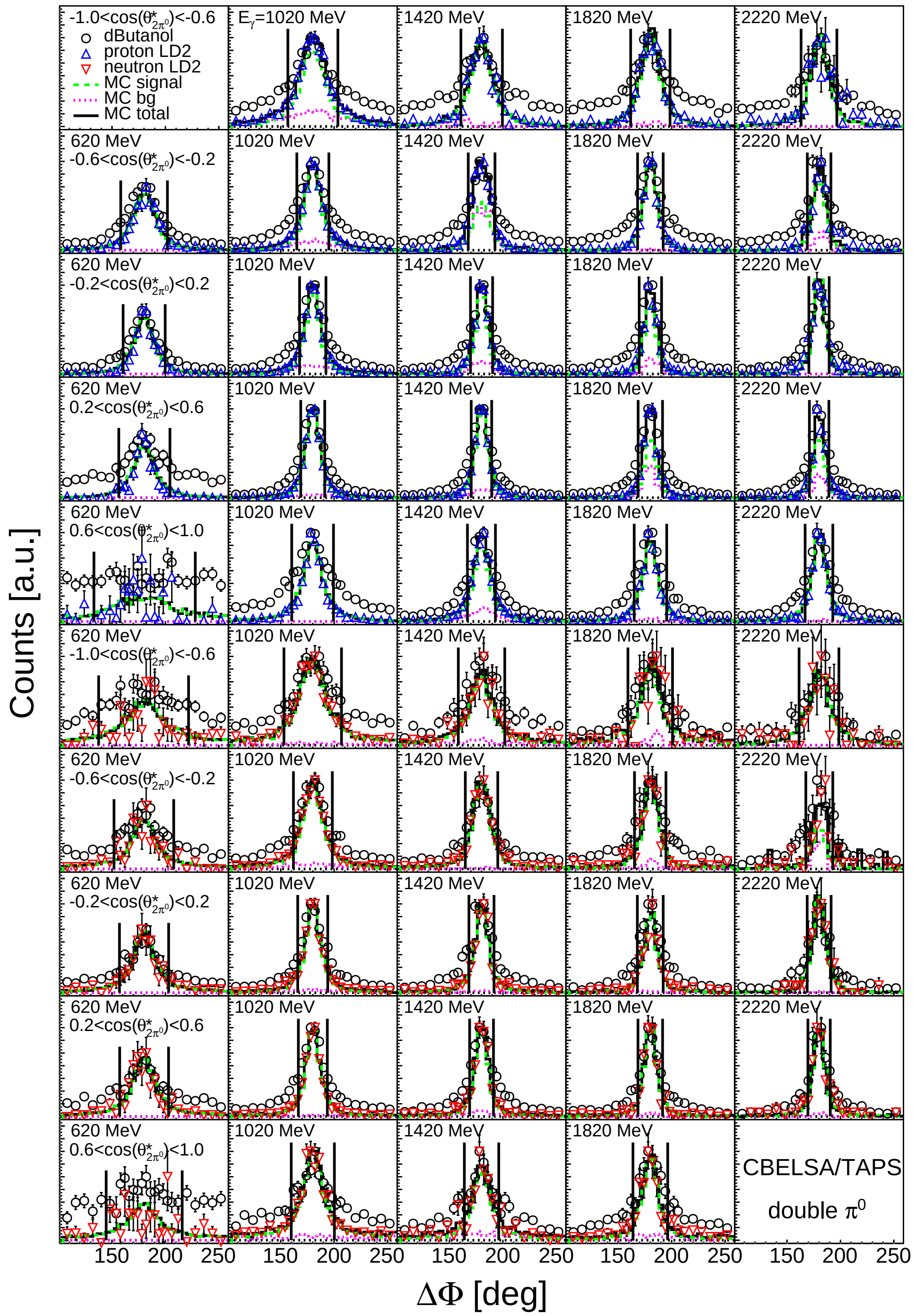

Figure 6.64: Coplanarity spectra for double π^0 photoproduction from deuterated butanol (black circles) compared to those from liquid deuterium (proton: blue triangles, upper half. Neutron: red triangles, lower half). Results from the CBELSA/TAPS data. Shown are five selected energy and angular bins. The PSA and invariant mass cuts were applied to the deuterium data. All cuts were applied to the deuterated butanol data. Notations are given in the figure and the vertical black lines indicate the $\pm 1.5\sigma$ cut positions.

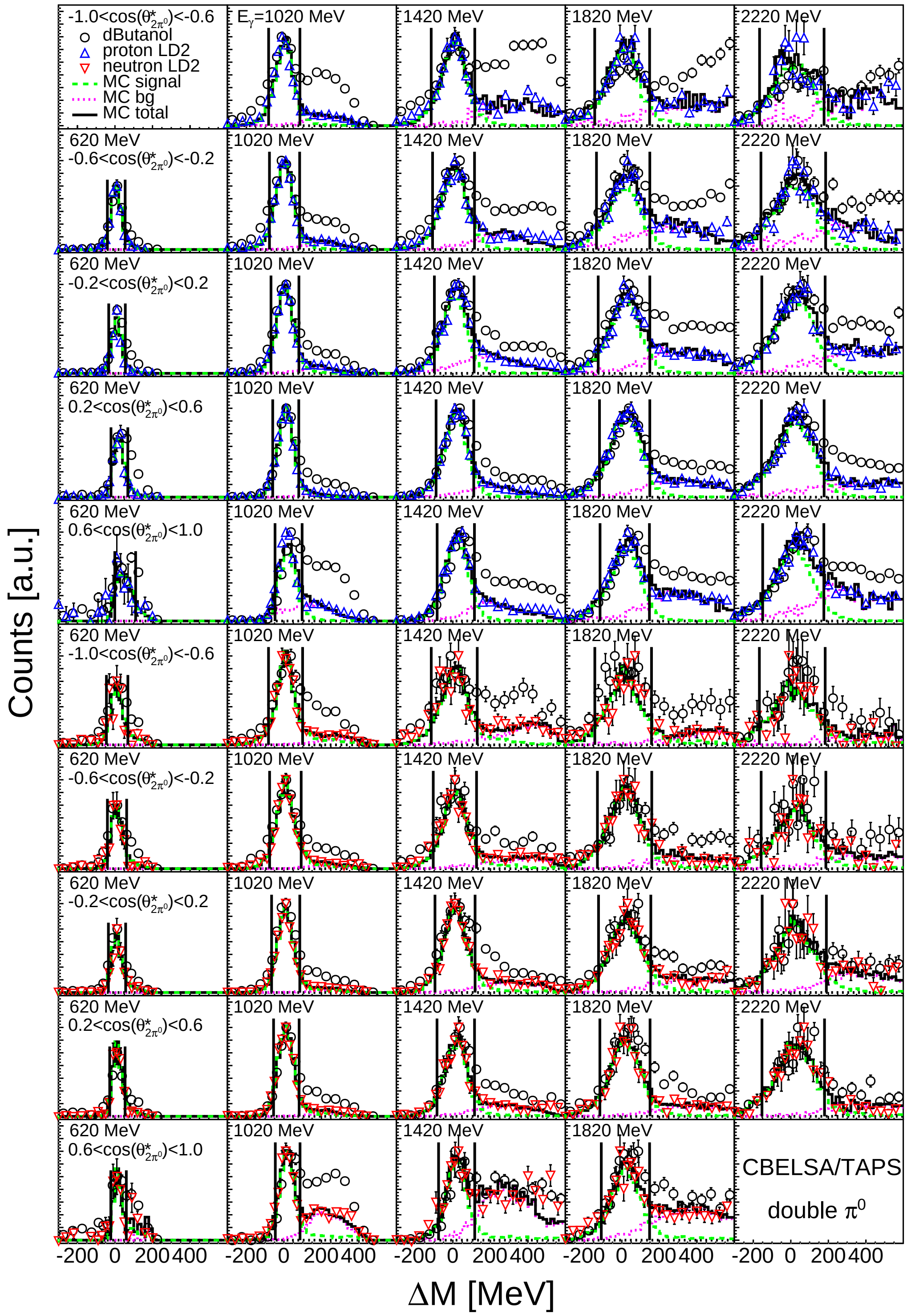

Figure 6.65: Missing mass spectra for double π^0 photoproduction from deuterated butanol (black circles) compared to those from liquid deuterium (proton: blue triangles, upper half. Neutron: red triangles, lower half). Results from the CBELSA/TAPS data. Shown are five selected energy and angular bins. The PSA, invariant mass, and coplanarity cuts were applied to the deuterium data. All cuts were applied to the deuterated butanol data. Notations are given in the figure and the vertical black lines indicate the $\pm 1.5\sigma$ cut positions.

6.5 Quality of the Particle Identification

The previous Section 6.4 described in detail the different conditions that had to be fulfilled by the collection of events as selected from the data sample. All the particles that passed the analysis cuts are supposed to stem from the reaction of interest and only such events that contain the reaction to be investigated are left. Possible remaining background might be due to combinatorial background or due to leftovers from competing channels. If they cannot be removed with a dedicated analysis cut, a proper subtraction from the invariant mass spectra is required, before they are used to determine the yield for the results.
Before the extraction of the results from the final data sample, it is important to check the quality of the different particles that survived all the different analysis cuts before their candidate status is removed. It will be shown that, except for single π^0 photoproduction where the punch-through protons had to be removed with an additional cut on the time of flight (see Section 6.4.1), the identification of the particles is sufficiently clean and no further analysis steps are required.
As previously mentioned in Section 6.4, the additional information of the different detector components were not used for the selection of the events, which instead almost purely consisted of conditions on the kinematics. This detector information however was used for the examination of the particle identification quality. Such information comprises the amount of deposited energies in the charged particle identification detectors (PID and Veto detectors at A2 and Veto detectors at CBELSA/TAPS), the PSA information (TAPS at A2 and MiniTAPS at CBELSA/TAPS), as well as the time of flight (TOF) (TAPS at A2 and MiniTAPS at CBELSA/TAPS). In the following sections, the methods which are based on this information, will be presented and used to discuss the quality of the particle identification for the example of single π^0 photoproduction. Subsequently, the identification quality of the other reactions will also be investigated.

6.5.1 Time of Flight Analysis

The comparatively large distance of the TAPS and MiniTAPS detectors to the target center of ~ 1.5 m (A2) and ~ 2.1 m (CBELSA/TAPS), respectively, in combination with the excellent time resolution of the BaF_2 crystals, can be used to distinguish different types of particles with the time of flight analysis, which is based on the characteristic properties of the individual particles. In contrast to photons, protons, as any massive particle, exhibit a longer time of flight from the target into TAPS/MiniTAPS, regardless of their kinetic energy. The time of flight t_{TOF} of a particle, normalized to 1 meter[4], is calculated as:

$$t_{\text{TOF}} = \frac{\Delta t}{s} + \frac{1}{c} \;, \tag{6.10}$$

where c is the speed of light, s the flight path and Δt is the measured time with respect to the tagged electron (which provides better resolution as the Crystal Ball or

[4] This is necessary in order to account for the different lengths of the flight paths.

Crystal Barrel and Forward Cone detectors). The normalized photon time of flight, $1/c$, had to be added as the time information of all detectors was calibrated such that the differences of the photon times were zero. The TOF analysis is then based on the fact that the time of flight of a massive particle depends on its energy. The higher the energy and the lower the mass of a particle, the shorter it needs to travel the distance from the target to the detector. In general, heavier particles exhibit longer time of flight values and particles of higher kinetic energies exhibit smaller time of flight values. However, a strict correlation is only achieved for charged particles. In contrast to massive charged particles, massive neutral particles deposit a rather statistically distributed amount of their energy in the detector. It is thus reasonable to investigate the time of flight as a function of the deposited energy. Figure 6.66 shows the deposited energy versus the time of flight for the different reaction channels of single π^0 photoproduction. The upper row shows the spectra of all events, i.e. before any of the analysis cuts were applied, and the lower row shows the final accepted event selection.

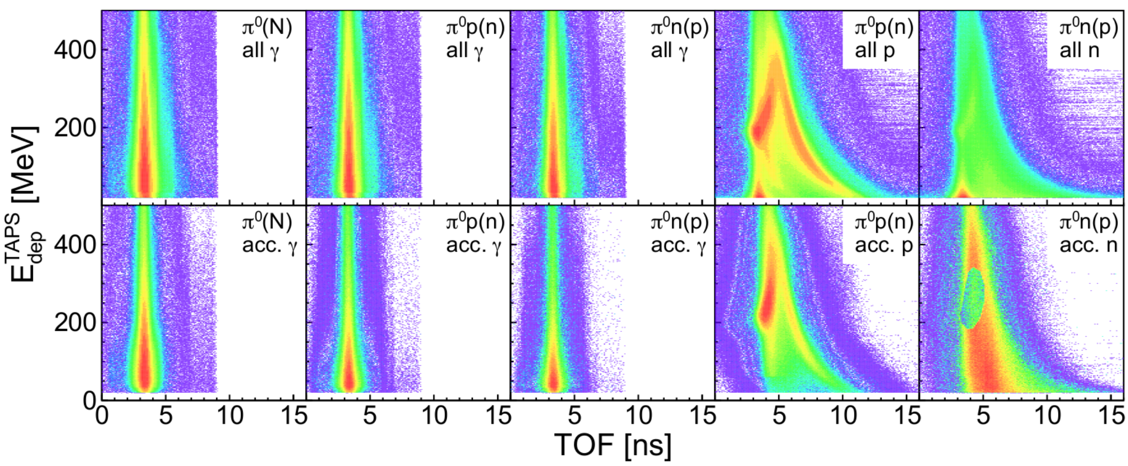

Figure 6.66: TOF spectra for single π^0 photoproduction from the deuteron from the A2 data. Shown is the deposited energy in the TAPS detector versus the time of flight. Columns: analysis channels (see labels). Upper row: no cut was applied to the data (all). Lower row: all cuts were applied to the data (acc.).

Figure 6.66 shows that the initial photon spectra (first three columns from left) are free of any contamination and that the analysis cuts mainly affect the relative contributions such that the average deposited photon energy in TAPS tends towards lower values. This demonstrates the effect of the cuts on the kinematics of the reaction. Although only photons contribute to the initial spectrum, a rather large fraction of photons, mainly those at higher deposited energies, stem from competing reactions and were successfully rejected by the different analysis cuts. In contrast, the initial TOF spectra of protons and neutrons show a lot of contamination from electrons and photons. The circular structure from the punch-through protons is clearly visible in the proton spectrum and partially in the neutron spectrum, as

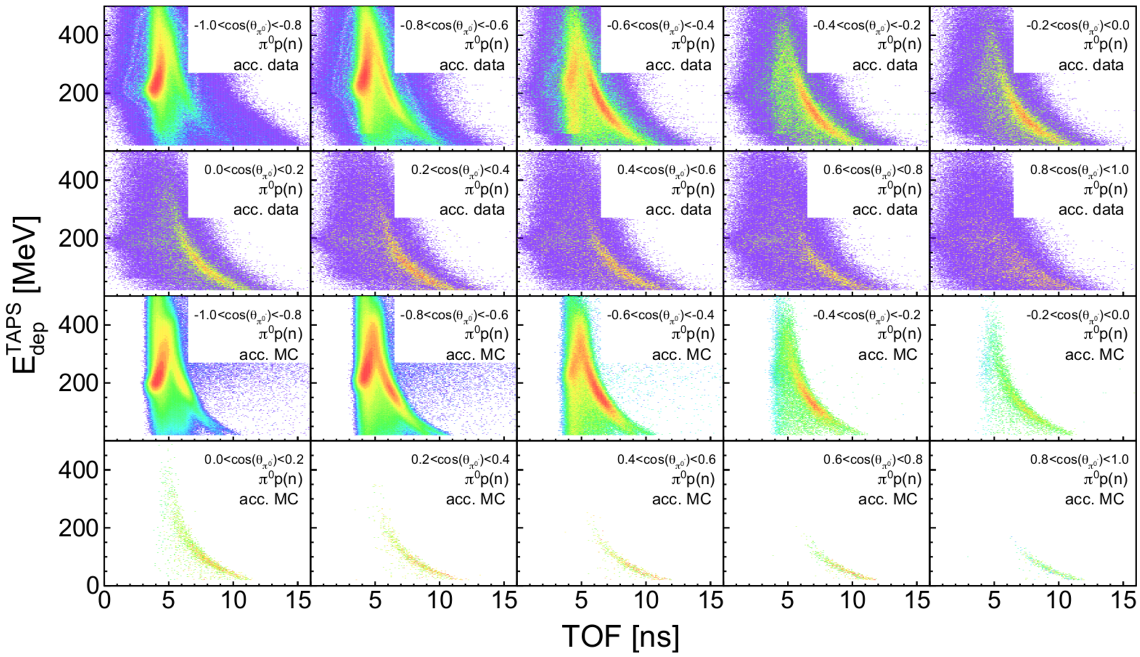

Figure 6.67: Proton TOF spectra for single π^0 photoproduction from the deuteron from the A2 data (upper two rows) and simulation (lower two rows). Shown is the deposited energy in the TAPS detector versus the time of flight for ten different $\cos(\theta^*_{\pi^0})$ bins. All cuts were applied to the data (acc.).

discussed in Section 6.4.1. In order to remove these punch-through protons that were misidentified as neutrons, neutron events within the circular border were rejected in the corresponding angular region (see Figure 6.30). As shown in Figure 6.31 and also visible in Figure 6.68, the cut works reasonably well and does not appear to affect the kinematics. Besides the location of the cut, a typical neutron TOF spectrum is visible, showing no direct correlation of the TOF and the deposited energy, but rather a region of kinematic probability. The final proton TOF spectra is also free from background contributions. The weak trace from charged pions is not visible anymore and the typical proton band is diminished. This again demonstrates the successful removal of competing reactions and also wrong particle candidates by the cuts on the kinematics of the reaction. As compared to double π^0 photoproduction, in single π^0 photoproduction the recoil proton has a much higher kinetic energy. A pure TOF spectrum does not significantly exhibit the typical proton band, but rather the circular minimum ionizing structure. Most of the events from within the proton band stem from competing reactions and thus had to be eliminated.
A closer look on the final proton TOF spectrum (lower row, second figure from the right) reveals a small trace below the circular structure of the punch through protons. This trace is located at nearly constant TOF values of ~ 4.5 ns. Since photons are located at TOF values of 3.3 ns and charged pions have an energy dependent TOF, this trace most have a different origin. A comparison of the proton TOF spectra from data and simulation indeed shows that this trace originates from the desired reaction. The situation is illustrated in Figure 6.67. It shows the proton TOF spectra from

data (upper two rows) and simulation (lower two rows) for ten different angular bins (see labels for the individual regions) after all cuts were applied. Good agreement between the spectra from data and simulation is visible and all prominent structures are equally present. The spectra at $\cos(\theta^*_{\pi^0}) < -0.4$ reveal that the small trace results from the very high energetic protons and not from charged particles from competing reactions and by that confirms the quality of the identification.

6.5.2 Pulse Shape Analysis (PSA)

The pulse shape analysis (PSA) was already discussed and described in detail in Section 6.4.1 and will not be repeated. The spectra of the different reaction channels of single π^0 photoproduction from the deuteron for the initial (top row), as well as the final selection of events (bottom row) are shown in Figure 6.68. All PSA spectra

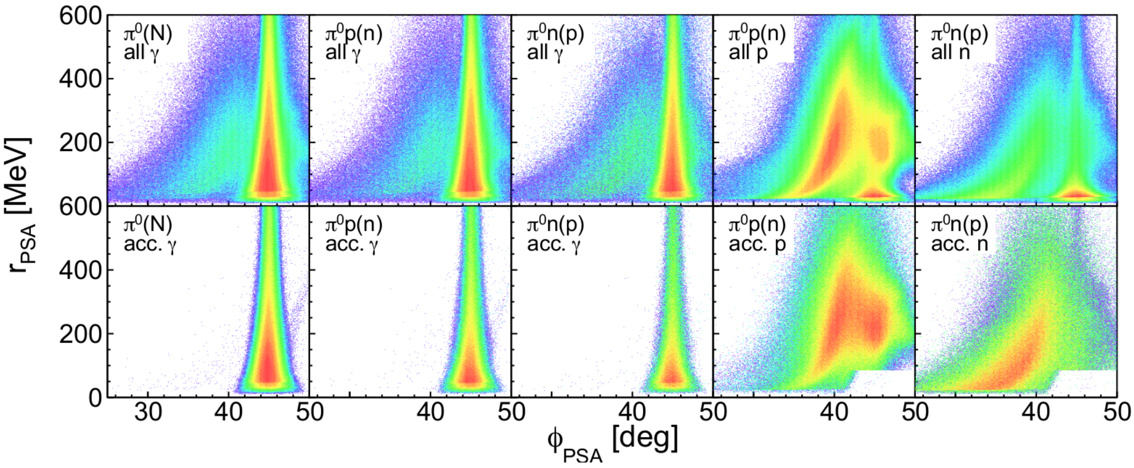

Figure 6.68: PSA spectra for single π^0 photoproduction from the deuteron from the A2 data. Shown is the PSA radius versus the PSA angle. Columns: analysis channels (see labels). Upper row: no cut was applied to the data (all). Lower row: all cuts were applied to the data (acc.).

of the photons are very clean, since the $\pm 3\sigma$ cut as a function of the PSA radius was applied. As the cut for the photons was determined and applied individually for every BaF_2 crystal, the outer area contains a few remaining events. The final proton spectrum is difficult to interpret as the high energy recoil region covers most of the photon area. Nevertheless, it appears to be sufficiently clean. The weak trace of the photon band, which is visible in the initial spectrum, vanished and the contributions from electrons were removed by the exclusion zone (see Figure 6.23). The most interesting effect of the cuts is visible in the neutron PSA spectrum. On the one hand, as observed for the proton, the contamination from photons (which obviously are much more present in the neutron channel) vanished, except for a small part at the top of the spectrum, which, since below the 1% level, is negligible. Furthermore, the cut on the neutron TOF (see Section 6.4.1) does not appear to have any influence on the kinematics of the neutron. A typical neutron PSA spectrum is visible, as seen in the lower row of the first column from the right in Figure 6.68.

6.5.3 ΔE versus E Analysis

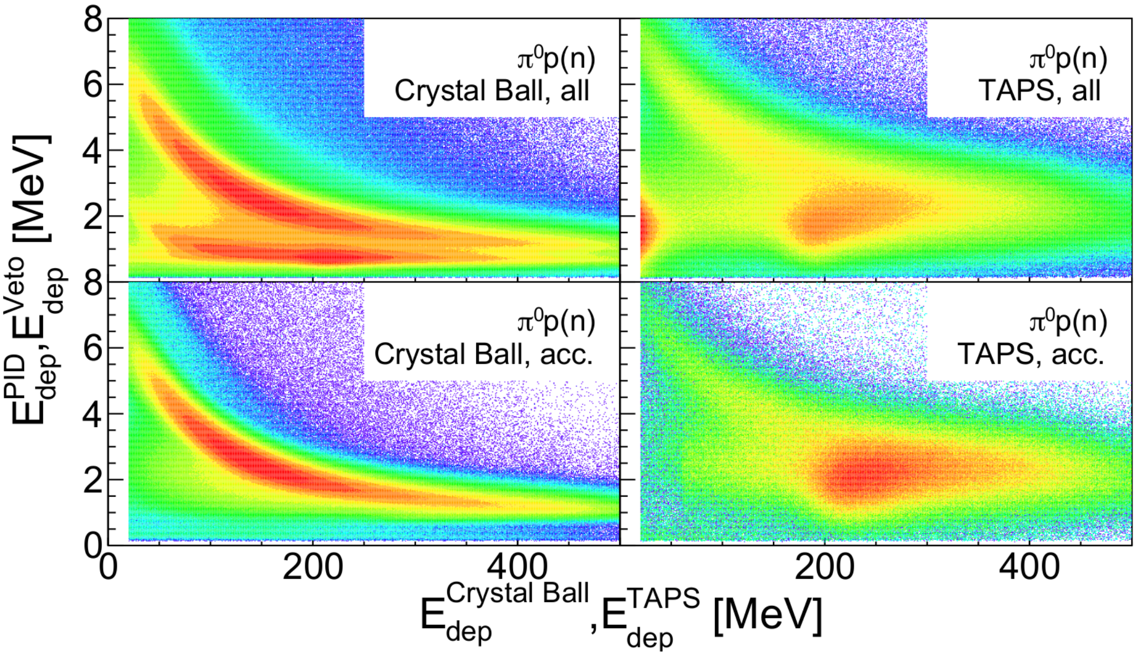

Figure 6.69: ΔE versus E analysis of the protons from single π^0 photoproduction from the deuteron from the A2 data. Shown is the deposited energy in the PID versus the deposited energy in the Crystal Ball (left column) and the deposited energy in the Veto detectors versus the deposited energy in TAPS (right column). Columns: analysis channels (see labels). Upper row: no cut was applied to the data (all). Lower row: all cuts were applied to the data (acc. data) and simulation (acc. MC).

For the identification of neutral or charged particles in the analysis, usually only logical information of the charged particle detectors is used to decide whether a particle is charged or not. This logical information is given if a coincident signal above a corresponding threshold was present in the individual detector component. However, except for the Inner Detector at CBELSA/TAPS, the charged particle detectors also allow access to the deposited energy. The amount of deposited energy contains information about the type of particle that passed through the detector. This energy (in relation to the total kinetic energy that the particle deposited in the corresponding calorimeter) depends on the charge, mass, and energy of an individual particle. Whereas just sufficient resolution for such an investigation is provided by the Veto detectors of the TAPS and MiniTAPS detectors, the PID detector is ideally suited for this type of analysis. Unfortunately, since the Inner detector does not provide any energy information, the ΔE versus E method is not feasible with the Crystal Barrel detector at CBELSA/TAPS. Therefore, the discrimination of charged particles over a large region is not possible.

The ΔE versus E spectra for the recoil protons in single π^0 photoproduction

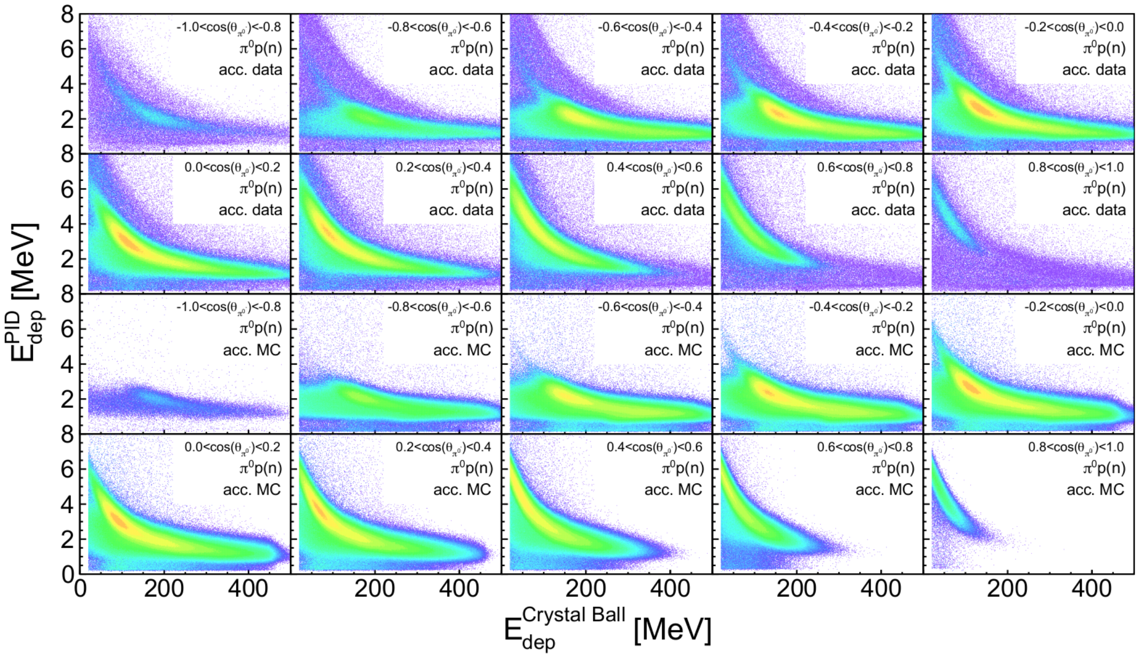

Figure 6.70: Proton ΔE versus E spectra for single π^0 photoproduction from the deuteron from the A2 data (upper two rows) and simulation (lower two rows). Shown is the deposited energy in the PID versus the deposited energy in the Crystal Ball for ten different $\cos(\theta^*_{\pi^0})$ bins. All cuts were applied to the data (acc. data) and simulations (acc. MC).

using the deposited energy in the PID versus the deposited energy in the Crystal Ball detector, as well as the deposited energy in the Veto detectors, combined with that from the TAPS detector, are shown in Figure 6.69.

Both initial spectra of the protons show a very prominent and strongly energy dependent band structure, as well as contributions from electrons and less energy dependent bands from charged mesons (mainly pions). The proton band in TAPS exhibits the typical circular punch through region, whereas in the Crystal Ball detector, almost no high energetic protons are visible. This was already assumed by means of the kinetic energy distribution of the recoil protons (see Figure 6.22), but was confirmed by this spectra. Hence, protons were not misidentified as neutrons in the Crystal Ball detector. The final spectra from both detectors are free of pions and electrons and exhibit almost purely the proton traces.

The small vertical trace, as observed in the proton TOF spectra (see Figure 6.66), is also visible in the ΔE versus E spectra from TAPS (see right spectrum in the bottom row of Figure 6.69) and does not correspond to background from charged pions as well. Even though the ΔE versus E spectra from the Crystal Ball detector (see left spectrum in the bottom row of Figure 6.69) mainly exhibit the typical proton band, the region at lower deposited energies was in addition investigated for remaining background. For this purpose, the final spectra of experimental and simulated data were compared for ten different angular regions, as shown in Figure 6.70. Although the calibration of the PID energy in the simulation is delicate (see Section

5.2.5), the spectra from data and simulation are in good agreement and indicate that the events at lower deposited energies, i.e. below the proton band, result from true signal events and not from competing reactions. No evidence for notable background contributions was observed.
From the different quality checks, it was concluded that the identification of the different particles was reliably performed and no further cuts were necessary.

6.5.4 Single π^0 Analysis on Polarized Nucleons

As the analysis of the polarized data was based on the analysis of liquid deuterium data (see Section 6.4.1) and the identical cuts were applied, it is important to check the effect of the cuts on this analysis. Nevertheless, a direct comparison might be difficult since the spectra from the polarized data still contain contributions from the reactions on unpolarized nucleons of the carbon and oxygen nuclei. For this reason, in order to investigate the quality of the particle identification on the analysis of polarized data, the corresponding spectra are not only shown for deuterated butanol, but also for carbon.

Primarily, the TOF spectra and the identification quality from the analysis of polarized data, i.e. Figure 6.71a, are very similar to those from liquid deuterium (Figure 6.66). The spectra of the final accepted events are nearly free of background and no contamination is visible. The main characteristics of the individual spectra (e.g. the small trace below the circular punch through region in the proton TOF) have already been discussed for the liquid deuterium case (see Section 6.5.1). However, it can be seen (on the number of events in the proton band) that the relative contribution of protons of lower energy has slightly increased (compared to Figure 6.66). Whereas on deuterium, most of the protons were found in the circular punch through region and the typical proton band structure was weak, here a more defined proton band is visible. The same can be observed by a comparison of the PSA spectra from deuterated butanol (see Figure 6.72a) with those from deuterium (see Figure 6.68). The strong region of overlap of the proton and photon bands is weaker in the polarized case. However, the corresponding spectra from the carbon background measurement (Figure 6.71b: TOF, Figure 6.72b: PSA) shed light on this characteristic. The protons from reactions on the nucleons of the carbon nuclei do not gain as much kinetic energy as on the deuterium. In the TOF and PSA spectra from the carbon data, only a small part of the protons is visible at the locations of high kinetic energy. Instead, moderate and rather typical proton spectra are obtained. This is also confirmed by the ΔE versus E analysis from the TAPS detector (right-hand side of Figure 6.73a), which also contains few high energetic protons. As the deuterated butanol target comprises reactions on nucleons in deuterium as well as in carbon, the resulting ΔE versus E spectrum exhibits characteristics from reactions on deuterium and carbon.
In contrast, the ΔE versus E spectra from the Crystal Ball detector of the polarized analysis (left-hand side of Figure 6.73a) are not only free of background, but are also more or less identically distributed compared to the deuterium spectrum (see

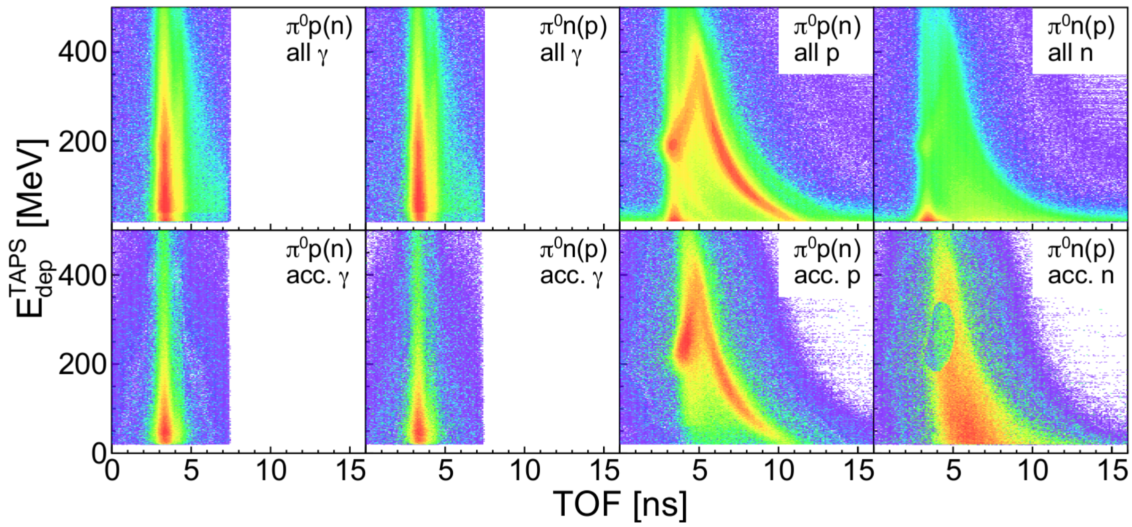

(a) A2 results from the deuterated butanol data

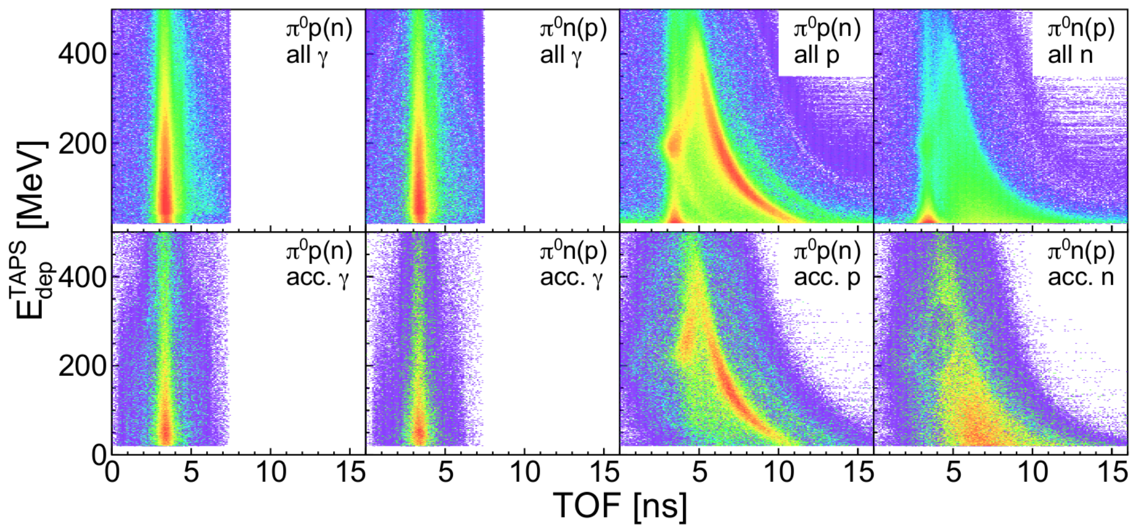

(b) A2 results from the carbon data

Figure 6.71: TOF spectra for single π^0 photoproduction from deuterated butanol (a) and carbon (b) from the A2 data. Shown is the deposited energy in the TAPS detector versus the time of flight. Columns: analysis channels (see labels). Upper row: no cut was applied to the data (all). Lower row: all cuts were applied to the data (acc.).

Figure 6.69). However, the width of the proton band is somewhat larger compared to that from the analysis of deuterium data, which results from the rather broad proton band from the carbon analysis (see Figure 6.73b) exhibits a broader proton band.
In total, the particle identification of the deuterated butanol data is in good agreement with that from the deuterium data and no significant background contribution was observed.

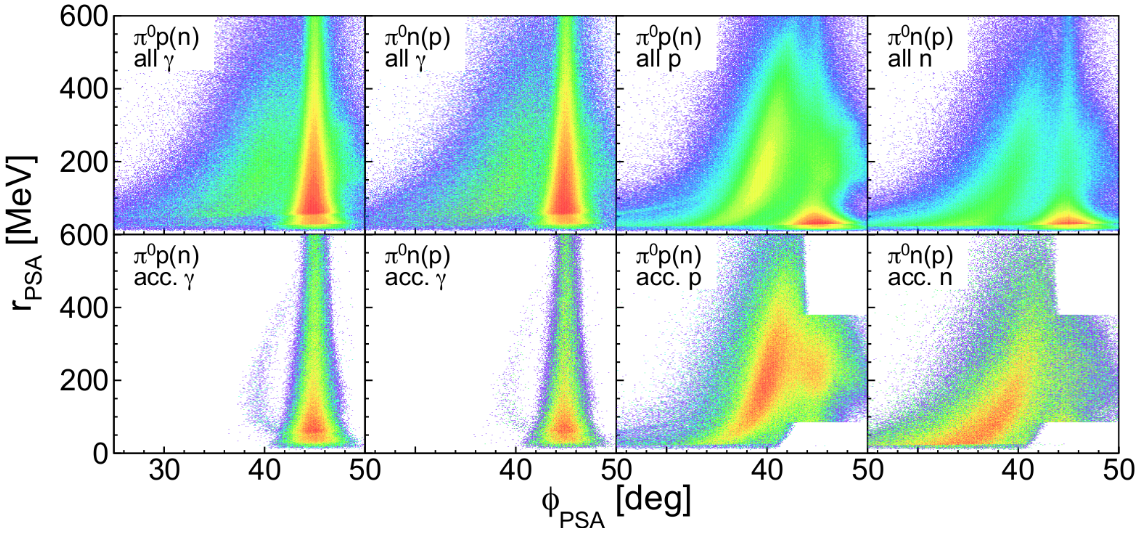

(a) A2 results from the deuterated butanol data

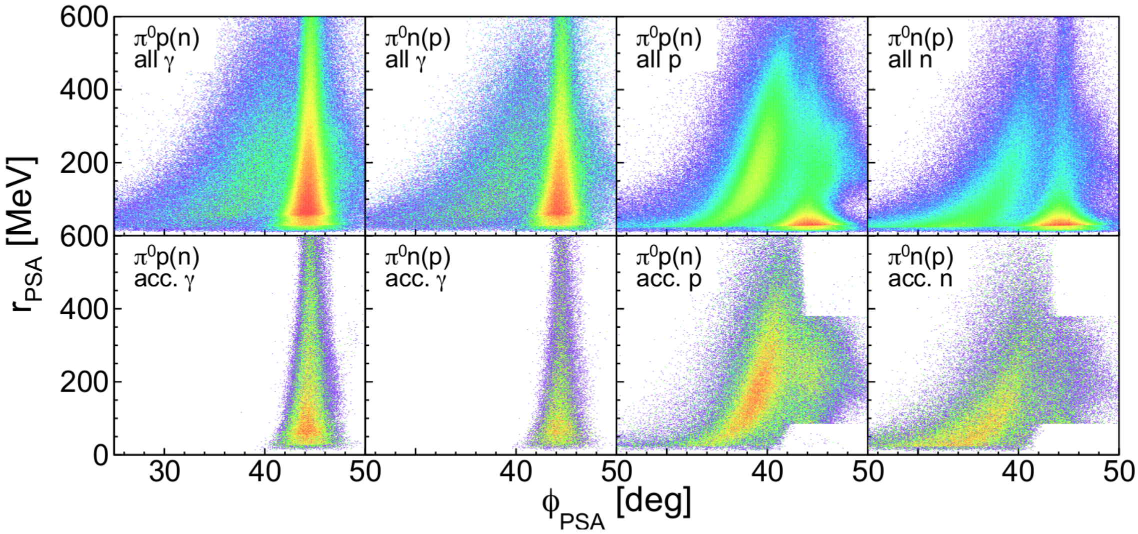

(b) A2 results from the carbon data

Figure 6.72: PSA spectra for single π^0 photoproduction from deuterated butanol (a) and carbon (b) from the A2 data. Shown is the PSA radius versus the PSA angle. Columns: analysis channels (see labels). Upper row: no cut was applied to the data (all). Lower row: all cuts were applied to the data (acc.).

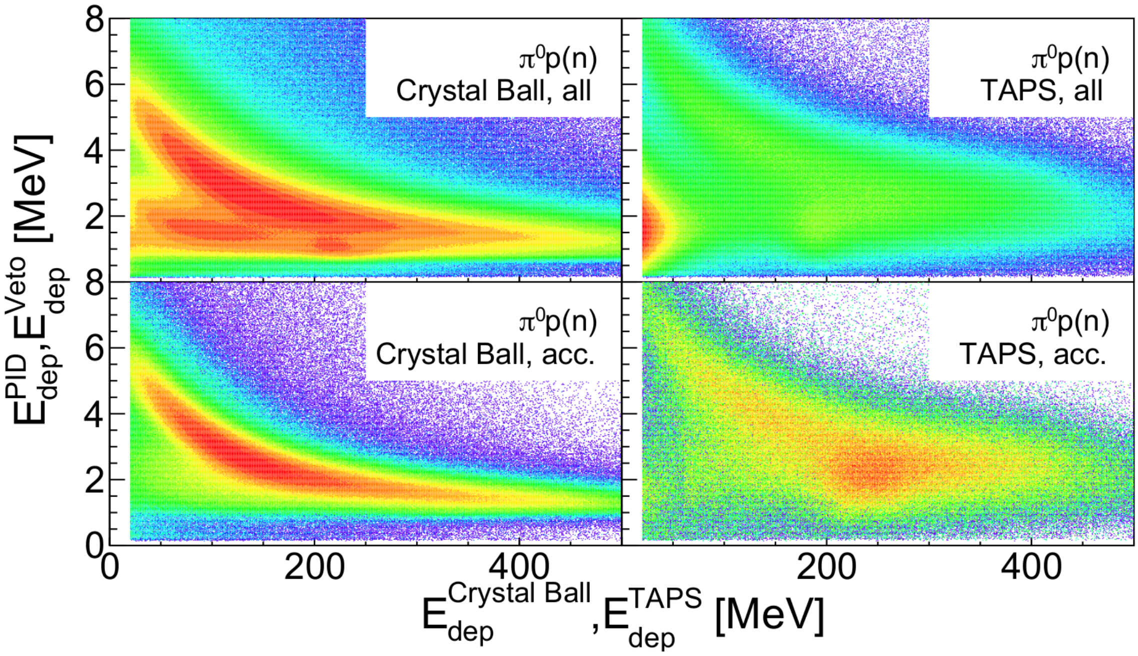

(a) A2 results from the deuterated butanol data

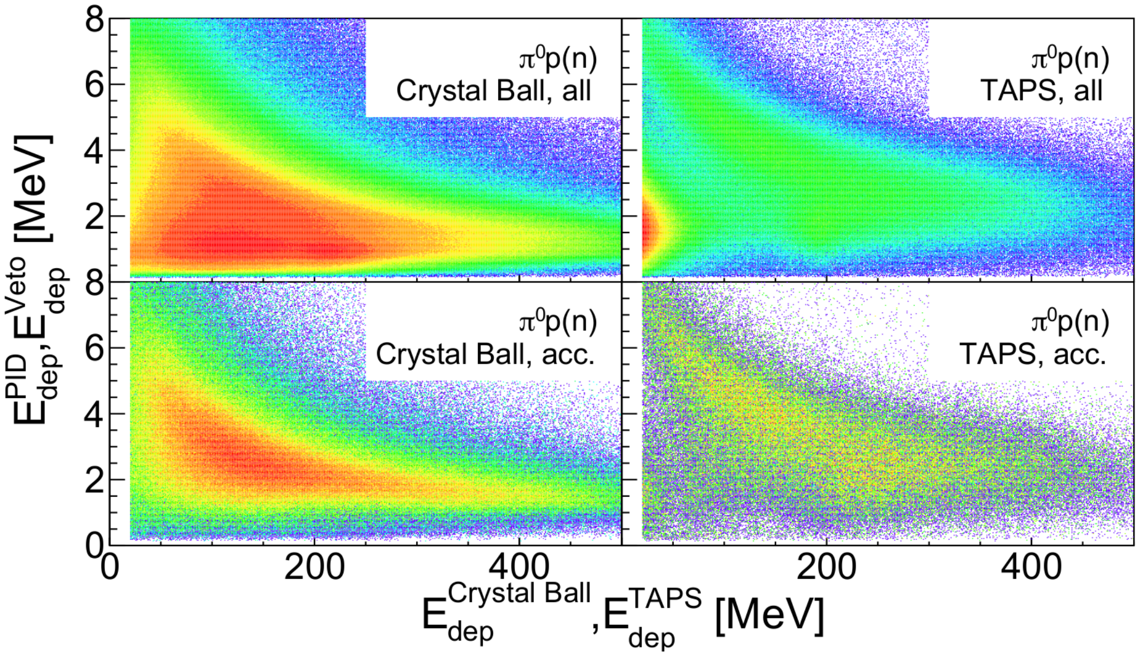

(b) A2 results from the carbon data

Figure 6.73: ΔE versus E analysis of the protons from single π^0 photoproduction from deuterated butanol (a) and carbon (b) from the A2 data. Shown is the deposited energy in the PID versus the deposited energy in the Crystal Ball (left column) and the deposited energy in the Veto detectors versus the deposited energy in TAPS (right column). Columns: analysis channels (see labels). Upper row: no cut was applied to the data (all). Lower row: all cuts were applied to the data (acc.).

6.5.5 Double π^0 Analysis on the Free Proton

The quality of the particle identification of double π^0 photoproduction from the free proton will be discussed in parallel for the analyses of the A2 and CBELSA/TAPS data in order to allow for a direct comparison. The time of flight spectra for the inclusive and exclusive analyses are shown in Figure 6.74a for A2 and in Figure 6.74b for CBELSA/TAPS. For each dataset, the TOF spectra for the photons and protons for all initial event candidates (upper row) and for the final event selection (lower row) are shown. For both experiments, no significant background is present in the final distributions and typical spectra, as expected for photons and protons, are visible.

The initial spectra from the analysis of the CBELSA/TAPS data show a higher contamination from other particles, where a prominent photon band is visible in the proton spectrum. Nevertheless, the final spectra are of comparable quality as observed with the A2 data.

For both datasets, the initial photon bands do not show a lot of contamination from protons and only a slightly blurred background is visible that disappears once all cuts were applied. On the other hand, contamination from photons, electrons and a few charged pions are observed in the initial proton spectra, but they were also successfully removed by the analysis cuts. The spectra also demonstrate the difference of the kinematics compared to single π^0 photoproduction. As previously mentioned in Section 6.4.1, most of the recoil protons in single π^0 photoproduction obtain a high kinetic energy such that they can punch-through the detector or can be identified as neutrons. This was predominantly the case for proton forward angles and was observed in the TOF, ΔE versus E and PSA spectra of the TAPS detector. As seen in Figure 6.74, most of the protons are located in the typical proton band and only a few protons tend to have higher kinetic energies. Therefore, effects from punch-through are not to be expected and were not further investigated in this analysis.

The results of the pulse shape analysis are shown in Figure 6.75. As for the TOF analysis, the final spectra are free of background and present typical spectra for photons and protons. The contamination of nucleons in the initial photon spectra was removed by the analysis cuts. The prominent electron structure and the photon band in the proton PSA were partially removed by the exclusion zone or rejected by the analysis cuts. The curved structure that is visible in the nucleon PSA and also weakly in the photon PSA is a calibration effect, but is negligible as the calibration was determined and applied for every crystal individually and is only a visual effect in this figure.

The ΔE versus E spectra are shown in Figure 6.76. The initial spectrum from the Crystal Ball detector comprises mainly of the dominant proton band, and the traces from charged pions and electrons. Besides electrons, the spectra from TAPS and MiniTAPS do not contain a lot of background. The different analysis cuts similarly affect all spectra and result in a reliable identification.

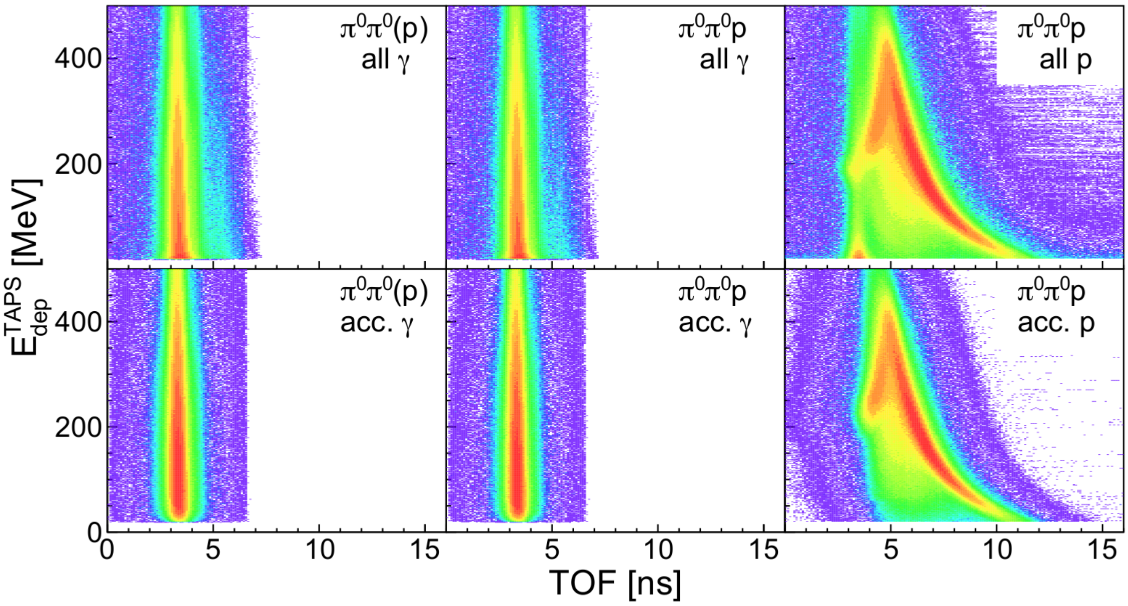

(a) A2 results from the hydrogen data

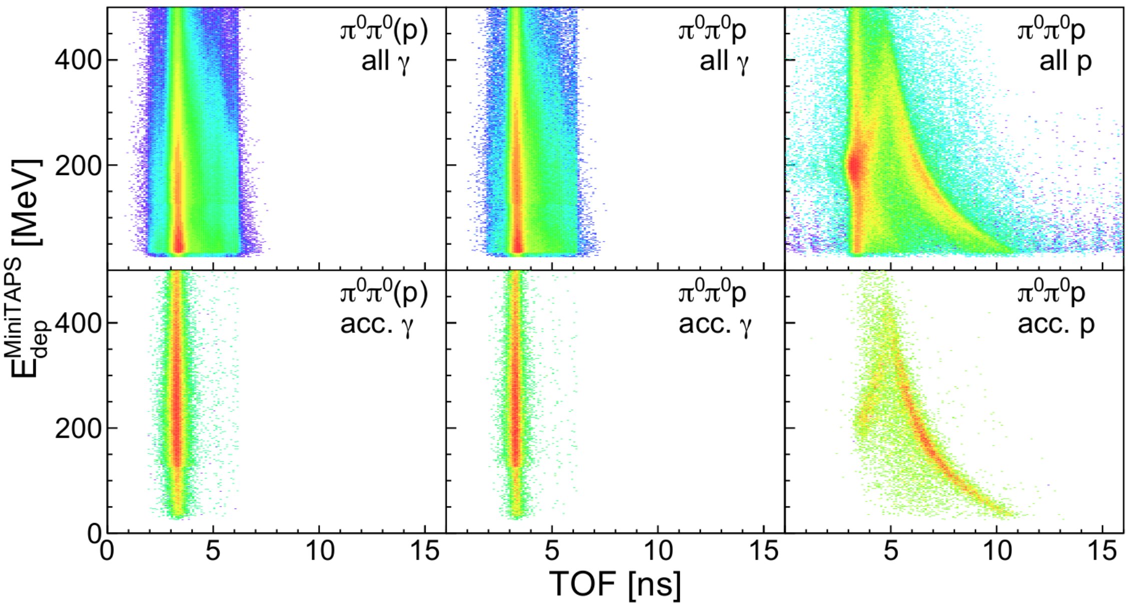

(b) CBELSA/TAPS results from the hydrogen data

Figure 6.74: TOF spectra for double π^0 photoproduction from free protons. Columns: analysis channels (see labels). Upper row: no cut was applied to the data (all). Lower row: all cuts were applied to the data (acc.). (a) Results from the A2 data. Shown is the deposited energy in the TAPS detector versus the time of flight. (b) Results from the CBELSA/TAPS data. Shown is the deposited energy in the MiniTAPS detector versus the time of flight.

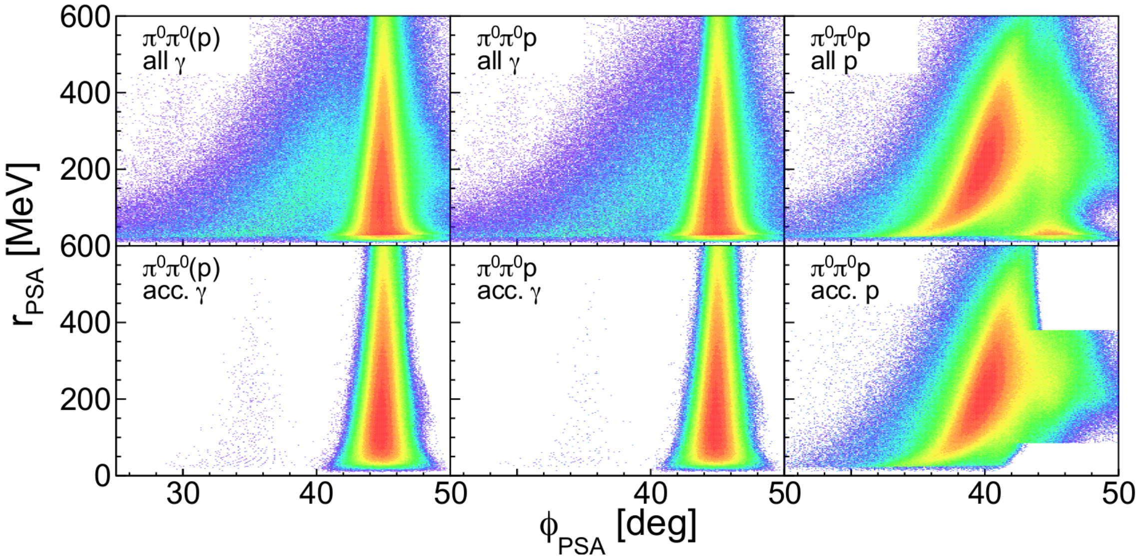

(a) A2 results from the hydrogen data

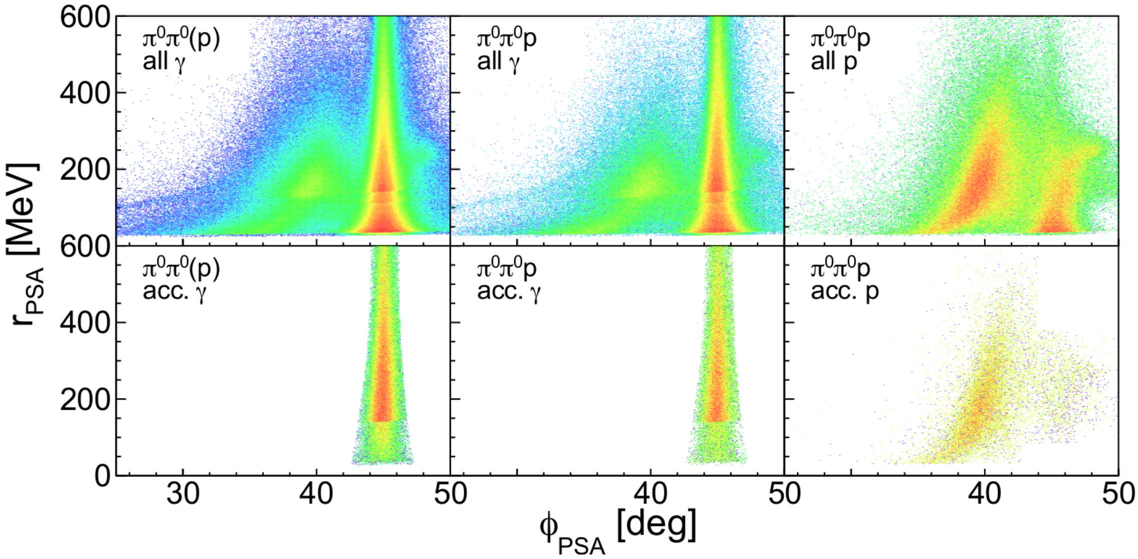

(b) CBELSA/TAPS results from the hydrogen data

Figure 6.75: PSA spectra for double π^0 photoproduction from free protons. Columns: analysis channels (see labels). Upper row: no cut was applied to the data (all). Lower row: all cuts were applied to the data (acc.). Shown is the PSA radius versus the PSA angle. (a) Results from the A2 data. (b) Results from the CBELSA/TAPS data.

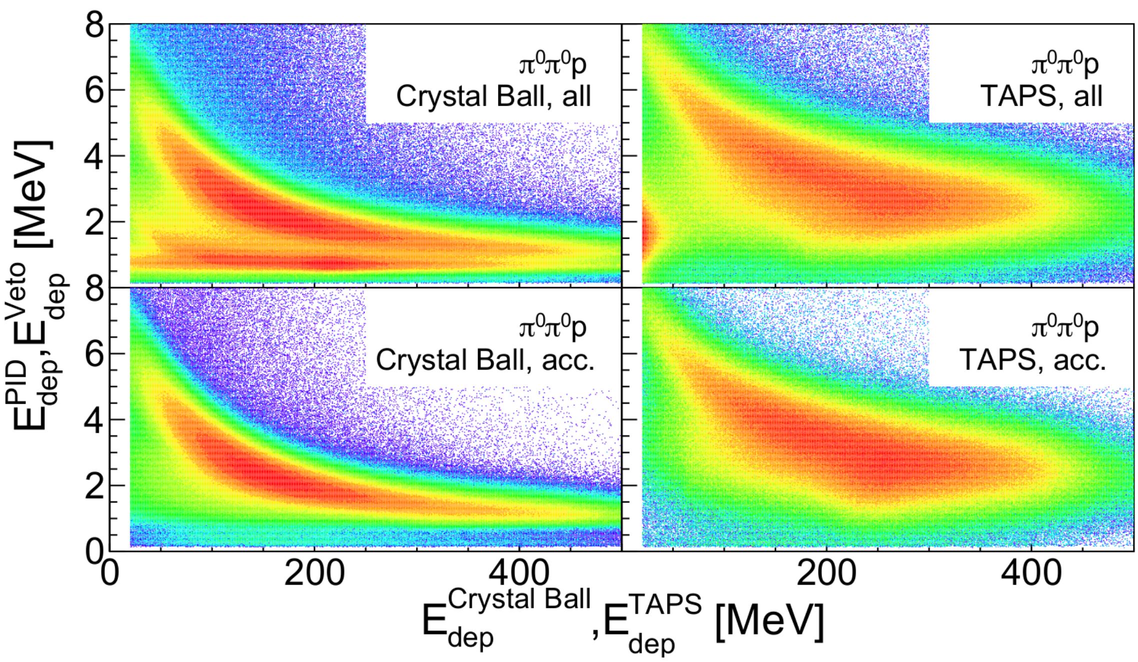

(a) A2 results from the hydrogen data

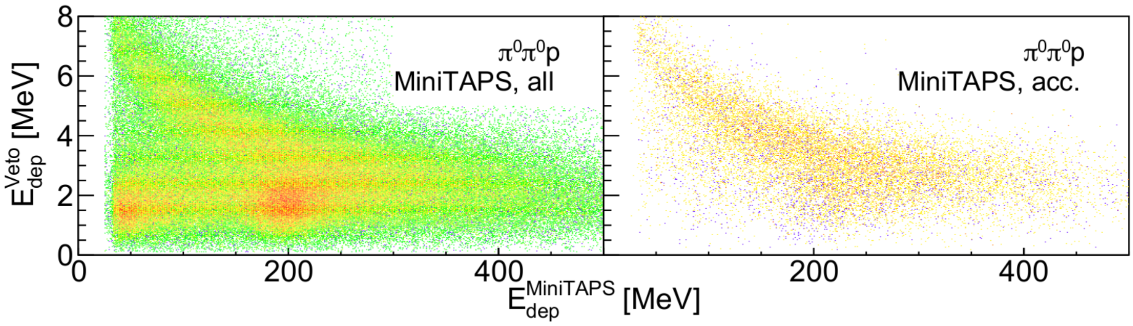

(b) CBELSA/TAPS results from the hydrogen data

Figure 6.76: ΔE versus E analysis of the protons from double π^0 photoproduction from free protons. (a) Results from the A2 data. Shown is the deposited energy in the PID versus the deposited energy in the Crystal Ball (left column) and the deposited energy in the Veto detectors versus the deposited energy in TAPS (right column). Upper row: All events. Lower row: Accepted events. (b) Results from the CBELSA/TAPS data. Shown is the deposited energy in the Veto detectors versus the deposited energy in MiniTAPS. Left column: no cut was applied to the data (all). Right column: all cuts were applied to the data (acc.).

6.5.6 Double π^0 Analysis on quasi-free Nucleons

The time of flight spectra for double π^0 photoproduction from quasi-free nucleons are presented in Figure 6.77a for the analysis of the A2 data and in Figure 6.77b for the analysis of the CBELSA/TAPS data. The characteristics and quality is very similar to the spectra from double π^0 photoproduction from free protons, except for the neutron channel, which was not available. The initial photon spectra from CBELSA/TAPS show slightly more background in the photon spectrum than is visible in those from A2, but after the different analysis cuts, all photon spectra are similarly free of contamination. The main background is from photons that were either identified as protons or that were sorted out by the χ^2 test, but are visible in the initial nucleon spectra. In addition, particles that were correctly identified, but originate from other reactions, also contribute to the initial spectra. After all cuts were applied, the photon bands in the nucleon spectra disappeared and typical nucleon spectra remain.

Figure 6.78 shows the results from the PSA for photons, protons, and neutrons. In the results from CBELSA/TAPS, a significant contribution from nucleons to the initial photon spectrum is visible, which disappeared due to the $\pm 3\sigma$ cut in the final spectra. The photon contribution to the nucleon spectra were eliminated by the analysis cuts. Reasonably clean spectra can be observed.
The ΔE versus E spectra for all detectors from A2 and CBELSA/TAPS do not exhibit significant background. The contamination from pions and electrons are not present in the final distributions and typical proton spectra are visible.

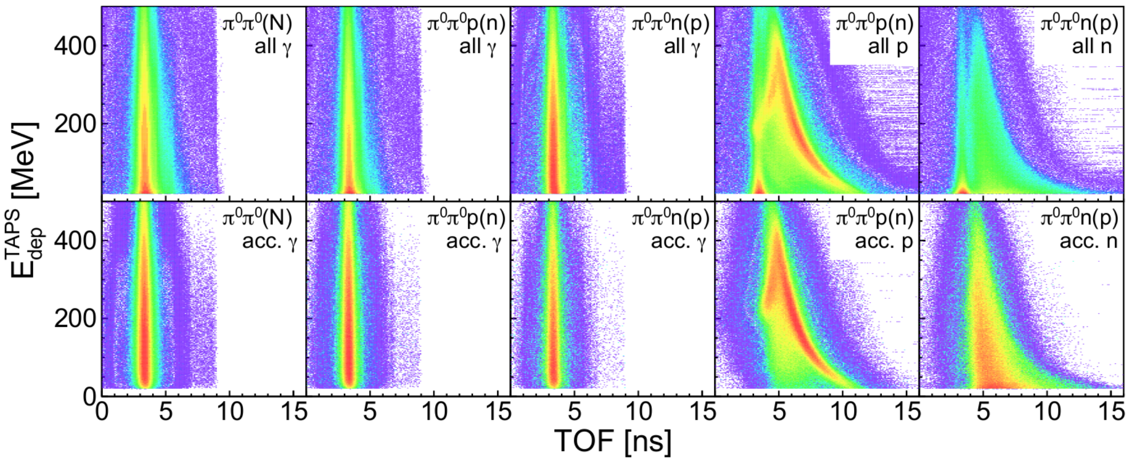

(a) A2 results from the deuterium data

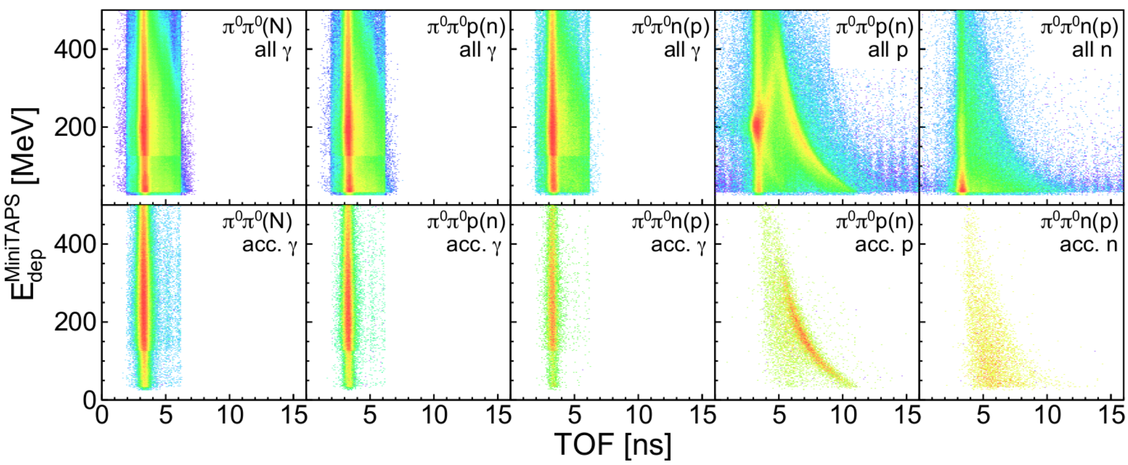

(b) CBELSA/TAPS results from the deuterium data

Figure 6.77: TOF spectra for double π^0 photoproduction from the deuteron. Columns: analysis channels (see labels). Upper row: no cut was applied to the data (all). Lower row: all cuts were applied to the data (acc.). (a) Results from the A2 data. Shown is the deposited energy in the TAPS detector versus the time of flight. (b) Results from the CBELSA/TAPS data. Shown is the deposited energy in the MiniTAPS detector versus the time of flight.

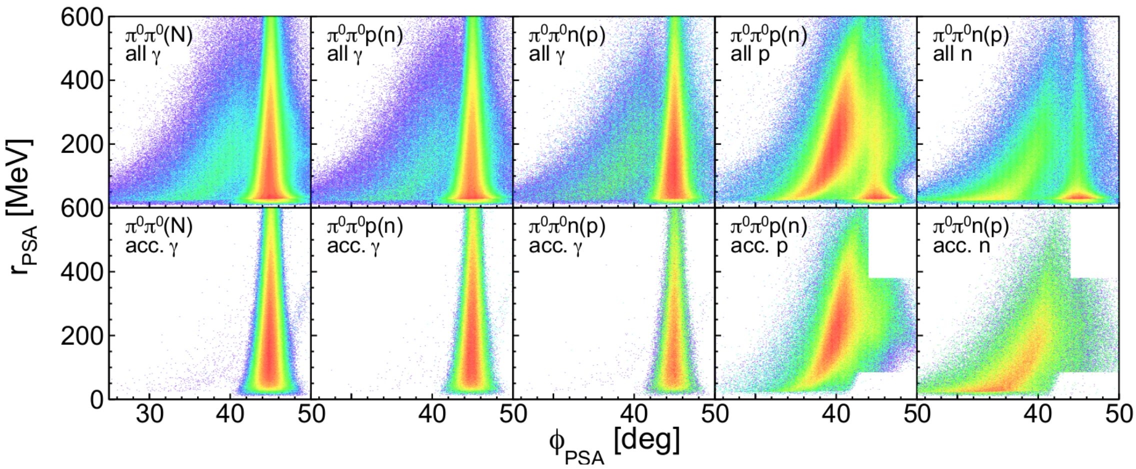

(a) A2 results from the deuterium data

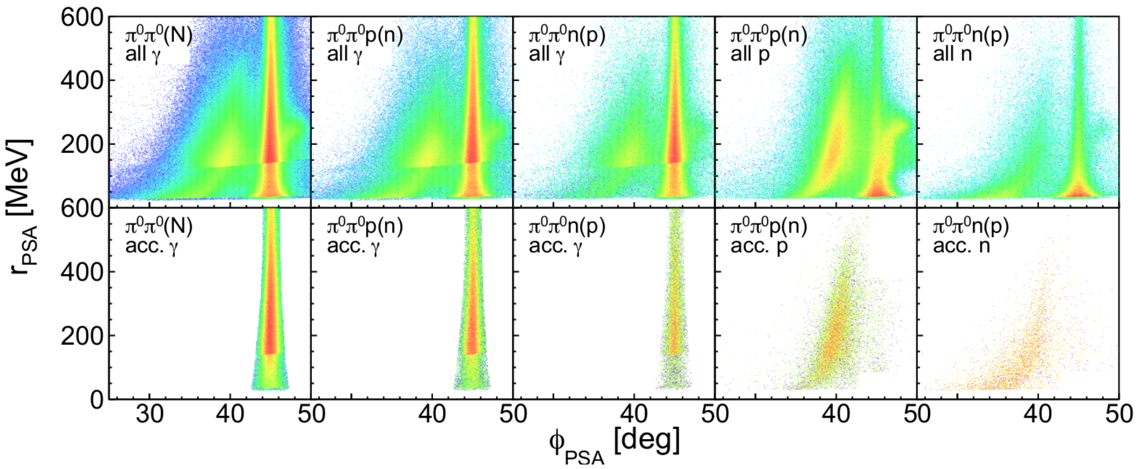

(b) CBELSA/TAPS results from the deuterium data

Figure 6.78: PSA spectra for double π^0 photoproduction from the deuteron. Columns: analysis channels (see labels). Upper row: no cut was applied to the data (all). Lower row: all cuts were applied to the data (acc.). Shown is the PSA radius versus the PSA angle. (a) Results from the A2 data. (b) Results from the CBELSA/TAPS data.

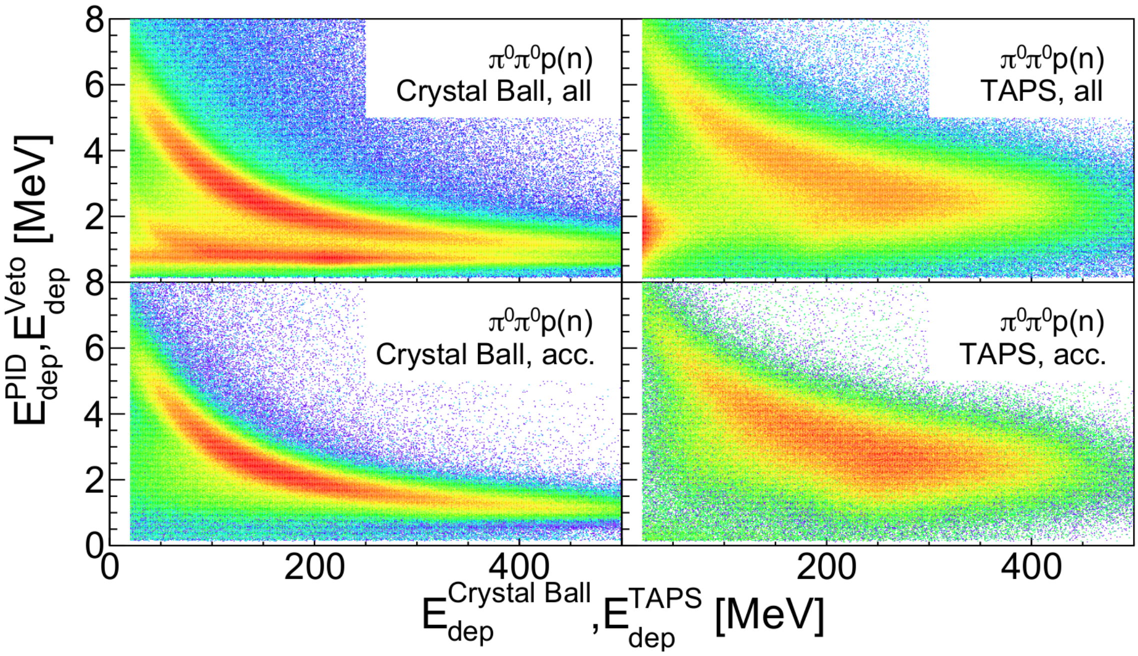

(a) A2 results from the deuterium data

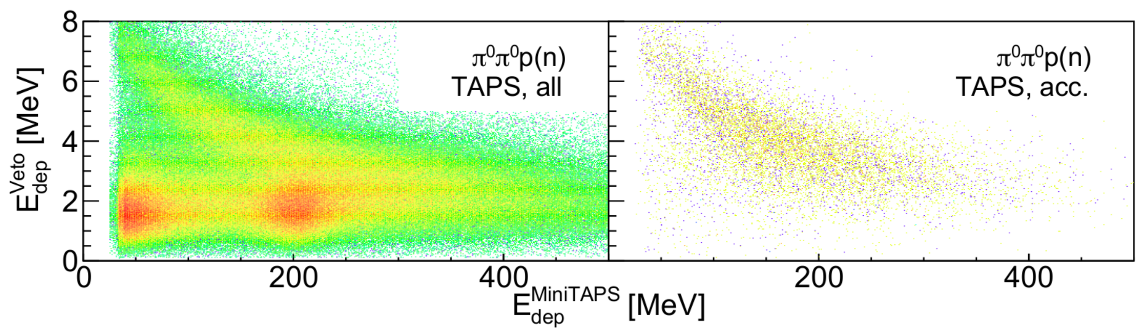

(b) CBELSA/TAPS results from the deuterium data

Figure 6.79: ΔE versus E analysis of the protons from double π^0 photoproduction from the deuteron. (a) Results from the A2 data. Shown is the deposited energy in the PID versus the deposited energy in the Crystal Ball (left column) and the deposited energy in the Veto detectors versus the deposited energy in TAPS (right column). Upper row: All events. Lower row: Accepted events. (b) Results from the CBELSA/TAPS data. Shown is the deposited energy in the Veto detectors versus the deposited energy in MiniTAPS. Left column: no cut was applied to the data (all). Right column: all cuts were applied to the data (acc.).

6.5.7 Double π^0 Analysis on Polarized Nucleons

The investigation of the quality of the particle identification in the analysis of double π^0 photoproduction from polarized nucleons from A2 and CBELSA/TAPS data will be discussed in the following sections. The relevant spectra obtained from the analysis of the deuterated butanol data will be compared with those from the analysis of the carbon foam data in order to have an estimation of the kinematical properties of the background reactions on the unpolarized nucleons. For this purpose, the quality of the identification of the A2 and CBELSA/TAPS analyses will be investigated individually.

A2 Analysis

For the polarized data, the situation is similar as discussed for double π^0 photoproduction from quasi-free nucleons and the same effect from reactions on carbon, as observed in single π^0 photoproduction, is visible. The time of flight spectra for the A2 analysis of the deuterated butanol data are shown in Figure 6.80a those of the carbon background measurement in Figure 6.80b. Observed contamination in the initial spectra are, as discussed before, mainly photons and electrons in the nucleon spectra that were reliably removed by the analysis cuts. In comparison to the spectra from the analysis of the deuterium data, more particles of lower energy are visible. This is also visible in the proton time of flight, which for deuterated butanol mostly comprises the proton band structure and a weaker high energy tail and for carbon is almost only characterized by the proton band.
The same observations and interpretations apply to the PSA (see Figure 6.81) and ΔE versus E spectra (see Figure 6.82). However, a weak photon band is visible in the neutron PSA spectrum from the carbon data (see the right spectrum in the bottom row of Figure 6.81b), which corresponds to 8% of all neutron events from the carbon sample. The deuterium spectrum (see Figure 6.78a) does not exhibit a notable contamination of the same percentage and the analysis cuts from deuterium were applied to the deuterated butanol data. Thus, it can be assumed, that possible contaminations from photons in the neutron PSA spectrum from the deuterated butanol data (see the right spectrum in the bottom row of Figure 6.81a), which are not visible, would result from reactions on the carbon nuclei and hence would be removed by the carbon subtraction (see Section 6.13.4).
The different conditions on the events in the analysis provide a sufficiently clean sample and typical spectra for all particles with little to no remaining background are visible.

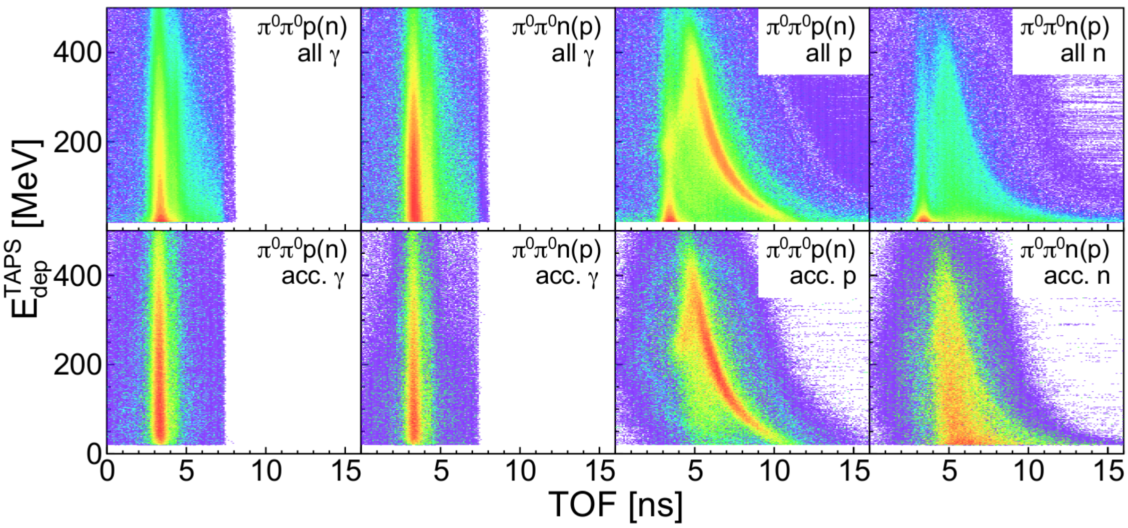

(a) A2 results from the deuterated butanol data

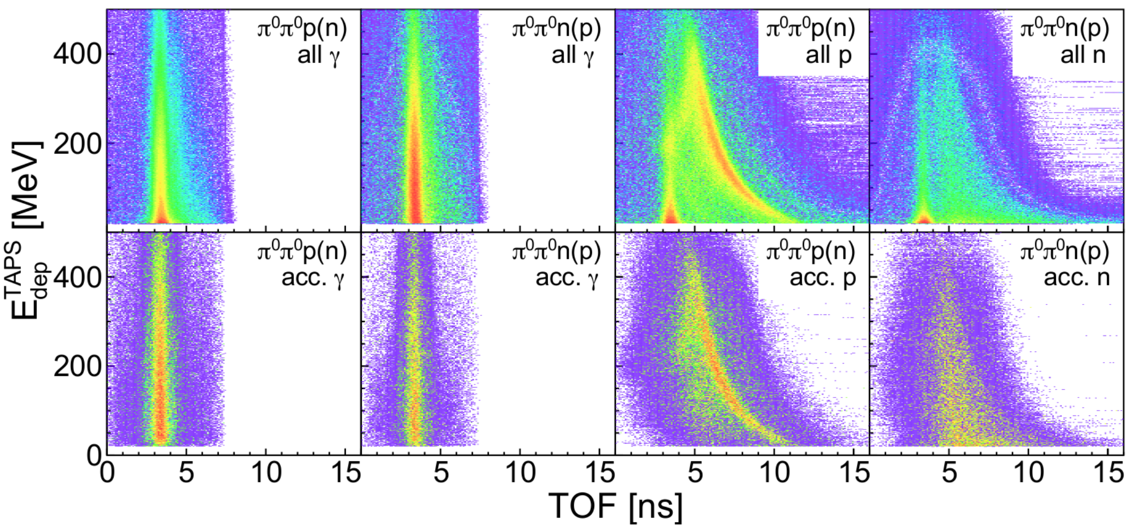

(b) A2 results from the carbon data

Figure 6.80: TOF spectra for double π^0 photoproduction from deuterated butanol (a) and carbon (b) from the A2 data. Shown is the deposited energy in the TAPS detector versus the time of flight. Columns: analysis channels (see labels). Upper row: no cut was applied to the data (all). Lower row: all cuts were applied to the data (acc.).

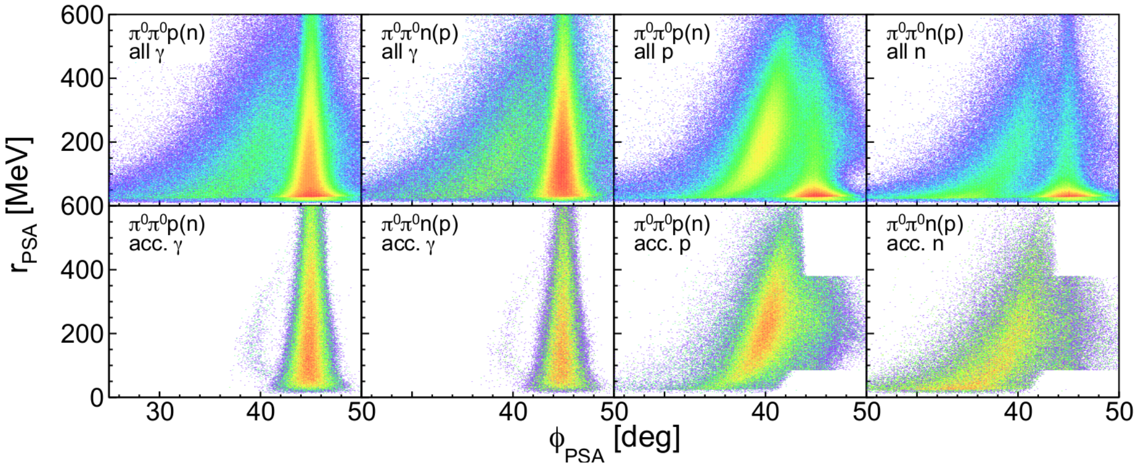

(a) A2 results from the deuterated butanol data

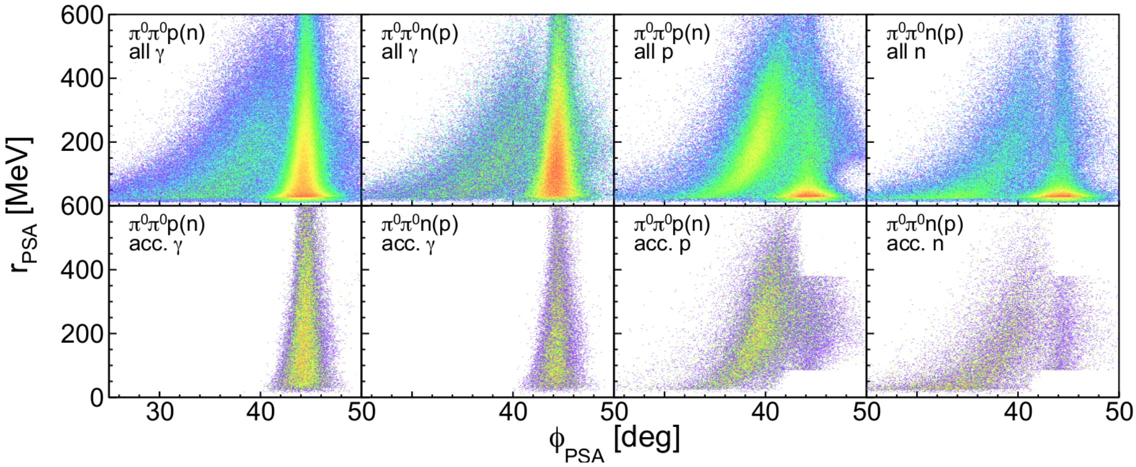

(b) A2 results from the carbon data

Figure 6.81: PSA spectra for double π^0 photoproduction from deuterated butanol (a) and carbon (b) from the A2 data. Shown is the PSA radius versus the PSA angle. Columns: analysis channels (see labels). Upper row: no cut was applied to the data (all). Lower row: all cuts were applied to the data (acc.).

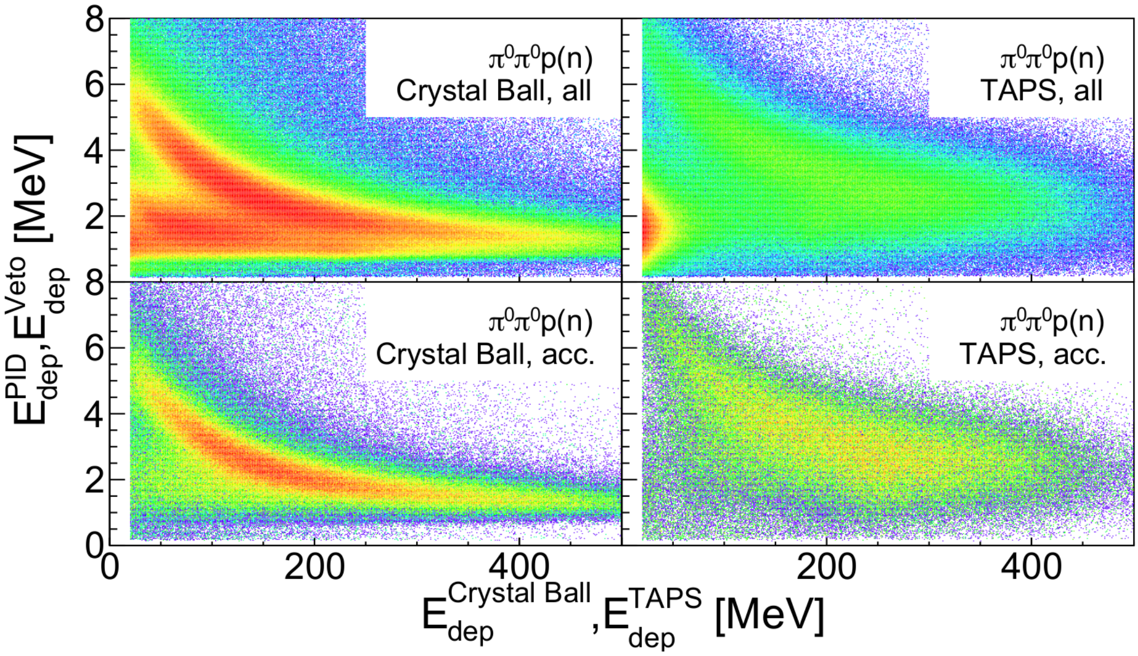

(a) A2 results from the deuterated butanol data

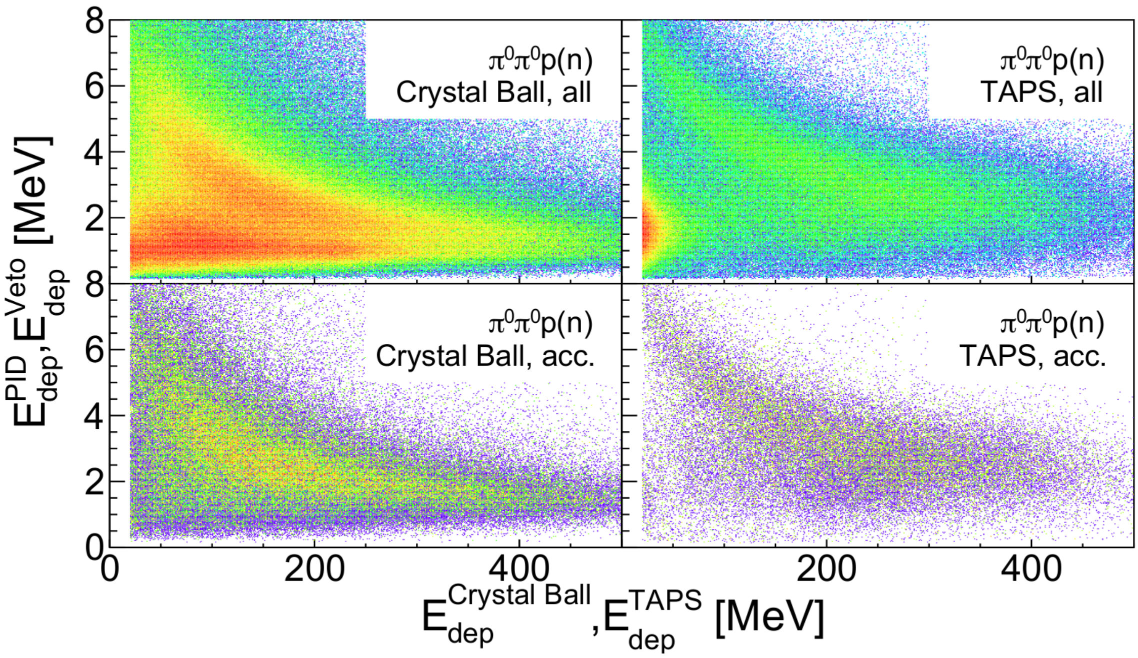

(b) A2 results from the carbon data

Figure 6.82: ΔE versus E analysis of the protons from double π^0 photoproduction from deuterated butanol (a) and carbon (b) from the A2 data. Shown is the deposited energy in the PID versus the deposited energy in the Crystal Ball (left column) and the deposited energy in the Veto detectors versus the deposited energy in TAPS (right column). Columns: analysis channels (see labels). Upper row: no cut was applied to the data (all). Lower row: all cuts were applied to the data (acc.).

CBELSA/TAPS Analysis

The TOF spectra of the analysis of polarized CBELSA/TAPS data are shown in Figure 6.83, the PSA spectra in Figure 6.84, and the ΔE versus E spectra in Figure 6.85.

In principle, the above mentioned discussions also apply to the analysis of the CBELSA/TAPS data. However, there are a few characteristics by which these spectra are different from the A2 ones. First, one immediately recognizes that all spectra from MiniTAPS exhibit the lack of events at low energies or PSA radii[5]. This is due to the fact that, in the deuterated butanol and carbon beamtimes, in order to suppress the high rates in the forward direction, the LED thresholds of the two most inner rings were set to high values.

The second difference can be observed in the TOF spectra. The oscillating structure in the time of flight is an artifact of the alternating field used for the acceleration of the electrons, as discussed in Section 6.3. The structure is only visible in the deuterated butanol and carbon data, since in the other beamtimes the tagger was in the first level trigger and hence, the effect cancelled out.

Besides these difference, which do not affect the quality of the particle identification, the analysis cuts result remove most of the background from charged pions, electrons, and photons. A negligible fraction of photons is visible in the final proton and neutron TOF spectra (see the two right spectra in the bottom row of Figure 6.83), which, most probably due to the poor statistics, is not visible in the spectra from the carbon data (see same spectrum in Figure 6.83). Slightly more contamination with photons is visible in the proton PSA spectrum (see second spectrum from the right in the bottom row of Figure 6.84a). A cut on the weak photon band would in principle be possible, but is not recommendable, as it could not be applied to the simulation as well. Since the fraction of the contamination is below 6% of all events and it only concerns the very forward angles covered by MiniTAPS, no further action was performed. Furthermore, a weak photon band is also visible in the corresponding spectrum from the carbon data (see Figure 6.84b) and thus might be removed by the carbon subtraction (see Section 6.13.4). The same discussion applies for the background contribution in the ΔE versus E spectra (see Figure 6.85a for the deuterated butanol data and Figure 6.85b for the carbon data).

[5] The PSA radius (see Equation (5.5) in Section 5.2.6) is related to the total deposited energy.

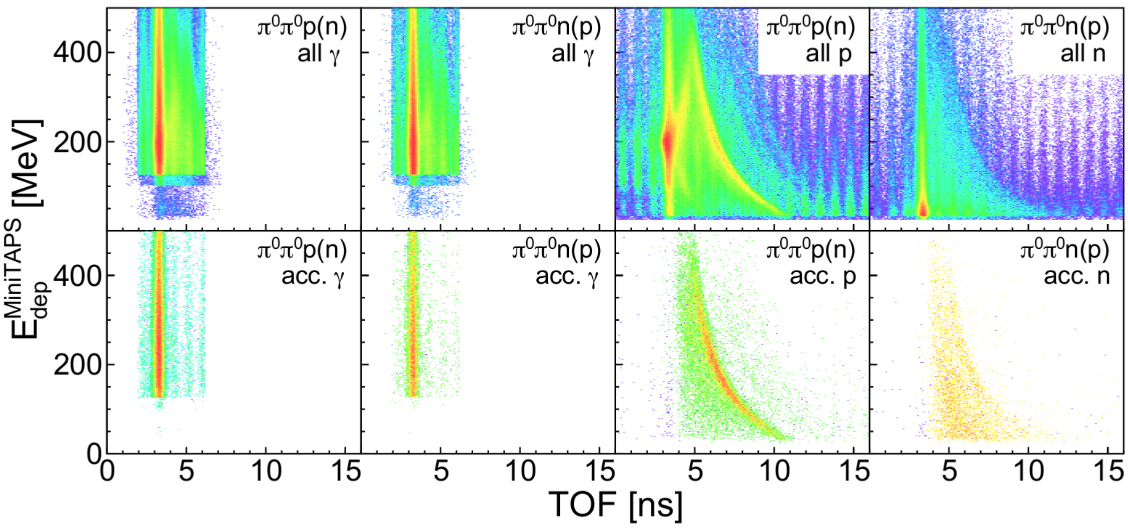

(a) CBELSA/TAPS results from the deuterated butanol data

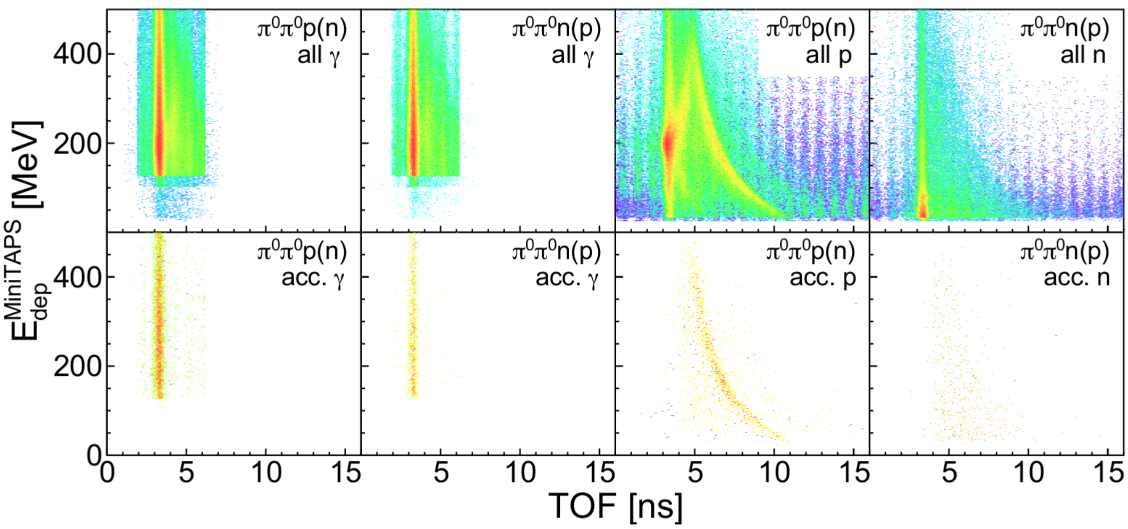

(b) CBELSA/TAPS results from the carbon data

Figure 6.83: TOF spectra for double π^0 photoproduction from deuterated butanol (a) and carbon (b) from the CBELSA/TAPS data. Shown is the deposited energy in the MiniTAPS detector versus the time of flight. Columns: analysis channels (see labels). Upper row: no cut was applied to the data (all). Lower row: all cuts were applied to the data (acc.).

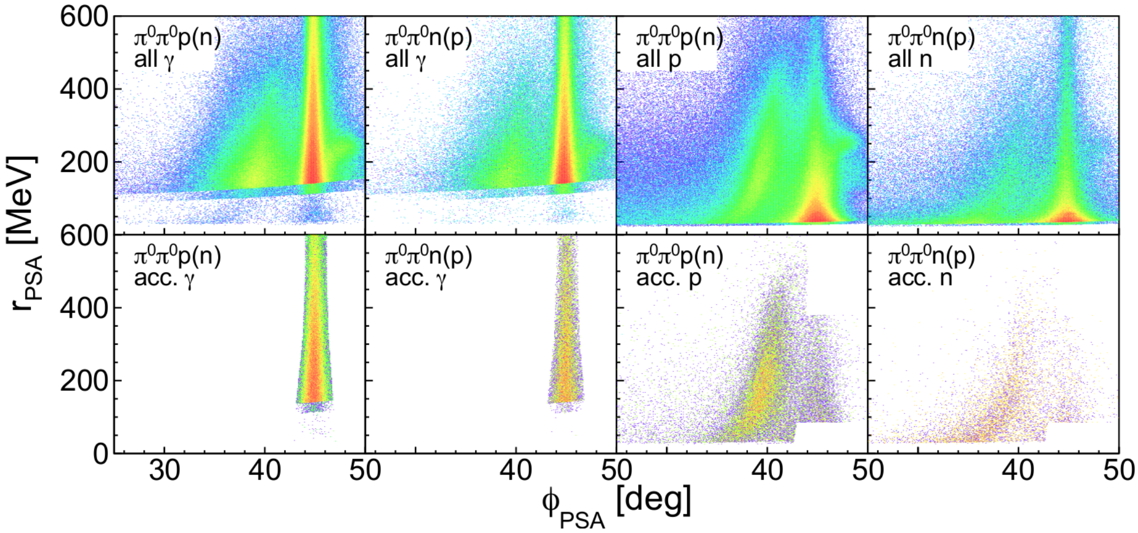

(a) CBELSA/TAPS results from the deuterated butanol data

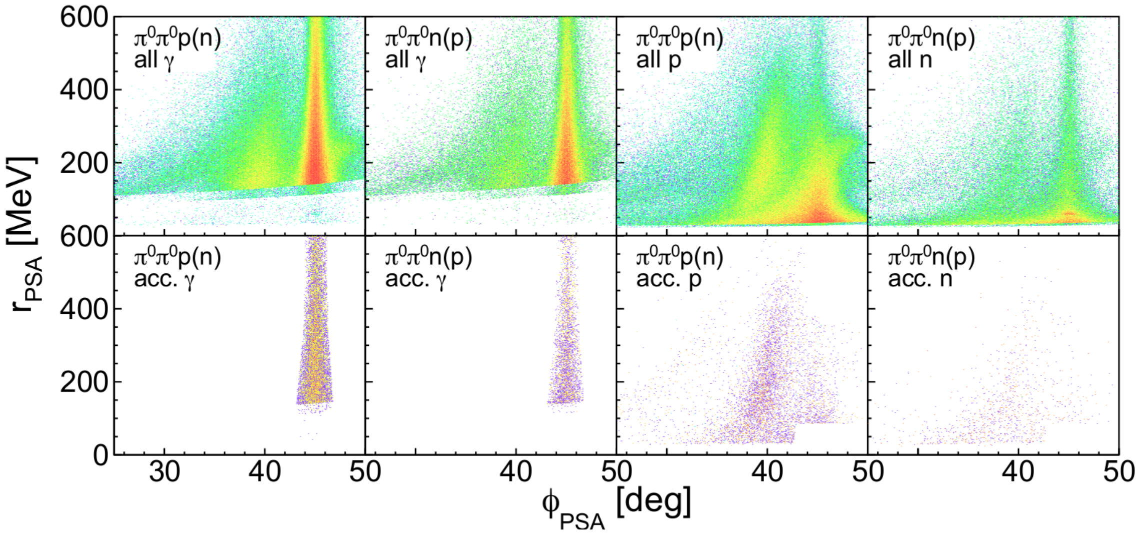

(b) CBELSA/TAPS results from the carbon data

Figure 6.84: PSA spectra for double π^0 photoproduction from deuterated butanol (a) and carbon (b) from the CBELSA/TAPS data. Shown is the PSA radius versus the PSA angle. Columns: analysis channels (see labels). Upper row: no cut was applied to the data (all). Lower row: all cuts were applied to the data (acc.).

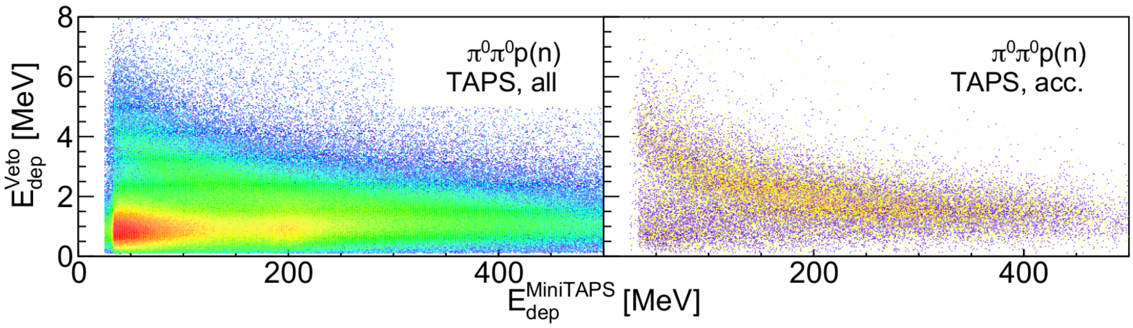

(a) CBELSA/TAPS results from the deuterated butanol data

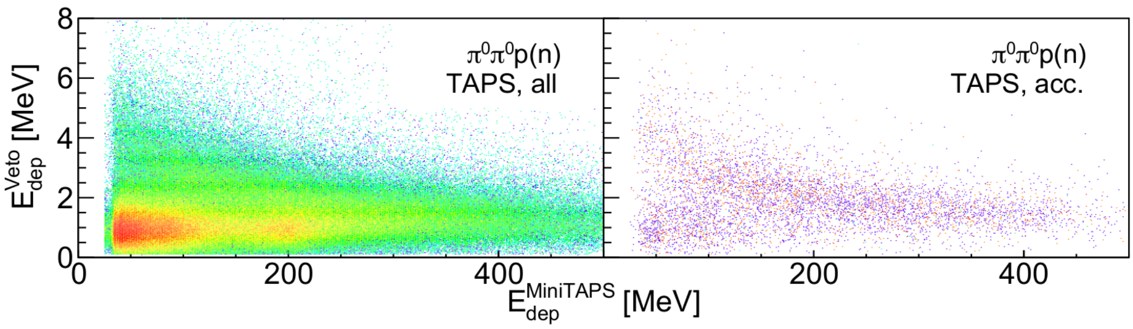

(b) CBELSA/TAPS results from the carbon data

Figure 6.85: ΔE versus E analysis of the protons from double π^0 photoproduction from deuterated butanol (a) and carbon (b) from the CBELSA/TAPS data. Shown is the deposited energy in the Veto detectors versus the deposited energy in MiniTAPS. Left column: no cut was applied to the data (all). Right column: all cuts were applied to the data (acc.).

6.6 Software Trigger

During the experiments, an initial selection of which events will be recorded was made by the hardware trigger, that was set up according to the aim of the experiment (see Sections 2.3.2, 2.3.3 for the trigger used at A2, Section 2.6.2 for that used in CBELSA/TAPS). Due to the imperfection of the detector setup and the electronics, not all particles can be detected and information can be lost. This has to be corrected by applying detection efficiencies (see Section 6.8) that are determined with the help of simulations. Therefore, the conditions of the hardware trigger need to be applied to the simulated data as well in order to have a simulation that is as close to the experiment as possible. For this purpose the software trigger was modeled in a way that all possible events that were rejected by the hardware trigger in the experiment were rejected in the software as well, i.e. in the analysis.
In order to allow for a better comparison between the results from reactions on the protons and from those on the neutrons, which is in particular important for the quasi-free inclusive analysis where the recoil nucleon is not required in coincidence, a more strict trigger was implemented in the software. Thereby the software trigger requires the trigger conditions to be fulfilled by the decay photons of the meson, whereas contributions from nucleons or other particles, as was the case in the experiment, were not considered.

6.6.1 Multiplicity Trigger

The requirement of a certain multiplicity is one of the main components of the hardware trigger. As previously discussed in Sections 2.3.2, 2.3.3, and 2.6.2, different conditions were set at the hardware level in order to correlate detector hits with clusters and thereby with the multiplicity. For the clustering at A2, the Crystal Ball detector was divided into 45 blocks, each of 16 neighboring crystals and TAPS was grouped into six sectors. A block of the Crystal Ball detector and a segment of TAPS then contributes to the multiplicity if at least one of its signals was above the set threshold value. At CBELSA/TAPS, the individual hits are compared to hit patterns which correspond to a certain multiplicity.
Depending on the beamtime that was analyzed, the multiplicity trigger in the software was extended by certain conditions on hits in the TAPS detector. TAPS elements from the most outer ring, as well as elements from the three most inner rings, were not considered for the multiplicity trigger decision if necessary in order to reduce the high rates close to the beam and to reduce inaccurate contributions from shower losses at the edge of the detector.
In order to check the trigger in the analysis, the multiplicity condition was verified with the decay photons of the mesons only. The signals of the involved photons in the individual crystals were compared to the thresholds that were obtained from the calibration of the data (see Sections 5.2.3, 5.2.8, and 5.2.9) and were also applied to the simulation. The individual total multiplicity conditions that were required for each experiment can be taken from Tables 2.5 - 2.8.

6.6.2 Crystal Ball Energy Sum Trigger

As already mentioned in the comparison of the experimental triggers from A2 and CBELSA/TAPS, in contrast to the Crystal Barrel detector at CBELSA/TAPS, the Crystal Ball detector at A2 is included in the first level trigger by means of the energy sum, i.e. the sum of the analog signals of all NaI(Tl) crystals. As this information was not available in the trigger system at CBELSA/TAPS[6], so this section only concerns the analysis of A2 data.

The implementation of the Crystal Ball energy sum trigger is especially important, as it strongly influenced the experimental data for events in which only a few particles were detected in the Crystal Ball detector. As long as this is not taken into consideration in the simulation, the determined detection efficiencies for such events will not be correct. By comparing the energy sum spectrum from the experimental data with that from the simulation, the threshold value as used in the experiment can be derived and applied to the simulation.
The Crystal Ball energy sum trigger is based on the sum of the analog signals of all NaI crystals, which is then compared to a threshold value that corresponds to a certain energy. As the threshold value is set in terms of voltage, since it is compared to analog and not digital signals, only uncalibrated raw signals have to be used for its consideration in the software trigger. For this purpose, the calibrated values in the analysis of data and simulation first had to be de-calibrated using the procedure described in [197, 204].
The Crystal Ball energy sum spectra for the different analyses of single and double π^0 photoproduction are shown in Figure 6.86 for the December 2007 beamtime. For the determination of the threshold value, the simulation was weighted with energy and angular dependent cross sections that were obtained from an initial analysis for which a fixed energy sum threshold value of 400 MeV was chosen. Weighting of the simulation is inevitable for the determination, since the energy sum strongly depends on the energy and the angular distribution of the reaction. As illustrated in the first and third row of Figure 6.86, the yield from data was then scaled to that from the simulation for energies above 400 MeV, where effects from the energy sum trigger are negligible. The ratio of the distribution from data and simulation are presented in the second and fourth row of Figure 6.86 and were used for the threshold determination. These distributions clearly show the effect of the threshold on the data. At the beginning, where the energy is well below the threshold value, the distribution is zero, i.e. all events were rejected, and at higher energies the ratio is around one, i.e. the threshold is always exceeded. In an ideal setup, the distribution should have the shape of a step function, where in reality the fixed threshold value is smeared out due to electronic fluctuations. The ratio was then fit with a cumulative distribution

[6]Currently the Crystal Barrel detector readout is upgraded with avalanche photo diodes which will then allow for an implementation of an analog to the energy sum on the first level trigger decision.

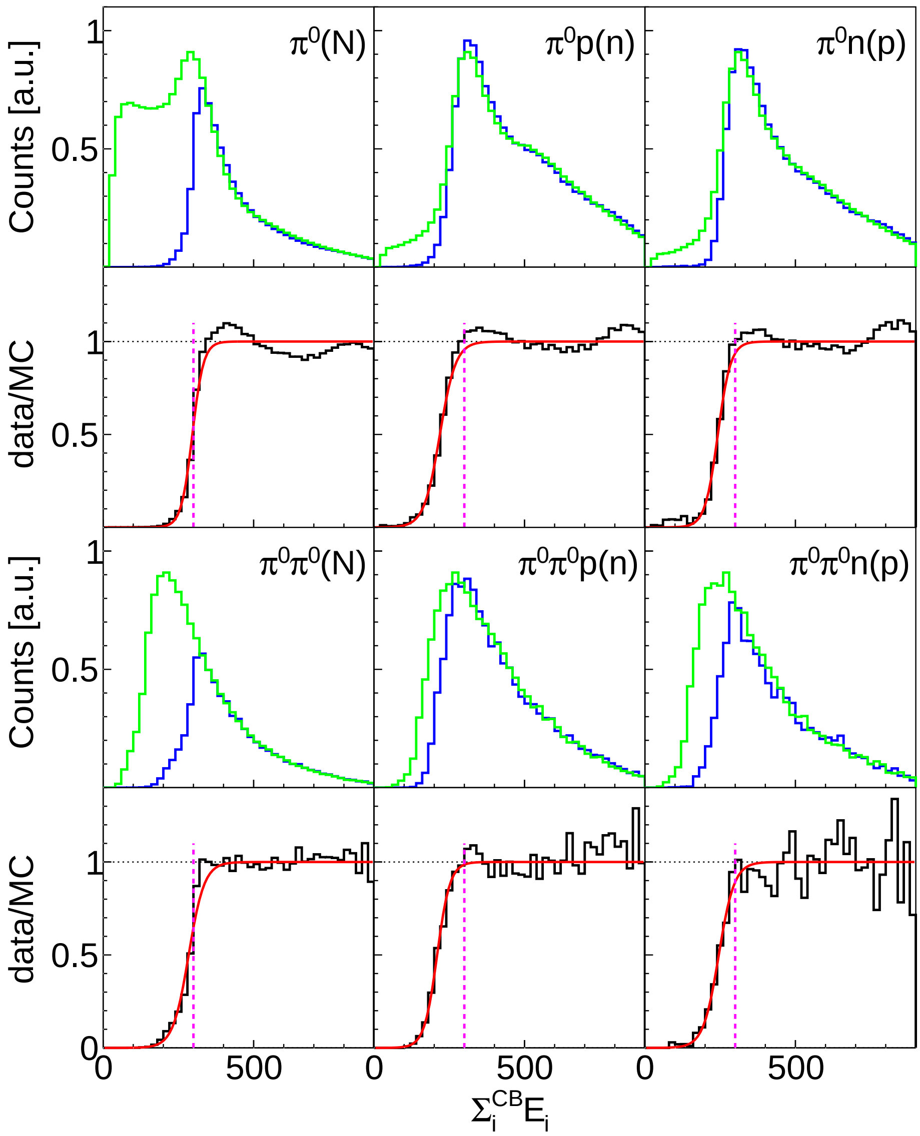

Figure 6.86: Determination of the Crystal Ball energy sum threshold for the A2 analysis for the example of the December 2007 deuterium beamtime. Columns: quasi-free inclusive and exclusive analysis channels. First and second row: single π^0 photoproduction. Third and fourth row: double π^0 photoproduction. First and third row: raw energy sum distribution for photons from data (blue histogram) and simulation (green histogram). Second and fourth row: ratio of the distribution from data and simulation (black histogram) and resulting fit with Equation (6.11) (red line). Dashed magenta line: hardware threshold.

function (red line in Figure 6.86) [205]:

$$f(E_{tot}^{CB}) = \frac{A}{1 + \exp\left(\frac{\overline{E} - E_{tot}^{CB}}{B}\right)} \ , \tag{6.11}$$

where A and B are fit parameters and correspond to the height and width of the function. $\overline{E}$ corresponds to the energy sum value where $f(E_{tot}^{CB}) = A/2$ and approximately corresponds to the value of the experimentally applied threshold value. The values from the fit vary from 250 to 300 MeV, which is close to the experimental value of 300 MeV. The fit functions were then used for the application of the Crystal Ball energy sum threshold in the analysis of the corresponding simulation. For this purpose, a random number in the interval [0,1] was generated for every event and compared to the value of the function evaluated at the actual energy sum value. If the random number was larger than the function value, the event was rejected. In this way, events below the threshold value were suppressed and events accepted above and in between increasingly accepted.

6.7 Reconstruction of the Final State Invariant Mass W

Instead of the incident photon beam energy E_γ, the center of mass energy $W = \sqrt{s}$ is often used as the significant quantity for the description of the energy dependence of an observable. For a reaction initiated by a photon beam of four momentum $\mathbb{P}_\gamma$ on a target of four momentum $\mathbb{P}_T$, producing n particles of four momentum $\mathbb{P}_1, \ldots, \mathbb{P}_n$, W is directly given from its definition as a Mandelstam variable:

$$W = \sqrt{s} = \sqrt{(\mathbb{P}_\gamma + \mathbb{P}_T)^2} = \sqrt{\left(\sum_{i=1}^{n} \mathbb{P}_i\right)^2} \tag{6.12}$$

For a target at rest, Equation (6.12) can be directly calculated from the initial state particles

$$\begin{aligned} W = \sqrt{s} &= \sqrt{(\mathbb{P}_\gamma + \mathbb{P}_T)^2} \\ &= \sqrt{2m_T E_\gamma + m_T^2} \end{aligned} \tag{6.13}$$

However, for reactions on quasi-free nucleons which are bound inside nuclei and hence exhibit Fermi motion, Equation (6.13) is not valid since the target is not at rest. The nucleons have a Fermi momentum that varies according to a probability density distribution (see section 3.4.1 for details and examples). Equation (6.13) can still be used when neglecting the Fermi momentum of the participant nucleon, but the results will be smeared out, which makes a comparison with models difficult. Nevertheless, the center of mass energy can be reconstructed from the invariant mass of the final state:

$$W = \sqrt{s} = \sqrt{\left(\sum_{i=1}^{n} \mathbb{P}_i\right)^2} \ . \tag{6.14}$$

In this case, effects from Fermi motion are eliminated, but as the reconstructed final state particles are involved in the calculation, the results are influenced by the experimental resolution instead.

For the determination of $W = \sqrt{s}$, knowledge of the four momenta of all final state particles is necessary. As already mentioned in Section 6.4.1, the experimental setup is optimized for the detection of photons and hence the reconstruction of nucleon four momenta can lead to rather large systematic uncertainties, especially in cases where the nucleon did not fully deposit its kinetic energy in the detector. In addition, the measurement of the impact position of the nucleon in the detector is less precise than for photons. This is due to the fact that the typical cluster size of nucleons is much smaller than that of photons (see Figure 6.1). Therefore, the position reconstruction depends on the center of mass of fewer crystals, which is less precise. In such cases, the kinetic energy of the recoil nucleon can be recalculated with Equation (B.29) from Section B.3. The recalculation is also possible by using the time of flight information, but was not used in this work. Details and results about the energy reconstruction with the time of flight can be found in Ref. [100].

6.8 Detection Efficiency Correction

The detection efficiency correction is necessary to correct the imperfect performance of the experimental detector setup. Due to holes in the setup or insensitive materials, not all particles and occurred reactions were registered during data taking. By simulating the reaction with a virtual experimental setup as implemented in the simulation, the comparison of all simulated events with those that have been registered, the inefficiency of the experiment can be determined and subsequently corrected. This requires the virtual setup to be in agreement with the real one, which is not easy to achieve as small differences in the geometry of the setup or slight differences in the material compositions or properties are unavoidable. In particular, the detection of nucleons, as required for the exclusive analyses, is strongly sensitive to variances, which show the importance of the choice of the appropriate physics model used in the simulation (see Sections 3.2.2 and 3.3.2). Nevertheless, the residual discrepancies afford special consideration by means of an additional nucleon detection efficiency correction, as discussed in Section 6.8.3. Thereby the analysis of $\pi^0\pi^0$ photoproduction from free protons using the hydrogen data did not only serve for a cross check of the analysis procedure, but also for an examination of the quality of the nucleon detection efficiency. The determination of the detection efficiency and the necessary corrections will be presented and discussed in the following sections.

The simulations used for the determination of the efficiency corrections were carried out within the simulation frameworks `A2` (based on `GEANT4` and used for the simulation of A2 data, see Section 3.2.2) and `CBGEANT` (based on `Geant3.21` and used for the simulation of CBELSA/TAPS data, see Section 3.3.2) with the corresponding virtual geometry of the setup as shown for the A2 setup in Figure 3.2 and for the CBELSA/TAPS setup in Figure 3.8. Detection efficiencies were then determined as a function of the polar angle $\cos(\theta^*_m)$ of the meson m (π^0 or $\pi^0\pi^0$) in the center of mass frame and for the incident photon energy E_γ and also for the final state invariant mass $W = \sqrt{s}$. The efficiencies were determined for each individual angular and energy bin, used for the extraction of the excitation functions. By comparing the generated N_{gen} with the detected events N_{det}, the effective efficiency ε of the detection of the reaction can be determined by:

$$\varepsilon\left(E_{\text{det}}, \cos(\theta^*_{m,\text{det}})\right) = \frac{N_{\text{det}}\left(E_{\text{det}}, \cos(\theta^*_{m,\text{det}})\right)}{N_{\text{gen}}\left(E_{\text{gen}}, \cos(\theta^*_{m,\text{gen}})\right)} \,. \tag{6.15}$$

Effective means that the reconstructed and not generated values of the polar angle $\cos(\theta^*_{m,\text{det}})$ and the energy E_{det} of the detected events were used for the calculation of Equation (6.15). This ensures that effects from the resolution are correctly taken into account.

For every reaction channel, the reaction of interest was generated for $20\cdot10^6$ to $100\cdot10^6$ events with the event generator `Pluto` (see Section 3.4.1) for photon energies from the production threshold (see Table 6.2) up to the energy of the last available tagger channel. For the reactions on quasi-free targets, the Fermi momentum was sampled according to the corresponding probability density distribution of the Fermi model (see Section 3.4.1).

In order to account for the bremsstrahlung spectrum of the incident photon distribution, the events were weighted with $1/E_\gamma$, whereas the meson decays were phase space distributed. Additional weighting of the events with cross sections was not performed in the event generators itself, as only an appropriate model for single π^0 photoproduction is available from the SAID partial wave analysis [39]. Instead, cross sections were determined in a first step with phase space event generators (except for the applied bremsstrahlung spectrum), which were then used as weights in the analysis of the simulation.

The `Pluto` output datafile contains the four momenta of the final state particles for each event that was then used as input for the corresponding simulation. Additional information about the reaction vertices were provided by the choice of a random position within a cylindrical volume of the same length as the target cell and diameter of the beam. For every event, the simulation then simulates the passage of the available particles through the virtual detector system and according to the physics model (see Sections 3.2.2 and 3.3.2), determines the amount of energy that was deposited at a certain time in a detector component. The output of the simulation is the same format as the experimental data and can then be directly and identically analyzed with the same analysis software.

6.8.1 Detection Efficiency for Double π^0 Photoproduction

The determination of the detection efficiencies for double π^0 photoproduction is complicated by the presence of different production mechanisms of the $\pi^0\pi^0 N$ final state. Depending on the incident photon energy, the final state can be achieved not only by a direct phase space decay of a low lying resonance R, i.e. $\gamma N \rightarrow R \rightarrow \pi^0\pi^0 N$, but also via sequential decays from higher lying resonances R' according to

$\gamma N \rightarrow R' \rightarrow R\pi^0 \rightarrow N\pi^0\pi^0$. Several sequential decays of different probabilities and branching ratios into this final state exist and each of them exhibits different energy and angular distributions. Therefore, the detection efficiency depends on the number and intensity of the contributions from the individual sequential decays. For this purpose, in addition to the direct phase space decay $\gamma N \rightarrow R \rightarrow N\pi^0\pi^0$, the most prominent sequential decay reactions with the $\pi^0\pi^0 N$ final state in the relevant energy range were simulated, i.e. contributions from $\gamma N \rightarrow R' \rightarrow \Delta(1232)3/2^+\pi^0 \rightarrow N\pi^0\pi^0$ and $\gamma N \rightarrow R' \rightarrow N(1520)3/2^-\pi^0 \rightarrow N\pi^0\pi^0$. The strength of each individual contribution was then determined by an investigation of the invariant mass of the nucleon-pion system. As in such cases one of the pions was produced together with the intermediate resonance and the other from the decay of the latter, signatures from the different contributions can be directly extracted from the shape of the nucleon-pion invariant mass spectra.
Such a spectrum was determined from the data, i.e. where all different possible decays contribute, and from each individual simulation. At this stage, the size of the contributions were not known and hence no detection efficiency could be established, such that an unnormalized raw mass distributions $dN(E_\gamma, \cos(\theta^*_{2\pi^0}))/dm_{\pi^0 N}$ had to be used. For every energy and angular bin, the line shape of the distributions from each simulation was then fit to the line shape of the data according to

$$\begin{aligned}\left(\frac{dN(E_\gamma,\cos\theta^*_{2\pi^0})}{dm_{\pi^0 N}}\right)_{\text{data}} = \; & a(E_\gamma,\cos\theta^*_{2\pi^0})\cdot\left(\frac{dN(E_\gamma,\cos\theta^*_{2\pi^0})}{dm_{\pi^0 N}}\right)_{\text{phase space}} + \\ & b(E_\gamma,\cos\theta^*_{2\pi^0})\cdot\left(\frac{dN(E_\gamma,\cos\theta^*_{2\pi^0})}{dm_{\pi^0 N}}\right)_{\Delta(1232)\pi^0} + \\ & c(E_\gamma,\cos\theta^*_{2\pi^0})\cdot\left(\frac{dN(E_\gamma,\cos\theta^*_{2\pi^0})}{dm_{\pi^0 N}}\right)_{N(1520)\pi^0},\end{aligned} \tag{6.16}$$

in order to determine the relative contributions a, b and c of the individual reactions to the $\pi^0\pi^0 N$ final state. In addition, a, b and c were normalized to meet the condition $a + b + c = 1$. The resulting spectra with the fit contributions for the analysis of double π^0 photoproduction from quasi-free protons and neutrons inside deuterium for the analysis of A2 data are shown in Figure 6.87 and for the analysis of CBELSA/TAPS data in Figure 6.88. The individual contributions are denoted with colored lines, i.e. phase space $\gamma N \rightarrow R \rightarrow N\pi^0\pi^0$ (green) and sequential decays via $\Delta(1232)3/2^+$ (magenta) and via $N(1520)3/2^-$ (cyan). The sum of all fit line shapes (black) is in good agreement with the data of the proton (blue upward triangles) and neutron (red downward triangles). The spectra show the contributions from sequential decays at the corresponding invariant mass of the pion-nucleon system and the characteristic line shape of each individual contribution.
As for the detection efficiencies, the relative contributions $a(E_\gamma, \cos\theta^*_{2\pi^0})$, $b(E_\gamma, \cos\theta^*_{2\pi^0})$, $c(E_\gamma, \cos\theta^*_{2\pi^0})$ were determined for the same energy and angular bins as used for the extraction of the excitation functions. The detection efficiency was then determined individually for every simulated contribution. Using the relative contributions from the fit of the pion-nucleon invariant mass, the overall detection efficiency ε_{all} was

determined as follows:

$$\varepsilon_{all} = a \cdot \varepsilon_{\text{phase space}} + b \cdot \varepsilon_{\Delta(1232)\pi^0} + c \cdot \varepsilon_{N(1520)\pi^0} \ . \tag{6.17}$$

6.8.2 Detection Efficiency for Helicity Dependent Double π^0 Photoproduction

The procedure for the determination of the detection efficiency for double π^0 photoproduction by considering contributions from sequential decays (see Section 6.8.1) can be directly applied to the analysis of polarized data. However, even though the same sequential decays are possible and contribute to the final state, energy and angular distributions might be affected by the spin configuration of the beam and target. For this reason, pion-nucleon invariant mass distributions were determined individually for both helicity states 1/2 (beam and target spin antiparallel) and 3/2 (beam and target spin parallel). For both configurations, the fit procedure discussed in Section 6.8.1 was carried out. As the measured distributions at this stage still contain contributions from the reactions on the unpolarized nucleons of the carbon and oxygen nuclei, the yield from the analysis of the carbon data was added as an additional fit contribution.

$$\begin{aligned}
\left(\frac{dN(E_\gamma, \cos\theta^*_{2\pi^0})}{dm_{\pi^0 N}}\right)_{\text{data}} = \; & a(E_\gamma, \cos\theta^*_{2\pi^0}) \cdot \left(\frac{dN(E_\gamma, \cos\theta^*_{2\pi^0})}{dm_{\pi^0 N}}\right)_{\text{phase space}} + \\
& b(E_\gamma, \cos\theta^*_{2\pi^0}) \cdot \left(\frac{dN(E_\gamma, \cos\theta^*_{2\pi^0})}{dm_{\pi^0 N}}\right)_{\Delta(1232)\pi^0} + \\
& c(E_\gamma, \cos\theta^*_{2\pi^0}) \cdot \left(\frac{dN(E_\gamma, \cos\theta^*_{2\pi^0})}{dm_{\pi^0 N}}\right)_{N(1520)\pi^0} + \\
& d(E_\gamma, \cos\theta^*_{2\pi^0}) \cdot \left(\frac{dN(E_\gamma, \cos\theta^*_{2\pi^0})}{dm_{\pi^0 N}}\right)_{\text{carbon}} .
\end{aligned} \tag{6.18}$$

Thereby the carbon distribution was only used for the fit and the fit parameters were also normalized in order to fulfill the condition $a + b + c = 1$. The result is shown in Figure 6.89 for the A2 data and in Figure 6.90 for the CBELSA/TAPS data. In order to allow for a better comparison, the pion-nucleon invariant mass distributions for both helicity states are shown in the same figure. As can be seen in Figures 6.89 and 6.90, the distributions exhibit a slight helicity dependence, especially at higher incident photon energies. This is better visible in the distributions from the CBELSA/TAPS analysis, although in this case the statistics are rather poor. Absolutely normalized helicity dependent invariant mass distributions will be shown in section 7.5.3.

As for the unpolarized analysis, the efficiencies ε^i_{all}, where $i = 1/2, 3/2$, were then determined by the summation of the relative individual contributions according to the fit result:

$$\varepsilon^i_{all} = a \cdot \varepsilon^i_{\text{phase space}} + b \cdot \varepsilon^i_{\Delta(1232)\pi^0} + c \cdot \varepsilon^i_{N(1520)\pi^0} \qquad \text{where } i = \frac{1}{2}, \frac{3}{2}. \tag{6.19}$$

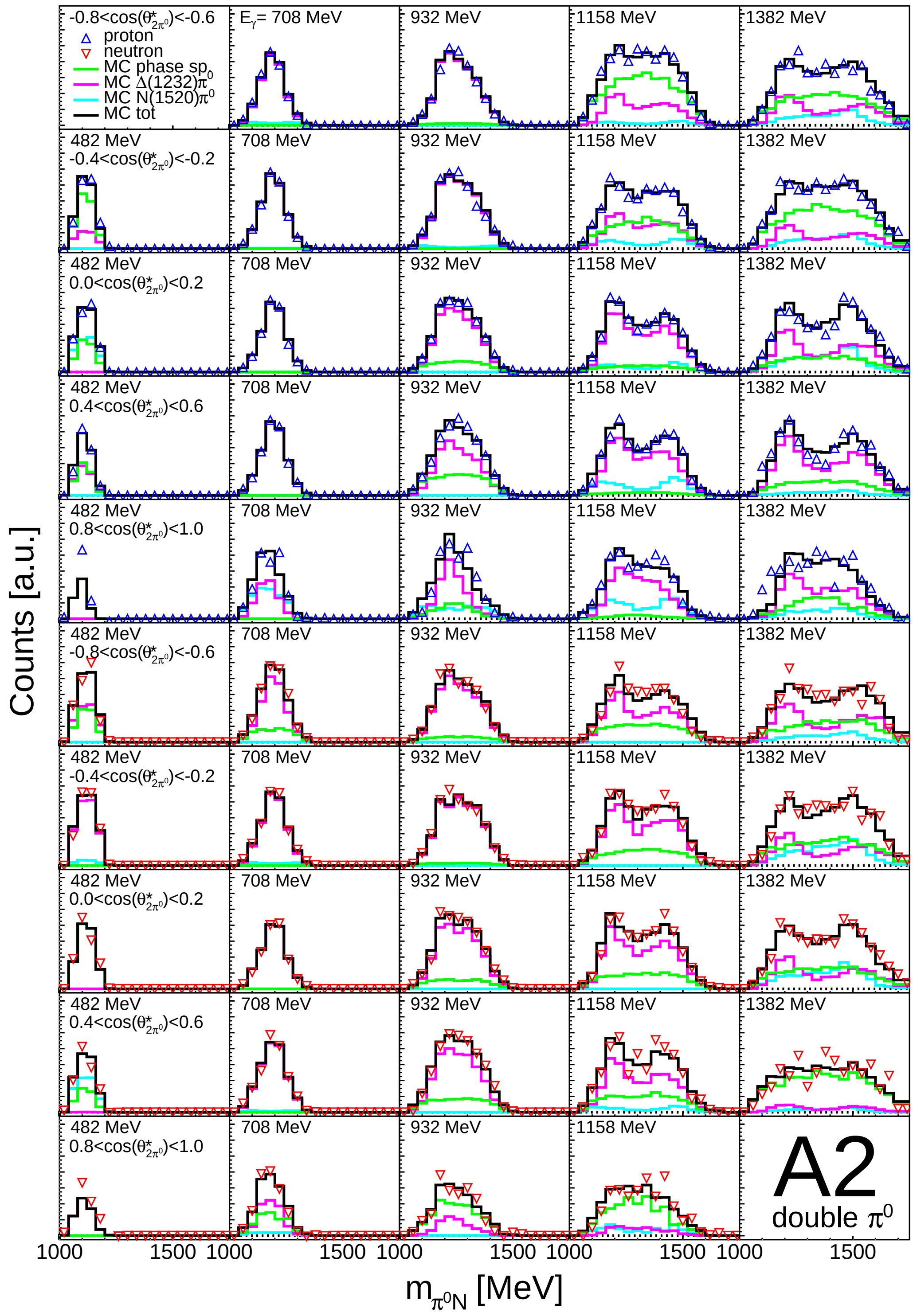

Figure 6.87: Unnormalized pion nucleon mass distributions for double π^0 photoproduction from quasi-free protons (upper half, blue triangles) and neutrons (lower half, red triangles) inside deuterium from the A2 data. Shown are five selected energy and angular bins. The data was fit with the line shape from phase space and intermediate $\Delta(1232)3/2^+$ and $N(1520)3/2^-$ states according to Equation (6.16). Notations are given in the figure.

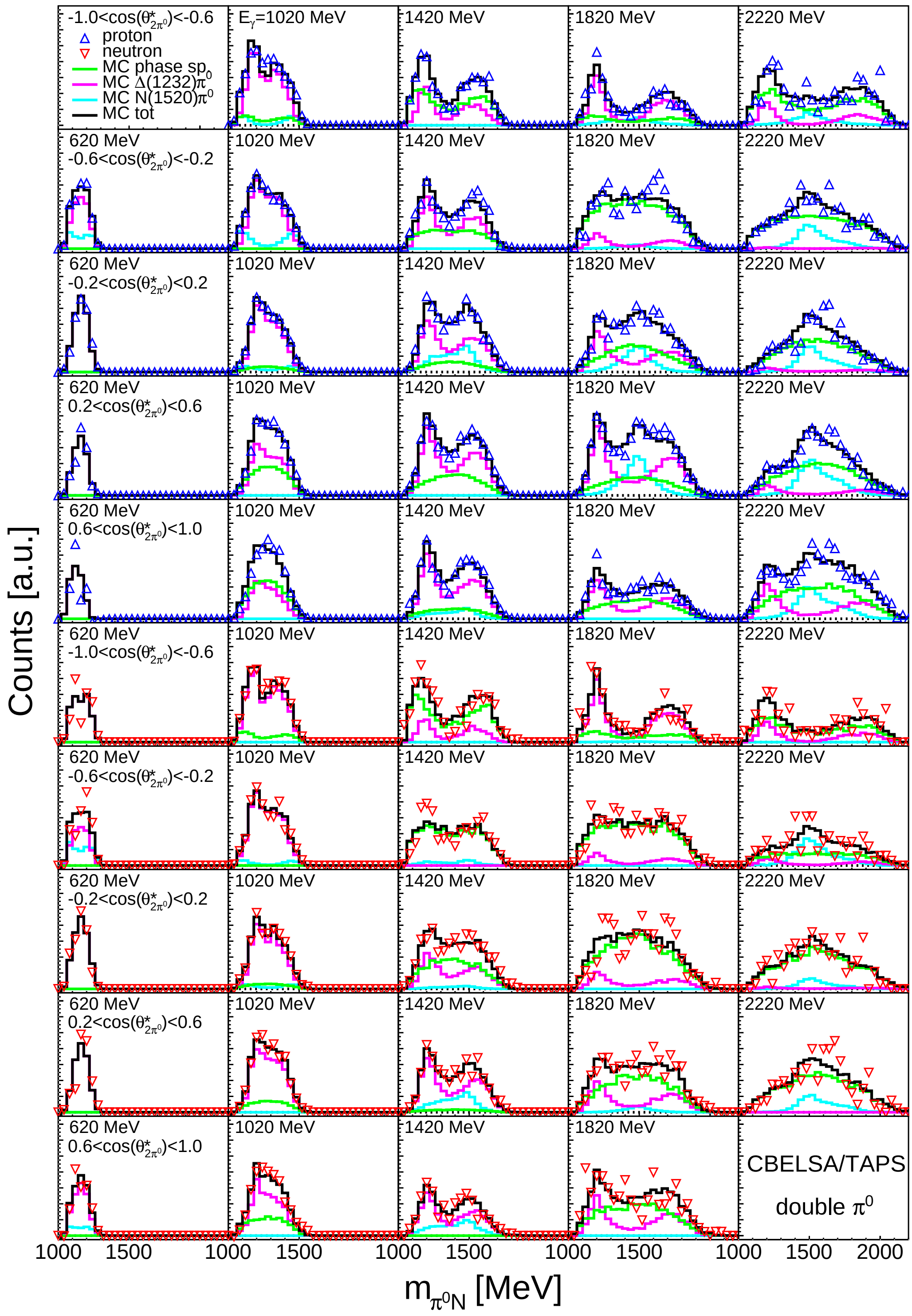

Figure 6.88: Unnormalized pion nucleon mass distributions for double π^0 photoproduction from quasi-free protons (upper half, blue upward triangles) and neutrons (lower half, red downward triangles) inside deuterium from the CBELSA/TAPS data. Shown are five selected energy and angular bins. The data was fit with the line shape from phase space and intermediate $\Delta(1232)3/2^+$ and $N(1520)3/2^-$ states according to Equation (6.16). Notations are given in the figure.

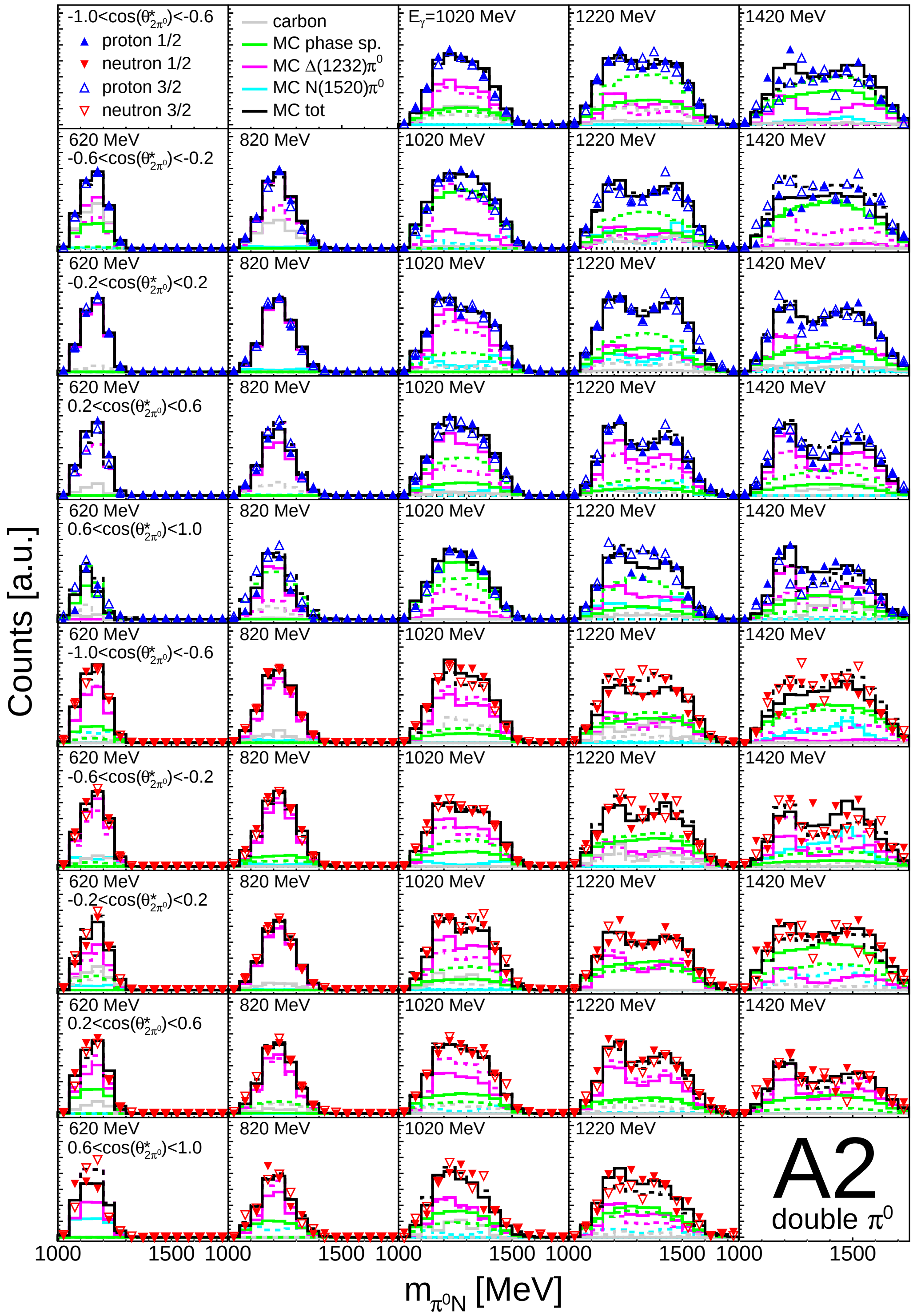

Figure 6.89: Unnormalized helicity dependent pion nucleon mass distributions for double π^0 photoproduction from quasi-free protons (upper half, blue triangles) and neutrons (lower half, red triangles) inside deuterated butanol from the A2 data. Shown are five selected energy and angular bins. The data was fit with the line shape from carbon, phase space and intermediate $\Delta(1232)3/2^+$ and $N(1520)3/2^-$ states according to Equation (6.18). Notations are given in the figure. Solid (dashed) lines: helicity 1/2 (3/2) results.

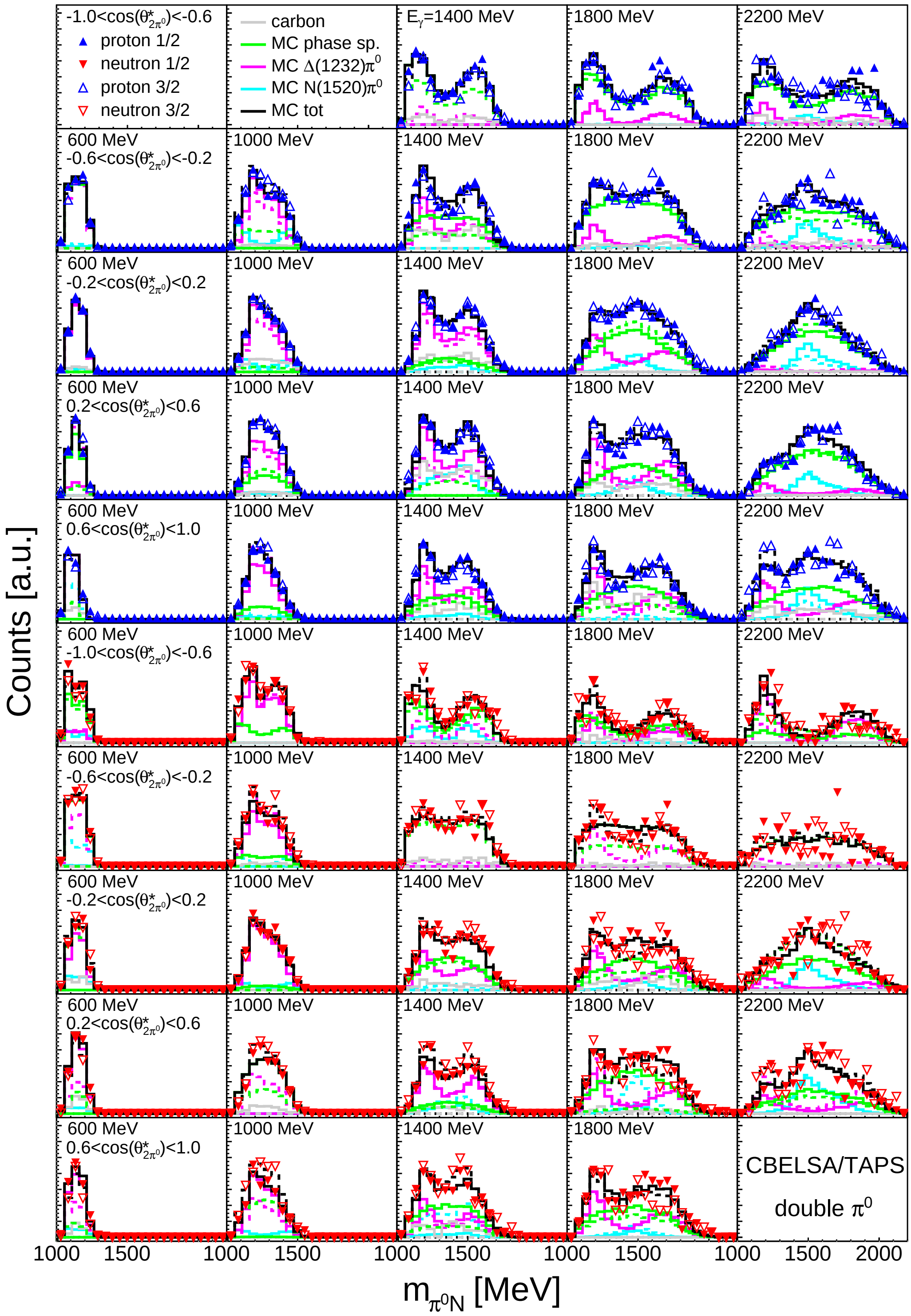

Figure 6.90: Unnormalized helicity dependent pion nucleon mass distributions for double π^0 photoproduction from quasi-free protons (upper half, blue upward triangles) and neutrons (lower half, red downward triangles) inside deuterated butanol from the CBELSA/TAPS data. Shown are five selected energy and angular bins. The data was fit with the line shape from carbon, phase space and intermediate $\Delta(1232)3/2^+$ and $N(1520)3/2^-$ states according to Equation (6.18). Notations are given in the figure. Solid (dashed) lines: helicity 1/2 (3/2) results.

6.8.3 Nucleon Detection Efficiency Correction

The analysis of reactions on bound nucleons in a nucleus requires the detection of the recoil nucleon in order to know, on which nucleon the reaction occurred. Analyses on free protons, as the case for experiments with liquid hydrogen targets, can be done inclusively, i.e. without the requirement of the detection of the recoil nucleon. In contrast, the analysis of exclusive reactions where the meson is detected in coincidence with the recoil nucleon relies on the detection efficiency of the nucleon. However, the simulation of interactions of nucleons with material is much more complicated than that for photons and strongly depends on the energy and by that on the physics model used for the calculation. Hence, the nucleon detection efficiency is very sensitive to inconsistencies between data and simulation. The behavior of neutrons is especially difficult to simulate, since their detection efficiency is much lower compared to that of protons and photons. An additional correction for the detection efficiency, discussed in Section 6.8, was carried out, which provides a much more reliable nucleon detection efficiency.

The determination of the detection efficiency of nucleons with the experimental setup is possible with the analysis of liquid hydrogen data. The advantage of using a liquid hydrogen target is that it is known that the reaction occurred on the proton, regardless if it is detected or not. In this case, the reaction can be measured inclusively as well as exclusively, i.e. with or without the coincident detection of the recoil nucleon. If the nucleon detection efficiency is correct, no difference between the two reactions should be observed. In any case, the comparison of the two reactions allows for the determination of the nucleon detection efficiency.
The reactions:

$$\begin{aligned} &\gamma p \rightarrow \pi^0 \pi^0 p \quad \text{and} \\ &\gamma p \rightarrow \pi^0 \pi^+ n \ , \end{aligned} \tag{6.20}$$

were analyzed for the determination of the detection efficiencies of the proton and neutron. The analysis of $\gamma p \rightarrow \pi^0 p$ was not possible due to the multiplicity condition of the experimental trigger. However, it was checked that the kinematic range was covered by the $\gamma p \rightarrow \pi^0 \pi^0 p$ reaction. Furthermore, a comparison of the proton detection efficiencies for $\gamma p \rightarrow \pi^0 \pi^0 p$ and $\gamma p \rightarrow \eta p$ showed good agreement, indicating that apart from the covered kinematic range, no severe dependence of the efficiency on the reaction is present. The reaction $\gamma p \rightarrow \pi^0 \pi^+ n$ was chosen for the determination for the neutron efficiency, since kinematically, it is the closest to single and double π^0 photoproduction. $\gamma p \rightarrow \pi^+ n$ was not possible due to the experimental trigger settings. However, its measurement would most likely lead to larger systematic uncertainties. The detection efficiencies of the charged pion and the neutron are rather small and therefore, the measurement would suffer from background contamination and misidentified particles. In addition, the absence of final state photons complicates the determination of a proper condition on time coincidences and the subtraction of the random background in the tagger.
The reactions from Equation (6.20) were measured inclusively, i.e. without the requirement of the coincident detection of the recoil nucleon and compared to the

exclusive measurement, i.e. when the nucleon was detected. The ratio of the number of exclusive events and the number of inclusive events denotes the nucleon detection efficiency ε_N and was determined dependent on the nucleon polar angle in the laboratory frame θ_N and on the nucleon kinetic energy T_N for data and simulation according to:

$$\begin{aligned}\varepsilon_p^{\mathrm{data,MC}}(T_p,\theta_p) &= \frac{N(\pi^0\pi^0 p)}{N(\pi^0\pi^0(p))}\\ \varepsilon_n^{\mathrm{data,MC}}(T_n,\theta_n) &= \frac{N(\pi^0\pi^+ n)}{N(\pi^0\pi^+(n))}\ ,\end{aligned} \tag{6.21}$$

where $N(\pi^0\pi^0 p)$ and $N(\pi^0\pi^+ n)$ denote the number of exclusive events, where the recoil nucleon was detected and $N(N(\pi^0\pi^0(p)))$ and $N(\pi^0\pi^+(n))$ the inclusive events, where the detection of the recoil nucleon was not required.

The polar angle and kinetic energy of the recoil nucleon were calculated from kinematics and not from measured quantities. This is necessary as the determination involves cases where the recoil nucleon was not detected. An additional dependence on the ϕ angle of the nucleon in the laboratory frame was implemented at first, but did not show any significant difference and therefore was omitted.
The additional determination of the nucleon detection efficiency in the simulation according to Equation (6.21) allows for the correction of possible discrepancies between the data and simulation, as mentioned in the beginning of this section. Since it does only cover the kinematic range of the considered reaction, it is not globally applicable nor valid. Therefore, the nucleon detection efficiencies from Equation (6.21) were not applied directly in the analyses. Instead, the ratio of both

$$\eta_c(T_N,\theta_N) = \frac{\varepsilon_N^{\mathrm{MC}}(T_N,\theta_N)}{\varepsilon_N^{\mathrm{data}}(T_N,\theta_N)} \tag{6.22}$$

was applied to the simulation. The ratio η_c serves as a nucleon detection efficiency correction of the simulation and adjusts the nucleon detection efficiency of the simulation to that of the experiment. For the determination of the final detection efficiencies of the exclusive analyses (see Section 6.8), the correction factor η_c was then applied to the analysis of the simulation by weighting every event with $1/\eta_c(T_N,\theta_N)$. For this purpose, the correction factor matrix was evaluated for a given measured polar angle θ_N and reconstructed kinetic energy T_N (see Section B.3). The evaluation of the correction factor matrix with the same quantities as it was determined, i.e. reconstructed values from kinematics instead of measured quantities, is only possible for analyses of data from free protons. However, the nucleon detection efficiency also had to be applied to analyses of quasi-free data, for which both values T_N and θ_N can not be obtained from kinematic considerations. Therefore, the correction factor was evaluated at the measured polar angle and the reconstructed kinetic energy of the nucleon. This approximation was investigated in the analysis of the free proton data. For this purpose, the correction factor was evaluated at the kinematically calculated values for T_N, θ_N, but also at the reconstructed value for T_N and the measured value for θ_N. No significant deviations between the two methods were observed.

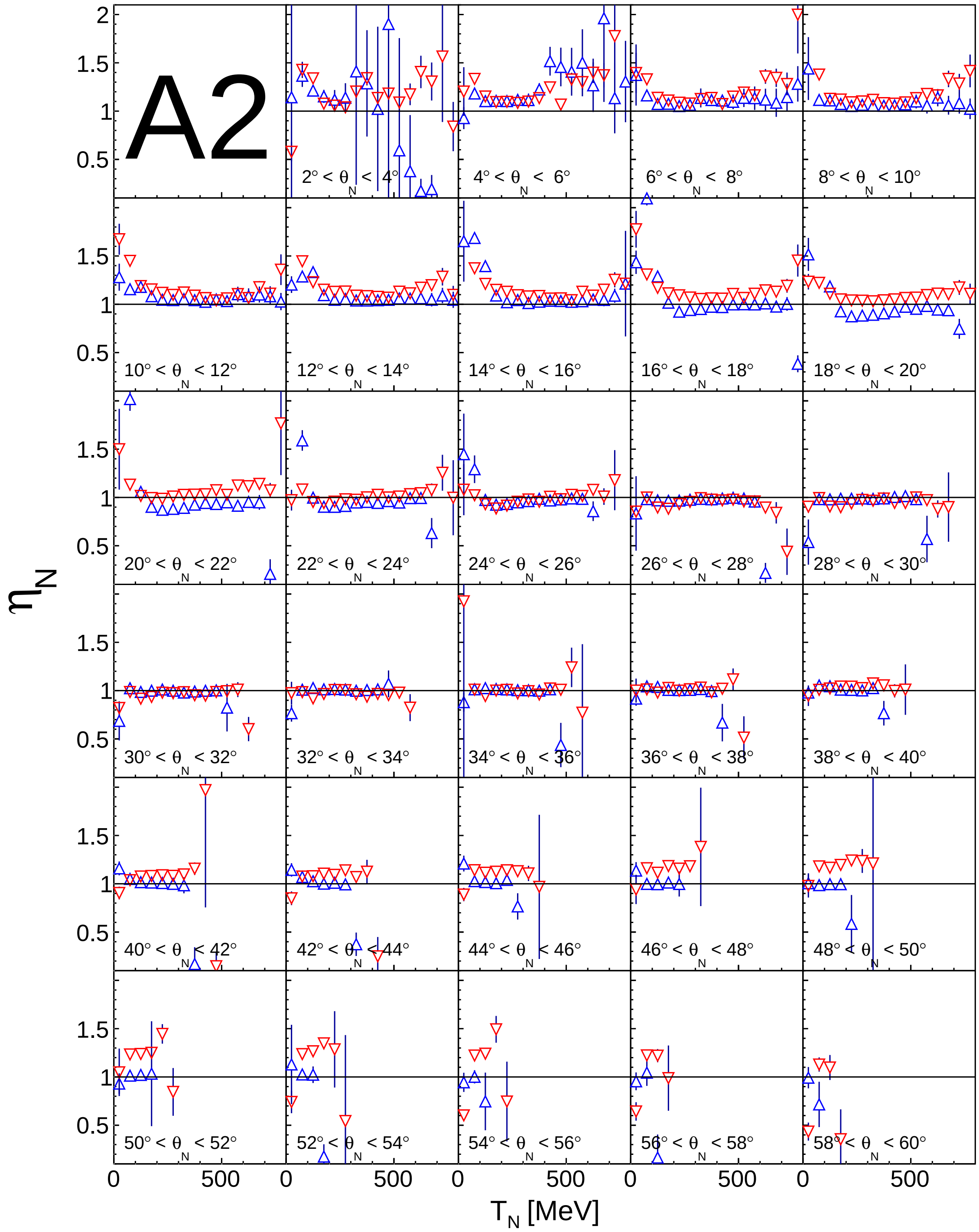

Figure 6.91: Nucleon detection efficiency correction η_N from the A2 data. The results were extracted from the ratio of the nucleon detection efficiency from simulation and data. Upward blue triangles: proton detection efficiency correction. Downward red triangles: neutron detection efficiency correction. The results were determined for the May 2009 beamtime.

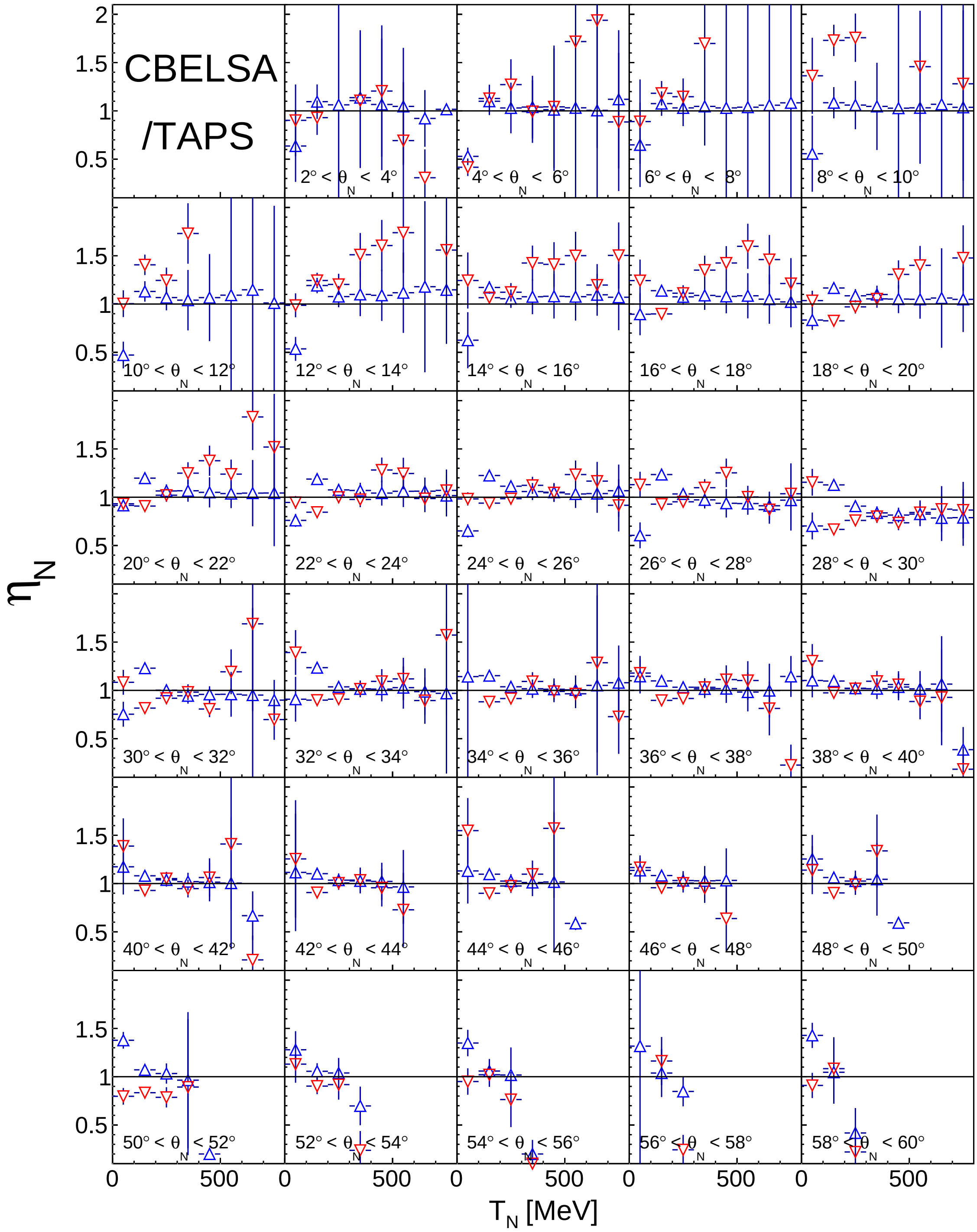

Figure 6.92: Nucleon detection efficiency correction η_N from the CBELSA/TAPS data. The results were extracted from the ratio of the nucleon detection efficiency from simulation and data. Upward blue triangles: proton detection efficiency correction. Downward red triangles: neutron detection efficiency correction. The results were determined for the December 2008 beamtime.

The nucleon efficiency correction factors for the analysis of A2 data are shown in Figure 6.91 and those for CBELSA/TAPS data in Figure 6.92. Due to several reasons, for the determination of the detection efficiency for CBELSA/TAPS data, only the proton detection efficiency correction was applied. A precise determination of the nucleon detection efficiency relies on a proper particle identification. However, the identification of the reaction $\gamma p \to \pi^0\pi^+ n$ is based on the reliability of the identification of the charged pion, which at CBELSA/TAPS can only be checked with the Forward detectors, i.e. Forward Cone and MiniTAPS. For the Inner detector, no information about the deposited energy of a particle was available. Therefore, the quality of the reaction identification for the angular region covered by the Crystal Barrel detector can not be verified and does not guarantee the proper determination of the neutron detection efficiency correction. Nevertheless, no significant change of the results were obtained when the correction was applied, which either indicates that there is no need for the correction or that it does not fit to its application. However, as its reliability could not be checked, its application would be unreliable and was omitted.

From the nucleon detection efficiencies of the A2 data (see Figure 6.91), it can be seen that for the forward region, the correction factor η_c deviates from one, especially at very low and very high kinetic energies. As values larger than one correspond to higher efficiencies in the simulation than in the data, this indicates that the simulated efficiencies are too large. In the forward region, more different materials and transitions are available and the BaF_2 crystals exhibit rather different signals from photons than from nucleons. Therefore, the TAPS detector is more difficult to properly implement in the simulation. For intermediate polar angles, both correction factors are almost one and identical, indicating that in this angular range, the nucleon detection efficiencies agree well with each other, independent of the kinetic energy. In higher energies, the proton correction factor is stable at one whereas the correction factor of the neutron drastically increases.

The correction factors obtained from the CBELSA/TAPS data show a different behavior. The proton detection efficiencies of data and simulation seem to agree well with each other for most angles and kinetic energies. At very low energies, at about 30° and at larger polar angles, significant deviations from one can be observed. Towards forward angles, the correction is slightly larger than one, which indicates similar, but smaller problems, as observed in the correction factors of the A2 data. In contrast, the neutron correction factor is, for most polar angles below 30°, significantly larger than one. Apart from some fluctuations at larger polar angles, it is in good agreement with the proton correction factor and around one. However, as previously mentioned, the particle identification of the reaction could not be checked to see if the determination of the neutron detection efficiency was correct. Therefore, the neutron detection efficiency correction factor was not applied to the simulated CBELSA/TAPS data.

The nucleon detection efficiency corrections presented in this section were determined from the April 2009 hydrogen beamtime for the application to the simulations

of A2 data and from the November 2008 hydrogen beamtime for the application to the simulations of CBELSA/TAPS data. They were determined by the comparison of the inclusive and exclusive reactions (see Equation (6.20)) and were applied to all exclusive analyses where the coincident detection of the recoil nucleon was required. Initially, an individual nucleon detection efficiency correction was established for the analysis of the deuterated butanol data, since different thresholds were used in the experiment. However, it was observed that the resulting nucleon detection efficiencies were within statistical fluctuations in good agreement. Therefore, the same nucleon detection efficiency correction as shown in Figures 6.91 and 6.92 were applied to all analyses of the same reaction.
The April 2009 beamtime from A2 was also used for the extraction of cross sections and mass distributions of $\pi^0\pi^0$ photoproduction from the free proton. Thereby it was observed that in this beamtime, a general problem with the detection of charged particles exists. As this could drastically influence the nucleon detection efficiency and with that all analyses that make use of that particular nucleon detection efficiency, this problem was investigated in detail and will be discussed in the next section. Even though the main reason for the problem could not be revealed, a correction was successfully established. Furthermore, and this is of great importance, it was shown that the problem does not seem to have an influence on the nucleon efficiency correction. In addition, similar problems with the used deuterium beamtimes could be excluded as well. Hence, according to the investigations done within this work, it was concluded that, although the developed correction has to be used for the quantitative analysis of the hydrogen beamtime, a consequence for the determination of the nucleon detection efficiency from this beamtime or an influence on other beamtimes is absent. However, it might be reasonable to further investigate the behavior of this particular beamtime or to use an independent, different hydrogen beamtime for future analyses.

6.8.4 Charged Particle Detection Efficiency Correction

During the analysis of $\pi^0\pi^0$ photoproduction from the free proton using the liquid hydrogen A2 data from April 2009, good agreement between the cross sections from both inclusive and exclusive analyses were obtained. However, significant discrepancies of about 10% to former results were observed, as illustrated by the open blue circles on the left-hand side of Figure 6.93. The problem could be traced back to a problem with the detection of charged particles. It was found that analyzing the data without using any information of the charged particle identification detectors (PID and Veto detectors) yields results (see solid blue circles in Figure 6.93) that are in good agreement with published results. Thereby the inclusive analysis without any information of the PID and Veto detectors was solely based on the χ^2 test. Whereas with the information from the charged particle detectors, events with four neutral clusters (for the decay photons of the two pions) and an optional charged particle (for the proton) were required, without any information from the PID and Veto detectors, all events with four or five clusters were selected. The χ^2 test was then used to find the best combination for the two pions and, if available, the re-

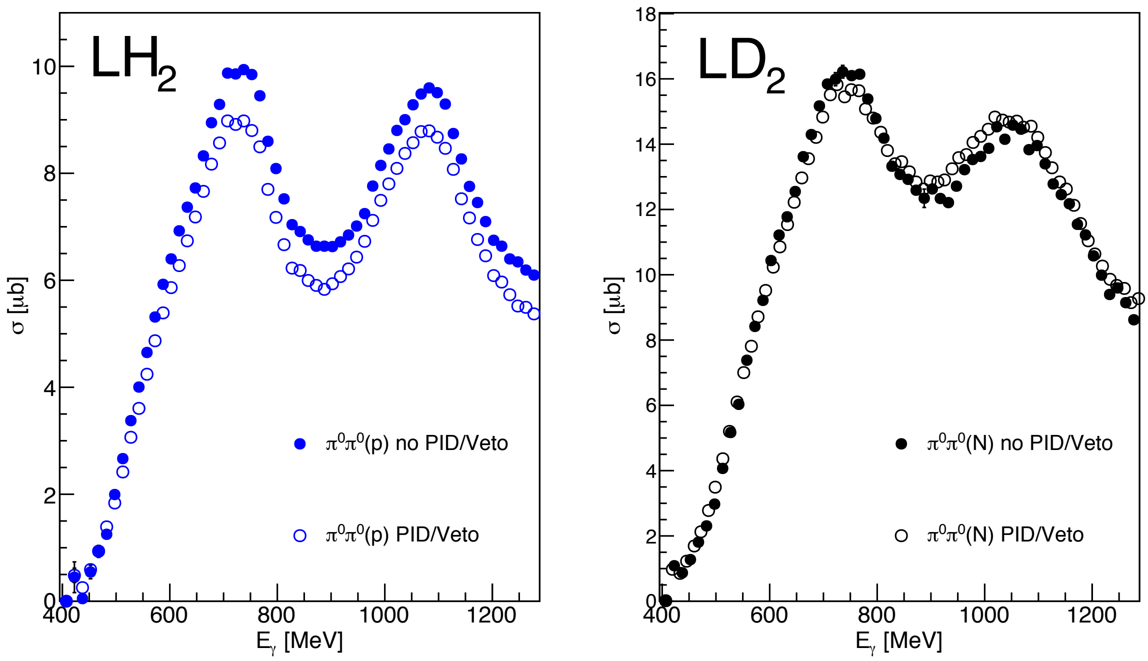

Figure 6.93: Investigation of the problem of the detection of charged particles in the analysis of the A2 data from the liquid hydrogen beamtime from April 2009. Left-hand side: inclusive $\pi^0\pi^0(p)$ total cross sections with (open blue circles) and without (filled blue circles) the usage of information from charged particle detectors. Right-hand side: quasi-free inclusive $\pi^0\pi^0(N)$ total cross sections with (open black circles) and without (filled black circles) the usage of information from charged particle detectors.

maining cluster was assigned to the proton. Even though no specific information of the proton was used, a very clean identification of the proton was achieved, which made this alternative analysis very reliable.

Nevertheless, the problem had to be solved, as the exclusive measurement was necessary to determine the nucleon detection efficiency correction, as discussed in Section 6.8.3, and required the results from the free proton for the estimation of the systematic uncertainties. As the analysis without any information about the charge of the particles achieved correct results whereas the analysis with this information failed, it was clear that the problem was related to the charged particle detectors. In order to investigate the problem, the same analysis was used where the identification of the particles was done without any information of the charged particle identification. However, the information of the charged particle detectors was used to determine the efficiencies of the PID and Veto detectors. The central detector element of the proton cluster obtained from the χ^2 test was checked for a coincidence with the corresponding charged particle detector. For every detector element, the ratio of the number of coincidences and the total number of hits was determined for data and simulation. The ratio of the efficiency obtained from simulation and data is shown on the left-hand side of Figure 6.94 for the 720 NaI(Tl) crystals of the Crystal

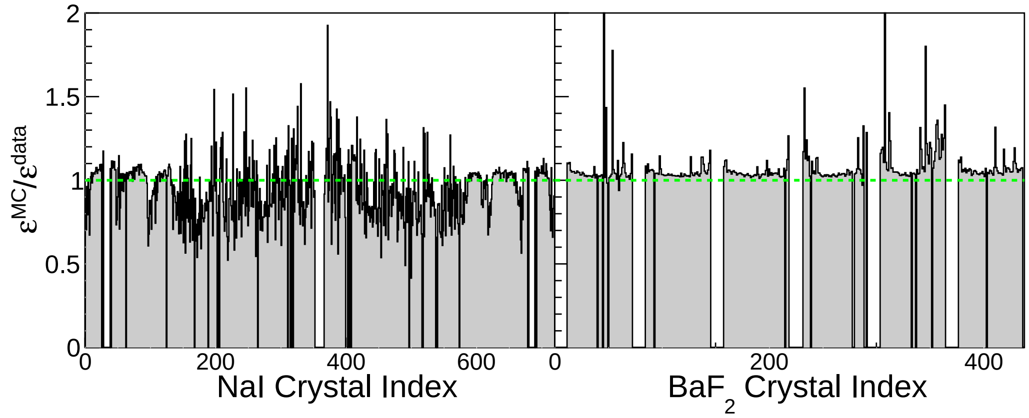

Figure 6.94: Efficiency of the charged particle identification detectors used in the liquid hydrogen beamtime from April 2009 at A2. Left-hand side: PID efficiency as a function of the NaI crystals of the Crystal Ball detector. Right-hand side: veto efficiency as a function of the BaF_2 and $PbWO_4$ crystals of TAPS.

Ball and on the right-hand side of Figure 6.94 for the 438 BaF_2 and $PbWO_4$ crystals of TAPS.
It is clearly visible in Figure 6.94 that the ratio of the PID and veto efficiencies is larger than one in the boundary area of the Crystal Ball detector and overall for the TAPS detector. As most of the detected clusters in the Crystal Ball detector were detected in the boundary area, i.e. below crystal index 120 and above crystal index 600, the mean ratio of the events in the Crystal Ball detector will be of a comparable magnitude. Therefore, the charged particle efficiency for $2\pi^0$ photoproduction in the liquid hydrogen simulation is about 10% larger than the data. As a consequence, the cross sections will be underestimated by about 10%, as seen in Figure 6.93.

While the source of the problem was not definitely revealed, a correction method was established, which is based on a comparison of the analysis without the information from PID and Veto detectors and the standard analysis, which makes use of the information.
The idea was to compare the inclusive and exclusive analyses of the data and simulation for the two different analysis methods. Thereby "w"("wo") denotes the analysis, where the information from PID and Veto were (not) used. Tables 6.8 presents the event selection that was chosen for the inclusive and exclusive analyses.For every analysis, the number of events with five clusters (denoted as H for *hit* in the following) and events with four clusters (denoted as NH for *no hit*) were determined and used to determine the individual nucleon detection efficiencies according to:

$$\begin{aligned} \varepsilon^{w}_{\mathrm{MC}} &= \frac{H^{w}_{\mathrm{MC}}}{NH^{w}_{\mathrm{MC}} + H^{w}_{\mathrm{MC}}} \qquad \varepsilon^{w}_{\mathrm{data}} = \frac{H^{w}_{\mathrm{data}}}{NH^{w}_{\mathrm{data}} + H^{w}_{\mathrm{data}}} \\ \varepsilon^{wo}_{\mathrm{MC}} &= \frac{H^{wo}_{\mathrm{MC}}}{NH^{wo}_{\mathrm{MC}} + H^{wo}_{\mathrm{MC}}} \qquad \varepsilon^{wo}_{\mathrm{data}} = \frac{H^{wo}_{\mathrm{data}}}{NH^{wo}_{\mathrm{data}} + H^{wo}_{\mathrm{data}}} \ . \end{aligned} \tag{6.23}$$

Analysis	inclusive	exclusive
with PID/Veto	5n && 0c 4n && 1c 4n && 0c	5n && 0c 4n && 1c
without PID/Veto	5N 4N	5N

Table 6.8: Event selection criteria for the analyses used for the determination of the charged particle detection efficiency correction. N: number of particles. n: number of neutral clusters. c: number of charged clusters. Multiple conditions were connected via logical "OR".

The ratio of the efficiencies of the analysis with the information from the charged particle detectors and the analysis without these information can be written as:

$$\xi = \varepsilon^{w}/\varepsilon^{wo} \ , \tag{6.24}$$

and is a measure for the reliability of the charged particle identification (CPI). Thereby it has to be mentioned that it is not primarily important that the ratio of the efficiencies (Equation (6.24)) is one, this would simply be the ideal case that indicates that the identification is perfect. However, the most important thing is that the ratio ξ is identical in the data and the simulation since imperfections in the data would then be corrected by the simulation. If they are not identical, the simulation would over or undercorrect the data. Using the individual efficiencies of the two analyses for data and simulation from equation 6.23 and the ratio of them as in Equation (6.24), the correction that has to be applied to the simulation is given by:

$$\zeta^{CPI} = \frac{\varepsilon^{w}_{\mathrm{MC}}}{\varepsilon^{wo}_{\mathrm{MC}}} \cdot \frac{\varepsilon^{wo}_{\mathrm{data}}}{\varepsilon^{w}_{\mathrm{data}}} = \frac{\xi_{\mathrm{MC}}}{\xi_{\mathrm{data}}} \tag{6.25}$$

The charged particle detection efficiency correction ζ^{CPI} was determined as a function of the proton kinetic energy T_p and polar angle θ_N as well as the azimuthal angle ϕ_N in the lab frame and then applied as a weight on an event by event base, which is identical to the application of the nucleon detection efficiency described in the last Section 6.8.3.
The application of the correction solves the problem such that the analysis of liquid hydrogen data with the information of the PID and Veto detectors yields results that are in good agreement with previous published measurements. Nevertheless, it is important to show that the nucleon detection efficiency obtained from the same liquid hydrogen data, as discussed in Section 6.8.3, is reliable. Furthermore, it was investigated, if the observed discrepancy between data and simulation was due to a general problem that would also affect the liquid deuterium data.

The effect of the charged particle efficiency correction on the standard nucleon detection efficiency had to be investigated. First of all, it is also based on the comparison of inclusive and exclusive analyses, except for the difference, that this case

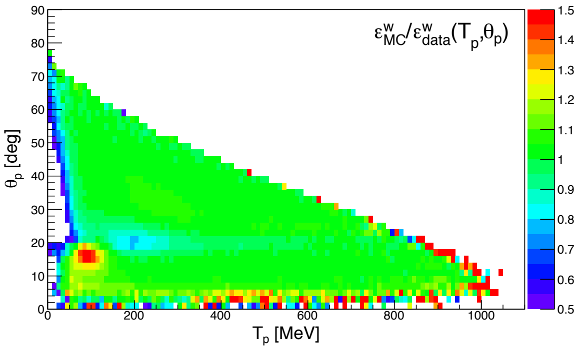

(a) Standard nucleon detection efficiency correction $\eta^w(T_p, \theta_p)$

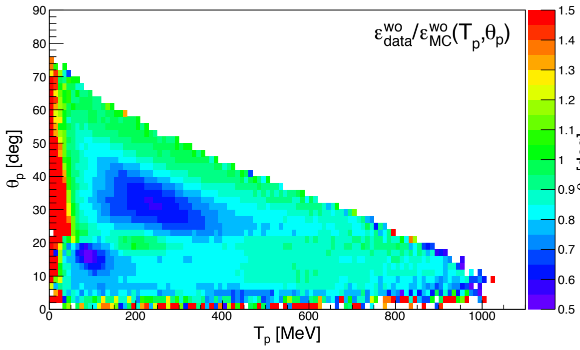

(b) Inverse modified nucleon detection efficiency correction $\eta^{wo}(T_p, \theta_p)^{-1}$

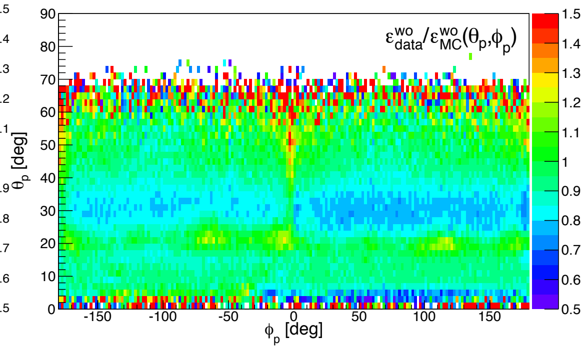

(c) Inverse modified nucleon detection efficiency correction $\eta^{wo}(\theta_p, \phi_p)^{-1}$

Figure 6.95: Visualization of the charged particle detection efficiency correction ζ^{CPI} and its decomposition into standard η^w and modified η^{wo} nucleon detection efficiency correction, according to Equation (6.27). (a) Extracted standard nucleon detection efficiency correction $\eta^w(T_p, \theta_p)$. (b) Inverse modified nucleon detection efficiency correction $\eta^{wo}(T_p, \theta_p, \phi_p)^{-1}$ integrated over ϕ_p. (c) Inverse modified nucleon detection efficiency $\eta^{wo}(T_p, \theta_p, \phi_p)^{-1}$ integrated over T_p.

includes additional events with five neutral clusters, which accounts for misidentified protons. Furthermore, an additional analysis without the information of the charged identification detectors was carried out. Besides that, the determination of the correction factor is based on the same type of efficiencies, i.e. comparing the number of events of the exclusive analysis, with the number of events of the inclusive analysis according to Equation (6.21). It was found that the correction factor for the charged particle efficiency correction can be factorized into two factors. One of them corresponds to the nucleon detection efficiency, as defined in Equation (6.22) and the other one to the nucleon detection efficiency correction obtained from the analysis without the charged particle information. The decomposition of Equation (6.25) into (6.22) is as follows:

$$\zeta^{CPI} = \frac{\varepsilon^{w}_{\mathrm{MC}}}{\varepsilon^{wo}_{\mathrm{MC}}} \cdot \frac{\varepsilon^{wo}_{\mathrm{data}}}{\varepsilon^{w}_{\mathrm{data}}} = \frac{\varepsilon^{w}_{\mathrm{MC}}}{\varepsilon^{w}_{\mathrm{data}}} \cdot \frac{\varepsilon^{wo}_{\mathrm{data}}}{\varepsilon^{wo}_{\mathrm{MC}}} = \eta^w \cdot \frac{1}{\eta^{wo}} \,, \tag{6.26}$$

where η^w corresponds to the earlier defined nucleon efficiency correction from Equation (6.22) of the standard analysis with the information of the charge sensitive detectors and η^{wo} is the nucleon detection efficiency correction where the charge information was ignored. The sole differences in this determination (compare to Equation (6.22)) are that, the additional event class of five neutral clusters was considered and that the correction was established dependent of the azimuthal angle of the proton ϕ_p additionally. Thereby ϕ_p was kept, since this factor accounts for the small ϕ_p dependence of the correction of the charged particle identification, as seen in Figure 6.95c.
In order to compare the standard nucleon detection efficiency with that obtained from the decomposition in Equation (6.26), the ϕ_p information was integrated in order to find:

$$\begin{aligned}\zeta^{CPI} = \eta^w \cdot \frac{1}{\eta^{wo}} &= \eta^w(T_p, \theta_p) \cdot \frac{1}{\eta^{wo}(T_p, \theta_p, \phi_p)} \\ &= \underbrace{\frac{\varepsilon^w_{\mathrm{MC}}(T_p, \theta_p)}{\varepsilon^w_{\mathrm{data}}(T_p, \theta_p)}}_{\text{std nucl. eff. corr.}} \cdot \underbrace{\frac{1}{\frac{\varepsilon^{wo}_{\mathrm{MC}}(T_p,\theta_p,\phi_p)}{\varepsilon^{wo}_{\mathrm{data}}(T_p,\theta_p,\phi_p)}}}_{\text{mod. nucl. eff. corr.}} \quad .\end{aligned} \tag{6.27}$$

The nucleon detection efficiency correction, as extracted from the charged particle detection efficiency, is in good agreement with the one obtained from the standard analysis, as shown in Figure 6.96. Shown are the standard nucleon detection efficiency correction from Equation (6.22) (upward black triangles), the extracted nucleon detection efficiency correction from Equation (6.27), and the additional modified nucleon detection efficiency correction from Equation (6.27).

As seen in Figure 6.96, both nucleon detection efficiency corrections η_p^{std} and η_p^w are in good agreement. The small deviations are most likely due to the difference in the event selection of the two analyses. The standard analysis only considers four neutral and one charged cluster or four neutral clusters, this analysis also considers events with five neutral and zero charged clusters in order to account for misidentified charged clusters. This explains the smaller statistical errors and the smaller correction factors at higher kinetic energies. Besides the small deviations, both results are in reasonable agreement. The decomposed charged particle efficiency correction is shown in Figure 6.95. The extracted standard nucleon detection efficiency correction $\eta^w(T_p, \theta_p)$ is shown in Figure 6.95a, the inverse[7] modified nucleon detection efficiency correction integrated over ϕ_p in Figure 6.95b, and integrated over T_p in Figure 6.95c for the illustration of the ϕ_p dependence of the correction.

In order to exclude the same problems from the analysis of liquid deuterium data, the quasi-free inclusive analysis was considered. The exclusive analyses require the coincident detection of the recoil nucleon in order to know which nucleon was the participant in the reaction, which is only possible in an analysis where information about the charged particles is available. For this reason, the quasi-free inclusive

[7] inverse as it appears in the denominator of the charged particle detection efficiency correction ζ^{CPI}

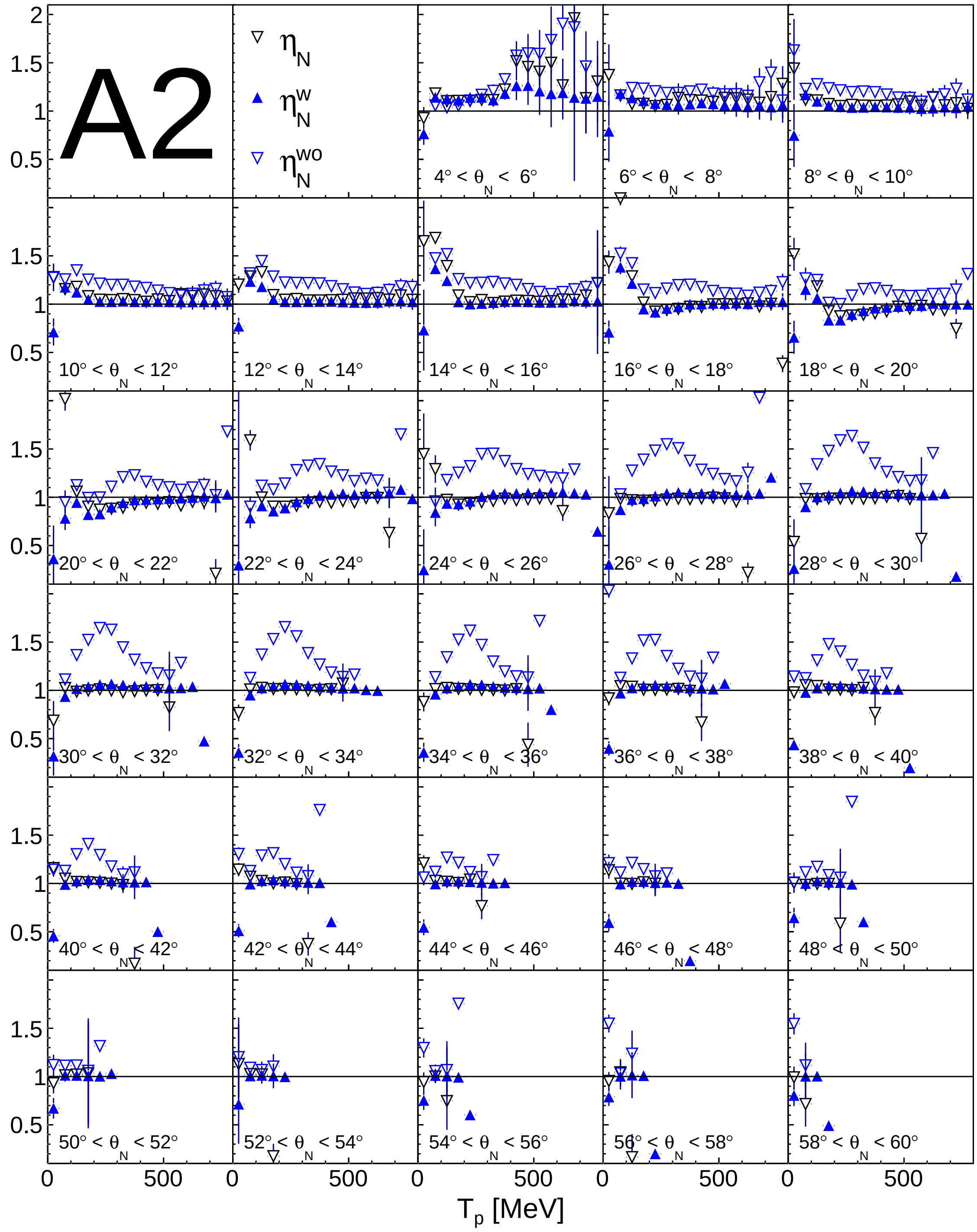

Figure 6.96: Decomposed components of the charged particle detection efficiency correction ζ^{CPI}. Open black triangles: standard nucleon detection efficiency correction η_N as obtained from the analysis with the charge sensitive detectors according to Equation (6.22). Filled blue triangles: extracted standard nucleon detection efficiency correction η_N^w from ζ^{CPI}. Open blue triangles: extracted modified nucleon detection efficiency correction η_N^{wo} from ζ^{CPI} as obtained from the analysis without the charge sensitive detectors.

analysis was also performed with the liquid deuterium beamtime from May 2009 but without using the PID and Veto detectors. A comparison of the result with that from the standard analysis is shown on the right-hand side of Figure 6.93. Both results are in good agreement with each other indicating no significant problem with the identification of charged particles in this deuterium beamtime. In addition, the crystal dependent PID and Veto detector efficiencies were determined for the deuterium beamtime, as shown on the right hand side of Figures **??** and **??**. As expected, in the range of interest, the ratio of the efficiencies of simulation and data are one, which confirms that the charged particle identification is understood.

It was concluded that the standard nucleon detection efficiency using the liquid hydrogen beamtime from April 2009 is reliable. The problem with the charged particle detection efficiency only seems to be present in this specific beamtime. A correction matrix was established which overcomes this problem. Application of the full correction factor to the inclusive analysis of the simulation and the extracted nucleon detection efficiency correction to the exclusive analysis of the simulation yielded consistent results among each other, as well as with published data. However, for future work it might be reasonable to use a different hydrogen beamtime instead, where no difficulties are observed. The established correction is only directly applicable to the analyses that cover the same kinematic range as double π^0 photoproduction that involves protons. The detection of other charged particles, i.e. charged pions, would require a separate correction.

6.8.5 Final Detection Efficiencies

Taking all corrections into account that have been presented in the Sections 6.8.3 and 6.8.4, the detection efficiencies for the individual reaction channels can be determined. For all analyses of simulated A2 data, the nucleon detection efficiency corrections from Figure 6.91 were applied and for the analyses of simulated CBELSA/TAPS data, only the proton detection efficiency correction from Figure 6.92 was applied due to an uncertainty in the identification of the corresponding reaction. The charged particle identification correction discussed in Section 6.8.4 was only applied to the analysis of the simulation of the liquid hydrogen data from A2 data in April 2009, but it was also used to verify the validation of the standard nucleon detection efficiency correction. No significant discrepancies were observed.

The detection efficiencies were determined individually for all analysis channels and all beamtimes and were calculated as a function of the meson (m) polar angle $\cos(\theta^*_m)$ and incident photon energy E_γ or final state invariant mass W. For single π^0 photoproduction, the determination of the detection efficiencies was based on Equation (6.15) and was directly obtained from the analysis of the simulated reaction channel of interest. For double π^0 photoproduction, at first efficiencies were determined for the individual contributions ($\gamma N \to \pi^0\pi^0 N$, $\gamma N \to \Delta(1232)\pi^0 \to \pi^0\pi^0 N$, $\gamma N \to N(1520)\pi^0 \to \pi^0\pi^0 N$) according to Equation (6.15) and then combined to an overall efficiency by using Equation (6.17) and the relative contributions a, b, c from Equation (6.16).

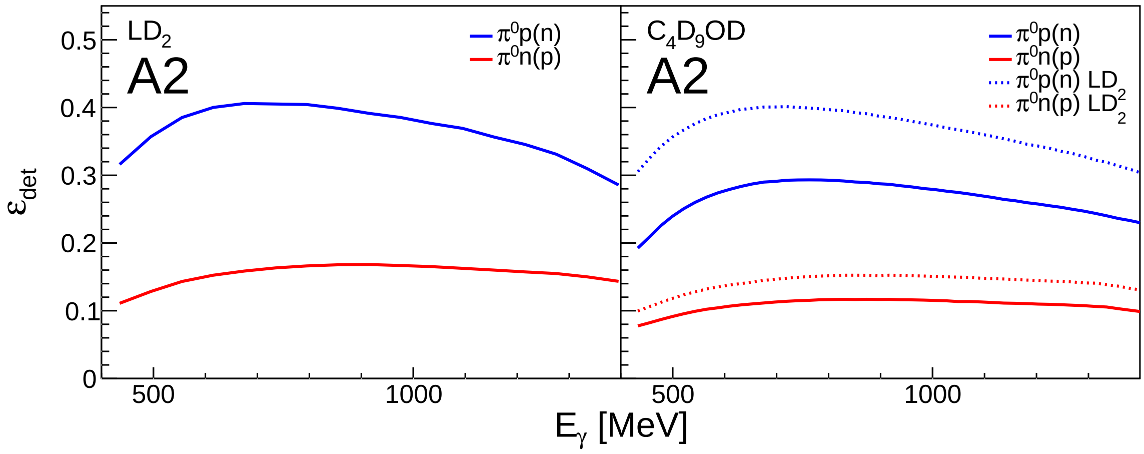

Figure 6.97: Detection efficiency of single π^0 photoproduction as a function of E_γ from the A2 data. Left-hand side: deuterium data. Right-hand side: deuterium and deuterated butanol data. Notations are given in the figure.

For the determination of the detection efficiencies for the deuterated butanol analyses, the event generators from the liquid deuterium simulations were used, but then simulated with the experimental setup from the deuterated butanol beamtime. Even though the reactions were generated on a deuterium target, the target in the simulation was filled with deuterated butanol in order to properly account for events on the polarized deuterons inside the deuterated butanol. For double π^0 photoproduction, the efficiencies of the individual contributions were determined individually and then used to calculate the efficiency for the two helicity states according to Equation (6.19) with the relative contributions a, b and c from Equation (6.18). For the determination of the detection efficiencies of the analyses of the carbon data, it was important to use simulations of reactions on deuterium inside a deuterated butanol target instead of reactions on carbon nuclei. This is due to the fact that the carbon beamtime was used to subtract the background contributions from unpolarized nucleons of carbon and oxygen from the deuterated butanol data and the carbon background in the data underlies the kinematics of the reaction on deuterium. Therefore, the efficiencies used for the deuterated butanol analyses were identically applied to the analyses of the carbon data.

Figure 6.97 illustrates the detection efficiencies used for the exclusive analyses of single π^0 photoproduction from quasi-free nucleons in deuterium (left-hand side) and deuterated butanol (right-hand side) from the A2 data. Shown are the detection efficiencies as a function of E_γ, which were obtained by integrating the detection efficiencies from Figures 6.98 and 6.99 over all angular bins. On the right-hand side of Figure 6.97, the deuterated butanol efficiencies are shown and are compared to those from liquid deuterium. On the left-hand side of the figure, the efficiencies for the extraction of cross sections from deuterium data are shown. Those on the right-hand side correspond to the same beamtimes, but obtained from the analysis with the same trigger and threshold settings as used for the appropriate comparison

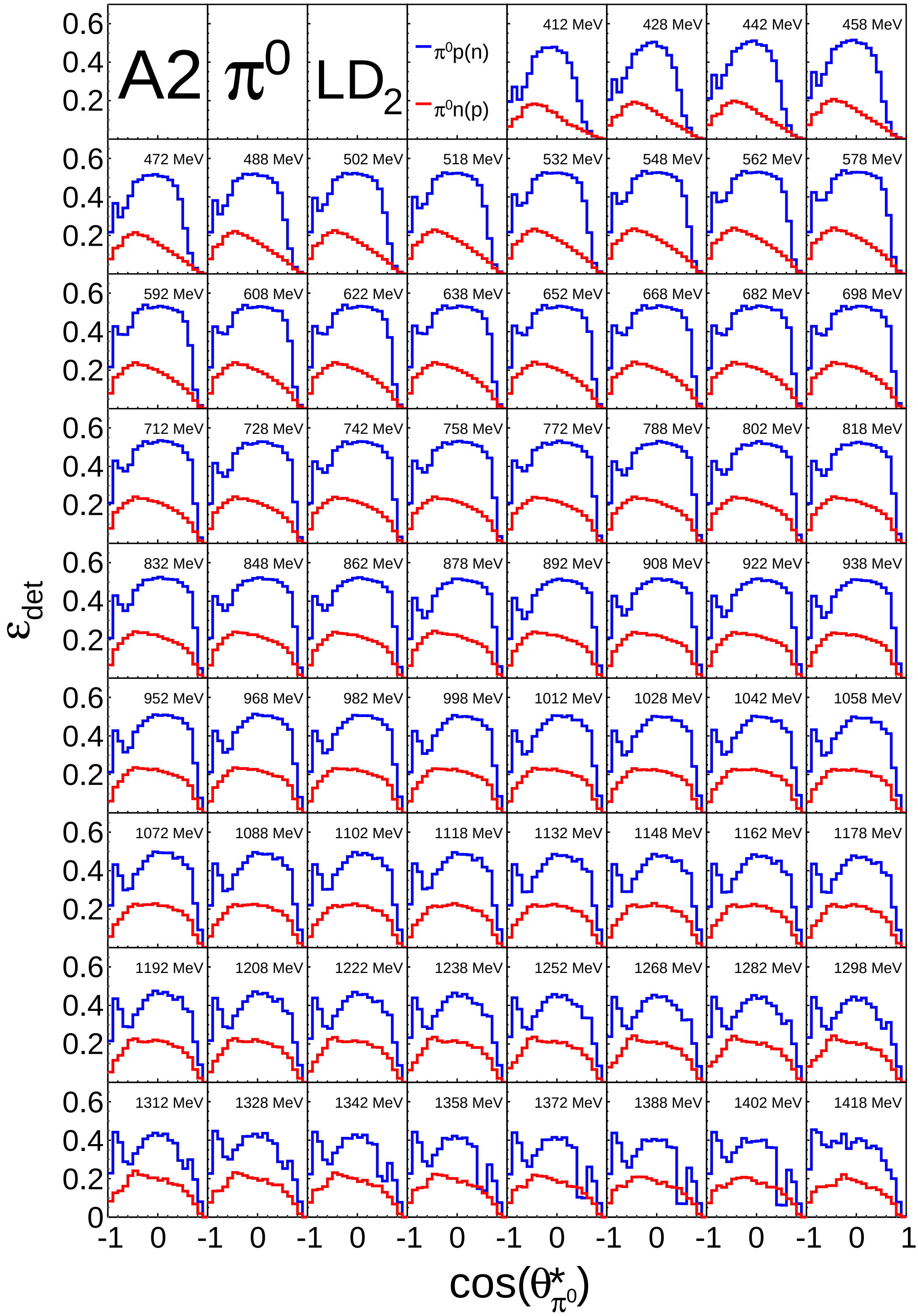

Figure 6.98: Angular detection efficiency of single π^0 photoproduction from the deuteron as a function of E_γ. Notations are given in the figure. Results from the A2 data.

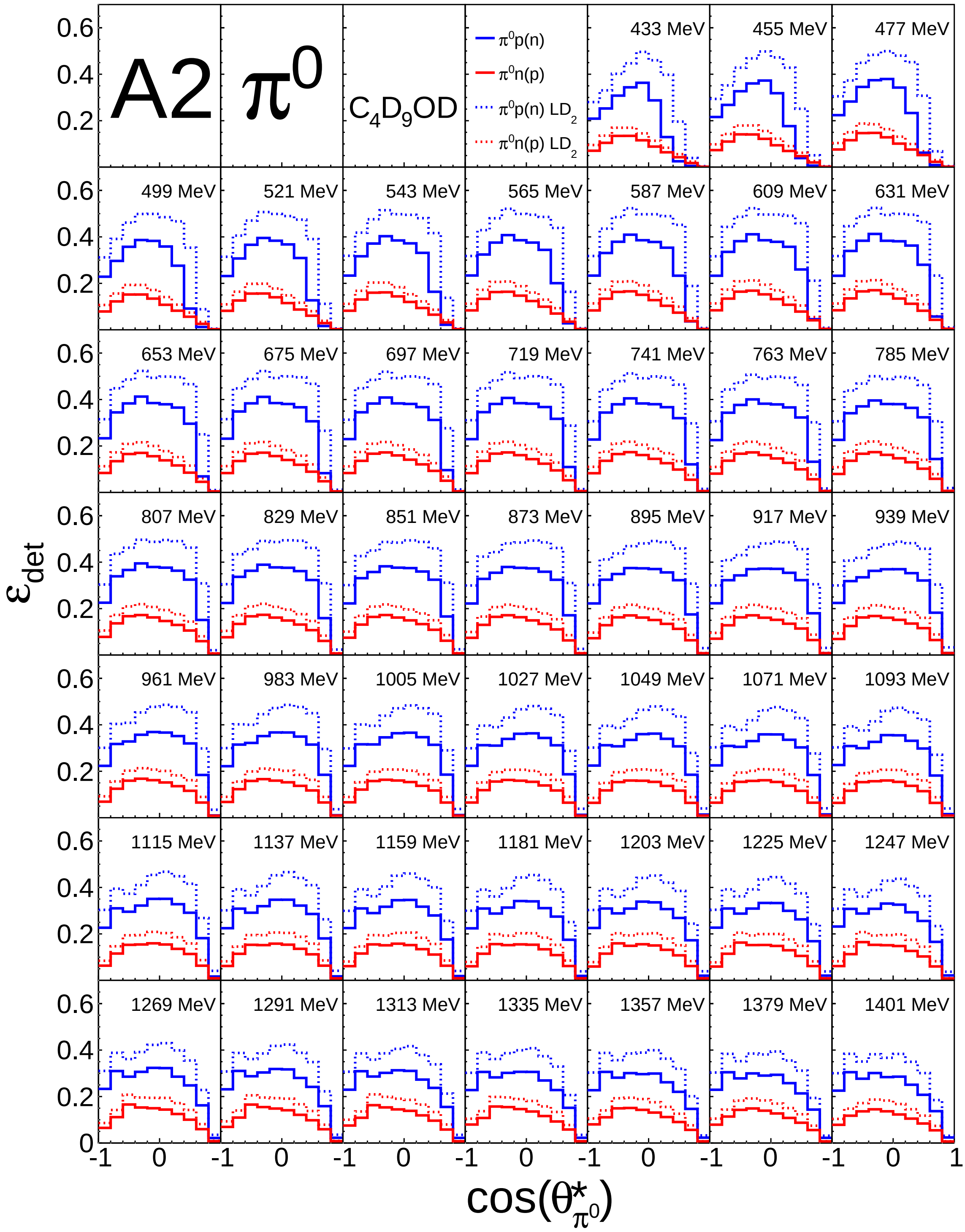

Figure 6.99: Angular detection efficiency of single π^0 photoproduction from deuterium (dotted histograms) and from deuterated butanol (solid histograms) as a function of E_γ. Notations are given in the figure. Results from the A2 data.

to the deuterated butanol data. Therefore, depending on the different trigger and threshold conditions, the deuterium efficiencies on the left and right-hand side do not necessarily have to coincide with each other.
The proton and neutron efficiencies of all three analyses are nearly identical in shape and differ only by their absolute values. The efficiencies first increase with photon energy and reach their maximum between 600 and 900 MeV and then slowly decrease again. The proton efficiency is about three times higher than that from the neutron, which is due to the different detection efficiencies for protons ($>$90%) and neutrons ($\sim$30%). By comparing the efficiencies of the analyses on deuterium from the left to those from the right-hand side, no significant differences can be seen indicating that the different trigger and threshold settings were comparable for this reaction. For the proton, the efficiencies are much smaller for the reactions inside deuterated butanol. This is due to the high atomic number Z of deuterated butanol compared to deuterium. With higher Z pair production and conversion processes strongly increase, which results in a reduction in the detection efficiency. Neutrons are not affected to the same amount, the efficiency for the deuterated butanol analysis is only slightly lower.
The angular detection efficiencies for the deuterium beamtime (corresponding to the left-hand side of Figure 6.97) are shown in Figure 6.98 and those for the deuterated butanol beamtime in Figure 6.99. Apart from the absolute value, the efficiencies from the deuterated butanol analysis are in good agreement with those from the deuterium analysis, which indicates no angular effect on the different target materials. The main observation from the angular efficiencies can be seen in those from the deuterium analysis in Figure 6.98. At backward angles of the π^0 in the pion-nucleon center of mass frame, i.e. at proton forward angles, a sudden and strong peak in the efficiency, especially for the proton, is visible. It will be discussed in Section 6.9 and is due to the correction of the insensitive gap between the Crystal Ball and TAPS detector, which results in a loss of protons and a drop in the efficiencies, which was counteracted with the correction. Due to the coarser angular binning in the deuterated butanol analysis, the structure in the corresponding angular efficiencies is smeared out and barely visible. In addition, it is visible that the efficiencies for meson forward angles tend towards zero. This is the consequence of the experimental trigger setting. As mentioned in Section 2.3.2, contributions to the multiplicity condition from the TAPS detector alone were not considered in the trigger. Therefore, events, where the two decay photons go into the TAPS detector are not recorded, which results in the low detection efficiencies at the very forward angles.

The detection efficiencies for double π^0 photoproduction from free protons in hydrogen and quasi-free nucleons in deuterium (left-hand side) and deuterated butanol (right-hand side) for the analysis of A2 data are shown in Figure 6.100 and for the CBELSA/TAPS analysis in Figure 6.101. For the unpolarized analysis (left-hand side), the efficiencies of the individual contributions as obtained from Equation (6.15) (see the legend in the figure for the labeling of the different contributions) and the combined efficiencies according to Equation (6.17) are shown. On the right-hand side, the efficiencies for the polarized analysis are shown, but the individual contri-

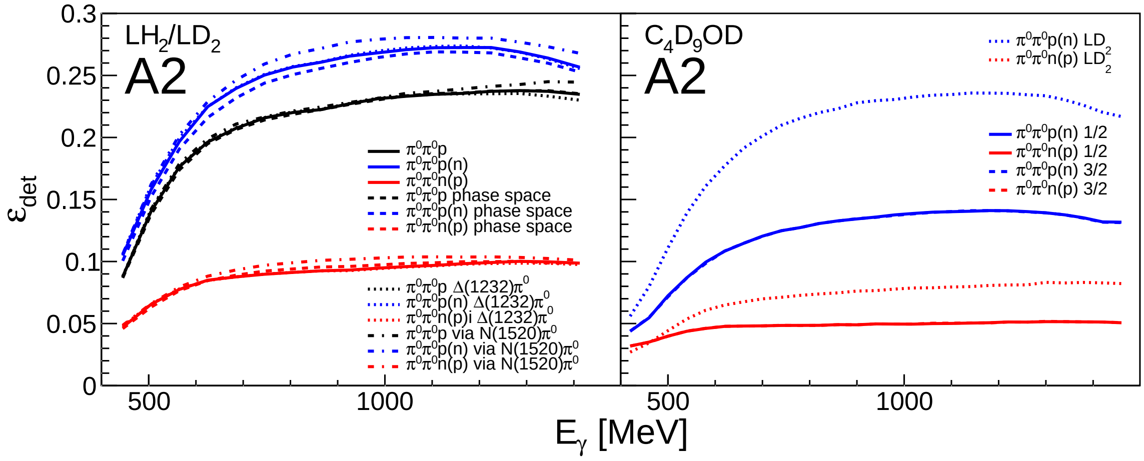

Figure 6.100: Detection efficiency of double π^0 photoproduction as a function of E_γ from the A2 data. Left-hand side: individual contributions and combined efficiencies for the hydrogen and deuterium data. Right-hand side: combined efficiencies for the deuterium and deuterated butanol data. The difference between the helicity dependent efficiencies is negligible. Notations are given in the figure.

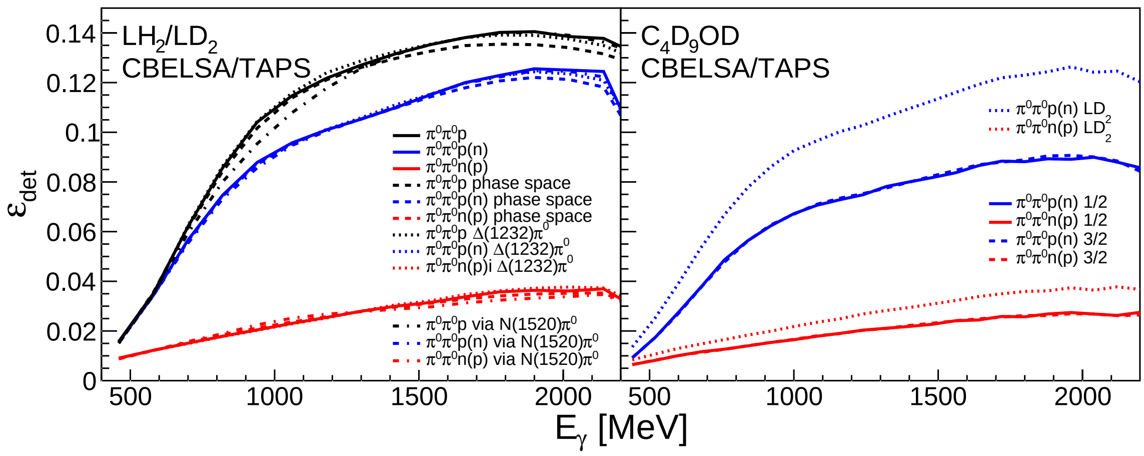

Figure 6.101: Detection efficiency of double π^0 photoproduction as a function of E_γ from the CBELSA/TAPS data. Left-hand side: individual contributions and combined efficiencies for the hydrogen and deuterium data. Right-hand side: combined efficiencies for the deuterium and deuterated butanol data. The difference between the helicity dependent efficiencies is negligible. Notations are given in the figure.

butions are omitted.

Apart from the different absolute values of the efficiencies, the most prominent observation in the comparison of the efficiencies from A2 and CBELSA/TAPS can be seen for the free proton. At CBELSA/TAPS, the efficiency of the exclusive analysis from the free proton is somewhat higher than that from the quasi-free proton and at A2 that is contrary to the case. This is due to the charged particle detection efficiency ζ^{CPI} (Section 6.8.4) that was applied to the free proton data at A2. It was observed that in the A2 liquid hydrogen beamtime from April 2009, the detection efficiency of charged particles in the simulation is about 10% higher than in the data, which results in 10% too low cross sections. This discrepancy was solved by the application of the charged particle detection efficiency correction, which has the effect that the efficiency of the simulation was adapted to that of the data. With that the detection efficiency was lowered by about 10%, as seen in Figure 6.100. Without this correction, the efficiency would be about 10% higher, which would result in good relative agreement between A2 and CBELSA/TAPS.

Overall, the detection efficiencies for all reactions are about two times higher at A2 compared to CBELSA/TAPS. This is due to the non-availability of a 4π trigger at CBELSA/TAPS. The trigger system at CBELSA/TAPS is mostly sensitive to the detectors at forward angles, whereas at A2, almost the full solid angle contributes to the trigger. All efficiencies are low at energies close to the production thresholds of the reactions and then increase with increasing energies and reach a plateau between 600 and 900 MeV. At higher energies, the efficiencies only slowly increase. Due to the different scales of the y-axes, the plateau seems to be steeper at CBELSA/TAPS, but this is primarily a visual effect. For all efficiencies, the dependence of the efficiency on the different contribution from phase space or sequential decays is negligible. Thus, the combined efficiency is of the same magnitude.

At CBELSA/TAPS, the trigger and threshold settings for the two different analyses of the deuterium beamtime are mostly identical and no significant difference of the corresponding efficiencies are visible. In contrast, the trigger and threshold settings at A2 are more strict for the polarized analysis. For single π^0, the different settings did not exhibit a noticeable difference (see Figure 6.97), whereas the detection efficiency for double π^0 photoproduction seems to be more sensitive to the different conditions. This results in considerably lower detection efficiencies on the right-hand side of Figure 6.100 compared to those on the left-hand side. As already discussed for single π^0 photoproduction, the efficiencies of the deuterated butanol data are reduced due to the different material properties, i.e. the higher atomic number of the target material.

The angular efficiencies for double π^0 photoproduction from the liquid deuterium analyses and deuterated butanol analyses are shown in Figures 6.103 and 6.104 and those from the CBELSA/TAPS analysis in Figures 6.102 and 6.105. The influence from the correction of the gap between the Crystal Ball detector and TAPS on the efficiencies of the A2 data (see Figure 6.103), as already observed in single π^0 photoproduction (see Figure 6.98), is similar, but somewhat smaller. Even more noticeable is the different shape of the angular efficiencies from A2 compared to CBELSA/TAPS, which now clearly shows the difference between a 4π trigger (A2) compared to one that is sensitive to forward angles (CBELSA/TAPS). Except for the very forward and backward angles, where, due to the beamline and the detector edges, the efficiencies decrease, the A2 efficiencies are rather flat. In contrast, the CBELSA/TAPS efficiencies strongly peak to forward angles of the combined meson.

The relative contributions of the angular efficiencies of the different reactions on quasi-free nucleons are in agreement between the A2 and CBELSA/TAPS data. Those from the free proton are different for the same reason as discussed for the integrated efficiencies and apart from that, are also in agreement.

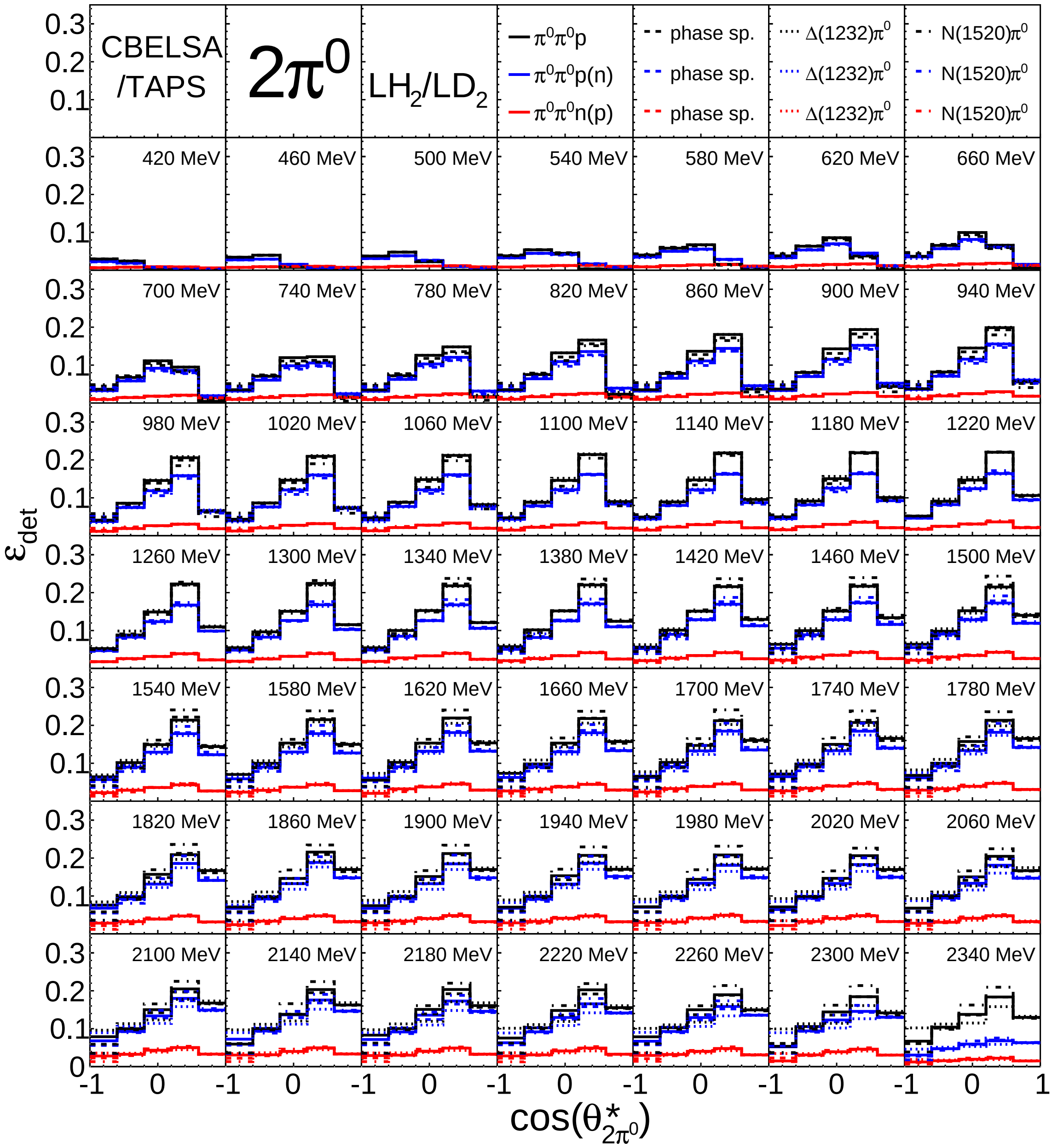

Figure 6.102: Angular detection efficiency of double π^0 photoproduction from hydrogen and deuterium as a function of E_γ from the CBELSA/TAPS data.

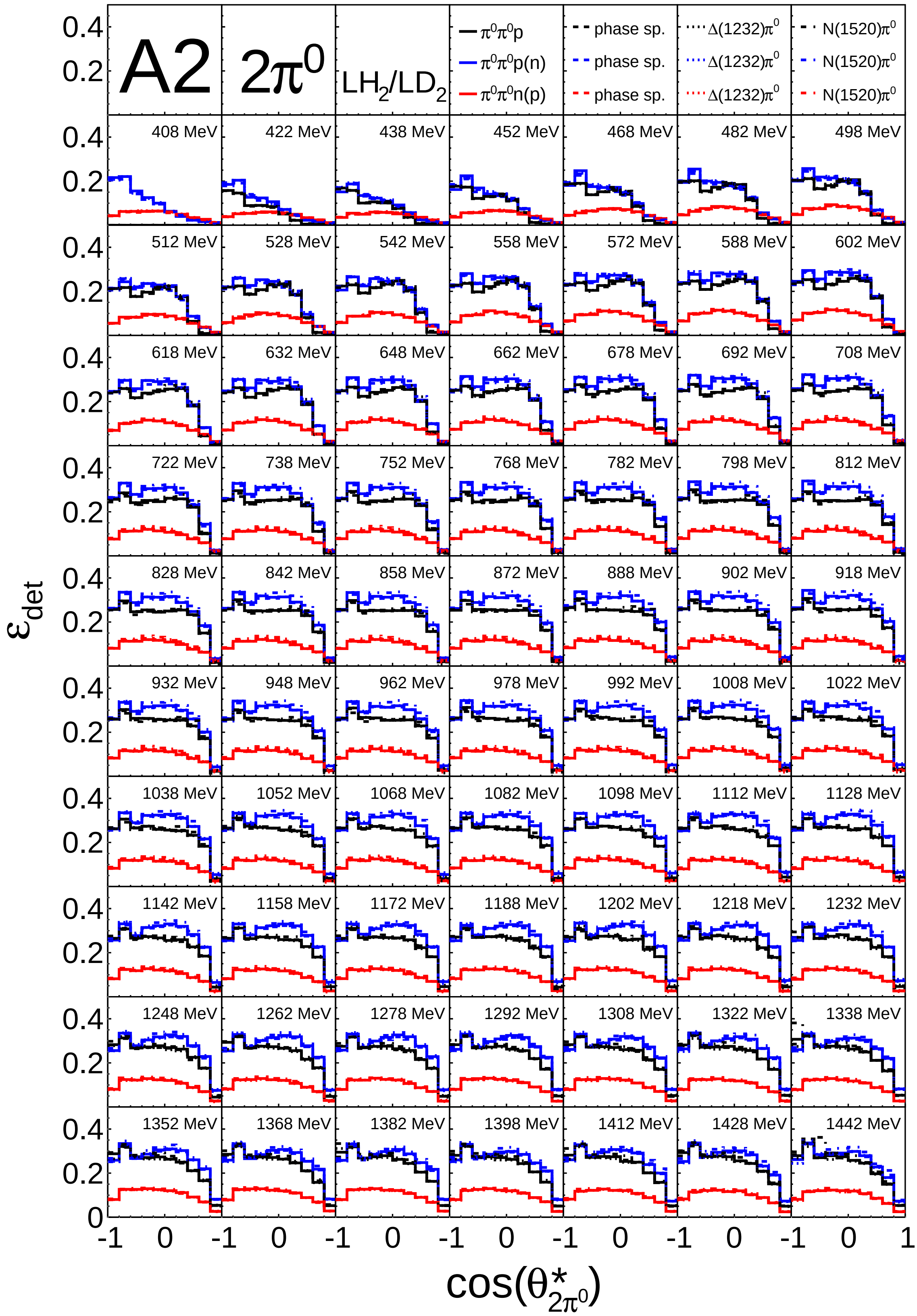

Figure 6.103: Angular detection efficiency of double π^0 photoproduction from hydrogen and deuterium as a function of E_γ from the A2 data.

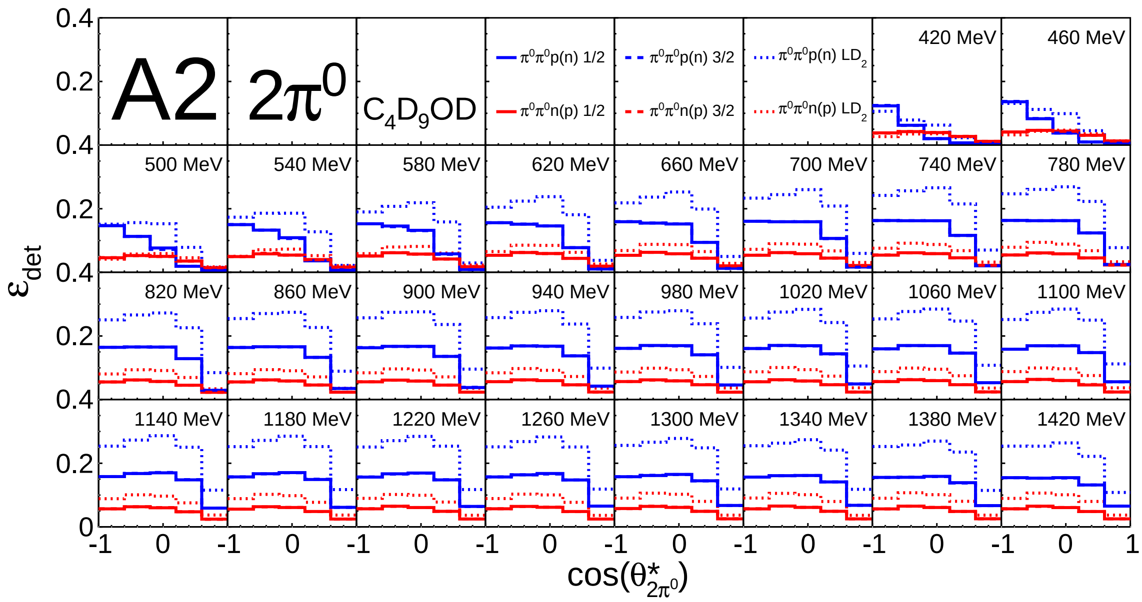

Figure 6.104: Angular detection efficiency of double π^0 photoproduction from deuterium (dotted histograms) and from deuterated butanol (1/2 : solid histograms, 3/2 : dashed histograms) as a function of E_γ from the A2 data. Only the combined efficiencies are shown. The difference between the helicity dependent efficiencies is negligible. Notations are given in the figure.

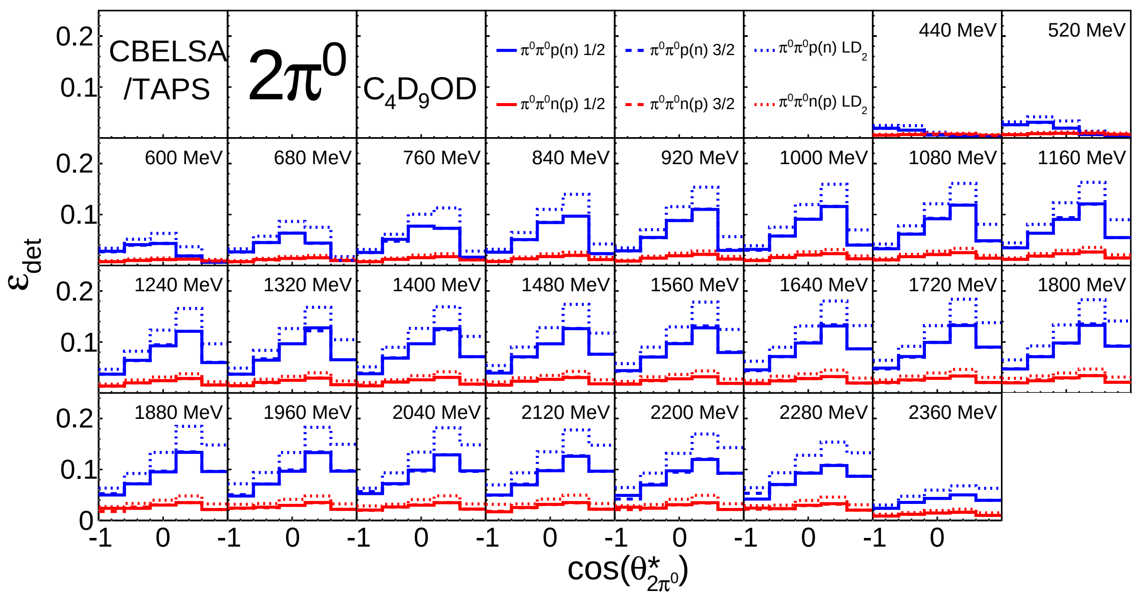

Figure 6.105: Angular detection efficiency of double π^0 photoproduction from deuterium (dotted histograms) and from deuterated butanol (1/2 : solid histograms, 3/2 : dashed histograms) as a function of E_γ from the CBELSA/TAPS data. Only the combined efficiencies are shown. The difference between the helicity dependent efficiencies is negligible. Notations are given in the figure.

6.9 Correction of the Gap between Crystal Ball and TAPS at A2

An additional correction was applied to the A2 data since the gap between the Crystal Ball detector and TAPS leads to a sudden drop of the detection efficiencies, which is visible in Figures 6.98 and 6.103. For this purpose, differential cross sections for every exclusive analysis were investigated in the influential region of the angular range of the gap that corresponds to nucleon polar angles in the laboratory frame of $18° < \theta_N < 24°$. For the liquid deuterium beamtime from December 2007, a larger range of $15° < \theta_N < 26°$ was chosen, as the PID detector was shifted by roughly 12.5 centimeters downstream, which enlarged the insensitive region [100]. The resulting spectra (open circles) are shown for the example of single π^0 photoproduction on the proton in Figure 6.106 and on the neutron in Figure 6.107. The effect of the drop in the efficiency is clearly visible. Within the sensitive region of the gap between the two detectors (indicated by the vertical black lines), the cross section exhibits a large peak. The size of the effect is much more prominent for the reaction from the proton than for the neutron, which can be seen in Figure 6.107, where the peak is much less pronounced. This is a result of the different sizes of the electromagnetic showers produced by protons and neutrons. Whereas neutrons as neutral particles usually deposit their energy over several neighboring crystals, protons mostly lose their energy in one or two crystals. As this has an effect on the resolution of the position reconstruction, the proton efficiency is more affected by the insensitive region of the gap than the neutron efficiency.
In order to correct this effect, the points within the vertical black lines were removed and the differential cross section were fit with a Legendre polynomial in the visible angular range. In the analysis of the simulation, an additional weight corresponding to a scale factor obtained from the ratio of the cross section value and the value of the fit function, was applied to events where the proton polar angle in the lab frame was within the insensitive regions. The successful result of the correction is visualized by the filled triangles in Figures 6.106 and 6.107.
This correction factor was determined for every liquid hydrogen and deuterium beamtime for all exclusive analyses of single and double π^0 photoproduction. The correction factor of the liquid deuterium beamtime was also applied to the corresponding deuterated butanol and carbon beamtime.

The effect was also investigated in the analysis of CBELSA/TAPS data for the transitions from the Crystal Barrel detector to the Forward Cone and MiniTAPS detectors, but was found to be absent.

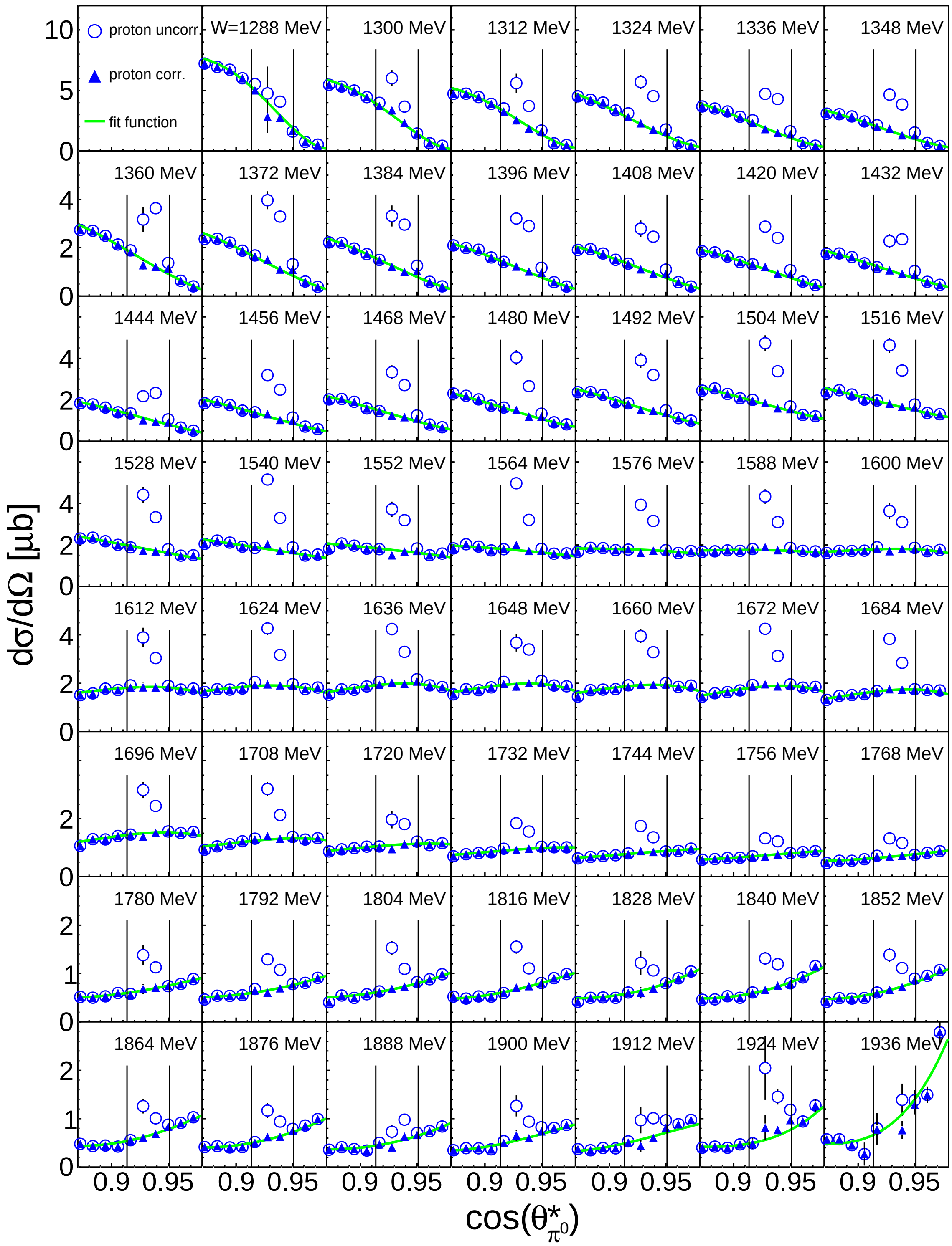

Figure 6.106: Correction of the gap between the Crystal Ball detector and TAPS for single π^0 photoproduction from quasi-free protons of the A2 liquid deuterium beamtime from May 2009. Shown are uncorrected (open circles) and corrected (filled triangles) differential cross sections as a function of the proton polar angle in the lab frame. The gap between the detectors is indicated by the vertical black lines.

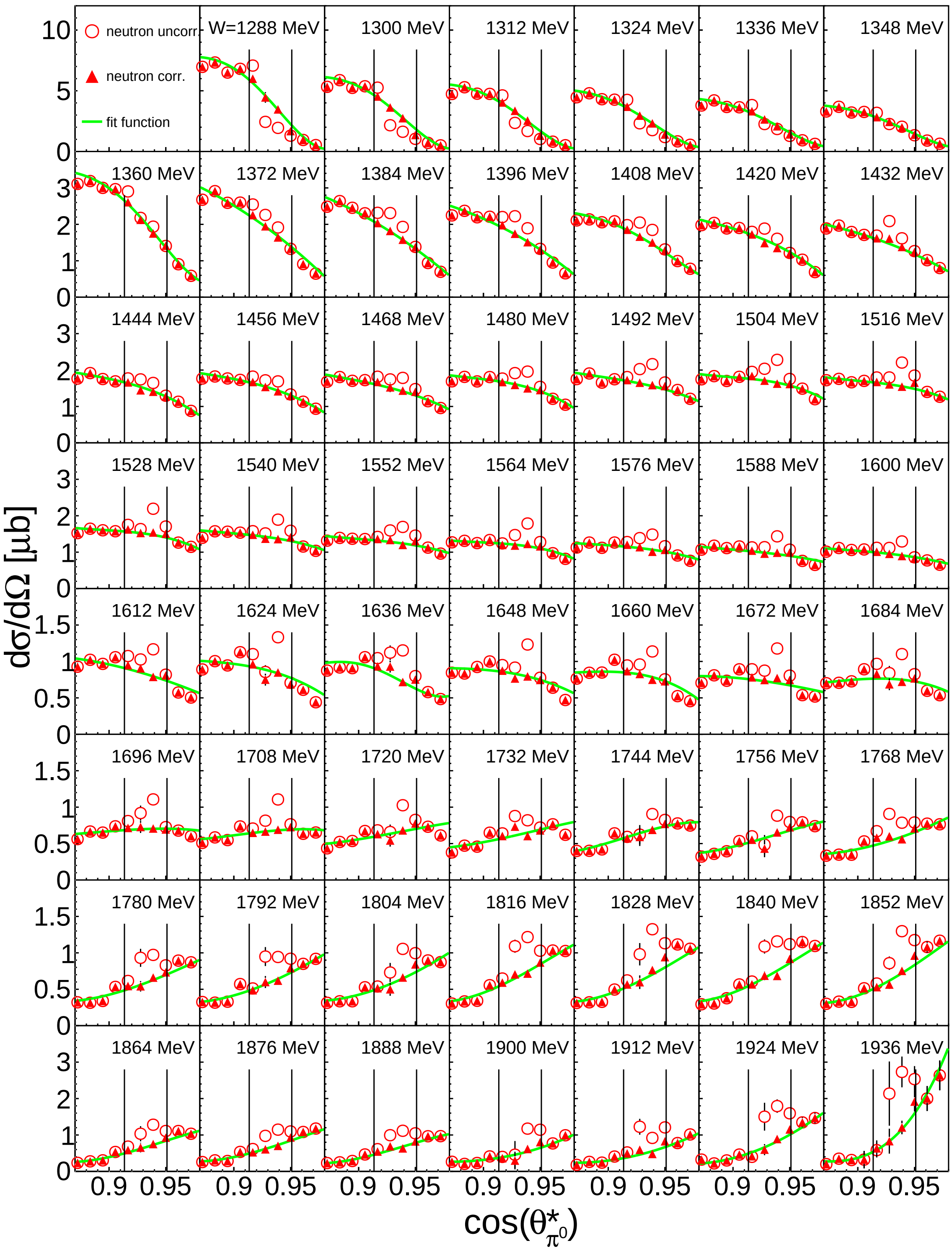

Figure 6.107: Correction of the gap between the Crystal Ball detector and TAPS for single π^0 photoproduction from quasi-free neutrons of the A2 liquid deuterium beamtime from May 2009. Shown are uncorrected (open circles) and corrected (filled triangles) differential cross sections as a function of the neutron polar angle in the lab frame. The gap between the detectors is indicated by the vertical black lines.

6.10 Determination of the Photon Flux

For the measurement of cross sections, σ, precise knowledge of the photon flux Φ is required. As the cross section is defined as:

$$\sigma = \frac{\dot{N}}{n \cdot \Phi} = \frac{\dot{N}}{\rho \cdot \dot{N}_\gamma} \ , \tag{6.28}$$

where $\dot{N}$ is the event rate and n is the number of reaction partners in the target of surface density $\rho = n/A$ and $\dot{N}_\gamma = \Phi \cdot A$ is the rate of incoming beam photons. In order to allow for measuring counts instead of rates, the time information can be integrated out and Equation (6.28) is given by:

$$\sigma = \frac{N}{\rho \cdot N_\gamma} \ . \tag{6.29}$$

Therefore, the number of photons N_γ that impinged on the target has to be determined, instead of the flux. This requires knowledge of the number of electrons N_{e^-} that radiated a bremsstrahlung photon and the fraction of those photons $\varepsilon_{\text{tagg}}$ that reached the target. The first is given by the number of electrons that have been detected by the tagging system and the latter is determined by means of a tagging efficiency measurement:

$$\varepsilon_{\text{tagg}} = \frac{N_\gamma}{N_{e^-}} \ . \tag{6.30}$$

At A2, the tagging efficiency is determined with periodic measurements in between data taking. At CBELSA/TAPS, it can be constantly measured during the dataruns. The following sections present the individual methods used at A2 and CBELSA/TAPS for the determination of the number of photons N_γ that impinged on the target.

6.10.1 Photon Flux Determination at A2

The magnetic field of the large tagger dipole magnet deflects electrons, that radiated a bremsstrahlung photon, onto the focal plane detector, where their energy can be deduced from the corresponding detector element (see Sections 2.2.1 and 5.2.11). The number of electrons that were detected by a certain tagger channel is measured with scaler modules. During the measurement, events are only recorded when the data acquisition is available and not reading out information from the detectors. Therefore, the electron scalers must be inhibited during the readout, i.e. during the deadtime, in order to count the correct number of electrons N_{e^-}. Typical tagger lifetimes range from 25% with the old readout system to 70% with the new readout system (depending on the experimental conditions).

As previously mentioned, tagging efficiency measurements were carried out regularly in order to determine the fraction of generated bremsstrahlung photons that

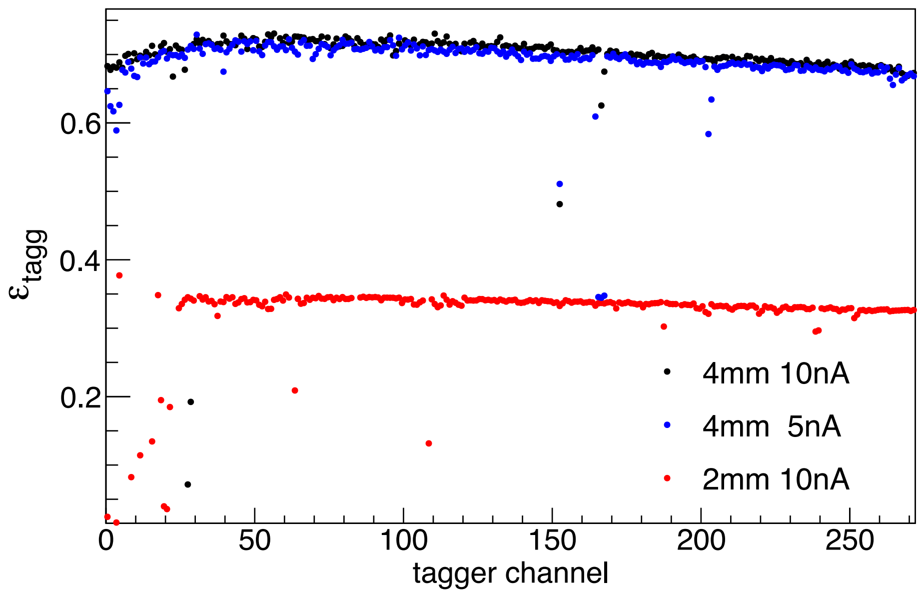

Figure 6.108: Tagging efficiency measurements from three different experimental conditions at A2. Black circles: December 2007 beamtime, electron beam current of 10 nA, 4 mm collimator. Blue circles: February 2009 beamtime, electron beam current of 5 nA, 4 mm collimator. Red circles: March 2015 beamtime, electron beam current of 10 nA, 2 mm collimator.

reached the target. Normal data taking is paused so dedicated runs of tagging efficiency may be taken. For this purpose, the lead glass detector (see Section 2.2.6) is moved into the beamline behind the TAPS detector in upstream direction to count the beam photons for roughly 30 minutes. This is only possible, since the probability that the photon interacts with the target is almost negligible. The lead glass detector is ideally suited for the tagging efficiency measurement, since it exhibits a photon detection efficiency of nearly 100%, even though this is only valid for low intensity beams. This is the reason that it is impossible to have an online tagging efficiency measurement at the usual high intensities during an experiment. However, the tagging efficiency primarily depends on the electron beam energy and the size of the photon beam collimator, that was used to focus the beam onto the target, and only weakly on the intensity of the photon beam. Therefore, it was assumed that the tagging efficiency measurement at low beam intensities can also be applied to high intensity beams. As the rate of tagger hits at low beam intensities is low, the measurement is significantly influenced by background contamination from cosmic radiation or from activated materials in the proximity of the tagging spectrometer. To account for such background contributions, an additional measurement without beam is carried out before and after the actual tagging efficiency measurement. The average of both background measurements is then subtracted from the tagging efficiency measurement. Figure 6.108 shows results of tagging efficiency measurements from the three different beamtimes used in this work. The tagging efficiencies of the same collimator diameter, but with half of the beam current are almost identical,

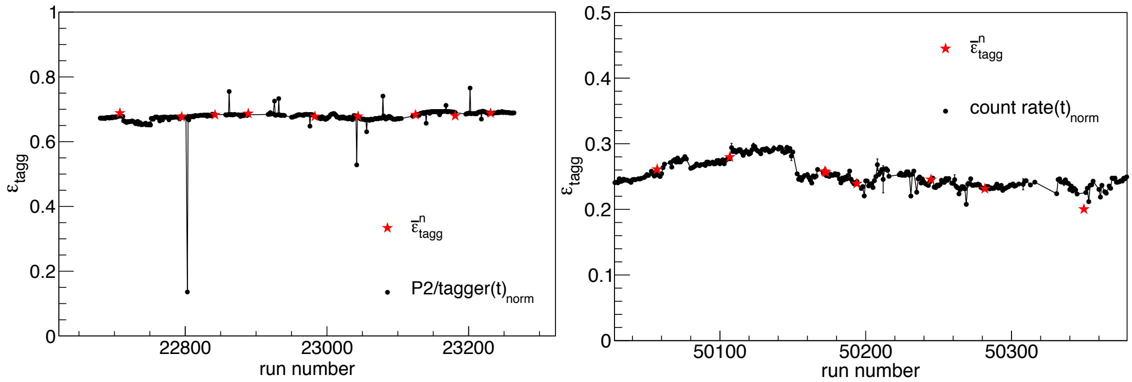

(a) From P2 to tagger ratio

(b) From $\pi^0 X$ count rate measurement

Figure 6.109: Illustration of the determination of the time dependent tagging efficiency at A2 obtained from the average values of the absolute values from the tagging efficiency measurements (red stars) and the time dependent relative values from (a) the P2 to tagger hit ratio from the May 2009 beamtime (black circles) and (b) the $\pi^0 X$ count rate measurement from the July 2013 beamtime (black circles).

indicating that the differences between the typical A2 electron beam currents has no strong influence on the tagging efficiency values. In contrast, the same beam current but a collimator of half sized diameter lowers the tagging efficiency by roughly a factor of two. This is reasonable, since the number of incident photons is proportional to the cross section area of the photon beam. In principle, a two times smaller collimator diameter would result in a four times smaller area and hence would lower the tagging efficiency by a factor of four. However, after the passage through the radiator, the photon beam is not parallel. Using a 4 mm collimator, the beam diameter at the target is about 1.3 cm and for a 2 mm collimator the beam diameter at the target is about 0.9 cm. Hence, the ratio of both areas is about two, which corresponds to the observed difference of the tagging efficiency values.

The instability of the beam position and quality require a time dependent determination of the tagging efficiency. Even though the tagging efficiency measurements were usually carried out periodically, i.e. once per day, this is not sufficient for an appropriate normalization of the data. In order to monitor the tagging efficiency during data taking, the P2 ionization chamber (see Section 2.2.7), which is permanently installed in the beamline, was used. Since its signals are proportional to the photon flux, the ratio of the registered hits to those in the tagger allow for a online relative measurement of the tagging efficiency. The time dependent relative measurement is then normalized to the n absolute tagging efficiency values. For every run, the average ratio of the hits in the P2 ionization chamber to those in the tagger, P2/tagger(t), was determined and a χ^2 minimization was then used to normalize the time (run) dependent relative values to the average of the absolute values $\bar{\varepsilon}^n_{\text{tagg}}$ of all n_c channels, as shown in Figure 6.109a. As this procedure was carried out

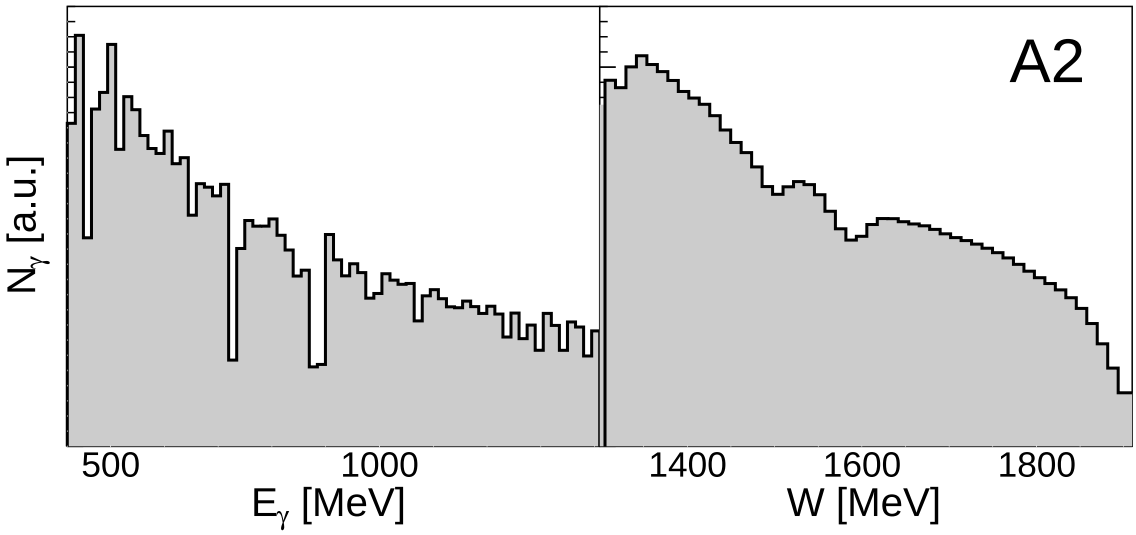

Figure 6.110: Number of photons N_γ per energy bin that impinged on the target. Left-hand side: N_γ as a function of the incident photon beam energy E_γ. Right-hand side: N_γ as a function of the final state invariant mass W (see Section 6.10.3). Results obtained from the May 2009 beamtime at A2.

with values that were averaged over all tagger channels, the channel dependency was recalculated as follows. For every run, the value from the normalized P2/tagger ratio, P2/tagger$(t)_{\mathrm{norm}}$, was taken as a reference value. From the n absolute tagging efficiency measurements, the average value $\overline{\varepsilon}_{\mathrm{tagg}}(c)$ for every tagger channel c and also the global average $\overline{\varepsilon}_{\mathrm{tagg}}$ of the tagging efficiency, was determined. The time and channel dependent tagging efficiency is then given by the value of the normalized P2/tagger ratio, multiplied by the average tagging efficiency of this channel, divided by the global average tagging efficiency value:

$$\varepsilon_{\mathrm{tagg}}(c,t) = \frac{\overline{\varepsilon}_{\mathrm{tagg}}(c)}{\overline{\varepsilon}_{\mathrm{tagg}}} \cdot \mathrm{P2/tagger}(t)_{\mathrm{norm}} \ , \tag{6.31}$$

where the averages were determined as follows:

$$\begin{aligned} \overline{\varepsilon}^{n}_{\mathrm{tagg}} &= \frac{1}{n_c}\sum_{i=1}^{n_c} \varepsilon^{n}_{\mathrm{tagg}}(i) \\ \overline{\varepsilon}_{\mathrm{tagg}}(c) &= \frac{1}{n}\sum_{i=1}^{n} \varepsilon^{i}_{\mathrm{tagg}}(c) \qquad . \\ \overline{\varepsilon}_{\mathrm{tagg}} &= \frac{1}{n_c}\sum_{i=1}^{n_c} \overline{\varepsilon}_{\mathrm{tagg}}(i) \ . \end{aligned} \tag{6.32}$$

For one of the deuterated butanol beamtimes (July 2013), the relative monitoring of the tagging efficiency with the P2/tagger ratio was not possible since the P2 scalers were not recorded in the data stream. For this reason, in order to reduce systematic effects, the monitoring for all deuterated butanol beamtimes was done with the count rate measurement of inclusive single π^0 photoproduction. As this reaction channel offers the highest statistics, it was possible to achieve a statistically relevant count rate value per run and a reliable alternative to the P2/tagger ratio, as shown in Figure 6.109b.

In the analysis, the number of incident beam photons $N_\gamma(c)$ that correspond to a certain tagger channel c are then determined as follows: for every run, the number of detected electrons $N_{e^-}(c,t)$ of every tagger channel c are multiplied with the corresponding tagging efficiency value $\varepsilon_{\text{tagg}}(c,t)$. Subsequent integration over the time (runs) yields the number of photons per tagger channel that impinged on the target:

$$N_\gamma(c) = N_{e^-}(c) \cdot \varepsilon_{\text{tagg}}(c)\ . \tag{6.33}$$

The obtained spectrum needs to be converted from photons per tagger channel to photons per bin of incident photon energy E_γ. Thereby the energy binning of the photon count spectrum was chosen to be identical to those used for the extraction of the results, to allow for a direct normalization of the results. For this purpose, the counts per tagger channel were converted to counts per energy bin by means of the bin-overlap method [206], which properly takes the finite and individual energy bin sizes of the tagger channels into account. A typical example of such a resulting spectrum is shown on the left-hand side of Figure 6.110.

6.10.2 Photon Flux Determination at CBELSA/TAPS

The determination of the number of photons that impinge on the target at the CBELSA/TAPS experiment is similar to that discussed at A2 in Section 6.10.1. The main difference is that it can be measured with the Gamma Intensity Monitor (GIM) (see Section 2.5.7) during data taking. However, the high beam intensities can lead to saturation of the detectors or the electronics. At high beam intensities, background contributions in the tagger from activated materials or cosmic radiation can be neglected, but the sample is contaminated with random electron hits in the tagger that have to be properly subtracted.

The determination of the number of photons that impinged on the target is based on the number of photons that were reconstructed out of the electrons that were detected in the tagging spectrometer (see Section 4.2.1). Due to the high beam intensities, this number contains true bremsstrahlung photons and also misidentified photons from random electron hits in the tagger. Furthermore, an additional reduction of the available photons results from the collimation of the photon beam. The determination of the correct number of photons that impinged on the target therefore requires a slightly different method than used at A2, which was described in Section 6.10.1.

The number of reconstructed beam photons $N_{\Delta t}$ (see Section 4.2.1) were counted within a certain time window Δt outside of the coincidence peak in their time spectrum in order to avoid influences of the trigger to the measured photon distribution. The fraction of photons of the initial sample, that do not stem from the reconstruction of random background electrons or were stopped by the collimator, can be determined with the tagging efficiency measurement. For this purpose, the GIM is

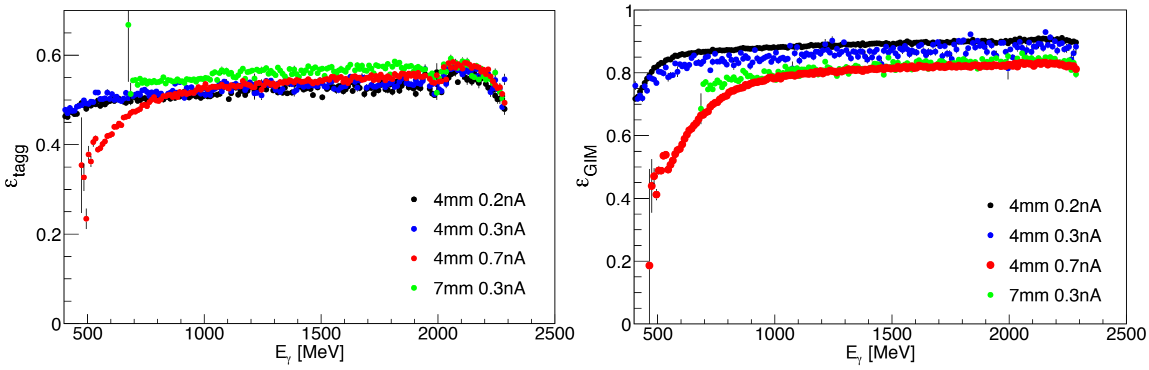

(a) Tagging efficiency **(b)** GIM efficiency

Figure 6.111: Tagging efficiency measurements (left-hand side) and GIM efficiency (right-hand side) of four different experimental conditions at CBELSA/TAPS. Black circles: November 2008 beamtime, electron beam current of 0.2 nA, 4 mm collimator. Blue circles: December 2008 beamtime, electron beam current of 0.3 nA, 4 mm collimator. Red circles: January 2011 beamtime, electron beam current of 0.7 nA, 4 mm collimator. Green circles: December 2008 beamtime, electron beam current 0.3 nA, 7mm collimator.

used, which is located in the photon beam at the end of the beamline and constantly counts the impinging photons. After a side-band analysis of the tagger-GIM time spectrum, the comparison of the coincident hits between the GIM and tagger with the total amount of tagger hits yields the tagging efficiency:

$$\varepsilon_{\text{tagg}} = \frac{N_{\text{tagger-GIM}}}{N_{\text{tagger}}} \, . \tag{6.34}$$

Figure 6.111a shows the tagging efficiencies $\varepsilon_{\text{tagg}}$ for four different settings using different electron currents and collimators. As seen in the A2 results in Figure 6.108, the tagging efficiency depends more on the size of the collimator than on the electron beam current.

However, an additional correction is necessary, since the intensity of the beam is already at the upper limit for a reliable measurement with the GIM. Due to the high rates, the electronics of the GIM (mainly the CFDs) became saturated over time, which resulted in a loss of detected photons. For this reason, the GIM efficiency, ε_{GIM}, was determined with the FluMo (see Section 2.5.7) and then used to correct the tagging efficiency. The measured GIM efficiencies (that correspond to the tagging efficiencies shown in Figure 6.111a) are shown in Figure 6.111b. It is clearly visible that with higher beam intensities the GIM efficiency decrease due to increasing saturation of the electronics, mainly of the discriminators. The latter are also responsible for the low efficiency at low photon energies, whereas at higher photon energies threshold effects can not contribute anymore. Due to the comparable high rates during the January 2011 beamtime, the thresholds of the GIM had to be increased in order to avoid immediate saturation. This resulted in an even stronger

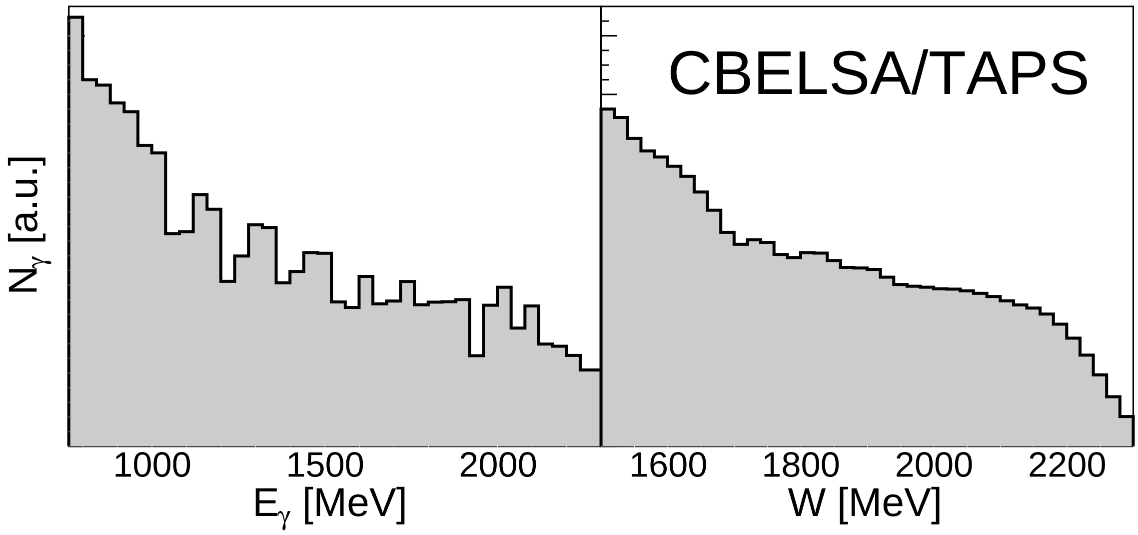

Figure 6.112: Number of photons N_γ per energy bin that impinged on the target. Left-hand side: N_γ as a function of the incident photon beam energy E_γ. Right-hand side: N_γ as a function of the final state invariant mass W (see Section 6.10.3). Results obtained from the December 2008 beamtime at CBELSA/TAPS.

decrease of the GIM efficiency at low photon energies, as can be seen in Figure 6.111b.

At this point, the true number of photons that impinged on the target during the time interval Δt can be determined. However, a proper normalization requires knowledge of the number of photons that reached the target within the time interval, t_{live}, when the events were recorded. The conversion from time interval Δt to the lifetime t_{live} can be carried out with the information from the tagger scalers that count the events N_{scaler} when the system is not busy. The conversion factor is then given by:

$$c_{\Delta t \to t_{\text{life}}} = \frac{N_{\text{scaler}}}{N_{\Delta t}} \ . \tag{6.35}$$

Additionally, beamtimes were corrected for deadtime if they included the Cherenkov detector in the setup. Since it is located in the forward region between the Crystal Barrel detector and MiniTAPS, it receives very high rates and exhibits a non negligible deadtime of 5% (deuterated butanol and carbon beamtimes) and 8% (liquid hydrogen and deuterium beamtimes) which is not considered in the system.

Finally the integrated photon flux, i.e. number of photon that impinged on the target within the lifetime t_{life} for a given energy bin ΔE_γ can be calculated as:

$$N_\gamma(\Delta E_\gamma, t_{\text{life}}) = N_\gamma(\Delta E_\gamma, \Delta t) \cdot \varepsilon_{\text{tagg}}(\Delta E_\gamma) \cdot \frac{c_{\Delta t \to t_{\text{life}}}}{\varepsilon_{\text{GIM}}(\Delta E_\gamma)} \ . \tag{6.36}$$

An example distribution of the obtained photon flux is shown on the left-hand side in Figure 6.112.

6.10.3 Determination of the W-dependent Flux

The photon flux determined with Equations (6.33) or (6.36) provides the number of photons of an energy E_γ within an energy interval (energy bin) ΔE_γ that impinged on the target during the time when the events were recorded. This ensures a proper normalization used for the extraction of cross sections as a function of E_γ. However, the extraction of normalized cross sections as a function of the final state invariant mass W is different. In the case of free targets (such as liquid hydrogen), the target nucleon is at rest and the results as a function of E_γ can directly be converted to W by using Equation (6.13). In the case of quasi-free targets, a reaction at a given incident photon energy E_γ does not correspond to a specific W, according to Equation (6.13), but rather to a distribution around this value, as shown in Figure 6.113. It can be seen that as the integral of each curve corresponds to the number of photons of the energy bin ΔE_γ, the integrals are decreasing with higher energy, reflecting the $1/E_\gamma$ bremsstrahlung spectrum.

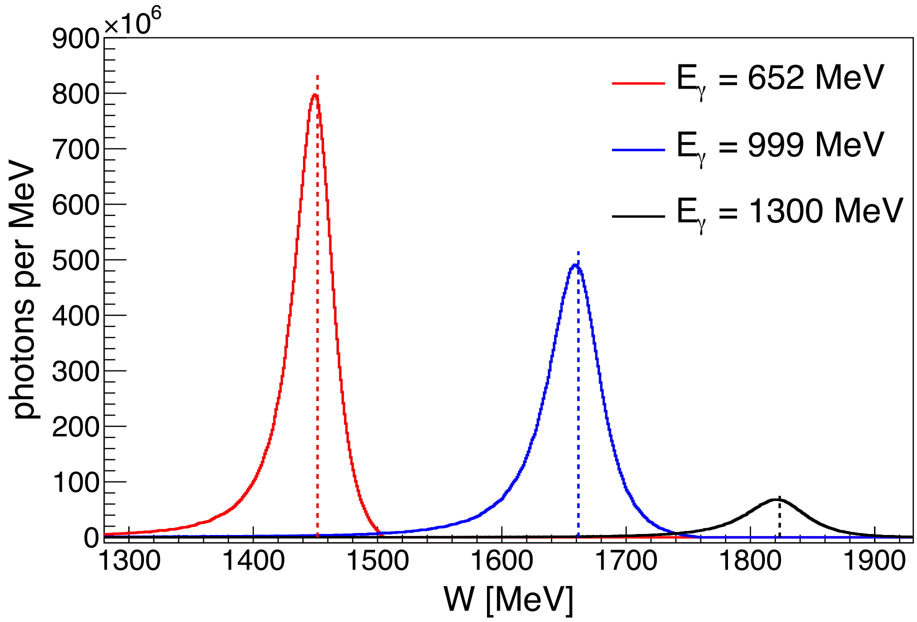

Figure 6.113: Illustration of the contributions of three individual tagger channels to the W-dependent photon flux in quasi-free kinematics (reaction on the proton, neutron treated as spectator). Solid lines: contributions to the photon flux. Dashed lines: corresponding W values in free kinematics according to Equation (6.13). Taken from [100].

The determination of the photon flux for energy intervals ΔW is based on a sampling method. For every initial energy bin ΔE_γ and corresponding number of photons $N_\gamma(c)$, a certain amount of events n are sampled and according to a randomly chosen Fermi momentum $\vec{p}_F$, the corresponding W value is calculated. For every event, the obtained W value is filled in a histogram and weighted with N_γ/n to ensure conservation of the normalization. Thereby, as for the E_γ-dependent photon

flux, the W histogram was also filled with the bin-overlap method.
The resulting photon flux as a function of W is shown on the right-hand side of Figures 6.110 and 6.112. Both distributions were obtained by applying the sampling method to the E_γ dependent photon flux on the left-hand side of each figure. The effects from Fermi motion are visible. Structures such as broken tagger channels and sharp edges at low and high energies are smeared out.

6.11 Determination of the Polarization Values

For the extraction of polarization observables from the deuterated butanol data, precise knowledge of the time dependent degree of polarization of the longitudinally polarized electron beam and the longitudinally polarized target is required. Furthermore, since the longitudinally polarized electrons transfer their polarization to circularly polarized photons, the photon beam polarization has to be extracted according to Equation (2.5), derived from Olsen and Maximon [133]. The next section present the methods that were used to determine the degree of beam and target polarization required for the analysis.
Only the product of the photon and target polarization has to be considered for the calculation of the double polarization observable E (see Equation (6.47)). In the analysis, this is realized by weighting the events with the inverse product of the two polarizations, i.e. $1/(p_\gamma \cdot p_T)$. Therefore, the statistical quality of the results is directly related to the size of the product of the two polarization degrees. For this reason, in the following, the determination of the photon and target polarization will be discussed separately, but the final polarization valued will be compared next to each other to allow for an immediate statement of their influence on the results.

6.11.1 Determination of the Photon Beam Polarization

As discussed in Section 2.7.2, the electron beam polarization can be determined from either a Mott or a Møller measurement. Whereas the Mott measurement is usually carried out near to the electron source, the Møller setup is located in the experimental hall next to the tagging spectrometer. As in general, the electron beam polarization is not conserved during the different accelerator stages of the beam, it is preferred to perform the measurement of the polarization with the Møller setup at the final stage, i.e. close to the radiator. At ELSA, Mott measurements were not used at all for the determination of the beam polarization, since the ramping of the magnets during the different accelerator stages strongly affects the beam polarization. For this reason, the beam polarization at CBELSA/TAPS was determined only with the Møller measurement. However, the microtron cascade at MAMI provides a very stable and highly continuous beam, which conserves the degree of beam polarization to a high degree. This allows for the measurement of the beam polarization with Møller and Mott measurements. The Mott measurement is performed at a beam energy of 3.65 MeV. With increasing energy, the beam starts to exhibit a non-negligible trans-

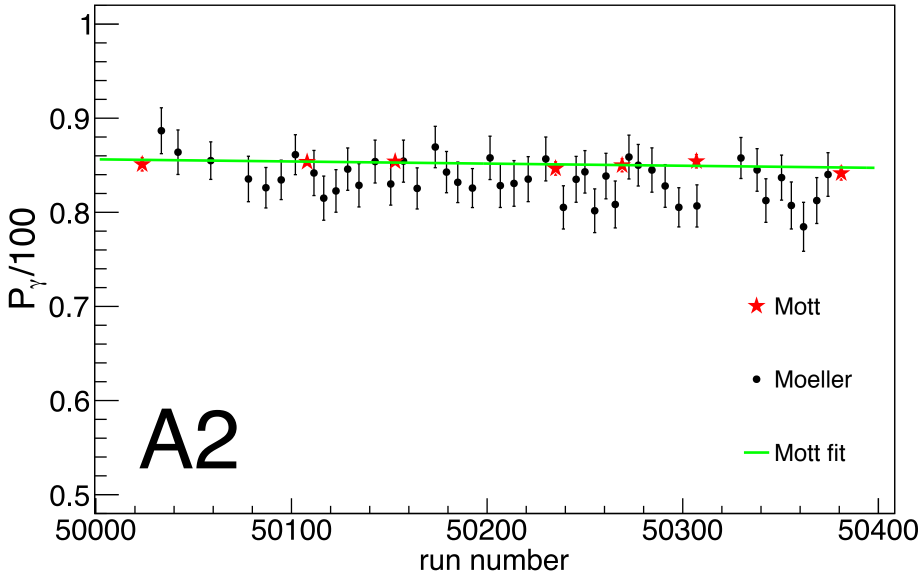

Figure 6.114: Example of the extraction of the electron beam polarization from the Mott measurements for the different dataruns of the July 2013 beamtime at A2. Black dots: electron polarization obtained from the online Møller measurements. Red stars: electron polarization obtained from the daily Mott measurements. Green line: fit of the Mott results, used for the extraction of the polarization values.

verse component of the polarization which influences the measurement. Therefore, a correction factor $k = 1.0551$ was applied to adapt the polarization value to the high energies used in the experiment.

The Mott measurement for a MAMI angle of $\phi_{\text{MAMI}} = 81°$ was normally performed once a day by the MAMI operators, which then provided the values of the measured asymmetry. To reduce systematic uncertainties, the measurement was carried out with and without the $\lambda/2$ plate (see Section 2.7.1), resulting in two values for the asymmetry. From the asymmetries, A_{Mott}, the resulting electron beam polarization is then given by:

$$P_{e^-} = \frac{A_{\text{Mott}}}{\sin(\phi_{\text{MAMI}}) \cdot 0.3930} \cdot k \ , \tag{6.37}$$

from which the mean value was taken as the degree of electron beam polarization for the analysis. Table 6.9 gives an example of the measured asymmetries A_{mott} and the resulting beam polarization.

In contrast to the Mott measurement only performed at MAMI, at A2 and CBELSA/TAPS, the Møller measurement was carried out in parallel to the data taking as the Møller foil was permanently used as a radiator. This allows for a permanent monitoring of the electron beam polarization. However, at CBELSA/TAPS, a Møller polarimeter is used for the measurement and at MAMI, the measurement is

Measurement #	Asymmetry A_{mott} [%] with $\lambda/2$ plate	without $\lambda/2$ plate	Electron beam polarization P_{e^-} [%]
1	-31.522 ± 0.267	+31.001 ± 0.256	84.975 ± 0.711
2	-31.525 ± 0.067	+31.278 ± 0.065	85.356 ± 0.179
3	-31.541 ± 0.070	+31.290 ± 0.068	85.394 ± 0.188
4	-30.964 ± 0.266	+31.323 ± 0.256	84.654 ± 0.709
5	-31.782 ± 0.258	+31.056 ± 0.251	84.995 ± 0.692
6	-31.818 ± 0.265	+31.033 ± 0.260	85.421 ± 0.714
7	-30.721 ± 0.271	+31.196 ± 0.266	84.151 ± 0.730

Table 6.9: Example of the calculation of the degree of the electron beam polarization from the measured Mott asymmetries. Values from July 2013 beamtime at A2.

carried out with the tagging spectrometer. As a consequence, the statistical errors of the measurement at A2 are rather large, especially compared to those from the Mott measurement. The electron polarization at A2 resulting from the Mott (see Table 6.9) and Møller measurements are shown in Figure 6.114. It shows the large statistical uncertainties of the Møller (black dots) compared to the Mott measurement (red stars), as well as the high stability of the electron beam polarization. Both results are compatible, but the Mott measurement is of higher precision. In order to obtain the time dependent electron beam polarization the Møller results were omitted and the Mott results were fit with a linear function (green line).
At CBELSA/TAPS, the precision of the Møller measurement is sufficient for the determination of the electron beam polarization, as illustrated in the left-hand side figure of Figure 6.116. In addition, the instability of the beam due to the ramping and extraction methods does not allow for an extrapolation of daily measurements. Therefore, the electron beam polarization at the A2 experiments was determined by a linear fit of the daily Mott measurements (as shown in Figure 6.114), whereas at CBELSA/TAPS, it was taken from the online Møller measurements. The resulting and final electron beam polarization used for the analysis of the A2 data is presented on the left-hand side of Figure 6.115 and for the analysis of CBELSA/TAPS data on the left-hand side of Figure 6.116. Shown are the electron beam polarization values as a function of an arbitrary run number for all analysed beamtimes (distinguished by colors). From the final values, a degree of polarization was assigned to every run, which was then available for the analysis.

In the analysis, the degree of photon polarization was determined event by event from the Olsen Maximon formula [133] (Equation (2.5)) and the corresponding incident photon energy. This formula describes the degree of circular polarization P_γ of a bremsstrahlung photon of energy E_γ after being radiated from a longitudinally polarized electron of energy E_{e^-} and polarization P_{e^-}:

$$P_\gamma = P_{e^-} \cdot \frac{4x - x^2}{4 - 4x + 3x^2} , \tag{6.38}$$

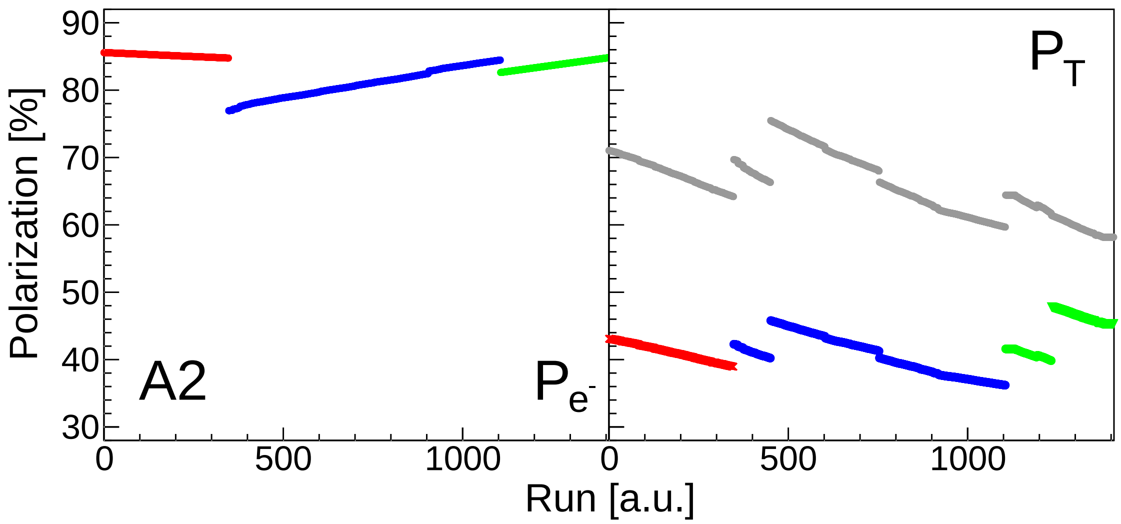

Figure 6.115: Final electron beam and target polarization values per run used in the A2 analysis of the July 2013 (red), February 2014 (blue) and March 2015 (green) beamtimes. Left-hand side: absolute electron beam polarization obtained from a linear fit of the individual contiguous Mott measurements. Right-hand side: gray dots: absolute target polarization obtained from the individual start and end values from NMR measurement and subsequent fitting with an exponential function. Colored dots: final values, i.e. gray values normalized with the polarization correction values and the *d*-wave contribution.

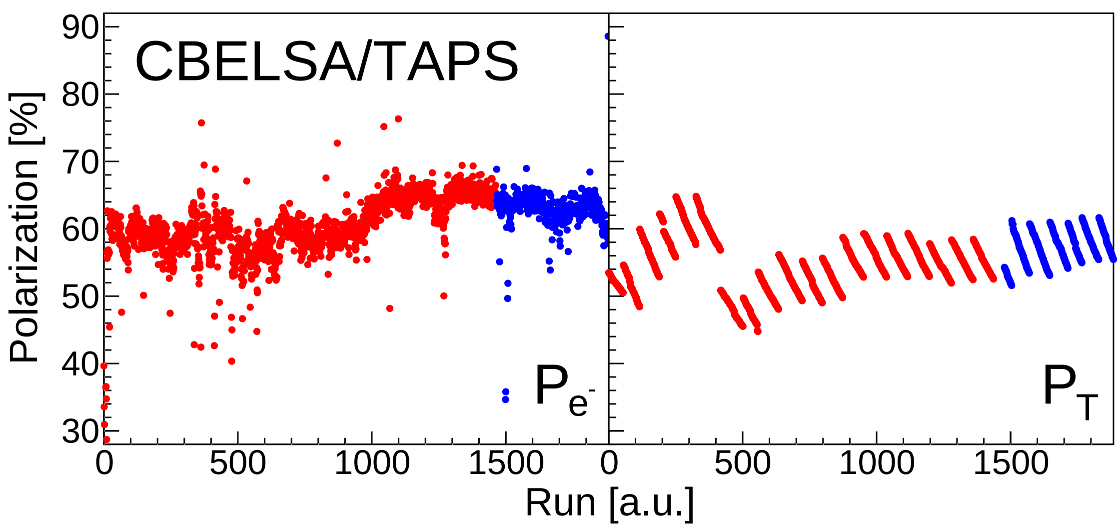

Figure 6.116: Final electron beam and target polarization values per run used in the CBELSA/TAPS analysis of the January 2011 (red) and June 2011 (blue) beamtimes. Left-hand side: absolute electron beam polarization obtained from the online Møller measurement. Right-hand side: absolute target polarization obtained from the individual start and end values from NMR measurement and subsequent fitting with an exponential function.

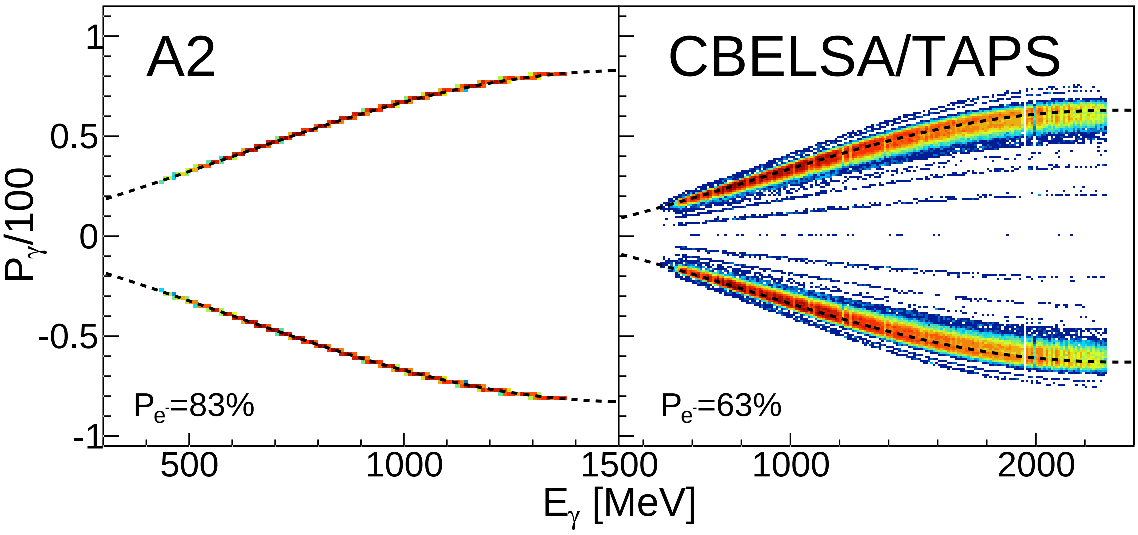

Figure 6.117: Photon polarization as a function of the incident photon energy for the July 2013 beamtime from A2 (left-hand side) and for the January 2011 beamtime from CBELSA/TAPS (right-hand side). Black fit lines: corresponding Olsen Maximon formulae for an electron beam energy of $E_{e^-} = 1557$ MeV and an electron beam polarization of $P_{e^-} = 83\%$ for A2 (left-hand side) and for $E_{e^-} = 2350$ MeV and $P_{e^-} = 63\%$ for CBELSA/TAPS (right-hand side).

where $x = E_\gamma/E_{e^-}$. The left-hand side of Figure 6.117 illustrates the photon polarization of one beamtime at A2 (July 2013) and the right-hand side of one beamtime at CBELSA/TAPS (January 2011). In addition, the measured distributions are compared to the theoretical formula (dotted black line) for the maximum electron beam energy of $E_{e^-} = 1557$ MeV and mean polarization $P_{e^-} = \pm 83\%$ for A2 and the maximum electron beam energy of $E_{e^-} = 2350$ MeV and mean polarization $P_{e^-} = \pm 63\%$ for CBELSA/TAPS. The distributions of the obtained photon polarizations of all runs at A2 are depicted on the left-hand side of Figure 6.124 and of all runs at CBELSA/TAPS on the left-hand side of Figure 6.125.

6.11.2 Determination of the Target Polarization

In contrast to the electron beam polarization, the target polarization can not be measured during data taking, as it requires a special setup for the NMR measurement. Hence it was measured before the experiment, once the target was polarized. Depending on the relaxation time of the target, the experiment was interrupted to allow for repolarization of the target or for changing the direction of polarization. The polarization was then remeasured before and after the repolarization process. From these measurements, start and end values of the target polarization were available, from which the corresponding values of the individual runs were extracted. For this purpose, the exponential decay of the polarization was used to calculate the polarization P at a time t:

$$P(t) = P_{\text{start}} \cdot \exp\left(-\frac{\Delta t}{\tau}\right) , \qquad \tau = \frac{\Delta t}{\ln\left(\frac{P_{\text{start}}}{P_{\text{end}}}\right)} , \tag{6.39}$$

where P_{start} is the initial polarization and P_{end} the final polarization, $\Delta t = t_{\text{end}} - t_{\text{start}}$ the time difference between the two measurements, and τ the corresponding relaxation time. The resulting target polarization values for all beamtimes (gray dots) at A2 are shown on the right-hand side of Figure 6.115 and for CBELSA/TAPS on the right-hand side of Figure 6.116. It can be seen that the relaxation times of the target at CBELSA/TAPS are much shorter than at A2 due to the lower temperatures at A2 (see Section 2.8.2) that maintain the polarization. Therefore, at CBELSA/TAPS, repolarization was necessary almost every second or third day ($\tau_{\text{CBELSA/TAPS}} \approx 340\text{h}$), whereas at A2 ($\tau_{\text{A2}} \approx 2000\text{h}$), repolarization was normally combined with changing the direction of polarization.

6.11.3 Target Polarization and Magnetic Field Inhomogeneities at A2

The photon beam and target polarization values shown in Figures 6.115 for A2 and 6.116 for CBELSA/TAPS were the basis for the analysis of A2 and CBELSA/TAPS data for the extraction of the polarization observable E and the helicity dependent cross sections $\sigma_{1/2}$ and $\sigma_{3/2}$. During the analysis of η photoproduction from polarized nucleons, which was the subject of the PhD thesis of Lilian Witthauer [173], significant differences between the results for E from CBELSA/TAPS and A2 were observed. Having isospin $I = 0$, the η meson has the special characteristics that it acts as isospin filter, i.e. can only originate from an intermediate N^* resonance of isospin $I = 1/2$ and not from Δ resonances of isospin $I = 3/2$. This immediately reduces the possible resonances that contribute to η photoproduction cross sections. In addition, for the first few hundred MeV above threshold (~ 630 MeV), the excitation spectrum is dominated by the contribution of the $N(1535)1/2^-$. Due to this dominant contribution, η photoproduction acts as a key reaction concerning helicity dependent cross sections. As resonances with total angular momentum $J = 1/2$ can only contribute to $\sigma_{1/2}$, the helicity dependent cross section $\sigma_{3/2}$ is expected to be negligible in the first energy range above the production threshold. Nuclear effects such as final state interactions could have an influence on the result, but the comparison of the free and quasi-free η photoproduction cross sections [207, 208] excludes such effects. Therefore, since $\sigma_{3/2}$ should not contribute in the region of the $N(1535)1/2^-$ and the double polarization observable is defined as the asymmetry of the helicity dependent cross sections, i.e. $E = (\sigma_{1/2} - \sigma_{3/2})/(\sigma_{1/2} + \sigma_{3/2})$, E is expected to be one at threshold.

The results of the analysis from the CBELSA/TAPS data confirm the expectations, as shown in Figure 6.118. Within the statistical errors, the double polarization observable E is one at threshold and with emerging contributions from resonances of

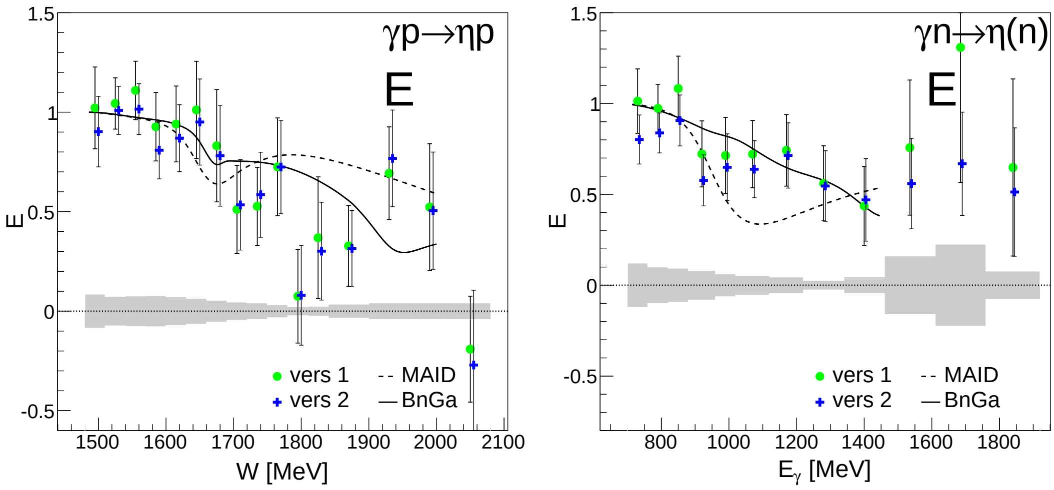

(a) $\gamma p \to \eta p$ **(b)** $\gamma n \to \eta(n)$

Figure 6.118: Double polarization observable E for η photoproduction from polarized nucleons from CBELSA/TAPS. Left-hand side: E as a function of W for the exclusive reaction $\gamma p \to \eta p$. Right-hand side: E as a function of E_γ for the inclusive reaction $\gamma n \to \eta(n)$. "vers1"("vers2") was extracted using Equation (6.57) ((6.56)). Figures taken from [173].

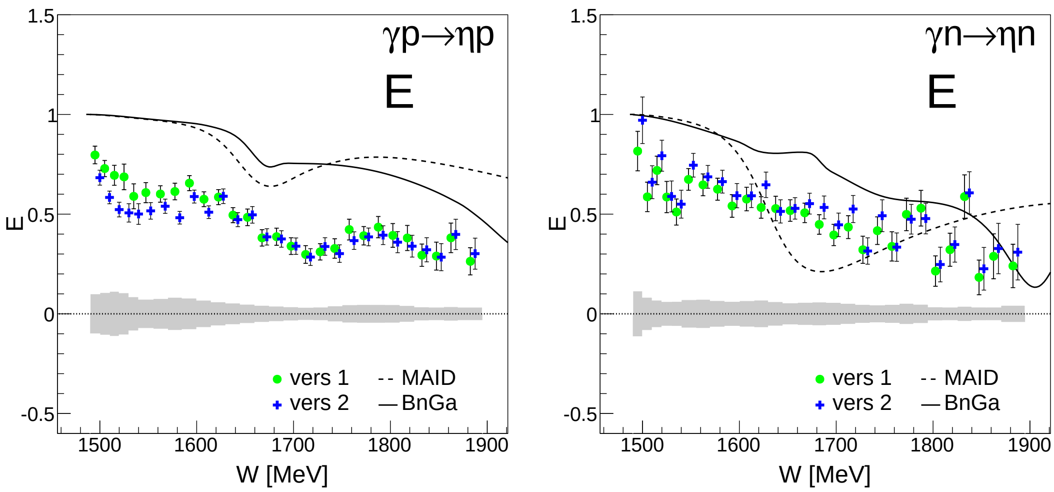

(a) $\gamma p \to \eta p$ **(b)** $\gamma n \to \eta n$

Figure 6.119: Double polarization observable E for η photoproduction from polarized nucleons from A2 obtained with the measured target polarization values (gray dots in Figure 6.115). Left-hand side: E as a function of W for the exclusive reaction $\gamma p \to \eta p$. Right-hand side: E as a function of W for the exclusive reaction $\gamma n \to \eta n$. "vers1"("vers2") was extracted using Equation (6.57) ((6.56)). Figures taken from [173].

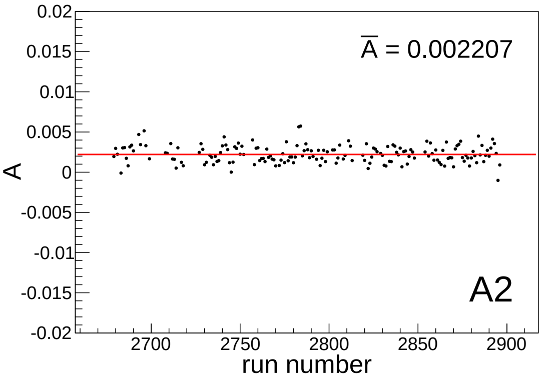

(a) Beam helicity asymmetry from the A2 data

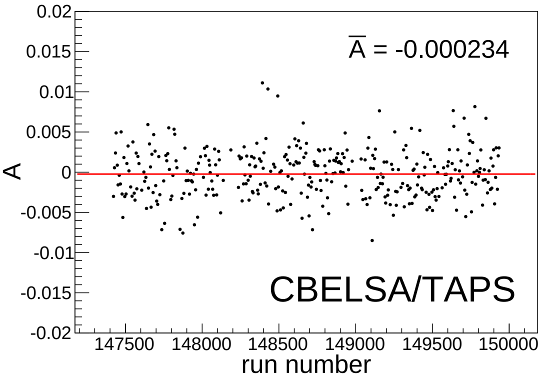

(b) Beam helicity asymmetry from the CBELSA/TAPS data

Figure 6.120: Example of the investigation of the asymmetry of the two photon helicity states. Left-hand side: February 2014 beamtime from A2. Right-hand side: January 2011 beamtime from CBELSA/TAPS. Red line: average asymmetry $\overline{A}$. Whereas the asymmetry at CBELSA/TAPS is negligible, that from A2 is one order of magnitude larger and hence considered in the analysis. Adapted from [173].

higher total angular momentum, starts to decrease. However, the equivalent analysis of the dataruns from A2 within the same work [173] were significantly lower than those from CBELSA/TAPS, as shown in Figure 6.119.
Several elaborate investigations excluded systematic errors in the general analysis procedure. Furthermore the same analysis was as well used for the extraction of the results from the CBELSA/TAPS data. An initially very promising explanation was found in the asymmetry of the helicity states of the photon. The direction of the target polarization was changed manually and it was discussed in Section 2.7.1, that the spin orientation of the electron and the photon beam depends on the helicity of the laser light with switches from positive to negative at a frequency of 0.5 Hz. Hence, one could assume that both helicity states are equally represented in the data. However, investigations of the raw photon helicity revealed a non-negligible asymmetry between the two states at A2 compared to CBELSA/TAPS. The resulting asymmetry A of both helicity states as a function of the time (run) is shown in Figure 6.120, on the left-hand side for A2 and on the right-hand side for CBELSA/TAPS. It is clearly visible that the asymmetries of the A2 data are on the order of one magnitude larger than the CBELSA/TAPS data, even though both asymmetries are below the 1% level. However, taking this asymmetry into account did not show any difference which, after all, is rather reasonable. At threshold, the double polarization observable almost purely consists of antiparallel beam target spin configurations ($\sigma_{1/2}$) and hence an asymmetry below 1% is negligible.

The agreement of the extracted beam helicity asymmetry $I^{\odot}$ for $2\pi^0$ photoproduction with published data [56] excluded errors in the determination of the beam

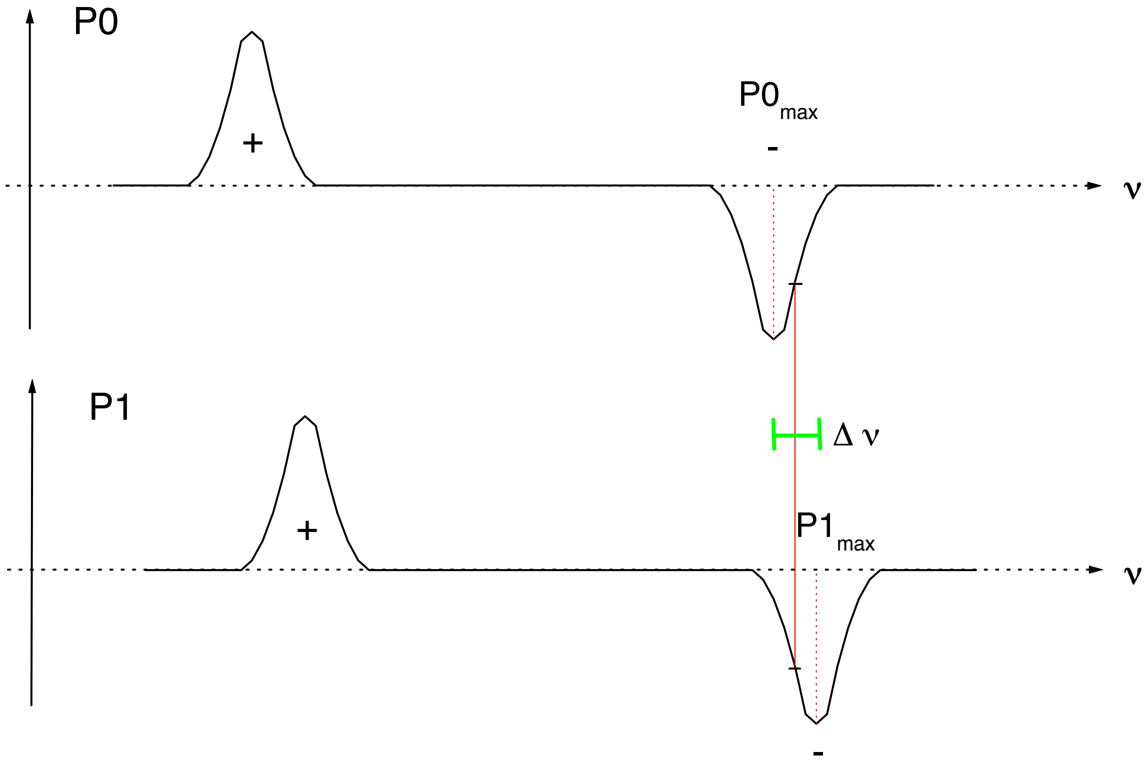

Figure 6.121: Schematic illustration of the influence of magnetic field inhomogeneities on the polarization frequency ν. Depending on the local magnetic field, a certain Larmor frequency is required for the polarization transfer within the DNP process (see Sections 2.8.3 and 2.8.2). Shown are the resonance peaks at two different locations at different magnetic field values. Whereas the same frequency ν might meet the resonance condition at one location, it is off by a value $\Delta\nu$ from the other resonance position.

polarization such that finally the determination of the target polarization was questioned. A comparison of the results from CBELSA/TAPS (see Figure 6.118) and A2 (see Figure 6.119) showed that if the target polarization was the reason for the discrepancy, it must be off by a factor of 1.5.

In the beginning it was suspected that the photon beam induced e^+e^--pair production locally heated up the target in the inner part where it is penetrated by the photon beam. This so-called *beam heating* process is known to lower the target polarization at least at high photon fluxes locally [209]. However, at typical photoproduction measurements, the photon flux is a few orders smaller and this behavior was not really expected. Nevertheless, as the target polarization was measured with a surface coil (see left-hand side of Figure 2.35) at the surface of the target material, but the reactions occurred around the target axis, an inhomogeneous polarized target would definitely be able to explain the observed discrepancies. It must be understood however, why the problem was only observed at A2 and how it could be corrected. For this reason, the local dependence of the target polarization of the A2 Frozen Spin Target was investigated within a bachelor thesis' work [158]. During the March 2015 beamtime, a series of investigations were carried out where an additional in-beam coil (see right-hand side of Figure 2.35) with the surface coil was used in order to have a reference value of the NMR measurement. This new NMR setup was capable of measuring effects from polarization inhomogeneities due to beam heating or other processes. It was observed that based on the measured start and end polarization values, beam heating did not occur within the systematic uncertainties of the polarization measurement. Nevertheless, the comparison of the obtained polarization values from the surface and the in-beam coil revealed inhomogeneities in the target polarization. Those were not induced by beam heating, but rather from inhomogeneities of the magnetic field and the consequentially locally dependent Larmor frequency of the material. The situation is depicted in Figure 6.121. It was found that with increasing frequency, the difference between surface and in-beam polarization decreased, which requires the magnetic field to be higher at the surface than inside. A calculation of the magnetic field inhomogeneity based on the polarization difference revealed even larger inhomogeneities than experimentally determined within a former measurement [210]. However, it was concluded that the size of the magnetic field inhomogeneities result in a locally dependent nuclear Larmor frequency. Since this was not known for the July 2013 and February 2014 beamtime and only one frequency was applied, it resulted in a lower target polarization in the target center than on the surface where the target polarization was measured. Furthermore, the size of the effect is large enough to explain a discrepancy on the order of the observed factor of 1.5.

This explanation is also in agreement with the absence of the problem at CBELSA/TAPS as the polarization magnet of the latter exhibits a much higher level of field homogeneity [211]. Finally, it also explains why the problem was not observed in A2 experiments on polarized protons in butanol. Due to the narrower NMR signal of the trityl doped deuterated butanol (see Section 2.8.2) it is more sensitive to field inhomogeneities than TEMPO doped butanol which has a rather broad NMR signal. Doping deuterated butanol with TEMPO could partially solve the inhomogeneous target polarization, but would not allow for high target polarizations.
Unfortunately, as the inhomogeneous magnetic field of the past beamtimes can not be redetermined and the resulting inhomogeneity of the polarization depends on the applied frequency, a method for the correction of the target polarization values was not feasible. While the reason for the problem was found after the first investigation in the March 2015 run, the inhomogeneity of the magnetic field could partially be restored in the second half of the beam time. This resulted in much lower differences of the polarization at the surface compared to the target center. However, this does not imply that the difference in between is of the same size. Therefore, the only possibility for the correction of the target polarization value was to scale it such that the double polarization E of η photoproduction from protons and neutrons is one at threshold.

Unfortunately, the statistics of the individual A2 beamtimes was not sufficient

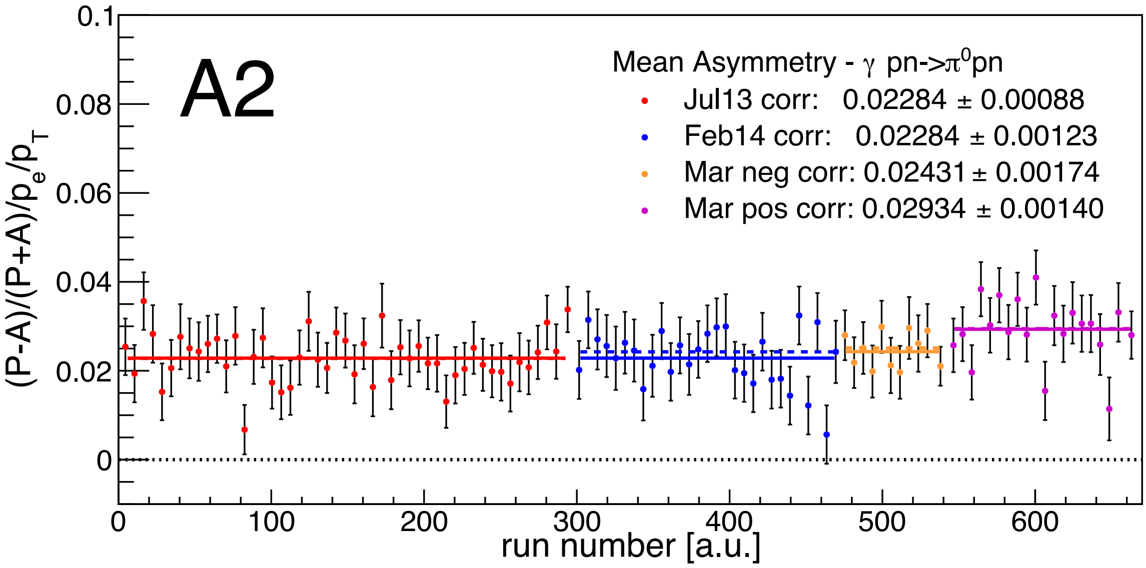

Figure 6.122: Illustration of the procedure used for the determination of the relative target polarization scale factors of the individual A2 beamtimes that were required due to the inhomogeneous magnetic field. Shown is the normalized average asymmetry of the parallel (antiparallel) (P) ((A)) photon and target spin states as a function of the dataruns (arbitrary run numbers) as obtained from the weighted mean of exclusive single π^0 photoproduction from quasi-free nucleons. Solid lines: mean asymmetries. Dashed lines: median values.

for the determination of the scale factor and was only possible with the combined statistics of all beamtimes. For this reason, the analysis of single π^0 photoproduction within this work was used to determine a relative scale factor c_{rel} for the target polarizations that ensures a comparable relative value of the individual target polarizations. Next, the absolute normalization factor c_{abs} was then determined from the investigation of the double polarization observable E of η photoproduction in the threshold region [173] such that the final corrected target polarization as used for the extraction of the results was given by $P_{\mathrm{abs}} = P_{\mathrm{meas}}/c_{\mathrm{rel}}/c_{\mathrm{abs}}$.

Due to the much higher cross section of single π^0 photoproduction, it was possible to determine a time (run) dependent average asymmetry of the parallel and antiparallel photon target spin configurations, i.e. $(P - A)/(P + A)/p_{e^-}/p_T$, using the number of events of parallel (P) and antiparallel (A) configuration, the electron beam polarization p_{e^-}, and the target polarization p_T. Thereby, the asymmetry in the photon helicity (see Figure 6.120) was already determined and corrected for. The resulting time dependent asymmetry is shown in Figure 6.122. Shown is the average asymmetry obtained from the weighted average from the exclusive single π^0 analysis on the quasi-free proton and neutron as a function of an arbitrary run number. The different colors represent the different beamtimes, i.e. the different intervals which were based on the same target polarization measurement. It is clearly visible that

Beamtime	Target Polarization [%]			c_{rel}	c_{abs}
	P_{meas}	$P_{rel} = P_{meas}/c_{rel}$	$P_{abs} = P_{meas}/c_{rel}/c_{abs}$		
July 2013	62	62	41	1	1.5
February 2014	-55	-55	-37	1	1.5
March 2015 I	-57	-61	-40	0.939717	1.5
March 2015 II	55	71	47	0.77843	1.5

Table 6.10: Overview of the correction of the target polarization values of the individual beamtimes. The measured target polarization, P_{meas}, was relatively scaled to P_{rel} with a scale factor c_{rel} such, that for all beamtimes the average asymmetry (Figure 6.122) of single π^0 photoproduction was in agreement. Subsequently the absolute scale factor c_{abs} (determined from the double polarization observable E in η photoproduction from polarized nucleons [173]) was applied to achieve the final absolute normalization. P_{abs} corresponds to the final corrected target polarization as applied in the analysis (see Figure 6.124 or colored dots in the right-hand figure of Figure 6.115).

the July 2013 (red) and February 2014 (blue) beamtime were already in agreement with each other, which is reasonable as they were based on an identical target polarization setup and measurement. Note that in order to solve the problem, the target polarization used in the analysis for the July 2013 and February 2015 beamtime must be wrong (and too high) by a factor of 1.5, which means that the correct average asymmetry should be larger than that achieved in Figure 6.122.

The first part of the March 2015 beamtime (orange) was used to investigate the problem. During this beamtime, the polarization was not only measured on the surface, but also in the center, and an average polarization value of the two measurements was provided [211]. In contrast, for the July 2013 and February 2014 beamtimes, the applied polarization value stem from the surface coil measurement. Therefore, in the first part of the March 2015 beamtime (since the problem was not yet discovered, but the resulting polarization value was the average of the surface and center measurement) an improvement was already visible. The situation further improved in the second part of the March 2015 beamtime (magenta), where the difference of the polarization inside and on the surface of the target was minimized by finding the best frequency of the microwave radiation, which was used for the polarization transfer from the electrons to the deuterons (see Section 2.8.2). A comparison of the average asymmetry from July 2013 or February 2014 with that from the second part of March 2015 yields a relative difference of 0.02934/0.02284 = 1.28 which is an improvement of about 52%. For the relative normalization of the target polarization values of the individual beamtimes, the two parts of the March 2015 beamtime were scaled to those from July 2013 and February 2014 such that the overall results should be off by a factor of 1.5, independent of the beamtime. Table 6.10 gives an overview of the obtained scale factors for the target polarizations and the final time (run) dependent target polarization values P_{abs} used in the analysis for

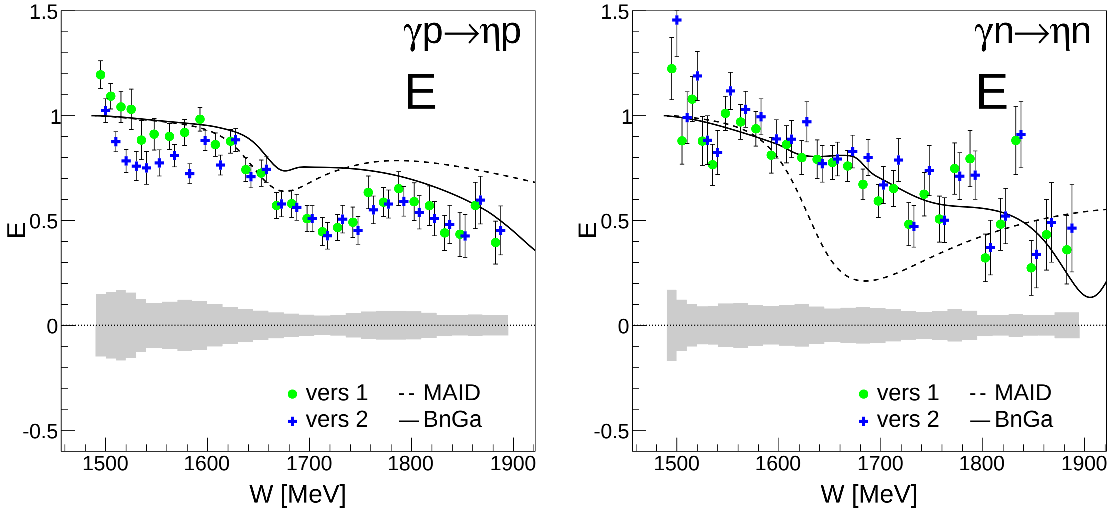

(a) $\gamma p \to \eta p$ **(b)** $\gamma n \to \eta n$

Figure 6.123: Double polarization observable E for η photoproduction from polarized nucleons from A2 as obtained with scaled target polarization values P_{abs}. Left-hand side: E as a function of W for the exclusive reaction $\gamma p \to \eta p(n)$. Right-hand side: E as a function of W for the exclusive reaction $\gamma n \to \eta n$. "vers1"("vers2") was extracted using Equation (6.57) ((6.56)). Figures taken from [173].

the extraction of the results. The results are shown on the right-hand side of Figure 6.115 (colored dots).

Figure 6.123 presents the final result of the double polarization observable E from η photoproduction from polarized protons (left-hand side) and neutrons (right-hand side) from the A2 data. The results were obtained by applying the relative target scale factor c_{rel} to the individual beamtimes. Subsequently, the weighted average of the double polarization observable E from all beamtimes was used to determine the absolute scaling factor $c_{\text{abs}} = 1.5$ such that E is one in the threshold region. Good agreement between the results from A2 and CBELSA/TAPS was achieved.

6.11.4 Final Photon Beam and Target Polarization

The distributions of the final photon beam and target polarization values are presented in Figure 6.124 for A2 and in Figure 6.125 for CBELSA/TAPS.

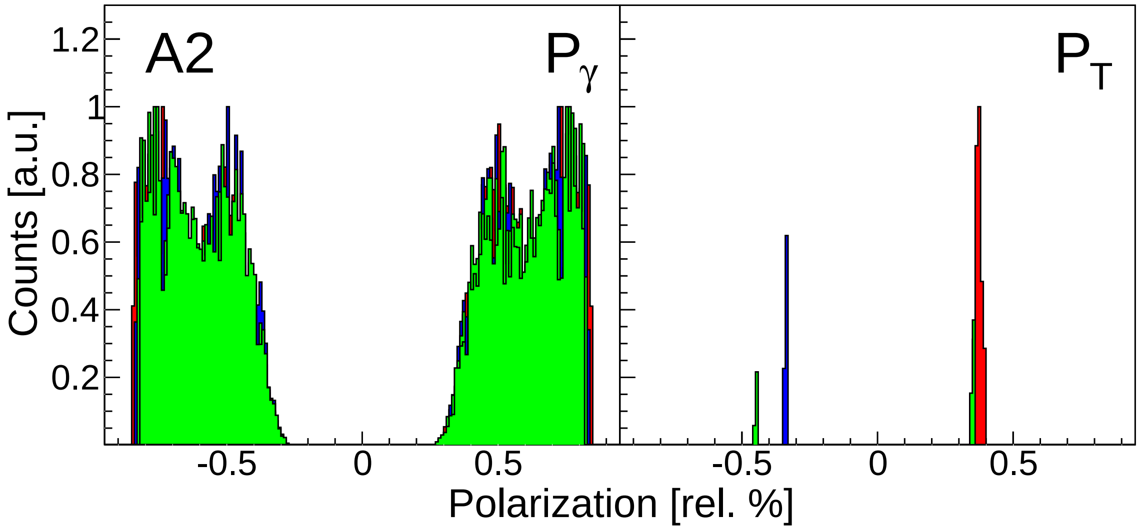

Figure 6.124: Final polarization values as used in the A2 analysis. Left-hand side: photon polarization. Right-hand side: target polarization (corrected, not measured values). Red histograms: July 2013 beamtime. Blue histograms: February 2014 beamtime. Green histograms: March 2015 beamtime.

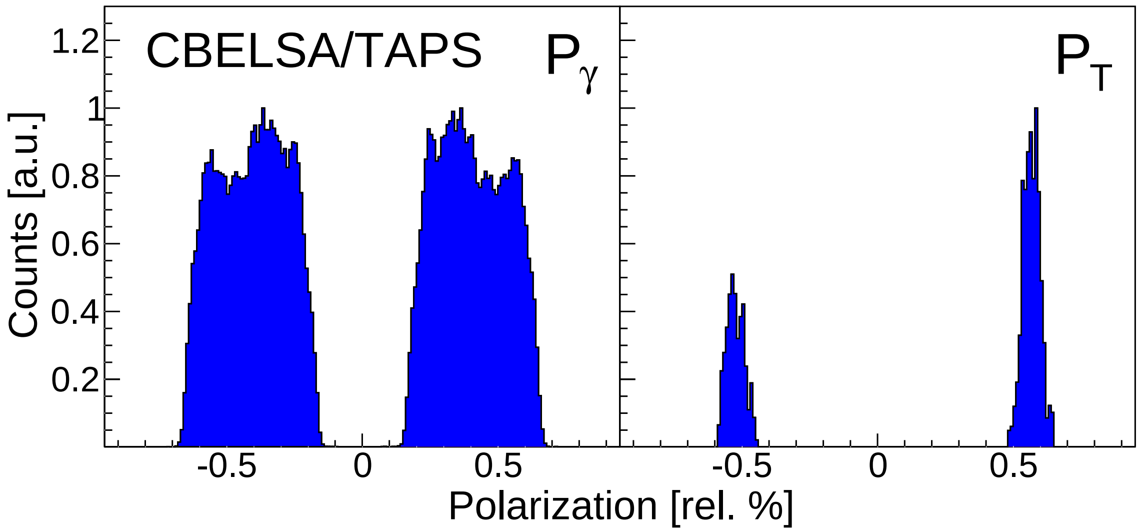

Figure 6.125: Final polarization values as used in the CBELSA/TAPS analysis. Left-hand side: photon polarization. Right-hand side: target polarization. Blue histograms: January and June 2011 beamtimes combined.

6.12 Estimation of the Free Neutron Cross Section

The analysis described in the previous sections allows for the extraction of cross sections for photoproduction from free protons from liquid hydrogen targets and quasi-free protons and neutrons bound in the deuteron. Due the non-existence of free neutron targets, the cross section for photoproduction from free neutrons can not be measured. However, an estimate of the free neutron cross section requires the elimination of nuclear final state interaction (FSI) effects from the quasi-free result, which can be deduced from a comparison of the free to quasi-free proton data.
As detailed model descriptions about FSI effects for protons and neutrons are not yet available, the only possibility for an estimation of the latter is to assume that the effects are similar for protons and neutrons. Such approximations were applied in previous analyses [68] and it is known from model results of other reactions [77, 82] that such approximations seem to be reliable. An exception are the cases where the relative momenta between the two final state nucleons are small, which is the case at very forward angles of the meson system. Within this approximation and the knowledge of the free $\sigma_{\mathrm{f}}(\gamma p)$ and quasi-free $\sigma_{\mathrm{qf}}(\gamma p)$ cross sections from the proton, the FSI effects in the quasi-free neutron cross section $\sigma_{\mathrm{qf}}(\gamma n)$ can be corrected via

$$\sigma_{\mathrm{f}}(\gamma n) = \sigma_{\mathrm{qf}}(\gamma n) \cdot \frac{\sigma_{\mathrm{f}}(\gamma p)}{\sigma_{\mathrm{qf}}(\gamma p)} \ . \tag{6.40}$$

Thereby it has to be noticed that the measured quasi-free cross section (as determined from the initial state) is influenced by Fermi motion or (if reconstructed from the final state according to Equation (6.14)) is affected by the experimental resolution. This leads to artifacts in the ratio of the free to quasi-free proton cross section and consequently and also in the estimated free neutron cross section. However, this problem can be circumvented by folding the free proton cross section with either Fermi motion or with experimental resolution, as shown in Figure 6.126. Shown are the free cross sections as prepared for the estimation of the neutron FSI correction used in the analysis of single π^0 photoproduction (left-hand side) and double π^0 photoproduction (right-hand side).

In this work, different methods were applied for the extraction of the free neutron cross section of single and double π^0 photoproduction since the analyzed data only allowed for the extraction of the free double π^0 cross section from the proton. However, the single π^0 cross section on the free proton is well known from measurement and theory. Thus, the $\gamma p \to \pi^0 p$ multipole solution of the SAID partial wave analysis [212] (dashed line on the left-hand side of Figure 6.126) was used for the free cross section on the proton and was compared to the measured quasi-free cross section. As previously mentioned, depending on the reconstruction, quasi-free data is influenced by Fermi motion or by experimental resolution. A reasonable estimation of the FSI correction for the neutron requires folding the free cross section with either of them. Since the SAID model provides user-defined energy and angular resolution, it was possible to fold it with experimental resolution and therefore, it does not rely on an appropriate parametrization of the corresponding Fermi model. For this purpose,

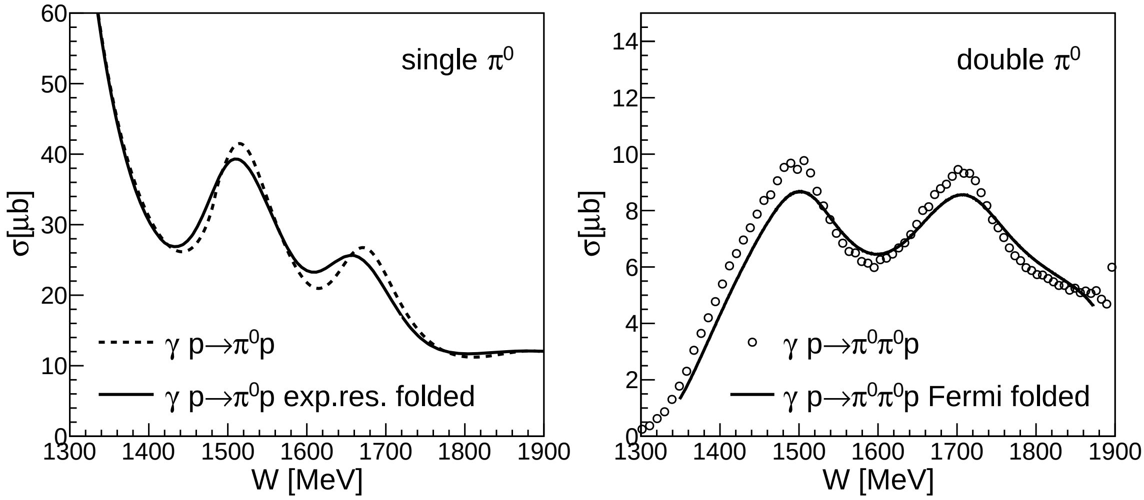

Figure 6.126: Illustration of the preparation of free cross sections for the extraction of the free neutron cross section. Left-hand side: single π^0. Solid line: SAID $\gamma p \to \pi^0 p$ [212]. Dashed line: SAID $\gamma p \to \pi^0 p$ folded with experimental resolution. Right-hand side: double π^0. Open circles: Free $\gamma p \to \pi^0\pi^0 p$ cross section. Dashed line: free $\gamma p \to \pi^0\pi^0 p$ cross section folded with Fermi motion. Double π^0 results obtained from A2 data.

the differential cross section data of the SAID solution was used as weight in the analysis of the simulation. Thereby the simulation was only used for the calculation of the final state invariant mass W and the corresponding polar angle of the neutral pion $\cos(\theta^*_{\pi^0})$. For every generated value of W and $\cos(\theta^*_{\pi^0})$, the corresponding value of the SAID model was extracted and filled as weight into a histogram at the reconstructed W and $\cos(\theta^*_{\pi^0})$ value. The result was then corrected with the appropriate detection efficiency in order to yield the free proton cross section smeared with the experimental resolution, as shown on the left-hand side of Figure 6.126 (solid line).

The correction factor for the estimation of the free double π^0 cross section on the neutron was obtained in a different way. Since the cross section of the free proton was determined as a function of E_γ and not reconstructed from the final state invariant mass W, it was free of effects from Fermi motion or experimental resolution. For the determination of the correction factor, the cross section had to be folded with Fermi motion and then converted to the center of mass energy according to Equation (6.13). In order to fold it with Fermi motion, 10^8 events were sampled and for each event the invariant mass of the initial state W was calculated from a randomly chosen incident photon energy and Fermi momentum from the deuteron Fermi distribution [181]. Using TGenPhaseSpace from `ROOT` [161], a decay at this value of W into the $\pi^0\pi^0 p$ final state was generated from which the $\cos(\theta^*_{2\pi^0})$ was determined. The free proton cross section was then transformed to W by Equation (6.13) and the differential cross section value at the generated W and $\cos(\theta^*_{2\pi^0})$ was extracted and filled into a histogram of the corresponding value of E_γ. The result

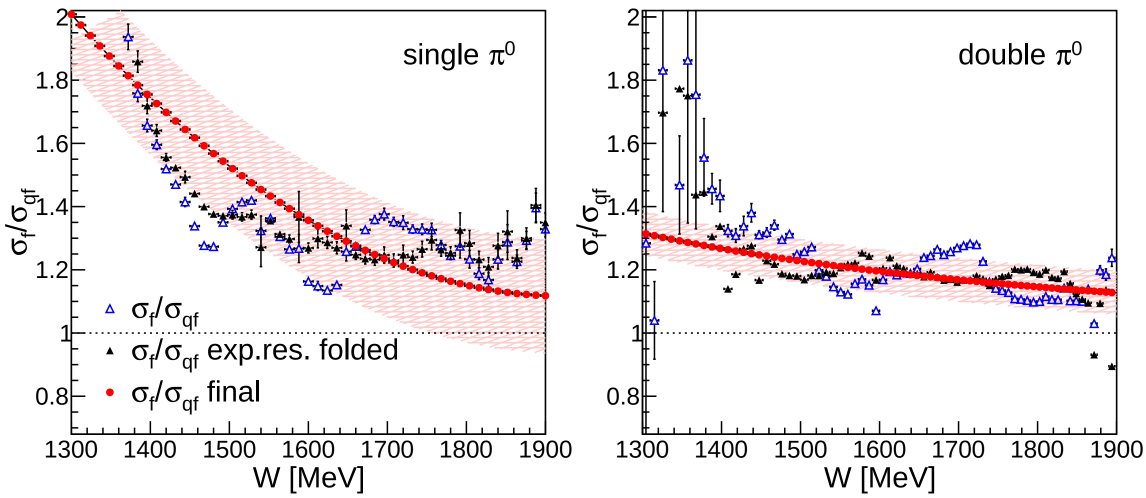

Figure 6.127: Illustration of the determination of the correction factors used for the estimation of the free neutron cross section for single (left-hand side) and double (right-hand side) π^0 photoproduction. Blue triangles: ratio of unfolded free to quasi-free cross section. Black triangles: ratio of folded free to quasi-free cross section. Red dots: final ratio of folded free to quasi-free ratio obtained from an energy-dependent fit. Red shaded area: estimated systematic error of the final correction. Results from the A2 data.

after proper normalization is shown on the right-hand side of Figure 6.126 (solid line).

The obtained correction factors (see Equation (6.40)) of the unfolded (blue triangles) and folded (black triangles) free to quasi-free cross sections σ_f/σ_{qf} for single π^0 (left-hand side) and double π^0 (right-hand side) photoproduction as a function of the final state invariant mass are shown in Figure 6.127. For both reactions, the effect of the folding procedure is clearly visible. Without effects from experimental resolution (left-hand side) or Fermi motion (right-hand side) in the free cross section (Figure 6.126), the resonance bumps in the excitation function are narrower than in the quasi-free cross section. As a consequence, the correction factor (blue triangles) is overestimated in the bump region and underestimated in between. After folding the free cross section with experimental resolution (black triangles), the sine shaped structure almost vanished. In order to optimize the removal of artifacts from Fermi motion or experimental resolution, the folded ratios (black triangles) were fit with an energy-dependent function. The fit result (red dots) were then used to normalize the angular dependent correction factor. The free neutron cross section was then estimated by applying the correction factor $q^p_{\mathrm{f}}(\cos(\theta^*_m), W)/q^p_{\mathrm{qf}}\cos(\theta^*_m), W$ to the quasi-free differential photoproduction cross section of the meson m from the neutron according to Equation (6.41).

$$\sigma^n_{\mathrm{f}}(\cos(\theta^*_m), W) = \sigma^n_{\mathrm{qf}}(\cos(\theta^*_m), W) \cdot \frac{\sigma^p_{\mathrm{f}}(\cos(\theta^*_m), W)}{\sigma^p_{\mathrm{qf}}(\cos(\theta^*_m), W)} \; . \tag{6.41}$$

6.13 Extraction of Observables

After the events were properly selected, the particles were identified and the photon flux, the detection efficiency, and additional corrections were applied, the data are ready to extract the observables of interest. The following section describes the different methods that were used to determine the yields of the event selection and the subsequent extraction of cross sections and polarization observables thereof.

6.13.1 Extraction of the Reaction Yields

Since all analyses involved neutral pions, the yields were determined from the $\gamma\gamma$ invariant mass distributions at the final stage of the analysis, i.e. when all cuts and corrections were applied. In case of double π^0, the yields were determined from the $\gamma\gamma$ invariant mass of one pion under the condition that the other pion passed the $\pm 3\sigma$ cut on the invariant mass. In all analyses, the invariant mass of the neutral pion was then filled into a histogram of a fixed binning in $\cos(\theta^*_{\pi^0,2\pi^0})$ and E_γ or $W = \sqrt{s}$. Thereby, as mentioned in Section 6.10.1, the E_γ dependent cross sections were filled using the bin-overlap method.
The yields were then determined by integrating the invariant mass spectra within the $\pm 3\sigma$ invariant mass cut range, as described in Section 6.4.1. For this purpose, the invariant mass spectra were fit with the simulated line shape of the reaction and a background polynomial of second or third order. The fit of the invariant mass spectra in the inclusive analyses revealed some residual background contributions, especially at the very forward angles. This is a result of the fewer cuts that could be applied to the event selection. In these cases, the yields were determined by integration of the fit results of the simulated line shape, while the statistical errors of the data were taken into consideration. The fit results of all exclusive analyses did not show significant background contributions and therefore the yields were directly obtained from integration of the measured invariant mass distribution within the $\pm 3\sigma$ cut range. In the following section, the final invariant mass spectra of the exclusive analyses are presented and discussed for five selected energy and angular bins.

Figure 6.128 shows the final invariant mass distributions from the analysis of quasi-free exclusive single π^0 photoproduction from protons and neutrons. They show a good agreement between the measured (colored triangles) and simulated (black lines) distributions except for energies around 682 MeV at very forward angles. On the proton, this contribution stems from the $\pi^0\pi^+n$ decay when one decay photon or the neutron were not detected and the π^+ was identified as proton. In contrast, on the neutron, it originates from $\eta \to 2\gamma$ decays when one decay photon and the neutron were permuted. However, the contribution of this background is negligible within the cut region. Furthermore only a few bins are involved and the cross section in the very forward region is rather small, which is visible by the size of the error bars. Investigations with subtracting this background showed that its effect on the results was well within the systematic uncertainty.
The same observations are valid for the final invariant mass spectra from the single

π^0 analysis of the deuterated butanol data (open black circles), as shown in Figure 6.129. At this stage, the deuterated butanol data still contains contributions from background reactions on the unpolarized nucleons in the carbon and oxygen nuclei. Therefore they are compared to the distributions of the corresponding deuterium analyses (blue and red triangles). Here, a coarser energy and angular binning is used compared to the main deuterium analysis in Figure 6.128. However, almost no difference between the spectra from deuterated butanol and deuterium is visible. This demonstrates, as will be discussed in Section 6.13.4, that the invariant mass distributions are not well suited for the subtraction of the carbon background from the deuterated butanol yield.

The final invariant mass distributions from the analysis of double π^0 photoproduction from the free proton are shown in Figure 6.130 for A2 and in Figure 6.131 for CBELSA/TAPS. For all energies and angles, no residual background contributions are visible. The comparison of the distributions from the analyses of the A2 and CBELSA/TAPS data demonstrate the slightly better energy resolution at CBELSA/TAPS (see Table 5.1), shown by the width of the $\gamma\gamma$ invariant mass peaks. The $\gamma\gamma$ invariant mass distributions for quasi-free exclusive double π^0 photoproduction from liquid deuterium are shown in Figure 6.132 for A2 and in Figure 6.133 for CBELSA/TAPS. As already observed in the distributions of the analyses on the free proton, good agreement overall between the data and simulation is visible for all energies and angular regions. Although, as observed for single π^0 photoproduction but less prominent in this case, some slight residual background around the η photoproduction threshold at the lower energies in the very forward region is present, but negligible within the range of the invariant mass cut. Also visible in the corresponding missing mass distributions in Figures 6.53 and 6.57, this contribution stems from $\eta \rightarrow 6\gamma$ decays where either two decay photons (reaction on the proton) or the recoil neutron and one decay photon (reaction on the neutron) were not detected.
Finally, Figures 6.134 and 6.135 show the final $\gamma\gamma$ invariant mass distributions from the quasi-free exclusive double π^0 analysis from the deuterated butanol data from A2 and CBELSA/TAPS, respectively. As discussed for single π^0 photoproduction, the distributions from the analysis of deuterated butanol data are of almost identical shape and are not suited for the subtraction of the carbon background.

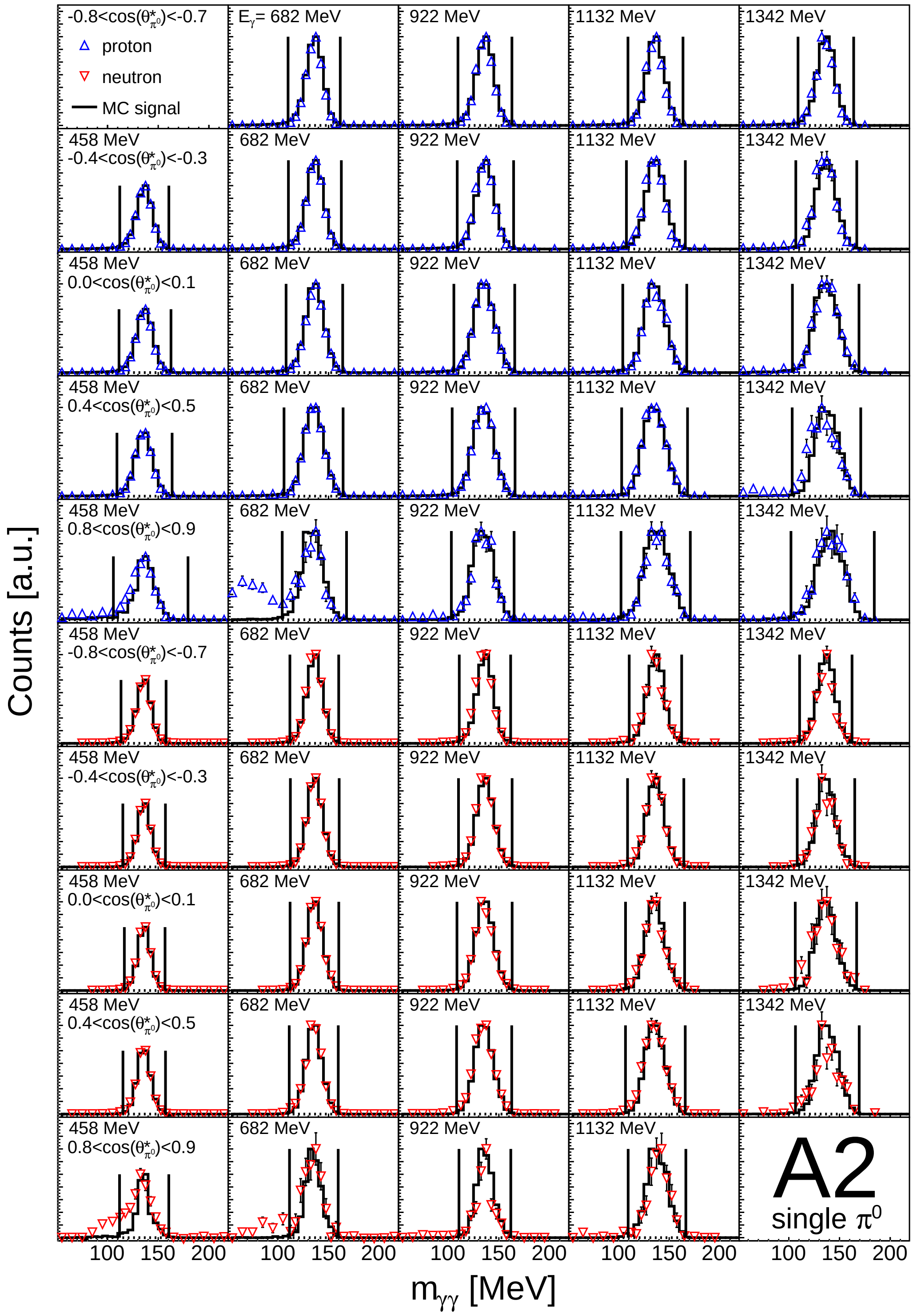

Figure 6.128: Final invariant mass spectra of exclusive single π^0 photoproduction from deuterium. Results from the A2 data. Blue triangles: proton. Red triangles: neutron. Black histograms: Simulated line shape. Shown are five selected energy and angular bins. All cuts were applied to the data. Notations are given in the figure and the vertical black lines indicate the $\pm 3\sigma$ cut positions.

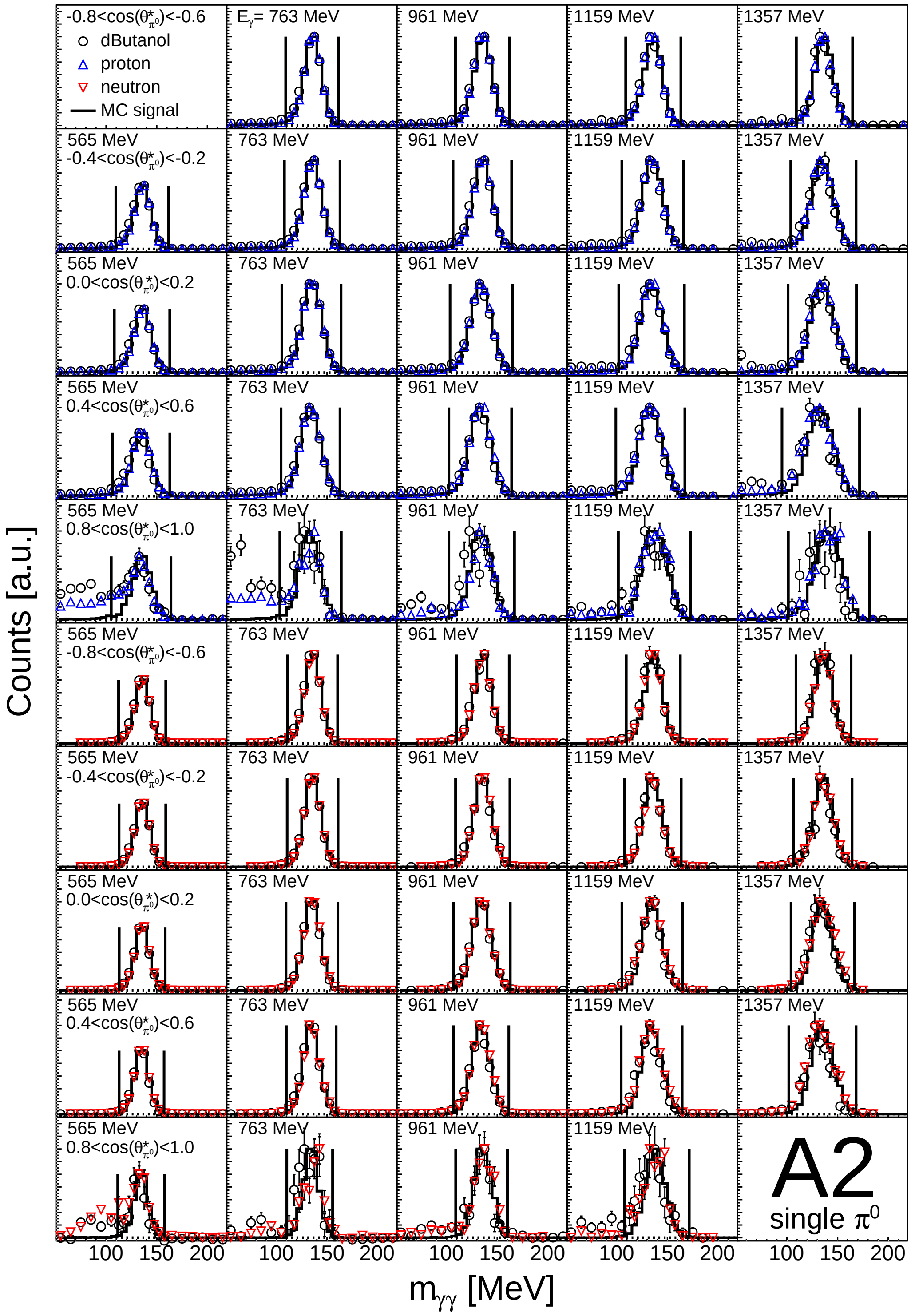

Figure 6.129: Final invariant mass spectra of exclusive single π^0 photoproduction from deuterated butanol (open circles) and deuterium (proton: blue triangles, upper half. Neutron: red triangles, lower half. Black histogram: simulated line shape). Results from the A2 data. Shown are five selected energy and angular bins. All cuts were applied to the data. Notations are given in the figure and the vertical black lines indicate the $\pm 3\sigma$ cut positions.

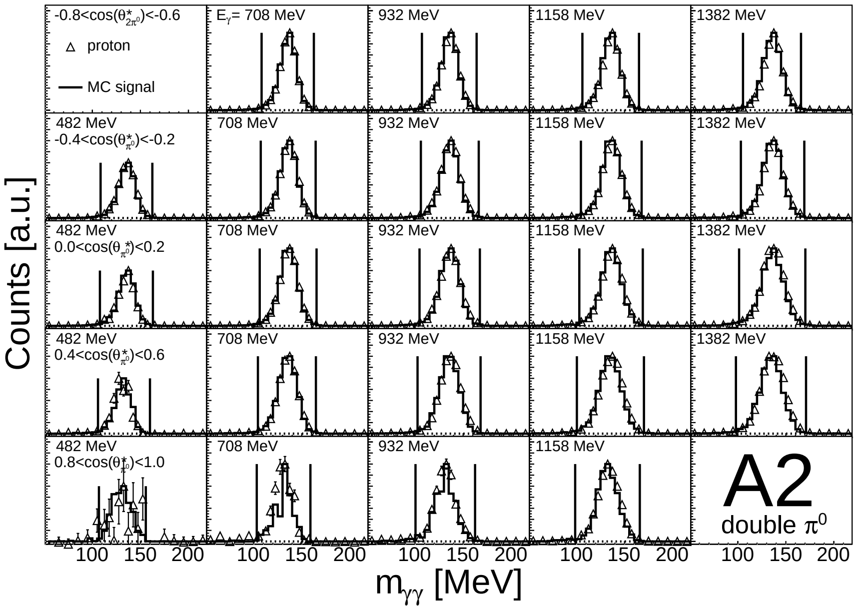

Figure 6.130: Final invariant mass spectra of exclusive double π^0 photoproduction from the free proton. Results from the A2 data. Black triangles: data. Black histograms: simulated line shape. Shown are five selected energy and angular bins. All cuts were applied to the data. Notations are given in the figure and the vertical black lines indicate the $\pm 3\sigma$ cut positions.

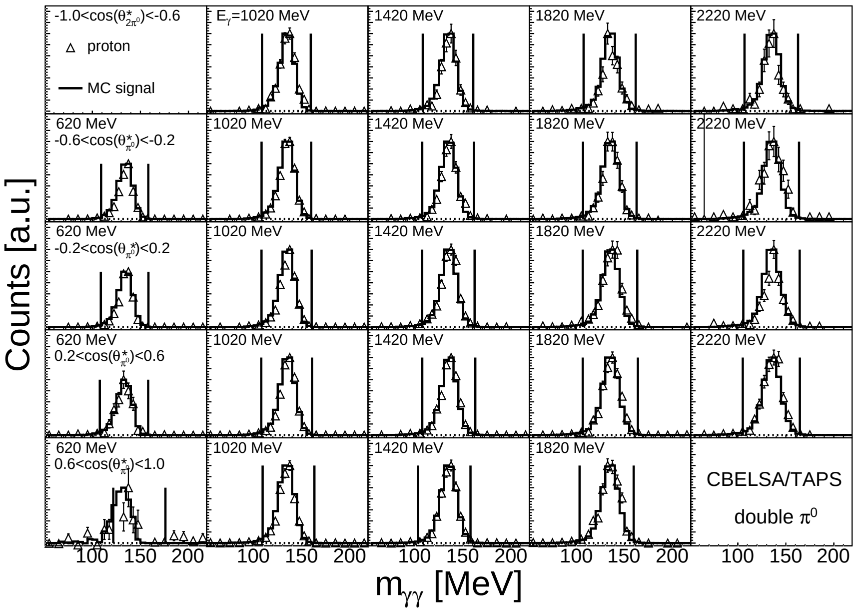

Figure 6.131: Final invariant mass spectra of exclusive double π^0 photoproduction from the free proton. Results from the CBELSA/TAPS data. Black triangles: data. Black histograms: simulated line shape. Shown are five selected energy and angular bins. All cuts were applied to the data. Notations are given in the figure and the vertical black lines indicate the $\pm 3\sigma$ cut positions.

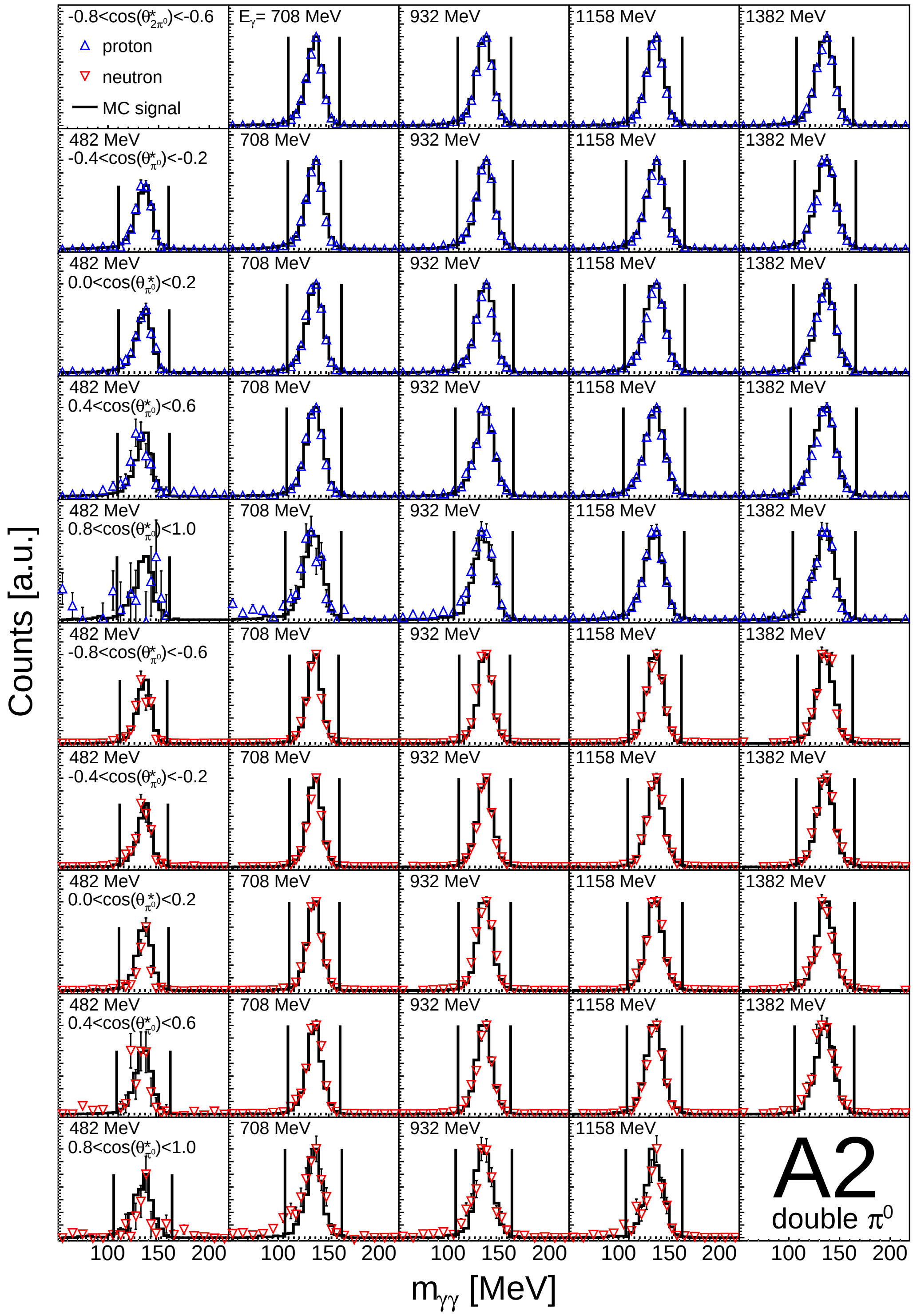

Figure 6.132: Final invariant mass spectra of exclusive double π^0 photoproduction from deuterium. Results from the A2 data. Blue triangles: proton. Red triangles: neutron. Black histograms: Simulated line shape. Shown are five selected energy and angular bins. All cuts were applied to the data. Notations are given in the figure and the vertical black lines indicate the $\pm 3\sigma$ cut positions.

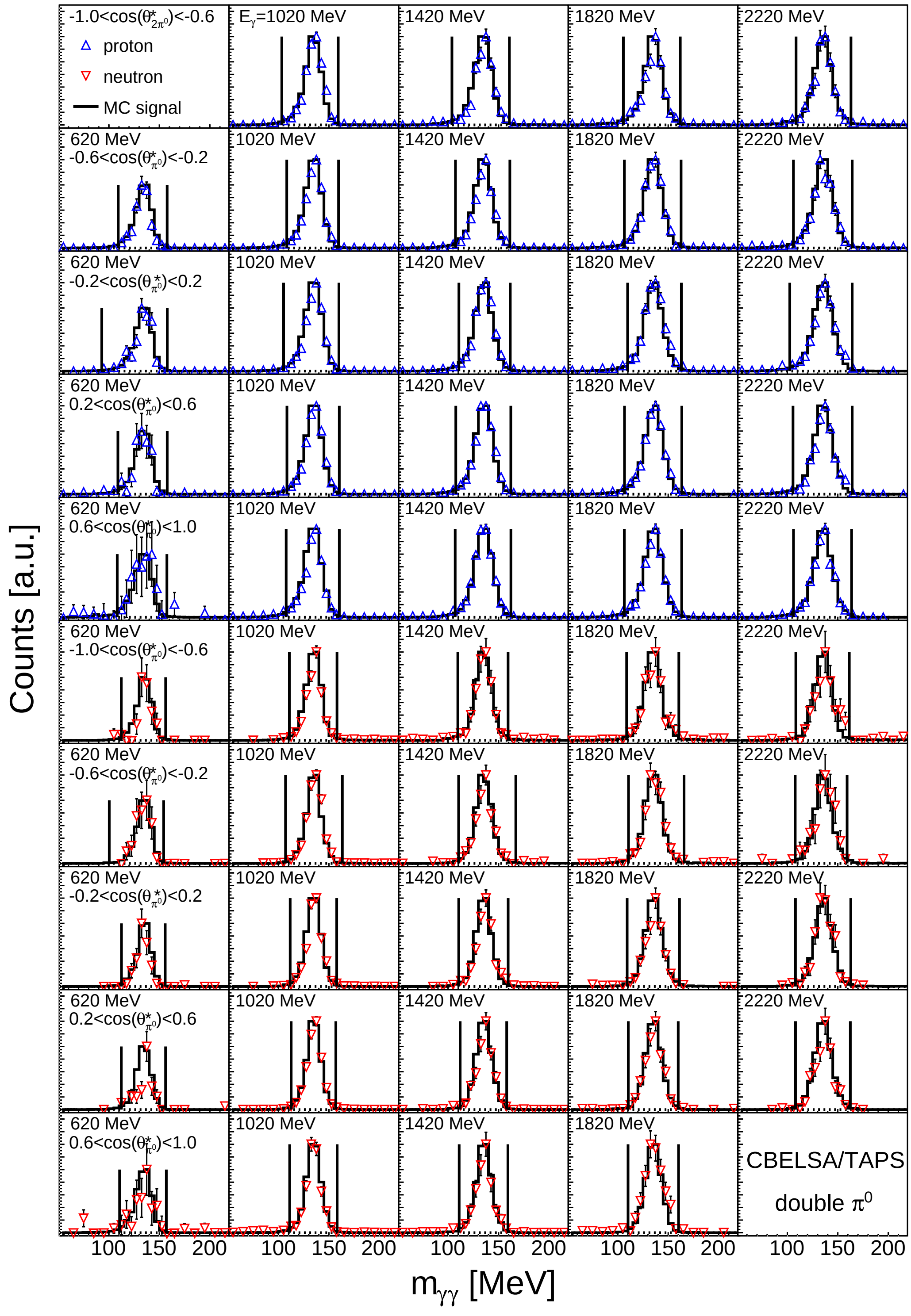

Figure 6.133: Final invariant mass spectra of exclusive double π^0 photoproduction from deuterium. Results from the CBELSA/TAPS data. Blue triangles: proton. Red triangles: neutron. Black histograms: Simulated line shape. Shown are five selected energy and angular bins. All cuts were applied to the data. Notations are given in the figure and the vertical black lines indicate the $\pm 3\sigma$ cut positions.

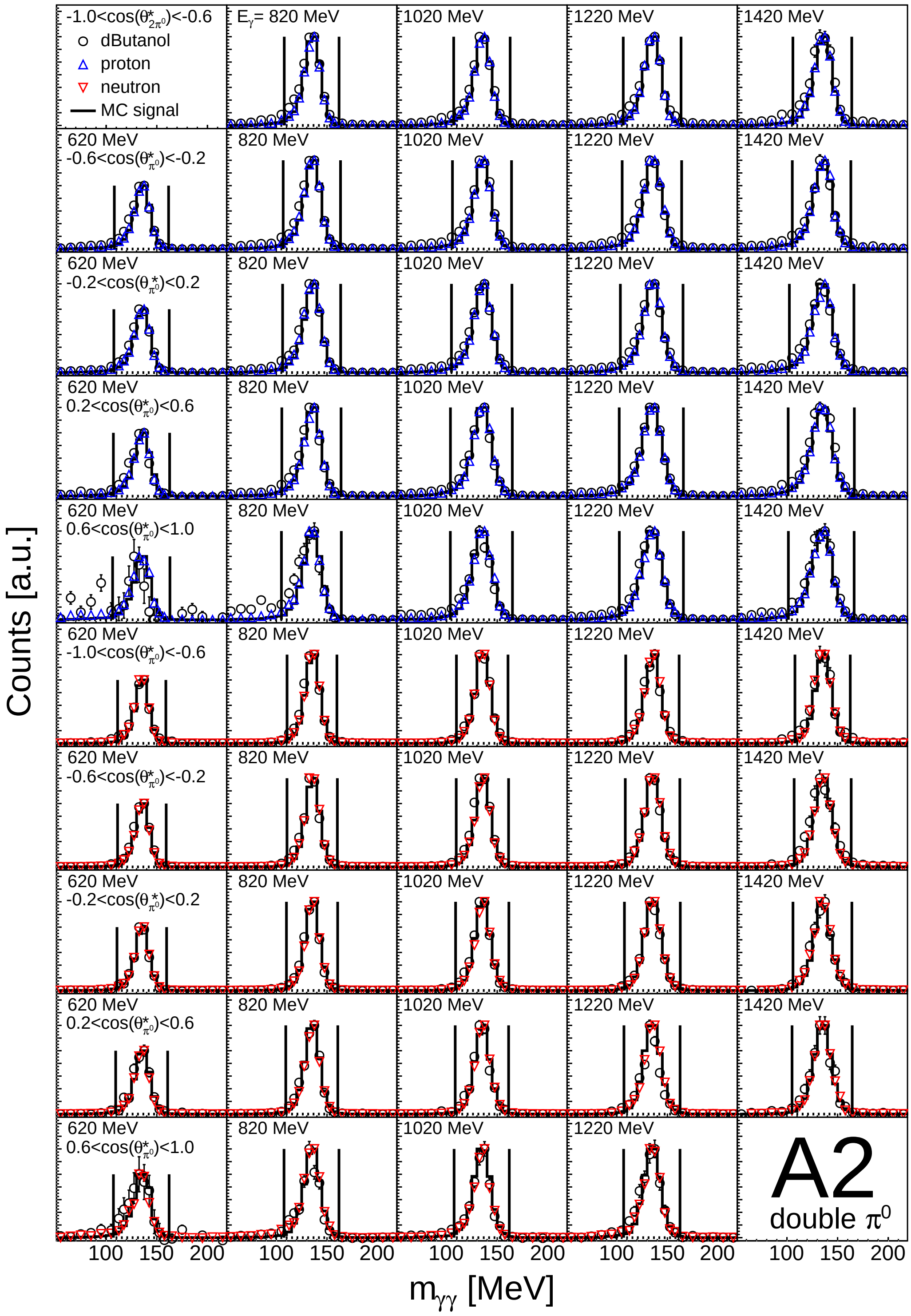

Figure 6.134: Final invariant mass spectra of exclusive double π^0 photoproduction from deuterated butanol (open circles) and deuterium (proton: blue triangles, upper half. Neutron: red triangles, lower half. Black histogram: simulated line shape). Results from the A2 data. Shown are five selected energy and angular bins. All cuts were applied to the data. Notations are given in the figure and the vertical black lines indicate the $\pm 3\sigma$ cut positions.

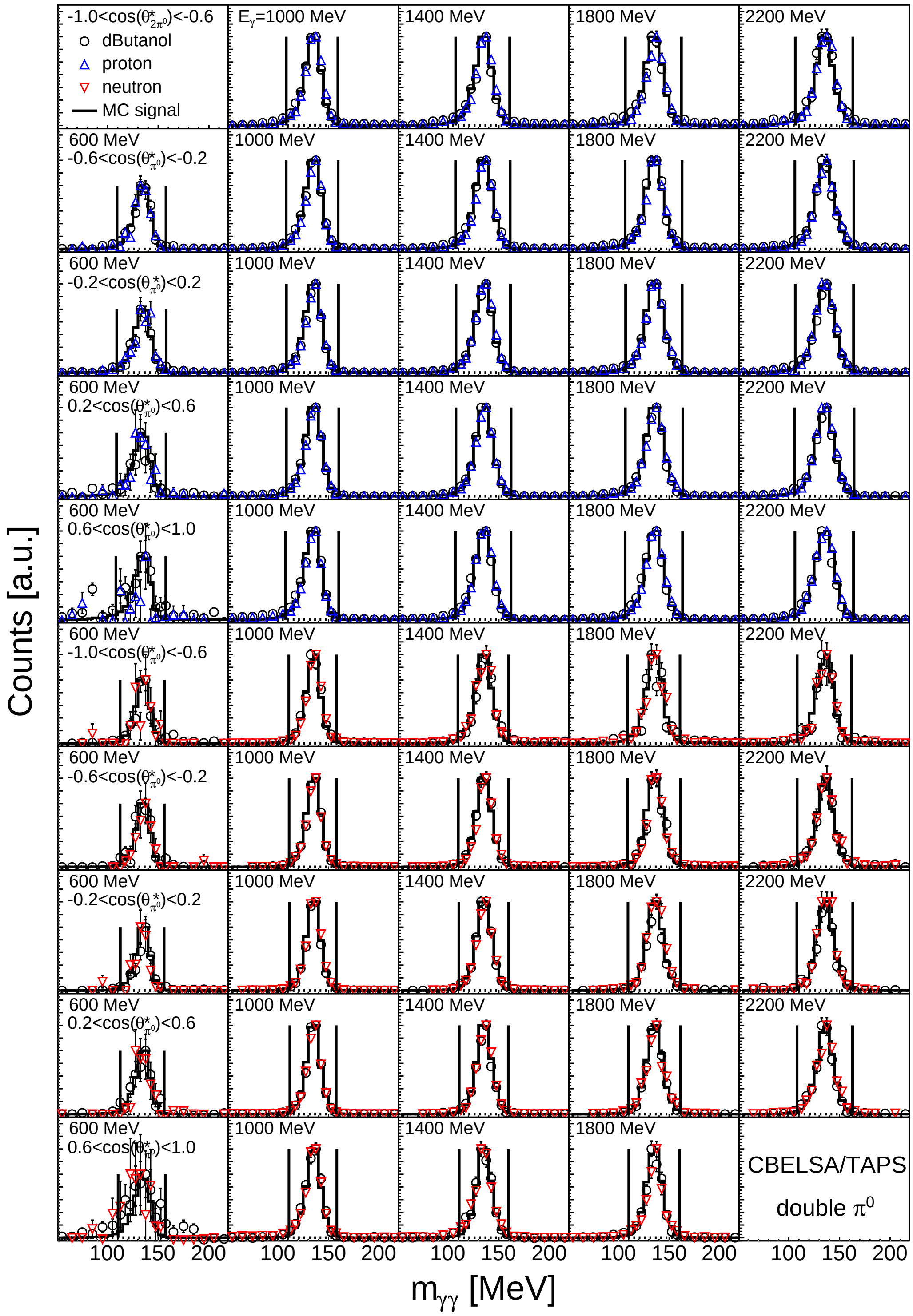

Figure 6.135: Final invariant mass spectra of exclusive double π^0 photoproduction from deuterated butanol (open circles) and deuterium (proton: blue triangles, upper half. Neutron: red triangles, lower half. Black histogram: simulated line shape). Results from the CBELSA/TAPS data. Shown are five selected energy and angular bins. All cuts were applied to the data. Notations are given in the figure and the vertical black lines indicate the $\pm 3\sigma$ cut positions.

6.13.2 Extraction of Cross Sections

For the determination of cross sections from the extracted yields, the number of detected events $N_{\text{det}}(\cos(\theta_m^*), E_\gamma/W)$ (see Section 6.13.1) of each energy and angular bin has to be corrected for the detection efficiency ε_{det} (see Equations (6.15), (6.17), (6.19)), the fraction of the considered decay branching ratio to the total branching ratio of the meson Γ_i/Γ, as well as the solid angle $\Delta\Omega$ of the individual $\cos(\theta_m^*)$ bin. This provides the true number of events $N(\cos(\theta_m^*), E_\gamma/W)$ independent from the experimental setup and the data acquisition. According to Equation (6.29), the differential cross section is then given by the normalization with the number of photons that hit the target $N_\gamma(E_\gamma/W)$ (see Sections 6.10.1 and 6.10.2) and the target surface density ρ:

$$\begin{aligned} \frac{d\sigma}{d\Omega}(\cos(\theta_m^*), E_\gamma/W) &= \frac{N(\cos(\theta_m^*), E_\gamma/W)}{\rho \cdot \Delta\Omega \cdot N_\gamma(E_\gamma/W)} \\ &= \frac{N_{\text{det}}(\cos(\theta_m^*), E_\gamma/W)}{\rho \cdot \Gamma_i/\Gamma \cdot \Delta\Omega \cdot \varepsilon_{\text{det}}(\cos(\theta_m^*), E_\gamma/W) \cdot N_\gamma(E_\gamma/W)} \ , \end{aligned} \tag{6.42}$$

where

$N_{\text{det}}(\cos(\theta_m^*), E_\gamma/W)$	number of detected events per angular and energy bin
ρ	target surface density [barn^{-1}]
Γ_i/Γ	fraction of meson branching ratio [202]:
	$\pi^0 \to 2\gamma$: (98.823 ± 0.034) %
	$\pi^0\pi^0 \to 4\gamma$: (97.660 ± 0.067) %
$\Delta\Omega$	solid angle per angular bin
$\varepsilon_{\text{det}}(\cos(\theta_m^*), E_\gamma/W)$	detection efficiency per angular and energy bin
$N_\gamma(E_\gamma/W)$	number of impinging photons per energy bin.

For n_b angular bins, the solid angle per angular bin is given by $\Delta\Omega = 4\pi/n_b$. The target surface density n_t for a target of length l_t, molar mass M_t, filling factor f_{fill}, and density ρ_t can be determined by using Avogadro's constant $N_A = 6.022 \cdot 10^{23}$ mol^{-1} as follows:

$$n_t = \frac{f_{\text{fill}} \cdot \rho_t \cdot l_t \cdot N_A}{M_t} \ , \tag{6.43}$$

where the filling factor denotes the fraction of the volume, which is filled with the target material. This is only for the deuterated butanol target, since the deuterated butanol beads have a spherical shape and can not completely fill the target cell. Therefore the filling factor is only different from one for the deuterated butanol beamtimes (see Table 6.11 for the exact values) and one for all other beamtimes.
The various target parameters of all analyzed beamtimes that were necessary to determine the target surface density are summarized in Table 6.11.

The total cross section is then given by integration of the differential cross sections

		Beamtime	l_t [cm]	ρ_t [g/cm^{-3}]	$\mathrm{f_{fill}}$	M_t [g/mol]	n_t [b^{-1}]
A2	LH_2	April 2009	10.0± 0.1	0.0705	1	1.0079	0.42150
	LD_2	December 2007	4.72 ± 0.05	0.16324	1	2.014	0.23039
		February 2009	4.72 ± 0.05	0.16324	1	2.014	0.23039
		May 2009	3.02 ± 0.03	0.16324	1	2.014	0.14741
	^{12}C	February 2014	1.98	0.57	1	12.011	0.05659
	C_4D_9OD	July 2013	2.00	1.1	0.6	84.1923	0.09442
		February 2014	2.00	1.1	0.6	84.1923	0.09442
		March 2015	2.00	1.1	0.6	84.1923	0.09442
CBELSA/TAPS	LH_2	November 2008	5.262	0.0756	1	1.0079	0.23776
	LD_2	December 2008	5.258	0.169	1	2.014	0.26570
	^{12}C	November 2011	1.88	0.5	1	12.011	0.04713
	C_4D_9OD	January 2011	1.88	1.1	0.59	84.1923	0.08727
		June 2011	1.88	1.1	0.59	84.1923	0.08727

Table 6.11: Overview of the target parameters of the different beamtimes from A2 and CBELSA/TAPS.

over the solid angle:

$$\begin{aligned} \sigma(E_\gamma, W) &= \int \frac{d\sigma}{d\Omega}(\cos(\theta^*_m), E_\gamma/W)d\Omega \\ &= \int \frac{d\sigma}{d\Omega}(\cos(\theta^*_m), E_\gamma/W)\sin(\theta^*_m)d\theta^*_m \\ &\sim \frac{4\pi}{n_b}\sum_{i=1}^{n_b}\frac{d\sigma}{d\Omega}(\cos(\theta^*_m), E_\gamma/W)\ . \end{aligned} \tag{6.44}$$

An alternative calculation is possible by means of a series of Legendre polynomials $P_l(\cos(\theta^*_m))$ of order l. For this purpose, the differential cross sections $d\sigma/d\Omega$ were first fit with a series of Legendre Polynomials of order l (depending on the reaction channel) and normalized to the polynomial of zeroth order:

$$\begin{aligned} f_L(\cos(\theta^*_m), E_\gamma/W) &= \frac{q^*_m}{k^*_\gamma}\sum_{l=0}^{n} A_l(E_\gamma, W)P_l(\cos(\theta^*_m)) = \sum_{l=0}^{n} B_l(E_\gamma, W)P_l(\cos(\theta^*_m)) \\ &= B_0(E_\gamma, W)P_0(\cos(\theta^*_m)) + \sum_{l=1}^{n}\frac{B_l(E_\gamma, W)}{B_0(E_\gamma, W)}P_l(\cos(\theta^*_m))\ , \end{aligned} \tag{6.45}$$

where A_l, B_l are the coefficients of the expansion and k^*_γ, q^*_m are the center of mass momenta of the incident photon and the meson m. From Equation (6.45), the total cross section is given by integration of the Legendre expansion $f_L(\cos(\theta_m^*), E_\gamma/W)$:

$$\sigma(E_\gamma, W) = \int_{-1}^{1} f_L(\cos(\theta_m^*), E_\gamma/W) d\cos(\theta_m^*) = 4\pi \cdot B_0(E_\gamma, W) \ . \quad (6.46)$$

In this work, Equation (6.46) was used for the extraction of the total cross sections from unpolarized data and Equation (6.44) was used for the determination of the helicity dependent cross sections. Due to the small asymmetries, the results were too sensitive to fit with Equation (6.45).

6.13.3 Extraction of the Double Polarization Observable E

For a circularly polarized photon beam of polarization p_γ and a longitudinally polarized target of polarization p_T, the double polarization observable E is given by:

$$E = \frac{\sigma_{1/2} - \sigma_{3/2}}{\sigma_{1/2} + \sigma_{3/2}} = \frac{\sigma_{1/2} - \sigma_{3/2}}{2 \cdot \sigma_{\text{unpol}}} = \frac{1}{p_\gamma p_T} \cdot \frac{N_{1/2} - N_{3/2}}{N_{1/2} + N_{3/2} + N_{\text{unpol}}} \ , \quad (6.47)$$

where $\sigma_{1/2}$ and $\sigma_{3/2}$ ($N_{1/2}$ and $N_{3/2}$) are the helicity dependent cross sections (count rates) for an antiparallel and parallel spin configuration, respectively, and σ_{unpol} (N_{unpol}) is the unpolarized cross section (count rate). In order to extract E and the helicity dependent cross sections $\sigma_{1/2}$ and $\sigma_{3/2}$, the events were divided into subgroups of measured yields from antiparallel $N^m_{1/2}$ and parallel $N^m_{3/2}$ spin configurations. The information about the spin configuration was obtained from the direction of the target polarization (constant until the target polarization was actively changed) and the helicity information of the photon beam (alternating at a frequency of 0.5 Hz), where the latter was available as helicity bit information for every event in the data. This reliably separates true $N_{1/2}$ yields from $N_{3/2}$ and provides a clear separation of events that contribute to $\sigma_{1/2}$ or $\sigma_{3/2}$. However, it also includes events from reactions on unpolarized nucleons inside deuterium N_{unpol} and from carbon and oxygen N_{CO}. Therefore, it was required to establish a strategy in which the contributions from reactions on unpolarized nucleons can be reliably subtracted in order to obtain clean samples of events that were truly of a parallel and antiparallel spin configuration. Whereas the degree of target polarization accounts for the contribution from reactions on unpolarized nucleons inside deuterium, the subtraction of contributions from the unpolarized nucleons inside the carbon and oxygen nuclei require the additional measurement of reactions on a carbon target of similar density as the deuterated butanol target. If the experiment was carried out under comparable conditions, it provides a reliable estimation of the contribution from reactions on the nucleons of carbon and oxygen nuclei inside deuterated butanol. Thereby the contributions from reactions on nucleons inside oxygen can be estimated by the carbon measurement, as the cross section on oxygen is comparable to that on carbon. Furthermore, the fraction of oxygen to carbon nuclei per deuterated butanol molecule (C_4D_9OD) is only 1:4.

In the following section, a detailed treatment and consideration of the reaction mechanism is carried out, which ensures the proper extraction of the double polarization observable E and the helicity dependent cross sections $\sigma_{1/2}$ and $\sigma_{3/2}$.

If a deuterated butanol target that is longitudinally polarized is considered and the deuterons are polarized to an amount of p_T, in relative percentage, and the target is impinged by circularly polarized photons of p_γ polarization, the total amount of measured events N^m is given by:

$$N^m = (N_1^p + N_3^p) \cdot p + N_{\text{unpol}} \cdot (1-p) + N_{\text{CO}} \ , \tag{6.48}$$

where $N_1^p = N_{1/2}^p$, $N_3^p = N_{3/2}^p$ are the yields of events with antiparallel and parallel spin configuration, N_{unpol}, N_{CO} the yield of events from reactions on unpolarized deuterons and nucleons in carbon and oxygen nuclei, and $p = p_\gamma \cdot p_T$ the product of photon and target polarization degree. If in the analysis the information about the spin configuration is used to separate the total amount N^m into yields of parallel N_3^m and antiparallel N_1^m events, the measured yields are given by:

$$\begin{aligned} N_1^m &= N_1^p \cdot p + N_{\text{unpol}}^1 \cdot (1-p) + N_{\text{CO}}^1 \\ N_3^m &= N_3^p \cdot p + N_{\text{unpol}}^3 \cdot (1-p) + N_{\text{CO}}^3 \ , \end{aligned} \tag{6.49}$$

where $N_{\text{unpol},CO}^{1,3}$ are the contributions of the reactions on unpolarized nuclei to the yields of parallel and antiparallel spin configuration. $N_{\text{unpol,CO}}^1 = N_{\text{unpol,CO}}^3$ only applies if no asymmetry in the photon beam helicity is given and if the photon fluxes F_1 and F_3 are equal. As an asymmetry in the helicity states of the photon beam was observed (see Section 6.11.3), the fluxes were treated as unequal, i.e. $F_1 \neq F_3$. Equation (6.49) shows that to extract the true yields of N_1 and N_3 for the determination of E according to Equation (6.47), the contributions from reactions on unpolarized nucleons has to be eliminated. The procedure of the determination of the true yields is described in the following paragraphs.

In terms of cross sections σ, i.e. $\sigma = N/(F \cdot n)$, where N are the yields, F the corresponding photon flux, and $n = \rho \cdot \varepsilon \cdot \Gamma_i/\Gamma$ is the normalization factor consisting of the target surface density ρ, the branching ratio Γ_i/Γ, and the detection efficiency ε, using Equation (6.47), Equation (6.49) can be written as:

$$\begin{aligned} N_1^m &= \sigma_1 F_1 np + \sigma_{\text{unpol}} F_1 n(1-p) + \sigma_{\text{CO}} F_1 n \\ &= \sigma_1 F_1 np + \frac{1}{2}(\sigma_1 + \sigma_3) F_1 n(1-p) + \sigma_{\text{CO}} F_1 n \end{aligned} \tag{6.50}$$

$$\begin{aligned} N_3^m &= \sigma_3 F_3 np + \sigma_{\text{unpol}} F_3 n(1-p) + \sigma_{\text{CO}} F_3 n \\ &= \sigma_3 F_3 np + \frac{1}{2}(\sigma_1 + \sigma_3) F_3 n(1-p) + \sigma_{\text{CO}} F_3 n \ . \end{aligned} \tag{6.51}$$

From Equations (6.50) and (6.51), it follows that the numerator $\sigma_1 - \sigma_3$ of Equation (6.47) is directly given by the difference of the cross sections σ_1^m, σ_3^m, as obtained from the measured yields:

$$\sigma_1^m - \sigma_3^m = \frac{N^m}{F_1 np} - \frac{N_3^m}{F_3 np} = \sigma_1 - \sigma_3 \ . \tag{6.52}$$

A subtraction of the contributions from reactions on unpolarized nucleons is hence not necessary for the determination of the numerator.
In contrast, the determination of the denominator of Equation (6.47) requires an elaborate subtraction of that background. This can be seen by considering the sum of the measured cross sections $\sigma_1^m + \sigma_3^m$ (note that the polarization weight p as necessary for Equation (6.47) was already considered in the numerator and hence in the following is not required anymore):

$$\sigma_1^m + \sigma_3^m = \frac{N_1^m}{F_1 n} + \frac{N_3^m}{F_3 n} = (\sigma_1 + \sigma_3) + 2\sigma_{\mathrm{CO}} \ . \tag{6.53}$$

Therefore it can be seen that the numerator and denominator of Equation (6.47) have to be determined from the measured yields from Equation (6.52) and (6.53) as follows:

$$\sigma_1 - \sigma_3 = \sigma_1^m - \sigma_3^m \stackrel{!}{=} \sigma_{\mathrm{diff}} \tag{6.54}$$

$$\sigma_1 + \sigma_3 = (\sigma_1^m + \sigma_3^m) - 2\sigma_{\mathrm{CO}} \stackrel{!}{=} \sigma_{\mathrm{sum}} \ . \tag{6.55}$$

From the measured difference and sum of the helicity dependent cross sections σ_{diff} and σ_{sum} (Equations (6.52) and (6.53)), the double polarization observable E can be determined in two ways that follow from Equation (6.47):

$$E^{\mathrm{version\ 1}} = \frac{\sigma_1 - \sigma_3}{2 \cdot \sigma_{\mathrm{unpol}}} = \frac{\sigma_{\mathrm{diff}}}{2 \cdot \sigma_{\mathrm{unpol}}} \tag{6.56}$$

$$E^{\mathrm{version\ 2}} = \frac{\sigma_1 - \sigma_3}{\sigma_1 + \sigma_3} = \frac{\sigma_{\mathrm{diff}}}{\sigma_{\mathrm{sum}}} \ . \tag{6.57}$$

Version 1 (Equation (6.56)) has the advantage that it is independent of the subtraction of the background from reactions on the unpolarized nucleons, as in the numerator such contributions cancel out (see Equation (6.52)) and the normalization is done by means of the unpolarized cross section. However, it involves results from different beamtimes and requires a delicate normalization of the latter which is sometimes not easy to achieve as it strongly depends on all individual experimental settings such as photon fluxes, detection efficiencies, and applied thresholds. In contrast to version 1, version 2 is independent of the normalization as the numerator and the denominator involve quantities from the same analysis and inconsistencies would cancel each other out. If the estimation of the background contributions from unpolarized nucleons is understood, version 2 is expected to be the most reliable extraction method.
The helicity dependent cross sections $\sigma_{1/2}$ and $\sigma_{3/2}$ can then be extracted from the two versions for the double polarization observable E (Equations (6.56) and (6.57)) in combination with the unpolarized cross section σ_{unpol}:

$$\begin{aligned} \sigma_{1/2}^{\mathrm{version\ 1/2}} &= \sigma_{\mathrm{unpol}} \cdot (E^{\mathrm{version\ 1/2}} + 1) \\ \sigma_{3/2}^{\mathrm{version\ 1/2}} &= \sigma_{\mathrm{unpol}} \cdot (E^{\mathrm{version\ 1/2}} - 1) \ , \end{aligned} \tag{6.58}$$

or directly from the measured difference (Equation (6.54)) and sum (Equation (6.55)) of the helicity dependent cross sections σ_{diff}, σ_{sum}:

$$\begin{aligned}\sigma_{1/2}^{\text{version 3}} &= \frac{1}{2}(\sigma_{\text{sum}} + \sigma_{\text{diff}}) \\ \sigma_{3/2}^{\text{version 3}} &= \frac{1}{2}(\sigma_{\text{sum}} - \sigma_{\text{diff}}) \; .\end{aligned} \tag{6.59}$$

The measured yields N_1^m and N_3^m can also be used to directly determine the helicity dependent cross sections $\sigma_{1/2}$ and $\sigma_{3/2}$. Solving Equation (6.50) for σ_1 and using in Equation (6.51) yields:

$$\sigma_{1/2}^{\text{version 4}} = \frac{N_1^m F_3(1+p) - N_3^m F_1(1-p)}{2F_1F_3np} - \sigma_{\text{CO}} \stackrel{!}{=} \sigma_1^{\text{direct}} \tag{6.60}$$

$$\sigma_{3/2}^{\text{version 4}} = \frac{N_3^m F_1(1+p) - N_1^m F_3(1-p)}{2F_1F_3np} - \sigma_{\text{CO}} \stackrel{!}{=} \sigma_3^{\text{direct}} \; . \tag{6.61}$$

From these direct measurements of the helicity dependent cross sections, a third version for the double polarization observable E results directly from Equation (6.47):

$$E^{\text{version 3}} = \frac{\sigma_1 - \sigma_3}{\sigma_1 + \sigma_3} = \frac{\sigma_1^{\text{direct}} - \sigma_3^{\text{direct}}}{\sigma_1^{\text{direct}} + \sigma_3^{\text{direct}}} \; . \tag{6.62}$$

Even though the direct calculation of the helicity dependent cross sections (Equations (6.60) and (6.61)) is the most intuitive, as it follows from the considerations made in the beginning (Equations (6.50) and (6.51)), they are not distinct. The extraction of the double polarization observable is theoretically identical with that from version 2 (Equation (6.57)). Nevertheless, since it relies on a different weighting of the events with the degree of polarization and a different extraction of the results, it allows for a further check of the analysis procedure. In general, the determination of E from the three versions (Equations (6.56), (6.57) and (6.62)) and $\sigma_{1/2}$, $\sigma_{3/2}$ from the four versions (Equations (6.58), (6.59), (6.60) and (6.61)), allows for a detailed and reliable investigation of the systematic uncertainties related to normalizations with photon fluxes, detection efficiencies, thresholds, analysis cuts, and the estimation of the background from reactions on unpolarized nucleons.
Table 6.12 summarizes the different extraction methods.

6.13.4 Carbon Background Subtraction

It is not possible to distinguish between reactions on polarized or unpolarized nucleons in the analysis. Therefore, the measured yields for antiparallel N_1^m and parallel N_3^m photon and target spin configurations (see Equation (6.49)) are contaminated by reactions on unpolarized nucleons inside the carbon and oxygen nuclei. As observed in Equations (6.56) and (6.58), the extraction of the double polarization observable E and the helicity dependent cross sections $\sigma_{1/2}$ and $\sigma_{3/2}$ does not necessarily require an appropriate estimation of such background contributions and could be circumvented by normalizing the yield with the unpolarized cross section. As already mentioned,

E	$\sigma_{1/2}$	$\sigma_{3/2}$
$\frac{\sigma_{\text{diff}}}{2\cdot\sigma_{\text{unpol}}}$	$\sigma_{\text{unpol}}\cdot(1+E)$	$\sigma_{\text{unpol}}\cdot(1-E)$
$\frac{\sigma_{\text{diff}}}{\sigma_{\text{sum}}}$	$\sigma_{\text{unpol}}\cdot(1+E)$	$\sigma_{\text{unpol}}\cdot(1-E)$
	$\frac{1}{2}(\sigma_{\text{sum}}+\sigma_{\text{diff}})$	$\frac{1}{2}(\sigma_{\text{sum}}-\sigma_{\text{diff}})$
$\frac{\sigma_{1/2}^{\text{direct}}-\sigma_{3/2}^{\text{direct}}}{\sigma_{1/2}^{\text{direct}}+\sigma_{3/2}^{\text{direct}}}$	$\sigma_{1/2}^{\text{direct}}$	$\sigma_{3/2}^{\text{direct}}$

Table 6.12: Overview of the different extraction methods for the double polarization observable E and the helicity dependent cross sections $\sigma_{1/2}$ and $\sigma_{3/2}$.

this though strongly depends on the proper normalization of both the polarized and unpolarized data. Although this might be understood, the extraction of the observables by means of an elaborate estimation and subtraction of the carbon background brings some advantages. On the one hand, it is not as sensitive to issues concerning the normalization of the results, on the other hand it also serves as an important cross check for the extraction with the unpolarized cross section.

For the estimation of the carbon background, extra beamtimes of identical setups and experimental settings were carried out, but the deuterated butanol target was replaced with a carbon foam target of approximately the same density. Whereas for the carbon measurement at A2 it was not feasible, at CBELSA/TAPS it was possible to fill the target cell with the ^{3}He/^{4}He mixture at the usual low temperatures and to apply the magnetic field of the holding coil. With the identical experimental trigger settings, data was taken for a few days in order to gain enough statistics for the background estimation. Besides the normalization with the photon flux, the identical analysis and detection efficiencies used for the deuterated butanol analysis were also applied to the carbon data.

The yield from the deuterated butanol analysis consists of contributions from the polarized and unpolarized nucleons from the deuterium, as well as from unpolarized nucleons from carbon and oxygen. A comparison of the missing mass spectra of the deuterium and carbon data with that from deuterated butanol allowed for the estimation of the background contributions. Missing mass spectra are especially suited for the estimation as influences from the different Fermi momenta of the different target nuclei are visible, which results in a rather distinct separation of the individual contributions. In addition, it ensures a rather strong separation of true signals and background events. However, as will be seen later, the estimation can also be carried out through coplanarity spectra and checked with the invariant mass spectra.

In order to estimate the contribution from carbon, a realistic relative normalization between the spectra of the analyses of data from the different beamtimes was achieved. This was realized by a first absolute normalization f_{abs} according to Equation (6.42), for which the corresponding target surface densities for deuterium $n_t^{\text{LD}_2}$, carbon $n_t^{^{12}\text{C}}$, and deuterated butanol n_t^{dB} were determined with the values from Table 6.11. At this stage, the individual missing mass yields correspond to cross sections per target nucleus, i.e. deuterium, carbon, and deuterated butanol. In order to obtain the proper relative normalization f_{rel}, an additional normalization with respect to the number of individual nucleons of interest n_i from the target nucleus is required and follows from the chemical formula for deuterated butanol C_4D_9OD. For deuterium, the number of deuterium nuclei d is identical to the number of protons and neutrons, i.e. $n_t^{d,\text{LD}_2} = n_t^{\text{LD}_2}$, and no additional normalization is required. In contrast, a deuterated butanol molecule contains 10 polarized deuterons and the relative normalization is achieved by:

$$n_t^{\text{d,dB}} = n_d^{\text{dB}} \cdot n_t^{dB} = 10 \cdot n_t^{dB} \ . \tag{6.63}$$

Since the carbon data was used for the estimation of the contributions from the oxygen nuclei, its scale factor contains an additional term with the ratio of the molar masses of oxygen and carbon. This term is used to approximate the oxygen yield from carbon and results from the assumption that the cross sections scale with the nuclear surface, i.e. $A^{2/3}$ [208, 213]:

$$n_t^{\text{CO,dB}} = n_{\text{CO}}^{\text{dB}} \cdot n_t^{dB} = \left[4 + \left(\frac{M_{^{16}\text{O}}}{M_{^{12}\text{C}}}\right)^{2/3}\right] \cdot n_t^{dB} \ . \tag{6.64}$$

As previously mentioned, the carbon target at A2 was not filled with the helium admixture that was used to cool down the deuterated butanol material. Therefore, contributions from reactions on these helium nuclei had to be approximated with the carbon data. For this purpose, the helium volume in the target was determined from the geometrical parameters, i.e. the length of the target l_{dB}, the target end caps l_{end}, and the filling factor. Using the molar mass of helium M_{He} and a density of $\rho_{\text{He}} = 0.14$ g/cm^3, the target surface density of the helium target is given by

$$n_t^{\text{He}} = \frac{[(1 - f_{\text{fill}}) \cdot l_{\text{dB}} + l_{\text{end}}] \cdot \rho_{\text{He}} \cdot N_A}{M_{\text{He}}} \ , \tag{6.65}$$

and its relative contribution to the deuterated butanol target is given by:

$$n_t^{^{3/4}\text{He,dB}} = n_{\text{He}}^{\text{dB}} \cdot n_t^{He} = \left(\frac{M_{^{3/4}\text{He}}}{M_{^{12}\text{C}}}\right)^{2/3} \cdot n_t^{He} \ . \tag{6.66}$$

The total normalization of the missing mass spectra from the analysis of the deuterium, carbon, and deuterated butanol beamtime was then carried out as follows:

$$N^{\text{rel}} = N^{\text{meas}}/f_{\text{abs}}/f_{\text{rel}} = N^{\text{abs}}/f_{\text{tot}} \ , \tag{6.67}$$

where

$$f_{\text{tot}} = \begin{cases} n_t^{\text{LD}} \cdot \varepsilon^{\text{LD}} \cdot N_\gamma^{\text{LD}} \cdot \Gamma_i/\Gamma & \text{LD}_2 \\ n_t^{\text{d,dB}} \cdot \varepsilon^{\text{dB}} \cdot N_\gamma^{\text{dB}} \cdot \Gamma_i/\Gamma & \text{C}_4\text{D}_9\text{OD} \\ \dfrac{n_t^{\text{C}} \cdot \varepsilon^{\text{dB}} \cdot N_\gamma^{\text{C}} \cdot \Gamma_i/\Gamma \cdot n_t^{\text{dB}}}{(n_t^{\text{CO,dB}} + n_t^{^{3/4}\text{He,dB}})} & {}^{12}\text{C (A2)} \\ \dfrac{((n_t^{\text{C}} + n_t^{^{3/4}\text{He,dB}}) \cdot \varepsilon^{\text{dB}} \cdot N_\gamma^{\text{C}} \cdot \Gamma_i/\Gamma) \cdot n_t^{\text{dB}}}{(n_t^{\text{CO,dB}} + n_t^{^{3/4}\text{He,dB}})} & {}^{12}\text{C (CBELSA/TAPS)} \ . \end{cases} \tag{6.68}$$

The resulting normalized missing mass yields of the different beamtimes are shown for single π^0 photoproduction in Figure 6.136, for double π^0 photoproduction from the A2 data in Figure 6.137 and for double π^0 photoproduction from the CBELSA/TAPS data in Figure 6.138. Shown are the missing mass spectra for five selected energy and angular bins for the reaction on the proton (upper half) and on the neutron (lower half). All cuts were applied to the deuterated butanol, deuterium and carbon data. The sum (solid black line) of the missing mass spectra from the analysis of the liquid deuterium (dashed green lines) and the carbon data (dotted magenta lines) are compared to those from the deuterated butanol data (open blue and red triangles). With the proper normalization and a realistic carbon measurement, the sum of deuterium and carbon yield (solid black line) should reproduce that from the deuterated butanol data (colored triangles). In order to demonstrate the effect of the carbon subtraction, the carbon subtracted yield from the deuterated butanol spectra is shown as the gray area.
For single π^0 photoproduction from the proton (upper half of Figure 6.136), an overall good agreement with almost negligible discrepancies can be observed for all energy and angular bins. For the reaction on the neutron (lower half of Figure 6.136), the agreement at low energies is of the same quality. However, at larger positive missing mass values, deviations occur for higher energies and center of mass forward angles of the pion. This might be due to the absence of helium in the target cell and the missing magnetic field of the holding coil. Due to the different Fermi momenta of nucleons inside helium, such contributions exhibit different kinematics than those from carbon and are therefore not reproduced by the missing mass spectra.
As the discrepancy increases with energy and the Lorentz force is proportional to the velocity of the particle that is exposed to a magnetic field, effects from the magnetic field are a plausible reason. As particles perpendicular to the magnetic field direction exhibit the strongest Lorentz force, the effect would mainly have an influence on the detection of charged particles with the PID. Due to the deflection the particles obtain a different azimuthal angle which might result in a wrong coincidence between hits in the PID and hits in the Crystal Ball. In this way, charged particles can be identified as neutral and vice versa. Besides the final state particles, the magnetic field spreads out the electromagnetic showers from the interaction of the photon beam with the target and could also interfere with the charged particle identification. However, effects from the magnetic field have been investigated with Monte Carlo simulations, but no influence on the extraction of the observables was observed. An influence of the magnetic field on charged particles hence is very unlikely. Nevertheless, an influence of the magnetic field on the electronics of the experimental setup, e.g. the PMTs of the PID, could result in differences that only affect the data and not the simulation. However, within the missing mass cut (vertical dashed lines) the spectra are in good agreement and only those events enter into the results.

The corresponding missing mass spectra for double π^0 photoproduction from polarized nucleons from the A2 data are shown in Figure 6.137. The agreement is mostly identical to that observed for single π^0 photoproduction. For the reaction on the proton, an overall good agreement can be seen, whereas with higher incident

photon energy and meson center of mass polar angle for the neutron, discrepancies at positive missing mass values arise. Nevertheless, the agreement within the missing mass cut is overall good such that the carbon background seems to be reliably estimated.
The nucleon missing mass of double π^0 photoproduction from the CBELSA/TAPS data are shown in Figure 6.138. As previously mentioned, at CBELSA/TAPS the magnetic field and helium were present during the carbon experiment. The discrepancy seems smaller than observed in the corresponding spectra from A2 (Figure 6.137), which emphasizes that the difference is most likely due to one or both of the mentioned reasons. Even though the overall agreement for the neutron outside the missing mass cut range is slightly better than observed in the spectra from the A2 data, for the proton the agreement at backward meson angles is somewhat poor which probably is due to the veto efficiency of the charged particles with the Forward Plug detector.

All the missing mass spectra from deuterated butanol of all beamtimes are in general well reproduced by those from liquid deuterium and carbon, especially in the region where the missing mass cut was applied. The fact that the agreement was achieved with an absolute normalization of all yields confirms the quality of the estimation of the contributions from reactions on unpolarized nucleons and seems to be well under control. The estimation of the carbon background can also be determined by means of the coplanarity spectra. Due to the Fermi motion, the spectra from different contributions have different resolution and are rather well separable. However, the separation is not as favorable as observed for the missing mass and hence was only used to verify the quality of the estimation. On the other hand, the invariant mass spectra were not suitable for the estimation. Due to the absence of effects from Fermi motion, the different spectra are too similar. The corresponding coplanarity spectra for single π^0 photoproduction are shown in Figure C.1, those for double π^0 photoproduction from the A2 data in Figure C.2 and from the CBELSA/TAPS data in Figure C.3. The invariant mass spectra for single π^0 photoproduction are shown in Figure C.4, those for double π^0 photoproduction from the A2 data in Figure C.5, and from the CBELSA/TAPS data in Figure C.6.

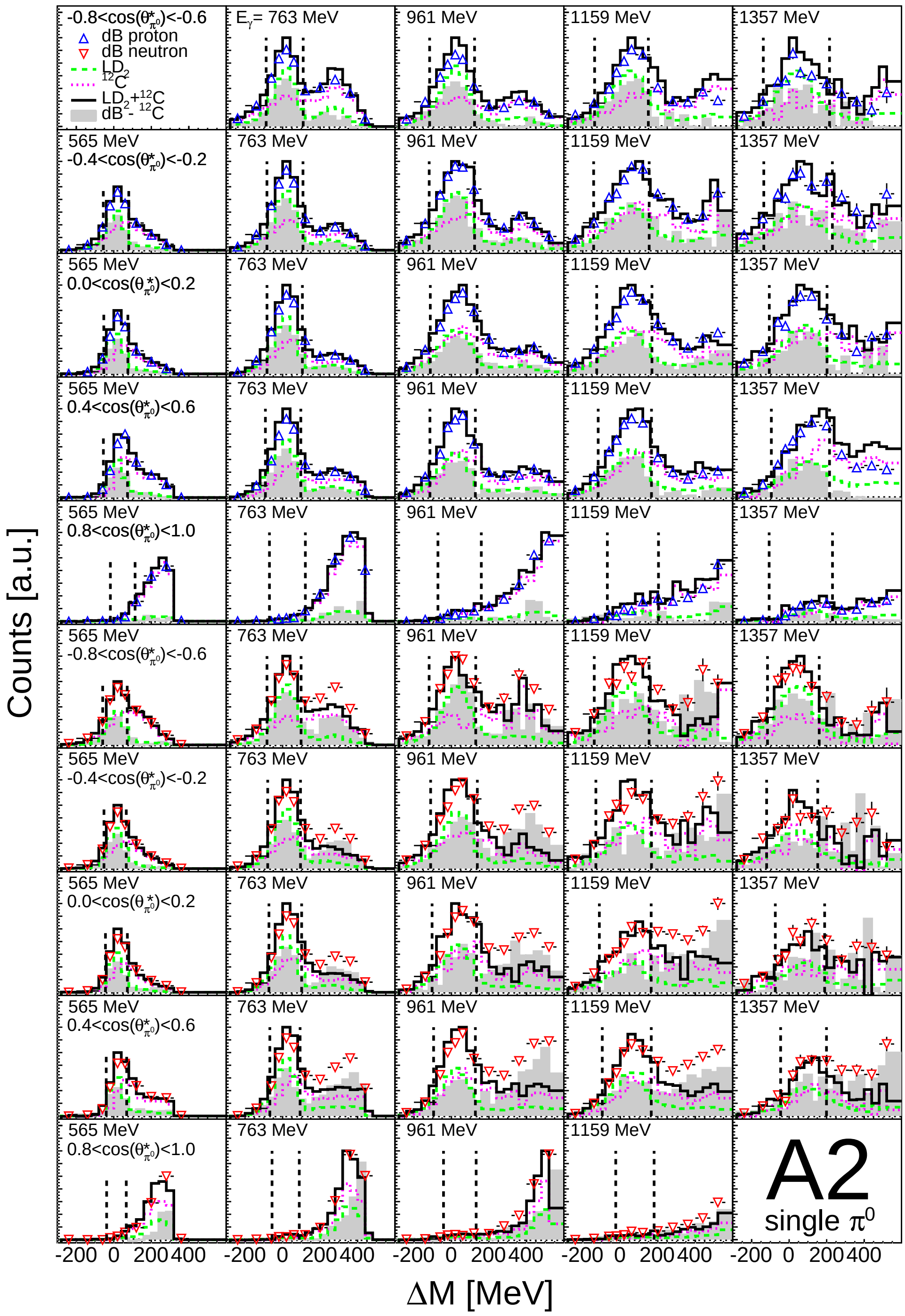

Figure 6.136: Illustration of the estimation of the carbon background by means of missing mass spectra for exclusive single π^0 photoproduction. Results from the A2 data. Shown are five selected energy and angular bins. All cuts were applied to the data. Red (blue) triangles: proton (neutron) distribution from the deuterated butanol data. Dashed green histogram: distribution from the deuterium data. Dotted magenta histogram: distribution from the carbon data. Black histogram: sum of deuterium and carbon data. Gray histogram: carbon subtracted yield from the deuterated butanol target. Dashed vertical black lines: missing mass cut from deuterium data.

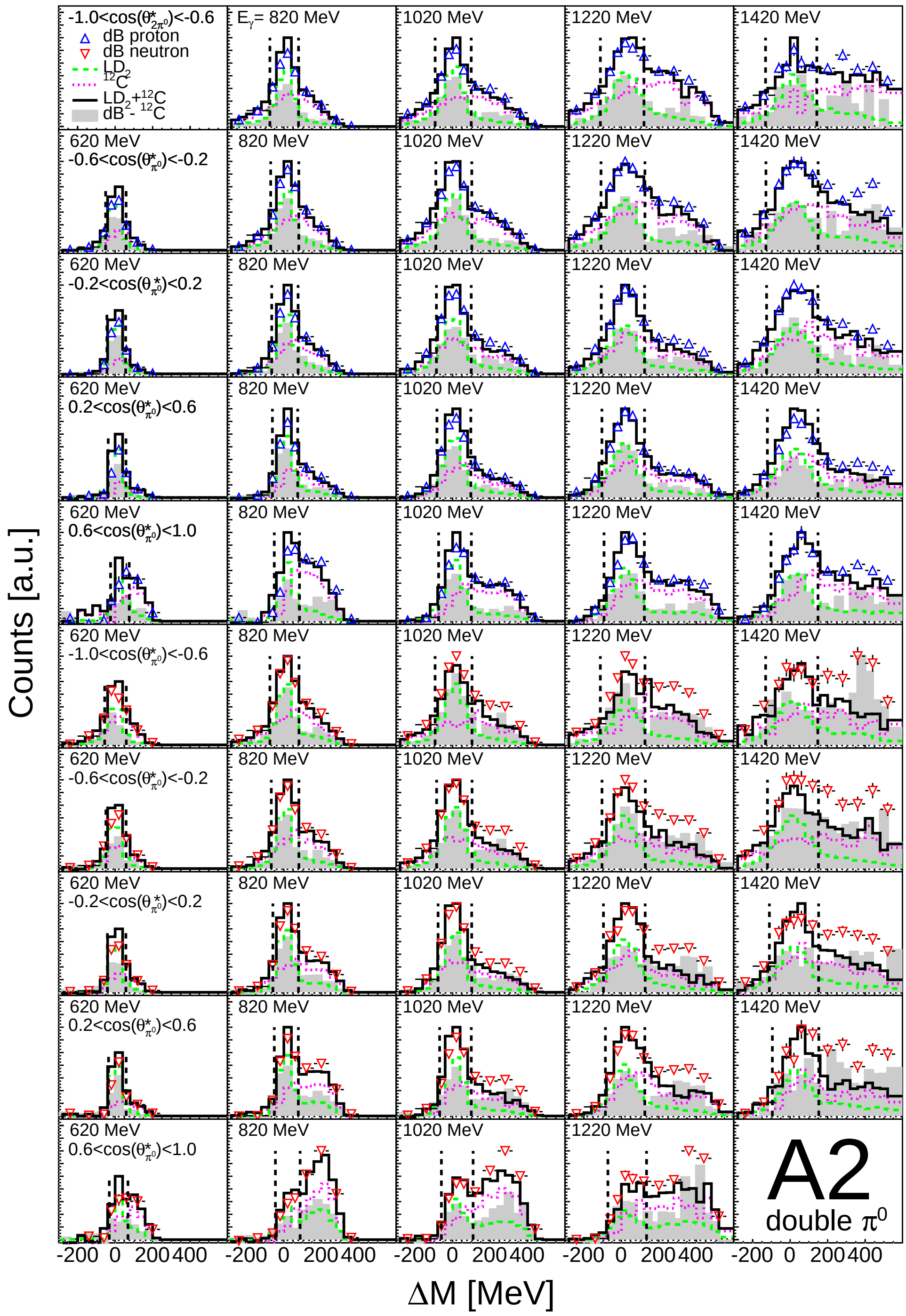

Figure 6.137: Illustration of the estimation of the carbon background by means of missing mass spectra for exclusive double π^0 photoproduction. Results from the A2 data. Shown are five selected energy and angular bins. All cuts were applied to the data. Red (blue) triangles: proton (neutron) distribution from the deuterated butanol data. Dashed green histogram: distribution from the deuterium data. Dotted magenta histogram: distribution from the carbon data. Black histogram: sum of deuterium and carbon data. Gray histogram: carbon subtracted yield from the deuterated butanol target. Dashed vertical black lines: missing mass cut from deuterium data.

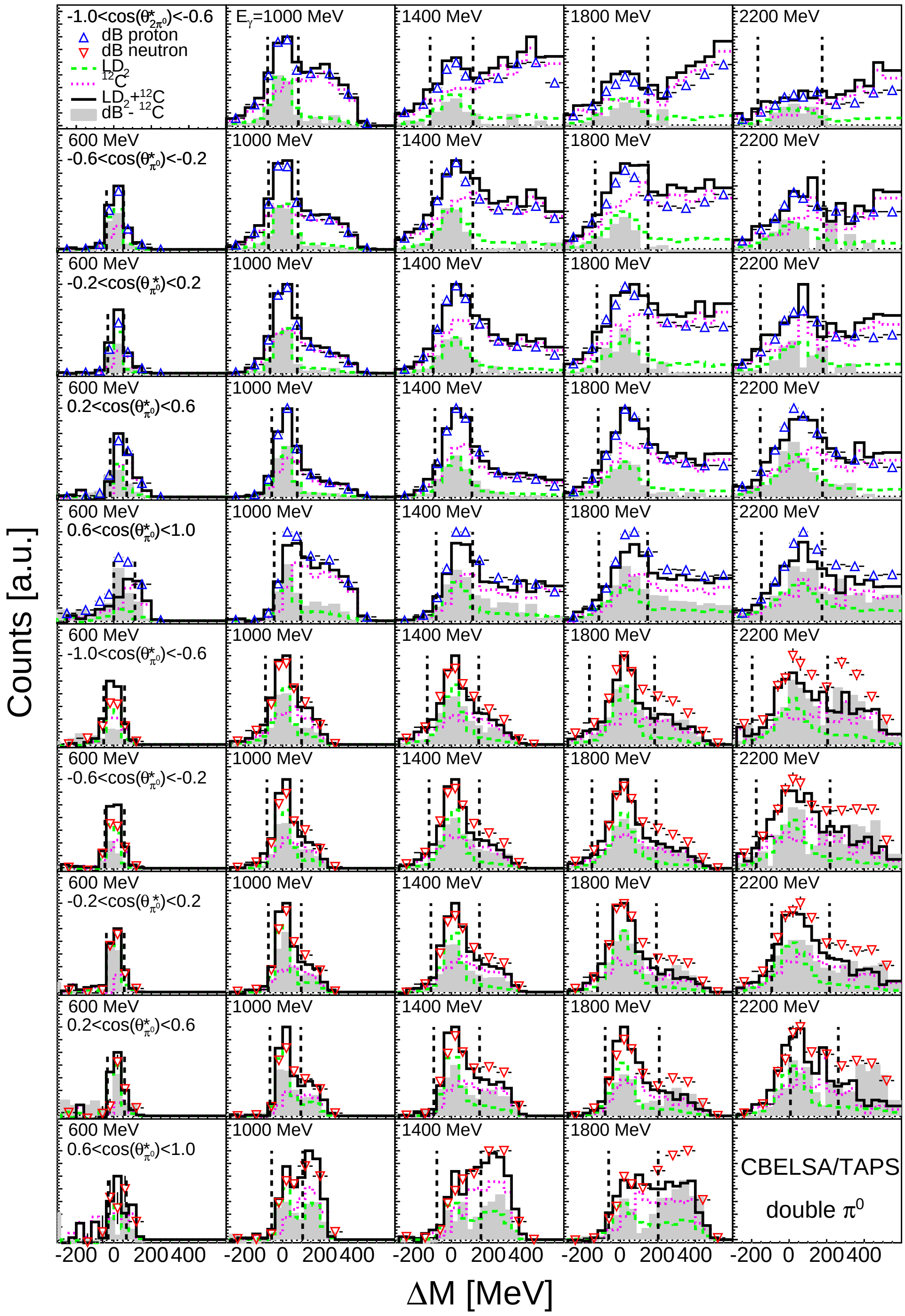

Figure 6.138: Illustration of the estimation of the carbon background by means of missing mass spectra for exclusive double π^0 photoproduction. Results from the CBELSA/TAPS data. Shown are five selected energy and angular bins. All cuts were applied to the data. Red (blue) triangles: proton (neutron) distribution from the deuterated butanol data. Dashed green histogram: distribution from the deuterium data. Dotted magenta histogram: distribution from the carbon data. Black histogram: sum of deuterium and carbon data. Gray histogram: carbon subtracted yield from the deuterated butanol target. Dashed vertical black lines: missing mass cut from deuterium data.

6.14 Empty Target Subtraction

Among the measured particles, not all of them originate from reactions on the photon beam with the target material. A certain amount of reactions stem from interactions of the photon beam with the different materials from the target cell, especially from reactions with the Kapton foils of the target windows. Kapton ($C_{22}H_{10}N_2O_5$) consists of nuclei that exhibit rather large cross sections for quasi-free meson photoproduction. Therefore, contributions from the target cell are non-negligible and have to be subtracted from the final yield. In this work, this only concerns the yields used for the extraction of unpolarized cross sections. For the double polarization observables, empty target contributions cancel out in the numerator as they equally contribute to both spin configuration yields. In the denominator, the contributions are removed with the subtraction of the carbon background, as the same target cell was used for the measurement with carbon foam.

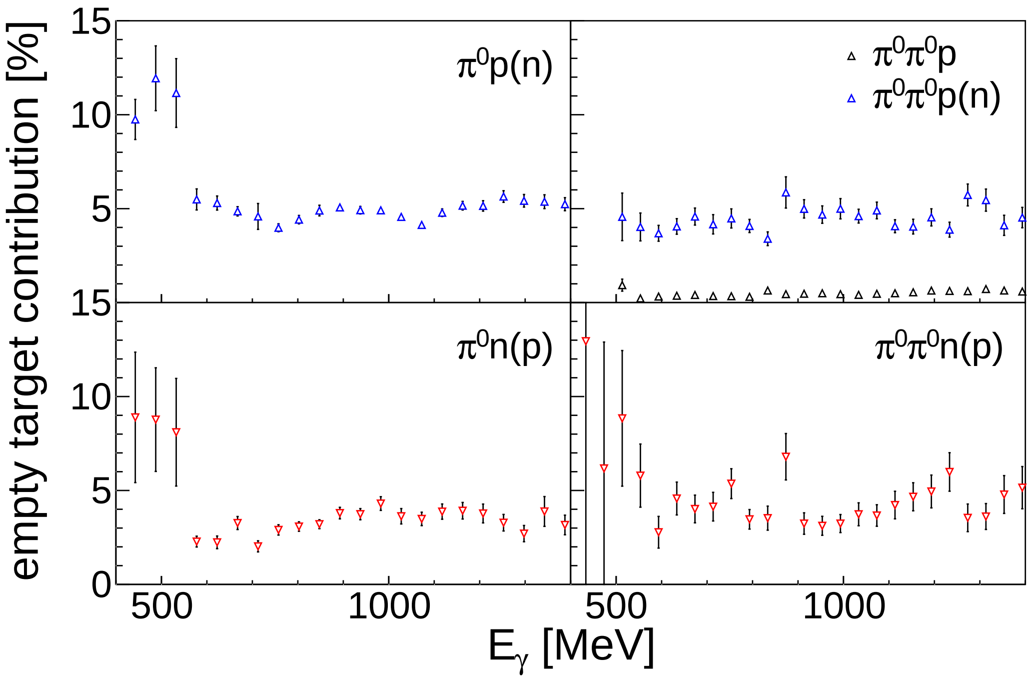

Figure 6.139: Relative empty target contributions to the total cross sections as a function of E_γ for single (left) and double π^0 photoproduction (right) from the A2 data. Black triangles: free proton. Blue triangles: quasi-free proton. Red triangles: quasi-free neutron.

In order to estimate the contributions from the target cell, the target material was removed from the target cell and the experiment was repeated for a few days with the identical settings and an empty target. The data was analyzed with the identical analysis and cuts and cross sections as a function of E_γ or W and $\cos(\theta^*_m)$ were determined. For every energy and angular bin, the empty target cross sections were then subtracted from the standard cross sections.

The relative contributions of the target cell to the energy dependent cross section for single and double π^0 photoproduction from free and quasi-free protons and quasi-free neutrons at A2 are shown in Figure 6.139. In general the contributions from the target container are independent of energy and on the order of 5% for single and double π^0 photoproduction from quasi-free nucleons. In contrast, the contribution to the free cross section is almost completely negligible, but increases with increasing energy. The much lower contribution for the reaction on the free proton is due to the absence of Fermi motion in liquid hydrogen. The 1.5σ cuts that were determined on the liquid hydrogen data correspond to a much more narrow cut on the carbon spectra than the 1.5σ cuts from liquid deuterium. Therefore, most of the events from carbon were automatically eliminated.

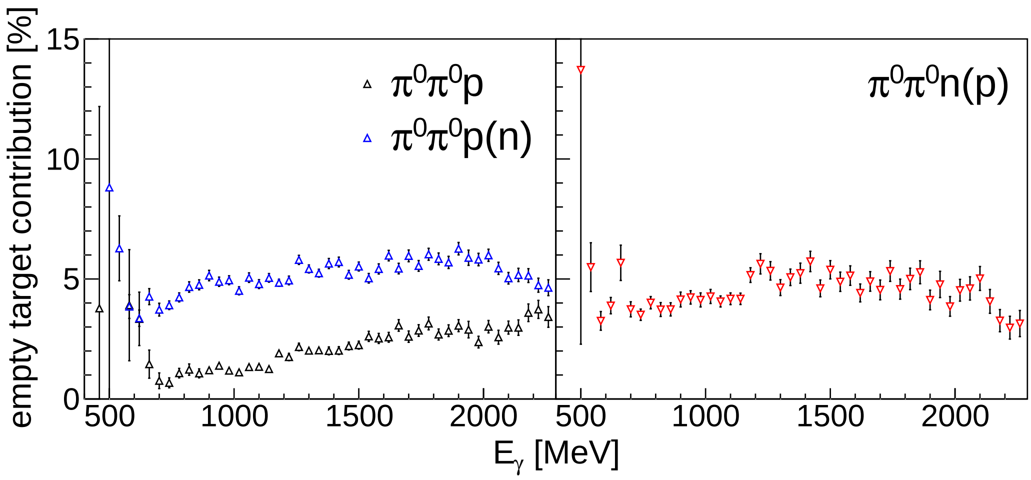

Figure 6.140: Relative empty target contributions to the total cross sections as a function of E_γ for double π^0 photoproduction from the CBELSA/TAPS data. Black triangles: free proton. Blue triangles: quasi-free proton. Red triangles: quasi-free neutron.

Such empty target experiments were only performed at A2 and not at CBELSA/TAPS. Therefore, at CBELSA/TAPS the contributions from the target cell had to be estimated by using the carbon foam experiment that served to estimate the carbon background for the deuterated butanol data. The contributions were then estimated by scaling the yield from the carbon measurement according to the ratio of carbon nuclei inside the carbon target and those inside the target cell. For this purpose the number of carbon nuclei inside the carbon target and the target cell were determined. The number of Kapton molecules inside the target cell can be calculated from its density $\rho_K = 1.42$ g/cm^3, the target window thickness $d_K = 2 \cdot 0.0125 = 0.025$ cm, and the molar mass of Kapton $M_K = 382.33$ g/mol, which directly follows from its chemical formula:

$$n_t^K = \frac{\rho_K \cdot d_K N_A}{M_K} = 5.59 \cdot 10^{-5} \text{ b}^{-1} \ . \qquad (6.69)$$

Neglecting contributions from the hydrogen atoms in Kapton, the number of carbon nuclei in the target windows is given by:

$$n_t^{C,K} = n_C^K \cdot n_t^K = 22 + 2 \cdot \left(\frac{M_\mathrm{N}}{M_\mathrm{C}}\right)^{2/3} + 5 \cdot \left(\frac{M_\mathrm{O}}{M_\mathrm{C}}\right)^{2/3} = 0.00163 \text{ b}^{-1} \ , \qquad (6.70)$$

where again the contribution from nitrogen and oxygen were approximated with carbon by assuming that the cross sections scale with $A^{2/3}$ [208, 213]. The resulting relative contributions of the empty target to the total cross section at CBELSA/TAPS are shown in Figure 6.140. The contributions are of similar size, i.e. 5% (<2%) for quasi-free (free) $2\pi^0$ photoproduction, as observed at A2, indicating that the estimation from the carbon data was reasonably carried out. The contribution to the free proton cross section exhibits the same behavior as at A2. Whereas at low energies it is almost zero, it increases with increasing energy. The rather large contributions at low energies are due to statistical fluctuations.

6.15 Systematic Uncertainties of Unpolarized Results

Besides the statistical errors, which contain information about the statistical quality of the data, it is necessary to have a measure of the effects of the different analysis steps and by that of the robustness of the identification and extraction of the results. In the following sections, the most relevant sources of systematic uncertainties will be estimated and discussed. Whereas some of the sources are independent of the reaction channel and of energy and angle, other sources have to be carefully determined as a function of energy and angle for the individual analyses.
The channel dependent systematic uncertainties were determined by an investigation of the effect of a small variation of the corresponding quantity to the total cross section. The relative difference of the varied cross section to the standard one was assigned to the relative systematic error and was determined for every analysis channel and type of result.

6.15.1 Reaction Independent Systematic Uncertainties

Systematic uncertainties from limitations from the experiment (target surface density, photon flux determination, empty target subtraction) or physical quantities (branching ratios) are independent of the reaction channel and only have to be determined once.

Target Surface Density

Fluctuations in the temperature and pressure of the target result in a systematic uncertainty of the target length $\Delta\sigma_\rho$, mainly from a deformation of the inner target window and target density. The systematic error for the deuterium beamtimes from A2 were estimated to be on the order of 4 % [214]. The same value, i.e. 4 %, was assumed for the uncertainty of the target surface density for the liquid hydrogen

target (l_t=10.0±0.1 cm) from A2.
For the liquid hydrogen and deuterium beamtimes at CBELSA/TAPS, a systematic error for the parameters of the liquid hydrogen and deuterium targets was not found. However, due to the similar operating conditions and target geometries, the systematic uncertainties were estimated to be of the same order of 4 %.

Empty Target Subtraction

The relative empty target contribution (see Section 6.14) was nearly independent of energy, reaction channel, analyzed beamtime and of the same order at A2 than at CBELSA/TAPS. Therefore, half of the relative contribution was assumed to be a realistic estimation for the systematic error of the empty target subtraction $\Delta\sigma_{\mathrm{ET}}$. This results in an error of 2.5 % for liquid deuterium and 1 % for liquid hydrogen at both A2 and CBELSA/TAPS.

Branching Ratio

The systematic uncertainty of the branching ratio of the decay of the neutral pion into two photons $\Delta\sigma_\Gamma$ of (98.823 ± 0.034) % [202] can be neglected as it is on the order of 0.03 % for single and 0.06 % for double π^0 photoproduction.

Photon Flux Determination

The systematic uncertainty of the determination of the photon flux $\Delta\sigma_\Phi$ at A2 is dominated by the uncertainty in the tagging efficiency measurement, whose time dependence was achieved by a χ^2 minimization of the P2/tagger ratio and the individual tagging efficiency measurements. The uncertainty of the absolute tagging efficiency value from the individual measurements and the relative value from the P2/tagger ratio contribute to the total systematic error. The same applies for the determination of the time dependent tagging efficiency from the count rate measurement. In both cases, the systematic uncertainty was estimated from a minimum and maximum value, as obtained from the absolute measurements. For the liquid hydrogen and deuterium beamtimes, the error was determined to be on the order of 3 % [214].
For CBELSA/TAPS, the main uncertainty is given by the GIM efficiency, which was estimated to be on the order of 7 % [118]. An additional error of 3.8 % results from the trigger electronics [118]. Hence, the absolute error is on the order of 8 %.

6.15.2 Reaction Dependent Systematic Uncertainties

In this section, the systematic uncertainties will be discussed that depend on the individual reaction channel. Therefore, they were determined for all energy and angular bins of the individual cross sections independently.

Analysis Cuts

The different requirements for the identification of the particles and the reaction that were applied to the different analysis steps have a strong influence on the quality of the results. Varying the strength of the individual conditions reveals the reliability of the individual condition. Whereas a reliable analysis condition would result in small effects of a variation, an unreliable condition may result in a drastic change of the result. Furthermore, it would directly reveal discrepancies between the simulation and data.

For this reason, the systematic uncertainty of the different analysis cuts $\Delta\sigma_{\text{cuts}}$ was investigated by inducing slight variations of ± 3 % to the applied conditions. The size of the variation was chosen such that only reasonable changes were allowed. Larger variations would not make sense as the individual conditions were already chosen to be at the upper limit in order to suppress as much background as possible while accepting a maximum number of true events. The cuts that were varied for the investigation were the cut on the meson-nucleon coplanarity, the nucleon missing mass, and the invariant mass cut. The analysis was then carried out with 3 % narrower cuts and also with 3 % wider cuts than used for the extraction of the results. The systematic error was then determined from the difference of the standard cross section to the average cross section obtained from the minimum and maximum cut.

Nucleon Detection Efficiency

The requirement of the coincident detection of the recoil nucleon in all exclusive analyses has a strong influence of the result. Hence, the systematic error of the result strongly depends on the reliability of the nucleon detection efficiency. A reasonable method for the estimation of this systematic error $\Delta\sigma_{\text{ND}}$ is the comparison of the (quasi-free) inclusive analysis (where the recoil nucleon detection is not required) with the exclusive analyses. For the analysis on the free proton, it can be investigated by comparing the inclusive to the exclusive cross section. In case where the proton detection efficiency is understood, both results should coincide with each other. In contrast, for the analyses of liquid deuterium data, the reaction can occur on either the proton or the neutron and hence the quasi-free inclusive cross section contains all events where the recoil proton or neutron was detected or not. In this case, a reliable nucleon detection efficiency is only achieved if the quasi-free inclusive cross section is equal to the sum of the exclusive proton and neutron result, by:

$$\begin{array}{lcll} \sigma(\gamma p \rightarrow \gamma(p)) & = & \sigma(\gamma p \rightarrow \gamma p) & \text{LH}_2 \\ \sigma(\gamma N \rightarrow \gamma(N)) & = & \sigma(\gamma p(n) \rightarrow \gamma p(n)) + \sigma(\gamma n(p) \rightarrow \gamma n(p)) & \text{LD}_2\ . \end{array} \tag{6.71}$$

Any discrepancy between the (quasi-free) inclusive and the exclusive analysis is related to the systematic error of the detection of the recoil nucleon. Therefore, the systematic error was determined as half of the difference of the two cross sections.

This method only accounts for relative systematic uncertainties between the inclusive and exclusive analyses. If the nucleon detection efficiency in the experiment was different than the behavior in the simulation, both cross sections might be in agreement, but the absolute scale can still be significantly different from the actual result. This was discussed in the analysis of hydrogen data from A2 (see Section 6.8.4). In this case, the inclusive and exclusive $2\pi^0$ cross sections were in agreement with each other, but both were about 10% lower than published results. However, such effects can be controlled by comparing results of the same analysis, but from the data of different beamtimes or even different experiments as it is rather unlikely that the same issue is present in different experiments. In addition, the comparison of results to published data or investigations of results with and without the information from charged particle sensitive detectors can give information about the accuracy of the absolute normalization. Within the results of this work, such effects were investigated and ruled out, yielding a reliable absolute normalization. Therefore, the comparison of the (quasi-free) inclusive to exclusive cross sections indeed yields a reliable estimation of the systematic uncertainty of the nucleon detection efficiency.

Crystal Ball Energy Sum Threshold

As the Crystal Ball energy sum threshold eliminates events of an energy sum below a certain threshold and only accepts events above a certain energy sum, it has an essential influence on the overall systematic uncertainty. Whereas software thresholds below the experimental threshold affect the detection efficiency determination and the normalization of the cross sections, software thresholds above the experimental threshold only have an influence on the statistical quality. Therefore, the systematic uncertainty of the applied threshold in the analysis $\Delta\sigma_{\mathrm{CDF}}$ was determined from a comparison of the cross section obtained with an analysis using a fixed threshold of 400 MeV (that is certainly above the experimental threshold of 300 MeV) to that using the established threshold from the cumulative distribution function (see Section 6.6.2). The induced deviations for single and double π^0 photoproduction supplied the leading contribution at low incident photon energies as in both cases the production threshold lies below the experimentally set value.

6.15.3 Total Systematic Uncertainty of the Unpolarized Results

The total systematic uncertainty from the reaction independent sources were not added to the energy and angular dependent values, which are shown together with the results and are listed as global values in Table 6.13. The resulting total systematic uncertainty was calculated by adding them quadratically.

The calculation of the energy and angle dependent total systematic uncertainty is based on the assumption that the individual errors are independent from each other and due to the different contributions cancellation effects may occur. For this reason for every energy and angular bin, the individual components of the systematic errors were added quadratically according to:

$$\Delta\sigma_{\mathrm{tot}}(E_\gamma/W, \cos(\theta^*_m)) = \sqrt{(\Delta\sigma^2_{\mathrm{cuts}} + \Delta\sigma^2_{\mathrm{ND}} + \underbrace{\Delta\sigma^2_{\mathrm{CDF}}}_{\text{only for A2}})(E_\gamma/W, \cos(\theta^*_m))}\ . \qquad (6.72)$$

	Beamtime	$\Delta\sigma_\rho$	$\Delta\sigma_{\mathrm{ET}}$	$\Delta\sigma_\Gamma$	$\Delta\sigma_\Phi$	$\Delta\sigma_{\mathrm{tot}}$
A2	LH_2	4%	1%	$<0.1\%$	3%	$\sim 5\%$
	LD_2	4%	2.5%	$<0.1\%$	3%	$\sim 6\%$
CBT	LH_2	4%	1%	$<0.1\%$	8%	$\sim 9\%$
	LD_2	4%	2.5%	$<0.1\%$	8%	$\sim 10\%$

Table 6.13: Overview of the reaction, energy, and angle independent systematic uncertainties for the A2 and CBELSA/TAPS (CBT) experiments involving liquid hydrogen and deuterium targets.

The total systematic error, which will be shown together with the results in chapter 7, corresponds to the energy and angular dependent error (Equation (6.72)) only. The result as a function of the incident photon energy E_γ for the analysis of A2 data is shown in Figure 6.141, and for the analysis of CBELSA/TAPS data in Figure 6.142. The angular dependence of the total systematic error is shown for single π^0 photoproduction in Figure 6.143, for double π^0 photoproduction from the A2 data in Figure 6.144, and for CBELSA/TAPS data in Figure 6.145.

The domination of the systematic error by the Crystal Ball energy sum threshold at low photon energies is clearly visible for the A2 data (Figures 6.141, 6.143 and 6.144), where especially at the forward and backward meson polar angles in the center of mass system, the systematic error reaches very high values. At these angles, the overall very high systematic error is accompanied by the systematic error from the detection efficiency, which drastically decreases at these angles, as the cross sections are very small. Furthermore, these meson center of mass polar angles correspond to nucleons going to TAPS where the detection is very sensitive to detector thresholds or to nucleons going to very backward angles where they escape the detection by the Crystal Ball detector. For higher photon energies, only the systematic error at forward angles remains high, which results from the trigger settings. As discussed in Section 2.3.2, the TAPS detector was not allowed to fulfill the multiplicity condition alone. Therefore events at very forward meson angles, where the two photons are going to TAPS, are not recorded.
In all other angular bins, the total relative systematic uncertainty for low energies is below 30 % at higher energies around 5 %.

The situation for double π^0 photoproduction is very similar to that observed for single π^0 photoproduction, but the size of the errors are much smaller due to the on average lower energies of the recoil nucleons. Except for the very forward and backward angular bin and for low energies, the systematic error for low energies is below 20 % at higher energies around 5 %.
From the systematic error at CBELSA/TAPS, it is directly visible that no energy sum condition could be applied to the Crystal Barrel detector. As a consequence, the systematic error at low energies is not that sensitive to the energy of the detected photons. Hence, the systematic error as a function of E_γ is only slightly dependent

on the incident photon energy. However, at low energies it is dominated by the low statistics, as the experimental conditions were optimized for η photoproduction. In general, the angular dependence of the systematic error is rather small, especially at higher energies. This is mostly due to the efficient charged particle identification with the Inner detector over most of the angular range.

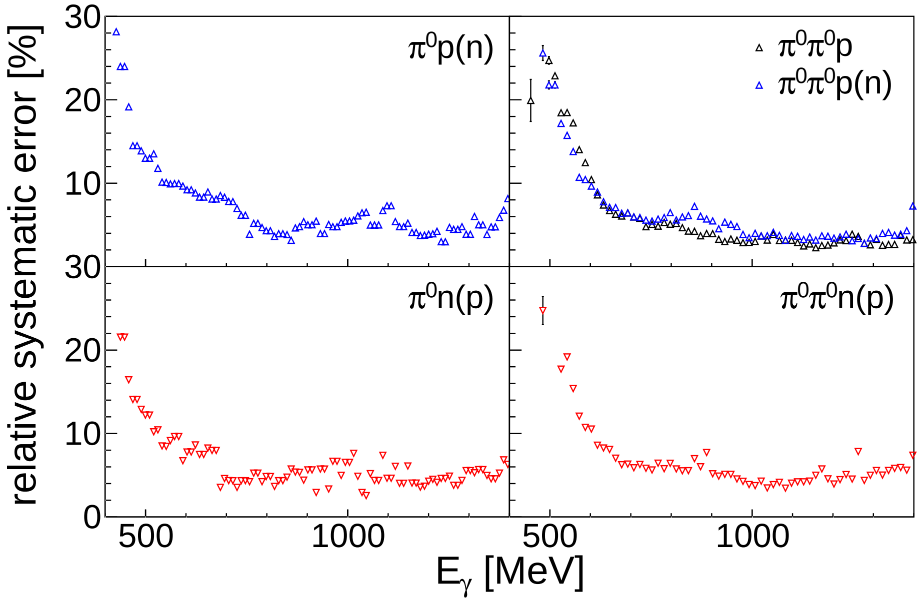

Figure 6.141: Relative systematic uncertainties as a function of E_γ for the analysis of the A2 data. Left column: single π^0. Right column: double π^0. Upper row: free (black) and quasi-free proton (blue). Lower row: quasi-free neutron (red).

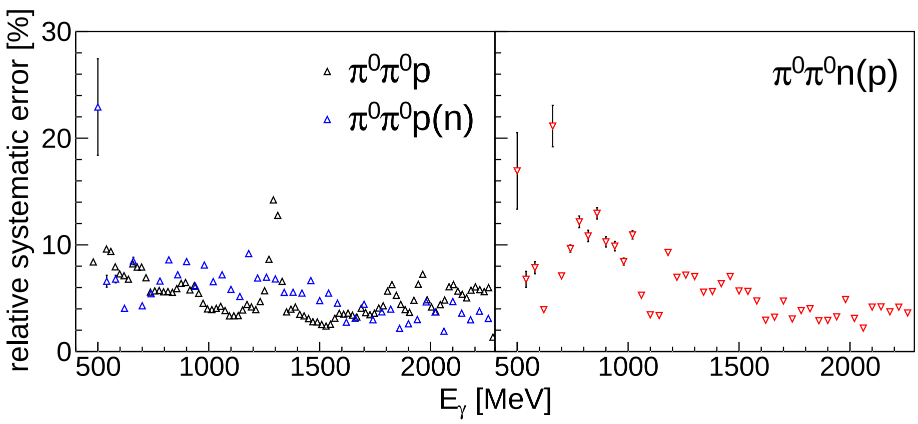

Figure 6.142: Relative systematic uncertainties as a function of E_γ for the analysis of double π^0 photoproduction of the CBELSA/TAPS data. Left column: free (black) and quasi-free proton (blue). Right column: quasi-free neutron (red).

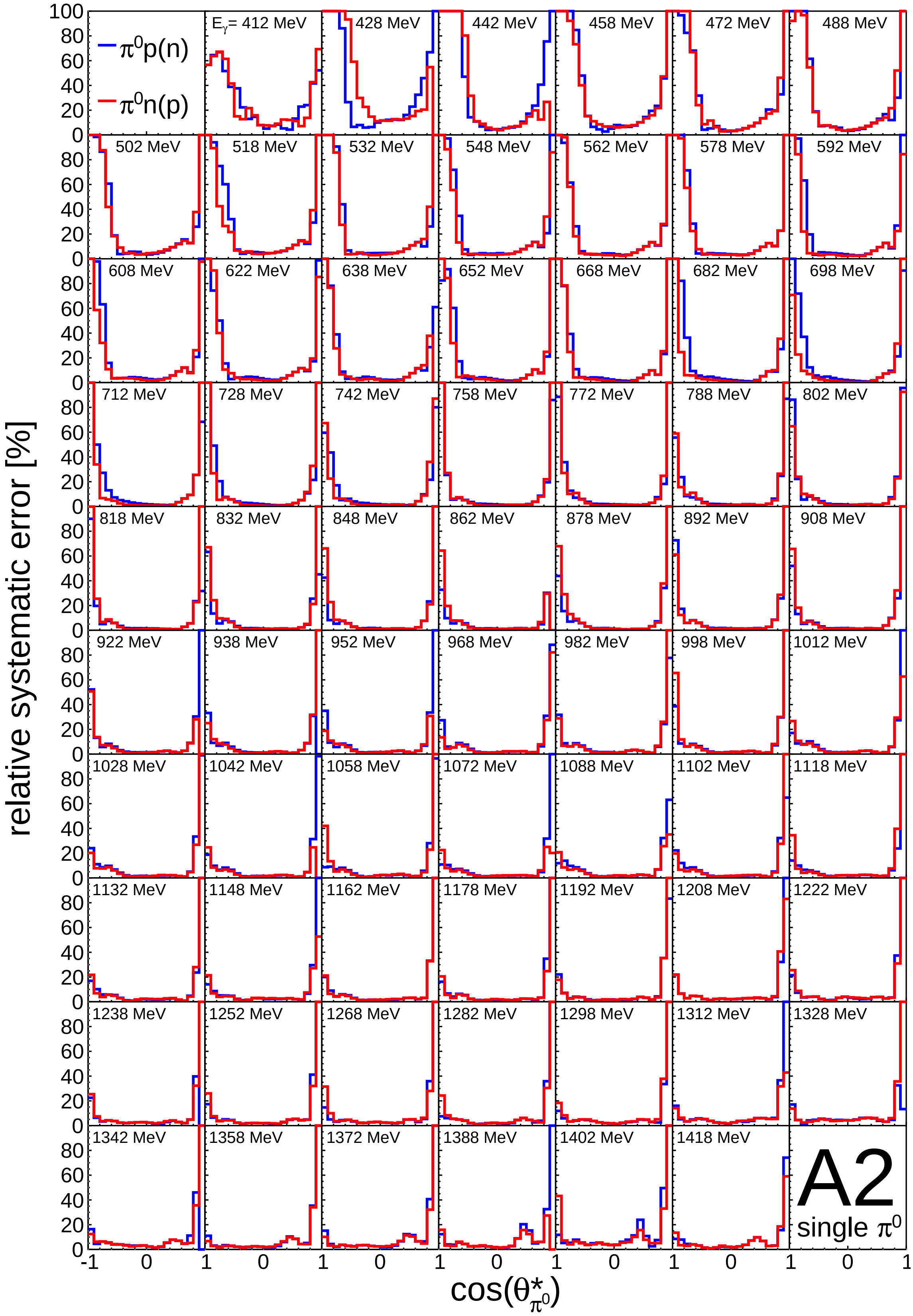

Figure 6.143: Relative systematic uncertainties for the analysis of single π^0 photoproduction from the deuterium beamtimes at A2. Blue histogram: quasi-free proton. Red histogram: quasi-free neutron.

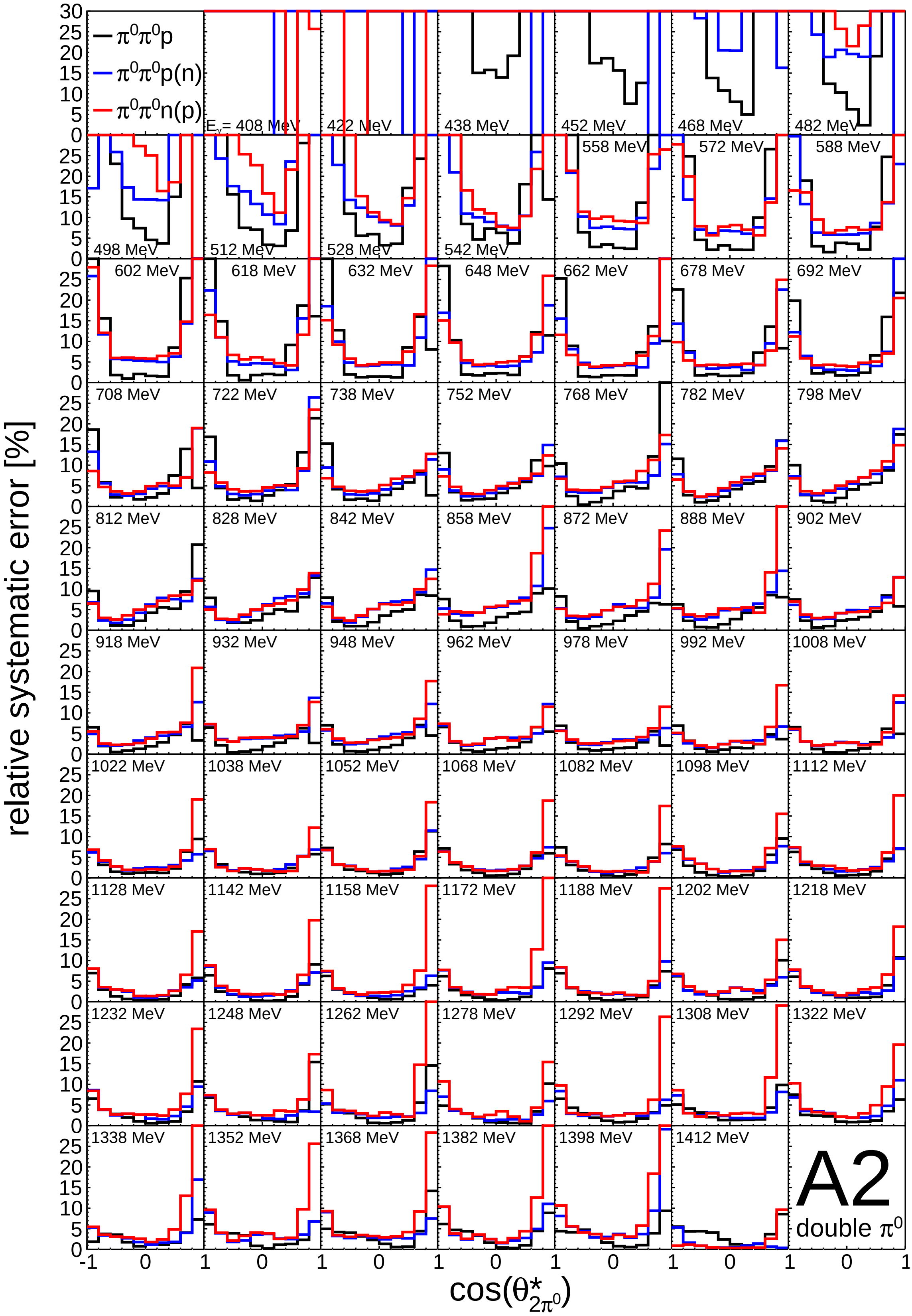

Figure 6.144: Relative systematic uncertainties for the analysis of double π^0 photoproduction from the hydrogen and deuterium beamtimes at A2. Black histogram: free proton. Blue histogram: quasi-free proton. Red histogram: quasi-free neutron.

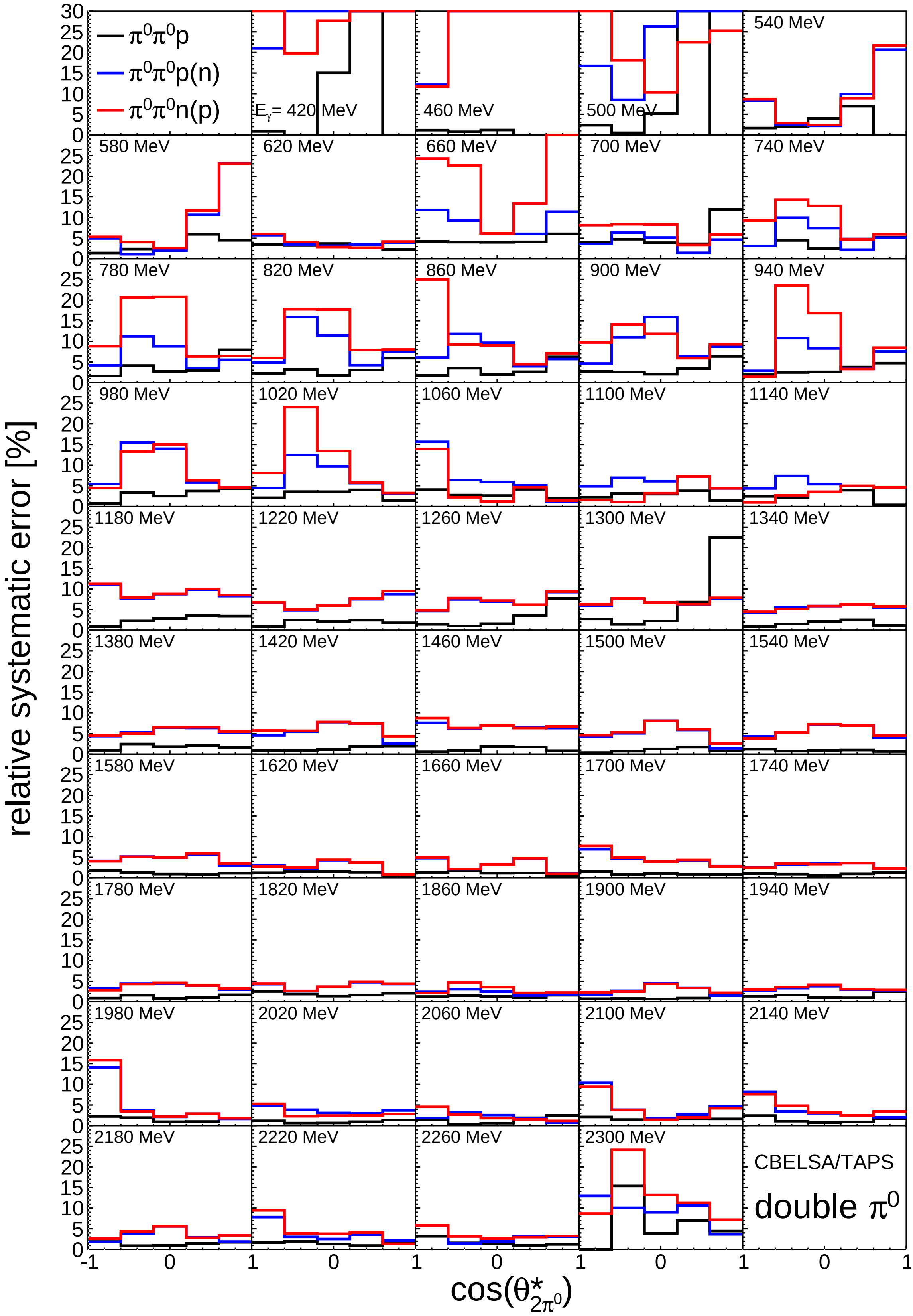

Figure 6.145: Relative systematic uncertainties for the analysis of double π^0 photoproduction from the hydrogen and deuterium beamtimes at CBELSA/TAPS. Black histogram: free proton. Blue histogram: quasi-free proton. Red histogram: quasi-free neutron.

6.16 Systematic Uncertainties of Polarized Results

The systematic errors of the double polarization observable E and the helicity dependent cross sections $\sigma_{1/2}$ and $\sigma_{3/2}$ are composed of the same sources as discussed for the unpolarized results (see Section 6.15). Additional uncertainties arise from the subtraction of the carbon background and the measurement and determination of the beam and target polarization. However, most of the polarization unrelated systematic uncertainties are automatically eliminated in the determination of E, as they are present in the numerator as well as the denominator. Effects from the detection of the recoil nucleon might be different for the helicity dependent yields and may also affect the uncertainty of the result, but were observed to be negligible. As the polarization observables were determined with different versions involving either carbon subtraction or unpolarized cross sections and also different extraction steps, a comparison of the results obtained from the individual methods is well suited for the investigation of the systematic uncertainty.
For this purpose, the systematic uncertainty of the double polarization observable ΔE_{sys} was determined from the maximal deviation between the three methods:

$$\Delta E_{\text{sys}} = \frac{1}{2}\max\left(\{\Delta E_{1,2}, \Delta E_{1,3}, \Delta E_{2,3}\}\right) \ , \tag{6.73}$$

where $\Delta E_{i,j} = E_i - E_j$ is the difference between the result for E from method i and j and $i \neq j$. The systematic uncertainty of the helicity dependent cross sections $\Delta\sigma_{1/2,3/2,\text{sys}}$ was also determined from the maximum difference between the individual methods, neglecting the systematic error of the unpolarized cross section $\Delta\sigma_{\text{sys}}$:

$$\begin{aligned}
\Delta\sigma_{1/2,\text{sys}} &= \frac{1}{2}\max\left(\left\{\Delta\sigma^{1,2}_{1/2}, \Delta\sigma^{1,3}_{1/2}, \Delta\sigma^{1,4}_{1/2}, \Delta\sigma^{2,3}_{1/2}, \Delta\sigma^{2,4}_{1/2}, \Delta\sigma^{3,4}_{1/2}\right\}\right) \\
\Delta\sigma_{3/2,\text{sys}} &= \frac{1}{2}\max\left(\left\{\Delta\sigma^{1,2}_{3/2}, \Delta\sigma^{1,3}_{3/2}, \Delta\sigma^{1,4}_{3/2}, \Delta\sigma^{2,3}_{3/2}, \Delta\sigma^{2,4}_{3/2}, \Delta\sigma^{3,4}_{3/2}\right\}\right) \ ,
\end{aligned} \tag{6.74}$$

where $\Delta\sigma^{i,j}_{1/2,3/2} = \Delta\sigma^{i}_{1/2,3/2} - \Delta\sigma^{j}_{1/2,3/2}$ is the difference between the results for $\sigma_{1/2,3/2}$ from method i and j and $i \neq j$.
This reliably allows for the determination of the systematic error of the carbon subtraction method, photon flux determination, analysis cuts, and the detection efficiency of the recoil nucleons. In addition, the influences of the systematic uncertainty of the beam and target polarization on the results were considered.

6.16.1 Systematic Uncertainty of the Photon Beam Polarization

The systematic uncertainty of the degree of photon beam polarization $\Delta P^{\text{sys}}_{\gamma}$ results, according to Equation (2.5), directly from the systematic error of the electron beam polarization.
At A2, the electron beam polarization results from the Mott measurements, which have an overall systematic uncertainty of 2.7 % [109, 134, 215]. This uncertainty is

composed of the uncertainty of the electron spin angle (1.1 %) due to the bending of the beam before its extraction into the A2 hall, the admixture of a transversal polarisation component (2.2 %), the finite thickness of the Mott radiator (1.0 %), and a statistical error (0.2 %).
At CBELSA/TAPS, the systematic error of the electron beam polarization arises from the Møller measurement, which has an overall uncertainty of 2.89 % [138]. It consists of the uncertainty from the polarization of the Møller foil, the error of the asymmetry coefficient, as well as of the count rate asymmetry (most likely 0.99 %, maximally 2.89 %).

6.16.2 Systematic Uncertainty of the Target Polarization

At A2, due to the observed problem with the target polarization (see Section 6.11.3), the systematic error of the target polarization ΔP_T^{sys} was estimated retrospectively. The final degree of target polarization, applied in the analysis, was determined from a renormalization of the double polarization observable E for η photoproduction in the region of the $N(1535)1/2^-$ [173] (see Section 6.11.3). The systematic error was determined by the difference between the minimum and maximum scale factor from. A maximum value of $\pm$ 10 % was found.
The systematic error of the degree of target polarization at CBELSA/TAPS was predominantly given by the determination of the parameters from the fit of the deuteron signals and was estimated to be on the order of 5 % [216].

6.16.3 Total Systematic Uncertainty of the Polarized Results

The total systematic uncertainty of the degree of polarization ΔP_{sys}, which results from the individual systematic error of the photon beam $\Delta P_\gamma^{\text{sys}}$ (Section 6.16.1) and the target polarization ΔP_T^{sys} (section (6.16.2)) is given by

$$\Delta P_{\text{sys}} = \sqrt{(\Delta P_\gamma^{\text{sys}})^2 + (\Delta P_T^{\text{sys}})^2} = \begin{cases} 11\% & \text{A2} \\ 6\% & \text{CBELSA/TAPS}\ . \end{cases} \tag{6.75}$$

In order to account for the systematic uncertainty of the degree of polarization to the total systematic error of the results, it was added in quadrature to the individual errors (Equations (6.73), and (6.74)), according to:

$$\begin{aligned} \Delta E_{\text{sys}}^{\text{tot}} &= \sqrt{\Delta E_{\text{sys}}^2 + \Delta P_{\text{sys}}^2} \\ \Delta \sigma_{1/2,\text{sys}}^{\text{tot}} &= \sqrt{\Delta \sigma_{1/2,\text{sys}}^2 + \Delta P_{\text{sys}}^2} \\ \Delta \sigma_{3/2,\text{sys}}^{\text{tot}} &= \sqrt{\Delta \sigma_{3/2,\text{sys}}^2 + \Delta P_{\text{sys}}^2}\ . \end{aligned} \tag{6.76}$$

6.17 Merging of Datasets

As the present work involves analyses of several beamtimes, the final results are the statistical averages of the corresponding results of the individual analyses. The statistical average was determined by the weighted arithmetic mean by means of cross sections. Whereas for the unpolarized results the individual cross sections were averaged, for the polarized results, the different ingredients used for the extraction of the double polarization observable E, i.e. σ_{diff} (Equation (6.54)), σ_{sum} (Equation (6.55)), $\sigma_{1/2}^{\text{direct}}$ (Equation (6.60)), and $\sigma_{3/2}^{\text{direct}}$ (Equation (6.61)), were taken. According to the weighted arithmetic mean, the statistical average of n results $\langle\sigma\rangle$ and their statistical error $\langle\Delta\sigma\rangle$ is then given by:

$$\langle\sigma\rangle = \frac{\sum_{i=1}^{n} \frac{\sigma_i}{\Delta\sigma_i^2}}{\sum_{i=1}^{n} \frac{1}{\Delta\sigma_i^2}} \qquad \langle\Delta\sigma\rangle = \frac{1}{\sum_{i=1}^{n} \sqrt{\frac{1}{\Delta\sigma_i^2}}} \ , \tag{6.77}$$

where $\sigma_i, \Delta\sigma_i$ denotes the individual cross section and statistical error of the result i.

7 Results and Discussion

This chapter presents the final results for single and double π^0 photoproduction from free and quasi-free nucleons obtained from the analyses of unpolarized and polarized data from the A2 and CBELSA/TAPS experiments.
The results were extracted as a function of the incident photon energy E_γ, as well as the final-state invariant mass $W = \sqrt{s}$. In the latter, effects from Fermi motion are absent due to the reconstruction out of the final state particles (see Section 6.7). This allows for a better comparison with results obtained from other experiments, especially if different types of targets (involving different nuclear effects) were used. However, the final state reconstruction requires the detection of the recoil nucleon, which is only present in the exclusive analyses. As discussed in Section 6.8.3, a reliable detection of the recoil nucleon strongly depends on the experimental settings and their precise modeling within the simulation. Comparisons of the (quasi-free) inclusive and exclusive analyses serve as a solid check of the quality of the coincident detection of the recoil nucleon. For this reason, the results of the differential and total cross sections were also extracted as a function of the incident photon energy E_γ.
In addition, the results for single and double π^0 photoproduction from the free neutron were estimated by applying a correction factor to the quasi-free neutron data. The correction factor was determined from a comparison of the free to quasi-free proton data, as discussed in Section 6.12 and is based on the assumption that the nuclear effects of the reactions involving quasi-free protons and neutrons are identical.

Unpolarized differential and total cross sections of single π^0 photoproduction from quasi-free protons and neutrons from the analysis of liquid deuterium data from A2 will be shown in Section 7.1. The unpolarized differential and total cross sections for double π^0 photoproduction from free protons will be discussed in Section 7.2 and those from quasi-free nucleons in Section 7.3. Whereas in the former, the results from the A2 data will be directly compared to those from the CBELSA/TAPS, the latter first presents the results from the analysis of A2 and CBELSA/TAPS data individually. Afterwards both results will be compared and discussed.

The results for the double polarization observable E and the helicity dependent cross sections $\sigma_{1/2}$ and $\sigma_{3/2}$ will be summarized for single π^0 photoproduction (A2 data) in Section 7.4, for double π^0 photoproduction from A2 and CBELSA/TAPS data in Section 7.5.1 and 7.5.2, respectively. The comparison of the polarized results from the A2 data with those from the CBELSA/TAPS data will be presented in Section 7.5.3.

7.1 Cross Sections for π^0 Photoproduction

Differential and total cross sections have been measured with high statistics in the second and third resonance region of the nucleon excitation spectrum for incident photon energies from ~ 450 MeV to ~ 1400 MeV. Due to the trigger settings (see Table 2.6) only two (December 2007 and May 2009) of three A2 beamtimes could be analyzed. For the same reason, the liquid deuterium beamtime from CBELSA/TAPS was not suited for the analysis of single π^0 photoproduction from quasi-free nucleons. The quasi-free inclusive reaction ($\gamma N \to \pi^0(N)$) as well as both quasi-free exclusive reactions ($\gamma p(n) \to \pi^0 p(n)$ and $\gamma n(p) \to \pi^0 n(p)$) were analyzed. Results as a function of the incident photon energy E_γ were primarily used for the investigation of the quality of the recoil nucleon detection efficiency by the comparison of the results from the quasi-free inclusive and the two quasi-free exclusive analyses. A selection of these results is presented in Section 7.1.1, the remaining results are shown in the Appendix, Section D.1.1. The main focus is on the results as a function of the final state invariant mass W that are presented and discussed in Section 7.1.2. This includes a full set of results from quasi-free nucleons, as well as the estimation of the corresponding results from the free neutron.

7.1.1 Results as a Function of the Incident Photon Energy E_γ

The total cross sections as a function of the incident photon energy E_γ for the exclusive analysis of photoproduction from quasi-free protons and neutrons are shown in Figure 7.1b. Differential cross sections for the reaction on the proton and the neutron can be found in the Appendix, in Figures D.1 - D.3. They were fit with Legendre coefficients according to Equation (6.45) in the angular range $-1 < \cos(\theta^*_{\pi^0}) < 0.9$. Due to the lack of statistics, the last bin was excluded from the fit. Total cross sections were then extracted using Equation (6.46) and the resulting Legendre coefficient ratios B_i/B_0 are shown in Figures D.4.
The cross sections on the proton (open blue circles) and the neutron (open red triangles) are of comparable size at the low incident photon energies, where they are dominated by contributions from the first resonance region, i.e. the $\Delta(1232)3/2^+$ resonance. With increasing photon energy, both cross sections in general decrease, but reveal the typical double-hump structure, corresponding to the second and third resonance region. Thereby the third resonance region is clearly visible in the proton cross section, but barely in the neutron cross section. In the second and third res-

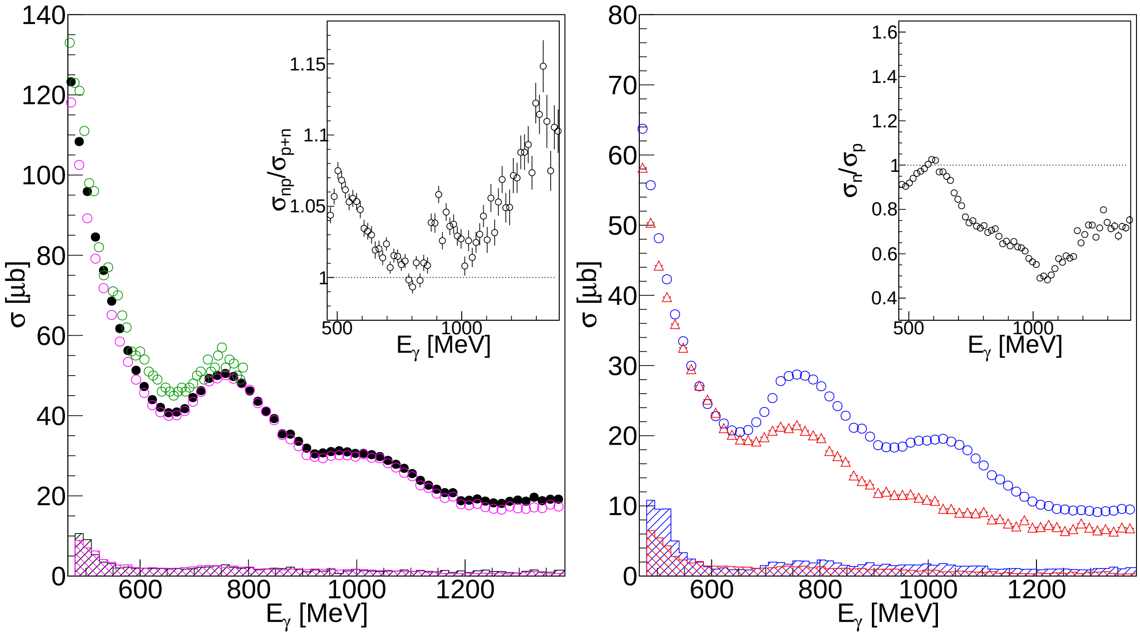

(a) $\gamma N \to \pi^0(N)$ **(b)** $\gamma N \to \pi^0 N$

Figure 7.1: Total cross sections for single π^0 photoproduction as a function of the incident photon energy E_γ. Results from the A2 data. Left-hand side: solid black circles: quasi-free inclusive reaction from the deuteron. Open magenta circles: sum of exclusive results from proton and neutron. Open green circles: $(\gamma d \to \pi^0 np) + (\gamma d \to \pi^0 d)$ (MAMI-B) [69]. Insert: ratio of quasi-free inclusive to sum of the exclusive cross sections. Right-hand side: open blue circles: exclusive reaction on the proton. Open red triangles: exclusive reaction on the neutron. Insert: ratio of neutron to proton cross sections. The hatched histograms at the bottom indicate the systematic uncertainties of the corresponding cross sections.

onance region, the proton cross section is up to 50% larger than the neutron cross section. This is shown in the insert, which shows the ratio of the two cross sections. However, at higher energies, the difference diminishes again, which points out significant differences in the involved processes for photoproduction of π^0 mesons from protons and neutrons in the second and third resonance region. The statistical errors are represented by the error bars, but due to the large statistics available, are barely visible. The systematic uncertainties are shown by the hatched histograms at the bottom of the figure. As already seen in Figures 6.141 and 6.143 the relative systematic uncertainty are of similar size for both results. The rather large systematic error at low incident photon energies results from the influence of the Crystal Ball energy sum threshold (see Section 6.15.3).

The quasi-free inclusive cross section is shown in Figure 7.1a (solid black circles) and is compared to published data from MAMI-B [69] (open green circles) and to

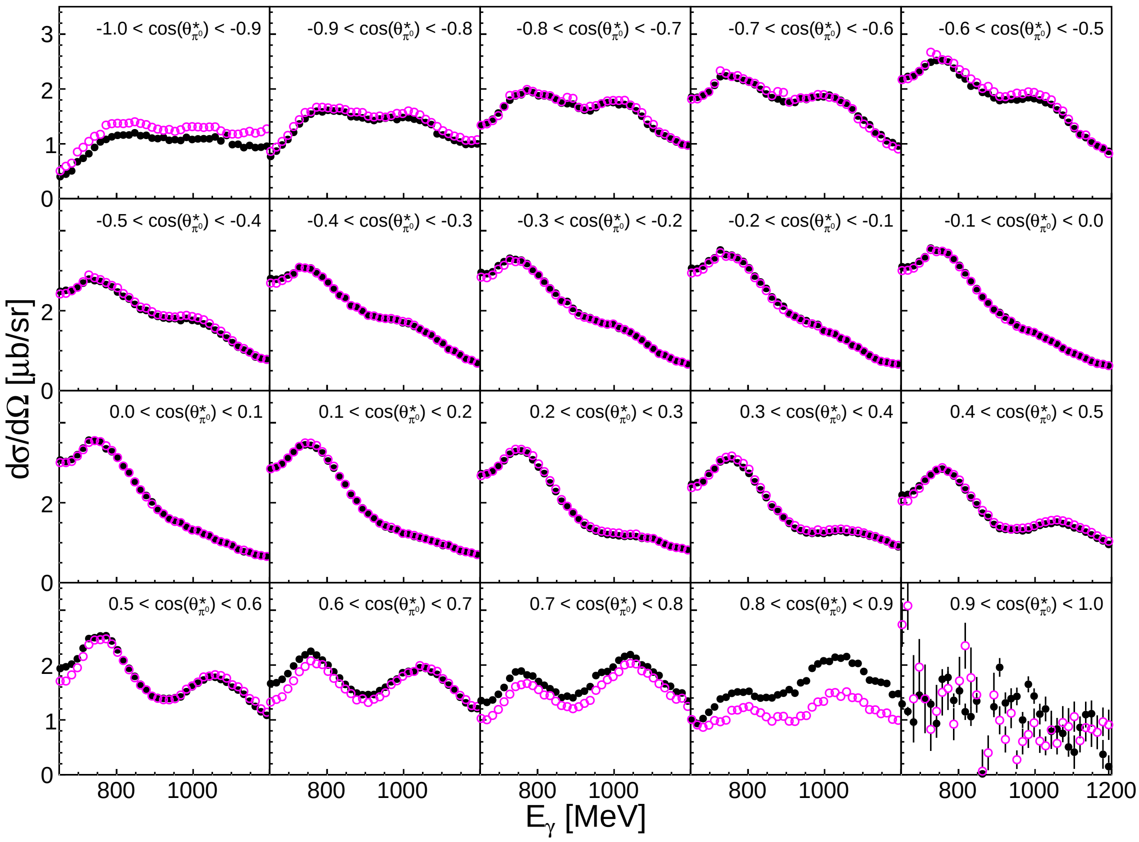

Figure 7.2: Differential cross sections for quasi-free inclusive π^0 photoproduction from the deuteron as a function of the incident photon beam energy E_γ. Results from the A2 data. Solid black circles: quasi-free inclusive reaction from the deuteron. Open magenta circles: sum of exclusive results from proton and neutron.

the sum of the exclusive proton and neutron cross section (open magenta circles). The insert shows the ratio of the quasi-free inclusive to the sum of the exclusive cross sections. Differential cross sections as a function of the incident photon energy are shown in Figure 7.2 and as a function of the meson polar angle in the $\pi^0 N$ center of mass frame in Figure 7.4.

Since the quasi-free inclusive analysis does not require the coincident detection of the recoil nucleon, the reconstruction of the final state invariant mass was not possible. Therefore, a comparison of the cross sections was only possible as a function of the incident photon energy. Contributions from coherent photoproduction of π^0 from the deuteron are negligible at these energies [69, 213, 217] and the quasi-free inclusive cross section should be reproduced by the sum of the exclusive cross section of the proton and neutron, i.e. $\sigma_{\text{incl}} \approx \sigma_{\text{p}} + \sigma_{\text{n}}$. Deviations are on average on the order of 5% and overall below 10%. As visible in the differential cross sections (Figures 7.2 and 7.4), the deviations are mainly present at the very forward and backward angles. For all other polar angles, the agreement for all energies is very good. At low energies, the deviations most likely stem from remaining coherent contributions.

Whereas the coherent cross section strongly peaks at forward angles, the incoherent cross section is much more in the backward direction. As no conditions on the recoil nucleon could be applied to the event selection in the quasi-free inclusive analysis, the discrepancies at low energies can partly be explained by a slight contamination of the quasi-free inclusive cross section with deuterons from the coherent process. In addition, the detection of the recoil nucleons at low energies is very sensitive for the detector thresholds, which is difficult to incorporate appropriately in the simulation. At higher energies the exclusive analyses are complicated by the reconstruction of the kinetic energy of the recoil nucleons or by punch through of protons. Overall, the agreement is very good, which indicates that the detection of the recoil nucleons is well understood.

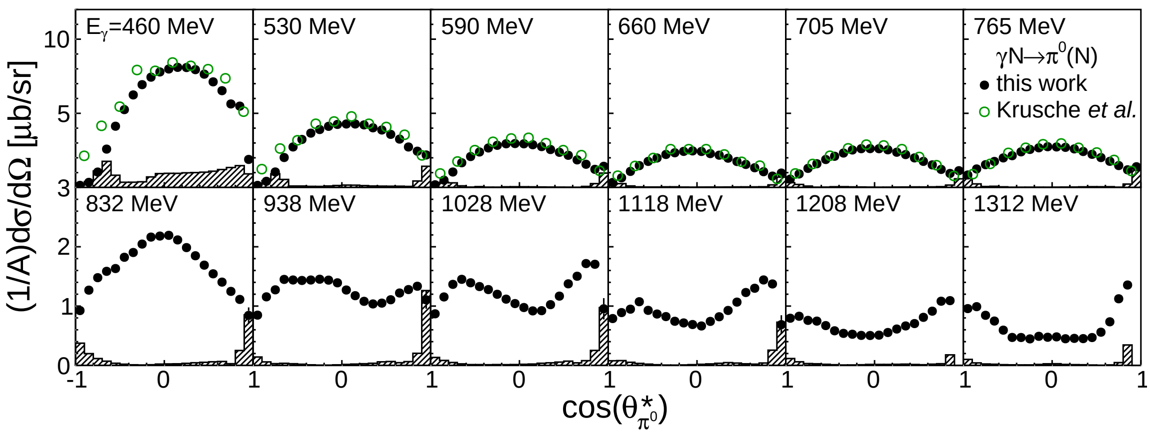

Figure 7.3: Differential cross sections for quasi-free inclusive π^0 photoproduction from the deuteron as a function of the incident photon energy E_γ. Results from the A2 data. Solid black circles: this work. Open green circles: MAMI-B [69]. Data from MAMI-B are only available for energies below 800 MeV. The hatched histograms at the bottom represent the systematic uncertainties of the quasi-free inclusive result from this work.

Within the systematic uncertainties, an overall good agreement between the present and the MAMI-B results is visible, especially at higher photon energies where contributions from the coherent cross section are absent and the systematic uncertainties are smaller. This is also confirmed by the comparison of the differential cross sections (Figure 7.3), which show an increasing agreement with the photon energy for all meson center of mass polar angles.

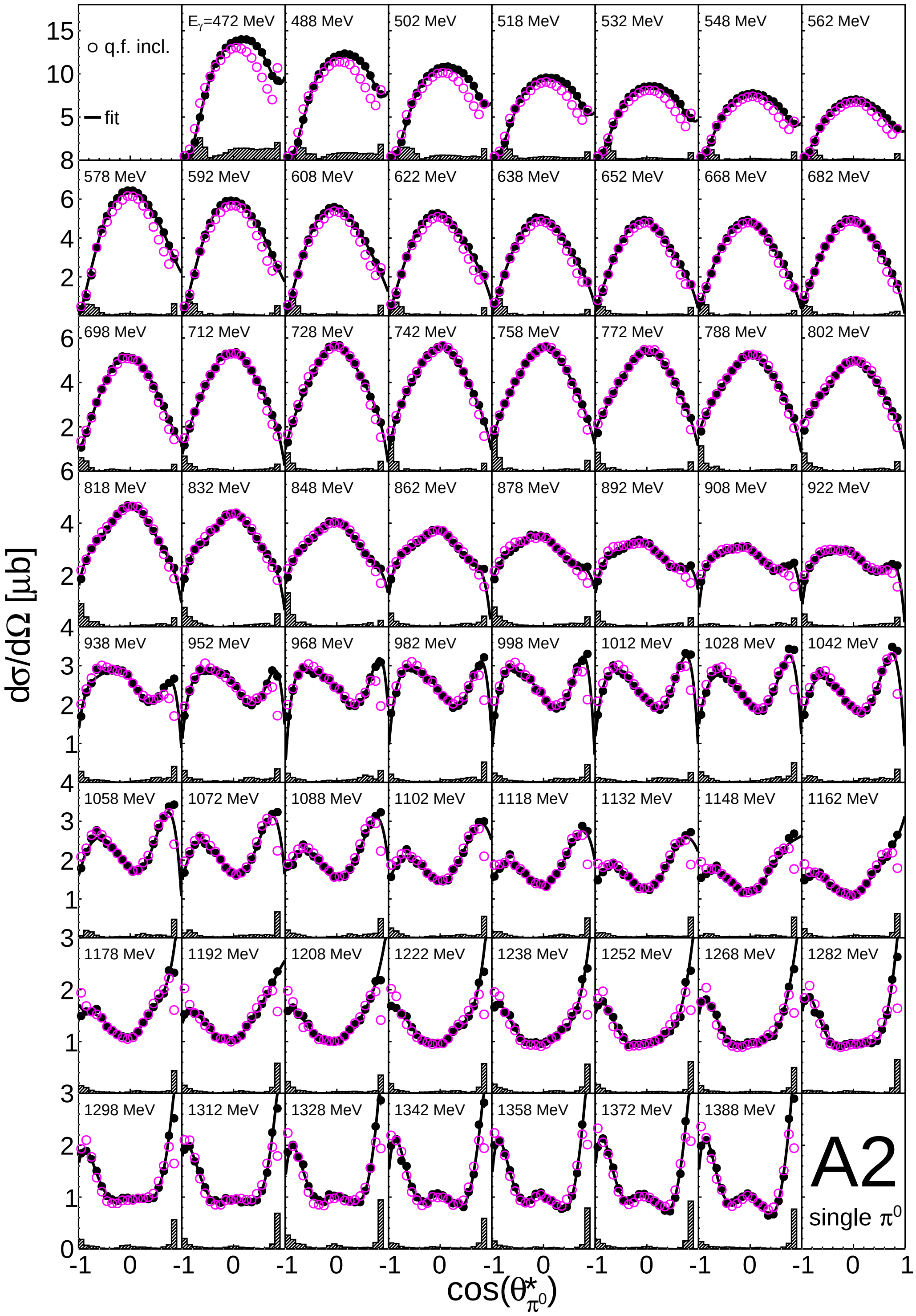

Figure 7.4: Differential cross sections for quasi-free inclusive π^0 photoproduction from the deuteron as a function of the polar angle of the pion in the $\pi^0 N$ center of mass system. Results from the A2 data. Solid black circles: quasi-free inclusive reaction from the deuteron. Open magenta circles: sum of exclusive results from proton and neutron. The hatched histograms at the bottom represent the systematic uncertainties of the quasi-free inclusive result.

7.1.2 Results as a Function of the Center of Mass Energy W

For the exclusive reaction channels (which require the detection of all final state particles except the spectator nucleon), the center of mass energy $W = \sqrt{s}$ was reconstructed from kinematics of the final state particles, according to Equation (6.14), discussed in Section 6.7. The total cross sections were obtained by fitting the differential cross sections with a series of Legendre coefficients (Equation (6.45)) of sixth order (see Figures D.5 and D.6 in the Appendix for the results of the fit). Due to the lack of statistics (see Figure 7.6) the most forward angular bin, i.e. $0.9 < \cos(\theta^*_{\pi^0}) < 1.0$, was excluded from the fit.

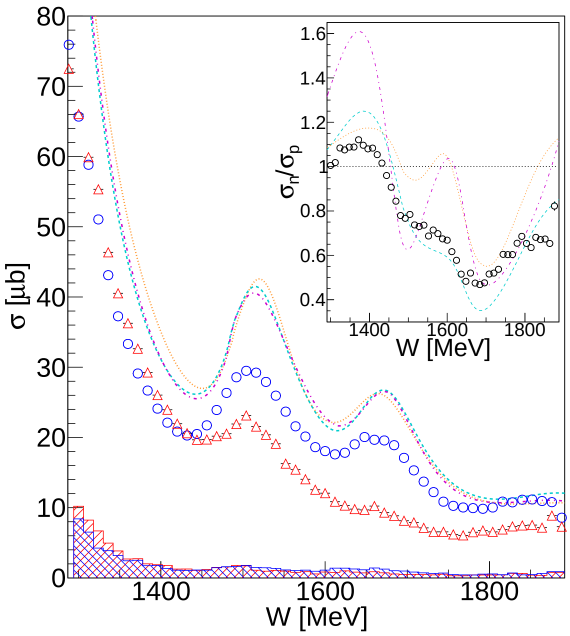

(a) $\gamma N(N) \to \pi^0 N(N)$

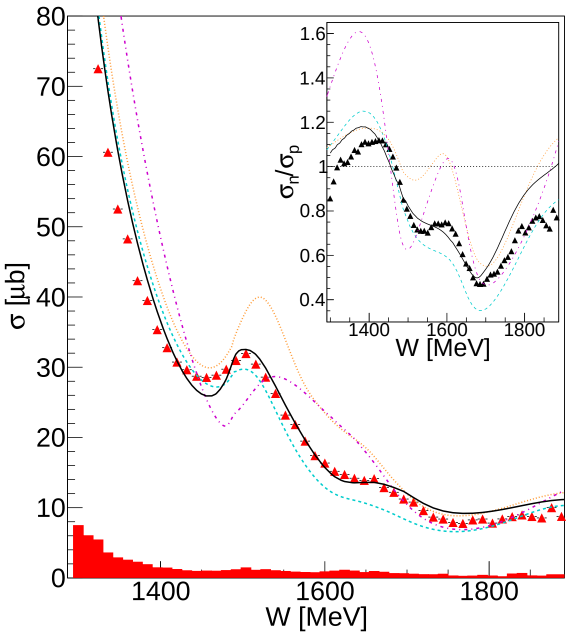

(b) $\gamma n \to \pi^0 n$

Figure 7.5: Total cross sections for single π^0 photoproduction from quasi-free nucleons as a function of the final-state invariant mass $W = \sqrt{s}$. Results from the A2 data. Left-hand side: open blue circles: exclusive reaction on the quasi-free proton. Open red triangles: exclusive reaction on the quasi-free neutron. Insert: ratio of quasi-free neutron to proton cross sections. Right-hand side: solid red triangles: estimated free neutron cross section. Insert: ratio of free neutron to proton cross sections. Model curves: left-hand side: $\gamma p \to \pi^0 p$. Right-hand side: $\gamma n \to \pi^0 n$. Dotted orange line: MAID [40]. Dashed cyan line: SAID [39]. Dashed-dotted magenta line: BnGa-2014-02 (proton, [43]), BnGa-2011-02 (neutron, [38]). Solid black line: BnGa-refit including the present free neutron data [218]. The histograms at the bottom represent the systematic uncertainties of the corresponding cross sections.

The resulting total cross sections for single π^0 photoproduction from quasi-free protons and neutrons are shown in Figure 7.5a. They are compared to model predic-

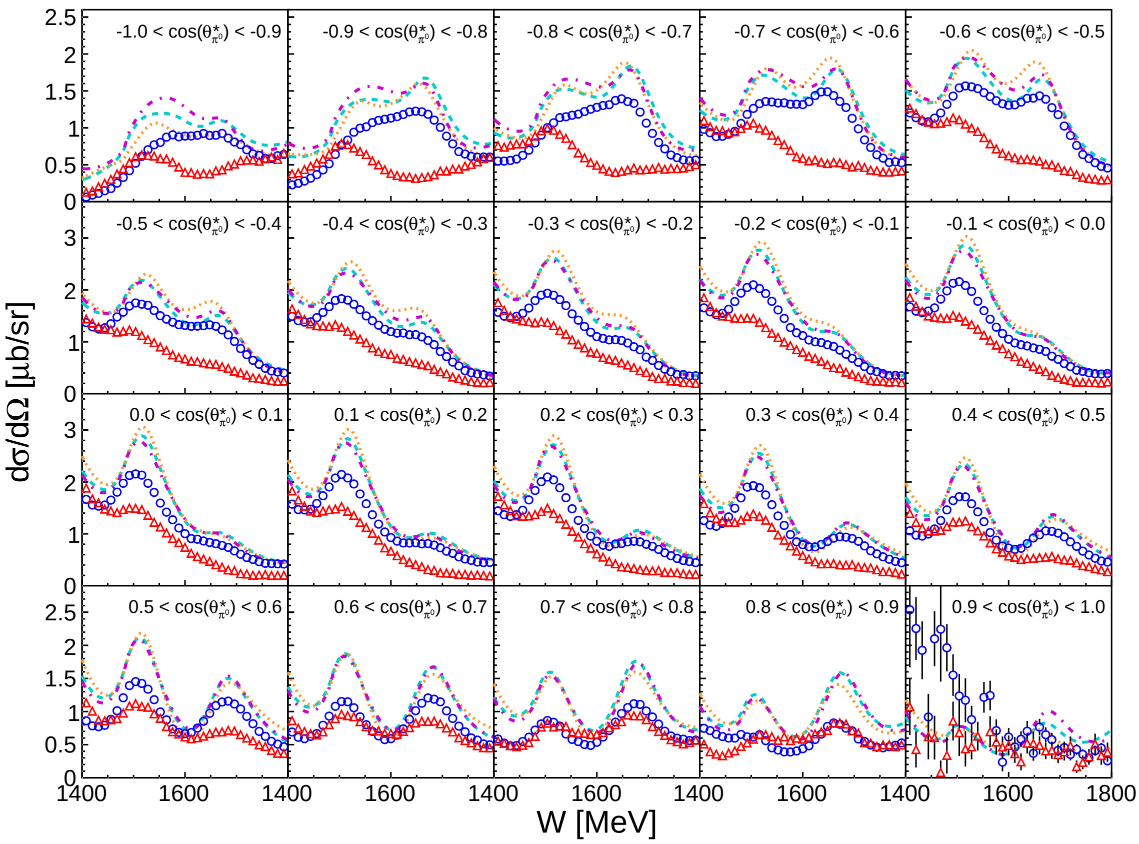

Figure 7.6: Differential cross sections for exclusive π^0 photoproduction from quasi-free nucleons as a function of the final state invariant mass W. Results from the A2 data. Notations as in Figure 7.5.

tions for free nucleons from the SAID partial wave analysis [39], the MAID unitary isobar model [40], and the Bonn-Gatchina (BnGa) coupled channel partial wave analysis [38, 43] (the model results for the reaction on the neutron are shown in Figure 7.5b). The insert illustrates the ratio of the neutron to proton cross section from data and model descriptions.

By comparing the total cross sections as a function of the incident photon energy E_γ (Figure 7.1b) with those as a function of the center of mass energy W (Figure 7.5a), the effect of the final state reconstruction is clearly visible. Due to the absence of Fermi motion in the latter, the bump structures are less smeared out and are more pronounced. However, the final state reconstruction depends on the experimental resolution, which, though energy dependent, is on the order of 30 MeV [100] and hence is only slightly lower than the most probable Fermi momentum of $\sim$40 MeV (see Figure 3.9). Thus, due to the absence of narrow structures, a significant effect holds off. The comparison of the proton (open blue circles) with the neutron cross section (open red triangles) again reveals that the peaks in the second and third resonance region of the neutron are strongly suppressed. As can be seen in the neutron to proton cross section ratio in the insert of Figure 7.5a, the different models only simultaneously predict such a suppression for the third resonance region at $\sim$ 1680

MeV, where all predict a much larger photon coupling of the N(1680)5/2$^+$ resonance for the proton than for the neutron [202]. In contrast, the predictions for the ratio of the neutron to proton cross section in the second resonance region vary strongly. Whereas the MAID model almost does not predict any suppression of the neutron cross section in this region, a substantial difference can be seen in the description of the SAID and BnGa model, which mainly results from different obtained coupling strengths for the N(1535)1/2$^-$.
In contrast to the different model predictions for the neutron, those for the proton are in very good agreement. This results from the large data base for the reaction on the proton to which the different models were fit. As available neutron data is sparse, the predictions primarily depend on input from other reactions, such as $\gamma n \rightarrow \pi^-\pi^0 p$, and therefore are much more sensitive to the individual description. In addition, the differential cross sections as a function of the center of mass energy (Figure 7.6) reveal, that the suppression of the neutron cross section is strongly dependent on the meson polar angle in the center of mass frame. Whereas the known reduction of the neutron cross section in the third resonance region is already clearly present at very backward angles and in the range of $-1 < \cos(\theta^*_{\pi^0}) < 0.6$, the suppression in the second resonance region is primarily dominant at medium meson polar angles, i.e. $-0.6 < \cos(\theta^*_{\pi^0}) < 0.6$.
Although all predictions for the free proton are very similar, the agreement with the quasi-free proton cross section is poor. This indicates that the reaction on quasi-free nucleons is strongly influenced by nuclear effects such as final state interactions (FSI) that are not included in the models. Such a substantial suppression was already observed in the second resonance peak for the inclusive $\gamma d \rightarrow \pi^0 np$ reaction (open green circles in Figure 7.1a [69]). A 30% smaller cross section was reported with respect to the sum of the model predictions for the free proton and neutron smeared with Fermi motion. Nevertheless, since it was not possible to measure the neutron cross section directly, it was not possible to assign the observation to FSI effects or to a much smaller than predicted neutron cross section. The present data clearly demonstrate that both effects contribute. It is very unlikely that the observed effect is due to any systematic uncertainty of the data or analysis. At first, the quasi-free inclusive cross section is in good agreement with former independent results [69] and similar effects were observed and modeled for the quasi-free $\gamma d \rightarrow pp\pi^-$ reaction [77]. In addition, the results for other reaction channels extracted from the same data exhibit different behavior. Whereas the observed effect in this work is on the order of up to 35% and energy dependent, for double $\pi^0\pi^0$ photoproduction it is energy independent and on the order of 15% [219]. For $\eta\pi^0$ and $\eta\pi^+$ photoproduction differences of 30% and 10% were observed [220], and for η photoproduction, the free and quasi-free cross sections were even in almost perfect agreement [207, 214].

The extraction of the cross section on the free neutron is complicated by the presence of FSI effects. Theoretical models describing the FSI effects for single π^0 photoproduction from the deuteron are under way [82], but not yet available. Therefore, it is only possible to estimate the free neutron cross section with the assumption that the FSI effects are similar for quasi-free π^0 photoproduction from

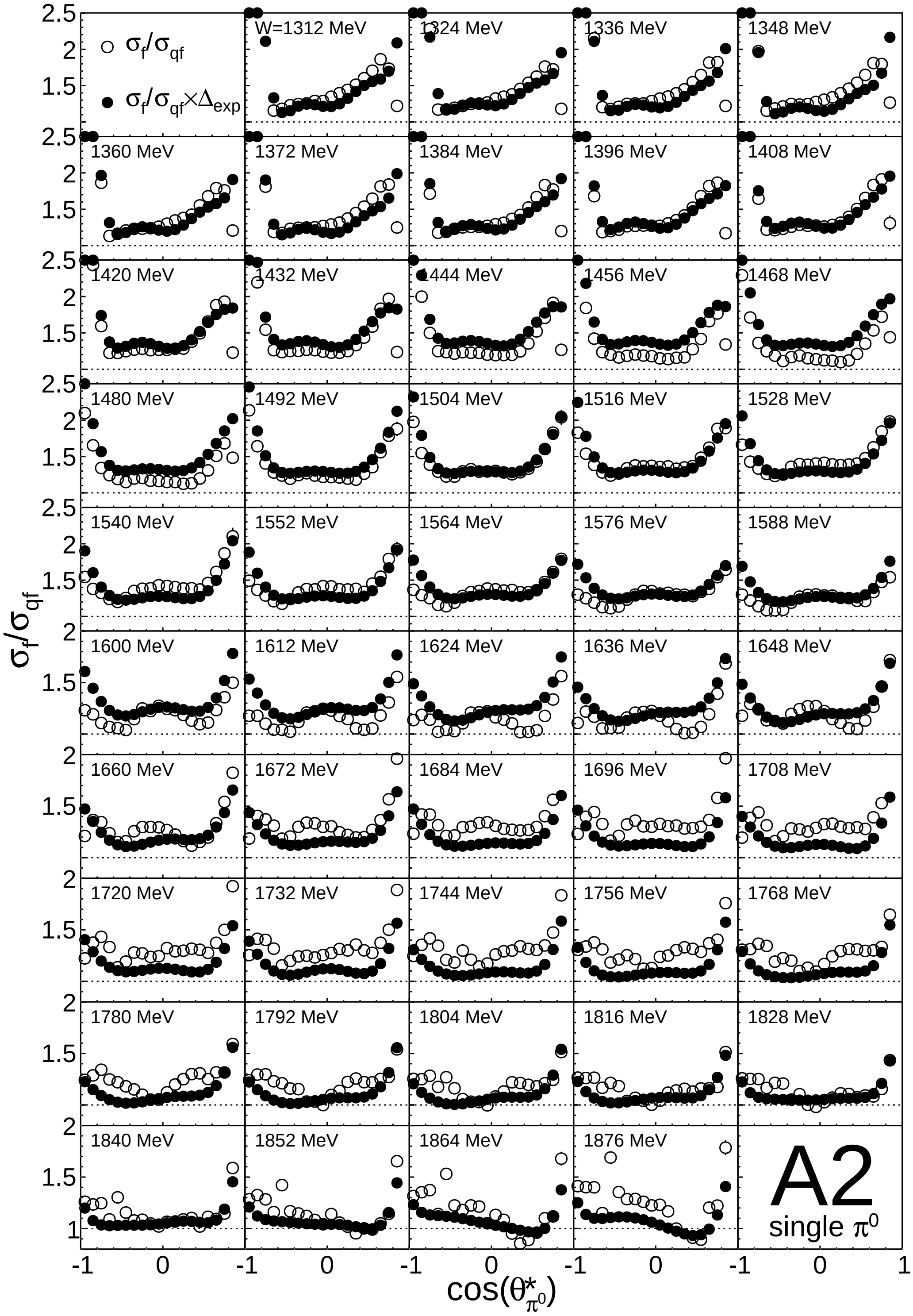

Figure 7.7: Differential ratio of the free $\pi^0 p$ cross section (SAID prediction) to the quasi-free $\pi^0 p(n)$ cross section (this work). Results from the A2 data. Open circles: bare ratio. Solid circles: smoothed ratio, i.e. ratio obtained from the SAID prediction smeared with the experimental resolution and an additional energy dependent smoothing factor (see Section 6.12).

protons and from neutrons. In this case, the FSI effects of the cross section from quasi-free neutrons can be corrected with the ratio of the free to quasi-free proton cross section according to Equation (6.40). Calculations for other reaction channels ($\gamma d \to pp\pi^-$, [77]) indicated that such approximations work reasonably well, except for very forward angles, where, due to the very small relative momenta between the participant and spectator nucleon, different behavior for protons than for neutrons are expected. Nevertheless, since in this work the statistics at such angles are poor, the most forward angular bin was rejected for the extraction of the results and at least partly circumvents this problem.
The difference of the quasi-free to free cross sections is shown by their ratio in Figure 7.7. Thereby the SAID model prediction was taken as the free cross section, which is reasonable, since it represents a fit to the world data of $\gamma p \to \pi^0 p$ and hence represents the free proton cross section reasonably well. The bare ratio, obtained from the SAID prediction and the measured quasi-free differential cross section, is shown as open black circles. However, as discussed in Section 6.12, this comparison is not truly realistic, as, in contrast to the measured quasi-free result, the SAID prediction is free from experimental resolution effects. Therefore, it was artificially folded with the same experimental resolution as present in the quasi-free data and the remaining resolution effects have been removed by applying an energy dependent correction factor (see Figure 6.127). The final correction factor is represented by the solid black circles in Figure 7.7. The effect of the folding procedure with the experimental resolution is clearly visible. Whereas both ratios in general exhibit similar behavior, the bare ratio (open black circles) has distinct wavy structures, especially at higher energies where the experimental resolution is worse. In contrast, the folded ratio is rather smooth and free of such structures. Apart from that, both ratios show a clear enhancement at forward and backward angles. The behavior at meson forward angles in the case of FSI effects is expected and predicted by model calculations [78], since in this case the relative momenta between the spectator and participant nucleon are comparatively small, which makes interactions between the two nucleons much more probable. Nevertheless, as the relative energy increases with the meson angle, an enhancement is also visible at meson backward angles, which is not understood. However, this effect was also observed in the quasi-free inclusive cross section in [69], but since recoil nucleons were not detected, contributions from protons and neutrons could not be separated.

The resulting estimate of the total cross section of single π^0 photoproduction from free neutrons is shown in Figure 7.5b. The insert illustrates the ratio of the estimated free neutron cross section to the SAID model prediction for the free proton. Differential cross sections as a function of the final state invariant mass are shown in Figure 7.8 and as a function of the meson polar angle in the center of mass frame in Figure 7.11. The latter were normalized to the corresponding total cross section in order to allow for a better comparison of the shapes of the different results. Standard differential cross sections are shown in the Appendix, in Figure D.7. In all figures, the results are compared to the available model predictions from MAID [40], SAID [39], and BnGa [38, 43]. As previously mentioned, the three different models are not

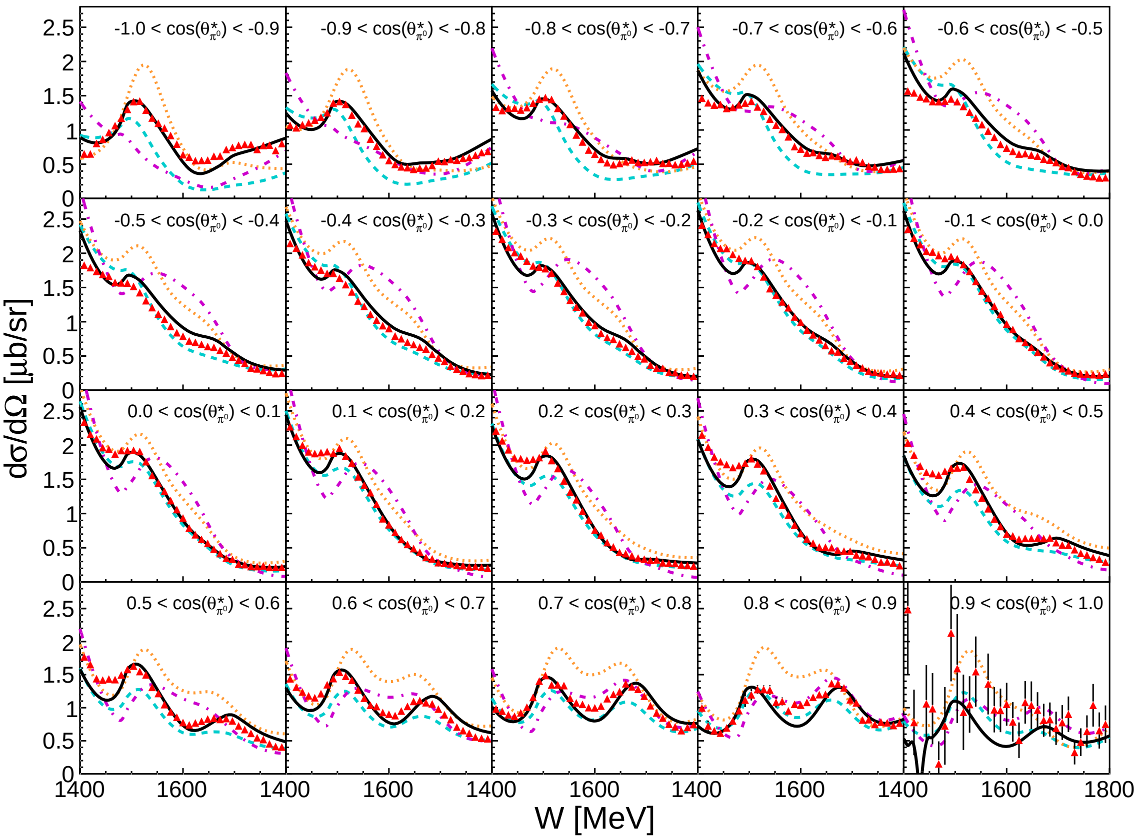

Figure 7.8: Estimated differential cross sections for exclusive π^0 photoproduction from the free neutron as a function of the final state invariant mass W. Results from the A2 data. Notations as in Figure 7.5.

in accordance with each other and none of them describes the estimated free neutron cross section reasonably well. Among the models, the SAID prediction achieves the best agreement with the data. Even though the shape is very similar to the data, it underestimates the free neutron result, especially in the second and third resonance, where mainly at backward and forward meson angles in the center of mass frame the data is higher (see Figure 7.8.

A refit of the BnGa coupled channel partial wave analysis (solid black line), which included the present data is also shown in the figures. However, the estimation was carried out with the raw correction factor (open black circles in Figure 7.7) at that time and hence does not correctly account for the experimental resolution, which is present in the quasi-free cross section. The data and results that were used for the fit can be found in [221]. Thus, the results of the refit, as shown in Figures 7.5b, 7.8, 7.9b and D.7, were obtained from a fit that included the old estimation, but is now compared to the final estimation of the free neutron cross section. As visible for all energies and angles, the free neutron data significantly improved the result of the fit, while still describing previous data reasonably well. The retrospective elimination of effects from the experimental resolution does not significantly degrade the quality

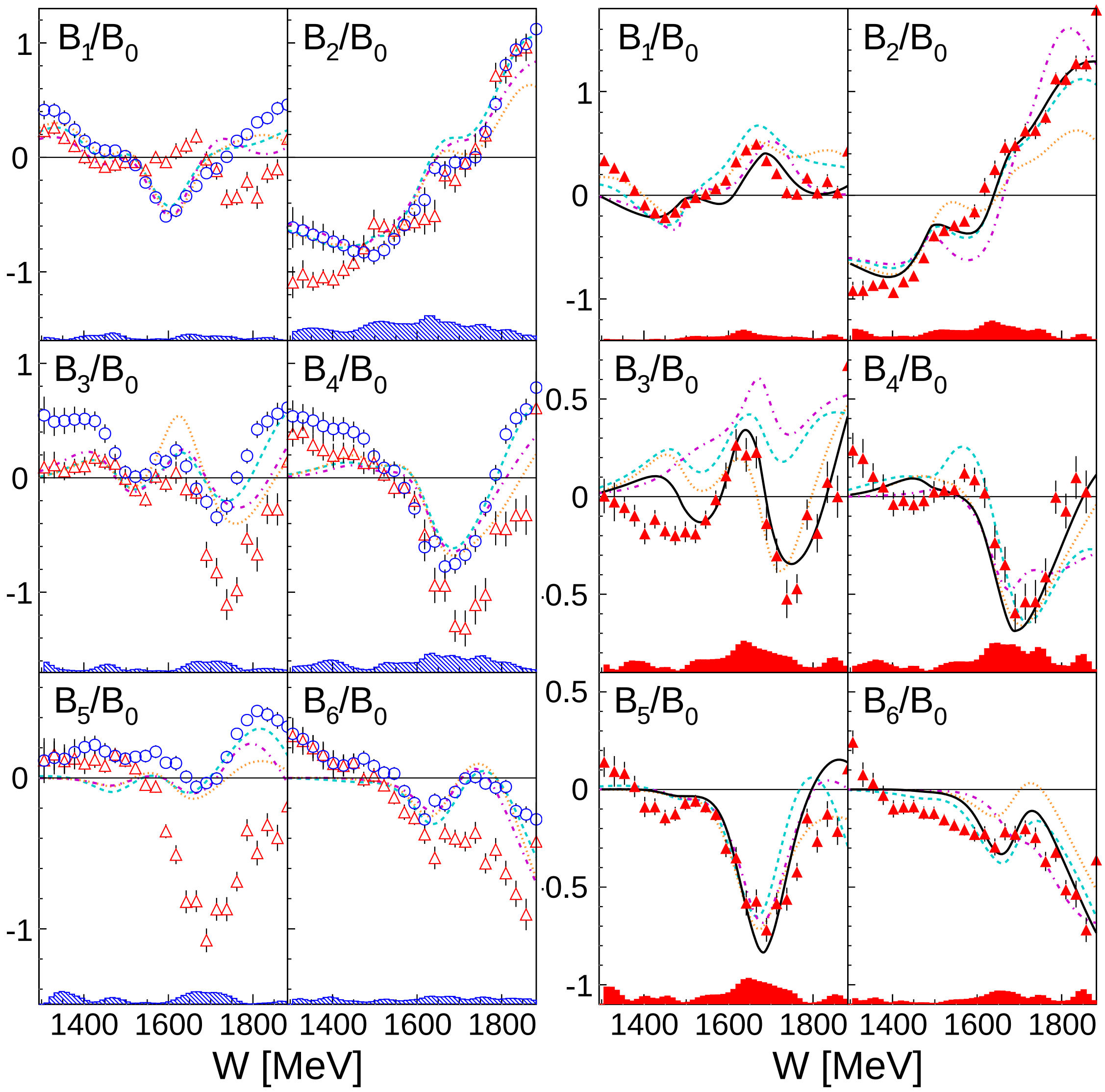

(a) $\gamma N(N) \to \pi^0 N(N)$

(b) $\gamma n \to \pi^0 n$

Figure 7.9: Legendre coefficient ratios for single π^0 photoproduction as a function of the final-state invariant mass $W = \sqrt{s}$. Results from the A2 data. Left-hand side: exclusive reactions on quasi-free nucleons. Right-hand side: exclusive reactions on the free neutron. Notations as in Figure 7.5. The histograms at the bottom represent the systematic uncertainties of the results.

of the agreement with the fit, but mainly differs in the width of the structures, as expected from the resolution effects. A first effect of the estimated neutron cross section can be seen in the ratios of the Legendre coefficients, as shown in Figure 7.9. The coefficient ratios for the reaction on quasi-free protons and neutrons are shown on the left-hand side and those for the free neutron on the right-hand side. Whereas the ratios with coefficients 2, 4, 5, and 6 do not show significant changes for the free compared to the quasi-free neutron result, those with coefficients 1 and

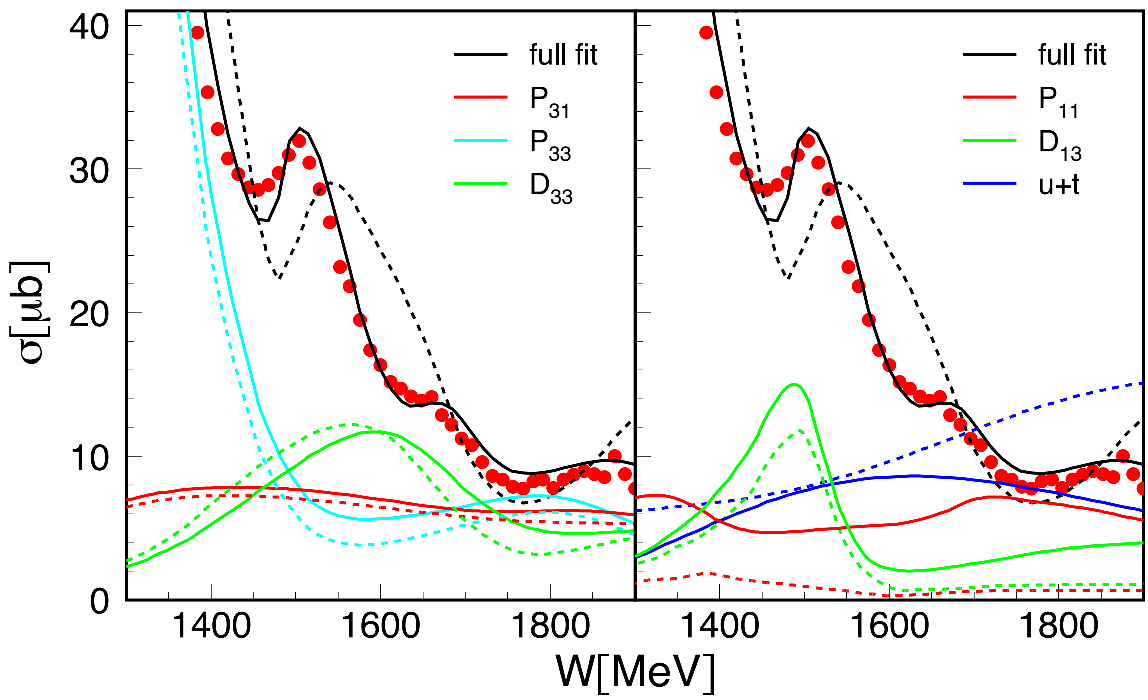

Figure 7.10: Impact of the Bonn-Gatchina refit on the different partial waves. Red circles: estimated free neutron total cross section from the A2 data. Dashed lines: previous BnGa results [38]. Solid lines: refit including the present data. Left-hand side: partial waves for Δ resonances (red: P_{31}, light blue: P_{33}, green: D_{33}). Right-hand side: partial waves for N^* resonances (red: P_{11}, green: D_{13}, blue: non-resonant background from u and t channel.)

3 exhibit drastic changes such as different zero crossings or even general sign changes.

The impact of the present results to the understanding of the nucleon excitation spectrum is demonstrated by its effect on the predictions of the BnGa partial wave analysis. In order to describe the present neutron data simultaneously with previous data, rather drastic changes had to be made. Due to the lack of neutron data, the model predictions mainly depended on the beam asymmetry for $\gamma n \to \pi^0 n$ from the GRAAL collaboration [46], as the other available neutron data is of poor statistical quality. For the refit the strength of several background contributions, e.g. $t-$, $u-$ and in particular vector meson exchange amplitudes, had to be changed. Furthermore, several resonance couplings had to be adjusted as depicted for a few partial waves in Figure 7.10. Shown is the measured estimate of the neutron total cross section (solid red circles) and the contributions from isospin $I = 3/2$ states (left-hand side) and isospin $I = 1/2$ states (right-hand side) together with the contributions from the previous BnGa result (dashed lines) and from the refit including the present data (solid lines). As expected, the most drastic changes are observed in the contributions with isospin $I = 1/2$, whereas the isospin $I = 3/2$ contributions are barely affected. This results from the fact that the latter are already sufficiently constrained by the results from the reaction on the free proton. In contrast, contributions of isospin $I = 1/2$ states and non-resonant $t-$ und $u-$ channels can not be limited by measurements on the proton alone and hence strongly depend on the available neutron data, which up to now was sparse and mainly consisted of either data from $\gamma n(p) \rightarrow p(n)\pi^-$ or the beam asymmetry data from $\gamma n(p) \rightarrow n(p)\pi^0$. As a consequence, the present data strongly influenced the model calculations and even revealed changes of well known four star states[1]. For example, the resonant P_{11} partial wave (red line) that contains contributions from the $N(1440)1/2^+$ roper resonance and the $N(1710)1/2^+$ changes significantly over the full energy range. At energies above 1600 MeV, drastic changes are also observed for the non-resonant $t-$ und $u-$channel background terms and contributions from D_{13} partial waves, mainly involving the $N(1700)3/2^-$ and $N(1720)3/2^+$ resonances.

[1]The reliability of an observed resonance is rated with one to four stars, where one star denotes *evidence of existence is poor* and four stars denote *existence is certain, and properties are at least fairly well explored* [37].

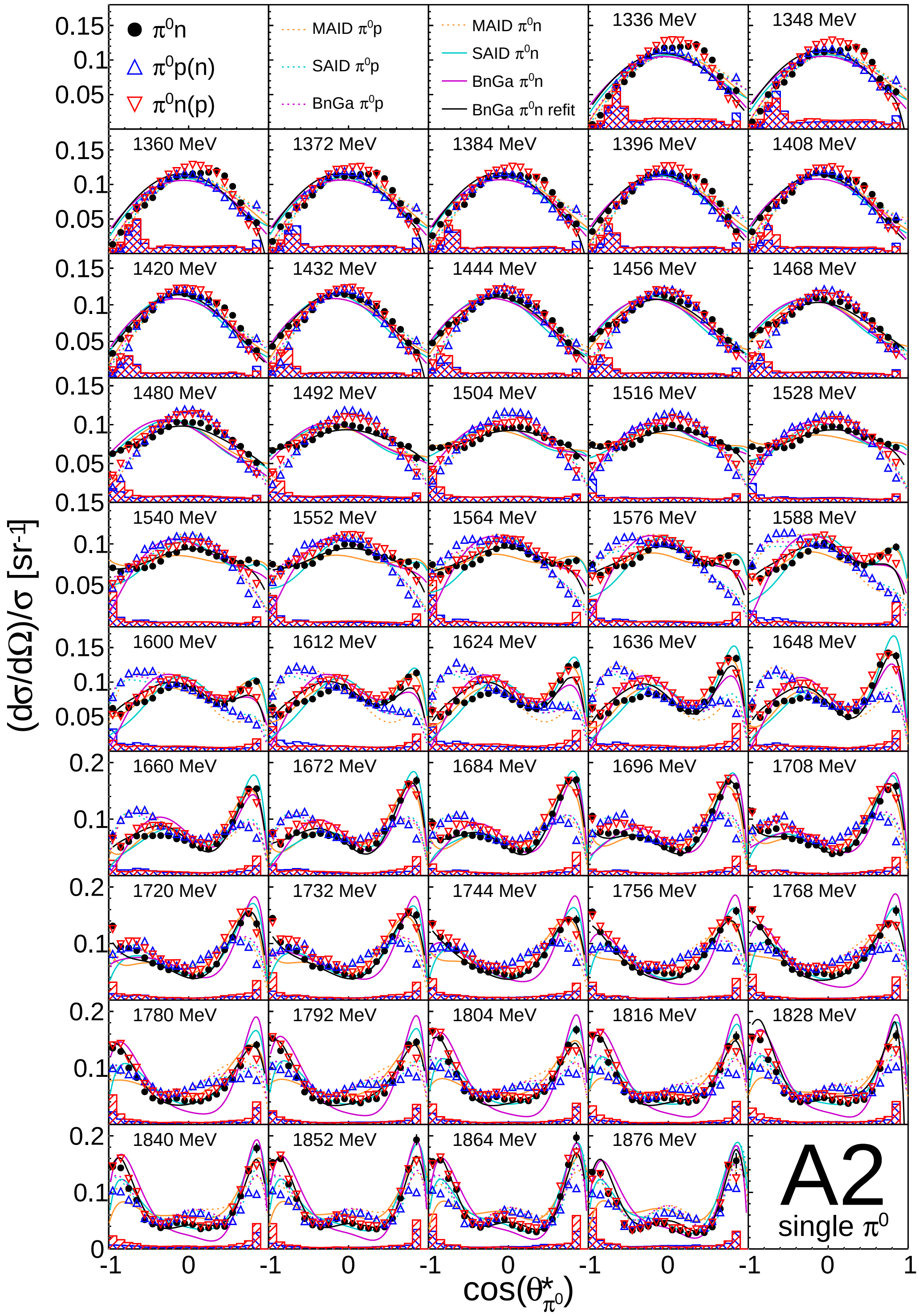

Figure 7.11: Normalized differential cross sections for exclusive π^0 photoproduction from quasi-free protons (open blue triangles), quasi-free neutrons (open red triangles), and free neutrons (solid black circles) as a function of the polar angle of the pion in the $\pi^0 N$ center of mass system. Results from the A2 data. Notations as in Figure 7.5. The hatched histograms at the bottom represent the systematic uncertainties of the quasi-free results.

7.2 Cross Sections for $\pi^0\pi^0$ Photoproduction from the Free Proton

In this section, the total and differential cross sections from the analysis of double π^0 photoproduction from free protons from A2 and CBELSA/TAPS data will be presented and compared. The analysis on the liquid hydrogen target was primarily used for the test of the analysis procedures. It was also used for the determination of the nucleon detection efficiency correction (see Section 6.8.3) and the investigation of final state interaction effects of the reaction from the quasi-free proton, from which the free neutron cross section was estimated (see Section 6.12).

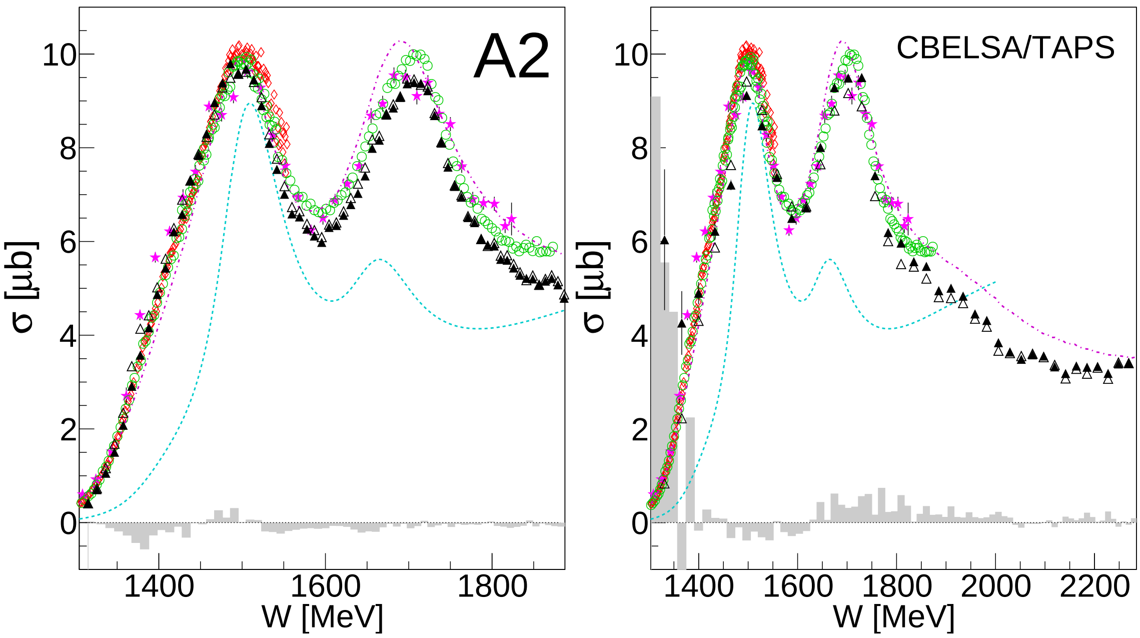

(a) Results from the A2 data **(b)** Results from the CBELSA/TAPS data

Figure 7.12: Total cross sections for double π^0 photoproduction from the free proton as a function of the final state invariant mass W. Left-hand side: A2 data. Right-hand side: CBELSA/TAPS data. Solid black triangles: exclusive reaction. Open black triangles: inclusive reaction. Solid magenta stars: ELSA-08 data [59]. Open green circles: MAMI1-12 data [55]. Open red diamonds: MAMI2-12 data [52]. Dashed cyan line: MAID [62]. Dashed-dotted magenta line: BnGa [43]. Gray histogram at the baseline: difference between inclusive and exclusive results.

The liquid hydrogen data from A2 and CBELSA/TAPS was analyzed with (exclusive) and without (inclusive) the coincident detection of the recoil proton. This allows for the investigation of the quality of the detection of the recoil proton. The resulting total cross sections for A2 and CBELSA/TAPS are shown in Figures 7.12a

and 7.12b, respectively. It can be seen that the inclusive (open black triangles) and the exclusive (solid black triangles) total cross section are in good agreement. The quality of the agreement is visualized by the gray histogram at the bottom, which represents the difference of the two results. The results are also compared to previous measurements from MAMI (without coincident detection of the proton, open red diamonds: [52], open green circles: [55]) and ELSA (with coincident detection of the proton, [59]) and solutions from the MAID isobar model (dashed cyan line, [62]) and BnGa coupled channel partial wave analysis (dashed-dotted magenta line, [43]). The agreement between the A2 data (Figure 7.12a) and previous results is overall satisfactory. The largest deviations (up to 10%) can be observed in the high energy tail between the A2 results and the MAMI data (open green circles). At the same time, the agreement with the data from ELSA (solid magenta diamonds) is much better. The results from CBELSA/TAPS (Figure 7.12b) are, apart from statistical fluctuations, in good agreement with both datasets. The large difference between the inclusive and exclusive measurements close to the threshold are due to the lack of statistics at low energies. As mentioned in Section 2.6.2, the trigger settings of the liquid hydrogen and deuterium beamtimes were optimized for η photoproduction and some of the lower tagger channels were switched off. The agreement of the measured data with the predictions from the MAID model is poor, which indicates that it neglects certain resonance contributions or contains incorrect contributions or wrong helicity couplings. The agreement with the BnGa solution is much better since it was fit to the ELSA data.
The differential cross sections of the exclusive measurements from both experiments are compared in Figure 7.13. In general, the agreement is good, especially for higher energies where influences from poor statistics of the CBELSA/TAPS data or from the energy sum trigger of the A2 data vanished. At low energies, small deviations occur, but are mostly within the systematical uncertainties. At low energies, the best agreement with the BnGa solution is achieved at meson backward angles and at higher energies the opposite is true, i.e. discrepancies mainly occur at backward angles. Even though several high statistics results are already available throughout the full angular and energy range in the second and third resonance region, the models still struggle with an appropriate description of the data. Further input from polarization observables or from measurements on the neutron seem to be necessary for solving the puzzle.

A full set of differential cross sections from the A2 and CBELSA/TAPS data are shown individually in Appendix D.2.1 and D.2.1. The $\pi^0 p$ and $\pi^0\pi^0$ invariant mass distributions are compared to each other in Appendix D.2.1.

The differential cross sections and $N\pi^0$ and $\pi^0\pi^0$ invariant mass distributions normalized to the total cross section are compared to those from quasi-free photoproduction in Section 7.3.1 and 7.3.2 for the analysis of the A2 and CBELSA/TAPS data, respectively.

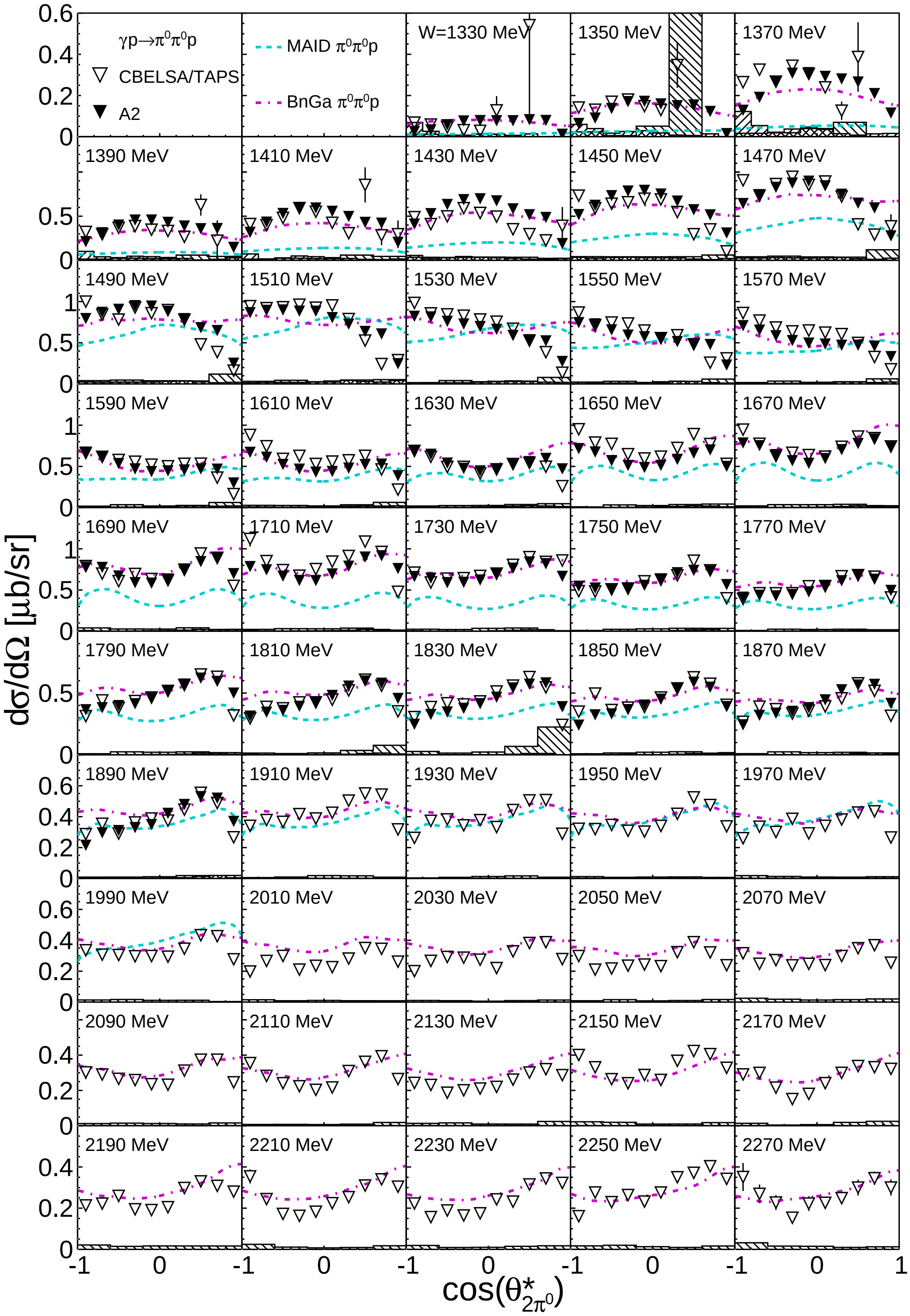

Figure 7.13: Differential cross sections for exclusive $2\pi^0$ photoproduction from the free proton as a function of the polar angle of the combined meson in the $2\pi^0 p$ center of mass system. Solid black triangles: results from the A2 data. Open black triangles: results from the CBELSA/TAPS data. Dashed cyan line: MAID [62]. Dashed-dotted magenta line: BnGa [43]. The hatched histograms at the bottom represent the systematic uncertainty of the exclusive result.

7.3 Cross Sections for $\pi^0\pi^0$ Photoproduction from Quasi-Free Nucleons

In this section, the analyses of double π^0 photoproduction from quasi-free protons and neutrons from the A2 and CBELSA/TAPS data will be presented. The results will be presented individually in Sections 7.3.1 and 7.3.2, respectively, and then compared to each other in Section 7.3.3.
Double π^0 photoproduction was analyzed with (exclusively) and without (quasi-free inclusively) the coincident detection of recoil protons and neutrons. Results were extracted as a function of the incident photon energy E_γ for the investigation of the quality of the nucleon detection efficiency and as a function of the final state invariant mass W to eliminate effects from Fermi motion. Total cross sections and differential cross sections as a function of the combined meson polar angle in the center of mass frame $\cos(\theta^*_{2\pi^0})$, as well as a function of the $N\pi^0$ and $\pi^0\pi^0$ invariant mass, have been extracted. In addition, the results from double π^0 photoproduction from the free and quasi-free proton were used to estimate the free neutron cross section. Finally, the results will be compared to the model predictions from the MAID isobar model [62] and the BnGa coupled channel partial wave analysis [43].

7.3.1 Cross Sections from A2 Data

This section presents the differential and total cross sections obtained from the analysis of double π^0 photoproduction from quasi-free protons and neutrons from the A2 data. For this analysis, all three liquid deuterium beamtimes were analyzed, i.e. December 2007, February 2009 and May 2009 (see Table 2.6 for details). First, the exclusive total cross sections from the proton and neutron are shown as a function of the incident photon energy E_γ and are compared to that of the quasi-free inclusive analysis. In the following, the results as a function of the center of mass energy W and the estimated free neutron cross section will be presented.

Results as a Function of the Incident Photon Energy E_γ

The total cross sections for the exclusive analyses of double π^0 photoproduction from quasi-free protons (open blue circles) and neutrons (open red triangles) as a function of the incident photon energy are shown in Figure 7.14b. Both cross sections exhibit the similar shape already observed on the free proton (Section 7.2) consisting of two rather broad bump structures representing the second and third resonance region. However, the proton cross section is steeper at threshold and reaches the maximum of the first resonance region earlier than that of the neutron. Similarly, the second bump in the proton cross section is shifted towards higher energies compared to the neutron, such that it exceeds the neutron cross sections in the high energy tail. In contrast, the neutron cross section does not exhibit a significantly deep valley in between the two bumps. This behavior is also visualized in the insert, which shows the ratio of the neutron to the proton cross section. In the minimum of the valley,

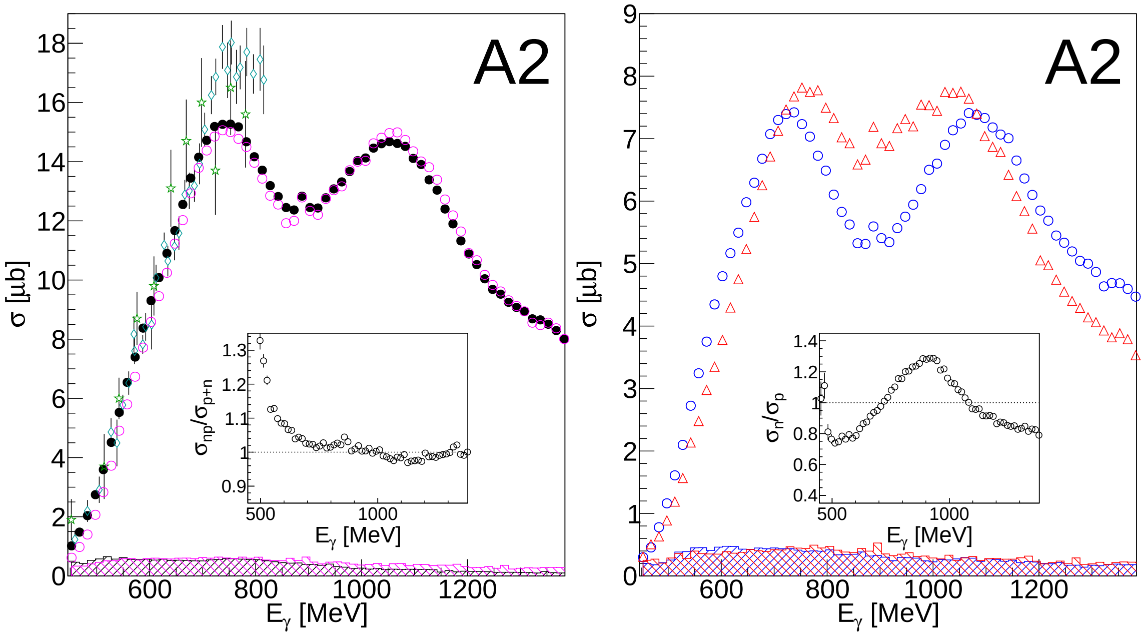

(a) $\gamma N \to 2\pi^0(N)$ (b) $\gamma N \to 2\pi^0 N$

Figure 7.14: Total cross sections for double π^0 photoproduction as a function of the incident photon energy E_γ. Results from the A2 data. Left-hand side: solid black circles: quasi-free inclusive reaction from the deuteron. Open magenta circles: sum of exclusive results from proton and neutron. Open green stars: $\gamma d \to 2\pi^0 np$ MAMI-B 99 [69]. Open cyan diamonds: $\gamma d \to \pi^0 np$ MAMI-B 2000 [70]. Insert: ratio of quasi-free inclusive to sum of the exclusive cross sections. Right-hand side: open blue circles: exclusive reaction on the proton. Open red triangles: exclusive reaction on the neutron. Insert: ratio of neutron to proton cross sections. The hatched histograms at the bottom indicate the systematic uncertainties of the corresponding cross sections.

both cross sections show a narrow structure of comparable size such that it is not visible in the ratio. The statistical errors are shown as error bars, but due to the large amount of statistics, fall below the size of the marker. The systematic uncertainties are indicated as hatched histograms in the bottom of the figure.

Figure 7.14a shows the total cross sections of the quasi-free inclusive analysis (solid black circles) compared to the sum of the exclusive proton and neutron cross section (open magenta circles) and two low statistics results from previous experiments from MAMI-B [69, 70]. Whereas one of the results from the older experiment [69] agrees well with the present data within the relatively large statistical errors, the other result [70] only agrees up to the η photoproduction threshold of $E_\gamma \approx 700$ MeV and then overshoots the present results by about 13%. Above these energies, the older experiments had to deal with large background contributions from the $\eta \to 3\pi^0$ decay, which was eliminated in this work due to the condition of the cluster

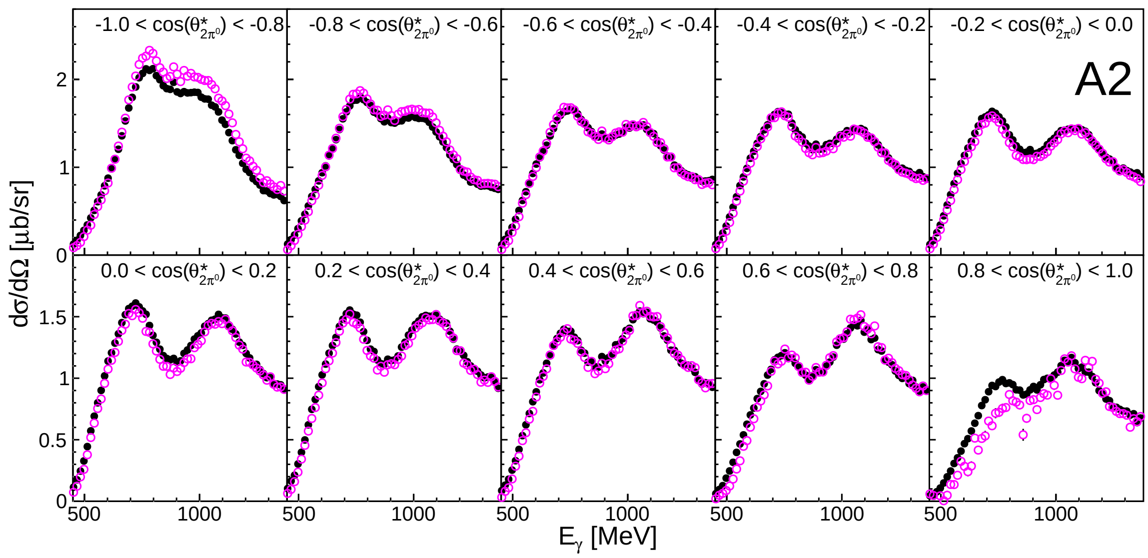

Figure 7.15: Differential cross sections for quasi-free inclusive $2\pi^0$ photoproduction from the deuteron as a function of the incident photon beam energy E_γ. Results from the A2 data. Solid black circles: quasi-free inclusive reaction from the deuteron. Open magenta circles: sum of exclusive results from proton and neutron.

multiplicity and the almost full angular coverage of the experimental setup.

The quasi-free inclusive result is in good agreement with the sum of the two exclusive cross sections, also visible in the insert, which shows the ratio of the quasi-free inclusive to the sum of the two exclusive cross sections. This equality must hold true as contributions from coherent $2\pi^0$ production are well below 100 nb [222] and thus, $\sigma_{\mathrm{incl}} \approx \sigma_{\mathrm{qfp}} + \sigma_{\mathrm{qfn}}$ applies. Except for the very low energies close to threshold, the ratio is almost one over all energies. The quality of the agreement can also be seen in the differential cross sections as a function of the incident photon energy (Figure 7.15) and as a function of the center of mass polar angle of the combined meson (Figure 7.16). Except for the very backward and forward angles and close to threshold, the agreement is excellent. This nicely demonstrates that no significant sources of systematic uncertainty due to the detection of the recoil nucleons are present.

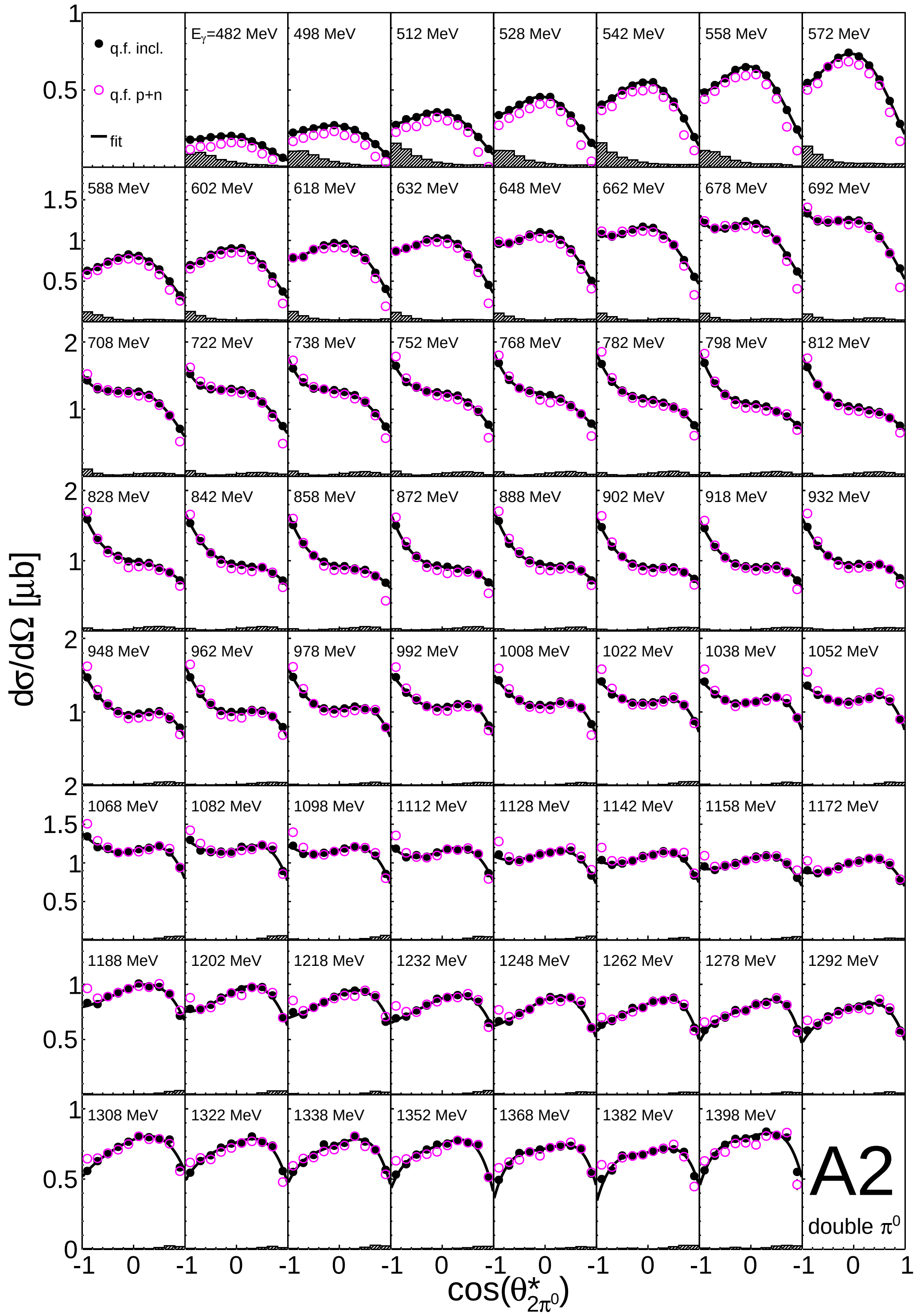

Figure 7.16: Differential cross sections for quasi-free inclusive $2\pi^0$ photoproduction from the deuteron as a function of the polar angle of the pion in the $\pi^0 N$ center of mass system. Results from the A2 data. Solid black circles: quasi-free inclusive reaction from the deuteron. Open magenta circles: sum of exclusive results from proton and neutron. The hatched histograms at the bottom represent the systematic uncertainties of the quasi-free inclusive result.

Results as a Function of the Final State Invariant Mass W

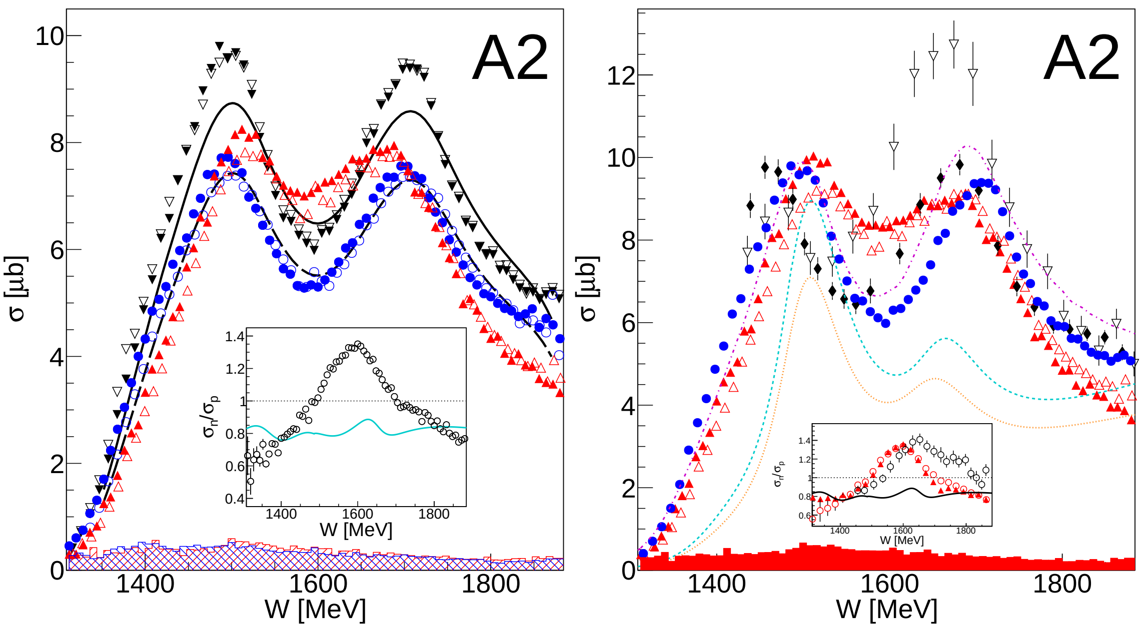

(a) $\gamma N(N) \rightarrow 2\pi^0 N(N)$ **(b)** $\gamma N \rightarrow 2\pi^0 N$

Figure 7.17: Total cross sections for double π^0 photoproduction from free and quasi-free nucleons as a function of the final-state invariant mass $W = \sqrt{s}$. Results from the A2 data. Left-hand side: open (solid) black triangles: inclusive (exclusive) free proton. Open (solid) blue circles: quasi-free proton from IS (FS). Open (solid) red triangles: quasi-free neutron from IS (FS). Solid (dashed) black line: free proton folded with Fermi motion (scaled with 0.85). Insert: ratio of quasi-free neutron to proton ratio. Solid cyan line: MAID neutron to proton ratio. Right-hand side: blue circles: free proton. Open (solid) red triangles: free neutron from IS (FS). Open black triangles: free proton from GRAAL [68]. Solid black diamonds: free neutron from GRAAL [68]. Dashed cyan (dotted orange) line: MAID proton (neutron) [62]. Dashed-dotted line: BnGa [43]. Insert: ratio of free neutron to proton ratio. Open (solid) red circles: this work from IS (FS). Open black circles: GRAAL data. Solid black line: MAID neutron to proton ratio. The histograms at the bottom represent the systematic uncertainties of the corresponding cross sections.

The total cross sections for double π^0 photoproduction from quasi-free protons and neutrons as a function of the center of mass energy are shown in Figure 7.17a. The center of mass energy $W = \sqrt{s}$ was reconstructed from the kinematics of the final state (FS) as discussed in Section 6.7. The resulting cross sections are shown as full symbols. In addition, the cross sections (shown as open symbols) were reconstructed from the initial state particles (IS) similarly to the free proton results (open black triangles: inclusive analysis, solid black triangles: exclusive analysis).

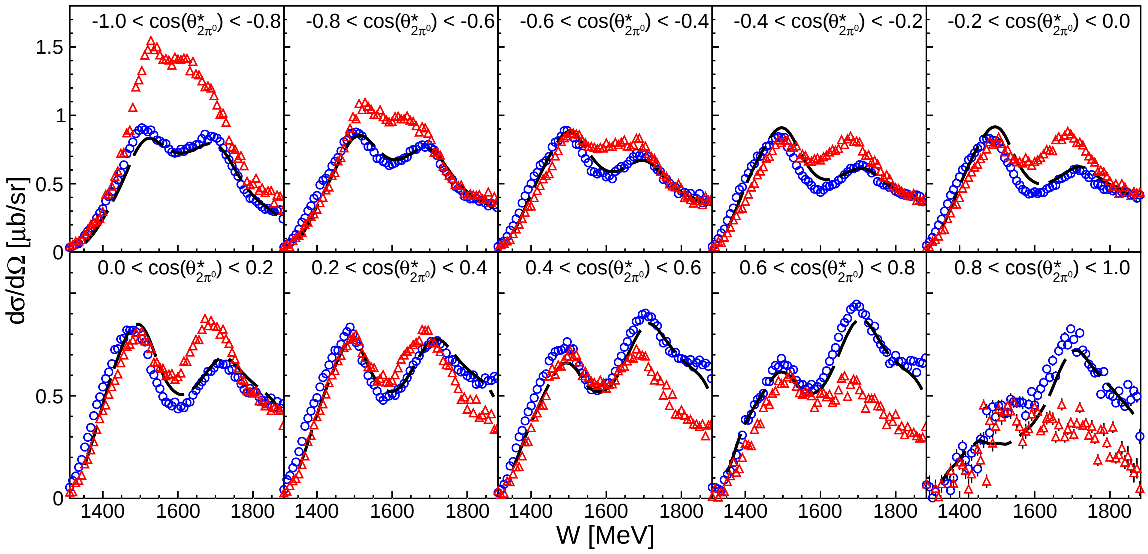

Figure 7.18: Differential cross sections for exclusive $2\pi^0$ photoproduction from quasi-free nucleons as a function of the final state invariant mass W. Results from the A2 data. Open blue circles: quasi-free proton. Open red triangles: quasi-free neutron. Dashed black line: free proton folded with Fermi motion and scaled with 0.85.

Whereas the IS cross sections are affected by Fermi motion, those from FS are subject to effects from experimental resolution. As previously mentioned, both effects are of similar order for the single π^0 results on deuterium. For this reason, the results of both reconstructions are very similar.
The comparison of the free and quasi-free proton cross sections show a rather strong reduction of the quasi-free cross section. The size of the effect was estimated by folding the free proton result with Fermi motion (shown as the solid black line). The folded free proton cross section is about 15% larger than the quasi-free result (indicated by the dashed line, which corresponds to the Fermi folded cross section scaled by 0.85). The curve almost perfectly fits the quasi-free result, indicating that the effect is nearly independent of energy. The angular dependence of the results reveal a similar behavior. The differential cross sections as a function of the final state invariant mass and the combined meson polar angle in the center of mass frame are shown in Figures 7.18 and 7.22. Thereby the differential cross sections as a function of the meson polar angle were normalized to the corresponding cross section to allow for a better comparison of the shapes of the distributions. The Fermi folded and scaled free proton cross section is also shown (dashed black line). Besides being independent of energy, the effect also seems to be of the same magnitude for all combined meson angles.

For almost all angular bins, the curve is nearly congruent with the quasi-free cross sections. This is somehow surprising, as the suppression of the quasi-free cross section with respect to the free result most likely indicates a moderate nuclear FSI effect which should not be independent of energy or angle. However, it should be noted that the present data does not cover the extreme forward angles where the FSI effects are predicted to be the most sizeable. In addition, the most forward angular bins exhibit the largest observed systematic uncertainties. Although the size of the effect is of similar size as the systematic uncertainties of the measured cross sections, it seems very unlikely that the effect is due to systematic errors in the analysis. On the one hand, the same analysis procedure used on the liquid hydrogen data achieved good agreement with published results. On the other hand, analyses of different reaction channels using the same data exhibit different behavior. As previously discussed in Section 7.1, the observed differences between free and quasi-free range from 0% (η photoproduction) to 35% (single π^0 photoproduction). Furthermore, the general trend of the effect is mostly in agreement with expectations, as it was observed to be larger for neutral pions than for charged pions (for the latter, due to charge exchange, two identical nucleons exist in the final state and nucleon-nucleon FSI effects are larger for proton-neutron than for neutron-neutron pairs [18]) and it was already known to be mostly absent in η photoproduction. Nevertheless, a detailed understanding of such effects are still required, even though first calculations for $\gamma d \to p(p)\pi^-$ and $\gamma d \to \pi^0 p(n)$ are under way [77, 82].

The high statistics results for the free and quasi-free proton cross sections were used to derive an estimation of the free neutron cross section, as discussed in Section 6.12. The ratio of the Fermi folded free to quasi-free cross section was smoothed as a function of energy (see right-hand side of Figure 6.126) and applied to the quasi-free neutron cross section. The correction factors for the bare (open circles) and smoothed ratio (filled circles) are shown in Figure 7.19. It is only slightly decreasing with energy as already seen in Figure 6.126, but also reveals a slight angular dependence that does not exhibit the predicted enhancement with forward meson angles from the associated low relative momenta between the final state nucleons. Instead, the largest ratios are observed at medium meson angles for all energies. Close inspection of the differential cross sections as a function of the final state invariant mass confirms the angular dependence of the correction factor. Towards medium meson angles, i.e. $-0.4 < \cos(\theta^*_{2\pi^0}) < 0.2$, the scaled Fermi folded proton result (dashed black line in Figure 7.18), is larger than the quasi-free cross section (open blue circles), whereas at backward and forward angles the opposite is the case. However, the angular dependence is
Since it was observed that the FSI effect for the quasi-free proton was on the order of 15% and is only weakly dependent on energy and angle, it can be expected that the free neutron cross section is of 15% larger magnitude than the quasi-free result, which is indeed the case. The obtained estimate for the free neutron cross section is shown in Figure 7.17b. Shown are the two estimates obtained from the quasi-free neutron cross section and were reconstructed from the initial state (open red triangles) and from the final state (solid red triangles). Both results are in very good agreement, since the effects of the Fermi motion in the initial state reconstruction are of similar size as those from the experimental resolution in the final state reconstruction and hence, both effects only affect the neutron cross section weakly. The insert shows the

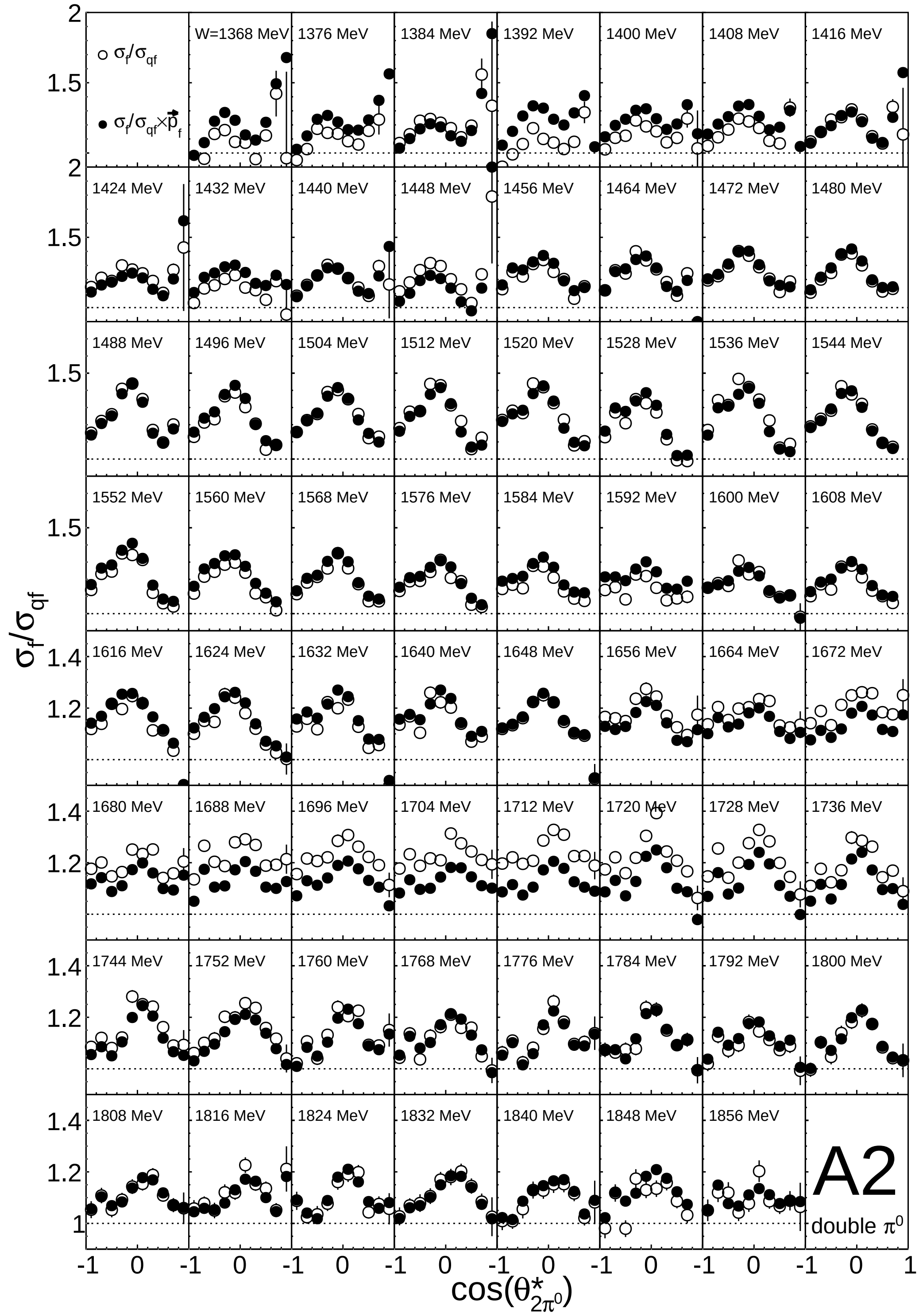

Figure 7.19: Differential ratio of free exclusive $2\pi^0 p$ cross section to the quasi-free $2\pi^0 p(n)$ cross section. Results from the A2 data. Open circles: bare ratio. Solid circles: ratio obtained from the free cross section smeared with Fermi motion and an additional energy dependent smoothing factor (see Section 6.12).

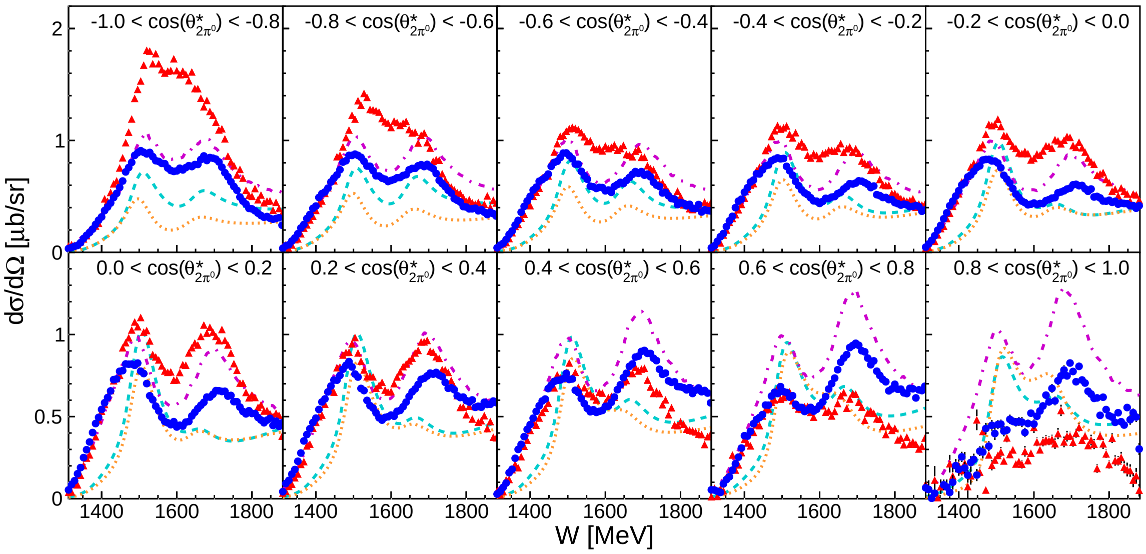

Figure 7.20: Differential cross sections for exclusive $2\pi^0$ photoproduction from the free proton (solid blue circles) and the estimated free neutron (solid red triangles) as a function of the final state invariant mass W. Results from the A2 data. Notations as in Figure 7.17.

ratio of the free neutron to free proton cross section that, free of normalization uncertainties, is equal to the quasi-free ratio. The estimated free neutron cross section is compared to the exclusive result for the free proton cross section (solid blue circles) and to available free proton and neutron results from the GRAAL collaboration [68]. They obtained the free neutron cross section with the ratio of free to quasi-free proton cross section reconstructed from the initial state. However, in contrast to the present work, they did not smear the free proton data with Fermi motion and their result for the free proton cross section exhibits significant discrepancies with published results. For this reason, their estimate for the neutron cross section exhibits a large enhancement in the third resonance region with respect to the proton cross section. Nevertheless, the present results can not confirm such behavior at all. In contrast, apart from the absolute magnitude, the free cross sections exhibit nearly the same characteristics as already discussed for the quasi-free results.
In addition to the already mentioned model results for the proton, the MAID calculation for the neutron (dotted orange line) is shown. However, compared to the already underestimating proton model, the prediction for the neutron seems to miss even more contributions. Nevertheless, it represents the only officially available prediction for double π^0 photoproduction from the neutron.

The nearly energy and angular independent effect of the FSI correction can also be seen in the normalized differential cross sections as a function of W and $\cos(\theta^*_{2\pi^0})$ for the free neutron compared to those for the quasi-free neutron in Figures 7.20, 7.18, and 7.22 which are almost of identical shape and only differ in magnitude. Besides the difference in absolute magnitude, the shape of the differential cross sec-

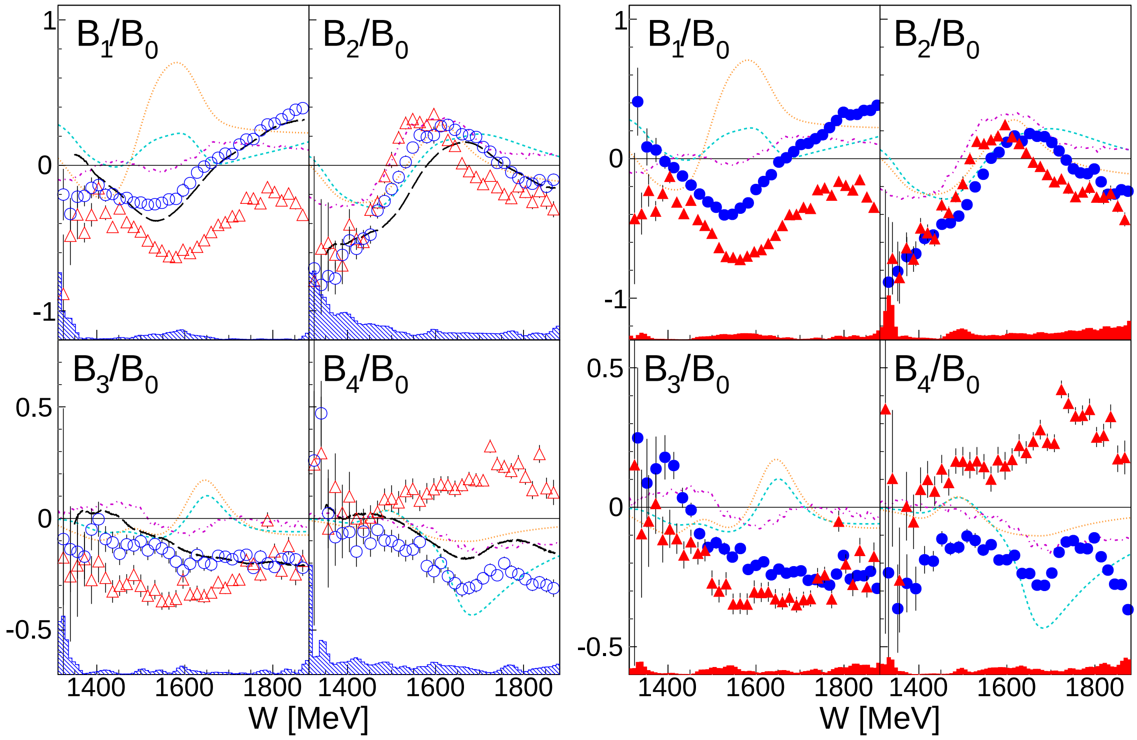

(a) $\gamma N(N) \rightarrow 2\pi^0 N(N)$ **(b)** $\gamma N \rightarrow 2\pi^0 N$

Figure 7.21: Legendre coefficient ratios for double π^0 photoproduction as a function of the final-state invariant mass $W = \sqrt{s}$. Results from the A2 data. Left-hand side: exclusive reactions on quasi-free nucleons. Right-hand side: exclusive reactions on the free nucleons. Notations as in Figure 7.17. The histograms at the bottom represent the systematic uncertainties of the corresponding results.

tion for free and quasi-free protons is similar to that for free and quasi-free neutrons for energies up to the region between the first bump and the subsequent valley at $W \approx 1600$ MeV. For higher energies, they exhibit rather different shapes, which is due to different contributions from the sequential decays. As expected, the agreement of the proton data with the prediction from the BnGa coupled-channel partial wave analysis is reasonably good over all energies, since their model was fit to similar data from previous CBELSA/TAPS data. In contrast, the solution from the MAID model does not accurately describe the proton or the neutron data. Due to the good agreement between free and quasi-free data, the Legendre coefficient ratios for the extraction of the quasi-free and free cross sections (Figure 7.21), apart from small differences, are very similar. The small deviations of the BnGa model in the differential cross sections result in rather large discrepancies in the coefficient ratios of the Legendre expansion.

Differential cross sections as a function of the $N\pi^0$ and $\pi^0\pi^0$ pairs normalized to the corresponding total cross section are shown in Figures 7.23 and 7.24, respectively. Thereby for every event one of the two available pions was randomly chosen for the

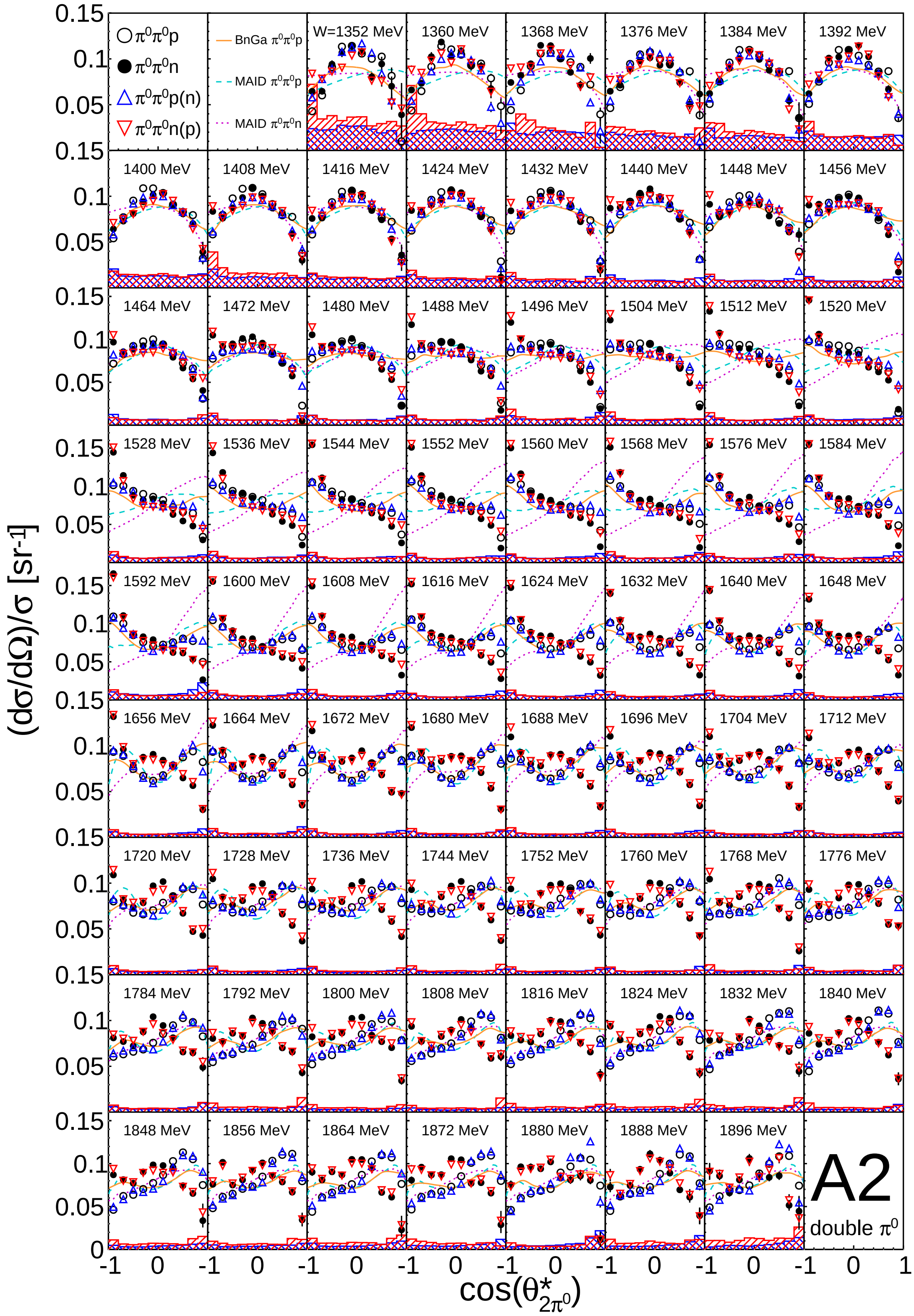

Figure 7.22: Normalized differential cross sections for exclusive $2\pi^0$ photoproduction from free and quasi-free nucleons as a function of the polar angle of the pion in the $2\pi^0 p$ center of mass system. Results from the A2 data. Notations are given in the Figure. The hatched histograms at the bottom represent the systematic uncertainties of the quasi-free results.

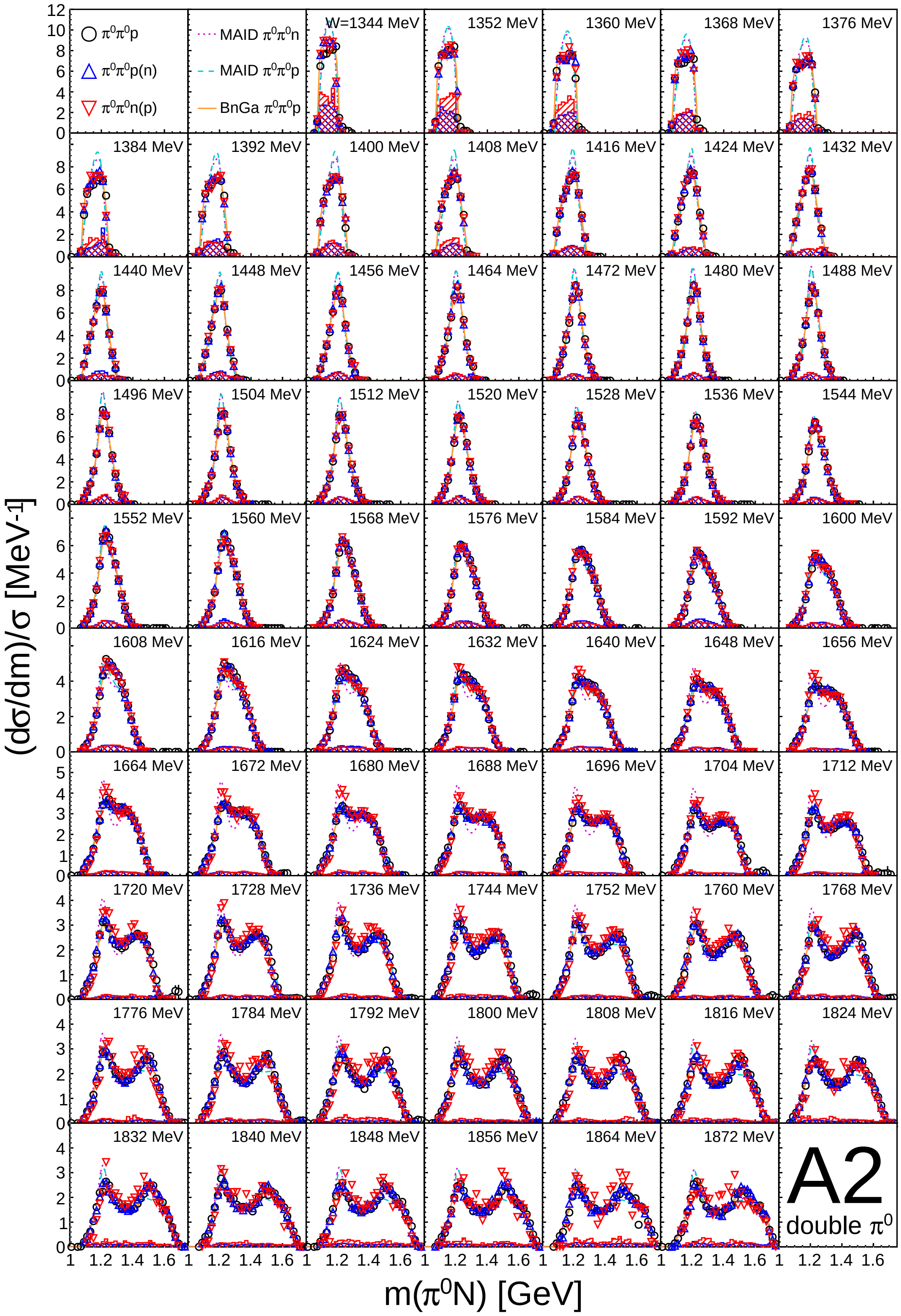

Figure 7.23: Normalized differential cross sections for exclusive $2\pi^0$ photoproduction from the free proton and from quasi-free nucleons as a function of the $N\pi^0$ invariant mass. Results from the A2 data. Notations are given in the Figure. The hatched histograms at the bottom represent the systematic uncertainties of the quasi-free results.

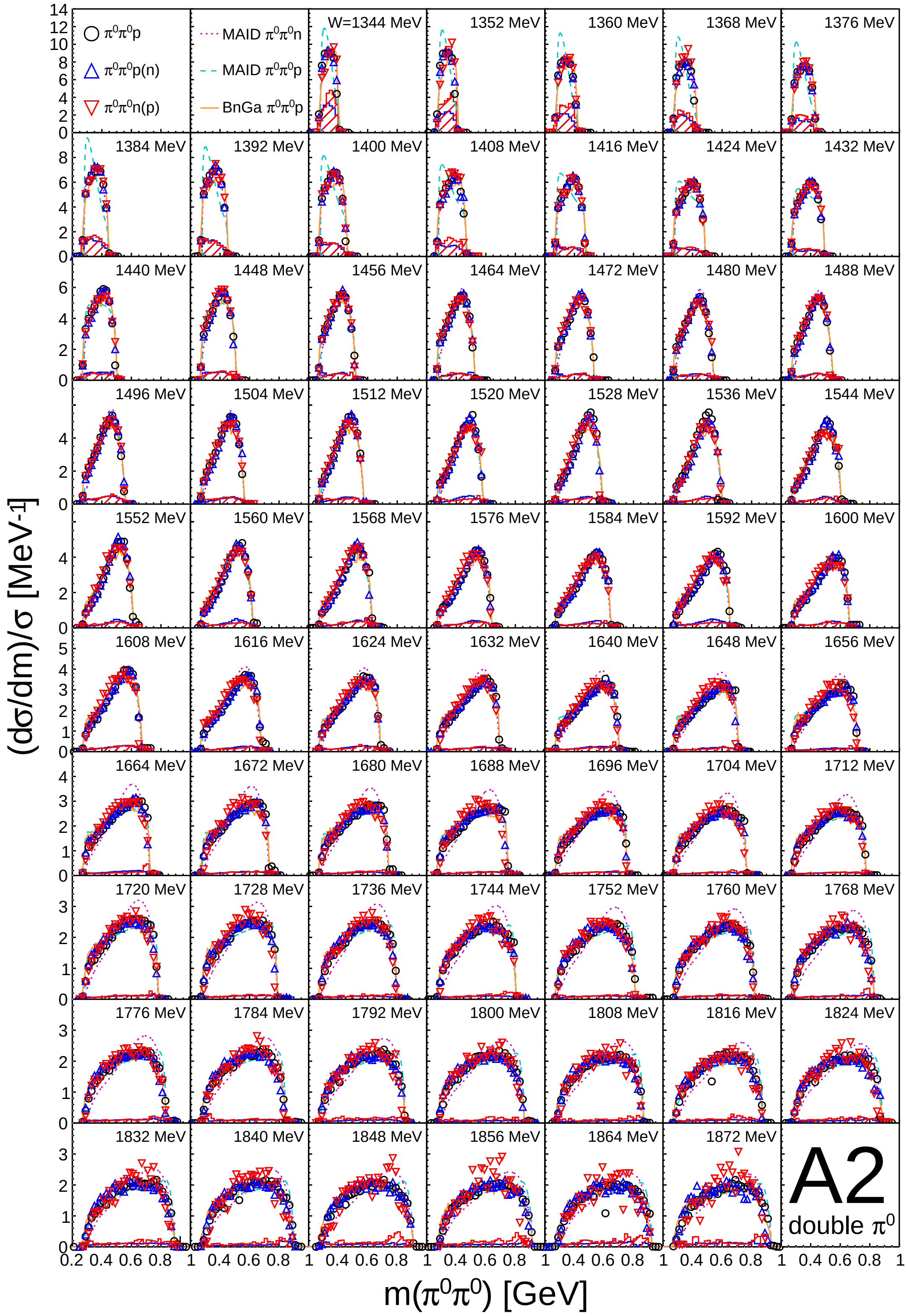

Figure 7.24: Normalized differential cross sections for exclusive $2\pi^0$ photoproduction from the free proton and from quasi-free nucleons as a function of the $\pi^0\pi^0$ invariant mass. Results from the A2 data. Notations are given in the Figure. The hatched histograms at the bottom represent the systematic uncertainties of the quasi-free results.

nucleon-pion pair to avoid correlations in the statistical uncertainty. This results in the same if the invariant masses from both $N\pi^0$ were used and the results were renormalized by a factor of 0.5. Shown are the results for the quasi-free proton (open blue triangles) and neutron (open red triangles) together with those for the free proton (open black circles). As expected from the comparison of the total cross sections, the results for the free and quasi-free proton are in good agreement and exhibit nearly identical shapes for all energies. The shapes of the proton and neutron cross sections again are very similar until energies of $W \approx 1600$ MeV, close to the valley between the two resonance regions. At higher energies, the shape remains similar, but the neutron cross section exhibits a more pronounced peak at the mass of the Δ resonance. This indicates a larger contribution from sequential decays via the $\Delta(1232)3/2^+$ intermediate state in the region of the second bump for the neutron compared to the proton.

In order to investigate this characteristic behavior in more detail, the total cross section was decomposed into contributions from phase space ($\gamma N \to N\pi^0\pi^0$) and the sequential decays via $\Delta(1232)3/2^+$ ($\gamma N \to \Delta(1232)3/2^+\pi^0 \to N\pi^0\pi^0$) or $N(1520)3/2^-$ ($\gamma N \to N(1520)3/2^-\pi^0 \to N\pi^0\pi^0$) resonances. These sequential decays were chosen within the energy range of interest as they tend to contribute most to the $N\pi^0\pi^0$ final state, also visible in the $N\pi^0$ differential cross sections. For this purpose, the relative contributions obtained from the determination of the detection efficiencies (see Equation (6.16) in Section 6.8.1) were used to produce total cross sections according to Equation (6.17). The quantum numbers of the intermediate states were not considered here and information about the angular distributions of the involved resonances were neglected. Similarly, the analysis does not account for the available information about the beam helicity asymmetries [56], nor for the interferences between the different contributions. Even though the data are compared to results from a PWA of previous ELSA data on the proton [59] and already reveal a few interesting aspects concerning the comparison of the reaction on the proton to the neutron, a more detailed analysis in the framework of coupled-channel partial wave analyses would be required. The results from the decomposition of the total cross section are shown in Figure 7.25 and the corresponding differential cross sections as a function of the final state invariant mass in Figure 7.26.

For all polar angles $\theta^*_{2\pi^0}$ in the second resonance region, the first bump in the proton and neutron cross sections is dominated by the sequential decay via the intermediate $\Delta(1232)3/2^+\pi^0$ state. Previous analyses of free proton data [50, 51, 59] found that this mainly originates from the $N(1520)3/2^- \to \Delta(1232)\pi^0 3/2^+$ decay. Subsequently, contributions from the $\Delta(1232)3/2^+\pi^0$ intermediate state diminish in the third resonance region (except for polar angles in the range $-0.2 < \cos(\theta^*_{2\pi^0}) < 0.4$) and are replaced by a strong resonance of the phase-space contribution and at forward angles also by the intermediate $N(1520)3/2^-$ state. In contrast, the contributions to the neutron cross section are, throughout all energies and meson polar angles, mostly dominated by a reaction chain via an intermediate $\Delta(1232)\pi^0$ state and contributions from phase-space or via $N(1520)3/2^-$ remain small. This shows that although

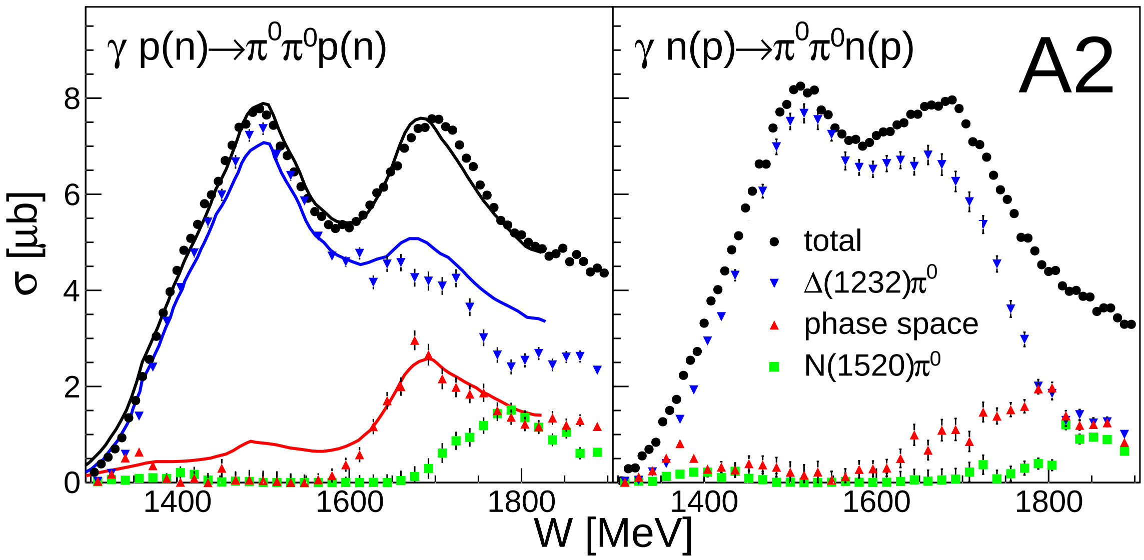

Figure 7.25: Contributions of $\gamma N \to \Delta(1232)\pi^0 \to N\pi^0\pi^0$ (blue triangles), $\gamma N \to N\pi^0\pi^0$ (red triangles) and $\gamma N \to N(1520)\pi^0 \to N\pi^0\pi^0$ (green squares) to the $2\pi^0$ total cross section (black circles) for quasi-free protons (left-hand side) and quasi-free neutrons (right-hand side). Solid lines: corresponding results from a PWA from previous ELSA proton data [59]. Results from the A2 data.

both cross sections exhibit a very similar shape, the origin of the bumps in the third resonance region is entirely different. Whereas for the proton, it mainly originates from phase space contributions, for the neutron intermediate $\Delta(1232)3/2^+\pi^0$ states are dominant and responsible for the more shallow peak.

A possible explanation for the observed behavior can be found in the origin of the phase-space contribution. As observed in the present data, the bump in the third resonance region in the PWA of the proton data is mainly caused by the resonant phase-space contribution (solid red line in Figure 7.25) which represents decays of the $N(\pi^0\pi^0)_S$ final state with the two pions in a relative s-wave. Such final states are sometimes assigned to the $N\sigma$ final state and the broad scalar-isoscalar σ-meson is used as an effective parametrization of this partial wave. In the MAID model, the second bump in the proton cross section is mainly caused by the $N(1680)5/2^+$ resonance, and in the neutron cross section primarily by the $N(1675)5/2^-$ resonance. This description is in agreement with expectations that would result from interpretations of the basic properties of these states as listed in the Review of Particle Physics [37]. The branching ratio of the $N(1680)5/2^+$ resonance to the $\Delta(1232)3/2^+\pi^0$ state is much lower (5-15%) than that of the $N(1675)5/2^-$ (50-60%). Due to the large electromagnetic coupling (all in units of 10^{-3} GeV$^{-1/2}$) of the $N(1680)5/2^+$ to the proton ($A^p_{1/2} = 15 \pm 6,\ A^p_{3/2} = 133 \pm 12$) compared to the neutron ($A^n_{1/2} = 29 \pm 10,\ A^n_{3/2} = 33 \pm 9$), it is much more probable that the proton is excited to the $N(1680)5/2^+$ than to the $N(1675)5/2^-$. In addition, the electromagnetic excitation of the latter is Moorehouse suppressed for the proton [223]

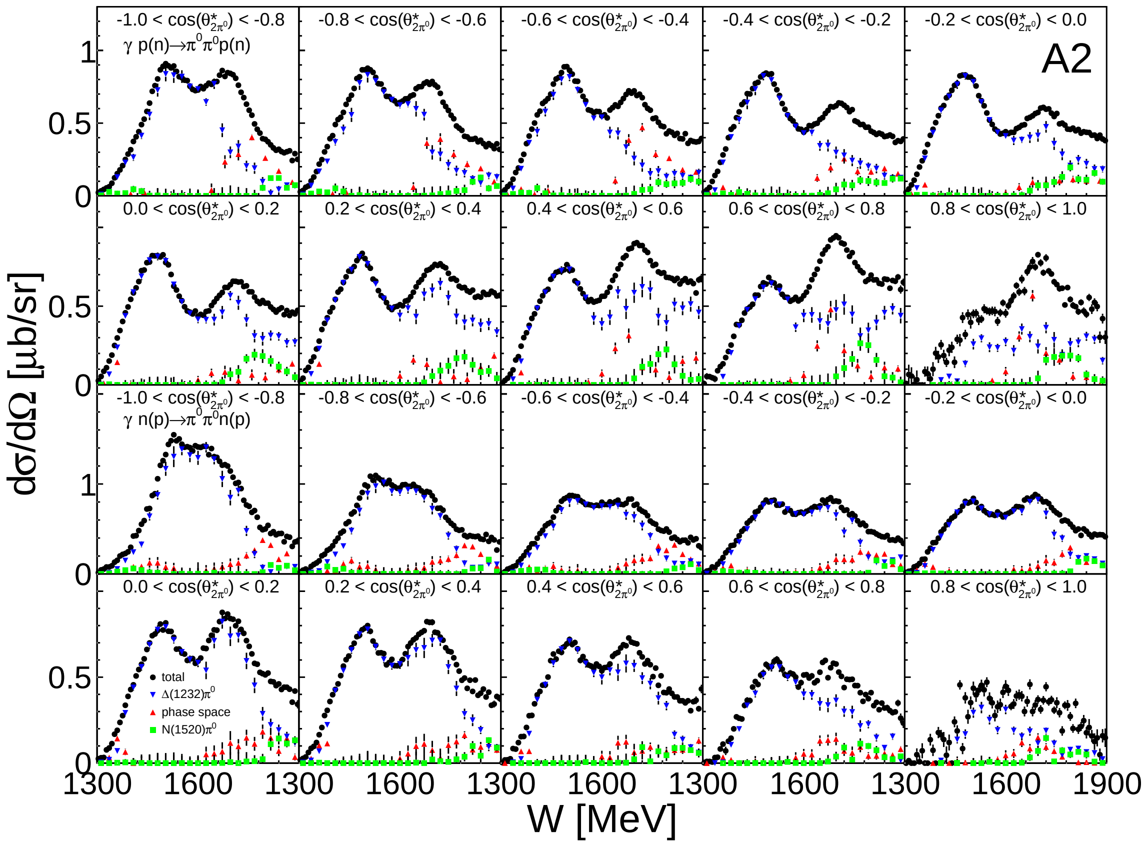

Figure 7.26: Contributions of $\gamma N \to \Delta(1232)\pi^0 \to N\pi^0\pi^0$ (blue triangles), $\gamma N \to N\pi^0\pi^0$ (red triangles), and $\gamma N \to N(1520)\pi^0 \to N\pi^0\pi^0$ (green squares) to the $2\pi^0$ differential cross sections as function of the final state invariant mass W (black circles) for quasi-free protons (upper two rows) and quasi-free neutrons (lower two rows). Results from the A2 data.

$(A^p_{1/2} = 19 \pm 8,\ A^p_{3/2} = 20 \pm 5)$ than for the neutron $(A^n_{1/2} = 60 \pm 5,\ A^n_{3/2} = 85 \pm 10)$. These considerations are also in agreement with the $N\sigma$ interpretation from the PWA [59]. The $N5/2^{\pm} \to N\sigma$ decay is possible with a relative angular momentum of the $N\sigma$ system of $l_{N\sigma} = 2$ for the $5/2^+$ state, but the $5/2^-$ state is only possible with $l_{N\sigma} \geq 3$. As a consequence, a larger contribution from the $N\sigma$ decay for the $N(1680)5/2^+$ state, which is the main contribution in the third resonance region of the proton cross section, is very plausible. However, a combined PWA involving both reactions, as well as information from angular distributions and polarization observables, will certainly shed more light on the puzzle.

A full set of differential cross sections for the quasi-free proton and neutron as well as for the free neutron are shown in the Appendix, in Figures D.12 - D.14 and are compared to the results from the CBELSA/TAPS data in Figures D.19 - D.21. Differential cross sections as function of the $N\pi^0$ and $\pi^0\pi^0$ invariant mass are compared to those from CBELSA/TAPS in Figures D.23, D.24 and Figures D.26, D.27.

7.3.2 Cross Sections from CBELSA/TAPS Data

In this section, the results for the differential and total cross sections for double π^0 photoproduction from quasi-free protons and neutrons bound in deuterium from the CBELSA/TAPS data will be presented. The data are taken from the December 2008 experiment with a liquid deuterium target and were analyzed with the equivalent analysis as used for the extraction of the results of the A2 data, presented in Section 7.3.1. The same observables using the identical techniques have been extracted for incident photon energies from ~ 0.45 GeV to ~ 2.3 GeV. Although the statistical quality of the data compared to that from A2 is rather poor and required a coarser energy and angular binning, the present results allow for the extension of the discussion and interpretation of the A2 results from section 7.3.1 beyond the third resonance region to roughly 1 GeV higher energies. Furthermore, applying the same analysis to data of a different experimental setup using different types of detectors and trigger settings allows for an important cross check and puts stringent limits on the systematic uncertainties among the individual results.

Results as a Function of the Incident Photon Energy E_γ

The total cross sections of the exclusive analysis of $2\pi^0$ photoproduction from quasi-free protons and neutrons bound in the deuteron are presented as a function of the incident photon energy in Figure 7.27b. Both cross sections exhibit the typical two bump shape. Due to the poor statistics that mostly affect the neutron channel, the cross sections show rather large fluctuations and error bars from threshold until roughly the second bump region. Compared to the Results from the A2, the high granularity of the Crystal Barrel detector results in a somewhat better energy resolution and by that the bumps appear sharper. In the second and third resonance region, the ratio of neutron to proton cross section strongly varies (see insert in Figure 7.27b), but remains rather stable at higher photon beam energies, indicating that at higher energies the neutron cross section is suppressed with respect to the proton result by roughly 20%. The sum of the two exclusive results is compared to the quasi-free inclusive cross section in Figure 7.27a. The comparison of the differential cross sections as a function of the incident photon energy and the meson polar angle in the center of mass frame are shown in Figures 7.28 and 7.29. Within the systematic uncertainties, the results are in good agreement for all meson polar angles and photon energies. The differences lie within 10% with a slight excess of about 15% at energies of ~ 1.3 GeV after the third resonance region and a somewhat too high sum of proton and neutron cross section at meson backward angles, which is compensated by a slightly too low sum in the proximate angular bin. The results are also compared to previous data from MAMI-B, illustrated with open green stars [69] and open cyan diamonds [70]. The same good agreement with the older MAMI-B data [69] as obtained with the A2 data is observable, whereas the newer MAMI-B data again exceeds the present result above the η photoproduction threshold at energies of $E_\gamma \approx 700$ MeV. The deviations are well within the systematic uncertainties and hence no significant problem with the detection of recoil nucleons was observed.

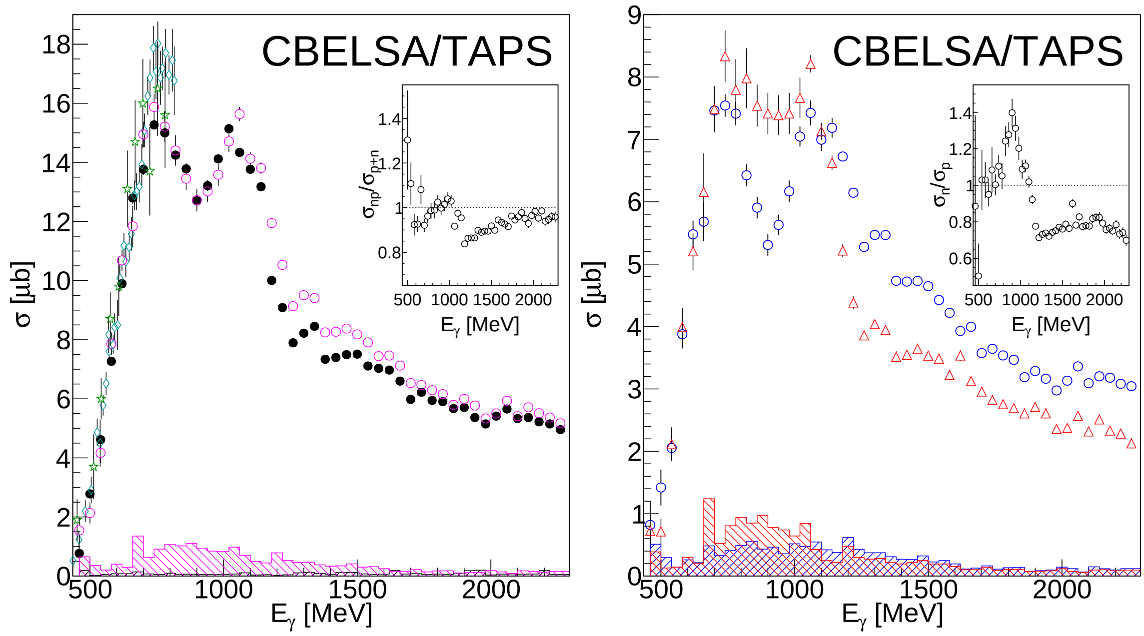

(a) $\gamma N \rightarrow 2\pi^0(N)$ **(b)** $\gamma N \rightarrow 2\pi^0 N$

Figure 7.27: Total cross sections for double π^0 photoproduction as a function of the incident photon energy E_γ. Results from the CBELSA/TAPS data. Left-hand side: solid black circles: quasi-free inclusive reaction from the deuteron. Open magenta circles: sum of exclusive results from proton and neutron. Open green stars: $\gamma d \rightarrow 2\pi^0 np$ MAMI-B 99 [69]. Open cyan diamonds: $\gamma d \rightarrow \pi^0 np$ MAMI-B 2000 [70]. Insert: ratio of quasi-free inclusive to sum of the exclusive cross sections. Right-hand side: open blue circles: exclusive reaction on the proton. Open red triangles: exclusive reaction on the neutron. Insert: ratio of neutron to proton cross sections. The hatched histograms at the bottom indicate the systematic uncertainties of the corresponding cross sections.

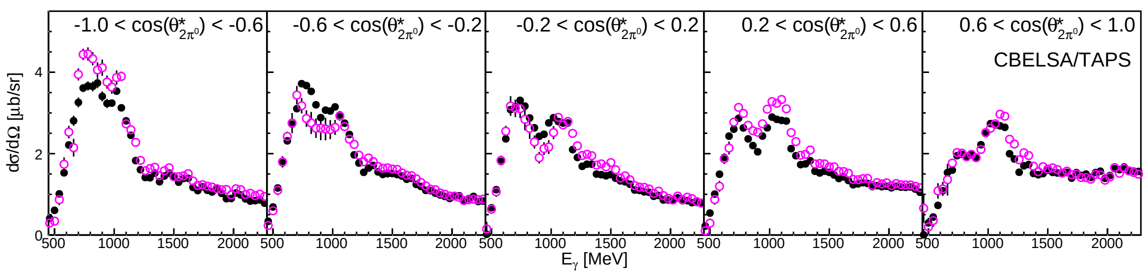

Figure 7.28: Differential cross sections for quasi-free inclusive $2\pi^0$ photoproduction from the deuteron as a function of the incident photon beam energy E_γ. Results from the CBELSA/TAPS data. Solid black circles: quasi-free inclusive reaction from the deuteron. Open magenta circles: sum of exclusive results from proton and neutron.

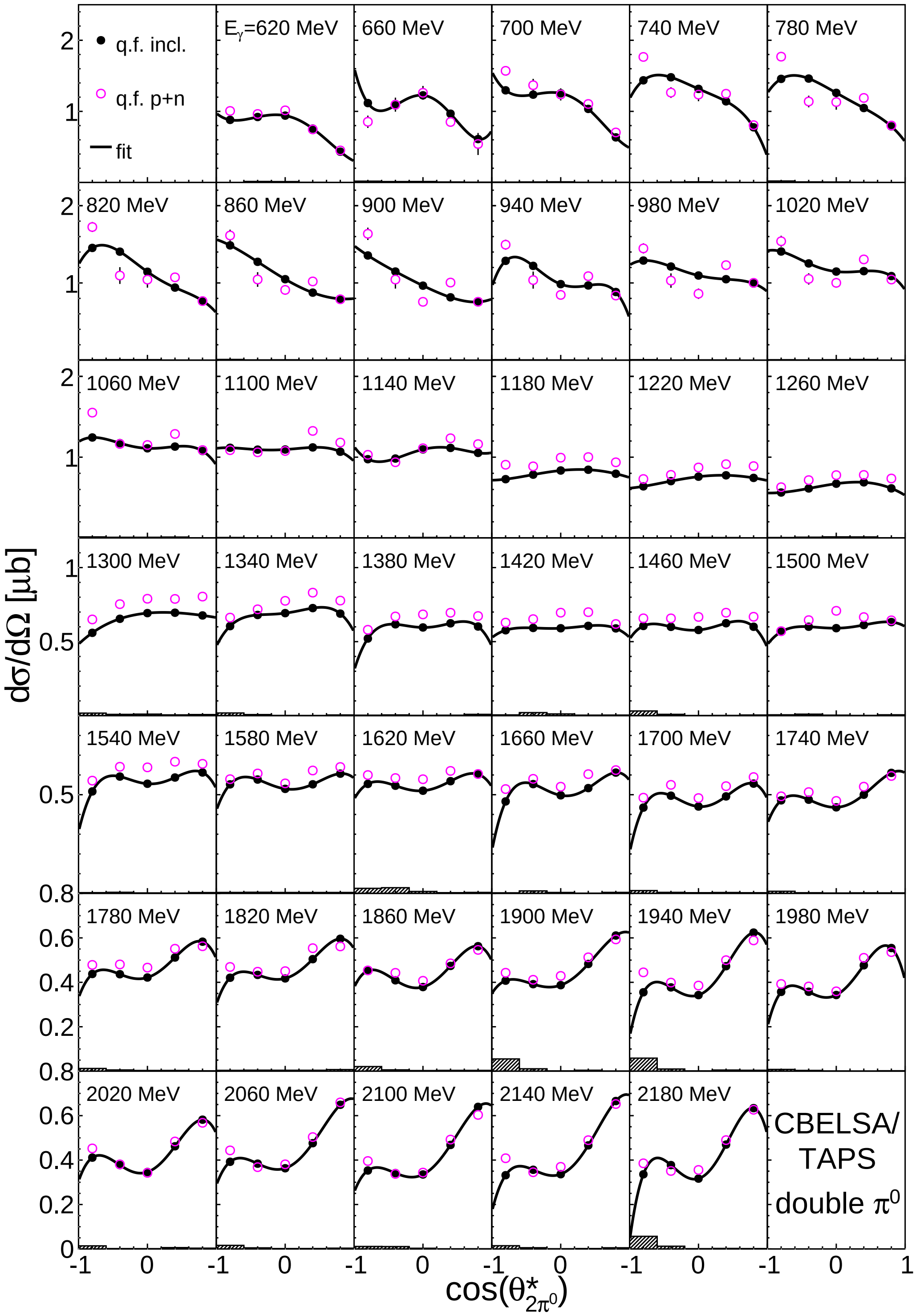

Figure 7.29: Differential cross sections for quasi-free inclusive $2\pi^0$ photoproduction from the deuteron as a function of the polar angle of the pion in the $\pi^0 N$ center of mass system. Results from the CBELSA/TAPS data. Solid black circles: quasi-free inclusive reaction from the deuteron. Open magenta circles: sum of exclusive results from proton and neutron. The hatched histograms at the bottom represent the systematic uncertainties of the quasi-free inclusive result.

Results as a Function of the Final State Invariant Mass W

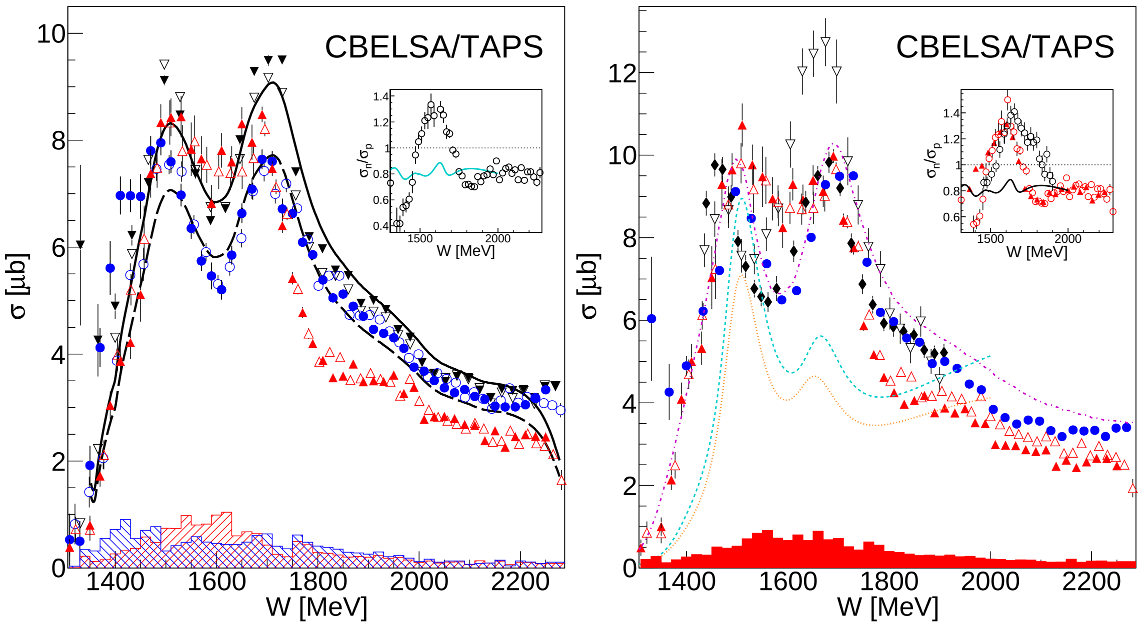

(a) $\gamma N(N) \rightarrow 2\pi^0 N(N)$ **(b)** $\gamma N \rightarrow 2\pi^0 N$

Figure 7.30: Total cross sections for double π^0 photoproduction from free and quasi-free nucleons as a function of the final-state invariant mass $W = \sqrt{s}$. Results from the CBELSA/TAPS data. Left-hand side: open (solid) black triangles: inclusive (exclusive) free proton. Open (solid) blue circles: quasi-free proton from IS (FS). Open (solid) red triangles: quasi-free neutron from IS (FS). Solid (dashed) black line: free proton folded with Fermi motion (scaled with 0.85). Insert: ratio of quasi-free neutron to proton ratio. Solid cyan line: MAID neutron to proton ratio. Right-hand side: blue circles: free proton. Open (solid) red triangles: free neutron from IS (FS). Open black triangles: free proton from GRAAL [68]. Solid black diamonds: free neutron from GRAAL [68]. Dashed cyan (dotted orange) line: MAID proton (neutron) [62]. Dashed-dotted line: BnGa [43]. Insert: ratio of free neutron to proton ratio. Open (solid) red circles (triangles): this work from IS (FS). Open black circles: GRAAL data. Solid black line: MAID neutron to proton ratio. The histograms at the bottom represent the systematic uncertainties of the corresponding cross sections.

Total cross sections as a function of the center of mass energy W have been reconstructed for the exclusive reactions from the final state (FS) according to Equation (6.14) and from the initial state (IS) under the assumption that the participant nucleon was at rest. The results (open symbols: IS reconstruction, full symbols: FS reconstruction) for the proton (blue circles) and the neutron (red circles) are shown in Figure 7.30a. Due to the slightly better energy resolution of the Crystal Barrel calorimeter compared to the Crystal Ball calorimeter from A2, the reconstruction from the final state achieves somewhat less smeared out structures. However, the agreement between both reconstructions is still in very good agreement. The quasi-free proton result is again compared to that of the free proton (black symbols: open triangles: inclusive analysis, full triangles: exclusive analysis) and to the free proton cross section smeared with Fermi motion (solid black line). In accordance with the observations from the A2 analysis but extending to higher energies, the quasi-free proton cross section is suppressed with respect to the free data by 15 %, as indicated by the Fermi smeared result scaled down by a factor of 0.85. The same observation applies for the differential cross sections as a function of the incident photon energy (Figure 7.31) and by that confirms the independence of the effect on photon energy and meson polar angle in the center of mass frame. No accurate information for very low photon energies in the most forward angular bin can be obtained as the poor statistics and small detection efficiencies result in an excess of the differential cross section.

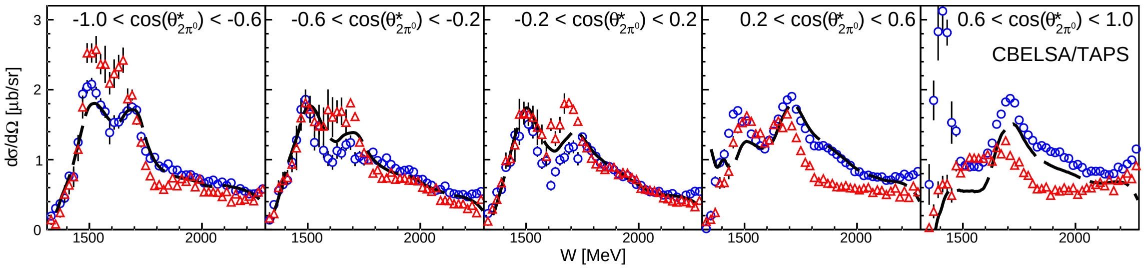

Figure 7.31: Differential cross sections for exclusive $2\pi^0$ photoproduction from quasi-free nucleons as a function of the final state invariant mass W. Results from the CBELSA/TAPS data. Open blue circles: quasi-free proton. Open red triangles: quasi-free neutron. Dashed black line: free proton folded with Fermi motion and scaled with 0.85.

The free neutron cross section was estimated with the same method as discussed in the results of the A2 analysis, in Section 7.3.1. The ratio of the free proton cross section folded with Fermi motion and the quasi-free proton data was applied as a correction factor to the quasi-free neutron data. The correction factor for the pure unfolded ratio (open black circles) and the final ratio (full black circles) is shown in Figure 7.32.

The correction factor is strongly influenced by the statistical fluctuations of the free and quasi-free protons. However, it exhibits by trend the same behavior as seen in the result of the A2 analysis: a slightly decreasing energy dependence with the highest values at medium meson polar angles. Figure 7.30b presents the free proton cross section compared to the resulting estimate for the free neutron as obtained from the correction of the quasi-free neutron data reconstructed from initial state (open red triangles) and final state (full red triangles). Both results are in good agreement and of similar shape and roughly 15% higher than the quasi-free neutron cross section. The comparison with the previous estimate from the GRAAL collaboration [68] disproves their observed enhancement of the free neutron result with respect to the free

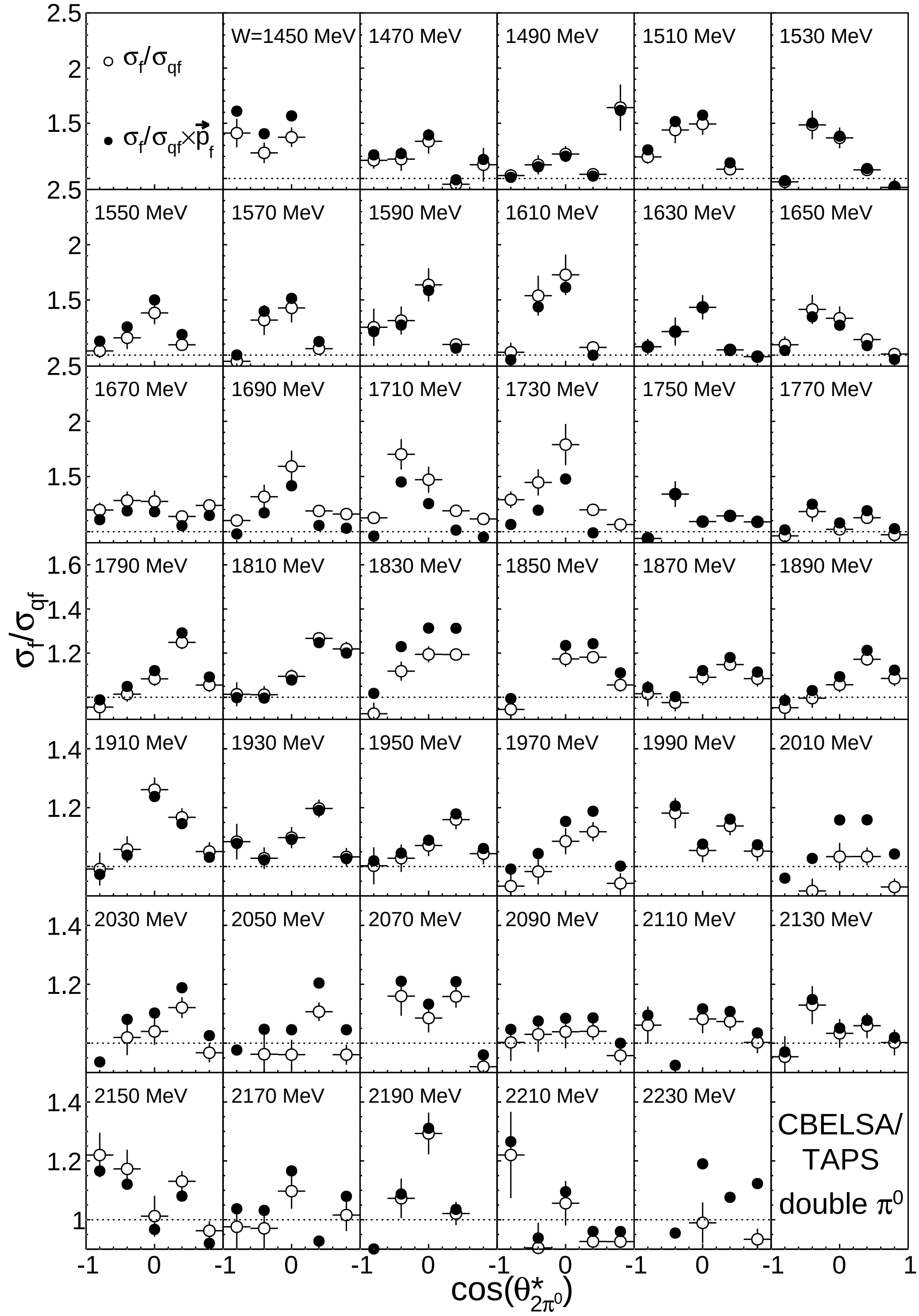

Figure 7.32: Differential ratio of free exclusive $2\pi^0 p$ cross section to the quasi-free $2\pi^0 p(n)$ cross section. Results from the CBELSA/TAPS data. Open circles: bare ratio. Solid circles: ratio obtained from the free cross section smeared with Fermi motion and an additional energy dependent smoothing factor (see Section 6.12).

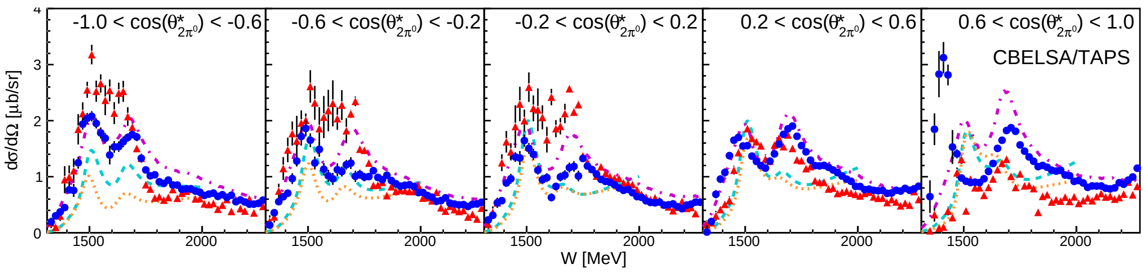

Figure 7.33: Differential cross sections for exclusive $2\pi^0$ photoproduction from the free proton (solid blue circles) and the estimated free neutron (solid red triangles) as a function of the final state invariant mass W. Results from the CBELSA/TAPS data. Notations as in Figure 7.30.

proton.

The energy and angular independent FSI effects are also confirmed by the comparison of the individual differential cross sections of the quasi-free and free nucleons normalized to the corresponding cross section as shown in Figure 7.35. For all energies, the free and quasi-free results are in reasonable good agreement. Furthermore, as already observed at the results from the A2 analysis (Figure 7.22) up to energies of $W \approx 1600$ MeV the proton and neutron results are of similar shape, but at higher energies, i.e. in the third resonance peak, start to differ. In contrast to the A2 data, for which the available photon beam energies only provided data up to $W \approx 1900$ MeV, the CBELSA/TAPS data now reveal that at energies beyond the third resonance, i.e. at $W \approx 2050$ MeV, the proton and neutron results recover similar shape. For all energies, the BnGa model describes the proton data rather well and agreement with the MAID model is generally poor for proton and neutron. Due to the similarity of the free and quasi-free differential cross sections, the Legendre coefficient ratios obtained from the fit of the differential cross sections are almost identical, as shown in Figure 7.34. Almost no change at all is seen in coefficients B_1 and B_2 and small deviations mainly occur at low energies in the coefficients B_3 and B_4.

Differential cross sections as a function of the invariant mass of the $N\pi^0$ and $\pi^0\pi^0$ pairs are shown in Figures 7.36 and 7.37, respectively. They were normalized to the corresponding total cross sections and are compared to the results from the free proton and to the theoretical model predictions. Overall, good agreement between the free and quasi-free proton is visible. The shapes of the proton and neutron cross section are almost identical from threshold up to energies of about $W \approx 1600$ MeV, corresponding to energies above the second resonance region, close to the valley between the two bumps. For energies throughout the third resonance region until $W \approx 1900$ MeV, the neutron result has a more pronounced peak at the mass of the $\Delta(1232)$ resonance. The higher incident photon beam energies achieved with the ELSA accelerator open access to higher lying excited states. For center of mass energies above $W \approx 1900$ MeV, contributions of many resonances with intermediate $\Delta\pi^0$ or $N\pi^0$ states (e.g. $\Delta(1600)3/2^+$, $\Delta(1620)1/2^-$, $\Delta(1700)3/2^-$ or $N(1650)1/2^-$, $N(1675)5/2^-$, $N(1680)5/2^+$, $N(1720)3/2^+$ might play a role) can be observed, but due to the statistical fluctuations, are hard to resolve. Within these fluctuations, the

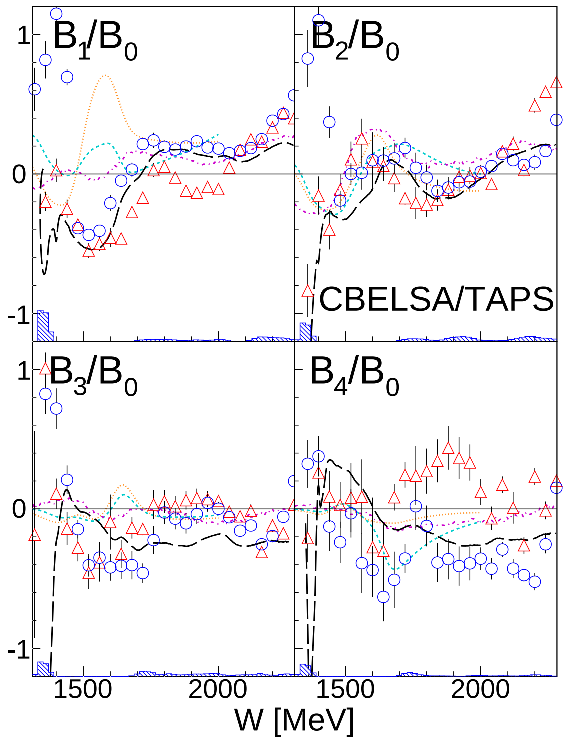

(a) $\gamma N(N) \rightarrow 2\pi^0 N(N)$

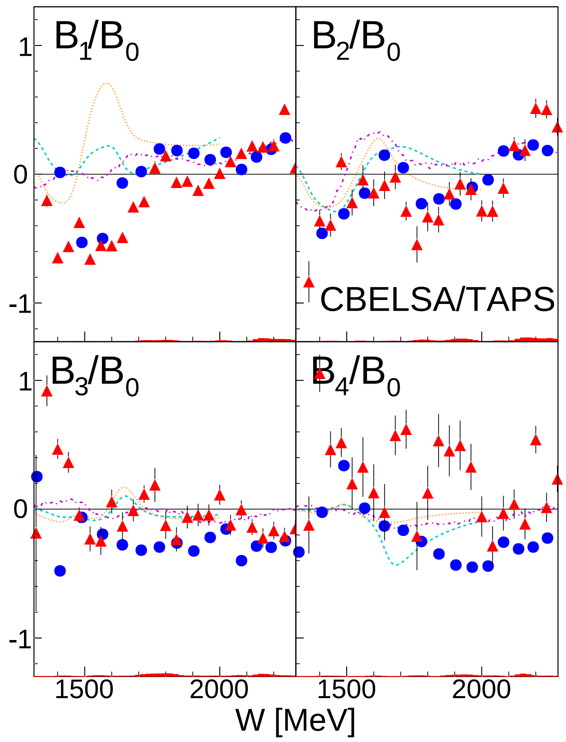

(b) $\gamma N \rightarrow 2\pi^0 N$

Figure 7.34: Legendre coefficient ratios for double π^0 photoproduction as a function of the final-state invariant mass $W = \sqrt{s}$. Results from the CBELSA/TAPS data. Left-hand side: exclusive reactions on quasi-free nucleons. Right-hand side: exclusive reactions on the free nucleons. Notations as in Figure 7.30. The histograms at the bottom represent the systematic uncertainties of the corresponding results.

shapes of the free and quasi-free proton and the quasi-free neutron are in comparable agreement.

The total and differential cross sections were also decomposed into the contributions from the phase-space and sequential decays via the intermediate $\Delta(1232)3/2^+\pi^0$ and $N(1520)3/2^-\pi^0$ states. The relative contributions from the fit of the simulated line shapes of the different components to the invariant mass distributions according to Equation (6.16) were used to extract the individual contributions to the cross sections. The resulting decomposition of the total cross sections are shown in Figure 7.38 and of the differential cross sections as a function of the center of mass energy in Figure 7.39. Even though CBELSA/TAPS has less statistics than the A2 data, the results are in good agreement. The achieved decomposition nicely reproduces the results of the PWA of the previous ELSA data [59] and shows the completely different origin of the bump of the proton and neutron cross sections in the third resonance region. The first bump in the second resonance region of both cross sections is entirely dominated by contributions from the $\Delta(1232)3/2^+\pi^0$ intermediate states. With increasing energy for the proton, the contributions of the sequential decay

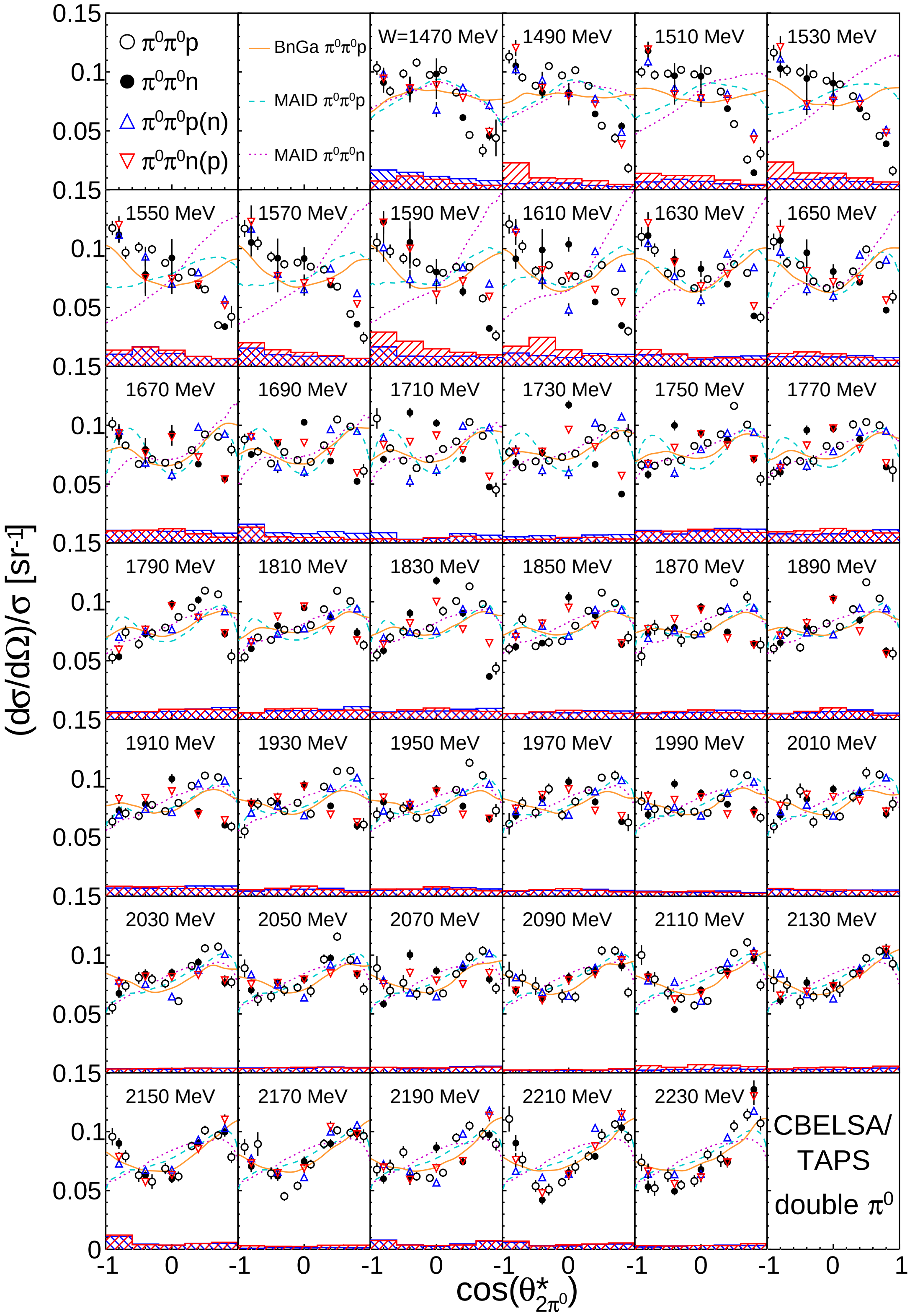

Figure 7.35: Normalized differential cross sections for exclusive $2\pi^0$ photoproduction from free and quasi-free nucleons as a function of the polar angle of the pion in the $2\pi^0p$ center of mass system. Results from the CBELSA/TAPS data. Notations are given in the Figure. The hatched histograms at the bottom represent the systematic uncertainties of the quasi-free results.

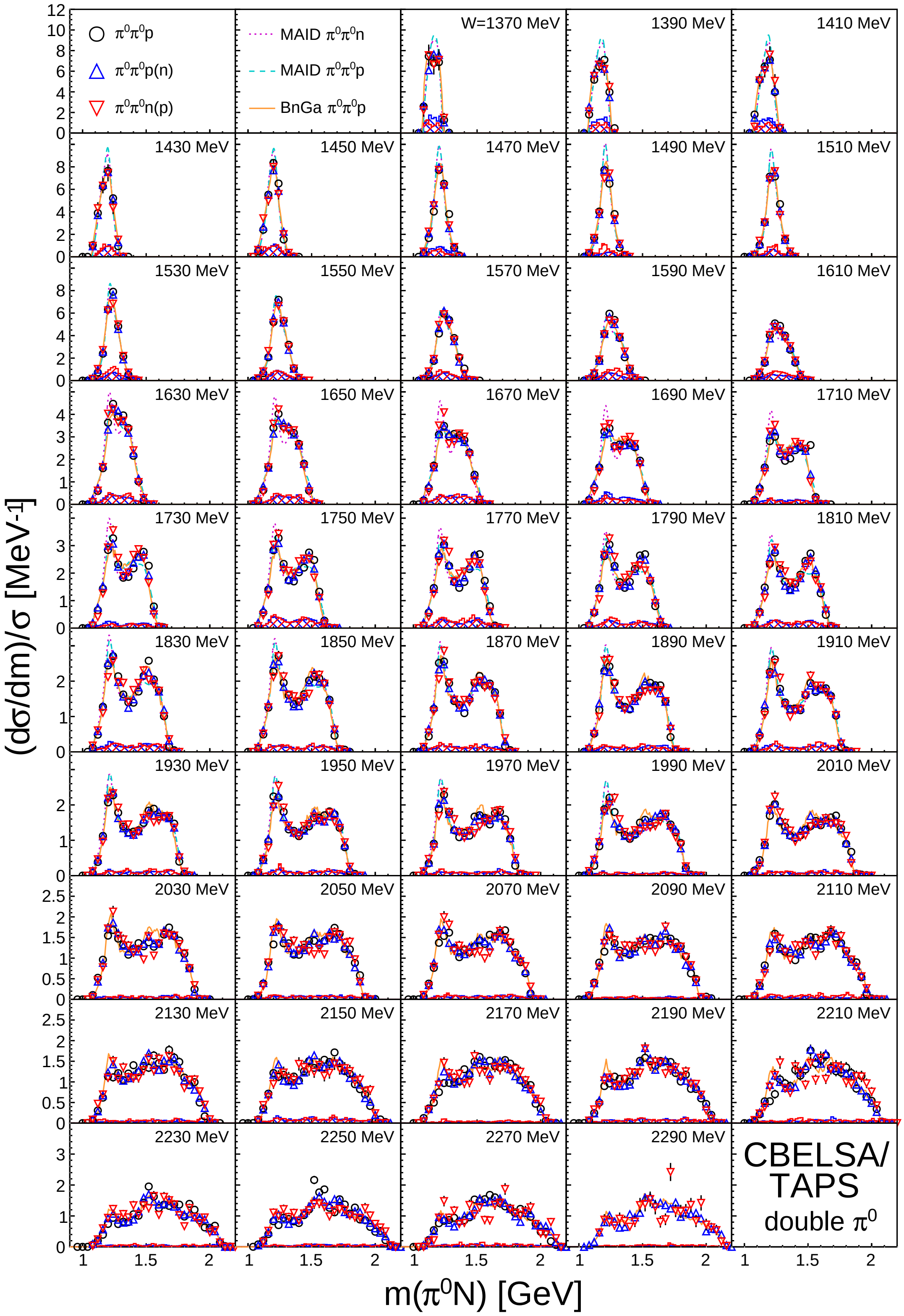

Figure 7.36: Normalized differential cross sections for exclusive $2\pi^0$ photoproduction from the free proton and from quasi-free nucleons as a function of the $N\pi^0$ invariant mass. Results from the CBELSA/TAPS data. Notations are given in the Figure. The hatched histograms at the bottom represent the systematic uncertainties of the quasi-free results.

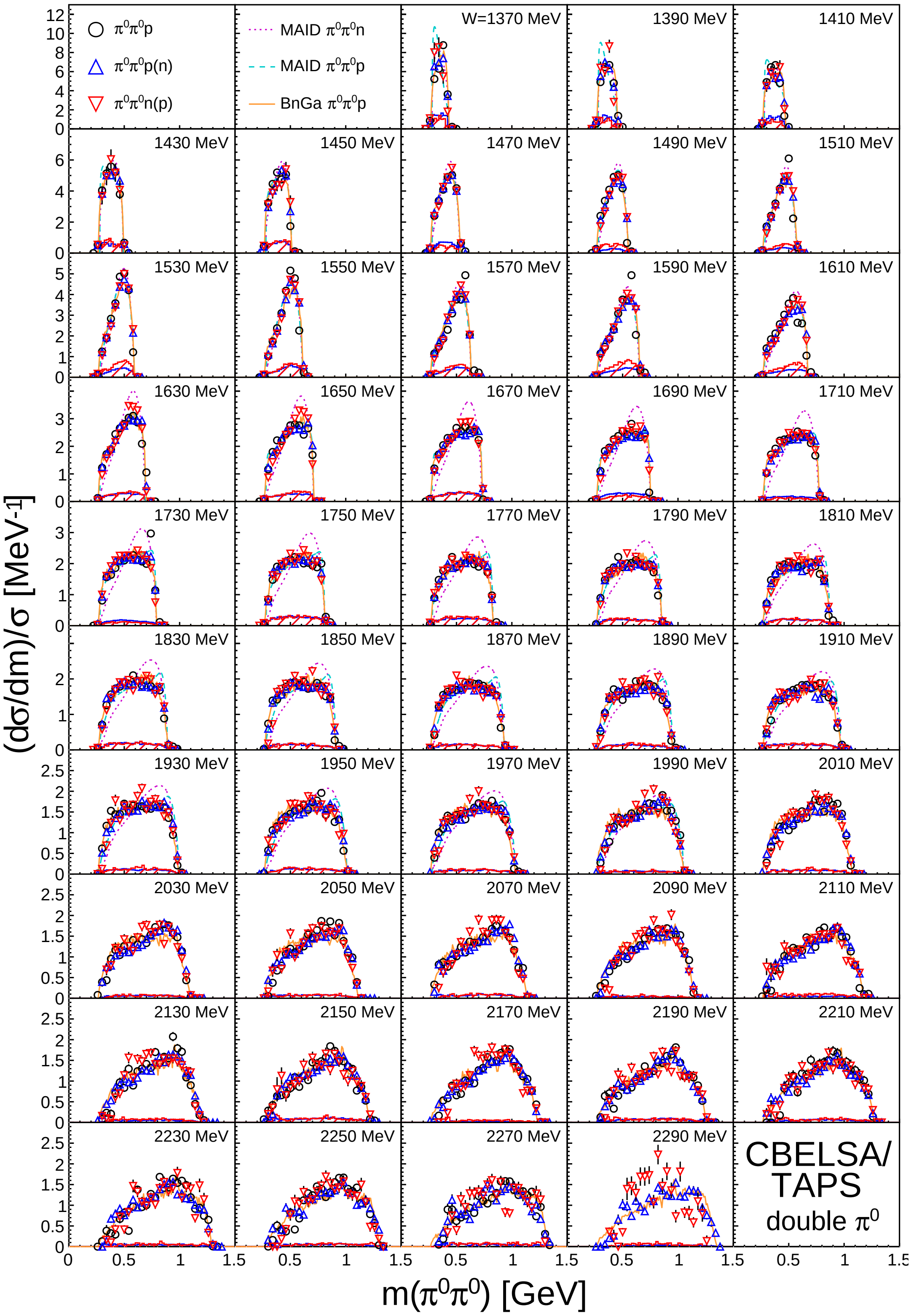

Figure 7.37: Normalized differential cross sections for exclusive $2\pi^0$ photoproduction from the free proton and from quasi-free nucleons as a function of the $\pi^0\pi^0$ invariant mass. Results from the CBELSA/TAPS data. Notations are given in the Figure. The hatched histograms at the bottom represent the systematic uncertainties of the quasi-free results.

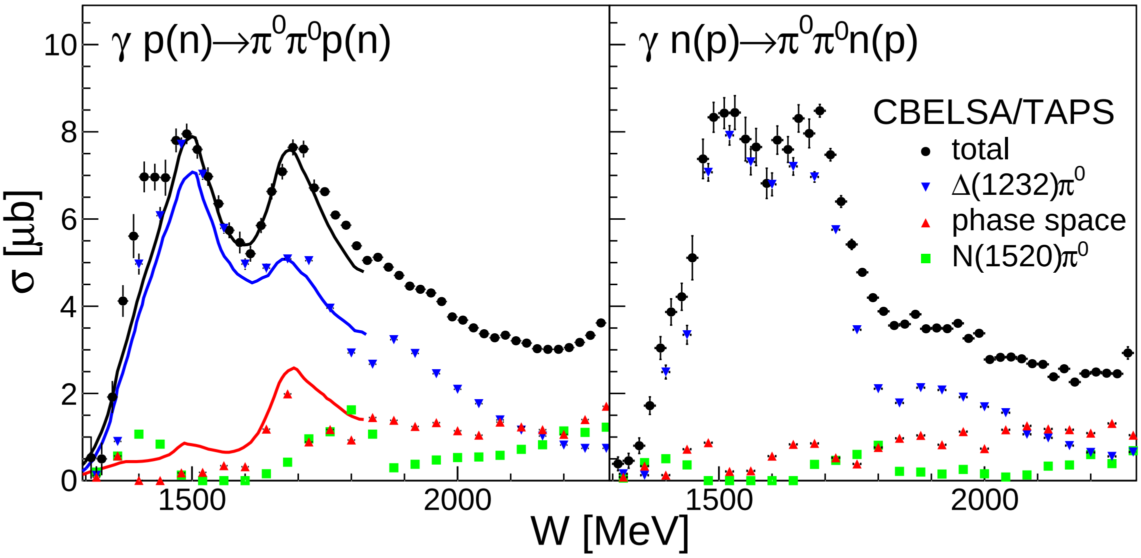

Figure 7.38: Contributions of $\gamma N \to \Delta(1232)\pi^0 \to N\pi^0\pi^0$ (blue triangles), $\gamma N \to N\pi^0\pi^0$ (red triangles) and $\gamma N \to N(1520)\pi^0 \to N\pi^0\pi^0$ (green squares) to the $2\pi^0$ total cross section (black circles) for quasi-free protons (left-hand side) and quasi-free neutrons (right-hand side). Solid lines: corresponding results from a PWA from previous ELSA proton data [59]. Results from the CBELSA/TAPS data.

via the $\Delta(1232)3/2^+\pi^0$ state decrease. They are accompanied by slowly increasing contributions from the $N(1520)3/2^-\pi^0$ intermediate state and the resonant contribution of the phase space component, which primarily causes the bump structure in the third resonance region. For the neutron, the contributions from phase space and the $N(1520)3/2^-\pi^0$ intermediate state increase with energy, but the second and third resonance region are throughout dominated by the strong contribution from the $\Delta(1232)3/2^+\pi^0$ intermediate state.

The relative contributions are also visible in the angular behavior of the individual contributions and are in reasonable agreement with the observations from A2. Additionally, the decomposition gives an explanation of the recovered shape of the differential cross sections at energies beyond the third resonance region for which no conclusion from the A2 data was possible. In the high energy tail of the cross section, the contributions of the individual components of the proton and neutron cross section become very similar. The dominant $\Delta(1232)3/2^+$ intermediate state only contributes to roughly 50%, but is slowly decreasing with energy whereas the phase space and $N(1520)3/2^-$ components slowly increase. Except for the third resonance region, the physical processes behind the reaction on the proton and neutron seem to be identical in nature and result in comparable total and differential cross sections. The main difference between the magnitude and angular distributions of the proton and neutron seem to originate from the excitation of the $N(1680)5/2^+$ resonance for the proton and that of the $N(1675)5/2^-$ resonance for the neutron that decay either via phase space (proton) or the $\Delta(1232)3/2^+\pi^0$ intermediate state (neutron).

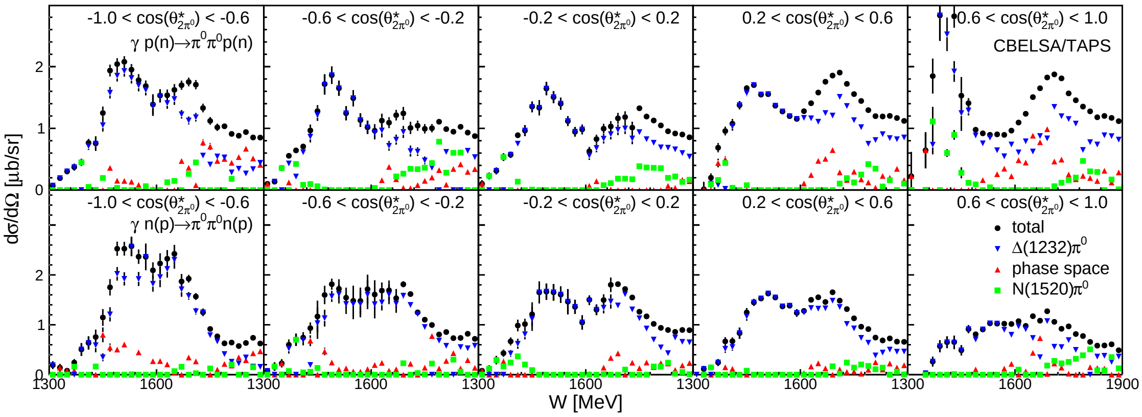

Figure 7.39: Contributions of $\gamma N \to \Delta(1232)\pi^0 \to N\pi^0\pi^0$ (blue triangles), $\gamma N \to N\pi^0\pi^0$ (red triangles), and $\gamma N \to N(1520)\pi^0 \to N\pi^0\pi^0$ (green squares) to the $2\pi^0$ differential cross sections as function of the final state invariant mass W (black circles) for quasi-free protons (upper two rows) and quasi-free neutrons (lower two rows). Results from the CBELSA/TAPS data.

A full set of differential cross sections for the quasi-free proton and neutron as well as for the free neutron are shown in the Appendix, in Figures D.16 - D.18 and are compared to the results from the A2 data in Figures D.19 - D.21. Differential cross sections as function of the $N\pi^0$ and $\pi^0\pi^0$ invariant mass are compared to those from A2 in Figure D.23, D.24 and Figures D.26, D.27.

7.3.3 Comparison of the A2 and CBELSA/TAPS Data

In this section, the most important results from the analysis of double π^0 photoproduction from quasi-free protons and neutrons from the A2 and CBELSA/TAPS data will be directly compared and discussed. From the discussion and comparison of the individual results with former data (Sections 7.3.1 and 7.3.2), a general agreement can already be expected. Nevertheless, only a direct comparison will allow for a quantitative investigation of the systematic quality of the results.

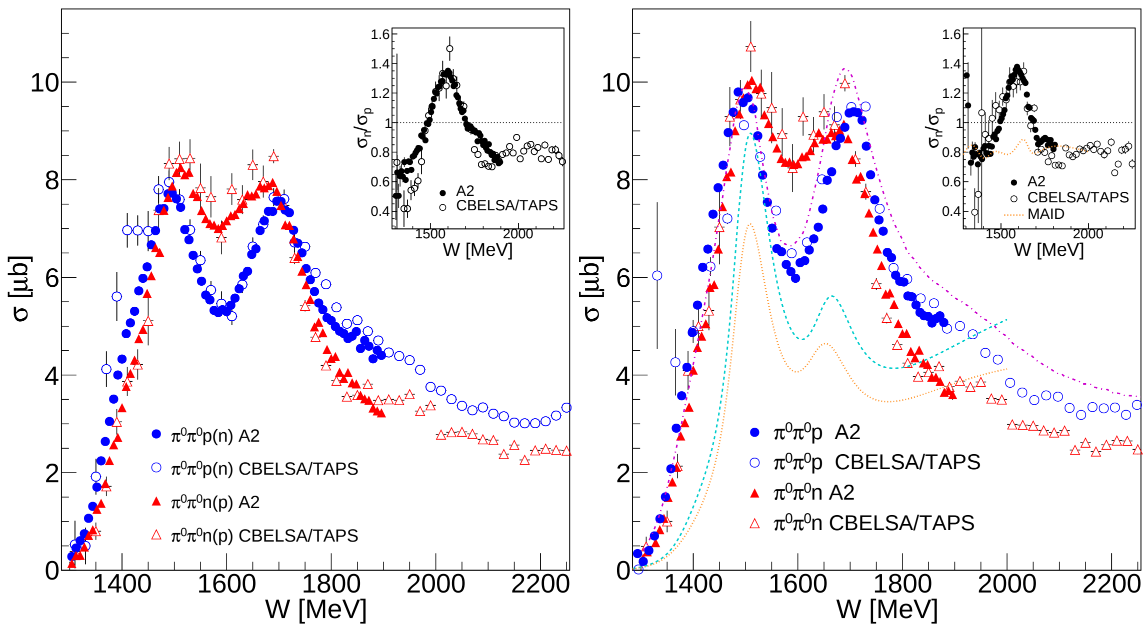

(a) $\gamma N(N) \rightarrow 2\pi^0 N(N)$ **(b)** $\gamma N \rightarrow 2\pi^0 N$

Figure 7.40: Total cross sections for double π^0 photoproduction from free nucleons (right-hand side) and quasi-free nucleons (left-hand side) as a function of the final-state invariant mass $W = \sqrt{s}$. Results from the A2 data (solid symbols) and CBELSA/TAPS data (open symbols). Dashed cyan (dotted orange) line: MAID proton (neutron) [62]. Dashed-dotted magenta line: BnGa [43]. Inserts: ratio of (quasi-free) free neutron to proton ratio. Dashed orange line: MAID neutron to proton ratio.

Figure 7.40 shows the total cross sections for free (right-hand side) and quasi-free (left-hand side) photoproduction from the A2 (full symbols) and CBELSA/TAPS data (open symbols). The free cross sections are also compared to the predictions from the BnGa coupled-channel PWA (only proton) [43] and the MAID isobar model [62]. As previously discussed, the MAID model clearly misses important resonance contributions and highly underestimates the measured cross sections, especially in the third resonance region. In contrast, the BnGa solution for the proton is in much better agreement with the free proton data, most notably compared to the

CBELSA/TAPS result, which is reasonable as it was fit to previous CBELSA/TAPS data. The insert in both figures shows the ratio of the quasi-free (qf) and free (f) neutron to proton cross sections, which have to be equal by definition of the correction factor $r_p = \sigma_{fp}/\sigma_{qfp}$ as it holds:

$$\frac{\sigma_{fn}}{\sigma_{fp}} = \frac{r_p \cdot \sigma_{qfn}}{\sigma_{fp}} = \frac{\frac{\sigma_{fp}}{\sigma_{qfp}} \cdot \sigma_{qfn}}{\sigma_{fp}} = \frac{\sigma_{qfn}}{\sigma_{qfp}} \; . \tag{7.1}$$

The small deviations are due to the subsequent fitting of the free and quasi-free differential cross sections with the Legendre series. Also shown is the ratio of the predicted solution by the MAID isobar model (dotted orange curve), which does not observe the strong suppression of the proton cross section in between the second and third resonance region, contrary to the measured results.

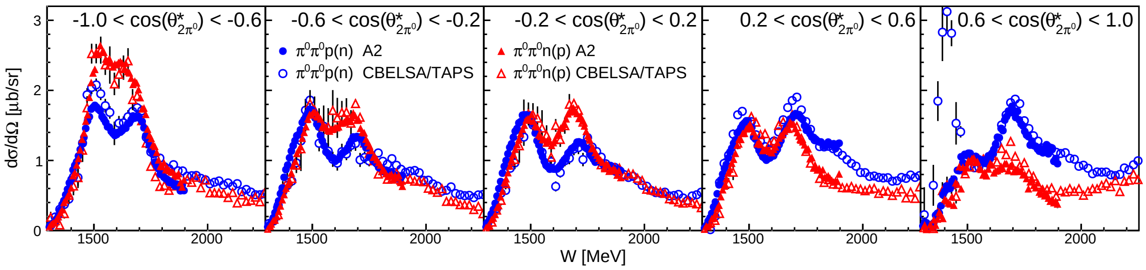

(a) $\gamma N(N) \rightarrow 2\pi^0 N(N)$

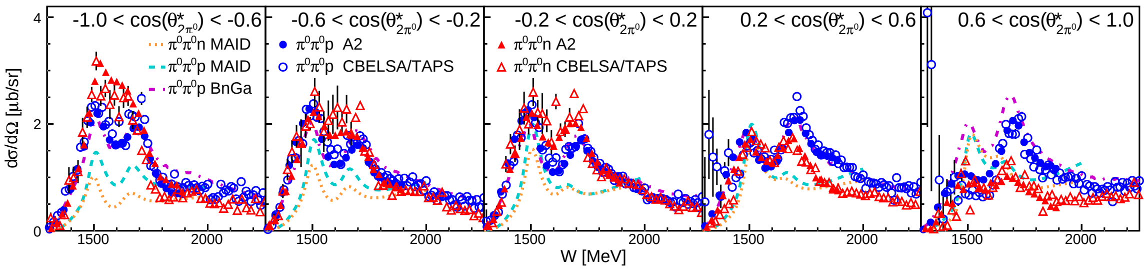

(b) $\gamma N \rightarrow 2\pi^0 N$

Figure 7.41: Differential cross sections for exclusive $2\pi^0$ photoproduction from quasi-free nucleons (a) and free nucleons (b) as a function of the final state invariant mass W. Results from the A2 data (solid symbols) and CBELSA/TAPS data (open symbols). Dashed cyan (dotted orange) line: MAID proton (neutron) [62]. Dashed-dotted magenta line: BnGa [43].

The results for the quasi-free (left-hand side) and free (right-hand side) proton and neutron cross sections from the individual analyses of both experiments are in good agreement. The biggest discrepancies can be found close to threshold, where the proton data from CBELA/TAPS is systematically too large due to the lack of statistics. In addition, the free proton cross section from CBELSA/TAPS exhibits a somewhat higher bump in the third resonance region. As previously mentioned in Section 7.2 (see Figure 7.12), the differences between the available results and the solution from the BnGa model in general are the most sizeable in this region. Although the effect is within the systematic uncertainties, it is unclear whether the discrepancies are due to effects from resolution or the detection of the recoil nucleons. Overall, the quasi-free and free cross sections are in reasonable good agreement and do not show any significant deviation. Both results obtained a reduction of the quasi-free cross section of 15 % with respect to the free result, which is nearly independent of energy and angle.

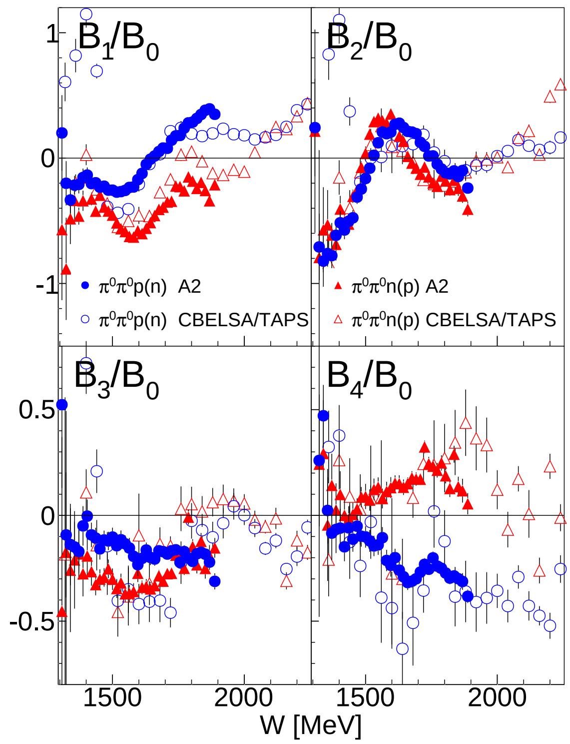

(a) $\gamma N(N) \to 2\pi^0 N(N)$

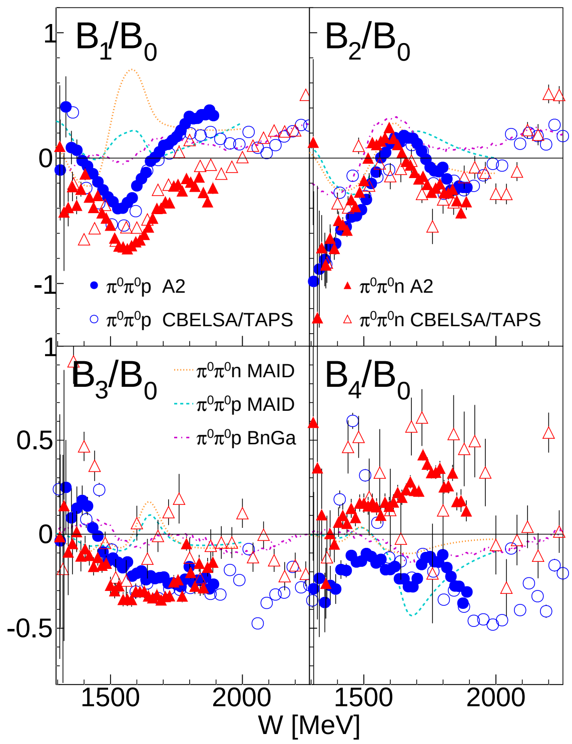

(b) $\gamma N \to 2\pi^0 N$

Figure 7.42: Legendre coefficient ratios for double π^0 photoproduction from quasi-free nucleons (a) and free nucleons (b) as a function of the final state invariant mass W. Results from the A2 data (solid symbols) and CBELSA/TAPS data (open symbols). Dashed cyan (dotted orange) line: MAID proton (neutron) [62]. Dashed-dotted magenta line: BnGa [43]

In Figure 7.41, the quality of the agreement of the quasi-free and free cross sections from the A2 and CBELSA/TAPS data is demonstrated by means of the differential cross sections as a function of the center of mass energy W. Reasonable agreement between the A2 and CBELSA/TAPS results was achieved for all angular bins. The differential cross sections demonstrate the different angular dependence of the individual contributions to the proton and neutron cross sections. For the neutron cross section, mainly the overall magnitude depends on the angle and has the largest values at meson backward angles. For the proton, the first bump behaves in a similar way, but the second bump increases in height towards forward meson

angles. This can be explained with the different mechanisms that were observed in the decomposition of the cross sections into the phase space and sequential decay components. It was observed (see Figures 7.25 and 7.38) that the first peak in both cross sections is dominated by contributions from the $\Delta(1232)3/2^+$ intermediate state, but the second peak results from resonant phase space contributions for the proton, and the $\Delta(1232)3/2^+$ contributes for the neutron. The angular dependence of the decomposition (Figures 7.26 and 7.39) revealed that the phase space and $N(1520)3/2^-$ contributions grow towards meson forward angles and thus nicely explains the angular dependence of the differential cross sections.
The Legendre coefficient ratios obtained from the fit of the differential cross sections are compared in Figure 7.42. Almost identical coefficient ratios were obtained for the fit of the quasi-free (see Figure 7.42a) and free (see Figure 7.42b) data. Even though the results from the fit of the CBELSA/TAPS data have rather larger statistical error bars, the coefficient ratios are in relatively good agreement. The largest discrepancies are visible in the ratio of the third coefficient B_3/B_0, which is most likely due to its sensitivity to the very forward and backward angles, where slight discrepancies in the differential cross sections are visible.

Differential cross sections as a function of the meson polar angle $\theta^*_{2\pi^0}$ in the center of mass frame and the comparison of the differential cross sections as a function of the nucleon-pion and pion-pion pairs for the individual reactions are shown in the Appendix D.2.1. Except for the first few energy bins, where due to the lack of the statistics of the CBELSA/TAPS data discrepancies in magnitude occur. However, the distributions for all reactions are in good agreement. The distributions are also compared to the model predictions from BnGa [43] and MAID [62]. Whereas the BnGa solution is in reasonable agreement with the shape and magnitude of the proton data, the MAID model only more or less agrees in shape, but drastically underestimates the results.

7.4 Double Polarization Observables for π^0 Photoproduction

In this section, the results from the analysis of single π^0 photoproduction from longitudinally polarized protons and neutrons inside deuterated butanol will be presented. The exclusive reactions $\gamma p(n) \to \pi^0 p(n)$ and $\gamma n(p) \to \pi^0 n(p)$ were analyzed for all deuterated butanol beamtimes from A2 (July 2013, February 2014, and March 2015) to extract the polarization weighted difference of the helicity dependent cross sections σ_{diff}, according to Equation (6.54), and the (not polarization weighted) sum of the helicity dependent cross sections σ_{sum}, according to Equation (6.55). In addition, the helicity dependent cross sections $\sigma_{1/2}$ and $\sigma_{3/2}$ were extracted directly, using Equations (6.60) and (6.61). Since σ_{sum} and the directly measured $\sigma_{1/2}$ and $\sigma_{3/2}$ contain contributions from reactions on the unpolarized nuclei of the deuterated butanol molecule, the same reactions were identically analyzed for the carbon foam beamtime (February 2014). The carbon background was then subtracted by absolute normalization of the corresponding data, as discussed in Section 6.13.4.

The results presented in this section were then obtained using the extracted cross sections σ_{diff}, σ_{sum}, $\sigma_{1/2}$, and $\sigma_{3/2}$ as well as the unpolarized cross sections σ_{unpol}, as discussed in Section 7.1. From these quantities, the final helicity dependent cross sections $\sigma_{1/2}$ and $\sigma_{3/2}$ were determined in four distinct versions (see Equations (6.58), (6.59), (6.60) and (6.61)) and the double polarization observable E in three different ways (see Equations (6.56), (6.57) and (6.62)). The different versions are summarized in Table 6.12.
As a normalization cross check, the unpolarized total cross section $\sigma_{\text{unpol}} = 0.5 \cdot (\sigma_{1/2} + \sigma_{3/2})$ was reconstructed from the four versions for the helicity dependent cross sections $\sigma_{1/2}$ and $\sigma_{3/2}$. However, as two of the four versions for $\sigma_{1/2}$ and $\sigma_{3/2}$ (version 1 and version 2) use the extracted observable E together with the unpolarized cross section σ_{unpol} itself, the cross check is redundant and not considered.
The four versions of the extracted helicity dependent cross sections $\sigma_{1/2}$ and $\sigma_{3/2}$, the three versions of the determined double polarization observable E, and the two reconstructed unpolarized cross sections compared to the reference cross section σ_{unpol} are shown in Figures 7.43 and 7.44 for the exclusive reaction on the proton and neutron, respectively. The corresponding results as a function of the incident photon energy are shown in the Appendix D.1.2. The error bars correspond to the statistical errors, the systematic uncertainties are shown as the gray histogram at the base line of each figure. In addition, the results are compared to the predictions from the SAID partial wave analysis [39], the MAID unitary isobar model [40], and the Bonn-Gatchina (BnGa) coupled-channel partial wave analysis (proton: [43], neutron: [38]).
For the reaction on the proton and the neutron, all different versions of the extraction are in perfect agreement. Small deviations occur at very low energies, where effects from the different Crystal Ball energy sum thresholds play an important role, and at the highest energies, which are sensitive to effects from the folding of the different photon fluxes with Fermi motion (and are not visible as a function of the

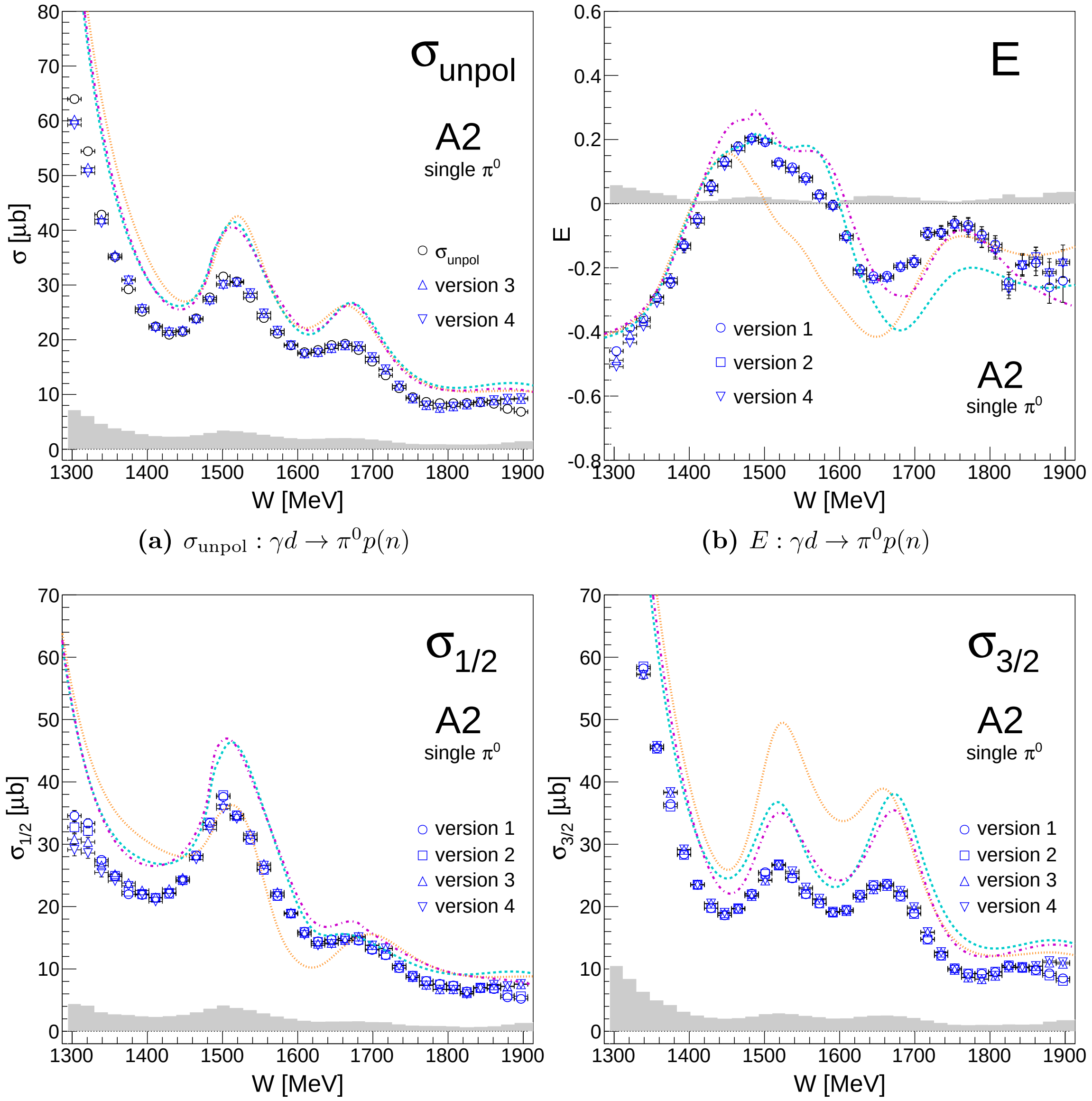

(a) $\sigma_{\text{unpol}} : \gamma d \to \pi^0 p(n)$ **(b)** $E : \gamma d \to \pi^0 p(n)$

(c) $\sigma_{1/2} : \gamma d \to \pi^0 p(n)$ **(d)** $\sigma_{3/2} : \gamma d \to \pi^0 p(n)$

Figure 7.43: Double polarization observables for single π^0 photoproduction from quasi-free protons as a function of the final state invariant mass W. Results from the A2 data. (a) Reconstructed unpolarized total cross section σ_{unpol}. (b) Double polarization observable E. (c) Helicity dependent cross section $\sigma_{1/2}$. (d) Helicity dependent cross section $\sigma_{3/2}$. The different versions are summarized in Table 6.12. Dotted orange line: MAID [40]. Dashed cyan line: SAID [39]. Dashed-dotted magenta line: BnGa [43]. The gray histogram at the base line of each figure represents the systematical uncertainties of the results.

incident photon energy in Figures D.8 and D.9). The good agreement of the different versions puts stringent limits on the systematic uncertainties of the results. As the different versions involve completely different analysis methods and even different beamtimes, the difference of the methods is a highly representative measure of the systematic quality of the results. The gray histogram at the bottom of each figure represents the systematic error that was determined from the maximal deviation of the different versions and the uncertainty of the polarization values (see Section 6.16.3) and is dominated by the systematic error of the degree of beam and target polarization.

Version 1 was determined from the measured difference of the helicity dependent cross sections σ_{diff} from the weighted average of the deuterated butanol beamtimes and the unpolarized cross section σ_{unpol} obtained from the weighted average of the different liquid deuterium data. The normalization with the unpolarized cross section is possible since the contributions of the reactions on unpolarized nuclei in the target cancel out in the difference (see Equation (6.52)). By that, this version is independent on the estimation of the carbon background, but strongly relies on the delicate absolute normalization of the deuterated butanol and the liquid deuterium data. Whereas the normalization of the liquid deuterium data can be checked by comparing the obtained total cross section with measured or published cross sections, the appropriate normalization of the deuterated butanol data is not guaranteed in this way.

Version 2 is the most straightforward version and is nearly independent of normalization. It makes use of the measured difference σ_{diff} and sum σ_{sum} of the helicity dependent cross sections $\sigma_{1/2}$ and $\sigma_{3/2}$ that were obtained from the same dataset. The double polarization observable E was determined as the ratio of the difference and the sum. In this way, apart from asymmetries in the helicity states of the photon beam, normalization of the individual quantities is unessential and by the definition of E is guaranteed. From the obtained double polarization observable E, the helicity dependent cross sections are then given by $\sigma_{1/2} = \sigma_{\mathrm{unpol}} \cdot (1 + E)$ and $\sigma_{3/2} = \sigma_{\mathrm{unpol}} \cdot (1 - E)$. If the unpolarized cross section is properly normalized, the same applies for the resulting helicity dependent cross sections. However, the sum σ_{sum} contains contributions from the carbon background that first has to be subtracted. This represents the sensitive part of this version.

In version 3, E is as well determined from the ratio of σ_{diff} and σ_{sum} and is identical to that from version 2. However, the helicity dependent cross sections are determined from $\sigma_{1/2} = 0.5 \cdot (\sigma_{\mathrm{sum}} + \sigma_{\mathrm{diff}})$ and $\sigma_{3/2} = 0.5 \cdot (\sigma_{\mathrm{sum}} - \sigma_{\mathrm{diff}})$. By that this version relies on the proper normalization of the deuterated butanol data.

Version 4 is the most elegant but also the most delicate one. All other versions make use of the polarization weighted difference σ_{diff} (which is free of contributions from unpolarized nucleons) and then use either the unpolarized cross section or the sum σ_{sum} (contaminated with carbon background), which was not weighted with the polarization degree. The latter is the crucial part since in the analysis, the individual counts are weighted with the degree of polarization on an event by event basis. As it is not known which events occur on unpolarized nucleons, it is important to only apply the weight to those quantities (i.e. σ_{diff}) for which the carbon background

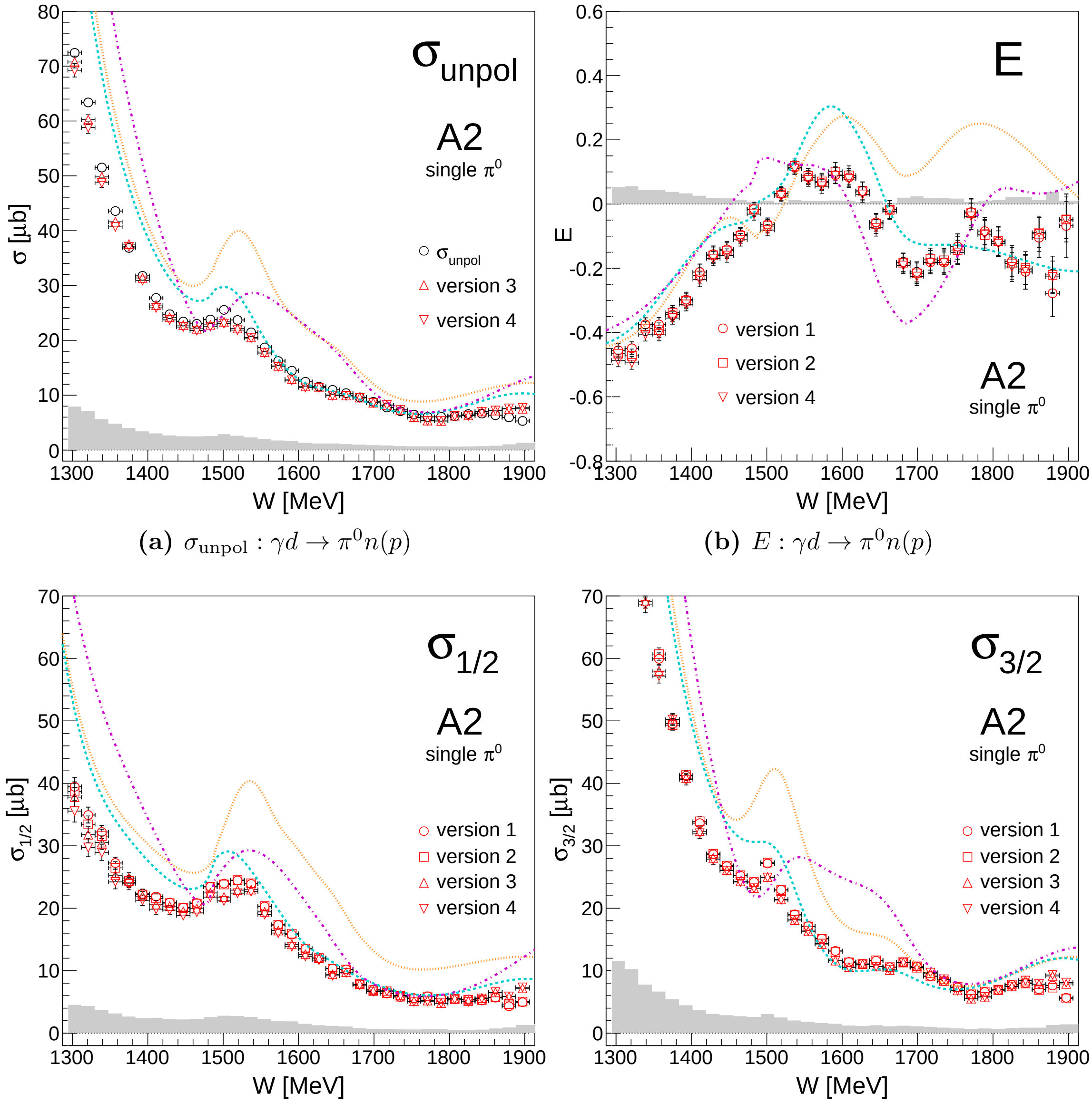

(a) $\sigma_{\text{unpol}} : \gamma d \to \pi^0 n(p)$ **(b)** $E : \gamma d \to \pi^0 n(p)$

(c) $\sigma_{1/2} : \gamma d \to \pi^0 n(p)$ **(d)** $\sigma_{3/2} : \gamma d \to \pi^0 n(p)$

Figure 7.44: Double polarization observables for single π^0 photoproduction from quasi-free neutrons as a function of the final state invariant mass W. Results from the A2 data. (a) Reconstructed unpolarized total cross section σ_{unpol}. (b) Double polarization observable E. (c) Helicity dependent cross section $\sigma_{1/2}$. (d) Helicity dependent cross section $\sigma_{3/2}$. The different versions are summarized in Table 6.12. Dotted orange line: MAID [40]. Dashed cyan line: SAID [39]. Dashed-dotted magenta line: BnGa [38]. The gray histogram at the base line of each figure represents the systematical uncertainties of the results.

cancels out. Otherwise, the carbon foam data has to be weighted with an average inverse weight, which is not exact and allows for unnecessary sources of systematic

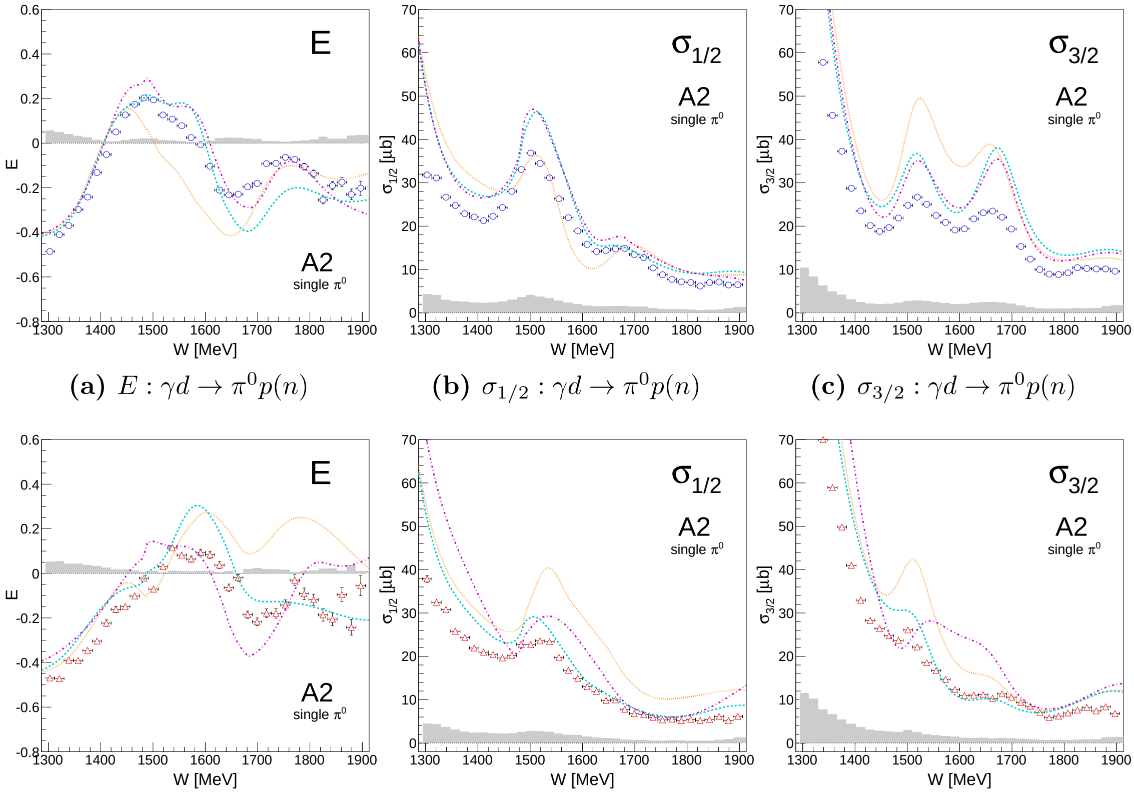

(a) $E : \gamma d \rightarrow \pi^0 p(n)$ **(b)** $\sigma_{1/2} : \gamma d \rightarrow \pi^0 p(n)$ **(c)** $\sigma_{3/2} : \gamma d \rightarrow \pi^0 p(n)$

(d) $E : \gamma d \rightarrow \pi^0 n(p)$ **(e)** $\sigma_{1/2} : \gamma d \rightarrow \pi^0 n(p)$ **(f)** $\sigma_{3/2} : \gamma d \rightarrow \pi^0 n(p)$

Figure 7.45: Final averaged double polarization observables for single π^0 photoproduction from quasi-free protons and neutrons as a function of the final state invariant mass W. Results from the A2 data. Shown are the average observables obtained from the arithmetic mean of the different versions. Figures (a)-(c): quasi-free proton. Figures (d)-(f): quasi-free neutron. (a) and (d): double polarization observable E. (b) and (e): helicity dependent cross section $\sigma_{1/2}$. (c) and (f): helicity dependent cross section $\sigma_{3/2}$. Dotted orange line: MAID [40]. Dashed cyan line: SAID [39]. Dashed-dotted magenta line: BnGa (proton: [43], neutron: [38]). The gray histogram at the base line of each figure represents the systematical uncertainties of the results.

uncertainties. This is the weak point of version 4, since all quantities, including the carbon background, are weighted with the degree of polarization. Therefore, for the direct extraction of the helicity dependent cross sections $\sigma_{1/2}$ and $\sigma_{3/2}$ according to Equations (6.60) and (6.61), the estimated carbon background was multiplied by the inverse of the corresponding average polarization weight.

The fact that all versions are in good agreement indicates that the normalization of the liquid deuterium, deuterated butanol, and carbon data together (at least relative to the different beamtimes) and the estimation of the carbon background are well understood. The good agreement of the reconstructed cross sections with

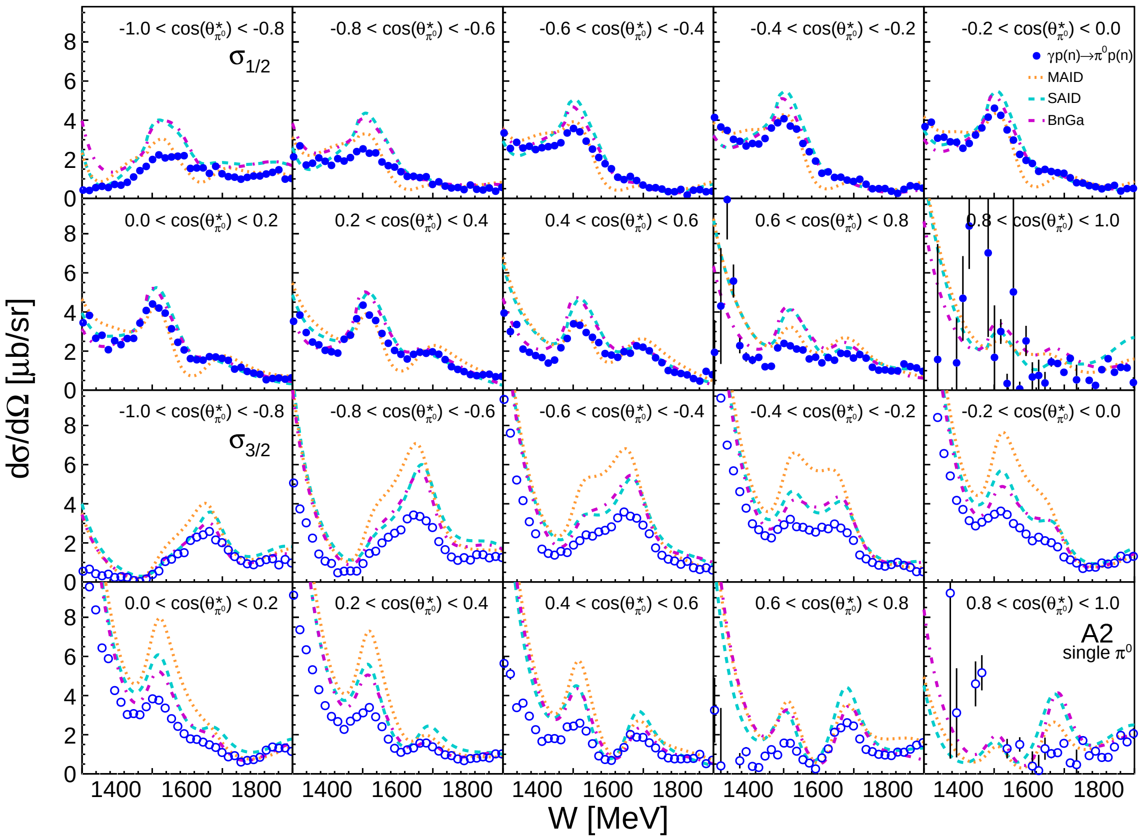

Figure 7.46: Helicity dependent differential cross sections as a function of the final state invariant mass W for single π^0 photoproduction from quasi-free protons. Results from the A2 data. Solid blue circles: $d\sigma_{1/2}/d\Omega$. Open blue circles: $d\sigma_{3/2}/d\Omega$. Dotted orange line: MAID [40]. Dashed cyan line: SAID [39]. Dashed-dotted magenta line: BnGa [43].

the reference cross sections indicates, that also the absolute normalization of the different beamtimes is understood. Furthermore, as the individual conditions in the analyses were adapted to the individual data that involve different kinematics and Fermi momenta, it also confirms that the analysis cuts are within the estimated systematic uncertainty.

Due to the precise agreement of the different versions, the arithmetic mean of the different versions was determined and will be used for the discussion of the results. The final results for the double polarization observable E and the helicity dependent cross sections $\sigma_{1/2}$ and $\sigma_{3/2}$ as a function of the final state invariant mass are shown in Figure 7.45 and the differential helicity dependent cross sections as a function of the center of mass energy in Figures 7.46 and 7.47 for the proton and neutron, respectively. Differential cross sections for E, $\sigma_{1/2}$, and $\sigma_{3/2}$ as a function of the pion polar angle in the center of mass system are shown in Figures 7.50 - 7.55. The differential results were then fit with a Legendre expansion of order 4, according to Equation (6.45). The resulting Legendre coefficient ratios are shown in Figure 7.48. However,

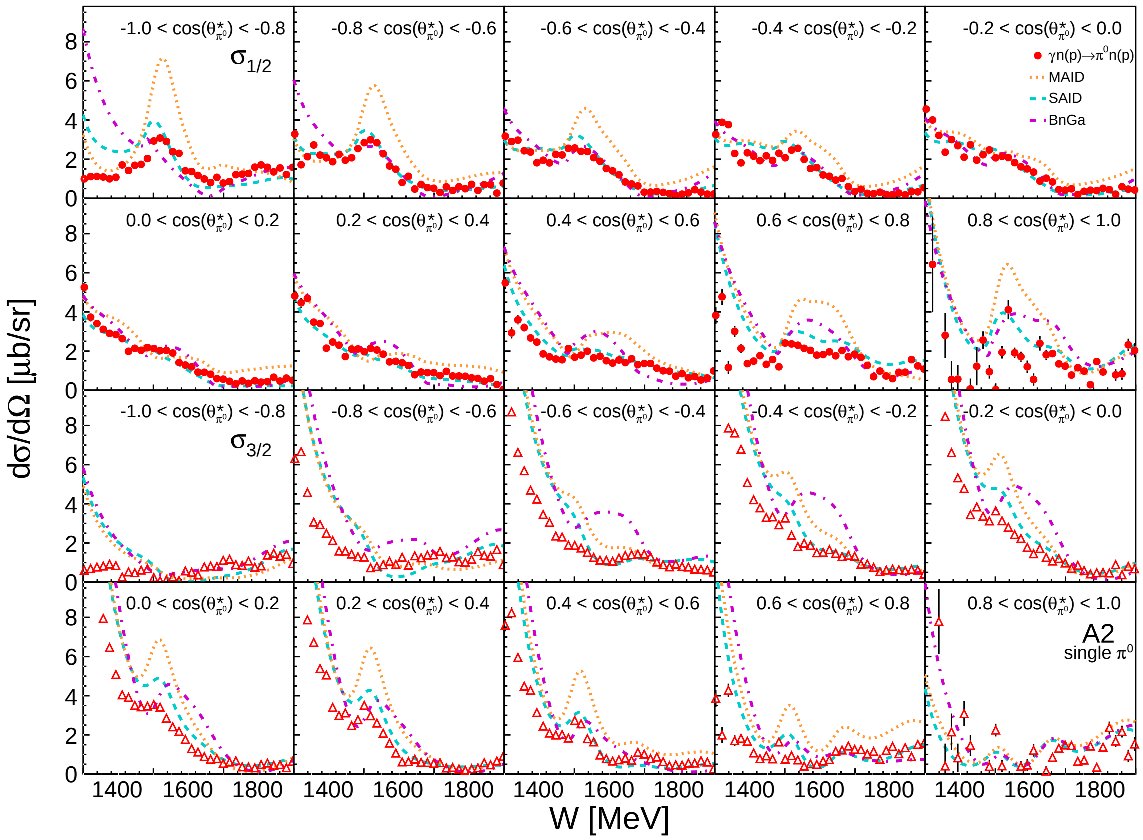

Figure 7.47: Helicity dependent differential cross sections as a function of the final state invariant mass W for single π^0 photoproduction from quasi-free neutrons. Results from the A2 data. Solid red circles: $d\sigma_{1/2}/d\Omega$. Open red triangles: $d\sigma_{3/2}/d\Omega$. Dotted orange line: MAID [40]. Dashed cyan line: SAID [39]. Dashed-dotted magenta line: BnGa [38].

due to the fluctuation in the resulting coefficient B_0, the total cross sections shown in Figures 7.45 were taken from the direct integration over the entire angular range. It was checked that the results only differ in statistical quality.

The obtained results of the helicity dependent total and differential cross sections as a function of the final state invariant mass (Figures 7.45, 7.46, and 7.47) are in good agreement with the expected resonance contributions available in the RPP [37]. Good agreement with the models was already achieved in the double polarization observable E [35], T, P, and H [224] in single π^0 photoproduction from the free proton, even though the data helped to further improve the individual descriptions and to clarify the type and strength of contributing resonances.
The tail of the $\Delta(1232)3/2^+$ resonance at low energies is visible in both $\sigma_{1/2}$ and $\sigma_{3/2}$, but is roughly twice as strong in $\sigma_{3/2}$, which twice as strong as expected from the actual helicity couplings (all in units of 10^{-3} GeV$^{-1/2}$) of $A_{1/2} = -135 \pm 6$ and $A_{3/2} = -255 \pm 5$. The bump in the second resonance region is clearly present in $\sigma_{1/2}$, which indicates contributions from the $N(1440)1/2^+$ (Roper resonance) and

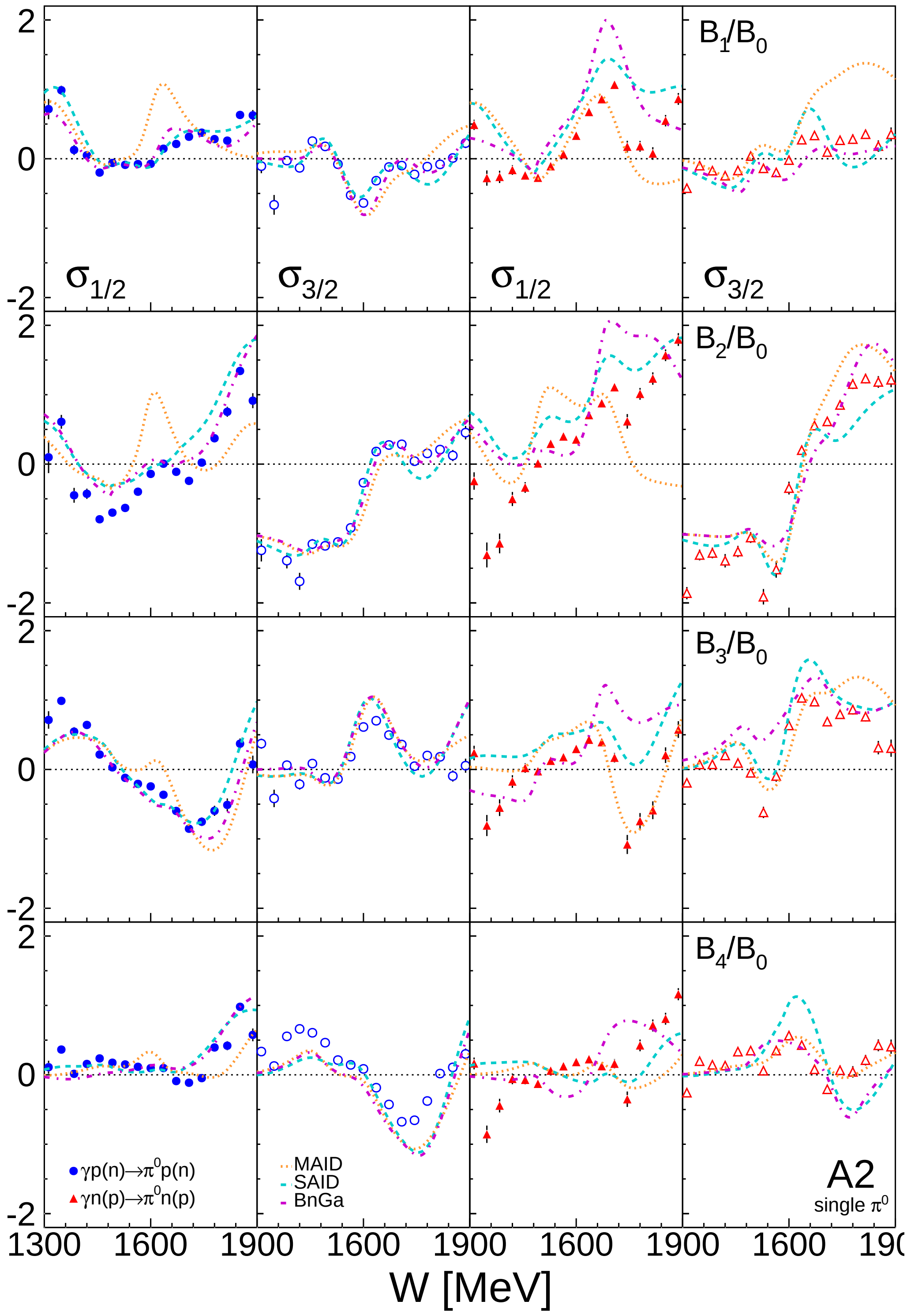

Figure 7.48: Legendre coefficient ratios for single π^0 photoproduction from polarized protons and neutrons. Results from the A2 data. Left two columns: quasi-free proton. Right two columns: quasi-free neutron. Solid (open) symbols: coefficient ratios from $\sigma_{1/2}$ ($\sigma_{3/2}$). Dotted orange line: MAID [40]. Dashed cyan line: SAID [39]. Dashed-dotted magenta line: BnGa (proton: [43], neutron: [38]).

the $N(1535)1/2^-$. The latter couples stronger to the proton ($A^p_{1/2} = 115 \pm 15$) than to the neutron ($A^n_{1/2} = -75 \pm 20$), which is visible by the larger height of the structure in $\sigma_{1/2}$ of the proton. However, the second resonance region is also visible in $\sigma_{3/2}$, which results from contributions of the $N(1520)3/2^-$. Nevertheless, its coupling is expected to be stronger for the proton ($A^p_{1/2} = -20 \pm 5$ and $A^p_{3/2} = 140 \pm 10$) than for the neutron ($A^n_{1/2} = -50 \pm 10$ and $A^n_{3/2} = -115 \pm 10$), which is in agreement with the measured data. Even though the second resonance region in $\sigma_{3/2}$ of proton and neutron are of similar magnitude, the peak in the proton result is much more pronounced than observed for the neutron.
In the third resonance region, a clear signature from the $N(1650)1/2^-$ is visible in $\sigma_{1/2}$ on the proton ($A^p_{1/2} = 45 \pm 10$ and $A^n_{1/2} = -50 \pm 20$), whereas for the neutron the bump in the third resonance region is almost only present in $\sigma_{3/2}$ and most likely results from contributions of the $N(1675)5/2^-$ ($A^p_{1/2} = 19 \pm 8$ and $A^p_{3/2} = 20 \pm 5$ for the proton and $A^n_{1/2} = -60 \pm 5$ and $A^n_{3/2} = -85 \pm 10$ for the neutron). Nevertheless, its coupling to total spin 1/2 states is not much lower than to 3/2 states, but clear evidence in $\sigma_{1/2}$ is missing. The dominant contribution of the $N(1680)5/2^+$ in $\sigma_{3/2}$ of the proton ($A^p_{1/2} = -15 \pm 6$, $A^p_{3/2} = 133 \pm 12$ and $A^n_{1/2} = 29 \pm 10$, $A^n_{3/2} = -33 \pm 9$) is clearly visible. Contributions from the $N(1700)3/2^-$ are difficult to identify as the coupling to 1/2 and 3/2 is similar and not very strong ($A^p_{1/2} = 15 \pm 25$, $A^p_{3/2} = -15 \pm 25$ and $A^n_{1/2} = 20 \pm 15$, $A^n_{3/2} = 30 \pm 20$).
Even though the results seem to coincide more or less with expected resonance contributions, strong deviations with the different model calculations can be seen. For the proton, the shape of $\sigma_{1/2}$ is consistent with the different predictions and the difference in magnitude might be due to the earlier observed FSI effect (see Section 7.1). In $\sigma_{3/2}$ for the proton, besides the difference in magnitude deviations in the shape also occur. The neutron result of the SAID model is not far away from the data, but still appears to miss certain contributions or needs to adjust the different coupling strengths. However, the SAID model also showed the best agreement with the unpolarized neutron cross section in Figure 7.5a. The solution from BnGa fails in describing the neutron data, but is also in good agreement with the proton results. The relative contributions to $\sigma_{1/2}$ and $\sigma_{3/2}$ seem to agree such that the model curve for the double polarization observable E sufficiently well describes the data. In contrast, the MAID model only achieves satisfying results for $\sigma_{1/2}$ for the proton. The situation is also nicely visible in the Legendre coefficient ratios for $\sigma_{1/2}$ and $\sigma_{3/2}$, as shown in Figure 7.48.

However, the former discussions involved results from quasi-free nucleons compared to model predictions for free nucleons, which due to the observed FSI effects, might be misleading. For this reason, the correction factor obtained from the comparison of the SAID result (describing accurately the available world data for single π^0 on the proton) to the measured unpolarized cross sections from quasi-free protons was used to deduce an estimation for the observables for the free proton and neutron. Thereby only the energy dependence of the correction factor was used. The correction was carried out by applying the factor to the initially measured quantities

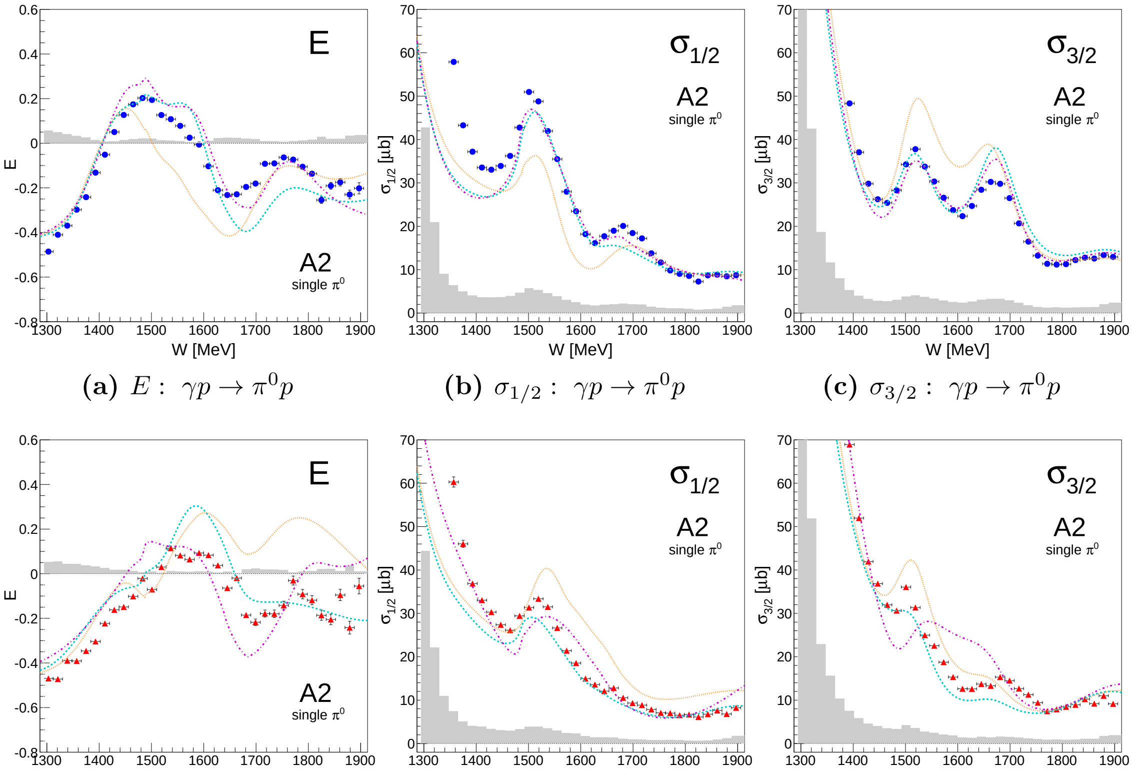

(a) $E: \ \gamma p \to \pi^0 p$ **(b)** $\sigma_{1/2}: \ \gamma p \to \pi^0 p$ **(c)** $\sigma_{3/2}: \ \gamma p \to \pi^0 p$

(d) $E: \ \gamma n \to \pi^0 n$ **(e)** $\sigma_{1/2}: \ \gamma n \to \pi^0 n$ **(f)** $\sigma_{3/2}: \ \gamma n \to \pi^0 n$

Figure 7.49: Final averaged double polarization observables for single π^0 photoproduction from free protons and neutrons (FSI corrected quasi-free results) as a function of the final state invariant mass W. Results from the A2 data. Shown are the average observables obtained from the arithmetic mean of the different versions. Figures (a)-(c): free proton. Figures (d)-(f): free neutron. (a) and (d): double polarization observable E. (b) and (e): helicity dependent cross section $\sigma_{1/2}$. (c) and (f): helicity dependent cross section $\sigma_{3/2}$. Dotted orange line: MAID [40]. Dashed cyan line: SAID [39]. Dashed-dotted magenta line: BnGa (proton: [43], neutron: [38]). The gray histogram at the base line of each figure represents the systematical uncertainties of the results.

σ_{diff}, σ_{sum}, $\sigma_{1/2}$, $\sigma_{3/2}$, and σ_{unpol} introduced in the beginning of this section. The final observables were then determined identically to the quasi-free results using versions 1 to 4. For this reason, the systematic uncertainty was also determined from the maximal deviation of the individual results combined with the error of the degree of polarization.

The results for the double polarization observable E and the helicity dependent cross sections $\sigma_{1/2}$ and $\sigma_{3/2}$ for the free proton and neutron, averaged over the different versions, are shown in Figure 7.49. Whereas the double polarization observable E remains unaltered by the definition of the correction factor (minor effects from the calculation using the different versions are visible at the lowest energies), the effect on $\sigma_{1/2}$ and $\sigma_{3/2}$ are clearly visible. The proton data is now in very good agreement with the SAID and BnGa solutions, but in the third resonance region the models overestimate $\sigma_{3/2}$ and underestimate $\sigma_{1/2}$. This could either point out some misinterpreted contributions of spin $J \geq 3/2$, which originate from a $J = 1/2$ state, or could be an effect from the correction. However, the correction was identical for the proton and neutron, but in the latter case in the same region results in an enhancement in $\sigma_{3/2}$ compared to the model predictions. Again, the SAID model achieves the best agreement with the data. It nicely describes $\sigma_{1/2}$ and is only somewhat poorer in the case of $\sigma_{3/2}$, where it seems to underestimates contributions of the $N(1520)3/2^-$ in the second resonance region and $N(1700)3/2^-$ or $N(1675)5/2^-$ in the third resonance region.

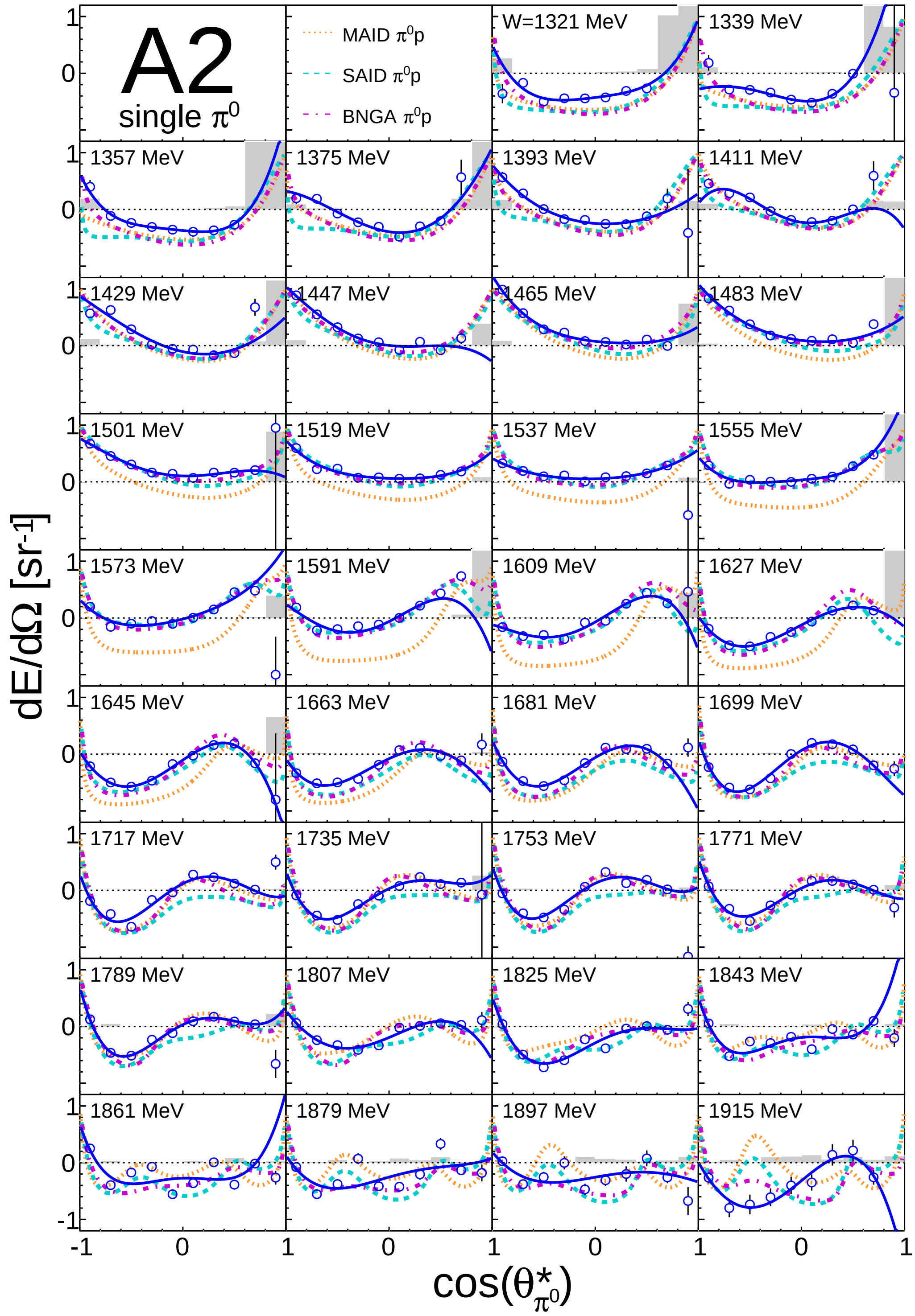

Figure 7.50: Differential double polarization observable E for single π^0 photoproduction from quasi-free protons (not FSI corrected) as a function of the meson polar angle in the $\pi^0 p$ center of mass frame. Solid blue line: Legendre fit. Dotted orange line: MAID [40]. Dashed cyan line: SAID [39]. Dashed-dotted magenta line: BnGa [43]. The gray histogram at the base line of each figure represents the systematical uncertainties of the results.

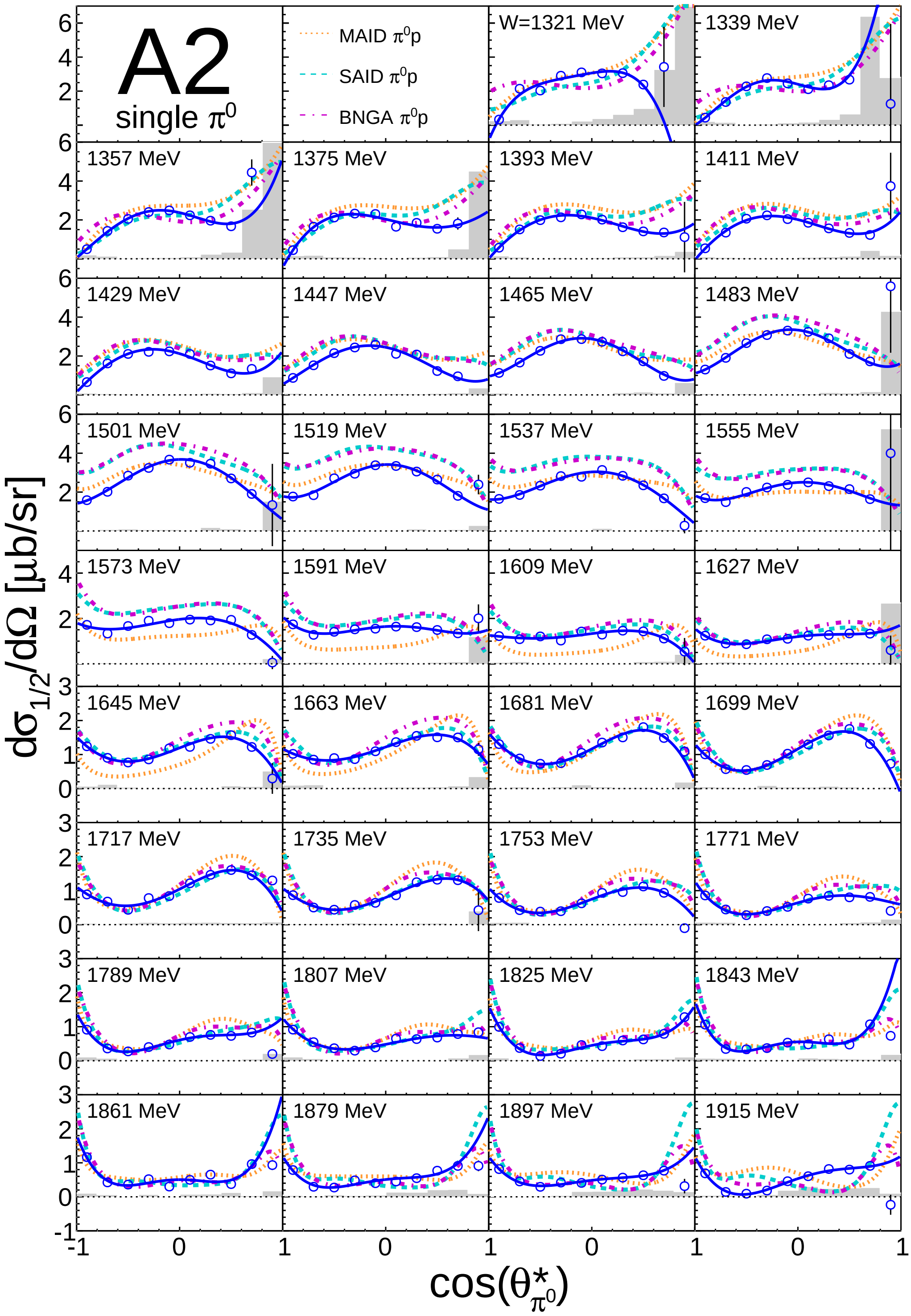

Figure 7.51: Differential helicity dependent cross section $\sigma_{1/2}$ for single π^0 photoproduction from quasi-free protons (not FSI corrected) as a function of the meson polar angle in the $\pi^0 p$ center of mass frame. Solid blue line: Legendre fit. Dotted orange line: MAID [40]. Dashed cyan line: SAID [39]. Dashed-dotted magenta line: BnGa [43]. The gray histogram at the base line of each figure represents the systematical uncertainties of the results.

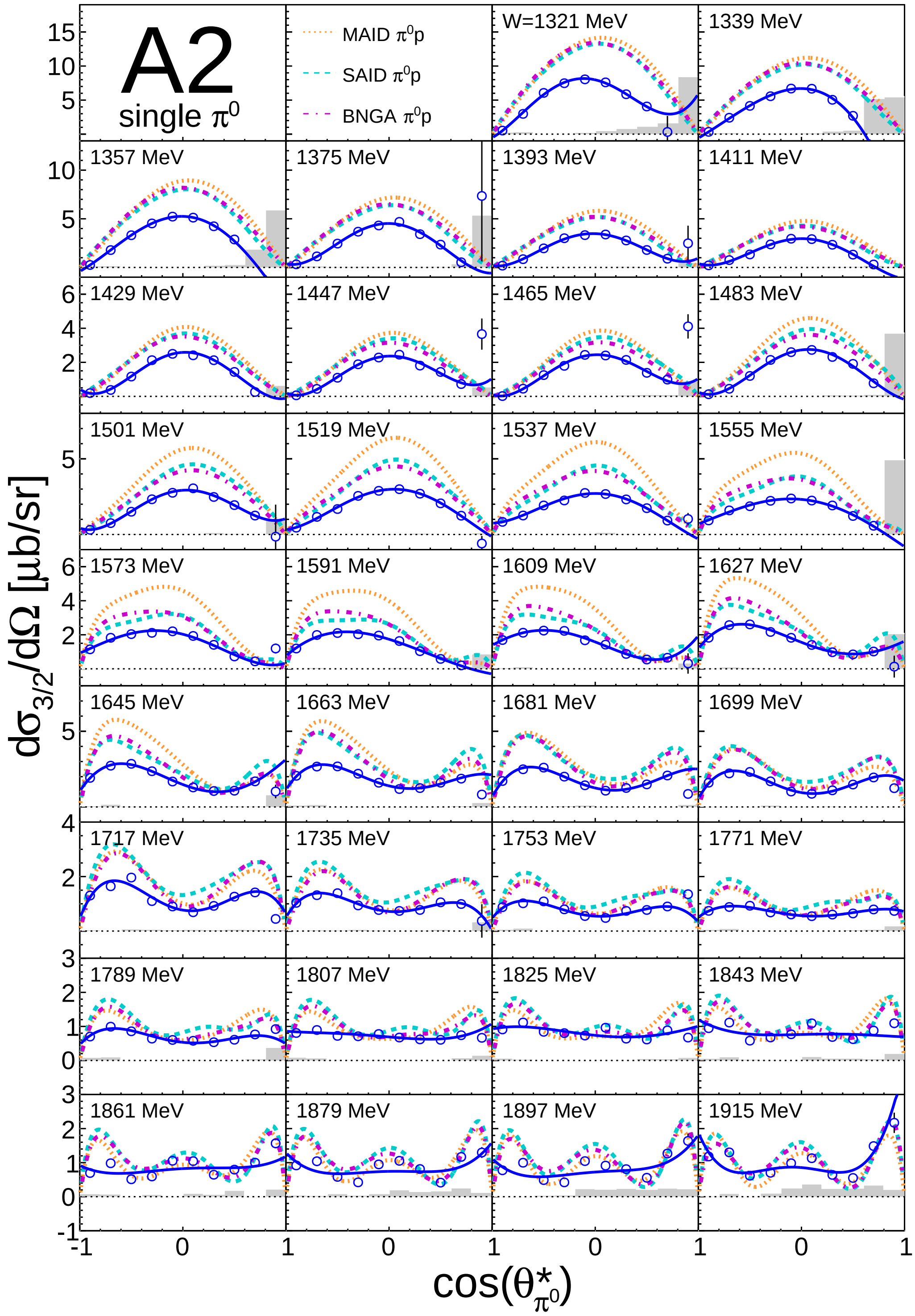

Figure 7.52: Differential helicity dependent cross section $\sigma_{3/2}$ for single π^0 photoproduction from quasi-free protons (not FSI corrected) as a function of the meson polar angle in the $\pi^0 p$ center of mass frame. Solid blue line: Legendre fit. Dotted orange line: MAID [40]. Dashed cyan line: SAID [39]. Dashed-dotted magenta line: BnGa [43]. The gray histogram at the base line of each figure represents the systematical uncertainties of the results.

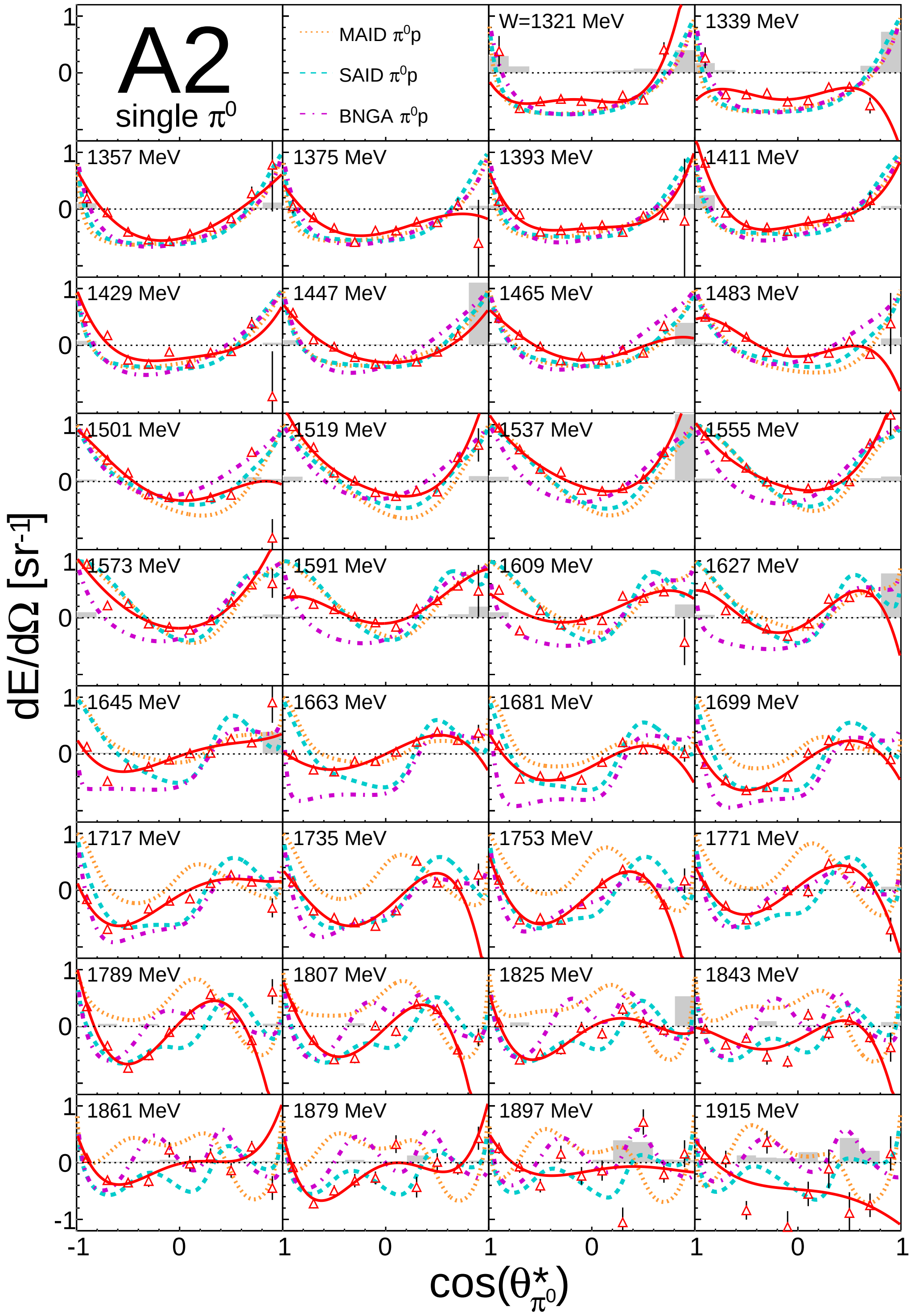

Figure 7.53: Differential double polarization observable E for single π^0 photoproduction from quasi-free neutrons (not FSI corrected) as a function of the meson polar angle in the $\pi^0 n$ center of mass frame. Solid red line: Legendre fit. Dotted orange line: MAID [40]. Dashed cyan line: SAID [39]. Dashed-dotted magenta line: BnGa [38]. The gray histogram at the base line of each figure represents the systematical uncertainties of the results.

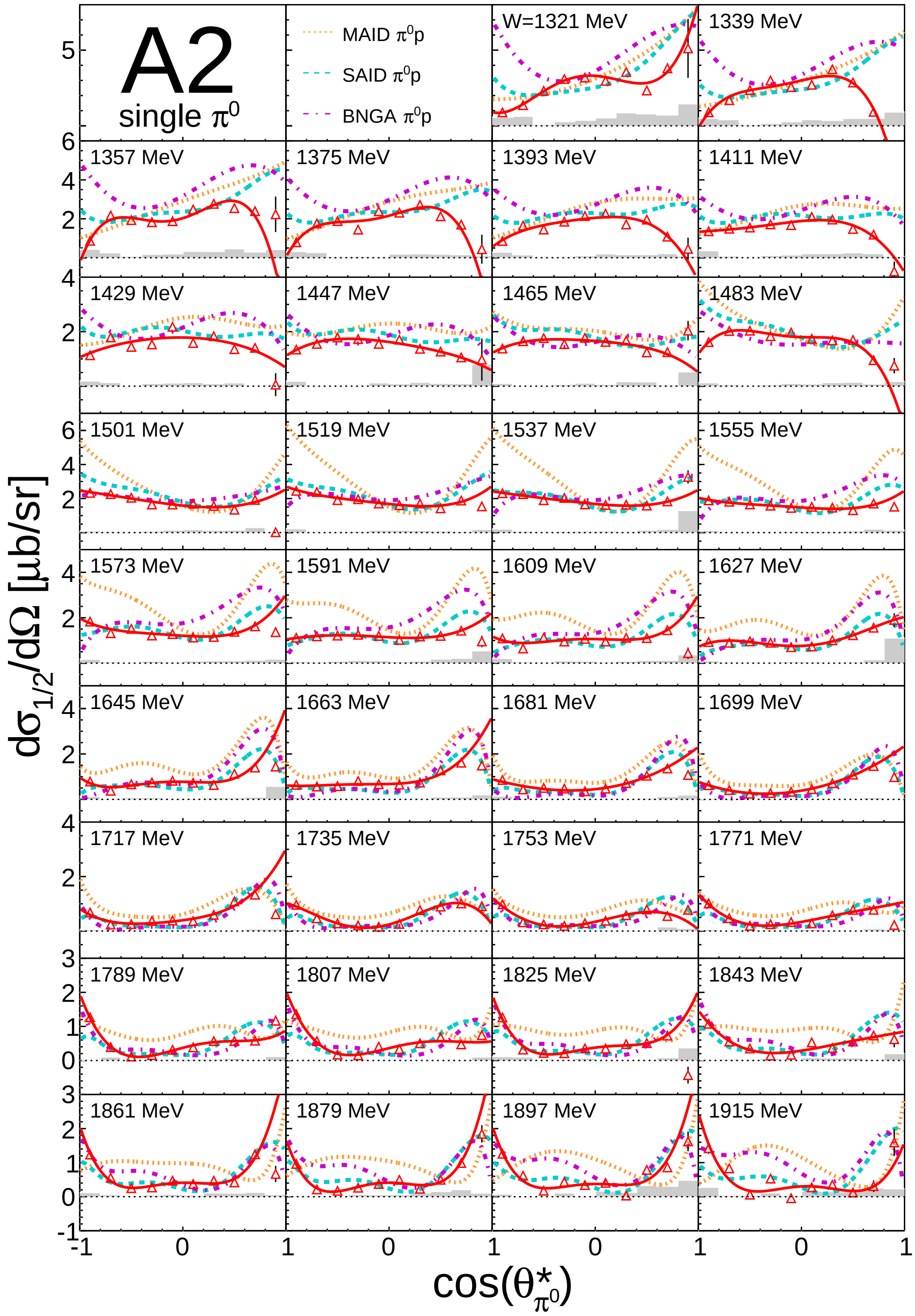

Figure 7.54: Differential helicity dependent cross section $\sigma_{1/2}$ for single π^0 photoproduction from quasi-free neutrons (not FSI corrected) as a function of the meson polar angle in the $\pi^0 n$ center of mass frame. Solid red line: Legendre fit. Dotted orange line: MAID [40]. Dashed cyan line: SAID [39]. Dashed-dotted magenta line: BnGa [38]. The gray histogram at the base line of each figure represents the systematical uncertainties of the results.

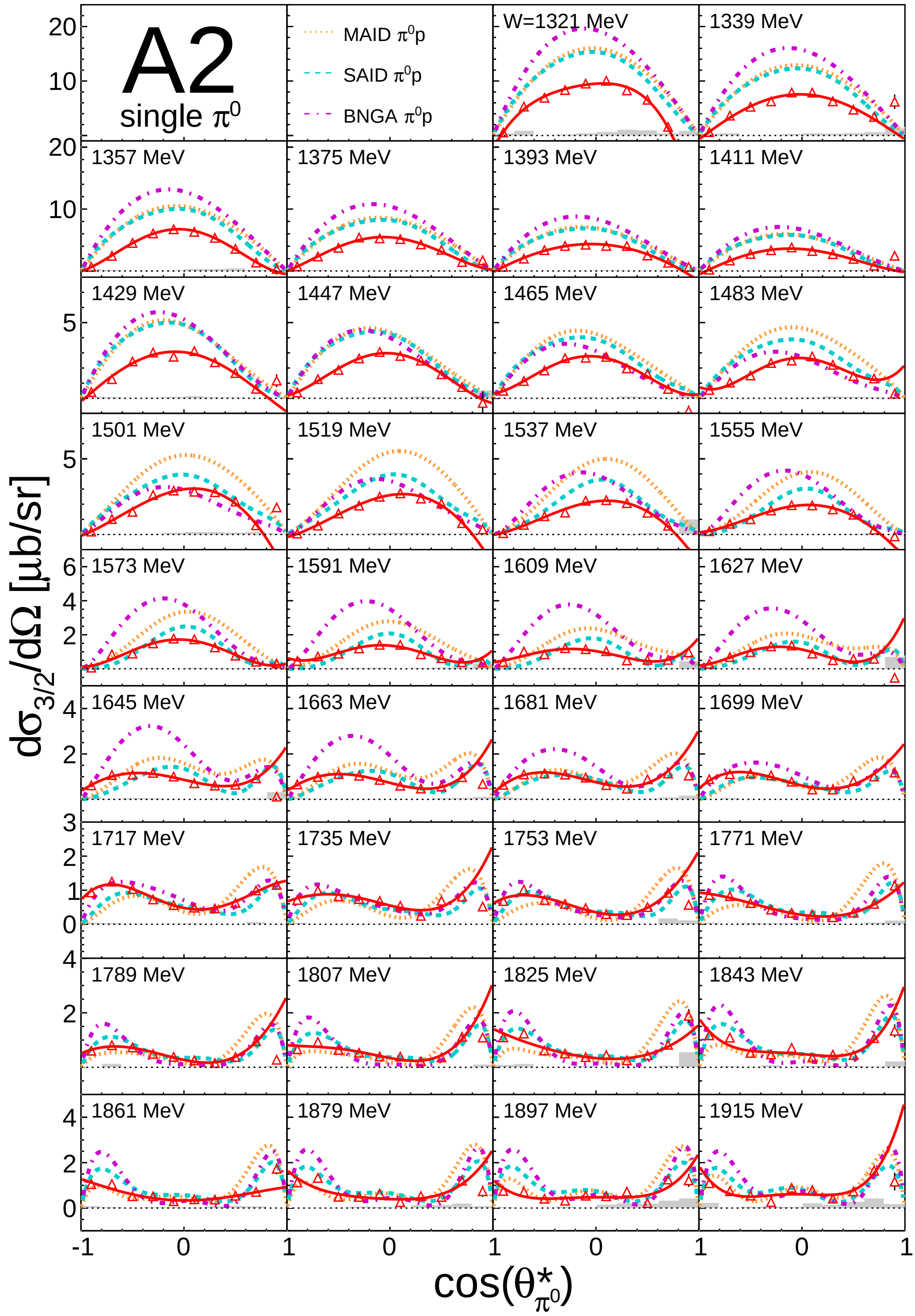

Figure 7.55: Differential helicity dependent cross section $\sigma_{3/2}$ for single π^0 photoproduction from quasi-free neutrons (not FSI corrected) as a function of the meson polar angle in the $\pi^0 n$ center of mass frame. Solid red line: Legendre fit. Dotted orange line: MAID [40]. Dashed cyan line: SAID [39]. Dashed-dotted magenta line: BnGa [38]. The gray histogram at the base line of each figure represents the systematical uncertainties of the results.

7.5 Double Polarization Observables for $\pi^0\pi^0$ Photoproduction

In this section, the final results of the double polarization observable E and the helicity dependent cross sections $\sigma_{1/2}$ and $\sigma_{3/2}$ of double π^0 photoproduction from quasi-free protons and neutrons from the analysis of the A2 and CBELSA/TAPS data will be presented. The observables were extracted with the same versions (three for E and four for $\sigma_{1/2}$ and $\sigma_{3/2}$) as discussed in Section 7.4 and introduced in Section 6.13.3. Deuterated butanol beamtimes (July 2013, February 2014, and March 2015 for A2 and January 2011 and June 2011 for CBELSA/TAPS) were analyzed for the extraction of the polarized results and carbon beamtimes (February 2014 for A2 and November 2011 for CBELSA/TAPS) for the estimation of the reactions on the unpolarized nucleons. In addition, the results of the unpolarized $2\pi^0$ cross sections shown in Sections 7.3.1 and 7.3.2 were used in two of the different versions to allow for a separate and independent normalization, which provides a distinct investigation of systematic uncertainties, as discussed in Section 7.4.
The observables extracted with the different versions from the A2 data will be presented and discussed in Section 7.5.1. Subsequently those from the CBELSA/TAPS analysis will be shown in Section 7.5.2. The final averaged results will be used to compare the results from the two independent analyses in Section 7.5.3 in order to discuss the features that can be deduced from the present data.

7.5.1 Double Polarization Observables from A2 Data

The helicity dependent cross sections $\sigma_{1/2}$ and $\sigma_{3/2}$, the double polarization observable E, and the reconstructed unpolarized cross sections $\sigma_{\mathrm{unpol}} = 0.5 \cdot (\sigma_{1/2} + \sigma_{3/2})$ as a function of the center of mass energy are shown in Figure 7.56 and 7.57 for the exclusive reaction on the quasi-free proton and neutron, respectively. Differential cross sections, mass distributions, and the decomposition into contributions from phase space and intermediate $\Delta(1232)3/2^+\pi^0$ and $N(1520)3/2^-\pi^0$ states will be presented while comparing the results with those from CBELSA/TAPS in Section 7.5.3. Individual results as a function of the center of mass energy and the average results from Figure 7.56 as a function of the incident photon energy are shown in the Appendix D.2.2.

As can be seen in Figure 7.56, the results from the different versions are overall in good agreement. All results exhibit the identical shape and small differences are only visible in the overall magnitude, but are within the systematic uncertainty. Versions 3 and 4 which involve the subtraction of the carbon background, result in somewhat smaller helicity dependent cross sections and therefore, the reconstructed unpolarized cross section is too small. Nevertheless, the resulting double polarization observable E is in good agreement with the other two versions. This indicates a small source of systematic error, which is related to the subtraction of the background from reactions on the unpolarized nucleons. Since the results, which are based on the carbon

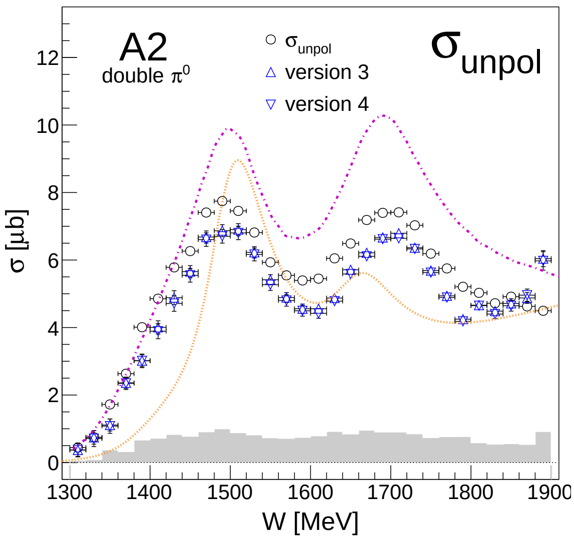

(a) $\sigma_{\text{unpol}} : \gamma d \to \pi^0\pi^0 p(n)$

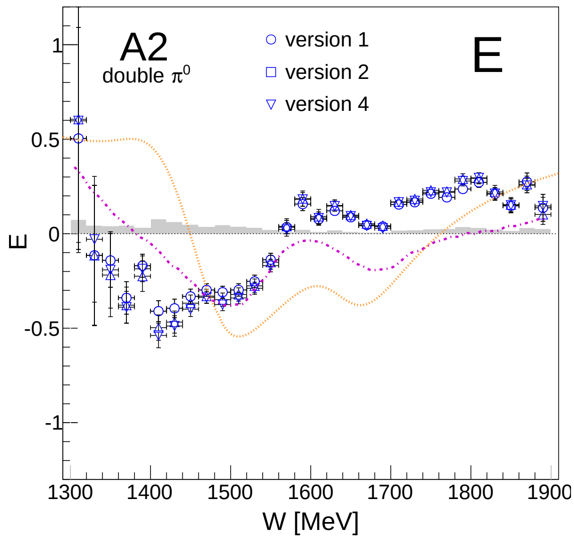

(b) $E : \gamma d \to \pi^0\pi^0 p(n)$

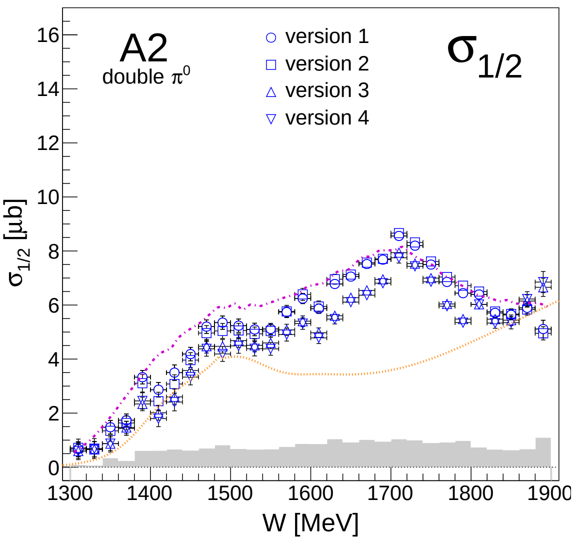

(c) $\sigma_{1/2} : \gamma d \to \pi^0\pi^0 p(n)$

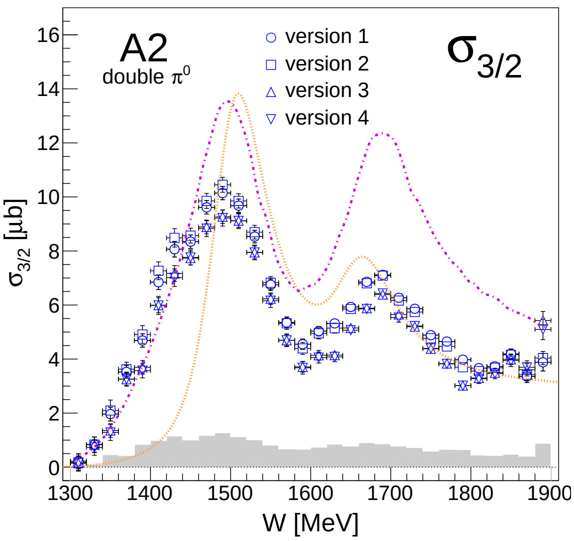

(d) $\sigma_{3/2} : \gamma d \to \pi^0\pi^0 p(n)$

Figure 7.56: Double polarization observables for double π^0 photoproduction from quasi-free protons as a function of the final state invariant mass W. Results from the A2 data. (a) Reconstructed unpolarized total cross section σ_{unpol}. (b) Double polarization observable E. (c) Helicity dependent cross section $\sigma_{1/2}$. (d) Helicity dependent cross section $\sigma_{3/2}$. The different versions are summarized in Table 6.12. Dotted orange line: MAID [40]. Dashed-dotted magenta line: BnGa [43]. The gray histogram at the base line of each figure represents the systematical uncertainties of the results.

subtraction, are lower than the reference cross sections (see top left plot in Figure 7.56), it seems that the contributions from carbon and oxygen were overestimated and too much carbon was subtracted from the results. In contrast, the results for the

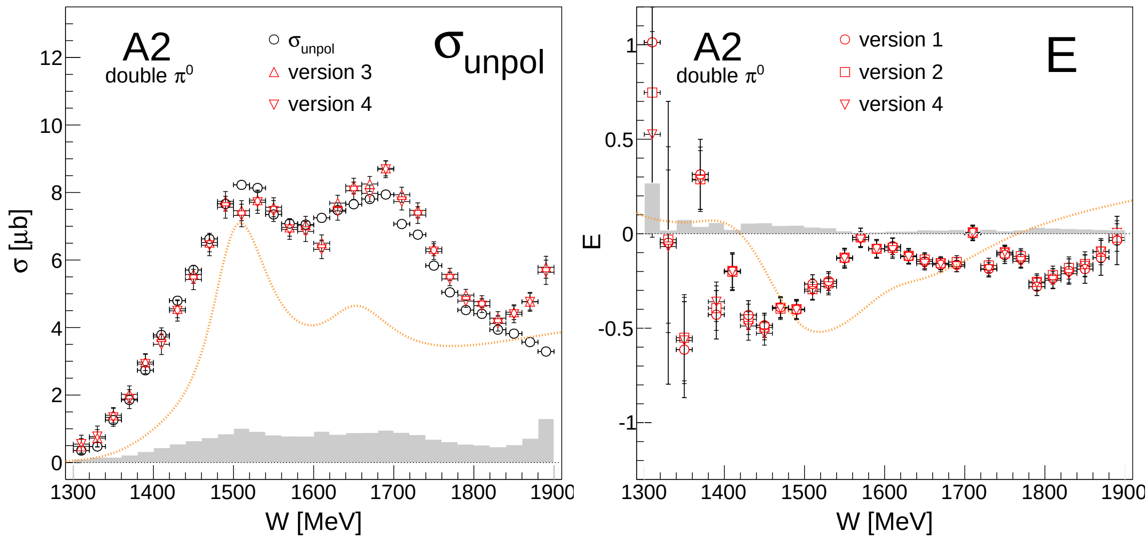

(a) $\sigma_{\mathrm{unpol}} : d\gamma d \to \pi^0\pi^0 n(p)$ **(b)** $E : \gamma d \to \pi^0\pi^0 n(p)$

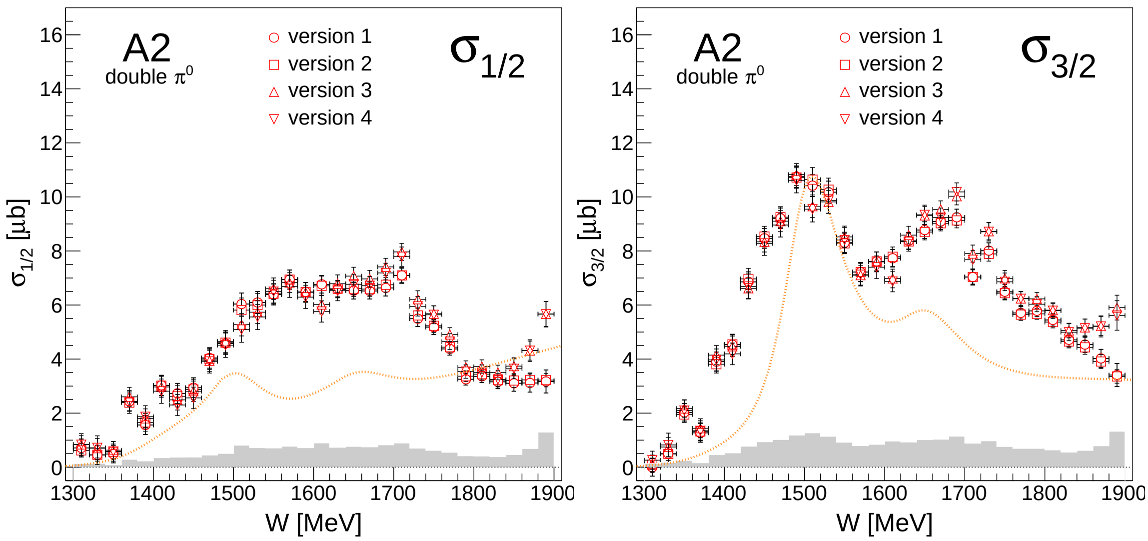

(c) $\sigma_{1/2} : \gamma d \to \pi^0\pi^0 n(p)$ **(d)** $\sigma_{3/2} : \gamma d \to \pi^0\pi^0 n(p)$

Figure 7.57: Double polarization observables for double π^0 photoproduction from quasi-free neutrons as a function of the final state invariant mass W. Results from the A2 data. (a) Reconstructed unpolarized total cross section σ_{unpol}. (b) Double polarization observable E. (c) Helicity dependent cross section $\sigma_{1/2}$. (d) Helicity dependent cross section $\sigma_{3/2}$. The different versions are summarized in Table 6.12. Dotted orange line: MAID [40]. The gray histogram at the base line of each figure represents the systematical uncertainties of the results.

reaction on the neutron using the different versions are in good agreement, except for the highest energies where influences from the W-dependent photon flux are visible. Nevertheless, the reconstructed cross sections are in good agreement with the reference unpolarized cross section besides some fluctuations in the third resonance region.

The missing mass spectra used for the estimation of the carbon background (see Figure 6.137) reveal that in the case of the proton (upper half of the figure), the estimation of the contamination was overestimated at intermediate energies, whereas the effect seems negligible for the neutron. However, the observed differences are rather energy dependent and a reliable improvement of the estimation is difficult. Simultaneous fitting of the missing mass, coplanarity, and invariant mass spectra from deuterated butanol with those from deuterium and carbon (as was used for the absolute normalization in Figures 6.137, C.2, and C.5) resulted in a flawless agreement between the different spectra, but strongly depends on the choice of fit parameters and limits. Furthermore, the problem could also be of a different origin such as an imperfect proton detection efficiency correction or related to the absolute scaling of the target polarization with the factor of 1.5 (see Section 6.11.3). As the differences are well within systematic uncertainties, it was decided that the extraction by absolute normalization is the most unbiased method and was retained.

7.5.2 Double Polarization Observables from CBELSA/TAPS Data

The double polarization observable E and the helicity dependent cross sections $\sigma_{1/2}$ and $\sigma_{3/2}$ for double π^0 photoproduction from quasi-free protons and neutrons resulting from the analysis of the CBELSA/TAPS data will be presented in this section. The results together with the reconstructed unpolarized cross section as a function of the final state invariant mass W are shown in Figures 7.58 and 7.59 for the proton and neutron, respectively. The differential cross sections and the decomposition into contributions from phase space and intermediate $\Delta(1232)3/2^+\pi^0$ and $N(1520)3/2^-\pi^0$ states will be presented in comparison to the A2 data in Section 7.5.3, the individual results are shown in the Appendix D.2.2 as well as the averaged results from Figure 7.58 as a function of the incident photon energy. Due to the lack of statistics, helicity dependent invariant mass distributions were omitted.

The observables for the reaction on the proton (see Figure 7.58) obtained with the different methods are in excellent agreement, except for the first two energy bins, which are dominated by low statistics. Due to the lower systematic uncertainty of the degree of polarization (6%) at CBELSA/TAPS compared to A2 (11%), the size of the systematic errors (gray histograms) are primarily dominated by the difference of the results from the different versions. The results for the exclusive reaction on the neutron are still in good agreement, but exhibit larger differences between the individual methods. However, as seen in the results from the A2 data on the proton, the helicity dependent cross sections obtained from versions 3 and 4 are somewhat smaller with respect to those from versions 1 and 2. The effect is best visible in the reconstruction of the unpolarized cross section that are roughly 10% too small, which indicates a slight discrepancy in the estimation of the carbon background. The neutron missing mass spectra used for the estimation of the degree of contamination with

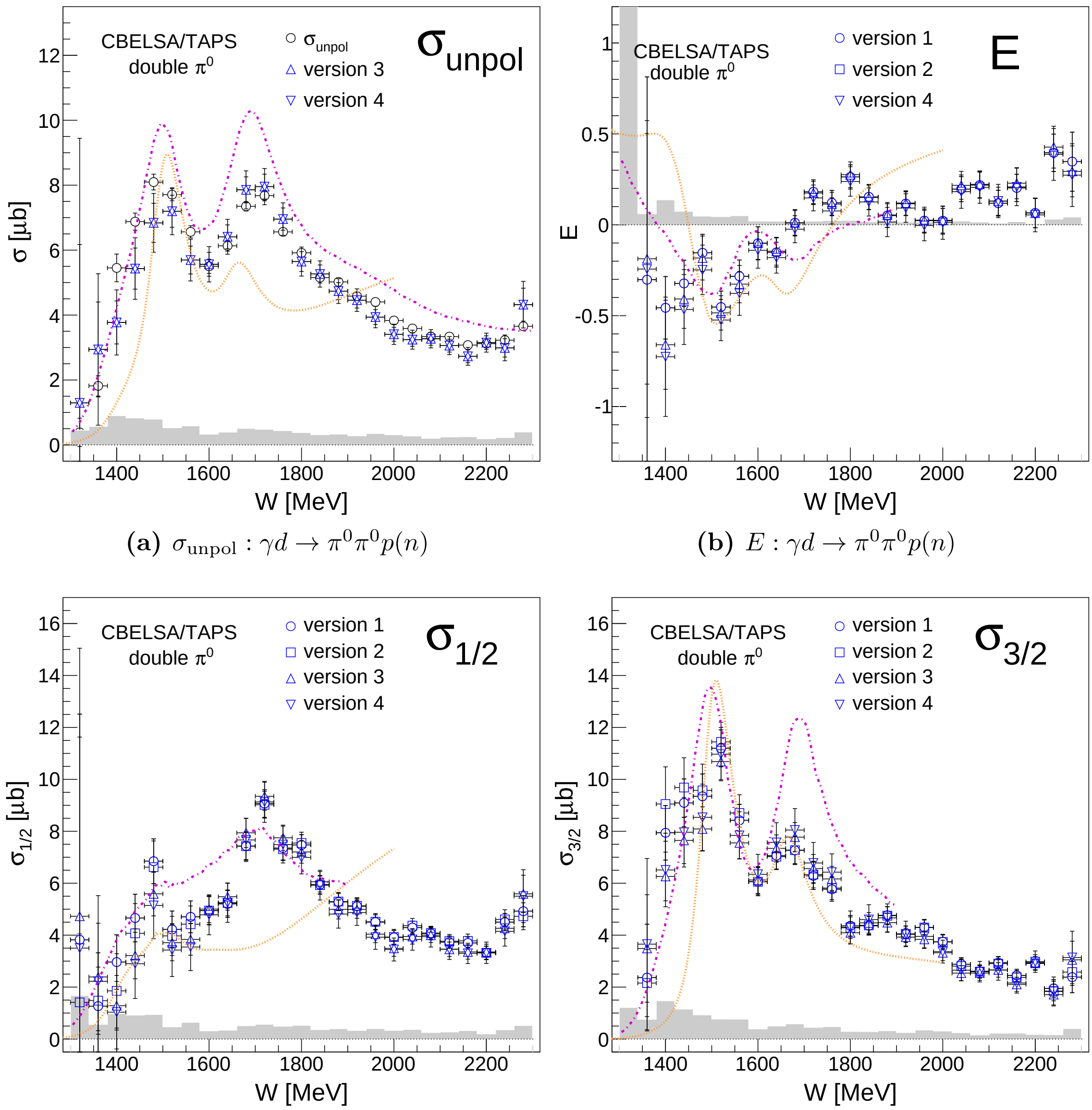

(a) $\sigma_{\mathrm{unpol}} : \gamma d \to \pi^0\pi^0 p(n)$

(b) $E : \gamma d \to \pi^0\pi^0 p(n)$

(c) $\sigma_{1/2} : \gamma d \to \pi^0\pi^0 p(n)$

(d) $\sigma_{3/2} : \gamma d \to \pi^0\pi^0 p(n)$

Figure 7.58: Double polarization observables for double π^0 photoproduction from quasi-free protons as a function of the final state invariant mass W. Results from the CBELSA/TAPS data. (a) Reconstructed unpolarized total cross section σ_{unpol}. (b) Double polarization observable E. (c) Helicity dependent cross section $\sigma_{1/2}$. (d) Helicity dependent cross section $\sigma_{3/2}$. The different versions are summarized in Table 6.12. Dotted orange line: MAID [40]. Dashed-dotted magenta line: BnGa [43]. The gray histogram at the base line of each figure represents the systematical uncertainties of the results.

reactions from unpolarized nucleons (lower half of Figure 6.138) show some evidence that at the energies of highest deviations, the carbon background was overestimated. This might be due to the fact that in the exclusive CBELSA/TAPS analysis for the

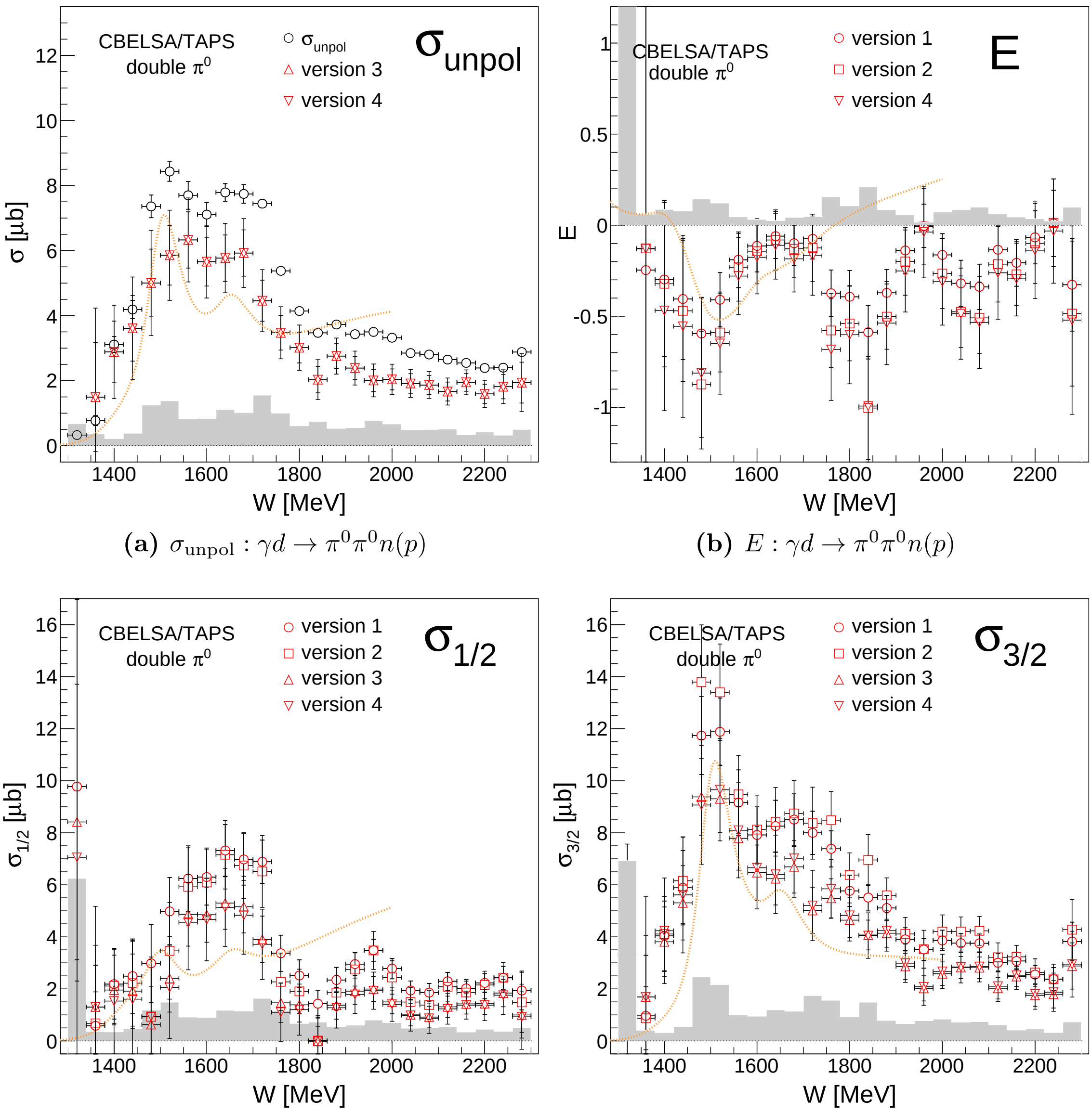

(a) $\sigma_{\mathrm{unpol}} : \gamma d \to \pi^0\pi^0 n(p)$ **(b)** $E : \gamma d \to \pi^0\pi^0 n(p)$

(c) $\sigma_{1/2} : \gamma d \to \pi^0\pi^0 n(p)$ **(d)** $\sigma_{3/2} : \gamma d \to \pi^0\pi^0 n(p)$

Figure 7.59: Double polarization observables for double π^0 photoproduction from quasi-free neutrons as a function of the final state invariant mass W. Results from the CBELSA/TAPS data. (a) Reconstructed unpolarized total cross section σ_{unpol}. (b) Double polarization observable E. (c) Helicity dependent cross section $\sigma_{1/2}$. (d) Helicity dependent cross section $\sigma_{3/2}$. The different versions are summarized in Table 6.12. Dotted orange line: MAID [40]. The gray histogram at the base line of each figure represents the systematical uncertainties of the results.

reaction on the neutron, the neutron detection efficiency could not be applied (see Section 6.8.3). However, it might also result from an inaccuracy in the subtraction of the carbon background. An issue with the photon flux determination could be ruled out, as it would also influence the results for the reaction on the proton. Concerning the statistical quality of the data, the deviations are overall in acceptable agreement.

7.5.3 Comparison of A2 and CBELSA/TAPS Data

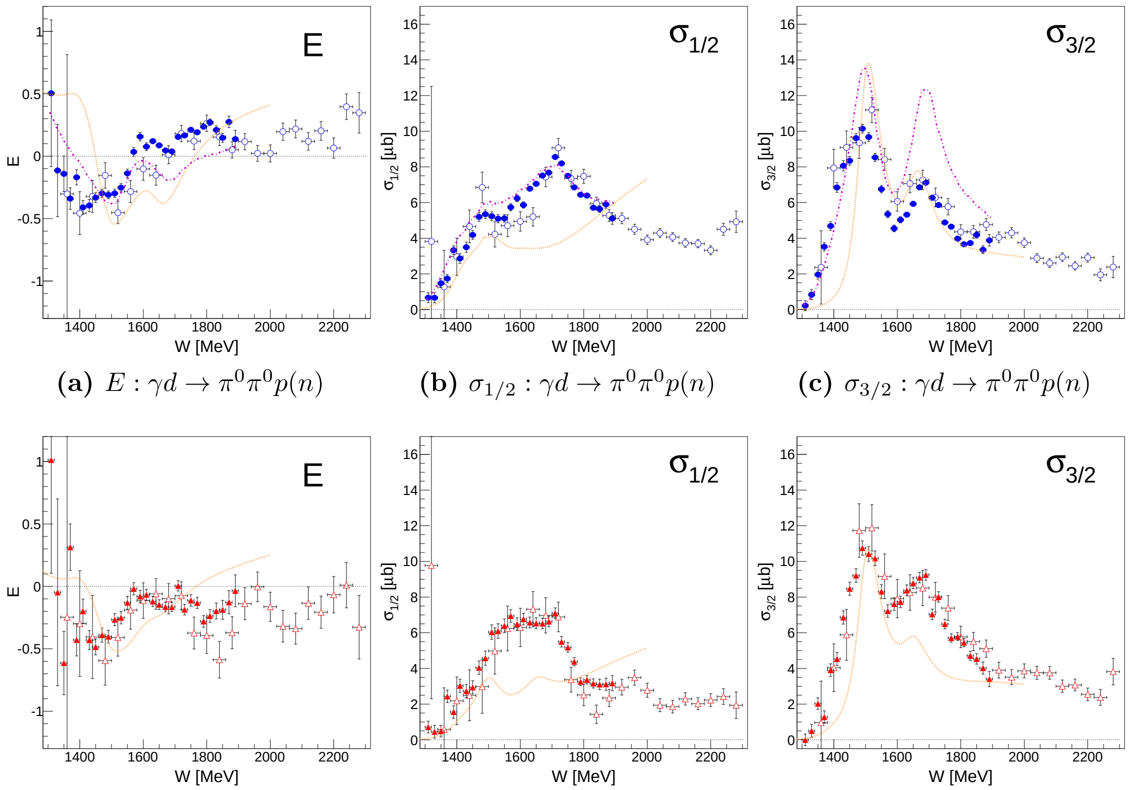

(a) $E : \gamma d \to \pi^0\pi^0 p(n)$ **(b)** $\sigma_{1/2} : \gamma d \to \pi^0\pi^0 p(n)$ **(c)** $\sigma_{3/2} : \gamma d \to \pi^0\pi^0 p(n)$

(d) $E : \gamma d \to \pi^0\pi^0 n(p)$ **(e)** $\sigma_{1/2} : \gamma d \to \pi^0\pi^0 n(p)$ **(f)** $\sigma_{3/2} : \gamma d \to \pi^0\pi^0 n(p)$

Figure 7.60: Final averaged double polarization observables for double π^0 photoproduction from quasi-free protons and neutrons as a function of the final state invariant mass W. Results from the A2 (solid symbols) and CBELSA/TAPS data (open symbols). Shown are the average observables obtained from the arithmetic mean of versions 1 and 2. Figures (a)-(c): quasi-free proton. Figures (d)-(f): quasi-free neutron. (a) and (d): double polarization observable E. (b) and (e): helicity dependent cross section $\sigma_{1/2}$. (c) and (f): helicity dependent cross section $\sigma_{3/2}$. Dotted orange line: MAID [62]. Dashed-dotted magenta line: BnGa [43] (only proton). The gray histogram at the base line of each figure represents the systematical uncertainties of the results.

For the comparison of the Results from the A2 and CBELSA/TAPS, only the results obtained with versions 1 and 2, i.e. those that achieved a proper reconstructed unpolarized cross section, were used. Although all different versions were overall in good agreement, the slight discrepancies in the proton results from A2 and the neutron results from CBELSA/TAPS would affect the arithmetic mean such, that the agreement between A2 and CBELSA/TAPS is not representative. As versions 1 and 2 achieved good agreement for both datasets, the final average was only computed out of these two versions. The arithmetic mean of the different versions of the double polarization observable E and the helicity dependent cross sections $\sigma_{1/2}$ and $\sigma_{3/2}$ from A2 and CBELSA/TAPS data are shown in Figure 7.60. The results from both experiments are in reasonable agreement. Due to the better energy resolution of the CBELSA/TAPS results, the bump structures in the second and third resonance region of the total cross sections are slightly narrower. This results in higher maxima and lower minima, which is also reflected in the helicity dependent cross sections. The results from both datasets for the proton are in rather good agreement. The largest differences are visible at the maxima of the peaks and the minimum of the valley in between, where effects from the different experimental resolutions are expected to be the largest. The neutron results are also in reasonable agreement, but somewhat poorer than those for the proton. The largest discrepancies are visible in $\sigma_{1/2}$, which is the smallest and by that the most sensitive of the four cross sections. In the second resonance region of the neutron, $\sigma_{3/2}$ of CBELSA/TAPS is larger in magnitude than at A2 and also results in a lower magnitude in $\sigma_{1/2}$. In addition, $\sigma_{1/2}$ from the CBELSA/TAPS data on the neutron shows a narrow dip above $W \approx 1800$ MeV, which is not visible in the result from A2. As a consequence, these two deviations are also reflected in the double polarization observable E.

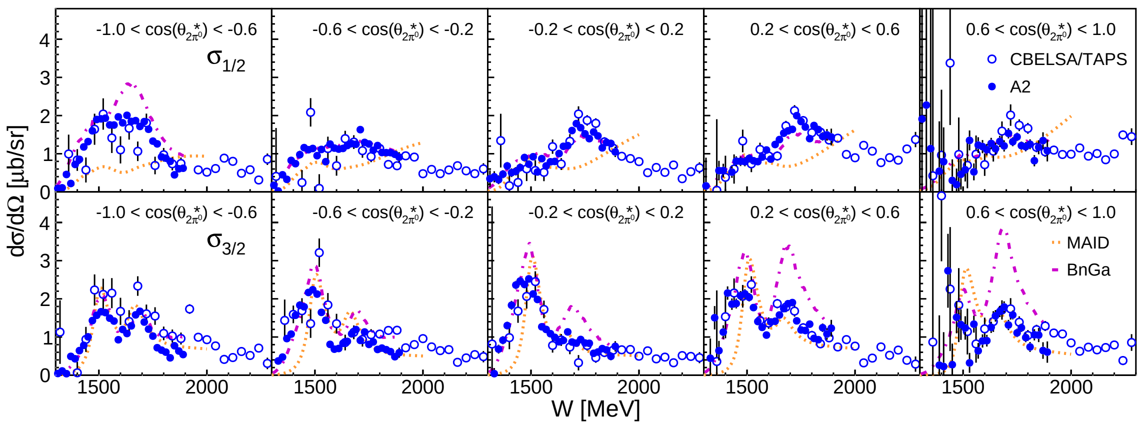

Figure 7.61: Helicity dependent differential cross sections as a function of the final state invariant mass W for double π^0 photoproduction from quasi-free protons. Results from the A2 (solid blue circles) and CBELSA/TAPS data (open blue circles). Upper row: $d\sigma_{1/2}/d\Omega$. Lower row: $d\sigma_{3/2}/d\Omega$. Dotted orange line: MAID [62]. Dashed-dotted magenta line: BnGa [43].

As shown in the differential cross sections as a function of the center of mass energy in Figures 7.61 and 7.62, the data also agree in the individual angular regions. However, the statistical quality of the CBELSA/TAPS data is hardly sufficient for angular distributions. This is even more reflected in the differential cross sections as a function of the meson polar angle $\theta^*_{2\pi^0}$, as shown in Figures 7.70-7.75. Although the CBELSA/TAPS data slightly scatters around the A2 results, the general agreement

is reasonable.
Also shown are the predictions from the MAID isobar model [62] (dotted lines) and from the BnGa coupled-channel partial wave analysis [43] (dashed-dotted magenta lines, only available for the proton). An overall discrepancy in magnitude is expected as moderate FSI effects were observed in the comparison of cross sections from free and quasi-free protons (see Section 7.3). In general, the shape of the BnGa predictions are in good agreement with the proton data. Their model even achieves a good agreement of the helicity dependent cross section $\sigma_{1/2}$. However, it predicts a more similar height of the two peaks in the second and third resonance region in $\sigma_{3/2}$ than observed in the data. Even though this might indicate a difference in the assignment of the contributing resonances, a slight excess of the prediction in the third resonance region was already observed in the unpolarized total cross section (see Figure 7.40). The good agreement from BnGa with the proton data is also confirmed in the differential cross sections as a function of the center of mass energy (Figure 7.61. Except for the most backward angular region, the agreement in $\sigma_{1/2}$ is excellent. The description of $\sigma_{3/2}$ mostly overestimates the data with increasing forward polar angles of the meson in the center of mass frame.

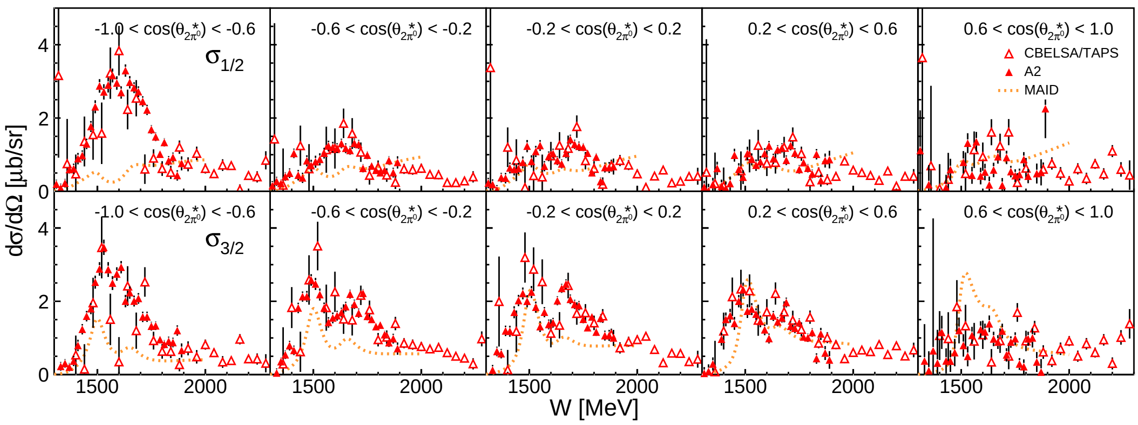

Figure 7.62: Helicity dependent differential cross sections as a function of the final state invariant mass W for double π^0 photoproduction from quasi-free neutrons. Results from the A2 (solid red circles) and CBELSA/TAPS data (open red circles). Upper row: $d\sigma_{1/2}/d\Omega$. Lower row: $d\sigma_{3/2}/d\Omega$. Dotted orange line: MAID [62].

At energies above $W \approx 1550$ MeV the MAID predictions for the proton achieve a good description of $\sigma_{3/2}$ from the proton, whereas the overall underestimation of the total cross section (see Figure 7.40) is reflected in $\sigma_{1/2}$, where the prediction is far too low in this energy range. This points out that spin $J = 1/2$ resonance or non-resonant background are missing in the model. The neutron result from MAID only agrees with the data up to the second resonance region of $\sigma_{1/2}$ and $\sigma_{3/2}$ at energies below $W \approx 1500$ MeV. Apart from that, the data is underestimated with missing contributions in both helicity dependent cross sections.

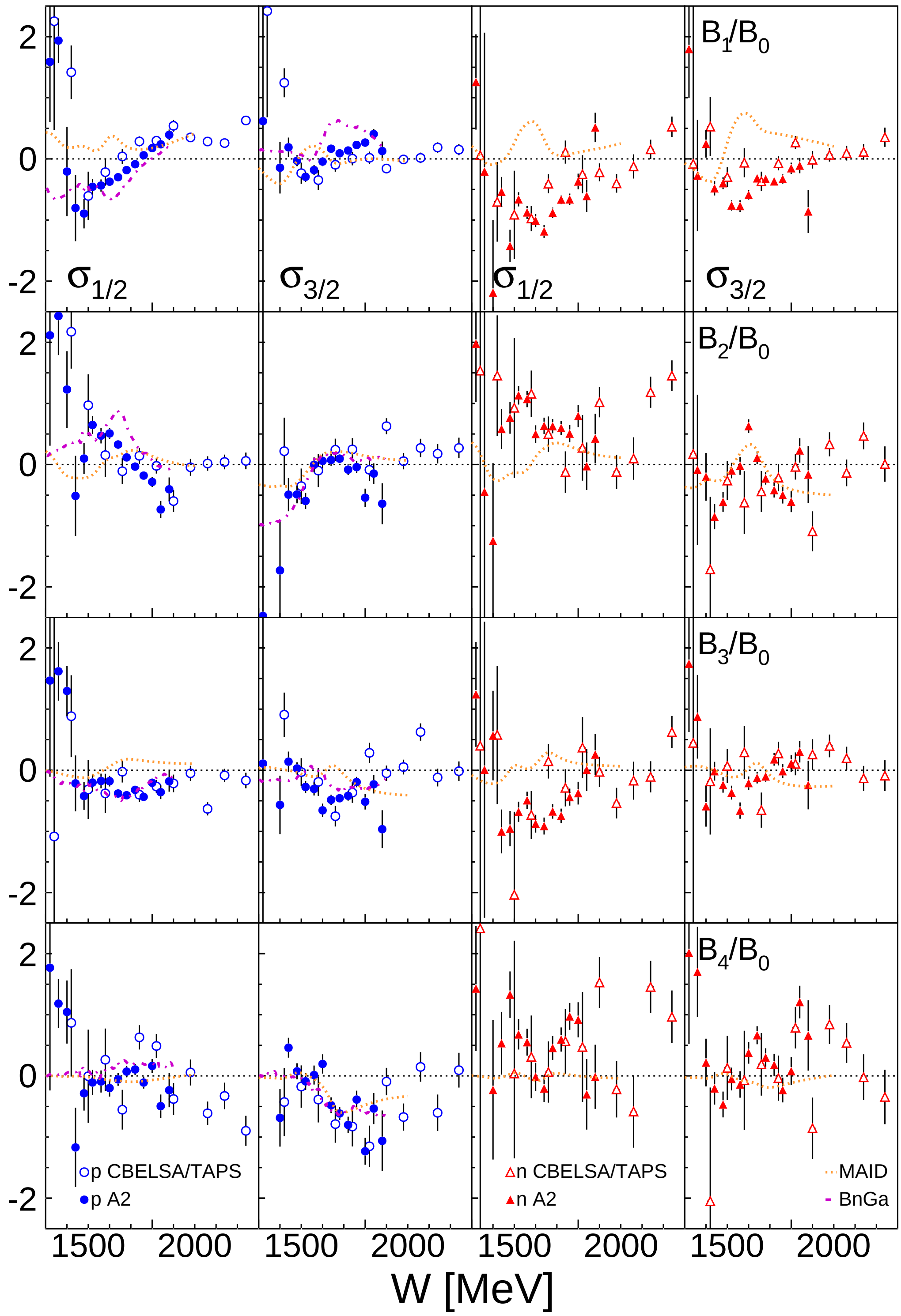

Figure 7.63: Legendre coefficient ratios for double π^0 photoproduction from polarized protons and neutrons. Results from the A2 (solid symbols) and CBELSA/TAPS data (open symbols). Left two columns: quasi-free proton. Right two columns: quasi-free neutron. First and third column: coefficient ratios from $\sigma_{1/2}$. Second and fourth column: coefficient ratios from ($\sigma_{3/2}$). Dotted orange line: MAID [62]. Dashed-dotted magenta line: BnGa [43] (only proton).

The differential observable E and helicity dependent cross sections as a function of the meson polar angle in the center of mass frame are shown in Figures 7.70 - 7.75. The agreement is satisfactory, the CBELSA/TAPS data by trend follows the results from A2. However, the statistical quality of the results from CBELSA/TAPS is barely sufficient for an interpretation of the angular dependence of the observables and is only meaningful by means of a comparison to the results from the A2 data. The complete set of differential results for all energy bins from the A2 data are shown in the Appendix D.2.2. Nevertheless, the Legendre expansion obtained from the fit of the differential results with a series of order 4 are in reasonable agreement, as shown in Figure 7.63 and also agree with the predictions from BnGa.

From the decomposition of the total cross sections into the contributions from phase space and $\Delta(1232)3/2^+\pi^0$ and $N(1520)3/2^-$ intermediate states (see Figures 7.25 and 7.38), it was observed that even though the shape of the proton and neutron cross sections are very similar, completely different processes are responsible for the peak in the third resonance region of the proton than of the neutron. Whereas the second and third resonance regions of the neutron are dominated by contributions from intermediate $\Delta(1232)3/2^+$ states, the second bump in the proton cross section originates from a resonant phase space contribution. A possible explanation for this behavior was found in the helicity couplings of the resonances that mainly contribute in this energy region, i.e. around $W \approx 1700$ MeV. The excitation of the $N(1680)5/2^+$ is much more likely for the proton ($A^p_{1/2} = 15 \pm 6$ and $A^p_{3/2} = 133 \pm 12$, units in 10^{-3} GeV$^{-1/2}$) than for the neutron ($A^n_{1/2} = 29 \pm 10$ and $A^n_{3/2} = 33 \pm 9$) and has a small branching ratio to the $\Delta(1232)3/2^+$ intermediate state (5-15%), but the decay to $N\sigma$ (phase space, i.e. $N(\pi^0\pi^0)_S$ final state) is possible with $l_{N\sigma} = 2$. In contrast, the excitation of the $N(1675)5/2^-$ is favored for the neutron ($A^p_{1/2} = 19 \pm 8$ and $A^p_{3/2} = 20 \pm 5$ for the proton and $A^n_{1/2} = 60 \pm 5$ and $A^n_{3/2} = 85 \pm 10$ for the neutron) and the branching ratio to $\Delta(1232)3/2^+\pi^0$ intermediate states is comparably large, whereas the decay to $N\sigma$ requires $l_{N\sigma} \geq 3$ and is more unlikely.

In order to further investigate this finding, the decomposition was also carried out using the helicity dependent cross sections $\sigma_{1/2}$ and $\sigma_{3/2}$. The decompositions are shown in Figures 7.64a for the A2 data in Figure 7.64b for the CBELSA/TAPS data. The strongest signature of the phase space component is visible in $\sigma_{3/2}$ of the proton, which is in agreement with the discussions above. However, its signal in $\sigma_{1/2}$ is not as negligible as expected from the much smaller helicity coupling ($A^p_{1/2} = 15 \pm 6$, $A^p_{3/2} = 133 \pm 12$, units in 10^{-3} GeV$^{-1/2}$). However, the general observations from the discussions of the unpolarized cross sections are qualitatively confirmed. Contributions from the intermediate $\Delta(1232)3/2^+\pi^0$ states dominate the neutron cross sections throughout the second and third resonance region, whereas a strong suppression is visible in the third resonance region of the proton. In this region, the phase space contributions exhibit a resonant structure and are stronger present in $\sigma_{3/2}$. Additionally, it seems that for the reaction on the proton above $W \approx 1700$ MeV, resonances that decay to intermediate $\Delta(1232)3/2^+$ states contribute stronger to $\sigma_{1/2}$

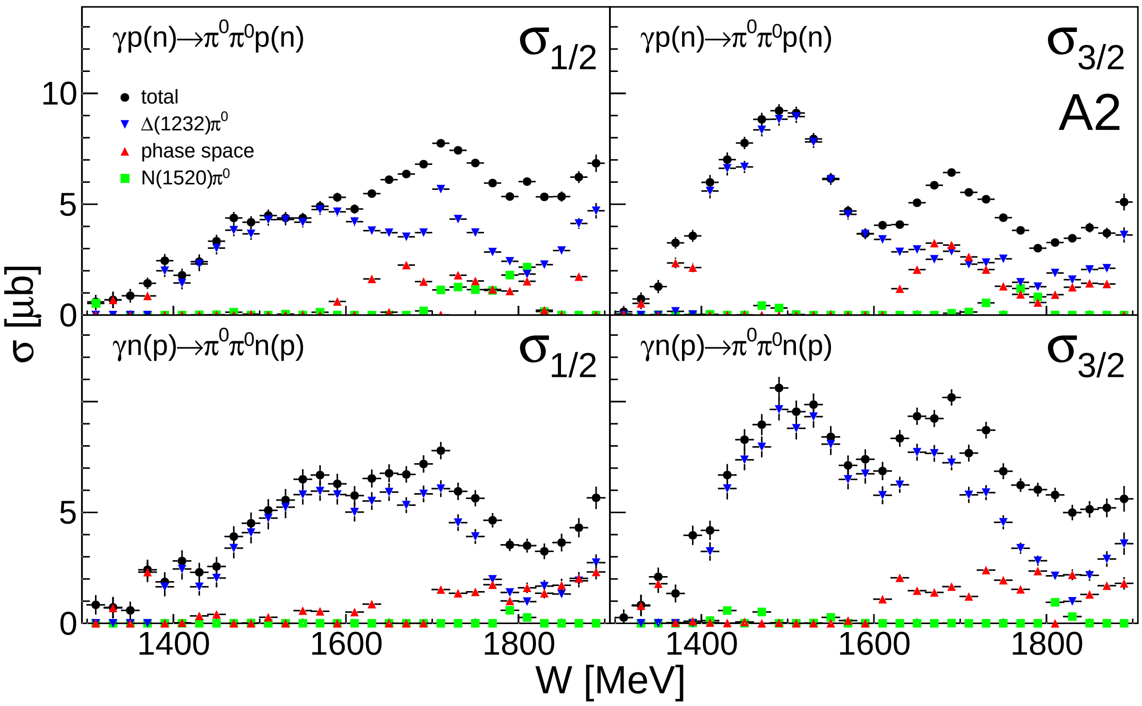

(a) Results from the A2 data

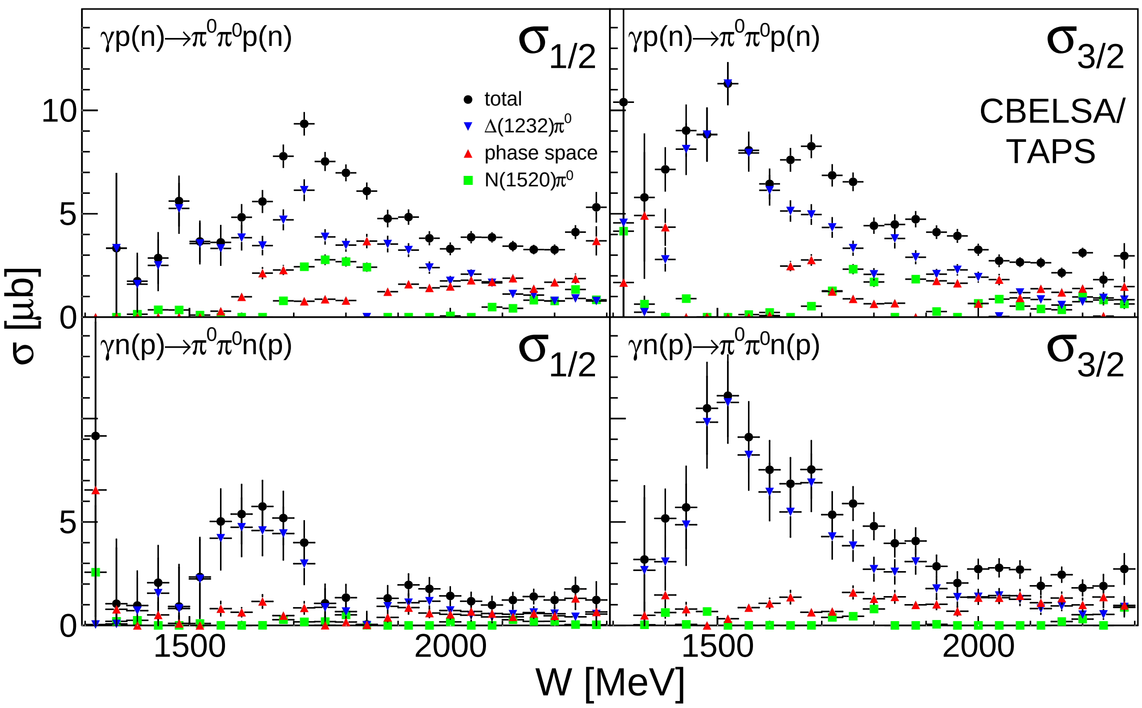

(b) Results from CBELSA/TAPS data

Figure 7.64: Contributions of $\gamma N \to \Delta(1232)\pi^0 \to N\pi^0\pi^0$ (blue triangles), $\gamma N \to N\pi^0\pi^0$ (red triangles) and $\gamma N \to N(1520)\pi^0 \to N\pi^0\pi^0$ (green squares) to the $2\pi^0$ helicity dependent cross sections $\sigma_{1/2}$ (black circles, left column) and $\sigma_{3/2}$ (black circles, right column) for quasi-free protons (top row) and neutrons (bottom row). (a) Results from the A2 data. (b) Results from the CBELSA/TAPS data.

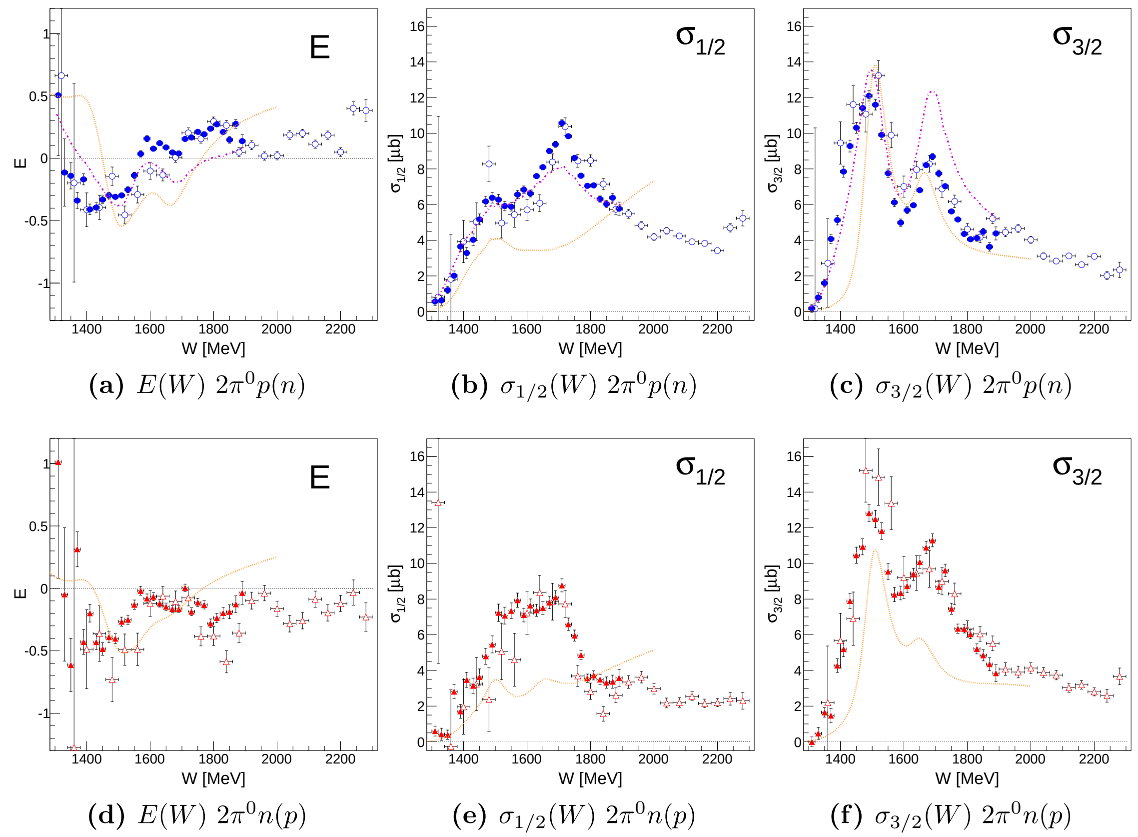

(a) $E(W)\ 2\pi^0 p(n)$ **(b)** $\sigma_{1/2}(W)\ 2\pi^0 p(n)$ **(c)** $\sigma_{3/2}(W)\ 2\pi^0 p(n)$

(d) $E(W)\ 2\pi^0 n(p)$ **(e)** $\sigma_{1/2}(W)\ 2\pi^0 n(p)$ **(f)** $\sigma_{3/2}(W)\ 2\pi^0 n(p)$

Figure 7.65: Final averaged double polarization observables for single π^0 photoproduction from free protons and neutrons (FSI corrected quasi-free results) as a function of the final state invariant mass W. Results from the A2 (solid symbols) and CBELSA/TAPS data (open symbols). Shown are the average observables obtained from the arithmetic mean of versions 1 and 2. Figures (a)-(c): free proton. Figures (d)-(f): free neutron. (a) and (d): double polarization observable E. (b) and (e): helicity dependent cross section $\sigma_{1/2}$. (c) and (f): helicity dependent cross section $\sigma_{3/2}$. Dotted orange line: MAID [62]. Dashed-dotted magenta line: BnGa [43] (only proton). The gray histogram at the base line of each figure represents the systematical uncertainties of the results.

than to $\sigma_{3/2}$, whereas for the neutron the opposite is true. The same observations can be found from the $N\pi^0$ and $\pi^0\pi^0$ mass distributions (see Figures 7.66-7.69). Above energies of $W \approx 1700$, $\mathrm{d}\sigma_{3/2}/\mathrm{d}m(\pi^0 p)$ exceeds $\mathrm{d}\sigma_{1/2}/\mathrm{d}m(\pi^0 p)$ whereas the opposite trend is visible in $\mathrm{d}\sigma/\mathrm{d}m(\pi^0 n)$. Furthermore, the shape of the proton $\mathrm{d}\sigma_{3/2}/\mathrm{d}m(\pi^0 p)$ distributions are similar to phase space and the characteristic resonance structures are visible in $\mathrm{d}\sigma_{1/2}/\mathrm{d}m(\pi^0 p)$. The distributions also show that for the neutron $\sigma_{3/2}$ is larger than $\sigma_{1/2}$ for all energies, while for the proton it is exceeded by $\sigma_{1/2}$ for energies above $W \approx 1550$ MeV. This is interesting, as this suggests that for the proton above $W \approx 1550$ MeV, spin 1/2 resonances strongly contribute to the excitation spectrum. However, at energies beyond the $N(1535)1/2^-$, spin 1/2 resonances become sparse. However, possible candidates are the $\Delta(1620)1/2^-$, $N(1650)1/2^-$, or the $N(1710)1/2^+$ of which the latter is the closest and the most narrow resonance of the three and might explain the rather sharp structure seen in $\sigma_{1/2}$ on the proton.

As for single π^0 photoproduction, an estimation of the results from the free proton and neutron were determined by applying the energy dependence of the correction factor (see Figures 7.19 and 7.32) to σ_{diff}, σ_{sum}, $\sigma_{1/2}$, $\sigma_{3/2}$, and σ_{unpol} and recalculation of the results with versions 1 to 4. The average results are shown in Figure 7.65 and are compared to the model predictions. As the correction factor is nearly independent of energy, the shape of the result was not much affected by the correction. In principle, the results are scaled up by a factor of 1/0.85. The MAID model is now in almost perfect agreement with $\sigma_{3/2}$ from the proton, but still totally underestimates $\sigma_{1/2}$. The solution from BnGa is also in very good agreement with $\sigma_{1/2}$, but seems to neglect some spin 1/2 contributions in the third resonance region. As a consequence, the corresponding data in $\sigma_{3/2}$ are overestimated. As previously mentioned, this might be due to a too weak helicity coupling of the $N(1710)1/2^+$ to the proton. In the absence of more detailed model predictions, especially for the neutron, the interpretation of the results is complicated by the large amount of spin 1/2 (N) and spin 3/2 (Δ) resonances that are present in the second and third resonance regions. However, the overall good agreement between the results from A2 and CBELSA/TAPS and the collection of different helicity dependent observables, ranging from total and differential cross sections to invariant mass distributions, provides a lot of valuable input for the understanding of the excitation spectrum of the nucleon.

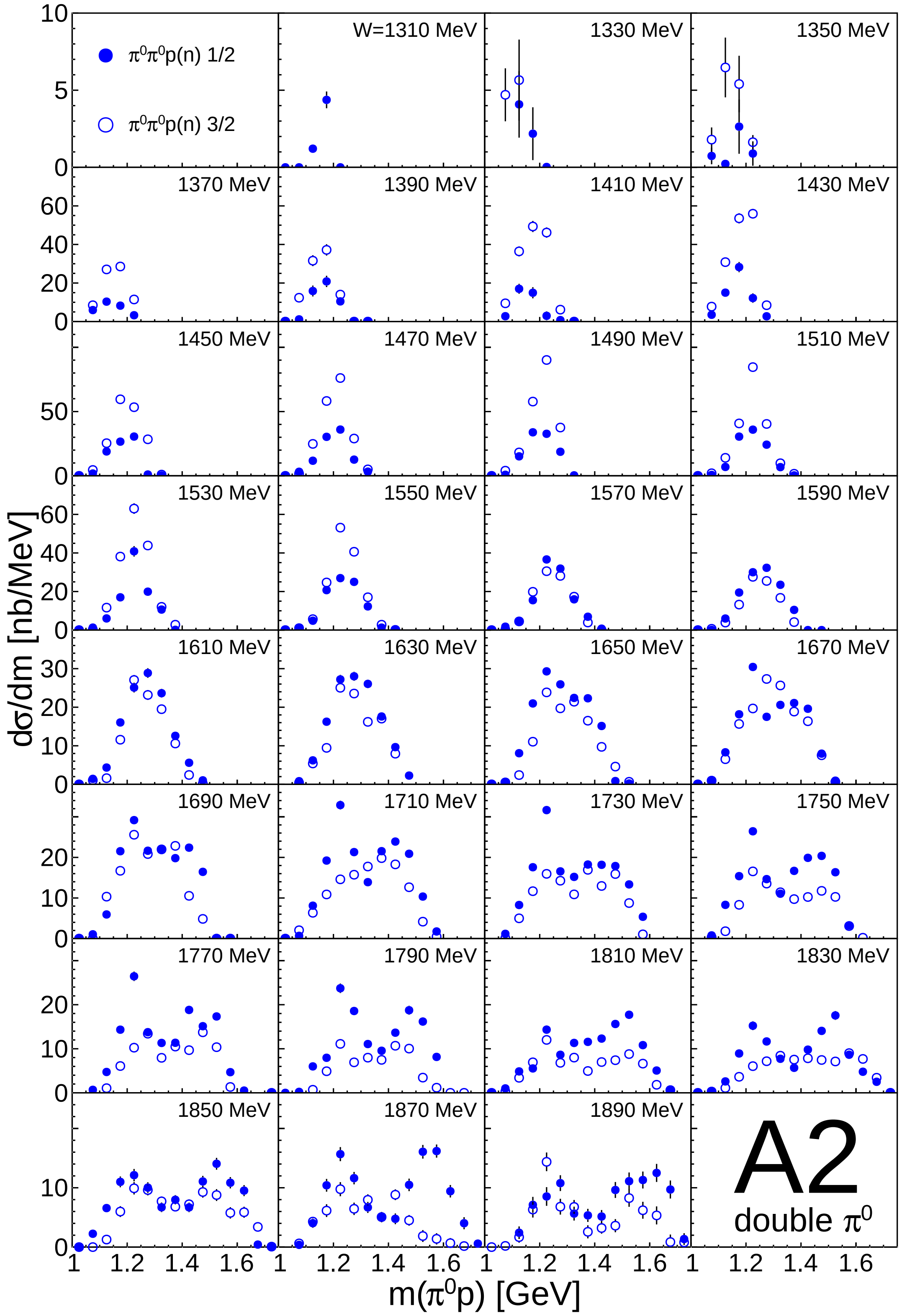

Figure 7.66: Differential helicity dependent cross sections $\sigma_{1/2}$ (solid symbols) and $\sigma_{3/2}$ (open symbols) for double π^0 photoproduction from quasi-free protons (not FSI corrected) as a function of the $\pi^0 p$ invariant mass. Results from the A2 data.

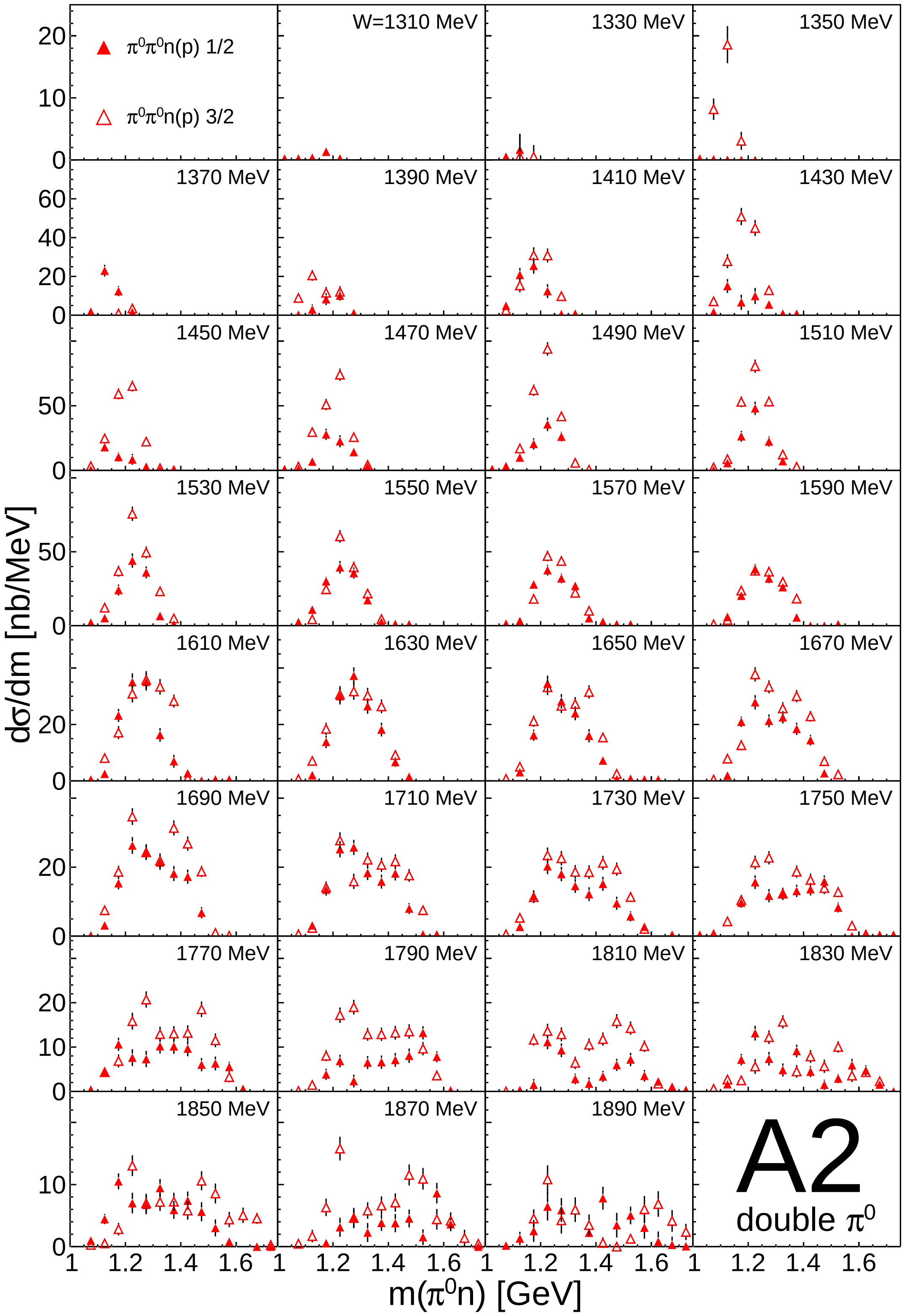

Figure 7.67: Differential helicity dependent cross sections $\sigma_{1/2}$ (solid symbols) and $\sigma_{3/2}$ (open symbols) for double π^0 photoproduction from quasi-free neutrons (not FSI corrected) as a function of the $\pi^0 n$ invariant mass. Results from the A2 data.

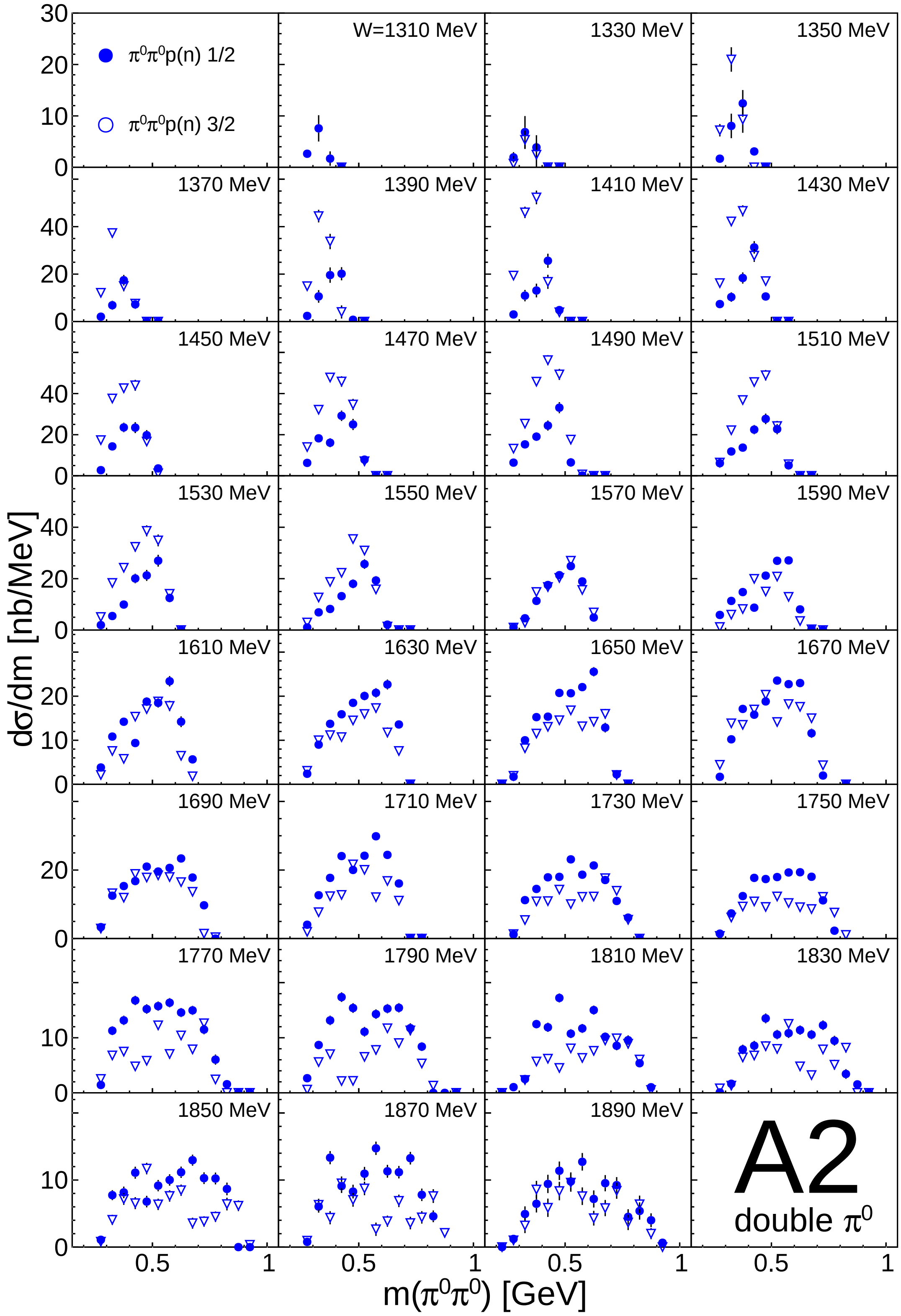

Figure 7.68: Differential helicity dependent cross sections $\sigma_{1/2}$ (solid symbols) and $\sigma_{3/2}$ (open symbols) for double π^0 photoproduction from quasi-free protons (not FSI corrected) as a function of the $\pi^0\pi^0$ invariant mass. Results from the A2 data.

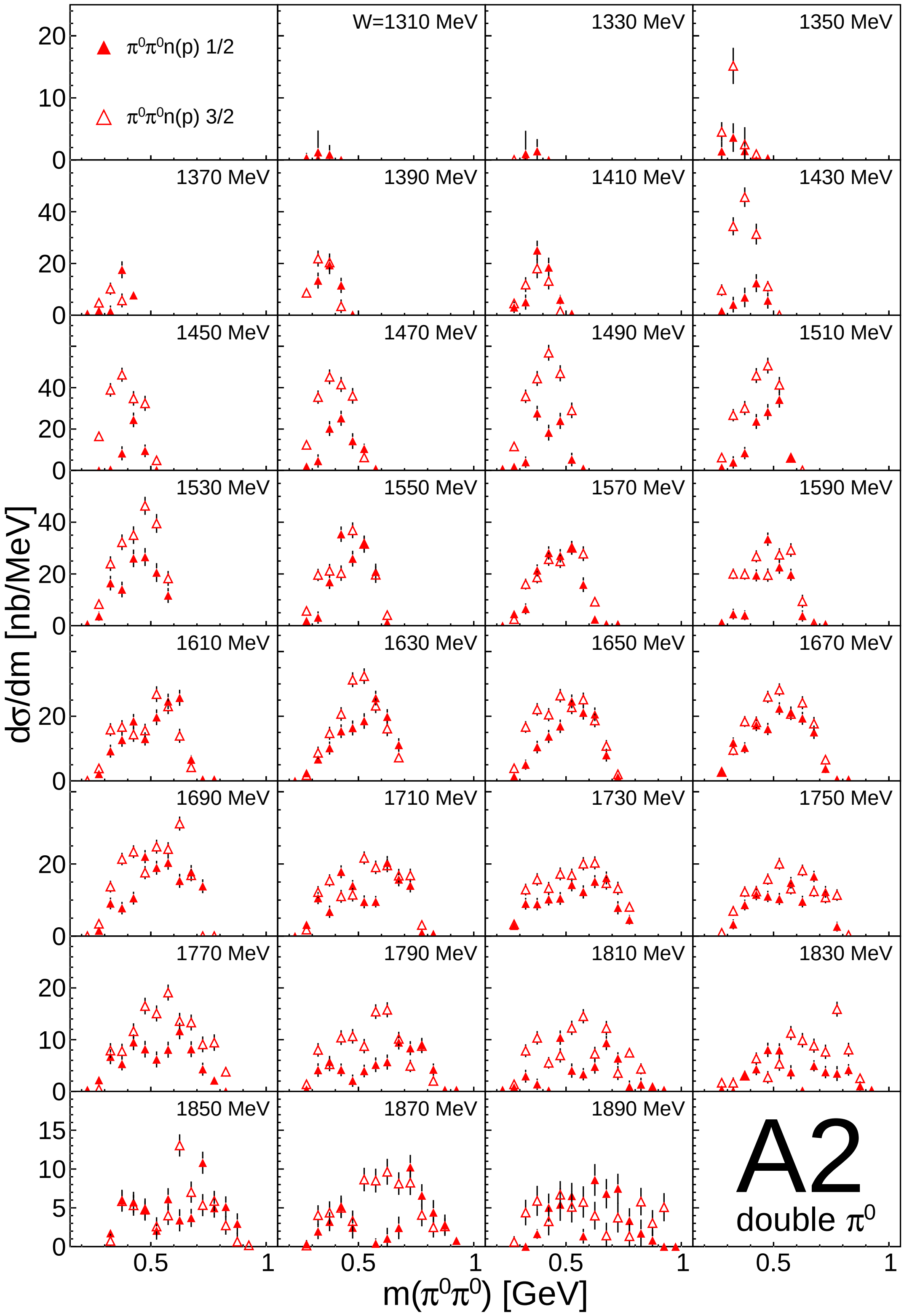

Figure 7.69: Differential helicity dependent cross sections $\sigma_{1/2}$ (solid symbols) and $\sigma_{3/2}$ (open symbols) for double π^0 photoproduction from quasi-free neutrons (not FSI corrected) as a function of the $\pi^0\pi^0$ invariant mass. Results from the A2 data.

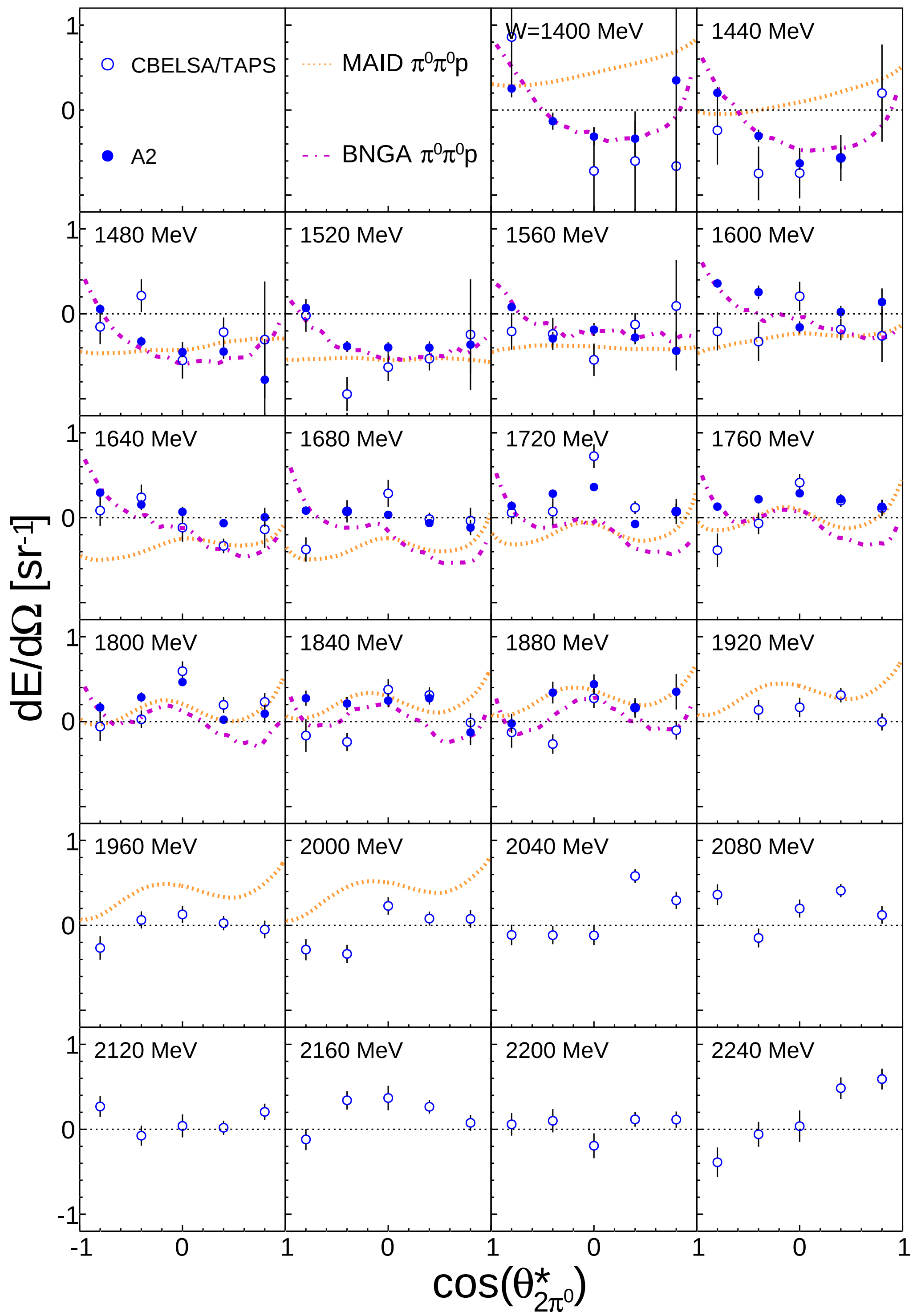

Figure 7.70: Differential double polarization observable E for double π^0 photoproduction from quasi-free protons (not FSI corrected) as a function of the meson polar angle in the $2\pi^0 p$ center of mass frame. Results from the A2 (solid symbols) and CBELSA/TAPS data (open symbols). Dotted orange line: MAID [62]. Dashed-dotted magenta line: BnGa [43].

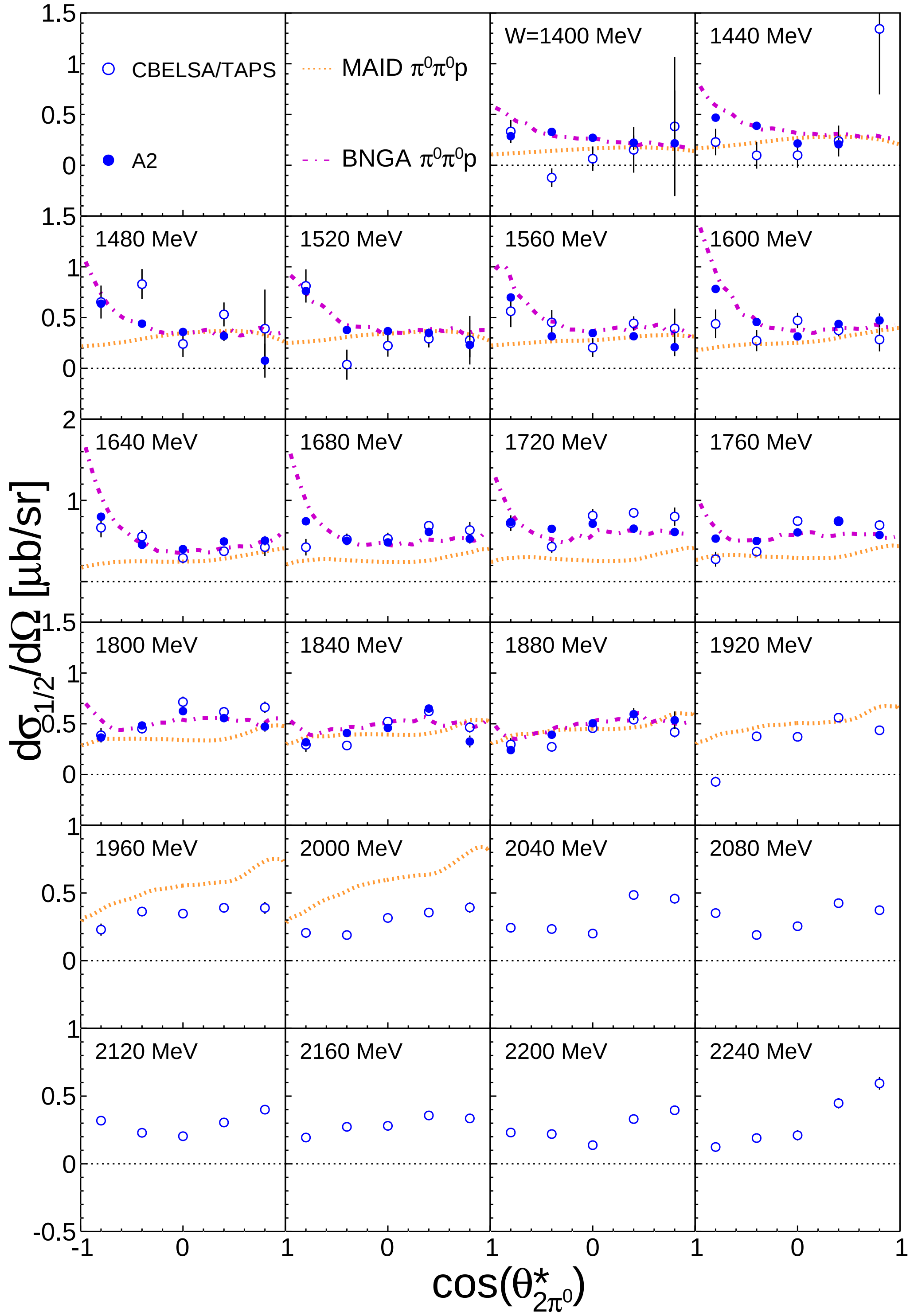

Figure 7.71: Differential helicity dependent cross section $\sigma_{1/2}$ for double π^0 photoproduction from quasi-free protons (not FSI corrected) as a function of the meson polar angle in the $2\pi^0 p$ center of mass frame. Results from the A2 (solid symbols) and CBELSA/TAPS data (open symbols). Dotted orange line: MAID [62]. Dashed-dotted magenta line: BnGa [43].

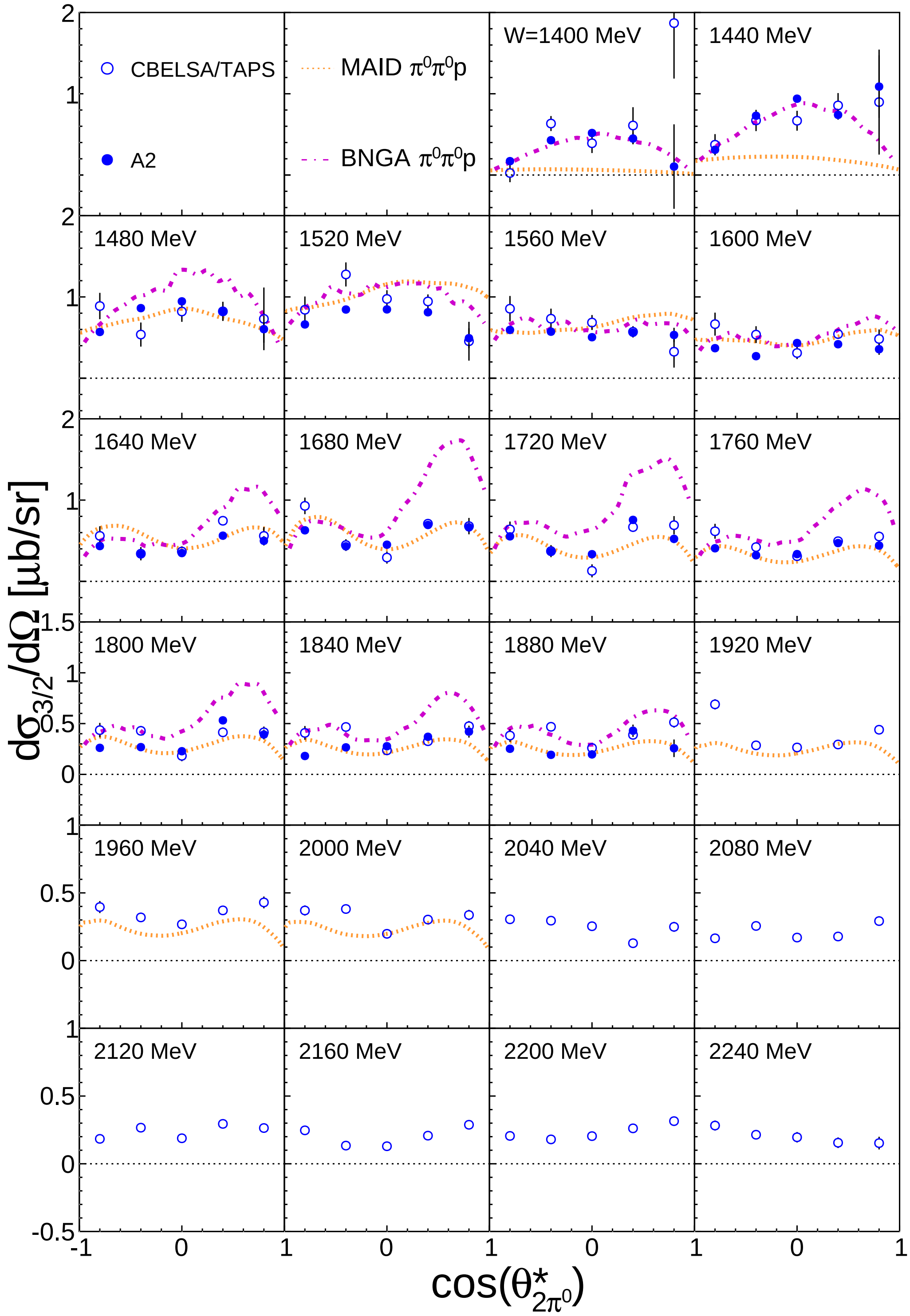

Figure 7.72: Differential helicity dependent cross section $\sigma_{3/2}$ for double π^0 photoproduction from quasi-free protons (not FSI corrected) as a function of the meson polar angle in the $2\pi^0 p$ center of mass frame. Results from the A2 (solid symbols) and CBELSA/TAPS data (open symbols). Dotted orange line: MAID [62]. Dashed-dotted magenta line: BnGa [43].

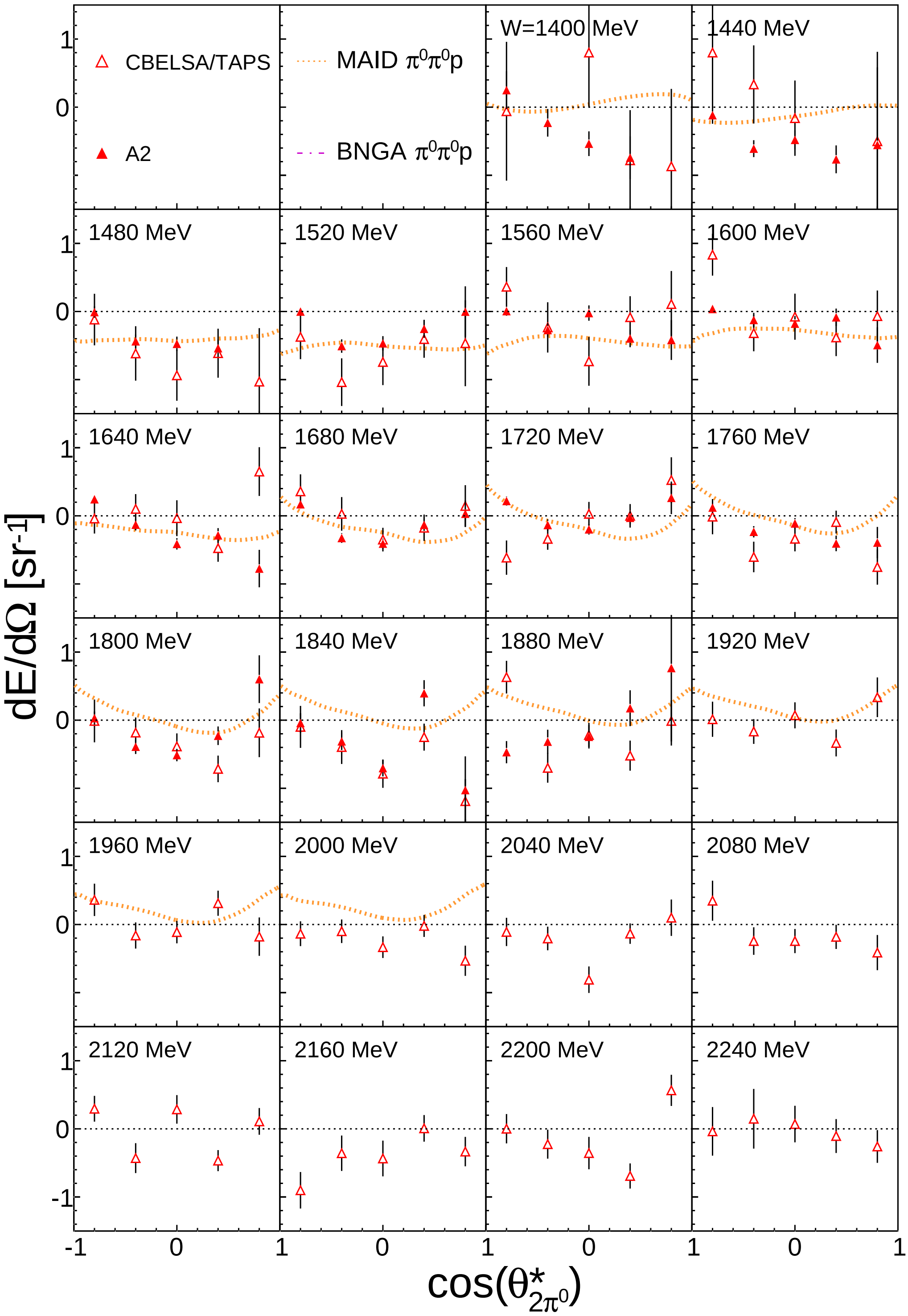

Figure 7.73: Differential double polarization observable E for double π^0 photoproduction from quasi-free neutrons (not FSI corrected) as a function of the meson polar angle in the $2\pi^0 n$ center of mass frame. Results from the A2 (solid symbols) and CBELSA/TAPS data (open symbols). Dotted orange line: MAID [62].

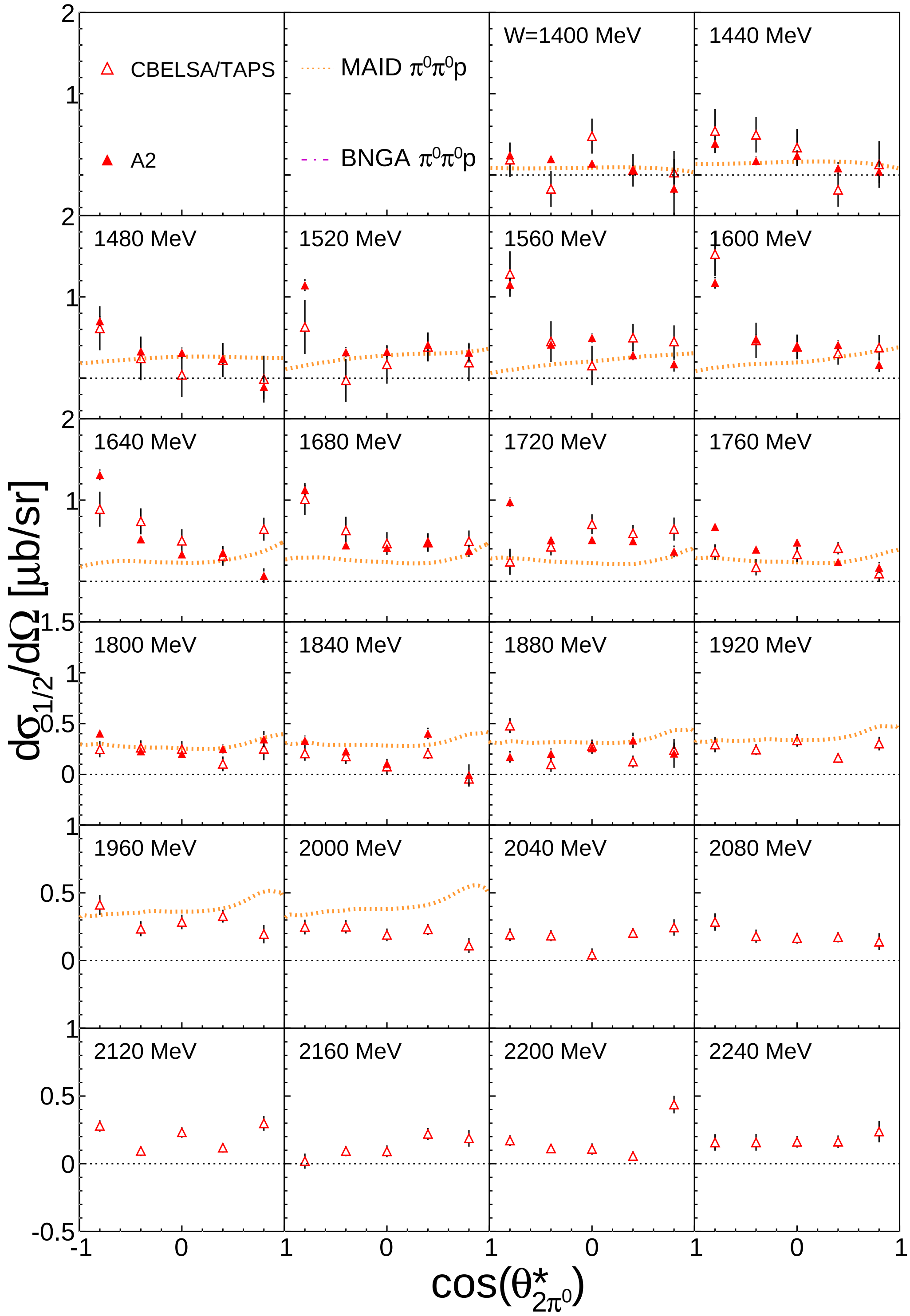

Figure 7.74: Differential helicity dependent cross section $\sigma_{1/2}$ for double π^0 photoproduction from quasi-free neutrons (not FSI corrected) as a function of the meson polar angle in the $2\pi^0 n$ center of mass frame. Results from the A2 (solid symbols) and CBELSA/TAPS data (open symbols). Dotted orange line: MAID [62].

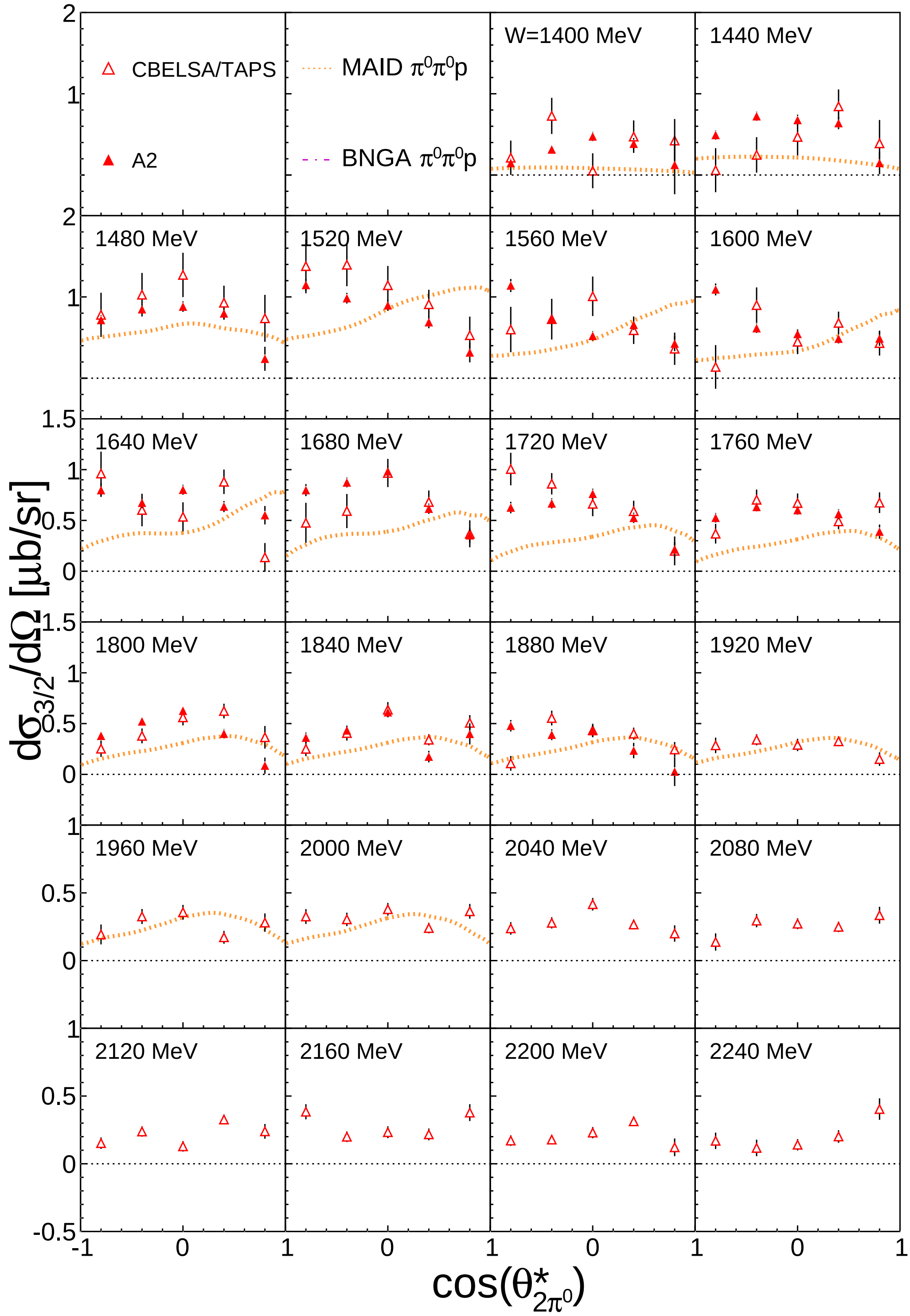

Figure 7.75: Differential helicity dependent cross section $\sigma_{3/2}$ for double π^0 photoproduction from quasi-free neutrons (not FSI corrected) as a function of the meson polar angle in the $2\pi^0 n$ center of mass frame. Results from the A2 (solid symbols) and CBELSA/TAPS data (open symbols). Dotted orange line: MAID [62].

8 Summary and Conclusions

In the present work, precise angular distributions, helicity dependent cross sections and the double polarization observable E have been measured for π^0 and $\pi^0\pi^0$ photoproduction from free and quasi-free nucleons bound in the deuteron.

Significant final state interaction effects ($\sim 35\%$ for single π^0 and $\sim 15\%$ for double π^0 with respect to the free proton cross sections) in the quasi-free proton cross sections were observed. From the comparison of the cross sections for quasi-free protons bound in the deuteron to the results for free protons, the influence of such nuclear effects was estimated. The estimation is based on the assumption that the effects are similar for protons and neutrons and was used to extract the results for free neutrons.

The obtained results comprise of analyses of data obtained within the A2 collaboration at MAMI and the CBELSA/TAPS collaboration at ELSA, which not only provide results of a different energy range and resolution, but also allow for an elaborate investigation of the systematic uncertainties that result from the individual measurements. The results provide an important contribution to the understanding of the excitation spectrum of the nucleon and are an important step towards the complete measurement.

In the following sections, the results and the discoveries of the analyses of single and double π^0 photoproduction from free and quasi-free nucleons will be summarized.

8.1 Single π^0 Photoproduction

Unpolarized cross sections and angular distributions for photoproduction of single π^0 mesons from quasi-free protons and neutrons in the second and third resonance region were measured with high precision at the tagged photon beam facility MAMI.

The comparison of the quasi-free proton and neutron cross sections revealed significant differences in the excitation spectrum of protons and neutrons. A comparison of the reaction on the neutron with the available model predictions from the MAID unitary isobar model [40], the SAID partial wave analysis [39] and the BnGa coupled-channel partial wave analysis [38, 43] clearly demonstrates that the other isospin channels ($p\pi^0$, $p\pi^-$, and $n\pi^+$) do not alone sufficiently constrain the isospin structure of single π^0 photoproduction. Knowledge of the reaction $\gamma n \to \pi^0 n$, as obtained in the present work, is essential for the determination of the neutron helicity couplings of N^* resonances.
A recalculation of the BnGa solution, including the free neutron data from this work, demonstrates the large impact of the present results on contributions from non-resonant background and on partial waves that are related to N^* resonances. The results mainly affect the properties of P_{11} and D_{13} partial waves, among which the well-known low lying Roper resonance ($N(1440)1/2^+$) and the higher-lying $N(1710)1/2^+$ drastically change throughout the first and second resonance region. Contributions from D_{13} partial waves mainly are affected at energies above $W = 1.6$ GeV among which a sign change in the photon coupling of the $N(1710)1/2^+$ was necessary. These results have been published in *Physical Review Letters* (see Ref. [221]). A more detailed version is in preparation for submission to *Physics Letters B*.

The measurement of double polarization observables for $\gamma n \to \pi^0 n$ provides the next step towards reliable neutron couplings. For this purpose, the double polarization observable E and the helicity dependent cross sections $\sigma_{1/2}$ and $\sigma_{3/2}$ were measured for photoproduction of π^0 mesons from quasi-free protons and neutrons with high statistics throughout the second and third resonance region.

In general, the results for the free proton are in good agreement with expectations from the available helicity couplings from the RPP [37]. Due to the much stronger helicity coupling of the $\Delta(1232)3/2^+$ to $\sigma_{3/2}$, in the high energy tail of the Δ-resonance region, the proton cross section is dominated by contributions from $\sigma_{3/2}$. In the second resonance region, $\sigma_{1/2}$ prevails due to the dominant contribution of the $N(1535)1/2^-$ and the third resonance region is again dominated by $\sigma_{3/2}$, due to the strong coupling of the $N(1680)5/2^+$. The neutron cross section is overall dominated by contributions from $\sigma_{3/2}$, with a slight excess of contributions from $\sigma_{1/2}$ in the second resonance region, where the coupling of the $N(1535)1/2^-$ exceeds that of the $N(1520)3/2^-$. The third resonance region is less pronounced with only a small contribution from the $N(1675)5/2^-$.
The FSI correction factor, established in the analysis of unpolarized data, was used to extract the helicity dependent results on the free proton and neutron. This allowed for a detailed comparison of the different resonance contributions to the helicity de-

pendent cross sections $\sigma_{1/2}$ and $\sigma_{3/2}$ for the proton and neutron with the available model predictions. Whereas the different models already predict a very different total cross section for the neutron, the different predictions for the free proton are in good agreement. However, the individual contributions to the helicity dependent cross sections $\sigma_{1/2}$ and $\sigma_{3/2}$ for the proton are strongly model dependent.
The MAID model for the proton drastically underestimates $\sigma_{1/2}$ and overestimates $\sigma_{3/2}$ throughout the second and third resonance region and is in poor agreement with the other two models. In contrast, the solution from SAID and BnGa are close to each other and are in reasonable agreement with the present free proton data, except for the third resonance region, where the contribution to $\sigma_{3/2}$ is overestimated (with respect to the data). By the same amount, the models underestimate the contributions to $\sigma_{1/2}$ in the same energy region, which indicates that more spin 1/2 resonances contribute to the third resonance region of the proton than expected. Thereby, contributions from the $N(1710)1/2^+$, which was affected by the recalculation of the BnGa solution, and from the $N(1720)3/2^+$ might play a role.
The SAID model, which already achieved the best description of the unpolarized neutron cross section (excluding the refit of the BnGa model), is the closest to the neutron data, but strongly differs from the other descriptions.
The high statistics and first time results of unpolarized and polarized data from single π^0 photoproduction from quasi-free and free nucleons provide an important contribution to the world database of single π^0 photoproduction, especially in the neutron sector. The simultaneous measurement of unpolarized cross sections, helicity dependent cross sections, and the double polarization observable E present a significant input for the understanding of the excitation spectrum of the nucleon. The results are ready for publication.

8.2 Double π^0 Photoproduction

A full set of observables comprising total cross sections, angular distributions, and invariant mass distributions, have been measured with high statistics for photoproduction of double π^0 photoproduction from free protons and quasi-free nucleons bound in the deuteron. Data from experiments within the A2 collaboration at MAMI and the CBELSA/TAPS collaboration at ELSA were analyzed with (exclusively) and without (inclusively) the coincident detection of the recoil nucleon. The free proton data are in good agreement with previous measurements and were primarily used as a cross check of the analysis procedures. The exclusive and inclusive measurements are in good agreement and put stringent limits on the systematic uncertainties. The results for free and quasi-free protons differ by about 15% in magnitude, but are of almost identical shape. This indicates the presence of moderate effects from FSI that exhibit an atypical energy and angular independent behavior. In the second resonance region, at energies up to $W \approx 1550$ MeV, the results for the proton and neutron are very similar and are dominated by the decay of the $N(1520)3/2^-$ resonance via the $\Delta(1232)3/2^+\pi^0$ intermediate state. In the third resonance region, the cross sections are still very similar, but the angular distributions and invariant mass distributions from the proton and neutron differ. A decomposition of the total cross section into contributions from phase space decays and decays via intermediate $\Delta(1232)3/2^+\pi^0$ and $N(1520)3/2^-\pi^0$ states showed, that the reaction on the proton is dominated by a strong contribution of $N^* \rightarrow N\sigma$ decays, while for the reaction on the neutron, contributions from the $\Delta(1232)3/2^+\pi^0$ intermediate states remain. The CBELSA/TAPS data is in good agreement with the results from A2 and provides information about the reaction at higher incident photon energies. In addition, it revealed that for energies above the third resonance region, i.e. above $W \approx 2050$ MeV, the proton and neutron cross section become again very similar. The data were compared to the available model predictions from the MAID isobar model [62] and the BnGa coupled-channel partial wave analysis [43] (only available for the proton). The MAID model predicts results of similar shape, but a suppression of the neutron results compared to those from the proton. It underestimates both data significantly, which indicates that it does not properly account for certain resonance contributions or even misses some. In contrast, the BnGa solution is in reasonable agreement with the proton data. The largest discrepancies were observed in the region of the peak in the third resonance region, where though the different previous results exhibit the largest disagreement. The results from the A2 data have been published in *The European Physics Journal A* (see Ref. [219]).

The measurement of the double polarization observable E, i.e. of the helicity dependent cross sections $\sigma_{1/2}$ and $\sigma_{3/2}$, shed some light on the situation. From both analyses, helicity dependent cross sections, angular distributions, and invariant mass distributions in the energy range of the second and third resonance region were extracted. In addition, the decomposition into contributions from phase space and $\Delta(1232)3/2^+$, as well as $N(1520)3/2^-$ intermediate states, was carried out using the helicity dependent cross sections. Signatures of the $N\sigma$ decay are dominantly seen in $\sigma_{3/2}$ from the proton, while $\sigma_{1/2}$ and $\sigma_{3/2}$ from the neutron are both dominated by intermediate $\Delta(1232)3/2^+\pi^0$ decays, which confirms the processes that were observed from the unpolarized results. In the second resonance region, i.e. until energies of $W \approx 1550$ MeV, the proton cross section is dominated by resonances with total angular momentum $J \geq 3/2$. At higher energies, resonances with $J = 1/2$ are dominant, which is not expected by the models. Both model results predict a change in the sign of the double polarization observable E at energies of $W \approx 1750$ MeV. In contrast, the neutron cross section is dominated by resonances with total angular momentum $J \geq 3/2$ throughout all energies. These observations indicate a significant underestimation of $\sigma_{1/2}$ by the models and can certainly provide important input for the improvement of the calculations.
Estimates for the helicity dependent cross sections and of the double polarization observable E on the free nucleons were determined by applying the correction factor (as used for the extraction of the unpolarized free neutron cross section) to the measured quantities σ_{diff}, σ_{sum}, $\sigma_{1/2}$, $\sigma_{3/2}$, and σ_{unpol}. The estimates of the observables were then extracted and averaged from the different versions in the same way as for the quasi-free results. Compared to the quasi-free results, the free proton and neutron cross sections are almost identical in shape, but are approximately 15%

higher in magnitude. The BnGa model is in good agreement with the free proton results, but underestimates $\sigma_{1/2}$ in the third resonance region. As a consequence, the prediction overestimates $\sigma_{3/2}$, which explains why the sign change in the double polarization observable E is predicted at too high energies and might be due to a wrong contribution of the $N(1710)1/2^+$. In contrast, the MAID model is in good agreement with $\sigma_{3/2}$ of the proton except in the threshold region, but significantly underestimates all the other results.

In summary, the results from the analyses from A2 and CBELSA/TAPS data provide a full set of unpolarized and helicity dependent quantities comprising total cross sections, helicity dependent cross sections, and invariant mass distributions for $2\pi^0$ photoproduction from free and quasi-free nucleons. Whereas the statistical quality of the A2 data is sufficient for the extraction of angular distributions of the unpolarized and polarized results in the second and third resonance regions, the CBELSA/TAPS data is just of adequate quality in order to confirm the A2 results up to the third resonance region and to draw conclusions for the extended energy range. These results present the first measurement of unpolarized and helicity dependent cross sections from the neutron and provide essential information for the understanding of the excitation spectrum of the nucleon. The results from the A2 and CBELSA/TAPS data are ready for publication.

Appendix

A Constants and Tables

A.1 Physical Properties of Scintillators

Table A.1 gives an overview of the physical properties of some of the scintillators used in the experimental setups at A2 and CBELSA/TAPS.

Scintillator	Type	Density [g/cm^3]	Radiation Length [cm]	Light Output [% Anthracene]	Decay constant, main component [ns]	Wavelength of maximum emission [nm]
NaI(Tl)	Crystal	3.67	2.59	230	230	413
CsI(Tl)	Crystal	4.51	1.86	95	1100	580
EJ-204	Plastic	1.023	$\sim$ 43	68	1.8	408
NE-104	Plastic	1.032	$\sim$ 43	68	1.9	406
BaF_2	Crystal	4.89	2.026	46 (slow) / 9.2 (fast)	620 (slow) / 0.6 (fast)	310 (slow) / 180-240 (fast)
$PbWO_4$	Crystal	8.30	0.8903	-	30 (slow) / 10 (fast)	420 nm

Table A.1: Physical properties of some of the scintillators used at A2 and CBELSA/TAPS. [120, 201]

$\mathcal{B}$

Supplementary Information

B.1 The χ^2 Distribution

The probability density function of a normally (or *Gaussian*) distributed sample of random variables x with expectation value μ and standard deviation σ is given by:

$$f(x) = \frac{1}{\sqrt{2\pi}\sigma} \exp\left[-\frac{(x-\mu)^2}{2\sigma^2}\right] . \tag{B.1}$$

For the simplified case of a standard normal distribution, i.e. a normally distributed sample of random variables x with expectation value $\mu = 0$ and standard deviation $\sigma = 1$, the sum of the squares of the elements of k subsamples

$$x^2 \stackrel{!}{=} \chi^2 = x_1^2 + x_2^2 + \ldots + x_k^2 , \tag{B.2}$$

follows the cumulative distribution function

$$\begin{aligned} F_k(\chi^2) &= \frac{1}{\Gamma(k/2)2^{k/2}} \cdot \int_0^{\chi^2} u^{k/2-1} \exp(-u/2)du \\ &= \frac{\gamma(k/2, \chi^2/2)}{\Gamma(k/2)}, \end{aligned} \tag{B.3}$$

where k is the number of degrees of freedom of the sample, $\Gamma(k/2)$ is the Gamma function, and $\gamma(k/2, \chi^2/2)$ is the lower incomplete Gamma function. The probability density function is then given by [225]:

$$f_k(\chi^2) = \frac{(\chi^2)^{k/2-1}}{\Gamma(k/2) \cdot 2^{k/2}} \cdot \exp(-\chi^2/2) . \tag{B.4}$$

Examples for the cumulative distribution function $F_k(\chi^2)$ and the probability density function $f_k(\chi^2)$ for a few different degrees of freedom are illustrated in Figure B.1.

For general normally distributed random variables of expectation value μ and standard deviation σ, the sum of squares of equation (B.2) is no longer directly described by a χ^2 distribution. However, this can be revised by considering the modified sum of squares

$$x^2 \stackrel{!}{=} \chi^2 = \frac{(x_1 - \mu)^2 + (x_2 - mu)^2 + \ldots + (x_k - mu)^2)^2}{\sigma^2}, \tag{B.5}$$

or for subsamples with different means μ_i and standard deviations σ_i

$$x^2 \stackrel{!}{=} \chi^2 = \frac{(x_1 - \mu_1)^2}{\sigma_1^2} + \frac{(x_2 - \mu_2)^2}{\sigma_2^2} + \ldots + \frac{(x_k - \mu_k)^2}{\sigma_k^2}, \tag{B.6}$$

which immediately again follows a χ^2 distribution.

The primary importance of the χ^2 distribution is given by the χ^2 test, where the quantity χ^2 is used as a measure of the confidence of a certain event. As in equation (B.6), the value χ^2 was defined as the sum of squares of deviations from the expectation value, the smaller the value of χ^2 the more plausible the event can be considered. Thereby, the cumulative distribution function $F_k(\chi^2)$ (equation (B.3)) represents the probability $P(x^2 < \chi^2)$ that a random variable x^2 will not exceed a value of χ^2.
A quantity that is often used to describe the degree of confidence is the *confidence level* $W_k(\chi^2)$ which represents the probability that a random value x^2 of the same distribution is greater than or equal to χ^2:

$$W_k(\chi^2) = 1 - F_k(\chi^2). \tag{B.7}$$

From the definition and interpretation of $F_k(\chi^2)$, it is reasonable that low values of χ^2 correspond to large values of $W_k(\chi^2)$ and vice versa. The confidence level distributions for a few degrees of freedom are illustrated on the right-hand side of Figure B.1. Note that the confidence level value $W_k(\chi^2)$ is given on the x-axis and was sampled according to the probability density function $f_k(\chi^2)$.

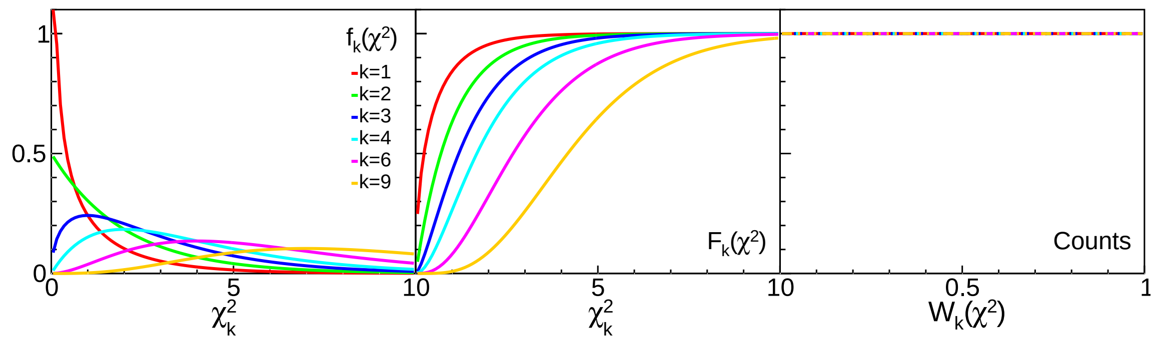

Figure B.1: Illustration of the χ^2 distribution. Left column: probability density function $f_k(\chi^2)$. Middle column: cumulative distribution function $F_k(\chi^2)$. Right column: normalized confidence level distributions $W_k(\chi^2)$. Shown are the representatives for different degrees of freedom k.

B.2 Determination of the Error in Invariant Mass

As discussed in section 6.1, the neutral clusters were assigned to the decay photons from the π^0 and $\pi^0\pi^0$ mesons with a χ^2 test on the invariant mass of the two photons. For every possible combination of two photons to a π^0 meson or four photons to a $\pi^0\pi^0$, pair the χ^2 value was determined as follows:

$$\left(\chi^2\right)_k^{ij} = \sum_{i=1}^{k} \left(\frac{m_{\gamma_i\gamma_j} - m_{\pi^0}}{\Delta m_{\gamma_i\gamma_j}}\right)^2 \begin{cases} k=1, & i,j=1,2,3, \qquad\qquad i \neq j \quad | \quad \pi^0 \\ k=2, & i,j=1,2,3,4,(5), \quad i \neq j \quad | \quad \pi^0\pi^0 \end{cases}, \tag{B.8}$$

where m_{π^0} is the nominal mass of the π^0 meson, $m_{\gamma_i\gamma_j}$ is the invariant mass of the two photons that form a π^0, and

$$m_{\gamma_i\gamma_j} = \sqrt{2E_{\gamma_i}E_{\gamma_j} \cdot \left(1 - \cos\phi_{\gamma_i\gamma_j}\right)}\ , \tag{B.9}$$

and $\phi_{\gamma_i\gamma_j}$ is the opening angle between the two photons that is given by the inner product of the two photon momenta p_{γ_i} and p_{γ_j}:

$$\begin{aligned} \cos\phi_{\gamma_i\gamma_j} &= \frac{\vec{p}_{\gamma_i} \cdot \vec{p}_{\gamma_j}}{|\vec{p}_{\gamma_i}| \cdot |\vec{p}_{\gamma_j}|} = \frac{p^x_{\gamma_i}p^x_{\gamma_j} + p^y_{\gamma_i}p^y_{\gamma_j} + p^z_{\gamma_i}p^z_{\gamma_j}}{|\vec{p}_{\gamma_i}| \cdot |\vec{p}_{\gamma_j}|} \\ &= \sin\theta_{\gamma_i}\sin\theta_{\gamma_j}\cos\phi_{\gamma_i}\cos\phi_{\gamma_j} + \\ &\quad \sin\theta_{\gamma_i}\sin\theta_{\gamma_j}\sin\phi_{\gamma_i}\sin\phi_{\gamma_j} + \\ &\quad \cos\theta_{\gamma_i}\cos\theta_{\gamma_j} . \end{aligned} \tag{B.10}$$

Therefore, the error of the invariant mass $\Delta m_{\gamma_i\gamma_j}$ is given by:

$$\begin{aligned} \Delta m_{\gamma_i\gamma_j} &= \sqrt{\left(\frac{\partial m_{\gamma_i\gamma_j}}{\partial E_{\gamma_i}}\Delta E_{\gamma_i}\right)^2 + \left(\frac{\partial m_{\gamma_i\gamma_j}}{\partial E_{\gamma_j}}\Delta E_{\gamma_j}\right)^2 + \left(\frac{\partial m_{\gamma_i\gamma_j}}{\partial \cos\phi_{\gamma_i\gamma_j}}\Delta\cos\phi_{\gamma_i\gamma_j}\right)^2} \\ &= \frac{1}{2}m_{\gamma_i\gamma_j}\sqrt{\left(\frac{\Delta E_{\gamma_i}}{E_{\gamma_i}}\right)^2 + \left(\frac{\Delta E_{\gamma_j}}{E_{\gamma_j}}\right)^2 + \left(\frac{\Delta\cos\phi_{\gamma_i\gamma_j}}{1 - \cos\phi_{\gamma_i\gamma_j}}\right)^2} \end{aligned}, \tag{B.11}$$

where the error of the opening angle $\Delta\cos\phi_{\gamma_i\gamma_j}$ is given by

$$\begin{aligned} \Delta\cos\phi_{\gamma_i\gamma_j} = \Big\{ & \left[-\sin\theta_{\gamma_i}\theta_{\gamma_j}\sin(\phi_{\gamma_i} - \phi_{\gamma_j})\right]^2 \cdot \Delta\phi^2_{\gamma_i} + \\ & \left[-\sin\theta_{\gamma_i}\theta_{\gamma_j}\sin(\phi_{\gamma_j} - \phi_{\gamma_i})\right]^2 \cdot \Delta\phi^2_{\gamma_j} + \\ & \left[\left(\cos\theta_{\gamma_i}\sin\theta_{\gamma_j}\cos(\phi_{\gamma_i} - \phi_{\gamma_j}) - \sin\theta_{\gamma_i}\cos\theta_{\gamma_j}\right)^2\right]^2 \cdot \Delta\theta^2_{\gamma_i} + \\ & \left[\left(\sin\theta_{\gamma_i}\cos\theta_{\gamma_j}\cos(\phi_{\gamma_j} - \phi_{\gamma_i}) - \cos\theta_{\gamma_i}\sin\theta_{\gamma_j}\right)^2\right]^2 \Delta\theta^2_{\gamma_j} \Big\}^{1/2} . \end{aligned} \tag{B.12}$$

For the determination of the error in the invariant mass that is used for the χ^2 test, the error of the energy ΔE, the azimuthal angle $\Delta\phi$, and the polar angle $\Delta\theta$ have to be known. They were determined by simulations and for the individual calorimeters are presented in section 5.4.1 and 5.4.3. For every χ^2 value of a photon pair ij the error is evaluated individually according to their energies E_{γ_i}, E_{γ_j}, azimuthal and polar angles ϕ_{γ_i}, ϕ_{γ_j}, θ_{γ_i}, θ_{γ_j}, and the corresponding errors ΔE_{γ_i}, ΔE_{γ_j}, $\Delta\phi_{\gamma_i}$, $\Delta\phi_{\gamma_j}$, $\Delta\theta_{\gamma_i}$, $\Delta\theta_{\gamma_j}$.

B.3 Kinetic Energy of the Recoil Nucleon

Under certain conditions nucleons may not fully deposit their kinetic energy in the detector and hence make a reconstruction of their energy from the measured energy impossible. However, the angular information as reconstructed from their impact in the detector is still valid and of the same precision as for all other particles. In such cases it is advantageous that their kinetic energy in free and quasi-free kinematics can be recalculated with the following formalisms.

For photoproduction of a meson m on a free target nucleon p, the kinetic energy of the recoil nucleon T_p is simply given by the difference of the incident photon energy E_γ and the energy of the meson E_m

$$T_p^{\text{free}} = E_\gamma - E_m \tag{B.13}$$

The derivation of the kinetic energy of the recoil participant nucleon in quasi-free kinematics needs some more effort. Consider a photoproduction reaction on a participant nucleon N_p inside a target nucleus d at rest

$$\gamma + d \rightarrow m + N_p + N_s \ , \tag{B.14}$$

which produces a final state meson m and distributes the remaining energy among the meson, the participant nucleon and the spectator nucleon N_s. In this case the kinetic energy of the participant nucleon in the final state can be determined exactly by knowing the mass of the target nucleon m_d, the incident photon energy E_γ, the energy of the meson E_m, the mass m_p, the polar and azimuthal angle θ_p, ϕ_p of the participant nucleon as well as the mass of the spectator nucleon m_n. The calculation is based on the energy and momentum conservation of the reaction with the photon beam in z-direction, where the index p denotes the participant nucleon and the index s the spectator nucleon

$$\begin{pmatrix} 0 \\ 0 \\ E_\gamma \\ E_\gamma \end{pmatrix} + \begin{pmatrix} 0 \\ 0 \\ 0 \\ m_d \end{pmatrix} = \begin{pmatrix} p_x^m \\ p_y^m \\ p_z^m \\ E_m \end{pmatrix} + \begin{pmatrix} p_x^p \\ p_y^p \\ p_z^p \\ E_p \end{pmatrix} + \begin{pmatrix} p_x^s \\ p_y^s \\ p_z^s \\ E_s \end{pmatrix} \ . \tag{B.15}$$

Inserting the momentum components of the spectator nucleon into the energy equation of equation (B.15) yields

$$\begin{aligned} E_\gamma + m_d &= E_m + E_p + \sqrt{p_{s,x}^2 + p_{s,y}^2 + p_{s,z}^2 + m_s^2} \\ &= E_m + E_p + \sqrt{\left(p_x^m + p_x^p\right)^2 + \left(p_y^m + p_y^p\right)^2 + \left(E_\gamma - \left(p_z^m + p_z^p\right)\right)^2 + m_s^2} \ . \end{aligned} \tag{B.16}$$

The participant energy E_p is therefore given by

$$\begin{aligned} E_p &= E_\gamma + m_d - E_m \\ &\quad - \sqrt{(p_x^m + p_x^p)^2 + \left(p_y^m + p_y^p\right)^2 + (E_\gamma - (p_z^m + p_z^p))^2 + m_s^2} \ . \end{aligned} \tag{B.17}$$

Inserting equation (B.17) into the definition of the kinetic energy of the participant nucleon:

$$T_p = E_p - m_p \tag{B.18}$$

yields

$$\begin{aligned} T_p &= E_\gamma - E_m + m_d - m_p \\ &\quad - \sqrt{p_m^2 + p_p^2 + 2\vec{p}_m\vec{p}_p + E_\gamma^2 - 2E_\gamma\left(p_z^m + p_z^p\right) + m_s^2} \ . \end{aligned} \tag{B.19}$$

Using the expression (B.18) for the kinetic energy of the participant nucleon, the absolute value of the participant momentum can be written as

$$\begin{aligned} |\vec{p}| &= \sqrt{E_p^2 - m_p^2} = \sqrt{(T_p + m_p)^2 - m_p^2} \\ &= \sqrt{T_p(T_p + 2m_p)} \ . \end{aligned} \tag{B.20}$$

The polar and azimuthal angle θ_p and ϕ_p of the participant nucleon can then be introduced as follows:

$$\begin{aligned} \vec{p}_p &= |\vec{p}_p| \begin{pmatrix} \sin(\theta_p)\cos(\phi_p) \\ \sin(\theta_p)\sin(\phi_p) \\ \cos(\theta_p) \end{pmatrix} \\ &= \sqrt{T_p\left(T_p + 2m_p\right)} \begin{pmatrix} \sin(\theta_p)\cos(\phi_p) \\ \sin(\theta_p)\sin(\phi_p) \\ \cos(\theta_p) \end{pmatrix} \ . \end{aligned} \tag{B.21}$$

Therefore the terms in the square root of equation (B.19) can be written as

$$\begin{aligned} p_p^2 &= T_p\left(T_p + 2m_p\right) \\ 2\vec{p}_m\vec{p}_p &= 2\sqrt{T_p\left(T_p + 2m_p\right)}\,[p_x^m \sin(\theta_p)\cos(\phi_p) \\ &\qquad + p_y^m \sin(\theta_p)\sin(\phi_p) + p_z^m \cos(\theta_p)] \\ -2E_\gamma p_z^p &= -2E_\gamma\sqrt{T_p\left(T_p + 2m_p\right)}\cos(\theta_p) \ . \end{aligned} \tag{B.22}$$

Defining

$$a := p_x^m \sin(\theta_p)\cos(\phi_p) + p_y^m \sin(\theta_p)\sin(\phi_p) + (p_z^m - E_\gamma)\cos(\theta_p) \tag{B.23}$$

and inserting this expression (B.23) into equation (B.19) yields

$$\begin{aligned} T_p &= E_\gamma - E_m + m_d - m_p \\ &\quad - \sqrt{p_m^2 + T_p\left(T_p + 2m_p\right) + 2\sqrt{T_p\left(T_p + 2m_p\right)}a + E_\gamma^2 - 2E_\gamma p_z^m + m_s^2} \ . \end{aligned} \tag{B.24}$$

Squaring equation (B.24) and substituting

$$\begin{aligned} b &:= E_m - E_\gamma - m_d \\ c &:= \left(E_m + m_p - E_\gamma - m_d\right)^2 - \left(m_s^2 + p_m^2 + E_\gamma^2 - 2E_\gamma p_z^m\right) \ , \end{aligned} \tag{B.25}$$

yields for equation (B.24)

$$\begin{aligned} \left(2T_p b + c\right)^2 &= 4a^2 T_p \left(T_p + 2m_p\right) \\ \rightarrow 4b^2T_p^2 + 4bcT_p + c^2 &= 4a^2T_p^2 + 4a^2 2m_p T_p \ . \end{aligned} \tag{B.26}$$

Finally the following quadratic equation of the kinetic energy of the recoil nucleon

$$T_p^2\left(4b^2 - 4a^2\right) + T_p\left(4bc - 8a^2 m_p\right) + c^2 = 0 \tag{B.27}$$

has to be solved to find the two solutions

$$T_p^{1,2} = \frac{-\left(4bc - 8a^2m_p\right) \pm \sqrt{\left(4bc - 8a^2m_p\right)^2 - 4\left(4b^2 - 4a^2\right)c^2}}{2\left(4b^2 - 4a^2\right)} \ , \tag{B.28}$$

where a, b and c are given by equations (B.23) and (B.25).

To use the achieved formula for the kinetic energy of the participant nucleon, T_p, one has to verify which solution of the two is the physically correct one. For this purpose $1 \cdot 10^5$ events of η photoproduction from the quasi-free neutron $\gamma + d \rightarrow \eta + n + p$ were generated with PLUTO (see section 3.4.1). The kinetic energy of the participant neutron was then recalculated according to the two possible solutions from equation (B.28) and compared to the generated value. Figure B.2 shows the difference of each solution and the generated values. It is clearly visible that the only

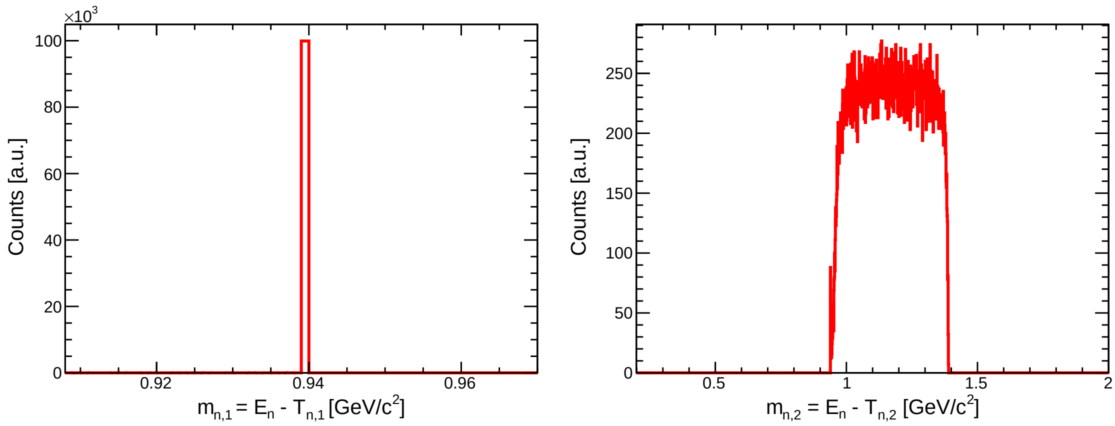

Figure B.2: Reconstructed mass of the neutron from the two solutions of equation (B.28).

physically correct solution of (B.28) is achieved in the left-hand side of figure B.2

which shows an exact value for m_n for all of the $100'000$ events. This corresponds to the following solution of (B.28)

$$T_p^{\text{quasi-free}} = \frac{-\left(4bc - 8a^2 m_p\right) + \sqrt{\left(4bc - 8a^2 m_p\right)^2 - 4\left(4b^2 - 4a^2\right)c^2}}{2\left(4b^2 - 4a^2\right)} \,, \tag{B.29}$$

where the parameters a, b and c are given by

$$\begin{aligned} a &= p_{m,x}\sin(\theta_p)\cos(\phi_p) + p_{m,y}\sin(\theta_p)\sin(\phi_p) + (p_{m,z} - E_\gamma)\cos(\theta_p) \\ b &= E_m - E_\gamma - m_d \\ c &= \left(E_m + m_p - E_\gamma - m_d\right)^2 - \left(m_s^2 + p_m^2 + E_\gamma^2 - 2E_\gamma p_{m,z}\right) \,. \end{aligned} \tag{B.30}$$

C Additional Spectra

C.1 Carbon Background Subtraction

This chapter presents the estimation of the background contribution from reactions on unpolarized nucleons inside the carbon and oxygen nuclei by means of coplanarity or invariant mass spectra, instead of missing mass spectra as discussed in Section 6.13.4.
Shown are the corresponding coplanarity and invariant mass spectra for the carbon subtraction in the analysis of single π^0 photoproduction (Figures C.1 and C.4) double π^0 photoproduction from the A2 data (Figures C.2 and C.5) and double π^0 photoproduction from the CBELSA/TAPS data (Figures C.3 and C.6).

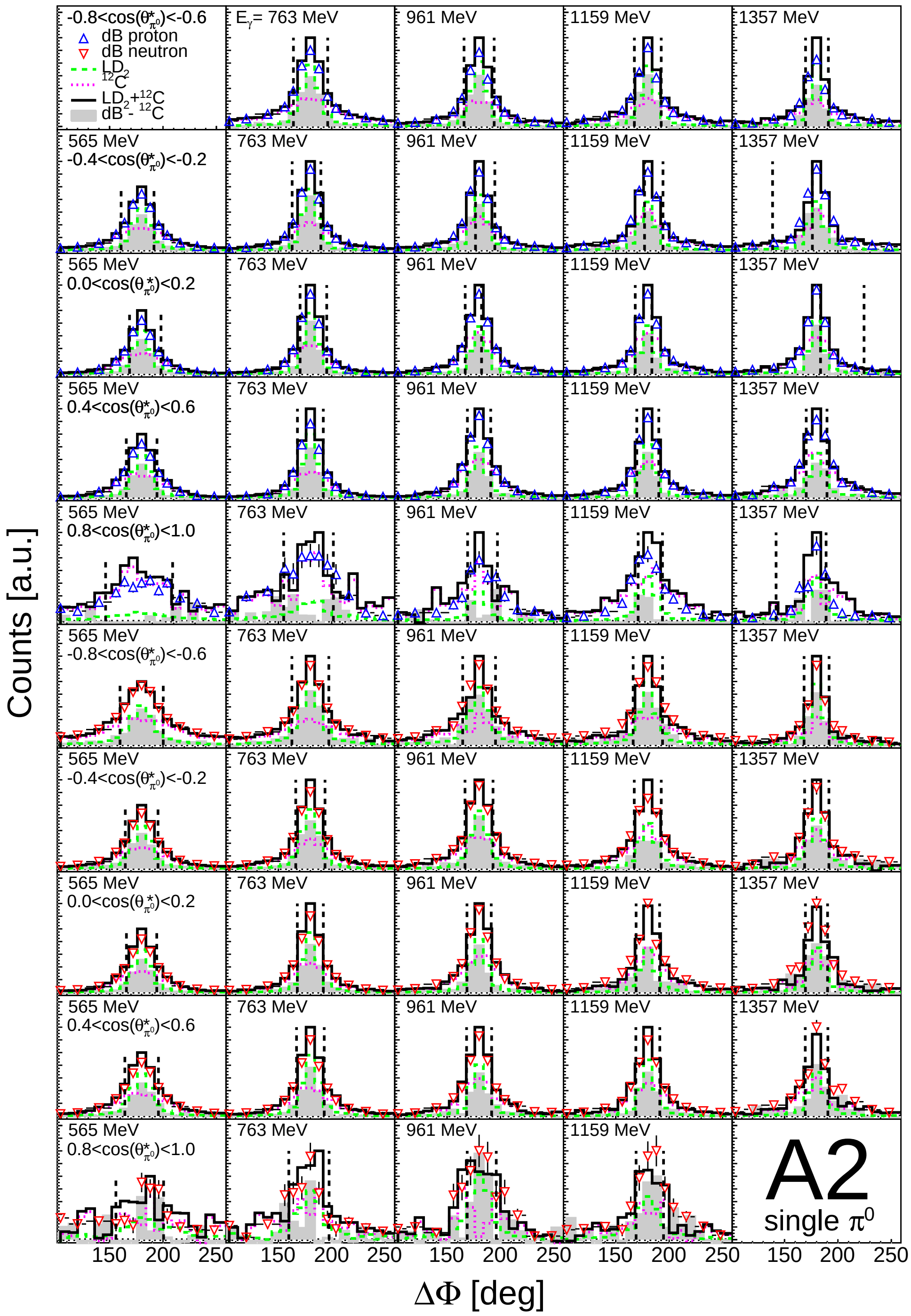

Figure C.1: Illustration of the estimation of the carbon background by means of coplanarity spectra for exclusive single π^0 photoproduction. Results from the A2 data. Shown are five selected energy and angular bins. All cuts were applied to the data. Red (blue) triangles: proton (neutron) distribution from the deuterated butanol data. Dashed green histogram: distribution from the deuterium data. Dotted magenta histogram: distribution from the carbon data. Black histogram: sum of deuterium and carbon data. Gray histogram: carbon subtracted yield from the deuterated butanol target. Dashed vertical black lines: coplanarity cut from deuterium data.

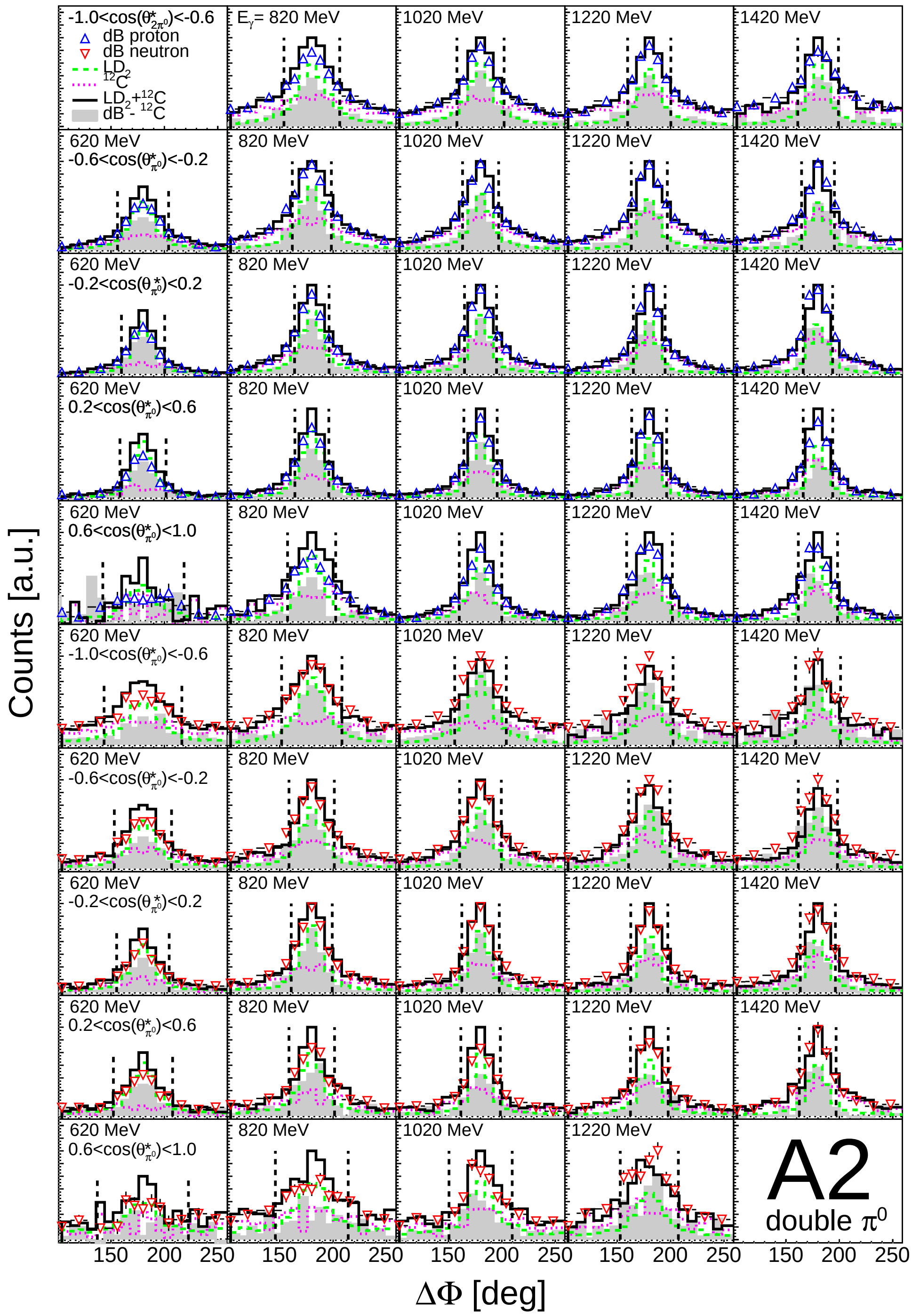

Figure C.2: Illustration of the estimation of the carbon background by means of coplanarity spectra for exclusive double π^0 photoproduction. Results from the A2 data. Shown are five selected energy and angular bins. All cuts were applied to the data. Red (blue) triangles: proton (neutron) distribution from the deuterated butanol data. Dashed green histogram: distribution from the deuterium data. Dotted magenta histogram: distribution from the carbon data. Black histogram: sum of deuterium and carbon data. Gray histogram: carbon subtracted yield from the deuterated butanol target. Dashed vertical black lines: coplanarity cut from deuterium data.

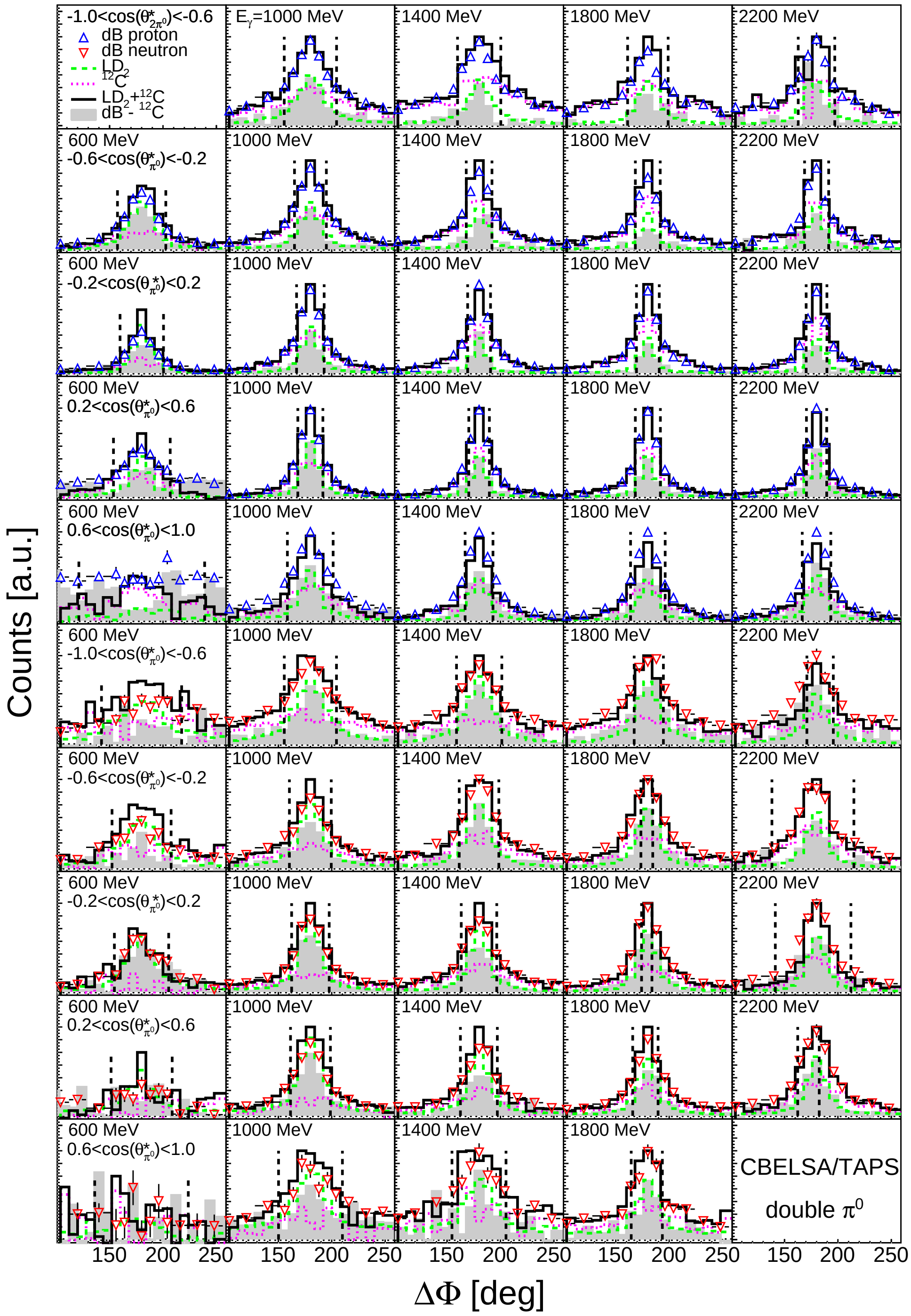

Figure C.3: Illustration of the estimation of the carbon background by means of coplanarity spectra for exclusive double π^0 photoproduction. Results from the CBELSA/TAPS data. Shown are five selected energy and angular bins. All cuts were applied to the data. Red (blue) triangles: proton (neutron) distribution from the deuterated butanol data. Dashed green histogram: distribution from the deuterium data. Dotted magenta histogram: distribution from the carbon data. Black histogram: sum of deuterium and carbon data. Gray histogram: carbon subtracted yield from the deuterated butanol target. Dashed vertical black lines: coplanarity cut from deuterium data.

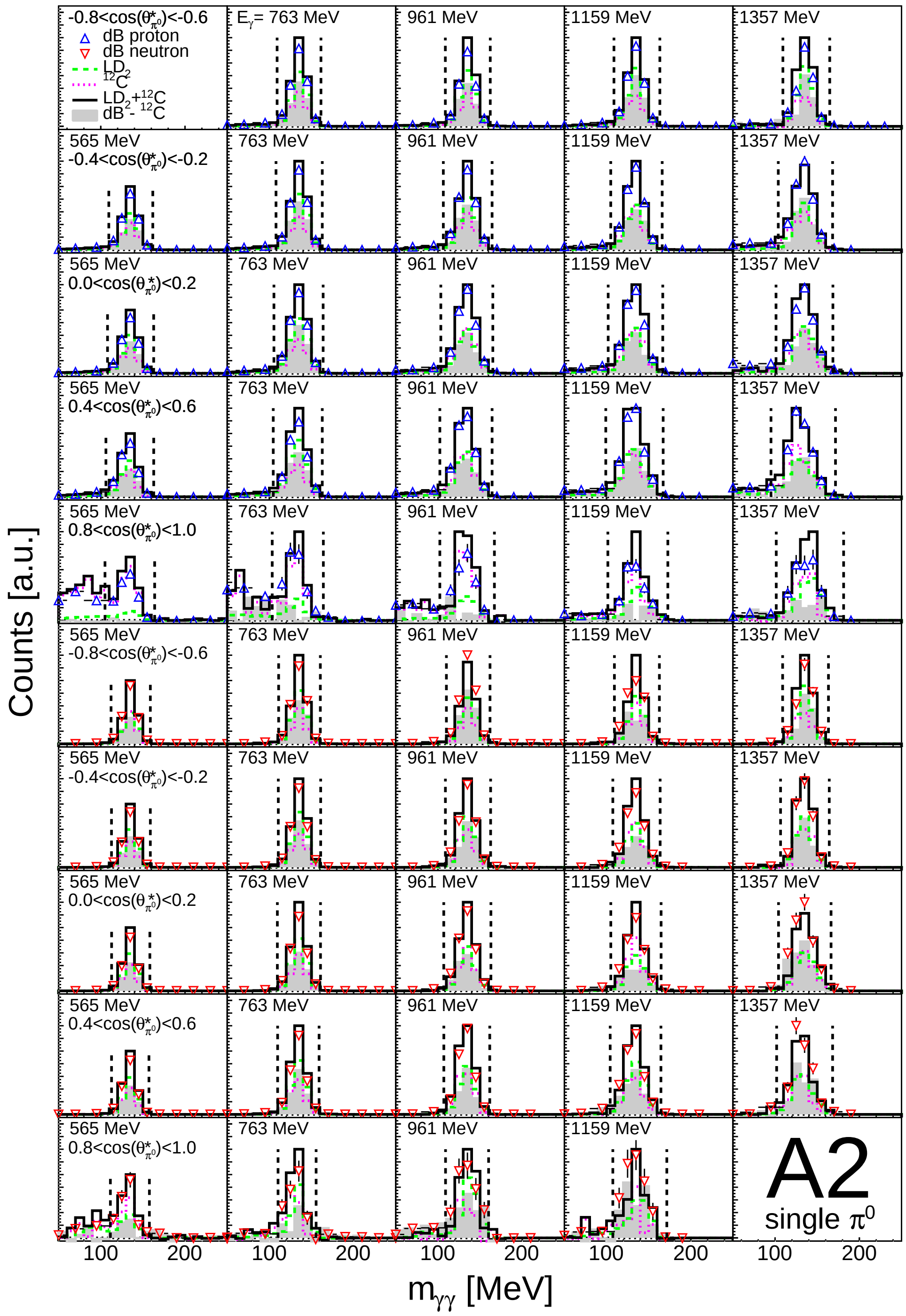

Figure C.4: Illustration of the estimation of the carbon background by means of invariant mass spectra for exclusive single π^0 photoproduction. Results from the A2 data. Shown are five selected energy and angular bins. All cuts were applied to the data. Red (blue) triangles: proton (neutron) distribution from the deuterated butanol data. Dashed green histogram: distribution from the deuterium data. Dotted magenta histogram: distribution from the carbon data. Black histogram: sum of deuterium and carbon data. Gray histogram: carbon subtracted yield from the deuterated butanol target. Dashed vertical black lines: invariant mass cut from deuterium data.

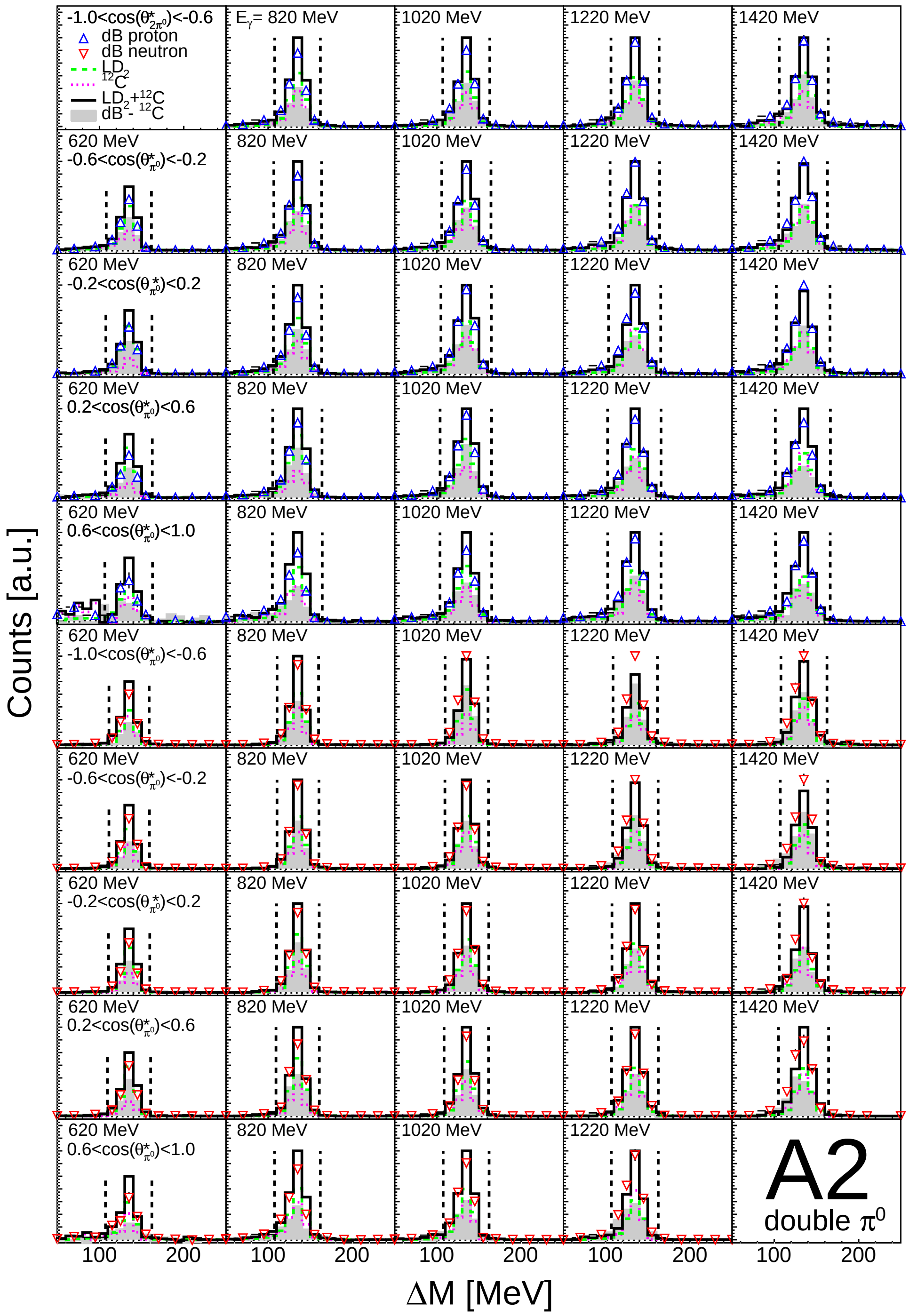

Figure C.5: Illustration of the estimation of the carbon background by means of invariant mass spectra for exclusive double π^0 photoproduction. Results from the A2 data. Shown are five selected energy and angular bins. All cuts were applied to the data. Red (blue) triangles: proton (neutron) distribution from the deuterated butanol data. Dashed green histogram: distribution from the deuterium data. Dotted magenta histogram: distribution from the carbon data. Black histogram: sum of deuterium and carbon data. Gray histogram: carbon subtracted yield from the deuterated butanol target. Dashed vertical black lines: invariant mass cut from deuterium data.

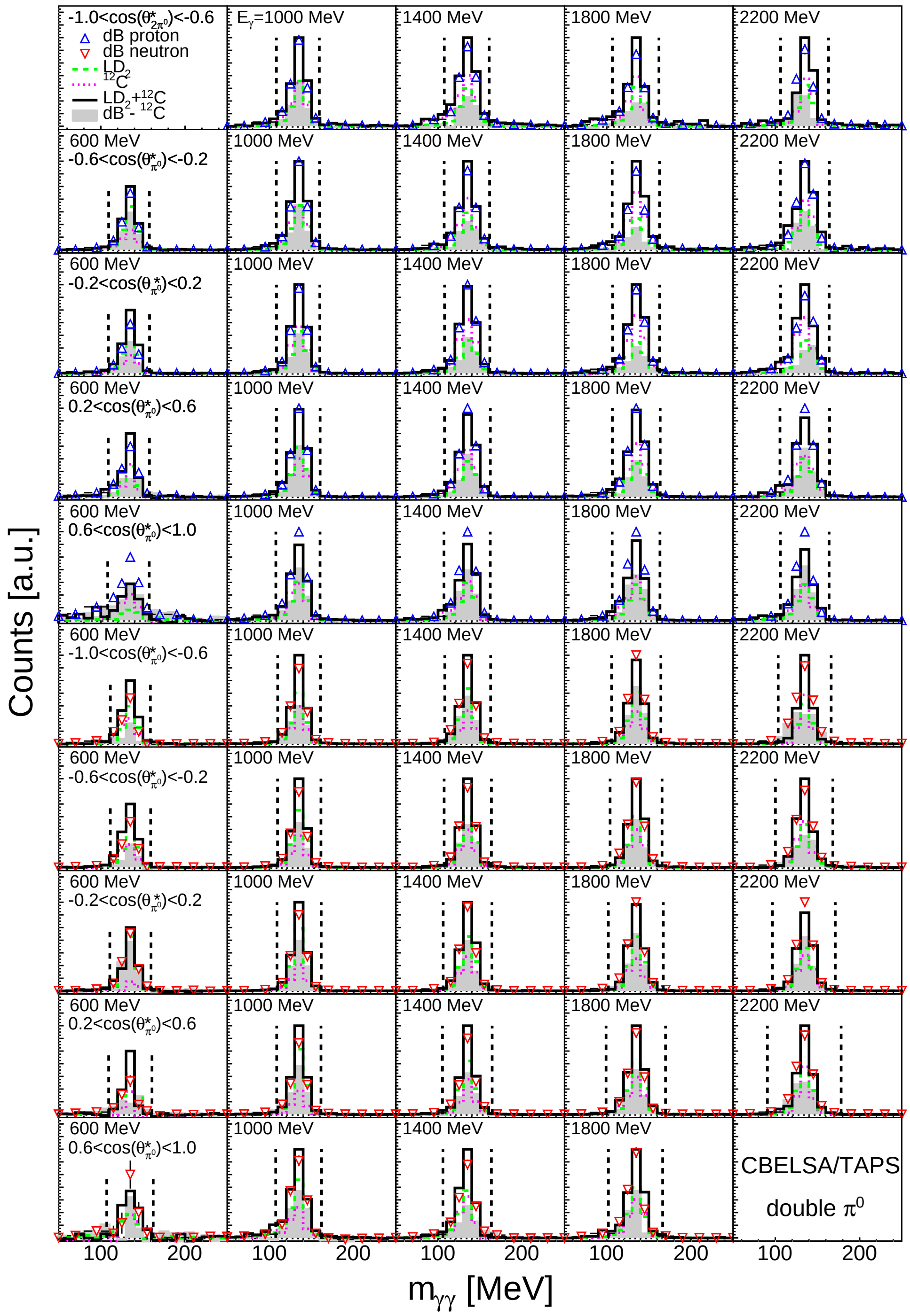

Figure C.6: Illustration of the estimation of the carbon background by means of invariant mass spectra for exclusive double π^0 photoproduction. Results from the CBELSA/TAPS data. Shown are five selected energy and angular bins. All cuts were applied to the data. Red (blue) triangles: proton (neutron) distribution from the deuterated butanol data. Dashed green histogram: distribution from the deuterium data. Dotted magenta histogram: distribution from the carbon data. Black histogram: sum of deuterium and carbon data. Gray histogram: carbon subtracted yield from the deuterated butanol target. Dashed vertical black lines: invariant mass cut from deuterium data.

D Supplementary Results

This chapter presents additional results that were not shown in the final results in Chapter 7.

D.1 Single π^0 Photoproduction

This section presents additional results from the analysis of single π^0 photoproduction from unpolarized and polarized A2 data discussed in Sections 7.1 and 7.4.

D.1.1 Unpolarized Cross Sections

This section presents additional results from the analysis of single π^0 photoproduction from the unpolarized A2 data discussed in Sections 7.1.

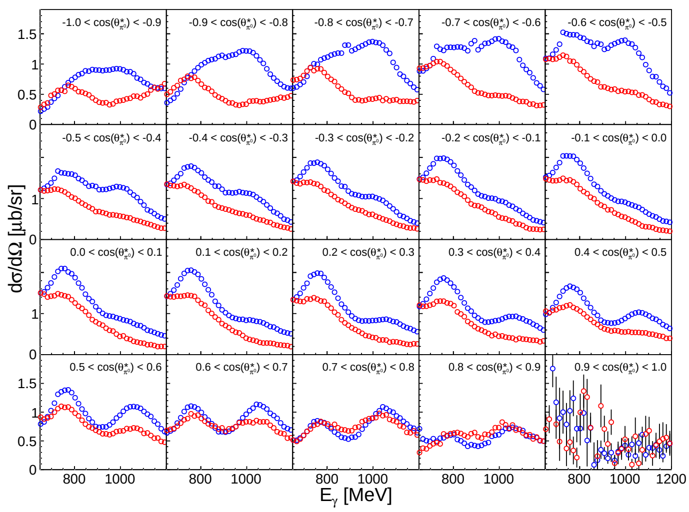

Figure D.1: Differential cross sections for exclusive π^0 photoproduction from quasi-free nucleons as a function of the incident photon energy E_γ. Results from the A2 data. Open blue circles: proton. Open red circles: neutron.

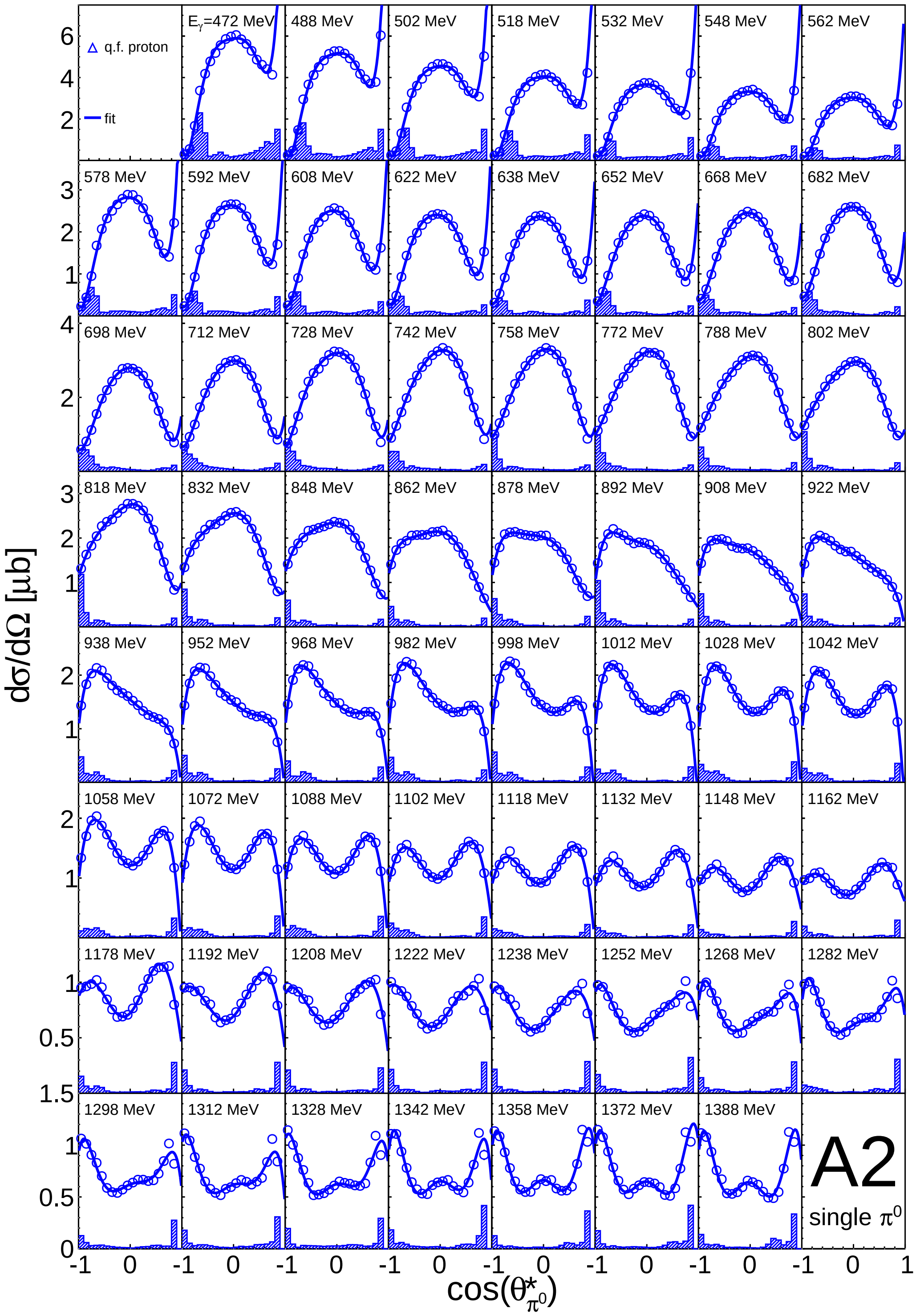

Figure D.2: Differential cross sections for exclusive π^0 photoproduction from the quasi-free proton as function of the polar angle of the pion in the $\pi^0 p$ center of mass system. Results from the A2 data. Shown is the result for energy bins of incident photon energy E_γ. Solid line: Legendre fit. Hatched histogram: systematic uncertainties.

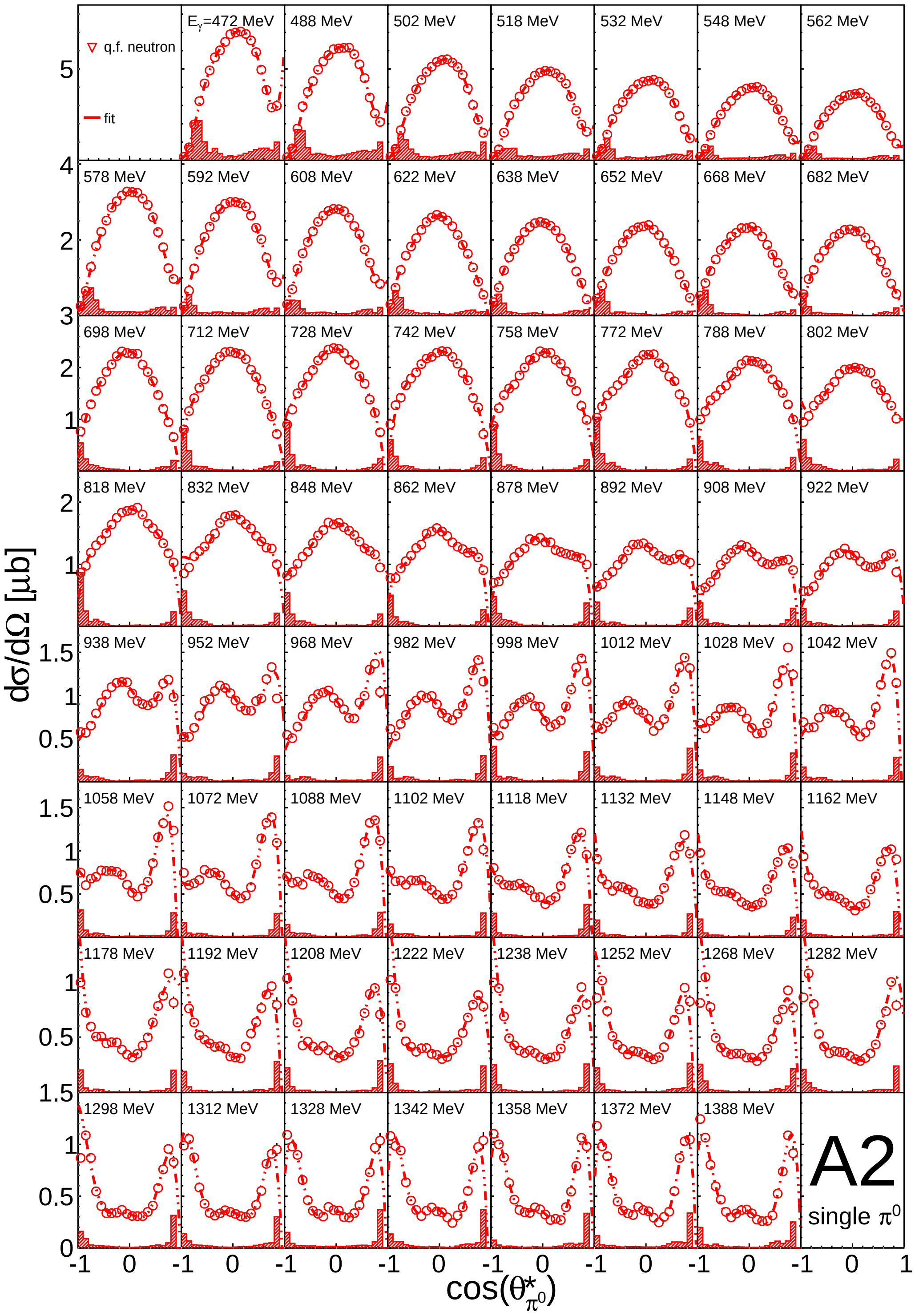

Figure D.3: Differential cross sections for exclusive π^0 photoproduction from the quasi-free neutron as function of the polar angle of the pion in the $\pi^0 p$ center of mass system. Results from the A2 data. Shown is the result for energy bins of incident photon energy E_γ. Solid line: Legendre fit. Hatched histogram: systematic uncertainties.

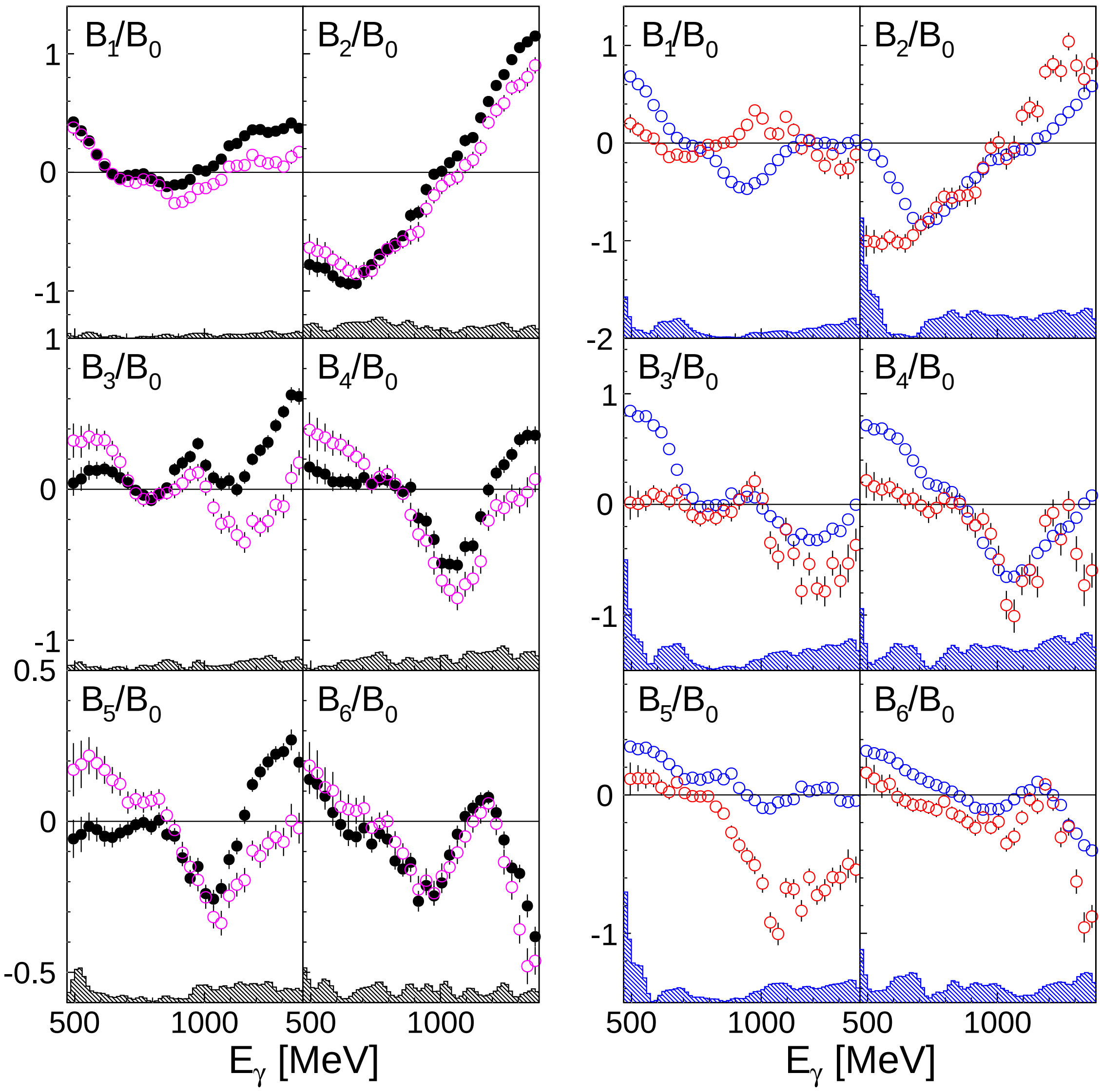

(a) $\gamma N \to \pi^0(N)$

(b) $\gamma N \to \pi^0 N$

Figure D.4: Legendre coefficient ratios for single π^0 photoproduction as function of the incident photon energy E_γ. Results from the A2 data. Left-hand side: Quasi-free inclusive reaction on the deuteron. Right-hand side: Quasi-free exclusive reactions on quasi-free nucleons. Solid black circles: quasi-free inclusive result. Open magenta circles: sum of exclusive proton and neutron results. Open blue circles: exclusive proton results. Open red circles: exclusive neutron result. The hatched histograms represent the systematic uncertainties of the corresponding cross sections.

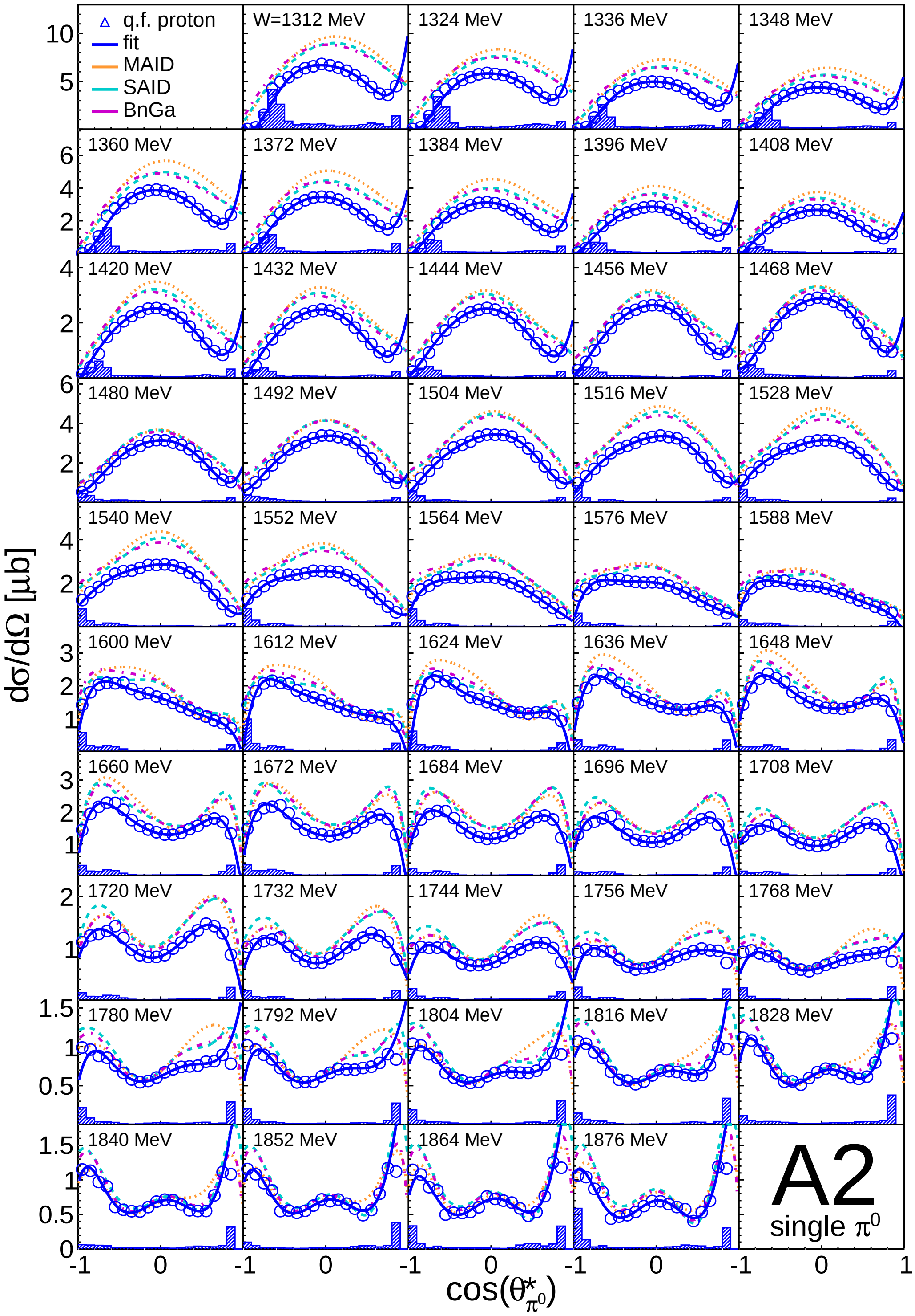

Figure D.5: Differential cross sections for exclusive π^0 photoproduction from quasi-free protons as a function of the polar angle of the pion in the $\pi^0 p$ center of mass system. Results from the A2 data. Notations as in Figure 7.5. The hatched histograms at the bottom represent the systematic uncertainties.

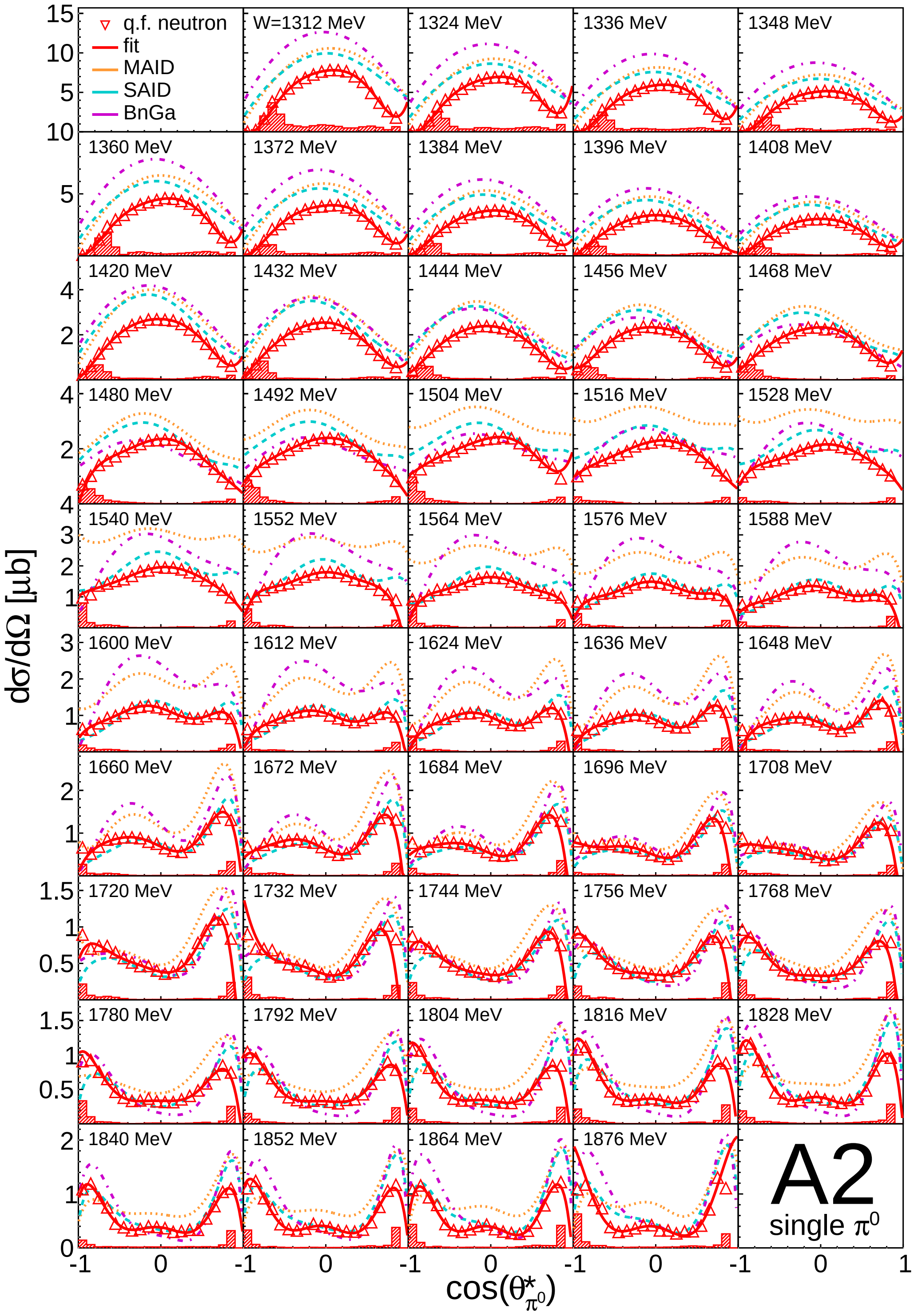

Figure D.6: Differential cross sections for exclusive π^0 photoproduction from quasi-free neutrons as a function of the polar angle of the pion in the $\pi^0 n$ center of mass system. Results from the A2 data. Notations as in Figure 7.5. The hatched histograms at the bottom represent the systematic uncertainties.

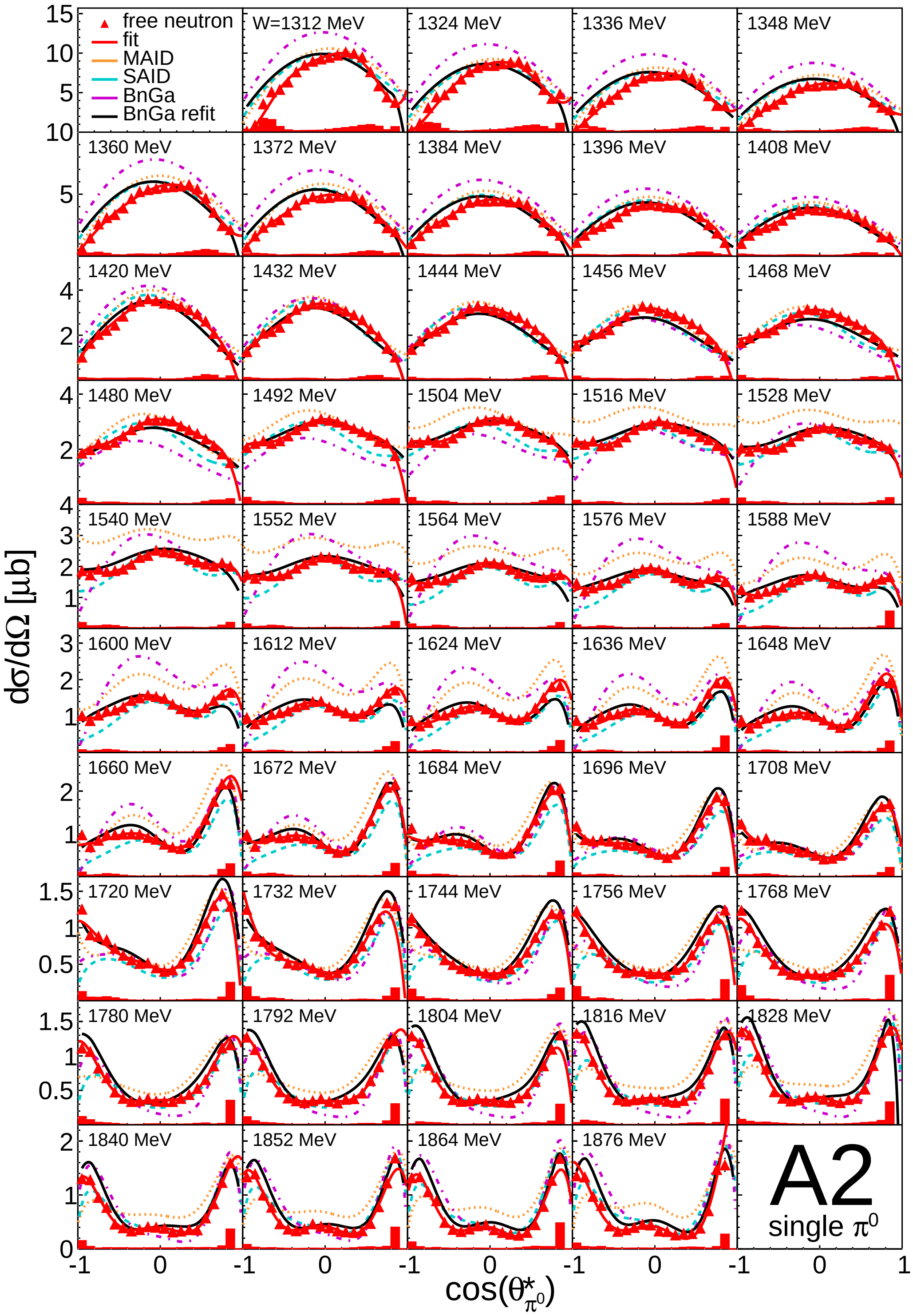

Figure D.7: Estimated differential cross sections for exclusive π^0 photoproduction from the free neutron as a function of the polar angle of the pion in the $\pi^0 n$ center of mass system. Results from the A2 data. Notations as in Figure 7.5. The hatched histograms at the bottom represent the systematic uncertainties.

D.1.2 Polarized Cross Sections

This section presents additional results from the analysis of single π^0 photoproduction from the polarized A2 data discussed in Sections 7.4.

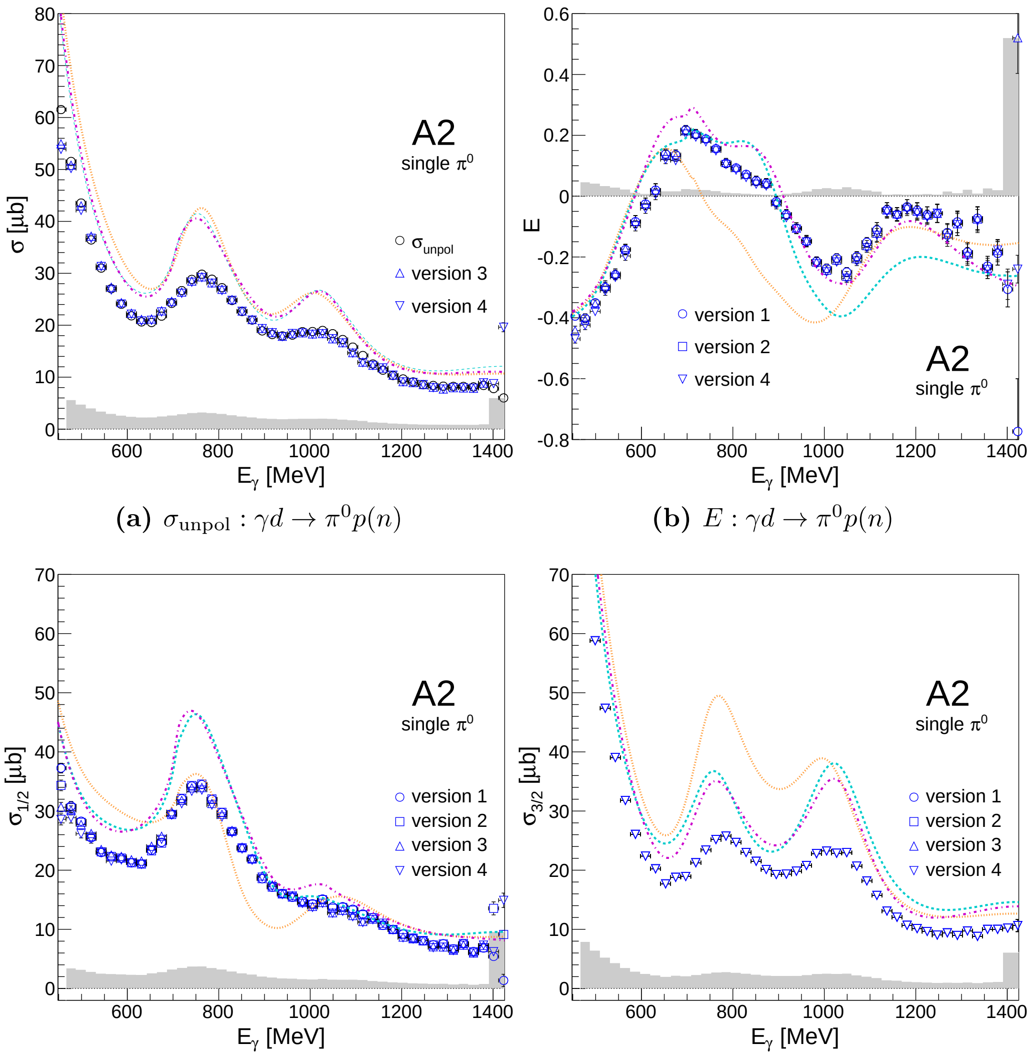

(a) $\sigma_{\text{unpol}} : \gamma d \to \pi^0 p(n)$

(b) $E : \gamma d \to \pi^0 p(n)$

(c) $\sigma_{1/2} : \gamma d \to \pi^0 p(n)$

(d) $\sigma_{3/2} : \gamma d \to \pi^0 p(n)$

Figure D.8: Double polarization observables for single π^0 photoproduction from quasi-free protons as a function of the incident photon energy E_γ. Results from the A2 data. (a) Reconstructed unpolarized total cross section σ_{unpol}. (b) Double polarization observable E. (c) Helicity dependent cross section $\sigma_{1/2}$. (d) Helicity dependent cross section $\sigma_{3/2}$. The different versions are summarized in Table 6.12. Dotted orange line: MAID [40]. Dashed cyan line: SAID [39]. Dashed-dotted magenta line: BnGa [43]. The gray histogram at the base line of each figure represents the systematical uncertainties of the results.

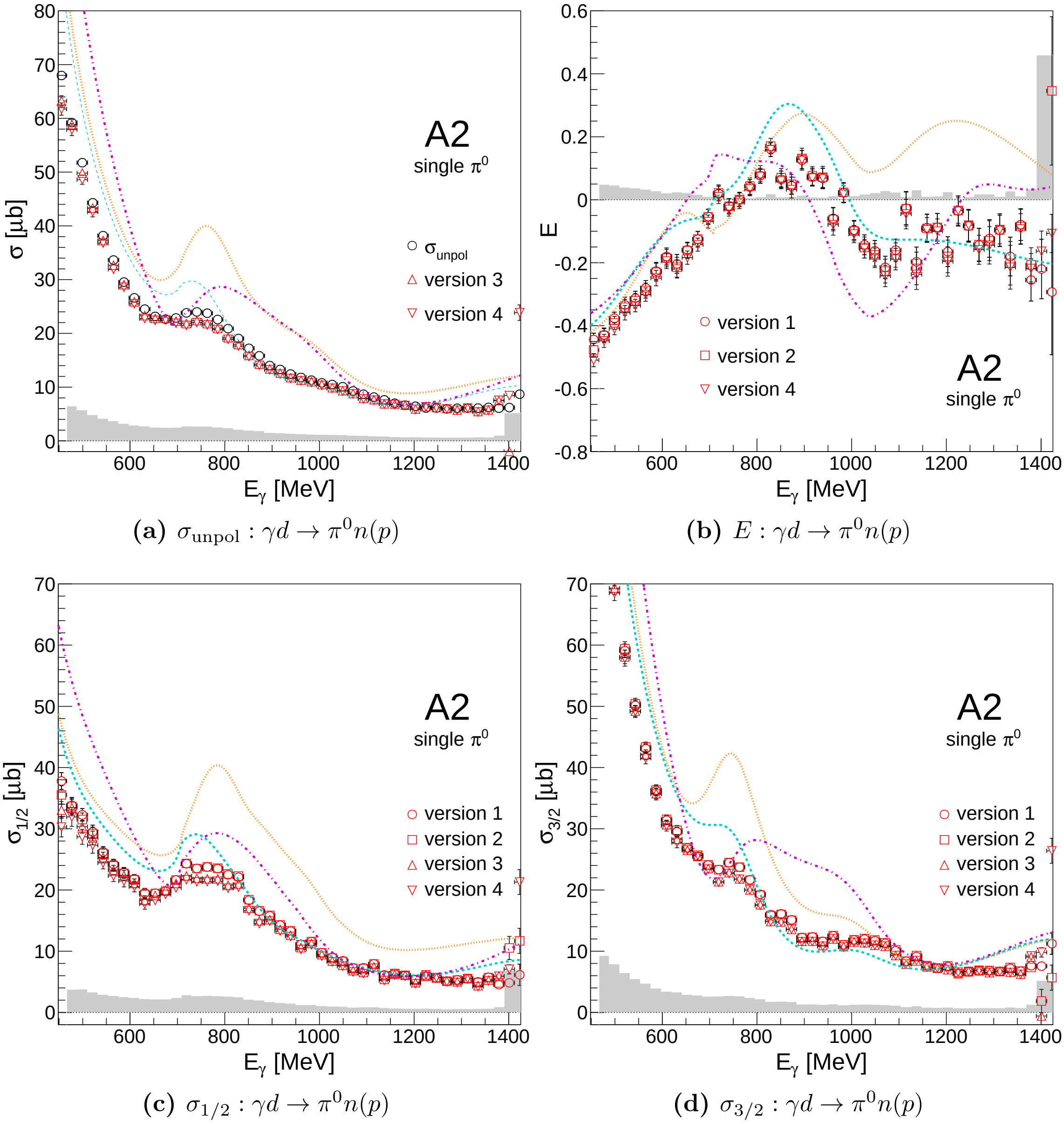

(a) $\sigma_{\text{unpol}} : \gamma d \to \pi^0 n(p)$

(b) $E : \gamma d \to \pi^0 n(p)$

(c) $\sigma_{1/2} : \gamma d \to \pi^0 n(p)$

(d) $\sigma_{3/2} : \gamma d \to \pi^0 n(p)$

Figure D.9: Double polarization observables for single π^0 photoproduction from quasi-free neutrons as a function of the incident photon energy E_γ. Results from the A2 data. (a) Reconstructed unpolarized total cross section σ_{unpol}. (b) Double polarization observable E. (c) Helicity dependent cross section $\sigma_{1/2}$. (d) Helicity dependent cross section $\sigma_{3/2}$. The different versions are summarized in Table 6.12. Dotted orange line: MAID [40]. Dashed cyan line: SAID [39]. Dashed-dotted magenta line: BnGa [38]. The gray histogram at the base line of each figure represents the systematical uncertainties of the results.

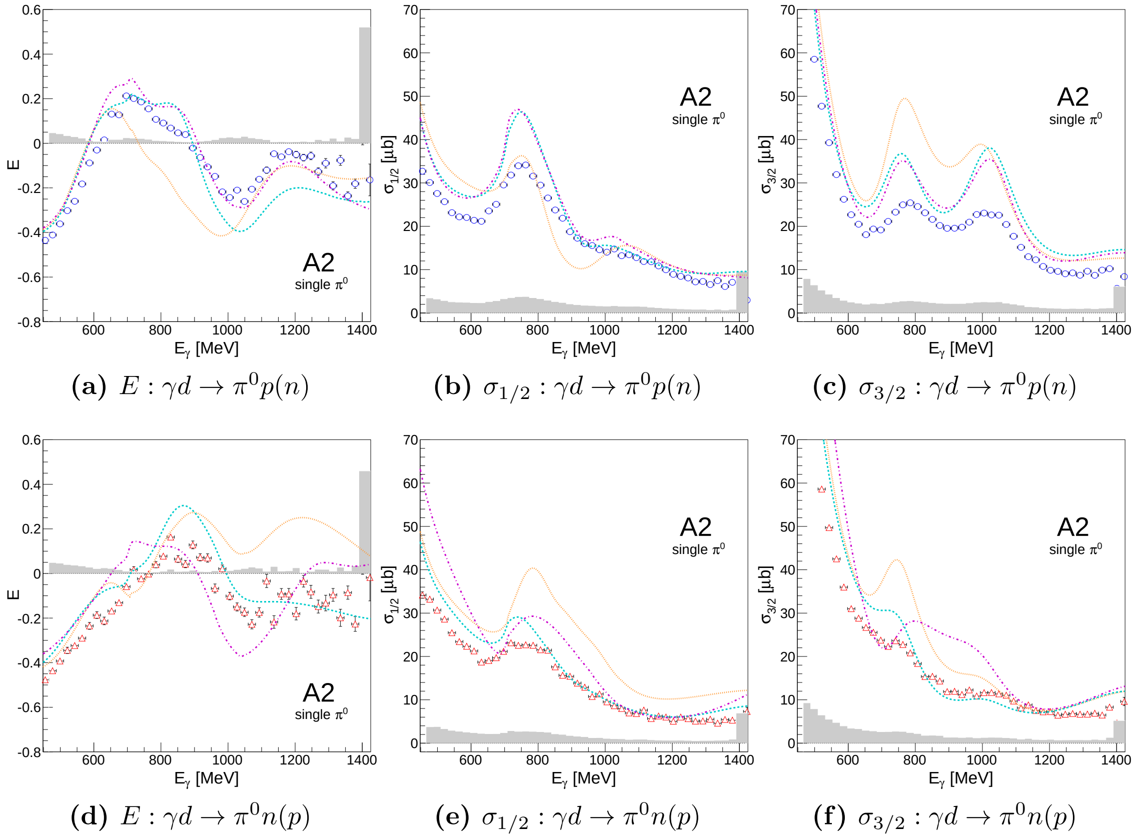

(a) $E : \gamma d \to \pi^0 p(n)$ **(b)** $\sigma_{1/2} : \gamma d \to \pi^0 p(n)$ **(c)** $\sigma_{3/2} : \gamma d \to \pi^0 p(n)$

(d) $E : \gamma d \to \pi^0 n(p)$ **(e)** $\sigma_{1/2} : \gamma d \to \pi^0 n(p)$ **(f)** $\sigma_{3/2} : \gamma d \to \pi^0 n(p)$

Figure D.10: Final averaged double polarization observables for single π^0 photoproduction from quasi-free protons and neutrons as a function of the incident photon energy E_γ. Results from the A2 data. Shown are the average observables obtained from the arithmetic mean of the different versions. Figures (a)-(c): quasi-free proton. Figures (d)-(f): quasi-free neutron. (a) and (d): double polarization observable E. (b) and (e): helicity dependent cross section $\sigma_{1/2}$. (c) and (f): helicity dependent cross section $\sigma_{3/2}$. Dotted orange line: MAID [40]. Dashed cyan line: SAID [39]. Dashed-dotted magenta line: BnGa (proton: [43], neutron: [38]). The gray histogram at the base line of each figure represents the systematical uncertainties of the results.

D.2 Double π^0 Photoproduction

This section presents additional results from the analysis of double π^0 photoproduction from unpolarized and polarized A2 and CBELSA/TAPS data discussed in Sections 7.2, 7.3 and 7.5.

D.2.1 Unpolarized Cross Sections

This section presents additional results from the analysis of double π^0 photoproduction from the unpolarized A2 and CBELSA/TAPS data discussed in Sections 7.2 and 7.3.

A2 Data

This section presents additional results from the analysis of double π^0 photoproduction from the unpolarized A2 data discussed in Sections 7.2 and 7.3.1.

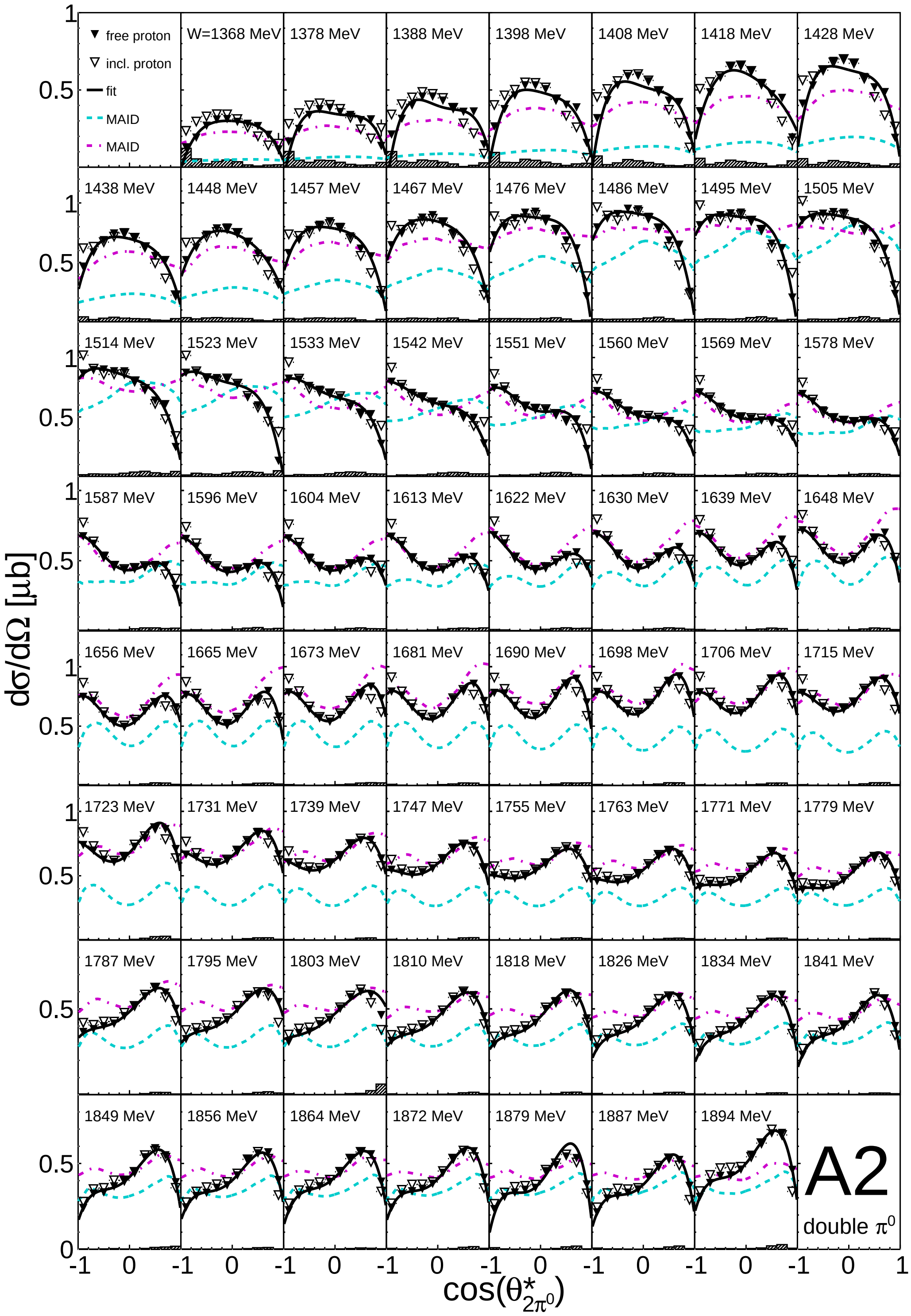

Figure D.11: Differential cross sections for $2\pi^0$ photoproduction from the free proton as function of the polar angle of the combined meson in the $2\pi^0 p$ center of mass system. Results from the A2 data. Open triangles: inclusive result. Solid triangles: exclusive result. Solid black line: Legendre fit of the exclusive result. Dashed cyan line: MAID [62]. Dashed-dotted magenta line: BnGa [43]. The hatched histograms represent the systematic uncertainties of the exclusive result.

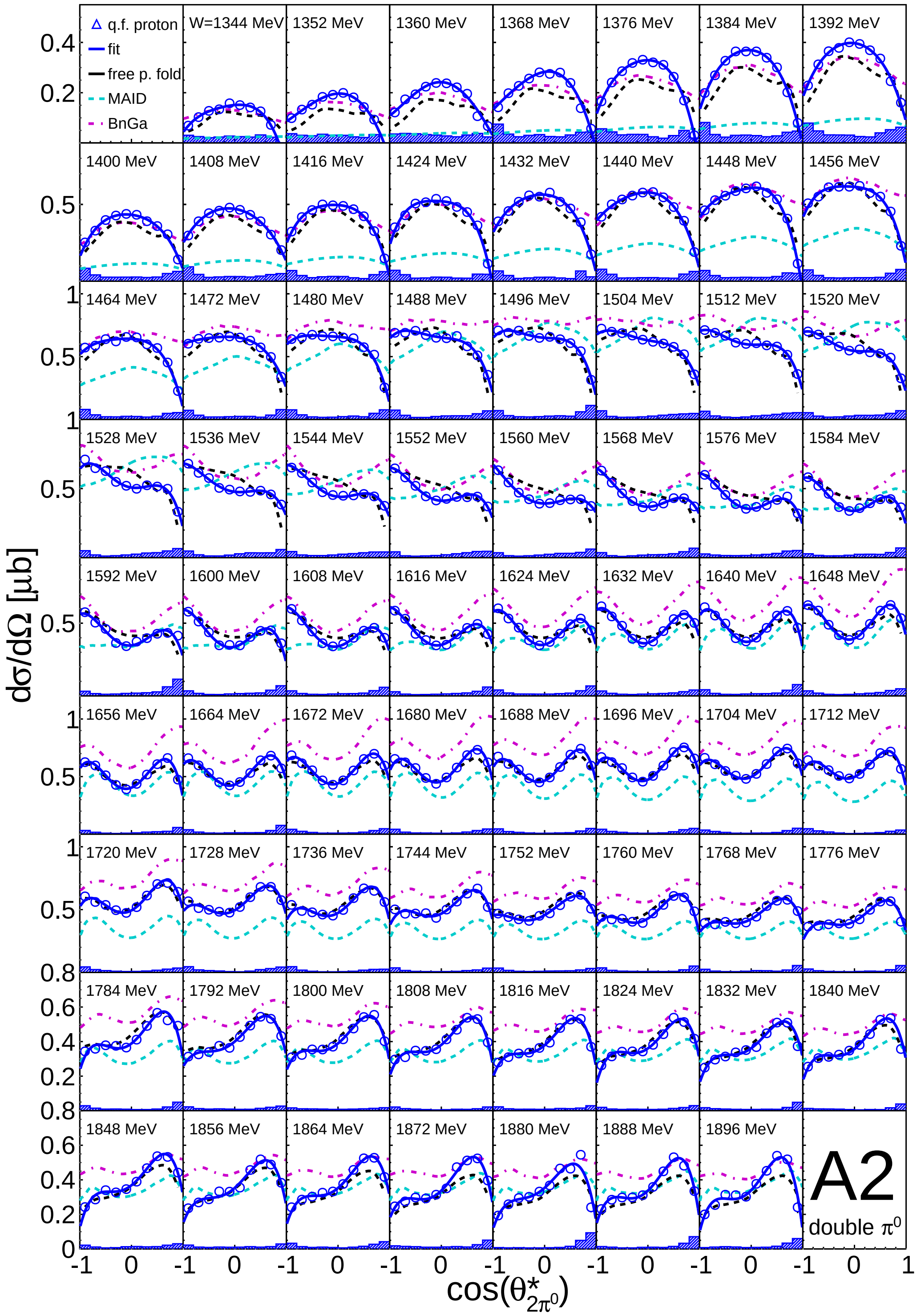

Figure D.12: Differential cross sections for $2\pi^0$ photoproduction from the quasi-free proton as function of the polar angle of the combined meson in the $2\pi^0 p$ center of mass system. Results from the A2 data. Solid blue line: Legendre fit of the data. Dashed black line: free proton result folded with Fermi motion and scaled with 0.85. Dashed cyan line: MAID [62]. Dashed-dotted magenta line: BnGa [43]. The hatched histograms represent the systematic uncertainties.

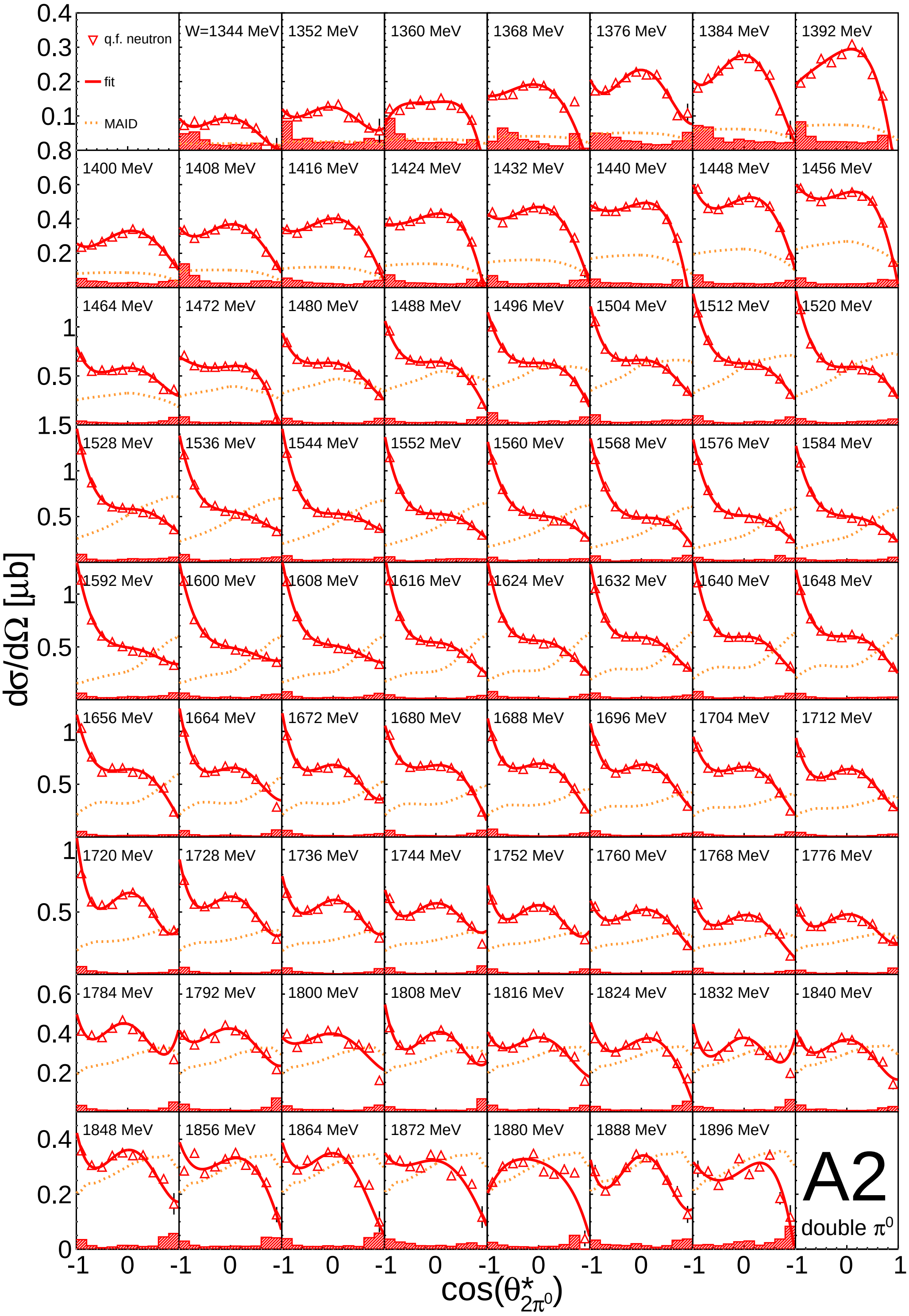

Figure D.13: Differential cross sections for $2\pi^0$ photoproduction from the quasi-free neutron as function of the polar angle of the combined meson in the $2\pi^0 n$ center of mass system. Results from the A2 data. Solid red line: Legendre fit of the data. Dotted orange line: MAID [62]. The hatched histograms represent the systematic uncertainties.

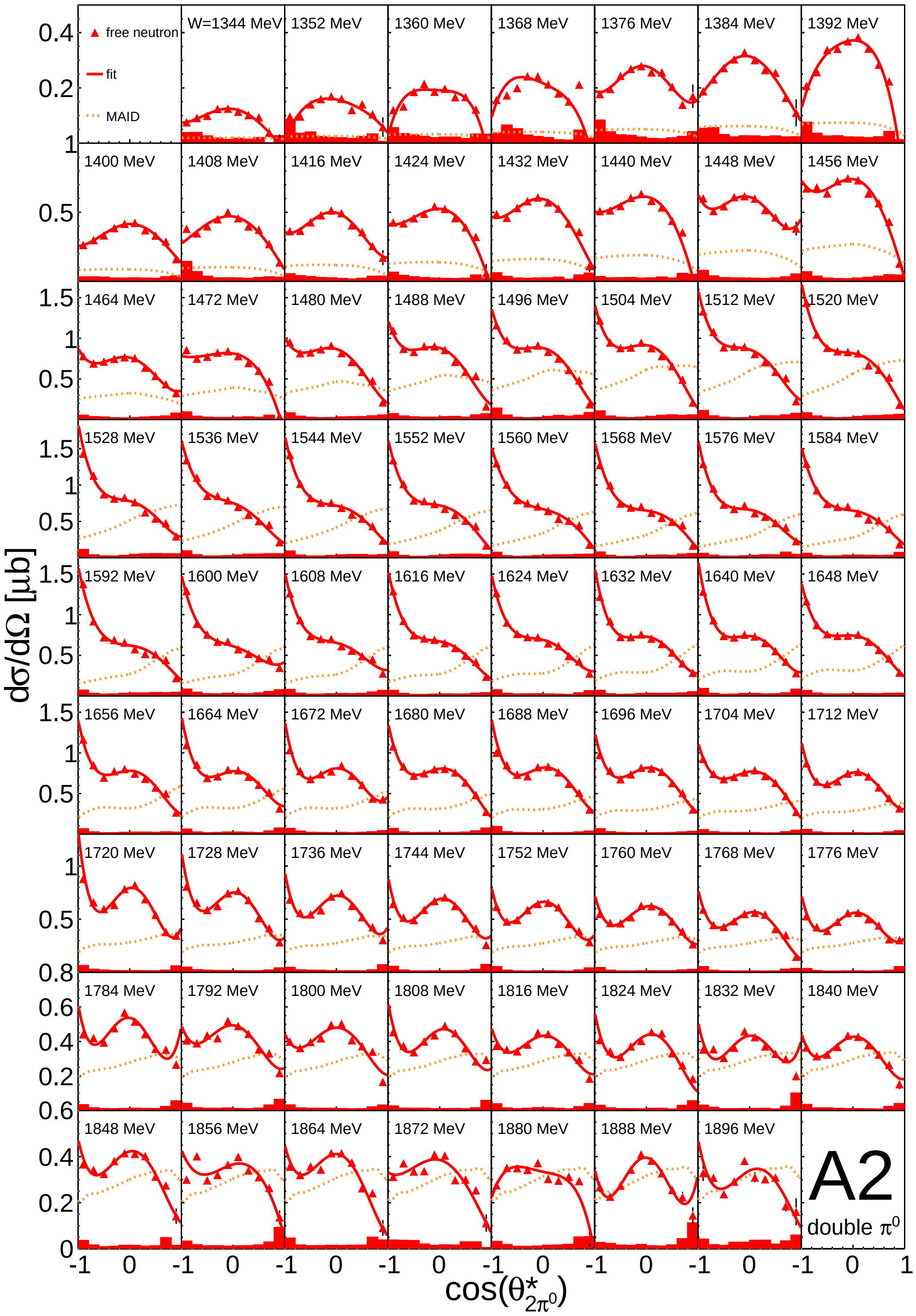

Figure D.14: Estimated differential cross sections for $2\pi^0$ photoproduction from the free neutron as function of the polar angle of the combined meson in the $2\pi^0 n$ center of mass system. Results from the A2 data. Solid red line: Legendre fit of the data. Dotted orange line: MAID [62]. The hatched histograms represent the systematic uncertainties.

CBELSA/TAPS Data

This section presents additional results from the analysis of double π^0 photoproduction from the unpolarized CBELSA/TAPS data discussed in Sections 7.2 and 7.3.2.

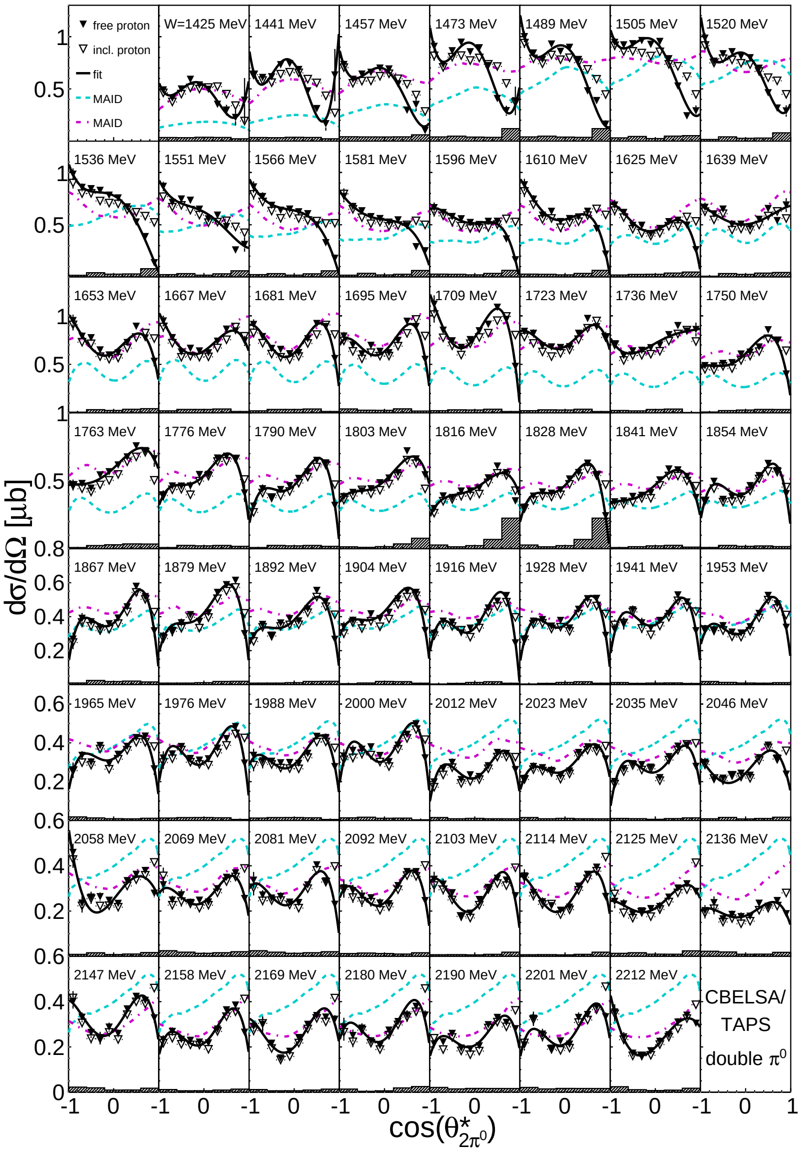

Figure D.15: Differential cross sections for $2\pi^0$ photoproduction from the free proton as function of the polar angle of the combined meson in the $2\pi^0 p$ center of mass system. Results from the CBELSA/TAPS data. Open triangles: inclusive result. Solid triangles: exclusive result. Solid black line: Legendre fit of the exclusive result. Dashed cyan line: MAID [62]. Dashed-dotted magenta line: BnGa [43]. The hatched histograms represent the systematic uncertainties of the exclusive result.

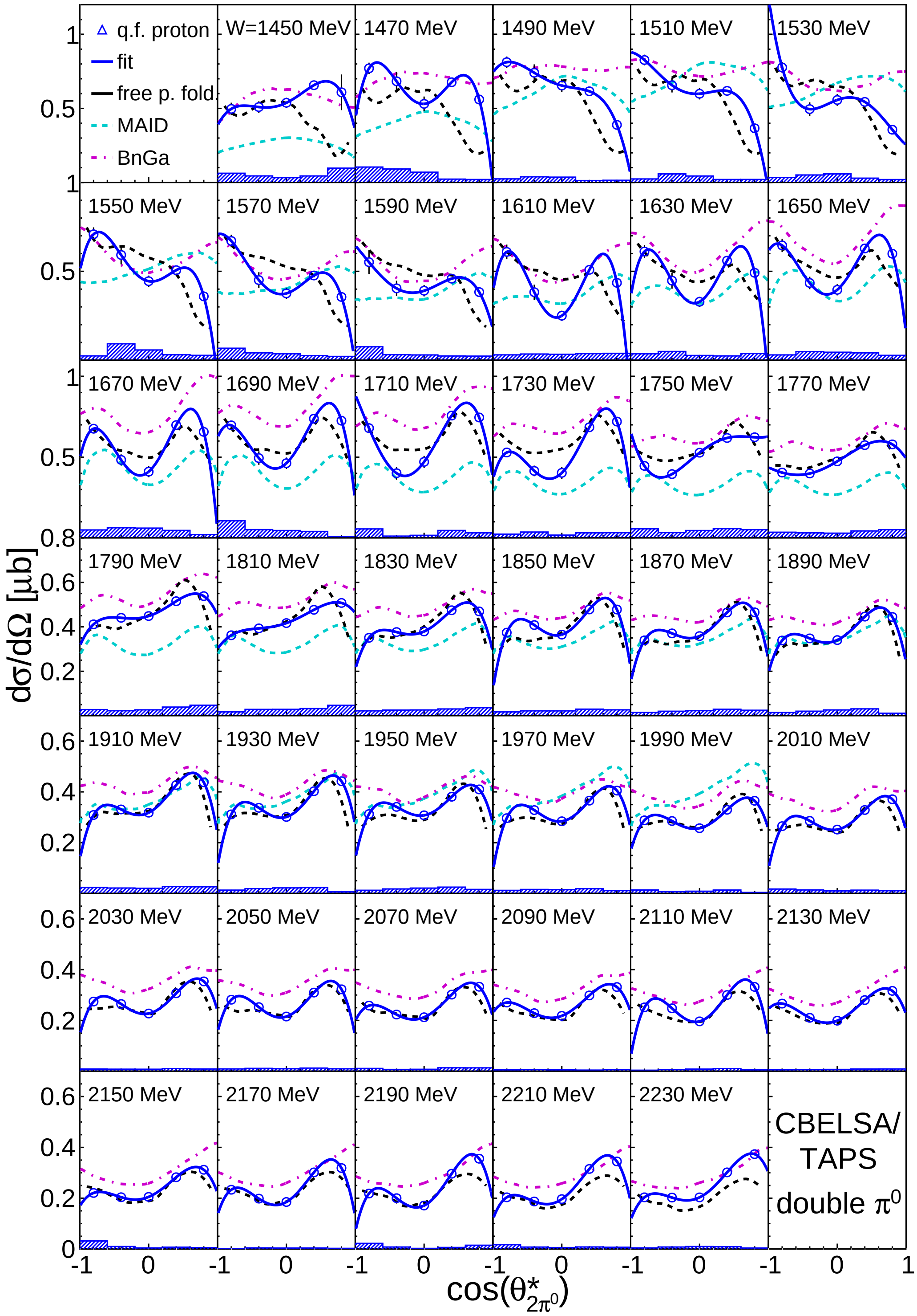

Figure D.16: Differential cross sections for $2\pi^0$ photoproduction from the quasi-free proton as function of the polar angle of the combined meson in the $2\pi^0 p$ center of mass system. Results from the A2 data. Solid blue line: Legendre fit of the data. Dashed black line: free proton result folded with Fermi motion and scaled with 0.85. Dashed cyan line: MAID [62]. Dashed-dotted magenta line: BnGa [43]. The hatched histograms represent the systematic uncertainties.

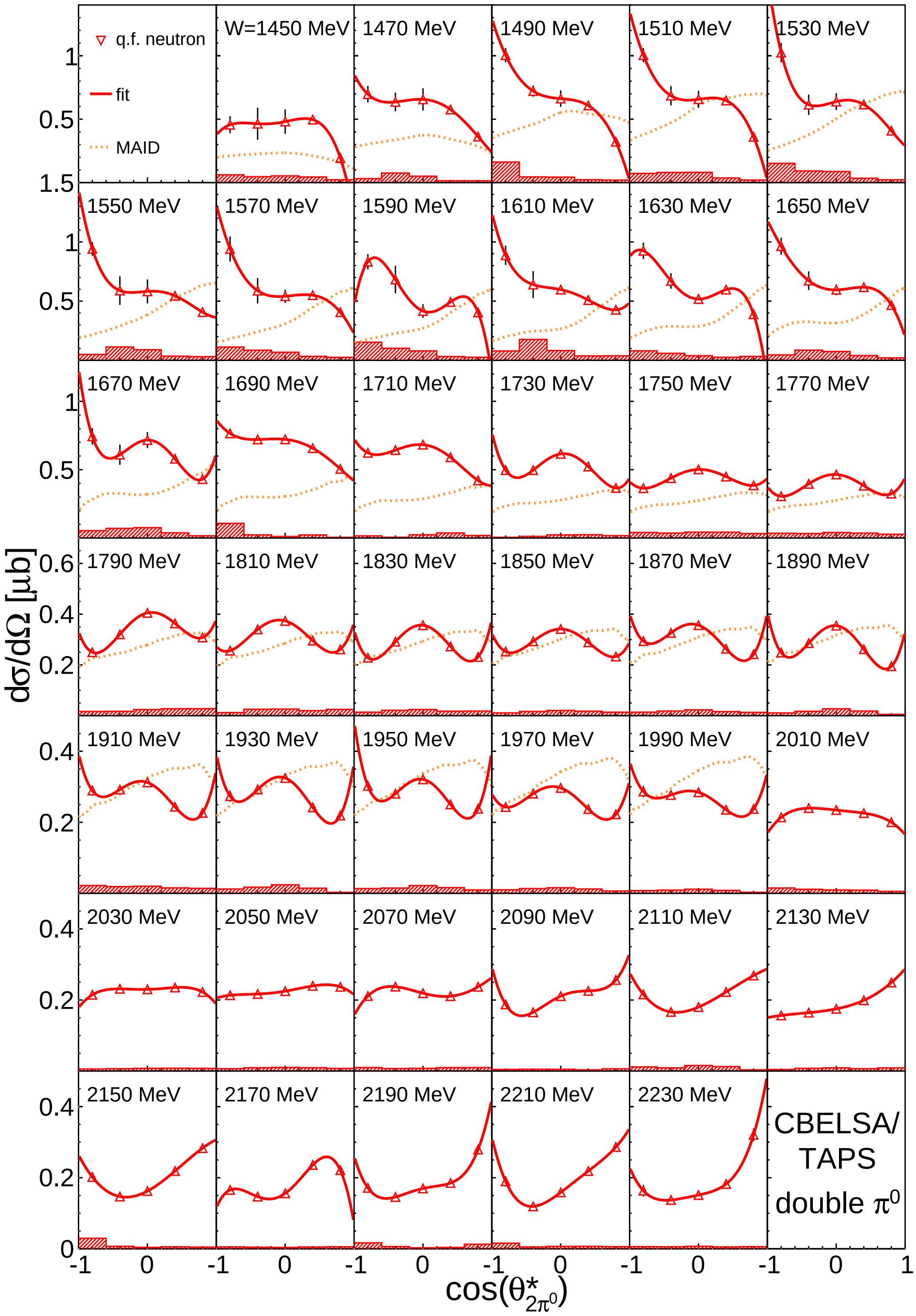

Figure D.17: Differential cross sections for $2\pi^0$ photoproduction from the quasi-free neutron as function of the polar angle of the combined meson in the $2\pi^0 n$ center of mass system. Results from the A2 data. Solid red line: Legendre fit of the data. Dotted orange line: MAID [62]. The hatched histograms represent the systematic uncertainties.

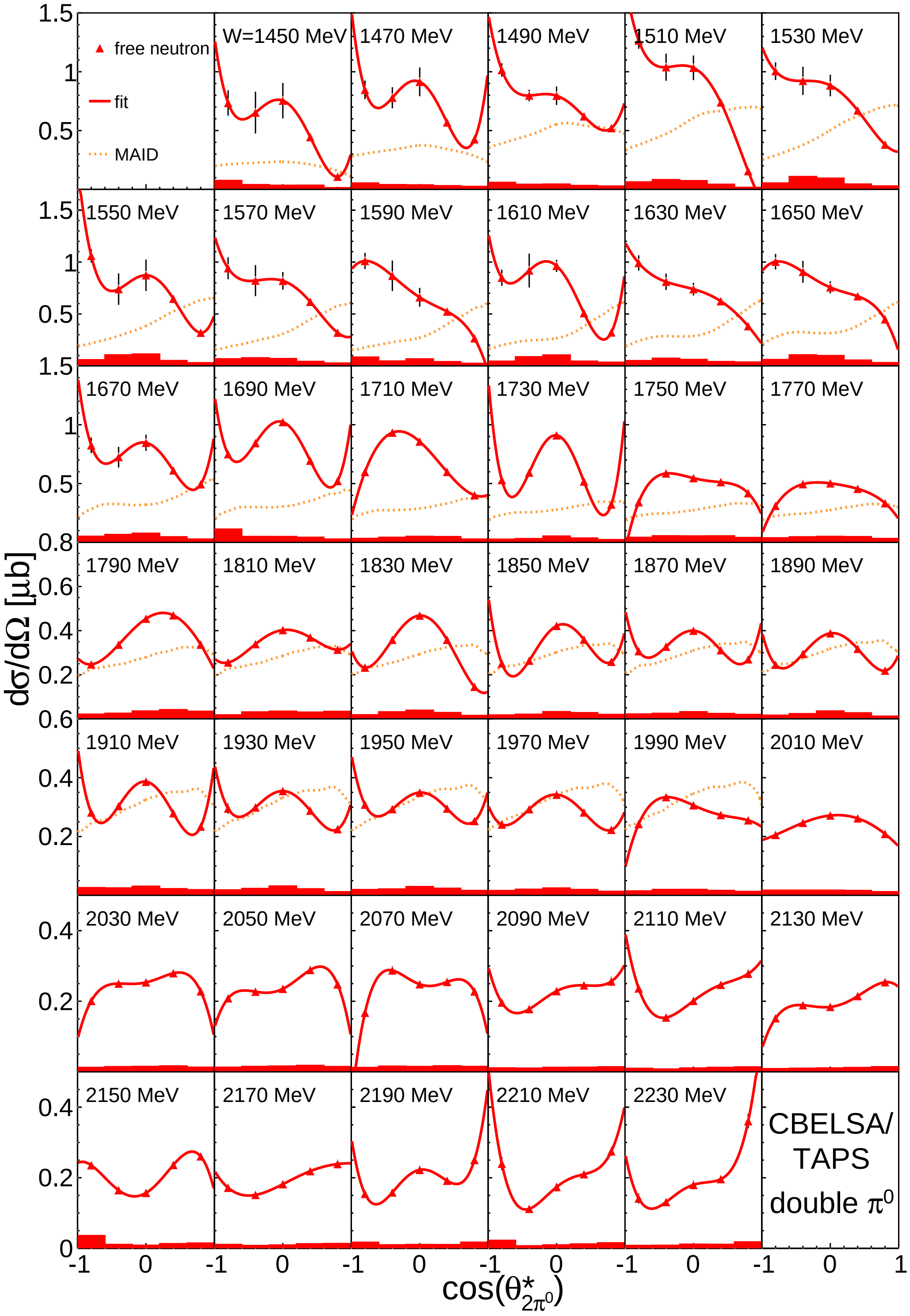

Figure D.18: Estimated differential cross sections for $2\pi^0$ photoproduction from the free neutron as function of the polar angle of the combined meson in the $2\pi^0 n$ center of mass system. Results from the A2 data. Solid red line: Legendre fit of the data. Dotted orange line: MAID [62]. The hatched histograms represent the systematic uncertainties.

Comparison of A2 and CBELSA/TAPS Data

This section presents additional results from the comparison of the analyses of double π^0 photoproduction from the unpolarized A2 and CBELSA/TAPS data discussed in Sections 7.2 and 7.3.3.

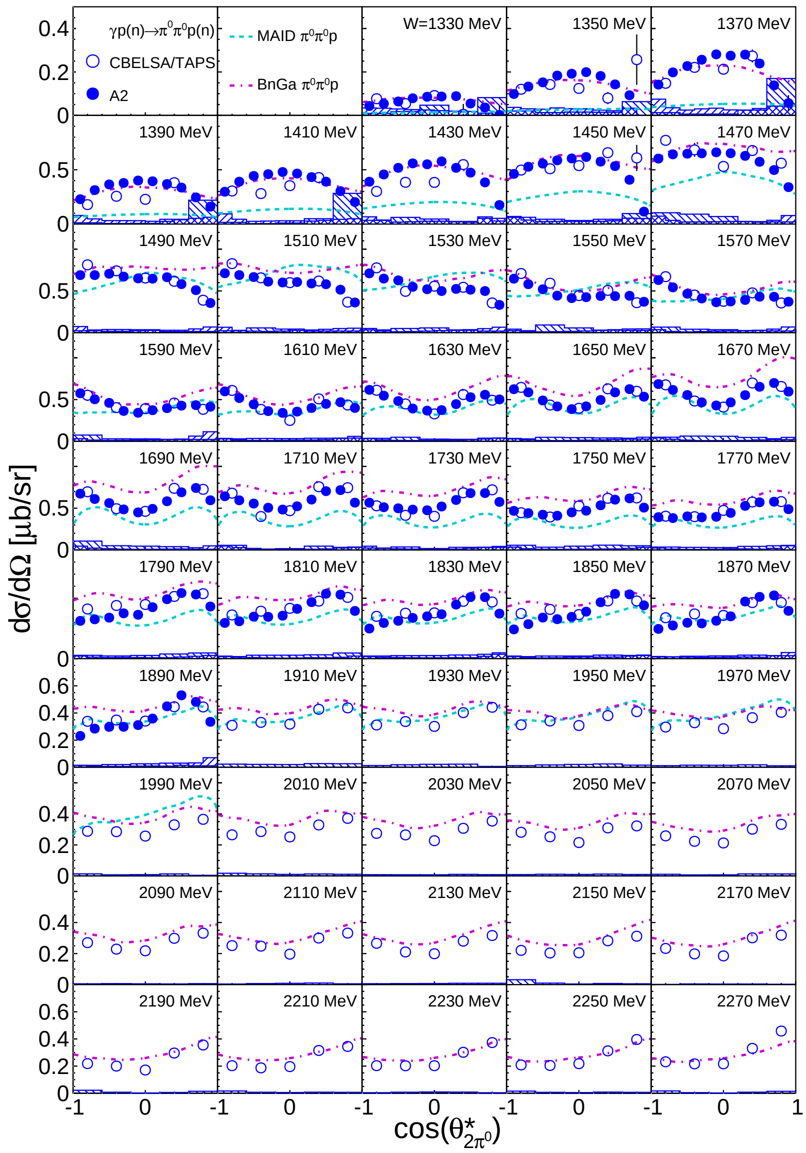

Figure D.19: Differential cross sections for exclusive $2\pi^0$ photoproduction from the quasi-free proton as a function of the polar angle of the combined meson in the $2\pi^0 p$ center of mass system. Solid blue circles: results from the A2 data. Open blue circles: results from the CBELSA/TAPS data. Dashed cyan line: MAID [62]. Dashed-dotted magenta line: BnGa [43]. The hatched histograms at the bottom represent the systematic uncertainty of the corresponding result.

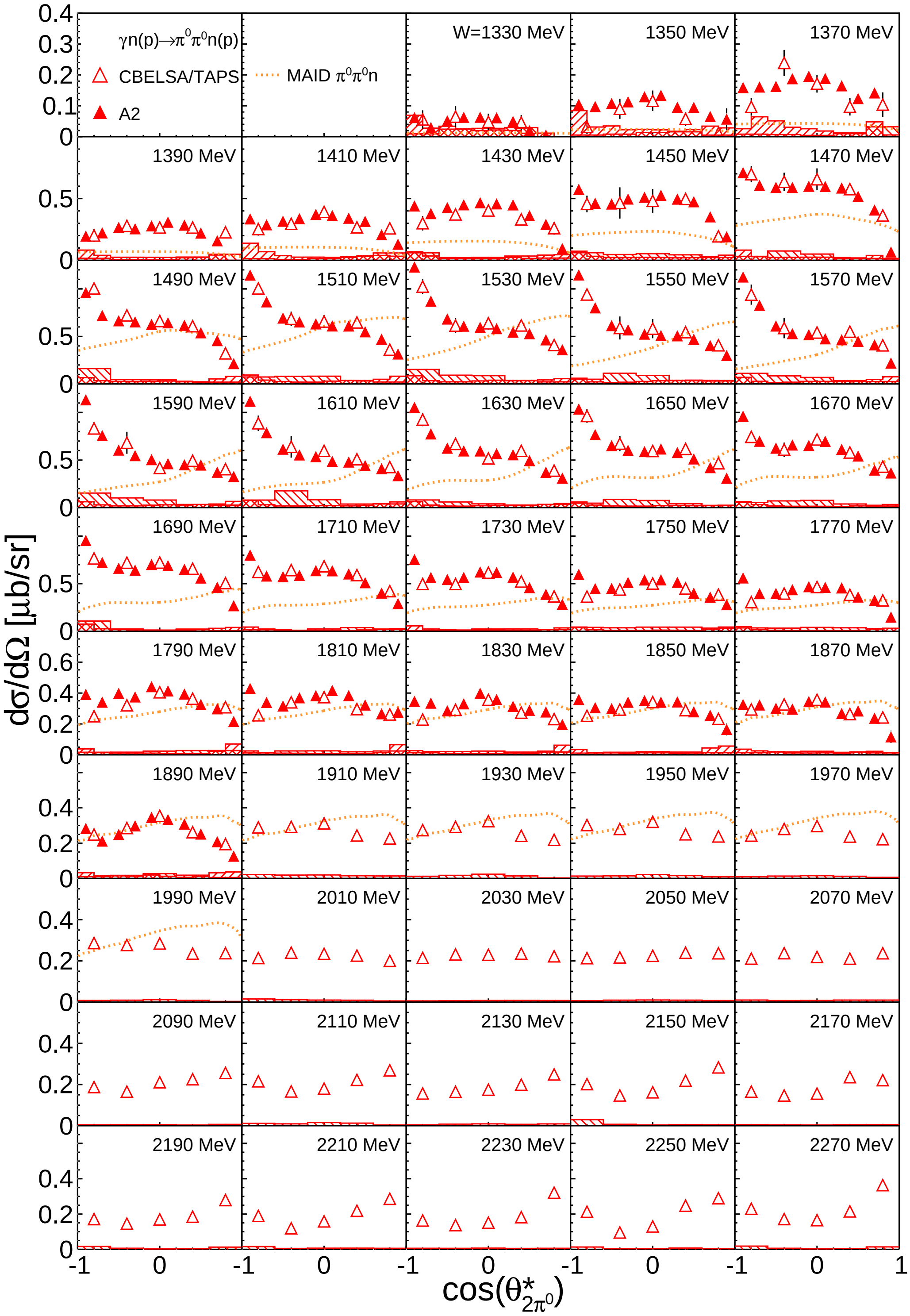

Figure D.20: Differential cross sections for exclusive $2\pi^0$ photoproduction from the quasi-free neutron as a function of the polar angle of the combined meson in the $2\pi^0 p$ center of mass system. Solid red circles: results from the A2 data. Open red circles: results from the CBELSA/TAPS data. Dotted orange line: MAID [62]. The hatched histograms at the bottom represent the systematic uncertainty of the corresponding result.

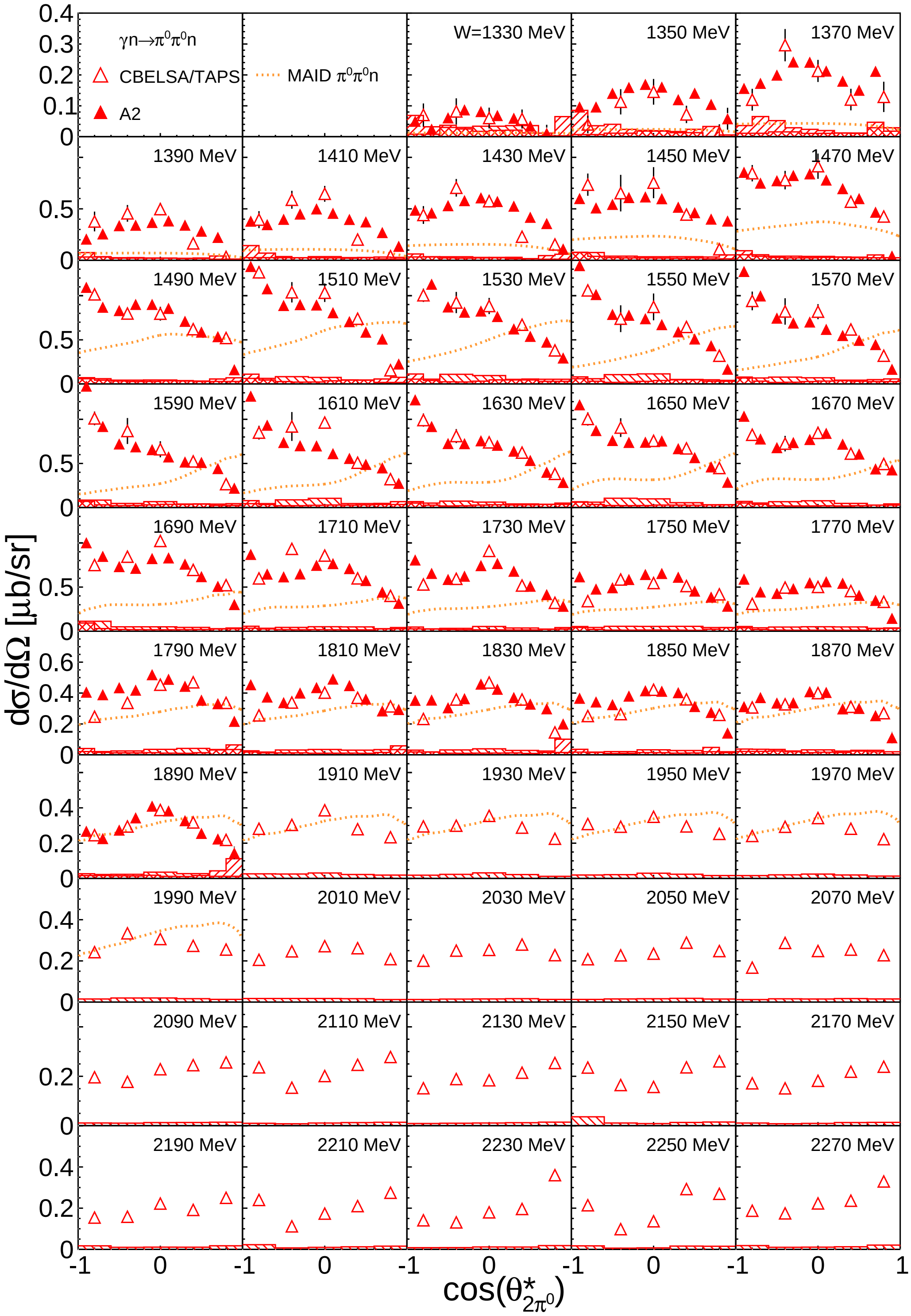

Figure D.21: Estimated differential cross sections for exclusive $2\pi^0$ photoproduction from the free neutron as a function of the polar angle of the combined meson in the $2\pi^0 p$ center of mass system. Solid red triangles: results from the A2 data. Open red triangles: results from the CBELSA/TAPS data. Dotted orange line: MAID [62]. The hatched histograms at the bottom represent the systematic uncertainty of the corresponding result.

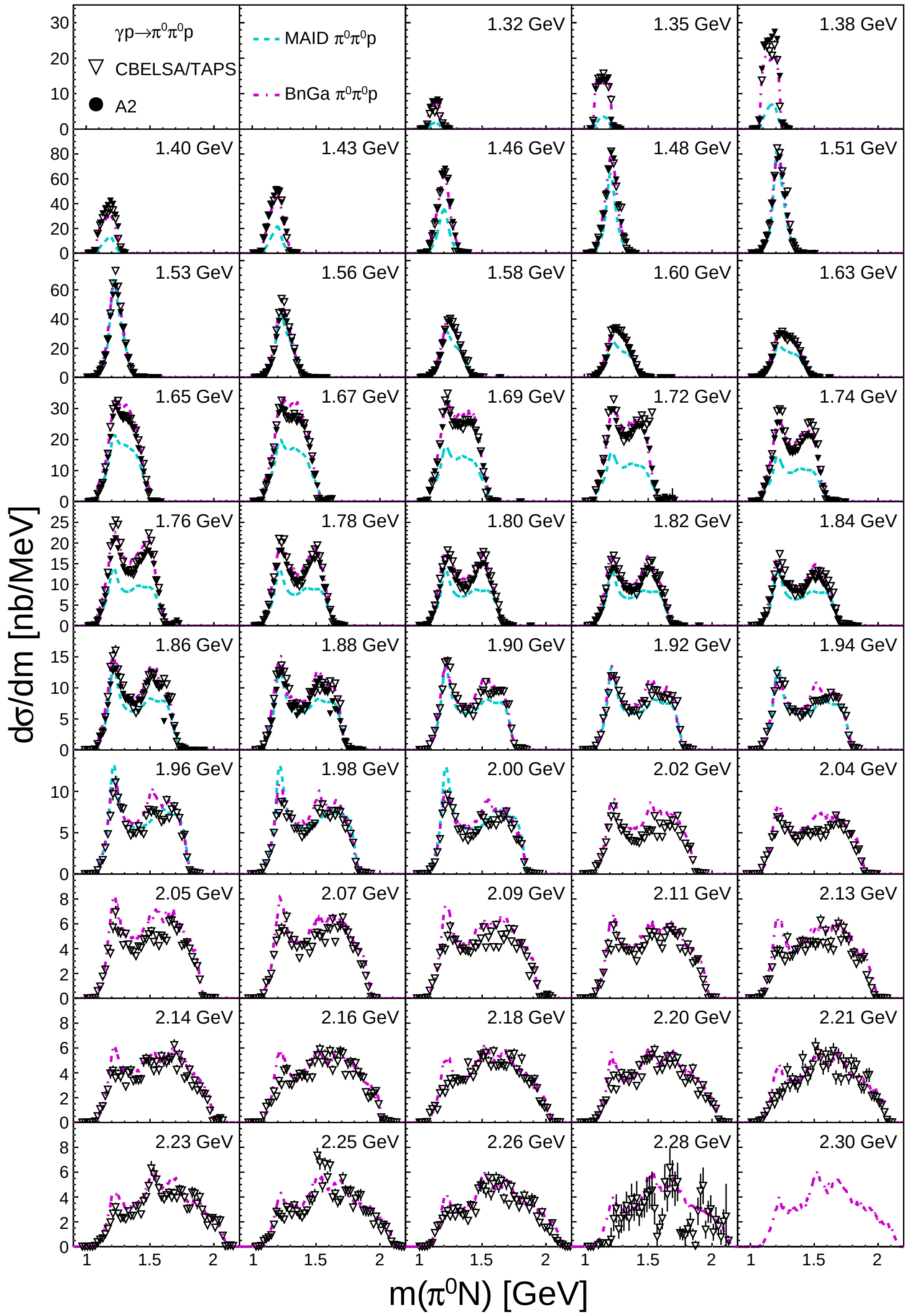

Figure D.22: Differential cross sections for exclusive $2\pi^0$ photoproduction from the free proton as a function of the $\pi^0 p$ invariant mass. Solid black triangles: results from the A2 data. Open black triangles: results from the CBELSA/TAPS data. Dashed cyan line: MAID [62]. Dashed-dotted magenta line: BnGa [43].

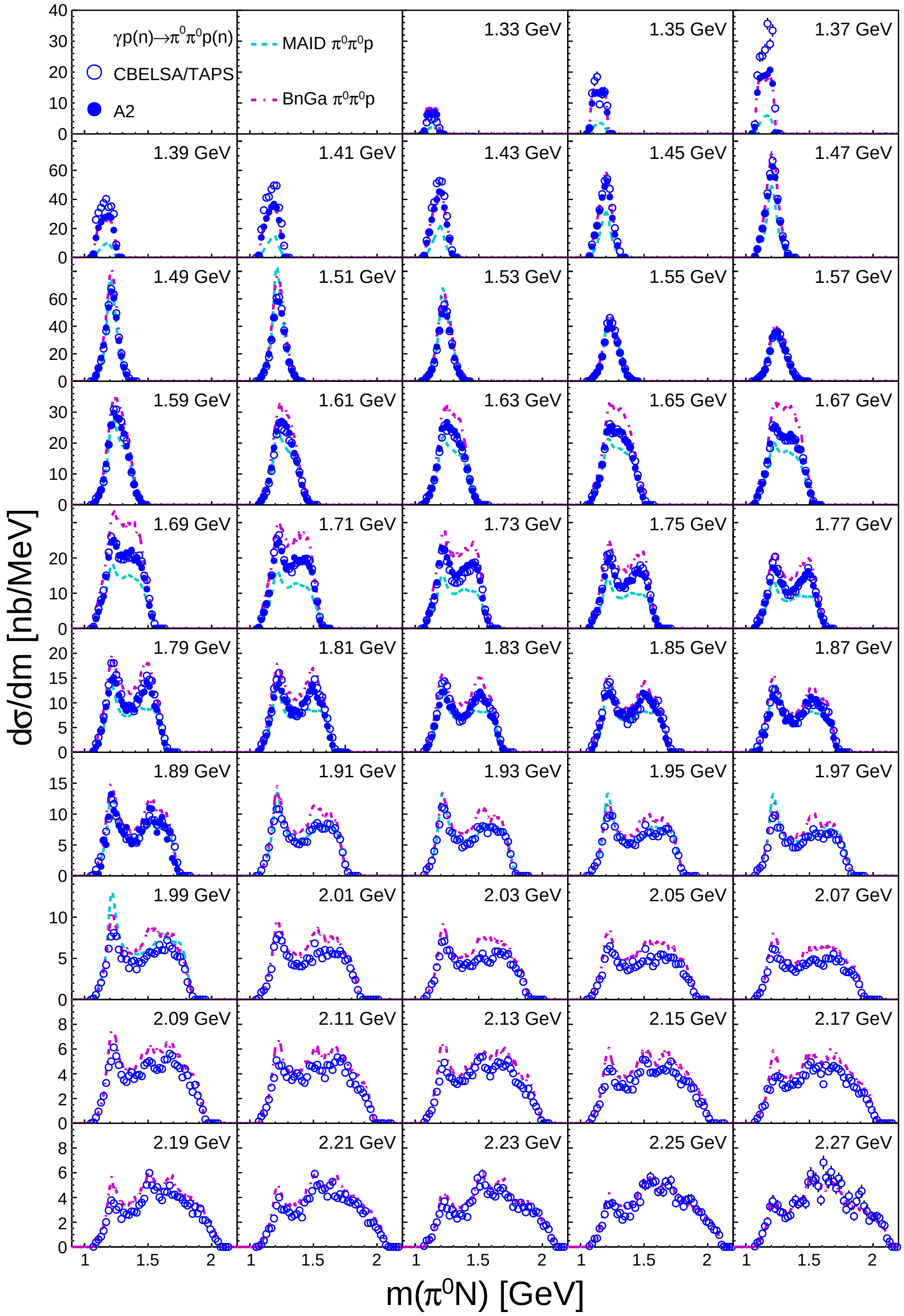

Figure D.23: Differential cross sections for exclusive $2\pi^0$ photoproduction from the quasi-free proton as a function of the $\pi^0 p$ invariant mass. Solid blue circles: results from the A2 data. Open blue circles: results from the CBELSA/TAPS data. Dashed cyan line: MAID [62]. Dashed-dotted magenta line: BnGa [43].

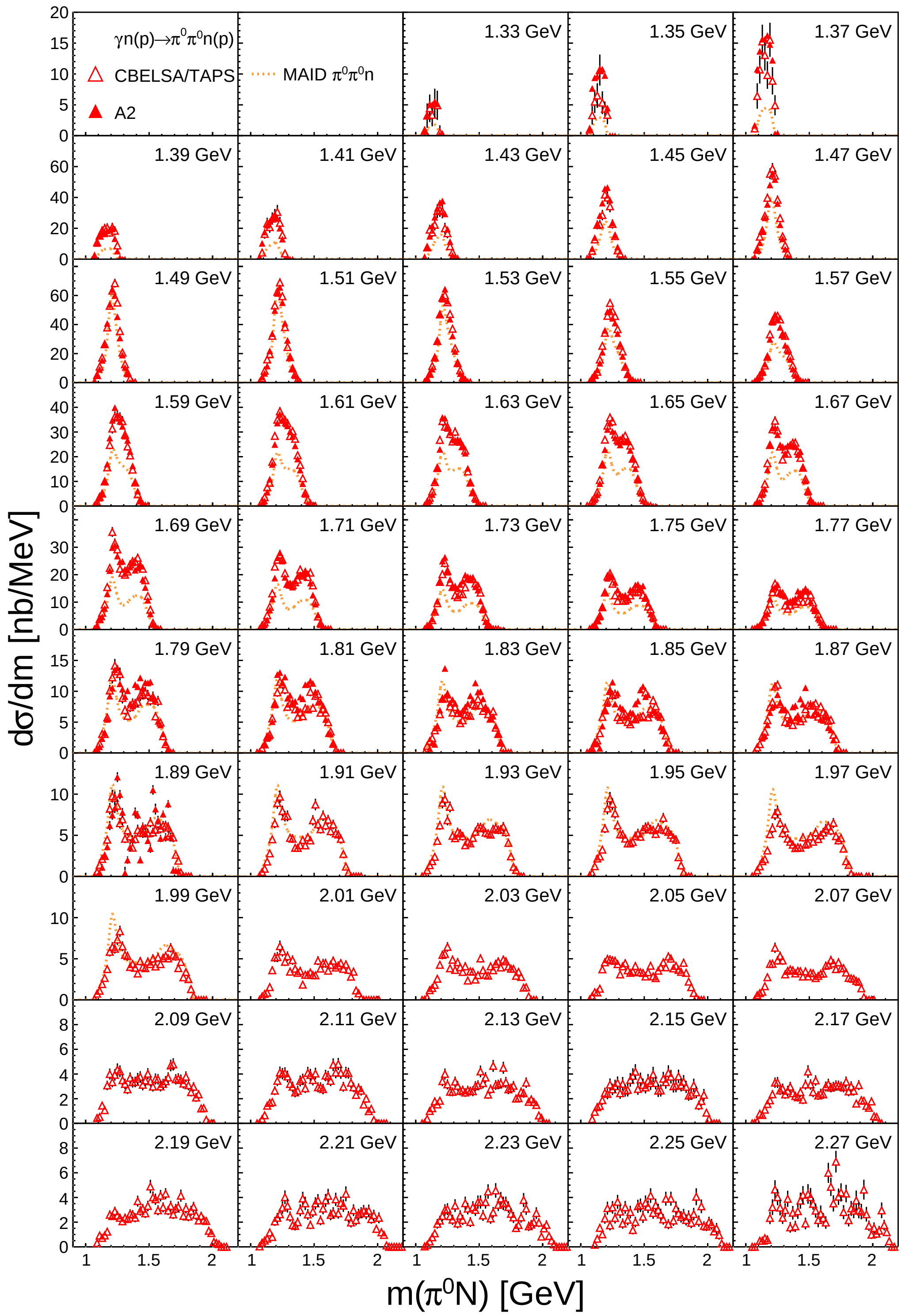

Figure D.24: Differential cross sections for exclusive $2\pi^0$ photoproduction from the quasi-free neutron as a function of the $\pi^0 n$ invariant mass. Solid red triangles: results from the A2 data. Open red triangles: results from the CBELSA/TAPS data. Dotted orange line: MAID [62].

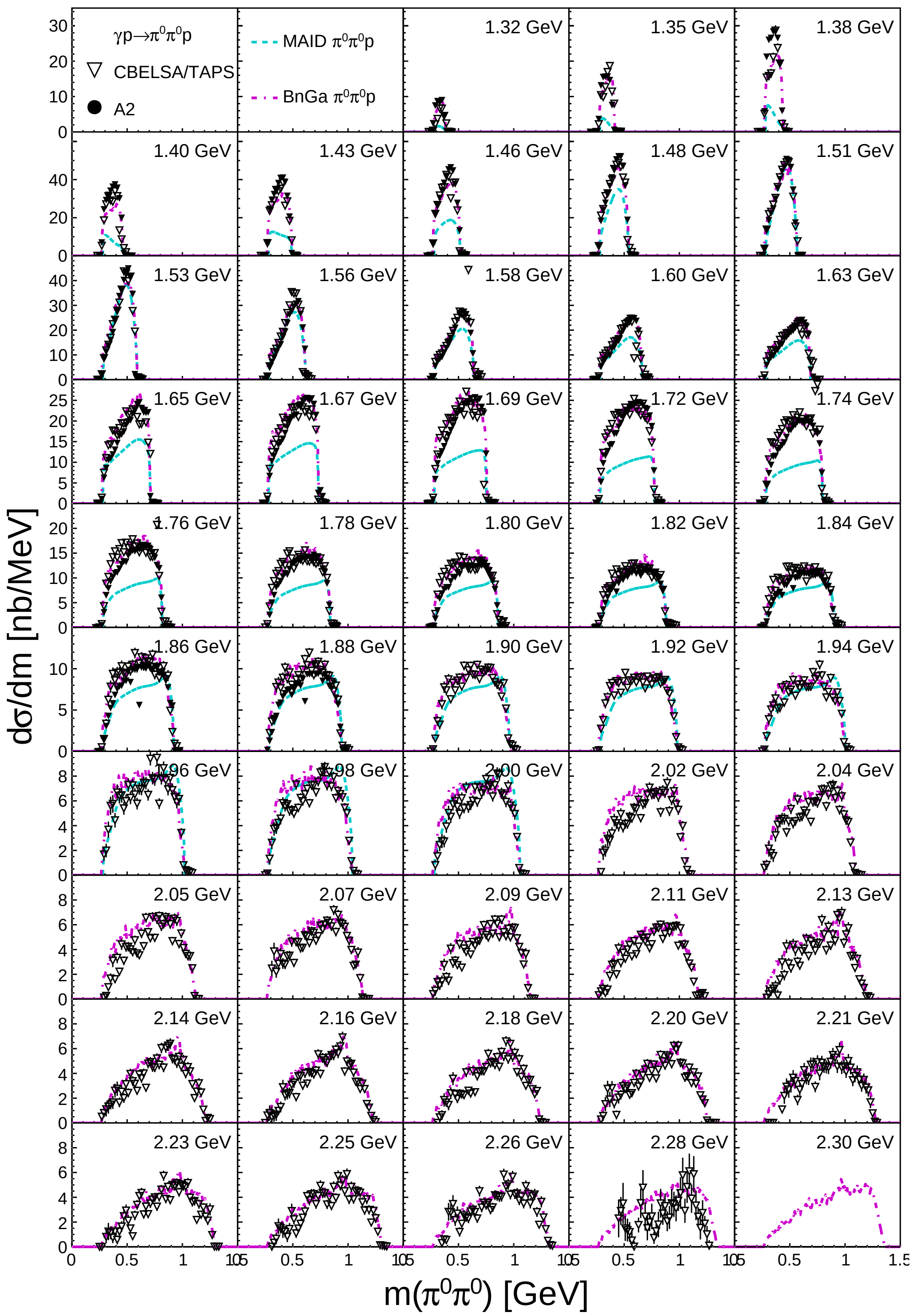

Figure D.25: Differential cross sections for exclusive $2\pi^0$ photoproduction from the free proton as a function of the $\pi^0\pi^0$ invariant mass. Solid black triangles: results from the A2 data. Open black triangles: results from the CBELSA/TAPS data. Dashed cyan line: MAID [62]. Dashed-dotted magenta line: BnGa [43].

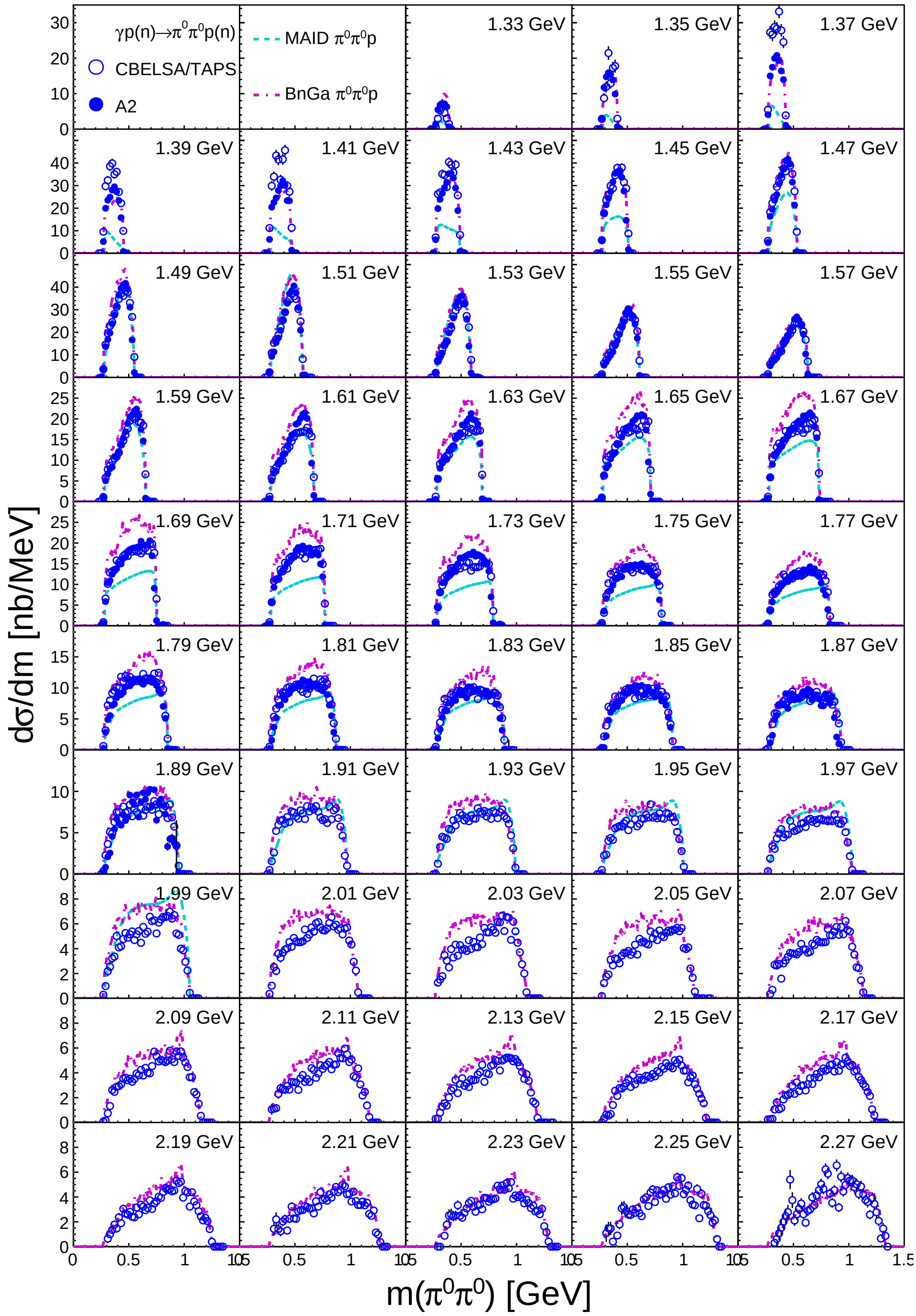

Figure D.26: Differential cross sections for exclusive $2\pi^0$ photoproduction from the quasi-free proton as a function of the $\pi^0\pi^0$ invariant mass. Solid blue circles: results from the A2 data. Open blue circles: results from the CBELSA/TAPS data. Dashed cyan line: MAID [62]. Dashed-dotted magenta line: BnGa [43].

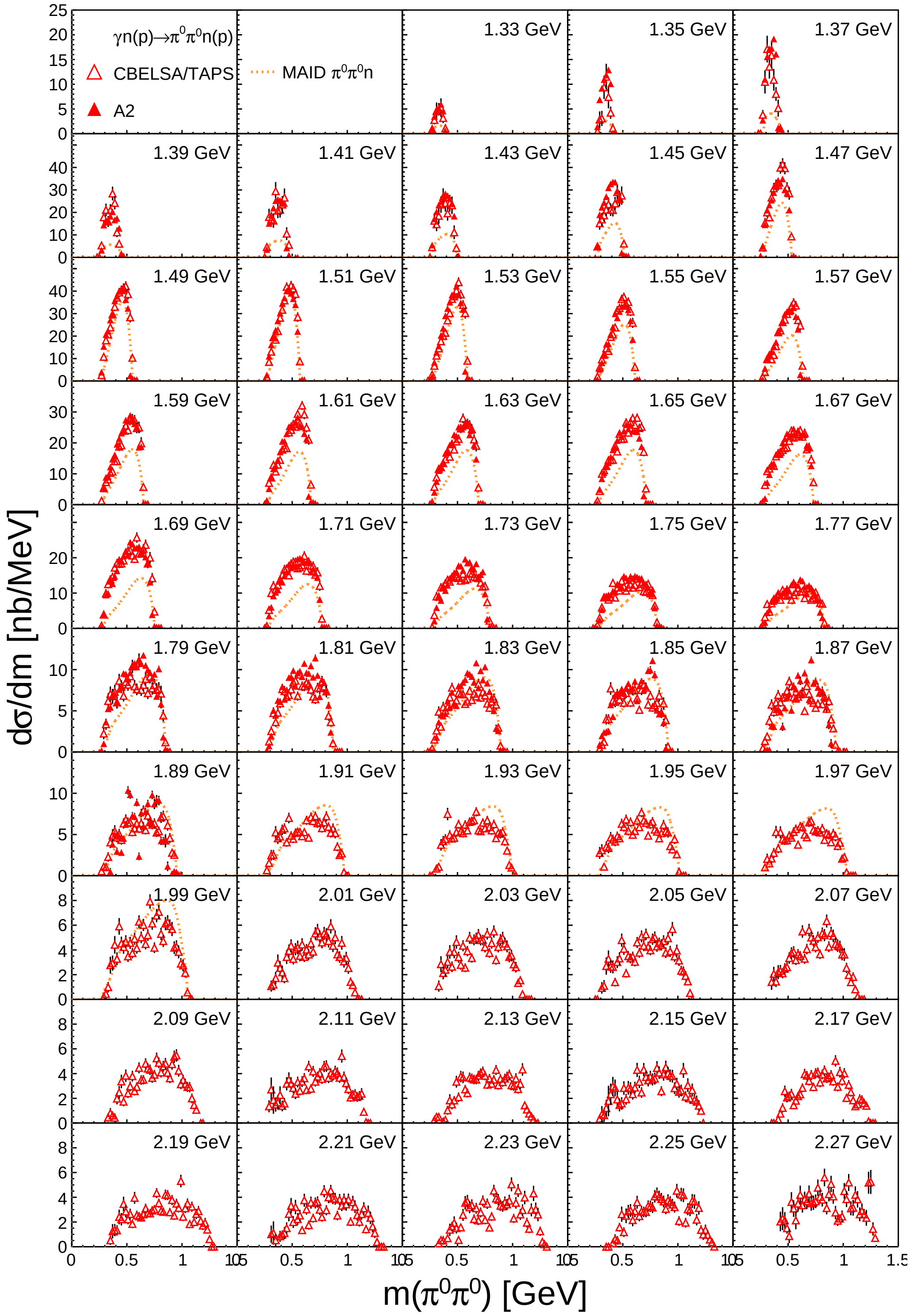

Figure D.27: Differential cross sections for exclusive $2\pi^0$ photoproduction from the quasi-free neutron as a function of the $\pi^0\pi^0$ invariant mass. Solid red triangles: results from the A2 data. Open red triangles: results from the CBELSA/TAPS data. Dotted orange line: MAID [62].

D.2.2 Polarized Cross Sections

This section presents additional results from the analysis of double π^0 photoproduction from the polarized A2 and CBELSA/TAPS data discussed in Section 7.5.

A2 Data

This section presents additional results from the analysis of double π^0 photoproduction from the polarized A2 data discussed in Section 7.5.1.

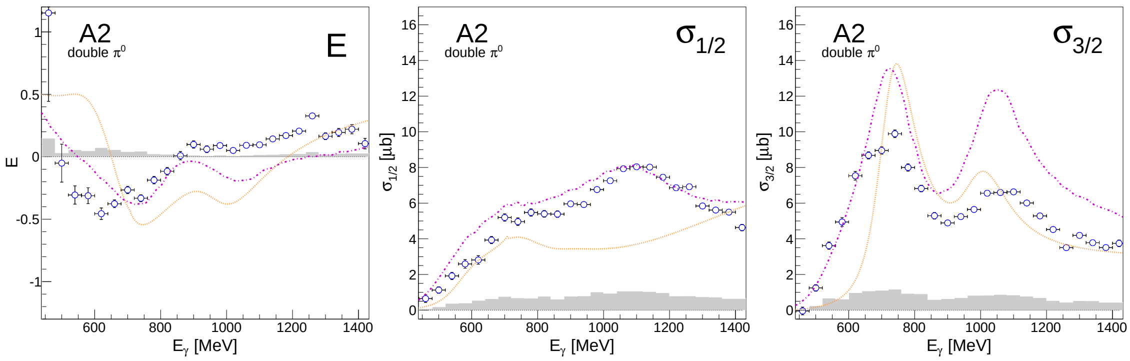

(a) $E : \gamma d \to \pi^0\pi^0 p(n)$ **(b)** $\sigma_{1/2} : \gamma d \to \pi^0\pi^0 p(n)$ **(c)** $\sigma_{3/2} : \gamma d \to \pi^0\pi^0 p(n)$

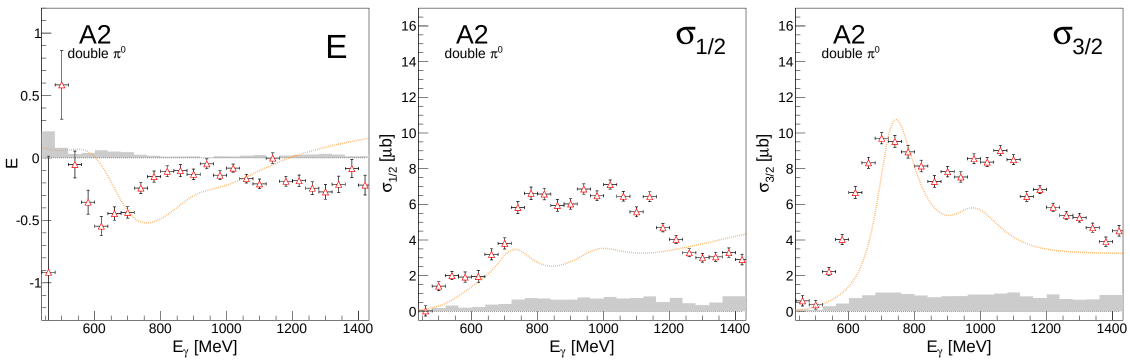

(d) $E : \gamma d \to \pi^0\pi^0 n(p)$ **(e)** $\sigma_{1/2} : \gamma d \to \pi^0\pi^0 n(p)$ **(f)** $\sigma_{3/2} : \gamma d \to \pi^0\pi^0 n(p)$

Figure D.28: Final averaged double polarization observables for double π^0 photoproduction from quasi-free protons and neutrons as a function of the incident photon energy E_γ. Results from the A2 data. Shown are the average observables obtained from the arithmetic mean of versions 1 and 2. Figures (a)-(c): quasi-free proton. Figures (d)-(f): quasi-free neutron. (a) and (d): double polarization observable E. (b) and (e): helicity dependent cross section $\sigma_{1/2}$. (c) and (f): helicity dependent cross section $\sigma_{3/2}$. Dotted orange line: MAID [62]. Dashed-dotted magenta line: BnGa (proton: [43], neutron: [38]). The gray histogram at the base line of each figure represents the systematical uncertainties of the results.

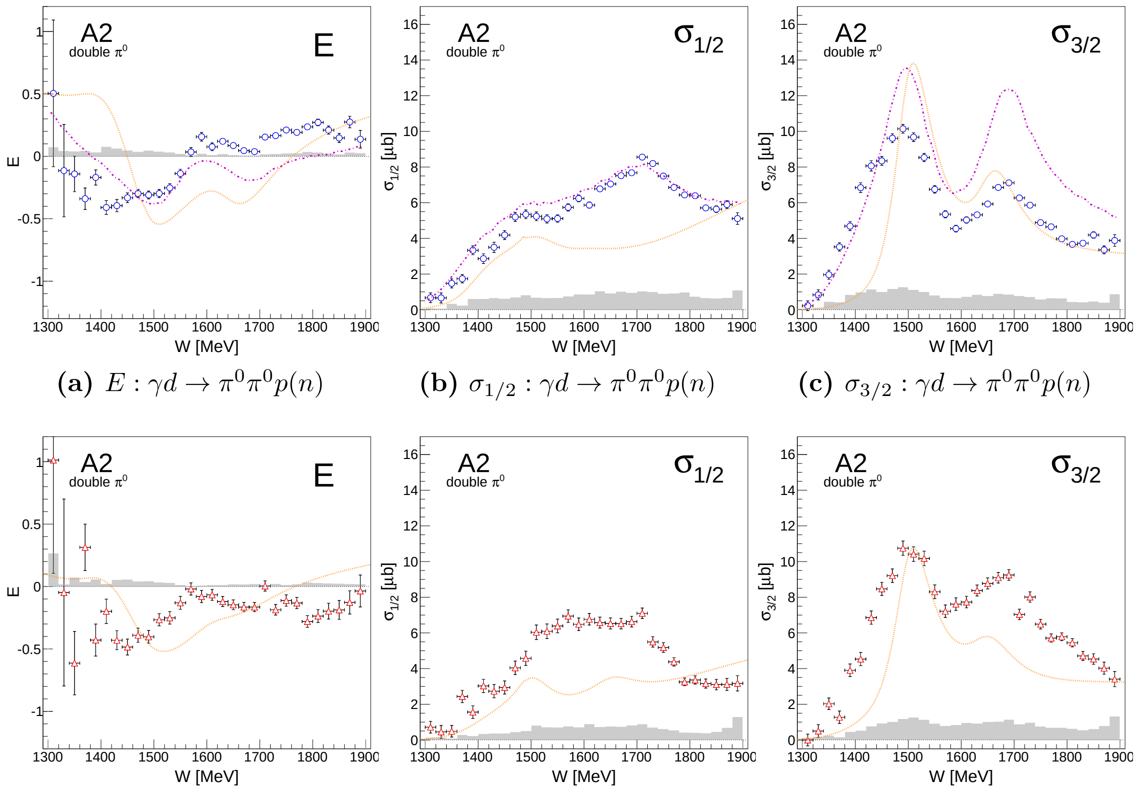

(a) $E : \gamma d \to \pi^0\pi^0 p(n)$ **(b)** $\sigma_{1/2} : \gamma d \to \pi^0\pi^0 p(n)$ **(c)** $\sigma_{3/2} : \gamma d \to \pi^0\pi^0 p(n)$

(d) $E : \gamma d \to \pi^0\pi^0 n(p)$ **(e)** $\sigma_{1/2} : \gamma d \to \pi^0\pi^0 n(p)$ **(f)** $\sigma_{3/2} : \gamma d \to \pi^0\pi^0 n(p)$

Figure D.29: Final averaged double polarization observables for double π^0 photoproduction from quasi-free protons and neutrons as a function of the final state invariant mass W. Results from the A2 data. Shown are the average observables obtained from the arithmetic mean of versions 1 and 2. Figures (a)-(c): quasi-free proton. Figures (d)-(f): quasi-free neutron. (a) and (d): double polarization observable E. (b) and (e): helicity dependent cross section $\sigma_{1/2}$. (c) and (f): helicity dependent cross section $\sigma_{3/2}$. Dotted orange line: MAID [62]. Dashed-dotted magenta line: BnGa (proton: [43], neutron: [38]). The gray histogram at the base line of each figure represents the systematical uncertainties of the results.

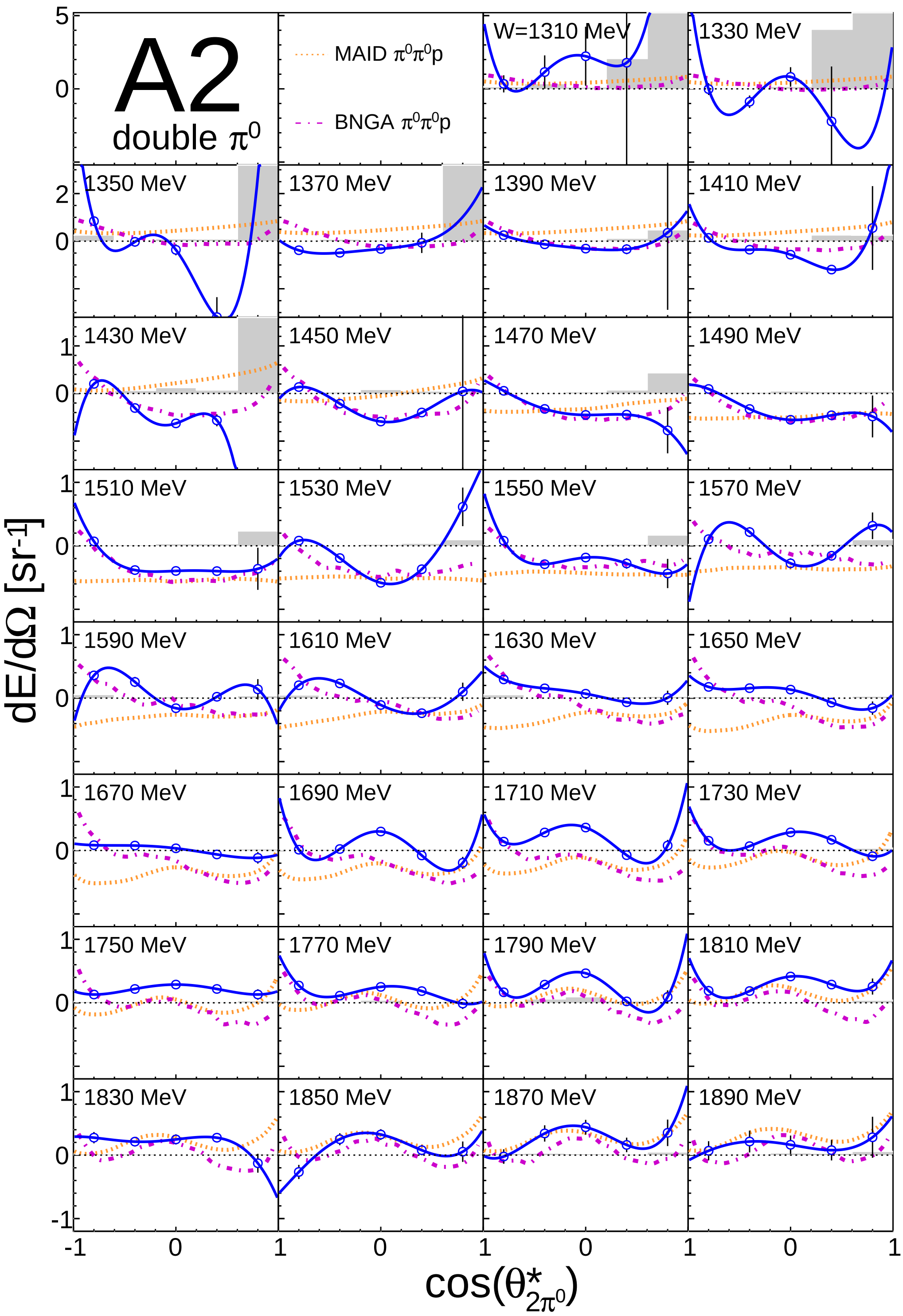

Figure D.30: Differential double polarization observable E for double π^0 photoproduction from quasi-free protons as a function of the meson polar angle in the $\pi^0 p$ center of mass frame. Results from the A2 data. Solid blue line: Legendre fit. Dotted orange line: MAID [62]. Dashed-dotted magenta line: BnGa [43]. The gray histogram at the base line of each figure represents the systematical uncertainties of the results.

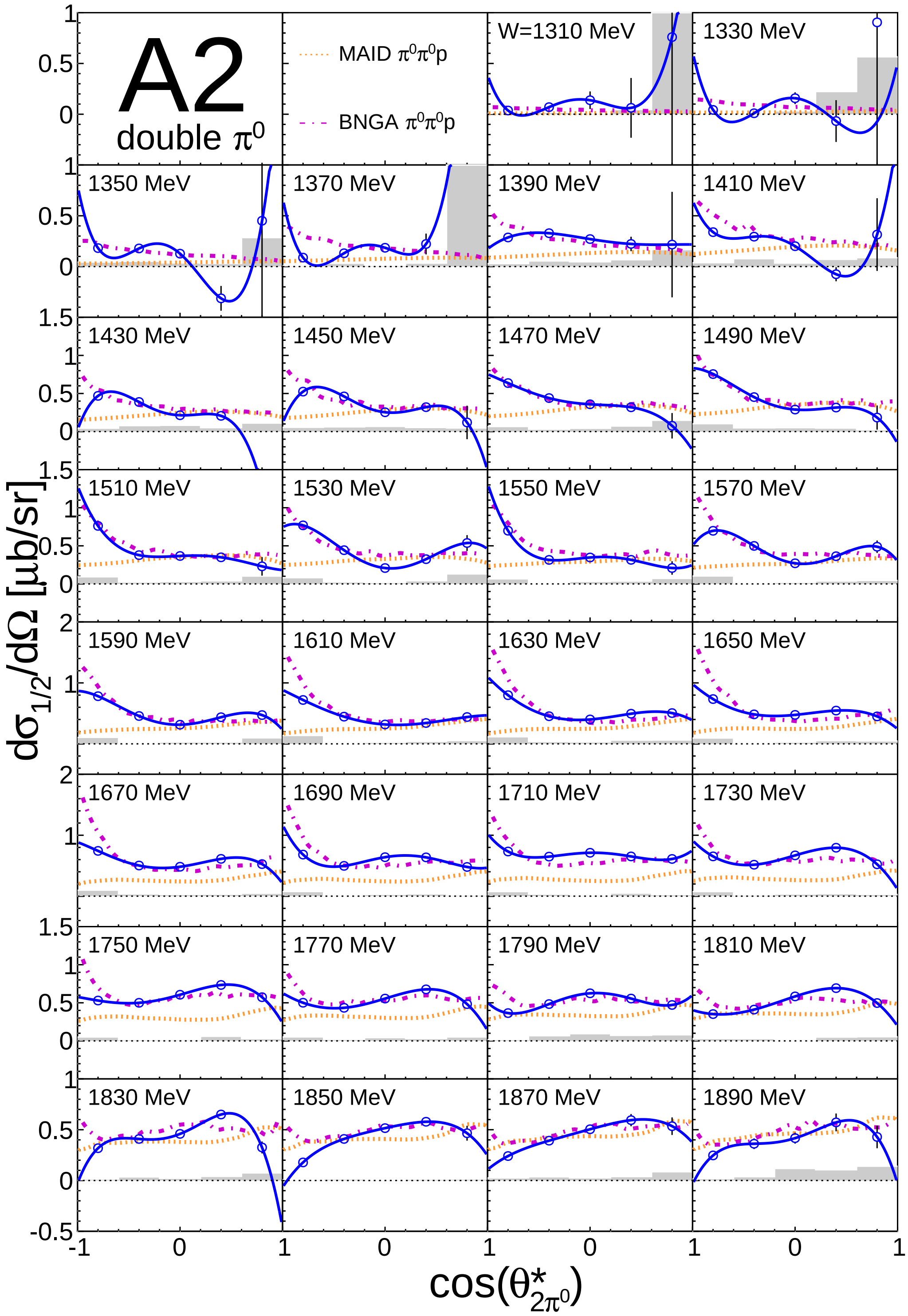

Figure D.31: Differential helicity dependent cross section $\sigma_{1/2}$ for double π^0 photoproduction from quasi-free protons as a function of the meson polar angle in the $\pi^0 p$ center of mass frame. Results from the A2 data. Solid blue line: Legendre fit. Dotted orange line: MAID [62]. Dashed-dotted magenta line: BnGa [43]. The gray histogram at the base line of each figure represents the systematical uncertainties of the results.

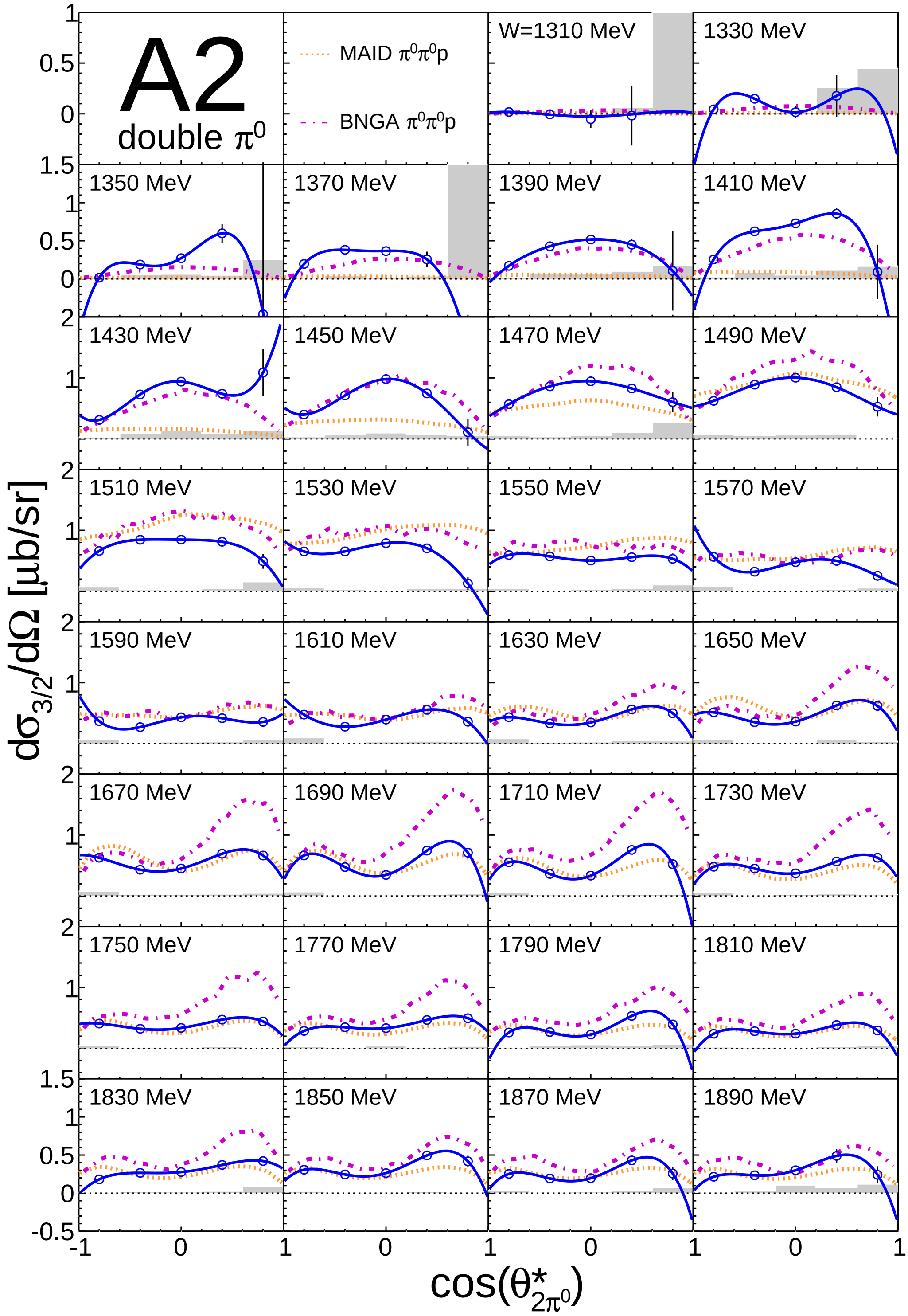

Figure D.32: Differential helicity dependent cross section $\sigma_{3/2}$ for double π^0 photoproduction from quasi-free protons as a function of the meson polar angle in the $\pi^0 p$ center of mass frame. Results from the A2 data. Solid blue line: Legendre fit. Dotted orange line: MAID [62]. Dashed-dotted magenta line: BnGa [43]. The gray histogram at the base line of each figure represents the systematical uncertainties of the results.

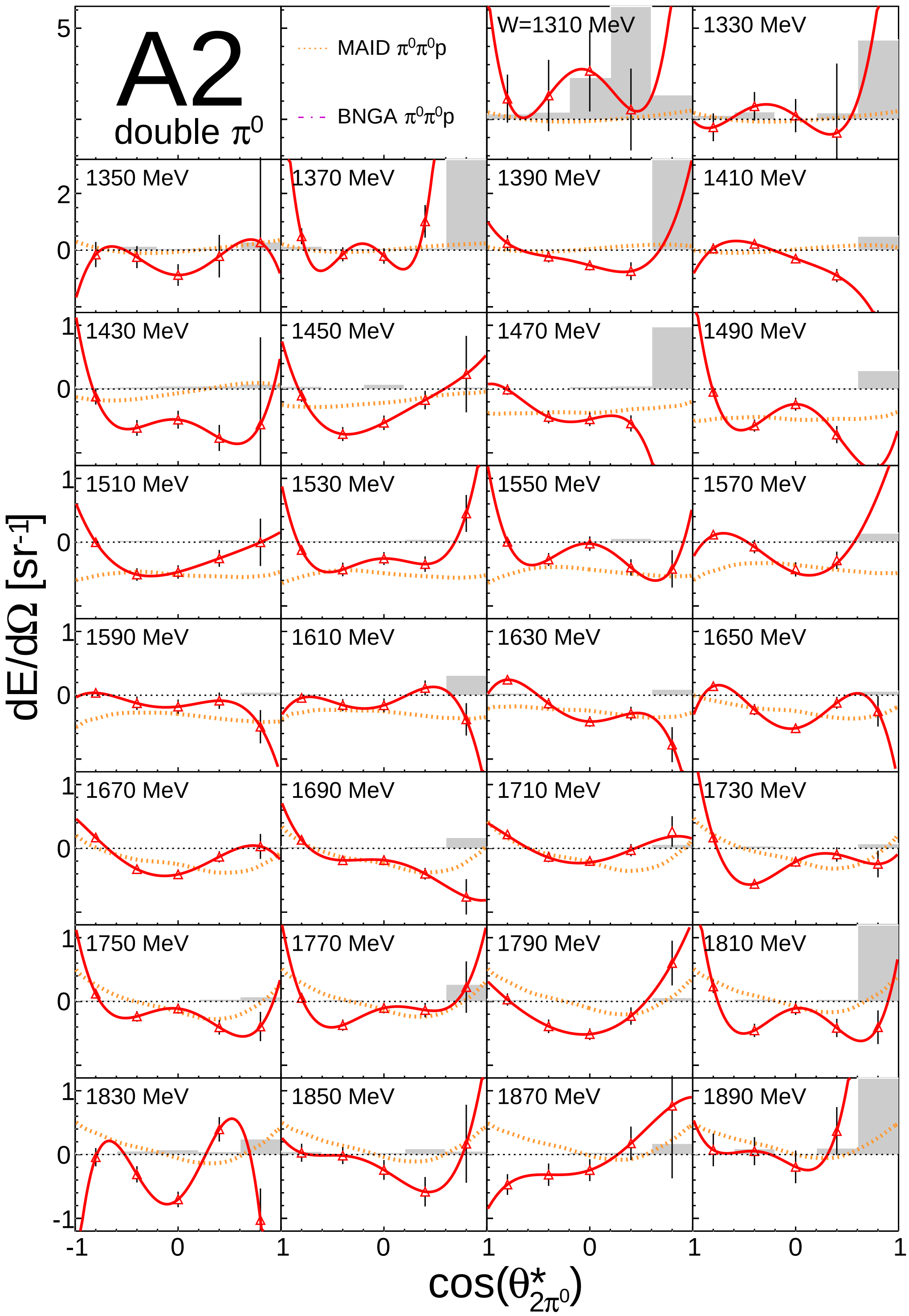

Figure D.33: Differential double polarization observable E for double π^0 photoproduction from quasi-free neutrons as a function of the meson polar angle in the $\pi^0 p$ center of mass frame. Results from the A2 data. Solid red line: Legendre fit. Dotted orange line: MAID [62]. The gray histogram at the base line of each figure represents the systematical uncertainties of the results.

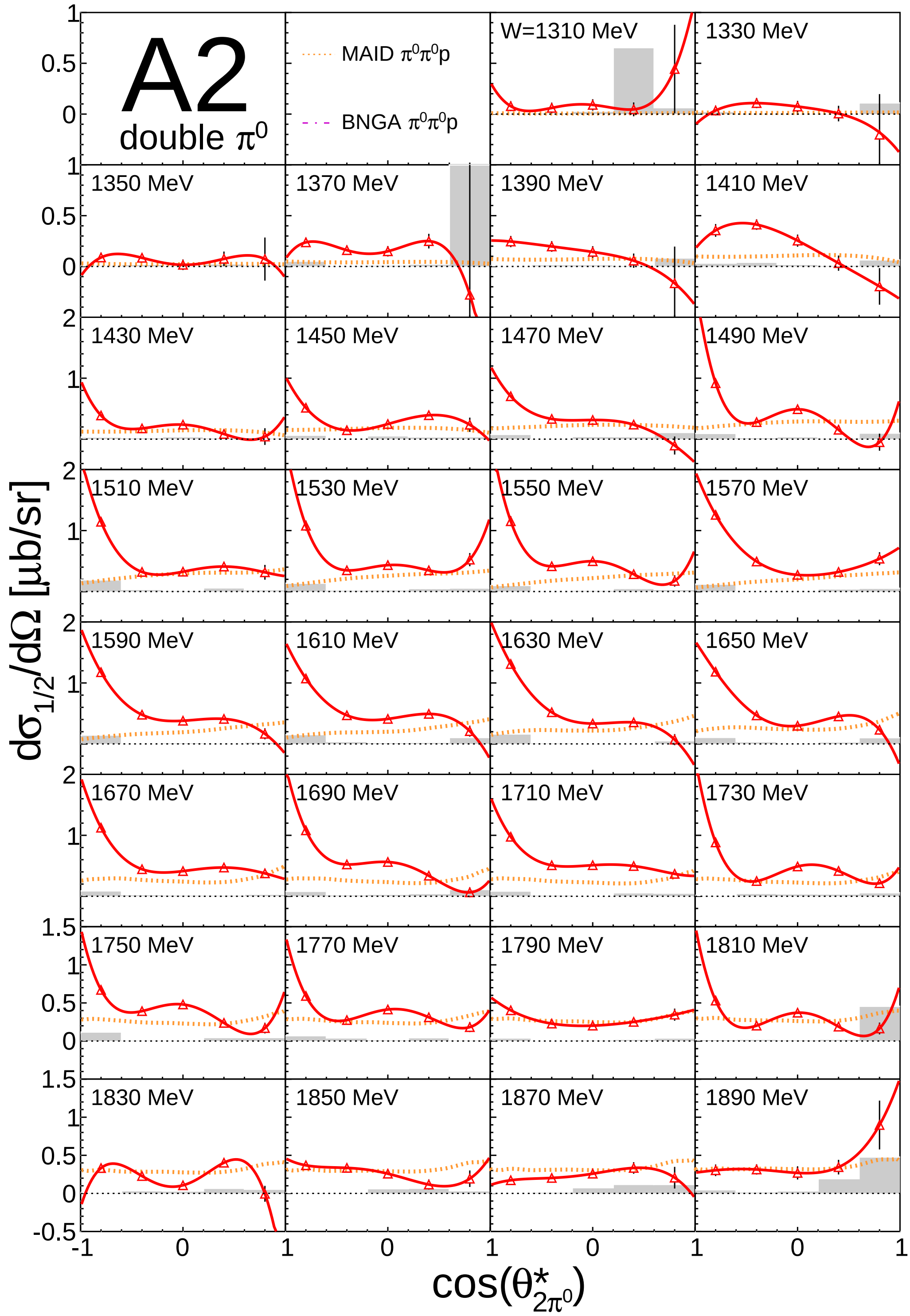

Figure D.34: Differential helicity dependent cross section $\sigma_{1/2}$ for double π^0 photoproduction from quasi-free neutrons as a function of the meson polar angle in the $\pi^0 p$ center of mass frame. Results from the A2 data. Solid red line: Legendre fit. Dotted orange line: MAID [62]. The gray histogram at the base line of each figure represents the systematical uncertainties of the results.

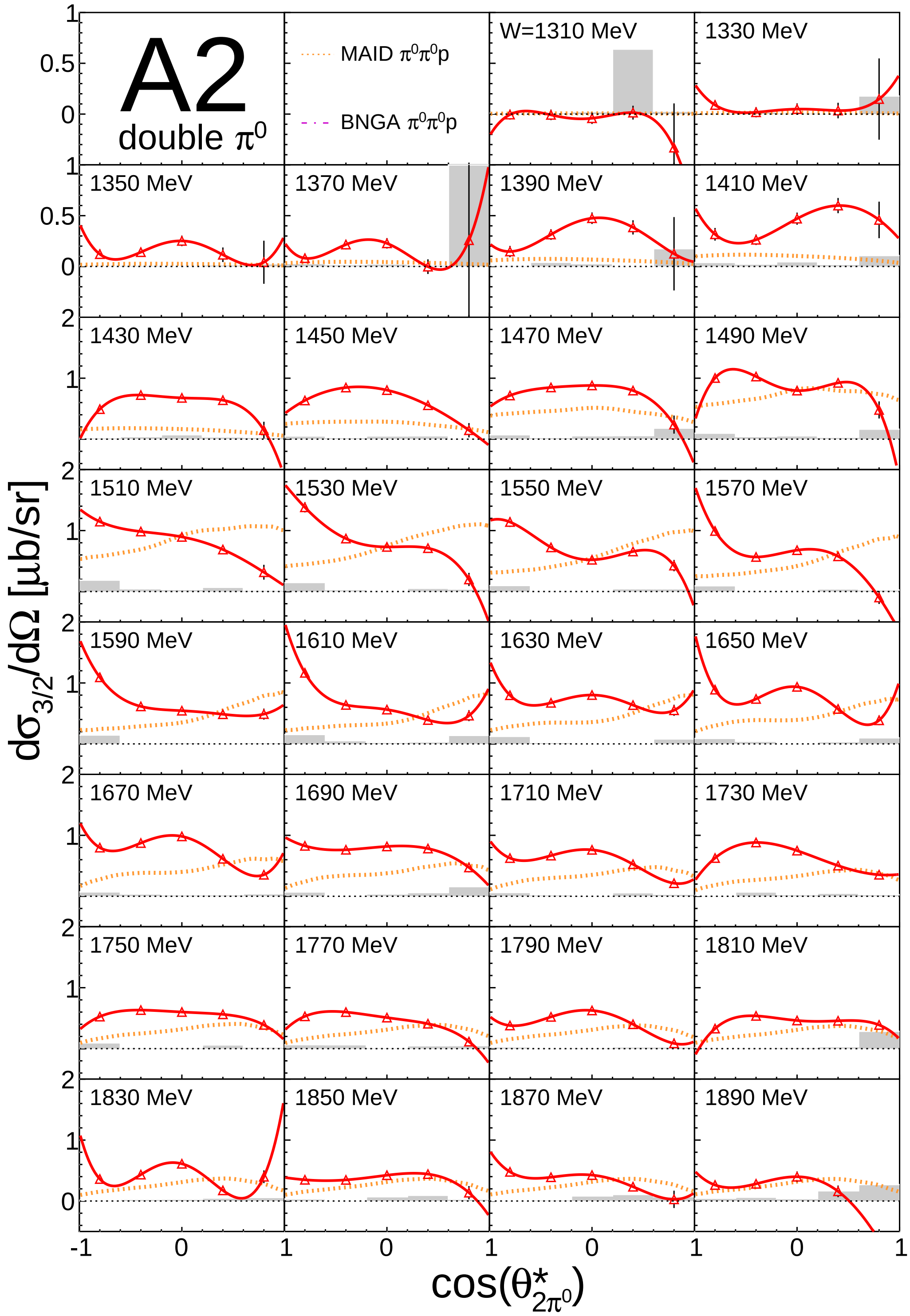

Figure D.35: Differential helicity dependent cross section $\sigma_{3/2}$ for double π^0 photoproduction from quasi-free neutrons as a function of the meson polar angle in the $\pi^0 p$ center of mass frame. Results from the A2 data. Solid red line: Legendre fit. Dotted orange line: MAID [62]. The gray histogram at the base line of each figure represents the systematical uncertainties of the results.

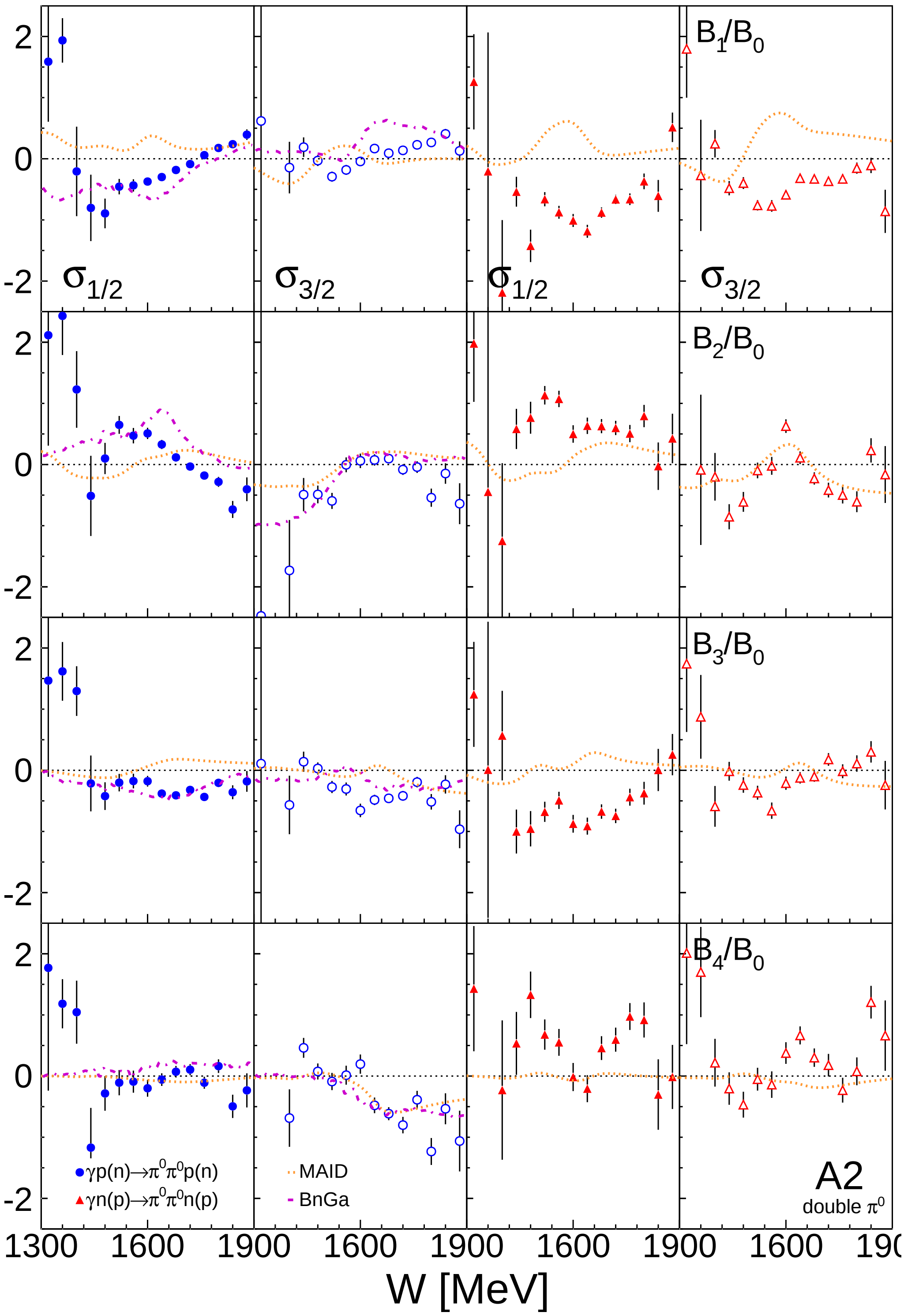

Figure D.36: Legendre coefficient ratios for double π^0 photoproduction from polarized protons and neutrons. Results from the A2 data. Left two columns: quasi-free proton. Right two columns: quasi-free neutron. Solid (open) symbols: coefficient ratios from $\sigma_{1/2}$ ($\sigma_{3/2}$). Dotted orange line: MAID [40]. Dashed-dotted magenta line: BnGa [43] (only proton).

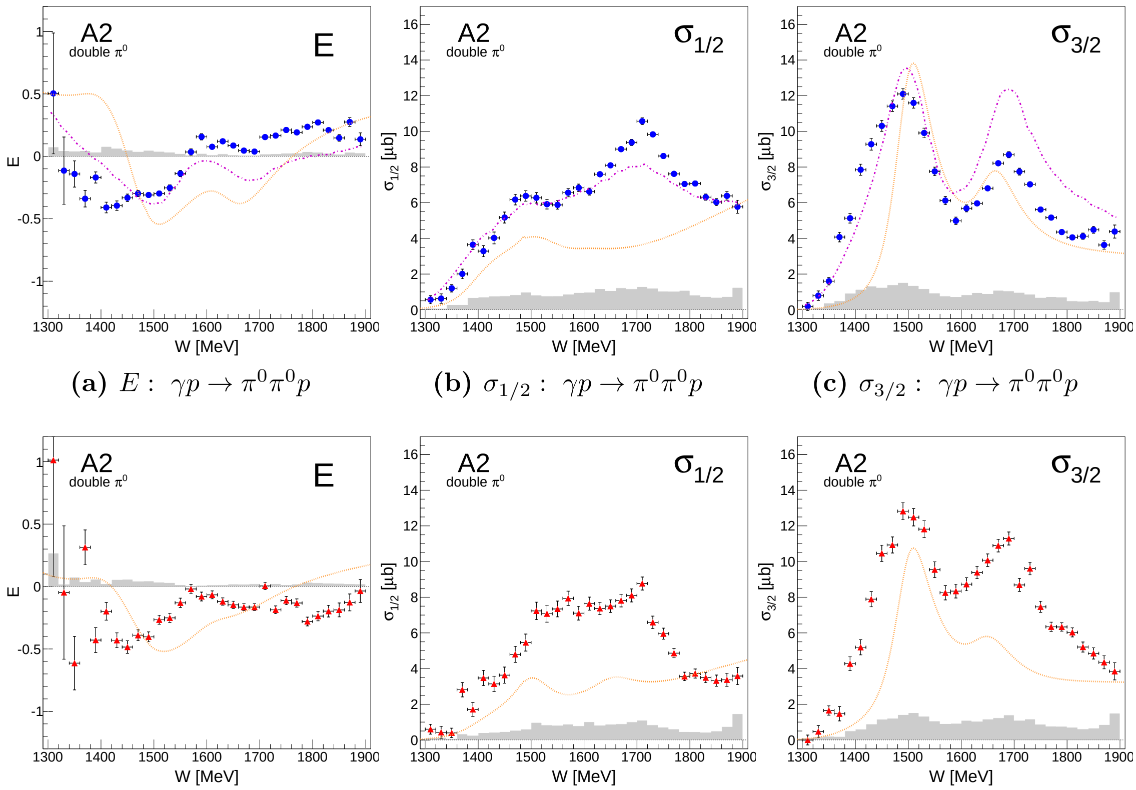

(a) $E: \ \gamma p \to \pi^0\pi^0 p$ **(b)** $\sigma_{1/2}: \ \gamma p \to \pi^0\pi^0 p$ **(c)** $\sigma_{3/2}: \ \gamma p \to \pi^0\pi^0 p$

(d) $E: \ \gamma n \to \pi^0\pi^0 n$ **(e)** $\sigma_{1/2}: \ \gamma n \to \pi^0\pi^0 n$ **(f)** $\sigma_{3/2}: \ \gamma n \to \pi^0\pi^0 n$

Figure D.37: Final averaged double polarization observables for double π^0 photoproduction from free protons and neutrons as a function of the final state invariant mass W. Results from the A2 data. Shown are the average observables obtained from the arithmetic mean of the different versions. Figures (a)-(c): free proton. Figures (d)-(f): free neutron. (a) and (d): double polarization observable E. (b) and (e): helicity dependent cross section $\sigma_{1/2}$. (c) and (f): helicity dependent cross section $\sigma_{3/2}$. Dotted orange line: MAID [62]. Dashed-dotted magenta line: BnGa [43] (only proton). The gray histogram at the base line of each figure represents the systematical uncertainties of the results.

CBELSA/TAPS Data

This section presents additional results from the analysis of double π^0 photoproduction from the polarized CBELSA/TAPS data discussed in Section 7.5.2.

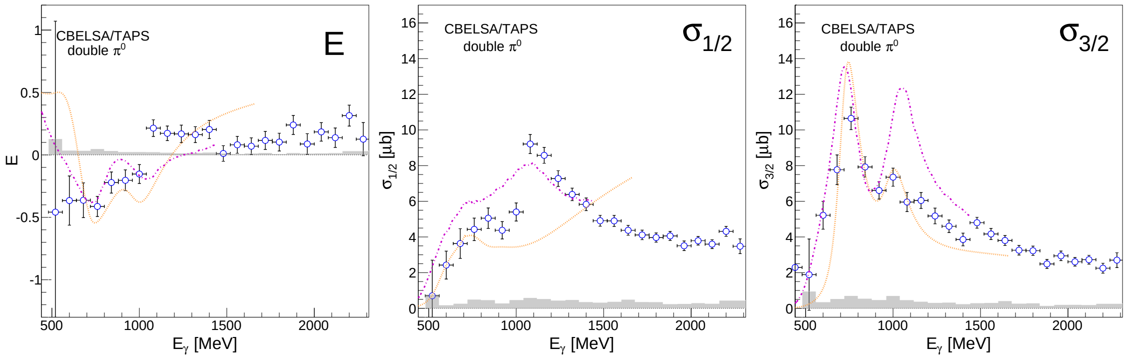

(a) $E : \gamma d \to \pi^0\pi^0 p(n)$ **(b)** $\sigma_{1/2} : \gamma d \to \pi^0\pi^0 p(n)$ **(c)** $\sigma_{3/2} : \gamma d \to \pi^0\pi^0 p(n)$

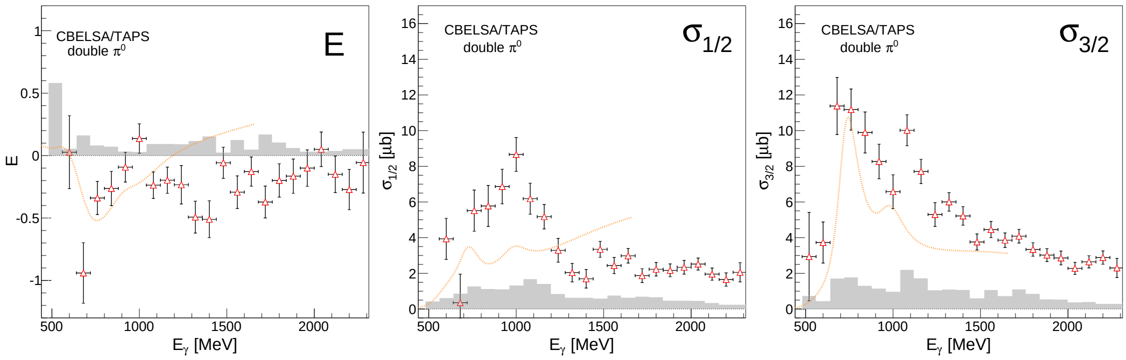

(d) $E : \gamma d \to \pi^0\pi^0 n(p)$ **(e)** $\sigma_{1/2} : \gamma d \to \pi^0\pi^0 n(p)$ **(f)** $\sigma_{3/2} : \gamma d \to \pi^0\pi^0 n(p)$

Figure D.38: Final averaged double polarization observables for double π^0 photoproduction from quasi-free protons and neutrons as a function of the incident photon energy E_γ. Results from the CBELSA/TAPS data. Shown are the average observables obtained from the arithmetic mean of versions 1 and 2. Figures (a)-(c): quasi-free proton. Figures (d)-(f): quasi-free neutron. (a) and (d): double polarization observable E. (b) and (e): helicity dependent cross section $\sigma_{1/2}$. (c) and (f): helicity dependent cross section $\sigma_{3/2}$. Dotted orange line: MAID [62]. Dashed-dotted magenta line: BnGa (proton: [43], neutron: [38]). The gray histogram at the base line of each figure represents the systematical uncertainties of the results.

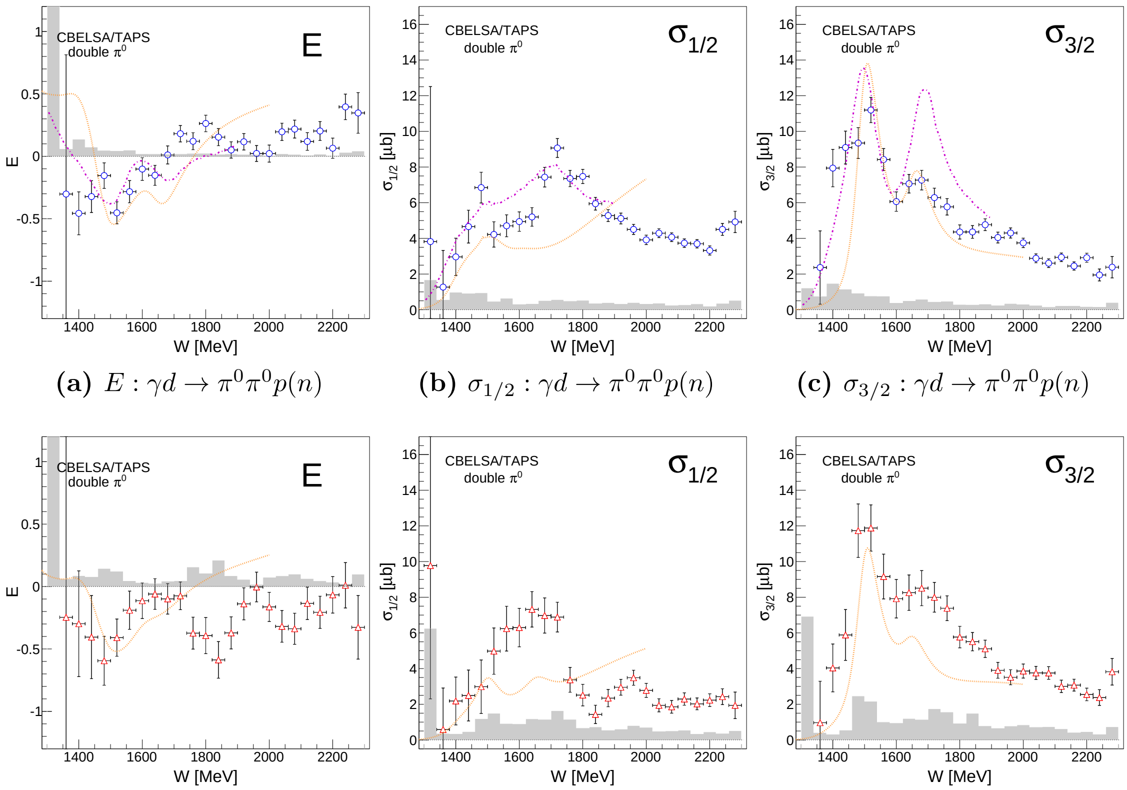

(a) $E : \gamma d \to \pi^0\pi^0 p(n)$ **(b)** $\sigma_{1/2} : \gamma d \to \pi^0\pi^0 p(n)$ **(c)** $\sigma_{3/2} : \gamma d \to \pi^0\pi^0 p(n)$

(d) $E : \gamma d \to \pi^0\pi^0 n(p)$ **(e)** $\sigma_{1/2} : \gamma d \to \pi^0\pi^0 n(p)$ **(f)** $\sigma_{3/2} : \gamma d \to \pi^0\pi^0 n(p)$

Figure D.39: Final averaged double polarization observables for double π^0 photoproduction from quasi-free protons and neutrons as a function of the final state invariant mass W. Results from the CBELSA/TAPS data. Shown are the average observables obtained from the arithmetic mean of versions 1 and 2. Figures (a)-(c): quasi-free proton. Figures (d)-(f): quasi-free neutron. (a) and (d): double polarization observable E. (b) and (e): helicity dependent cross section $\sigma_{1/2}$. (c) and (f): helicity dependent cross section $\sigma_{3/2}$. Dotted orange line: MAID [62]. Dashed-dotted magenta line: BnGa (proton: [43], neutron: [38]). The gray histogram at the base line of each figure represents the systematical uncertainties of the results.

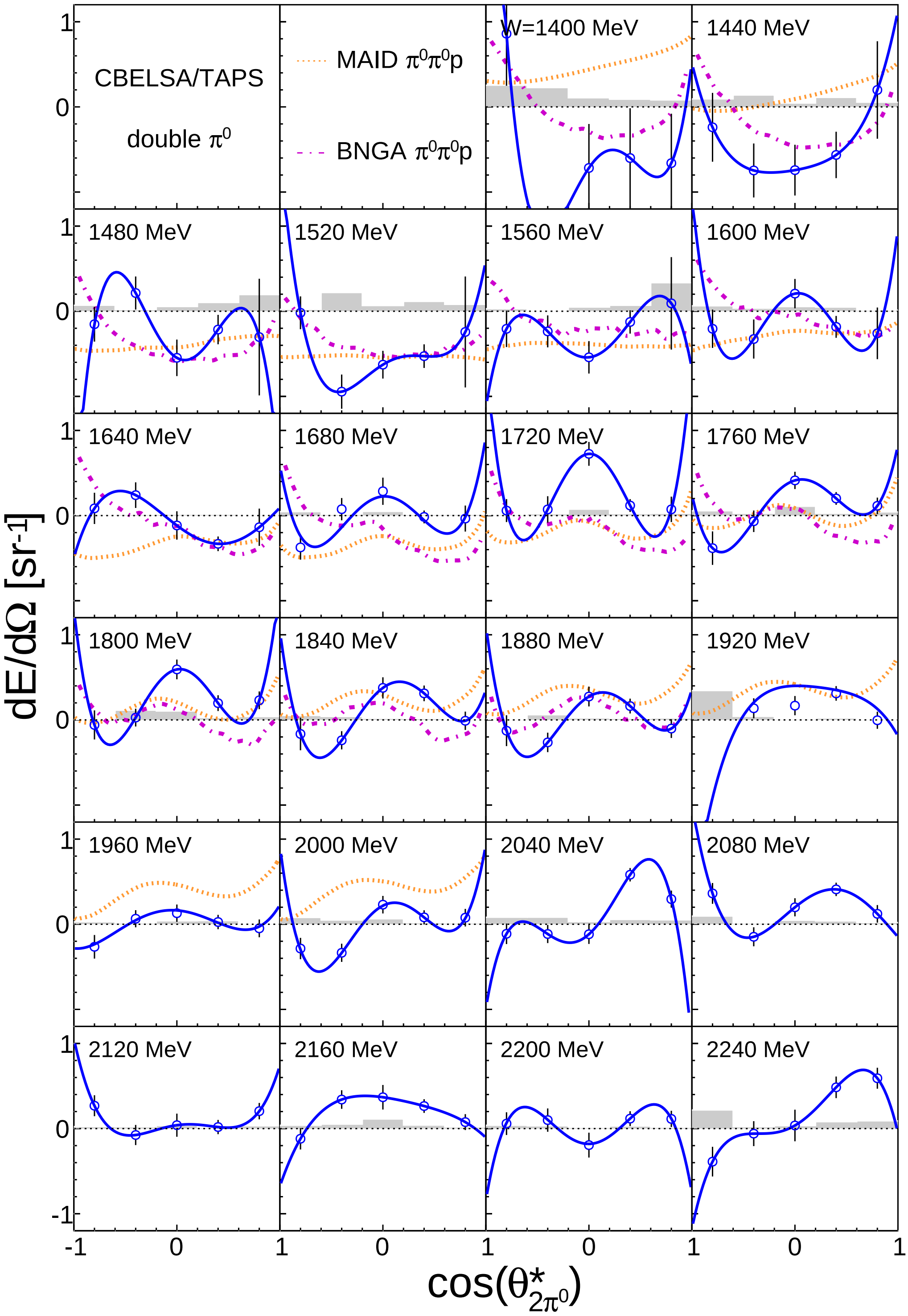

Figure D.40: Differential double polarization observable E for double π^0 photoproduction from quasi-free protons as a function of the meson polar angle in the $\pi^0 p$ center of mass frame. Results from the CBELSA/TAPS data. Solid blue line: Legendre fit. Dotted orange line: MAID [62]. Dashed-dotted magenta line: BnGa [43]. The gray histogram at the base line of each figure represents the systematical uncertainties of the results.

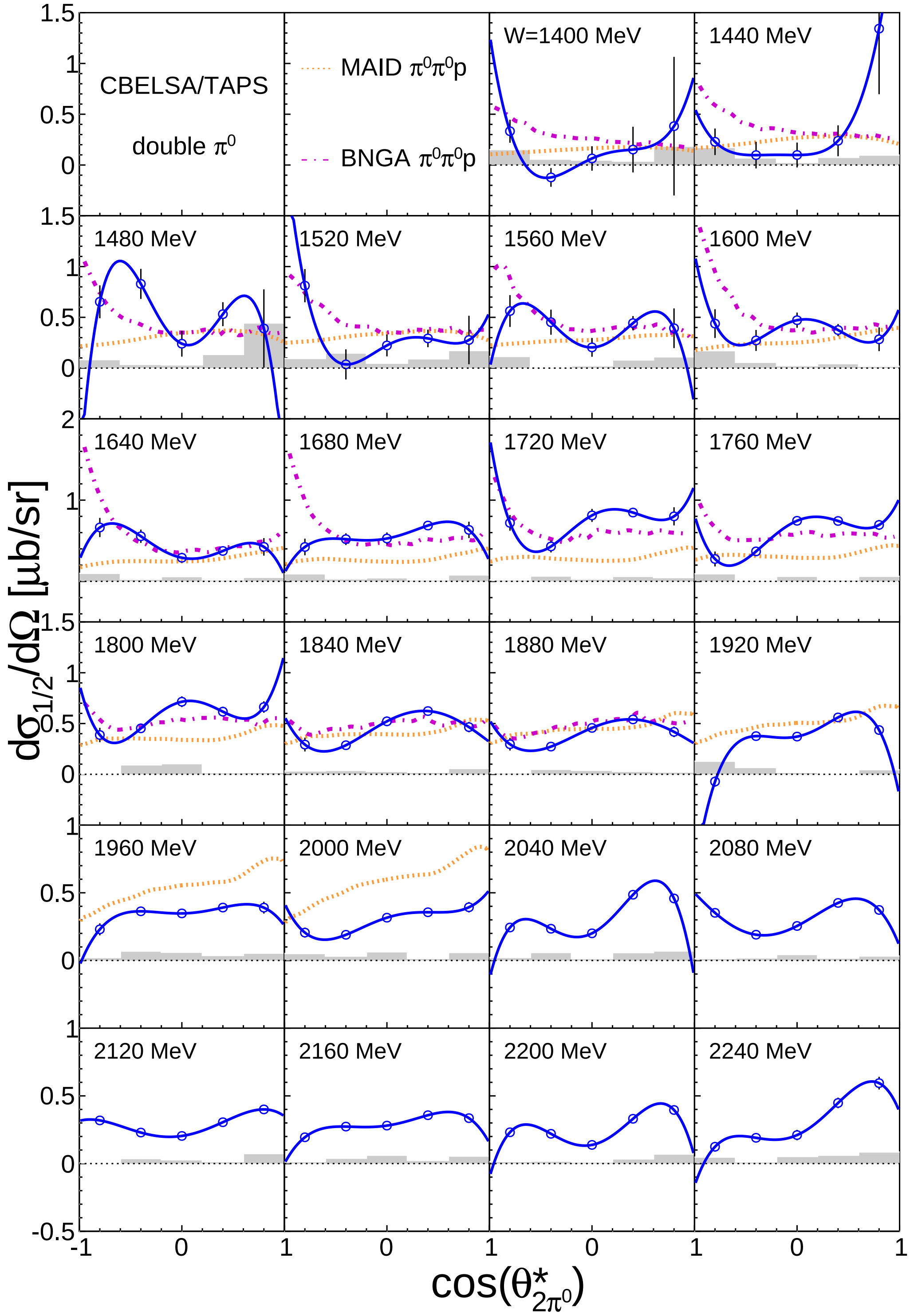

Figure D.41: Differential helicity dependent cross section $\sigma_{1/2}$ for double π^0 photoproduction from quasi-free protons as a function of the meson polar angle in the $\pi^0 p$ center of mass frame. Results from the CBELSA/TAPS data. Solid blue line: Legendre fit. Dotted orange line: MAID [62]. Dashed-dotted magenta line: BnGa [43]. The gray histogram at the base line of each figure represents the systematical uncertainties of the results.

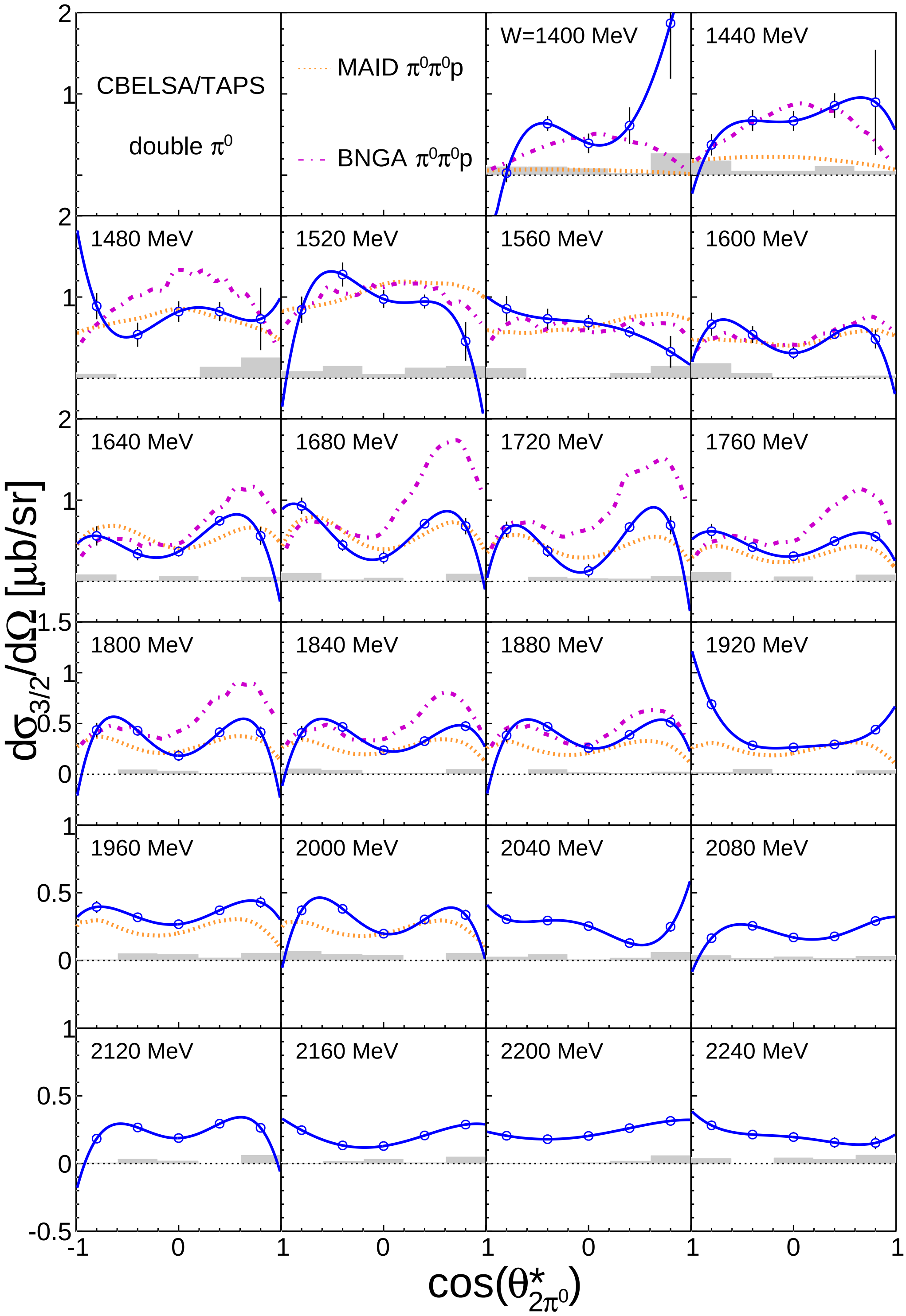

Figure D.42: Differential helicity dependent cross section $\sigma_{3/2}$ for double π^0 photoproduction from quasi-free protons as a function of the meson polar angle in the $\pi^0 p$ center of mass frame. Results from the CBELSA/TAPS data. Solid blue line: Legendre fit. Dotted orange line: MAID [62]. Dashed-dotted magenta line: BnGa [43]. The gray histogram at the base line of each figure represents the systematical uncertainties of the results.

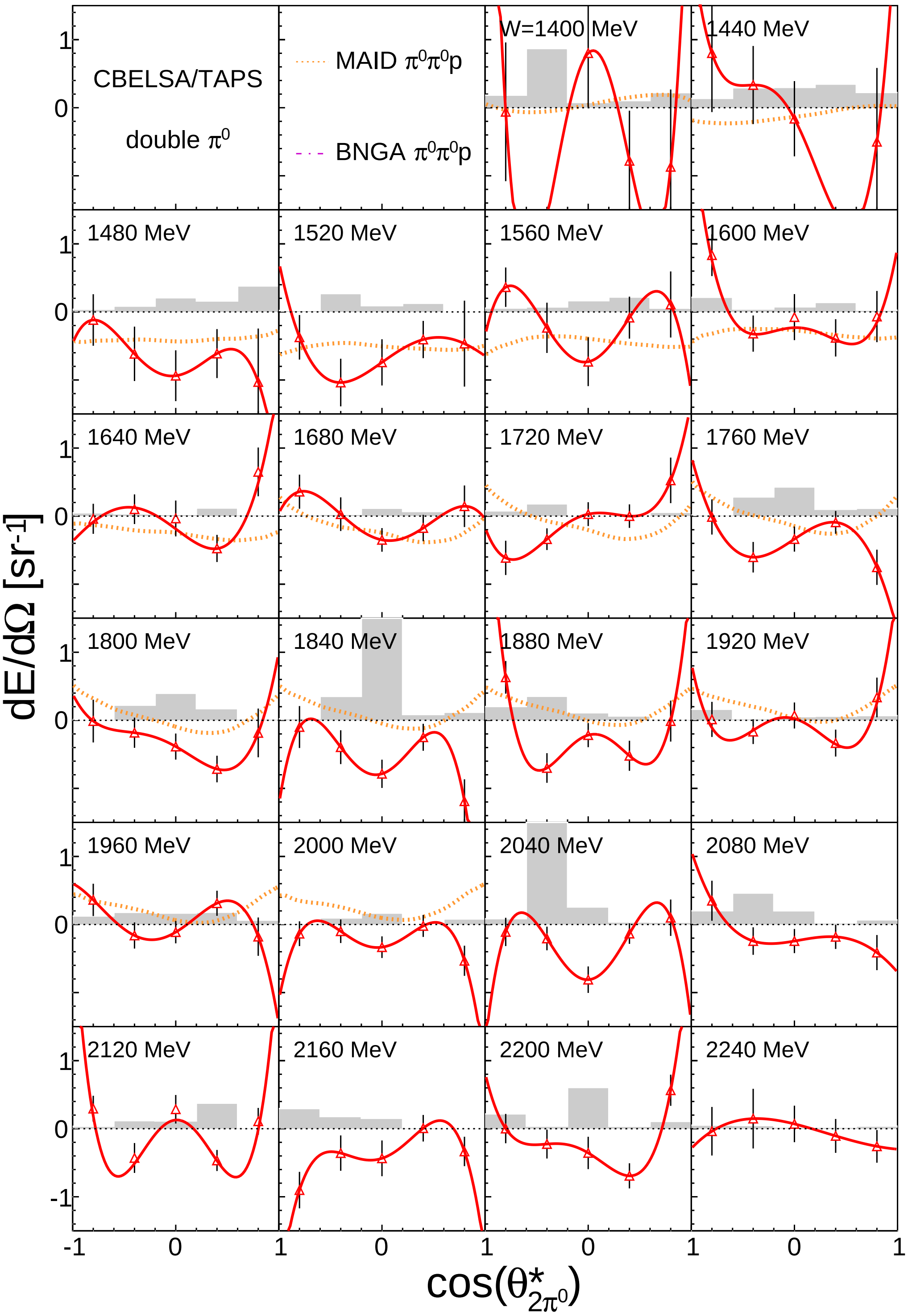

Figure D.43: Differential double polarization observable E for double π^0 photoproduction from quasi-free neutrons as a function of the meson polar angle in the $\pi^0 p$ center of mass frame. Results from the CBELSA/TAPS data. Solid red line: Legendre fit. Dotted orange line: MAID [62]. The gray histogram at the base line of each figure represents the systematical uncertainties of the results.

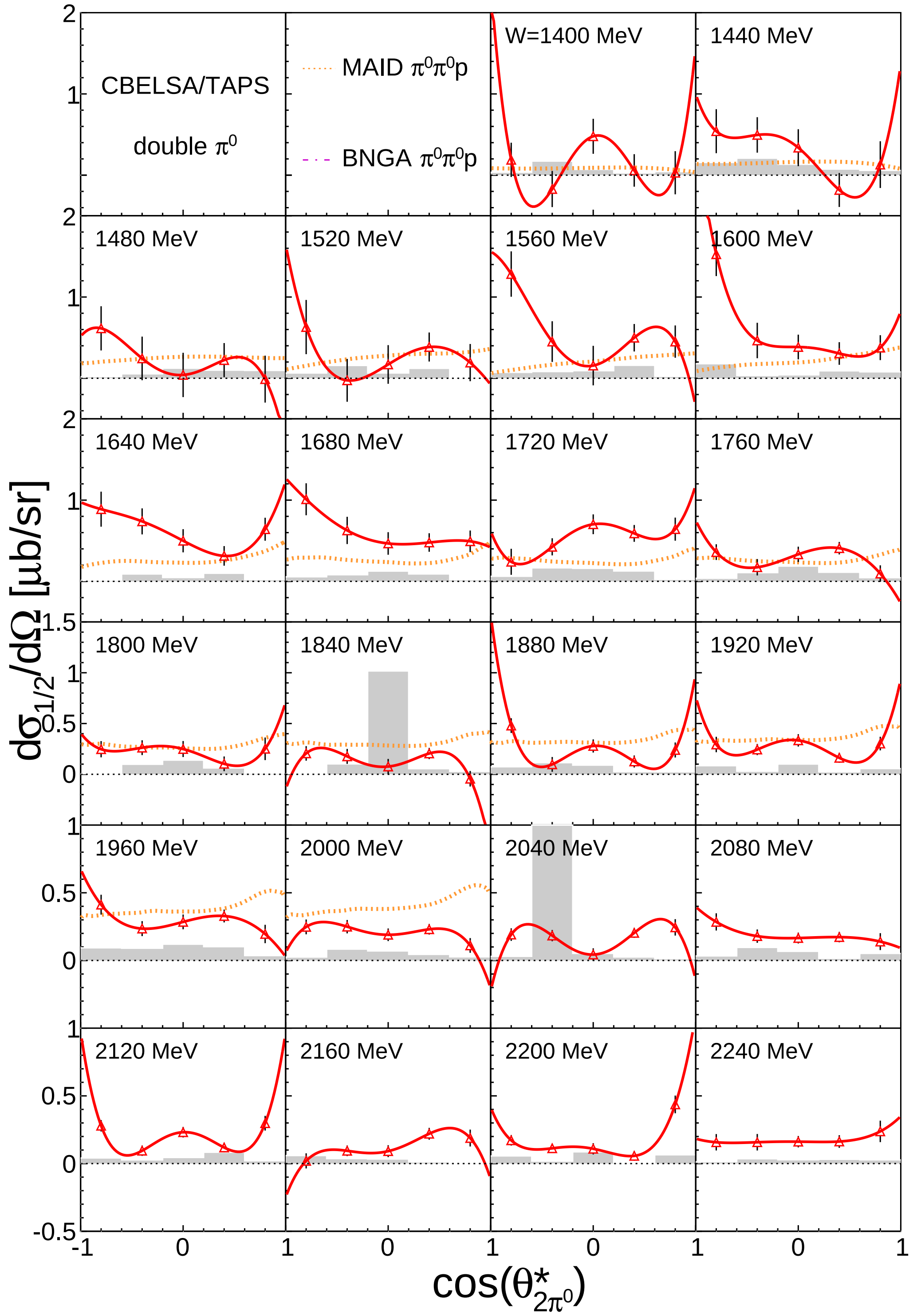

Figure D.44: Differential helicity dependent cross section $\sigma_{1/2}$ for double π^0 photoproduction from quasi-free neutrons as a function of the meson polar angle in the $\pi^0 p$ center of mass frame. Results from the CBELSA/TAPS data. Solid red line: Legendre fit. Dotted orange line: MAID [62]. The gray histogram at the base line of each figure represents the systematical uncertainties of the results.

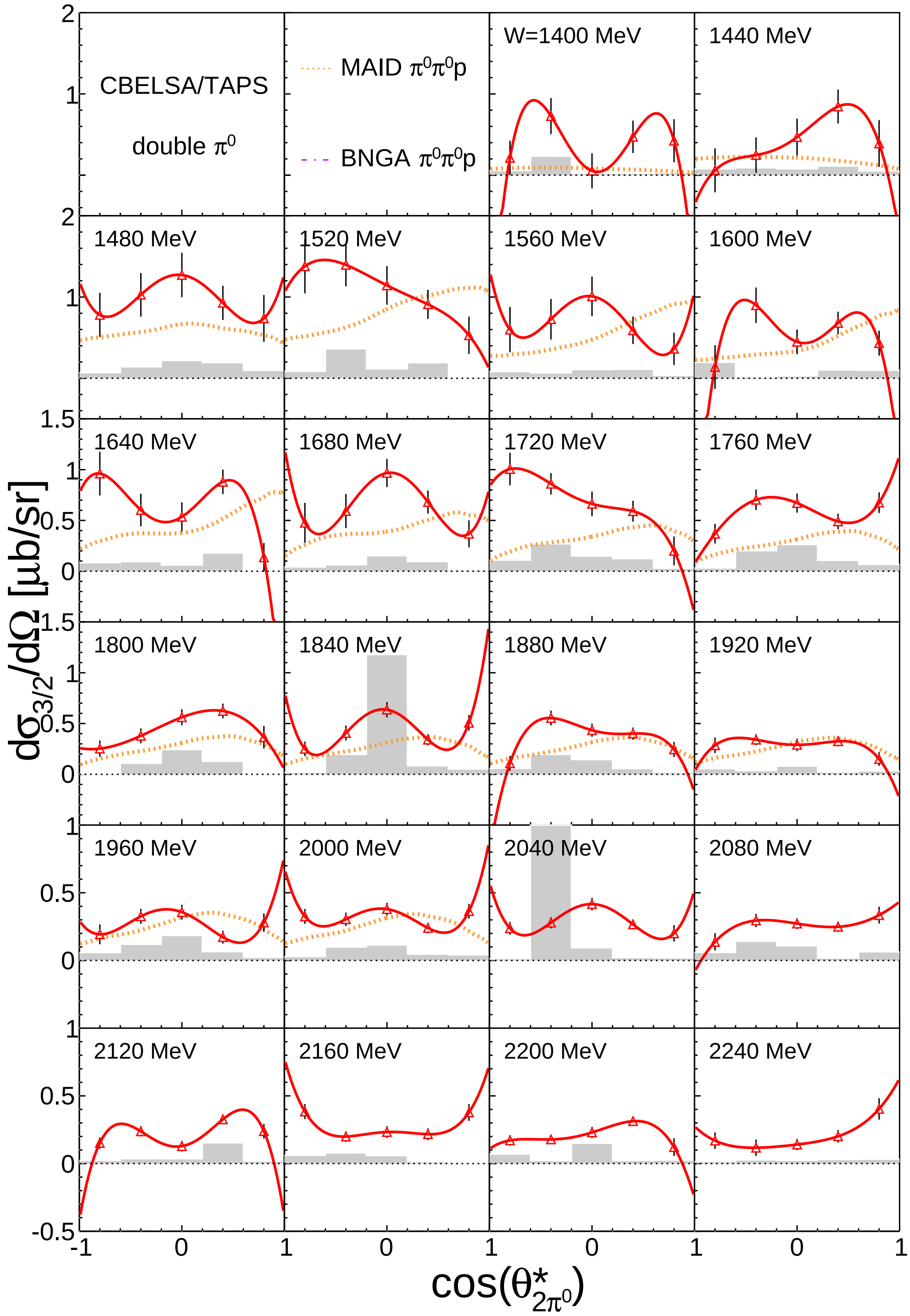

Figure D.45: Differential helicity dependent cross section $\sigma_{3/2}$ for double π^0 photoproduction from quasi-free neutrons as a function of the meson polar angle in the $\pi^0 p$ center of mass frame. Results from the CBELSA/TAPS data. Solid red line: Legendre fit. Dotted orange line: MAID [62]. The gray histogram at the base line of each figure represents the systematical uncertainties of the results.

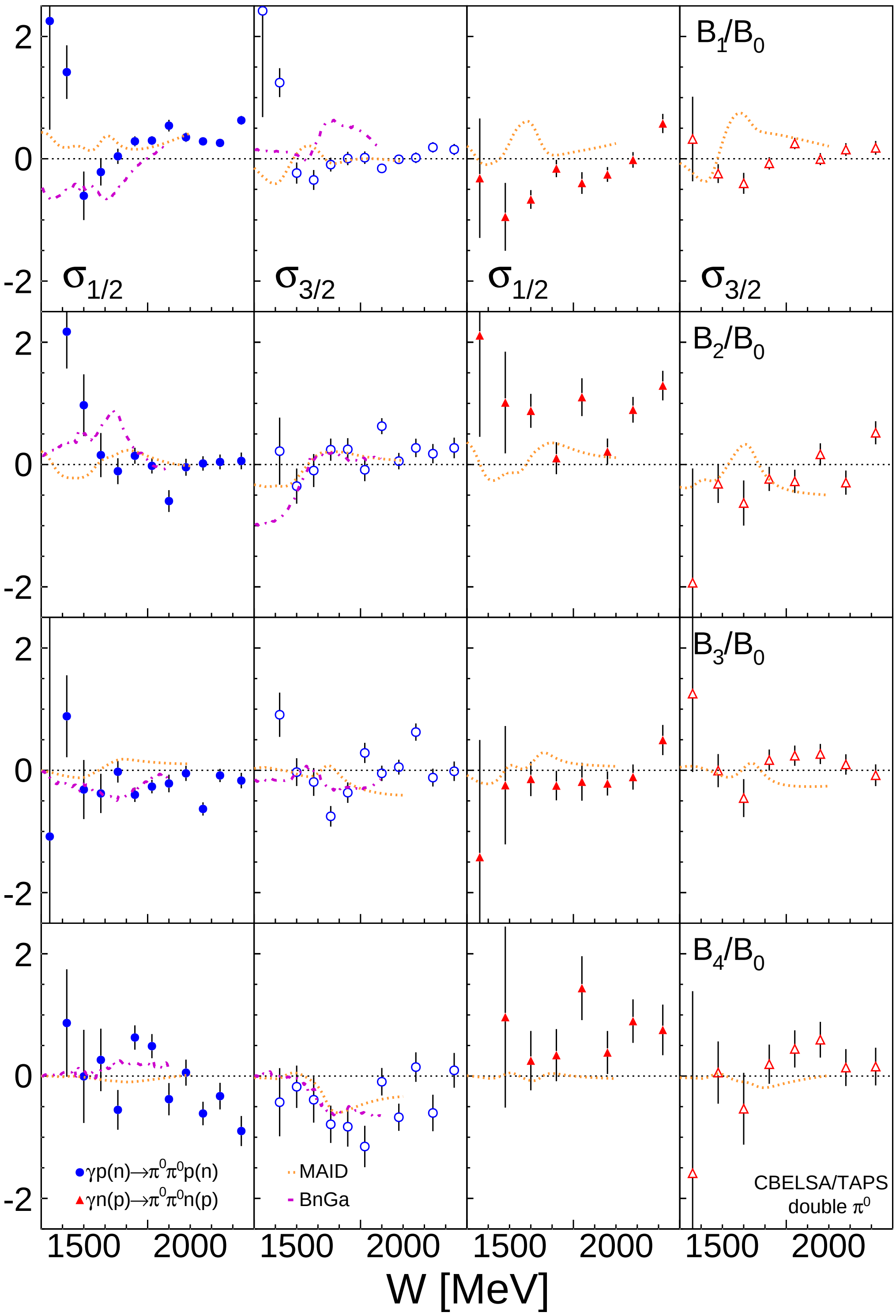

Figure D.46: Legendre coefficient ratios for double π^0 photoproduction from polarized protons and neutrons. Results from the CBELA/TAPS data. Left two columns: quasi-free proton. Right two columns: quasi-free neutron. Solid (open) symbols: coefficient ratios from $\sigma_{1/2}$ ($\sigma_{3/2}$). Dotted orange line: MAID [40]. Dashed-dotted magenta line: BnGa [43] (only proton).

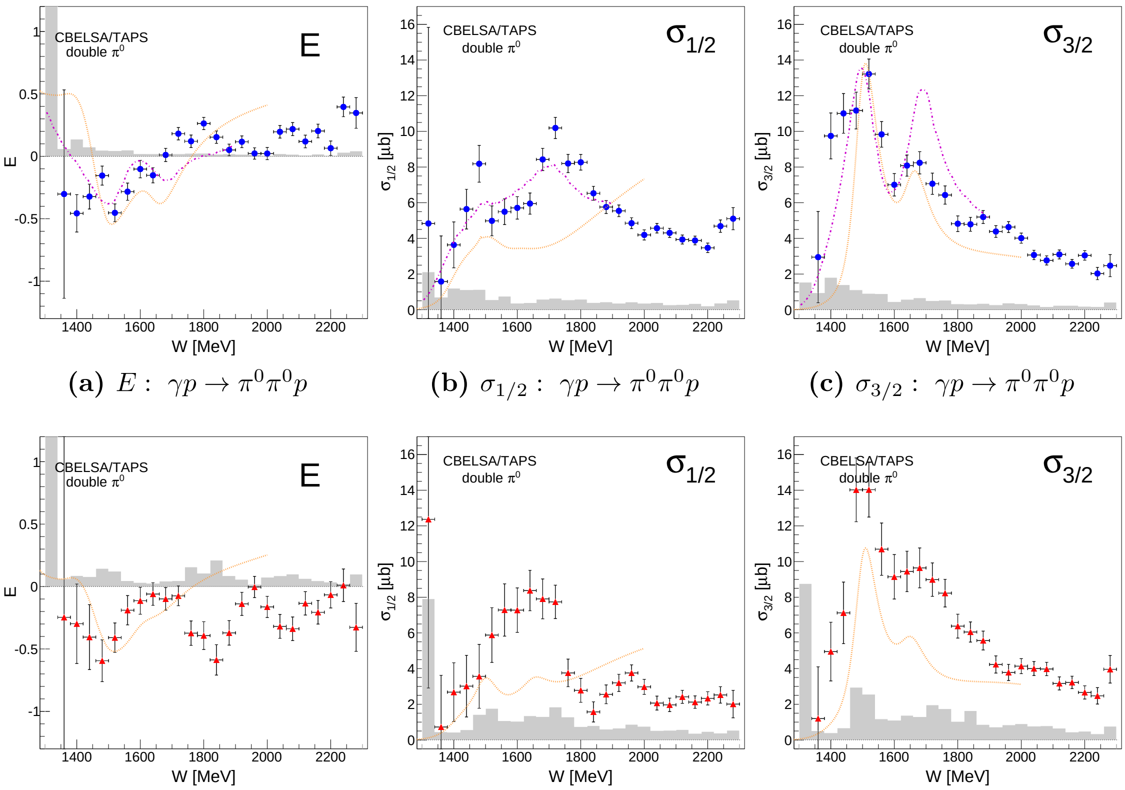

(a) $E: \ \gamma p \rightarrow \pi^0\pi^0 p$ **(b)** $\sigma_{1/2}: \ \gamma p \rightarrow \pi^0\pi^0 p$ **(c)** $\sigma_{3/2}: \ \gamma p \rightarrow \pi^0\pi^0 p$

(d) $E: \ \gamma n \rightarrow \pi^0\pi^0 n$ **(e)** $\sigma_{1/2}: \ \gamma n \rightarrow \pi^0\pi^0 n$ **(f)** $\sigma_{3/2}: \ \gamma n \rightarrow \pi^0\pi^0 n$

Figure D.47: Final averaged double polarization observables for double π^0 photoproduction from free protons and neutrons as a function of the final state invariant mass W. Results from the A2 data. Shown are the average observables obtained from the arithmetic mean of the different versions. Figures (a)-(c): free proton. Figures (d)-(f): free neutron. (a) and (d): double polarization observable E. (b) and (e): helicity dependent cross section $\sigma_{1/2}$. (c) and (f): helicity dependent cross section $\sigma_{3/2}$. Dotted orange line: MAID [62]. Dashed-dotted magenta line: BnGa [43] (only proton). The gray histogram at the base line of each figure represents the systematical uncertainties of the results.

E Data Tables

The following data tables contain most of the results of the measured cross sections and polarization observables. Shown are the individual observables together with the corresponding statistical and (if available) systematic uncertainties.
Section E.1 contains the data from the differential and total cross sections for single π^0 photoproduction from the A2 data. Section E.2 presents the differential and total cross section data of the double polarization observable E and the helicity dependent cross sections $\sigma_{1/2}$ and $\sigma_{3/2}$ for single π^0 photoproduction from the A2 data.
Section E.3 (E.5) shows the differential and total cross sections for double π^0 photoproduction from A2 (CBELSA/TAPS) data as well as the decomposition of the contributions from intermediate excited states. The data for the double polarization observable E and the helicity dependent cross sections $\sigma_{1/2}$ and $\sigma_{3/2}$ for double π^0 photoproduction from A2 (CBELSA/TAPS) data are shown in Sections E.4 (E.6).
The data for the results as function of the incident photon energy E_γ are only given for the total cross sections.

E.1 Unpolarized Results for Single π^0 from the A2 Data

E.1.1 Total Cross Sections as a Function of E_γ

E_γ [MeV]	ΔE_γ [MeV]	σ_{qf-inc} [μb]	Δ_{stat} [μb]	Δ_{sys} [μb]	σ_p [μb]	Δ_{stat} [μb]	Δ_{sys} [μb]	σ_n [μb]	Δ_{stat} [μb]	Δ_{sys} [μb]
457.5	7.5	141.4821	0.1513	5.3213	74.9837	0.5187	9.5700	66.8859	0.5619	4.3109
472.5	7.5	123.2560	0.1355	3.4777	63.7430	0.4244	5.0109	58.1992	0.4351	2.8045
487.5	7.5	108.3517	0.1210	3.1052	55.6968	0.3622	3.3248	50.3520	0.3755	2.2971
502.5	7.5	95.9017	0.1159	2.0117	48.1427	0.3143	2.4351	44.2452	0.3494	1.8676
517.5	7.5	84.5504	0.1144	2.2393	42.2911	0.2857	1.9912	39.7596	0.3395	2.0811
532.5	7.5	76.2117	0.1104	1.9346	37.2945	0.2425	1.3237	35.9047	0.2934	1.4378
547.5	7.5	68.5697	0.1044	1.9441	33.4638	0.2209	0.9878	32.5279	0.2541	1.4042
562.5	7.5	61.7227	0.0998	1.8769	29.9749	0.2007	1.1724	29.4814	0.2359	1.4227
577.5	7.5	56.2482	0.0949	1.8787	27.0379	0.1856	0.9025	27.1374	0.1950	1.3458
592.5	7.5	51.3141	0.0922	1.7596	24.5180	0.1674	0.9163	25.1375	0.1892	1.2837
607.5	7.5	47.2732	0.0896	1.8536	22.7883	0.1495	0.8657	23.2758	0.1742	1.2626
622.5	7.5	43.9993	0.0886	1.7280	21.7439	0.1348	1.1075	21.0716	0.1727	1.0816
637.5	7.5	42.0640	0.0885	1.8263	20.7564	0.1312	1.4905	20.1280	0.1762	1.1393
652.5	7.5	40.7309	0.0886	2.1704	20.5143	0.1290	1.9824	19.4668	0.1759	1.1829
667.5	7.5	40.9156	0.0882	2.2840	20.8075	0.1277	1.9250	19.3720	0.1429	1.3257
682.5	7.5	41.7462	0.0861	2.5600	21.9292	0.1165	1.6859	19.1801	0.1451	1.4200
697.5	7.5	44.5032	0.0930	2.8038	23.3858	0.1166	2.1677	19.7810	0.1233	1.3115
712.5	7.5	46.2446	0.0928	2.1833	25.3646	0.1123	2.1332	20.7109	0.1277	1.4069
727.5	7.5	49.2927	0.1054	1.9457	27.7852	0.1289	1.8766	21.2898	0.1633	1.1747
742.5	7.5	50.0326	0.1029	2.0996	28.5008	0.1176	2.2965	21.0758	0.1691	1.3427
757.5	7.5	50.5257	0.1056	1.5575	28.7167	0.1193	2.1708	21.5094	0.1426	1.0440
772.5	7.5	49.7686	0.1116	1.7934	28.5517	0.1215	1.8661	20.6917	0.1753	1.0902
787.5	7.5	47.9989	0.1051	1.9535	28.0102	0.1079	1.5287	20.0546	0.1539	1.1170
802.5	7.5	46.1664	0.1021	1.8671	27.0441	0.0930	1.3560	19.6558	0.1662	1.0217
817.5	7.5	43.5807	0.0982	2.2191	25.6020	0.0903	1.6109	17.8258	0.1475	1.0961
832.5	7.5	40.9937	0.1050	1.6590	24.2185	0.0994	1.9028	17.0885	0.1445	0.8954
847.5	7.5	39.2798	0.1134	1.0626	22.8550	0.1054	1.5336	16.2882	0.1561	0.9704
862.5	7.5	35.4708	0.1100	1.5499	21.1256	0.0978	1.6877	14.3419	0.1340	0.9695
877.5	7.5	35.3979	0.1153	1.2166	21.0101	0.0989	1.4756	13.5538	0.1446	0.9898
892.5	7.5	33.6009	0.1176	1.7889	19.8691	0.0982	1.5844	13.0486	0.1533	0.8733
907.5	7.5	31.8969	0.0987	0.6462	18.6480	0.0706	1.5922	11.8509	0.1236	0.8141
922.5	7.5	30.4881	0.1003	1.2837	18.3543	0.0762	1.5838	12.0215	0.1243	0.7100
937.5	7.5	30.7138	0.1039	1.6718	18.3188	0.0784	1.7406	11.5567	0.1185	0.8558
952.5	7.5	31.0502	0.1084	1.3554	18.4502	0.0803	1.5440	11.5594	0.1181	0.8307
967.5	7.5	31.2597	0.1066	1.2414	19.0074	0.0786	1.7785	11.6432	0.1495	0.6002
982.5	7.5	30.9780	0.1225	1.1195	19.2788	0.0938	1.5723	11.1575	0.1322	0.6098
997.5	7.5	30.5875	0.1205	1.2582	19.3027	0.0909	1.3990	10.8716	0.1319	0.7100
1012.5	7.5	30.6042	0.1251	1.2228	19.4418	0.0891	1.4108	10.7230	0.1319	0.6314
1027.5	7.5	30.2750	0.1220	1.5263	19.5567	0.0898	1.4402	9.5870	0.1467	0.5705
1042.5	7.5	29.8014	0.1232	1.1713	19.1565	0.0908	1.4230	9.5663	0.1250	0.5118
1057.5	7.5	28.8407	0.1234	1.4105	18.6975	0.0897	1.0013	9.0210	0.1320	0.6377
1072.5	7.5	27.8772	0.1260	1.1752	17.9237	0.0890	0.9662	9.0377	0.1375	0.4126
1087.5	7.5	26.8676	0.1167	1.0596	16.7612	0.0810	1.0334	8.9364	0.1324	0.5057
1102.5	7.5	25.5539	0.1315	1.4094	15.7624	0.0887	1.0799	9.1110	0.1548	0.3480
1117.5	7.5	23.8700	0.1378	0.9276	14.3718	0.0886	0.9608	8.0732	0.1385	0.3358
1132.5	7.5	22.6581	0.1226	1.2867	13.7668	0.0865	0.9715	8.1306	0.1256	0.3241
1147.5	7.5	21.6536	0.1268	0.8890	12.8947	0.0776	0.8985	7.4833	0.1222	0.4306
1162.5	7.5	20.8054	0.1138	1.3061	12.0378	0.0718	0.9934	7.0714	0.1163	0.3538
1177.5	7.5	20.7850	0.1278	1.4974	11.2969	0.0784	1.0051	7.9544	0.1292	0.4635
1192.5	7.5	18.7893	0.1343	1.1034	10.6224	0.0800	1.0117	6.8972	0.1483	0.3942
1207.5	7.5	18.9149	0.1257	1.1435	10.1665	0.0802	0.9336	6.9822	0.1408	0.5479
1222.5	7.5	19.2385	0.1241	0.8650	9.9899	0.0712	0.8959	7.2885	0.1142	0.3370
1237.5	7.5	18.6865	0.1275	0.7303	9.5639	0.0785	0.8818	6.9749	0.1206	0.5499
1252.5	7.5	18.2515	0.1353	1.1865	9.4893	0.0796	1.0767	6.4040	0.1222	0.5513
1267.5	7.5	18.1192	0.1391	1.5347	9.3353	0.0770	1.0848	6.6893	0.1286	0.6252
1282.5	7.5	18.6368	0.1327	1.0330	9.3917	0.0837	1.2784	7.4967	0.1195	0.3690
1297.5	7.5	18.9507	0.1530	0.9479	9.2867	0.0891	1.0354	6.8857	0.1376	0.2939
1312.5	7.5	18.6707	0.1488	1.4639	9.1186	0.0761	1.1981	6.5026	0.1361	0.3254
1327.5	7.5	19.6574	0.2123	1.4402	9.2346	0.1103	1.0494	6.6939	0.1648	0.4132
1342.5	7.5	18.7888	0.2114	0.0000	9.3172	0.1217	0.0000	6.3391	0.1712	0.0000
1357.5	7.5	19.1582	0.1662	7.5000	9.5651	0.0954	0.0000	6.9168	0.1448	0.0000
1372.5	7.5	19.1715	0.1760	7.5000	9.4915	0.1018	0.0000	6.8044	0.1524	0.0000
1387.5	7.5	18.9929	0.1704	7.5000	9.2391	0.0941	0.0000	6.9537	0.1518	0.0000

E.1.2 Total Cross Sections as a Function of W

W [MeV]	ΔW [MeV]	σ_{qfp} [μb]	Δ_{stat} [μb]	Δ_{sys} [μb]	σ_{qfn} [μb]	Δ_{stat} [μb]	Δ_{sys} [μb]	σ_n [μb]	Δ_{stat} [μb]	Δ_{sys} [μb]
1300.0	6.0	65.6836	0.4335	1.1239	66.0411	0.4488	1.0688	86.0307	0.8114	0.9441
1312.0	6.0	58.8285	0.3868	1.0991	59.9008	0.4210	1.2026	80.4752	0.7255	0.9893
1324.0	6.0	51.0458	0.3264	1.4539	55.3337	0.3253	1.4964	72.5061	0.5638	0.9699
1336.0	6.0	43.1044	0.2680	1.5961	46.3585	0.3090	1.5753	60.6112	0.5400	1.0601
1348.0	6.0	37.2543	0.2340	1.6280	40.5256	0.2617	1.7738	52.5279	0.4716	1.1796
1360.0	6.0	33.3189	0.2003	1.7859	36.2577	0.2461	1.7137	48.2736	0.4215	1.4443
1372.0	6.0	29.1071	0.1800	1.4892	32.6308	0.2058	1.0918	42.3233	0.3634	1.0995
1384.0	6.0	26.6761	0.1590	1.4461	29.2484	0.1870	0.9536	39.5022	0.3294	1.1927
1396.0	6.0	24.1009	0.1494	1.3563	26.0318	0.1694	1.0751	35.3526	0.2920	1.0410
1408.0	6.0	22.1031	0.1392	1.1361	23.9460	0.1322	0.9694	32.7853	0.2400	0.9324
1420.0	6.0	20.8300	0.1237	1.0482	21.9547	0.1515	0.7937	30.7336	0.2675	0.8427
1432.0	6.0	20.2764	0.1153	1.1058	20.6002	0.1137	0.8894	29.6440	0.1981	0.7866
1444.0	6.0	20.4852	0.1122	0.9493	19.6654	0.1103	0.5676	28.7212	0.1936	0.7576
1456.0	6.0	21.7272	0.1026	1.1082	19.7050	0.1170	0.8379	28.5527	0.2058	0.8803
1468.0	6.0	23.9073	0.1075	1.3887	20.1816	0.1184	0.7860	28.8691	0.2140	0.9829
1480.0	6.0	26.3454	0.1119	1.3853	20.5345	0.1204	1.0045	29.7176	0.2212	1.1078
1492.0	6.0	28.5708	0.1116	1.2717	21.9158	0.1615	0.8240	30.9619	0.2939	0.9911
1504.0	6.0	29.4865	0.1103	1.1578	23.1305	0.1503	0.7162	31.9483	0.2730	0.7770
1516.0	6.0	29.2223	0.0982	1.4124	21.5433	0.1353	0.8771	30.4430	0.2404	0.9282
1528.0	6.0	27.9083	0.0976	1.2559	20.3773	0.1282	0.7247	28.5869	0.2254	0.8226
1540.0	6.0	25.9466	0.0972	1.0254	19.0984	0.1334	0.5611	26.2697	0.2361	0.6330
1552.0	6.0	23.6707	0.0897	0.9794	16.2680	0.1441	0.5011	23.1829	0.2455	0.6164
1564.0	6.0	21.5870	0.0774	0.8325	15.4164	0.1309	0.5077	21.8279	0.2127	0.5455
1576.0	6.0	20.1267	0.0760	0.7234	14.0455	0.1164	0.4709	19.4774	0.1832	0.4812
1588.0	6.0	18.6175	0.0769	0.6399	12.5563	0.1093	0.4345	17.4116	0.1743	0.4705
1600.0	6.0	18.0527	0.0758	0.6915	12.0649	0.1118	0.5234	16.3544	0.1792	0.5424
1612.0	6.0	17.5953	0.0728	0.4797	10.8496	0.1069	0.3067	15.1799	0.1694	0.2944
1624.0	6.0	17.8201	0.0728	0.4358	10.2951	0.1083	0.3042	14.7292	0.1703	0.2461
1636.0	6.0	19.0213	0.0811	0.4129	9.7982	0.1054	0.4385	14.1916	0.1650	0.2790
1648.0	6.0	20.0556	0.0815	0.5400	9.6860	0.1092	0.4116	13.8881	0.1688	0.3813
1660.0	6.0	19.6685	0.0822	0.5657	10.2290	0.1126	0.4185	14.1379	0.1713	0.2906
1672.0	6.0	19.5742	0.0802	0.4522	9.2952	0.1267	0.4449	12.8591	0.1886	0.1855
1684.0	6.0	18.8967	0.0810	0.7015	8.8448	0.1124	0.6356	12.1912	0.1649	0.5732
1696.0	6.0	17.0947	0.0740	0.4371	8.1392	0.1095	0.6454	11.2313	0.1597	0.6526
1708.0	6.0	15.3166	0.0733	0.4726	7.8988	0.1066	0.3949	10.7970	0.1548	0.3059
1720.0	6.0	13.7059	0.0696	0.6438	7.1252	0.1094	0.3670	9.5882	0.1540	0.2746
1732.0	6.0	12.2132	0.0656	0.8907	6.5597	0.0937	0.7495	8.6607	0.1340	0.4644
1744.0	6.0	10.8517	0.0647	0.0000	6.5601	0.0991	0.0000	8.3826	0.1399	0.0000
1756.0	6.0	10.2629	0.0610	0.0000	6.1900	0.0939	0.0000	7.8991	0.1329	0.0000
1768.0	6.0	10.0301	0.0631	0.0000	6.0540	0.1062	0.0000	7.7638	0.1486	0.0000
1780.0	6.0	9.9356	0.0651	0.0000	6.5035	0.0899	0.0000	8.2585	0.1262	0.0000
1792.0	6.0	9.8428	0.0664	0.0000	6.7485	0.0944	0.0000	8.3870	0.1321	0.0000
1804.0	6.0	10.0245	0.0734	0.0000	6.5555	0.0980	0.0000	7.8083	0.1371	0.0000
1816.0	6.0	10.8570	0.0742	0.0000	6.8929	0.1157	0.0000	8.4004	0.1545	0.0000
1828.0	6.0	10.7634	0.0765	0.0000	7.3317	0.1287	−0.4125	8.7291	0.1696	0.0000
1840.0	6.0	11.1283	0.0887	0.0000	7.4652	0.1250	−95.7505	8.9681	0.1660	0.0000
1852.0	6.0	11.1685	0.1023	2.9484	7.5229	0.1372	−111.8617	8.7481	0.1786	0.0000
1864.0	6.0	10.9509	0.1168	0.0000	7.1568	0.1506	−23.4946	8.5427	0.1944	0.0000
1876.0	6.0	10.7847	0.1246	0.0000	8.8685	0.1954	0.7346	10.0051	0.2488	0.0000

E.1.3 Angular Distributions $\gamma d \to \pi^0 p(n)$ as a Function of W

	W=(1300.0±6.0) MeV			W=(1312.0±6.0) MeV			W=(1324.0±6.0) MeV			W=(1336.0±6.0) MeV		
$\cos(\theta^*_{\pi^0})$	$d\sigma/d\Omega$ [μb/sr]	Δ_{stat} [μb/sr]	Δ_{sys} [μb/sr]	$d\sigma/d\Omega$ [μb/sr]	Δ_{stat} [μb/sr]	Δ_{sys} [μb/sr]	$d\sigma/d\Omega$ [μb/sr]	Δ_{stat} [μb/sr]	Δ_{sys} [μb/sr]	$d\sigma/d\Omega$ [μb/sr]	Δ_{stat} [μb/sr]	Δ_{sys} [μb/sr]
−0.95	0.0115	0.0015	0.0168	0.0136	0.0023	0.0198	0.0191	0.0023	0.0250	0.0281	0.0022	0.0360
−0.85	0.1603	0.0043	0.1891	0.1863	0.0044	0.2201	0.2007	0.0049	0.2318	0.2039	0.0048	0.2313
−0.75	1.4151	0.0176	1.7115	1.5123	0.0178	1.7673	1.3789	0.0155	1.5255	1.2205	0.0133	1.3389
−0.65	4.8700	0.0275	3.7854	4.2229	0.0231	4.1693	3.4714	0.0211	3.4030	2.8567	0.0179	2.5577
−0.55	5.7702	0.0218	1.5159	4.9414	0.0192	2.6007	4.1721	0.0175	2.3134	3.5396	0.0154	1.2632
−0.45	6.0660	0.0208	0.7014	5.4241	0.0193	0.8323	4.7067	0.0178	0.6488	3.9842	0.0160	0.2894
−0.35	6.5739	0.0220	0.9345	5.9332	0.0205	0.4569	5.1279	0.0187	0.1353	4.3007	0.0167	0.2022
−0.25	7.0884	0.0224	1.0928	6.3694	0.0204	0.5582	5.4328	0.0189	0.2761	4.6431	0.0172	0.2133
−0.15	7.4105	0.0222	0.9780	6.5628	0.0206	0.5096	5.7287	0.0192	0.2723	4.9219	0.0173	0.1875
−0.05	7.3959	0.0226	0.6833	6.8191	0.0214	0.5617	5.8762	0.0197	0.1827	4.9776	0.0175	0.1504
0.05	7.3521	0.0229	0.6462	6.6699	0.0212	0.4175	5.7626	0.0194	0.1746	4.9436	0.0174	0.1670
0.15	7.1673	0.0226	0.5525	6.4256	0.0201	0.3194	5.6353	0.0189	0.2324	4.8122	0.0172	0.2161
0.25	6.7717	0.0225	0.4229	6.1081	0.0202	0.3381	5.3951	0.0188	0.3081	4.5506	0.0171	0.2579
0.35	6.2071	0.0227	0.4113	5.6219	0.0206	0.3911	4.9246	0.0189	0.3809	4.2056	0.0168	0.3120
0.45	5.5177	0.0250	0.5264	5.0398	0.0224	0.4921	4.4130	0.0199	0.4593	3.7218	0.0171	0.3661
0.55	4.8550	0.0324	0.7706	4.4185	0.0281	0.6388	3.8986	0.0240	0.5406	3.2524	0.0196	0.4221
0.65	3.8349	0.0493	0.6850	3.7110	0.0429	0.5363	3.2950	0.0358	0.5020	2.6998	0.0280	0.3502
0.75	3.8171	0.0995	0.3847	3.5878	0.0937	0.2512	3.0378	0.0770	0.3525	2.4314	0.0602	0.1690
0.85	4.6607	0.3161	1.5000	4.4988	0.2761	1.3847	3.9396	0.2301	0.7932	3.2411	0.1885	0.9545

$\cos(\theta^*_{\pi^0})$	$W=(1348.0\pm6.0)$ MeV			$W=(1360.0\pm6.0)$ MeV			$W=(1372.0\pm6.0)$ MeV			$W=(1384.0\pm6.0)$ MeV		
	$d\sigma/d\Omega$ [μb/sr]	$\Delta_{\rm stat}$ [μb/sr]	$\Delta_{\rm sys}$ [μb/sr]	$d\sigma/d\Omega$ [μb/sr]	$\Delta_{\rm stat}$ [μb/sr]	$\Delta_{\rm sys}$ [μb/sr]	$d\sigma/d\Omega$ [μb/sr]	$\Delta_{\rm stat}$ [μb/sr]	$\Delta_{\rm sys}$ [μb/sr]	$d\sigma/d\Omega$ [μb/sr]	$\Delta_{\rm stat}$ [μb/sr]	$\Delta_{\rm sys}$ [μb/sr]
−0.95	0.0267	0.0030	0.0345	0.0330	0.0036	0.0396	0.0435	0.0033	0.0508	0.0579	0.0038	0.0635
−0.85	0.2349	0.0046	0.2603	0.2480	0.0048	0.2616	0.2785	0.0049	0.3078	0.3043	0.0052	0.3230
−0.75	1.1382	0.0119	1.1878	1.0557	0.0113	1.0663	0.9754	0.0108	0.9673	0.9458	0.0101	0.8640
−0.65	2.5719	0.0168	2.0231	2.3108	0.0168	1.5984	1.9842	0.0153	1.1535	1.8345	0.0148	0.8156
−0.55	3.0542	0.0147	0.9322	2.7567	0.0138	0.4496	2.4616	0.0133	0.3567	2.2278	0.0128	0.1327
−0.45	3.4571	0.0145	0.1981	3.0828	0.0140	0.1057	2.7300	0.0135	0.1527	2.4989	0.0132	0.1199
−0.35	3.7573	0.0159	0.1320	3.3823	0.0151	0.1818	3.0158	0.0143	0.1526	2.7499	0.0139	0.1132
−0.25	4.1061	0.0158	0.1366	3.6632	0.0153	0.1386	3.2572	0.0145	0.1119	2.9529	0.0139	0.0953
−0.15	4.3205	0.0159	0.1349	3.8502	0.0154	0.1153	3.4234	0.0145	0.0974	3.1029	0.0140	0.0894
−0.05	4.3763	0.0162	0.1249	3.9114	0.0157	0.1131	3.4765	0.0150	0.1048	3.1447	0.0148	0.0891
0.05	4.3412	0.0163	0.1370	3.8294	0.0158	0.1136	3.4339	0.0150	0.1094	3.0830	0.0143	0.0887
0.15	4.1959	0.0163	0.1615	3.6511	0.0153	0.1327	3.2997	0.0145	0.1105	2.9556	0.0137	0.0830
0.25	3.9146	0.0157	0.1920	3.4449	0.0150	0.1617	3.0418	0.0140	0.1230	2.7111	0.0135	0.0983
0.35	3.5833	0.0157	0.2368	3.1704	0.0145	0.1940	2.7240	0.0139	0.1504	2.4432	0.0131	0.1291
0.45	3.1925	0.0152	0.2866	2.7226	0.0144	0.2255	2.3855	0.0134	0.1898	2.1012	0.0127	0.1595
0.55	2.7652	0.0173	0.3356	2.3223	0.0154	0.2655	2.0384	0.0142	0.2254	1.7453	0.0131	0.1894
0.65	2.2995	0.0239	0.3085	1.9816	0.0202	0.2656	1.6746	0.0173	0.2070	1.4279	0.0154	0.1769
0.75	2.0934	0.0486	0.2061	1.8175	0.0440	0.1807	1.4816	0.0367	0.1506	1.3186	0.0290	0.1191
0.85	2.6573	0.1764	0.6806	2.3685	0.1326	0.6109	1.9456	0.1239	0.6251	1.7262	0.1151	0.4511

$\cos(\theta^*_{\pi^0})$	$W=(1396.0\pm6.0)$ MeV			$W=(1408.0\pm6.0)$ MeV			$W=(1420.0\pm6.0)$ MeV			$W=(1432.0\pm6.0)$ MeV		
	$d\sigma/d\Omega$ [μb/sr]	$\Delta_{\rm stat}$ [μb/sr]	$\Delta_{\rm sys}$ [μb/sr]	$d\sigma/d\Omega$ [μb/sr]	$\Delta_{\rm stat}$ [μb/sr]	$\Delta_{\rm sys}$ [μb/sr]	$d\sigma/d\Omega$ [μb/sr]	$\Delta_{\rm stat}$ [μb/sr]	$\Delta_{\rm sys}$ [μb/sr]	$d\sigma/d\Omega$ [μb/sr]	$\Delta_{\rm stat}$ [μb/sr]	$\Delta_{\rm sys}$ [μb/sr]
−0.95	0.0781	0.0046	0.0855	0.0991	0.0049	0.1088	0.1435	0.0056	0.1488	0.1791	0.0067	0.1863
−0.85	0.3318	0.0051	0.3249	0.3635	0.0058	0.3372	0.3965	0.0063	0.3943	0.4458	0.0066	0.2966
−0.75	0.9022	0.0098	0.6872	0.8764	0.0100	0.4210	0.8755	0.0099	0.6100	0.8889	0.0106	0.3724
−0.65	1.6947	0.0144	0.6445	1.5579	0.0146	0.2122	1.4866	0.0144	0.3785	1.4033	0.0140	0.2483
−0.55	2.0513	0.0124	0.2104	1.9138	0.0124	0.1251	1.8096	0.0121	0.0933	1.7383	0.0126	0.0773
−0.45	2.3445	0.0128	0.1137	2.1822	0.0125	0.1317	2.0521	0.0123	0.0891	1.9841	0.0125	0.0566
−0.35	2.5154	0.0137	0.1188	2.3723	0.0133	0.1020	2.2399	0.0133	0.0814	2.1974	0.0134	0.0759
−0.25	2.6995	0.0136	0.0922	2.4971	0.0131	0.0954	2.3793	0.0133	0.0766	2.3252	0.0130	0.0782
−0.15	2.8163	0.0138	0.0791	2.6337	0.0134	0.0791	2.5132	0.0130	0.0700	2.4224	0.0136	0.0660
−0.05	2.8791	0.0140	0.0769	2.6662	0.0140	0.0672	2.5324	0.0138	0.0583	2.4839	0.0138	0.0578
0.05	2.8526	0.0140	0.0677	2.6491	0.0139	0.0600	2.4756	0.0137	0.0433	2.4409	0.0137	0.0471
0.15	2.6886	0.0136	0.0579	2.5021	0.0133	0.0533	2.3347	0.0136	0.0381	2.3257	0.0132	0.0355
0.25	2.4633	0.0132	0.0727	2.2976	0.0127	0.0571	2.1797	0.0129	0.0480	2.1271	0.0129	0.0406
0.35	2.1841	0.0127	0.1050	1.9981	0.0122	0.0789	1.8619	0.0123	0.0647	1.8239	0.0124	0.0628
0.45	1.8580	0.0122	0.1339	1.6830	0.0118	0.1077	1.5513	0.0115	0.0899	1.5225	0.0116	0.0882
0.55	1.5181	0.0118	0.1570	1.3706	0.0111	0.1354	1.2483	0.0111	0.1169	1.2275	0.0111	0.1099
0.65	1.2519	0.0132	0.1575	1.0996	0.0124	0.1241	0.9728	0.0113	0.1024	0.9400	0.0118	0.1007
0.75	1.0838	0.0273	0.1133	0.9314	0.0244	0.0680	0.8340	0.0198	0.0598	0.7675	0.0182	0.0645
0.85	1.5221	0.1048	0.3538	1.1886	0.0974	0.3200	1.1344	0.0843	0.3240	1.0466	0.0732	0.2275

$\cos(\theta^*_{\pi^0})$	$W=(1444.0\pm6.0)$ MeV			$W=(1456.0\pm6.0)$ MeV			$W=(1468.0\pm6.0)$ MeV			$W=(1480.0\pm6.0)$ MeV		
	$d\sigma/d\Omega$ [μb/sr]	$\Delta_{\rm stat}$ [μb/sr]	$\Delta_{\rm sys}$ [μb/sr]	$d\sigma/d\Omega$ [μb/sr]	$\Delta_{\rm stat}$ [μb/sr]	$\Delta_{\rm sys}$ [μb/sr]	$d\sigma/d\Omega$ [μb/sr]	$\Delta_{\rm stat}$ [μb/sr]	$\Delta_{\rm sys}$ [μb/sr]	$d\sigma/d\Omega$ [μb/sr]	$\Delta_{\rm stat}$ [μb/sr]	$\Delta_{\rm sys}$ [μb/sr]
−0.95	0.2364	0.0083	0.2471	0.2837	0.0093	0.2931	0.3997	0.0090	0.3743	0.5232	0.0107	0.4670
−0.85	0.5068	0.0074	0.3531	0.5828	0.0081	0.4027	0.6854	0.0089	0.4713	0.8178	0.0097	0.3563
−0.75	0.9194	0.0104	0.4204	0.9993	0.0109	0.3780	1.1104	0.0115	0.3432	1.2674	0.0129	0.1544
−0.65	1.4096	0.0150	0.2831	1.4539	0.0149	0.2075	1.5164	0.0152	0.1383	1.6873	0.0171	0.0911
−0.55	1.7222	0.0123	0.0699	1.8019	0.0128	0.0938	1.9122	0.0132	0.1172	2.0987	0.0147	0.1247
−0.45	2.0218	0.0130	0.0637	2.1447	0.0134	0.0986	2.3538	0.0142	0.1085	2.5023	0.0151	0.1247
−0.35	2.2048	0.0139	0.0767	2.3340	0.0145	0.0869	2.4928	0.0154	0.0946	2.6694	0.0160	0.1076
−0.25	2.3739	0.0137	0.0794	2.4660	0.0145	0.0659	2.6280	0.0151	0.0711	2.8570	0.0157	0.0858
−0.15	2.4684	0.0141	0.0696	2.5898	0.0146	0.0569	2.8281	0.0153	0.0596	3.0869	0.0161	0.0616
−0.05	2.5367	0.0145	0.0588	2.6332	0.0154	0.0485	2.9017	0.0160	0.0551	3.1543	0.0166	0.0452
0.05	2.4753	0.0147	0.0427	2.6266	0.0150	0.0333	2.8704	0.0156	0.0450	3.1434	0.0169	0.0396
0.15	2.3479	0.0138	0.0314	2.5240	0.0145	0.0258	2.7598	0.0154	0.0319	3.0305	0.0163	0.0371
0.25	2.1804	0.0135	0.0308	2.3158	0.0141	0.0234	2.6328	0.0149	0.0257	2.9205	0.0160	0.0306
0.35	1.9152	0.0131	0.0432	2.1113	0.0138	0.0384	2.3762	0.0144	0.0232	2.6941	0.0157	0.0259
0.45	1.5862	0.0122	0.0700	1.7419	0.0128	0.0660	1.9998	0.0135	0.0417	2.3266	0.0148	0.0426
0.55	1.2609	0.0113	0.1004	1.4043	0.0121	0.0989	1.6114	0.0130	0.0871	1.9225	0.0143	0.0818
0.65	0.9951	0.0114	0.1044	1.0629	0.0121	0.0811	1.2623	0.0130	0.1012	1.4819	0.0142	0.1008
0.75	0.7767	0.0176	0.0728	0.8717	0.0175	0.0410	0.9761	0.0173	0.0788	1.1465	0.0186	0.1065
0.85	0.9910	0.0671	0.2387	0.9552	0.0523	0.2872	0.9531	0.0563	0.2618	1.0418	0.0558	0.2282

$\cos(\theta^*_{\pi^0})$	$W=(1492.0\pm6.0)$ MeV			$W=(1504.0\pm6.0)$ MeV			$W=(1516.0\pm6.0)$ MeV			$W=(1528.0\pm6.0)$ MeV		
	$d\sigma/d\Omega$ [μb/sr]	$\Delta_{\rm stat}$ [μb/sr]	$\Delta_{\rm sys}$ [μb/sr]	$d\sigma/d\Omega$ [μb/sr]	$\Delta_{\rm stat}$ [μb/sr]	$\Delta_{\rm sys}$ [μb/sr]	$d\sigma/d\Omega$ [μb/sr]	$\Delta_{\rm stat}$ [μb/sr]	$\Delta_{\rm sys}$ [μb/sr]	$d\sigma/d\Omega$ [μb/sr]	$\Delta_{\rm stat}$ [μb/sr]	$\Delta_{\rm sys}$ [μb/sr]
−0.95	0.6689	0.0125	0.3758	0.8297	0.0143	0.6059	0.9771	0.0152	0.8655	1.1199	0.0169	0.6750
−0.85	1.0193	0.0111	0.3120	1.2186	0.0117	0.3320	1.3287	0.0127	0.2481	1.4975	0.0129	0.2535
−0.75	1.4334	0.0134	0.2226	1.5949	0.0138	0.1177	1.6999	0.0142	0.0571	1.8116	0.0146	0.1329
−0.65	1.8806	0.0185	0.1770	2.0101	0.0193	0.1304	2.1130	0.0204	0.1419	2.1593	0.0221	0.1541
−0.55	2.2761	0.0153	0.1468	2.4525	0.0160	0.1405	2.4952	0.0172	0.1445	2.4763	0.0169	0.1530
−0.45	2.6894	0.0154	0.1074	2.7842	0.0162	0.1000	2.7456	0.0159	0.0942	2.7123	0.0157	0.0876
−0.35	2.8624	0.0170	0.0871	2.9141	0.0174	0.0706	2.8711	0.0167	0.0562	2.7434	0.0175	0.0493
−0.25	3.0245	0.0165	0.0704	3.0815	0.0169	0.0612	3.0208	0.0169	0.0445	2.8864	0.0168	0.0427
−0.15	3.2584	0.0172	0.0609	3.3400	0.0174	0.0538	3.2266	0.0172	0.0412	3.0724	0.0168	0.0385
−0.05	3.3886	0.0177	0.0511	3.4356	0.0179	0.0535	3.3195	0.0174	0.0438	3.1397	0.0175	0.0437
0.05	3.3824	0.0172	0.0459	3.4290	0.0177	0.0502	3.3921	0.0180	0.0477	3.1431	0.0178	0.0520
0.15	3.3029	0.0171	0.0416	3.4108	0.0177	0.0475	3.3052	0.0175	0.0450	3.1219	0.0170	0.0494
0.25	3.1907	0.0172	0.0362	3.3346	0.0170	0.0538	3.2464	0.0172	0.0433	3.0030	0.0169	0.0392
0.35	3.0251	0.0163	0.0296	3.0697	0.0170	0.0440	3.0061	0.0171	0.0391	2.7839	0.0163	0.0309
0.45	2.6111	0.0164	0.0356	2.7309	0.0170	0.0276	2.7257	0.0167	0.0370	2.5136	0.0165	0.0283
0.55	2.2156	0.0155	0.0758	2.3107	0.0167	0.0324	2.2676	0.0163	0.0423	2.1295	0.0159	0.0333
0.65	1.7180	0.0157	0.1042	1.8321	0.0156	0.0751	1.8265	0.0164	0.0707	1.6828	0.0151	0.0487
0.75	1.2951	0.0199	0.1191	1.3761	0.0193	0.1221	1.3338	0.0178	0.1233	1.2428	0.0179	0.0805
0.85	0.9852	0.0520	0.2353	0.9759	0.0500	0.2597	1.0349	0.0403	0.2385	0.8915	0.0400	0.2117

$\cos(\theta^*_{\pi^0})$	$W=(1540.0\pm6.0)$ MeV			$W=(1552.0\pm6.0)$ MeV			$W=(1564.0\pm6.0)$ MeV			$W=(1576.0\pm6.0)$ MeV		
	$d\sigma/d\Omega$ [μb/sr]	Δ_{stat} [μb/sr]	Δ_{sys} [μb/sr]	$d\sigma/d\Omega$ [μb/sr]	Δ_{stat} [μb/sr]	Δ_{sys} [μb/sr]	$d\sigma/d\Omega$ [μb/sr]	Δ_{stat} [μb/sr]	Δ_{sys} [μb/sr]	$d\sigma/d\Omega$ [μb/sr]	Δ_{stat} [μb/sr]	Δ_{sys} [μb/sr]
−0.95	1.2260	0.0166	0.8251	1.2773	0.0181	0.8404	1.3909	0.0183	0.8214	1.4411	0.0194	0.6241
−0.85	1.5846	0.0136	0.2845	1.6137	0.0139	0.3033	1.7052	0.0148	0.2897	1.7522	0.0148	0.1845
−0.75	1.8305	0.0152	0.0991	1.8630	0.0154	0.0953	1.8870	0.0165	0.0933	1.9432	0.0168	0.0964
−0.65	2.1499	0.0208	0.1734	2.1274	0.0220	0.1633	2.1309	0.0222	0.1688	2.1015	0.0225	0.1469
−0.55	2.4377	0.0175	0.1681	2.3498	0.0172	0.1480	2.2662	0.0177	0.1580	2.1763	0.0177	0.1288
−0.45	2.5528	0.0156	0.0901	2.3921	0.0165	0.0748	2.2873	0.0156	0.0762	2.1959	0.0160	0.0670
−0.35	2.5756	0.0167	0.0479	2.3872	0.0166	0.0351	2.2380	0.0165	0.0300	2.1024	0.0164	0.0321
−0.25	2.7027	0.0165	0.0353	2.4502	0.0168	0.0257	2.2560	0.0164	0.0250	2.0613	0.0158	0.0265
−0.15	2.8340	0.0167	0.0358	2.5706	0.0164	0.0311	2.3094	0.0158	0.0329	2.0298	0.0148	0.0295
−0.05	2.8350	0.0170	0.0389	2.5482	0.0165	0.0345	2.2849	0.0162	0.0330	2.0409	0.0154	0.0286
0.05	2.8624	0.0171	0.0405	2.5354	0.0165	0.0345	2.2575	0.0162	0.0271	2.0229	0.0150	0.0243
0.15	2.8137	0.0166	0.0405	2.5140	0.0162	0.0339	2.1787	0.0152	0.0245	1.8899	0.0147	0.0234
0.25	2.7002	0.0164	0.0468	2.3611	0.0151	0.0289	2.0064	0.0149	0.0277	1.7571	0.0144	0.0254
0.35	2.4858	0.0163	0.0429	2.1405	0.0154	0.0221	1.8498	0.0150	0.0270	1.5702	0.0142	0.0228
0.45	2.2674	0.0159	0.0282	1.9653	0.0148	0.0165	1.6311	0.0140	0.0190	1.3985	0.0136	0.0158
0.55	1.8768	0.0152	0.0194	1.5819	0.0148	0.0184	1.3922	0.0137	0.0168	1.1726	0.0133	0.0119
0.65	1.4650	0.0140	0.0302	1.2761	0.0137	0.0332	1.1130	0.0134	0.0223	1.0065	0.0131	0.0276
0.75	1.0530	0.0172	0.0698	0.9218	0.0170	0.0484	0.8693	0.0160	0.0450	0.7995	0.0144	0.0588
0.85	0.7195	0.0405	0.1588	0.6664	0.0353	0.1834	0.6228	0.0274	0.1036	0.6200	0.0268	0.1707

$\cos(\theta^*_{\pi^0})$	$W=(1588.0\pm6.0)$ MeV			$W=(1600.0\pm6.0)$ MeV			$W=(1612.0\pm6.0)$ MeV			$W=(1624.0\pm6.0)$ MeV		
	$d\sigma/d\Omega$ [μb/sr]	Δ_{stat} [μb/sr]	Δ_{sys} [μb/sr]	$d\sigma/d\Omega$ [μb/sr]	Δ_{stat} [μb/sr]	Δ_{sys} [μb/sr]	$d\sigma/d\Omega$ [μb/sr]	Δ_{stat} [μb/sr]	Δ_{sys} [μb/sr]	$d\sigma/d\Omega$ [μb/sr]	Δ_{stat} [μb/sr]	Δ_{sys} [μb/sr]
−0.95	1.3976	0.0197	0.3444	1.4148	0.0201	0.5734	1.4165	0.0203	0.9827	1.4313	0.0189	0.6150
−0.85	1.7764	0.0151	0.1771	1.8021	0.0156	0.1721	1.8336	0.0151	0.2391	1.8787	0.0156	0.2057
−0.75	1.9928	0.0162	0.1218	2.0337	0.0170	0.1247	2.0733	0.0168	0.1158	2.0900	0.0168	0.1265
−0.65	2.1013	0.0221	0.1717	2.0931	0.0215	0.1794	2.1550	0.0226	0.1686	2.2871	0.0244	0.1816
−0.55	2.1112	0.0180	0.1363	2.0781	0.0172	0.1386	2.0871	0.0176	0.1301	2.1467	0.0186	0.1269
−0.45	2.1175	0.0157	0.0694	2.0957	0.0154	0.0715	2.0675	0.0153	0.0638	2.0734	0.0156	0.0604
−0.35	1.9777	0.0160	0.0346	1.9031	0.0154	0.0304	1.8589	0.0152	0.0294	1.8635	0.0149	0.0274
−0.25	1.8863	0.0153	0.0274	1.7519	0.0147	0.0232	1.6966	0.0148	0.0184	1.6518	0.0146	0.0187
−0.15	1.8701	0.0146	0.0271	1.7819	0.0139	0.0265	1.6482	0.0135	0.0178	1.5926	0.0135	0.0180
−0.05	1.8468	0.0146	0.0250	1.6726	0.0138	0.0266	1.5577	0.0133	0.0219	1.5036	0.0132	0.0181
0.05	1.7712	0.0147	0.0209	1.5959	0.0141	0.0252	1.4463	0.0137	0.0210	1.4266	0.0129	0.0199
0.15	1.6490	0.0144	0.0130	1.4766	0.0135	0.0207	1.3686	0.0128	0.0214	1.3120	0.0122	0.0239
0.25	1.5225	0.0137	0.0105	1.3659	0.0125	0.0162	1.2430	0.0124	0.0269	1.2089	0.0119	0.0256
0.35	1.3470	0.0136	0.0145	1.2590	0.0124	0.0166	1.1957	0.0123	0.0299	1.1921	0.0123	0.0205
0.45	1.2189	0.0132	0.0138	1.1560	0.0124	0.0163	1.1150	0.0116	0.0209	1.1502	0.0125	0.0111
0.55	1.0919	0.0133	0.0145	1.0600	0.0129	0.0135	1.0864	0.0123	0.0133	1.1933	0.0133	0.0128
0.65	0.9171	0.0135	0.0147	0.9396	0.0126	0.0303	1.0237	0.0137	0.0275	1.1752	0.0137	0.0389
0.75	0.7776	0.0152	0.0426	0.8527	0.0150	0.0709	0.9791	0.0145	0.0826	1.1365	0.0165	0.1063
0.85	0.6445	0.0277	0.2532	0.6980	0.0279	0.1986	0.7681	0.0260	0.2437	0.9216	0.0259	0.2543

$\cos(\theta^*_{\pi^0})$	$W=(1636.0\pm6.0)$ MeV			$W=(1648.0\pm6.0)$ MeV			$W=(1660.0\pm6.0)$ MeV			$W=(1672.0\pm6.0)$ MeV		
	$d\sigma/d\Omega$ [μb/sr]	Δ_{stat} [μb/sr]	Δ_{sys} [μb/sr]	$d\sigma/d\Omega$ [μb/sr]	Δ_{stat} [μb/sr]	Δ_{sys} [μb/sr]	$d\sigma/d\Omega$ [μb/sr]	Δ_{stat} [μb/sr]	Δ_{sys} [μb/sr]	$d\sigma/d\Omega$ [μb/sr]	Δ_{stat} [μb/sr]	Δ_{sys} [μb/sr]
−0.95	1.4702	0.0193	0.3508	1.4271	0.0205	0.1421	1.4322	0.0207	0.3223	1.4717	0.0206	0.3433
−0.85	1.9348	0.0158	0.1560	1.9509	0.0156	0.1344	1.9379	0.0154	0.1438	1.8842	0.0162	0.1587
−0.75	2.1814	0.0163	0.1209	2.2174	0.0174	0.1489	2.1577	0.0175	0.1263	2.1200	0.0167	0.1574
−0.65	2.3661	0.0241	0.1934	2.3696	0.0228	0.1957	2.2870	0.0222	0.1890	2.1619	0.0216	0.1976
−0.55	2.2266	0.0182	0.1570	2.2318	0.0193	0.1536	2.2814	0.0197	0.1608	2.2078	0.0205	0.1656
−0.45	2.0862	0.0155	0.0698	2.1128	0.0158	0.0773	2.0683	0.0165	0.0767	1.9569	0.0159	0.0819
−0.35	1.8090	0.0155	0.0222	1.8115	0.0160	0.0321	1.7433	0.0158	0.0304	1.6331	0.0152	0.0331
−0.25	1.6559	0.0144	0.0168	1.6330	0.0142	0.0220	1.5563	0.0142	0.0174	1.4399	0.0147	0.0181
−0.15	1.5679	0.0132	0.0227	1.5016	0.0132	0.0241	1.4483	0.0131	0.0176	1.3382	0.0127	0.0192
−0.05	1.4660	0.0128	0.0245	1.4054	0.0133	0.0207	1.3613	0.0131	0.0215	1.2966	0.0129	0.0198
0.05	1.3731	0.0127	0.0228	1.3272	0.0129	0.0150	1.2895	0.0127	0.0229	1.2366	0.0128	0.0178
0.15	1.3094	0.0125	0.0245	1.3195	0.0127	0.0201	1.2855	0.0133	0.0230	1.2927	0.0126	0.0207
0.25	1.2819	0.0119	0.0311	1.2942	0.0122	0.0347	1.3447	0.0123	0.0291	1.3655	0.0131	0.0256
0.35	1.2670	0.0123	0.0330	1.3551	0.0128	0.0447	1.4589	0.0127	0.0349	1.5025	0.0136	0.0299
0.45	1.2924	0.0128	0.0230	1.4648	0.0134	0.0402	1.5635	0.0139	0.0286	1.6827	0.0150	0.0330
0.55	1.3578	0.0138	0.0165	1.5498	0.0146	0.0208	1.7340	0.0152	0.0137	1.8215	0.0162	0.0226
0.65	1.4049	0.0151	0.0318	1.6123	0.0161	0.0173	1.7924	0.0165	0.0303	1.9189	0.0180	0.0187
0.75	1.3378	0.0182	0.0890	1.5435	0.0190	0.0899	1.6880	0.0197	0.1310	1.7795	0.0212	0.0955
0.85	1.0489	0.0310	0.3444	1.2340	0.0306	0.3568	1.3175	0.0306	0.3258	1.2864	0.0290	0.3164

$\cos(\theta^*_{\pi^0})$	$W=(1684.0\pm6.0)$ MeV			$W=(1696.0\pm6.0)$ MeV			$W=(1708.0\pm6.0)$ MeV			$W=(1720.0\pm6.0)$ MeV		
	$d\sigma/d\Omega$ [μb/sr]	Δ_{stat} [μb/sr]	Δ_{sys} [μb/sr]	$d\sigma/d\Omega$ [μb/sr]	Δ_{stat} [μb/sr]	Δ_{sys} [μb/sr]	$d\sigma/d\Omega$ [μb/sr]	Δ_{stat} [μb/sr]	Δ_{sys} [μb/sr]	$d\sigma/d\Omega$ [μb/sr]	Δ_{stat} [μb/sr]	Δ_{sys} [μb/sr]
−0.95	1.3703	0.0199	0.2215	1.2871	0.0199	0.1211	1.2297	0.0179	0.1420	1.1192	0.0176	0.1432
−0.85	1.7585	0.0154	0.1093	1.6018	0.0149	0.0851	1.4136	0.0139	0.0813	1.2472	0.0133	0.0723
−0.75	1.9313	0.0162	0.1075	1.6939	0.0158	0.0983	1.4720	0.0147	0.1059	1.2771	0.0141	0.0705
−0.65	2.0306	0.0216	0.1497	1.7966	0.0209	0.1352	1.5715	0.0210	0.1269	1.3327	0.0191	0.0939
−0.55	2.0263	0.0197	0.1374	1.8761	0.0209	0.1201	1.6307	0.0187	0.1131	1.4270	0.0185	0.0893
−0.45	1.8048	0.0157	0.0626	1.6038	0.0150	0.0535	1.3855	0.0144	0.0504	1.1987	0.0133	0.0425
−0.35	1.5048	0.0144	0.0192	1.2935	0.0146	0.0187	1.1398	0.0135	0.0190	0.9707	0.0127	0.0161
−0.25	1.3483	0.0139	0.0135	1.1243	0.0139	0.0106	1.0213	0.0124	0.0123	0.8661	0.0118	0.0094
−0.15	1.2115	0.0132	0.0166	1.0844	0.0120	0.0128	0.9654	0.0118	0.0120	0.8343	0.0110	0.0107
−0.05	1.1509	0.0123	0.0171	1.0552	0.0113	0.0201	0.9270	0.0115	0.0145	0.8336	0.0108	0.0119
0.05	1.1752	0.0129	0.0173	1.0684	0.0123	0.0232	0.9669	0.0123	0.0178	0.8668	0.0121	0.0126
0.15	1.2472	0.0130	0.0206	1.1649	0.0123	0.0247	1.0602	0.0125	0.0176	0.9947	0.0117	0.0160
0.25	1.3455	0.0131	0.0274	1.2728	0.0134	0.0313	1.2094	0.0129	0.0174	1.1139	0.0119	0.0206
0.35	1.4899	0.0138	0.0337	1.4489	0.0137	0.0380	1.3642	0.0135	0.0267	1.2216	0.0128	0.0249
0.45	1.6680	0.0149	0.0307	1.6138	0.0146	0.0340	1.4995	0.0143	0.0380	1.3461	0.0140	0.0280
0.55	1.8429	0.0166	0.0148	1.7729	0.0171	0.0193	1.6533	0.0156	0.0317	1.4758	0.0156	0.0196
0.65	1.8883	0.0176	0.0145	1.8249	0.0175	0.0184	1.6094	0.0177	0.0253	1.4262	0.0160	0.0107
0.75	1.7630	0.0201	0.0825	1.6046	0.0205	0.0875	1.4626	0.0200	0.0914	1.2908	0.0190	0.0554
0.85	1.1913	0.0299	0.3357	1.1277	0.0255	0.2733	0.9320	0.0260	0.2229	0.8744	0.0248	0.2456

$\cos(\theta^*_{\pi^0})$	$W=(1732.0\pm6.0)$ MeV			$W=(1744.0\pm6.0)$ MeV			$W=(1756.0\pm6.0)$ MeV			$W=(1768.0\pm6.0)$ MeV		
	$d\sigma/d\Omega$ [μb/sr]	Δ_{stat} [μb/sr]	Δ_{sys} [μb/sr]	$d\sigma/d\Omega$ [μb/sr]	Δ_{stat} [μb/sr]	Δ_{sys} [μb/sr]	$d\sigma/d\Omega$ [μb/sr]	Δ_{stat} [μb/sr]	Δ_{sys} [μb/sr]	$d\sigma/d\Omega$ [μb/sr]	Δ_{stat} [μb/sr]	Δ_{sys} [μb/sr]
−0.95	1.0303	0.0178	0.1839	0.9976	0.0156	0.2254	0.9332	0.0175	0.2486	0.9306	0.0172	0.2391
−0.85	1.0800	0.0130	0.0707	1.0279	0.0120	0.0751	0.9759	0.0123	0.0672	0.9589	0.0121	0.0732
−0.75	1.1388	0.0137	0.0447	1.0068	0.0134	0.0326	0.9491	0.0127	0.0311	0.9008	0.0123	0.0219
−0.65	1.1692	0.0168	0.0643	1.0118	0.0161	0.0454	0.9391	0.0155	0.0533	0.8456	0.0147	0.0290
−0.55	1.2131	0.0178	0.0675	1.0164	0.0163	0.0502	0.9293	0.0172	0.0503	0.8404	0.0160	0.0291
−0.45	1.0237	0.0133	0.0289	0.9021	0.0117	0.0219	0.7810	0.0110	0.0198	0.6971	0.0113	0.0126
−0.35	0.8535	0.0117	0.0093	0.7069	0.0116	0.0082	0.6459	0.0108	0.0083	0.6058	0.0107	0.0073
−0.25	0.7525	0.0112	0.0084	0.6723	0.0111	0.0115	0.5905	0.0102	0.0072	0.5891	0.0108	0.0081
−0.15	0.7195	0.0107	0.0116	0.6765	0.0105	0.0179	0.6148	0.0106	0.0091	0.5559	0.0101	0.0103
−0.05	0.7220	0.0100	0.0150	0.6852	0.0099	0.0189	0.6432	0.0100	0.0102	0.6137	0.0100	0.0112
0.05	0.8067	0.0112	0.0156	0.7374	0.0115	0.0171	0.6883	0.0113	0.0114	0.6801	0.0112	0.0105
0.15	0.8868	0.0115	0.0148	0.8210	0.0110	0.0196	0.7786	0.0113	0.0121	0.7277	0.0116	0.0094
0.25	1.0118	0.0117	0.0194	0.9207	0.0117	0.0213	0.8363	0.0112	0.0112	0.7738	0.0108	0.0105
0.35	1.0731	0.0131	0.0257	0.9776	0.0124	0.0244	0.8875	0.0116	0.0157	0.8137	0.0120	0.0192
0.45	1.2076	0.0134	0.0307	1.0617	0.0129	0.0277	0.9429	0.0133	0.0224	0.8442	0.0123	0.0308
0.55	1.2986	0.0149	0.0192	1.1147	0.0151	0.0198	0.9958	0.0140	0.0221	0.8757	0.0134	0.0276
0.65	1.2401	0.0162	0.0101	1.1042	0.0156	0.0221	0.9593	0.0158	0.0084	0.9054	0.0145	0.0106
0.75	1.1197	0.0185	0.0532	1.0050	0.0169	0.0753	0.9514	0.0162	0.0294	0.9266	0.0165	0.0284
0.85	0.7858	0.0227	0.1900	0.7333	0.0233	0.1628	0.7192	0.0211	0.2149	0.7490	0.0227	0.2555

$\cos(\theta^*_{\pi^0})$	$W=(1780.0\pm6.0)$ MeV			$W=(1792.0\pm6.0)$ MeV			$W=(1804.0\pm6.0)$ MeV			$W=(1816.0\pm6.0)$ MeV		
	$d\sigma/d\Omega$ [μb/sr]	Δ_{stat} [μb/sr]	Δ_{sys} [μb/sr]	$d\sigma/d\Omega$ [μb/sr]	Δ_{stat} [μb/sr]	Δ_{sys} [μb/sr]	$d\sigma/d\Omega$ [μb/sr]	Δ_{stat} [μb/sr]	Δ_{sys} [μb/sr]	$d\sigma/d\Omega$ [μb/sr]	Δ_{stat} [μb/sr]	Δ_{sys} [μb/sr]
−0.95	0.9912	0.0169	0.2191	1.0187	0.0172	0.2033	1.0406	0.0200	0.1896	1.0686	0.0199	0.1465
−0.85	0.9647	0.0126	0.0857	0.9636	0.0127	0.0613	1.0180	0.0128	0.0562	1.0389	0.0136	0.0673
−0.75	0.8826	0.0122	0.0364	0.8965	0.0129	0.0315	0.9046	0.0126	0.0331	0.9275	0.0135	0.0548
−0.65	0.8598	0.0159	0.0326	0.8386	0.0151	0.0338	0.8572	0.0158	0.0358	0.8547	0.0163	0.0436
−0.55	0.7623	0.0163	0.0277	0.7267	0.0169	0.0244	0.6657	0.0152	0.0305	0.6782	0.0180	0.0239
−0.45	0.6656	0.0120	0.0136	0.6344	0.0108	0.0148	0.6037	0.0117	0.0194	0.5752	0.0116	0.0107
−0.35	0.5800	0.0112	0.0054	0.5421	0.0106	0.0107	0.5670	0.0121	0.0132	0.5655	0.0128	0.0054
−0.25	0.5444	0.0106	0.0083	0.5494	0.0111	0.0134	0.5360	0.0121	0.0118	0.5182	0.0127	0.0065
−0.15	0.5607	0.0101	0.0176	0.5502	0.0104	0.0151	0.5481	0.0115	0.0145	0.5533	0.0105	0.0105
−0.05	0.6048	0.0101	0.0235	0.6202	0.0100	0.0165	0.6209	0.0109	0.0180	0.6319	0.0118	0.0134
0.05	0.6722	0.0110	0.0224	0.6661	0.0113	0.0152	0.6659	0.0126	0.0167	0.6954	0.0134	0.0121
0.15	0.7102	0.0112	0.0182	0.7147	0.0119	0.0117	0.6943	0.0123	0.0139	0.6857	0.0127	0.0105
0.25	0.7422	0.0114	0.0152	0.7084	0.0120	0.0118	0.6683	0.0125	0.0123	0.6760	0.0130	0.0160
0.35	0.7478	0.0119	0.0179	0.7058	0.0115	0.0203	0.6679	0.0119	0.0186	0.6400	0.0118	0.0290
0.45	0.7576	0.0129	0.0270	0.7268	0.0129	0.0259	0.6649	0.0127	0.0309	0.6281	0.0159	0.0356
0.55	0.8089	0.0144	0.0294	0.7446	0.0136	0.0197	0.6928	0.0138	0.0319	0.6375	0.0141	0.0294
0.65	0.8139	0.0144	0.0108	0.7922	0.0145	0.0126	0.7703	0.0157	0.0234	0.7659	0.0152	0.0113
0.75	0.8951	0.0172	0.0189	0.9053	0.0191	0.0501	0.9259	0.0214	0.0532	1.0007	0.0209	0.0387
0.85	0.7812	0.0235	0.2911	0.8372	0.0243	0.2756	0.9016	0.0276	0.3043	0.9683	0.0276	0.3379

$\cos(\theta^*_{\pi^0})$	$W=(1828.0\pm6.0)$ MeV			$W=(1840.0\pm6.0)$ MeV			$W=(1852.0\pm6.0)$ MeV			$W=(1864.0\pm6.0)$ MeV		
	$d\sigma/d\Omega$ [μb/sr]	Δ_{stat} [μb/sr]	Δ_{sys} [μb/sr]	$d\sigma/d\Omega$ [μb/sr]	Δ_{stat} [μb/sr]	Δ_{sys} [μb/sr]	$d\sigma/d\Omega$ [μb/sr]	Δ_{stat} [μb/sr]	Δ_{sys} [μb/sr]	$d\sigma/d\Omega$ [μb/sr]	Δ_{stat} [μb/sr]	Δ_{sys} [μb/sr]
−0.95	1.1146	0.0197	0.1156	1.1503	0.0219	0.0628	1.1563	0.0223	0.0982	1.1448	0.0237	0.3335
−0.85	1.0808	0.0149	0.0545	1.1320	0.0149	0.0567	1.0815	0.0166	0.0513	1.0764	0.0160	0.0771
−0.75	0.9511	0.0139	0.0357	0.9699	0.0159	0.0527	0.9530	0.0159	0.0255	0.8943	0.0160	0.0254
−0.65	0.8500	0.0196	0.0395	0.9056	0.0205	0.0453	0.8461	0.0200	0.0220	0.8490	0.0239	0.0397
−0.55	0.6631	0.0174	0.0387	0.6075	0.0166	0.0235	0.5478	0.0157	0.0152	0.4978	0.0165	0.0231
−0.45	0.5504	0.0123	0.0282	0.5668	0.0125	0.0206	0.5558	0.0134	0.0114	0.5246	0.0152	0.0146
−0.35	0.5550	0.0136	0.0203	0.5461	0.0145	0.0178	0.5237	0.0148	0.0083	0.5204	0.0167	0.0130
−0.25	0.5121	0.0133	0.0123	0.5420	0.0149	0.0139	0.5521	0.0156	0.0101	0.5352	0.0173	0.0141
−0.15	0.5981	0.0111	0.0111	0.6049	0.0133	0.0171	0.6279	0.0142	0.0153	0.6023	0.0162	0.0135
−0.05	0.6731	0.0131	0.0121	0.6857	0.0132	0.0206	0.7172	0.0170	0.0167	0.7599	0.0171	0.0134
0.05	0.7189	0.0152	0.0189	0.7139	0.0168	0.0165	0.6917	0.0194	0.0136	0.7246	0.0200	0.0101
0.15	0.7089	0.0145	0.0237	0.7084	0.0160	0.0112	0.7150	0.0165	0.0145	0.6998	0.0187	0.0083
0.25	0.6603	0.0135	0.0215	0.6439	0.0152	0.0153	0.6565	0.0157	0.0218	0.6710	0.0209	0.0214
0.35	0.6120	0.0139	0.0248	0.5593	0.0148	0.0296	0.5837	0.0163	0.0369	0.5871	0.0209	0.0564
0.45	0.5887	0.0147	0.0333	0.5488	0.0178	0.0403	0.4889	0.0191	0.0475	0.4801	0.0199	0.0815
0.55	0.6157	0.0147	0.0381	0.5495	0.0184	0.0377	0.5638	0.0189	0.0502	0.5349	0.0199	0.0764
0.65	0.7975	0.0184	0.0354	0.7752	0.0224	0.0308	0.7999	0.0213	0.0296	0.7635	0.0258	0.0433
0.75	1.0549	0.0241	0.0552	1.1126	0.0242	0.0507	1.1700	0.0306	0.0519	1.2526	0.0310	0.0730
0.85	1.1056	0.0277	0.3790	1.0809	0.0338	0.3180	1.1192	0.0409	0.3801	1.1754	0.0468	0.3308

$\cos(\theta^*_{\pi^0})$	$W=(1876.0\pm6.0)$ MeV		
	$d\sigma/d\Omega$ [μb/sr]	Δ_{stat} [μb/sr]	Δ_{sys} [μb/sr]
−0.95	1.0626	0.0241	0.5874
−0.85	1.0403	0.0188	0.1342
−0.75	0.8699	0.0187	0.0290
−0.65	0.8242	0.0238	0.0461
−0.55	0.4383	0.0151	0.0234
−0.45	0.4682	0.0146	0.0169
−0.35	0.4882	0.0169	0.0171
−0.25	0.5374	0.0192	0.0196
−0.15	0.6204	0.0174	0.0204
−0.05	0.6946	0.0249	0.0215
0.05	0.6896	0.0223	0.0243
0.15	0.6490	0.0230	0.0291
0.25	0.6062	0.0238	0.0371
0.35	0.5755	0.0231	0.0568
0.45	0.4039	0.0218	0.0501
0.55	0.5309	0.0244	0.0426
0.65	0.6988	0.0249	0.0172
0.75	1.1899	0.0439	0.0323
0.85	1.1621	0.0488	0.3070

E.1.4 Angular Distributions $\gamma d \to \pi^0 n(p)$ as a Function of W

$\cos(\theta^*_{\pi^0})$	W=(1300.0±6.0) MeV			W=(1312.0±6.0) MeV			W=(1324.0±6.0) MeV			W=(1336.0±6.0) MeV		
	$d\sigma/d\Omega$ [μb/sr]	Δ_{stat} [μb/sr]	Δ_{sys} [μb/sr]	$d\sigma/d\Omega$ [μb/sr]	Δ_{stat} [μb/sr]	Δ_{sys} [μb/sr]	$d\sigma/d\Omega$ [μb/sr]	Δ_{stat} [μb/sr]	Δ_{sys} [μb/sr]	$d\sigma/d\Omega$ [μb/sr]	Δ_{stat} [μb/sr]	Δ_{sys} [μb/sr]
−0.95	0.0178	0.0028	0.0274	0.0190	0.0034	0.0327	0.0354	0.0043	0.0418	0.0557	0.0049	0.0602
−0.85	0.1768	0.0104	0.2139	0.2250	0.0103	0.2749	0.2865	0.0096	0.3112	0.3120	0.0093	0.3686
−0.75	1.5756	0.0282	1.7443	1.7064	0.0253	2.0109	1.4413	0.0225	1.3474	1.3724	0.0202	1.5624
−0.65	4.3294	0.0324	3.2575	3.8384	0.0285	3.6818	3.2261	0.0242	2.6114	2.7720	0.0212	2.5004
−0.55	5.5281	0.0293	2.1123	4.7986	0.0257	2.2390	4.0616	0.0231	1.7085	3.5902	0.0204	1.4797
−0.45	6.0790	0.0306	1.0549	5.5151	0.0274	0.9125	4.7855	0.0251	0.6930	4.1308	0.0229	0.4054
−0.35	6.7904	0.0337	0.7319	6.2834	0.0315	0.7389	5.4664	0.0287	0.3636	4.7197	0.0262	0.2723
−0.25	7.4356	0.0365	0.7549	6.8268	0.0339	0.6206	6.0583	0.0314	0.3549	5.2081	0.0279	0.4269
−0.15	8.0064	0.0393	0.7717	7.2657	0.0361	0.7769	6.5195	0.0334	0.5239	5.5833	0.0296	0.4344
−0.05	8.1965	0.0417	0.9135	7.6344	0.0393	0.8960	6.8570	0.0364	0.5345	5.9161	0.0322	0.3610
0.05	8.3856	0.0461	1.0784	7.8270	0.0415	0.8220	6.9004	0.0380	0.4379	5.9680	0.0339	0.3005
0.15	8.6032	0.0492	1.0829	7.8156	0.0440	0.6878	6.9385	0.0413	0.3886	5.9470	0.0357	0.2847
0.25	8.2583	0.0517	0.8624	7.6691	0.0479	0.4951	6.7624	0.0430	0.4056	5.7047	0.0380	0.3274
0.35	7.6934	0.0556	0.6385	7.0339	0.0491	0.4944	6.4337	0.0442	0.5058	5.4898	0.0401	0.3875
0.45	6.9674	0.0580	0.6899	6.3334	0.0536	0.6360	5.6548	0.0479	0.5934	4.7993	0.0428	0.4466
0.55	5.4598	0.0586	0.8295	4.9326	0.0529	0.7320	4.6570	0.0498	0.6342	4.0358	0.0411	0.5151
0.65	4.0058	0.0628	0.7654	3.6975	0.0525	0.5711	3.4249	0.0520	0.5019	2.9577	0.0467	0.4126
0.75	2.8354	0.0873	0.7617	2.6371	0.0809	0.2730	2.5764	0.0688	0.2862	2.0162	0.0670	0.1704
0.85	2.1878	0.2815	1.0000	1.8112	0.2609	0.6500	2.4892	0.1767	0.9246	1.6830	0.1706	0.5065

$\cos(\theta^*_{\pi^0})$	W=(1348.0±6.0) MeV			W=(1360.0±6.0) MeV			W=(1372.0±6.0) MeV			W=(1384.0±6.0) MeV		
	$d\sigma/d\Omega$ [μb/sr]	Δ_{stat} [μb/sr]	Δ_{sys} [μb/sr]	$d\sigma/d\Omega$ [μb/sr]	Δ_{stat} [μb/sr]	Δ_{sys} [μb/sr]	$d\sigma/d\Omega$ [μb/sr]	Δ_{stat} [μb/sr]	Δ_{sys} [μb/sr]	$d\sigma/d\Omega$ [μb/sr]	Δ_{stat} [μb/sr]	Δ_{sys} [μb/sr]
−0.95	0.0766	0.0052	0.0918	0.0928	0.0060	0.1056	0.1126	0.0081	0.1309	0.1702	0.0086	0.1788
−0.85	0.3728	0.0097	0.4049	0.4124	0.0106	0.4672	0.4773	0.0108	0.4826	0.5200	0.0114	0.5624
−0.75	1.3433	0.0176	1.3778	1.3321	0.0173	1.4404	1.2282	0.0174	0.9049	1.2567	0.0161	1.1920
−0.65	2.5662	0.0202	1.7939	2.3759	0.0196	1.8122	2.1565	0.0191	0.8973	2.0270	0.0182	0.9851
−0.55	3.1958	0.0190	0.8349	2.9222	0.0180	0.7126	2.5648	0.0172	0.3430	2.3435	0.0170	0.2016
−0.45	3.6656	0.0212	0.2391	3.3069	0.0198	0.1096	3.0461	0.0195	0.1605	2.7561	0.0184	0.0993
−0.35	4.2108	0.0248	0.3195	3.7715	0.0227	0.2680	3.3875	0.0219	0.1781	3.0809	0.0208	0.1570
−0.25	4.6122	0.0257	0.4265	4.1445	0.0246	0.3240	3.7352	0.0234	0.1975	3.3697	0.0226	0.1621
−0.15	4.9374	0.0275	0.3822	4.3269	0.0262	0.2618	3.9553	0.0239	0.1622	3.5114	0.0226	0.1441
−0.05	5.0600	0.0288	0.2303	4.5072	0.0275	0.1856	3.9843	0.0265	0.1207	3.5946	0.0248	0.1170
0.05	5.2017	0.0312	0.1755	4.6553	0.0289	0.1491	4.0700	0.0276	0.1175	3.6763	0.0260	0.0955
0.15	5.0923	0.0332	0.1872	4.6019	0.0302	0.1708	4.0949	0.0284	0.1292	3.6381	0.0277	0.0908
0.25	4.9818	0.0347	0.2384	4.4263	0.0314	0.2111	3.9053	0.0290	0.1559	3.4268	0.0274	0.1204
0.35	4.7390	0.0351	0.3070	4.2202	0.0340	0.2572	3.7255	0.0300	0.2048	3.2069	0.0285	0.1685
0.45	4.2530	0.0360	0.3726	3.7182	0.0336	0.3027	3.2549	0.0312	0.2575	2.8801	0.0283	0.2188
0.55	3.5216	0.0377	0.4218	3.0685	0.0333	0.3491	2.6200	0.0316	0.2906	2.2752	0.0284	0.2472
0.65	2.5421	0.0397	0.3510	2.2514	0.0356	0.2993	1.9975	0.0349	0.2451	1.7279	0.0313	0.2148
0.75	1.8891	0.0568	0.1936	1.4967	0.0507	0.1454	1.3936	0.0446	0.1349	1.2255	0.0414	0.1154
0.85	1.3104	0.1393	0.3450	1.1298	0.1343	0.2778	1.0050	0.1031	0.2396	0.8859	0.0907	0.1847

$\cos(\theta^*_{\pi^0})$	W=(1396.0±6.0) MeV			W=(1408.0±6.0) MeV			W=(1420.0±6.0) MeV			W=(1432.0±6.0) MeV		
	$d\sigma/d\Omega$ [μb/sr]	Δ_{stat} [μb/sr]	Δ_{sys} [μb/sr]	$d\sigma/d\Omega$ [μb/sr]	Δ_{stat} [μb/sr]	Δ_{sys} [μb/sr]	$d\sigma/d\Omega$ [μb/sr]	Δ_{stat} [μb/sr]	Δ_{sys} [μb/sr]	$d\sigma/d\Omega$ [μb/sr]	Δ_{stat} [μb/sr]	Δ_{sys} [μb/sr]
−0.95	0.1992	0.0099	0.2114	0.2050	0.0109	0.2300	0.2305	0.0128	0.2447	0.3218	0.0131	0.3345
−0.85	0.5552	0.0120	0.6071	0.6003	0.0116	0.6019	0.6206	0.0131	0.5903	0.6936	0.0132	0.7030
−0.75	1.2020	0.0165	1.1136	1.2088	0.0165	0.9635	1.1749	0.0165	0.6646	1.2196	0.0162	0.8309
−0.65	1.8169	0.0177	0.7651	1.7476	0.0181	0.6356	1.6164	0.0175	0.3587	1.5378	0.0180	0.3116
−0.55	2.1860	0.0161	0.1654	2.0175	0.0163	0.1841	1.9001	0.0161	0.1137	1.7675	0.0157	0.0688
−0.45	2.5417	0.0179	0.1161	2.2948	0.0177	0.1231	2.1650	0.0171	0.0640	2.0428	0.0170	0.0762
−0.35	2.8083	0.0199	0.1497	2.6028	0.0200	0.1401	2.4337	0.0195	0.0713	2.2764	0.0189	0.0619
−0.25	3.0352	0.0218	0.1402	2.7945	0.0209	0.1203	2.5608	0.0205	0.0699	2.3818	0.0199	0.0628
−0.15	3.1653	0.0230	0.1086	2.9441	0.0222	0.0852	2.6782	0.0207	0.0644	2.4841	0.0207	0.0552
−0.05	3.2920	0.0240	0.0915	2.9495	0.0230	0.0668	2.6848	0.0219	0.0525	2.5259	0.0221	0.0435
0.05	3.2942	0.0251	0.0754	2.9966	0.0238	0.0573	2.6646	0.0226	0.0385	2.5429	0.0236	0.0346
0.15	3.1967	0.0258	0.0637	2.9086	0.0245	0.0558	2.6317	0.0239	0.0353	2.4401	0.0235	0.0298
0.25	3.0444	0.0263	0.0865	2.7416	0.0254	0.0656	2.4802	0.0244	0.0489	2.3031	0.0227	0.0403
0.35	2.8383	0.0267	0.1349	2.5193	0.0251	0.0978	2.2326	0.0243	0.0750	2.0620	0.0230	0.0684
0.45	2.4918	0.0263	0.1792	2.2174	0.0250	0.1406	1.9432	0.0241	0.1114	1.7684	0.0237	0.1010
0.55	2.0259	0.0258	0.2106	1.8006	0.0249	0.1779	1.6009	0.0241	0.1509	1.3844	0.0231	0.1239
0.65	1.5475	0.0285	0.1949	1.3731	0.0265	0.1554	1.1904	0.0238	0.1251	1.1105	0.0218	0.1193
0.75	1.0962	0.0341	0.1118	0.8790	0.0356	0.0650	0.8280	0.0314	0.0628	0.7713	0.0271	0.0685
0.85	0.6166	0.0820	0.2012	0.8106	0.0545	0.2305	0.6259	0.0704	0.2026	0.5684	0.0450	0.1365

$\cos(\theta^*_{\pi^0})$	W=(1444.0±6.0) MeV			W=(1456.0±6.0) MeV			W=(1468.0±6.0) MeV			W=(1480.0±6.0) MeV		
	$d\sigma/d\Omega$ [μb/sr]	Δ_{stat} [μb/sr]	Δ_{sys} [μb/sr]	$d\sigma/d\Omega$ [μb/sr]	Δ_{stat} [μb/sr]	Δ_{sys} [μb/sr]	$d\sigma/d\Omega$ [μb/sr]	Δ_{stat} [μb/sr]	Δ_{sys} [μb/sr]	$d\sigma/d\Omega$ [μb/sr]	Δ_{stat} [μb/sr]	Δ_{sys} [μb/sr]
−0.95	0.3961	0.0152	0.2040	0.4814	0.0154	0.3647	0.5987	0.0184	0.6117	0.7071	0.0200	0.7148
−0.85	0.7670	0.0137	0.6430	0.8344	0.0143	0.6164	0.9213	0.0146	0.6625	1.0210	0.0177	0.5470
−0.75	1.2446	0.0171	0.5976	1.2470	0.0181	0.5363	1.3071	0.0183	0.4317	1.4137	0.0193	0.3026
−0.65	1.5297	0.0185	0.2113	1.4834	0.0185	0.2248	1.5067	0.0191	0.1563	1.5775	0.0194	0.1357
−0.55	1.7119	0.0156	0.1053	1.6803	0.0157	0.0840	1.6906	0.0161	0.0961	1.7257	0.0167	0.0953
−0.45	1.9777	0.0165	0.0619	1.9633	0.0163	0.0576	1.8915	0.0178	0.0618	1.9168	0.0175	0.0661
−0.35	2.1418	0.0188	0.0518	2.0859	0.0193	0.0576	2.0789	0.0195	0.0443	2.0631	0.0195	0.0507
−0.25	2.2934	0.0208	0.0544	2.2367	0.0207	0.0493	2.2090	0.0207	0.0304	2.1736	0.0209	0.0327
−0.15	2.3846	0.0206	0.0521	2.3649	0.0202	0.0436	2.3193	0.0208	0.0274	2.3017	0.0211	0.0218
−0.05	2.3849	0.0219	0.0410	2.3438	0.0221	0.0339	2.3230	0.0222	0.0230	2.3121	0.0227	0.0162
0.05	2.3511	0.0230	0.0312	2.2948	0.0221	0.0206	2.2440	0.0227	0.0160	2.3350	0.0231	0.0121
0.15	2.2910	0.0229	0.0243	2.2443	0.0229	0.0116	2.2900	0.0226	0.0085	2.3325	0.0235	0.0074
0.25	2.1440	0.0233	0.0243	2.1307	0.0232	0.0157	2.1393	0.0234	0.0048	2.1831	0.0228	0.0057
0.35	1.9795	0.0224	0.0407	1.9467	0.0225	0.0321	1.9416	0.0221	0.0085	2.0147	0.0240	0.0094
0.45	1.6783	0.0228	0.0728	1.6755	0.0233	0.0565	1.7017	0.0231	0.0321	1.8164	0.0230	0.0287
0.55	1.3703	0.0230	0.1097	1.3919	0.0230	0.0955	1.4228	0.0226	0.0760	1.5543	0.0235	0.0651
0.65	1.0586	0.0215	0.1116	1.0283	0.0224	0.0941	1.1026	0.0234	0.0886	1.2763	0.0212	0.0883
0.75	0.7455	0.0231	0.0678	0.7815	0.0287	0.0653	0.8469	0.0258	0.0690	0.9933	0.0328	0.0875
0.85	0.5283	0.0433	0.1310	0.5935	0.0468	0.1426	0.6464	0.0476	0.1799	0.7530	0.0472	0.1669

$\cos(\theta^*_{\pi^0})$	W=(1492.0±6.0) MeV			W=(1504.0±6.0) MeV			W=(1516.0±6.0) MeV			W=(1528.0±6.0) MeV		
	$d\sigma/d\Omega$ [μb/sr]	Δ_{stat} [μb/sr]	Δ_{sys} [μb/sr]	$d\sigma/d\Omega$ [μb/sr]	Δ_{stat} [μb/sr]	Δ_{sys} [μb/sr]	$d\sigma/d\Omega$ [μb/sr]	Δ_{stat} [μb/sr]	Δ_{sys} [μb/sr]	$d\sigma/d\Omega$ [μb/sr]	Δ_{stat} [μb/sr]	Δ_{sys} [μb/sr]
−0.95	0.8430	0.0226	0.8603	0.9704	0.0263	0.9756	1.0083	0.0271	0.2527	0.9965	0.0268	0.2242
−0.85	1.1985	0.0189	0.5902	1.2577	0.0191	0.4481	1.2301	0.0212	0.1205	1.1563	0.0195	0.0930
−0.75	1.5291	0.0209	0.2466	1.5772	0.0211	0.1867	1.5401	0.0191	0.1015	1.4521	0.0203	0.0870
−0.65	1.6506	0.0204	0.1247	1.6935	0.0214	0.1199	1.5848	0.0208	0.0977	1.5395	0.0216	0.1024
−0.55	1.8071	0.0178	0.0932	1.7655	0.0182	0.0971	1.6715	0.0167	0.0815	1.5871	0.0162	0.0831
−0.45	1.9602	0.0182	0.0457	1.9058	0.0183	0.0641	1.7865	0.0171	0.0536	1.6572	0.0171	0.0526
−0.35	2.1174	0.0198	0.0307	2.0362	0.0205	0.0325	1.9120	0.0200	0.0279	1.8012	0.0199	0.0241
−0.25	2.2107	0.0210	0.0215	2.1806	0.0212	0.0208	2.0883	0.0204	0.0115	1.9372	0.0207	0.0139
−0.15	2.3208	0.0216	0.0181	2.3099	0.0219	0.0203	2.1901	0.0214	0.0104	2.0265	0.0205	0.0147
−0.05	2.4016	0.0235	0.0189	2.3505	0.0229	0.0207	2.2276	0.0230	0.0128	2.1191	0.0217	0.0174
0.05	2.3846	0.0236	0.0168	2.3739	0.0236	0.0163	2.3361	0.0231	0.0159	2.1604	0.0223	0.0240
0.15	2.3546	0.0226	0.0135	2.4297	0.0229	0.0119	2.2843	0.0230	0.0190	2.1567	0.0231	0.0259
0.25	2.2745	0.0232	0.0122	2.3814	0.0229	0.0127	2.2118	0.0235	0.0224	2.0657	0.0227	0.0240
0.35	2.1303	0.0244	0.0117	2.2047	0.0248	0.0139	2.1262	0.0232	0.0227	2.0111	0.0231	0.0197
0.45	1.9532	0.0239	0.0221	1.9572	0.0242	0.0224	1.9871	0.0233	0.0209	1.8057	0.0230	0.0173
0.55	1.7248	0.0230	0.0583	1.7831	0.0246	0.0465	1.7162	0.0255	0.0300	1.6951	0.0235	0.0256
0.65	1.4206	0.0243	0.0889	1.5257	0.0264	0.0828	1.4916	0.0277	0.0587	1.4668	0.0248	0.0471
0.75	1.2174	0.0281	0.1085	1.3120	0.0305	0.1494	1.2196	0.0337	0.1098	1.2445	0.0308	0.0829
0.85	0.8364	0.0789	0.2556	0.9267	0.0664	0.2399	1.0404	0.0555	0.2310	1.0359	0.0517	0.2145

$\cos(\theta^*_{\pi^0})$	W=(1540.0±6.0) MeV			W=(1552.0±6.0) MeV			W=(1564.0±6.0) MeV			W=(1576.0±6.0) MeV		
	$d\sigma/d\Omega$ [μb/sr]	Δ_{stat} [μb/sr]	Δ_{sys} [μb/sr]	$d\sigma/d\Omega$ [μb/sr]	Δ_{stat} [μb/sr]	Δ_{sys} [μb/sr]	$d\sigma/d\Omega$ [μb/sr]	Δ_{stat} [μb/sr]	Δ_{sys} [μb/sr]	$d\sigma/d\Omega$ [μb/sr]	Δ_{stat} [μb/sr]	Δ_{sys} [μb/sr]
−0.95	0.9830	0.0275	0.8010	0.9278	0.0285	0.6113	0.9221	0.0287	0.8583	0.8520	0.0293	0.4599
−0.85	1.0832	0.0195	0.1682	1.0176	0.0187	0.1708	0.8821	0.0192	0.1441	0.7935	0.0166	0.1054
−0.75	1.3659	0.0210	0.0828	1.2263	0.0193	0.0539	1.0502	0.0187	0.0536	0.9460	0.0179	0.0514
−0.65	1.4316	0.0213	0.0969	1.3178	0.0212	0.0819	1.2301	0.0188	0.0811	1.1058	0.0180	0.0762
−0.55	1.5128	0.0171	0.0766	1.3806	0.0163	0.0741	1.2479	0.0155	0.0704	1.1374	0.0153	0.0572
−0.45	1.5677	0.0163	0.0408	1.4354	0.0165	0.0377	1.3264	0.0156	0.0390	1.1916	0.0153	0.0291
−0.35	1.6777	0.0185	0.0140	1.5641	0.0187	0.0149	1.4050	0.0179	0.0141	1.2963	0.0180	0.0111
−0.25	1.8261	0.0199	0.0095	1.6515	0.0198	0.0116	1.5148	0.0197	0.0092	1.4057	0.0188	0.0103
−0.15	1.8547	0.0208	0.0116	1.7251	0.0201	0.0157	1.5855	0.0199	0.0148	1.4748	0.0191	0.0148
−0.05	1.9770	0.0207	0.0149	1.7965	0.0209	0.0160	1.6389	0.0205	0.0176	1.4920	0.0197	0.0151
0.05	1.9461	0.0211	0.0164	1.8021	0.0212	0.0174	1.6193	0.0202	0.0146	1.4513	0.0200	0.0131
0.15	1.9432	0.0226	0.0211	1.7864	0.0207	0.0195	1.6080	0.0197	0.0147	1.3992	0.0196	0.0144
0.25	1.8862	0.0219	0.0304	1.6719	0.0207	0.0174	1.4943	0.0214	0.0197	1.2878	0.0193	0.0173
0.35	1.7943	0.0226	0.0290	1.5564	0.0214	0.0136	1.3976	0.0202	0.0199	1.2216	0.0197	0.0177
0.45	1.6826	0.0222	0.0169	1.5255	0.0204	0.0096	1.3120	0.0192	0.0136	1.1308	0.0187	0.0141
0.55	1.5370	0.0218	0.0139	1.4279	0.0209	0.0151	1.2300	0.0222	0.0147	1.1059	0.0191	0.0114
0.65	1.3475	0.0253	0.0280	1.2273	0.0223	0.0296	1.1362	0.0208	0.0234	1.1240	0.0215	0.0302
0.75	1.2330	0.0286	0.0718	1.0887	0.0305	0.0812	1.0706	0.0284	0.0494	1.0681	0.0255	0.0790
0.85	0.9880	0.0561	0.2197	0.8995	0.0646	0.2460	0.9847	0.0562	0.2622	0.8922	0.0475	0.2377

$\cos(\theta^*_{\pi^0})$	W=(1588.0±6.0) MeV			W=(1600.0±6.0) MeV			W=(1612.0±6.0) MeV			W=(1624.0±6.0) MeV		
	$d\sigma/d\Omega$ [μb/sr]	Δ_{stat} [μb/sr]	Δ_{sys} [μb/sr]	$d\sigma/d\Omega$ [μb/sr]	Δ_{stat} [μb/sr]	Δ_{sys} [μb/sr]	$d\sigma/d\Omega$ [μb/sr]	Δ_{stat} [μb/sr]	Δ_{sys} [μb/sr]	$d\sigma/d\Omega$ [μb/sr]	Δ_{stat} [μb/sr]	Δ_{sys} [μb/sr]
−0.95	0.7473	0.0247	0.1849	0.6326	0.0287	0.1859	0.6276	0.0241	0.3817	0.5911	0.0238	0.4034
−0.85	0.6885	0.0172	0.0555	0.6099	0.0175	0.1037	0.5655	0.0170	0.0628	0.5366	0.0163	0.0799
−0.75	0.8464	0.0177	0.0476	0.7841	0.0170	0.0613	0.7085	0.0166	0.0443	0.6566	0.0171	0.0388
−0.65	0.9676	0.0181	0.0684	0.9324	0.0180	0.0690	0.8788	0.0182	0.0553	0.8981	0.0178	0.0627
−0.55	1.0414	0.0144	0.0602	0.9883	0.0144	0.0592	0.9456	0.0145	0.0469	0.9042	0.0141	0.0449
−0.45	1.1123	0.0156	0.0353	1.0673	0.0148	0.0334	0.9988	0.0136	0.0225	0.9874	0.0136	0.0259
−0.35	1.2331	0.0171	0.0177	1.2043	0.0166	0.0159	1.0856	0.0159	0.0081	1.0546	0.0149	0.0113
−0.25	1.2775	0.0187	0.0140	1.2369	0.0174	0.0117	1.1111	0.0162	0.0079	1.0596	0.0162	0.0065
−0.15	1.3515	0.0187	0.0157	1.2719	0.0177	0.0154	1.1486	0.0174	0.0137	1.0856	0.0159	0.0079
−0.05	1.3827	0.0181	0.0135	1.2232	0.0174	0.0170	1.1351	0.0160	0.0164	0.9910	0.0164	0.0094
0.05	1.3220	0.0183	0.0102	1.1785	0.0174	0.0175	0.9979	0.0183	0.0142	0.8947	0.0176	0.0112
0.15	1.1614	0.0192	0.0075	1.0617	0.0174	0.0153	0.9213	0.0164	0.0110	0.8009	0.0157	0.0146
0.25	1.1528	0.0176	0.0071	0.9764	0.0171	0.0118	0.8785	0.0149	0.0109	0.7431	0.0138	0.0162
0.35	1.0630	0.0180	0.0105	0.9236	0.0164	0.0123	0.8163	0.0162	0.0118	0.7329	0.0149	0.0134
0.45	1.0273	0.0182	0.0113	0.9124	0.0177	0.0128	0.8732	0.0163	0.0113	0.8033	0.0163	0.0078
0.55	1.0503	0.0180	0.0148	0.9813	0.0179	0.0125	0.9374	0.0185	0.0134	0.9601	0.0161	0.0102
0.65	1.0655	0.0222	0.0191	1.0626	0.0206	0.0329	1.0447	0.0211	0.0411	1.1142	0.0222	0.0369
0.75	1.0377	0.0257	0.0533	1.0453	0.0271	0.0970	1.0859	0.0259	0.1106	1.2011	0.0269	0.1117
0.85	0.9513	0.0446	0.3680	0.9279	0.0462	0.2053	0.9729	0.0449	0.2595	1.0534	0.0466	0.2911

$\cos(\theta^*_{\pi^0})$	W=(1636.0±6.0) MeV			W=(1648.0±6.0) MeV			W=(1660.0±6.0) MeV			W=(1672.0±6.0) MeV		
	$d\sigma/d\Omega$ [μb/sr]	Δ_{stat} [μb/sr]	Δ_{sys} [μb/sr]	$d\sigma/d\Omega$ [μb/sr]	Δ_{stat} [μb/sr]	Δ_{sys} [μb/sr]	$d\sigma/d\Omega$ [μb/sr]	Δ_{stat} [μb/sr]	Δ_{sys} [μb/sr]	$d\sigma/d\Omega$ [μb/sr]	Δ_{stat} [μb/sr]	Δ_{sys} [μb/sr]
−0.95	0.6075	0.0237	0.4145	0.6002	0.0236	0.3204	0.6664	0.0303	0.2699	0.6871	0.0270	0.1861
−0.85	0.5326	0.0162	0.0700	0.5014	0.0176	0.0645	0.5217	0.0178	0.0610	0.5382	0.0187	0.0532
−0.75	0.6288	0.0173	0.0426	0.6548	0.0151	0.0387	0.6849	0.0180	0.0416	0.7271	0.0188	0.0531
−0.65	0.8510	0.0191	0.0606	0.8213	0.0178	0.0598	0.8488	0.0191	0.0603	0.8376	0.0203	0.0681
−0.55	0.9164	0.0133	0.0517	0.8983	0.0132	0.0521	0.8746	0.0141	0.0492	0.8056	0.0137	0.0516
−0.45	0.9482	0.0138	0.0250	0.9144	0.0130	0.0251	0.9011	0.0129	0.0285	0.8288	0.0132	0.0268
−0.35	0.9862	0.0163	0.0093	0.9479	0.0153	0.0119	0.9010	0.0145	0.0144	0.8560	0.0139	0.0138
−0.25	1.0244	0.0161	0.0056	0.9472	0.0164	0.0094	0.8816	0.0154	0.0080	0.8035	0.0158	0.0098
−0.15	0.9969	0.0161	0.0100	0.8919	0.0154	0.0113	0.7993	0.0150	0.0074	0.7786	0.0139	0.0092
−0.05	0.9287	0.0148	0.0135	0.8397	0.0146	0.0103	0.7516	0.0148	0.0110	0.6740	0.0138	0.0093
0.05	0.8210	0.0146	0.0134	0.7498	0.0137	0.0078	0.6471	0.0147	0.0111	0.5709	0.0139	0.0085
0.15	0.7209	0.0138	0.0141	0.6484	0.0141	0.0104	0.5869	0.0133	0.0106	0.4934	0.0135	0.0096
0.25	0.6741	0.0142	0.0165	0.5786	0.0140	0.0163	0.5612	0.0135	0.0125	0.5305	0.0122	0.0141
0.35	0.6717	0.0148	0.0184	0.6766	0.0141	0.0230	0.6810	0.0122	0.0172	0.6408	0.0133	0.0180
0.45	0.8296	0.0150	0.0149	0.8400	0.0161	0.0228	0.8621	0.0158	0.0165	0.8747	0.0154	0.0164
0.55	1.0003	0.0185	0.0118	1.0605	0.0172	0.0147	1.0992	0.0203	0.0093	1.1019	0.0200	0.0087
0.65	1.2038	0.0218	0.0257	1.3153	0.0224	0.0145	1.3591	0.0227	0.0233	1.3537	0.0231	0.0151
0.75	1.2773	0.0282	0.0848	1.3483	0.0318	0.0857	1.5089	0.0312	0.1204	1.4894	0.0318	0.0978
0.85	1.1001	0.0446	0.3794	1.1354	0.0468	0.2744	1.3121	0.0482	0.3338	1.3188	0.0588	0.2929

$\cos(\theta^*_{\pi^0})$	$W=(1684.0\pm6.0)$ MeV			$W=(1696.0\pm6.0)$ MeV			$W=(1708.0\pm6.0)$ MeV			$W=(1720.0\pm6.0)$ MeV		
	$d\sigma/d\Omega$ [μb/sr]	Δ_{stat} [μb/sr]	Δ_{sys} [μb/sr]	$d\sigma/d\Omega$ [μb/sr]	Δ_{stat} [μb/sr]	Δ_{sys} [μb/sr]	$d\sigma/d\Omega$ [μb/sr]	Δ_{stat} [μb/sr]	Δ_{sys} [μb/sr]	$d\sigma/d\Omega$ [μb/sr]	Δ_{stat} [μb/sr]	Δ_{sys} [μb/sr]
−0.95	0.7728	0.0321	0.1749	0.8113	0.0324	0.0784	0.8823	0.0330	0.1236	0.8953	0.0308	0.2170
−0.85	0.5793	0.0166	0.0574	0.6628	0.0193	0.0448	0.6606	0.0195	0.0520	0.7032	0.0204	0.0628
−0.75	0.6855	0.0166	0.0392	0.6933	0.0181	0.0436	0.7050	0.0200	0.0511	0.7390	0.0203	0.0390
−0.65	0.7999	0.0188	0.0510	0.7484	0.0196	0.0493	0.7811	0.0174	0.0579	0.7380	0.0196	0.0478
−0.55	0.7938	0.0143	0.0432	0.7440	0.0141	0.0402	0.6713	0.0146	0.0379	0.6525	0.0144	0.0349
−0.45	0.7780	0.0133	0.0226	0.6916	0.0127	0.0196	0.6403	0.0128	0.0196	0.5734	0.0114	0.0175
−0.35	0.7493	0.0133	0.0087	0.6744	0.0144	0.0070	0.6106	0.0124	0.0083	0.5130	0.0119	0.0073
−0.25	0.7070	0.0148	0.0075	0.6503	0.0132	0.0034	0.5278	0.0142	0.0051	0.4634	0.0132	0.0040
−0.15	0.6627	0.0140	0.0091	0.5934	0.0131	0.0066	0.5199	0.0129	0.0063	0.4650	0.0121	0.0057
−0.05	0.5635	0.0133	0.0088	0.4997	0.0126	0.0104	0.4447	0.0120	0.0076	0.4020	0.0117	0.0065
0.05	0.4852	0.0125	0.0084	0.4645	0.0117	0.0106	0.3691	0.0130	0.0078	0.3604	0.0116	0.0060
0.15	0.4719	0.0124	0.0096	0.3994	0.0130	0.0087	0.3879	0.0118	0.0075	0.3811	0.0116	0.0064
0.25	0.4918	0.0129	0.0115	0.4752	0.0131	0.0129	0.4559	0.0112	0.0077	0.4687	0.0105	0.0090
0.35	0.6353	0.0143	0.0160	0.6469	0.0142	0.0181	0.5792	0.0146	0.0117	0.5601	0.0139	0.0118
0.45	0.9016	0.0154	0.0177	0.8268	0.0163	0.0181	0.7897	0.0159	0.0208	0.7817	0.0146	0.0173
0.55	1.1411	0.0198	0.0101	1.1237	0.0187	0.0130	1.0364	0.0189	0.0203	0.9548	0.0180	0.0138
0.65	1.3624	0.0243	0.0110	1.2965	0.0238	0.0140	1.1965	0.0233	0.0180	1.1018	0.0229	0.0118
0.75	1.4852	0.0291	0.0763	1.3949	0.0327	0.0752	1.2275	0.0313	0.0802	1.1111	0.0273	0.0491
0.85	1.2902	0.0483	0.3556	1.1262	0.0456	0.2698	1.0758	0.0445	0.2449	0.8415	0.0484	0.2383

$\cos(\theta^*_{\pi^0})$	$W=(1732.0\pm6.0)$ MeV			$W=(1744.0\pm6.0)$ MeV			$W=(1756.0\pm6.0)$ MeV			$W=(1768.0\pm6.0)$ MeV		
	$d\sigma/d\Omega$ [μb/sr]	Δ_{stat} [μb/sr]	Δ_{sys} [μb/sr]	$d\sigma/d\Omega$ [μb/sr]	Δ_{stat} [μb/sr]	Δ_{sys} [μb/sr]	$d\sigma/d\Omega$ [μb/sr]	Δ_{stat} [μb/sr]	Δ_{sys} [μb/sr]	$d\sigma/d\Omega$ [μb/sr]	Δ_{stat} [μb/sr]	Δ_{sys} [μb/sr]
−0.95	0.9024	0.0298	0.3111	0.8727	0.0320	0.2367	0.9258	0.0372	0.1886	0.9621	0.0332	0.2709
−0.85	0.7037	0.0192	0.0715	0.7691	0.0212	0.0629	0.8041	0.0216	0.0539	0.8583	0.0220	0.0683
−0.75	0.6998	0.0203	0.0281	0.7159	0.0195	0.0263	0.7124	0.0195	0.0241	0.7244	0.0194	0.0197
−0.65	0.6814	0.0195	0.0359	0.6669	0.0201	0.0292	0.6398	0.0199	0.0355	0.6373	0.0205	0.0212
−0.55	0.5843	0.0141	0.0282	0.5262	0.0132	0.0221	0.5008	0.0130	0.0250	0.4855	0.0132	0.0163
−0.45	0.4886	0.0114	0.0121	0.4708	0.0107	0.0105	0.4386	0.0098	0.0104	0.4054	0.0097	0.0068
−0.35	0.4628	0.0114	0.0041	0.4193	0.0106	0.0039	0.3690	0.0107	0.0043	0.3523	0.0095	0.0025
−0.25	0.4695	0.0115	0.0039	0.3906	0.0113	0.0060	0.3860	0.0109	0.0043	0.3404	0.0115	0.0043
−0.15	0.4054	0.0114	0.0065	0.3868	0.0115	0.0100	0.3786	0.0112	0.0051	0.3573	0.0110	0.0066
−0.05	0.3552	0.0111	0.0080	0.3516	0.0098	0.0098	0.3431	0.0099	0.0051	0.3407	0.0097	0.0058
0.05	0.3214	0.0110	0.0068	0.3302	0.0114	0.0085	0.3458	0.0101	0.0057	0.3164	0.0114	0.0047
0.15	0.3468	0.0099	0.0067	0.3496	0.0111	0.0090	0.3226	0.0106	0.0051	0.3332	0.0110	0.0045
0.25	0.4086	0.0113	0.0091	0.4024	0.0119	0.0103	0.3988	0.0111	0.0055	0.3656	0.0113	0.0054
0.35	0.5463	0.0128	0.0141	0.4904	0.0124	0.0139	0.4310	0.0136	0.0082	0.4325	0.0122	0.0108
0.45	0.7002	0.0151	0.0179	0.6171	0.0148	0.0173	0.5847	0.0140	0.0148	0.5252	0.0139	0.0197
0.55	0.8865	0.0180	0.0134	0.7906	0.0172	0.0153	0.7505	0.0167	0.0169	0.6568	0.0169	0.0213
0.65	0.9610	0.0200	0.0070	0.8942	0.0211	0.0205	0.8388	0.0214	0.0102	0.7701	0.0199	0.0120
0.75	1.0184	0.0283	0.0587	0.9138	0.0237	0.0659	0.8669	0.0253	0.0274	0.8122	0.0291	0.0353
0.85	0.8332	0.0382	0.1981	0.7508	0.0422	0.1851	0.7910	0.0377	0.2324	0.7943	0.0460	0.2435

$\cos(\theta^*_{\pi^0})$	$W=(1780.0\pm6.0)$ MeV			$W=(1792.0\pm6.0)$ MeV			$W=(1804.0\pm6.0)$ MeV			$W=(1816.0\pm6.0)$ MeV		
	$d\sigma/d\Omega$ [μb/sr]	Δ_{stat} [μb/sr]	Δ_{sys} [μb/sr]	$d\sigma/d\Omega$ [μb/sr]	Δ_{stat} [μb/sr]	Δ_{sys} [μb/sr]	$d\sigma/d\Omega$ [μb/sr]	Δ_{stat} [μb/sr]	Δ_{sys} [μb/sr]	$d\sigma/d\Omega$ [μb/sr]	Δ_{stat} [μb/sr]	Δ_{sys} [μb/sr]
−0.95	0.9103	0.0285	0.3346	1.0429	0.0328	0.1505	1.0727	0.0311	0.2263	1.0827	0.0358	0.2154
−0.85	0.9276	0.0251	0.1030	0.9530	0.0232	0.0666	1.0640	0.0275	0.0588	1.1189	0.0274	0.0882
−0.75	0.7567	0.0207	0.0314	0.7983	0.0203	0.0315	0.8137	0.0217	0.0298	0.8651	0.0205	0.0490
−0.65	0.6523	0.0180	0.0270	0.6641	0.0170	0.0262	0.6765	0.0184	0.0309	0.7128	0.0204	0.0360
−0.55	0.4658	0.0127	0.0184	0.4717	0.0141	0.0151	0.4573	0.0144	0.0213	0.4725	0.0132	0.0189
−0.45	0.3798	0.0100	0.0085	0.3867	0.0101	0.0092	0.3660	0.0097	0.0128	0.3607	0.0105	0.0075
−0.35	0.3341	0.0098	0.0033	0.3458	0.0105	0.0067	0.3396	0.0101	0.0068	0.3368	0.0112	0.0044
−0.25	0.3410	0.0108	0.0057	0.3165	0.0122	0.0070	0.3423	0.0117	0.0063	0.3509	0.0120	0.0044
−0.15	0.3672	0.0101	0.0116	0.3380	0.0123	0.0086	0.3690	0.0108	0.0090	0.3544	0.0113	0.0061
−0.05	0.3280	0.0102	0.0132	0.3620	0.0109	0.0092	0.3290	0.0129	0.0095	0.3700	0.0134	0.0075
0.05	0.3179	0.0108	0.0114	0.3209	0.0111	0.0073	0.3242	0.0112	0.0083	0.3455	0.0128	0.0060
0.15	0.3159	0.0106	0.0090	0.2989	0.0119	0.0057	0.3100	0.0123	0.0068	0.3207	0.0111	0.0050
0.25	0.3556	0.0114	0.0076	0.3487	0.0111	0.0066	0.3036	0.0116	0.0064	0.3072	0.0121	0.0078
0.35	0.4068	0.0128	0.0103	0.3573	0.0132	0.0111	0.3668	0.0138	0.0107	0.3336	0.0137	0.0163
0.45	0.4858	0.0138	0.0175	0.4305	0.0151	0.0169	0.4226	0.0137	0.0200	0.4069	0.0133	0.0243
0.55	0.5876	0.0155	0.0223	0.5833	0.0161	0.0164	0.5773	0.0165	0.0270	0.5504	0.0160	0.0254
0.65	0.7224	0.0214	0.0100	0.7173	0.0210	0.0117	0.7420	0.0215	0.0263	0.7083	0.0235	0.0117
0.75	0.8463	0.0268	0.0394	0.9028	0.0279	0.0511	0.8522	0.0337	0.0454	0.9172	0.0272	0.0487
0.85	0.7463	0.0366	0.2542	0.7858	0.0382	0.2341	0.8483	0.0398	0.2402	0.8819	0.0520	0.2748

$\cos(\theta^*_{\pi^0})$	$W=(1828.0\pm6.0)$ MeV			$W=(1840.0\pm6.0)$ MeV			$W=(1852.0\pm6.0)$ MeV			$W=(1864.0\pm6.0)$ MeV		
	$d\sigma/d\Omega$ [μb/sr]	Δ_{stat} [μb/sr]	Δ_{sys} [μb/sr]	$d\sigma/d\Omega$ [μb/sr]	Δ_{stat} [μb/sr]	Δ_{sys} [μb/sr]	$d\sigma/d\Omega$ [μb/sr]	Δ_{stat} [μb/sr]	Δ_{sys} [μb/sr]	$d\sigma/d\Omega$ [μb/sr]	Δ_{stat} [μb/sr]	Δ_{sys} [μb/sr]
−0.95	1.1051	0.0321	0.1887	1.0887	0.0365	0.1429	1.1067	0.0417	0.3307	1.0730	0.0366	0.4356
−0.85	1.1681	0.0313	0.0911	1.1931	0.0309	0.0605	1.2422	0.0319	0.0640	1.1579	0.0353	0.1009
−0.75	0.9315	0.0226	0.0322	0.9250	0.0255	0.0195	0.9215	0.0269	0.0175	0.9387	0.0285	0.0178
−0.65	0.7655	0.0200	0.0350	0.7517	0.0209	0.0224	0.7230	0.0263	0.0250	0.7965	0.0282	0.0280
−0.55	0.4567	0.0160	0.0249	0.4497	0.0136	0.0184	0.4393	0.0171	0.0125	0.4418	0.0178	0.0136
−0.45	0.3687	0.0110	0.0185	0.3820	0.0098	0.0188	0.3492	0.0107	0.0074	0.3279	0.0100	0.0092
−0.35	0.3314	0.0119	0.0120	0.3248	0.0133	0.0156	0.3222	0.0146	0.0053	0.2971	0.0159	0.0097
−0.25	0.3475	0.0143	0.0079	0.3498	0.0145	0.0142	0.3562	0.0168	0.0067	0.3447	0.0206	0.0118
−0.15	0.3890	0.0132	0.0061	0.3997	0.0163	0.0181	0.4471	0.0154	0.0107	0.4056	0.0190	0.0114
−0.05	0.3927	0.0124	0.0066	0.3878	0.0159	0.0173	0.4067	0.0178	0.0089	0.4315	0.0204	0.0111
0.05	0.3546	0.0145	0.0098	0.3661	0.0172	0.0170	0.3789	0.0161	0.0068	0.3478	0.0216	0.0091
0.15	0.3256	0.0118	0.0112	0.2979	0.0150	0.0148	0.3252	0.0143	0.0073	0.3026	0.0179	0.0072
0.25	0.3049	0.0132	0.0108	0.3117	0.0144	0.0190	0.3088	0.0162	0.0108	0.2756	0.0207	0.0093
0.35	0.3464	0.0130	0.0153	0.3366	0.0157	0.0222	0.3020	0.0198	0.0195	0.2605	0.0188	0.0200
0.45	0.3624	0.0165	0.0213	0.3364	0.0165	0.0195	0.3391	0.0208	0.0301	0.3196	0.0162	0.0353
0.55	0.4851	0.0207	0.0291	0.5469	0.0211	0.0217	0.4762	0.0223	0.0388	0.4679	0.0237	0.0480
0.65	0.7779	0.0220	0.0348	0.7756	0.0239	0.0186	0.7608	0.0347	0.0261	0.7898	0.0286	0.0433
0.75	0.9929	0.0374	0.0539	1.0394	0.0365	0.0546	1.0618	0.0363	0.0463	1.1408	0.0462	0.0413
0.85	0.9622	0.0576	0.2855	1.0986	0.0537	0.3188	1.1699	0.0593	0.3795	1.2218	0.0651	0.4170

$\cos(\theta^*_{\pi^0})$	$W=(1876.0\pm6.0)$ MeV		
	$d\sigma/d\Omega$ [μb/sr]	Δ_{stat} [μb/sr]	Δ_{sys} [μb/sr]
−0.95	1.0863	0.0456	0.6293
−0.85	1.1747	0.0359	0.1123
−0.75	0.8884	0.0303	0.0428
−0.65	0.7365	0.0273	0.0425
−0.55	0.3871	0.0144	0.0182
−0.45	0.2958	0.0106	0.0097
−0.35	0.3213	0.0138	0.0101
−0.25	0.3636	0.0201	0.0125
−0.15	0.4230	0.0220	0.0137
−0.05	0.4208	0.0240	0.0135
0.05	0.3242	0.0221	0.0117
0.15	0.3233	0.0167	0.0147
0.25	0.2690	0.0251	0.0167
0.35	0.3061	0.0185	0.0301
0.45	0.3085	0.0185	0.0359
0.55	0.4133	0.0216	0.0303
0.65	0.7144	0.0299	0.0197
0.75	1.3037	0.0475	0.0527
0.85	1.1079	0.0954	0.2598

E.1.5 Angular Distributions $\gamma n \to \pi^0 n$ as a Function of W

$\cos(\theta^*_{\pi^0})$	$W=(1300.0\pm6.0)$ MeV			$W=(1312.0\pm6.0)$ MeV			$W=(1324.0\pm6.0)$ MeV			$W=(1336.0\pm6.0)$ MeV		
	$d\sigma/d\Omega$ [μb/sr]	Δ_{stat} [μb/sr]	Δ_{sys} [μb/sr]	$d\sigma/d\Omega$ [μb/sr]	Δ_{stat} [μb/sr]	Δ_{sys} [μb/sr]	$d\sigma/d\Omega$ [μb/sr]	Δ_{stat} [μb/sr]	Δ_{sys} [μb/sr]	$d\sigma/d\Omega$ [μb/sr]	Δ_{stat} [μb/sr]	Δ_{sys} [μb/sr]
−0.95	0.1525	0.0237	0.0796	0.1521	0.0271	0.0641	0.2759	0.0337	0.0789	0.4188	0.0367	0.1059
−0.85	0.7410	0.0435	0.4207	0.9100	0.0415	0.4625	1.1550	0.0387	0.4674	1.2172	0.0362	0.3386
−0.75	3.2799	0.0587	1.7688	3.6005	0.0533	1.7252	3.1222	0.0486	1.2181	2.8941	0.0426	0.6719
−0.65	5.3899	0.0404	1.9667	5.1134	0.0380	1.5739	4.4843	0.0336	1.0871	3.7843	0.0290	0.4909
−0.55	5.7438	0.0305	0.9365	5.4258	0.0290	0.6987	4.7498	0.0270	0.4512	4.1473	0.0236	0.1931
−0.45	6.5434	0.0329	0.4025	6.3656	0.0317	0.2786	5.6290	0.0295	0.1683	4.8007	0.0266	0.0985
−0.35	7.8325	0.0389	0.2933	7.6487	0.0383	0.1761	6.7365	0.0354	0.1178	5.7339	0.0318	0.1425
−0.25	8.8534	0.0435	0.3052	8.5116	0.0423	0.1958	7.6507	0.0396	0.1609	6.4659	0.0346	0.1823
−0.15	9.4705	0.0464	0.2346	8.9894	0.0447	0.2096	8.1917	0.0420	0.2131	6.8779	0.0365	0.1815
−0.05	9.5061	0.0484	0.1974	9.2764	0.0478	0.2362	8.4620	0.0450	0.2492	7.1376	0.0388	0.1944
0.05	9.7010	0.0533	0.3725	9.4890	0.0503	0.3318	8.4487	0.0465	0.2894	7.1235	0.0405	0.2363
0.15	10.2905	0.0588	0.5659	9.7617	0.0549	0.4521	8.6588	0.0515	0.3719	7.2169	0.0434	0.2905
0.25	10.5483	0.0661	0.5958	10.1595	0.0635	0.5603	8.8489	0.0562	0.4981	7.2474	0.0483	0.3585
0.35	10.6102	0.0767	0.6876	9.9846	0.0697	0.6728	8.9574	0.0616	0.6697	7.4208	0.0542	0.4932
0.45	10.2486	0.0853	0.9236	9.5208	0.0806	0.8461	8.3376	0.0706	0.8096	6.8873	0.0615	0.6263
0.55	8.3764	0.0898	1.0407	7.6698	0.0823	0.9412	7.1452	0.0764	0.8933	6.0635	0.0617	0.7411
0.65	6.3879	0.1001	0.8110	5.8793	0.0834	0.7331	5.4019	0.0820	0.6919	4.6208	0.0729	0.5675
0.75	5.0023	0.1541	0.4123	4.4778	0.1374	0.2948	4.2895	0.1146	0.4002	3.3851	0.1125	0.2308
0.85	5.0177	0.6456	0.9972	3.7812	0.5446	0.6781	4.8612	0.3450	1.1047	3.3815	0.3429	0.5962

$\cos(\theta^*_{\pi^0})$	$W=(1348.0\pm6.0)$ MeV			$W=(1360.0\pm6.0)$ MeV			$W=(1372.0\pm6.0)$ MeV			$W=(1384.0\pm6.0)$ MeV		
	$d\sigma/d\Omega$ [μb/sr]	Δ_{stat} [μb/sr]	Δ_{sys} [μb/sr]	$d\sigma/d\Omega$ [μb/sr]	Δ_{stat} [μb/sr]	Δ_{sys} [μb/sr]	$d\sigma/d\Omega$ [μb/sr]	Δ_{stat} [μb/sr]	Δ_{sys} [μb/sr]	$d\sigma/d\Omega$ [μb/sr]	Δ_{stat} [μb/sr]	Δ_{sys} [μb/sr]
−0.95	0.5517	0.0374	0.1486	0.6433	0.0415	0.1512	0.7468	0.0535	0.1855	1.0244	0.0516	0.2223
−0.85	1.3647	0.0354	0.3109	1.4810	0.0380	0.2510	1.6423	0.0370	0.2316	1.6690	0.0366	0.1910
−0.75	2.6260	0.0344	0.4509	2.6175	0.0340	0.3175	2.3354	0.0331	0.1941	2.3277	0.0299	0.1517
−0.65	3.2875	0.0259	0.3187	3.1261	0.0257	0.2271	2.7927	0.0248	0.1482	2.6747	0.0241	0.1202
−0.55	3.5595	0.0212	0.1367	3.3710	0.0208	0.1155	2.9447	0.0197	0.0954	2.8005	0.0203	0.0895
−0.45	4.1713	0.0242	0.0948	3.9022	0.0234	0.1031	3.5778	0.0229	0.1051	3.3757	0.0226	0.1004
−0.35	5.0094	0.0295	0.1420	4.6621	0.0281	0.1512	4.1470	0.0269	0.1329	3.9262	0.0265	0.1304
−0.25	5.5658	0.0310	0.1719	5.2170	0.0309	0.1765	4.6288	0.0290	0.1408	4.3488	0.0292	0.1407
−0.15	5.8631	0.0326	0.1667	5.3786	0.0326	0.1610	4.8154	0.0291	0.1330	4.4611	0.0287	0.1236
−0.05	5.8586	0.0334	0.1633	5.4665	0.0333	0.1472	4.7150	0.0313	0.1256	4.4433	0.0307	0.1071
0.05	5.9689	0.0357	0.1845	5.5778	0.0346	0.1595	4.7467	0.0322	0.1319	4.4679	0.0316	0.1037
0.15	5.9799	0.0390	0.2211	5.6144	0.0369	0.2039	4.8548	0.0336	0.1566	4.4692	0.0340	0.1181
0.25	6.1641	0.0430	0.2941	5.6757	0.0403	0.2695	4.8575	0.0360	0.1982	4.3906	0.0352	0.1593
0.35	6.2479	0.0463	0.4058	5.7858	0.0466	0.3534	4.9428	0.0399	0.2752	4.3734	0.0388	0.2329
0.45	5.9223	0.0502	0.5207	5.4320	0.0491	0.4428	4.5917	0.0441	0.3647	4.1922	0.0412	0.3202
0.55	5.0934	0.0545	0.6089	4.6931	0.0510	0.5339	3.8709	0.0467	0.4293	3.4960	0.0437	0.3800
0.65	3.8277	0.0598	0.5223	3.5509	0.0561	0.4723	3.0687	0.0536	0.3770	2.7717	0.0503	0.3472
0.75	3.1580	0.0950	0.3015	2.4801	0.0841	0.2410	2.3042	0.0737	0.2070	2.0787	0.0702	0.1825
0.85	2.8367	0.3015	0.2440	2.1568	0.2564	0.1997	1.9987	0.2051	0.2556	1.7019	0.1742	0.1565

$\cos(\theta^*_{\pi^0})$	$W=(1396.0\pm6.0)$ MeV			$W=(1408.0\pm6.0)$ MeV			$W=(1420.0\pm6.0)$ MeV			$W=(1432.0\pm6.0)$ MeV		
	$d\sigma/d\Omega$ [μb/sr]	$\Delta_{\rm stat}$ [μb/sr]	$\Delta_{\rm sys}$ [μb/sr]	$d\sigma/d\Omega$ [μb/sr]	$\Delta_{\rm stat}$ [μb/sr]	$\Delta_{\rm sys}$ [μb/sr]	$d\sigma/d\Omega$ [μb/sr]	$\Delta_{\rm stat}$ [μb/sr]	$\Delta_{\rm sys}$ [μb/sr]	$d\sigma/d\Omega$ [μb/sr]	$\Delta_{\rm stat}$ [μb/sr]	$\Delta_{\rm sys}$ [μb/sr]
−0.95	1.1284	0.0564	0.1286	1.0340	0.0551	0.1714	1.0356	0.0576	0.1125	1.2785	0.0522	0.1197
−0.85	1.7068	0.0368	0.1330	1.6979	0.0328	0.1314	1.6425	0.0346	0.0882	1.7125	0.0325	0.0913
−0.75	2.1889	0.0300	0.1204	2.1206	0.0290	0.0902	2.0423	0.0287	0.0750	2.0946	0.0278	0.0690
−0.65	2.4185	0.0236	0.0938	2.3291	0.0241	0.0837	2.2233	0.0241	0.0868	2.1689	0.0254	0.0653
−0.55	2.6696	0.0197	0.0756	2.4964	0.0202	0.0728	2.4535	0.0208	0.0861	2.3583	0.0209	0.0684
−0.45	3.1912	0.0225	0.0898	2.9058	0.0224	0.0834	2.8502	0.0225	0.0856	2.7606	0.0229	0.0738
−0.35	3.6703	0.0261	0.1176	3.4096	0.0262	0.1111	3.3015	0.0265	0.0972	3.1475	0.0261	0.0858
−0.25	4.0191	0.0289	0.1220	3.6992	0.0276	0.1161	3.5093	0.0281	0.0980	3.3161	0.0278	0.0886
−0.15	4.1259	0.0299	0.1059	3.8382	0.0289	0.1027	3.6218	0.0280	0.0871	3.4131	0.0285	0.0789
−0.05	4.1669	0.0303	0.0969	3.7389	0.0292	0.0856	3.5361	0.0288	0.0705	3.3837	0.0296	0.0647
0.05	4.0817	0.0311	0.0861	3.7158	0.0295	0.0758	3.4308	0.0291	0.0563	3.3285	0.0309	0.0536
0.15	3.9818	0.0322	0.0827	3.6102	0.0304	0.0727	3.3823	0.0307	0.0542	3.1782	0.0306	0.0478
0.25	3.9407	0.0340	0.1155	3.5125	0.0325	0.0876	3.2830	0.0323	0.0710	3.0743	0.0303	0.0598
0.35	3.9146	0.0368	0.1883	3.4197	0.0341	0.1354	3.1366	0.0342	0.1087	2.9095	0.0324	0.0991
0.45	3.6902	0.0390	0.2662	3.2305	0.0364	0.2062	2.9504	0.0366	0.1709	2.6954	0.0361	0.1556
0.55	3.1925	0.0406	0.3312	2.8144	0.0390	0.2783	2.6306	0.0396	0.2480	2.2913	0.0383	0.2061
0.65	2.5514	0.0471	0.3222	2.2879	0.0442	0.2595	2.0865	0.0417	0.2195	1.9702	0.0386	0.2126
0.75	1.8757	0.0584	0.1901	1.5637	0.0633	0.1108	1.5094	0.0572	0.0962	1.4224	0.0499	0.1117
0.85	1.1248	0.1496	0.1077	1.5849	0.1065	0.2408	1.1529	0.1296	0.1907	1.0382	0.0822	0.0985

$\cos(\theta^*_{\pi^0})$	$W=(1444.0\pm6.0)$ MeV			$W=(1456.0\pm6.0)$ MeV			$W=(1468.0\pm6.0)$ MeV			$W=(1480.0\pm6.0)$ MeV		
	$d\sigma/d\Omega$ [μb/sr]	$\Delta_{\rm stat}$ [μb/sr]	$\Delta_{\rm sys}$ [μb/sr]	$d\sigma/d\Omega$ [μb/sr]	$\Delta_{\rm stat}$ [μb/sr]	$\Delta_{\rm sys}$ [μb/sr]	$d\sigma/d\Omega$ [μb/sr]	$\Delta_{\rm stat}$ [μb/sr]	$\Delta_{\rm sys}$ [μb/sr]	$d\sigma/d\Omega$ [μb/sr]	$\Delta_{\rm stat}$ [μb/sr]	$\Delta_{\rm sys}$ [μb/sr]
−0.95	1.3751	0.0529	0.1310	1.5311	0.0489	0.1823	1.6920	0.0520	0.2145	1.8655	0.0527	0.2172
−0.85	1.7579	0.0314	0.0800	1.8204	0.0312	0.1048	1.8886	0.0299	0.0998	1.9920	0.0346	0.0930
−0.75	2.0985	0.0289	0.0665	2.0560	0.0299	0.0749	2.1104	0.0295	0.0695	2.2141	0.0302	0.0627
−0.65	2.1828	0.0265	0.0730	2.0921	0.0261	0.0803	2.1162	0.0269	0.0862	2.1753	0.0267	0.0800
−0.55	2.3182	0.0211	0.0673	2.2510	0.0211	0.0786	2.2485	0.0214	0.0796	2.2606	0.0219	0.0785
−0.45	2.6926	0.0225	0.0643	2.6454	0.0219	0.0672	2.5057	0.0235	0.0521	2.4954	0.0228	0.0571
−0.35	2.9669	0.0261	0.0686	2.8709	0.0266	0.0606	2.7933	0.0263	0.0398	2.7154	0.0257	0.0429
−0.25	3.1984	0.0290	0.0797	3.1203	0.0289	0.0661	3.0034	0.0282	0.0418	2.8906	0.0278	0.0399
−0.15	3.2953	0.0285	0.0770	3.2920	0.0281	0.0660	3.1557	0.0282	0.0448	3.0669	0.0282	0.0377
−0.05	3.2308	0.0296	0.0602	3.2132	0.0303	0.0537	3.1281	0.0299	0.0419	3.0597	0.0300	0.0337
0.05	3.1236	0.0306	0.0471	3.0856	0.0297	0.0384	2.9761	0.0301	0.0346	3.0560	0.0302	0.0311
0.15	3.0265	0.0302	0.0415	2.9860	0.0305	0.0301	3.0078	0.0296	0.0289	3.0306	0.0306	0.0288
0.25	2.8874	0.0314	0.0426	2.8676	0.0312	0.0324	2.8321	0.0309	0.0257	2.8535	0.0299	0.0264
0.35	2.7971	0.0316	0.0628	2.7307	0.0315	0.0508	2.6616	0.0303	0.0254	2.7069	0.0322	0.0264
0.45	2.5473	0.0347	0.1121	2.5201	0.0351	0.0876	2.4873	0.0337	0.0511	2.5739	0.0326	0.0464
0.55	2.2567	0.0379	0.1815	2.2821	0.0377	0.1582	2.2677	0.0361	0.1228	2.3792	0.0360	0.1024
0.65	1.8781	0.0382	0.1980	1.8314	0.0398	0.1665	1.9296	0.0409	0.1568	2.1445	0.0356	0.1495
0.75	1.3869	0.0429	0.1189	1.4689	0.0540	0.0894	1.6046	0.0490	0.1246	1.8393	0.0607	0.1555
0.85	0.9809	0.0803	0.1053	1.1049	0.0871	0.1749	1.2728	0.0937	0.1860	1.5212	0.0953	0.2034

$\cos(\theta^*_{\pi^0})$	$W=(1492.0\pm6.0)$ MeV			$W=(1504.0\pm6.0)$ MeV			$W=(1516.0\pm6.0)$ MeV			$W=(1528.0\pm6.0)$ MeV		
	$d\sigma/d\Omega$ [μb/sr]	$\Delta_{\rm stat}$ [μb/sr]	$\Delta_{\rm sys}$ [μb/sr]	$d\sigma/d\Omega$ [μb/sr]	$\Delta_{\rm stat}$ [μb/sr]	$\Delta_{\rm sys}$ [μb/sr]	$d\sigma/d\Omega$ [μb/sr]	$\Delta_{\rm stat}$ [μb/sr]	$\Delta_{\rm sys}$ [μb/sr]	$d\sigma/d\Omega$ [μb/sr]	$\Delta_{\rm stat}$ [μb/sr]	$\Delta_{\rm sys}$ [μb/sr]
−0.95	2.0708	0.0554	0.2502	2.2503	0.0611	0.2458	2.2627	0.0608	0.1437	2.0514	0.0552	0.2286
−0.85	2.2189	0.0350	0.1244	2.2525	0.0342	0.1091	2.1875	0.0377	0.0635	1.9384	0.0327	0.0944
−0.75	2.3106	0.0316	0.0932	2.3447	0.0313	0.0935	2.3012	0.0285	0.0724	2.0944	0.0292	0.0863
−0.65	2.2175	0.0274	0.1051	2.2577	0.0285	0.1209	2.1273	0.0279	0.0978	2.0265	0.0284	0.1082
−0.55	2.3126	0.0228	0.0921	2.2490	0.0232	0.1103	2.1386	0.0214	0.0913	2.0058	0.0205	0.0921
−0.45	2.4904	0.0231	0.0567	2.4130	0.0232	0.0690	2.2679	0.0217	0.0596	2.0811	0.0215	0.0561
−0.35	2.7156	0.0254	0.0363	2.6060	0.0263	0.0344	2.4546	0.0256	0.0321	2.2862	0.0252	0.0315
−0.25	2.8642	0.0272	0.0332	2.8252	0.0275	0.0299	2.7197	0.0266	0.0262	2.4943	0.0266	0.0262
−0.15	3.0172	0.0281	0.0349	3.0103	0.0285	0.0347	2.8754	0.0281	0.0283	2.6349	0.0266	0.0282
−0.05	3.1081	0.0304	0.0360	3.0558	0.0298	0.0356	2.9202	0.0302	0.0306	2.7600	0.0283	0.0336
0.05	3.0566	0.0303	0.0338	3.0608	0.0304	0.0322	3.0332	0.0299	0.0347	2.7980	0.0289	0.0415
0.15	2.9926	0.0288	0.0314	3.1067	0.0292	0.0310	2.9310	0.0295	0.0372	2.7684	0.0296	0.0433
0.25	2.8930	0.0295	0.0305	3.0444	0.0292	0.0317	2.8232	0.0300	0.0393	2.6379	0.0289	0.0390
0.35	2.7604	0.0316	0.0285	2.8666	0.0323	0.0311	2.7462	0.0300	0.0387	2.5878	0.0297	0.0340
0.45	2.6445	0.0323	0.0373	2.6534	0.0328	0.0382	2.6653	0.0312	0.0370	2.3936	0.0305	0.0297
0.55	2.5130	0.0335	0.0871	2.5935	0.0358	0.0697	2.4626	0.0366	0.0481	2.3821	0.0331	0.0410
0.65	2.2931	0.0392	0.1411	2.4462	0.0424	0.1331	2.3494	0.0437	0.0935	2.2525	0.0381	0.0682
0.75	2.2323	0.0515	0.1867	2.3670	0.0550	0.2573	2.1394	0.0591	0.1570	2.1423	0.0530	0.1292
0.85	1.7752	0.1675	0.2152	1.9024	0.1364	0.3060	2.0299	0.1082	0.2128	2.0313	0.1014	0.2405

$\cos(\theta^*_{\pi^0})$	$W=(1540.0\pm6.0)$ MeV			$W=(1552.0\pm6.0)$ MeV			$W=(1564.0\pm6.0)$ MeV			$W=(1576.0\pm6.0)$ MeV		
	$d\sigma/d\Omega$ [μb/sr]	$\Delta_{\rm stat}$ [μb/sr]	$\Delta_{\rm sys}$ [μb/sr]	$d\sigma/d\Omega$ [μb/sr]	$\Delta_{\rm stat}$ [μb/sr]	$\Delta_{\rm sys}$ [μb/sr]	$d\sigma/d\Omega$ [μb/sr]	$\Delta_{\rm stat}$ [μb/sr]	$\Delta_{\rm sys}$ [μb/sr]	$d\sigma/d\Omega$ [μb/sr]	$\Delta_{\rm stat}$ [μb/sr]	$\Delta_{\rm sys}$ [μb/sr]
−0.95	1.8701	0.0523	0.1876	1.7483	0.0536	0.1423	1.6377	0.0510	0.1433	1.4635	0.0504	0.1079
−0.85	1.7352	0.0312	0.0828	1.6239	0.0299	0.0590	1.3785	0.0299	0.0582	1.2157	0.0255	0.0435
−0.75	1.9174	0.0295	0.0853	1.7216	0.0271	0.0712	1.4756	0.0263	0.0651	1.3133	0.0249	0.0551
−0.65	1.8449	0.0275	0.1070	1.7033	0.0274	0.1014	1.6053	0.0245	0.1015	1.4328	0.0234	0.0846
−0.55	1.8699	0.0211	0.0922	1.7154	0.0203	0.0861	1.5668	0.0195	0.0879	1.4228	0.0191	0.0700
−0.45	1.9205	0.0200	0.0517	1.7706	0.0204	0.0483	1.6501	0.0194	0.0481	1.4814	0.0190	0.0383
−0.35	2.0757	0.0229	0.0251	1.9500	0.0233	0.0255	1.7645	0.0225	0.0212	1.6305	0.0227	0.0207
−0.25	2.2953	0.0250	0.0224	2.0915	0.0251	0.0213	1.9340	0.0251	0.0197	1.8004	0.0241	0.0206
−0.15	2.3607	0.0265	0.0246	2.2101	0.0257	0.0249	2.0541	0.0258	0.0253	1.9176	0.0249	0.0261
−0.05	2.5275	0.0264	0.0292	2.3082	0.0269	0.0278	2.1386	0.0268	0.0288	1.9529	0.0258	0.0268
0.05	2.4763	0.0269	0.0310	2.3008	0.0271	0.0298	2.1097	0.0263	0.0264	1.8938	0.0262	0.0238
0.15	2.4458	0.0284	0.0346	2.2537	0.0261	0.0326	2.0775	0.0255	0.0263	1.8072	0.0253	0.0250
0.25	2.3496	0.0273	0.0430	2.0872	0.0259	0.0294	1.9128	0.0274	0.0297	1.6453	0.0247	0.0268
0.35	2.2362	0.0281	0.0410	1.9453	0.0268	0.0242	1.7862	0.0259	0.0290	1.5568	0.0251	0.0260
0.45	2.1480	0.0284	0.0287	1.9534	0.0261	0.0210	1.7038	0.0249	0.0228	1.4641	0.0242	0.0200
0.55	2.0817	0.0296	0.0258	1.9340	0.0284	0.0264	1.6656	0.0301	0.0239	1.4920	0.0258	0.0188
0.65	2.0180	0.0378	0.0445	1.8197	0.0331	0.0467	1.6506	0.0302	0.0363	1.6205	0.0310	0.0448
0.75	2.1239	0.0492	0.1032	1.8187	0.0509	0.0863	1.7080	0.0454	0.0770	1.6728	0.0399	0.1205
0.85	2.0169	0.1146	0.1937	1.7210	0.1236	0.2219	1.7443	0.0996	0.1877	1.5161	0.0808	0.1542

$\cos(\theta^*_{\pi^0})$	$W=(1588.0\pm6.0)$ MeV			$W=(1600.0\pm6.0)$ MeV			$W=(1612.0\pm6.0)$ MeV			$W=(1624.0\pm6.0)$ MeV		
	$d\sigma/d\Omega$ [μb/sr]	$\Delta_{\rm stat}$ [μb/sr]	$\Delta_{\rm sys}$ [μb/sr]	$d\sigma/d\Omega$ [μb/sr]	$\Delta_{\rm stat}$ [μb/sr]	$\Delta_{\rm sys}$ [μb/sr]	$d\sigma/d\Omega$ [μb/sr]	$\Delta_{\rm stat}$ [μb/sr]	$\Delta_{\rm sys}$ [μb/sr]	$d\sigma/d\Omega$ [μb/sr]	$\Delta_{\rm stat}$ [μb/sr]	$\Delta_{\rm sys}$ [μb/sr]
−0.95	1.2635	0.0418	0.0920	1.0168	0.0462	0.0730	0.9625	0.0370	0.0825	0.8797	0.0354	0.0752
−0.85	1.0167	0.0253	0.0417	0.8812	0.0252	0.0397	0.7907	0.0238	0.0343	0.7350	0.0223	0.0342
−0.75	1.1268	0.0236	0.0580	1.0317	0.0224	0.0594	0.9090	0.0213	0.0408	0.8305	0.0217	0.0471
−0.65	1.2053	0.0226	0.0832	1.1464	0.0221	0.0835	1.0562	0.0219	0.0624	1.0665	0.0211	0.0732
−0.55	1.2573	0.0174	0.0713	1.1714	0.0171	0.0674	1.0953	0.0167	0.0531	1.0330	0.0161	0.0510
−0.45	1.3376	0.0188	0.0421	1.2549	0.0174	0.0392	1.1465	0.0156	0.0284	1.1132	0.0153	0.0293
−0.35	1.5014	0.0208	0.0251	1.4333	0.0197	0.0230	1.2614	0.0184	0.0150	1.1977	0.0169	0.0172
−0.25	1.5846	0.0232	0.0222	1.5038	0.0211	0.0198	1.3217	0.0193	0.0151	1.2275	0.0187	0.0141
−0.15	1.7043	0.0236	0.0247	1.5793	0.0219	0.0238	1.4012	0.0212	0.0206	1.2881	0.0189	0.0156
−0.05	1.7606	0.0230	0.0233	1.5399	0.0218	0.0252	1.4120	0.0200	0.0237	1.2010	0.0198	0.0159
0.05	1.6851	0.0233	0.0193	1.4886	0.0220	0.0248	1.2534	0.0230	0.0207	1.0998	0.0216	0.0170
0.15	1.4708	0.0244	0.0145	1.3314	0.0218	0.0210	1.1557	0.0205	0.0167	0.9902	0.0194	0.0199
0.25	1.4458	0.0221	0.0147	1.2076	0.0212	0.0176	1.0917	0.0185	0.0164	0.9181	0.0170	0.0213
0.35	1.3254	0.0225	0.0174	1.1282	0.0200	0.0180	1.0035	0.0199	0.0174	0.9040	0.0184	0.0176
0.45	1.2911	0.0229	0.0176	1.1158	0.0216	0.0185	1.0724	0.0201	0.0173	0.9975	0.0203	0.0131
0.55	1.3635	0.0234	0.0216	1.2357	0.0226	0.0192	1.1792	0.0232	0.0200	1.2253	0.0205	0.0169
0.65	1.4771	0.0308	0.0267	1.4356	0.0279	0.0461	1.4007	0.0282	0.0565	1.5113	0.0301	0.0516
0.75	1.5943	0.0395	0.0775	1.5880	0.0412	0.1315	1.6311	0.0389	0.1589	1.8082	0.0405	0.1626
0.85	1.6749	0.0785	0.5584	1.6542	0.0823	0.2176	1.7203	0.0794	0.2967	1.8415	0.0815	0.3265

$\cos(\theta^*_{\pi^0})$	$W=(1636.0\pm6.0)$ MeV			$W=(1648.0\pm6.0)$ MeV			$W=(1660.0\pm6.0)$ MeV			$W=(1672.0\pm6.0)$ MeV		
	$d\sigma/d\Omega$ [μb/sr]	$\Delta_{\rm stat}$ [μb/sr]	$\Delta_{\rm sys}$ [μb/sr]	$d\sigma/d\Omega$ [μb/sr]	$\Delta_{\rm stat}$ [μb/sr]	$\Delta_{\rm sys}$ [μb/sr]	$d\sigma/d\Omega$ [μb/sr]	$\Delta_{\rm stat}$ [μb/sr]	$\Delta_{\rm sys}$ [μb/sr]	$d\sigma/d\Omega$ [μb/sr]	$\Delta_{\rm stat}$ [μb/sr]	$\Delta_{\rm sys}$ [μb/sr]
−0.95	0.8839	0.0345	0.0670	0.8904	0.0350	0.0782	0.9818	0.0446	0.1036	0.9880	0.0388	0.1059
−0.85	0.7156	0.0217	0.0280	0.6769	0.0238	0.0363	0.7052	0.0241	0.0356	0.7108	0.0247	0.0474
−0.75	0.7840	0.0216	0.0391	0.8127	0.0187	0.0466	0.8538	0.0224	0.0458	0.8949	0.0232	0.0616
−0.65	1.0017	0.0225	0.0687	0.9573	0.0207	0.0671	0.9931	0.0224	0.0682	0.9791	0.0238	0.0775
−0.55	1.0421	0.0151	0.0583	1.0098	0.0148	0.0569	0.9837	0.0159	0.0543	0.9132	0.0155	0.0559
−0.45	1.0663	0.0155	0.0306	1.0166	0.0144	0.0316	0.9983	0.0143	0.0330	0.9281	0.0148	0.0317
−0.35	1.1167	0.0185	0.0135	1.0622	0.0171	0.0170	1.0024	0.0162	0.0179	0.9598	0.0155	0.0179
−0.25	1.1801	0.0185	0.0127	1.0812	0.0187	0.0144	0.9960	0.0174	0.0125	0.9093	0.0179	0.0134
−0.15	1.1719	0.0190	0.0171	1.0394	0.0179	0.0161	0.9200	0.0173	0.0118	0.8912	0.0159	0.0132
−0.05	1.1107	0.0176	0.0193	0.9954	0.0173	0.0152	0.8787	0.0174	0.0148	0.7785	0.0160	0.0126
0.05	0.9923	0.0177	0.0180	0.8978	0.0164	0.0121	0.7634	0.0174	0.0148	0.6620	0.0161	0.0117
0.15	0.8744	0.0167	0.0182	0.7783	0.0169	0.0138	0.6935	0.0158	0.0140	0.5713	0.0157	0.0118
0.25	0.8167	0.0172	0.0214	0.6928	0.0167	0.0197	0.6608	0.0160	0.0156	0.6113	0.0141	0.0166
0.35	0.8138	0.0179	0.0226	0.8093	0.0169	0.0277	0.7999	0.0144	0.0208	0.7359	0.0152	0.0211
0.45	1.0154	0.0184	0.0204	1.0138	0.0194	0.0292	1.0206	0.0187	0.0214	1.0111	0.0178	0.0206
0.55	1.2641	0.0234	0.0188	1.3196	0.0214	0.0215	1.3401	0.0247	0.0164	1.3098	0.0238	0.0154
0.65	1.6232	0.0294	0.0375	1.7428	0.0296	0.0240	1.7636	0.0294	0.0335	1.7119	0.0292	0.0252
0.75	1.9132	0.0423	0.1287	1.9775	0.0466	0.1127	2.1689	0.0449	0.1660	2.0940	0.0447	0.1155
0.85	1.9060	0.0772	0.4524	1.9157	0.0790	0.3145	2.1735	0.0799	0.2976	2.1620	0.0964	0.3074

$\cos(\theta^*_{\pi^0})$	$W=(1684.0\pm6.0)$ MeV			$W=(1696.0\pm6.0)$ MeV			$W=(1708.0\pm6.0)$ MeV			$W=(1720.0\pm6.0)$ MeV		
	$d\sigma/d\Omega$ [μb/sr]	$\Delta_{\rm stat}$ [μb/sr]	$\Delta_{\rm sys}$ [μb/sr]	$d\sigma/d\Omega$ [μb/sr]	$\Delta_{\rm stat}$ [μb/sr]	$\Delta_{\rm sys}$ [μb/sr]	$d\sigma/d\Omega$ [μb/sr]	$\Delta_{\rm stat}$ [μb/sr]	$\Delta_{\rm sys}$ [μb/sr]	$d\sigma/d\Omega$ [μb/sr]	$\Delta_{\rm stat}$ [μb/sr]	$\Delta_{\rm sys}$ [μb/sr]
−0.95	1.1383	0.0474	0.1246	1.1854	0.0473	0.0860	1.2359	0.0462	0.0454	1.2571	0.0432	0.1234
−0.85	0.7674	0.0220	0.0443	0.8676	0.0253	0.0369	0.8573	0.0252	0.0432	0.9049	0.0263	0.0482
−0.75	0.8386	0.0203	0.0429	0.8389	0.0219	0.0418	0.8540	0.0242	0.0555	0.8844	0.0243	0.0454
−0.65	0.9275	0.0218	0.0577	0.8616	0.0225	0.0549	0.8975	0.0200	0.0640	0.8386	0.0223	0.0532
−0.55	0.8929	0.0161	0.0478	0.8347	0.0158	0.0440	0.7465	0.0163	0.0420	0.7197	0.0159	0.0386
−0.45	0.8646	0.0148	0.0262	0.7696	0.0142	0.0230	0.7023	0.0140	0.0226	0.6261	0.0124	0.0201
−0.35	0.8332	0.0148	0.0114	0.7525	0.0161	0.0108	0.6703	0.0136	0.0112	0.5621	0.0131	0.0094
−0.25	0.7922	0.0165	0.0094	0.7312	0.0149	0.0076	0.5848	0.0157	0.0072	0.5130	0.0147	0.0063
−0.15	0.7495	0.0158	0.0116	0.6724	0.0148	0.0090	0.5824	0.0144	0.0080	0.5204	0.0135	0.0076
−0.05	0.6421	0.0151	0.0108	0.5687	0.0143	0.0118	0.5018	0.0135	0.0088	0.4528	0.0132	0.0076
0.05	0.5548	0.0143	0.0095	0.5281	0.0132	0.0125	0.4166	0.0147	0.0085	0.4058	0.0131	0.0070
0.15	0.5389	0.0142	0.0106	0.4511	0.0147	0.0106	0.4347	0.0132	0.0085	0.4258	0.0129	0.0082
0.25	0.5590	0.0146	0.0130	0.5313	0.0147	0.0144	0.5041	0.0124	0.0091	0.5172	0.0116	0.0110
0.35	0.7196	0.0162	0.0183	0.7167	0.0157	0.0208	0.6321	0.0160	0.0140	0.6112	0.0152	0.0142
0.45	1.0262	0.0176	0.0216	0.9165	0.0181	0.0220	0.8599	0.0173	0.0235	0.8526	0.0159	0.0200
0.55	1.3312	0.0231	0.0166	1.2737	0.0212	0.0198	1.1546	0.0211	0.0248	1.0658	0.0201	0.0172
0.65	1.6840	0.0300	0.0180	1.5587	0.0286	0.0218	1.4211	0.0277	0.0260	1.3060	0.0271	0.0153
0.75	2.0362	0.0399	0.0939	1.8698	0.0439	0.0966	1.6395	0.0418	0.0922	1.4653	0.0360	0.0486
0.85	2.0687	0.0774	0.3626	1.7817	0.0721	0.2146	1.7084	0.0707	0.2126	1.2961	0.0746	0.2506

$\cos(\theta^*_{\pi^0})$	$W=(1732.0\pm6.0)$ MeV			$W=(1744.0\pm6.0)$ MeV			$W=(1756.0\pm6.0)$ MeV			$W=(1768.0\pm6.0)$ MeV		
	$d\sigma/d\Omega$ [μb/sr]	$\Delta_{\rm stat}$ [μb/sr]	$\Delta_{\rm sys}$ [μb/sr]	$d\sigma/d\Omega$ [μb/sr]	$\Delta_{\rm stat}$ [μb/sr]	$\Delta_{\rm sys}$ [μb/sr]	$d\sigma/d\Omega$ [μb/sr]	$\Delta_{\rm stat}$ [μb/sr]	$\Delta_{\rm sys}$ [μb/sr]	$d\sigma/d\Omega$ [μb/sr]	$\Delta_{\rm stat}$ [μb/sr]	$\Delta_{\rm sys}$ [μb/sr]
−0.95	1.2537	0.0414	0.1895	1.1397	0.0418	0.1576	1.2319	0.0495	0.1924	1.2399	0.0428	0.2062
−0.85	0.8891	0.0243	0.0545	0.9329	0.0257	0.0537	0.9521	0.0255	0.0527	1.0035	0.0257	0.0637
−0.75	0.8157	0.0237	0.0302	0.8203	0.0223	0.0252	0.7850	0.0215	0.0262	0.7981	0.0214	0.0207
−0.65	0.7500	0.0215	0.0372	0.7334	0.0221	0.0304	0.6785	0.0211	0.0369	0.6784	0.0218	0.0228
−0.55	0.6237	0.0151	0.0287	0.5637	0.0142	0.0235	0.5229	0.0136	0.0262	0.5071	0.0137	0.0171
−0.45	0.5179	0.0121	0.0135	0.4979	0.0113	0.0111	0.4572	0.0102	0.0113	0.4199	0.0101	0.0075
−0.35	0.4953	0.0122	0.0060	0.4425	0.0112	0.0053	0.3872	0.0112	0.0051	0.3645	0.0098	0.0041
−0.25	0.5113	0.0126	0.0056	0.4146	0.0120	0.0069	0.4090	0.0116	0.0055	0.3540	0.0119	0.0051
−0.15	0.4491	0.0126	0.0078	0.4145	0.0123	0.0112	0.4054	0.0120	0.0065	0.3753	0.0116	0.0075
−0.05	0.3980	0.0124	0.0090	0.3807	0.0106	0.0110	0.3707	0.0107	0.0065	0.3622	0.0103	0.0073
0.05	0.3607	0.0124	0.0077	0.3600	0.0124	0.0092	0.3756	0.0110	0.0069	0.3405	0.0123	0.0060
0.15	0.3860	0.0110	0.0074	0.3818	0.0121	0.0096	0.3506	0.0115	0.0061	0.3618	0.0120	0.0058
0.25	0.4479	0.0124	0.0098	0.4379	0.0129	0.0114	0.4320	0.0120	0.0074	0.3985	0.0123	0.0067
0.35	0.5897	0.0138	0.0158	0.5303	0.0134	0.0147	0.4647	0.0147	0.0099	0.4711	0.0133	0.0123
0.45	0.7527	0.0162	0.0208	0.6666	0.0160	0.0190	0.6312	0.0151	0.0170	0.5716	0.0152	0.0217
0.55	0.9744	0.0197	0.0173	0.8693	0.0189	0.0184	0.8261	0.0184	0.0201	0.7230	0.0186	0.0245
0.65	1.1268	0.0234	0.0131	1.0407	0.0246	0.0229	0.9770	0.0250	0.0125	0.8866	0.0229	0.0135
0.75	1.3432	0.0373	0.0606	1.1960	0.0310	0.0832	1.1321	0.0330	0.0230	1.0393	0.0373	0.0188
0.85	1.3038	0.0598	0.1741	1.1895	0.0669	0.1724	1.2448	0.0593	0.2876	1.2289	0.0712	0.3464

$\cos(\theta^*_{\pi^0})$	$W=(1780.0\pm6.0)$ MeV			$W=(1792.0\pm6.0)$ MeV			$W=(1804.0\pm6.0)$ MeV			$W=(1816.0\pm6.0)$ MeV		
	$d\sigma/d\Omega$ [μb/sr]	Δ_{stat} [μb/sr]	Δ_{sys} [μb/sr]	$d\sigma/d\Omega$ [μb/sr]	Δ_{stat} [μb/sr]	Δ_{sys} [μb/sr]	$d\sigma/d\Omega$ [μb/sr]	Δ_{stat} [μb/sr]	Δ_{sys} [μb/sr]	$d\sigma/d\Omega$ [μb/sr]	Δ_{stat} [μb/sr]	Δ_{sys} [μb/sr]
−0.95	1.1153	0.0349	0.1181	1.2754	0.0401	0.1151	1.2929	0.0375	0.0138	1.3291	0.0440	0.0309
−0.85	1.0661	0.0288	0.0720	1.0943	0.0266	0.0569	1.1943	0.0309	0.0417	1.2632	0.0309	0.0653
−0.75	0.8258	0.0226	0.0341	0.8694	0.0221	0.0324	0.8671	0.0232	0.0325	0.9233	0.0218	0.0522
−0.65	0.6855	0.0189	0.0270	0.6955	0.0179	0.0269	0.6965	0.0190	0.0289	0.7366	0.0211	0.0368
−0.55	0.4783	0.0131	0.0185	0.4823	0.0144	0.0170	0.4621	0.0146	0.0209	0.4818	0.0134	0.0189
−0.45	0.3864	0.0102	0.0089	0.3918	0.0103	0.0099	0.3679	0.0097	0.0123	0.3680	0.0107	0.0081
−0.35	0.3406	0.0099	0.0041	0.3512	0.0107	0.0074	0.3431	0.0102	0.0075	0.3467	0.0115	0.0044
−0.25	0.3512	0.0111	0.0058	0.3248	0.0125	0.0077	0.3501	0.0120	0.0076	0.3658	0.0126	0.0052
−0.15	0.3837	0.0106	0.0123	0.3517	0.0128	0.0095	0.3834	0.0112	0.0104	0.3743	0.0120	0.0077
−0.05	0.3479	0.0108	0.0139	0.3816	0.0115	0.0106	0.3472	0.0136	0.0103	0.3949	0.0143	0.0090
0.05	0.3411	0.0115	0.0118	0.3415	0.0118	0.0084	0.3462	0.0120	0.0091	0.3708	0.0137	0.0071
0.15	0.3415	0.0115	0.0094	0.3195	0.0128	0.0060	0.3333	0.0132	0.0073	0.3443	0.0119	0.0060
0.25	0.3856	0.0123	0.0093	0.3729	0.0119	0.0073	0.3267	0.0125	0.0067	0.3286	0.0130	0.0087
0.35	0.4419	0.0139	0.0119	0.3821	0.0141	0.0119	0.3941	0.0148	0.0116	0.3554	0.0146	0.0166
0.45	0.5316	0.0151	0.0198	0.4637	0.0163	0.0178	0.4550	0.0147	0.0217	0.4345	0.0142	0.0257
0.55	0.6590	0.0174	0.0254	0.6453	0.0178	0.0190	0.6333	0.0181	0.0299	0.5997	0.0175	0.0278
0.65	0.8577	0.0254	0.0118	0.8439	0.0247	0.0134	0.8588	0.0248	0.0259	0.8130	0.0270	0.0137
0.75	1.1176	0.0354	0.0194	1.1866	0.0366	0.0554	1.0993	0.0434	0.0520	1.1626	0.0345	0.0325
0.85	1.1635	0.0571	0.3538	1.2223	0.0594	0.3037	1.3064	0.0613	0.2968	1.3070	0.0771	0.3708

$\cos(\theta^*_{\pi^0})$	$W=(1828.0\pm6.0)$ MeV			$W=(1840.0\pm6.0)$ MeV			$W=(1852.0\pm6.0)$ MeV			$W=(1864.0\pm6.0)$ MeV		
	$d\sigma/d\Omega$ [μb/sr]	Δ_{stat} [μb/sr]	Δ_{sys} [μb/sr]	$d\sigma/d\Omega$ [μb/sr]	Δ_{stat} [μb/sr]	Δ_{sys} [μb/sr]	$d\sigma/d\Omega$ [μb/sr]	Δ_{stat} [μb/sr]	Δ_{sys} [μb/sr]	$d\sigma/d\Omega$ [μb/sr]	Δ_{stat} [μb/sr]	Δ_{sys} [μb/sr]
−0.95	1.3522	0.0393	0.0781	1.3057	0.0438	0.1509	1.3384	0.0505	0.0802	1.3215	0.0451	0.1272
−0.85	1.3062	0.0350	0.0492	1.2853	0.0333	0.0440	1.3941	0.0358	0.0303	1.3404	0.0409	0.0396
−0.75	1.0010	0.0243	0.0341	0.9577	0.0264	0.0141	1.0017	0.0292	0.0173	1.0629	0.0323	0.0175
−0.65	0.8114	0.0212	0.0375	0.7727	0.0214	0.0209	0.7762	0.0282	0.0209	0.8961	0.0317	0.0256
−0.55	0.4820	0.0169	0.0272	0.4635	0.0140	0.0187	0.4685	0.0182	0.0134	0.4948	0.0199	0.0146
−0.45	0.3882	0.0116	0.0201	0.3945	0.0101	0.0197	0.3701	0.0113	0.0083	0.3642	0.0111	0.0100
−0.35	0.3479	0.0125	0.0130	0.3355	0.0137	0.0164	0.3392	0.0154	0.0060	0.3257	0.0174	0.0105
−0.25	0.3640	0.0149	0.0092	0.3614	0.0150	0.0157	0.3728	0.0176	0.0078	0.3719	0.0223	0.0128
−0.15	0.4071	0.0138	0.0083	0.4144	0.0169	0.0179	0.4663	0.0161	0.0121	0.4307	0.0202	0.0133
−0.05	0.4120	0.0130	0.0081	0.4050	0.0166	0.0175	0.4238	0.0185	0.0104	0.4514	0.0213	0.0116
0.05	0.3738	0.0152	0.0102	0.3863	0.0182	0.0168	0.3949	0.0167	0.0080	0.3588	0.0223	0.0072
0.15	0.3451	0.0125	0.0118	0.3176	0.0160	0.0160	0.3381	0.0149	0.0069	0.3079	0.0182	0.0061
0.25	0.3244	0.0141	0.0113	0.3341	0.0154	0.0203	0.3187	0.0167	0.0102	0.2760	0.0207	0.0088
0.35	0.3689	0.0138	0.0158	0.3600	0.0168	0.0232	0.3073	0.0201	0.0195	0.2562	0.0185	0.0180
0.45	0.3859	0.0176	0.0221	0.3569	0.0175	0.0204	0.3396	0.0208	0.0317	0.3094	0.0157	0.0335
0.55	0.5208	0.0222	0.0315	0.5776	0.0223	0.0241	0.4747	0.0222	0.0387	0.4521	0.0229	0.0469
0.65	0.8633	0.0244	0.0387	0.8395	0.0259	0.0206	0.7852	0.0358	0.0289	0.7917	0.0287	0.0417
0.75	1.2004	0.0452	0.0619	1.2352	0.0434	0.0536	1.2272	0.0419	0.0463	1.2748	0.0516	0.0409
0.85	1.3731	0.0823	0.3310	1.5974	0.0781	0.3661	1.6886	0.0856	0.4010	1.6812	0.0896	0.4807

$\cos(\theta^*_{\pi^0})$	$W=(1876.0\pm6.0)$ MeV		
	$d\sigma/d\Omega$ [μb/sr]	Δ_{stat} [μb/sr]	Δ_{sys} [μb/sr]
−0.95	1.3586	0.0570	0.1062
−0.85	1.3364	0.0409	0.0428
−0.75	0.9773	0.0333	0.0333
−0.65	0.8086	0.0299	0.0438
−0.55	0.4285	0.0159	0.0209
−0.45	0.3294	0.0118	0.0112
−0.35	0.3575	0.0153	0.0117
−0.25	0.4010	0.0222	0.0136
−0.15	0.4590	0.0239	0.0149
−0.05	0.4468	0.0255	0.0139
0.05	0.3353	0.0228	0.0117
0.15	0.3248	0.0168	0.0147
0.25	0.2623	0.0244	0.0162
0.35	0.2904	0.0175	0.0284
0.45	0.2877	0.0172	0.0336
0.55	0.3885	0.0203	0.0283
0.65	0.7104	0.0298	0.0141
0.75	1.4757	0.0538	0.0415
0.85	1.5597	0.1343	0.2716

E.2 Polarized Results for Single π^0 from the A2 Data

E.2.1 Observables for $\gamma d \to \pi^0 p(n)$ as a Function of E_γ

E_γ [MeV]	ΔE_γ [MeV]	E	Δ_{stat}	Δ_{sys}	$\sigma_{1/2}$ [μb]	Δ_{stat} [μb]	Δ_{sys} [μb]	$\sigma_{3/2}$ [μb]	Δ_{stat} [μb]	Δ_{sys} [μb]
433.0	11.0	−0.4540	0.0085	0.0617	50.1601	0.7332	8.6198	133.9163	0.7344	16.6603
455.0	11.0	−0.4352	0.0079	0.0608	32.7078	0.4320	5.6317	83.2171	0.4327	10.3250
477.0	11.0	−0.4113	0.0083	0.0467	30.0904	0.3994	3.4543	71.9513	0.4001	7.9316
499.0	11.0	−0.3615	0.0077	0.0423	27.5582	0.3129	3.2116	58.5253	0.3135	6.4537
521.0	11.0	−0.3020	0.0096	0.0342	25.6740	0.3335	2.8577	47.6964	0.3340	5.2703
543.0	11.0	−0.2601	0.0088	0.0292	23.1349	0.2600	2.5581	39.2849	0.2604	4.3385
565.0	11.0	−0.1824	0.0092	0.0230	22.1685	0.2387	2.4929	31.9213	0.2390	3.5154
587.0	11.0	−0.0882	0.0108	0.0122	22.0326	0.2510	2.4413	26.2242	0.2512	2.8918
609.0	11.0	−0.0304	0.0105	0.0084	21.3763	0.2222	2.3657	22.6581	0.2223	2.5149
631.0	11.0	0.0152	0.0116	0.0070	21.1495	0.2329	2.3433	20.4732	0.2329	2.2648
653.0	11.0	0.1309	0.0090	0.0170	23.5405	0.1810	2.6172	18.0630	0.1809	2.0217
675.0	11.0	0.1277	0.0086	0.0170	25.0612	0.1838	2.8161	19.3667	0.1837	2.2055
697.0	11.0	0.2125	0.0079	0.0244	29.5255	0.1864	3.2600	19.1546	0.1861	2.1181
719.0	11.0	0.2009	0.0078	0.0228	31.8152	0.2007	3.5295	21.1200	0.2004	2.3278
741.0	11.0	0.1856	0.0074	0.0212	33.9484	0.2053	3.7652	23.2608	0.2050	2.5640
763.0	11.0	0.1545	0.0067	0.0176	34.1366	0.1915	3.7891	24.9447	0.1912	2.7557
785.0	11.0	0.1074	0.0076	0.0122	31.5739	0.2110	3.5115	25.4137	0.2107	2.8173
807.0	11.0	0.0907	0.0072	0.0108	29.4908	0.1904	3.2682	24.5438	0.1902	2.7046
829.0	11.0	0.0682	0.0072	0.0091	26.5310	0.1756	2.9249	23.1084	0.1755	2.5456
851.0	11.0	0.0467	0.0083	0.0075	23.7573	0.1831	2.6173	21.5992	0.1830	2.3805
873.0	11.0	0.0391	0.0086	0.0061	21.8587	0.1768	2.4087	20.1847	0.1768	2.2220
895.0	11.0	−0.0211	0.0094	0.0052	18.7478	0.1770	2.0750	19.5268	0.1770	2.1715
917.0	11.0	−0.0635	0.0085	0.0090	17.2534	0.1539	1.9075	19.5515	0.1540	2.1699
939.0	11.0	−0.1062	0.0097	0.0118	15.9950	0.1701	1.7617	19.7855	0.1703	2.1769
961.0	11.0	−0.1485	0.0099	0.0165	15.5505	0.1773	1.7167	20.9537	0.1776	2.3145
983.0	11.0	−0.2179	0.0083	0.0243	14.5894	0.1510	1.6145	22.7070	0.1515	2.5013
1005.0	11.0	−0.2434	0.0080	0.0274	14.0262	0.1457	1.5736	23.0497	0.1463	2.5515
1027.0	11.0	−0.2101	0.0081	0.0240	14.7646	0.1488	1.6644	22.6194	0.1493	2.5141
1049.0	11.0	−0.2609	0.0086	0.0305	13.2107	0.1504	1.5484	22.5646	0.1510	2.5588
1071.0	11.0	−0.2059	0.0091	0.0239	13.4460	0.1520	1.5297	20.4147	0.1525	2.2756
1093.0	11.0	−0.1614	0.0093	0.0199	12.7714	0.1398	1.5389	17.6941	0.1402	2.0453
1115.0	11.0	−0.1206	0.0142	0.0161	11.8783	0.1892	1.4926	15.1391	0.1897	1.8136
1137.0	11.0	−0.0470	0.0131	0.0061	11.8262	0.1612	1.3123	12.9829	0.1615	1.4339
1159.0	11.0	−0.0609	0.0119	0.0073	10.8592	0.1363	1.2091	12.2534	0.1365	1.3735
1181.0	11.0	−0.0377	0.0128	0.0060	9.9703	0.1315	1.0975	10.7365	0.1317	1.1839
1203.0	11.0	−0.0505	0.0148	0.0068	8.9135	0.1382	1.0278	9.8571	0.1384	1.1189
1225.0	11.0	−0.0644	0.0149	0.0082	8.4485	0.1330	0.9335	9.6010	0.1333	1.0582
1247.0	11.0	−0.0566	0.0172	0.0062	8.0724	0.1485	0.8883	9.0409	0.1487	0.9947
1269.0	11.0	−0.1272	0.0172	0.0165	7.1721	0.1400	0.8270	9.2493	0.1404	1.0360
1291.0	11.0	−0.0895	0.0212	0.0107	7.2739	0.1692	0.8507	8.7086	0.1697	1.0049
1313.0	11.0	−0.1907	0.0181	0.0221	6.5581	0.1449	0.7364	9.6438	0.1456	1.0708
1335.0	11.0	−0.0765	0.0222	0.0096	7.4624	0.1793	0.8351	8.6921	0.1797	0.9686

E.2.2 Observables for $\gamma d \to \pi^0 p(n)$ as a Function of W

W [MeV]	ΔW [MeV]	E	Δ_{stat}	Δ_{sys}	$\sigma_{1/2}$ [μb]	Δ_{stat} [μb]	Δ_{sys} [μb]	$\sigma_{3/2}$ [μb]	Δ_{stat} [μb]	Δ_{sys} [μb]
1321.0	9.0	−0.4103	0.0077	0.0508	31.1067	0.3833	4.1714	74.2960	0.3840	8.4541
1339.0	9.0	−0.3693	0.0079	0.0425	26.6833	0.3162	3.1057	57.8031	0.3167	6.3952
1357.0	9.0	−0.2977	0.0084	0.0343	24.7678	0.2803	2.7779	45.5695	0.2807	5.0181
1375.0	9.0	−0.2416	0.0084	0.0275	22.8700	0.2408	2.6718	37.2768	0.2412	4.2661
1393.0	9.0	−0.1317	0.0090	0.0160	22.1131	0.2199	2.4589	28.7368	0.2201	3.1922
1411.0	9.0	−0.0512	0.0099	0.0093	21.2755	0.2132	2.3627	23.5101	0.2133	2.5864
1429.0	9.0	0.0503	0.0095	0.0099	22.2916	0.1944	2.4815	20.1166	0.1943	2.2464
1447.0	9.0	0.1267	0.0086	0.0160	24.2956	0.1799	2.6868	18.7926	0.1798	2.0783
1465.0	9.0	0.1744	0.0076	0.0204	28.0310	0.1749	3.1000	19.6573	0.1746	2.1634
1483.0	9.0	0.2027	0.0069	0.0230	33.0812	0.1830	3.6812	21.8741	0.1827	2.4141
1501.0	9.0	0.1942	0.0063	0.0219	36.8663	0.1883	4.1975	24.7981	0.1880	2.8087
1519.0	9.0	0.1264	0.0062	0.0148	34.4665	0.1830	3.8019	26.6813	0.1827	2.9368
1537.0	9.0	0.1078	0.0064	0.0136	31.1299	0.1734	3.4562	25.0448	0.1732	2.8141
1555.0	9.0	0.0780	0.0069	0.0104	26.3118	0.1631	2.9328	22.4856	0.1629	2.5316
1573.0	9.0	0.0250	0.0075	0.0063	21.9423	0.1571	2.4338	20.8406	0.1570	2.3262
1591.0	9.0	−0.0060	0.0081	0.0035	18.8990	0.1506	2.0818	19.1056	0.1506	2.1035
1609.0	9.0	−0.1031	0.0083	0.0124	15.7785	0.1432	1.7526	19.3812	0.1434	2.1354
1627.0	9.0	−0.2106	0.0080	0.0243	14.1441	0.1394	1.5908	21.6649	0.1398	2.3946
1645.0	9.0	−0.2321	0.0074	0.0261	14.3789	0.1351	1.6216	23.0783	0.1356	2.5646
1663.0	9.0	−0.2288	0.0070	0.0255	14.7391	0.1309	1.6337	23.4807	0.1314	2.5898
1681.0	9.0	−0.1959	0.0072	0.0218	14.8652	0.1290	1.6679	22.0590	0.1295	2.4731
1699.0	9.0	−0.1806	0.0080	0.0203	13.4559	0.1283	1.5295	19.3368	0.1288	2.1978
1717.0	9.0	−0.0920	0.0092	0.0108	12.7477	0.1258	1.5122	15.3127	0.1261	1.7923
1735.0	9.0	−0.0903	0.0108	0.0105	10.3600	0.1212	1.1632	12.3968	0.1215	1.3971
1753.0	9.0	−0.0635	0.0123	0.0077	8.7901	0.1141	0.9788	9.9778	0.1143	1.1056
1771.0	9.0	−0.0733	0.0136	0.0112	7.7299	0.1125	0.9249	8.9414	0.1128	1.0393
1789.0	9.0	−0.1054	0.0149	0.0140	7.1323	0.1179	0.9091	8.8200	0.1183	1.0871
1807.0	9.0	−0.1366	0.0161	0.0176	7.0048	0.1294	0.8436	9.2196	0.1298	1.0696
1825.0	9.0	−0.2547	0.0177	0.0302	6.1907	0.1444	0.7117	10.4105	0.1451	1.1593
1843.0	9.0	−0.1909	0.0188	0.0210	6.9658	0.1589	0.7686	10.2434	0.1596	1.1300
1861.0	9.0	−0.1749	0.0207	0.0214	7.1191	0.1739	0.8606	10.1239	0.1746	1.1722
1879.0	9.0	−0.2299	0.0242	0.0352	6.4196	0.1908	1.1418	10.1297	0.1918	1.6089
1897.0	9.0	−0.2020	0.0316	0.0377	6.4830	0.2382	1.3953	9.6119	0.2394	1.8357
1915.0	9.0	−0.3550	0.0469	0.0776	5.7605	0.3738	1.6944	11.6306	0.3763	2.4888

Angular Distributions

	$W=(1321.0\pm9.0)$ MeV			$W=(1339.0\pm9.0)$ MeV			$W=(1357.0\pm9.0)$ MeV			$W=(1375.0\pm9.0)$ MeV		
$\cos(\theta^*_{\pi^0})$	E	Δ_{stat}	Δ_{sys}	E	Δ_{stat}	Δ_{sys}	E	Δ_{stat}	Δ_{sys}	E	Δ_{stat}	Δ_{sys}
−0.90	−0.3608	0.1686	0.2751	0.1826	0.1378	0.1152	0.3985	0.1206	0.2029	0.1969	0.1029	0.1030
−0.70	−0.1693	0.0341	0.0221	−0.2865	0.0364	0.0263	−0.1149	0.0376	0.0263	0.1878	0.0367	0.0292
−0.50	−0.4987	0.0191	0.0126	−0.2923	0.0197	0.0098	−0.2375	0.0213	0.0114	−0.0727	0.0215	0.0032
−0.30	−0.4416	0.0169	0.0138	−0.3392	0.0176	0.0133	−0.3085	0.0194	0.0142	−0.2263	0.0196	0.0068
−0.10	−0.4431	0.0155	0.0228	−0.4644	0.0164	0.0200	−0.3563	0.0175	0.0135	−0.3057	0.0181	0.0074
0.10	−0.4257	0.0166	0.0323	−0.5187	0.0172	0.0267	−0.3935	0.0183	0.0190	−0.4798	0.0191	0.0092
0.30	−0.3114	0.0233	0.0430	−0.3620	0.0215	0.0335	−0.3679	0.0216	0.0386	−0.2979	0.0213	0.0115
0.50	−0.2666	0.0768	0.0867	−0.0080	0.0557	0.0160	−0.2707	0.0446	0.0647	−0.2064	0.0376	0.0180
0.70	1.2518	4.7324	1.0331	4.9750	5.8393	3.2433	2.8009	1.6436	1.4126	0.5673	0.3108	0.2015
0.90	−7.4181	40.4657	5.2720	−0.3439	1.8704	0.8317	4.4811	17.2332	2.5834	−5.4929	30.8331	3.7792

	$W=(1393.0\pm9.0)$ MeV			$W=(1411.0\pm9.0)$ MeV			$W=(1429.0\pm9.0)$ MeV			$W=(1447.0\pm9.0)$ MeV		
$\cos(\theta^*_{\pi^0})$	E	Δ_{stat}	Δ_{sys}	E	Δ_{stat}	Δ_{sys}	E	Δ_{stat}	Δ_{sys}	E	Δ_{stat}	Δ_{sys}
−0.90	0.5673	0.0927	0.1848	0.4561	0.0911	0.1138	0.5680	0.0784	0.1316	0.8865	0.0720	0.1069
−0.70	0.2838	0.0394	0.0182	0.2840	0.0420	0.0177	0.6279	0.0419	0.0296	0.5509	0.0387	0.0156
−0.50	0.0063	0.0229	0.0024	0.2123	0.0258	0.0042	0.2886	0.0246	0.0129	0.3236	0.0229	0.0071
−0.30	−0.1706	0.0210	0.0043	−0.0306	0.0226	0.0093	0.0191	0.0223	0.0096	0.1257	0.0209	0.0133
−0.10	−0.1850	0.0197	0.0012	−0.1838	0.0216	0.0103	−0.0567	0.0209	0.0106	0.0595	0.0189	0.0111
0.10	−0.2541	0.0203	0.0081	−0.2225	0.0225	0.0124	−0.0700	0.0218	0.0097	−0.0762	0.0202	0.0137
0.30	−0.2610	0.0232	0.0146	−0.1975	0.0252	0.0152	−0.1698	0.0248	0.0172	0.0677	0.0217	0.0057
0.50	−0.1205	0.0364	0.0124	0.0017	0.0394	0.0126	−0.1324	0.0352	0.0201	−0.0805	0.0304	0.0191
0.70	0.1923	0.1736	0.0295	0.5929	0.2555	0.1666	0.6771	0.1502	0.0860	0.1303	0.0985	0.0324
0.90	−0.4127	1.1301	0.1656	2.1050	2.3373	0.1519	6.0742	7.0737	1.1590	−2.1262	1.0818	0.3967

	$W=(1465.0\pm9.0)$ MeV			$W=(1483.0\pm9.0)$ MeV			$W=(1501.0\pm9.0)$ MeV			$W=(1519.0\pm9.0)$ MeV		
$\cos(\theta^*_{\pi^0})$	E	Δ_{stat}	Δ_{sys}	E	Δ_{stat}	Δ_{sys}	E	Δ_{stat}	Δ_{sys}	E	Δ_{stat}	Δ_{sys}
−0.90	0.9864	0.0589	0.0959	0.8326	0.0489	0.0480	0.6714	0.0384	0.0027	0.5944	0.0334	0.0117
−0.70	0.5725	0.0341	0.0086	0.6183	0.0321	0.0121	0.4542	0.0273	0.0179	0.2223	0.0245	0.0131
−0.50	0.2867	0.0202	0.0094	0.3769	0.0191	0.0073	0.3062	0.0172	0.0095	0.2324	0.0167	0.0042
−0.30	0.2297	0.0188	0.0036	0.1782	0.0172	0.0098	0.1630	0.0163	0.0057	0.0708	0.0161	0.0062
−0.10	0.0799	0.0168	0.0114	0.1189	0.0157	0.0091	0.1409	0.0147	0.0054	0.0779	0.0145	0.0082
0.10	0.0635	0.0177	0.0051	0.0852	0.0160	0.0053	0.0687	0.0148	0.0057	0.0546	0.0149	0.0055
0.30	0.0207	0.0192	0.0106	0.1120	0.0173	0.0049	0.1629	0.0159	0.0077	0.0614	0.0160	0.0023
0.50	0.1064	0.0261	0.0136	0.0471	0.0215	0.0070	0.1609	0.0196	0.0105	0.1230	0.0190	0.0055
0.70	−0.0049	0.0726	0.0006	0.3782	0.0567	0.0352	0.2058	0.0417	0.0048	0.1820	0.0400	0.0108
0.90	−2.8440	1.0178	0.7524	12.6498	71.4942	10.3370	0.9510	3.8292	0.8950	1.6331	0.7833	0.0945

	$W=(1537.0\pm9.0)$ MeV			$W=(1555.0\pm9.0)$ MeV			$W=(1573.0\pm9.0)$ MeV			$W=(1591.0\pm9.0)$ MeV		
$\cos(\theta^*_{\pi^0})$	E	Δ_{stat}	Δ_{sys}	E	Δ_{stat}	Δ_{sys}	E	Δ_{stat}	Δ_{sys}	E	Δ_{stat}	Δ_{sys}
−0.90	0.3258	0.0295	0.0066	0.2884	0.0282	0.0059	0.1993	0.0259	0.0019	0.1854	0.0254	0.0039
−0.70	0.1910	0.0235	0.0044	−0.0355	0.0234	0.0030	−0.1554	0.0231	0.0090	−0.2172	0.0226	0.0124
−0.50	0.0964	0.0167	0.0025	0.0353	0.0175	0.0036	−0.1007	0.0180	0.0018	−0.1967	0.0189	0.0072
−0.30	0.1126	0.0167	0.0061	0.0015	0.0180	0.0027	−0.0542	0.0192	0.0043	−0.1445	0.0210	0.0042
−0.10	0.0065	0.0154	0.0097	−0.0019	0.0167	0.0068	−0.1035	0.0190	0.0018	−0.1161	0.0205	0.0041
0.10	0.0798	0.0154	0.0074	0.0535	0.0176	0.0070	0.0033	0.0203	0.0074	0.0019	0.0224	0.0050
0.30	0.0996	0.0167	0.0093	0.0915	0.0188	0.0111	0.1502	0.0226	0.0063	0.2167	0.0263	0.0072
0.50	0.1477	0.0206	0.0066	0.2749	0.0231	0.0148	0.4540	0.0279	0.0064	0.4340	0.0341	0.0176
0.70	0.2870	0.0420	0.0189	0.4785	0.0440	0.0213	0.4817	0.0525	0.0263	0.7373	0.0600	0.0721
0.90	−0.5862	0.6657	0.0844	16.6420	167.7133	15.4052	−0.9994	0.6705	0.4069	4.5804	6.5334	2.4917

	$W=(1609.0\pm9.0)$ MeV			$W=(1627.0\pm9.0)$ MeV			$W=(1645.0\pm9.0)$ MeV			$W=(1663.0\pm9.0)$ MeV		
$\cos(\theta^*_{\pi^0})$	E	Δ_{stat}	Δ_{sys}	E	Δ_{stat}	Δ_{sys}	E	Δ_{stat}	Δ_{sys}	E	Δ_{stat}	Δ_{sys}
−0.90	−0.1612	0.0251	0.0121	−0.1909	0.0236	0.0072	−0.2131	0.0224	0.0120	−0.3349	0.0225	0.0238
−0.70	−0.3206	0.0228	0.0216	−0.4807	0.0212	0.0254	−0.4991	0.0197	0.0360	−0.5133	0.0195	0.0350
−0.50	−0.2998	0.0189	0.0060	−0.5003	0.0193	0.0149	−0.5740	0.0185	0.0145	−0.4979	0.0180	0.0069
−0.30	−0.3718	0.0224	0.0059	−0.3339	0.0217	0.0022	−0.4681	0.0212	0.0073	−0.4363	0.0212	0.0113
−0.10	−0.0822	0.0216	0.0017	−0.2471	0.0221	0.0055	−0.1748	0.0211	0.0037	−0.1878	0.0211	0.0053
0.10	−0.0500	0.0252	0.0013	−0.0632	0.0245	0.0131	−0.0266	0.0243	0.0039	0.0715	0.0230	0.0056
0.30	0.2506	0.0277	0.0103	0.1293	0.0276	0.0116	0.1614	0.0237	0.0076	0.1087	0.0209	0.0065
0.50	0.4425	0.0341	0.0277	0.2219	0.0293	0.0092	0.1865	0.0246	0.0098	−0.0307	0.0209	0.0017
0.70	0.2592	0.0466	0.0234	0.1313	0.0344	0.0069	−0.1603	0.0286	0.0103	−0.1093	0.0253	0.0088
0.90	0.4627	2.0253	0.4544	1.8235	1.5900	2.1159	−0.8026	1.1685	0.6677	0.1678	0.1996	0.0480

	$W=(1681.0\pm9.0)$ MeV			$W=(1699.0\pm9.0)$ MeV			$W=(1717.0\pm9.0)$ MeV			$W=(1735.0\pm9.0)$ MeV		
$\cos(\theta^*_{\pi^0})$	E	Δ_{stat}	Δ_{sys}	E	Δ_{stat}	Δ_{sys}	E	Δ_{stat}	Δ_{sys}	E	Δ_{stat}	Δ_{sys}
−0.90	−0.1338	0.0222	0.0023	−0.2283	0.0256	0.0129	−0.1888	0.0295	0.0091	−0.0893	0.0318	0.0080
−0.70	−0.4736	0.0194	0.0140	−0.5886	0.0231	0.0191	−0.4173	0.0252	0.0064	−0.4445	0.0299	0.0155
−0.50	−0.5622	0.0193	0.0116	−0.6207	0.0225	0.0146	−0.6414	0.0263	0.0276	−0.5218	0.0322	0.0250
−0.30	−0.4607	0.0230	0.0189	−0.4259	0.0259	0.0363	−0.1707	0.0312	0.0207	−0.2423	0.0368	0.0171
−0.10	−0.1563	0.0221	0.0154	0.0027	0.0263	0.0042	−0.0367	0.0302	0.0058	−0.0940	0.0362	0.0053
0.10	0.1150	0.0239	0.0121	0.1981	0.0268	0.0143	0.2777	0.0303	0.0261	0.0762	0.0349	0.0099
0.30	0.0900	0.0216	0.0087	0.1752	0.0227	0.0140	0.2290	0.0258	0.0103	0.2351	0.0297	0.0099
0.50	0.0941	0.0204	0.0066	0.0841	0.0214	0.0036	0.1195	0.0242	0.0104	0.1104	0.0286	0.0218
0.70	−0.1665	0.0245	0.0035	−0.1969	0.0270	0.0086	0.0120	0.0308	0.0009	0.1360	0.0372	0.0091
0.90	0.1166	0.1609	0.0213	−0.2581	0.1300	0.0125	0.4977	0.1318	0.0332	−0.0769	1.5015	0.2713

$\cos(\theta^*_{\pi^0})$	$W=(1753.0\pm9.0)$ MeV			$W=(1771.0\pm9.0)$ MeV			$W=(1789.0\pm9.0)$ MeV			$W=(1807.0\pm9.0)$ MeV		
	E	Δ_{stat}	Δ_{sys}	E	Δ_{stat}	Δ_{sys}	E	Δ_{stat}	Δ_{sys}	E	Δ_{stat}	Δ_{sys}
−0.90	−0.0555	0.0341	0.0053	0.0713	0.0347	0.0061	0.1270	0.0364	0.0151	0.0604	0.0366	0.0070
−0.70	−0.4045	0.0353	0.0414	−0.3258	0.0371	0.0359	−0.4638	0.0381	0.0583	−0.2405	0.0370	0.0247
−0.50	−0.4793	0.0372	0.0078	−0.5401	0.0444	0.0133	−0.5144	0.0480	0.0102	−0.3279	0.0520	0.0149
−0.30	−0.3401	0.0439	0.0111	−0.2654	0.0473	0.0095	−0.2333	0.0523	0.0212	−0.4111	0.0634	0.0196
−0.10	0.0627	0.0410	0.0032	−0.0773	0.0414	0.0052	−0.1163	0.0465	0.0049	−0.3331	0.0488	0.0116
0.10	0.3218	0.0383	0.0098	0.1667	0.0407	0.0029	0.0929	0.0450	0.0042	−0.0194	0.0491	0.0031
0.30	0.1264	0.0331	0.0101	0.1648	0.0376	0.0084	0.1727	0.0436	0.0071	0.0112	0.0493	0.0143
0.50	0.1846	0.0333	0.0088	0.1047	0.0430	0.0113	0.0883	0.0474	0.0088	0.0576	0.0529	0.0021
0.70	0.0170	0.0428	0.0066	0.0107	0.0491	0.0160	0.0398	0.0515	0.0033	0.0289	0.0615	0.0031
0.90	−1.1688	0.1811	0.0621	−0.3032	0.1748	0.1062	−0.6581	0.2474	0.2375	0.1121	0.1451	0.0222

$\cos(\theta^*_{\pi^0})$	$W=(1825.0\pm9.0)$ MeV			$W=(1843.0\pm9.0)$ MeV			$W=(1861.0\pm9.0)$ MeV			$W=(1879.0\pm9.0)$ MeV		
	E	Δ_{stat}	Δ_{sys}	E	Δ_{stat}	Δ_{sys}	E	Δ_{stat}	Δ_{sys}	E	Δ_{stat}	Δ_{sys}
−0.90	0.0417	0.0357	0.0070	0.0545	0.0360	0.0065	0.2510	0.0402	0.0264	−0.0769	0.0461	0.0070
−0.70	−0.4962	0.0397	0.0221	−0.5220	0.0452	0.0556	−0.3953	0.0495	0.0436	−0.5551	0.0597	0.0238
−0.50	−0.7198	0.0662	0.0183	−0.2643	0.0671	0.0170	−0.1740	0.0690	0.0059	−0.3765	0.0739	0.0604
−0.30	−0.5936	0.0713	0.0126	−0.2914	0.0732	0.0230	−0.0702	0.0740	0.0173	0.0697	0.0954	0.0134
−0.10	−0.2259	0.0556	0.0048	−0.1822	0.0573	0.0156	−0.5558	0.0662	0.0023	−0.4151	0.0776	0.0369
0.10	−0.3843	0.0578	0.0238	−0.3995	0.0583	0.0467	−0.3611	0.0681	0.0423	−0.4235	0.0813	0.0852
0.30	−0.0363	0.0575	0.0095	−0.0443	0.0640	0.0102	0.0067	0.0796	0.0170	−0.2052	0.0955	0.0544
0.50	0.0078	0.0604	0.0029	−0.1410	0.0774	0.0153	−0.3865	0.0869	0.0950	0.3311	0.1022	0.1086
0.70	−0.0575	0.0623	0.0130	0.0988	0.0610	0.0126	−0.0164	0.0709	0.0214	−0.1333	0.0795	0.0295
0.90	0.3104	0.1253	0.0339	−0.2019	0.1579	0.0582	−0.2629	0.1230	0.0391	−0.1803	0.1487	0.0167

$\cos(\theta^*_{\pi^0})$	$W=(1897.0\pm9.0)$ MeV			$W=(1915.0\pm9.0)$ MeV		
	E	Δ_{stat}	Δ_{sys}	E	Δ_{stat}	Δ_{sys}
−0.90	0.0246	0.0602	0.0019	−0.2656	0.0969	0.0265
−0.70	−0.3783	0.0748	0.0057	−0.7985	0.1619	0.0593
−0.50	−0.2539	0.0927	0.0213	−0.7367	0.1743	0.0143
−0.30	−0.0033	0.1153	0.0105	−0.6088	0.1565	0.1084
−0.10	−0.4700	0.0992	0.1150	−0.4005	0.1548	0.1208
0.10	−0.3087	0.1073	0.0777	−0.3491	0.1421	0.1443
0.30	−0.1992	0.1342	0.0656	0.1383	0.1891	0.0691
0.50	0.0759	0.1397	0.0321	0.2155	0.1889	0.1168
0.70	−0.2591	0.1043	0.0525	−0.2581	0.1295	0.0619
0.90	−0.6745	0.2430	0.1128	−1.2747	0.3693	0.1259

$\cos(\theta^*_{\pi^0})$	$W=(1321.0\pm9.0)$ MeV			$W=(1339.0\pm9.0)$ MeV			$W=(1357.0\pm9.0)$ MeV			$W=(1375.0\pm9.0)$ MeV		
	$d\sigma_{1/2}/d\Omega$ [μb/sr]	Δ_{stat} [μb/sr]	Δ_{sys} [μb/sr]	$d\sigma_{1/2}/d\Omega$ [μb/sr]	Δ_{stat} [μb/sr]	Δ_{sys} [μb/sr]	$d\sigma_{1/2}/d\Omega$ [μb/sr]	Δ_{stat} [μb/sr]	Δ_{sys} [μb/sr]	$d\sigma_{1/2}/d\Omega$ [μb/sr]	Δ_{stat} [μb/sr]	Δ_{sys} [μb/sr]
−0.90	0.3273	0.0384	0.2716	0.4408	0.0341	0.2326	0.4947	0.0327	0.2106	0.4451	0.0296	0.1752
−0.70	2.1404	0.0807	0.3340	1.3598	0.0640	0.1768	1.4335	0.0570	0.1483	1.6503	0.0476	0.1943
−0.50	2.0348	0.0718	0.0730	2.2812	0.0601	0.0438	2.0510	0.0545	0.0446	2.1237	0.0469	0.1014
−0.30	2.9051	0.0821	0.1176	2.7668	0.0695	0.0720	2.4052	0.0639	0.0671	2.3260	0.0559	0.0897
−0.10	3.1008	0.0813	0.2528	2.4528	0.0702	0.1490	2.4899	0.0640	0.0763	2.3049	0.0568	0.0599
0.10	3.0431	0.0836	0.3999	2.1141	0.0704	0.1913	2.2365	0.0635	0.1125	1.6497	0.0567	0.0407
0.30	3.0569	0.0994	0.6453	2.3479	0.0757	0.3511	1.9600	0.0635	0.2476	1.8484	0.0536	0.0870
0.50	2.3861	0.2305	0.9917	2.6744	0.1439	0.6699	1.6734	0.0968	0.3537	1.5452	0.0704	0.1221
0.70	3.4245	2.3556	3.2837	7.7529	1.6219	6.4123	4.4404	0.6738	2.5613	1.8140	0.3125	0.5210
0.90	−14.9642	10.1657	7.0368	1.2516	4.6978	2.8075	9.3205	9.3664	7.0310	−4.5689	6.7278	4.5232

$\cos(\theta^*_{\pi^0})$	$W=(1393.0\pm9.0)$ MeV			$W=(1411.0\pm9.0)$ MeV			$W=(1429.0\pm9.0)$ MeV			$W=(1447.0\pm9.0)$ MeV		
	$d\sigma_{1/2}/d\Omega$ [μb/sr]	Δ_{stat} [μb/sr]	Δ_{sys} [μb/sr]	$d\sigma_{1/2}/d\Omega$ [μb/sr]	Δ_{stat} [μb/sr]	Δ_{sys} [μb/sr]	$d\sigma_{1/2}/d\Omega$ [μb/sr]	Δ_{stat} [μb/sr]	Δ_{sys} [μb/sr]	$d\sigma_{1/2}/d\Omega$ [μb/sr]	Δ_{stat} [μb/sr]	Δ_{sys} [μb/sr]
−0.90	0.5717	0.0290	0.1634	0.5406	0.0305	0.1097	0.6573	0.0301	0.1015	0.8734	0.0297	0.0917
−0.70	1.5114	0.0439	0.0954	1.3469	0.0418	0.0801	1.6186	0.0384	0.0749	1.5219	0.0355	0.0218
−0.50	1.9879	0.0435	0.0335	2.0636	0.0423	0.0602	2.1073	0.0385	0.0508	2.1473	0.0355	0.0218
−0.30	2.1334	0.0516	0.0641	2.2362	0.0501	0.0444	2.2152	0.0466	0.0337	2.4388	0.0437	0.0392
−0.10	2.2842	0.0530	0.0076	2.0419	0.0518	0.0438	2.2383	0.0478	0.0376	2.5797	0.0446	0.0348
0.10	2.0147	0.0526	0.0681	1.8535	0.0516	0.0879	2.1023	0.0477	0.0505	2.1115	0.0448	0.0696
0.30	1.6231	0.0490	0.1060	1.5650	0.0474	0.1124	1.5121	0.0437	0.0922	2.0755	0.0409	0.0586
0.50	1.4101	0.0566	0.1064	1.3313	0.0510	0.1523	1.1060	0.0434	0.0764	1.2277	0.0394	0.0870
0.70	1.3544	0.1887	0.1824	1.2271	0.1714	0.4416	1.3376	0.1071	0.1274	0.9565	0.0806	0.1158
0.90	1.1152	1.8125	0.3923	3.7384	1.7177	0.1846	6.6800	1.7490	0.9409	−1.2515	0.9125	0.3689

$\cos(\theta^*_{\pi^0})$	$W=(1465.0\pm9.0)$ MeV			$W=(1483.0\pm9.0)$ MeV			$W=(1501.0\pm9.0)$ MeV			$W=(1519.0\pm9.0)$ MeV		
	$d\sigma_{1/2}/d\Omega$ [μb/sr]	Δ_{stat} [μb/sr]	Δ_{sys} [μb/sr]	$d\sigma_{1/2}/d\Omega$ [μb/sr]	Δ_{stat} [μb/sr]	Δ_{sys} [μb/sr]	$d\sigma_{1/2}/d\Omega$ [μb/sr]	Δ_{stat} [μb/sr]	Δ_{sys} [μb/sr]	$d\sigma_{1/2}/d\Omega$ [μb/sr]	Δ_{stat} [μb/sr]	Δ_{sys} [μb/sr]
−0.90	1.1310	0.0295	0.1042	1.3033	0.0313	0.0731	1.5843	0.0337	0.0190	1.7716	0.0347	0.0152
−0.70	1.6626	0.0336	0.0133	1.9051	0.0351	0.0497	2.0160	0.0361	0.0884	1.8406	0.0358	0.0549
−0.50	2.2655	0.0342	0.0531	2.6633	0.0353	0.0713	2.8458	0.0361	0.1125	2.7096	0.0357	0.0598
−0.30	2.8642	0.0422	0.0196	3.0773	0.0435	0.0370	3.2432	0.0443	0.0816	2.9445	0.0429	0.0338
−0.10	2.8695	0.0433	0.0396	3.3069	0.0450	0.0389	3.6701	0.0462	0.0832	3.3800	0.0443	0.0299
0.10	2.7319	0.0440	0.0273	3.2438	0.0464	0.0585	3.5080	0.0474	0.0431	3.3434	0.0459	0.0443
0.30	2.2412	0.0410	0.1250	2.9095	0.0442	0.1334	3.4607	0.0461	0.1926	3.0562	0.0451	0.1142
0.50	1.7271	0.0397	0.1589	2.1051	0.0423	0.1106	2.7027	0.0446	0.1204	2.6439	0.0436	0.0466
0.70	0.9753	0.0696	0.1088	1.7218	0.0675	0.1792	1.9049	0.0639	0.0567	1.8062	0.0594	0.0852
0.90	−1.8514	0.7117	0.6473	5.5852	3.4178	4.3089	1.3356	2.1166	1.5449	2.3889	0.5035	0.2945

$\cos(\theta^*_{\pi^0})$	W=(1537.0±9.0) MeV			W=(1555.0±9.0) MeV			W=(1573.0±9.0) MeV			W=(1591.0±9.0) MeV		
	$d\sigma_{1/2}/d\Omega$ [μb/sr]	Δ_{stat} [μb/sr]	Δ_{sys} [μb/sr]	$d\sigma_{1/2}/d\Omega$ [μb/sr]	Δ_{stat} [μb/sr]	Δ_{sys} [μb/sr]	$d\sigma_{1/2}/d\Omega$ [μb/sr]	Δ_{stat} [μb/sr]	Δ_{sys} [μb/sr]	$d\sigma_{1/2}/d\Omega$ [μb/sr]	Δ_{stat} [μb/sr]	Δ_{sys} [μb/sr]
−0.90	1.6491	0.0353	0.0316	1.6884	0.0358	0.0394	1.7182	0.0361	0.0105	1.7398	0.0364	0.0404
−0.70	1.8532	0.0357	0.0478	1.4841	0.0353	0.0462	1.3341	0.0357	0.0521	1.2769	0.0360	0.0748
−0.50	2.3310	0.0347	0.0416	2.0071	0.0332	0.0251	1.6668	0.0326	0.0050	1.4122	0.0324	0.0333
−0.30	2.8224	0.0412	0.0433	2.2350	0.0391	0.0405	1.9002	0.0377	0.0401	1.5208	0.0365	0.0193
−0.10	2.7876	0.0416	0.0272	2.3754	0.0388	0.0347	1.7918	0.0370	0.0228	1.5494	0.0351	0.0198
0.10	3.1371	0.0432	0.1468	2.5005	0.0406	0.0507	1.9485	0.0385	0.0369	1.6404	0.0357	0.0672
0.30	2.8375	0.0418	0.0399	2.3087	0.0386	0.0562	1.9114	0.0367	0.0127	1.6181	0.0342	0.0255
0.50	2.3484	0.0411	0.0198	2.1531	0.0378	0.0521	1.9389	0.0356	0.0117	1.4917	0.0341	0.0744
0.70	1.6780	0.0529	0.0794	1.6381	0.0463	0.0251	1.2749	0.0430	0.0556	1.3440	0.0419	0.0991
0.90	0.2750	0.3972	0.0575	3.9975	8.4067	5.2678	0.0564	0.2930	0.2373	2.0057	0.6148	1.2067

$\cos(\theta^*_{\pi^0})$	W=(1609.0±9.0) MeV			W=(1627.0±9.0) MeV			W=(1645.0±9.0) MeV			W=(1663.0±9.0) MeV		
	$d\sigma_{1/2}/d\Omega$ [μb/sr]	Δ_{stat} [μb/sr]	Δ_{sys} [μb/sr]	$d\sigma_{1/2}/d\Omega$ [μb/sr]	Δ_{stat} [μb/sr]	Δ_{sys} [μb/sr]	$d\sigma_{1/2}/d\Omega$ [μb/sr]	Δ_{stat} [μb/sr]	Δ_{sys} [μb/sr]	$d\sigma_{1/2}/d\Omega$ [μb/sr]	Δ_{stat} [μb/sr]	Δ_{sys} [μb/sr]
−0.90	1.2221	0.0358	0.0753	1.2408	0.0355	0.0485	1.2433	0.0347	0.0786	1.0199	0.0337	0.1058
−0.70	1.0866	0.0355	0.1049	0.8964	0.0349	0.0888	0.9028	0.0339	0.1303	0.8502	0.0325	0.1183
−0.50	1.2084	0.0316	0.0288	0.8640	0.0318	0.0537	0.7666	0.0315	0.0453	0.8959	0.0307	0.0237
−0.30	1.0250	0.0349	0.0155	1.0818	0.0340	0.0088	0.8573	0.0325	0.0213	0.8652	0.0310	0.0379
−0.10	1.4230	0.0327	0.0324	1.1033	0.0314	0.0111	1.1823	0.0295	0.0306	1.0961	0.0278	0.0379
0.10	1.2868	0.0334	0.0177	1.2409	0.0316	0.0318	1.2245	0.0301	0.0076	1.3655	0.0287	0.0443
0.30	1.4625	0.0316	0.0184	1.2716	0.0306	0.0440	1.4603	0.0292	0.0125	1.5489	0.0285	0.0448
0.50	1.4313	0.0324	0.1038	1.3400	0.0315	0.0676	1.5691	0.0320	0.0885	1.5068	0.0321	0.0536
0.70	1.1148	0.0402	0.1222	1.3293	0.0397	0.0416	1.2223	0.0410	0.0689	1.5021	0.0422	0.0877
0.90	0.5401	0.5995	0.4261	0.6020	0.6424	2.6861	0.2961	0.4509	0.5216	1.1512	0.1889	0.3578

$\cos(\theta^*_{\pi^0})$	W=(1681.0±9.0) MeV			W=(1699.0±9.0) MeV			W=(1717.0±9.0) MeV			W=(1735.0±9.0) MeV		
	$d\sigma_{1/2}/d\Omega$ [μb/sr]	Δ_{stat} [μb/sr]	Δ_{sys} [μb/sr]	$d\sigma_{1/2}/d\Omega$ [μb/sr]	Δ_{stat} [μb/sr]	Δ_{sys} [μb/sr]	$d\sigma_{1/2}/d\Omega$ [μb/sr]	Δ_{stat} [μb/sr]	Δ_{sys} [μb/sr]	$d\sigma_{1/2}/d\Omega$ [μb/sr]	Δ_{stat} [μb/sr]	Δ_{sys} [μb/sr]
−0.90	1.3073	0.0329	0.0275	1.0051	0.0327	0.0574	0.8881	0.0318	0.0461	0.8667	0.0298	0.0308
−0.70	0.8842	0.0312	0.0518	0.5710	0.0302	0.0420	0.6774	0.0280	0.0168	0.5032	0.0261	0.0334
−0.50	0.7295	0.0302	0.0298	0.5456	0.0300	0.0336	0.4362	0.0293	0.0513	0.4394	0.0278	0.0372
−0.30	0.7471	0.0300	0.0560	0.6923	0.0292	0.0973	0.7815	0.0284	0.0730	0.5786	0.0269	0.0525
−0.10	1.0503	0.0263	0.1172	1.0250	0.0262	0.0492	0.8395	0.0257	0.0598	0.6413	0.0249	0.0392
0.10	1.3527	0.0283	0.0570	1.2966	0.0284	0.0476	1.2163	0.0280	0.0709	0.8616	0.0275	0.0244
0.30	1.5042	0.0293	0.0367	1.5623	0.0295	0.0762	1.4647	0.0300	0.0770	1.2476	0.0293	0.0459
0.50	1.8056	0.0332	0.0372	1.7517	0.0340	0.0495	1.6054	0.0340	0.0662	1.3211	0.0333	0.0484
0.70	1.4868	0.0427	0.0051	1.3108	0.0431	0.0114	1.4520	0.0433	0.0620	1.3064	0.0421	0.0265
0.90	1.0883	0.1543	0.1974	0.7302	0.1248	0.0436	1.2987	0.1087	0.0861	0.4250	0.6149	0.4095

$\cos(\theta^*_{\pi^0})$	W=(1753.0±9.0) MeV			W=(1771.0±9.0) MeV			W=(1789.0±9.0) MeV			W=(1807.0±9.0) MeV		
	$d\sigma_{1/2}/d\Omega$ [μb/sr]	Δ_{stat} [μb/sr]	Δ_{sys} [μb/sr]	$d\sigma_{1/2}/d\Omega$ [μb/sr]	Δ_{stat} [μb/sr]	Δ_{sys} [μb/sr]	$d\sigma_{1/2}/d\Omega$ [μb/sr]	Δ_{stat} [μb/sr]	Δ_{sys} [μb/sr]	$d\sigma_{1/2}/d\Omega$ [μb/sr]	Δ_{stat} [μb/sr]	Δ_{sys} [μb/sr]
−0.90	0.7844	0.0282	0.0713	0.8585	0.0277	0.0787	0.9123	0.0293	0.1179	0.9148	0.0315	0.1182
−0.70	0.4268	0.0247	0.0764	0.4456	0.0240	0.0745	0.3606	0.0246	0.0809	0.5461	0.0262	0.0687
−0.50	0.3835	0.0260	0.0089	0.2792	0.0253	0.0095	0.2745	0.0258	0.0082	0.3673	0.0274	0.0217
−0.30	0.3955	0.0252	0.0196	0.3995	0.0249	0.0196	0.4024	0.0267	0.0137	0.2959	0.0307	0.0206
−0.10	0.6268	0.0240	0.0072	0.5230	0.0231	0.0110	0.4770	0.0249	0.0167	0.3920	0.0276	0.0205
0.10	0.9338	0.0265	0.0053	0.7653	0.0264	0.0132	0.6981	0.0286	0.0324	0.6489	0.0323	0.0124
0.30	0.9585	0.0278	0.0078	0.8469	0.0270	0.0108	0.7602	0.0280	0.0243	0.6370	0.0308	0.0220
0.50	1.1229	0.0311	0.0444	0.8027	0.0310	0.0650	0.7300	0.0316	0.0282	0.6814	0.0337	0.0177
0.70	0.9359	0.0391	0.0208	0.8162	0.0394	0.0851	0.8284	0.0409	0.0555	0.7861	0.0469	0.0882
0.90	−0.1028	0.0922	0.0357	0.4040	0.0948	0.1687	0.1980	0.1199	0.2216	0.8382	0.1073	0.1877

$\cos(\theta^*_{\pi^0})$	W=(1825.0±9.0) MeV			W=(1843.0±9.0) MeV			W=(1861.0±9.0) MeV			W=(1879.0±9.0) MeV		
	$d\sigma_{1/2}/d\Omega$ [μb/sr]	Δ_{stat} [μb/sr]	Δ_{sys} [μb/sr]	$d\sigma_{1/2}/d\Omega$ [μb/sr]	Δ_{stat} [μb/sr]	Δ_{sys} [μb/sr]	$d\sigma_{1/2}/d\Omega$ [μb/sr]	Δ_{stat} [μb/sr]	Δ_{sys} [μb/sr]	$d\sigma_{1/2}/d\Omega$ [μb/sr]	Δ_{stat} [μb/sr]	Δ_{sys} [μb/sr]
−0.90	0.9949	0.0340	0.0896	1.0618	0.0360	0.0823	1.1663	0.0371	0.1127	0.7873	0.0389	0.0472
−0.70	0.3740	0.0281	0.0317	0.3458	0.0312	0.0779	0.4244	0.0335	0.0702	0.2956	0.0375	0.0281
−0.50	0.1379	0.0296	0.0098	0.3361	0.0302	0.0296	0.3592	0.0294	0.0040	0.2729	0.0289	0.0656
−0.30	0.2071	0.0337	0.0107	0.3712	0.0372	0.0243	0.5182	0.0393	0.0764	0.4838	0.0417	0.0447
−0.10	0.4608	0.0326	0.0127	0.5320	0.0365	0.0275	0.3016	0.0423	0.0034	0.4004	0.0494	0.0586
0.10	0.4292	0.0388	0.0285	0.4799	0.0433	0.0886	0.4991	0.0499	0.0838	0.4505	0.0555	0.1447
0.30	0.5947	0.0350	0.0274	0.6320	0.0408	0.0740	0.6518	0.0497	0.0891	0.5484	0.0598	0.1409
0.50	0.6262	0.0365	0.0595	0.4756	0.0411	0.0593	0.3748	0.0454	0.1335	0.7680	0.0521	0.2157
0.70	0.7907	0.0520	0.0648	1.0709	0.0583	0.0513	0.9618	0.0684	0.0419	0.9088	0.0752	0.2244
0.90	1.2824	0.1200	0.1156	0.7321	0.1412	0.1916	0.9327	0.1445	0.1811	0.9109	0.1581	0.1054

$\cos(\theta^*_{\pi^0})$	W=(1897.0±9.0) MeV			W=(1915.0±9.0) MeV		
	$d\sigma_{1/2}/d\Omega$ [μb/sr]	Δ_{stat} [μb/sr]	Δ_{sys} [μb/sr]	$d\sigma_{1/2}/d\Omega$ [μb/sr]	Δ_{stat} [μb/sr]	Δ_{sys} [μb/sr]
−0.90	0.8153	0.0472	0.0124	0.6898	0.0881	0.0516
−0.70	0.4520	0.0518	0.0109	0.1427	0.1039	0.0551
−0.50	0.2940	0.0344	0.0328	0.0923	0.0560	0.0069
−0.30	0.4188	0.0463	0.0480	0.1845	0.0628	0.0726
−0.10	0.4092	0.0637	0.1648	0.4586	0.0967	0.1984
0.10	0.5067	0.0680	0.1707	0.6058	0.1006	0.3092
0.30	0.5645	0.0785	0.2131	0.8173	0.1171	0.2532
0.50	0.6336	0.0667	0.2332	0.8001	0.1057	0.2685
0.70	0.7690	0.0975	0.1994	0.9099	0.1392	0.2791
0.90	0.3149	0.2134	0.1585	−0.2335	0.2938	0.1111

$\cos(\theta^*_{\pi^0})$	$W=(1321.0\pm9.0)$ MeV			$W=(1339.0\pm9.0)$ MeV			$W=(1357.0\pm9.0)$ MeV			$W=(1375.0\pm9.0)$ MeV		
	$d\sigma_{3/2}/d\Omega$ [μb/sr]	Δ_{stat} [μb/sr]	Δ_{sys} [μb/sr]	$d\sigma_{3/2}/d\Omega$ [μb/sr]	Δ_{stat} [μb/sr]	Δ_{sys} [μb/sr]	$d\sigma_{3/2}/d\Omega$ [μb/sr]	Δ_{stat} [μb/sr]	Δ_{sys} [μb/sr]	$d\sigma_{3/2}/d\Omega$ [μb/sr]	Δ_{stat} [μb/sr]	Δ_{sys} [μb/sr]
−0.90	0.5258	0.0384	0.3173	0.3368	0.0341	0.2113	0.2542	0.0326	0.1675	0.3206	0.0296	0.1550
−0.70	2.9746	0.0808	0.3834	2.4087	0.0641	0.2365	1.7865	0.0570	0.1900	1.1394	0.0475	0.1709
−0.50	6.0560	0.0720	0.0224	4.1494	0.0602	0.0226	3.3113	0.0546	0.0626	2.4530	0.0470	0.1085
−0.30	7.4801	0.0823	0.0691	5.5686	0.0696	0.1058	4.5225	0.0640	0.0604	3.6751	0.0560	0.1127
−0.10	8.0470	0.0814	0.2827	6.6918	0.0704	0.1211	5.2249	0.0641	0.0239	4.3142	0.0569	0.0931
0.10	7.6024	0.0838	0.5419	6.6669	0.0706	0.1879	5.1199	0.0636	0.0709	4.6838	0.0568	0.0233
0.30	5.8595	0.0995	0.8532	5.0449	0.0759	0.4738	4.2319	0.0636	0.2438	3.4211	0.0537	0.0956
0.50	4.0624	0.2306	1.1831	2.6923	0.1439	0.6033	2.8762	0.0969	0.3159	2.3475	0.0705	0.1171
0.70	0.3231	2.3557	1.6845	−4.6715	1.6215	5.2538	−1.9297	0.6734	1.8995	0.5329	0.3124	0.3953
0.90	21.7398	10.1669	8.4629	−1.0519	4.6923	5.4980	−5.5479	9.3648	5.9314	7.3481	6.7278	5.3952

$\cos(\theta^*_{\pi^0})$	$W=(1393.0\pm9.0)$ MeV			$W=(1411.0\pm9.0)$ MeV			$W=(1429.0\pm9.0)$ MeV			$W=(1447.0\pm9.0)$ MeV		
	$d\sigma_{3/2}/d\Omega$ [μb/sr]	Δ_{stat} [μb/sr]	Δ_{sys} [μb/sr]	$d\sigma_{3/2}/d\Omega$ [μb/sr]	Δ_{stat} [μb/sr]	Δ_{sys} [μb/sr]	$d\sigma_{3/2}/d\Omega$ [μb/sr]	Δ_{stat} [μb/sr]	Δ_{sys} [μb/sr]	$d\sigma_{3/2}/d\Omega$ [μb/sr]	Δ_{stat} [μb/sr]	Δ_{sys} [μb/sr]
−0.90	0.1861	0.0289	0.1139	0.2158	0.0304	0.0805	0.1917	0.0299	0.0796	0.0627	0.0295	0.0535
−0.70	0.8508	0.0439	0.0752	0.7565	0.0418	0.0630	0.3771	0.0383	0.0466	0.4409	0.0354	0.0186
−0.50	1.9618	0.0435	0.0333	1.3384	0.0423	0.0422	1.1643	0.0384	0.0434	1.0943	0.0354	0.0069
−0.30	3.0049	0.0517	0.0748	2.3695	0.0502	0.0510	2.1261	0.0466	0.0371	1.8855	0.0437	0.0213
−0.10	3.3212	0.0530	0.0142	2.9519	0.0519	0.0098	2.4982	0.0478	0.0293	2.2825	0.0445	0.0423
0.10	3.3878	0.0527	0.0685	2.9118	0.0517	0.0762	2.4114	0.0477	0.0175	2.4493	0.0448	0.0304
0.30	2.7736	0.0491	0.1177	2.3351	0.0475	0.1118	2.1246	0.0438	0.0734	1.8080	0.0409	0.0344
0.50	1.7952	0.0567	0.1011	1.3192	0.0510	0.1224	1.4369	0.0434	0.0553	1.4348	0.0394	0.0632
0.70	0.9008	0.1886	0.0953	0.3036	0.1714	0.2323	0.2569	0.1068	0.0968	0.7234	0.0806	0.0703
0.90	2.4815	1.8127	0.5330	−1.3310	1.7157	0.1181	−4.7614	1.7463	0.6554	3.6586	0.9149	0.5625

$\cos(\theta^*_{\pi^0})$	$W=(1465.0\pm9.0)$ MeV			$W=(1483.0\pm9.0)$ MeV			$W=(1501.0\pm9.0)$ MeV			$W=(1519.0\pm9.0)$ MeV		
	$d\sigma_{3/2}/d\Omega$ [μb/sr]	Δ_{stat} [μb/sr]	Δ_{sys} [μb/sr]	$d\sigma_{3/2}/d\Omega$ [μb/sr]	Δ_{stat} [μb/sr]	Δ_{sys} [μb/sr]	$d\sigma_{3/2}/d\Omega$ [μb/sr]	Δ_{stat} [μb/sr]	Δ_{sys} [μb/sr]	$d\sigma_{3/2}/d\Omega$ [μb/sr]	Δ_{stat} [μb/sr]	Δ_{sys} [μb/sr]
−0.90	0.0195	0.0293	0.0542	0.1263	0.0311	0.0406	0.3109	0.0334	0.0058	0.4503	0.0345	0.0152
−0.70	0.4516	0.0335	0.0096	0.4466	0.0350	0.0255	0.7517	0.0359	0.0579	1.1639	0.0357	0.0252
−0.50	1.2500	0.0341	0.0213	1.2002	0.0352	0.0376	1.5034	0.0360	0.0677	1.6828	0.0356	0.0354
−0.30	1.7937	0.0421	0.0140	2.1412	0.0434	0.0290	2.3269	0.0442	0.0478	2.5514	0.0429	0.0420
−0.10	2.4363	0.0433	0.0317	2.5984	0.0450	0.0391	2.7561	0.0461	0.0473	2.8854	0.0442	0.0477
0.10	2.4015	0.0439	0.0031	2.7287	0.0464	0.0248	3.0506	0.0473	0.0107	2.9934	0.0459	0.0520
0.30	2.1409	0.0410	0.0885	2.3162	0.0441	0.0958	2.4803	0.0461	0.1395	2.6987	0.0451	0.0948
0.50	1.3839	0.0397	0.1163	1.9092	0.0423	0.0832	1.9426	0.0445	0.0756	2.0598	0.0436	0.0268
0.70	0.9849	0.0696	0.1092	0.7699	0.0674	0.1251	1.2513	0.0638	0.0370	1.2423	0.0593	0.0553
0.90	4.1101	0.7155	0.9214	−4.3890	3.4171	3.7203	−0.1430	2.1164	0.9383	−0.5947	0.5017	0.1265

$\cos(\theta^*_{\pi^0})$	$W=(1537.0\pm9.0)$ MeV			$W=(1555.0\pm9.0)$ MeV			$W=(1573.0\pm9.0)$ MeV			$W=(1591.0\pm9.0)$ MeV		
	$d\sigma_{3/2}/d\Omega$ [μb/sr]	Δ_{stat} [μb/sr]	Δ_{sys} [μb/sr]	$d\sigma_{3/2}/d\Omega$ [μb/sr]	Δ_{stat} [μb/sr]	Δ_{sys} [μb/sr]	$d\sigma_{3/2}/d\Omega$ [μb/sr]	Δ_{stat} [μb/sr]	Δ_{sys} [μb/sr]	$d\sigma_{3/2}/d\Omega$ [μb/sr]	Δ_{stat} [μb/sr]	Δ_{sys} [μb/sr]
−0.90	0.8354	0.0351	0.0128	0.9289	0.0356	0.0212	1.1462	0.0360	0.0028	1.1937	0.0363	0.0309
−0.70	1.2550	0.0356	0.0325	1.5925	0.0353	0.0416	1.8236	0.0358	0.0461	1.9872	0.0361	0.0787
−0.50	1.9187	0.0347	0.0303	1.8678	0.0332	0.0117	2.0386	0.0327	0.0072	2.1026	0.0325	0.0303
−0.30	2.2494	0.0412	0.0542	2.2263	0.0391	0.0469	2.1142	0.0377	0.0497	2.0308	0.0366	0.0260
−0.10	2.7433	0.0416	0.0509	2.3795	0.0388	0.0529	2.2034	0.0370	0.0282	1.9530	0.0352	0.0241
0.10	2.6745	0.0432	0.1490	2.2433	0.0406	0.0628	1.9312	0.0385	0.0489	1.6321	0.0357	0.0714
0.30	2.3188	0.0418	0.0587	1.9179	0.0386	0.0699	1.4097	0.0366	0.0117	1.0384	0.0342	0.0102
0.50	1.7397	0.0410	0.0152	1.2244	0.0376	0.0547	0.7278	0.0355	0.0132	0.5829	0.0339	0.0421
0.70	0.9198	0.0528	0.0405	0.5764	0.0461	0.0309	0.4384	0.0429	0.0209	0.2016	0.0416	0.0731
0.90	1.0244	0.3975	0.0632	−3.2466	8.4067	4.9497	1.1945	0.2945	0.1290	−1.1940	0.6141	0.8846

$\cos(\theta^*_{\pi^0})$	$W=(1609.0\pm9.0)$ MeV			$W=(1627.0\pm9.0)$ MeV			$W=(1645.0\pm9.0)$ MeV			$W=(1663.0\pm9.0)$ MeV		
	$d\sigma_{3/2}/d\Omega$ [μb/sr]	Δ_{stat} [μb/sr]	Δ_{sys} [μb/sr]	$d\sigma_{3/2}/d\Omega$ [μb/sr]	Δ_{stat} [μb/sr]	Δ_{sys} [μb/sr]	$d\sigma_{3/2}/d\Omega$ [μb/sr]	Δ_{stat} [μb/sr]	Δ_{sys} [μb/sr]	$d\sigma_{3/2}/d\Omega$ [μb/sr]	Δ_{stat} [μb/sr]	Δ_{sys} [μb/sr]
−0.90	1.6914	0.0359	0.0727	1.8275	0.0356	0.0516	1.9199	0.0349	0.0879	2.0571	0.0339	0.1348
−0.70	2.1207	0.0357	0.1319	2.5686	0.0352	0.1191	2.7261	0.0343	0.1868	2.6683	0.0328	0.1695
−0.50	2.2450	0.0317	0.0324	2.6092	0.0320	0.0830	2.8494	0.0318	0.0685	2.6787	0.0310	0.0325
−0.30	2.2302	0.0351	0.0247	2.1656	0.0341	0.0081	2.3618	0.0328	0.0293	2.1960	0.0313	0.0506
−0.10	1.6764	0.0327	0.0351	1.8234	0.0315	0.0121	1.6800	0.0296	0.0359	1.5992	0.0278	0.0459
0.10	1.4214	0.0335	0.0186	1.4019	0.0317	0.0474	1.2897	0.0301	0.0076	1.1832	0.0287	0.0473
0.30	0.8752	0.0315	0.0200	0.9754	0.0305	0.0230	1.0523	0.0292	0.0125	1.2454	0.0284	0.0445
0.50	0.5470	0.0322	0.0631	0.8479	0.0314	0.0449	1.0728	0.0319	0.0734	1.6022	0.0321	0.0542
0.70	0.6501	0.0401	0.0844	1.0175	0.0396	0.0216	1.6901	0.0411	0.0737	1.8710	0.0423	0.0922
0.90	0.3156	0.5994	0.3504	0.1305	0.6427	2.0748	1.0229	0.4510	0.8163	0.8212	0.1887	0.3022

$\cos(\theta^*_{\pi^0})$	$W=(1681.0\pm9.0)$ MeV			$W=(1699.0\pm9.0)$ MeV			$W=(1717.0\pm9.0)$ MeV			$W=(1735.0\pm9.0)$ MeV		
	$d\sigma_{3/2}/d\Omega$ [μb/sr]	Δ_{stat} [μb/sr]	Δ_{sys} [μb/sr]	$d\sigma_{3/2}/d\Omega$ [μb/sr]	Δ_{stat} [μb/sr]	Δ_{sys} [μb/sr]	$d\sigma_{3/2}/d\Omega$ [μb/sr]	Δ_{stat} [μb/sr]	Δ_{sys} [μb/sr]	$d\sigma_{3/2}/d\Omega$ [μb/sr]	Δ_{stat} [μb/sr]	Δ_{sys} [μb/sr]
−0.90	1.7124	0.0330	0.0318	1.6011	0.0328	0.0613	1.3036	0.0319	0.0516	1.0351	0.0299	0.0266
−0.70	2.4888	0.0316	0.0798	2.2169	0.0306	0.0594	1.6443	0.0283	0.0220	1.3164	0.0264	0.0517
−0.50	2.5970	0.0305	0.0366	2.3141	0.0304	0.0533	1.9637	0.0297	0.0831	1.3907	0.0281	0.0448
−0.30	2.0029	0.0303	0.0913	1.6922	0.0294	0.1310	1.1004	0.0285	0.0727	0.9412	0.0271	0.0674
−0.10	1.4304	0.0264	0.1331	1.0185	0.0262	0.0555	0.9034	0.0257	0.0559	0.7727	0.0250	0.0436
0.10	1.0736	0.0283	0.0626	0.8686	0.0283	0.0497	0.6907	0.0279	0.0660	0.7384	0.0275	0.0291
0.30	1.2542	0.0292	0.0443	1.0987	0.0294	0.0743	0.9239	0.0299	0.0536	0.7750	0.0292	0.0392
0.50	1.4909	0.0332	0.0267	1.4808	0.0339	0.0494	1.2633	0.0339	0.0717	1.0547	0.0333	0.0655
0.70	2.0784	0.0429	0.0082	1.9473	0.0433	0.0261	1.4176	0.0433	0.0624	0.9927	0.0420	0.0336
0.90	0.8592	0.1541	0.1761	1.2406	0.1252	0.0504	0.4461	0.1078	0.0588	0.3726	0.6149	0.3452

	W=(1753.0±9.0) MeV			W=(1771.0±9.0) MeV			W=(1789.0±9.0) MeV			W=(1807.0±9.0) MeV		
$\cos(\theta^*_{\pi^0})$	$d\sigma_{3/2}/d\Omega$ [μb/sr]	Δ_{stat} [μb/sr]	Δ_{sys} [μb/sr]	$d\sigma_{3/2}/d\Omega$ [μb/sr]	Δ_{stat} [μb/sr]	Δ_{sys} [μb/sr]	$d\sigma_{3/2}/d\Omega$ [μb/sr]	Δ_{stat} [μb/sr]	Δ_{sys} [μb/sr]	$d\sigma_{3/2}/d\Omega$ [μb/sr]	Δ_{stat} [μb/sr]	Δ_{sys} [μb/sr]
−0.90	0.8772	0.0282	0.0740	0.7420	0.0277	0.0679	0.7027	0.0292	0.0976	0.8072	0.0314	0.1019
−0.70	1.0196	0.0249	0.1144	0.8831	0.0243	0.0988	0.9922	0.0249	0.1100	0.8947	0.0264	0.0803
−0.50	1.0891	0.0263	0.0097	0.9294	0.0256	0.0034	0.8571	0.0261	0.0064	0.7228	0.0276	0.0260
−0.30	0.7970	0.0254	0.0276	0.6838	0.0250	0.0269	0.6419	0.0268	0.0140	0.7110	0.0310	0.0253
−0.10	0.5521	0.0240	0.0049	0.6093	0.0232	0.0145	0.6030	0.0250	0.0186	0.7777	0.0278	0.0280
0.10	0.4810	0.0264	0.0078	0.5463	0.0264	0.0115	0.5784	0.0286	0.0292	0.6739	0.0323	0.0089
0.30	0.7414	0.0277	0.0142	0.6052	0.0270	0.0065	0.5357	0.0279	0.0207	0.6197	0.0308	0.0135
0.50	0.7747	0.0310	0.0399	0.6462	0.0310	0.0523	0.6090	0.0316	0.0219	0.6073	0.0337	0.0175
0.70	0.9026	0.0391	0.0128	0.7931	0.0394	0.0709	0.7647	0.0408	0.0544	0.7413	0.0469	0.0855
0.90	1.3532	0.0938	0.0246	0.7394	0.0951	0.1967	0.9219	0.1203	0.3876	0.6653	0.1073	0.1589

	W=(1825.0±9.0) MeV			W=(1843.0±9.0) MeV			W=(1861.0±9.0) MeV			W=(1879.0±9.0) MeV		
$\cos(\theta^*_{\pi^0})$	$d\sigma_{3/2}/d\Omega$ [μb/sr]	Δ_{stat} [μb/sr]	Δ_{sys} [μb/sr]	$d\sigma_{3/2}/d\Omega$ [μb/sr]	Δ_{stat} [μb/sr]	Δ_{sys} [μb/sr]	$d\sigma_{3/2}/d\Omega$ [μb/sr]	Δ_{stat} [μb/sr]	Δ_{sys} [μb/sr]	$d\sigma_{3/2}/d\Omega$ [μb/sr]	Δ_{stat} [μb/sr]	Δ_{sys} [μb/sr]
−0.90	0.9117	0.0340	0.0745	0.9486	0.0360	0.0683	0.6958	0.0368	0.0941	0.9185	0.0390	0.0508
−0.70	1.1151	0.0286	0.0415	1.1130	0.0316	0.1131	0.9822	0.0339	0.0836	1.0410	0.0381	0.0407
−0.50	0.8416	0.0301	0.0071	0.5821	0.0305	0.0401	0.5117	0.0296	0.0009	0.5813	0.0293	0.0950
−0.30	0.8034	0.0341	0.0185	0.6757	0.0374	0.0272	0.5947	0.0394	0.0727	0.4213	0.0418	0.0479
−0.10	0.7318	0.0327	0.0181	0.7699	0.0366	0.0211	1.0546	0.0427	0.0093	0.9487	0.0498	0.0950
0.10	0.9622	0.0390	0.0240	1.0909	0.0436	0.1216	1.0447	0.0502	0.1049	1.0534	0.0559	0.2066
0.30	0.6406	0.0350	0.0239	0.6898	0.0408	0.0739	0.6453	0.0496	0.0754	0.8128	0.0600	0.1571
0.50	0.6165	0.0364	0.0617	0.6265	0.0412	0.0735	0.7952	0.0456	0.1904	0.4140	0.0518	0.1755
0.70	0.8844	0.0521	0.0554	0.8780	0.0582	0.0554	1.0000	0.0683	0.0205	1.1684	0.0754	0.2623
0.90	0.6724	0.1194	0.0942	1.0931	0.1418	0.2109	1.5660	0.1455	0.2273	1.2970	0.1588	0.1310

	W=(1897.0±9.0) MeV			W=(1915.0±9.0) MeV		
$\cos(\theta^*_{\pi^0})$	$d\sigma_{3/2}/d\Omega$ [μb/sr]	Δ_{stat} [μb/sr]	Δ_{sys} [μb/sr]	$d\sigma_{3/2}/d\Omega$ [μb/sr]	Δ_{stat} [μb/sr]	Δ_{sys} [μb/sr]
−0.90	0.7756	0.0472	0.0121	1.1811	0.0888	0.0282
−0.70	0.9979	0.0525	0.0173	1.3012	0.1057	0.1007
−0.50	0.4882	0.0348	0.0456	0.6161	0.0567	0.0196
−0.30	0.4208	0.0464	0.0549	0.7027	0.0634	0.1095
−0.10	1.0454	0.0643	0.2407	0.9828	0.0974	0.2616
0.10	0.9132	0.0684	0.2242	1.1304	0.1012	0.3776
0.30	0.8094	0.0787	0.2501	0.6402	0.1170	0.2465
0.50	0.5564	0.0666	0.2215	0.5501	0.1053	0.2555
0.70	1.2682	0.0980	0.2566	1.4865	0.1400	0.3472
0.90	1.6376	0.2153	0.2381	2.1705	0.2988	0.2188

E.2.3 Observables for $\gamma d \to \pi^0 n(p)$ as a Function of E_γ

E_γ [MeV]	ΔE_γ [MeV]	E	Δ_{stat}	Δ_{sys}	$\sigma_{1/2}$ [μb]	Δ_{stat} [μb]	Δ_{sys} [μb]	$\sigma_{3/2}$ [μb]	Δ_{stat} [μb]	Δ_{sys} [μb]
433.0	11.0	−0.4931	0.0131	0.0620	51.5809	1.2414	7.7506	151.7067	1.2436	17.4853
455.0	11.0	−0.4769	0.0120	0.0618	34.1676	0.7337	5.3145	96.2834	0.7350	11.1939
477.0	11.0	−0.4363	0.0125	0.0490	33.2094	0.6870	3.7704	84.3681	0.6883	9.2917
499.0	11.0	−0.3925	0.0114	0.0463	30.6976	0.5455	3.8220	70.2584	0.5465	7.9225
521.0	11.0	−0.3448	0.0141	0.0399	28.6140	0.5819	3.3323	58.6086	0.5829	6.4926
543.0	11.0	−0.3233	0.0127	0.0374	25.4720	0.4528	2.9420	49.7326	0.4536	5.5067
565.0	11.0	−0.2900	0.0132	0.0336	23.4230	0.4162	2.7478	42.5089	0.4169	4.7637
587.0	11.0	−0.2352	0.0155	0.0282	22.3501	0.4332	2.5544	35.9967	0.4339	3.9736
609.0	11.0	−0.1868	0.0151	0.0218	21.2709	0.3811	2.4241	31.0144	0.3816	3.4521
631.0	11.0	−0.2128	0.0173	0.0249	18.7031	0.3952	2.2402	28.8296	0.3958	3.3223
653.0	11.0	−0.1683	0.0136	0.0222	19.0717	0.2997	2.1795	26.6924	0.3002	2.9444
675.0	11.0	−0.1309	0.0135	0.0169	19.7059	0.2951	2.1924	25.5626	0.2955	2.8139
697.0	11.0	−0.0590	0.0132	0.0105	21.1716	0.2877	2.4170	23.7662	0.2879	2.6385
719.0	11.0	0.0170	0.0136	0.0062	23.1485	0.3036	2.8671	22.3159	0.3036	2.6634
741.0	11.0	−0.0238	0.0133	0.0063	22.5601	0.2999	2.7109	23.6206	0.3001	2.7486
763.0	11.0	−0.0025	0.0124	0.0047	22.6828	0.2751	2.7650	22.7546	0.2752	2.6903
785.0	11.0	0.0393	0.0140	0.0063	22.5737	0.2965	2.7001	20.8204	0.2965	2.4381
807.0	11.0	0.0778	0.0136	0.0097	21.5406	0.2660	2.6391	18.3802	0.2658	2.2103
829.0	11.0	0.1633	0.0134	0.0188	21.4448	0.2420	2.5293	15.3676	0.2417	1.7848
851.0	11.0	0.0647	0.0155	0.0089	17.5953	0.2505	2.1357	15.4114	0.2503	1.8238
873.0	11.0	0.0420	0.0164	0.0097	15.6533	0.2422	2.0158	14.3336	0.2422	1.7605
895.0	11.0	0.1281	0.0177	0.0144	15.4158	0.2374	1.7583	11.8949	0.2371	1.3560
917.0	11.0	0.0723	0.0161	0.0086	13.8478	0.2042	1.6044	11.9587	0.2041	1.3695
939.0	11.0	0.0695	0.0187	0.0079	12.8994	0.2217	1.4916	11.2123	0.2215	1.2968
961.0	11.0	−0.0671	0.0201	0.0124	10.7605	0.2280	1.2526	12.2761	0.2282	1.3795
983.0	11.0	0.0211	0.0171	0.0038	11.3574	0.1880	1.2754	10.8753	0.1879	1.2102
1005.0	11.0	−0.1015	0.0172	0.0128	9.5257	0.1789	1.0847	11.6629	0.1792	1.3003
1027.0	11.0	−0.1501	0.0181	0.0177	8.6252	0.1813	1.0144	11.6794	0.1816	1.3404
1049.0	11.0	−0.1739	0.0192	0.0222	7.9991	0.1828	0.9855	11.3674	0.1832	1.3252
1071.0	11.0	−0.2279	0.0207	0.0286	6.9702	0.1833	0.8390	11.0725	0.1839	1.2531
1093.0	11.0	−0.1748	0.0208	0.0239	6.8266	0.1698	0.8876	9.7163	0.1702	1.1619
1115.0	11.0	−0.0336	0.0296	0.0100	7.6247	0.2296	0.9088	8.1319	0.2298	0.9295
1137.0	11.0	−0.2175	0.0282	0.0312	5.6762	0.2010	0.7702	8.8240	0.2017	1.0700
1159.0	11.0	−0.0919	0.0244	0.0107	6.2648	0.1665	0.7015	7.5286	0.1668	0.8357
1181.0	11.0	−0.0917	0.0245	0.0118	6.0227	0.1606	0.6663	7.2240	0.1609	0.7947
1203.0	11.0	−0.1803	0.0281	0.0252	5.0517	0.1705	0.6537	7.2677	0.1711	0.8610
1225.0	11.0	−0.0348	0.0260	0.0039	6.0200	0.1599	0.6747	6.4530	0.1601	0.7223
1247.0	11.0	−0.0823	0.0292	0.0092	5.6523	0.1803	0.6232	6.6669	0.1807	0.7346
1269.0	11.0	−0.1483	0.0291	0.0183	5.0853	0.1711	0.5641	6.8354	0.1717	0.7535
1291.0	11.0	−0.1326	0.0351	0.0182	5.1165	0.2054	0.6059	6.6703	0.2059	0.7565
1313.0	11.0	−0.0959	0.0287	0.0106	5.5214	0.1729	0.6080	6.6924	0.1733	0.7368
1335.0	11.0	−0.1988	0.0386	0.0277	4.6111	0.2203	0.6411	6.9027	0.2211	0.8617

E.2.4 Observables for $\gamma d \to \pi^0 n(p)$ as a Function of W

W [MeV]	ΔW [MeV]	E	Δ_{stat}	Δ_{sys}	$\sigma_{1/2}$ [μb]	Δ_{stat} [μb]	Δ_{sys} [μb]	$\sigma_{3/2}$ [μb]	Δ_{stat} [μb]	Δ_{sys} [μb]
1321.0	9.0	−0.4720	0.0117	0.0567	32.4622	0.6739	4.4131	90.4432	0.6752	10.3162
1339.0	9.0	−0.3897	0.0118	0.0458	30.7924	0.5634	3.7669	69.9964	0.5644	7.8354
1357.0	9.0	−0.3909	0.0125	0.0455	25.7982	0.5023	3.2144	58.9414	0.5033	6.7191
1375.0	9.0	−0.3459	0.0123	0.0390	24.3244	0.4313	2.7164	49.8301	0.4323	5.5006
1393.0	9.0	−0.3036	0.0129	0.0342	21.9263	0.3867	2.4665	40.9846	0.3874	4.5232
1411.0	9.0	−0.2230	0.0143	0.0270	20.9599	0.3708	2.5161	32.9666	0.3713	3.7492
1429.0	9.0	−0.1618	0.0142	0.0191	20.4403	0.3326	2.3275	28.2961	0.3330	3.1496
1447.0	9.0	−0.1487	0.0134	0.0190	19.6172	0.2972	2.2513	26.4148	0.2976	2.9322
1465.0	9.0	−0.1016	0.0126	0.0138	20.2147	0.2751	2.3411	24.7443	0.2754	2.7745
1483.0	9.0	−0.0213	0.0120	0.0082	22.7699	0.2704	2.6357	23.6990	0.2706	2.6540
1501.0	9.0	−0.0708	0.0113	0.0119	22.6804	0.2688	2.8518	26.0955	0.2691	3.1099
1519.0	9.0	0.0301	0.0114	0.0055	23.5715	0.2546	2.7962	22.1492	0.2546	2.5704
1537.0	9.0	0.1143	0.0117	0.0132	23.3798	0.2384	2.6567	18.5403	0.2381	2.0901
1555.0	9.0	0.0819	0.0125	0.0110	19.7627	0.2227	2.2758	16.7212	0.2225	1.8879
1573.0	9.0	0.0641	0.0137	0.0103	16.7831	0.2125	1.9650	14.7113	0.2123	1.6779
1591.0	9.0	0.0931	0.0152	0.0121	14.9410	0.2045	1.9455	12.3452	0.2044	1.5663
1609.0	9.0	0.0834	0.0160	0.0108	12.9880	0.1887	1.5601	10.9543	0.1885	1.2835
1627.0	9.0	0.0373	0.0155	0.0068	11.9346	0.1750	1.3232	11.0559	0.1749	1.2166
1645.0	9.0	−0.0641	0.0161	0.0110	9.8182	0.1667	1.2292	11.1471	0.1668	1.3276
1663.0	9.0	−0.0194	0.0156	0.0034	9.9469	0.1559	1.1278	10.3334	0.1560	1.1602
1681.0	9.0	−0.1852	0.0161	0.0209	7.8071	0.1507	0.8636	11.3417	0.1512	1.2480
1699.0	9.0	−0.2176	0.0177	0.0250	6.8143	0.1504	0.7621	10.5926	0.1510	1.1703
1717.0	9.0	−0.1784	0.0193	0.0204	6.5649	0.1501	0.7544	9.3830	0.1506	1.0768
1735.0	9.0	−0.1797	0.0211	0.0201	5.9114	0.1482	0.6628	8.4812	0.1487	0.9460
1753.0	9.0	−0.1421	0.0231	0.0181	5.3344	0.1421	0.6502	7.1021	0.1424	0.8287
1771.0	9.0	−0.0305	0.0246	0.0074	5.5244	0.1393	0.7265	5.8624	0.1395	0.7369
1789.0	9.0	−0.0915	0.0258	0.0117	5.1596	0.1457	0.6844	6.2125	0.1460	0.8105
1807.0	9.0	−0.1186	0.0251	0.0136	5.4700	0.1534	0.6034	6.9305	0.1539	0.7638
1825.0	9.0	−0.1863	0.0278	0.0223	5.2257	0.1753	0.6039	7.6123	0.1761	0.8512
1843.0	9.0	−0.2051	0.0290	0.0233	5.4329	0.1930	0.6284	8.2114	0.1940	0.9332
1861.0	9.0	−0.0953	0.0317	0.0132	6.1353	0.2085	0.8091	7.4133	0.2090	0.9369
1879.0	9.0	−0.2416	0.0353	0.0389	5.1714	0.2249	0.9689	8.3472	0.2265	1.3729
1897.0	9.0	−0.0552	0.0448	0.0117	6.1212	0.2668	1.3708	6.8010	0.2674	1.4745
1915.0	9.0	−0.3379	0.0637	0.0861	4.5887	0.3815	1.5665	8.8358	0.3847	2.2007

Angular Distributions

	W=(1321.0±9.0) MeV			W=(1339.0±9.0) MeV			W=(1357.0±9.0) MeV			W=(1375.0±9.0) MeV		
$\cos(\theta^*_{\pi^0})$	E	Δ_{stat}	Δ_{sys}	E	Δ_{stat}	Δ_{sys}	E	Δ_{stat}	Δ_{sys}	E	Δ_{stat}	Δ_{sys}
−0.90	0.3810	0.2681	0.3097	0.2654	0.1837	0.1841	0.1879	0.1567	0.1147	0.0509	0.1245	0.0487
−0.70	−0.6239	0.0497	0.1256	−0.3804	0.0471	0.0610	−0.0593	0.0473	0.0166	−0.1468	0.0460	0.0203
−0.50	−0.5012	0.0277	0.0116	−0.3815	0.0277	0.0095	−0.4016	0.0296	0.0106	−0.3325	0.0292	0.0069
−0.30	−0.4593	0.0254	0.0250	−0.3538	0.0262	0.0164	−0.5381	0.0284	0.0284	−0.5813	0.0287	0.0163
−0.10	−0.4962	0.0254	0.0281	−0.5086	0.0265	0.0268	−0.5648	0.0283	0.0306	−0.3782	0.0273	0.0120
0.10	−0.5404	0.0289	0.0436	−0.4858	0.0297	0.0397	−0.4351	0.0310	0.0337	−0.3799	0.0313	0.0257
0.30	−0.3965	0.0359	0.0573	−0.2511	0.0339	0.0168	−0.3159	0.0364	0.0240	−0.2256	0.0354	0.0201
0.50	−0.4746	0.0554	0.0877	−0.2466	0.0502	0.0355	−0.1663	0.0544	0.0251	−0.2325	0.0493	0.0247
0.70	0.4099	0.1300	0.0828	−0.5753	0.1399	0.1368	0.2751	0.1212	0.0418	0.0768	0.1126	0.0065
0.90	1.7075	1.6029	0.4123	−3.0568	1.3192	0.7355	0.7801	0.8228	0.1271	−0.5989	0.7614	0.0703

	W=(1393.0±9.0) MeV			W=(1411.0±9.0) MeV			W=(1429.0±9.0) MeV			W=(1447.0±9.0) MeV		
$\cos(\theta^*_{\pi^0})$	E	Δ_{stat}	Δ_{sys}	E	Δ_{stat}	Δ_{sys}	E	Δ_{stat}	Δ_{sys}	E	Δ_{stat}	Δ_{sys}
−0.90	0.1423	0.1085	0.0773	0.8133	0.1062	0.2592	0.4862	0.0950	0.0894	0.5733	0.0806	0.1033
−0.70	−0.0939	0.0462	0.0081	−0.0656	0.0513	0.0132	0.1751	0.0502	0.0148	0.1022	0.0495	0.0055
−0.50	−0.3998	0.0312	0.0030	−0.2812	0.0330	0.0081	−0.2561	0.0336	0.0042	−0.0253	0.0316	0.0058
−0.30	−0.3728	0.0294	0.0065	−0.3237	0.0329	0.0211	−0.3281	0.0331	0.0214	−0.2083	0.0303	0.0067
−0.10	−0.3283	0.0293	0.0116	−0.3879	0.0329	0.0223	−0.1138	0.0318	0.0046	−0.3276	0.0310	0.0252
0.10	−0.2829	0.0327	0.0236	−0.2112	0.0364	0.0218	−0.3243	0.0368	0.0182	−0.2423	0.0335	0.0133
0.30	−0.4041	0.0382	0.0285	−0.1624	0.0428	0.0253	−0.1289	0.0414	0.0046	−0.2892	0.0407	0.0271
0.50	−0.1215	0.0521	0.0114	−0.1358	0.0658	0.0187	−0.1041	0.0615	0.0198	−0.1140	0.0562	0.0237
0.70	−0.1087	0.1282	0.0386	0.1567	0.1426	0.0250	0.3832	0.1157	0.0044	0.1730	0.1101	0.0146
0.90	−0.2073	1.0956	0.1036	−1.8128	0.8205	0.0673	−0.8998	0.7946	0.0577	2.1255	5.1106	1.1161

	W=(1465.0±9.0) MeV			W=(1483.0±9.0) MeV			W=(1501.0±9.0) MeV			W=(1519.0±9.0) MeV		
$\cos(\theta^*_{\pi^0})$	E	Δ_{stat}	Δ_{sys}	E	Δ_{stat}	Δ_{sys}	E	Δ_{stat}	Δ_{sys}	E	Δ_{stat}	Δ_{sys}
−0.90	0.4828	0.0702	0.0512	0.5012	0.0625	0.0525	0.8559	0.0584	0.0466	0.9734	0.0601	0.0977
−0.70	0.1817	0.0465	0.0048	0.3239	0.0419	0.0236	0.3814	0.0385	0.0206	0.6036	0.0426	0.0075
−0.50	−0.0202	0.0294	0.0034	0.1476	0.0297	0.0104	0.1538	0.0288	0.0042	0.1560	0.0297	0.0103
−0.30	−0.2672	0.0294	0.0198	−0.1216	0.0286	0.0131	−0.2255	0.0276	0.0174	0.0127	0.0284	0.0056
−0.10	−0.2033	0.0292	0.0149	−0.1188	0.0284	0.0158	−0.2750	0.0278	0.0234	−0.1886	0.0280	0.0197
0.10	−0.2576	0.0321	0.0204	−0.2281	0.0304	0.0112	−0.2497	0.0302	0.0231	−0.2568	0.0299	0.0213
0.30	−0.0823	0.0394	0.0116	−0.1347	0.0362	0.0080	−0.2781	0.0321	0.0168	−0.1624	0.0322	0.0111
0.50	−0.1323	0.0520	0.0312	0.0738	0.0460	0.0077	−0.2357	0.0419	0.0242	−0.1779	0.0394	0.0157
0.70	0.3377	0.0951	0.0135	−0.1541	0.0781	0.0110	0.5194	0.0781	0.0902	0.4282	0.0649	0.0131
0.90	2.3521	1.0893	0.4074	0.3839	0.5385	0.1328	−0.9918	0.3300	0.0576	0.6446	0.2937	0.1079

$\cos(\theta^*_{\pi^0})$	$W=(1537.0\pm9.0)$ MeV			$W=(1555.0\pm9.0)$ MeV			$W=(1573.0\pm9.0)$ MeV			$W=(1591.0\pm9.0)$ MeV		
	E	Δ_{stat}	Δ_{sys}	E	Δ_{stat}	Δ_{sys}	E	Δ_{stat}	Δ_{sys}	E	Δ_{stat}	Δ_{sys}
−0.90	0.9477	0.0605	0.0965	0.8092	0.0650	0.0635	0.9479	0.0715	0.1097	0.4246	0.0775	0.0410
−0.70	0.5649	0.0412	0.0281	0.4391	0.0445	0.0197	0.2170	0.0495	0.0218	0.2414	0.0545	0.0246
−0.50	0.2212	0.0295	0.0122	0.2417	0.0326	0.0090	0.2535	0.0347	0.0096	0.1496	0.0382	0.0112
−0.30	0.1671	0.0298	0.0048	−0.0019	0.0304	0.0054	−0.1032	0.0345	0.0123	0.0184	0.0372	0.0143
−0.10	−0.1489	0.0281	0.0155	−0.1424	0.0300	0.0095	−0.1623	0.0316	0.0113	−0.0835	0.0359	0.0174
0.10	−0.1676	0.0308	0.0153	−0.1202	0.0320	0.0148	−0.2120	0.0368	0.0210	−0.1607	0.0397	0.0233
0.30	−0.1173	0.0323	0.0053	−0.0619	0.0352	0.0065	−0.0461	0.0430	0.0179	0.1581	0.0477	0.0139
0.50	0.0477	0.0423	0.0080	0.0020	0.0442	0.0065	0.2786	0.0505	0.0193	0.3092	0.0579	0.0407
0.70	0.5152	0.0697	0.0496	0.6707	0.0806	0.0715	0.5832	0.0724	0.0427	0.5639	0.0790	0.0743
0.90	3.4063	1.1947	1.2461	1.1759	0.3731	0.1003	0.6065	0.2560	0.0707	0.4736	0.4568	0.2079

$\cos(\theta^*_{\pi^0})$	$W=(1609.0\pm9.0)$ MeV			$W=(1627.0\pm9.0)$ MeV			$W=(1645.0\pm9.0)$ MeV			$W=(1663.0\pm9.0)$ MeV		
	E	Δ_{stat}	Δ_{sys}	E	Δ_{stat}	Δ_{sys}	E	Δ_{stat}	Δ_{sys}	E	Δ_{stat}	Δ_{sys}
−0.90	0.4903	0.0814	0.1081	0.5336	0.0970	0.0634	0.1259	0.0817	0.0360	−0.0142	0.0841	0.0097
−0.70	−0.2267	0.0596	0.0149	0.1301	0.0600	0.0125	−0.4780	0.0659	0.0342	−0.2771	0.0567	0.0158
−0.50	0.1334	0.0383	0.0032	−0.0134	0.0373	0.0096	−0.2380	0.0405	0.0237	−0.3109	0.0391	0.0108
−0.30	−0.1225	0.0394	0.0229	−0.1922	0.0356	0.0070	−0.2223	0.0403	0.0253	−0.1253	0.0385	0.0043
−0.10	−0.0402	0.0392	0.0094	−0.3229	0.0390	0.0271	−0.1015	0.0403	0.0047	−0.1258	0.0443	0.0100
0.10	−0.0426	0.0441	0.0108	−0.1007	0.0494	0.0195	0.0121	0.0499	0.0145	0.0388	0.0518	0.0163
0.30	0.3837	0.0543	0.0249	0.3316	0.0506	0.0065	0.0190	0.0566	0.0083	0.2132	0.0531	0.0124
0.50	0.3483	0.0581	0.0333	0.3619	0.0465	0.0198	0.2684	0.0458	0.0130	0.3870	0.0436	0.0325
0.70	0.4619	0.0664	0.0361	0.4480	0.0598	0.0362	0.2003	0.0516	0.0124	0.2446	0.0465	0.0181
0.90	−0.4289	0.4061	0.2464	1.8499	0.7337	0.7930	0.9072	0.3582	0.4021	0.3705	0.1442	0.0440

$\cos(\theta^*_{\pi^0})$	$W=(1681.0\pm9.0)$ MeV			$W=(1699.0\pm9.0)$ MeV			$W=(1717.0\pm9.0)$ MeV			$W=(1735.0\pm9.0)$ MeV		
	E	Δ_{stat}	Δ_{sys}	E	Δ_{stat}	Δ_{sys}	E	Δ_{stat}	Δ_{sys}	E	Δ_{stat}	Δ_{sys}
−0.90	0.1521	0.0766	0.0314	−0.1776	0.0784	0.0118	−0.1585	0.0755	0.0132	0.1501	0.0736	0.0144
−0.70	−0.4378	0.0571	0.0300	−0.4676	0.0598	0.0329	−0.6861	0.0656	0.0242	−0.3608	0.0671	0.0017
−0.50	−0.3883	0.0389	0.0122	−0.6400	0.0486	0.0098	−0.6099	0.0520	0.0182	−0.4848	0.0595	0.0049
−0.30	−0.3928	0.0437	0.0052	−0.5859	0.0515	0.0268	−0.3256	0.0581	0.0016	−0.5693	0.0676	0.0340
−0.10	−0.4571	0.0510	0.0300	−0.3987	0.0567	0.0173	−0.1871	0.0637	0.0120	−0.6314	0.0730	0.0197
0.10	−0.1414	0.0552	0.0085	0.0193	0.0677	0.0014	−0.1482	0.0686	0.0128	−0.3581	0.0736	0.0424
0.30	0.2054	0.0524	0.0107	0.2417	0.0539	0.0111	0.1246	0.0599	0.0047	0.5165	0.0643	0.0246
0.50	0.0810	0.0410	0.0049	0.1469	0.0423	0.0018	0.2693	0.0489	0.0041	0.1318	0.0512	0.0127
0.70	0.0877	0.0504	0.0082	0.1829	0.0504	0.0187	0.1478	0.0537	0.0167	0.1090	0.0682	0.0055
0.90	0.0120	0.1478	0.0041	−0.0942	0.1320	0.0093	−0.3118	0.1685	0.0574	0.2728	0.1976	0.0131

$\cos(\theta^*_{\pi^0})$	$W=(1753.0\pm9.0)$ MeV			$W=(1771.0\pm9.0)$ MeV			$W=(1789.0\pm9.0)$ MeV			$W=(1807.0\pm9.0)$ MeV		
	E	Δ_{stat}	Δ_{sys}	E	Δ_{stat}	Δ_{sys}	E	Δ_{stat}	Δ_{sys}	E	Δ_{stat}	Δ_{sys}
−0.90	0.1811	0.0716	0.0050	0.0817	0.0619	0.0092	0.3536	0.0654	0.0092	0.3469	0.0660	0.0041
−0.70	−0.5200	0.0711	0.0279	−0.2744	0.0655	0.0144	−0.3426	0.0788	0.0577	−0.2414	0.0601	0.0155
−0.50	−0.4901	0.0633	0.0116	−0.5183	0.0721	0.0441	−0.7318	0.0696	0.0189	−0.5814	0.0751	0.0123
−0.30	−0.5232	0.0715	0.0154	−0.2644	0.0789	0.0336	−0.5094	0.0882	0.0545	−0.5590	0.0910	0.0676
−0.10	−0.2473	0.0729	0.0039	−0.0032	0.0852	0.0125	−0.0998	0.0852	0.0131	0.0130	0.0768	0.0024
0.10	0.1204	0.0843	0.0083	−0.0201	0.1081	0.0196	0.2063	0.0974	0.0401	−0.0822	0.0917	0.0146
0.30	0.3659	0.0734	0.0363	0.4745	0.0788	0.0316	0.5647	0.0893	0.0324	0.3948	0.0926	0.0216
0.50	0.2197	0.0600	0.0046	0.3880	0.0699	0.0144	0.2046	0.0872	0.0255	0.3028	0.0836	0.0012
0.70	−0.2518	0.0876	0.0590	0.1271	0.0846	0.0131	−0.2444	0.0782	0.0111	−0.4091	0.0828	0.0119
0.90	0.1683	0.2151	0.0626	−0.6935	0.2105	0.0737	0.6110	0.2223	0.0602	−0.1941	0.1570	0.0264

$\cos(\theta^*_{\pi^0})$	$W=(1825.0\pm9.0)$ MeV			$W=(1843.0\pm9.0)$ MeV			$W=(1861.0\pm9.0)$ MeV			$W=(1879.0\pm9.0)$ MeV		
	E	Δ_{stat}	Δ_{sys}	E	Δ_{stat}	Δ_{sys}	E	Δ_{stat}	Δ_{sys}	E	Δ_{stat}	Δ_{sys}
−0.90	0.0708	0.0587	0.0082	−0.0441	0.0652	0.0093	0.0814	0.0648	0.0084	−0.0792	0.0749	0.0079
−0.70	−0.5870	0.0706	0.0833	−0.3224	0.0679	0.0143	−0.3088	0.0745	0.0264	−0.7212	0.0874	0.0147
−0.50	−0.4750	0.0771	0.0245	−0.2036	0.0707	0.0223	−0.3509	0.0810	0.0256	−0.4937	0.0958	0.0375
−0.30	−0.4014	0.0949	0.0270	−0.5331	0.1406	0.1043	−0.3248	0.1020	0.0455	−0.3169	0.1174	0.0612
−0.10	−0.0250	0.1067	0.0059	−0.6213	0.1030	0.0233	0.2275	0.1357	0.0627	−0.2688	0.1127	0.0330
0.10	−0.1263	0.0976	0.0061	0.2047	0.1038	0.0368	−0.0175	0.1367	0.0026	0.3259	0.1566	0.0366
0.30	0.3080	0.1080	0.0062	−0.1171	0.1113	0.0232	0.1198	0.1311	0.0297	−0.4317	0.1825	0.1387
0.50	0.0706	0.0988	0.0049	0.1126	0.1104	0.0207	−0.1361	0.1285	0.0352	0.0120	0.1531	0.0091
0.70	−0.0621	0.0984	0.0099	−0.1914	0.0945	0.0192	0.2799	0.1033	0.0301	−0.1028	0.1091	0.0206
0.90	−1.6373	0.5375	0.5435	−0.3682	0.2534	0.0888	−0.4470	0.2098	0.0412	0.4300	0.2040	0.0486

$\cos(\theta^*_{\pi^0})$	$W=(1897.0\pm9.0)$ MeV			$W=(1915.0\pm9.0)$ MeV		
	E	Δ_{stat}	Δ_{sys}	E	Δ_{stat}	Δ_{sys}
−0.90	0.2554	0.0967	0.0168	0.1392	0.1437	0.0372
−0.70	−0.0700	0.1082	0.0069	0.0605	0.1493	0.0224
−0.50	−0.4054	0.1191	0.0223	−0.8401	0.1644	0.1402
−0.30	0.1546	0.1454	0.0420	0.3614	0.2007	0.1013
−0.10	−0.2321	0.1558	0.0121	−1.1342	0.2796	0.0900
0.10	−0.1409	0.1768	0.0621	−0.5506	0.2156	0.1973
0.30	−1.0517	0.2611	0.4056	−0.1066	0.3390	0.0462
0.50	0.7164	0.2234	0.3752	−0.8871	0.3666	0.4466
0.70	−0.2068	0.1474	0.0667	−0.7511	0.2078	0.2202
0.90	0.1580	0.2366	0.0593	0.1623	0.3035	0.0234

$\cos(\theta^*_{\pi^0})$	$W=(1321.0\pm9.0)$ MeV			$W=(1339.0\pm9.0)$ MeV			$W=(1357.0\pm9.0)$ MeV			$W=(1375.0\pm9.0)$ MeV		
	$d\sigma_{1/2}/d\Omega$ [μb/sr]	Δ_{stat} [μb/sr]	Δ_{sys} [μb/sr]	$d\sigma_{1/2}/d\Omega$ [μb/sr]	Δ_{stat} [μb/sr]	Δ_{sys} [μb/sr]	$d\sigma_{1/2}/d\Omega$ [μb/sr]	Δ_{stat} [μb/sr]	Δ_{sys} [μb/sr]	$d\sigma_{1/2}/d\Omega$ [μb/sr]	Δ_{stat} [μb/sr]	Δ_{sys} [μb/sr]
−0.90	0.8842	0.0903	0.5709	0.8895	0.0796	0.5032	0.8679	0.0765	0.4406	0.7928	0.0704	0.3255
−0.70	1.3654	0.1450	0.6389	1.6953	0.1139	0.4140	2.1688	0.1020	0.2586	1.7578	0.0867	0.2722
−0.50	2.3095	0.1186	0.0756	2.3638	0.1000	0.0745	1.9328	0.0903	0.0788	1.8822	0.0776	0.0516
−0.30	3.0892	0.1362	0.2786	2.9948	0.1149	0.1611	1.8240	0.1039	0.1784	1.4429	0.0905	0.0647
−0.10	3.1843	0.1508	0.3758	2.5583	0.1289	0.2769	1.8751	0.1126	0.2025	2.3871	0.0983	0.0614
0.10	2.9699	0.1743	0.5322	2.7105	0.1469	0.4139	2.4767	0.1286	0.3340	2.3133	0.1107	0.1996
0.30	3.5548	0.2003	0.8644	3.7374	0.1633	0.3628	2.7673	0.1411	0.3254	2.7123	0.1190	0.2084
0.50	2.3310	0.2285	0.7984	2.8600	0.1835	0.4958	2.5475	0.1611	0.4633	2.1254	0.1310	0.1915
0.70	3.7974	0.3276	0.7205	0.9234	0.2719	0.5100	2.3926	0.2183	0.2998	1.6988	0.1726	0.1661
0.90	5.1145	1.9469	1.4608	−2.9757	1.3104	0.9173	2.2316	0.9120	0.4314	0.4385	0.7456	0.1032

$\cos(\theta^*_{\pi^0})$	$W=(1393.0\pm9.0)$ MeV			$W=(1411.0\pm9.0)$ MeV			$W=(1429.0\pm9.0)$ MeV			$W=(1447.0\pm9.0)$ MeV		
	$d\sigma_{1/2}/d\Omega$ [μb/sr]	Δ_{stat} [μb/sr]	Δ_{sys} [μb/sr]	$d\sigma_{1/2}/d\Omega$ [μb/sr]	Δ_{stat} [μb/sr]	Δ_{sys} [μb/sr]	$d\sigma_{1/2}/d\Omega$ [μb/sr]	Δ_{stat} [μb/sr]	Δ_{sys} [μb/sr]	$d\sigma_{1/2}/d\Omega$ [μb/sr]	Δ_{stat} [μb/sr]	Δ_{sys} [μb/sr]
−0.90	0.8584	0.0663	0.2915	1.3574	0.0680	0.3665	1.1332	0.0658	0.1932	1.3424	0.0628	0.1863
−0.70	1.6500	0.0789	0.1572	1.4900	0.0776	0.0925	1.7890	0.0724	0.1393	1.5511	0.0672	0.0145
−0.50	1.4461	0.0709	0.0085	1.5493	0.0676	0.0304	1.4408	0.0621	0.0191	1.7852	0.0560	0.0309
−0.30	1.8509	0.0820	0.0393	1.7139	0.0794	0.1207	1.5310	0.0717	0.1038	1.7278	0.0635	0.0271
−0.10	2.1398	0.0892	0.1096	1.6732	0.0854	0.1515	2.1780	0.0758	0.1181	1.5522	0.0681	0.1268
0.10	2.2624	0.0989	0.2055	2.0978	0.0935	0.2164	1.5837	0.0828	0.1386	1.7040	0.0726	0.0927
0.30	1.7098	0.1037	0.1659	1.9601	0.0969	0.2191	1.8324	0.0844	0.0968	1.3704	0.0754	0.1454
0.50	1.9569	0.1127	0.1697	1.4775	0.1095	0.2616	1.3570	0.0903	0.1262	1.2680	0.0779	0.1089
0.70	1.0826	0.1505	0.2178	1.1847	0.1415	0.2165	1.4052	0.1116	0.0315	1.0542	0.0961	0.1000
0.90	0.4519	0.5788	0.0931	−0.7021	0.5060	0.0655	0.0551	0.4221	0.0397	0.9745	0.7747	0.8103

$\cos(\theta^*_{\pi^0})$	$W=(1465.0\pm9.0)$ MeV			$W=(1483.0\pm9.0)$ MeV			$W=(1501.0\pm9.0)$ MeV			$W=(1519.0\pm9.0)$ MeV		
	$d\sigma_{1/2}/d\Omega$ [μb/sr]	Δ_{stat} [μb/sr]	Δ_{sys} [μb/sr]	$d\sigma_{1/2}/d\Omega$ [μb/sr]	Δ_{stat} [μb/sr]	Δ_{sys} [μb/sr]	$d\sigma_{1/2}/d\Omega$ [μb/sr]	Δ_{stat} [μb/sr]	Δ_{sys} [μb/sr]	$d\sigma_{1/2}/d\Omega$ [μb/sr]	Δ_{stat} [μb/sr]	Δ_{sys} [μb/sr]
−0.90	1.3799	0.0608	0.1079	1.6175	0.0629	0.1287	2.3317	0.0661	0.1029	2.4518	0.0664	0.2317
−0.70	1.6488	0.0626	0.0163	2.0233	0.0611	0.0574	2.2636	0.0601	0.0713	2.3789	0.0589	0.0433
−0.50	1.7639	0.0511	0.0211	2.0340	0.0508	0.0277	2.0446	0.0497	0.0618	1.9074	0.0475	0.0509
−0.30	1.5420	0.0591	0.0702	1.8338	0.0578	0.0529	1.6497	0.0569	0.0966	1.9610	0.0536	0.0784
−0.10	1.7731	0.0629	0.1156	1.9673	0.0614	0.1045	1.6475	0.0611	0.1560	1.7055	0.0573	0.1457
0.10	1.6236	0.0670	0.0661	1.7354	0.0660	0.0851	1.6932	0.0662	0.1845	1.6075	0.0627	0.1421
0.30	1.6712	0.0701	0.1686	1.6789	0.0686	0.1365	1.5678	0.0677	0.1404	1.7048	0.0639	0.1254
0.50	1.2390	0.0721	0.1629	1.6934	0.0711	0.1476	1.3449	0.0716	0.1522	1.4266	0.0665	0.1050
0.70	1.2472	0.0851	0.0436	0.9528	0.0859	0.0859	1.9178	0.0917	0.3037	1.8827	0.0818	0.0745
0.90	2.0380	0.3560	0.5275	0.7516	0.2791	0.1757	0.0233	0.2574	0.0536	1.5398	0.2501	0.1931

$\cos(\theta^*_{\pi^0})$	$W=(1537.0\pm9.0)$ MeV			$W=(1555.0\pm9.0)$ MeV			$W=(1573.0\pm9.0)$ MeV			$W=(1591.0\pm9.0)$ MeV		
	$d\sigma_{1/2}/d\Omega$ [μb/sr]	Δ_{stat} [μb/sr]	Δ_{sys} [μb/sr]	$d\sigma_{1/2}/d\Omega$ [μb/sr]	Δ_{stat} [μb/sr]	Δ_{sys} [μb/sr]	$d\sigma_{1/2}/d\Omega$ [μb/sr]	Δ_{stat} [μb/sr]	Δ_{sys} [μb/sr]	$d\sigma_{1/2}/d\Omega$ [μb/sr]	Δ_{stat} [μb/sr]	Δ_{sys} [μb/sr]
−0.90	2.3112	0.0639	0.2188	1.8942	0.0618	0.1286	1.8284	0.0601	0.1754	1.1190	0.0577	0.0736
−0.70	2.2610	0.0558	0.0885	1.8125	0.0533	0.0495	1.3157	0.0515	0.0648	1.1823	0.0501	0.0480
−0.50	1.9024	0.0445	0.0352	1.6549	0.0422	0.0605	1.5077	0.0405	0.0285	1.2121	0.0395	0.0942
−0.30	2.0331	0.0506	0.0733	1.5811	0.0472	0.0454	1.2158	0.0459	0.0936	1.2482	0.0448	0.1265
−0.10	1.6560	0.0531	0.0856	1.4520	0.0497	0.0755	1.2814	0.0471	0.0486	1.1981	0.0461	0.1176
0.10	1.6203	0.0583	0.0920	1.5140	0.0536	0.0730	1.1276	0.0513	0.1015	1.0236	0.0472	0.0630
0.30	1.6363	0.0584	0.0646	1.4661	0.0539	0.0745	1.1534	0.0510	0.1094	1.1752	0.0475	0.1010
0.50	1.5869	0.0630	0.1551	1.3150	0.0569	0.1077	1.3819	0.0530	0.1160	1.2006	0.0513	0.1853
0.70	1.8300	0.0793	0.2019	1.7032	0.0754	0.2141	1.6207	0.0691	0.1403	1.4274	0.0670	0.2215
0.90	3.2699	0.3873	1.3074	1.5200	0.2140	0.1549	1.3652	0.2036	0.1831	0.9562	0.2514	0.5481

$\cos(\theta^*_{\pi^0})$	$W=(1609.0\pm9.0)$ MeV			$W=(1627.0\pm9.0)$ MeV			$W=(1645.0\pm9.0)$ MeV			$W=(1663.0\pm9.0)$ MeV		
	$d\sigma_{1/2}/d\Omega$ [μb/sr]	Δ_{stat} [μb/sr]	Δ_{sys} [μb/sr]	$d\sigma_{1/2}/d\Omega$ [μb/sr]	Δ_{stat} [μb/sr]	Δ_{sys} [μb/sr]	$d\sigma_{1/2}/d\Omega$ [μb/sr]	Δ_{stat} [μb/sr]	Δ_{sys} [μb/sr]	$d\sigma_{1/2}/d\Omega$ [μb/sr]	Δ_{stat} [μb/sr]	Δ_{sys} [μb/sr]
−0.90	1.0903	0.0541	0.2146	0.9311	0.0550	0.1080	0.7870	0.0526	0.1334	0.6392	0.0510	0.0916
−0.70	0.6443	0.0472	0.0553	0.8959	0.0462	0.0451	0.3777	0.0455	0.0416	0.5643	0.0423	0.0438
−0.50	1.1147	0.0369	0.0336	0.9579	0.0355	0.0430	0.6659	0.0347	0.0778	0.5834	0.0323	0.0297
−0.30	0.9509	0.0418	0.1050	0.8979	0.0383	0.0237	0.7428	0.0377	0.0802	0.8073	0.0350	0.0330
−0.10	1.0668	0.0430	0.0974	0.7016	0.0389	0.0601	0.8189	0.0362	0.0342	0.6662	0.0333	0.0389
0.10	0.9515	0.0431	0.0484	0.7349	0.0397	0.0523	0.7310	0.0355	0.0415	0.6506	0.0316	0.0361
0.30	1.1162	0.0422	0.0910	1.0064	0.0370	0.0120	0.6307	0.0346	0.0753	0.7392	0.0318	0.0495
0.50	1.1044	0.0460	0.1294	1.2292	0.0404	0.0432	1.1246	0.0398	0.0688	1.2797	0.0390	0.1088
0.70	1.4509	0.0630	0.1318	1.5608	0.0619	0.1539	1.4004	0.0593	0.1062	1.6146	0.0593	0.1115
0.90	0.4367	0.2497	0.3730	1.9038	0.2917	1.1129	1.4420	0.2052	0.5787	1.4897	0.1530	0.2074

$\cos(\theta^*_{\pi^0})$	$W=(1681.0\pm9.0)$ MeV			$W=(1699.0\pm9.0)$ MeV			$W=(1717.0\pm9.0)$ MeV			$W=(1735.0\pm9.0)$ MeV		
	$d\sigma_{1/2}/d\Omega$ [μb/sr]	Δ_{stat} [μb/sr]	Δ_{sys} [μb/sr]	$d\sigma_{1/2}/d\Omega$ [μb/sr]	Δ_{stat} [μb/sr]	Δ_{sys} [μb/sr]	$d\sigma_{1/2}/d\Omega$ [μb/sr]	Δ_{stat} [μb/sr]	Δ_{sys} [μb/sr]	$d\sigma_{1/2}/d\Omega$ [μb/sr]	Δ_{stat} [μb/sr]	Δ_{sys} [μb/sr]
−0.90	0.8541	0.0525	0.1473	0.6215	0.0574	0.0090	0.6813	0.0584	0.0605	0.9621	0.0595	0.0612
−0.70	0.4370	0.0413	0.0518	0.4099	0.0428	0.0532	0.2374	0.0449	0.0260	0.4660	0.0471	0.0034
−0.50	0.5054	0.0306	0.0256	0.2489	0.0314	0.0112	0.2545	0.0311	0.0192	0.2822	0.0311	0.0012
−0.30	0.4742	0.0328	0.0024	0.2756	0.0320	0.0241	0.3700	0.0309	0.0009	0.2036	0.0299	0.0238
−0.10	0.3561	0.0319	0.0398	0.3338	0.0303	0.0209	0.3863	0.0292	0.0265	0.1561	0.0283	0.0090
0.10	0.4735	0.0294	0.0334	0.4508	0.0296	0.0188	0.3645	0.0282	0.0364	0.2619	0.0278	0.0470
0.30	0.7160	0.0305	0.0350	0.7114	0.0304	0.0204	0.5957	0.0313	0.0092	0.7681	0.0311	0.0054
0.50	1.0396	0.0391	0.0624	1.0876	0.0396	0.0129	1.0878	0.0410	0.0047	0.8982	0.0397	0.0411
0.70	1.3613	0.0625	0.1314	1.4673	0.0614	0.0773	1.3337	0.0606	0.0786	1.0123	0.0612	0.0036
0.90	1.0726	0.1556	0.1988	0.9805	0.1385	0.0301	0.6173	0.1440	0.0795	0.9155	0.1392	0.0385

$\cos(\theta^*_{\pi^0})$	W=(1753.0±9.0) MeV			W=(1771.0±9.0) MeV			W=(1789.0±9.0) MeV			W=(1807.0±9.0) MeV		
	$d\sigma_{1/2}/d\Omega$ [μb/sr]	Δ_{stat} [μb/sr]	Δ_{sys} [μb/sr]	$d\sigma_{1/2}/d\Omega$ [μb/sr]	Δ_{stat} [μb/sr]	Δ_{sys} [μb/sr]	$d\sigma_{1/2}/d\Omega$ [μb/sr]	Δ_{stat} [μb/sr]	Δ_{sys} [μb/sr]	$d\sigma_{1/2}/d\Omega$ [μb/sr]	Δ_{stat} [μb/sr]	Δ_{sys} [μb/sr]
−0.90	0.9815	0.0584	0.0140	1.0104	0.0559	0.0654	1.2672	0.0596	0.0090	1.3584	0.0649	0.0199
−0.70	0.3207	0.0452	0.0307	0.4714	0.0415	0.0155	0.3917	0.0460	0.1066	0.5690	0.0440	0.0295
−0.50	0.2432	0.0287	0.0082	0.1948	0.0278	0.0365	0.1147	0.0270	0.0108	0.1705	0.0284	0.0073
−0.30	0.1885	0.0266	0.0072	0.2493	0.0262	0.0402	0.1579	0.0271	0.0320	0.1512	0.0291	0.0359
−0.10	0.2859	0.0271	0.0071	0.3302	0.0281	0.0388	0.3128	0.0294	0.0368	0.4051	0.0302	0.0138
0.10	0.3787	0.0282	0.0333	0.2813	0.0304	0.0678	0.3842	0.0306	0.0385	0.3293	0.0325	0.0050
0.30	0.5791	0.0302	0.0384	0.5777	0.0297	0.0253	0.5682	0.0308	0.0397	0.5028	0.0324	0.0167
0.50	0.7909	0.0383	0.0233	0.7771	0.0380	0.0264	0.5713	0.0409	0.0620	0.6757	0.0424	0.0008
0.70	0.5513	0.0627	0.1585	0.7794	0.0580	0.0904	0.5805	0.0591	0.0351	0.4720	0.0633	0.0214
0.90	0.7780	0.1404	0.1037	0.2241	0.1299	0.0746	1.1677	0.1501	0.1209	0.7435	0.1373	0.1068

$\cos(\theta^*_{\pi^0})$	W=(1825.0±9.0) MeV			W=(1843.0±9.0) MeV			W=(1861.0±9.0) MeV			W=(1879.0±9.0) MeV		
	$d\sigma_{1/2}/d\Omega$ [μb/sr]	Δ_{stat} [μb/sr]	Δ_{sys} [μb/sr]	$d\sigma_{1/2}/d\Omega$ [μb/sr]	Δ_{stat} [μb/sr]	Δ_{sys} [μb/sr]	$d\sigma_{1/2}/d\Omega$ [μb/sr]	Δ_{stat} [μb/sr]	Δ_{sys} [μb/sr]	$d\sigma_{1/2}/d\Omega$ [μb/sr]	Δ_{stat} [μb/sr]	Δ_{sys} [μb/sr]
−0.90	1.2628	0.0667	0.1178	1.0774	0.0720	0.0137	1.2365	0.0709	0.1218	0.9641	0.0762	0.0334
−0.70	0.3196	0.0508	0.1072	0.5536	0.0542	0.0377	0.5553	0.0587	0.0607	0.2129	0.0612	0.0160
−0.50	0.2221	0.0306	0.0214	0.3506	0.0298	0.0333	0.2517	0.0300	0.0225	0.1715	0.0298	0.0248
−0.30	0.2125	0.0328	0.0244	0.1418	0.0401	0.0634	0.2706	0.0378	0.0529	0.2634	0.0402	0.0708
−0.10	0.3543	0.0382	0.0725	0.1663	0.0421	0.0143	0.4710	0.0513	0.0682	0.3737	0.0540	0.0594
0.10	0.3478	0.0379	0.0131	0.5294	0.0428	0.0900	0.3724	0.0494	0.0464	0.4937	0.0557	0.0623
0.30	0.4795	0.0386	0.0095	0.3688	0.0427	0.0785	0.4691	0.0497	0.1164	0.2333	0.0585	0.1128
0.50	0.5081	0.0460	0.0298	0.5557	0.0525	0.0815	0.4192	0.0559	0.1094	0.4962	0.0632	0.1566
0.70	0.7294	0.0759	0.0847	0.7341	0.0828	0.0358	1.2435	0.0963	0.1298	0.9896	0.1095	0.2108
0.90	−0.4320	0.2446	0.3737	0.6239	0.2364	0.2034	0.6681	0.2376	0.0666	1.8445	0.2537	0.1096

$\cos(\theta^*_{\pi^0})$				W=(1897.0±9.0) MeV						W=(1915.0±9.0) MeV		
				$d\sigma_{1/2}/d\Omega$ [μb/sr]	Δ_{stat} [μb/sr]	Δ_{sys} [μb/sr]				$d\sigma_{1/2}/d\Omega$ [μb/sr]	Δ_{stat} [μb/sr]	Δ_{sys} [μb/sr]
−0.90				1.2604	0.0932	0.0817				1.4247	0.1642	0.2803
−0.70				0.6172	0.0708	0.0210				0.8303	0.1138	0.0424
−0.50				0.1750	0.0329	0.0159				0.0590	0.0436	0.0477
−0.30				0.4319	0.0483	0.1129				0.5311	0.0709	0.1175
−0.10				0.3404	0.0663	0.0277				−0.0449	0.0968	0.0353
0.10				0.4059	0.0656	0.1695				0.2740	0.0940	0.1703
0.30				0.0326	0.0761	0.1295				0.3478	0.1006	0.1505
0.50				0.7862	0.0796	0.3347				0.1209	0.1121	0.1855
0.70				0.8597	0.1337	0.3098				0.3098	0.1712	0.2635
0.90				1.6228	0.2873	0.4859				1.5918	0.3930	0.2353

$\cos(\theta^*_{\pi^0})$	W=(1321.0±9.0) MeV			W=(1339.0±9.0) MeV			W=(1357.0±9.0) MeV			W=(1375.0±9.0) MeV		
	$d\sigma_{3/2}/d\Omega$ [μb/sr]	Δ_{stat} [μb/sr]	Δ_{sys} [μb/sr]	$d\sigma_{3/2}/d\Omega$ [μb/sr]	Δ_{stat} [μb/sr]	Δ_{sys} [μb/sr]	$d\sigma_{3/2}/d\Omega$ [μb/sr]	Δ_{stat} [μb/sr]	Δ_{sys} [μb/sr]	$d\sigma_{3/2}/d\Omega$ [μb/sr]	Δ_{stat} [μb/sr]	Δ_{sys} [μb/sr]
−0.90	0.5517	0.0902	0.4954	0.6138	0.0795	0.4440	0.6548	0.0764	0.3979	0.7329	0.0703	0.3263
−0.70	5.3030	0.1453	0.9797	3.6424	0.1141	0.5523	2.4394	0.1021	0.2698	2.3393	0.0867	0.3096
−0.50	6.9192	0.1189	0.0185	5.2739	0.1002	0.0637	4.5285	0.0905	0.0904	3.7388	0.0777	0.0698
−0.30	8.3454	0.1365	0.3149	6.2635	0.1152	0.1363	6.0622	0.1042	0.1685	5.4005	0.0908	0.0312
−0.10	9.5205	0.1511	0.5638	7.8947	0.1292	0.3936	6.7324	0.1129	0.1958	5.2630	0.0986	0.0308
0.10	10.0371	0.1747	0.7871	7.8639	0.1472	0.5384	6.3231	0.1289	0.4436	5.1432	0.1109	0.1882
0.30	8.2744	0.2007	1.1725	6.2666	0.1635	0.4606	5.3492	0.1413	0.4304	4.2867	0.1192	0.1897
0.50	6.5535	0.2289	1.0730	4.7376	0.1837	0.5684	3.5715	0.1612	0.5327	3.4052	0.1312	0.1726
0.70	1.5874	0.3273	0.5388	3.4045	0.2722	0.7309	1.3582	0.2181	0.2581	1.4501	0.1726	0.1338
0.90	−1.3547	1.9453	0.9654	6.1998	1.3139	1.4570	0.3280	0.9096	0.2072	1.7143	0.7462	0.0732

$\cos(\theta^*_{\pi^0})$	W=(1393.0±9.0) MeV			W=(1411.0±9.0) MeV			W=(1429.0±9.0) MeV			W=(1447.0±9.0) MeV		
	$d\sigma_{3/2}/d\Omega$ [μb/sr]	Δ_{stat} [μb/sr]	Δ_{sys} [μb/sr]	$d\sigma_{3/2}/d\Omega$ [μb/sr]	Δ_{stat} [μb/sr]	Δ_{sys} [μb/sr]	$d\sigma_{3/2}/d\Omega$ [μb/sr]	Δ_{stat} [μb/sr]	Δ_{sys} [μb/sr]	$d\sigma_{3/2}/d\Omega$ [μb/sr]	Δ_{stat} [μb/sr]	Δ_{sys} [μb/sr]
−0.90	0.6711	0.0662	0.2739	0.2076	0.0676	0.2247	0.4156	0.0655	0.1357	0.3844	0.0624	0.1349
−0.70	1.9834	0.0790	0.1708	1.6905	0.0776	0.1130	1.2630	0.0723	0.1194	1.2617	0.0672	0.0108
−0.50	3.3734	0.0710	0.0200	2.7495	0.0677	0.0371	2.4295	0.0623	0.0107	1.8743	0.0560	0.0111
−0.30	4.0451	0.0822	0.0296	3.3492	0.0795	0.1043	3.0191	0.0719	0.0841	2.6294	0.0636	0.0169
−0.10	4.2396	0.0893	0.1352	3.8049	0.0857	0.1909	2.7407	0.0759	0.1339	3.0572	0.0683	0.1083
0.10	4.0452	0.0991	0.2040	3.2204	0.0936	0.2221	3.1148	0.0829	0.1825	2.7931	0.0728	0.0897
0.30	4.0256	0.1039	0.1642	2.7098	0.0970	0.1899	2.3787	0.0845	0.1173	2.4850	0.0756	0.1499
0.50	2.4990	0.1127	0.1765	1.9476	0.1095	0.3020	1.6648	0.0904	0.0986	1.5847	0.0780	0.0817
0.70	1.3322	0.1506	0.1961	0.8572	0.1414	0.1719	0.6256	0.1114	0.0186	0.7401	0.0960	0.0809
0.90	0.6592	0.5784	0.0278	2.4539	0.5079	0.0808	1.1636	0.4226	0.0881	−0.3094	0.7744	0.5635

$\cos(\theta^*_{\pi^0})$	W=(1465.0±9.0) MeV			W=(1483.0±9.0) MeV			W=(1501.0±9.0) MeV			W=(1519.0±9.0) MeV		
	$d\sigma_{3/2}/d\Omega$ [μb/sr]	Δ_{stat} [μb/sr]	Δ_{sys} [μb/sr]	$d\sigma_{3/2}/d\Omega$ [μb/sr]	Δ_{stat} [μb/sr]	Δ_{sys} [μb/sr]	$d\sigma_{3/2}/d\Omega$ [μb/sr]	Δ_{stat} [μb/sr]	Δ_{sys} [μb/sr]	$d\sigma_{3/2}/d\Omega$ [μb/sr]	Δ_{stat} [μb/sr]	Δ_{sys} [μb/sr]
−0.90	0.4897	0.0605	0.0831	0.5479	0.0624	0.0975	0.1895	0.0654	0.0662	0.0588	0.0655	0.1223
−0.70	1.1400	0.0625	0.0006	1.0322	0.0610	0.0619	1.0161	0.0599	0.0645	0.5847	0.0586	0.0184
−0.50	1.8344	0.0511	0.0214	1.5059	0.0507	0.0170	1.4958	0.0497	0.0381	1.3864	0.0475	0.0197
−0.30	2.6521	0.0592	0.0306	2.3318	0.0579	0.0177	2.6040	0.0570	0.0747	1.9076	0.0536	0.0562
−0.10	2.6764	0.0630	0.1096	2.4881	0.0615	0.0676	2.8984	0.0613	0.1619	2.4947	0.0575	0.1357
0.10	2.7324	0.0672	0.0202	2.7609	0.0661	0.0844	2.8246	0.0664	0.2071	2.7186	0.0628	0.1455
0.30	1.9694	0.0701	0.1648	2.2072	0.0687	0.1618	2.7922	0.0679	0.1961	2.3687	0.0640	0.1373
0.50	1.6054	0.0722	0.1373	1.4600	0.0710	0.1420	2.1772	0.0717	0.1658	2.0419	0.0666	0.0986
0.70	0.6157	0.0849	0.0351	1.3042	0.0860	0.1024	0.6041	0.0913	0.2165	0.7480	0.0814	0.0404
0.90	−0.8317	0.3544	0.2983	0.3055	0.2789	0.0609	1.7875	0.2591	0.1073	0.3335	0.2490	0.1468

$\cos(\theta^*_{\pi^0})$	$W=(1537.0\pm9.0)$ MeV			$W=(1555.0\pm9.0)$ MeV			$W=(1573.0\pm9.0)$ MeV			$W=(1591.0\pm9.0)$ MeV		
	$d\sigma_{3/2}/d\Omega$ [μb/sr]	$\Delta_{\rm stat}$ [μb/sr]	$\Delta_{\rm sys}$ [μb/sr]	$d\sigma_{3/2}/d\Omega$ [μb/sr]	$\Delta_{\rm stat}$ [μb/sr]	$\Delta_{\rm sys}$ [μb/sr]	$d\sigma_{3/2}/d\Omega$ [μb/sr]	$\Delta_{\rm stat}$ [μb/sr]	$\Delta_{\rm sys}$ [μb/sr]	$d\sigma_{3/2}/d\Omega$ [μb/sr]	$\Delta_{\rm stat}$ [μb/sr]	$\Delta_{\rm sys}$ [μb/sr]
−0.90	0.0858	0.0631	0.1187	0.2123	0.0610	0.0800	0.0676	0.0593	0.1070	0.4568	0.0572	0.0649
−0.70	0.6350	0.0554	0.0660	0.7082	0.0530	0.0428	0.8477	0.0513	0.0674	0.7222	0.0499	0.0537
−0.50	1.2075	0.0444	0.0145	1.0051	0.0421	0.0341	0.8941	0.0404	0.0102	0.8901	0.0395	0.0674
−0.30	1.4468	0.0506	0.0498	1.5839	0.0472	0.0291	1.4936	0.0460	0.0858	1.1951	0.0449	0.0958
−0.10	2.2285	0.0532	0.0637	1.9337	0.0498	0.0716	1.7742	0.0473	0.0341	1.4112	0.0462	0.1023
0.10	2.2684	0.0584	0.0819	1.9209	0.0538	0.0485	1.7328	0.0515	0.0972	1.4063	0.0473	0.0327
0.30	2.0715	0.0585	0.0652	1.6578	0.0540	0.0662	1.2575	0.0511	0.0837	0.8528	0.0474	0.0890
0.50	1.4360	0.0629	0.1319	1.3062	0.0568	0.0914	0.7720	0.0528	0.0749	0.6242	0.0511	0.1231
0.70	0.5740	0.0789	0.1189	0.3207	0.0750	0.1098	0.4187	0.0686	0.0767	0.3904	0.0666	0.1305
0.90	−1.7523	0.3850	1.0418	−0.1266	0.2126	0.0623	0.3153	0.2028	0.0961	0.3652	0.2511	0.3373

$\cos(\theta^*_{\pi^0})$	$W=(1609.0\pm9.0)$ MeV			$W=(1627.0\pm9.0)$ MeV			$W=(1645.0\pm9.0)$ MeV			$W=(1663.0\pm9.0)$ MeV		
	$d\sigma_{3/2}/d\Omega$ [μb/sr]	$\Delta_{\rm stat}$ [μb/sr]	$\Delta_{\rm sys}$ [μb/sr]	$d\sigma_{3/2}/d\Omega$ [μb/sr]	$\Delta_{\rm stat}$ [μb/sr]	$\Delta_{\rm sys}$ [μb/sr]	$d\sigma_{3/2}/d\Omega$ [μb/sr]	$\Delta_{\rm stat}$ [μb/sr]	$\Delta_{\rm sys}$ [μb/sr]	$d\sigma_{3/2}/d\Omega$ [μb/sr]	$\Delta_{\rm stat}$ [μb/sr]	$\Delta_{\rm sys}$ [μb/sr]
−0.90	0.4008	0.0535	0.1536	0.2942	0.0545	0.0715	0.6176	0.0523	0.1371	0.6562	0.0508	0.1069
−0.70	1.0121	0.0474	0.0775	0.6903	0.0461	0.0461	1.0720	0.0457	0.0512	0.9900	0.0425	0.0584
−0.50	0.8506	0.0369	0.0230	0.9806	0.0355	0.0260	1.0843	0.0348	0.0883	1.1164	0.0325	0.0494
−0.30	1.2110	0.0419	0.0879	1.3201	0.0384	0.0280	1.1662	0.0378	0.0785	1.0407	0.0351	0.0416
−0.10	1.1536	0.0431	0.0872	1.3662	0.0391	0.0484	1.0040	0.0362	0.0349	0.8576	0.0334	0.0369
0.10	1.0328	0.0432	0.0317	0.8948	0.0398	0.0368	0.7094	0.0355	0.0241	0.6003	0.0316	0.0391
0.30	0.4926	0.0420	0.0571	0.5052	0.0368	0.0071	0.6046	0.0346	0.0643	0.4767	0.0317	0.0356
0.50	0.5271	0.0458	0.0804	0.5777	0.0402	0.0329	0.6443	0.0396	0.0428	0.5616	0.0388	0.0791
0.70	0.5262	0.0625	0.0789	0.5864	0.0614	0.0889	0.9262	0.0590	0.0717	0.9768	0.0590	0.0928
0.90	0.9644	0.2501	0.4850	−0.5274	0.2906	0.7441	0.1196	0.2039	0.3509	0.6766	0.1521	0.1404

$\cos(\theta^*_{\pi^0})$	$W=(1681.0\pm9.0)$ MeV			$W=(1699.0\pm9.0)$ MeV			$W=(1717.0\pm9.0)$ MeV			$W=(1735.0\pm9.0)$ MeV		
	$d\sigma_{3/2}/d\Omega$ [μb/sr]	$\Delta_{\rm stat}$ [μb/sr]	$\Delta_{\rm sys}$ [μb/sr]	$d\sigma_{3/2}/d\Omega$ [μb/sr]	$\Delta_{\rm stat}$ [μb/sr]	$\Delta_{\rm sys}$ [μb/sr]	$d\sigma_{3/2}/d\Omega$ [μb/sr]	$\Delta_{\rm stat}$ [μb/sr]	$\Delta_{\rm sys}$ [μb/sr]	$d\sigma_{3/2}/d\Omega$ [μb/sr]	$\Delta_{\rm stat}$ [μb/sr]	$\Delta_{\rm sys}$ [μb/sr]
−0.90	0.6375	0.0523	0.1346	0.8859	0.0575	0.0305	0.9340	0.0584	0.0668	0.7130	0.0592	0.0603
−0.70	1.0987	0.0416	0.0822	1.1098	0.0432	0.0863	1.2515	0.0455	0.0534	0.9908	0.0475	0.0084
−0.50	1.1405	0.0308	0.0354	1.1385	0.0317	0.0192	1.0338	0.0315	0.0362	0.8156	0.0313	0.0090
−0.30	1.0907	0.0330	0.0125	1.0526	0.0323	0.0215	0.7275	0.0311	0.0014	0.7414	0.0302	0.0248
−0.10	0.9588	0.0321	0.0485	0.7778	0.0305	0.0236	0.5599	0.0293	0.0350	0.6815	0.0286	0.0110
0.10	0.6265	0.0295	0.0378	0.4334	0.0296	0.0172	0.4882	0.0283	0.0423	0.5405	0.0280	0.0627
0.30	0.4690	0.0304	0.0197	0.4343	0.0302	0.0204	0.4627	0.0312	0.0055	0.2470	0.0307	0.0170
0.50	0.8830	0.0390	0.0581	0.8087	0.0394	0.0116	0.6267	0.0408	0.0067	0.6893	0.0396	0.0379
0.70	1.1381	0.0624	0.1173	1.0043	0.0613	0.0434	0.9918	0.0605	0.0797	0.8120	0.0611	0.0086
0.90	1.0482	0.1555	0.1994	1.1799	0.1388	0.0416	1.1548	0.1450	0.0333	0.5189	0.1390	0.0226

$\cos(\theta^*_{\pi^0})$	$W=(1753.0\pm9.0)$ MeV			$W=(1771.0\pm9.0)$ MeV			$W=(1789.0\pm9.0)$ MeV			$W=(1807.0\pm9.0)$ MeV		
	$d\sigma_{3/2}/d\Omega$ [μb/sr]	$\Delta_{\rm stat}$ [μb/sr]	$\Delta_{\rm sys}$ [μb/sr]	$d\sigma_{3/2}/d\Omega$ [μb/sr]	$\Delta_{\rm stat}$ [μb/sr]	$\Delta_{\rm sys}$ [μb/sr]	$d\sigma_{3/2}/d\Omega$ [μb/sr]	$\Delta_{\rm stat}$ [μb/sr]	$\Delta_{\rm sys}$ [μb/sr]	$d\sigma_{3/2}/d\Omega$ [μb/sr]	$\Delta_{\rm stat}$ [μb/sr]	$\Delta_{\rm sys}$ [μb/sr]
−0.90	0.6803	0.0581	0.0156	0.8588	0.0557	0.0673	0.6066	0.0590	0.0100	0.6598	0.0644	0.0135
−0.70	1.0186	0.0457	0.0373	0.8257	0.0418	0.0118	0.8097	0.0463	0.1517	0.9293	0.0444	0.0234
−0.50	0.7103	0.0290	0.0075	0.6215	0.0281	0.0570	0.7297	0.0274	0.0186	0.6368	0.0288	0.0153
−0.30	0.5986	0.0269	0.0038	0.4297	0.0263	0.0475	0.4892	0.0273	0.0427	0.5334	0.0294	0.0409
−0.10	0.4742	0.0272	0.0091	0.3343	0.0281	0.0445	0.3823	0.0295	0.0383	0.3950	0.0302	0.0136
0.10	0.2957	0.0282	0.0247	0.2899	0.0304	0.0606	0.2544	0.0304	0.0421	0.3899	0.0325	0.0092
0.30	0.2687	0.0300	0.0356	0.2060	0.0294	0.0232	0.1545	0.0305	0.0207	0.2187	0.0322	0.0128
0.50	0.5043	0.0381	0.0128	0.3417	0.0377	0.0203	0.3762	0.0408	0.0533	0.3618	0.0421	0.0014
0.70	0.9214	0.0629	0.1898	0.5996	0.0580	0.0705	0.9584	0.0593	0.0430	1.1207	0.0638	0.0300
0.90	0.5665	0.1396	0.1337	1.1351	0.1321	0.1287	0.2750	0.1491	0.0731	1.0904	0.1382	0.1261

$\cos(\theta^*_{\pi^0})$	$W=(1825.0\pm9.0)$ MeV			$W=(1843.0\pm9.0)$ MeV			$W=(1861.0\pm9.0)$ MeV			$W=(1879.0\pm9.0)$ MeV		
	$d\sigma_{3/2}/d\Omega$ [μb/sr]	$\Delta_{\rm stat}$ [μb/sr]	$\Delta_{\rm sys}$ [μb/sr]	$d\sigma_{3/2}/d\Omega$ [μb/sr]	$\Delta_{\rm stat}$ [μb/sr]	$\Delta_{\rm sys}$ [μb/sr]	$d\sigma_{3/2}/d\Omega$ [μb/sr]	$\Delta_{\rm stat}$ [μb/sr]	$\Delta_{\rm sys}$ [μb/sr]	$d\sigma_{3/2}/d\Omega$ [μb/sr]	$\Delta_{\rm stat}$ [μb/sr]	$\Delta_{\rm sys}$ [μb/sr]
−0.90	1.0987	0.0666	0.1129	1.1732	0.0722	0.0210	1.0538	0.0707	0.1138	1.1264	0.0765	0.0421
−0.70	1.2373	0.0516	0.1485	1.0881	0.0547	0.0646	1.0549	0.0592	0.0731	1.3234	0.0625	0.0271
−0.50	0.6151	0.0309	0.0344	0.5273	0.0300	0.0399	0.5209	0.0303	0.0260	0.4950	0.0302	0.0417
−0.30	0.5029	0.0331	0.0353	0.4726	0.0404	0.0996	0.5185	0.0382	0.0686	0.4887	0.0406	0.0957
−0.10	0.3723	0.0382	0.0734	0.7119	0.0426	0.0146	0.3003	0.0511	0.0713	0.6392	0.0543	0.0726
0.10	0.4469	0.0380	0.0146	0.3566	0.0427	0.0764	0.3851	0.0494	0.0493	0.2579	0.0552	0.0439
0.30	0.2543	0.0383	0.0073	0.4608	0.0427	0.0869	0.3755	0.0494	0.1016	0.5287	0.0590	0.1610
0.50	0.4418	0.0458	0.0279	0.4465	0.0524	0.0775	0.5412	0.0559	0.1195	0.4860	0.0631	0.1600
0.70	0.8253	0.0760	0.0840	1.0721	0.0834	0.0504	0.7108	0.0957	0.1034	1.2034	0.1099	0.2297
0.90	1.8857	0.2477	0.5812	1.3387	0.2380	0.2380	1.7265	0.2406	0.0306	0.7396	0.2513	0.1088

$\cos(\theta^*_{\pi^0})$	$W=(1897.0\pm9.0)$ MeV			$W=(1915.0\pm9.0)$ MeV		
	$d\sigma_{3/2}/d\Omega$ [μb/sr]	$\Delta_{\rm stat}$ [μb/sr]	$\Delta_{\rm sys}$ [μb/sr]	$d\sigma_{3/2}/d\Omega$ [μb/sr]	$\Delta_{\rm stat}$ [μb/sr]	$\Delta_{\rm sys}$ [μb/sr]
−0.90	0.7534	0.0926	0.0651	1.0933	0.1635	0.2571
−0.70	0.7092	0.0712	0.0205	0.7418	0.1136	0.0424
−0.50	0.4086	0.0333	0.0262	0.5464	0.0445	0.0888
−0.30	0.3245	0.0483	0.0967	0.2638	0.0706	0.0978
−0.10	0.5433	0.0667	0.0365	0.8871	0.0985	0.0793
0.10	0.5179	0.0658	0.1815	0.7935	0.0951	0.2417
0.30	0.7213	0.0772	0.2460	0.4166	0.1007	0.1635
0.50	0.2155	0.0786	0.2233	0.7298	0.1133	0.3019
0.70	1.2559	0.1345	0.3554	1.6510	0.1740	0.4517
0.90	1.2205	0.2863	0.4515	1.1653	0.3911	0.2075

E.2.5 Observables for $\gamma p \to \pi^0 p$ as a Function of W

W [MeV]	ΔW [MeV]	E	Δ_{stat}	Δ_{sys}	$\sigma_{1/2}$ [μb]	Δ_{stat} [μb]	Δ_{sys} [μb]	$\sigma_{3/2}$ [μb]	Δ_{stat} [μb]	Δ_{sys} [μb]
1321.0	9.0	−0.4103	0.0065	0.0508	156.6226	1.9301	21.0029	374.0808	1.9335	42.5662
1339.0	9.0	−0.3693	0.0066	0.0425	78.2560	0.9272	9.1084	169.5231	0.9289	18.7556
1357.0	9.0	−0.2977	0.0069	0.0343	57.8899	0.6551	6.4928	106.5099	0.6561	11.7288
1375.0	9.0	−0.2416	0.0068	0.0275	43.2774	0.4557	5.0560	70.5395	0.4564	8.0729
1393.0	9.0	−0.1317	0.0072	0.0160	37.1936	0.3699	4.1358	48.3346	0.3703	5.3693
1411.0	9.0	−0.0512	0.0079	0.0093	33.5432	0.3361	3.7251	37.0663	0.3363	4.0777
1429.0	9.0	0.0503	0.0076	0.0099	33.0458	0.2881	3.6787	29.8216	0.2881	3.3301
1447.0	9.0	0.1267	0.0069	0.0160	33.9065	0.2511	3.7496	26.2266	0.2509	2.9004
1465.0	9.0	0.1744	0.0061	0.0204	36.2224	0.2260	4.0059	25.4017	0.2257	2.7956
1483.0	9.0	0.2027	0.0056	0.0230	42.7623	0.2366	4.7585	28.2754	0.2362	3.1206
1501.0	9.0	0.1942	0.0051	0.0219	50.9584	0.2603	5.8020	34.2772	0.2598	3.8823
1519.0	9.0	0.1264	0.0050	0.0148	48.7952	0.2591	5.3824	37.7735	0.2587	4.1578
1537.0	9.0	0.1078	0.0051	0.0136	41.9497	0.2336	4.6575	33.7496	0.2333	3.7922
1555.0	9.0	0.0780	0.0055	0.0104	35.4832	0.2199	3.9550	30.3233	0.2197	3.4140
1573.0	9.0	0.0250	0.0060	0.0063	27.9788	0.2003	3.1034	26.5740	0.2002	2.9661
1591.0	9.0	−0.0060	0.0065	0.0035	23.4643	0.1870	2.5847	23.7208	0.1870	2.6117
1609.0	9.0	−0.1031	0.0067	0.0124	18.1834	0.1650	2.0197	22.3353	0.1652	2.4608
1627.0	9.0	−0.2106	0.0066	0.0243	16.1135	0.1588	1.8123	24.6815	0.1593	2.7281
1645.0	9.0	−0.2321	0.0061	0.0261	17.7057	0.1664	1.9968	28.4178	0.1670	3.1580
1663.0	9.0	−0.2288	0.0058	0.0255	18.9745	0.1685	2.1032	30.2280	0.1691	3.3340
1681.0	9.0	−0.1959	0.0059	0.0218	20.0797	0.1743	2.2529	29.7970	0.1750	3.3406
1699.0	9.0	−0.1806	0.0065	0.0203	18.4366	0.1758	2.0956	26.4942	0.1764	3.0113
1717.0	9.0	−0.0920	0.0074	0.0108	17.2071	0.1699	2.0413	20.6695	0.1702	2.4193
1735.0	9.0	−0.0903	0.0088	0.0105	13.7651	0.1610	1.5455	16.4714	0.1614	1.8564
1753.0	9.0	−0.0635	0.0100	0.0077	11.6630	0.1513	1.2987	13.2389	0.1517	1.4670
1771.0	9.0	−0.0733	0.0111	0.0112	9.8188	0.1429	1.1749	11.3577	0.1432	1.3202
1789.0	9.0	−0.1054	0.0122	0.0140	9.0387	0.1495	1.1521	11.1774	0.1499	1.3777
1807.0	9.0	−0.1366	0.0132	0.0176	8.5610	0.1582	1.0310	11.2680	0.1587	1.3072
1825.0	9.0	−0.2547	0.0147	0.0302	7.2624	0.1694	0.8349	12.2127	0.1703	1.3600
1843.0	9.0	−0.1909	0.0154	0.0210	8.6841	0.1981	0.9582	12.7701	0.1990	1.4087
1861.0	9.0	−0.1749	0.0168	0.0214	8.8372	0.2159	1.0683	12.5671	0.2167	1.4551
1879.0	9.0	−0.2299	0.0196	0.0352	8.4654	0.2516	1.5057	13.3578	0.2530	2.1216
1897.0	9.0	−0.2020	0.0253	0.0377	8.7237	0.3205	1.8775	12.9340	0.3221	2.4701
1915.0	9.0	−0.3550	0.0388	0.0776	7.9554	0.5162	2.3401	16.0624	0.5197	3.4371

Angular Distributions

	W=(1321.0±9.0) MeV			W=(1339.0±9.0) MeV			W=(1357.0±9.0) MeV			W=(1375.0±9.0) MeV		
$\cos(\theta^*_{\pi^0})$	E	Δ_{stat}	Δ_{sys}	E	Δ_{stat}	Δ_{sys}	E	Δ_{stat}	Δ_{sys}	E	Δ_{stat}	Δ_{sys}
−0.90	−0.3608	0.1472	0.2751	0.1826	0.1056	0.1152	0.3985	0.1032	0.2029	0.1969	0.0796	0.1030
−0.70	−0.1693	0.0270	0.0221	−0.2865	0.0297	0.0263	−0.1149	0.0298	0.0263	0.1878	0.0292	0.0292
−0.50	−0.4987	0.0165	0.0126	−0.2923	0.0161	0.0098	−0.2375	0.0173	0.0114	−0.0727	0.0170	0.0032
−0.30	−0.4416	0.0143	0.0138	−0.3392	0.0146	0.0133	−0.3085	0.0160	0.0142	−0.2263	0.0158	0.0068
−0.10	−0.4431	0.0132	0.0228	−0.4644	0.0140	0.0200	−0.3563	0.0146	0.0135	−0.3057	0.0148	0.0074
0.10	−0.4257	0.0142	0.0323	−0.5187	0.0150	0.0267	−0.3935	0.0154	0.0190	−0.4798	0.0164	0.0092
0.30	−0.3114	0.0196	0.0430	−0.3620	0.0182	0.0335	−0.3679	0.0182	0.0386	−0.2979	0.0175	0.0115
0.50	−0.2666	0.0661	0.0867	−0.0080	0.0463	0.0160	−0.2707	0.0372	0.0647	−0.2064	0.0306	0.0180
0.70	1.2518	4.7540	1.0331	4.9750	6.6335	3.2433	2.8009	1.8687	1.4126	0.5673	0.2839	0.2015
0.90	−7.4181	41.5596	5.2720	−0.3439	1.7570	0.8317	4.4811	22.7131	2.5834	−5.4929	34.2174	3.7792

	W=(1393.0±9.0) MeV			W=(1411.0±9.0) MeV			W=(1429.0±9.0) MeV			W=(1447.0±9.0) MeV		
$\cos(\theta^*_{\pi^0})$	E	Δ_{stat}	Δ_{sys}	E	Δ_{stat}	Δ_{sys}	E	Δ_{stat}	Δ_{sys}	E	Δ_{stat}	Δ_{sys}
−0.90	0.5673	0.0838	0.1848	0.4561	0.0778	0.1138	0.5680	0.0699	0.1316	0.8865	0.0718	0.1069
−0.70	0.2838	0.0321	0.0182	0.2840	0.0343	0.0177	0.6279	0.0377	0.0296	0.5509	0.0341	0.0156
−0.50	0.0063	0.0182	0.0024	0.2123	0.0210	0.0042	0.2886	0.0202	0.0129	0.3236	0.0190	0.0071
−0.30	−0.1706	0.0169	0.0043	−0.0306	0.0180	0.0093	0.0191	0.0177	0.0096	0.1257	0.0168	0.0133
−0.10	−0.1850	0.0159	0.0012	−0.1838	0.0175	0.0103	−0.0567	0.0167	0.0106	0.0595	0.0152	0.0111
0.10	−0.2541	0.0166	0.0081	−0.2225	0.0184	0.0124	−0.0700	0.0175	0.0097	−0.0762	0.0163	0.0137
0.30	−0.2610	0.0191	0.0146	−0.1975	0.0205	0.0152	−0.1698	0.0202	0.0172	0.0677	0.0174	0.0057
0.50	−0.1205	0.0295	0.0124	0.0017	0.0320	0.0126	−0.1324	0.0285	0.0201	−0.0805	0.0245	0.0191
0.70	0.1923	0.1442	0.0295	0.5929	0.2372	0.1666	0.6771	0.1376	0.0860	0.1303	0.0805	0.0324
0.90	−0.4127	0.9461	0.1656	2.1050	2.8371	0.1519	6.0742	10.1511	1.1590	−2.1262	1.5792	0.3967

	W=(1465.0±9.0) MeV			W=(1483.0±9.0) MeV			W=(1501.0±9.0) MeV			W=(1519.0±9.0) MeV		
$\cos(\theta^*_{\pi^0})$	E	Δ_{stat}	Δ_{sys}	E	Δ_{stat}	Δ_{sys}	E	Δ_{stat}	Δ_{sys}	E	Δ_{stat}	Δ_{sys}
−0.90	0.9864	0.0608	0.0959	0.8326	0.0473	0.0480	0.6714	0.0352	0.0027	0.5944	0.0299	0.0117
−0.70	0.5725	0.0302	0.0086	0.6183	0.0290	0.0121	0.4542	0.0235	0.0179	0.2223	0.0200	0.0131
−0.50	0.2867	0.0166	0.0094	0.3769	0.0161	0.0073	0.3062	0.0143	0.0095	0.2324	0.0137	0.0042
−0.30	0.2297	0.0153	0.0036	0.1782	0.0140	0.0098	0.1630	0.0133	0.0057	0.0708	0.0129	0.0062
−0.10	0.0799	0.0135	0.0114	0.1189	0.0127	0.0091	0.1409	0.0120	0.0054	0.0779	0.0117	0.0082
0.10	0.0635	0.0142	0.0051	0.0852	0.0129	0.0053	0.0687	0.0119	0.0057	0.0546	0.0120	0.0055
0.30	0.0207	0.0154	0.0106	0.1120	0.0140	0.0049	0.1629	0.0130	0.0077	0.0614	0.0129	0.0023
0.50	0.1064	0.0212	0.0136	0.0471	0.0174	0.0070	0.1609	0.0160	0.0105	0.1230	0.0154	0.0055
0.70	−0.0049	0.0590	0.0006	0.3782	0.0483	0.0352	0.2058	0.0341	0.0048	0.1820	0.0326	0.0108
0.90	−2.8440	1.8488	0.7524	12.6498	79.4096	10.3370	0.9510	5.1467	0.8950	1.6331	0.9128	0.0945

$\cos(\theta^*_{\pi^0})$	$W=(1537.0\pm9.0)$ MeV			$W=(1555.0\pm9.0)$ MeV			$W=(1573.0\pm9.0)$ MeV			$W=(1591.0\pm9.0)$ MeV		
	E	Δ_{stat}	Δ_{sys}	E	Δ_{stat}	Δ_{sys}	E	Δ_{stat}	Δ_{sys}	E	Δ_{stat}	Δ_{sys}
−0.90	0.3258	0.0245	0.0066	0.2884	0.0233	0.0059	0.1993	0.0211	0.0019	0.1854	0.0207	0.0039
−0.70	0.1910	0.0192	0.0044	−0.0355	0.0189	0.0030	−0.1554	0.0188	0.0090	−0.2172	0.0186	0.0124
−0.50	0.0964	0.0135	0.0025	0.0353	0.0141	0.0036	−0.1007	0.0146	0.0018	−0.1967	0.0154	0.0072
−0.30	0.1126	0.0135	0.0061	0.0015	0.0144	0.0027	−0.0542	0.0155	0.0043	−0.1445	0.0171	0.0042
−0.10	0.0065	0.0124	0.0097	−0.0019	0.0134	0.0068	−0.1035	0.0153	0.0018	−0.1161	0.0167	0.0041
0.10	0.0798	0.0123	0.0074	0.0535	0.0141	0.0070	0.0033	0.0164	0.0074	0.0019	0.0180	0.0050
0.30	0.0996	0.0134	0.0093	0.0915	0.0151	0.0111	0.1502	0.0184	0.0063	0.2167	0.0217	0.0072
0.50	0.1477	0.0167	0.0066	0.2749	0.0191	0.0148	0.4540	0.0242	0.0064	0.4340	0.0295	0.0176
0.70	0.2870	0.0349	0.0189	0.4785	0.0381	0.0213	0.4817	0.0459	0.0263	0.7373	0.0564	0.0721
0.90	−0.5862	0.5887	0.0844	16.6420	245.7999	15.4052	−0.9994	0.6447	0.4069	4.5804	7.7662	2.4917

$\cos(\theta^*_{\pi^0})$	$W=(1609.0\pm9.0)$ MeV			$W=(1627.0\pm9.0)$ MeV			$W=(1645.0\pm9.0)$ MeV			$W=(1663.0\pm9.0)$ MeV		
	E	Δ_{stat}	Δ_{sys}	E	Δ_{stat}	Δ_{sys}	E	Δ_{stat}	Δ_{sys}	E	Δ_{stat}	Δ_{sys}
−0.90	−0.1612	0.0204	0.0121	−0.1909	0.0193	0.0072	−0.2131	0.0184	0.0120	−0.3349	0.0190	0.0238
−0.70	−0.3206	0.0192	0.0216	−0.4807	0.0185	0.0254	−0.4991	0.0173	0.0360	−0.5133	0.0172	0.0350
−0.50	−0.2998	0.0157	0.0060	−0.5003	0.0169	0.0149	−0.5740	0.0166	0.0145	−0.4979	0.0158	0.0069
−0.30	−0.3718	0.0189	0.0059	−0.3339	0.0182	0.0022	−0.4681	0.0185	0.0073	−0.4363	0.0183	0.0113
−0.10	−0.0822	0.0174	0.0017	−0.2471	0.0182	0.0055	−0.1748	0.0173	0.0037	−0.1878	0.0173	0.0053
0.10	−0.0500	0.0204	0.0013	−0.0632	0.0198	0.0131	−0.0266	0.0197	0.0039	0.0715	0.0186	0.0056
0.30	0.2506	0.0229	0.0103	0.1293	0.0226	0.0116	0.1614	0.0194	0.0076	0.1087	0.0169	0.0065
0.50	0.4425	0.0296	0.0277	0.2219	0.0243	0.0092	0.1865	0.0203	0.0098	−0.0307	0.0170	0.0017
0.70	0.2592	0.0391	0.0234	0.1313	0.0281	0.0069	−0.1603	0.0234	0.0103	−0.1093	0.0207	0.0088
0.90	0.4627	1.9077	0.4544	1.8235	2.5009	2.1159	−0.8026	1.1456	0.6677	0.1678	0.1698	0.0480

$\cos(\theta^*_{\pi^0})$	$W=(1681.0\pm9.0)$ MeV			$W=(1699.0\pm9.0)$ MeV			$W=(1717.0\pm9.0)$ MeV			$W=(1735.0\pm9.0)$ MeV		
	E	Δ_{stat}	Δ_{sys}	E	Δ_{stat}	Δ_{sys}	E	Δ_{stat}	Δ_{sys}	E	Δ_{stat}	Δ_{sys}
−0.90	−0.1338	0.0180	0.0023	−0.2283	0.0211	0.0129	−0.1888	0.0242	0.0091	−0.0893	0.0257	0.0080
−0.70	−0.4736	0.0169	0.0140	−0.5886	0.0208	0.0191	−0.4173	0.0216	0.0064	−0.4445	0.0259	0.0155
−0.50	−0.5622	0.0172	0.0116	−0.6207	0.0205	0.0146	−0.6414	0.0241	0.0276	−0.5218	0.0283	0.0250
−0.30	−0.4607	0.0199	0.0189	−0.4259	0.0221	0.0363	−0.1707	0.0253	0.0207	−0.2423	0.0301	0.0171
−0.10	−0.1563	0.0178	0.0154	0.0027	0.0211	0.0042	−0.0367	0.0243	0.0058	−0.0940	0.0291	0.0053
0.10	0.1150	0.0193	0.0121	0.1981	0.0219	0.0143	0.2777	0.0251	0.0261	0.0762	0.0283	0.0099
0.30	0.0900	0.0175	0.0087	0.1752	0.0185	0.0140	0.2290	0.0211	0.0103	0.2351	0.0244	0.0099
0.50	0.0941	0.0166	0.0066	0.0841	0.0173	0.0036	0.1195	0.0196	0.0104	0.1104	0.0231	0.0218
0.70	−0.1665	0.0200	0.0035	−0.1969	0.0222	0.0086	0.0120	0.0248	0.0009	0.1360	0.0303	0.0091
0.90	0.1166	0.1337	0.0213	−0.2581	0.1079	0.0125	0.4977	0.1151	0.0332	−0.0769	1.2915	0.2713

$\cos(\theta^*_{\pi^0})$	$W=(1753.0\pm9.0)$ MeV			$W=(1771.0\pm9.0)$ MeV			$W=(1789.0\pm9.0)$ MeV			$W=(1807.0\pm9.0)$ MeV		
	E	Δ_{stat}	Δ_{sys}	E	Δ_{stat}	Δ_{sys}	E	Δ_{stat}	Δ_{sys}	E	Δ_{stat}	Δ_{sys}
−0.90	−0.0555	0.0278	0.0053	0.0713	0.0284	0.0061	0.1270	0.0300	0.0151	0.0604	0.0301	0.0070
−0.70	−0.4045	0.0305	0.0414	−0.3258	0.0315	0.0359	−0.4638	0.0334	0.0583	−0.2405	0.0308	0.0247
−0.50	−0.4793	0.0323	0.0078	−0.5401	0.0394	0.0133	−0.5144	0.0423	0.0102	−0.3279	0.0435	0.0149
−0.30	−0.3401	0.0368	0.0111	−0.2654	0.0391	0.0095	−0.2333	0.0432	0.0212	−0.4111	0.0544	0.0196
−0.10	0.0627	0.0334	0.0032	−0.0773	0.0336	0.0052	−0.1163	0.0381	0.0049	−0.3331	0.0410	0.0116
0.10	0.3218	0.0322	0.0098	0.1667	0.0335	0.0029	0.0929	0.0369	0.0042	−0.0194	0.0400	0.0031
0.30	0.1264	0.0269	0.0101	0.1648	0.0309	0.0084	0.1727	0.0359	0.0071	0.0112	0.0401	0.0143
0.50	0.1846	0.0273	0.0088	0.1047	0.0354	0.0113	0.0883	0.0388	0.0088	0.0576	0.0428	0.0021
0.70	0.0170	0.0349	0.0066	0.0107	0.0403	0.0160	0.0398	0.0422	0.0033	0.0289	0.0507	0.0031
0.90	−1.1688	0.1911	0.0621	−0.3032	0.1513	0.1062	−0.6581	0.2350	0.2375	0.1121	0.1221	0.0222

$\cos(\theta^*_{\pi^0})$	$W=(1825.0\pm9.0)$ MeV			$W=(1843.0\pm9.0)$ MeV			$W=(1861.0\pm9.0)$ MeV			$W=(1879.0\pm9.0)$ MeV		
	E	Δ_{stat}	Δ_{sys}	E	Δ_{stat}	Δ_{sys}	E	Δ_{stat}	Δ_{sys}	E	Δ_{stat}	Δ_{sys}
−0.90	0.0417	0.0292	0.0070	0.0545	0.0292	0.0065	0.2510	0.0334	0.0264	−0.0769	0.0372	0.0070
−0.70	−0.4962	0.0349	0.0221	−0.5220	0.0401	0.0556	−0.3953	0.0424	0.0436	−0.5551	0.0529	0.0238
−0.50	−0.7198	0.0618	0.0183	−0.2643	0.0560	0.0170	−0.1740	0.0561	0.0059	−0.3765	0.0615	0.0604
−0.30	−0.5936	0.0642	0.0126	−0.2914	0.0608	0.0230	−0.0702	0.0586	0.0173	0.0697	0.0760	0.0134
−0.10	−0.2259	0.0460	0.0048	−0.1822	0.0466	0.0156	−0.5558	0.0586	0.0023	−0.4151	0.0656	0.0369
0.10	−0.3843	0.0493	0.0238	−0.3995	0.0494	0.0467	−0.3611	0.0569	0.0423	−0.4235	0.0688	0.0852
0.30	−0.0363	0.0465	0.0095	−0.0443	0.0509	0.0102	0.0067	0.0632	0.0170	−0.2052	0.0762	0.0544
0.50	0.0078	0.0482	0.0029	−0.1410	0.0621	0.0153	−0.3865	0.0728	0.0950	0.3311	0.0835	0.1086
0.70	−0.0575	0.0512	0.0130	0.0988	0.0492	0.0126	−0.0164	0.0569	0.0214	−0.1333	0.0628	0.0295
0.90	0.3104	0.1059	0.0339	−0.2019	0.1328	0.0582	−0.2629	0.1005	0.0391	−0.1803	0.1207	0.0167

$\cos(\theta^*_{\pi^0})$	$W=(1897.0\pm9.0)$ MeV			$W=(1915.0\pm9.0)$ MeV		
	E	Δ_{stat}	Δ_{sys}	E	Δ_{stat}	Δ_{sys}
−0.90	0.0246	0.0482	0.0019	−0.2656	0.0803	0.0265
−0.70	−0.3783	0.0630	0.0057	−0.7985	0.1544	0.0593
−0.50	−0.2539	0.0752	0.0213	−0.7367	0.1626	0.0143
−0.30	−0.0033	0.0914	0.0105	−0.6088	0.1417	0.1084
−0.10	−0.4700	0.0858	0.1150	−0.4005	0.1309	0.1208
0.10	−0.3087	0.0876	0.0777	−0.3491	0.1183	0.1443
0.30	−0.1992	0.1056	0.0656	0.1383	0.1468	0.0691
0.50	0.0759	0.1061	0.0321	0.2155	0.1497	0.1168
0.70	−0.2591	0.0845	0.0525	−0.2581	0.1038	0.0619
0.90	−0.6745	0.2240	0.1128	−1.2747	0.4267	0.1259

$\cos(\theta^*_{\pi^0})$	W=(1321.0±9.0) MeV			W=(1339.0±9.0) MeV			W=(1357.0±9.0) MeV			W=(1375.0±9.0) MeV		
	$d\sigma_{1/2}/d\Omega$ [μb/sr]	Δ_{stat} [μb/sr]	Δ_{sys} [μb/sr]	$d\sigma_{1/2}/d\Omega$ [μb/sr]	Δ_{stat} [μb/sr]	Δ_{sys} [μb/sr]	$d\sigma_{1/2}/d\Omega$ [μb/sr]	Δ_{stat} [μb/sr]	Δ_{sys} [μb/sr]	$d\sigma_{1/2}/d\Omega$ [μb/sr]	Δ_{stat} [μb/sr]	Δ_{sys} [μb/sr]
−0.90	1.6482	0.1932	1.3673	1.2928	0.1000	0.6822	1.1563	0.0764	0.4921	0.8423	0.0560	0.3315
−0.70	10.7769	0.4064	1.6819	3.9879	0.1878	0.5185	3.3504	0.1331	0.3465	3.1229	0.0900	0.3676
−0.50	10.2452	0.3617	0.3675	6.6903	0.1763	0.1286	4.7939	0.1274	0.1043	4.0187	0.0888	0.1918
−0.30	14.6272	0.4134	0.5923	8.1145	0.2037	0.2113	5.6216	0.1493	0.1568	4.4016	0.1057	0.1698
−0.10	15.6126	0.4092	1.2727	7.1936	0.2060	0.4369	5.8196	0.1496	0.1784	4.3616	0.1075	0.1134
0.10	15.3219	0.4212	2.0136	6.2000	0.2065	0.5610	5.2275	0.1484	0.2629	3.1218	0.1072	0.0769
0.30	15.3914	0.5003	3.2489	6.8857	0.2221	1.0296	4.5811	0.1484	0.5787	3.4977	0.1015	0.1645
0.50	12.0140	1.1604	4.9934	7.8433	0.4220	1.9646	3.9113	0.2262	0.8268	2.9240	0.1332	0.2310
0.70	17.2424	11.8607	16.5333	22.7376	4.7565	18.8059	10.3786	1.5748	5.9865	3.4327	0.5914	0.9858
0.90	−75.3449	51.1842	35.4305	3.6706	13.7775	8.2338	21.7849	21.8921	16.4336	−8.6458	12.7312	8.5594

$\cos(\theta^*_{\pi^0})$	W=(1393.0±9.0) MeV			W=(1411.0±9.0) MeV			W=(1429.0±9.0) MeV			W=(1447.0±9.0) MeV		
	$d\sigma_{1/2}/d\Omega$ [μb/sr]	Δ_{stat} [μb/sr]	Δ_{sys} [μb/sr]	$d\sigma_{1/2}/d\Omega$ [μb/sr]	Δ_{stat} [μb/sr]	Δ_{sys} [μb/sr]	$d\sigma_{1/2}/d\Omega$ [μb/sr]	Δ_{stat} [μb/sr]	Δ_{sys} [μb/sr]	$d\sigma_{1/2}/d\Omega$ [μb/sr]	Δ_{stat} [μb/sr]	Δ_{sys} [μb/sr]
−0.90	0.9617	0.0487	0.2748	0.8522	0.0481	0.1730	0.9743	0.0446	0.1505	1.2189	0.0415	0.1279
−0.70	2.5421	0.0739	0.1605	2.1236	0.0660	0.1263	2.3994	0.0570	0.1110	2.1240	0.0495	0.0305
−0.50	3.3436	0.0732	0.0564	3.2535	0.0667	0.0949	3.1240	0.0570	0.0752	2.9967	0.0496	0.0304
−0.30	3.5883	0.0868	0.1078	3.5256	0.0790	0.0700	3.2838	0.0691	0.0500	3.4035	0.0610	0.0547
−0.10	3.8419	0.0891	0.0127	3.2193	0.0817	0.0691	3.3181	0.0709	0.0557	3.6002	0.0622	0.0486
0.10	3.3887	0.0884	0.1145	2.9222	0.0814	0.1385	3.1165	0.0706	0.0749	2.9467	0.0625	0.0971
0.30	2.7301	0.0824	0.1783	2.4674	0.0747	0.1773	2.2415	0.0648	0.1366	2.8966	0.0571	0.0818
0.50	2.3717	0.0952	0.1790	2.0989	0.0804	0.2402	1.6396	0.0643	0.1133	1.7133	0.0550	0.1215
0.70	2.2780	0.3174	0.3067	1.9347	0.2703	0.6962	1.9829	0.1587	0.1888	1.3349	0.1125	0.1616
0.90	1.8758	3.0485	0.6598	5.8940	2.7081	0.2911	9.9026	2.5928	1.3949	−1.7466	1.2734	0.5148

$\cos(\theta^*_{\pi^0})$	W=(1465.0±9.0) MeV			W=(1483.0±9.0) MeV			W=(1501.0±9.0) MeV			W=(1519.0±9.0) MeV		
	$d\sigma_{1/2}/d\Omega$ [μb/sr]	Δ_{stat} [μb/sr]	Δ_{sys} [μb/sr]	$d\sigma_{1/2}/d\Omega$ [μb/sr]	Δ_{stat} [μb/sr]	Δ_{sys} [μb/sr]	$d\sigma_{1/2}/d\Omega$ [μb/sr]	Δ_{stat} [μb/sr]	Δ_{sys} [μb/sr]	$d\sigma_{1/2}/d\Omega$ [μb/sr]	Δ_{stat} [μb/sr]	Δ_{sys} [μb/sr]
−0.90	1.4615	0.0382	0.1346	1.6847	0.0405	0.0944	2.1898	0.0465	0.0263	2.5081	0.0492	0.0216
−0.70	2.1484	0.0434	0.0171	2.4626	0.0454	0.0642	2.7866	0.0499	0.1221	2.6058	0.0507	0.0778
−0.50	2.9275	0.0442	0.0687	3.4427	0.0456	0.0922	3.9336	0.0499	0.1555	3.8360	0.0505	0.0847
−0.30	3.7012	0.0545	0.0253	3.9779	0.0562	0.0478	4.4829	0.0612	0.1128	4.1686	0.0608	0.0478
−0.10	3.7080	0.0560	0.0512	4.2746	0.0582	0.0503	5.0729	0.0638	0.1150	4.7852	0.0627	0.0424
0.10	3.5303	0.0568	0.0353	4.1931	0.0600	0.0756	4.8489	0.0655	0.0596	4.7333	0.0650	0.0627
0.30	2.8962	0.0530	0.1615	3.7610	0.0571	0.1724	4.7835	0.0638	0.2663	4.3267	0.0639	0.1617
0.50	2.2318	0.0513	0.2053	2.7211	0.0547	0.1429	3.7357	0.0616	0.1664	3.7431	0.0618	0.0660
0.70	1.2603	0.0899	0.1406	2.2257	0.0873	0.2316	2.6330	0.0883	0.0783	2.5571	0.0841	0.1206
0.90	−2.3924	0.9196	0.8364	7.2197	4.4180	5.5698	1.8461	2.9256	2.1355	3.3821	0.7128	0.4169

$\cos(\theta^*_{\pi^0})$	W=(1537.0±9.0) MeV			W=(1555.0±9.0) MeV			W=(1573.0±9.0) MeV			W=(1591.0±9.0) MeV		
	$d\sigma_{1/2}/d\Omega$ [μb/sr]	Δ_{stat} [μb/sr]	Δ_{sys} [μb/sr]	$d\sigma_{1/2}/d\Omega$ [μb/sr]	Δ_{stat} [μb/sr]	Δ_{sys} [μb/sr]	$d\sigma_{1/2}/d\Omega$ [μb/sr]	Δ_{stat} [μb/sr]	Δ_{sys} [μb/sr]	$d\sigma_{1/2}/d\Omega$ [μb/sr]	Δ_{stat} [μb/sr]	Δ_{sys} [μb/sr]
−0.90	2.2223	0.0476	0.0426	2.2769	0.0482	0.0531	2.1908	0.0460	0.0134	2.1601	0.0453	0.0502
−0.70	2.4973	0.0481	0.0644	2.0014	0.0476	0.0623	1.7011	0.0455	0.0665	1.5853	0.0447	0.0929
−0.50	3.1411	0.0468	0.0560	2.7067	0.0448	0.0339	2.1253	0.0416	0.0064	1.7534	0.0402	0.0414
−0.30	3.8034	0.0556	0.0584	3.0140	0.0527	0.0546	2.4230	0.0480	0.0512	1.8882	0.0453	0.0240
−0.10	3.7565	0.0561	0.0366	3.2034	0.0523	0.0467	2.2848	0.0471	0.0290	1.9237	0.0436	0.0246
0.10	4.2274	0.0582	0.1978	3.3721	0.0548	0.0684	2.4846	0.0491	0.0470	2.0367	0.0443	0.0834
0.30	3.8237	0.0564	0.0537	3.1135	0.0521	0.0758	2.4373	0.0468	0.0162	2.0090	0.0425	0.0317
0.50	3.1647	0.0553	0.0267	2.9036	0.0509	0.0703	2.4723	0.0454	0.0149	1.8521	0.0423	0.0924
0.70	2.2613	0.0713	0.1070	2.2091	0.0625	0.0339	1.6256	0.0549	0.0709	1.6686	0.0521	0.1231
0.90	0.3706	0.5352	0.0775	5.3909	11.3370	7.1039	0.0719	0.3737	0.3025	2.4903	0.7633	1.4983

$\cos(\theta^*_{\pi^0})$	W=(1609.0±9.0) MeV			W=(1627.0±9.0) MeV			W=(1645.0±9.0) MeV			W=(1663.0±9.0) MeV		
	$d\sigma_{1/2}/d\Omega$ [μb/sr]	Δ_{stat} [μb/sr]	Δ_{sys} [μb/sr]	$d\sigma_{1/2}/d\Omega$ [μb/sr]	Δ_{stat} [μb/sr]	Δ_{sys} [μb/sr]	$d\sigma_{1/2}/d\Omega$ [μb/sr]	Δ_{stat} [μb/sr]	Δ_{sys} [μb/sr]	$d\sigma_{1/2}/d\Omega$ [μb/sr]	Δ_{stat} [μb/sr]	Δ_{sys} [μb/sr]
−0.90	1.4083	0.0413	0.0868	1.4136	0.0404	0.0553	1.5310	0.0428	0.0968	1.3130	0.0434	0.1362
−0.70	1.2522	0.0409	0.1209	1.0212	0.0398	0.1012	1.1116	0.0418	0.1604	1.0945	0.0418	0.1523
−0.50	1.3925	0.0364	0.0332	0.9843	0.0362	0.0612	0.9440	0.0388	0.0558	1.1534	0.0395	0.0304
−0.30	1.1813	0.0402	0.0179	1.2324	0.0387	0.0101	1.0556	0.0401	0.0262	1.1139	0.0400	0.0488
−0.10	1.6399	0.0377	0.0374	1.2569	0.0358	0.0126	1.4558	0.0364	0.0377	1.4110	0.0357	0.0488
0.10	1.4829	0.0385	0.0204	1.4137	0.0360	0.0362	1.5079	0.0370	0.0093	1.7579	0.0370	0.0570
0.30	1.6854	0.0364	0.0211	1.4487	0.0348	0.0502	1.7982	0.0360	0.0154	1.9940	0.0367	0.0576
0.50	1.6495	0.0373	0.1196	1.5266	0.0359	0.0770	1.9322	0.0394	0.1090	1.9397	0.0413	0.0690
0.70	1.2847	0.0463	0.1409	1.5144	0.0452	0.0474	1.5051	0.0505	0.0849	1.9337	0.0544	0.1129
0.90	0.6224	0.6909	0.4910	0.6858	0.7319	3.0602	0.3646	0.5552	0.6423	1.4819	0.2432	0.4606

$\cos(\theta^*_{\pi^0})$	W=(1681.0±9.0) MeV			W=(1699.0±9.0) MeV			W=(1717.0±9.0) MeV			W=(1735.0±9.0) MeV		
	$d\sigma_{1/2}/d\Omega$ [μb/sr]	Δ_{stat} [μb/sr]	Δ_{sys} [μb/sr]	$d\sigma_{1/2}/d\Omega$ [μb/sr]	Δ_{stat} [μb/sr]	Δ_{sys} [μb/sr]	$d\sigma_{1/2}/d\Omega$ [μb/sr]	Δ_{stat} [μb/sr]	Δ_{sys} [μb/sr]	$d\sigma_{1/2}/d\Omega$ [μb/sr]	Δ_{stat} [μb/sr]	Δ_{sys} [μb/sr]
−0.90	1.7658	0.0445	0.0371	1.3771	0.0448	0.0787	1.1988	0.0429	0.0622	1.1515	0.0396	0.0409
−0.70	1.1943	0.0422	0.0700	0.7824	0.0413	0.0576	0.9144	0.0378	0.0226	0.6686	0.0347	0.0443
−0.50	0.9854	0.0407	0.0402	0.7475	0.0411	0.0461	0.5887	0.0395	0.0692	0.5838	0.0369	0.0494
−0.30	1.0092	0.0406	0.0756	0.9486	0.0400	0.1334	1.0548	0.0384	0.0986	0.7687	0.0358	0.0698
−0.10	1.4187	0.0355	0.1583	1.4044	0.0359	0.0674	1.1331	0.0346	0.0808	0.8521	0.0331	0.0521
0.10	1.8272	0.0383	0.0770	1.7766	0.0389	0.0652	1.6418	0.0378	0.0957	1.1447	0.0365	0.0324
0.30	2.0318	0.0395	0.0496	2.1406	0.0404	0.1043	1.9772	0.0405	0.1039	1.6577	0.0390	0.0609
0.50	2.4390	0.0449	0.0503	2.4001	0.0466	0.0678	2.1670	0.0459	0.0894	1.7553	0.0443	0.0643
0.70	2.0084	0.0577	0.0069	1.7959	0.0591	0.0157	1.9600	0.0585	0.0837	1.7357	0.0559	0.0352
0.90	1.4701	0.2085	0.2666	1.0005	0.1710	0.0597	1.7530	0.1468	0.1162	0.5647	0.8170	0.5441

$\cos(\theta^*_{\pi^0})$	$W=(1753.0\pm9.0)$ MeV			$W=(1771.0\pm9.0)$ MeV			$W=(1789.0\pm9.0)$ MeV			$W=(1807.0\pm9.0)$ MeV		
	$d\sigma_{1/2}/d\Omega$ [μb/sr]	$\Delta_{\rm stat}$ [μb/sr]	$\Delta_{\rm sys}$ [μb/sr]	$d\sigma_{1/2}/d\Omega$ [μb/sr]	$\Delta_{\rm stat}$ [μb/sr]	$\Delta_{\rm sys}$ [μb/sr]	$d\sigma_{1/2}/d\Omega$ [μb/sr]	$\Delta_{\rm stat}$ [μb/sr]	$\Delta_{\rm sys}$ [μb/sr]	$d\sigma_{1/2}/d\Omega$ [μb/sr]	$\Delta_{\rm stat}$ [μb/sr]	$\Delta_{\rm sys}$ [μb/sr]
−0.90	1.0408	0.0374	0.0945	1.0905	0.0352	0.1000	1.1561	0.0371	0.1494	1.1180	0.0385	0.1445
−0.70	0.5663	0.0328	0.1014	0.5660	0.0305	0.0946	0.4570	0.0312	0.1025	0.6675	0.0320	0.0840
−0.50	0.5088	0.0345	0.0118	0.3547	0.0321	0.0121	0.3479	0.0327	0.0103	0.4489	0.0334	0.0265
−0.30	0.5248	0.0334	0.0260	0.5074	0.0316	0.0249	0.5099	0.0338	0.0174	0.3616	0.0376	0.0252
−0.10	0.8316	0.0318	0.0095	0.6643	0.0294	0.0140	0.6045	0.0316	0.0211	0.4791	0.0338	0.0251
0.10	1.2390	0.0351	0.0070	0.9721	0.0336	0.0167	0.8847	0.0363	0.0411	0.7930	0.0394	0.0151
0.30	1.2718	0.0368	0.0103	1.0758	0.0343	0.0137	0.9633	0.0355	0.0308	0.7786	0.0376	0.0269
0.50	1.4899	0.0412	0.0589	1.0197	0.0394	0.0825	0.9251	0.0401	0.0357	0.8327	0.0412	0.0216
0.70	1.2418	0.0519	0.0276	1.0367	0.0500	0.1081	1.0498	0.0518	0.0704	0.9607	0.0573	0.1078
0.90	−0.1364	0.1223	0.0474	0.5132	0.1204	0.2142	0.2509	0.1519	0.2808	1.0245	0.1311	0.2294

$\cos(\theta^*_{\pi^0})$	$W=(1825.0\pm9.0)$ MeV			$W=(1843.0\pm9.0)$ MeV			$W=(1861.0\pm9.0)$ MeV			$W=(1879.0\pm9.0)$ MeV		
	$d\sigma_{1/2}/d\Omega$ [μb/sr]	$\Delta_{\rm stat}$ [μb/sr]	$\Delta_{\rm sys}$ [μb/sr]	$d\sigma_{1/2}/d\Omega$ [μb/sr]	$\Delta_{\rm stat}$ [μb/sr]	$\Delta_{\rm sys}$ [μb/sr]	$d\sigma_{1/2}/d\Omega$ [μb/sr]	$\Delta_{\rm stat}$ [μb/sr]	$\Delta_{\rm sys}$ [μb/sr]	$d\sigma_{1/2}/d\Omega$ [μb/sr]	$\Delta_{\rm stat}$ [μb/sr]	$\Delta_{\rm sys}$ [μb/sr]
−0.90	1.1671	0.0399	0.1051	1.3237	0.0449	0.1027	1.4477	0.0460	0.1399	1.0383	0.0513	0.0622
−0.70	0.4387	0.0330	0.0372	0.4311	0.0388	0.0971	0.5269	0.0416	0.0871	0.3898	0.0494	0.0371
−0.50	0.1618	0.0348	0.0115	0.4190	0.0377	0.0369	0.4459	0.0365	0.0050	0.3599	0.0382	0.0865
−0.30	0.2429	0.0396	0.0126	0.4628	0.0463	0.0303	0.6432	0.0487	0.0949	0.6379	0.0550	0.0589
−0.10	0.5406	0.0383	0.0150	0.6632	0.0455	0.0343	0.3743	0.0525	0.0042	0.5280	0.0652	0.0772
0.10	0.5035	0.0455	0.0335	0.5983	0.0539	0.1104	0.6196	0.0620	0.1041	0.5941	0.0733	0.1908
0.30	0.6976	0.0411	0.0322	0.7879	0.0509	0.0923	0.8092	0.0617	0.1106	0.7232	0.0789	0.1858
0.50	0.7346	0.0428	0.0698	0.5929	0.0513	0.0739	0.4653	0.0563	0.1657	1.0127	0.0687	0.2844
0.70	0.9276	0.0610	0.0760	1.3350	0.0727	0.0639	1.1939	0.0848	0.0520	1.1984	0.0991	0.2960
0.90	1.5044	0.1407	0.1356	0.9127	0.1761	0.2389	1.1577	0.1794	0.2247	1.2012	0.2085	0.1389

$\cos(\theta^*_{\pi^0})$				$W=(1897.0\pm9.0)$ MeV						$W=(1915.0\pm9.0)$ MeV		
				$d\sigma_{1/2}/d\Omega$ [μb/sr]	$\Delta_{\rm stat}$ [μb/sr]	$\Delta_{\rm sys}$ [μb/sr]				$d\sigma_{1/2}/d\Omega$ [μb/sr]	$\Delta_{\rm stat}$ [μb/sr]	$\Delta_{\rm sys}$ [μb/sr]
−0.90				1.0971	0.0635	0.0166				0.9527	0.1217	0.0713
−0.70				0.6082	0.0697	0.0147				0.1971	0.1435	0.0761
−0.50				0.3957	0.0464	0.0441				0.1275	0.0773	0.0096
−0.30				0.5636	0.0623	0.0646				0.2549	0.0867	0.1003
−0.10				0.5506	0.0857	0.2217				0.6333	0.1336	0.2741
0.10				0.6818	0.0916	0.2297				0.8367	0.1389	0.4270
0.30				0.7595	0.1056	0.2868				1.1287	0.1617	0.3497
0.50				0.8526	0.0898	0.3137				1.1050	0.1460	0.3708
0.70				1.0348	0.1312	0.2683				1.2566	0.1922	0.3855
0.90				0.4237	0.2871	0.2133				−0.3224	0.4058	0.1534

$\cos(\theta^*_{\pi^0})$	$W=(1321.0\pm9.0)$ MeV			$W=(1339.0\pm9.0)$ MeV			$W=(1357.0\pm9.0)$ MeV			$W=(1375.0\pm9.0)$ MeV		
	$d\sigma_{3/2}/d\Omega$ [μb/sr]	$\Delta_{\rm stat}$ [μb/sr]	$\Delta_{\rm sys}$ [μb/sr]	$d\sigma_{3/2}/d\Omega$ [μb/sr]	$\Delta_{\rm stat}$ [μb/sr]	$\Delta_{\rm sys}$ [μb/sr]	$d\sigma_{3/2}/d\Omega$ [μb/sr]	$\Delta_{\rm stat}$ [μb/sr]	$\Delta_{\rm sys}$ [μb/sr]	$d\sigma_{3/2}/d\Omega$ [μb/sr]	$\Delta_{\rm stat}$ [μb/sr]	$\Delta_{\rm sys}$ [μb/sr]
−0.90	2.6472	0.1933	1.5978	0.9876	0.1000	0.6197	0.5942	0.0763	0.3916	0.6067	0.0560	0.2934
−0.70	14.9770	0.4068	1.9304	7.0642	0.1880	0.6936	4.1756	0.1332	0.4440	2.1561	0.0900	0.3235
−0.50	30.4922	0.3625	0.1128	12.1692	0.1765	0.0663	7.7395	0.1275	0.1463	4.6419	0.0889	0.2052
−0.30	37.6621	0.4142	0.3477	16.3313	0.2040	0.3103	10.5705	0.1496	0.1411	6.9545	0.1059	0.2133
−0.10	40.5167	0.4101	1.4234	19.6255	0.2065	0.3551	12.2121	0.1499	0.0560	8.1638	0.1078	0.1762
0.10	38.2783	0.4220	2.7283	19.5523	0.2071	0.5511	11.9668	0.1487	0.1657	8.8632	0.1075	0.0441
0.30	29.5028	0.5010	4.2957	14.7954	0.2225	1.3897	9.8912	0.1487	0.5699	6.4738	0.1017	0.1809
0.50	20.4543	1.1611	5.9567	7.8959	0.4220	1.7692	6.7226	0.2265	0.7383	4.4422	0.1334	0.2217
0.70	1.6268	11.8608	8.4816	−13.7004	4.7556	15.4081	−4.5102	1.5738	4.4396	1.0084	0.5911	0.7480
0.90	109.4600	51.1901	42.6108	−3.0849	13.7616	16.1242	−12.9670	21.8883	13.8634	13.9049	12.7312	10.2094

$\cos(\theta^*_{\pi^0})$	$W=(1393.0\pm9.0)$ MeV			$W=(1411.0\pm9.0)$ MeV			$W=(1429.0\pm9.0)$ MeV			$W=(1447.0\pm9.0)$ MeV		
	$d\sigma_{3/2}/d\Omega$ [μb/sr]	$\Delta_{\rm stat}$ [μb/sr]	$\Delta_{\rm sys}$ [μb/sr]	$d\sigma_{3/2}/d\Omega$ [μb/sr]	$\Delta_{\rm stat}$ [μb/sr]	$\Delta_{\rm sys}$ [μb/sr]	$d\sigma_{3/2}/d\Omega$ [μb/sr]	$\Delta_{\rm stat}$ [μb/sr]	$\Delta_{\rm sys}$ [μb/sr]	$d\sigma_{3/2}/d\Omega$ [μb/sr]	$\Delta_{\rm stat}$ [μb/sr]	$\Delta_{\rm sys}$ [μb/sr]
−0.90	0.3130	0.0485	0.1916	0.3402	0.0480	0.1269	0.2843	0.0444	0.1180	0.0875	0.0412	0.0747
−0.70	1.4310	0.0738	0.1265	1.1928	0.0658	0.0993	0.5591	0.0567	0.0691	0.6153	0.0493	0.0259
−0.50	3.2998	0.0732	0.0559	2.1101	0.0667	0.0665	1.7259	0.0569	0.0644	1.5272	0.0494	0.0097
−0.30	5.0542	0.0869	0.1257	3.7359	0.0791	0.0805	3.1518	0.0691	0.0550	2.6314	0.0610	0.0298
−0.10	5.5861	0.0892	0.0239	4.6541	0.0818	0.0155	3.7034	0.0709	0.0434	3.1855	0.0622	0.0591
0.10	5.6982	0.0886	0.1153	4.5908	0.0815	0.1201	3.5747	0.0707	0.0260	3.4182	0.0626	0.0424
0.30	4.6652	0.0826	0.1980	3.6816	0.0748	0.1763	3.1495	0.0649	0.1088	2.5233	0.0570	0.0480
0.50	3.0194	0.0953	0.1700	2.0798	0.0804	0.1930	2.1302	0.0644	0.0820	2.0023	0.0550	0.0882
0.70	1.5152	0.3173	0.1603	0.4787	0.2702	0.3663	0.3808	0.1584	0.1435	1.0095	0.1125	0.0981
0.90	4.1739	3.0489	0.8964	−2.0984	2.7051	0.1863	−7.0584	2.5888	0.9716	5.1058	1.2768	0.7850

$\cos(\theta^*_{\pi^0})$	$W=(1465.0\pm9.0)$ MeV			$W=(1483.0\pm9.0)$ MeV			$W=(1501.0\pm9.0)$ MeV			$W=(1519.0\pm9.0)$ MeV		
	$d\sigma_{3/2}/d\Omega$ [μb/sr]	$\Delta_{\rm stat}$ [μb/sr]	$\Delta_{\rm sys}$ [μb/sr]	$d\sigma_{3/2}/d\Omega$ [μb/sr]	$\Delta_{\rm stat}$ [μb/sr]	$\Delta_{\rm sys}$ [μb/sr]	$d\sigma_{3/2}/d\Omega$ [μb/sr]	$\Delta_{\rm stat}$ [μb/sr]	$\Delta_{\rm sys}$ [μb/sr]	$d\sigma_{3/2}/d\Omega$ [μb/sr]	$\Delta_{\rm stat}$ [μb/sr]	$\Delta_{\rm sys}$ [μb/sr]
−0.90	0.0251	0.0379	0.0700	0.1633	0.0401	0.0525	0.4298	0.0462	0.0080	0.6375	0.0488	0.0215
−0.70	0.5836	0.0432	0.0124	0.5772	0.0452	0.0330	1.0390	0.0496	0.0800	1.6477	0.0506	0.0357
−0.50	1.6152	0.0441	0.0275	1.5515	0.0455	0.0486	2.0780	0.0498	0.0936	2.3824	0.0504	0.0501
−0.30	2.3179	0.0544	0.0180	2.7678	0.0561	0.0375	3.2164	0.0611	0.0661	3.6121	0.0607	0.0595
−0.10	3.1482	0.0559	0.0410	3.3589	0.0581	0.0505	3.8097	0.0637	0.0654	4.0849	0.0626	0.0675
0.10	3.1033	0.0568	0.0040	3.5273	0.0599	0.0321	4.2167	0.0654	0.0147	4.2379	0.0650	0.0736
0.30	2.7665	0.0530	0.1144	2.9940	0.0570	0.1239	3.4284	0.0637	0.1928	3.8206	0.0639	0.1342
0.50	1.7883	0.0512	0.1503	2.4680	0.0546	0.1076	2.6852	0.0615	0.1045	2.9162	0.0617	0.0379
0.70	1.2727	0.0899	0.1411	0.9952	0.0871	0.1617	1.7295	0.0882	0.0512	1.7587	0.0839	0.0782
0.90	5.3112	0.9246	1.1907	−5.6734	4.4171	4.8090	−0.1976	2.9254	1.2970	−0.8420	0.7103	0.1790

$\cos(\theta^*_{\pi^0})$	$W=(1537.0\pm9.0)$ MeV			$W=(1555.0\pm9.0)$ MeV			$W=(1573.0\pm9.0)$ MeV			$W=(1591.0\pm9.0)$ MeV		
	$d\sigma_{3/2}/d\Omega$ [μb/sr]	Δ_{stat} [μb/sr]	Δ_{sys} [μb/sr]	$d\sigma_{3/2}/d\Omega$ [μb/sr]	Δ_{stat} [μb/sr]	Δ_{sys} [μb/sr]	$d\sigma_{3/2}/d\Omega$ [μb/sr]	Δ_{stat} [μb/sr]	Δ_{sys} [μb/sr]	$d\sigma_{3/2}/d\Omega$ [μb/sr]	Δ_{stat} [μb/sr]	Δ_{sys} [μb/sr]
−0.90	1.1257	0.0474	0.0172	1.2527	0.0480	0.0286	1.4615	0.0459	0.0035	1.4820	0.0451	0.0384
−0.70	1.6913	0.0480	0.0437	2.1476	0.0477	0.0561	2.3253	0.0457	0.0588	2.4672	0.0448	0.0977
−0.50	2.5856	0.0467	0.0408	2.5189	0.0448	0.0158	2.5994	0.0417	0.0092	2.6105	0.0403	0.0377
−0.30	3.0312	0.0555	0.0731	3.0023	0.0527	0.0632	2.6958	0.0481	0.0634	2.5214	0.0454	0.0323
−0.10	3.6968	0.0561	0.0685	3.2089	0.0523	0.0713	2.8096	0.0472	0.0360	2.4248	0.0437	0.0300
0.10	3.6040	0.0582	0.2007	3.0253	0.0548	0.0846	2.4625	0.0491	0.0623	2.0264	0.0443	0.0886
0.30	3.1247	0.0563	0.0791	2.5864	0.0521	0.0942	1.7975	0.0467	0.0149	1.2892	0.0424	0.0127
0.50	2.3444	0.0552	0.0204	1.6512	0.0507	0.0737	0.9280	0.0452	0.0168	0.7238	0.0421	0.0523
0.70	1.2395	0.0711	0.0545	0.7773	0.0621	0.0416	0.5590	0.0546	0.0267	0.2503	0.0517	0.0908
0.90	1.3804	0.5356	0.0852	−4.3782	11.3369	6.6750	1.5231	0.3755	0.1645	−1.4825	0.7624	1.0983

$\cos(\theta^*_{\pi^0})$	$W=(1609.0\pm9.0)$ MeV			$W=(1627.0\pm9.0)$ MeV			$W=(1645.0\pm9.0)$ MeV			$W=(1663.0\pm9.0)$ MeV		
	$d\sigma_{3/2}/d\Omega$ [μb/sr]	Δ_{stat} [μb/sr]	Δ_{sys} [μb/sr]	$d\sigma_{3/2}/d\Omega$ [μb/sr]	Δ_{stat} [μb/sr]	Δ_{sys} [μb/sr]	$d\sigma_{3/2}/d\Omega$ [μb/sr]	Δ_{stat} [μb/sr]	Δ_{sys} [μb/sr]	$d\sigma_{3/2}/d\Omega$ [μb/sr]	Δ_{stat} [μb/sr]	Δ_{sys} [μb/sr]
−0.90	1.9492	0.0414	0.0837	2.0819	0.0406	0.0588	2.3641	0.0429	0.1082	2.6483	0.0437	0.1736
−0.70	2.4439	0.0411	0.1520	2.9262	0.0401	0.1357	3.3568	0.0422	0.2300	3.4350	0.0423	0.2182
−0.50	2.5872	0.0366	0.0374	2.9725	0.0365	0.0945	3.5086	0.0392	0.0843	3.4484	0.0398	0.0418
−0.30	2.5701	0.0404	0.0285	2.4671	0.0389	0.0093	2.9082	0.0404	0.0361	2.8271	0.0403	0.0651
−0.10	1.9319	0.0377	0.0404	2.0772	0.0359	0.0138	2.0687	0.0364	0.0442	2.0587	0.0359	0.0591
0.10	1.6381	0.0386	0.0214	1.5971	0.0361	0.0540	1.5880	0.0370	0.0093	1.5232	0.0370	0.0608
0.30	1.0086	0.0363	0.0230	1.1112	0.0348	0.0262	1.2958	0.0359	0.0154	1.6032	0.0366	0.0573
0.50	0.6304	0.0371	0.0728	0.9660	0.0358	0.0512	1.3211	0.0393	0.0904	2.0625	0.0413	0.0698
0.70	0.7492	0.0462	0.0973	1.1591	0.0451	0.0246	2.0812	0.0506	0.0907	2.4086	0.0545	0.1187
0.90	0.3637	0.6908	0.4038	0.1486	0.7322	2.3636	1.2596	0.5554	1.0051	1.0571	0.2429	0.3890

$\cos(\theta^*_{\pi^0})$	$W=(1681.0\pm9.0)$ MeV			$W=(1699.0\pm9.0)$ MeV			$W=(1717.0\pm9.0)$ MeV			$W=(1735.0\pm9.0)$ MeV		
	$d\sigma_{3/2}/d\Omega$ [μb/sr]	Δ_{stat} [μb/sr]	Δ_{sys} [μb/sr]	$d\sigma_{3/2}/d\Omega$ [μb/sr]	Δ_{stat} [μb/sr]	Δ_{sys} [μb/sr]	$d\sigma_{3/2}/d\Omega$ [μb/sr]	Δ_{stat} [μb/sr]	Δ_{sys} [μb/sr]	$d\sigma_{3/2}/d\Omega$ [μb/sr]	Δ_{stat} [μb/sr]	Δ_{sys} [μb/sr]
−0.90	2.3131	0.0446	0.0429	2.1938	0.0450	0.0840	1.7596	0.0431	0.0697	1.3753	0.0397	0.0353
−0.70	3.3618	0.0426	0.1077	3.0375	0.0419	0.0814	2.2196	0.0382	0.0297	1.7491	0.0351	0.0687
−0.50	3.5080	0.0412	0.0495	3.1706	0.0416	0.0730	2.6507	0.0400	0.1122	1.8477	0.0373	0.0595
−0.30	2.7056	0.0409	0.1234	2.3186	0.0403	0.1795	1.4853	0.0385	0.0981	1.2505	0.0360	0.0896
−0.10	1.9322	0.0356	0.1797	1.3954	0.0360	0.0760	1.2194	0.0347	0.0754	1.0267	0.0332	0.0580
0.10	1.4503	0.0382	0.0846	1.1902	0.0388	0.0681	0.9323	0.0377	0.0890	0.9811	0.0365	0.0386
0.30	1.6942	0.0395	0.0598	1.5054	0.0403	0.1018	1.2471	0.0404	0.0724	1.0297	0.0388	0.0521
0.50	2.0139	0.0448	0.0360	2.0289	0.0465	0.0677	1.7052	0.0457	0.0968	1.4014	0.0442	0.0871
0.70	2.8075	0.0579	0.0110	2.6681	0.0593	0.0357	1.9135	0.0585	0.0843	1.3190	0.0558	0.0447
0.90	1.1606	0.2082	0.2378	1.6998	0.1716	0.0691	0.6021	0.1455	0.0794	0.4950	0.8170	0.4586

$\cos(\theta^*_{\pi^0})$	$W=(1753.0\pm9.0)$ MeV			$W=(1771.0\pm9.0)$ MeV			$W=(1789.0\pm9.0)$ MeV			$W=(1807.0\pm9.0)$ MeV		
	$d\sigma_{3/2}/d\Omega$ [μb/sr]	Δ_{stat} [μb/sr]	Δ_{sys} [μb/sr]	$d\sigma_{3/2}/d\Omega$ [μb/sr]	Δ_{stat} [μb/sr]	Δ_{sys} [μb/sr]	$d\sigma_{3/2}/d\Omega$ [μb/sr]	Δ_{stat} [μb/sr]	Δ_{sys} [μb/sr]	$d\sigma_{3/2}/d\Omega$ [μb/sr]	Δ_{stat} [μb/sr]	Δ_{sys} [μb/sr]
−0.90	1.1639	0.0375	0.0982	0.9425	0.0352	0.0862	0.8905	0.0371	0.1237	0.9865	0.0384	0.1245
−0.70	1.3529	0.0331	0.1517	1.1218	0.0308	0.1254	1.2574	0.0316	0.1394	1.0935	0.0323	0.0982
−0.50	1.4451	0.0349	0.0129	1.1806	0.0325	0.0043	1.0862	0.0331	0.0081	0.8834	0.0337	0.0318
−0.30	1.0575	0.0337	0.0366	0.8686	0.0318	0.0341	0.8134	0.0340	0.0177	0.8690	0.0378	0.0309
−0.10	0.7326	0.0318	0.0066	0.7740	0.0294	0.0185	0.7642	0.0316	0.0236	0.9504	0.0340	0.0342
0.10	0.6381	0.0350	0.0104	0.6939	0.0335	0.0146	0.7331	0.0362	0.0370	0.8236	0.0394	0.0108
0.30	0.9837	0.0368	0.0188	0.7688	0.0343	0.0083	0.6788	0.0354	0.0262	0.7573	0.0376	0.0165
0.50	1.0279	0.0411	0.0530	0.8208	0.0394	0.0665	0.7718	0.0400	0.0278	0.7423	0.0411	0.0214
0.70	1.1976	0.0519	0.0170	1.0074	0.0501	0.0901	0.9691	0.0518	0.0690	0.9060	0.0573	0.1045
0.90	1.7954	0.1244	0.0326	0.9392	0.1208	0.2499	1.1683	0.1525	0.4912	0.8132	0.1312	0.1942

$\cos(\theta^*_{\pi^0})$	$W=(1825.0\pm9.0)$ MeV			$W=(1843.0\pm9.0)$ MeV			$W=(1861.0\pm9.0)$ MeV			$W=(1879.0\pm9.0)$ MeV		
	$d\sigma_{3/2}/d\Omega$ [μb/sr]	Δ_{stat} [μb/sr]	Δ_{sys} [μb/sr]	$d\sigma_{3/2}/d\Omega$ [μb/sr]	Δ_{stat} [μb/sr]	Δ_{sys} [μb/sr]	$d\sigma_{3/2}/d\Omega$ [μb/sr]	Δ_{stat} [μb/sr]	Δ_{sys} [μb/sr]	$d\sigma_{3/2}/d\Omega$ [μb/sr]	Δ_{stat} [μb/sr]	Δ_{sys} [μb/sr]
−0.90	1.0696	0.0399	0.0874	1.1825	0.0448	0.0851	0.8638	0.0456	0.1168	1.2112	0.0514	0.0670
−0.70	1.3082	0.0335	0.0487	1.3875	0.0394	0.1411	1.2193	0.0421	0.1037	1.3728	0.0503	0.0536
−0.50	0.9873	0.0353	0.0083	0.7257	0.0380	0.0500	0.6351	0.0368	0.0011	0.7666	0.0387	0.1252
−0.30	0.9425	0.0400	0.0217	0.8424	0.0466	0.0339	0.7382	0.0489	0.0902	0.5555	0.0551	0.0632
−0.10	0.8585	0.0384	0.0213	0.9598	0.0457	0.0263	1.3091	0.0530	0.0115	1.2511	0.0656	0.1253
0.10	1.1288	0.0458	0.0282	1.3600	0.0543	0.1516	1.2969	0.0623	0.1303	1.3892	0.0737	0.2724
0.30	0.7515	0.0411	0.0281	0.8599	0.0509	0.0922	0.8011	0.0616	0.0936	1.0718	0.0791	0.2072
0.50	0.7232	0.0428	0.0724	0.7810	0.0513	0.0916	0.9871	0.0566	0.2364	0.5459	0.0683	0.2314
0.70	1.0375	0.0611	0.0649	1.0946	0.0726	0.0690	1.2414	0.0848	0.0255	1.5407	0.0994	0.3459
0.90	0.7889	0.1400	0.1105	1.3627	0.1767	0.2630	1.9439	0.1806	0.2822	1.7103	0.2094	0.1727

$\cos(\theta^*_{\pi^0})$	$W=(1897.0\pm9.0)$ MeV			$W=(1915.0\pm9.0)$ MeV		
	$d\sigma_{3/2}/d\Omega$ [μb/sr]	Δ_{stat} [μb/sr]	Δ_{sys} [μb/sr]	$d\sigma_{3/2}/d\Omega$ [μb/sr]	Δ_{stat} [μb/sr]	Δ_{sys} [μb/sr]
−0.90	1.0437	0.0635	0.0162	1.6311	0.1227	0.0389
−0.70	1.3427	0.0707	0.0232	1.7970	0.1459	0.1391
−0.50	0.6569	0.0468	0.0614	0.8508	0.0783	0.0271
−0.30	0.5662	0.0625	0.0739	0.9704	0.0876	0.1512
−0.10	1.4067	0.0865	0.3238	1.3573	0.1345	0.3613
0.10	1.2288	0.0920	0.3017	1.5612	0.1397	0.5215
0.30	1.0891	0.1059	0.3365	0.8841	0.1615	0.3404
0.50	0.7487	0.0897	0.2981	0.7597	0.1454	0.3528
0.70	1.7065	0.1319	0.3453	2.0529	0.1933	0.4795
0.90	2.2035	0.2897	0.3204	2.9975	0.4126	0.3021

E.2.6 Observables for $\gamma n \to \pi^0 n$ as a Function of W

W [MeV]	ΔW [MeV]	E	Δ_{stat}	Δ_{sys}	$\sigma_{1/2}$ [μb]	Δ_{stat} [μb]	Δ_{sys} [μb]	$\sigma_{3/2}$ [μb]	Δ_{stat} [μb]	Δ_{sys} [μb]
1321.0	9.0	−0.4720	0.0101	0.0567	163.4471	3.3930	22.2200	455.3820	3.3998	51.9419
1339.0	9.0	−0.3897	0.0100	0.0458	90.3071	1.6522	11.0474	205.2835	1.6554	22.9795
1357.0	9.0	−0.3909	0.0106	0.0455	60.2984	1.1740	7.5131	137.7642	1.1763	15.7046
1375.0	9.0	−0.3459	0.0102	0.0390	46.0295	0.8162	5.1403	94.2943	0.8180	10.4090
1393.0	9.0	−0.3036	0.0106	0.0342	36.8794	0.6504	4.1487	68.9351	0.6517	7.6079
1411.0	9.0	−0.2230	0.0117	0.0270	33.0456	0.5845	3.9670	51.9755	0.5854	5.9111
1429.0	9.0	−0.1618	0.0114	0.0191	30.3014	0.4930	3.4503	41.9470	0.4937	4.6691
1447.0	9.0	−0.1487	0.0108	0.0190	27.3774	0.4148	3.1418	36.8640	0.4154	4.0922
1465.0	9.0	−0.1016	0.0101	0.0138	26.1220	0.3555	3.0252	31.9753	0.3559	3.5853
1483.0	9.0	−0.0213	0.0096	0.0082	29.4333	0.3496	3.4070	30.6344	0.3497	3.4307
1501.0	9.0	−0.0708	0.0091	0.0119	31.3499	0.3716	3.9419	36.0705	0.3719	4.2987
1519.0	9.0	0.0301	0.0092	0.0055	33.3709	0.3605	3.9587	31.3573	0.3604	3.6390
1537.0	9.0	0.1143	0.0094	0.0132	31.5060	0.3213	3.5801	24.9844	0.3209	2.8166
1555.0	9.0	0.0819	0.0101	0.0110	26.6513	0.3003	3.0690	22.5496	0.3001	2.5460
1573.0	9.0	0.0641	0.0111	0.0103	21.4002	0.2709	2.5056	18.7585	0.2707	2.1395
1591.0	9.0	0.0931	0.0124	0.0121	18.5502	0.2540	2.4155	15.3274	0.2538	1.9446
1609.0	9.0	0.0834	0.0130	0.0108	14.9676	0.2174	1.7979	12.6239	0.2172	1.4791
1627.0	9.0	0.0373	0.0125	0.0068	13.5964	0.1993	1.5074	12.5954	0.1992	1.3860
1645.0	9.0	−0.0641	0.0131	0.0110	12.0898	0.2052	1.5136	13.7261	0.2054	1.6348
1663.0	9.0	−0.0194	0.0126	0.0034	12.8052	0.2007	1.4519	13.3028	0.2008	1.4936
1681.0	9.0	−0.1852	0.0132	0.0209	10.5457	0.2036	1.1665	15.3203	0.2042	1.6858
1699.0	9.0	−0.2176	0.0145	0.0250	9.3366	0.2061	1.0442	14.5134	0.2069	1.6035
1717.0	9.0	−0.1784	0.0157	0.0204	8.8615	0.2026	1.0183	12.6655	0.2033	1.4535
1735.0	9.0	−0.1797	0.0172	0.0201	7.8543	0.1970	0.8807	11.2688	0.1976	1.2569
1753.0	9.0	−0.1421	0.0190	0.0181	7.0779	0.1885	0.8627	9.4233	0.1890	1.0995
1771.0	9.0	−0.0305	0.0201	0.0074	7.0173	0.1770	0.9228	7.4467	0.1772	0.9361
1789.0	9.0	−0.0915	0.0211	0.0117	6.5387	0.1846	0.8674	7.8730	0.1850	1.0272
1807.0	9.0	−0.1186	0.0204	0.0136	6.6853	0.1875	0.7375	8.4702	0.1881	0.9335
1825.0	9.0	−0.1863	0.0228	0.0223	6.1303	0.2057	0.7085	8.9301	0.2065	0.9986
1843.0	9.0	−0.2051	0.0237	0.0233	6.7730	0.2406	0.7833	10.2369	0.2418	1.1634
1861.0	9.0	−0.0953	0.0254	0.0132	7.6160	0.2588	1.0044	9.2024	0.2594	1.1630
1879.0	9.0	−0.2416	0.0285	0.0389	6.8194	0.2966	1.2777	11.0073	0.2986	1.8105
1897.0	9.0	−0.0552	0.0349	0.0117	8.2368	0.3590	1.8446	9.1516	0.3599	1.9842
1915.0	9.0	−0.3379	0.0522	0.0861	6.3371	0.5269	2.1634	12.2026	0.5312	3.0393

Angular Distributions

	W=(1321.0±9.0) MeV			W=(1339.0±9.0) MeV			W=(1357.0±9.0) MeV			W=(1375.0±9.0) MeV		
$\cos(\theta^*_{\pi^0})$	E	Δ_{stat}	Δ_{sys}	E	Δ_{stat}	Δ_{sys}	E	Δ_{stat}	Δ_{sys}	E	Δ_{stat}	Δ_{sys}
−0.90	0.3810	0.2397	0.3097	0.2654	0.1472	0.1841	0.1879	0.1200	0.1147	0.0509	0.0929	0.0487
−0.70	−0.6239	0.0450	0.1256	−0.3804	0.0390	0.0610	−0.0593	0.0372	0.0166	−0.1468	0.0361	0.0203
−0.50	−0.5012	0.0239	0.0116	−0.3815	0.0232	0.0095	−0.4016	0.0250	0.0106	−0.3325	0.0241	0.0069
−0.30	−0.4593	0.0218	0.0250	−0.3538	0.0219	0.0164	−0.5381	0.0249	0.0284	−0.5813	0.0253	0.0163
−0.10	−0.4962	0.0220	0.0281	−0.5086	0.0230	0.0268	−0.5648	0.0250	0.0306	−0.3782	0.0227	0.0120
0.10	−0.5404	0.0254	0.0436	−0.4858	0.0258	0.0397	−0.4351	0.0266	0.0337	−0.3799	0.0263	0.0257
0.30	−0.3965	0.0307	0.0573	−0.2511	0.0280	0.0168	−0.3159	0.0303	0.0240	−0.2256	0.0288	0.0201
0.50	−0.4746	0.0485	0.0877	−0.2466	0.0417	0.0355	−0.1663	0.0448	0.0251	−0.2325	0.0402	0.0247
0.70	0.4099	0.1126	0.0828	−0.5753	0.1265	0.1368	0.2751	0.1013	0.0418	0.0768	0.0911	0.0065
0.90	1.7075	1.8606	0.4123	−3.0568	2.7346	0.7355	0.7801	0.7846	0.1271	−0.5989	0.6759	0.0703

	W=(1393.0±9.0) MeV			W=(1411.0±9.0) MeV			W=(1429.0±9.0) MeV			W=(1447.0±9.0) MeV		
$\cos(\theta^*_{\pi^0})$	E	Δ_{stat}	Δ_{sys}	E	Δ_{stat}	Δ_{sys}	E	Δ_{stat}	Δ_{sys}	E	Δ_{stat}	Δ_{sys}
−0.90	0.1423	0.0831	0.0773	0.8133	0.1098	0.2592	0.4862	0.0814	0.0894	0.5733	0.0714	0.1033
−0.70	−0.0939	0.0364	0.0081	−0.0656	0.0406	0.0132	0.1751	0.0401	0.0148	0.1022	0.0396	0.0055
−0.50	−0.3998	0.0262	0.0030	−0.2812	0.0270	0.0081	−0.2561	0.0274	0.0042	−0.0253	0.0252	0.0058
−0.30	−0.3728	0.0246	0.0065	−0.3237	0.0273	0.0211	−0.3281	0.0275	0.0214	−0.2083	0.0246	0.0067
−0.10	−0.3283	0.0243	0.0116	−0.3879	0.0278	0.0223	−0.1138	0.0257	0.0046	−0.3276	0.0258	0.0252
0.10	−0.2829	0.0270	0.0236	−0.2112	0.0298	0.0218	−0.3243	0.0307	0.0182	−0.2423	0.0275	0.0133
0.30	−0.4041	0.0324	0.0285	−0.1624	0.0350	0.0253	−0.1289	0.0335	0.0046	−0.2892	0.0338	0.0271
0.50	−0.1215	0.0422	0.0114	−0.1358	0.0542	0.0187	−0.1041	0.0499	0.0198	−0.1140	0.0455	0.0237
0.70	−0.1087	0.1052	0.0386	0.1567	0.1180	0.0250	0.3832	0.0973	0.0044	0.1730	0.0899	0.0146
0.90	−0.2073	0.9039	0.1036	−1.8128	0.9958	0.0673	−0.8998	0.7735	0.0577	2.1255	6.0450	1.1161

	W=(1465.0±9.0) MeV			W=(1483.0±9.0) MeV			W=(1501.0±9.0) MeV			W=(1519.0±9.0) MeV		
$\cos(\theta^*_{\pi^0})$	E	Δ_{stat}	Δ_{sys}	E	Δ_{stat}	Δ_{sys}	E	Δ_{stat}	Δ_{sys}	E	Δ_{stat}	Δ_{sys}
−0.90	0.4828	0.0600	0.0512	0.5012	0.0540	0.0525	0.8559	0.0570	0.0466	0.9734	0.0621	0.0977
−0.70	0.1817	0.0376	0.0048	0.3239	0.0347	0.0236	0.3814	0.0323	0.0206	0.6036	0.0381	0.0075
−0.50	−0.0202	0.0234	0.0034	0.1476	0.0239	0.0104	0.1538	0.0234	0.0042	0.1560	0.0240	0.0103
−0.30	−0.2672	0.0241	0.0198	−0.1216	0.0231	0.0131	−0.2255	0.0226	0.0174	0.0127	0.0228	0.0056
−0.10	−0.2033	0.0238	0.0149	−0.1188	0.0229	0.0158	−0.2750	0.0231	0.0234	−0.1886	0.0229	0.0197
0.10	−0.2576	0.0263	0.0204	−0.2281	0.0249	0.0112	−0.2497	0.0250	0.0231	−0.2568	0.0247	0.0213
0.30	−0.0823	0.0320	0.0116	−0.1347	0.0295	0.0080	−0.2781	0.0267	0.0168	−0.1624	0.0262	0.0111
0.50	−0.1323	0.0424	0.0312	0.0738	0.0374	0.0077	−0.2357	0.0346	0.0242	−0.1779	0.0322	0.0157
0.70	0.3377	0.0795	0.0135	−0.1541	0.0636	0.0110	0.5194	0.0693	0.0902	0.4282	0.0557	0.0131
0.90	2.3521	1.3608	0.4074	0.3839	0.4749	0.1328	−0.9918	0.3383	0.0576	0.6446	0.2669	0.1079

$\cos(\theta^*_{\pi^0})$	W=(1537.0±9.0) MeV			W=(1555.0±9.0) MeV			W=(1573.0±9.0) MeV			W=(1591.0±9.0) MeV		
	E	Δ_{stat}	Δ_{sys}	E	Δ_{stat}	Δ_{sys}	E	Δ_{stat}	Δ_{sys}	E	Δ_{stat}	Δ_{sys}
−0.90	0.9477	0.0617	0.0965	0.8092	0.0625	0.0635	0.9479	0.0735	0.1097	0.4246	0.0656	0.0410
−0.70	0.5649	0.0364	0.0281	0.4391	0.0379	0.0197	0.2170	0.0401	0.0218	0.2414	0.0445	0.0246
−0.50	0.2212	0.0241	0.0122	0.2417	0.0268	0.0090	0.2535	0.0286	0.0096	0.1496	0.0313	0.0112
−0.30	0.1671	0.0243	0.0048	−0.0019	0.0245	0.0054	−0.1032	0.0282	0.0123	0.0184	0.0304	0.0143
−0.10	−0.1489	0.0228	0.0155	−0.1424	0.0245	0.0095	−0.1623	0.0258	0.0113	−0.0835	0.0294	0.0174
0.10	−0.1676	0.0250	0.0153	−0.1202	0.0260	0.0148	−0.2120	0.0304	0.0210	−0.1607	0.0326	0.0233
0.30	−0.1173	0.0261	0.0053	−0.0619	0.0285	0.0065	−0.0461	0.0351	0.0179	0.1581	0.0393	0.0139
0.50	0.0477	0.0344	0.0080	0.0020	0.0358	0.0065	0.2786	0.0422	0.0193	0.3092	0.0491	0.0407
0.70	0.5152	0.0615	0.0496	0.6707	0.0746	0.0715	0.5832	0.0650	0.0427	0.5639	0.0713	0.0743
0.90	3.4063	1.6731	1.2461	1.1759	0.4018	0.1003	0.6065	0.2335	0.0707	0.4736	0.4231	0.2079

$\cos(\theta^*_{\pi^0})$	W=(1609.0±9.0) MeV			W=(1627.0±9.0) MeV			W=(1645.0±9.0) MeV			W=(1663.0±9.0) MeV		
	E	Δ_{stat}	Δ_{sys}	E	Δ_{stat}	Δ_{sys}	E	Δ_{stat}	Δ_{sys}	E	Δ_{stat}	Δ_{sys}
−0.90	0.4903	0.0708	0.1081	0.5336	0.0849	0.0634	0.1259	0.0639	0.0360	−0.0142	0.0660	0.0097
−0.70	−0.2267	0.0484	0.0149	0.1301	0.0484	0.0125	−0.4780	0.0573	0.0342	−0.2771	0.0467	0.0158
−0.50	0.1334	0.0311	0.0032	−0.0134	0.0301	0.0096	−0.2380	0.0336	0.0237	−0.3109	0.0328	0.0108
−0.30	−0.1225	0.0323	0.0229	−0.1922	0.0290	0.0070	−0.2223	0.0335	0.0253	−0.1253	0.0314	0.0043
−0.10	−0.0402	0.0321	0.0094	−0.3229	0.0328	0.0271	−0.1015	0.0329	0.0047	−0.1258	0.0363	0.0100
0.10	−0.0426	0.0360	0.0108	−0.1007	0.0404	0.0195	0.0121	0.0406	0.0145	0.0388	0.0418	0.0163
0.30	0.3837	0.0465	0.0249	0.3316	0.0424	0.0065	0.0190	0.0465	0.0083	0.2132	0.0439	0.0124
0.50	0.3483	0.0496	0.0333	0.3619	0.0392	0.0198	0.2684	0.0382	0.0130	0.3870	0.0374	0.0325
0.70	0.4619	0.0579	0.0361	0.4480	0.0522	0.0362	0.2003	0.0427	0.0124	0.2446	0.0386	0.0181
0.90	−0.4289	0.3656	0.2464	1.8499	0.8821	0.7930	0.9072	0.3550	0.4021	0.3705	0.1246	0.0440

$\cos(\theta^*_{\pi^0})$	W=(1681.0±9.0) MeV			W=(1699.0±9.0) MeV			W=(1717.0±9.0) MeV			W=(1735.0±9.0) MeV		
	E	Δ_{stat}	Δ_{sys}	E	Δ_{stat}	Δ_{sys}	E	Δ_{stat}	Δ_{sys}	E	Δ_{stat}	Δ_{sys}
−0.90	0.1521	0.0604	0.0314	−0.1776	0.0632	0.0118	−0.1585	0.0602	0.0132	0.1501	0.0589	0.0144
−0.70	−0.4378	0.0488	0.0300	−0.4676	0.0517	0.0329	−0.6861	0.0607	0.0242	−0.3608	0.0565	0.0017
−0.50	−0.3883	0.0330	0.0122	−0.6400	0.0445	0.0098	−0.6099	0.0469	0.0182	−0.4848	0.0518	0.0049
−0.30	−0.3928	0.0372	0.0052	−0.5859	0.0463	0.0268	−0.3256	0.0488	0.0016	−0.5693	0.0603	0.0340
−0.10	−0.4571	0.0442	0.0300	−0.3987	0.0484	0.0173	−0.1871	0.0518	0.0120	−0.6314	0.0662	0.0197
0.10	−0.1414	0.0447	0.0085	0.0193	0.0550	0.0014	−0.1482	0.0554	0.0128	−0.3581	0.0617	0.0424
0.30	0.2054	0.0431	0.0107	0.2417	0.0447	0.0111	0.1246	0.0487	0.0047	0.5165	0.0566	0.0246
0.50	0.0810	0.0335	0.0049	0.1469	0.0345	0.0018	0.2693	0.0405	0.0041	0.1318	0.0414	0.0127
0.70	0.0877	0.0412	0.0082	0.1829	0.0413	0.0187	0.1478	0.0433	0.0167	0.1090	0.0552	0.0055
0.90	0.0120	0.1213	0.0041	−0.0942	0.1057	0.0093	−0.3118	0.1418	0.0574	0.2728	0.1648	0.0131

$\cos(\theta^*_{\pi^0})$	W=(1753.0±9.0) MeV			W=(1771.0±9.0) MeV			W=(1789.0±9.0) MeV			W=(1807.0±9.0) MeV		
	E	Δ_{stat}	Δ_{sys}	E	Δ_{stat}	Δ_{sys}	E	Δ_{stat}	Δ_{sys}	E	Δ_{stat}	Δ_{sys}
−0.90	0.1811	0.0581	0.0050	0.0817	0.0492	0.0092	0.3536	0.0549	0.0092	0.3469	0.0554	0.0041
−0.70	−0.5200	0.0628	0.0279	−0.2744	0.0545	0.0144	−0.3426	0.0678	0.0577	−0.2414	0.0497	0.0155
−0.50	−0.4901	0.0552	0.0116	−0.5183	0.0639	0.0441	−0.7318	0.0660	0.0189	−0.5814	0.0673	0.0123
−0.30	−0.5232	0.0631	0.0154	−0.2644	0.0663	0.0336	−0.5094	0.0782	0.0545	−0.5590	0.0815	0.0676
−0.10	−0.2473	0.0604	0.0039	−0.0032	0.0701	0.0125	−0.0998	0.0703	0.0131	0.0130	0.0619	0.0024
0.10	0.1204	0.0695	0.0083	−0.0201	0.0907	0.0196	0.2063	0.0815	0.0401	−0.0822	0.0745	0.0146
0.30	0.3659	0.0626	0.0363	0.4745	0.0691	0.0316	0.5647	0.0802	0.0324	0.3948	0.0792	0.0216
0.50	0.2197	0.0496	0.0046	0.3880	0.0596	0.0144	0.2046	0.0728	0.0255	0.3028	0.0697	0.0012
0.70	−0.2518	0.0742	0.0590	0.1271	0.0700	0.0131	−0.2444	0.0650	0.0111	−0.4091	0.0709	0.0119
0.90	0.1683	0.1804	0.0626	−0.6935	0.1991	0.0737	0.6110	0.2014	0.0602	−0.1941	0.1277	0.0264

$\cos(\theta^*_{\pi^0})$	W=(1825.0±9.0) MeV			W=(1843.0±9.0) MeV			W=(1861.0±9.0) MeV			W=(1879.0±9.0) MeV		
	E	Δ_{stat}	Δ_{sys}	E	Δ_{stat}	Δ_{sys}	E	Δ_{stat}	Δ_{sys}	E	Δ_{stat}	Δ_{sys}
−0.90	0.0708	0.0468	0.0082	−0.0441	0.0524	0.0093	0.0814	0.0513	0.0084	−0.0792	0.0599	0.0079
−0.70	−0.5870	0.0637	0.0833	−0.3224	0.0572	0.0143	−0.3088	0.0627	0.0264	−0.7212	0.0814	0.0147
−0.50	−0.4750	0.0669	0.0245	−0.2036	0.0572	0.0223	−0.3509	0.0678	0.0256	−0.4937	0.0828	0.0375
−0.30	−0.4014	0.0815	0.0270	−0.5331	0.1263	0.1043	−0.3248	0.0849	0.0455	−0.3169	0.0964	0.0612
−0.10	−0.0250	0.0888	0.0059	−0.6213	0.0933	0.0233	0.2275	0.1139	0.0627	−0.2688	0.0918	0.0330
0.10	−0.1263	0.0789	0.0061	0.2047	0.0829	0.0368	−0.0175	0.1077	0.0026	0.3259	0.1290	0.0366
0.30	0.3080	0.0896	0.0062	−0.1171	0.0877	0.0232	0.1198	0.1030	0.0297	−0.4317	0.1567	0.1387
0.50	0.0706	0.0796	0.0049	0.1126	0.0874	0.0207	−0.1361	0.1014	0.0352	0.0120	0.1162	0.0091
0.70	−0.0621	0.0810	0.0099	−0.1914	0.0769	0.0192	0.2799	0.0844	0.0301	−0.1028	0.0851	0.0206
0.90	−1.6373	0.6102	0.5435	−0.3682	0.2183	0.0888	−0.4470	0.1797	0.0412	0.4300	0.1755	0.0486

$\cos(\theta^*_{\pi^0})$				W=(1897.0±9.0) MeV						W=(1915.0±9.0) MeV		
				E	Δ_{stat}	Δ_{sys}				E	Δ_{stat}	Δ_{sys}
−0.90				0.2554	0.0782	0.0168				0.1392	0.1125	0.0372
−0.70				−0.0700	0.0874	0.0069				0.0605	0.1196	0.0224
−0.50				−0.4054	0.1002	0.0223				−0.8401	0.1651	0.1402
−0.30				0.1546	0.1139	0.0420				0.3614	0.1654	0.1013
−0.10				−0.2321	0.1261	0.0121				−1.1342	0.2934	0.0900
0.10				−0.1409	0.1351	0.0621				−0.5506	0.1961	0.1973
0.30				−1.0517	0.3194	0.4056				−0.1066	0.2556	0.0462
0.50				0.7164	0.2475	0.3752				−0.8871	0.4543	0.4466
0.70				−0.2068	0.1161	0.0667				−0.7511	0.2097	0.2202
0.90				0.1580	0.1863	0.0593				0.1623	0.2410	0.0234

$\cos(\theta^*_{\pi^0})$	$W=(1321.0\pm9.0)$ MeV			$W=(1339.0\pm9.0)$ MeV			$W=(1357.0\pm9.0)$ MeV			$W=(1375.0\pm9.0)$ MeV		
	$d\sigma_{1/2}/d\Omega$ [μb/sr]	Δ_{stat} [μb/sr]	Δ_{sys} [μb/sr]	$d\sigma_{1/2}/d\Omega$ [μb/sr]	Δ_{stat} [μb/sr]	Δ_{sys} [μb/sr]	$d\sigma_{1/2}/d\Omega$ [μb/sr]	Δ_{stat} [μb/sr]	Δ_{sys} [μb/sr]	$d\sigma_{1/2}/d\Omega$ [μb/sr]	Δ_{stat} [μb/sr]	Δ_{sys} [μb/sr]
−0.90	4.4519	0.4545	2.8747	2.6088	0.2334	1.4758	2.0285	0.1788	1.0299	1.5002	0.1332	0.6159
−0.70	6.8747	0.7301	3.2171	4.9719	0.3341	1.2143	5.0692	0.2385	0.6044	3.3264	0.1640	0.5152
−0.50	11.6284	0.5973	0.3808	6.9325	0.2932	0.2184	4.5175	0.2110	0.1842	3.5616	0.1468	0.0976
−0.30	15.5542	0.6857	1.4026	8.7831	0.3371	0.4725	4.2633	0.2428	0.4169	2.7304	0.1712	0.1225
−0.10	16.0330	0.7591	1.8922	7.5030	0.3781	0.8122	4.3826	0.2632	0.4734	4.5172	0.1860	0.1163
0.10	14.9536	0.8777	2.6795	7.9493	0.4307	1.2138	5.7889	0.3007	0.7806	4.3775	0.2095	0.3777
0.30	17.8983	1.0087	4.3523	10.9609	0.4788	1.0640	6.4679	0.3298	0.7606	5.1325	0.2253	0.3943
0.50	11.7364	1.1504	4.0198	8.3876	0.5380	1.4541	5.9544	0.3765	1.0829	4.0220	0.2480	0.3624
0.70	19.1199	1.6496	3.6277	2.7080	0.7974	1.4957	5.5923	0.5102	0.7008	3.2147	0.3266	0.3143
0.90	25.7513	9.8024	7.3553	−8.7271	3.8430	2.6904	5.2160	2.1317	1.0084	0.8298	1.4109	0.1952

$\cos(\theta^*_{\pi^0})$	$W=(1393.0\pm9.0)$ MeV			$W=(1411.0\pm9.0)$ MeV			$W=(1429.0\pm9.0)$ MeV			$W=(1447.0\pm9.0)$ MeV		
	$d\sigma_{1/2}/d\Omega$ [μb/sr]	Δ_{stat} [μb/sr]	Δ_{sys} [μb/sr]	$d\sigma_{1/2}/d\Omega$ [μb/sr]	Δ_{stat} [μb/sr]	Δ_{sys} [μb/sr]	$d\sigma_{1/2}/d\Omega$ [μb/sr]	Δ_{stat} [μb/sr]	Δ_{sys} [μb/sr]	$d\sigma_{1/2}/d\Omega$ [μb/sr]	Δ_{stat} [μb/sr]	Δ_{sys} [μb/sr]
−0.90	1.4438	0.1116	0.4903	2.1402	0.1072	0.5778	1.6799	0.0975	0.2864	1.8734	0.0877	0.2600
−0.70	2.7753	0.1328	0.2643	2.3491	0.1224	0.1458	2.6521	0.1073	0.2065	2.1646	0.0939	0.0203
−0.50	2.4324	0.1192	0.0143	2.4426	0.1065	0.0480	2.1359	0.0921	0.0283	2.4914	0.0781	0.0432
−0.30	3.1132	0.1379	0.0662	2.7021	0.1251	0.1904	2.2696	0.1063	0.1539	2.4113	0.0886	0.0378
−0.10	3.5992	0.1499	0.1843	2.6380	0.1347	0.2388	3.2287	0.1123	0.1751	2.1662	0.0951	0.1770
0.10	3.8053	0.1664	0.3456	3.3073	0.1473	0.3412	2.3477	0.1227	0.2055	2.3780	0.1013	0.1294
0.30	2.8758	0.1743	0.2791	3.0903	0.1528	0.3454	2.7164	0.1252	0.1435	1.9126	0.1053	0.2030
0.50	3.2914	0.1895	0.2855	2.3295	0.1726	0.4124	2.0116	0.1339	0.1871	1.7696	0.1087	0.1520
0.70	1.8208	0.2532	0.3663	1.8679	0.2231	0.3414	2.0832	0.1655	0.0467	1.4713	0.1341	0.1395
0.90	0.7601	0.9735	0.1565	−1.1070	0.7977	0.1033	0.0817	0.6257	0.0588	1.3601	1.0812	1.1308

$\cos(\theta^*_{\pi^0})$	$W=(1465.0\pm9.0)$ MeV			$W=(1483.0\pm9.0)$ MeV			$W=(1501.0\pm9.0)$ MeV			$W=(1519.0\pm9.0)$ MeV		
	$d\sigma_{1/2}/d\Omega$ [μb/sr]	Δ_{stat} [μb/sr]	Δ_{sys} [μb/sr]	$d\sigma_{1/2}/d\Omega$ [μb/sr]	Δ_{stat} [μb/sr]	Δ_{sys} [μb/sr]	$d\sigma_{1/2}/d\Omega$ [μb/sr]	Δ_{stat} [μb/sr]	Δ_{sys} [μb/sr]	$d\sigma_{1/2}/d\Omega$ [μb/sr]	Δ_{stat} [μb/sr]	Δ_{sys} [μb/sr]
−0.90	1.7831	0.0786	0.1395	2.0908	0.0812	0.1664	3.2230	0.0914	0.1422	3.4711	0.0939	0.3280
−0.70	2.1306	0.0810	0.0211	2.6154	0.0790	0.0743	3.1289	0.0831	0.0986	3.3679	0.0834	0.0613
−0.50	2.2793	0.0660	0.0272	2.6292	0.0656	0.0357	2.8262	0.0687	0.0854	2.7003	0.0673	0.0720
−0.30	1.9926	0.0763	0.0907	2.3705	0.0747	0.0684	2.2802	0.0786	0.1335	2.7762	0.0759	0.1110
−0.10	2.2913	0.0812	0.1494	2.5431	0.0794	0.1350	2.2772	0.0845	0.2156	2.4145	0.0811	0.2063
0.10	2.0980	0.0866	0.0854	2.2433	0.0853	0.1100	2.3404	0.0915	0.2551	2.2757	0.0887	0.2011
0.30	2.1596	0.0906	0.2178	2.1702	0.0887	0.1765	2.1671	0.0936	0.1940	2.4136	0.0904	0.1775
0.50	1.6011	0.0932	0.2105	2.1890	0.0919	0.1909	1.8589	0.0989	0.2104	2.0196	0.0941	0.1486
0.70	1.6117	0.1100	0.0564	1.2317	0.1111	0.1110	2.6509	0.1267	0.4198	2.6654	0.1158	0.1054
0.90	2.6336	0.4600	0.6817	0.9715	0.3608	0.2271	0.0323	0.3558	0.0741	2.1799	0.3541	0.2734

$\cos(\theta^*_{\pi^0})$	$W=(1537.0\pm9.0)$ MeV			$W=(1555.0\pm9.0)$ MeV			$W=(1573.0\pm9.0)$ MeV			$W=(1591.0\pm9.0)$ MeV		
	$d\sigma_{1/2}/d\Omega$ [μb/sr]	Δ_{stat} [μb/sr]	Δ_{sys} [μb/sr]	$d\sigma_{1/2}/d\Omega$ [μb/sr]	Δ_{stat} [μb/sr]	Δ_{sys} [μb/sr]	$d\sigma_{1/2}/d\Omega$ [μb/sr]	Δ_{stat} [μb/sr]	Δ_{sys} [μb/sr]	$d\sigma_{1/2}/d\Omega$ [μb/sr]	Δ_{stat} [μb/sr]	Δ_{sys} [μb/sr]
−0.90	3.1145	0.0862	0.2949	2.5544	0.0833	0.1734	2.3314	0.0767	0.2236	1.3893	0.0717	0.0914
−0.70	3.0469	0.0751	0.1193	2.4442	0.0718	0.0667	1.6777	0.0656	0.0826	1.4679	0.0622	0.0596
−0.50	2.5636	0.0600	0.0474	2.2317	0.0570	0.0816	1.9225	0.0516	0.0364	1.5049	0.0491	0.1170
−0.30	2.7398	0.0682	0.0988	2.1322	0.0636	0.0612	1.5502	0.0586	0.1194	1.5497	0.0557	0.1571
−0.10	2.2315	0.0716	0.1154	1.9581	0.0670	0.1018	1.6340	0.0601	0.0619	1.4875	0.0573	0.1461
0.10	2.1835	0.0785	0.1239	2.0417	0.0723	0.0985	1.4378	0.0654	0.1294	1.2708	0.0585	0.0782
0.30	2.2051	0.0787	0.0870	1.9772	0.0727	0.1004	1.4707	0.0651	0.1395	1.4591	0.0590	0.1254
0.50	2.1384	0.0848	0.2089	1.7734	0.0767	0.1452	1.7620	0.0676	0.1479	1.4906	0.0637	0.2301
0.70	2.4660	0.1069	0.2720	2.2969	0.1017	0.2887	2.0665	0.0882	0.1789	1.7722	0.0832	0.2749
0.90	4.4064	0.5220	1.7619	2.0498	0.2886	0.2088	1.7407	0.2596	0.2334	1.1872	0.3121	0.6804

$\cos(\theta^*_{\pi^0})$	$W=(1609.0\pm9.0)$ MeV			$W=(1627.0\pm9.0)$ MeV			$W=(1645.0\pm9.0)$ MeV			$W=(1663.0\pm9.0)$ MeV		
	$d\sigma_{1/2}/d\Omega$ [μb/sr]	Δ_{stat} [μb/sr]	Δ_{sys} [μb/sr]	$d\sigma_{1/2}/d\Omega$ [μb/sr]	Δ_{stat} [μb/sr]	Δ_{sys} [μb/sr]	$d\sigma_{1/2}/d\Omega$ [μb/sr]	Δ_{stat} [μb/sr]	Δ_{sys} [μb/sr]	$d\sigma_{1/2}/d\Omega$ [μb/sr]	Δ_{stat} [μb/sr]	Δ_{sys} [μb/sr]
−0.90	1.2565	0.0624	0.2473	1.0607	0.0627	0.1231	0.9691	0.0648	0.1642	0.8229	0.0657	0.1180
−0.70	0.7426	0.0544	0.0638	1.0207	0.0527	0.0514	0.4651	0.0560	0.0513	0.7264	0.0545	0.0564
−0.50	1.2847	0.0425	0.0387	1.0913	0.0404	0.0490	0.8199	0.0427	0.0958	0.7511	0.0416	0.0383
−0.30	1.0958	0.0482	0.1210	1.0229	0.0437	0.0270	0.9146	0.0464	0.0987	1.0393	0.0451	0.0425
−0.10	1.2294	0.0496	0.1122	0.7993	0.0444	0.0685	1.0083	0.0445	0.0421	0.8576	0.0429	0.0501
0.10	1.0966	0.0497	0.0558	0.8372	0.0452	0.0596	0.9001	0.0437	0.0511	0.8375	0.0407	0.0465
0.30	1.2863	0.0486	0.1048	1.1466	0.0421	0.0136	0.7766	0.0426	0.0928	0.9517	0.0409	0.0637
0.50	1.2727	0.0530	0.1491	1.4003	0.0461	0.0492	1.3848	0.0490	0.0847	1.6474	0.0502	0.1400
0.70	1.6720	0.0725	0.1519	1.7781	0.0705	0.1753	1.7244	0.0730	0.1307	2.0786	0.0764	0.1436
0.90	0.5032	0.2878	0.4299	2.1688	0.3323	1.2678	1.7756	0.2527	0.7126	1.9177	0.1969	0.2670

$\cos(\theta^*_{\pi^0})$	$W=(1681.0\pm9.0)$ MeV			$W=(1699.0\pm9.0)$ MeV			$W=(1717.0\pm9.0)$ MeV			$W=(1735.0\pm9.0)$ MeV		
	$d\sigma_{1/2}/d\Omega$ [μb/sr]	Δ_{stat} [μb/sr]	Δ_{sys} [μb/sr]	$d\sigma_{1/2}/d\Omega$ [μb/sr]	Δ_{stat} [μb/sr]	Δ_{sys} [μb/sr]	$d\sigma_{1/2}/d\Omega$ [μb/sr]	Δ_{stat} [μb/sr]	Δ_{sys} [μb/sr]	$d\sigma_{1/2}/d\Omega$ [μb/sr]	Δ_{stat} [μb/sr]	Δ_{sys} [μb/sr]
−0.90	1.1537	0.0709	0.1990	0.8516	0.0787	0.0124	0.9196	0.0789	0.0817	1.2783	0.0791	0.0813
−0.70	0.5903	0.0558	0.0700	0.5616	0.0587	0.0728	0.3205	0.0606	0.0350	0.6191	0.0626	0.0046
−0.50	0.6826	0.0414	0.0346	0.3410	0.0430	0.0153	0.3435	0.0420	0.0260	0.3750	0.0413	0.0015
−0.30	0.6406	0.0444	0.0033	0.3776	0.0439	0.0331	0.4994	0.0418	0.0012	0.2705	0.0397	0.0316
−0.10	0.4810	0.0431	0.0538	0.4574	0.0415	0.0286	0.5214	0.0394	0.0357	0.2075	0.0376	0.0120
0.10	0.6396	0.0398	0.0450	0.6177	0.0406	0.0257	0.4920	0.0381	0.0491	0.3480	0.0370	0.0624
0.30	0.9672	0.0412	0.0472	0.9747	0.0417	0.0279	0.8041	0.0422	0.0124	1.0206	0.0413	0.0071
0.50	1.4043	0.0528	0.0843	1.4902	0.0542	0.0177	1.4683	0.0554	0.0063	1.1934	0.0527	0.0547
0.70	1.8388	0.0845	0.1776	2.0104	0.0842	0.1060	1.8003	0.0818	0.1061	1.3450	0.0814	0.0047
0.90	1.4488	0.2102	0.2686	1.3434	0.1897	0.0413	0.8333	0.1943	0.1073	1.2164	0.1850	0.0512

	$W=(1753.0\pm9.0)$ MeV			$W=(1771.0\pm9.0)$ MeV			$W=(1789.0\pm9.0)$ MeV			$W=(1807.0\pm9.0)$ MeV		
$\cos(\theta^*_{\pi^0})$	$d\sigma_{1/2}/d\Omega$ [μb/sr]	$\Delta_{\rm stat}$ [μb/sr]	$\Delta_{\rm sys}$ [μb/sr]	$d\sigma_{1/2}/d\Omega$ [μb/sr]	$\Delta_{\rm stat}$ [μb/sr]	$\Delta_{\rm sys}$ [μb/sr]	$d\sigma_{1/2}/d\Omega$ [μb/sr]	$\Delta_{\rm stat}$ [μb/sr]	$\Delta_{\rm sys}$ [μb/sr]	$d\sigma_{1/2}/d\Omega$ [μb/sr]	$\Delta_{\rm stat}$ [μb/sr]	$\Delta_{\rm sys}$ [μb/sr]
−0.90	1.3022	0.0774	0.0186	1.2834	0.0710	0.0831	1.6059	0.0755	0.0114	1.6601	0.0793	0.0243
−0.70	0.4256	0.0600	0.0407	0.5988	0.0527	0.0196	0.4963	0.0583	0.1351	0.6954	0.0538	0.0361
−0.50	0.3227	0.0381	0.0108	0.2475	0.0353	0.0464	0.1454	0.0342	0.0137	0.2084	0.0347	0.0089
−0.30	0.2501	0.0353	0.0095	0.3166	0.0332	0.0511	0.2001	0.0343	0.0406	0.1848	0.0355	0.0439
−0.10	0.3793	0.0359	0.0094	0.4195	0.0357	0.0493	0.3964	0.0372	0.0467	0.4951	0.0369	0.0168
0.10	0.5024	0.0374	0.0442	0.3573	0.0386	0.0862	0.4868	0.0388	0.0488	0.4024	0.0397	0.0062
0.30	0.7684	0.0401	0.0510	0.7338	0.0377	0.0322	0.7200	0.0390	0.0503	0.6145	0.0396	0.0204
0.50	1.0494	0.0508	0.0309	0.9871	0.0483	0.0335	0.7240	0.0519	0.0786	0.8258	0.0519	0.0010
0.70	0.7315	0.0832	0.2103	0.9900	0.0737	0.1149	0.7356	0.0749	0.0445	0.5769	0.0774	0.0261
0.90	1.0323	0.1862	0.1375	0.2847	0.1650	0.0948	1.4798	0.1902	0.1532	0.9087	0.1678	0.1305

	$W=(1825.0\pm9.0)$ MeV			$W=(1843.0\pm9.0)$ MeV			$W=(1861.0\pm9.0)$ MeV			$W=(1879.0\pm9.0)$ MeV		
$\cos(\theta^*_{\pi^0})$	$d\sigma_{1/2}/d\Omega$ [μb/sr]	$\Delta_{\rm stat}$ [μb/sr]	$\Delta_{\rm sys}$ [μb/sr]	$d\sigma_{1/2}/d\Omega$ [μb/sr]	$\Delta_{\rm stat}$ [μb/sr]	$\Delta_{\rm sys}$ [μb/sr]	$d\sigma_{1/2}/d\Omega$ [μb/sr]	$\Delta_{\rm stat}$ [μb/sr]	$\Delta_{\rm sys}$ [μb/sr]	$d\sigma_{1/2}/d\Omega$ [μb/sr]	$\Delta_{\rm stat}$ [μb/sr]	$\Delta_{\rm sys}$ [μb/sr]
−0.90	1.4814	0.0783	0.1381	1.3432	0.0898	0.0170	1.5349	0.0880	0.1512	1.2714	0.1005	0.0440
−0.70	0.3749	0.0596	0.1258	0.6902	0.0676	0.0470	0.6893	0.0728	0.0753	0.2808	0.0807	0.0210
−0.50	0.2606	0.0359	0.0251	0.4371	0.0372	0.0416	0.3124	0.0372	0.0279	0.2262	0.0393	0.0327
−0.30	0.2493	0.0385	0.0287	0.1767	0.0500	0.0790	0.3359	0.0470	0.0657	0.3473	0.0530	0.0934
−0.10	0.4156	0.0448	0.0850	0.2073	0.0525	0.0178	0.5847	0.0637	0.0847	0.4928	0.0712	0.0783
0.10	0.4080	0.0445	0.0153	0.6599	0.0534	0.1122	0.4622	0.0613	0.0575	0.6510	0.0734	0.0821
0.30	0.5625	0.0453	0.0111	0.4598	0.0532	0.0979	0.5823	0.0616	0.1445	0.3077	0.0772	0.1488
0.50	0.5961	0.0539	0.0350	0.6927	0.0655	0.1016	0.5204	0.0694	0.1358	0.6544	0.0833	0.2065
0.70	0.8557	0.0890	0.0994	0.9152	0.1032	0.0446	1.5436	0.1196	0.1611	1.3050	0.1444	0.2779
0.90	−0.5067	0.2870	0.4384	0.7777	0.2947	0.2535	0.8294	0.2949	0.0827	2.4322	0.3346	0.1445

	$W=(1897.0\pm9.0)$ MeV			$W=(1915.0\pm9.0)$ MeV		
$\cos(\theta^*_{\pi^0})$	$d\sigma_{1/2}/d\Omega$ [μb/sr]	$\Delta_{\rm stat}$ [μb/sr]	$\Delta_{\rm sys}$ [μb/sr]	$d\sigma_{1/2}/d\Omega$ [μb/sr]	$\Delta_{\rm stat}$ [μb/sr]	$\Delta_{\rm sys}$ [μb/sr]
−0.90	1.6960	0.1254	0.1100	1.9676	0.2268	0.3871
−0.70	0.8305	0.0953	0.0282	1.1467	0.1572	0.0586
−0.50	0.2354	0.0442	0.0213	0.0815	0.0602	0.0659
−0.30	0.5812	0.0650	0.1520	0.7334	0.0979	0.1623
−0.10	0.4580	0.0892	0.0373	−0.0620	0.1336	0.0487
0.10	0.5461	0.0883	0.2281	0.3784	0.1298	0.2352
0.30	0.0438	0.1024	0.1742	0.4804	0.1389	0.2078
0.50	1.0580	0.1072	0.4504	0.1670	0.1548	0.2561
0.70	1.1568	0.1799	0.4169	0.4279	0.2364	0.3639
0.90	2.1837	0.3865	0.6538	2.1983	0.5427	0.3249

	$W=(1321.0\pm9.0)$ MeV			$W=(1339.0\pm9.0)$ MeV			$W=(1357.0\pm9.0)$ MeV			$W=(1375.0\pm9.0)$ MeV		
$\cos(\theta^*_{\pi^0})$	$d\sigma_{3/2}/d\Omega$ [μb/sr]	$\Delta_{\rm stat}$ [μb/sr]	$\Delta_{\rm sys}$ [μb/sr]	$d\sigma_{3/2}/d\Omega$ [μb/sr]	$\Delta_{\rm stat}$ [μb/sr]	$\Delta_{\rm sys}$ [μb/sr]	$d\sigma_{3/2}/d\Omega$ [μb/sr]	$\Delta_{\rm stat}$ [μb/sr]	$\Delta_{\rm sys}$ [μb/sr]	$d\sigma_{3/2}/d\Omega$ [μb/sr]	$\Delta_{\rm stat}$ [μb/sr]	$\Delta_{\rm sys}$ [μb/sr]
−0.90	2.7779	0.4542	2.4943	1.8001	0.2332	1.3021	1.5304	0.1786	0.9300	1.3868	0.1330	0.6175
−0.70	26.7007	0.7316	4.9329	10.6822	0.3346	1.6199	5.7017	0.2385	0.6305	4.4267	0.1641	0.5859
−0.50	34.8384	0.5986	0.0933	15.4671	0.2938	0.1867	10.5846	0.2114	0.2114	7.0750	0.1471	0.1320
−0.30	42.0190	0.6871	1.5857	18.3693	0.3377	0.3997	14.1692	0.2435	0.3938	10.2195	0.1718	0.0590
−0.10	47.9357	0.7608	2.8385	23.1534	0.3790	1.1543	15.7358	0.2639	0.4577	9.9593	0.1865	0.0583
0.10	50.5369	0.8796	3.9630	23.0631	0.4317	1.5790	14.7790	0.3013	1.0369	9.7326	0.2099	0.3560
0.30	41.6615	1.0103	5.9035	18.3786	0.4795	1.3507	12.5027	0.3303	1.0059	8.1118	0.2256	0.3590
0.50	32.9971	1.1523	5.4027	13.8944	0.5386	1.6671	8.3476	0.3768	1.2451	6.4437	0.2483	0.3267
0.70	7.9927	1.6480	2.7127	9.9847	0.7983	2.1435	3.1745	0.5097	0.6033	2.7441	0.3266	0.2533
0.90	−6.8207	9.7945	4.8610	18.1826	3.8534	4.2732	0.7666	2.1260	0.4843	3.2439	1.4120	0.1384

	$W=(1393.0\pm9.0)$ MeV			$W=(1411.0\pm9.0)$ MeV			$W=(1429.0\pm9.0)$ MeV			$W=(1447.0\pm9.0)$ MeV		
$\cos(\theta^*_{\pi^0})$	$d\sigma_{3/2}/d\Omega$ [μb/sr]	$\Delta_{\rm stat}$ [μb/sr]	$\Delta_{\rm sys}$ [μb/sr]	$d\sigma_{3/2}/d\Omega$ [μb/sr]	$\Delta_{\rm stat}$ [μb/sr]	$\Delta_{\rm sys}$ [μb/sr]	$d\sigma_{3/2}/d\Omega$ [μb/sr]	$\Delta_{\rm stat}$ [μb/sr]	$\Delta_{\rm sys}$ [μb/sr]	$d\sigma_{3/2}/d\Omega$ [μb/sr]	$\Delta_{\rm stat}$ [μb/sr]	$\Delta_{\rm sys}$ [μb/sr]
−0.90	1.1288	0.1114	0.4608	0.3272	0.1066	0.3542	0.6161	0.0971	0.2012	0.5365	0.0871	0.1882
−0.70	3.3361	0.1329	0.2873	2.6653	0.1224	0.1781	1.8723	0.1072	0.1770	1.7608	0.0938	0.0151
−0.50	5.6739	0.1195	0.0336	4.3349	0.1067	0.0584	3.6015	0.0923	0.0159	2.6157	0.0782	0.0155
−0.30	6.8038	0.1382	0.0497	5.2804	0.1254	0.1644	4.4755	0.1066	0.1247	3.6696	0.0887	0.0236
−0.10	7.1309	0.1503	0.2274	5.9989	0.1350	0.3009	4.0628	0.1125	0.1985	4.2665	0.0954	0.1511
0.10	6.8040	0.1666	0.3431	5.0773	0.1476	0.3502	4.6175	0.1230	0.2705	3.8979	0.1016	0.1252
0.30	6.7710	0.1748	0.2762	4.2722	0.1529	0.2994	3.5263	0.1253	0.1738	3.4680	0.1055	0.2092
0.50	4.2033	0.1896	0.2968	3.0706	0.1727	0.4761	2.4679	0.1340	0.1462	2.2116	0.1089	0.1140
0.70	2.2407	0.2533	0.3299	1.3515	0.2229	0.2710	0.9274	0.1651	0.0275	1.0328	0.1339	0.1129
0.90	1.1088	0.9729	0.0468	3.8688	0.8008	0.1274	1.7249	0.6265	0.1305	−0.4317	1.0807	0.7864

	$W=(1465.0\pm9.0)$ MeV			$W=(1483.0\pm9.0)$ MeV			$W=(1501.0\pm9.0)$ MeV			$W=(1519.0\pm9.0)$ MeV		
$\cos(\theta^*_{\pi^0})$	$d\sigma_{3/2}/d\Omega$ [μb/sr]	$\Delta_{\rm stat}$ [μb/sr]	$\Delta_{\rm sys}$ [μb/sr]	$d\sigma_{3/2}/d\Omega$ [μb/sr]	$\Delta_{\rm stat}$ [μb/sr]	$\Delta_{\rm sys}$ [μb/sr]	$d\sigma_{3/2}/d\Omega$ [μb/sr]	$\Delta_{\rm stat}$ [μb/sr]	$\Delta_{\rm sys}$ [μb/sr]	$d\sigma_{3/2}/d\Omega$ [μb/sr]	$\Delta_{\rm stat}$ [μb/sr]	$\Delta_{\rm sys}$ [μb/sr]
−0.90	0.6328	0.0781	0.1074	0.7083	0.0807	0.1260	0.2619	0.0904	0.0915	0.0833	0.0927	0.1731
−0.70	1.4731	0.0808	0.0008	1.3343	0.0788	0.0800	1.4045	0.0828	0.0891	0.8278	0.0829	0.0260
−0.50	2.3704	0.0661	0.0277	1.9466	0.0655	0.0220	2.0675	0.0687	0.0527	1.9628	0.0672	0.0280
−0.30	3.4271	0.0765	0.0395	3.0141	0.0748	0.0229	3.5994	0.0788	0.1032	2.7006	0.0759	0.0796
−0.10	3.4585	0.0814	0.1416	3.2162	0.0795	0.0874	4.0063	0.0847	0.2238	3.5318	0.0813	0.1921
0.10	3.5309	0.0868	0.0260	3.5689	0.0855	0.1091	3.9043	0.0918	0.2863	3.8487	0.0890	0.2060
0.30	2.5450	0.0906	0.2130	2.8531	0.0888	0.2091	3.8595	0.0939	0.2711	3.3534	0.0906	0.1943
0.50	2.0746	0.0933	0.1774	1.8873	0.0918	0.1836	3.0095	0.0991	0.2292	2.8908	0.0943	0.1396
0.70	0.7957	0.1097	0.0453	1.6859	0.1111	0.1323	0.8350	0.1262	0.2993	1.0590	0.1153	0.0572
0.90	−1.0747	0.4580	0.3854	0.3949	0.3605	0.0787	2.4708	0.3582	0.1483	0.4721	0.3525	0.2078

$\cos(\theta^*_{\pi^0})$	$W=(1537.0\pm9.0)$ MeV			$W=(1555.0\pm9.0)$ MeV			$W=(1573.0\pm9.0)$ MeV			$W=(1591.0\pm9.0)$ MeV		
	$d\sigma_{3/2}/d\Omega$ [μb/sr]	$\Delta_{\rm stat}$ [μb/sr]	$\Delta_{\rm sys}$ [μb/sr]	$d\sigma_{3/2}/d\Omega$ [μb/sr]	$\Delta_{\rm stat}$ [μb/sr]	$\Delta_{\rm sys}$ [μb/sr]	$d\sigma_{3/2}/d\Omega$ [μb/sr]	$\Delta_{\rm stat}$ [μb/sr]	$\Delta_{\rm sys}$ [μb/sr]	$d\sigma_{3/2}/d\Omega$ [μb/sr]	$\Delta_{\rm stat}$ [μb/sr]	$\Delta_{\rm sys}$ [μb/sr]
−0.90	0.1156	0.0850	0.1600	0.2863	0.0823	0.1079	0.0862	0.0756	0.1365	0.5672	0.0710	0.0806
−0.70	0.8557	0.0746	0.0889	0.9551	0.0714	0.0577	1.0809	0.0654	0.0859	0.8966	0.0620	0.0666
−0.50	1.6273	0.0598	0.0196	1.3555	0.0568	0.0460	1.1401	0.0515	0.0131	1.1051	0.0490	0.0837
−0.30	1.9497	0.0681	0.0670	2.1360	0.0636	0.0392	1.9045	0.0587	0.1094	1.4838	0.0557	0.1189
−0.10	3.0031	0.0717	0.0858	2.6078	0.0672	0.0966	2.2623	0.0603	0.0434	1.7522	0.0574	0.1270
0.10	3.0569	0.0787	0.1103	2.5904	0.0725	0.0654	2.2095	0.0656	0.1239	1.7460	0.0587	0.0406
0.30	2.7915	0.0788	0.0879	2.2356	0.0728	0.0893	1.6035	0.0651	0.1067	1.0588	0.0588	0.1105
0.50	1.9351	0.0848	0.1777	1.7615	0.0767	0.1232	0.9844	0.0674	0.0956	0.7750	0.0635	0.1528
0.70	0.7735	0.1063	0.1602	0.4324	0.1011	0.1481	0.5339	0.0875	0.0978	0.4847	0.0827	0.1621
0.90	−2.3613	0.5189	1.4039	−0.1707	0.2867	0.0841	0.4020	0.2585	0.1225	0.4534	0.3118	0.4188

$\cos(\theta^*_{\pi^0})$	$W=(1609.0\pm9.0)$ MeV			$W=(1627.0\pm9.0)$ MeV			$W=(1645.0\pm9.0)$ MeV			$W=(1663.0\pm9.0)$ MeV		
	$d\sigma_{3/2}/d\Omega$ [μb/sr]	$\Delta_{\rm stat}$ [μb/sr]	$\Delta_{\rm sys}$ [μb/sr]	$d\sigma_{3/2}/d\Omega$ [μb/sr]	$\Delta_{\rm stat}$ [μb/sr]	$\Delta_{\rm sys}$ [μb/sr]	$d\sigma_{3/2}/d\Omega$ [μb/sr]	$\Delta_{\rm stat}$ [μb/sr]	$\Delta_{\rm sys}$ [μb/sr]	$d\sigma_{3/2}/d\Omega$ [μb/sr]	$\Delta_{\rm stat}$ [μb/sr]	$\Delta_{\rm sys}$ [μb/sr]
−0.90	0.4619	0.0617	0.1770	0.3351	0.0620	0.0815	0.7605	0.0644	0.1688	0.8448	0.0655	0.1376
−0.70	1.1664	0.0546	0.0893	0.7864	0.0526	0.0525	1.3200	0.0563	0.0631	1.2744	0.0547	0.0752
−0.50	0.9803	0.0425	0.0265	1.1171	0.0405	0.0296	1.3351	0.0428	0.1088	1.4372	0.0418	0.0636
−0.30	1.3956	0.0483	0.1013	1.5039	0.0438	0.0319	1.4361	0.0466	0.0967	1.3397	0.0452	0.0536
−0.10	1.3295	0.0496	0.1004	1.5564	0.0446	0.0551	1.2362	0.0446	0.0429	1.1040	0.0430	0.0475
0.10	1.1902	0.0498	0.0366	1.0194	0.0453	0.0420	0.8735	0.0437	0.0296	0.7727	0.0407	0.0503
0.30	0.5677	0.0484	0.0657	0.5755	0.0419	0.0081	0.7445	0.0426	0.0792	0.6137	0.0408	0.0458
0.50	0.6074	0.0528	0.0927	0.6581	0.0458	0.0375	0.7934	0.0487	0.0527	0.7230	0.0499	0.1019
0.70	0.6064	0.0721	0.0909	0.6681	0.0700	0.1012	1.1406	0.0727	0.0883	1.2575	0.0760	0.1195
0.90	1.1114	0.2882	0.5589	−0.6008	0.3311	0.8477	0.1472	0.2511	0.4321	0.8710	0.1958	0.1808

$\cos(\theta^*_{\pi^0})$	$W=(1681.0\pm9.0)$ MeV			$W=(1699.0\pm9.0)$ MeV			$W=(1717.0\pm9.0)$ MeV			$W=(1735.0\pm9.0)$ MeV		
	$d\sigma_{3/2}/d\Omega$ [μb/sr]	$\Delta_{\rm stat}$ [μb/sr]	$\Delta_{\rm sys}$ [μb/sr]	$d\sigma_{3/2}/d\Omega$ [μb/sr]	$\Delta_{\rm stat}$ [μb/sr]	$\Delta_{\rm sys}$ [μb/sr]	$d\sigma_{3/2}/d\Omega$ [μb/sr]	$\Delta_{\rm stat}$ [μb/sr]	$\Delta_{\rm sys}$ [μb/sr]	$d\sigma_{3/2}/d\Omega$ [μb/sr]	$\Delta_{\rm stat}$ [μb/sr]	$\Delta_{\rm sys}$ [μb/sr]
−0.90	0.8611	0.0706	0.1818	1.2138	0.0787	0.0419	1.2608	0.0788	0.0902	0.9474	0.0787	0.0801
−0.70	1.4842	0.0563	0.1111	1.5206	0.0592	0.1182	1.6894	0.0614	0.0721	1.3165	0.0631	0.0112
−0.50	1.5406	0.0416	0.0478	1.5599	0.0434	0.0263	1.3955	0.0425	0.0489	1.0836	0.0416	0.0120
−0.30	1.4733	0.0446	0.0169	1.4422	0.0443	0.0294	0.9820	0.0420	0.0018	0.9851	0.0401	0.0329
−0.10	1.2951	0.0434	0.0655	1.0657	0.0418	0.0324	0.7557	0.0396	0.0472	0.9055	0.0380	0.0146
0.10	0.8463	0.0399	0.0510	0.5939	0.0406	0.0236	0.6590	0.0382	0.0571	0.7181	0.0372	0.0833
0.30	0.6335	0.0411	0.0265	0.5951	0.0414	0.0279	0.6246	0.0421	0.0074	0.3282	0.0409	0.0226
0.50	1.1927	0.0527	0.0785	1.1081	0.0540	0.0159	0.8459	0.0551	0.0091	0.9159	0.0526	0.0503
0.70	1.5373	0.0843	0.1584	1.3760	0.0839	0.0594	1.3388	0.0816	0.1076	1.0789	0.0812	0.0114
0.90	1.4158	0.2101	0.2694	1.6167	0.1902	0.0570	1.5587	0.1957	0.0450	0.6895	0.1847	0.0301

$\cos(\theta^*_{\pi^0})$	$W=(1753.0\pm9.0)$ MeV			$W=(1771.0\pm9.0)$ MeV			$W=(1789.0\pm9.0)$ MeV			$W=(1807.0\pm9.0)$ MeV		
	$d\sigma_{3/2}/d\Omega$ [μb/sr]	$\Delta_{\rm stat}$ [μb/sr]	$\Delta_{\rm sys}$ [μb/sr]	$d\sigma_{3/2}/d\Omega$ [μb/sr]	$\Delta_{\rm stat}$ [μb/sr]	$\Delta_{\rm sys}$ [μb/sr]	$d\sigma_{3/2}/d\Omega$ [μb/sr]	$\Delta_{\rm stat}$ [μb/sr]	$\Delta_{\rm sys}$ [μb/sr]	$d\sigma_{3/2}/d\Omega$ [μb/sr]	$\Delta_{\rm stat}$ [μb/sr]	$\Delta_{\rm sys}$ [μb/sr]
−0.90	0.9027	0.0770	0.0207	1.0909	0.0708	0.0855	0.7688	0.0748	0.0127	0.8064	0.0787	0.0165
−0.70	1.3515	0.0606	0.0495	1.0489	0.0531	0.0150	1.0262	0.0587	0.1923	1.1358	0.0542	0.0286
−0.50	0.9424	0.0384	0.0099	0.7895	0.0356	0.0724	0.9247	0.0347	0.0236	0.7783	0.0351	0.0186
−0.30	0.7942	0.0357	0.0050	0.5458	0.0334	0.0604	0.6199	0.0346	0.0541	0.6519	0.0359	0.0500
−0.10	0.6292	0.0361	0.0120	0.4247	0.0357	0.0565	0.4844	0.0373	0.0485	0.4828	0.0370	0.0166
0.10	0.3924	0.0374	0.0328	0.3682	0.0386	0.0769	0.3224	0.0386	0.0534	0.4766	0.0398	0.0113
0.30	0.3566	0.0398	0.0473	0.2617	0.0373	0.0294	0.1958	0.0387	0.0263	0.2673	0.0393	0.0157
0.50	0.6692	0.0506	0.0170	0.4340	0.0479	0.0258	0.4768	0.0517	0.0675	0.4422	0.0514	0.0017
0.70	1.2225	0.0835	0.2519	0.7616	0.0736	0.0896	1.2146	0.0752	0.0544	1.3697	0.0780	0.0366
0.90	0.7516	0.1852	0.1774	1.4419	0.1678	0.1635	0.3485	0.1889	0.0926	1.3326	0.1689	0.1541

$\cos(\theta^*_{\pi^0})$	$W=(1825.0\pm9.0)$ MeV			$W=(1843.0\pm9.0)$ MeV			$W=(1861.0\pm9.0)$ MeV			$W=(1879.0\pm9.0)$ MeV		
	$d\sigma_{3/2}/d\Omega$ [μb/sr]	$\Delta_{\rm stat}$ [μb/sr]	$\Delta_{\rm sys}$ [μb/sr]	$d\sigma_{3/2}/d\Omega$ [μb/sr]	$\Delta_{\rm stat}$ [μb/sr]	$\Delta_{\rm sys}$ [μb/sr]	$d\sigma_{3/2}/d\Omega$ [μb/sr]	$\Delta_{\rm stat}$ [μb/sr]	$\Delta_{\rm sys}$ [μb/sr]	$d\sigma_{3/2}/d\Omega$ [μb/sr]	$\Delta_{\rm stat}$ [μb/sr]	$\Delta_{\rm sys}$ [μb/sr]
−0.90	1.2889	0.0781	0.1324	1.4626	0.0900	0.0262	1.3081	0.0878	0.1412	1.4853	0.1008	0.0555
−0.70	1.4515	0.0605	0.1742	1.3564	0.0682	0.0805	1.3095	0.0735	0.0907	1.7452	0.0824	0.0357
−0.50	0.7216	0.0363	0.0404	0.6573	0.0374	0.0497	0.6467	0.0376	0.0323	0.6527	0.0399	0.0550
−0.30	0.5900	0.0388	0.0414	0.5892	0.0503	0.1242	0.6436	0.0474	0.0852	0.6444	0.0536	0.1262
−0.10	0.4368	0.0448	0.0862	0.8875	0.0531	0.0182	0.3728	0.0635	0.0886	0.8428	0.0716	0.0957
0.10	0.5242	0.0446	0.0171	0.4445	0.0533	0.0953	0.4780	0.0613	0.0612	0.3400	0.0728	0.0580
0.30	0.2983	0.0449	0.0085	0.5744	0.0532	0.1084	0.4661	0.0613	0.1261	0.6972	0.0778	0.2123
0.50	0.5182	0.0538	0.0327	0.5566	0.0653	0.0966	0.6718	0.0694	0.1483	0.6409	0.0831	0.2110
0.70	0.9681	0.0891	0.0986	1.3365	0.1040	0.0629	0.8823	0.1188	0.1283	1.5869	0.1449	0.3029
0.90	2.2122	0.2906	0.6818	1.6689	0.2967	0.2967	2.1432	0.2987	0.0380	0.9752	0.3314	0.1435

$\cos(\theta^*_{\pi^0})$	$W=(1897.0\pm9.0)$ MeV			$W=(1915.0\pm9.0)$ MeV		
	$d\sigma_{3/2}/d\Omega$ [μb/sr]	$\Delta_{\rm stat}$ [μb/sr]	$\Delta_{\rm sys}$ [μb/sr]	$d\sigma_{3/2}/d\Omega$ [μb/sr]	$\Delta_{\rm stat}$ [μb/sr]	$\Delta_{\rm sys}$ [μb/sr]
−0.90	1.0139	0.1246	0.0875	1.5098	0.2258	0.3550
−0.70	0.9544	0.0958	0.0277	1.0244	0.1568	0.0585
−0.50	0.5498	0.0448	0.0352	0.7546	0.0614	0.1226
−0.30	0.4366	0.0649	0.1302	0.3642	0.0974	0.1351
−0.10	0.7311	0.0898	0.0491	1.2252	0.1360	0.1095
0.10	0.6969	0.0886	0.2442	1.0959	0.1314	0.3338
0.30	0.9705	0.1039	0.3310	0.5754	0.1391	0.2259
0.50	0.2900	0.1058	0.3005	1.0079	0.1565	0.4170
0.70	1.6900	0.1809	0.4783	2.2801	0.2403	0.6238
0.90	1.6424	0.3852	0.6076	1.6093	0.5401	0.2866

E.3 Unpolarized Results for Double π^0 from the A2 Data

E.3.1 Total Cross Sections as a Function of E_γ

E_γ [MeV]	ΔE_γ [MeV]	σ_{qf-inc} [μb]	Δ_{stat} [μb]	Δ_{sys} [μb]	σ_p [μb]	Δ_{stat} [μb]	Δ_{sys} [μb]	σ_n [μb]	Δ_{stat} [μb]	Δ_{sys} [μb]
422.5	7.5	0.4636	0.0077	0.4079	0.0477	0.0214	0.1687	0.1781	0.0274	0.1683
437.5	7.5	0.4594	0.0086	0.4644	0.1757	0.0216	0.2007	0.1589	0.0325	0.2511
452.5	7.5	1.0176	0.0102	0.4209	0.2992	0.0195	0.1795	0.3072	0.0261	0.2695
467.5	7.5	1.4816	0.0117	0.5268	0.4565	0.0228	0.2134	0.5069	0.0287	0.2051
482.5	7.5	2.0382	0.0122	0.5761	0.7796	0.0267	0.2548	0.6325	0.0338	0.2876
497.5	7.5	2.7466	0.0134	0.6523	1.1627	0.0253	0.3831	0.8881	0.0304	0.3585
512.5	7.5	3.5929	0.0151	0.5700	1.6106	0.0277	0.3898	1.1898	0.0312	0.2787
527.5	7.5	4.5139	0.0162	0.6195	2.0982	0.0253	0.4507	1.5670	0.0308	0.3985
542.5	7.5	5.5274	0.0173	0.5572	2.7252	0.0246	0.4534	2.1362	0.0321	0.3575
557.5	7.5	6.5429	0.0192	0.5633	3.2442	0.0262	0.4071	2.4793	0.0319	0.3520
572.5	7.5	7.3971	0.0206	0.5680	3.7512	0.0283	0.4615	2.9768	0.0327	0.3495
587.5	7.5	8.3751	0.0213	0.5370	4.3462	0.0306	0.4751	3.3489	0.0356	0.3888
602.5	7.5	9.3029	0.0229	0.5667	4.7975	0.0342	0.4711	3.7768	0.0360	0.3646
617.5	7.5	10.0812	0.0240	0.5205	5.1659	0.0340	0.4294	4.2965	0.0390	0.3788
632.5	7.5	10.9010	0.0254	0.5326	5.4947	0.0308	0.4261	4.7491	0.0431	0.4225
647.5	7.5	11.6688	0.0273	0.5247	5.9813	0.0324	0.4477	5.2325	0.0409	0.4036
662.5	7.5	12.5540	0.0284	0.5125	6.2939	0.0324	0.4359	5.7474	0.0452	0.3902
677.5	7.5	13.4454	0.0293	0.5101	6.6778	0.0319	0.4489	6.2543	0.0445	0.4196
692.5	7.5	14.1487	0.0307	0.5461	7.0727	0.0334	0.4360	6.7143	0.0503	0.4152
707.5	7.5	14.7191	0.0315	0.5553	7.2985	0.0328	0.4369	7.1255	0.0479	0.4676
722.5	7.5	15.1874	0.0357	0.5826	7.3924	0.0352	0.4138	7.4663	0.0523	0.4463
737.5	7.5	15.2608	0.0347	0.5824	7.4206	0.0370	0.3953	7.6757	0.0530	0.4398
752.5	7.5	15.2685	0.0338	0.5688	7.2319	0.0322	0.4015	7.8175	0.0537	0.4933
767.5	7.5	15.1759	0.0364	0.5523	7.0317	0.0355	0.3960	7.7473	0.0565	0.4481
782.5	7.5	14.6723	0.0332	0.5510	6.7261	0.0299	0.4182	7.7741	0.0517	0.4740
797.5	7.5	14.1660	0.0342	0.5140	6.4880	0.0331	0.3386	7.4951	0.0505	0.4132
812.5	7.5	13.7106	0.0337	0.4825	6.1041	0.0299	0.3465	7.3291	0.0515	0.3832
827.5	7.5	13.1897	0.0343	0.4508	5.8269	0.0285	0.3476	7.0210	0.0506	0.3771
842.5	7.5	12.8214	0.0356	0.4323	5.6257	0.0325	0.3847	6.9263	0.0533	0.4397
857.5	7.5	12.4494	0.0438	0.4399	5.3251	0.0367	0.3192	6.5868	0.0709	0.3978
872.5	7.5	12.3673	0.0361	0.3896	5.3141	0.0325	0.3274	6.6636	0.0514	0.5276
887.5	7.5	12.8328	0.0397	0.3868	5.5944	0.0329	0.3008	7.1894	0.0555	0.3529
902.5	7.5	12.4498	0.0349	0.3601	5.4075	0.0296	0.2445	6.9262	0.0483	0.3247
917.5	7.5	12.4341	0.0351	0.4014	5.3429	0.0278	0.2964	6.8830	0.0511	0.3494
932.5	7.5	12.7795	0.0362	0.3167	5.5674	0.0294	0.2924	7.1673	0.0513	0.3723
947.5	7.5	13.0798	0.0363	0.2963	5.7509	0.0270	0.2849	7.3133	0.0477	0.3099
962.5	7.5	13.3157	0.0375	0.2570	5.9422	0.0282	0.2425	7.1968	0.0484	0.3192
977.5	7.5	13.6668	0.0371	0.2651	6.1916	0.0270	0.2263	7.5447	0.0502	0.2879
992.5	7.5	14.0354	0.0401	0.2325	6.5005	0.0310	0.2628	7.5349	0.0542	0.2732
1007.5	7.5	14.1242	0.0391	0.2559	6.6003	0.0290	0.2565	7.4456	0.0501	0.3325
1022.5	7.5	14.4574	0.0398	0.2145	6.9004	0.0286	0.2736	7.7474	0.0503	0.2501
1037.5	7.5	14.6049	0.0431	0.2295	7.1337	0.0299	0.2961	7.7322	0.0512	0.2894
1052.5	7.5	14.6750	0.0429	0.2189	7.2426	0.0305	0.2843	7.7507	0.0479	0.3109
1067.5	7.5	14.6145	0.0430	0.2271	7.4088	0.0307	0.2346	7.6398	0.0511	0.2469
1082.5	7.5	14.5158	0.0426	0.2172	7.3811	0.0300	0.2731	7.4002	0.0501	0.2777
1097.5	7.5	14.1092	0.0432	0.2224	7.3303	0.0289	0.2638	7.0396	0.0496	0.2815
1112.5	7.5	13.9037	0.0474	0.2108	7.1796	0.0321	0.2353	6.8686	0.0542	0.2690
1127.5	7.5	13.3860	0.0418	0.1322	7.0658	0.0262	0.2521	6.7863	0.0471	0.2692
1142.5	7.5	13.0373	0.0428	0.1824	7.0060	0.0259	0.2130	6.4204	0.0458	0.2911
1157.5	7.5	12.3998	0.0423	0.1398	6.6501	0.0280	0.2323	6.0804	0.0443	0.3176
1172.5	7.5	11.8983	0.0403	0.1611	6.3627	0.0253	0.2221	5.8388	0.0407	0.2366
1187.5	7.5	11.3236	0.0413	0.1553	6.0988	0.0265	0.2010	5.5600	0.0445	0.1934
1202.5	7.5	10.8805	0.0420	0.1522	5.8494	0.0248	0.1964	5.0519	0.0425	0.2150
1217.5	7.5	10.5225	0.0400	0.1444	5.6874	0.0242	0.2152	4.9738	0.0433	0.2383
1232.5	7.5	10.0424	0.0431	0.1238	5.4493	0.0256	0.1719	4.7422	0.0439	0.2025
1247.5	7.5	9.6834	0.0404	0.1247	5.3335	0.0242	0.1730	4.5512	0.0396	0.2896
1262.5	7.5	9.5220	0.0415	0.1254	5.1945	0.0253	0.1406	4.4001	0.0418	0.1853
1277.5	7.5	9.2482	0.0400	0.1184	5.0432	0.0236	0.1717	4.2895	0.0369	0.1941
1292.5	7.5	9.0744	0.0432	0.1189	4.9994	0.0263	0.1643	4.1394	0.0446	0.2190
1307.5	7.5	8.9318	0.0387	0.1014	4.8655	0.0210	0.1856	4.0615	0.0347	0.1854
1322.5	7.5	8.6892	0.0468	0.1532	4.6349	0.0295	0.1904	3.9296	0.0426	0.2160
1337.5	7.5	8.6541	0.0483	0.1123	4.6881	0.0289	0.1783	3.8198	0.0468	0.2249
1352.5	7.5	8.5068	0.0413	0.1023	4.6843	0.0258	0.1808	3.8855	0.0360	0.2208
1367.5	7.5	8.2932	0.0405	0.1416	4.5945	0.0259	0.1934	3.7894	0.0359	0.1800
1382.5	7.5	8.0081	0.0405	0.2068	4.4714	0.0251	0.3665	3.5321	0.0382	0.2779
1397.5	7.5	9.2680	0.0627	0.0476	5.0246	0.0380	0.0447	3.9315	0.0628	0.0365
1412.5	7.5	7.7638	0.0804	0.0374	4.1541	0.0497	0.0593	3.6006	0.0566	0.0732
1427.5	7.5	7.7783	0.0868	0.0578	4.0377	0.0581	0.0728	3.4620	0.0789	0.0631
1442.5	7.5	9.5649	0.1843	0.0000	5.1489	0.1052	0.0000	4.5131	0.1405	0.0000

E.3.2 Total Cross Sections as a Function of W

W [MeV]	ΔW [MeV]	σ_{qfp} [μb]	Δ_{stat} [μb]	Δ_{sys} [μb]	σ_{qfn} [μb]	Δ_{stat} [μb]	Δ_{sys} [μb]
1304.0	4.0	0.2813	0.0554	0.1714	0.1420	0.0364	0.1282
1312.0	4.0	0.4555	0.0534	0.2778	0.3018	0.0409	0.2789
1320.0	4.0	0.6057	0.0494	0.3229	0.3057	0.0427	0.2812
1328.0	4.0	0.7493	0.0475	0.2794	0.4777	0.0434	0.2465
1336.0	4.0	1.0644	0.0549	0.2169	0.7138	0.0377	0.4248
1344.0	4.0	1.3095	0.0431	0.2332	0.8302	0.0414	0.2391
1352.0	4.0	1.7044	0.0501	0.2964	1.2489	0.0421	0.3714
1360.0	4.0	2.2422	0.0387	0.3977	1.3730	0.0431	0.3258
1368.0	4.0	2.6381	0.0448	0.4416	1.7763	0.0409	0.3220
1376.0	4.0	3.0483	0.0398	0.3952	2.2476	0.0433	0.3970
1384.0	4.0	3.5068	0.0446	0.4499	2.5712	0.0423	0.4250
1392.0	4.0	4.0004	0.0443	0.5248	2.7218	0.0450	0.3283
1400.0	4.0	4.3266	0.0424	0.4917	3.3307	0.0420	0.4097
1408.0	4.0	4.8469	0.0410	0.4984	3.7640	0.0435	0.5604
1416.0	4.0	5.0684	0.0439	0.4492	4.0329	0.0515	0.3967
1424.0	4.0	5.3062	0.0395	0.4046	4.3072	0.0591	0.3959
1432.0	4.0	5.7241	0.0454	0.3552	4.7436	0.0576	0.3919
1440.0	4.0	5.9806	0.0448	0.4476	4.9329	0.0576	0.2750
1448.0	4.0	6.2155	0.0453	0.4434	5.6739	0.0514	0.3888
1456.0	4.0	6.6670	0.0416	0.4703	6.0329	0.0531	0.3781
1464.0	4.0	6.9574	0.0476	0.4295	6.6080	0.0521	0.4033
1472.0	4.0	7.4021	0.0453	0.4347	6.5138	0.0556	0.3386
1480.0	4.0	7.4106	0.0433	0.4512	7.3762	0.0591	0.4283
1488.0	4.0	7.7123	0.0448	0.4566	7.6395	0.0638	0.4659
1496.0	4.0	7.7261	0.0483	0.5196	7.8720	0.0660	0.5909
1504.0	4.0	7.6086	0.0422	0.4191	8.1514	0.0674	0.5391
1512.0	4.0	7.4352	0.0416	0.4404	8.2495	0.0682	0.5321
1520.0	4.0	6.9798	0.0429	0.4576	8.1010	0.0601	0.4866
1528.0	4.0	6.7698	0.0394	0.4099	8.1550	0.0628	0.5130
1536.0	4.0	6.4530	0.0410	0.3779	7.7222	0.0672	0.4813
1544.0	4.0	6.1733	0.0383	0.3587	7.6574	0.0604	0.4542
1552.0	4.0	5.9217	0.0398	0.3333	7.3699	0.0623	0.4134
1560.0	4.0	5.6386	0.0399	0.3526	7.2033	0.0614	0.3807
1568.0	4.0	5.5385	0.0391	0.3497	7.1023	0.0627	0.4554
1576.0	4.0	5.3239	0.0390	0.3343	7.0728	0.0652	0.4063
1584.0	4.0	5.2793	0.0373	0.3339	7.0028	0.0625	0.3818
1592.0	4.0	5.3381	0.0356	0.4198	7.0679	0.0619	0.4323
1600.0	4.0	5.2991	0.0374	0.3130	7.1586	0.0629	0.4035
1608.0	4.0	5.4304	0.0348	0.2933	7.2622	0.0595	0.4057
1616.0	4.0	5.5757	0.0347	0.2709	7.2904	0.0579	0.2820
1624.0	4.0	5.7659	0.0341	0.3174	7.4067	0.0598	0.3598
1632.0	4.0	6.0280	0.0329	0.2616	7.5163	0.0579	0.3593
1640.0	4.0	6.1253	0.0344	0.3296	7.6954	0.0568	0.3882
1648.0	4.0	6.4698	0.0350	0.2871	7.6685	0.0566	0.3076
1656.0	4.0	6.5851	0.0358	0.2497	7.7096	0.0589	0.2613
1664.0	4.0	6.9602	0.0349	0.2896	7.8713	0.0603	0.3364
1672.0	4.0	7.1577	0.0352	0.2735	7.8338	0.0599	0.2913
1680.0	4.0	7.3533	0.0368	0.2506	7.8784	0.0567	0.3242
1688.0	4.0	7.3518	0.0338	0.2650	7.9459	0.0596	0.3005
1696.0	4.0	7.5606	0.0325	0.2880	7.7651	0.0555	0.2915
1704.0	4.0	7.5558	0.0341	0.2597	7.4757	0.0545	0.2756
1712.0	4.0	7.3787	0.0321	0.2527	7.0762	0.0543	0.2300
1720.0	4.0	7.3256	0.0338	0.2447	7.0687	0.0536	0.2669
1728.0	4.0	6.9657	0.0313	0.2537	6.7884	0.0493	0.2556
1736.0	4.0	6.7005	0.0311	0.2013	6.4298	0.0499	0.2468
1744.0	4.0	6.5019	0.0301	0.1967	6.1294	0.0481	0.2655
1752.0	4.0	6.1810	0.0292	0.2065	5.8488	0.0524	0.2263
1760.0	4.0	5.9508	0.0285	0.2188	5.5497	0.0465	0.2102
1768.0	4.0	5.7099	0.0275	0.2007	4.9866	0.0458	0.2063
1776.0	4.0	5.4750	0.0273	0.1970	5.0838	0.0446	0.2143
1784.0	4.0	5.3379	0.0281	0.2049	4.8664	0.0487	0.2014
1792.0	4.0	5.1732	0.0299	0.1710	4.5230	0.0442	0.2469
1800.0	4.0	5.1162	0.0294	0.1416	4.3391	0.0434	0.1937
1808.0	4.0	4.9933	0.0277	0.1324	4.3795	0.0447	0.1893
1816.0	4.0	4.8984	0.0309	0.1673	4.0593	0.0432	0.2023
1824.0	4.0	4.8503	0.0316	0.1602	3.9289	0.0447	0.2172
1832.0	4.0	4.7472	0.0347	0.1726	4.0513	0.0486	0.2218
1840.0	4.0	4.7954	0.0347	0.1469	3.8405	0.0493	0.1742
1848.0	4.0	4.8905	0.0367	0.1853	3.8187	0.0597	0.2528
1856.0	4.0	4.5430	0.0421	0.1698	3.5869	0.0514	0.2187
1864.0	4.0	4.7088	0.0427	0.2120	3.5135	0.0625	0.2563
1872.0	4.0	4.5911	0.0481	0.2130	3.4838	0.0643	0.2242
1880.0	4.0	4.3316	0.0539	0.2415	3.3253	0.0627	0.0948
1888.0	4.0	4.5074	0.0571	0.2175	3.2658	0.0736	0.2327
1896.0	4.0	4.4030	0.0656	0.2218	3.2257	0.0927	0.3290

W [MeV]	ΔW [MeV]	σ_p [μb]	Δ_{stat} [μb]	Δ_{sys} [μb]	σ_n [μb]	Δ_{stat} [μb]	Δ_{sys} [μb]
1282.6	5.5	0.0000	0.0000	0.0000	0.2455	0.0264	0.2232
1293.5	5.5	0.3424	0.0765	0.0504	0.3795	0.0519	0.3085
1304.4	5.4	0.1807	0.0246	0.0274	−0.0014	0.0540	0.3057
1315.1	5.3	0.4047	0.0318	0.0581	0.5670	0.0510	0.3444
1325.8	5.3	0.7040	0.0328	0.0800	0.8325	0.0672	0.4340
1336.3	5.3	1.0554	0.0330	0.2198	1.0636	0.0453	0.2167
1346.8	5.3	1.5039	0.0255	0.2115	1.4926	0.0539	0.3415
1357.2	5.2	2.0791	0.0266	0.3184	1.8105	0.0467	0.3525
1367.6	5.2	2.9113	0.0266	0.3786	2.1082	0.0584	0.3429
1377.8	5.2	3.5748	0.0260	0.4486	2.7525	0.0604	0.3952
1388.0	5.1	4.1588	0.0174	0.4111	3.0233	0.0628	0.3779
1398.1	5.1	4.8706	0.0194	0.4019	3.3432	0.0542	0.3466
1408.1	5.0	5.4323	0.0192	0.3056	4.1020	0.0515	0.3520
1418.1	5.0	6.2076	0.0243	0.3641	4.5650	0.0514	0.5305
1428.0	4.9	6.5794	0.0215	0.3223	4.7986	0.0690	0.3894
1437.8	4.9	7.2945	0.0208	0.3208	5.0499	0.0784	0.3798
1447.6	4.9	7.8367	0.0252	0.3231	5.7968	0.0692	0.4087
1457.2	4.8	8.2982	0.0234	0.3079	5.8501	0.0741	0.3828
1466.9	4.8	8.9666	0.0257	0.3097	6.5816	0.0710	0.4287
1476.4	4.8	9.3851	0.0224	0.2918	7.4480	0.0592	0.4326
1485.9	4.7	9.7973	0.0264	0.2958	8.0638	0.0591	0.4594
1495.4	4.7	9.5822	0.0255	0.2973	8.1588	0.0587	0.4000
1504.8	4.7	9.6794	0.0355	0.2966	9.0044	0.0637	0.4990
1514.1	4.7	9.4512	0.0228	0.3163	9.3488	0.0685	0.5335
1523.4	4.6	8.8995	0.0398	0.2858	9.6804	0.0705	0.6614
1532.6	4.6	8.0947	0.0216	0.2597	9.9477	0.0698	0.5972
1541.7	4.6	7.5394	0.0197	0.2348	10.0367	0.0724	0.6004
1550.8	4.5	7.0091	0.0211	0.1979	9.8665	0.0666	0.5676
1559.9	4.5	6.5890	0.0262	0.1888	9.8971	0.0693	0.6112
1568.9	4.5	6.5248	0.0220	0.1854	9.3294	0.0692	0.5668
1577.8	4.5	6.2649	0.0197	0.1637	9.1537	0.0660	0.5108
1586.7	4.5	6.1175	0.0217	0.1618	8.8824	0.0657	0.5017
1595.6	4.4	5.9816	0.0383	0.1577	8.6505	0.0659	0.4727
1604.3	4.4	6.3010	0.0177	0.1448	8.4363	0.0681	0.4747
1613.1	4.4	6.3425	0.0188	0.1502	8.3596	0.0712	0.4722
1621.8	4.4	6.5600	0.0218	0.1528	8.3652	0.0666	0.4684
1630.5	4.3	6.7890	0.0182	0.1478	8.3160	0.0666	0.4718
1639.1	4.3	7.0280	0.0185	0.1137	8.3268	0.0705	0.5391
1647.6	4.3	7.3996	0.0184	0.1236	8.4696	0.0650	0.4804
1656.1	4.3	7.9895	0.0242	0.1147	8.4851	0.0654	0.3726
1664.6	4.2	8.1630	0.0183	0.1143	8.5977	0.0670	0.4305
1673.1	4.2	8.6983	0.0192	0.1373	8.7582	0.0643	0.4320
1681.4	4.2	8.8495	0.0192	0.1155	8.9647	0.0630	0.4930
1689.8	4.2	9.0749	0.0187	0.1322	8.8327	0.0625	0.3999
1698.1	4.1	9.3666	0.0235	0.1055	8.8342	0.0671	0.3342
1706.4	4.1	9.3922	0.0200	0.0961	8.9679	0.0680	0.4114
1714.6	4.1	9.3761	0.0193	0.1083	8.9015	0.0681	0.3736
1722.8	4.1	9.2192	0.0184	0.0996	9.0166	0.0644	0.4136
1730.9	4.1	8.6882	0.0190	0.0743	9.1399	0.0668	0.3504
1739.1	4.0	8.1013	0.0182	0.0555	8.8393	0.0619	0.3250
1747.1	4.0	7.5886	0.0181	0.0530	8.4177	0.0610	0.3356
1755.2	4.0	7.1763	0.0174	0.0719	8.0148	0.0607	0.3161
1763.2	4.0	6.9467	0.0176	0.0731	8.0697	0.0590	0.3330
1771.1	4.0	6.5116	0.0159	0.0576	7.7165	0.0543	0.2904
1779.1	3.9	6.4037	0.0170	0.0601	7.3193	0.0554	0.3132
1787.0	3.9	6.0447	0.0170	0.0450	6.9284	0.0535	0.3270
1794.8	3.9	5.9218	0.0205	0.0614	6.5823	0.0572	0.2655
1802.6	3.9	5.9046	0.0173	0.1231	6.2448	0.0516	0.2438
1810.4	3.9	5.6197	0.0186	0.0557	5.6589	0.0495	0.2573
1818.2	3.9	5.6019	0.0179	0.0529	5.6826	0.0497	0.2456
1825.9	3.8	5.4351	0.0165	0.0507	5.4492	0.0527	0.2452
1833.6	3.8	5.2820	0.0171	0.0355	5.0515	0.0477	0.2873
1841.3	3.8	5.2133	0.0197	0.0486	4.8476	0.0466	0.2106
1848.9	3.8	5.2019	0.0164	0.0663	4.8526	0.0484	0.2115
1856.5	3.8	5.0649	0.0183	0.0338	4.4843	0.0480	0.2420
1864.0	3.8	5.1553	0.0220	0.0420	4.3531	0.0490	0.2347
1871.6	3.7	5.2126	0.0190	0.0467	4.5118	0.0520	0.2621
1879.1	3.7	5.0755	0.0163	0.0407	4.2484	0.0533	0.2209
1886.6	3.7	4.7896	0.0186	0.0534	4.2149	0.0598	0.1861
1894.0	3.7	6.2185	0.0346	0.0727	3.9570	0.0558	0.2926
1901.4	3.7	0.0000	0.0000	0.0000	3.9567	0.0639	0.2620
1908.8	3.6	0.0000	0.0000	0.0000	3.8698	0.0667	0.2945
1916.2	3.6	0.0000	0.0000	0.0000	3.6481	0.0676	0.2804
1923.5	3.6	0.0000	0.0000	0.0000	3.6813	0.0800	0.3553
1930.8	3.6	0.0000	0.0000	0.0000	3.5984	0.1079	0.3863

E.3.3 $\gamma d \to \pi^0\pi^0 p(n)$ as a Function of W

Angular Distributions

$\cos(\theta^*_{2\pi^0})$	W=(1304.0±4.0) MeV			W=(1312.0±4.0) MeV			W=(1320.0±4.0) MeV			W=(1328.0±4.0) MeV		
	$d\sigma/d\Omega$ [μb/sr]	Δ_{stat} [μb/sr]	Δ_{sys} [μb/sr]	$d\sigma/d\Omega$ [μb/sr]	Δ_{stat} [μb/sr]	Δ_{sys} [μb/sr]	$d\sigma/d\Omega$ [μb/sr]	Δ_{stat} [μb/sr]	Δ_{sys} [μb/sr]	$d\sigma/d\Omega$ [μb/sr]	Δ_{stat} [μb/sr]	Δ_{sys} [μb/sr]
−0.90	0.0182	0.0016	0.0211	0.0271	0.0015	0.0274	0.0350	0.0018	0.0324	0.0433	0.0019	0.0343
−0.70	0.0219	0.0017	0.0226	0.0293	0.0018	0.0258	0.0471	0.0019	0.0353	0.0542	0.0017	0.0330
−0.50	0.0203	0.0025	0.0177	0.0326	0.0025	0.0244	0.0514	0.0022	0.0347	0.0642	0.0026	0.0298
−0.30	0.0212	0.0022	0.0195	0.0325	0.0023	0.0234	0.0465	0.0029	0.0354	0.0789	0.0027	0.0268
−0.10	0.0191	0.0018	0.0210	0.0375	0.0025	0.0178	0.0599	0.0030	0.0233	0.0858	0.0034	0.0250
0.10	0.0213	0.0028	0.0200	0.0428	0.0027	0.0154	0.0692	0.0029	0.0208	0.0869	0.0028	0.0220
0.30	0.0184	0.0037	0.0116	0.0341	0.0039	0.0142	0.0734	0.0037	0.0298	0.0888	0.0042	0.0197
0.50	0.0084	0.0079	0.0028	0.0225	0.0068	0.0081	0.0342	0.0075	0.0090	0.0548	0.0050	0.0184
0.70	0.0064	0.0162	0.0020	0.0431	0.0168	0.0192	0.0420	0.0143	0.0285	0.0366	0.0147	0.0103
0.90	0.0448	0.0568	0.0062	0.0528	0.0495	0.0500	0.0450	0.0443	0.0307	0.0022	0.0449	0.0040

$\cos(\theta^*_{2\pi^0})$	W=(1336.0±4.0) MeV			W=(1344.0±4.0) MeV			W=(1352.0±4.0) MeV			W=(1360.0±4.0) MeV		
	$d\sigma/d\Omega$ [μb/sr]	Δ_{stat} [μb/sr]	Δ_{sys} [μb/sr]	$d\sigma/d\Omega$ [μb/sr]	Δ_{stat} [μb/sr]	Δ_{sys} [μb/sr]	$d\sigma/d\Omega$ [μb/sr]	Δ_{stat} [μb/sr]	Δ_{sys} [μb/sr]	$d\sigma/d\Omega$ [μb/sr]	Δ_{stat} [μb/sr]	Δ_{sys} [μb/sr]
−0.90	0.0498	0.0021	0.0431	0.0691	0.0020	0.0305	0.0987	0.0028	0.0369	0.1214	0.0024	0.0356
−0.70	0.0809	0.0024	0.0195	0.1029	0.0022	0.0253	0.1328	0.0025	0.0305	0.1736	0.0026	0.0378
−0.50	0.0912	0.0027	0.0148	0.1277	0.0025	0.0208	0.1523	0.0036	0.0287	0.1936	0.0037	0.0367
−0.30	0.1115	0.0037	0.0218	0.1341	0.0029	0.0236	0.1834	0.0032	0.0346	0.2241	0.0045	0.0334
−0.10	0.1181	0.0029	0.0237	0.1579	0.0032	0.0273	0.1919	0.0033	0.0308	0.2387	0.0044	0.0312
0.10	0.1208	0.0034	0.0178	0.1507	0.0031	0.0251	0.1993	0.0041	0.0303	0.2373	0.0041	0.0280
0.30	0.1192	0.0044	0.0148	0.1413	0.0045	0.0233	0.1814	0.0046	0.0243	0.2213	0.0044	0.0245
0.50	0.0759	0.0073	0.0200	0.1259	0.0055	0.0320	0.1429	0.0068	0.0216	0.1959	0.0060	0.0315
0.70	0.0303	0.0168	−0.0003	0.0719	0.0116	0.0228	0.0929	0.0137	0.0332	0.1066	0.0126	0.0378
0.90	0.0265	0.0467	0.0089	−0.0351	0.0424	−0.0779	−0.0062	0.0476	−0.0179	0.0673	0.0258	0.0240

$\cos(\theta^*_{2\pi^0})$	W=(1368.0±4.0) MeV			W=(1376.0±4.0) MeV			W=(1384.0±4.0) MeV			W=(1392.0±4.0) MeV		
	$d\sigma/d\Omega$ [μb/sr]	Δ_{stat} [μb/sr]	Δ_{sys} [μb/sr]	$d\sigma/d\Omega$ [μb/sr]	Δ_{stat} [μb/sr]	Δ_{sys} [μb/sr]	$d\sigma/d\Omega$ [μb/sr]	Δ_{stat} [μb/sr]	Δ_{sys} [μb/sr]	$d\sigma/d\Omega$ [μb/sr]	Δ_{stat} [μb/sr]	Δ_{sys} [μb/sr]
−0.90	0.1419	0.0030	0.0749	0.1654	0.0034	0.0563	0.1988	0.0037	0.0815	0.2287	0.0038	0.0790
−0.70	0.1982	0.0033	0.0353	0.2407	0.0033	0.0440	0.2693	0.0029	0.0336	0.3127	0.0039	0.0479
−0.50	0.2272	0.0045	0.0246	0.2857	0.0045	0.0322	0.3272	0.0049	0.0232	0.3650	0.0055	0.0321
−0.30	0.2563	0.0046	0.0302	0.3183	0.0048	0.0341	0.3642	0.0042	0.0303	0.3783	0.0057	0.0319
−0.10	0.2810	0.0048	0.0332	0.3311	0.0043	0.0339	0.3641	0.0049	0.0314	0.4006	0.0053	0.0313
0.10	0.2749	0.0049	0.0256	0.3207	0.0052	0.0246	0.3642	0.0051	0.0293	0.3939	0.0052	0.0256
0.30	0.2800	0.0046	0.0244	0.3109	0.0049	0.0189	0.3392	0.0057	0.0248	0.3690	0.0060	0.0240
0.50	0.2389	0.0066	0.0318	0.2634	0.0071	0.0293	0.3007	0.0070	0.0282	0.3360	0.0069	0.0401
0.70	0.1383	0.0118	0.0427	0.1690	0.0109	0.0496	0.2015	0.0118	0.0426	0.2455	0.0120	0.0528
0.90	0.0569	0.0366	0.0438	0.0306	0.0290	0.0196	0.0798	0.0354	0.0472	0.1603	0.0323	0.0625

$\cos(\theta^*_{2\pi^0})$	W=(1400.0±4.0) MeV			W=(1408.0±4.0) MeV			W=(1416.0±4.0) MeV			W=(1424.0±4.0) MeV		
	$d\sigma/d\Omega$ [μb/sr]	Δ_{stat} [μb/sr]	Δ_{sys} [μb/sr]	$d\sigma/d\Omega$ [μb/sr]	Δ_{stat} [μb/sr]	Δ_{sys} [μb/sr]	$d\sigma/d\Omega$ [μb/sr]	Δ_{stat} [μb/sr]	Δ_{sys} [μb/sr]	$d\sigma/d\Omega$ [μb/sr]	Δ_{stat} [μb/sr]	Δ_{sys} [μb/sr]
−0.90	0.2524	0.0039	0.0842	0.2976	0.0041	0.0937	0.3231	0.0044	0.0694	0.3510	0.0046	0.0709
−0.70	0.3294	0.0042	0.0411	0.3903	0.0046	0.0442	0.4176	0.0047	0.0370	0.4295	0.0051	0.0424
−0.50	0.3985	0.0049	0.0265	0.4431	0.0054	0.0250	0.4635	0.0056	0.0230	0.5057	0.0065	0.0197
−0.30	0.4276	0.0053	0.0263	0.4594	0.0056	0.0279	0.4998	0.0059	0.0288	0.5141	0.0061	0.0214
−0.10	0.4383	0.0058	0.0266	0.4793	0.0056	0.0305	0.4940	0.0064	0.0310	0.5364	0.0063	0.0267
0.10	0.4325	0.0058	0.0273	0.4648	0.0060	0.0301	0.4903	0.0062	0.0305	0.5222	0.0064	0.0259
0.30	0.3905	0.0059	0.0242	0.4324	0.0061	0.0273	0.4689	0.0063	0.0223	0.4836	0.0067	0.0202
0.50	0.3591	0.0075	0.0273	0.3902	0.0073	0.0332	0.4230	0.0078	0.0171	0.4503	0.0076	0.0196
0.70	0.3053	0.0112	0.0500	0.3033	0.0134	0.0433	0.3266	0.0122	0.0426	0.3633	0.0116	0.0460
0.90	0.1416	0.0306	0.0638	0.2028	0.0247	0.0495	0.1486	0.0292	0.0621	0.1141	0.0233	0.0450

$\cos(\theta^*_{2\pi^0})$	W=(1432.0±4.0) MeV			W=(1440.0±4.0) MeV			W=(1448.0±4.0) MeV			W=(1456.0±4.0) MeV		
	$d\sigma/d\Omega$ [μb/sr]	Δ_{stat} [μb/sr]	Δ_{sys} [μb/sr]	$d\sigma/d\Omega$ [μb/sr]	Δ_{stat} [μb/sr]	Δ_{sys} [μb/sr]	$d\sigma/d\Omega$ [μb/sr]	Δ_{stat} [μb/sr]	Δ_{sys} [μb/sr]	$d\sigma/d\Omega$ [μb/sr]	Δ_{stat} [μb/sr]	Δ_{sys} [μb/sr]
−0.90	0.3898	0.0052	0.0668	0.4196	0.0058	0.0779	0.4619	0.0055	0.0698	0.5074	0.0063	0.0736
−0.70	0.4567	0.0046	0.0373	0.5006	0.0050	0.0450	0.5277	0.0053	0.0369	0.5506	0.0058	0.0378
−0.50	0.5176	0.0067	0.0182	0.5323	0.0069	0.0210	0.5566	0.0069	0.0229	0.6117	0.0066	0.0223
−0.30	0.5590	0.0061	0.0217	0.5575	0.0066	0.0218	0.5869	0.0068	0.0241	0.6148	0.0071	0.0212
−0.10	0.5504	0.0068	0.0258	0.5773	0.0067	0.0231	0.6042	0.0067	0.0254	0.6151	0.0072	0.0220
0.10	0.5771	0.0066	0.0263	0.5804	0.0068	0.0233	0.6174	0.0068	0.0245	0.6208	0.0071	0.0229
0.30	0.5175	0.0066	0.0212	0.5460	0.0068	0.0210	0.5749	0.0071	0.0246	0.5743	0.0074	0.0231
0.50	0.4734	0.0076	0.0171	0.4830	0.0074	0.0195	0.5336	0.0078	0.0306	0.5510	0.0079	0.0252
0.70	0.3837	0.0122	0.0664	0.3936	0.0125	0.0463	0.4075	0.0122	0.0542	0.4537	0.0117	0.0517
0.90	0.1755	0.0305	0.0284	0.1900	0.0283	0.0635	0.1146	0.0294	0.0510	0.2304	0.0236	0.0763

$\cos(\theta^*_{2\pi^0})$	W=(1464.0±4.0) MeV			W=(1472.0±4.0) MeV			W=(1480.0±4.0) MeV			W=(1488.0±4.0) MeV		
	$d\sigma/d\Omega$ [μb/sr]	Δ_{stat} [μb/sr]	Δ_{sys} [μb/sr]	$d\sigma/d\Omega$ [μb/sr]	Δ_{stat} [μb/sr]	Δ_{sys} [μb/sr]	$d\sigma/d\Omega$ [μb/sr]	Δ_{stat} [μb/sr]	Δ_{sys} [μb/sr]	$d\sigma/d\Omega$ [μb/sr]	Δ_{stat} [μb/sr]	Δ_{sys} [μb/sr]
−0.90	0.5720	0.0065	0.0796	0.6029	0.0068	0.0728	0.6397	0.0073	0.0765	0.6895	0.0076	0.0740
−0.70	0.5878	0.0058	0.0366	0.6418	0.0062	0.0338	0.6514	0.0071	0.0367	0.6895	0.0072	0.0329
−0.50	0.6393	0.0078	0.0214	0.6477	0.0079	0.0196	0.6743	0.0079	0.0205	0.7058	0.0084	0.0161
−0.30	0.6211	0.0074	0.0206	0.6510	0.0073	0.0198	0.6624	0.0077	0.0168	0.6716	0.0078	0.0160
−0.10	0.6565	0.0073	0.0246	0.6608	0.0072	0.0219	0.6611	0.0076	0.0180	0.6501	0.0076	0.0233
0.10	0.6530	0.0071	0.0235	0.6519	0.0074	0.0242	0.6525	0.0076	0.0222	0.6464	0.0075	0.0282
0.30	0.5976	0.0073	0.0190	0.6278	0.0073	0.0243	0.6466	0.0076	0.0271	0.6643	0.0076	0.0292
0.50	0.5685	0.0082	0.0252	0.5734	0.0085	0.0179	0.5750	0.0089	0.0213	0.5816	0.0080	0.0294
0.70	0.4532	0.0122	0.0484	0.4973	0.0121	0.0347	0.5156	0.0115	0.0487	0.5096	0.0116	0.0453
0.90	0.2262	0.0311	0.0544	0.3400	0.0273	0.0783	0.2547	0.0240	0.0766	0.3554	0.0260	0.0684

$\cos(\theta^*_{2\pi^0})$	W=(1496.0±4.0) MeV			W=(1504.0±4.0) MeV			W=(1512.0±4.0) MeV			W=(1520.0±4.0) MeV		
	$d\sigma/d\Omega$ [μb/sr]	Δ_{stat} [μb/sr]	Δ_{sys} [μb/sr]	$d\sigma/d\Omega$ [μb/sr]	Δ_{stat} [μb/sr]	Δ_{sys} [μb/sr]	$d\sigma/d\Omega$ [μb/sr]	Δ_{stat} [μb/sr]	Δ_{sys} [μb/sr]	$d\sigma/d\Omega$ [μb/sr]	Δ_{stat} [μb/sr]	Δ_{sys} [μb/sr]
−0.90	0.7083	0.0080	0.0704	0.7230	0.0077	0.0691	0.7115	0.0082	0.0653	0.7001	0.0082	0.0538
−0.70	0.6894	0.0075	0.0305	0.6983	0.0077	0.0242	0.6895	0.0073	0.0282	0.6758	0.0078	0.0266
−0.50	0.7069	0.0088	0.0216	0.6869	0.0088	0.0173	0.6662	0.0084	0.0189	0.6277	0.0081	0.0184
−0.30	0.6649	0.0079	0.0202	0.6677	0.0079	0.0180	0.6115	0.0076	0.0154	0.5807	0.0077	0.0203
−0.10	0.6489	0.0079	0.0223	0.6350	0.0073	0.0209	0.6013	0.0074	0.0197	0.5479	0.0072	0.0272
0.10	0.6572	0.0073	0.0266	0.6180	0.0077	0.0268	0.6065	0.0074	0.0281	0.5579	0.0071	0.0327
0.30	0.6383	0.0078	0.0292	0.6041	0.0080	0.0338	0.5895	0.0075	0.0330	0.5344	0.0075	0.0326
0.50	0.6074	0.0086	0.0261	0.5779	0.0089	0.0396	0.5802	0.0085	0.0408	0.5255	0.0081	0.0347
0.70	0.5430	0.0113	0.0608	0.5188	0.0114	0.0443	0.5147	0.0111	0.0500	0.4921	0.0102	0.0483
0.90	0.3158	0.0314	0.1115	0.3591	0.0220	0.0477	0.3616	0.0217	0.0540	0.3276	0.0253	0.0697

$\cos(\theta^*_{2\pi^0})$	$W=(1528.0\pm4.0)$ MeV			$W=(1536.0\pm4.0)$ MeV			$W=(1544.0\pm4.0)$ MeV			$W=(1552.0\pm4.0)$ MeV		
	$d\sigma/d\Omega$ [μb/sr]	Δ_{stat} [μb/sr]	Δ_{sys} [μb/sr]	$d\sigma/d\Omega$ [μb/sr]	Δ_{stat} [μb/sr]	Δ_{sys} [μb/sr]	$d\sigma/d\Omega$ [μb/sr]	Δ_{stat} [μb/sr]	Δ_{sys} [μb/sr]	$d\sigma/d\Omega$ [μb/sr]	Δ_{stat} [μb/sr]	Δ_{sys} [μb/sr]
−0.90	0.7104	0.0086	0.0506	0.6808	0.0085	0.0482	0.6519	0.0081	0.0443	0.6463	0.0088	0.0424
−0.70	0.6477	0.0078	0.0201	0.6139	0.0078	0.0208	0.6118	0.0075	0.0199	0.5808	0.0076	0.0138
−0.50	0.6265	0.0084	0.0118	0.5762	0.0079	0.0127	0.5443	0.0083	0.0155	0.5199	0.0081	0.0110
−0.30	0.5487	0.0075	0.0145	0.5049	0.0069	0.0124	0.4737	0.0069	0.0153	0.4437	0.0074	0.0131
−0.10	0.5205	0.0069	0.0198	0.4927	0.0071	0.0185	0.4534	0.0067	0.0194	0.4143	0.0068	0.0159
0.10	0.4987	0.0069	0.0255	0.4794	0.0067	0.0282	0.4483	0.0066	0.0255	0.4256	0.0065	0.0211
0.30	0.5240	0.0072	0.0336	0.4764	0.0070	0.0354	0.4508	0.0068	0.0294	0.4397	0.0071	0.0285
0.50	0.5147	0.0074	0.0363	0.4851	0.0070	0.0347	0.4610	0.0081	0.0357	0.4376	0.0077	0.0361
0.70	0.4990	0.0106	0.0488	0.4575	0.0105	0.0356	0.4434	0.0102	0.0410	0.4421	0.0103	0.0448
0.90	0.3327	0.0198	0.0660	0.3847	0.0228	0.0589	0.3752	0.0194	0.0416	0.3704	0.0208	0.0462

$\cos(\theta^*_{2\pi^0})$	$W=(1560.0\pm4.0)$ MeV			$W=(1568.0\pm4.0)$ MeV			$W=(1576.0\pm4.0)$ MeV			$W=(1584.0\pm4.0)$ MeV		
	$d\sigma/d\Omega$ [μb/sr]	Δ_{stat} [μb/sr]	Δ_{sys} [μb/sr]	$d\sigma/d\Omega$ [μb/sr]	Δ_{stat} [μb/sr]	Δ_{sys} [μb/sr]	$d\sigma/d\Omega$ [μb/sr]	Δ_{stat} [μb/sr]	Δ_{sys} [μb/sr]	$d\sigma/d\Omega$ [μb/sr]	Δ_{stat} [μb/sr]	Δ_{sys} [μb/sr]
−0.90	0.6330	0.0087	0.0359	0.6306	0.0087	0.0366	0.5995	0.0089	0.0271	0.5823	0.0092	0.0284
−0.70	0.5444	0.0074	0.0145	0.5429	0.0073	0.0147	0.5273	0.0076	0.0193	0.5200	0.0078	0.0168
−0.50	0.4705	0.0078	0.0113	0.4662	0.0076	0.0095	0.4547	0.0079	0.0158	0.4620	0.0077	0.0133
−0.30	0.4229	0.0068	0.0140	0.4098	0.0069	0.0136	0.3881	0.0070	0.0149	0.3665	0.0068	0.0138
−0.10	0.3907	0.0066	0.0188	0.3649	0.0068	0.0185	0.3536	0.0067	0.0161	0.3383	0.0063	0.0176
0.10	0.3949	0.0071	0.0245	0.3738	0.0070	0.0215	0.3677	0.0067	0.0197	0.3587	0.0066	0.0243
0.30	0.4159	0.0068	0.0312	0.3921	0.0067	0.0227	0.3807	0.0069	0.0240	0.3939	0.0067	0.0251
0.50	0.4214	0.0077	0.0317	0.4310	0.0079	0.0288	0.4183	0.0079	0.0309	0.4233	0.0071	0.0239
0.70	0.4229	0.0103	0.0385	0.4302	0.0080	0.0432	0.4424	0.0085	0.0479	0.4243	0.0089	0.0374
0.90	0.3742	0.0216	0.0623	0.3710	0.0241	0.0687	0.3209	0.0225	0.0521	0.3647	0.0196	0.0704

$\cos(\theta^*_{2\pi^0})$	$W=(1592.0\pm4.0)$ MeV			$W=(1600.0\pm4.0)$ MeV			$W=(1608.0\pm4.0)$ MeV			$W=(1616.0\pm4.0)$ MeV		
	$d\sigma/d\Omega$ [μb/sr]	Δ_{stat} [μb/sr]	Δ_{sys} [μb/sr]	$d\sigma/d\Omega$ [μb/sr]	Δ_{stat} [μb/sr]	Δ_{sys} [μb/sr]	$d\sigma/d\Omega$ [μb/sr]	Δ_{stat} [μb/sr]	Δ_{sys} [μb/sr]	$d\sigma/d\Omega$ [μb/sr]	Δ_{stat} [μb/sr]	Δ_{sys} [μb/sr]
−0.90	0.5757	0.0086	0.0323	0.5791	0.0090	0.0350	0.5982	0.0093	0.0351	0.5862	0.0090	0.0289
−0.70	0.5039	0.0074	0.0160	0.5114	0.0078	0.0175	0.5186	0.0075	0.0167	0.5306	0.0074	0.0125
−0.50	0.4608	0.0077	0.0115	0.4376	0.0079	0.0103	0.4433	0.0072	0.0113	0.4266	0.0071	0.0090
−0.30	0.3640	0.0065	0.0133	0.3481	0.0066	0.0097	0.3623	0.0055	0.0105	0.3844	0.0061	0.0099
−0.10	0.3424	0.0066	0.0172	0.3509	0.0062	0.0138	0.3408	0.0059	0.0136	0.3474	0.0051	0.0116
0.10	0.3733	0.0061	0.0194	0.3475	0.0054	0.0160	0.3562	0.0058	0.0152	0.3519	0.0058	0.0141
0.30	0.3973	0.0063	0.0219	0.4052	0.0065	0.0182	0.3996	0.0059	0.0160	0.4235	0.0065	0.0169
0.50	0.4275	0.0075	0.0279	0.4473	0.0061	0.0208	0.4485	0.0065	0.0196	0.4675	0.0066	0.0208
0.70	0.4334	0.0091	0.0628	0.4510	0.0082	0.0393	0.4686	0.0075	0.0363	0.4950	0.0081	0.0318
0.90	0.4145	0.0175	0.1151	0.3620	0.0220	0.0700	0.3997	0.0195	0.0595	0.4255	0.0190	0.0612

$\cos(\theta^*_{2\pi^0})$	$W=(1624.0\pm4.0)$ MeV			$W=(1632.0\pm4.0)$ MeV			$W=(1640.0\pm4.0)$ MeV			$W=(1648.0\pm4.0)$ MeV		
	$d\sigma/d\Omega$ [μb/sr]	Δ_{stat} [μb/sr]	Δ_{sys} [μb/sr]	$d\sigma/d\Omega$ [μb/sr]	Δ_{stat} [μb/sr]	Δ_{sys} [μb/sr]	$d\sigma/d\Omega$ [μb/sr]	Δ_{stat} [μb/sr]	Δ_{sys} [μb/sr]	$d\sigma/d\Omega$ [μb/sr]	Δ_{stat} [μb/sr]	Δ_{sys} [μb/sr]
−0.90	0.6024	0.0090	0.0409	0.6164	0.0086	0.0339	0.6100	0.0085	0.0426	0.6243	0.0082	0.0351
−0.70	0.5324	0.0065	0.0204	0.5465	0.0068	0.0179	0.5524	0.0066	0.0175	0.5867	0.0067	0.0194
−0.50	0.4694	0.0073	0.0134	0.4825	0.0069	0.0117	0.4978	0.0063	0.0111	0.4895	0.0061	0.0112
−0.30	0.3825	0.0061	0.0133	0.3928	0.0057	0.0100	0.3971	0.0057	0.0105	0.4179	0.0054	0.0092
−0.10	0.3472	0.0059	0.0126	0.3678	0.0055	0.0125	0.3749	0.0061	0.0133	0.3858	0.0053	0.0108
0.10	0.3711	0.0055	0.0129	0.3742	0.0062	0.0147	0.4009	0.0057	0.0151	0.4189	0.0056	0.0145
0.30	0.4281	0.0058	0.0158	0.4458	0.0058	0.0168	0.4681	0.0059	0.0159	0.4953	0.0061	0.0186
0.50	0.4927	0.0059	0.0196	0.5283	0.0063	0.0208	0.5519	0.0061	0.0199	0.5864	0.0061	0.0235
0.70	0.5317	0.0074	0.0356	0.5578	0.0076	0.0293	0.5846	0.0079	0.0391	0.6251	0.0079	0.0373
0.90	0.4495	0.0188	0.0686	0.5019	0.0170	0.0406	0.4693	0.0193	0.0780	0.5345	0.0216	0.0491

$\cos(\theta^*_{2\pi^0})$	$W=(1656.0\pm4.0)$ MeV			$W=(1664.0\pm4.0)$ MeV			$W=(1672.0\pm4.0)$ MeV			$W=(1680.0\pm4.0)$ MeV		
	$d\sigma/d\Omega$ [μb/sr]	Δ_{stat} [μb/sr]	Δ_{sys} [μb/sr]	$d\sigma/d\Omega$ [μb/sr]	Δ_{stat} [μb/sr]	Δ_{sys} [μb/sr]	$d\sigma/d\Omega$ [μb/sr]	Δ_{stat} [μb/sr]	Δ_{sys} [μb/sr]	$d\sigma/d\Omega$ [μb/sr]	Δ_{stat} [μb/sr]	Δ_{sys} [μb/sr]
−0.90	0.6254	0.0081	0.0324	0.6602	0.0085	0.0386	0.6856	0.0076	0.0423	0.6534	0.0077	0.0427
−0.70	0.5966	0.0062	0.0166	0.5978	0.0058	0.0183	0.6155	0.0064	0.0247	0.6235	0.0060	0.0177
−0.50	0.5113	0.0062	0.0089	0.5323	0.0062	0.0101	0.5547	0.0061	0.0152	0.5745	0.0072	0.0107
−0.30	0.4279	0.0055	0.0064	0.4507	0.0056	0.0088	0.4670	0.0054	0.0091	0.4882	0.0057	0.0101
−0.10	0.3893	0.0057	0.0087	0.4235	0.0054	0.0117	0.4293	0.0058	0.0092	0.4377	0.0057	0.0089
0.10	0.4370	0.0059	0.0117	0.4527	0.0058	0.0124	0.4670	0.0063	0.0096	0.4924	0.0063	0.0082
0.30	0.5179	0.0060	0.0181	0.5318	0.0063	0.0127	0.5533	0.0069	0.0112	0.5784	0.0070	0.0103
0.50	0.6080	0.0074	0.0212	0.6416	0.0067	0.0136	0.6530	0.0070	0.0178	0.6864	0.0070	0.0189
0.70	0.6613	0.0085	0.0248	0.6820	0.0080	0.0318	0.6981	0.0080	0.0316	0.7326	0.0086	0.0316
0.90	0.4738	0.0211	0.0581	0.5719	0.0205	0.0764	0.5952	0.0215	0.0474	0.6237	0.0225	0.0451

$\cos(\theta^*_{2\pi^0})$	$W=(1688.0\pm4.0)$ MeV			$W=(1696.0\pm4.0)$ MeV			$W=(1704.0\pm4.0)$ MeV			$W=(1712.0\pm4.0)$ MeV		
	$d\sigma/d\Omega$ [μb/sr]	Δ_{stat} [μb/sr]	Δ_{sys} [μb/sr]	$d\sigma/d\Omega$ [μb/sr]	Δ_{stat} [μb/sr]	Δ_{sys} [μb/sr]	$d\sigma/d\Omega$ [μb/sr]	Δ_{stat} [μb/sr]	Δ_{sys} [μb/sr]	$d\sigma/d\Omega$ [μb/sr]	Δ_{stat} [μb/sr]	Δ_{sys} [μb/sr]
−0.90	0.6740	0.0078	0.0462	0.6699	0.0075	0.0427	0.6628	0.0076	0.0357	0.6433	0.0071	0.0476
−0.70	0.6102	0.0061	0.0225	0.6256	0.0060	0.0238	0.6069	0.0060	0.0236	0.5948	0.0060	0.0289
−0.50	0.5617	0.0068	0.0158	0.5743	0.0061	0.0161	0.5490	0.0063	0.0156	0.5561	0.0061	0.0192
−0.30	0.4860	0.0052	0.0105	0.4930	0.0056	0.0101	0.5086	0.0057	0.0088	0.5059	0.0052	0.0100
−0.10	0.4502	0.0057	0.0079	0.4563	0.0064	0.0084	0.4802	0.0060	0.0079	0.4839	0.0056	0.0054
0.10	0.4925	0.0066	0.0088	0.5060	0.0070	0.0088	0.5237	0.0069	0.0094	0.5232	0.0064	0.0067
0.30	0.5835	0.0068	0.0110	0.5948	0.0069	0.0114	0.6087	0.0075	0.0104	0.6036	0.0076	0.0094
0.50	0.6908	0.0071	0.0130	0.7135	0.0074	0.0212	0.7184	0.0075	0.0148	0.7043	0.0071	0.0136
0.70	0.7425	0.0087	0.0277	0.7533	0.0088	0.0387	0.7435	0.0081	0.0311	0.7171	0.0081	0.0253
0.90	0.5951	0.0177	0.0497	0.6576	0.0150	0.0502	0.6165	0.0183	0.0513	0.5668	0.0166	0.0359

$\cos(\theta^*_{2\pi^0})$	$W=(1720.0\pm4.0)$ MeV			$W=(1728.0\pm4.0)$ MeV			$W=(1736.0\pm4.0)$ MeV			$W=(1744.0\pm4.0)$ MeV		
	$d\sigma/d\Omega$ [μb/sr]	$\Delta_{\rm stat}$ [μb/sr]	$\Delta_{\rm sys}$ [μb/sr]	$d\sigma/d\Omega$ [μb/sr]	$\Delta_{\rm stat}$ [μb/sr]	$\Delta_{\rm sys}$ [μb/sr]	$d\sigma/d\Omega$ [μb/sr]	$\Delta_{\rm stat}$ [μb/sr]	$\Delta_{\rm sys}$ [μb/sr]	$d\sigma/d\Omega$ [μb/sr]	$\Delta_{\rm stat}$ [μb/sr]	$\Delta_{\rm sys}$ [μb/sr]
−0.90	0.6054	0.0070	0.0441	0.5665	0.0071	0.0457	0.5376	0.0063	0.0458	0.5016	0.0064	0.0364
−0.70	0.5608	0.0055	0.0226	0.5120	0.0054	0.0204	0.4891	0.0060	0.0183	0.4673	0.0051	0.0156
−0.50	0.5372	0.0067	0.0146	0.4989	0.0057	0.0147	0.4786	0.0059	0.0091	0.4686	0.0055	0.0084
−0.30	0.4956	0.0052	0.0095	0.4833	0.0049	0.0115	0.4606	0.0051	0.0053	0.4716	0.0049	0.0070
−0.10	0.4740	0.0058	0.0073	0.4758	0.0063	0.0066	0.4523	0.0057	0.0050	0.4343	0.0051	0.0065
0.10	0.5197	0.0068	0.0081	0.5207	0.0067	0.0053	0.4972	0.0072	0.0064	0.5004	0.0068	0.0070
0.30	0.6119	0.0072	0.0115	0.5989	0.0074	0.0105	0.5914	0.0079	0.0094	0.5637	0.0063	0.0088
0.50	0.7037	0.0077	0.0176	0.6807	0.0074	0.0223	0.6692	0.0074	0.0181	0.6274	0.0077	0.0147
0.70	0.7117	0.0081	0.0262	0.6812	0.0075	0.0306	0.6492	0.0081	0.0241	0.6679	0.0077	0.0200
0.90	0.6415	0.0189	0.0348	0.5754	0.0158	0.0426	0.5606	0.0150	0.0257	0.5207	0.0155	0.0342

$\cos(\theta^*_{2\pi^0})$	$W=(1752.0\pm4.0)$ MeV			$W=(1760.0\pm4.0)$ MeV			$W=(1768.0\pm4.0)$ MeV			$W=(1776.0\pm4.0)$ MeV		
	$d\sigma/d\Omega$ [μb/sr]	$\Delta_{\rm stat}$ [μb/sr]	$\Delta_{\rm sys}$ [μb/sr]	$d\sigma/d\Omega$ [μb/sr]	$\Delta_{\rm stat}$ [μb/sr]	$\Delta_{\rm sys}$ [μb/sr]	$d\sigma/d\Omega$ [μb/sr]	$\Delta_{\rm stat}$ [μb/sr]	$\Delta_{\rm sys}$ [μb/sr]	$d\sigma/d\Omega$ [μb/sr]	$\Delta_{\rm stat}$ [μb/sr]	$\Delta_{\rm sys}$ [μb/sr]
−0.90	0.4684	0.0062	0.0346	0.4414	0.0062	0.0366	0.3935	0.0065	0.0250	0.3642	0.0057	0.0273
−0.70	0.4412	0.0052	0.0162	0.4219	0.0050	0.0164	0.3823	0.0049	0.0107	0.3704	0.0046	0.0136
−0.50	0.4225	0.0061	0.0091	0.4263	0.0056	0.0103	0.4025	0.0053	0.0067	0.3828	0.0055	0.0084
−0.30	0.4103	0.0045	0.0072	0.4035	0.0045	0.0087	0.3905	0.0049	0.0064	0.3904	0.0049	0.0065
−0.10	0.4505	0.0057	0.0088	0.3939	0.0052	0.0077	0.3978	0.0051	0.0095	0.3871	0.0046	0.0059
0.10	0.4705	0.0067	0.0113	0.4699	0.0055	0.0083	0.4439	0.0054	0.0147	0.4228	0.0057	0.0081
0.30	0.5350	0.0066	0.0122	0.5376	0.0062	0.0074	0.5283	0.0064	0.0137	0.4987	0.0062	0.0105
0.50	0.6027	0.0076	0.0132	0.6087	0.0065	0.0085	0.5711	0.0070	0.0099	0.5638	0.0061	0.0088
0.70	0.6179	0.0072	0.0199	0.5973	0.0065	0.0210	0.5780	0.0070	0.0194	0.5666	0.0078	0.0217
0.90	0.5072	0.0144	0.0318	0.4862	0.0158	0.0508	0.4885	0.0129	0.0550	0.4040	0.0130	0.0549

$\cos(\theta^*_{2\pi^0})$	$W=(1784.0\pm4.0)$ MeV			$W=(1792.0\pm4.0)$ MeV			$W=(1800.0\pm4.0)$ MeV			$W=(1808.0\pm4.0)$ MeV		
	$d\sigma/d\Omega$ [μb/sr]	$\Delta_{\rm stat}$ [μb/sr]	$\Delta_{\rm sys}$ [μb/sr]	$d\sigma/d\Omega$ [μb/sr]	$\Delta_{\rm stat}$ [μb/sr]	$\Delta_{\rm sys}$ [μb/sr]	$d\sigma/d\Omega$ [μb/sr]	$\Delta_{\rm stat}$ [μb/sr]	$\Delta_{\rm sys}$ [μb/sr]	$d\sigma/d\Omega$ [μb/sr]	$\Delta_{\rm stat}$ [μb/sr]	$\Delta_{\rm sys}$ [μb/sr]
−0.90	0.3433	0.0059	0.0286	0.3129	0.0056	0.0222	0.3092	0.0053	0.0162	0.2960	0.0063	0.0211
−0.70	0.3583	0.0047	0.0144	0.3259	0.0044	0.0121	0.3226	0.0042	0.0109	0.3095	0.0046	0.0120
−0.50	0.3785	0.0058	0.0091	0.3397	0.0055	0.0093	0.3547	0.0058	0.0104	0.3479	0.0056	0.0091
−0.30	0.3754	0.0048	0.0097	0.3757	0.0050	0.0106	0.3541	0.0055	0.0094	0.3465	0.0049	0.0066
−0.10	0.3653	0.0051	0.0084	0.3636	0.0054	0.0092	0.3706	0.0046	0.0076	0.3559	0.0050	0.0046
0.10	0.4112	0.0057	0.0063	0.4263	0.0058	0.0077	0.4131	0.0056	0.0081	0.4128	0.0059	0.0058
0.30	0.4904	0.0055	0.0065	0.4925	0.0063	0.0081	0.4756	0.0064	0.0092	0.4684	0.0069	0.0082
0.50	0.5665	0.0063	0.0095	0.5437	0.0063	0.0135	0.5420	0.0064	0.0108	0.5379	0.0074	0.0077
0.70	0.5227	0.0072	0.0214	0.5318	0.0079	0.0196	0.5546	0.0072	0.0134	0.5304	0.0078	0.0112
0.90	0.4918	0.0145	0.0491	0.4318	0.0160	0.0265	0.4021	0.0170	0.0172	0.3955	0.0121	0.0214

$\cos(\theta^*_{2\pi^0})$	$W=(1816.0\pm4.0)$ MeV			$W=(1824.0\pm4.0)$ MeV			$W=(1832.0\pm4.0)$ MeV			$W=(1840.0\pm4.0)$ MeV		
	$d\sigma/d\Omega$ [μb/sr]	$\Delta_{\rm stat}$ [μb/sr]	$\Delta_{\rm sys}$ [μb/sr]	$d\sigma/d\Omega$ [μb/sr]	$\Delta_{\rm stat}$ [μb/sr]	$\Delta_{\rm sys}$ [μb/sr]	$d\sigma/d\Omega$ [μb/sr]	$\Delta_{\rm stat}$ [μb/sr]	$\Delta_{\rm sys}$ [μb/sr]	$d\sigma/d\Omega$ [μb/sr]	$\Delta_{\rm stat}$ [μb/sr]	$\Delta_{\rm sys}$ [μb/sr]
−0.90	0.2789	0.0052	0.0224	0.2624	0.0055	0.0192	0.2496	0.0051	0.0173	0.2548	0.0053	0.0127
−0.70	0.3098	0.0045	0.0110	0.3141	0.0052	0.0098	0.2957	0.0047	0.0115	0.3043	0.0047	0.0103
−0.50	0.3309	0.0054	0.0083	0.3417	0.0060	0.0074	0.3135	0.0059	0.0096	0.3117	0.0064	0.0098
−0.30	0.3362	0.0057	0.0086	0.3433	0.0050	0.0088	0.3375	0.0054	0.0079	0.3245	0.0053	0.0088
−0.10	0.3632	0.0048	0.0078	0.3429	0.0055	0.0079	0.3508	0.0052	0.0070	0.3477	0.0056	0.0064
0.10	0.3938	0.0058	0.0091	0.3813	0.0063	0.0071	0.3680	0.0061	0.0074	0.3807	0.0071	0.0048
0.30	0.4787	0.0068	0.0128	0.4428	0.0069	0.0083	0.4480	0.0074	0.0085	0.4433	0.0077	0.0066
0.50	0.5275	0.0081	0.0119	0.5381	0.0087	0.0130	0.5099	0.0093	0.0080	0.5262	0.0099	0.0062
0.70	0.5310	0.0085	0.0152	0.5130	0.0086	0.0181	0.5094	0.0105	0.0187	0.5350	0.0095	0.0167
0.90	0.3700	0.0164	0.0286	0.4167	0.0163	0.0291	0.3731	0.0184	0.0484	0.3570	0.0186	0.0387

$\cos(\theta^*_{2\pi^0})$	$W=(1848.0\pm4.0)$ MeV			$W=(1856.0\pm4.0)$ MeV			$W=(1864.0\pm4.0)$ MeV			$W=(1872.0\pm4.0)$ MeV		
	$d\sigma/d\Omega$ [μb/sr]	$\Delta_{\rm stat}$ [μb/sr]	$\Delta_{\rm sys}$ [μb/sr]	$d\sigma/d\Omega$ [μb/sr]	$\Delta_{\rm stat}$ [μb/sr]	$\Delta_{\rm sys}$ [μb/sr]	$d\sigma/d\Omega$ [μb/sr]	$\Delta_{\rm stat}$ [μb/sr]	$\Delta_{\rm sys}$ [μb/sr]	$d\sigma/d\Omega$ [μb/sr]	$\Delta_{\rm stat}$ [μb/sr]	$\Delta_{\rm sys}$ [μb/sr]
−0.90	0.2424	0.0058	0.0216	0.2356	0.0053	0.0221	0.2414	0.0058	0.0327	0.2465	0.0073	0.0179
−0.70	0.2862	0.0051	0.0111	0.2692	0.0055	0.0106	0.2855	0.0057	0.0133	0.2752	0.0063	0.0145
−0.50	0.3401	0.0070	0.0060	0.2872	0.0070	0.0087	0.3029	0.0083	0.0087	0.2976	0.0086	0.0130
−0.30	0.3274	0.0067	0.0072	0.3331	0.0058	0.0109	0.3255	0.0063	0.0105	0.2923	0.0066	0.0099
−0.10	0.3462	0.0057	0.0127	0.3316	0.0058	0.0097	0.3325	0.0063	0.0084	0.3139	0.0075	0.0099
0.10	0.3894	0.0073	0.0139	0.3550	0.0078	0.0104	0.3758	0.0089	0.0061	0.3507	0.0097	0.0115
0.30	0.4675	0.0083	0.0120	0.4568	0.0079	0.0131	0.4577	0.0096	0.0101	0.4732	0.0108	0.0136
0.50	0.5367	0.0100	0.0133	0.5184	0.0106	0.0104	0.5245	0.0118	0.0153	0.5120	0.0135	0.0112
0.70	0.5326	0.0108	0.0216	0.4885	0.0123	0.0133	0.5276	0.0142	0.0269	0.5239	0.0152	0.0244
0.90	0.4418	0.0183	0.0299	0.3829	0.0245	0.0286	0.4167	0.0208	0.0417	0.3960	0.0240	0.0507

$\cos(\theta^*_{2\pi^0})$	$W=(1880.0\pm4.0)$ MeV			$W=(1888.0\pm4.0)$ MeV			$W=(1896.0\pm4.0)$ MeV		
	$d\sigma/d\Omega$ [μb/sr]	$\Delta_{\rm stat}$ [μb/sr]	$\Delta_{\rm sys}$ [μb/sr]	$d\sigma/d\Omega$ [μb/sr]	$\Delta_{\rm stat}$ [μb/sr]	$\Delta_{\rm sys}$ [μb/sr]	$d\sigma/d\Omega$ [μb/sr]	$\Delta_{\rm stat}$ [μb/sr]	$\Delta_{\rm sys}$ [μb/sr]
−0.90	0.1933	0.0065	0.0077	0.2311	0.0070	0.0136	0.1998	0.0099	0.0077
−0.70	0.2585	0.0060	0.0063	0.2848	0.0077	0.0102	0.2542	0.0080	0.0109
−0.50	0.2947	0.0081	0.0070	0.2976	0.0115	0.0060	0.3138	0.0140	0.0130
−0.30	0.3017	0.0093	0.0058	0.2982	0.0101	0.0059	0.3113	0.0111	0.0112
−0.10	0.3320	0.0081	0.0060	0.3111	0.0102	0.0091	0.3022	0.0106	0.0079
0.10	0.3676	0.0111	0.0070	0.3588	0.0127	0.0098	0.3767	0.0105	0.0088
0.30	0.4655	0.0121	0.0086	0.4492	0.0126	0.0086	0.4523	0.0160	0.0097
0.50	0.4645	0.0150	0.0150	0.5305	0.0161	0.0143	0.5394	0.0213	0.0156
0.70	0.5451	0.0156	0.0494	0.4818	0.0206	0.0326	0.5185	0.0187	0.0336
0.90	0.2408	0.0291	0.0933	0.3349	0.0247	0.0708	0.2409	0.0339	0.0599

Decomposed Total Cross Sections

W [MeV]	ΔW [MeV]	$\sigma_{PhaseSpace}$ [μb]	Δ_{stat} [μb]	$\sigma_{\Delta(1232)}$ [μb]	Δ_{stat} [μb]	$\sigma_{N(1520)}$ [μb]	Δ_{stat} [μb]
1308.0	8.0	0.0290	0.0068	0.0253	0.0051	0.0193	0.0067
1324.0	8.0	0.1782	0.0165	0.1909	0.0162	0.0615	0.0151
1340.0	8.0	0.5143	0.0335	0.5879	0.0245	0.0489	0.0281
1356.0	8.0	0.6369	0.0525	1.3818	0.0355	0.0858	0.0465
1372.0	8.0	0.3520	0.0780	2.4025	0.0443	0.1003	0.0727
1388.0	8.0	0.0872	0.0974	3.3601	0.0622	0.0839	0.1097
1404.0	8.0	0.0078	0.1127	4.0574	0.0846	0.2060	0.1318
1420.0	8.0	0.0876	0.1500	4.7790	0.1010	0.1701	0.1593
1436.0	8.0	0.0000	0.1553	5.4220	0.1109	0.0535	0.1454
1452.0	8.0	0.3000	0.1913	5.9866	0.1283	0.0148	0.1689
1468.0	8.0	0.0560	0.1784	6.6745	0.1427	0.0309	0.1901
1484.0	8.0	0.0567	0.2082	7.2241	0.1310	0.0210	0.2104
1500.0	8.0	0.0422	0.2069	7.3646	0.1313	0.0016	0.2058
1516.0	8.0	0.0253	0.2097	6.8364	0.1172	0.0006	0.2044
1532.0	8.0	0.0040	0.1884	6.3899	0.1086	0.0000	0.1829
1548.0	8.0	0.0000	0.1671	5.8617	0.0873	0.0001	0.1626
1564.0	8.0	0.0605	0.1346	5.1280	0.0921	0.0010	0.1351
1580.0	8.0	0.1461	0.1500	4.7126	0.0906	0.0000	0.1295
1596.0	8.0	0.3717	0.1467	4.5948	0.1096	0.0024	0.1209
1612.0	8.0	0.5808	0.1585	4.7697	0.1260	0.0000	0.1578
1628.0	8.0	1.1652	0.1603	4.1666	0.1446	0.0041	0.1660
1644.0	8.0	1.7046	0.1816	4.5487	0.1660	0.0000	0.1739
1660.0	8.0	1.9976	0.1912	4.5770	0.1806	0.0419	0.2067
1676.0	8.0	2.9608	0.2066	4.2633	0.1853	0.1267	0.2147
1692.0	8.0	2.6619	0.2246	4.1930	0.1989	0.2924	0.2151
1708.0	8.0	2.1616	0.2207	4.0910	0.1853	0.6147	0.2067
1724.0	8.0	1.9846	0.2091	4.2517	0.1878	0.8695	0.1901
1740.0	8.0	1.8437	0.1923	3.6501	0.1858	0.9408	0.1942
1756.0	8.0	1.8689	0.1908	3.0127	0.1738	1.1853	0.1723
1772.0	8.0	1.4978	0.1715	2.6545	0.1627	1.4348	0.1555
1788.0	8.0	1.3617	0.1612	2.4075	0.1570	1.5100	0.1541
1804.0	8.0	1.2188	0.1501	2.5430	0.1476	1.3518	0.1519
1820.0	8.0	1.1627	0.1416	2.6853	0.1367	1.1513	0.1430
1836.0	8.0	1.3450	0.1439	2.4481	0.1317	0.8889	0.1365
1852.0	8.0	1.1953	0.1373	2.6128	0.1265	1.0466	0.1315
1868.0	8.0	1.2942	0.1256	2.6246	0.1250	0.6083	0.1271
1888.0	10.0	1.1688	0.0905	2.3377	0.0971	0.6304	0.0961

E.3.4 $\gamma d \to \pi^0\pi^0 n(p)$ as a Function of W

Angular Distributions

$\cos(\theta^*_{2\pi^0})$	$W=(1304.0\pm4.0)$ MeV			$W=(1312.0\pm4.0)$ MeV			$W=(1320.0\pm4.0)$ MeV			$W=(1328.0\pm4.0)$ MeV		
	$d\sigma/d\Omega$ [μb/sr]	Δ_{stat} [μb/sr]	Δ_{sys} [μb/sr]	$d\sigma/d\Omega$ [μb/sr]	Δ_{stat} [μb/sr]	Δ_{sys} [μb/sr]	$d\sigma/d\Omega$ [μb/sr]	Δ_{stat} [μb/sr]	Δ_{sys} [μb/sr]	$d\sigma/d\Omega$ [μb/sr]	Δ_{stat} [μb/sr]	Δ_{sys} [μb/sr]
−0.90	0.0246	0.0049	0.0428	0.0365	0.0047	0.0308	0.0437	0.0068	0.0616	0.0622	0.0063	0.0696
−0.70	0.0179	0.0031	0.0202	0.0342	0.0034	0.0296	0.0440	0.0045	0.0535	0.0296	0.0043	0.0277
−0.50	0.0067	0.0032	0.0077	0.0205	0.0039	0.0280	0.0432	0.0033	0.0395	0.0516	0.0041	0.0339
−0.30	0.0116	0.0031	0.0123	0.0263	0.0031	0.0302	0.0319	0.0032	0.0222	0.0630	0.0033	0.0257
−0.10	0.0149	0.0036	0.0205	0.0237	0.0040	0.0225	0.0289	0.0036	0.0216	0.0631	0.0044	0.0199
0.10	0.0202	0.0036	0.0173	0.0247	0.0037	0.0255	0.0261	0.0042	0.0172	0.0614	0.0043	0.0218
0.30	0.0142	0.0042	0.0128	0.0217	0.0043	0.0135	0.0285	0.0046	0.0158	0.0496	0.0045	0.0205
0.50	0.0025	0.0068	−0.0087	0.0302	0.0053	0.0256	0.0155	0.0070	0.0090	0.0200	0.0082	0.0110
0.70	0.0241	0.0093	0.0171	0.0077	0.0108	0.0062	0.0404	0.0100	0.0265	0.0052	0.0125	0.0116
0.90	−0.0001	0.0291	−0.0079	0.0566	0.0346	0.0510	−0.0267	0.0394	−0.0213	−0.0276	0.0306	−0.0563

$\cos(\theta^*_{2\pi^0})$	$W=(1336.0\pm4.0)$ MeV			$W=(1344.0\pm4.0)$ MeV			$W=(1352.0\pm4.0)$ MeV			$W=(1360.0\pm4.0)$ MeV		
	$d\sigma/d\Omega$ [μb/sr]	Δ_{stat} [μb/sr]	Δ_{sys} [μb/sr]	$d\sigma/d\Omega$ [μb/sr]	Δ_{stat} [μb/sr]	Δ_{sys} [μb/sr]	$d\sigma/d\Omega$ [μb/sr]	Δ_{stat} [μb/sr]	Δ_{sys} [μb/sr]	$d\sigma/d\Omega$ [μb/sr]	Δ_{stat} [μb/sr]	Δ_{sys} [μb/sr]
−0.90	0.0623	0.0047	0.0668	0.0728	0.0055	0.0481	0.1048	0.0054	0.0846	0.1211	0.0064	0.0930
−0.70	0.0671	0.0044	0.0507	0.0847	0.0045	0.0533	0.0979	0.0050	0.0314	0.1165	0.0050	0.0476
−0.50	0.0649	0.0042	0.0417	0.0735	0.0048	0.0304	0.1077	0.0048	0.0349	0.1347	0.0065	0.0286
−0.30	0.0562	0.0036	0.0314	0.0870	0.0034	0.0162	0.1130	0.0052	0.0226	0.1455	0.0044	0.0221
−0.10	0.0725	0.0045	0.0216	0.0932	0.0046	0.0134	0.1294	0.0045	0.0239	0.1318	0.0051	0.0219
0.10	0.0701	0.0037	0.0156	0.0901	0.0038	0.0166	0.1339	0.0055	0.0223	0.1518	0.0054	0.0231
0.30	0.0685	0.0041	0.0132	0.0773	0.0062	0.0147	0.0954	0.0054	0.0177	0.1315	0.0066	0.0234
0.50	0.0674	0.0060	0.0198	0.0649	0.0057	0.0203	0.0950	0.0079	0.0231	0.1226	0.0062	0.0175
0.70	0.0257	0.0098	0.0226	0.0273	0.0124	0.0010	0.0655	0.0099	0.0342	0.0881	0.0098	0.0308
0.90	0.0392	0.0292	0.0659	0.0064	0.0295	0.0125	0.0572	0.0348	0.0287	−0.0258	0.0376	−0.0295

$\cos(\theta^*_{2\pi^0})$	$W=(1368.0\pm4.0)$ MeV			$W=(1376.0\pm4.0)$ MeV			$W=(1384.0\pm4.0)$ MeV			$W=(1392.0\pm4.0)$ MeV		
	$d\sigma/d\Omega$ [μb/sr]	Δ_{stat} [μb/sr]	Δ_{sys} [μb/sr]	$d\sigma/d\Omega$ [μb/sr]	Δ_{stat} [μb/sr]	Δ_{sys} [μb/sr]	$d\sigma/d\Omega$ [μb/sr]	Δ_{stat} [μb/sr]	Δ_{sys} [μb/sr]	$d\sigma/d\Omega$ [μb/sr]	Δ_{stat} [μb/sr]	Δ_{sys} [μb/sr]
−0.90	0.1592	0.0068	0.0260	0.1734	0.0071	0.0498	0.1816	0.0061	0.0719	0.1963	0.0085	0.0830
−0.70	0.1610	0.0042	0.0646	0.1749	0.0049	0.0478	0.2094	0.0052	0.0675	0.2227	0.0049	0.0404
−0.50	0.1627	0.0060	0.0514	0.1966	0.0065	0.0376	0.2318	0.0053	0.0355	0.2669	0.0063	0.0251
−0.30	0.1878	0.0045	0.0308	0.2120	0.0063	0.0275	0.2511	0.0063	0.0234	0.2556	0.0059	0.0251
−0.10	0.1957	0.0063	0.0259	0.2283	0.0061	0.0257	0.2765	0.0076	0.0320	0.2793	0.0069	0.0248
0.10	0.1884	0.0060	0.0185	0.2198	0.0069	0.0182	0.2678	0.0065	0.0277	0.3090	0.0073	0.0239
0.30	0.1648	0.0070	0.0128	0.2203	0.0058	0.0158	0.2443	0.0076	0.0237	0.2853	0.0067	0.0211
0.50	0.1236	0.0081	0.0124	0.1650	0.0083	0.0168	0.2194	0.0090	0.0248	0.2209	0.0094	0.0247
0.70	0.1419	0.0082	0.0483	0.1012	0.0116	0.0270	0.1153	0.0108	0.0212	0.1587	0.0103	0.0434
0.90	−0.0101	0.0379	0.0058	0.1085	0.0273	0.0520	0.0594	0.0267	0.0227	−0.0203	0.0310	−0.0155

$\cos(\theta^*_{2\pi^0})$	$W=(1400.0\pm4.0)$ MeV			$W=(1408.0\pm4.0)$ MeV			$W=(1416.0\pm4.0)$ MeV			$W=(1424.0\pm4.0)$ MeV		
	$d\sigma/d\Omega$ [μb/sr]	Δ_{stat} [μb/sr]	Δ_{sys} [μb/sr]	$d\sigma/d\Omega$ [μb/sr]	Δ_{stat} [μb/sr]	Δ_{sys} [μb/sr]	$d\sigma/d\Omega$ [μb/sr]	Δ_{stat} [μb/sr]	Δ_{sys} [μb/sr]	$d\sigma/d\Omega$ [μb/sr]	Δ_{stat} [μb/sr]	Δ_{sys} [μb/sr]
−0.90	0.2363	0.0076	0.0531	0.3358	0.0083	0.1385	0.3397	0.0076	0.0552	0.3840	0.0094	0.0743
−0.70	0.2497	0.0062	0.0381	0.2880	0.0068	0.0704	0.3181	0.0068	0.0415	0.3618	0.0079	0.0397
−0.50	0.2681	0.0059	0.0351	0.3169	0.0061	0.0384	0.3582	0.0070	0.0312	0.3869	0.0077	0.0280
−0.30	0.2959	0.0059	0.0265	0.3375	0.0070	0.0259	0.3783	0.0062	0.0256	0.4003	0.0080	0.0269
−0.10	0.3169	0.0060	0.0270	0.3718	0.0084	0.0259	0.3972	0.0084	0.0245	0.4350	0.0081	0.0246
0.10	0.3408	0.0079	0.0298	0.3624	0.0091	0.0239	0.4036	0.0089	0.0218	0.4332	0.0088	0.0221
0.30	0.3168	0.0081	0.0238	0.3413	0.0096	0.0243	0.3668	0.0096	0.0174	0.4049	0.0096	0.0206
0.50	0.2746	0.0106	0.0207	0.3159	0.0099	0.0380	0.3318	0.0096	0.0219	0.3609	0.0106	0.0233
0.70	0.2142	0.0105	0.0347	0.2077	0.0113	0.0400	0.2044	0.0130	0.0374	0.2674	0.0146	0.0484
0.90	0.1415	0.0260	0.0420	0.1308	0.0231	0.0333	0.1093	0.0348	0.0429	0.0365	0.0410	0.0286

$\cos(\theta^*_{2\pi^0})$	$W=(1432.0\pm4.0)$ MeV			$W=(1440.0\pm4.0)$ MeV			$W=(1448.0\pm4.0)$ MeV			$W=(1456.0\pm4.0)$ MeV		
	$d\sigma/d\Omega$ [μb/sr]	Δ_{stat} [μb/sr]	Δ_{sys} [μb/sr]	$d\sigma/d\Omega$ [μb/sr]	Δ_{stat} [μb/sr]	Δ_{sys} [μb/sr]	$d\sigma/d\Omega$ [μb/sr]	Δ_{stat} [μb/sr]	Δ_{sys} [μb/sr]	$d\sigma/d\Omega$ [μb/sr]	Δ_{stat} [μb/sr]	Δ_{sys} [μb/sr]
−0.90	0.4405	0.0095	0.0698	0.4721	0.0111	0.0495	0.5747	0.0114	0.0739	0.5792	0.0123	0.0563
−0.70	0.3786	0.0072	0.0353	0.4451	0.0092	0.0289	0.4623	0.0089	0.0326	0.5306	0.0088	0.0297
−0.50	0.4263	0.0074	0.0224	0.4448	0.0080	0.0263	0.4560	0.0082	0.0231	0.5023	0.0096	0.0207
−0.30	0.4497	0.0083	0.0215	0.4714	0.0081	0.0275	0.4964	0.0091	0.0224	0.5467	0.0098	0.0214
−0.10	0.4663	0.0090	0.0240	0.4945	0.0091	0.0233	0.5107	0.0094	0.0248	0.5438	0.0102	0.0212
0.10	0.4574	0.0098	0.0234	0.4827	0.0099	0.0218	0.5261	0.0108	0.0235	0.5563	0.0105	0.0222
0.30	0.4490	0.0097	0.0243	0.4790	0.0106	0.0215	0.4956	0.0108	0.0206	0.5337	0.0122	0.0221
0.50	0.3617	0.0110	0.0157	0.3985	0.0118	0.0186	0.4743	0.0121	0.0222	0.5051	0.0121	0.0259
0.70	0.2908	0.0146	0.0423	0.2894	0.0147	0.0455	0.3521	0.0137	0.0288	0.3777	0.0132	0.0468
0.90	0.0954	0.0368	0.0457	−0.0012	0.0350	−0.0100	0.1911	0.0251	0.0418	0.1492	0.0260	0.0436

$\cos(\theta^*_{2\pi^0})$	$W=(1464.0\pm4.0)$ MeV			$W=(1472.0\pm4.0)$ MeV			$W=(1480.0\pm4.0)$ MeV			$W=(1488.0\pm4.0)$ MeV		
	$d\sigma/d\Omega$ [μb/sr]	Δ_{stat} [μb/sr]	Δ_{sys} [μb/sr]	$d\sigma/d\Omega$ [μb/sr]	Δ_{stat} [μb/sr]	Δ_{sys} [μb/sr]	$d\sigma/d\Omega$ [μb/sr]	Δ_{stat} [μb/sr]	Δ_{sys} [μb/sr]	$d\sigma/d\Omega$ [μb/sr]	Δ_{stat} [μb/sr]	Δ_{sys} [μb/sr]
−0.90	0.6937	0.0129	0.0398	0.7098	0.0130	0.0828	0.8418	0.0147	0.0674	0.9606	0.0168	0.0666
−0.70	0.5493	0.0098	0.0287	0.6065	0.0105	0.0298	0.6713	0.0106	0.0393	0.7207	0.0125	0.0339
−0.50	0.5593	0.0093	0.0250	0.5902	0.0104	0.0235	0.6437	0.0103	0.0252	0.6650	0.0109	0.0247
−0.30	0.5565	0.0096	0.0212	0.5901	0.0100	0.0247	0.6251	0.0104	0.0207	0.6534	0.0105	0.0239
−0.10	0.5607	0.0109	0.0187	0.5995	0.0100	0.0255	0.6422	0.0113	0.0217	0.6271	0.0119	0.0261
0.10	0.5900	0.0108	0.0211	0.5977	0.0116	0.0255	0.6142	0.0120	0.0230	0.6437	0.0117	0.0308
0.30	0.5548	0.0117	0.0219	0.5853	0.0114	0.0224	0.5920	0.0131	0.0201	0.6175	0.0126	0.0289
0.50	0.4815	0.0140	0.0277	0.5179	0.0125	0.0198	0.5130	0.0145	0.0197	0.5386	0.0142	0.0161
0.70	0.3642	0.0141	0.0417	0.4076	0.0156	0.0396	0.4171	0.0162	0.0360	0.4566	0.0149	0.0536
0.90	0.3622	0.0217	0.0770	0.0672	0.0257	0.0111	0.3022	0.0264	0.0678	0.2147	0.0326	0.0805

$\cos(\theta^*_{2\pi^0})$	$W=(1496.0\pm4.0)$ MeV			$W=(1504.0\pm4.0)$ MeV			$W=(1512.0\pm4.0)$ MeV			$W=(1520.0\pm4.0)$ MeV		
	$d\sigma/d\Omega$ [μb/sr]	Δ_{stat} [μb/sr]	Δ_{sys} [μb/sr]	$d\sigma/d\Omega$ [μb/sr]	Δ_{stat} [μb/sr]	Δ_{sys} [μb/sr]	$d\sigma/d\Omega$ [μb/sr]	Δ_{stat} [μb/sr]	Δ_{sys} [μb/sr]	$d\sigma/d\Omega$ [μb/sr]	Δ_{stat} [μb/sr]	Δ_{sys} [μb/sr]
−0.90	1.0020	0.0193	0.1246	1.0557	0.0180	0.1035	1.1457	0.0192	0.0940	1.1784	0.0192	0.0641
−0.70	0.7875	0.0124	0.0477	0.7754	0.0132	0.0355	0.8641	0.0147	0.0406	0.8287	0.0145	0.0376
−0.50	0.6761	0.0123	0.0270	0.6941	0.0118	0.0260	0.6936	0.0117	0.0252	0.6870	0.0129	0.0253
−0.30	0.6372	0.0113	0.0203	0.6485	0.0120	0.0254	0.6530	0.0109	0.0204	0.6085	0.0113	0.0214
−0.10	0.6377	0.0120	0.0246	0.6686	0.0122	0.0309	0.6322	0.0121	0.0198	0.5829	0.0115	0.0223
0.10	0.6163	0.0126	0.0355	0.6491	0.0123	0.0322	0.6108	0.0128	0.0301	0.6095	0.0122	0.0322
0.30	0.6251	0.0140	0.0420	0.6365	0.0135	0.0384	0.6104	0.0140	0.0373	0.5650	0.0126	0.0373
0.50	0.5521	0.0149	0.0309	0.5723	0.0143	0.0497	0.5493	0.0145	0.0321	0.5582	0.0140	0.0384
0.70	0.4451	0.0177	0.0428	0.4471	0.0187	0.0472	0.4712	0.0171	0.0492	0.4805	0.0151	0.0489
0.90	0.2800	0.0288	0.0813	0.3468	0.0308	0.0561	0.3160	0.0323	0.0814	0.3381	0.0222	0.0610

$\cos(\theta^*_{2\pi^0})$	$W=(1528.0\pm4.0)$ MeV			$W=(1536.0\pm4.0)$ MeV			$W=(1544.0\pm4.0)$ MeV			$W=(1552.0\pm4.0)$ MeV		
	$d\sigma/d\Omega$ [μb/sr]	Δ_{stat} [μb/sr]	Δ_{sys} [μb/sr]	$d\sigma/d\Omega$ [μb/sr]	Δ_{stat} [μb/sr]	Δ_{sys} [μb/sr]	$d\sigma/d\Omega$ [μb/sr]	Δ_{stat} [μb/sr]	Δ_{sys} [μb/sr]	$d\sigma/d\Omega$ [μb/sr]	Δ_{stat} [μb/sr]	Δ_{sys} [μb/sr]
−0.90	1.2307	0.0189	0.0867	1.1773	0.0200	0.0849	1.1941	0.0199	0.0720	1.1471	0.0194	0.0606
−0.70	0.8713	0.0139	0.0341	0.8489	0.0136	0.0335	0.8314	0.0139	0.0289	0.8011	0.0143	0.0226
−0.50	0.6835	0.0125	0.0230	0.6509	0.0129	0.0172	0.6363	0.0125	0.0204	0.6143	0.0130	0.0145
−0.30	0.6084	0.0113	0.0229	0.6179	0.0117	0.0206	0.5476	0.0117	0.0229	0.5691	0.0109	0.0188
−0.10	0.5964	0.0116	0.0321	0.5593	0.0111	0.0234	0.5416	0.0113	0.0283	0.5249	0.0115	0.0264
0.10	0.5824	0.0130	0.0395	0.5277	0.0118	0.0294	0.5283	0.0115	0.0334	0.5091	0.0113	0.0339
0.30	0.5458	0.0130	0.0360	0.5100	0.0117	0.0353	0.5107	0.0128	0.0352	0.5069	0.0115	0.0388
0.50	0.5293	0.0131	0.0377	0.4758	0.0147	0.0365	0.4932	0.0133	0.0345	0.4705	0.0142	0.0401
0.70	0.4645	0.0163	0.0427	0.4347	0.0185	0.0485	0.4098	0.0157	0.0334	0.4044	0.0141	0.0386
0.90	0.3605	0.0258	0.0564	0.3392	0.0303	0.0583	0.3747	0.0227	0.0547	0.3001	0.0277	0.0365

$\cos(\theta^*_{2\pi^0})$	$W=(1560.0\pm4.0)$ MeV			$W=(1568.0\pm4.0)$ MeV			$W=(1576.0\pm4.0)$ MeV			$W=(1584.0\pm4.0)$ MeV		
	$d\sigma/d\Omega$ [μb/sr]	Δ_{stat} [μb/sr]	Δ_{sys} [μb/sr]	$d\sigma/d\Omega$ [μb/sr]	Δ_{stat} [μb/sr]	Δ_{sys} [μb/sr]	$d\sigma/d\Omega$ [μb/sr]	Δ_{stat} [μb/sr]	Δ_{sys} [μb/sr]	$d\sigma/d\Omega$ [μb/sr]	Δ_{stat} [μb/sr]	Δ_{sys} [μb/sr]
−0.90	1.1207	0.0195	0.0553	1.1255	0.0186	0.0698	1.1172	0.0206	0.0535	1.0876	0.0194	0.0457
−0.70	0.7992	0.0136	0.0233	0.8276	0.0145	0.0285	0.7873	0.0133	0.0311	0.7713	0.0146	0.0267
−0.50	0.6145	0.0122	0.0168	0.6099	0.0123	0.0140	0.6014	0.0138	0.0222	0.6088	0.0122	0.0200
−0.30	0.5608	0.0114	0.0215	0.5297	0.0119	0.0191	0.5284	0.0113	0.0215	0.5423	0.0115	0.0209
−0.10	0.5270	0.0108	0.0257	0.5183	0.0119	0.0275	0.5487	0.0112	0.0240	0.5284	0.0114	0.0265
0.10	0.5049	0.0119	0.0290	0.4755	0.0127	0.0274	0.4817	0.0120	0.0234	0.4840	0.0115	0.0289
0.30	0.4550	0.0131	0.0294	0.4655	0.0124	0.0280	0.4803	0.0117	0.0310	0.4513	0.0118	0.0232
0.50	0.4544	0.0132	0.0289	0.4493	0.0140	0.0254	0.4392	0.0151	0.0275	0.4587	0.0126	0.0237
0.70	0.4170	0.0145	0.0385	0.4121	0.0143	0.0477	0.3980	0.0159	0.0739	0.3523	0.0139	0.0334
0.90	0.2790	0.0260	0.0388	0.2203	0.0272	0.0758	0.2610	0.0291	0.0451	0.2703	0.0284	0.0556

$\cos(\theta^*_{2\pi^0})$	$W=(1592.0\pm4.0)$ MeV			$W=(1600.0\pm4.0)$ MeV			$W=(1608.0\pm4.0)$ MeV			$W=(1616.0\pm4.0)$ MeV		
	$d\sigma/d\Omega$ [μb/sr]	Δ_{stat} [μb/sr]	Δ_{sys} [μb/sr]	$d\sigma/d\Omega$ [μb/sr]	Δ_{stat} [μb/sr]	Δ_{sys} [μb/sr]	$d\sigma/d\Omega$ [μb/sr]	Δ_{stat} [μb/sr]	Δ_{sys} [μb/sr]	$d\sigma/d\Omega$ [μb/sr]	Δ_{stat} [μb/sr]	Δ_{sys} [μb/sr]
−0.90	1.1341	0.0195	0.0619	1.1230	0.0195	0.0629	1.1195	0.0196	0.0755	1.1288	0.0230	0.0463
−0.70	0.7575	0.0137	0.0290	0.7605	0.0155	0.0334	0.7885	0.0143	0.0301	0.7904	0.0150	0.0225
−0.50	0.6053	0.0128	0.0188	0.6346	0.0131	0.0223	0.6146	0.0132	0.0180	0.6145	0.0124	0.0152
−0.30	0.5471	0.0116	0.0189	0.5358	0.0123	0.0199	0.5543	0.0111	0.0172	0.5645	0.0111	0.0134
−0.10	0.5048	0.0113	0.0256	0.5266	0.0111	0.0257	0.5368	0.0103	0.0209	0.5502	0.0120	0.0156
0.10	0.4621	0.0117	0.0295	0.4720	0.0118	0.0215	0.4864	0.0110	0.0214	0.5324	0.0109	0.0172
0.30	0.4507	0.0126	0.0268	0.4577	0.0115	0.0177	0.4795	0.0127	0.0190	0.5063	0.0120	0.0129
0.50	0.4481	0.0133	0.0314	0.4274	0.0121	0.0286	0.4421	0.0118	0.0241	0.4442	0.0135	0.0150
0.70	0.3724	0.0145	0.0376	0.4079	0.0135	0.0468	0.4095	0.0129	0.0411	0.3939	0.0121	0.0294
0.90	0.3275	0.0262	0.0651	0.3556	0.0285	0.0529	0.3366	0.0255	0.0600	0.2623	0.0175	0.0401

$\cos(\theta^*_{2\pi^0})$	$W=(1624.0\pm4.0)$ MeV			$W=(1632.0\pm4.0)$ MeV			$W=(1640.0\pm4.0)$ MeV			$W=(1648.0\pm4.0)$ MeV		
	$d\sigma/d\Omega$ [μb/sr]	Δ_{stat} [μb/sr]	Δ_{sys} [μb/sr]	$d\sigma/d\Omega$ [μb/sr]	Δ_{stat} [μb/sr]	Δ_{sys} [μb/sr]	$d\sigma/d\Omega$ [μb/sr]	Δ_{stat} [μb/sr]	Δ_{sys} [μb/sr]	$d\sigma/d\Omega$ [μb/sr]	Δ_{stat} [μb/sr]	Δ_{sys} [μb/sr]
−0.90	1.1271	0.0208	0.0771	1.0545	0.0191	0.0630	1.1089	0.0183	0.0774	1.0372	0.0179	0.0592
−0.70	0.7755	0.0154	0.0301	0.7755	0.0139	0.0264	0.7923	0.0137	0.0269	0.7679	0.0136	0.0270
−0.50	0.6379	0.0117	0.0221	0.6256	0.0127	0.0163	0.6394	0.0120	0.0155	0.6525	0.0117	0.0178
−0.30	0.5824	0.0109	0.0226	0.5965	0.0108	0.0151	0.5921	0.0104	0.0164	0.6026	0.0103	0.0157
−0.10	0.5717	0.0116	0.0211	0.5964	0.0098	0.0203	0.5939	0.0104	0.0215	0.5895	0.0115	0.0154
0.10	0.5304	0.0114	0.0170	0.5678	0.0113	0.0236	0.5917	0.0125	0.0212	0.6168	0.0115	0.0207
0.30	0.5397	0.0122	0.0129	0.5561	0.0110	0.0216	0.5709	0.0118	0.0172	0.5799	0.0117	0.0221
0.50	0.4590	0.0116	0.0123	0.4949	0.0143	0.0254	0.5064	0.0121	0.0249	0.5123	0.0108	0.0206
0.70	0.4037	0.0140	0.0293	0.3720	0.0126	0.0323	0.3815	0.0117	0.0348	0.4209	0.0119	0.0234
0.90	0.2739	0.0226	0.0504	0.3108	0.0242	0.0439	0.3168	0.0238	0.0597	0.3096	0.0240	0.0249

$\cos(\theta^*_{2\pi^0})$	$W=(1656.0\pm4.0)$ MeV			$W=(1664.0\pm4.0)$ MeV			$W=(1672.0\pm4.0)$ MeV			$W=(1680.0\pm4.0)$ MeV		
	$d\sigma/d\Omega$ [μb/sr]	Δ_{stat} [μb/sr]	Δ_{sys} [μb/sr]	$d\sigma/d\Omega$ [μb/sr]	Δ_{stat} [μb/sr]	Δ_{sys} [μb/sr]	$d\sigma/d\Omega$ [μb/sr]	Δ_{stat} [μb/sr]	Δ_{sys} [μb/sr]	$d\sigma/d\Omega$ [μb/sr]	Δ_{stat} [μb/sr]	Δ_{sys} [μb/sr]
−0.90	1.0310	0.0183	0.0531	0.9959	0.0181	0.0610	0.9617	0.0193	0.0634	0.9668	0.0160	0.0634
−0.70	0.7602	0.0150	0.0243	0.7352	0.0127	0.0217	0.6984	0.0126	0.0305	0.7298	0.0128	0.0223
−0.50	0.6166	0.0131	0.0146	0.6132	0.0128	0.0118	0.6257	0.0115	0.0171	0.6618	0.0125	0.0122
−0.30	0.6537	0.0117	0.0126	0.6254	0.0121	0.0140	0.6588	0.0111	0.0140	0.6744	0.0121	0.0146
−0.10	0.6539	0.0121	0.0150	0.6711	0.0131	0.0186	0.6540	0.0133	0.0143	0.6802	0.0120	0.0138
0.10	0.6153	0.0137	0.0164	0.6552	0.0135	0.0172	0.6977	0.0130	0.0135	0.6696	0.0127	0.0101
0.30	0.5965	0.0130	0.0175	0.6050	0.0133	0.0127	0.6128	0.0122	0.0107	0.6550	0.0129	0.0099
0.50	0.5331	0.0134	0.0147	0.5480	0.0119	0.0101	0.5434	0.0136	0.0186	0.5792	0.0123	0.0181
0.70	0.4663	0.0114	0.0211	0.4755	0.0128	0.0315	0.3954	0.0134	0.0244	0.4416	0.0122	0.0352
0.90	0.2391	0.0229	0.0214	0.2855	0.0246	0.0678	0.3645	0.0234	0.0321	0.2391	0.0227	0.0647

$\cos(\theta^*_{2\pi^0})$	$W=(1688.0\pm4.0)$ MeV			$W=(1696.0\pm4.0)$ MeV			$W=(1704.0\pm4.0)$ MeV			$W=(1712.0\pm4.0)$ MeV		
	$d\sigma/d\Omega$ [μb/sr]	Δ_{stat} [μb/sr]	Δ_{sys} [μb/sr]	$d\sigma/d\Omega$ [μb/sr]	Δ_{stat} [μb/sr]	Δ_{sys} [μb/sr]	$d\sigma/d\Omega$ [μb/sr]	Δ_{stat} [μb/sr]	Δ_{sys} [μb/sr]	$d\sigma/d\Omega$ [μb/sr]	Δ_{stat} [μb/sr]	Δ_{sys} [μb/sr]
−0.90	0.9544	0.0189	0.0751	0.9100	0.0165	0.0587	0.8557	0.0181	0.0470	0.8012	0.0170	0.0439
−0.70	0.7227	0.0132	0.0264	0.6912	0.0135	0.0266	0.6543	0.0113	0.0267	0.5812	0.0138	0.0232
−0.50	0.6628	0.0116	0.0175	0.6078	0.0117	0.0164	0.6168	0.0120	0.0177	0.5738	0.0121	0.0149
−0.30	0.6427	0.0118	0.0145	0.6457	0.0107	0.0128	0.6406	0.0100	0.0123	0.5880	0.0099	0.0099
−0.10	0.7026	0.0135	0.0116	0.6875	0.0128	0.0142	0.6637	0.0118	0.0112	0.6374	0.0118	0.0103
0.10	0.6900	0.0127	0.0099	0.6695	0.0123	0.0146	0.6660	0.0116	0.0121	0.6359	0.0121	0.0100
0.30	0.6518	0.0137	0.0124	0.6523	0.0146	0.0137	0.6058	0.0133	0.0106	0.6030	0.0137	0.0092
0.50	0.5601	0.0119	0.0161	0.5556	0.0128	0.0164	0.5521	0.0133	0.0097	0.5106	0.0129	0.0136
0.70	0.4624	0.0130	0.0304	0.4589	0.0127	0.0262	0.4214	0.0120	0.0252	0.4017	0.0109	0.0230
0.90	0.2687	0.0229	0.0400	0.2946	0.0193	0.0352	0.2486	0.0198	0.0485	0.2909	0.0199	0.0277

$\cos(\theta^*_{2\pi^0})$	$W=(1720.0\pm4.0)$ MeV			$W=(1728.0\pm4.0)$ MeV			$W=(1736.0\pm4.0)$ MeV			$W=(1744.0\pm4.0)$ MeV		
	$d\sigma/d\Omega$ [μb/sr]	Δ_{stat} [μb/sr]	Δ_{sys} [μb/sr]	$d\sigma/d\Omega$ [μb/sr]	Δ_{stat} [μb/sr]	Δ_{sys} [μb/sr]	$d\sigma/d\Omega$ [μb/sr]	Δ_{stat} [μb/sr]	Δ_{sys} [μb/sr]	$d\sigma/d\Omega$ [μb/sr]	Δ_{stat} [μb/sr]	Δ_{sys} [μb/sr]
−0.90	0.8089	0.0161	0.0628	0.7552	0.0156	0.0566	0.6517	0.0152	0.0520	0.6101	0.0132	0.0531
−0.70	0.5828	0.0114	0.0284	0.5645	0.0094	0.0233	0.5011	0.0099	0.0224	0.4743	0.0095	0.0188
−0.50	0.5560	0.0099	0.0189	0.5445	0.0108	0.0143	0.5155	0.0096	0.0160	0.4686	0.0103	0.0094
−0.30	0.5623	0.0095	0.0118	0.5664	0.0092	0.0107	0.5235	0.0113	0.0127	0.5332	0.0094	0.0073
−0.10	0.6398	0.0118	0.0083	0.6234	0.0106	0.0115	0.5874	0.0108	0.0084	0.5596	0.0116	0.0081
0.10	0.6566	0.0115	0.0097	0.6189	0.0121	0.0126	0.6009	0.0109	0.0060	0.5671	0.0120	0.0099
0.30	0.5829	0.0138	0.0124	0.5691	0.0129	0.0117	0.5340	0.0111	0.0101	0.5183	0.0122	0.0093
0.50	0.4918	0.0122	0.0132	0.4591	0.0094	0.0114	0.4747	0.0128	0.0130	0.4557	0.0111	0.0111
0.70	0.3498	0.0122	0.0156	0.3883	0.0118	0.0173	0.3868	0.0109	0.0191	0.3882	0.0109	0.0225
0.90	0.3535	0.0212	0.0365	0.2838	0.0180	0.0353	0.2929	0.0189	0.0462	0.2451	0.0174	0.0685

$\cos(\theta^*_{2\pi^0})$	$W=(1752.0\pm4.0)$ MeV			$W=(1760.0\pm4.0)$ MeV			$W=(1768.0\pm4.0)$ MeV			$W=(1776.0\pm4.0)$ MeV		
	$d\sigma/d\Omega$ [μb/sr]	Δ_{stat} [μb/sr]	Δ_{sys} [μb/sr]	$d\sigma/d\Omega$ [μb/sr]	Δ_{stat} [μb/sr]	Δ_{sys} [μb/sr]	$d\sigma/d\Omega$ [μb/sr]	Δ_{stat} [μb/sr]	Δ_{sys} [μb/sr]	$d\sigma/d\Omega$ [μb/sr]	Δ_{stat} [μb/sr]	Δ_{sys} [μb/sr]
−0.90	0.5985	0.0128	0.0439	0.5452	0.0136	0.0413	0.5608	0.0121	0.0487	0.5021	0.0141	0.0338
−0.70	0.4481	0.0102	0.0160	0.4289	0.0090	0.0169	0.3957	0.0080	0.0169	0.3866	0.0081	0.0148
−0.50	0.4502	0.0092	0.0095	0.4398	0.0095	0.0097	0.3968	0.0092	0.0100	0.3852	0.0088	0.0084
−0.30	0.5127	0.0100	0.0082	0.4702	0.0084	0.0090	0.4373	0.0086	0.0091	0.4498	0.0082	0.0080
−0.10	0.5399	0.0112	0.0096	0.5237	0.0094	0.0103	0.4689	0.0093	0.0092	0.4767	0.0087	0.0121
0.10	0.5405	0.0110	0.0114	0.5057	0.0097	0.0114	0.4617	0.0100	0.0085	0.4579	0.0098	0.0142
0.30	0.5146	0.0111	0.0100	0.4877	0.0100	0.0118	0.4559	0.0107	0.0070	0.4259	0.0092	0.0120
0.50	0.4004	0.0125	0.0080	0.4400	0.0116	0.0124	0.3602	0.0092	0.0088	0.4041	0.0108	0.0099
0.70	0.3592	0.0116	0.0208	0.3587	0.0094	0.0241	0.3261	0.0097	0.0230	0.2860	0.0109	0.0143
0.90	0.2797	0.0253	0.0440	0.2332	0.0216	0.0256	0.1490	0.0220	0.0311	0.2678	0.0180	0.0509

$\cos(\theta^*_{2\pi^0})$	$W=(1784.0\pm4.0)$ MeV			$W=(1792.0\pm4.0)$ MeV			$W=(1800.0\pm4.0)$ MeV			$W=(1808.0\pm4.0)$ MeV		
	$d\sigma/d\Omega$ [μb/sr]	Δ_{stat} [μb/sr]	Δ_{sys} [μb/sr]	$d\sigma/d\Omega$ [μb/sr]	Δ_{stat} [μb/sr]	Δ_{sys} [μb/sr]	$d\sigma/d\Omega$ [μb/sr]	Δ_{stat} [μb/sr]	Δ_{sys} [μb/sr]	$d\sigma/d\Omega$ [μb/sr]	Δ_{stat} [μb/sr]	Δ_{sys} [μb/sr]
−0.90	0.4122	0.0132	0.0325	0.3914	0.0120	0.0386	0.3984	0.0134	0.0302	0.4300	0.0127	0.0256
−0.70	0.3906	0.0079	0.0149	0.3413	0.0095	0.0144	0.3291	0.0082	0.0139	0.3397	0.0093	0.0122
−0.50	0.3792	0.0097	0.0084	0.3983	0.0082	0.0109	0.3705	0.0075	0.0110	0.3165	0.0091	0.0111
−0.30	0.4270	0.0081	0.0071	0.3751	0.0079	0.0108	0.3749	0.0077	0.0109	0.3696	0.0080	0.0105
−0.10	0.4674	0.0088	0.0074	0.4416	0.0086	0.0111	0.4143	0.0074	0.0108	0.3831	0.0077	0.0079
0.10	0.4202	0.0088	0.0094	0.4141	0.0079	0.0076	0.4085	0.0090	0.0082	0.4168	0.0074	0.0083
0.30	0.3837	0.0104	0.0094	0.3938	0.0088	0.0071	0.3462	0.0082	0.0068	0.3838	0.0105	0.0084
0.50	0.3271	0.0100	0.0076	0.3258	0.0103	0.0093	0.3429	0.0089	0.0083	0.3229	0.0091	0.0074
0.70	0.3174	0.0114	0.0185	0.2983	0.0111	0.0224	0.3262	0.0106	0.0229	0.2661	0.0102	0.0149
0.90	0.2670	0.0250	0.0497	0.2162	0.0203	0.0703	0.1605	0.0199	0.0340	0.2767	0.0221	0.0662

$\cos(\theta^*_{2\pi^0})$	$W=(1816.0\pm4.0)$ MeV			$W=(1824.0\pm4.0)$ MeV			$W=(1832.0\pm4.0)$ MeV			$W=(1840.0\pm4.0)$ MeV		
	$d\sigma/d\Omega$ [μb/sr]	Δ_{stat} [μb/sr]	Δ_{sys} [μb/sr]	$d\sigma/d\Omega$ [μb/sr]	Δ_{stat} [μb/sr]	Δ_{sys} [μb/sr]	$d\sigma/d\Omega$ [μb/sr]	Δ_{stat} [μb/sr]	Δ_{sys} [μb/sr]	$d\sigma/d\Omega$ [μb/sr]	Δ_{stat} [μb/sr]	Δ_{sys} [μb/sr]
−0.90	0.3584	0.0111	0.0335	0.3740	0.0110	0.0274	0.3468	0.0098	0.0267	0.3574	0.0104	0.0343
−0.70	0.3334	0.0075	0.0125	0.3300	0.0093	0.0125	0.3348	0.0083	0.0211	0.3100	0.0083	0.0125
−0.50	0.3259	0.0088	0.0080	0.3055	0.0088	0.0081	0.2852	0.0099	0.0100	0.2985	0.0079	0.0139
−0.30	0.3543	0.0071	0.0102	0.3411	0.0081	0.0094	0.3305	0.0080	0.0088	0.3273	0.0075	0.0104
−0.10	0.3980	0.0074	0.0125	0.3416	0.0079	0.0088	0.3986	0.0084	0.0080	0.3790	0.0074	0.0079
0.10	0.3782	0.0075	0.0123	0.3760	0.0092	0.0090	0.3588	0.0086	0.0093	0.3667	0.0085	0.0068
0.30	0.3320	0.0090	0.0113	0.3847	0.0099	0.0087	0.3140	0.0113	0.0109	0.3235	0.0118	0.0067
0.50	0.3065	0.0099	0.0089	0.3060	0.0118	0.0082	0.2886	0.0104	0.0086	0.2884	0.0119	0.0089
0.70	0.2812	0.0112	0.0207	0.2473	0.0110	0.0314	0.2779	0.0124	0.0240	0.2552	0.0133	0.0200
0.90	0.1568	0.0214	0.0329	0.1698	0.0207	0.0538	0.1967	0.0262	0.0625	0.1406	0.0265	0.0266

$\cos(\theta^*_{2\pi^0})$	$W=(1848.0\pm4.0)$ MeV			$W=(1856.0\pm4.0)$ MeV			$W=(1864.0\pm4.0)$ MeV			$W=(1872.0\pm4.0)$ MeV		
	$d\sigma/d\Omega$ [μb/sr]	Δ_{stat} [μb/sr]	Δ_{sys} [μb/sr]	$d\sigma/d\Omega$ [μb/sr]	Δ_{stat} [μb/sr]	Δ_{sys} [μb/sr]	$d\sigma/d\Omega$ [μb/sr]	Δ_{stat} [μb/sr]	Δ_{sys} [μb/sr]	$d\sigma/d\Omega$ [μb/sr]	Δ_{stat} [μb/sr]	Δ_{sys} [μb/sr]
−0.90	0.3587	0.0117	0.0347	0.2852	0.0128	0.0292	0.3323	0.0160	0.0382	0.3257	0.0173	0.0366
−0.70	0.3057	0.0105	0.0128	0.3497	0.0102	0.0140	0.2891	0.0090	0.0140	0.3231	0.0099	0.0259
−0.50	0.2993	0.0083	0.0055	0.2759	0.0080	0.0083	0.3241	0.0091	0.0097	0.3011	0.0101	0.0207
−0.30	0.3408	0.0081	0.0081	0.3004	0.0083	0.0104	0.3026	0.0092	0.0097	0.2966	0.0102	0.0126
−0.10	0.3512	0.0083	0.0139	0.3284	0.0097	0.0099	0.3529	0.0099	0.0121	0.3447	0.0100	0.0120
0.10	0.3410	0.0097	0.0135	0.3516	0.0104	0.0111	0.3513	0.0100	0.0098	0.3422	0.0107	0.0136
0.30	0.3428	0.0106	0.0095	0.3062	0.0092	0.0105	0.3283	0.0096	0.0123	0.2677	0.0131	0.0102
0.50	0.2790	0.0110	0.0110	0.2887	0.0118	0.0113	0.2427	0.0133	0.0096	0.2844	0.0124	0.0193
0.70	0.2562	0.0146	0.0447	0.2430	0.0114	0.0432	0.2339	0.0140	0.0418	0.2373	0.0133	0.0229
0.90	0.1651	0.0390	0.0569	0.1259	0.0280	0.0412	0.0999	0.0381	0.0583	0.1169	0.0395	0.0124

$\cos(\theta^*_{2\pi^0})$	$W=(1880.0\pm4.0)$ MeV			$W=(1888.0\pm4.0)$ MeV			$W=(1896.0\pm4.0)$ MeV		
	$d\sigma/d\Omega$ [μb/sr]	Δ_{stat} [μb/sr]	Δ_{sys} [μb/sr]	$d\sigma/d\Omega$ [μb/sr]	Δ_{stat} [μb/sr]	Δ_{sys} [μb/sr]	$d\sigma/d\Omega$ [μb/sr]	Δ_{stat} [μb/sr]	Δ_{sys} [μb/sr]
−0.90	0.2441	0.0156	0.0246	0.2831	0.0236	0.0329	0.2921	0.0305	0.0147
−0.70	0.3017	0.0115	0.0148	0.2122	0.0144	0.0169	0.2840	0.0164	0.0167
−0.50	0.3120	0.0137	0.0093	0.2494	0.0140	0.0149	0.2326	0.0154	0.0124
−0.30	0.3171	0.0101	0.0086	0.2982	0.0122	0.0130	0.2708	0.0138	0.0188
−0.10	0.3483	0.0107	0.0069	0.3462	0.0142	0.0198	0.3298	0.0162	0.0268
0.10	0.2822	0.0129	0.0099	0.3337	0.0134	0.0125	0.2725	0.0189	0.0297
0.30	0.2736	0.0159	0.0101	0.3084	0.0139	0.0070	0.2998	0.0165	0.0142
0.50	0.2910	0.0178	0.0165	0.2518	0.0137	0.0125	0.3433	0.0196	0.0234
0.70	0.2782	0.0157	0.0502	0.2083	0.0215	0.0324	0.1852	0.0226	0.0368
0.90	0.0389	0.0288	−0.0445	0.1266	0.0309	0.0369	0.1175	0.0428	0.0832

Decomposed Total Cross Sections

W [MeV]	ΔW [MeV]	$\sigma_{PhaseSpace}$ [μb]	Δ_{stat} [μb]	$\sigma_{\Delta(1232)}$ [μb]	Δ_{stat} [μb]	$\sigma_{N(1520)}$ [μb]	Δ_{stat} [μb]
1308.0	8.0	0.0118	0.0050	0.0273	0.0050	0.0014	0.0021
1324.0	8.0	0.1152	0.0134	0.0476	0.0103	0.0303	0.0109
1340.0	8.0	0.2470	0.0216	0.2212	0.0207	0.0246	0.0169
1356.0	8.0	0.5098	0.0317	0.3954	0.0280	0.1290	0.0346
1372.0	8.0	0.8115	0.0505	1.3157	0.0406	0.1756	0.0525
1388.0	8.0	0.5053	0.0638	1.9285	0.0594	0.2171	0.0736
1404.0	8.0	0.2802	0.0872	2.9465	0.0740	0.2180	0.0957
1420.0	8.0	0.3223	0.1106	3.4516	0.0878	0.1036	0.1032
1436.0	8.0	0.2662	0.1446	4.3146	0.1117	0.2361	0.1251
1452.0	8.0	0.3945	0.1594	5.3003	0.1291	0.0878	0.1600
1468.0	8.0	0.3702	0.1816	6.0646	0.1382	0.0603	0.1702
1484.0	8.0	0.3201	0.2009	6.9874	0.1581	0.0056	0.1828
1500.0	8.0	0.2169	0.2134	7.5158	0.1668	0.0097	0.1966
1516.0	8.0	0.1565	0.2149	7.6840	0.1946	0.0002	0.2340
1532.0	8.0	0.2208	0.2190	7.5522	0.2016	0.0001	0.2109
1548.0	8.0	0.0546	0.1779	7.2451	0.1331	0.0082	0.2222
1564.0	8.0	0.1249	0.1613	6.6932	0.1839	0.0218	0.1769
1580.0	8.0	0.2751	0.1786	6.5595	0.1599	0.0071	0.2104
1596.0	8.0	0.2888	0.1601	6.5204	0.1644	0.0031	0.2081
1612.0	8.0	0.3052	0.1742	6.6373	0.1639	0.0075	0.1883
1628.0	8.0	0.5026	0.1899	6.7090	0.1733	0.0225	0.2073
1644.0	8.0	0.9938	0.2166	6.5812	0.1783	0.0565	0.2184
1660.0	8.0	0.6748	0.2011	6.8168	0.1969	0.0310	0.2262
1676.0	8.0	1.0906	0.2207	6.6165	0.2214	0.0547	0.2258
1692.0	8.0	1.1057	0.2289	6.2666	0.2094	0.0733	0.2201
1708.0	8.0	0.8562	0.2082	5.8431	0.2017	0.2191	0.2006
1724.0	8.0	1.4680	0.2039	5.3697	0.1831	0.3720	0.1974
1740.0	8.0	1.3853	0.1649	4.5495	0.1655	0.0782	0.1764
1756.0	8.0	1.5181	0.1437	3.6130	0.1710	0.1845	0.1529
1772.0	8.0	1.5871	0.1358	2.9800	0.1494	0.3008	0.1434
1788.0	8.0	1.9516	0.1059	2.0064	0.1373	0.3947	0.1115
1804.0	8.0	1.9728	0.1133	1.8545	0.1287	0.3610	0.1098
1820.0	8.0	1.3912	0.1052	1.2926	0.1176	1.2036	0.1001
1836.0	8.0	1.1926	0.0993	1.4123	0.1083	0.9058	0.0990
1852.0	8.0	1.2103	0.0884	1.2387	0.1077	0.9460	0.0885
1868.0	8.0	1.2457	0.0951	1.2632	0.0980	0.8945	0.0895
1888.0	10.0	0.8355	0.0576	1.0027	0.0691	0.6531	0.0652

E.3.5 $\gamma p \to \pi^0\pi^0 p$ as a Function of W

Angular Distributions

	W=(1282.6±5.5) MeV			W=(1293.5±5.4) MeV			W=(1304.4±5.4) MeV			W=(1315.1±5.4) MeV		
$\cos(\theta^*_{2\pi^0})$	$d\sigma/d\Omega$ [μb/sr]	Δ_{stat} [μb/sr]	Δ_{sys} [μb/sr]	$d\sigma/d\Omega$ [μb/sr]	Δ_{stat} [μb/sr]	Δ_{sys} [μb/sr]	$d\sigma/d\Omega$ [μb/sr]	Δ_{stat} [μb/sr]	Δ_{sys} [μb/sr]	$d\sigma/d\Omega$ [μb/sr]	Δ_{stat} [μb/sr]	Δ_{sys} [μb/sr]
−0.90	0.0000	0.0000	0.0000	0.0026	0.0008	0.0212	0.0046	0.0004	0.0186	0.0111	0.0007	0.0111
−0.70	0.0000	0.0000	0.0000	0.0063	0.0008	−0.0133	0.0078	0.0005	0.0214	0.0165	0.0009	0.0150
−0.50	0.0000	0.0000	0.0000	0.0123	0.0013	0.0139	0.0176	0.0009	0.0105	0.0294	0.0013	0.0086
−0.30	0.0000	0.0000	0.0000	0.0224	0.0021	0.0110	0.0244	0.0011	0.0005	0.0418	0.0012	0.0051
−0.10	0.0000	0.0000	0.0000	0.0173	0.0018	0.0149	0.0233	0.0010	0.0018	0.0414	0.0014	0.0098
0.10	0.0000	0.0000	0.0000	0.0169	0.0025	0.0192	0.0241	0.0013	0.0058	0.0394	0.0012	0.0100
0.30	0.0000	0.0000	0.0000	0.0175	0.0053	0.0082	0.0218	0.0022	0.0091	0.0395	0.0023	0.0039
0.50	0.0000	0.0000	0.0000	0.0217	0.0216	0.0339	0.0380	0.0076	0.0179	0.0431	0.0071	0.0065
0.70	0.0000	0.0000	0.0000	0.0396	0.0212	0.0693	0.0088	0.0056	−0.0036	0.0240	0.0086	0.0370
0.90	0.0000	0.0000	0.0000	0.1020	0.0776	−0.0656	0.0007	0.0504	−0.0970	−0.0212	0.0313	−0.0637

	W=(1325.8±5.3) MeV			W=(1336.3±5.3) MeV			W=(1346.8±5.2) MeV			W=(1357.2±5.2) MeV		
$\cos(\theta^*_{2\pi^0})$	$d\sigma/d\Omega$ [μb/sr]	Δ_{stat} [μb/sr]	Δ_{sys} [μb/sr]	$d\sigma/d\Omega$ [μb/sr]	Δ_{stat} [μb/sr]	Δ_{sys} [μb/sr]	$d\sigma/d\Omega$ [μb/sr]	Δ_{stat} [μb/sr]	Δ_{sys} [μb/sr]	$d\sigma/d\Omega$ [μb/sr]	Δ_{stat} [μb/sr]	Δ_{sys} [μb/sr]
−0.90	0.0253	0.0009	0.0691	0.0401	0.0011	0.0915	0.0645	0.0011	0.0599	0.0908	0.0014	0.1041
−0.70	0.0332	0.0011	0.0262	0.0550	0.0010	0.0303	0.0905	0.0008	0.0395	0.1348	0.0017	0.0530
−0.50	0.0583	0.0014	0.0037	0.0917	0.0018	0.0032	0.1370	0.0014	0.0171	0.1902	0.0017	0.0223
−0.30	0.0764	0.0017	0.0066	0.1119	0.0019	0.0113	0.1705	0.0014	0.0252	0.2370	0.0023	0.0315
−0.10	0.0784	0.0012	0.0138	0.1111	0.0018	0.0193	0.1718	0.0014	0.0294	0.2295	0.0022	0.0365
0.10	0.0776	0.0018	0.0127	0.1047	0.0017	0.0160	0.1592	0.0018	0.0184	0.2175	0.0021	0.0263
0.30	0.0777	0.0017	0.0064	0.1047	0.0015	0.0058	0.1506	0.0016	0.0080	0.1934	0.0023	0.0090
0.50	0.0826	0.0058	0.0137	0.1034	0.0034	0.0081	0.1542	0.0027	0.0058	0.1973	0.0040	0.0108
0.70	0.0789	0.0133	−0.0220	0.0886	0.0149	0.0218	0.1226	0.0137	0.0140	0.1639	0.0103	0.0310
0.90	0.0121	0.0217	−0.0428	0.0579	0.0246	−0.0972	0.0151	0.0175	−0.0476	0.1006	0.0174	0.0086

	W=(1367.6±5.1) MeV			W=(1377.8±5.1) MeV			W=(1388.0±5.1) MeV			W=(1398.1±5.0) MeV		
$\cos(\theta^*_{2\pi^0})$	$d\sigma/d\Omega$ [μb/sr]	Δ_{stat} [μb/sr]	Δ_{sys} [μb/sr]	$d\sigma/d\Omega$ [μb/sr]	Δ_{stat} [μb/sr]	Δ_{sys} [μb/sr]	$d\sigma/d\Omega$ [μb/sr]	Δ_{stat} [μb/sr]	Δ_{sys} [μb/sr]	$d\sigma/d\Omega$ [μb/sr]	Δ_{stat} [μb/sr]	Δ_{sys} [μb/sr]
−0.90	0.1284	0.0017	0.1224	0.1656	0.0018	0.1021	0.2112	0.0018	0.1016	0.2635	0.0021	0.0957
−0.70	0.1911	0.0021	0.0540	0.2474	0.0017	0.0458	0.3126	0.0019	0.0401	0.3755	0.0023	0.0315
−0.50	0.2683	0.0021	0.0218	0.3378	0.0017	0.0317	0.3992	0.0025	0.0308	0.4639	0.0030	0.0301
−0.30	0.3083	0.0027	0.0372	0.3751	0.0027	0.0458	0.4565	0.0030	0.0468	0.5296	0.0033	0.0516
−0.10	0.3110	0.0025	0.0468	0.3842	0.0027	0.0435	0.4566	0.0029	0.0420	0.5292	0.0033	0.0447
0.10	0.2929	0.0025	0.0354	0.3566	0.0025	0.0322	0.4303	0.0027	0.0323	0.5044	0.0033	0.0327
0.30	0.2804	0.0027	0.0149	0.3375	0.0022	0.0188	0.3887	0.0027	0.0214	0.4427	0.0032	0.0227
0.50	0.2656	0.0040	0.0079	0.3044	0.0038	0.0135	0.3583	0.0037	0.0045	0.4040	0.0041	0.0119
0.70	0.2094	0.0073	0.0140	0.3091	0.0096	0.0149	0.3602	0.0075	0.0124	0.3869	0.0066	0.0216
0.90	0.1149	0.0213	0.0159	0.1376	0.0169	0.0311	0.1469	0.0087	0.0285	0.1565	0.0103	0.0254

$\cos(\theta^*_{2\pi^0})$	$W=(1408.1\pm5.0)$ MeV			$W=(1418.1\pm5.0)$ MeV			$W=(1428.0\pm4.9)$ MeV			$W=(1437.8\pm4.9)$ MeV		
	$d\sigma/d\Omega$ [μb/sr]	Δ_{stat} [μb/sr]	Δ_{sys} [μb/sr]	$d\sigma/d\Omega$ [μb/sr]	Δ_{stat} [μb/sr]	Δ_{sys} [μb/sr]	$d\sigma/d\Omega$ [μb/sr]	Δ_{stat} [μb/sr]	Δ_{sys} [μb/sr]	$d\sigma/d\Omega$ [μb/sr]	Δ_{stat} [μb/sr]	Δ_{sys} [μb/sr]
−0.90	0.3171	0.0019	0.0726	0.3618	0.0020	0.0578	0.4112	0.0022	0.0556	0.4636	0.0025	0.0420
−0.70	0.4326	0.0026	0.0168	0.4849	0.0022	0.0191	0.5286	0.0028	0.0175	0.5836	0.0031	0.0195
−0.50	0.5307	0.0032	0.0284	0.5807	0.0034	0.0297	0.6328	0.0035	0.0300	0.6859	0.0038	0.0304
−0.30	0.5880	0.0033	0.0498	0.6514	0.0035	0.0459	0.6873	0.0036	0.0433	0.7422	0.0039	0.0383
−0.10	0.5929	0.0033	0.0417	0.6583	0.0035	0.0381	0.6971	0.0037	0.0351	0.7526	0.0039	0.0308
0.10	0.5555	0.0032	0.0307	0.6206	0.0034	0.0299	0.6734	0.0036	0.0300	0.7125	0.0038	0.0269
0.30	0.4967	0.0031	0.0214	0.5450	0.0033	0.0235	0.5831	0.0034	0.0237	0.6327	0.0036	0.0242
0.50	0.4302	0.0037	0.0117	0.4722	0.0039	0.0078	0.5166	0.0038	0.0133	0.5525	0.0041	0.0148
0.70	0.4211	0.0063	0.0095	0.4482	0.0065	0.0144	0.4855	0.0068	0.0088	0.5188	0.0075	0.0118
0.90	0.2040	0.0104	0.0158	0.1920	0.0168	0.0415	0.1900	0.0121	0.0218	0.2271	0.0103	0.0269

$\cos(\theta^*_{2\pi^0})$	$W=(1447.6\pm4.9)$ MeV			$W=(1457.2\pm4.8)$ MeV			$W=(1466.9\pm4.8)$ MeV			$W=(1476.4\pm4.8)$ MeV		
	$d\sigma/d\Omega$ [μb/sr]	Δ_{stat} [μb/sr]	Δ_{sys} [μb/sr]	$d\sigma/d\Omega$ [μb/sr]	Δ_{stat} [μb/sr]	Δ_{sys} [μb/sr]	$d\sigma/d\Omega$ [μb/sr]	Δ_{stat} [μb/sr]	Δ_{sys} [μb/sr]	$d\sigma/d\Omega$ [μb/sr]	Δ_{stat} [μb/sr]	Δ_{sys} [μb/sr]
−0.90	0.5182	0.0029	0.0350	0.5773	0.0034	0.0291	0.6435	0.0034	0.0273	0.7272	0.0037	0.0268
−0.70	0.6233	0.0030	0.0245	0.6880	0.0033	0.0230	0.7441	0.0036	0.0272	0.7963	0.0039	0.0268
−0.50	0.7321	0.0041	0.0326	0.7713	0.0042	0.0305	0.8269	0.0043	0.0312	0.8706	0.0043	0.0269
−0.30	0.7848	0.0042	0.0355	0.8155	0.0043	0.0331	0.8754	0.0044	0.0288	0.9170	0.0046	0.0255
−0.10	0.7927	0.0042	0.0309	0.8449	0.0044	0.0294	0.8965	0.0045	0.0260	0.9251	0.0046	0.0256
0.10	0.7512	0.0040	0.0298	0.7978	0.0042	0.0294	0.8439	0.0043	0.0287	0.8660	0.0043	0.0292
0.30	0.6713	0.0039	0.0276	0.7182	0.0040	0.0309	0.7486	0.0041	0.0319	0.7804	0.0041	0.0341
0.50	0.5728	0.0041	0.0146	0.6147	0.0042	0.0163	0.6476	0.0042	0.0185	0.6833	0.0043	0.0239
0.70	0.5145	0.0074	0.0086	0.5498	0.0070	0.0076	0.5936	0.0069	0.0117	0.6173	0.0065	0.0100
0.90	0.3098	0.0150	0.0210	0.2329	0.0125	0.0210	0.2772	0.0154	0.0242	0.2140	0.0110	0.0150

$\cos(\theta^*_{2\pi^0})$	$W=(1485.9\pm4.7)$ MeV			$W=(1495.4\pm4.7)$ MeV			$W=(1504.8\pm4.7)$ MeV			$W=(1514.1\pm4.6)$ MeV		
	$d\sigma/d\Omega$ [μb/sr]	Δ_{stat} [μb/sr]	Δ_{sys} [μb/sr]	$d\sigma/d\Omega$ [μb/sr]	Δ_{stat} [μb/sr]	Δ_{sys} [μb/sr]	$d\sigma/d\Omega$ [μb/sr]	Δ_{stat} [μb/sr]	Δ_{sys} [μb/sr]	$d\sigma/d\Omega$ [μb/sr]	Δ_{stat} [μb/sr]	Δ_{sys} [μb/sr]
−0.90	0.7934	0.0040	0.0243	0.8119	0.0050	0.0201	0.8539	0.0066	0.0150	0.8651	0.0046	0.0140
−0.70	0.8692	0.0037	0.0212	0.8524	0.0048	0.0251	0.8699	0.0065	0.0229	0.8935	0.0045	0.0211
−0.50	0.9057	0.0047	0.0223	0.8954	0.0056	0.0245	0.9087	0.0075	0.0212	0.8982	0.0050	0.0194
−0.30	0.9501	0.0047	0.0228	0.9111	0.0056	0.0216	0.9222	0.0073	0.0211	0.8835	0.0049	0.0186
−0.10	0.9449	0.0047	0.0248	0.9177	0.0056	0.0255	0.9169	0.0073	0.0277	0.8829	0.0049	0.0268
0.10	0.8822	0.0044	0.0319	0.8541	0.0053	0.0357	0.8311	0.0068	0.0350	0.8049	0.0046	0.0364
0.30	0.7929	0.0042	0.0387	0.7804	0.0051	0.0424	0.7693	0.0066	0.0433	0.7260	0.0044	0.0428
0.50	0.6830	0.0043	0.0263	0.6567	0.0051	0.0314	0.6563	0.0065	0.0328	0.6371	0.0044	0.0305
0.70	0.6480	0.0066	0.0147	0.6192	0.0071	0.0144	0.6140	0.0086	0.0160	0.6069	0.0061	0.0235
0.90	0.2521	0.0160	0.0202	0.2035	0.0112	0.0208	0.2337	0.0183	0.0264	0.2464	0.0103	0.0415

$\cos(\theta^*_{2\pi^0})$	$W=(1523.4\pm4.6)$ MeV			$W=(1532.6\pm4.6)$ MeV			$W=(1541.7\pm4.6)$ MeV			$W=(1550.8\pm4.5)$ MeV		
	$d\sigma/d\Omega$ [μb/sr]	Δ_{stat} [μb/sr]	Δ_{sys} [μb/sr]	$d\sigma/d\Omega$ [μb/sr]	Δ_{stat} [μb/sr]	Δ_{sys} [μb/sr]	$d\sigma/d\Omega$ [μb/sr]	Δ_{stat} [μb/sr]	Δ_{sys} [μb/sr]	$d\sigma/d\Omega$ [μb/sr]	Δ_{stat} [μb/sr]	Δ_{sys} [μb/sr]
−0.90	0.8712	0.0087	0.0119	0.8215	0.0046	0.0081	0.7953	0.0044	0.0045	0.7443	0.0044	0.0037
−0.70	0.8740	0.0084	0.0266	0.8136	0.0044	0.0156	0.7537	0.0041	0.0120	0.7297	0.0042	0.0126
−0.50	0.8299	0.0087	0.0205	0.7600	0.0047	0.0140	0.7018	0.0043	0.0109	0.6564	0.0043	0.0101
−0.30	0.8263	0.0090	0.0154	0.7282	0.0045	0.0145	0.6719	0.0042	0.0129	0.5934	0.0041	0.0108
−0.10	0.8183	0.0090	0.0259	0.6971	0.0045	0.0224	0.6254	0.0040	0.0201	0.5731	0.0040	0.0177
0.10	0.7727	0.0086	0.0375	0.6633	0.0043	0.0323	0.5896	0.0039	0.0285	0.5601	0.0039	0.0270
0.30	0.6647	0.0079	0.0399	0.5880	0.0040	0.0379	0.5486	0.0038	0.0345	0.5140	0.0038	0.0341
0.50	0.5967	0.0084	0.0334	0.5369	0.0041	0.0346	0.5040	0.0040	0.0322	0.4743	0.0038	0.0308
0.70	0.5520	0.0110	0.0192	0.5230	0.0053	0.0219	0.4916	0.0049	0.0215	0.4789	0.0050	0.0170
0.90	0.1307	0.0162	0.0478	0.2730	0.0104	0.0196	0.2770	0.0090	0.0213	0.2295	0.0111	0.0111

$\cos(\theta^*_{2\pi^0})$	$W=(1559.9\pm4.5)$ MeV			$W=(1568.9\pm4.5)$ MeV			$W=(1577.8\pm4.5)$ MeV			$W=(1586.7\pm4.4)$ MeV		
	$d\sigma/d\Omega$ [μb/sr]	Δ_{stat} [μb/sr]	Δ_{sys} [μb/sr]	$d\sigma/d\Omega$ [μb/sr]	Δ_{stat} [μb/sr]	Δ_{sys} [μb/sr]	$d\sigma/d\Omega$ [μb/sr]	Δ_{stat} [μb/sr]	Δ_{sys} [μb/sr]	$d\sigma/d\Omega$ [μb/sr]	Δ_{stat} [μb/sr]	Δ_{sys} [μb/sr]
−0.90	0.7172	0.0061	0.0044	0.7071	0.0048	0.0074	0.6925	0.0050	0.0106	0.6734	0.0054	0.0058
−0.70	0.6749	0.0056	0.0087	0.6535	0.0045	0.0077	0.6302	0.0043	0.0069	0.6201	0.0048	0.0078
−0.50	0.6148	0.0057	0.0091	0.5854	0.0045	0.0072	0.5543	0.0044	0.0052	0.5354	0.0049	0.0059
−0.30	0.5532	0.0054	0.0110	0.5264	0.0043	0.0086	0.4950	0.0041	0.0073	0.4696	0.0046	0.0065
−0.10	0.5164	0.0052	0.0147	0.4966	0.0042	0.0128	0.4655	0.0041	0.0117	0.4368	0.0044	0.0101
0.10	0.4969	0.0052	0.0220	0.4847	0.0041	0.0196	0.4615	0.0040	0.0171	0.4461	0.0043	0.0160
0.30	0.4832	0.0050	0.0288	0.4700	0.0040	0.0265	0.4651	0.0039	0.0227	0.4567	0.0043	0.0220
0.50	0.4648	0.0052	0.0262	0.4708	0.0041	0.0254	0.4561	0.0039	0.0232	0.4692	0.0044	0.0222
0.70	0.4396	0.0058	0.0171	0.4590	0.0052	0.0176	0.4690	0.0049	0.0166	0.4665	0.0049	0.0175
0.90	0.2770	0.0130	0.0170	0.3317	0.0115	0.0238	0.2906	0.0084	0.0108	0.2991	0.0100	0.0202

$\cos(\theta^*_{2\pi^0})$	$W=(1595.6\pm4.4)$ MeV			$W=(1604.3\pm4.4)$ MeV			$W=(1613.1\pm4.4)$ MeV			$W=(1621.8\pm4.3)$ MeV		
	$d\sigma/d\Omega$ [μb/sr]	Δ_{stat} [μb/sr]	Δ_{sys} [μb/sr]	$d\sigma/d\Omega$ [μb/sr]	Δ_{stat} [μb/sr]	Δ_{sys} [μb/sr]	$d\sigma/d\Omega$ [μb/sr]	Δ_{stat} [μb/sr]	Δ_{sys} [μb/sr]	$d\sigma/d\Omega$ [μb/sr]	Δ_{stat} [μb/sr]	Δ_{sys} [μb/sr]
−0.90	0.6544	0.0091	0.0072	0.6591	0.0044	0.0064	0.6707	0.0048	0.0069	0.6814	0.0048	0.0106
−0.70	0.5997	0.0087	0.0087	0.6043	0.0039	0.0066	0.6114	0.0041	0.0067	0.6224	0.0042	0.0078
−0.50	0.5082	0.0088	0.0072	0.5212	0.0039	0.0044	0.5231	0.0041	0.0042	0.5226	0.0041	0.0035
−0.30	0.4533	0.0078	0.0073	0.4618	0.0037	0.0059	0.4665	0.0040	0.0052	0.4695	0.0039	0.0036
−0.10	0.4210	0.0082	0.0100	0.4357	0.0036	0.0089	0.4304	0.0038	0.0080	0.4392	0.0037	0.0071
0.10	0.4335	0.0077	0.0147	0.4374	0.0035	0.0126	0.4383	0.0037	0.0117	0.4510	0.0035	0.0119
0.30	0.4522	0.0077	0.0205	0.4741	0.0033	0.0182	0.4789	0.0034	0.0176	0.4887	0.0034	0.0180
0.50	0.4815	0.0067	0.0246	0.5007	0.0033	0.0221	0.5218	0.0036	0.0209	0.5298	0.0037	0.0228
0.70	0.4622	0.0088	0.0148	0.5134	0.0041	0.0166	0.5275	0.0040	0.0184	0.5593	0.0042	0.0184
0.90	0.2983	0.0177	0.0187	0.4136	0.0081	0.0158	0.3872	0.0089	0.0219	0.4594	0.0146	0.0199

$\cos(\theta^*_{2\pi^0})$	$W\!=\!(1630.5\pm4.3)$ MeV			$W\!=\!(1639.1\pm4.3)$ MeV			$W\!=\!(1647.6\pm4.3)$ MeV			$W\!=\!(1656.1\pm4.2)$ MeV		
	$d\sigma/d\Omega$ [μb/sr]	$\Delta_{\rm stat}$ [μb/sr]	$\Delta_{\rm sys}$ [μb/sr]	$d\sigma/d\Omega$ [μb/sr]	$\Delta_{\rm stat}$ [μb/sr]	$\Delta_{\rm sys}$ [μb/sr]	$d\sigma/d\Omega$ [μb/sr]	$\Delta_{\rm stat}$ [μb/sr]	$\Delta_{\rm sys}$ [μb/sr]	$d\sigma/d\Omega$ [μb/sr]	$\Delta_{\rm stat}$ [μb/sr]	$\Delta_{\rm sys}$ [μb/sr]
−0.90	0.6874	0.0047	0.0092	0.6902	0.0047	0.0106	0.7159	0.0048	0.0097	0.7456	0.0052	0.0089
−0.70	0.6474	0.0042	0.0072	0.6577	0.0042	0.0055	0.6744	0.0043	0.0049	0.7099	0.0041	0.0046
−0.50	0.5403	0.0041	0.0040	0.5556	0.0037	0.0027	0.5697	0.0037	0.0027	0.5964	0.0040	0.0032
−0.30	0.4768	0.0037	0.0042	0.4966	0.0038	0.0035	0.5115	0.0036	0.0042	0.5363	0.0038	0.0039
−0.10	0.4452	0.0037	0.0079	0.4661	0.0036	0.0065	0.4865	0.0038	0.0065	0.4941	0.0041	0.0045
0.10	0.4701	0.0035	0.0127	0.4984	0.0037	0.0096	0.5124	0.0037	0.0090	0.5421	0.0040	0.0067
0.30	0.5202	0.0035	0.0175	0.5466	0.0034	0.0143	0.5850	0.0036	0.0145	0.6275	0.0041	0.0141
0.50	0.5581	0.0034	0.0226	0.6012	0.0036	0.0207	0.6608	0.0039	0.0214	0.6984	0.0044	0.0231
0.70	0.5967	0.0041	0.0197	0.6495	0.0041	0.0171	0.6992	0.0044	0.0185	0.7501	0.0050	0.0216
0.90	0.4699	0.0085	0.0126	0.4481	0.0090	0.0023	0.4999	0.0082	0.0100	0.6569	0.0162	0.0101

$\cos(\theta^*_{2\pi^0})$	$W\!=\!(1664.6\pm4.2)$ MeV			$W\!=\!(1673.1\pm4.2)$ MeV			$W\!=\!(1681.4\pm4.2)$ MeV			$W\!=\!(1689.8\pm4.2)$ MeV		
	$d\sigma/d\Omega$ [μb/sr]	$\Delta_{\rm stat}$ [μb/sr]	$\Delta_{\rm sys}$ [μb/sr]	$d\sigma/d\Omega$ [μb/sr]	$\Delta_{\rm stat}$ [μb/sr]	$\Delta_{\rm sys}$ [μb/sr]	$d\sigma/d\Omega$ [μb/sr]	$\Delta_{\rm stat}$ [μb/sr]	$\Delta_{\rm sys}$ [μb/sr]	$d\sigma/d\Omega$ [μb/sr]	$\Delta_{\rm stat}$ [μb/sr]	$\Delta_{\rm sys}$ [μb/sr]
−0.90	0.7622	0.0040	0.0073	0.7836	0.0042	0.0085	0.7899	0.0041	0.0105	0.7791	0.0039	0.0082
−0.70	0.7328	0.0033	0.0043	0.7512	0.0034	0.0045	0.7567	0.0034	0.0040	0.7741	0.0035	0.0029
−0.50	0.6272	0.0033	0.0030	0.6429	0.0033	0.0024	0.6585	0.0033	0.0020	0.6702	0.0034	0.0019
−0.30	0.5408	0.0032	0.0030	0.5690	0.0032	0.0030	0.5772	0.0033	0.0033	0.5892	0.0031	0.0032
−0.10	0.5162	0.0038	0.0040	0.5371	0.0038	0.0050	0.5634	0.0038	0.0057	0.5834	0.0037	0.0053
0.10	0.5637	0.0039	0.0068	0.5953	0.0036	0.0074	0.6083	0.0038	0.0083	0.6344	0.0041	0.0077
0.30	0.6650	0.0036	0.0126	0.7032	0.0037	0.0128	0.7279	0.0039	0.0137	0.7548	0.0042	0.0130
0.50	0.7308	0.0038	0.0201	0.7776	0.0039	0.0215	0.7968	0.0041	0.0221	0.8447	0.0042	0.0224
0.70	0.7949	0.0044	0.0213	0.8319	0.0045	0.0245	0.8554	0.0048	0.0210	0.8982	0.0049	0.0216
0.90	0.5798	0.0094	0.0131	0.7328	0.0106	0.0226	0.7111	0.0100	0.0081	0.6986	0.0091	0.0229

$\cos(\theta^*_{2\pi^0})$	$W\!=\!(1698.1\pm4.1)$ MeV			$W\!=\!(1706.4\pm4.1)$ MeV			$W\!=\!(1714.6\pm4.1)$ MeV			$W\!=\!(1722.8\pm4.1)$ MeV		
	$d\sigma/d\Omega$ [μb/sr]	$\Delta_{\rm stat}$ [μb/sr]	$\Delta_{\rm sys}$ [μb/sr]	$d\sigma/d\Omega$ [μb/sr]	$\Delta_{\rm stat}$ [μb/sr]	$\Delta_{\rm sys}$ [μb/sr]	$d\sigma/d\Omega$ [μb/sr]	$\Delta_{\rm stat}$ [μb/sr]	$\Delta_{\rm sys}$ [μb/sr]	$d\sigma/d\Omega$ [μb/sr]	$\Delta_{\rm stat}$ [μb/sr]	$\Delta_{\rm sys}$ [μb/sr]
−0.90	0.7873	0.0042	0.0095	0.7844	0.0041	0.0075	0.7793	0.0040	0.0076	0.7379	0.0038	0.0052
−0.70	0.7593	0.0038	0.0041	0.7447	0.0037	0.0032	0.7260	0.0038	0.0036	0.6945	0.0036	0.0030
−0.50	0.6841	0.0039	0.0022	0.6686	0.0037	0.0026	0.6641	0.0035	0.0027	0.6240	0.0035	0.0020
−0.30	0.6064	0.0035	0.0033	0.6162	0.0033	0.0041	0.6186	0.0031	0.0030	0.6075	0.0031	0.0021
−0.10	0.6052	0.0042	0.0053	0.6145	0.0039	0.0050	0.6473	0.0038	0.0036	0.6489	0.0038	0.0023
0.10	0.6818	0.0046	0.0077	0.6952	0.0047	0.0070	0.6971	0.0043	0.0071	0.7248	0.0042	0.0063
0.30	0.7720	0.0044	0.0131	0.7892	0.0047	0.0122	0.8067	0.0048	0.0146	0.7906	0.0047	0.0146
0.50	0.8805	0.0048	0.0239	0.8999	0.0050	0.0212	0.8769	0.0046	0.0240	0.8674	0.0049	0.0277
0.70	0.9182	0.0052	0.0233	0.9156	0.0050	0.0216	0.8970	0.0046	0.0243	0.8616	0.0044	0.0302
0.90	0.7587	0.0152	0.0036	0.7604	0.0098	0.0045	0.7521	0.0098	0.0082	0.7067	0.0087	0.0087

$\cos(\theta^*_{2\pi^0})$	$W\!=\!(1730.9\pm4.1)$ MeV			$W\!=\!(1739.1\pm4.0)$ MeV			$W\!=\!(1747.1\pm4.0)$ MeV			$W\!=\!(1755.2\pm4.0)$ MeV		
	$d\sigma/d\Omega$ [μb/sr]	$\Delta_{\rm stat}$ [μb/sr]	$\Delta_{\rm sys}$ [μb/sr]	$d\sigma/d\Omega$ [μb/sr]	$\Delta_{\rm stat}$ [μb/sr]	$\Delta_{\rm sys}$ [μb/sr]	$d\sigma/d\Omega$ [μb/sr]	$\Delta_{\rm stat}$ [μb/sr]	$\Delta_{\rm sys}$ [μb/sr]	$d\sigma/d\Omega$ [μb/sr]	$\Delta_{\rm stat}$ [μb/sr]	$\Delta_{\rm sys}$ [μb/sr]
−0.90	0.6636	0.0038	0.0051	0.6034	0.0038	0.0050	0.5459	0.0035	0.0067	0.5026	0.0034	0.0031
−0.70	0.6445	0.0034	0.0018	0.5772	0.0034	0.0029	0.5240	0.0032	0.0025	0.4889	0.0031	0.0021
−0.50	0.5900	0.0036	0.0014	0.5425	0.0032	0.0020	0.5082	0.0032	0.0016	0.4778	0.0030	0.0020
−0.30	0.5930	0.0032	0.0013	0.5462	0.0029	0.0014	0.5269	0.0030	0.0025	0.4988	0.0028	0.0026
−0.10	0.6215	0.0037	0.0018	0.5975	0.0034	0.0014	0.5565	0.0035	0.0022	0.5414	0.0034	0.0019
0.10	0.6949	0.0043	0.0055	0.6530	0.0043	0.0024	0.6359	0.0044	0.0024	0.5963	0.0036	0.0025
0.30	0.7649	0.0048	0.0114	0.7447	0.0049	0.0064	0.7096	0.0047	0.0077	0.6763	0.0045	0.0079
0.50	0.8402	0.0050	0.0181	0.7767	0.0046	0.0161	0.7380	0.0048	0.0179	0.7114	0.0045	0.0165
0.70	0.8194	0.0049	0.0186	0.7780	0.0046	0.0179	0.7297	0.0047	0.0195	0.7089	0.0048	0.0187
0.90	0.6660	0.0089	0.0070	0.6334	0.0087	0.0045	0.5658	0.0084	0.0049	0.5506	0.0082	0.0130

$\cos(\theta^*_{2\pi^0})$	$W\!=\!(1763.2\pm4.0)$ MeV			$W\!=\!(1771.1\pm4.0)$ MeV			$W\!=\!(1779.1\pm4.0)$ MeV			$W\!=\!(1787.0\pm3.9)$ MeV		
	$d\sigma/d\Omega$ [μb/sr]	$\Delta_{\rm stat}$ [μb/sr]	$\Delta_{\rm sys}$ [μb/sr]	$d\sigma/d\Omega$ [μb/sr]	$\Delta_{\rm stat}$ [μb/sr]	$\Delta_{\rm sys}$ [μb/sr]	$d\sigma/d\Omega$ [μb/sr]	$\Delta_{\rm stat}$ [μb/sr]	$\Delta_{\rm sys}$ [μb/sr]	$d\sigma/d\Omega$ [μb/sr]	$\Delta_{\rm stat}$ [μb/sr]	$\Delta_{\rm sys}$ [μb/sr]
−0.90	0.4585	0.0033	0.0063	0.4131	0.0031	0.0058	0.3909	0.0032	0.0058	0.3650	0.0032	0.0046
−0.70	0.4664	0.0031	0.0023	0.4361	0.0031	0.0030	0.4104	0.0028	0.0021	0.3814	0.0030	0.0012
−0.50	0.4481	0.0032	0.0013	0.4286	0.0027	0.0010	0.4035	0.0026	0.0013	0.3985	0.0027	0.0007
−0.30	0.4675	0.0029	0.0015	0.4454	0.0026	0.0022	0.4180	0.0025	0.0023	0.4135	0.0026	0.0017
−0.10	0.5138	0.0030	0.0012	0.4779	0.0028	0.0041	0.4661	0.0029	0.0019	0.4577	0.0037	0.0023
0.10	0.5815	0.0042	0.0033	0.5556	0.0036	0.0025	0.5482	0.0032	0.0023	0.5156	0.0035	0.0025
0.30	0.6572	0.0040	0.0079	0.6121	0.0037	0.0061	0.6006	0.0039	0.0069	0.5727	0.0039	0.0064
0.50	0.7002	0.0046	0.0140	0.6867	0.0045	0.0147	0.6396	0.0043	0.0136	0.6207	0.0042	0.0138
0.70	0.6637	0.0044	0.0158	0.6303	0.0039	0.0158	0.6331	0.0046	0.0137	0.5942	0.0046	0.0134
0.90	0.5546	0.0092	0.0122	0.4950	0.0083	0.0069	0.5250	0.0092	0.0094	0.4996	0.0085	0.0044

$\cos(\theta^*_{2\pi^0})$	$W\!=\!(1794.8\pm3.9)$ MeV			$W\!=\!(1802.6\pm3.9)$ MeV			$W\!=\!(1810.4\pm3.9)$ MeV			$W\!=\!(1818.2\pm3.9)$ MeV		
	$d\sigma/d\Omega$ [μb/sr]	$\Delta_{\rm stat}$ [μb/sr]	$\Delta_{\rm sys}$ [μb/sr]	$d\sigma/d\Omega$ [μb/sr]	$\Delta_{\rm stat}$ [μb/sr]	$\Delta_{\rm sys}$ [μb/sr]	$d\sigma/d\Omega$ [μb/sr]	$\Delta_{\rm stat}$ [μb/sr]	$\Delta_{\rm sys}$ [μb/sr]	$d\sigma/d\Omega$ [μb/sr]	$\Delta_{\rm stat}$ [μb/sr]	$\Delta_{\rm sys}$ [μb/sr]
−0.90	0.3234	0.0027	0.0046	0.3079	0.0028	0.0059	0.3133	0.0034	0.0051	0.2934	0.0031	0.0036
−0.70	0.3667	0.0031	0.0013	0.3589	0.0026	0.0016	0.3453	0.0028	0.0017	0.3393	0.0025	0.0010
−0.50	0.3756	0.0028	0.0012	0.3671	0.0027	0.0005	0.3595	0.0027	0.0012	0.3532	0.0028	0.0008
−0.30	0.4086	0.0027	0.0018	0.4100	0.0026	0.0009	0.3925	0.0028	0.0021	0.3834	0.0027	0.0014
−0.10	0.4356	0.0031	0.0018	0.4370	0.0030	0.0014	0.4217	0.0031	0.0021	0.4188	0.0036	0.0020
0.10	0.4968	0.0038	0.0028	0.5017	0.0034	0.0024	0.4807	0.0036	0.0030	0.4989	0.0035	0.0029
0.30	0.5664	0.0040	0.0064	0.5672	0.0040	0.0062	0.5561	0.0042	0.0053	0.5448	0.0041	0.0061
0.50	0.5840	0.0044	0.0138	0.5997	0.0045	0.0079	0.5975	0.0045	0.0113	0.5946	0.0047	0.0142
0.70	0.5941	0.0054	0.0174	0.5827	0.0044	0.0237	0.5793	0.0052	0.0146	0.5738	0.0054	0.0153
0.90	0.5387	0.0130	0.0104	0.4634	0.0099	0.0619	0.4564	0.0099	0.0074	0.4440	0.0086	0.0076

$\cos(\theta^*_{2\pi^0})$	W=(1825.9±3.9) MeV			W=(1833.6±3.8) MeV			W=(1841.3±3.8) MeV			W=(1848.9±3.8) MeV		
	$d\sigma/d\Omega$ [μb/sr]	Δ_{stat} [μb/sr]	Δ_{sys} [μb/sr]	$d\sigma/d\Omega$ [μb/sr]	Δ_{stat} [μb/sr]	Δ_{sys} [μb/sr]	$d\sigma/d\Omega$ [μb/sr]	Δ_{stat} [μb/sr]	Δ_{sys} [μb/sr]	$d\sigma/d\Omega$ [μb/sr]	Δ_{stat} [μb/sr]	Δ_{sys} [μb/sr]
−0.90	0.2755	0.0029	0.0074	0.2473	0.0025	0.0038	0.2323	0.0025	0.0019	0.2405	0.0020	0.0024
−0.70	0.3293	0.0023	0.0018	0.3268	0.0024	0.0019	0.3159	0.0026	0.0017	0.3239	0.0022	0.0010
−0.50	0.3548	0.0027	0.0004	0.3468	0.0024	0.0012	0.3407	0.0030	0.0031	0.3313	0.0024	0.0024
−0.30	0.3795	0.0027	0.0012	0.3764	0.0025	0.0009	0.3631	0.0032	0.0046	0.3660	0.0026	0.0041
−0.10	0.4121	0.0028	0.0011	0.4141	0.0028	0.0009	0.4024	0.0035	0.0031	0.4026	0.0028	0.0020
0.10	0.4829	0.0037	0.0026	0.4664	0.0034	0.0017	0.4576	0.0040	0.0022	0.4510	0.0036	0.0012
0.30	0.5352	0.0037	0.0077	0.5412	0.0039	0.0055	0.5225	0.0055	0.0058	0.5353	0.0042	0.0052
0.50	0.5694	0.0045	0.0140	0.5718	0.0049	0.0108	0.5787	0.0061	0.0105	0.5880	0.0047	0.0112
0.70	0.5683	0.0052	0.0143	0.5818	0.0054	0.0111	0.5608	0.0067	0.0101	0.5471	0.0054	0.0137
0.90	0.4275	0.0077	0.0060	0.3894	0.0085	0.0015	0.3993	0.0085	0.0060	0.3903	0.0076	0.0178

$\cos(\theta^*_{2\pi^0})$	W=(1856.5±3.8) MeV			W=(1864.0±3.8) MeV			W=(1871.6±3.8) MeV			W=(1879.1±3.7) MeV		
	$d\sigma/d\Omega$ [μb/sr]	Δ_{stat} [μb/sr]	Δ_{sys} [μb/sr]	$d\sigma/d\Omega$ [μb/sr]	Δ_{stat} [μb/sr]	Δ_{sys} [μb/sr]	$d\sigma/d\Omega$ [μb/sr]	Δ_{stat} [μb/sr]	Δ_{sys} [μb/sr]	$d\sigma/d\Omega$ [μb/sr]	Δ_{stat} [μb/sr]	Δ_{sys} [μb/sr]
−0.90	0.2437	0.0022	0.0018	0.2263	0.0028	0.0020	0.2429	0.0022	0.0056	0.2338	0.0021	0.0095
−0.70	0.3104	0.0023	0.0017	0.3135	0.0025	0.0024	0.3195	0.0023	0.0024	0.3048	0.0022	0.0025
−0.50	0.3287	0.0026	0.0014	0.3419	0.0029	0.0024	0.3375	0.0027	0.0021	0.3305	0.0027	0.0011
−0.30	0.3578	0.0026	0.0013	0.3665	0.0030	0.0012	0.3520	0.0027	0.0022	0.3464	0.0025	0.0016
−0.10	0.3726	0.0029	0.0011	0.3920	0.0032	0.0015	0.3814	0.0029	0.0011	0.3578	0.0027	0.0006
0.10	0.4296	0.0034	0.0015	0.4479	0.0038	0.0026	0.4447	0.0037	0.0016	0.4546	0.0037	0.0018
0.30	0.5231	0.0043	0.0040	0.5288	0.0047	0.0047	0.5263	0.0047	0.0043	0.4903	0.0039	0.0051
0.50	0.5582	0.0047	0.0094	0.5661	0.0055	0.0079	0.5648	0.0053	0.0119	0.5400	0.0050	0.0146
0.70	0.5643	0.0059	0.0108	0.5529	0.0065	0.0062	0.5705	0.0061	0.0157	0.5311	0.0057	0.0190
0.90	0.4028	0.0095	0.0027	0.3935	0.0127	0.0035	0.4163	0.0098	0.0058	0.3776	0.0071	0.0029

$\cos(\theta^*_{2\pi^0})$	W=(1886.6±3.7) MeV			W=(1894.0±3.7) MeV			W=(1901.4±3.7) MeV			W=(1908.8±3.7) MeV		
	$d\sigma/d\Omega$ [μb/sr]	Δ_{stat} [μb/sr]	Δ_{sys} [μb/sr]	$d\sigma/d\Omega$ [μb/sr]	Δ_{stat} [μb/sr]	Δ_{sys} [μb/sr]	$d\sigma/d\Omega$ [μb/sr]	Δ_{stat} [μb/sr]	Δ_{sys} [μb/sr]	$d\sigma/d\Omega$ [μb/sr]	Δ_{stat} [μb/sr]	Δ_{sys} [μb/sr]
−0.90	0.2148	0.0022	0.0072	0.3050	0.0050	0.0030	0.0000	0.0000	0.0000	0.0000	0.0000	0.0000
−0.70	0.2956	0.0023	0.0027	0.3857	0.0048	0.0023	0.0000	0.0000	0.0000	0.0000	0.0000	0.0000
−0.50	0.3100	0.0027	0.0025	0.4271	0.0063	0.0044	0.0000	0.0000	0.0000	0.0000	0.0000	0.0000
−0.30	0.3295	0.0028	0.0015	0.4301	0.0048	0.0041	0.0000	0.0000	0.0000	0.0000	0.0000	0.0000
−0.10	0.3487	0.0029	0.0010	0.4639	0.0060	0.0027	0.0000	0.0000	0.0000	0.0000	0.0000	0.0000
0.10	0.4215	0.0038	0.0026	0.5504	0.0068	0.0049	0.0000	0.0000	0.0000	0.0000	0.0000	0.0000
0.30	0.4788	0.0045	0.0050	0.6207	0.0077	0.0080	0.0000	0.0000	0.0000	0.0000	0.0000	0.0000
0.50	0.5294	0.0053	0.0140	0.6745	0.0099	0.0202	0.0000	0.0000	0.0000	0.0000	0.0000	0.0000
0.70	0.5198	0.0061	0.0194	0.6773	0.0121	0.0274	0.0000	0.0000	0.0000	0.0000	0.0000	0.0000
0.90	0.3692	0.0092	0.0045	0.4624	0.0159	0.0064	0.0000	0.0000	0.0000	0.0000	0.0000	0.0000

$\cos(\theta^*_{2\pi^0})$	W=(1916.2±3.7) MeV			W=(1923.5±3.7) MeV			W=(1930.8±3.6) MeV		
	$d\sigma/d\Omega$ [μb/sr]	Δ_{stat} [μb/sr]	Δ_{sys} [μb/sr]	$d\sigma/d\Omega$ [μb/sr]	Δ_{stat} [μb/sr]	Δ_{sys} [μb/sr]	$d\sigma/d\Omega$ [μb/sr]	Δ_{stat} [μb/sr]	Δ_{sys} [μb/sr]
−0.90	0.0000	0.0000	0.0000	0.0000	0.0000	0.0000	0.0000	0.0000	0.0000
−0.70	0.0000	0.0000	0.0000	0.0000	0.0000	0.0000	0.0000	0.0000	0.0000
−0.50	0.0000	0.0000	0.0000	0.0000	0.0000	0.0000	0.0000	0.0000	0.0000
−0.30	0.0000	0.0000	0.0000	0.0000	0.0000	0.0000	0.0000	0.0000	0.0000
−0.10	0.0000	0.0000	0.0000	0.0000	0.0000	0.0000	0.0000	0.0000	0.0000
0.10	0.0000	0.0000	0.0000	0.0000	0.0000	0.0000	0.0000	0.0000	0.0000
0.30	0.0000	0.0000	0.0000	0.0000	0.0000	0.0000	0.0000	0.0000	0.0000
0.50	0.0000	0.0000	0.0000	0.0000	0.0000	0.0000	0.0000	0.0000	0.0000
0.70	0.0000	0.0000	0.0000	0.0000	0.0000	0.0000	0.0000	0.0000	0.0000
0.90	0.0000	0.0000	0.0000	0.0000	0.0000	0.0000	0.0000	0.0000	0.0000

E.3.6 $\gamma n \to \pi^0\pi^0 n$ as a Function of W

Angular Distributions

$\cos(\theta^*_{2\pi^0})$	W=(1304.0±4.0) MeV			W=(1312.0±4.0) MeV			W=(1320.0±4.0) MeV			W=(1328.0±4.0) MeV		
	$d\sigma/d\Omega$ [μb/sr]	Δ_{stat} [μb/sr]	Δ_{sys} [μb/sr]	$d\sigma/d\Omega$ [μb/sr]	Δ_{stat} [μb/sr]	Δ_{sys} [μb/sr]	$d\sigma/d\Omega$ [μb/sr]	Δ_{stat} [μb/sr]	Δ_{sys} [μb/sr]	$d\sigma/d\Omega$ [μb/sr]	Δ_{stat} [μb/sr]	Δ_{sys} [μb/sr]
−0.90	0.0105	0.0021	0.0417	0.0463	0.0059	0.0367	0.0553	0.0087	0.0608	0.0501	0.0051	0.0688
−0.70	0.0111	0.0019	0.0142	0.0434	0.0043	0.0444	0.0557	0.0057	0.0529	0.0246	0.0035	0.0322
−0.50	0.0092	0.0044	0.0079	0.0261	0.0049	0.0292	0.0547	0.0042	0.0365	0.0613	0.0049	0.0370
−0.30	0.0209	0.0056	0.0118	0.0334	0.0039	0.0267	0.0403	0.0041	0.0196	0.0871	0.0045	0.0252
−0.10	0.0276	0.0067	0.0216	0.0301	0.0051	0.0169	0.0366	0.0046	0.0209	0.0816	0.0057	0.0173
0.10	0.0353	0.0063	0.0186	0.0314	0.0047	0.0213	0.0330	0.0054	0.0195	0.0687	0.0049	0.0206
0.30	0.0242	0.0071	0.0142	0.0276	0.0054	0.0129	0.0361	0.0059	0.0164	0.0600	0.0054	0.0212
0.50	0.0042	0.0112	0.0117	0.0383	0.0068	0.0237	0.0196	0.0089	0.0105	0.0345	0.0142	0.0123
0.70	0.0319	0.0123	0.0088	0.0098	0.0137	0.0140	0.0511	0.0126	0.0268	0.0114	0.0273	0.0116
0.90	−0.0000	0.0068	0.0297	0.0719	0.0439	0.0607	−0.0338	0.0499	0.0019	−0.0238	0.0263	0.0651

$\cos(\theta^*_{2\pi^0})$	$W=(1336.0\pm4.0)$ MeV			$W=(1344.0\pm4.0)$ MeV			$W=(1352.0\pm4.0)$ MeV			$W=(1360.0\pm4.0)$ MeV		
	$d\sigma/d\Omega$ [μb/sr]	Δ_{stat} [μb/sr]	Δ_{sys} [μb/sr]	$d\sigma/d\Omega$ [μb/sr]	Δ_{stat} [μb/sr]	Δ_{sys} [μb/sr]	$d\sigma/d\Omega$ [μb/sr]	Δ_{stat} [μb/sr]	Δ_{sys} [μb/sr]	$d\sigma/d\Omega$ [μb/sr]	Δ_{stat} [μb/sr]	Δ_{sys} [μb/sr]
−0.90	0.0549	0.0042	0.0662	0.0756	0.0058	0.0381	0.0963	0.0050	0.0853	0.1196	0.0063	0.0559
−0.70	0.0530	0.0035	0.0593	0.0913	0.0048	0.0385	0.0964	0.0049	0.0356	0.1328	0.0057	0.0345
−0.50	0.0710	0.0046	0.0437	0.0990	0.0064	0.0261	0.1405	0.0063	0.0402	0.1855	0.0089	0.0296
−0.30	0.0675	0.0044	0.0320	0.1240	0.0048	0.0181	0.1595	0.0073	0.0237	0.2144	0.0065	0.0244
−0.10	0.0790	0.0049	0.0215	0.1249	0.0061	0.0130	0.1696	0.0059	0.0206	0.1861	0.0072	0.0194
0.10	0.0675	0.0036	0.0142	0.1140	0.0048	0.0172	0.1607	0.0067	0.0194	0.1971	0.0070	0.0217
0.30	0.0705	0.0042	0.0130	0.1018	0.0082	0.0142	0.1201	0.0068	0.0168	0.1666	0.0084	0.0217
0.50	0.0916	0.0081	0.0200	0.0935	0.0082	0.0198	0.1410	0.0117	0.0240	0.1668	0.0085	0.0164
0.70	0.0477	0.0181	0.0236	0.0384	0.0174	0.0013	0.1047	0.0158	0.0331	0.1222	0.0135	0.0328
0.90	0.0906	0.0675	0.0615	0.0056	0.0258	0.0270	0.0583	0.0354	0.0058	−0.0194	0.0282	0.0321

$\cos(\theta^*_{2\pi^0})$	$W=(1368.0\pm4.0)$ MeV			$W=(1376.0\pm4.0)$ MeV			$W=(1384.0\pm4.0)$ MeV			$W=(1392.0\pm4.0)$ MeV		
	$d\sigma/d\Omega$ [μb/sr]	Δ_{stat} [μb/sr]	Δ_{sys} [μb/sr]	$d\sigma/d\Omega$ [μb/sr]	Δ_{stat} [μb/sr]	Δ_{sys} [μb/sr]	$d\sigma/d\Omega$ [μb/sr]	Δ_{stat} [μb/sr]	Δ_{sys} [μb/sr]	$d\sigma/d\Omega$ [μb/sr]	Δ_{stat} [μb/sr]	Δ_{sys} [μb/sr]
−0.90	0.1566	0.0067	0.0361	0.1780	0.0073	0.0832	0.1879	0.0063	0.0533	0.2072	0.0089	0.0754
−0.70	0.1729	0.0045	0.0653	0.1961	0.0055	0.0408	0.2309	0.0057	0.0559	0.2571	0.0057	0.0357
−0.50	0.1996	0.0073	0.0521	0.2439	0.0080	0.0303	0.2717	0.0063	0.0310	0.3372	0.0080	0.0257
−0.30	0.2420	0.0058	0.0290	0.2688	0.0080	0.0280	0.3033	0.0076	0.0225	0.3414	0.0079	0.0266
−0.10	0.2413	0.0078	0.0239	0.2788	0.0075	0.0219	0.3279	0.0090	0.0265	0.3685	0.0091	0.0224
0.10	0.2126	0.0067	0.0200	0.2564	0.0081	0.0168	0.3007	0.0073	0.0259	0.3833	0.0091	0.0216
0.30	0.1800	0.0076	0.0121	0.2562	0.0068	0.0156	0.2647	0.0083	0.0237	0.3421	0.0081	0.0193
0.50	0.1506	0.0099	0.0108	0.2039	0.0103	0.0191	0.2546	0.0104	0.0260	0.2840	0.0121	0.0229
0.70	0.2119	0.0122	0.0468	0.1392	0.0159	0.0244	0.1642	0.0154	0.0223	0.2235	0.0145	0.0419
0.90	−0.0170	0.0637	0.0180	0.1697	0.0426	0.0414	0.1098	0.0494	0.0230	−0.0212	0.0324	0.0122

$\cos(\theta^*_{2\pi^0})$	$W=(1400.0\pm4.0)$ MeV			$W=(1408.0\pm4.0)$ MeV			$W=(1416.0\pm4.0)$ MeV			$W=(1424.0\pm4.0)$ MeV		
	$d\sigma/d\Omega$ [μb/sr]	Δ_{stat} [μb/sr]	Δ_{sys} [μb/sr]	$d\sigma/d\Omega$ [μb/sr]	Δ_{stat} [μb/sr]	Δ_{sys} [μb/sr]	$d\sigma/d\Omega$ [μb/sr]	Δ_{stat} [μb/sr]	Δ_{sys} [μb/sr]	$d\sigma/d\Omega$ [μb/sr]	Δ_{stat} [μb/sr]	Δ_{sys} [μb/sr]
−0.90	0.2635	0.0085	0.0319	0.3810	0.0094	0.1435	0.3636	0.0081	0.0547	0.4266	0.0104	0.0657
−0.70	0.2988	0.0074	0.0324	0.3473	0.0081	0.0701	0.3658	0.0078	0.0405	0.4200	0.0091	0.0428
−0.50	0.3326	0.0073	0.0302	0.3989	0.0076	0.0367	0.4279	0.0083	0.0341	0.4570	0.0090	0.0329
−0.30	0.3859	0.0076	0.0237	0.4501	0.0094	0.0248	0.4791	0.0078	0.0275	0.4893	0.0098	0.0268
−0.10	0.4166	0.0078	0.0232	0.5000	0.0112	0.0252	0.5132	0.0109	0.0249	0.5418	0.0101	0.0232
0.10	0.4241	0.0098	0.0249	0.4572	0.0115	0.0240	0.4933	0.0109	0.0211	0.5247	0.0106	0.0207
0.30	0.3702	0.0094	0.0231	0.3977	0.0112	0.0211	0.4054	0.0106	0.0164	0.4578	0.0109	0.0196
0.50	0.3313	0.0128	0.0214	0.3740	0.0117	0.0273	0.3567	0.0103	0.0218	0.3913	0.0115	0.0225
0.70	0.2879	0.0141	0.0327	0.2704	0.0147	0.0322	0.2563	0.0163	0.0364	0.3218	0.0176	0.0455
0.90	0.1609	0.0296	0.0394	0.1369	0.0241	0.0291	0.1719	0.0547	0.0376	0.0591	0.0663	0.0200

$\cos(\theta^*_{2\pi^0})$	$W=(1432.0\pm4.0)$ MeV			$W=(1440.0\pm4.0)$ MeV			$W=(1448.0\pm4.0)$ MeV			$W=(1456.0\pm4.0)$ MeV		
	$d\sigma/d\Omega$ [μb/sr]	Δ_{stat} [μb/sr]	Δ_{sys} [μb/sr]	$d\sigma/d\Omega$ [μb/sr]	Δ_{stat} [μb/sr]	Δ_{sys} [μb/sr]	$d\sigma/d\Omega$ [μb/sr]	Δ_{stat} [μb/sr]	Δ_{sys} [μb/sr]	$d\sigma/d\Omega$ [μb/sr]	Δ_{stat} [μb/sr]	Δ_{sys} [μb/sr]
−0.90	0.4877	0.0106	0.0619	0.5086	0.0120	0.0345	0.6005	0.0119	0.0785	0.6727	0.0143	0.0689
−0.70	0.4602	0.0087	0.0356	0.5136	0.0106	0.0246	0.5094	0.0098	0.0390	0.6804	0.0113	0.0367
−0.50	0.5314	0.0093	0.0238	0.5454	0.0098	0.0258	0.5438	0.0098	0.0264	0.6369	0.0122	0.0234
−0.30	0.5801	0.0107	0.0214	0.6047	0.0104	0.0274	0.6101	0.0111	0.0242	0.7246	0.0130	0.0195
−0.10	0.6073	0.0117	0.0238	0.6326	0.0116	0.0231	0.6163	0.0114	0.0234	0.7455	0.0140	0.0183
0.10	0.5718	0.0122	0.0248	0.5827	0.0119	0.0248	0.5990	0.0123	0.0223	0.7317	0.0138	0.0232
0.30	0.5265	0.0114	0.0297	0.5350	0.0118	0.0311	0.5165	0.0112	0.0205	0.6351	0.0145	0.0284
0.50	0.4186	0.0127	0.0150	0.4383	0.0130	0.0234	0.4634	0.0118	0.0237	0.5661	0.0136	0.0367
0.70	0.3578	0.0179	0.0459	0.3546	0.0180	0.0569	0.4010	0.0156	0.0324	0.4317	0.0151	0.0475
0.90	0.1111	0.0429	0.0593	−0.0017	0.0502	0.0504	0.3822	0.0501	0.0529	0.1288	0.0224	0.0449

$\cos(\theta^*_{2\pi^0})$	$W=(1464.0\pm4.0)$ MeV			$W=(1472.0\pm4.0)$ MeV			$W=(1480.0\pm4.0)$ MeV			$W=(1488.0\pm4.0)$ MeV		
	$d\sigma/d\Omega$ [μb/sr]	Δ_{stat} [μb/sr]	Δ_{sys} [μb/sr]	$d\sigma/d\Omega$ [μb/sr]	Δ_{stat} [μb/sr]	Δ_{sys} [μb/sr]	$d\sigma/d\Omega$ [μb/sr]	Δ_{stat} [μb/sr]	Δ_{sys} [μb/sr]	$d\sigma/d\Omega$ [μb/sr]	Δ_{stat} [μb/sr]	Δ_{sys} [μb/sr]
−0.90	0.7805	0.0146	0.0519	0.8551	0.0157	0.0934	0.9486	0.0166	0.0820	1.0950	0.0191	0.0713
−0.70	0.6901	0.0123	0.0357	0.7501	0.0130	0.0399	0.8167	0.0129	0.0409	0.8700	0.0151	0.0429
−0.50	0.7136	0.0119	0.0307	0.7733	0.0136	0.0287	0.8255	0.0132	0.0268	0.8321	0.0136	0.0332
−0.30	0.7471	0.0129	0.0221	0.8240	0.0140	0.0242	0.8647	0.0144	0.0219	0.9017	0.0145	0.0284
−0.10	0.7665	0.0150	0.0194	0.8402	0.0140	0.0247	0.9101	0.0161	0.0239	0.9015	0.0171	0.0288
0.10	0.7564	0.0139	0.0234	0.7802	0.0152	0.0288	0.8179	0.0160	0.0317	0.8567	0.0156	0.0357
0.30	0.6383	0.0135	0.0306	0.6965	0.0135	0.0325	0.7091	0.0157	0.0343	0.7103	0.0145	0.0381
0.50	0.5373	0.0156	0.0359	0.6001	0.0144	0.0262	0.5864	0.0165	0.0360	0.5884	0.0155	0.0288
0.70	0.4347	0.0169	0.0432	0.4679	0.0178	0.0526	0.4788	0.0186	0.0454	0.5367	0.0175	0.0566
0.90	0.3262	0.0196	0.0787	0.0422	0.0162	0.0017	0.2123	0.0186	0.0553	0.1621	0.0246	0.0701

$\cos(\theta^*_{2\pi^0})$	$W=(1496.0\pm4.0)$ MeV			$W=(1504.0\pm4.0)$ MeV			$W=(1512.0\pm4.0)$ MeV			$W=(1520.0\pm4.0)$ MeV		
	$d\sigma/d\Omega$ [μb/sr]	Δ_{stat} [μb/sr]	Δ_{sys} [μb/sr]	$d\sigma/d\Omega$ [μb/sr]	Δ_{stat} [μb/sr]	Δ_{sys} [μb/sr]	$d\sigma/d\Omega$ [μb/sr]	Δ_{stat} [μb/sr]	Δ_{sys} [μb/sr]	$d\sigma/d\Omega$ [μb/sr]	Δ_{stat} [μb/sr]	Δ_{sys} [μb/sr]
−0.90	1.1592	0.0224	0.1400	1.2187	0.0208	0.1056	1.3314	0.0223	0.1109	1.4366	0.0234	0.0829
−0.70	0.9752	0.0154	0.0544	0.9479	0.0161	0.0427	1.0787	0.0183	0.0447	1.0467	0.0183	0.0432
−0.50	0.8619	0.0157	0.0262	0.8800	0.0150	0.0270	0.8896	0.0150	0.0271	0.8821	0.0166	0.0275
−0.30	0.8768	0.0155	0.0214	0.8859	0.0164	0.0230	0.8988	0.0150	0.0212	0.8403	0.0156	0.0223
−0.10	0.9113	0.0172	0.0253	0.9468	0.0173	0.0290	0.8952	0.0172	0.0226	0.8314	0.0163	0.0254
0.10	0.8339	0.0170	0.0371	0.8785	0.0167	0.0385	0.8077	0.0169	0.0357	0.8152	0.0163	0.0373
0.30	0.7506	0.0168	0.0497	0.7815	0.0166	0.0512	0.7066	0.0162	0.0461	0.6666	0.0149	0.0465
0.50	0.6111	0.0165	0.0413	0.6580	0.0164	0.0569	0.5878	0.0155	0.0444	0.6126	0.0154	0.0484
0.70	0.4828	0.0192	0.0513	0.4914	0.0206	0.0506	0.5096	0.0184	0.0566	0.5177	0.0163	0.0555
0.90	0.1877	0.0193	0.0858	0.2100	0.0186	0.0567	0.2267	0.0232	0.0751	0.1830	0.0120	0.0635

$\cos(\theta^*_{2\pi^0})$	$W=(1528.0\pm4.0)$ MeV			$W=(1536.0\pm4.0)$ MeV			$W=(1544.0\pm4.0)$ MeV			$W=(1552.0\pm4.0)$ MeV		
	$d\sigma/d\Omega$ [μb/sr]	$\Delta_{\rm stat}$ [μb/sr]	$\Delta_{\rm sys}$ [μb/sr]	$d\sigma/d\Omega$ [μb/sr]	$\Delta_{\rm stat}$ [μb/sr]	$\Delta_{\rm sys}$ [μb/sr]	$d\sigma/d\Omega$ [μb/sr]	$\Delta_{\rm stat}$ [μb/sr]	$\Delta_{\rm sys}$ [μb/sr]	$d\sigma/d\Omega$ [μb/sr]	$\Delta_{\rm stat}$ [μb/sr]	$\Delta_{\rm sys}$ [μb/sr]
−0.90	1.4310	0.0220	0.1131	1.3415	0.0228	0.0932	1.4132	0.0235	0.0916	1.3413	0.0227	0.0806
−0.70	1.1305	0.0180	0.0395	1.1024	0.0177	0.0413	1.0169	0.0170	0.0365	1.0135	0.0181	0.0308
−0.50	0.8731	0.0160	0.0248	0.8513	0.0168	0.0232	0.8220	0.0161	0.0228	0.7885	0.0166	0.0179
−0.30	0.8141	0.0151	0.0229	0.8509	0.0161	0.0243	0.7569	0.0161	0.0234	0.7792	0.0149	0.0194
−0.10	0.8267	0.0161	0.0320	0.7900	0.0156	0.0278	0.7567	0.0158	0.0305	0.7398	0.0162	0.0295
0.10	0.7648	0.0171	0.0462	0.6990	0.0156	0.0377	0.6874	0.0149	0.0387	0.6729	0.0149	0.0390
0.30	0.6242	0.0149	0.0525	0.5914	0.0136	0.0489	0.5942	0.0149	0.0430	0.5910	0.0134	0.0469
0.50	0.5400	0.0134	0.0559	0.5034	0.0155	0.0491	0.5385	0.0145	0.0437	0.5104	0.0154	0.0486
0.70	0.4749	0.0167	0.0535	0.4534	0.0193	0.0539	0.4349	0.0167	0.0358	0.4333	0.0151	0.0476
0.90	0.2950	0.0212	0.0535	0.2144	0.0192	0.0545	0.2366	0.0144	0.0433	0.1682	0.0155	0.0411

$\cos(\theta^*_{2\pi^0})$	$W=(1560.0\pm4.0)$ MeV			$W=(1568.0\pm4.0)$ MeV			$W=(1576.0\pm4.0)$ MeV			$W=(1584.0\pm4.0)$ MeV		
	$d\sigma/d\Omega$ [μb/sr]	$\Delta_{\rm stat}$ [μb/sr]	$\Delta_{\rm sys}$ [μb/sr]	$d\sigma/d\Omega$ [μb/sr]	$\Delta_{\rm stat}$ [μb/sr]	$\Delta_{\rm sys}$ [μb/sr]	$d\sigma/d\Omega$ [μb/sr]	$\Delta_{\rm stat}$ [μb/sr]	$\Delta_{\rm sys}$ [μb/sr]	$d\sigma/d\Omega$ [μb/sr]	$\Delta_{\rm stat}$ [μb/sr]	$\Delta_{\rm sys}$ [μb/sr]
−0.90	1.2994	0.0226	0.0739	1.2751	0.0211	0.0784	1.2890	0.0237	0.0595	1.2932	0.0231	0.0603
−0.70	1.0073	0.0172	0.0269	0.9978	0.0175	0.0322	0.9523	0.0161	0.0347	0.9292	0.0175	0.0305
−0.50	0.7939	0.0158	0.0186	0.7463	0.0151	0.0174	0.7319	0.0168	0.0221	0.7412	0.0148	0.0229
−0.30	0.7497	0.0152	0.0224	0.6909	0.0155	0.0193	0.6710	0.0143	0.0204	0.7006	0.0148	0.0250
−0.10	0.7075	0.0146	0.0294	0.7026	0.0161	0.0277	0.7177	0.0146	0.0260	0.7023	0.0151	0.0336
0.10	0.6440	0.0152	0.0360	0.6192	0.0166	0.0330	0.6127	0.0152	0.0314	0.6149	0.0146	0.0356
0.30	0.5353	0.0154	0.0394	0.5495	0.0146	0.0369	0.5643	0.0137	0.0411	0.5267	0.0137	0.0339
0.50	0.5085	0.0147	0.0396	0.4950	0.0154	0.0307	0.4785	0.0164	0.0386	0.5163	0.0142	0.0297
0.70	0.4457	0.0155	0.0459	0.4471	0.0155	0.0493	0.4187	0.0167	0.0762	0.3951	0.0156	0.0322
0.90	0.1798	0.0168	0.0486	0.1672	0.0207	0.0572	0.2294	0.0256	0.0454	0.1850	0.0195	0.0723

$\cos(\theta^*_{2\pi^0})$	$W=(1592.0\pm4.0)$ MeV			$W=(1600.0\pm4.0)$ MeV			$W=(1608.0\pm4.0)$ MeV			$W=(1616.0\pm4.0)$ MeV		
	$d\sigma/d\Omega$ [μb/sr]	$\Delta_{\rm stat}$ [μb/sr]	$\Delta_{\rm sys}$ [μb/sr]	$d\sigma/d\Omega$ [μb/sr]	$\Delta_{\rm stat}$ [μb/sr]	$\Delta_{\rm sys}$ [μb/sr]	$d\sigma/d\Omega$ [μb/sr]	$\Delta_{\rm stat}$ [μb/sr]	$\Delta_{\rm sys}$ [μb/sr]	$d\sigma/d\Omega$ [μb/sr]	$\Delta_{\rm stat}$ [μb/sr]	$\Delta_{\rm sys}$ [μb/sr]
−0.90	1.3766	0.0237	0.0709	1.2924	0.0224	0.0833	1.2631	0.0221	0.0789	1.2886	0.0263	0.0679
−0.70	0.9194	0.0167	0.0313	0.8882	0.0181	0.0452	0.9337	0.0169	0.0340	0.9236	0.0175	0.0309
−0.50	0.7216	0.0153	0.0216	0.7561	0.0156	0.0270	0.7382	0.0158	0.0213	0.7471	0.0150	0.0180
−0.30	0.6891	0.0147	0.0240	0.6681	0.0154	0.0254	0.7015	0.0140	0.0218	0.7080	0.0139	0.0176
−0.10	0.6572	0.0147	0.0314	0.6683	0.0141	0.0328	0.6996	0.0134	0.0261	0.6915	0.0150	0.0218
0.10	0.5748	0.0145	0.0367	0.5758	0.0144	0.0279	0.6119	0.0139	0.0294	0.6500	0.0133	0.0242
0.30	0.5172	0.0145	0.0359	0.5191	0.0131	0.0263	0.5578	0.0148	0.0273	0.5903	0.0140	0.0225
0.50	0.5120	0.0152	0.0412	0.4663	0.0132	0.0364	0.4901	0.0131	0.0307	0.4961	0.0151	0.0237
0.70	0.4428	0.0173	0.0397	0.4525	0.0150	0.0542	0.4505	0.0142	0.0475	0.4190	0.0129	0.0335
0.90	0.2206	0.0177	0.0446	0.3460	0.0278	0.0752	0.2755	0.0209	0.0675	0.2370	0.0158	0.0394

$\cos(\theta^*_{2\pi^0})$	$W=(1624.0\pm4.0)$ MeV			$W=(1632.0\pm4.0)$ MeV			$W=(1640.0\pm4.0)$ MeV			$W=(1648.0\pm4.0)$ MeV		
	$d\sigma/d\Omega$ [μb/sr]	$\Delta_{\rm stat}$ [μb/sr]	$\Delta_{\rm sys}$ [μb/sr]	$d\sigma/d\Omega$ [μb/sr]	$\Delta_{\rm stat}$ [μb/sr]	$\Delta_{\rm sys}$ [μb/sr]	$d\sigma/d\Omega$ [μb/sr]	$\Delta_{\rm stat}$ [μb/sr]	$\Delta_{\rm sys}$ [μb/sr]	$d\sigma/d\Omega$ [μb/sr]	$\Delta_{\rm stat}$ [μb/sr]	$\Delta_{\rm sys}$ [μb/sr]
−0.90	1.2659	0.0234	0.0742	1.2210	0.0221	0.0677	1.2831	0.0212	0.0915	1.1649	0.0201	0.0663
−0.70	0.9031	0.0179	0.0321	0.9189	0.0164	0.0273	0.9315	0.0161	0.0318	0.8735	0.0155	0.0351
−0.50	0.7642	0.0141	0.0235	0.7263	0.0148	0.0185	0.7386	0.0139	0.0199	0.7608	0.0137	0.0240
−0.30	0.7245	0.0135	0.0249	0.7249	0.0132	0.0213	0.7201	0.0127	0.0223	0.7390	0.0127	0.0227
−0.10	0.7210	0.0147	0.0265	0.7574	0.0124	0.0290	0.7543	0.0133	0.0301	0.7414	0.0145	0.0238
0.10	0.6472	0.0139	0.0238	0.7067	0.0141	0.0322	0.7322	0.0155	0.0301	0.7551	0.0141	0.0288
0.30	0.6148	0.0139	0.0209	0.6402	0.0127	0.0300	0.6528	0.0135	0.0242	0.6682	0.0135	0.0282
0.50	0.4917	0.0124	0.0179	0.5345	0.0155	0.0316	0.5523	0.0132	0.0262	0.5666	0.0120	0.0267
0.70	0.4252	0.0147	0.0374	0.4012	0.0136	0.0368	0.4233	0.0130	0.0371	0.4617	0.0131	0.0311
0.90	0.2767	0.0228	0.0643	0.2857	0.0222	0.0510	0.2806	0.0211	0.0821	0.2878	0.0223	0.0326

$\cos(\theta^*_{2\pi^0})$	$W=(1656.0\pm4.0)$ MeV			$W=(1664.0\pm4.0)$ MeV			$W=(1672.0\pm4.0)$ MeV			$W=(1680.0\pm4.0)$ MeV		
	$d\sigma/d\Omega$ [μb/sr]	$\Delta_{\rm stat}$ [μb/sr]	$\Delta_{\rm sys}$ [μb/sr]	$d\sigma/d\Omega$ [μb/sr]	$\Delta_{\rm stat}$ [μb/sr]	$\Delta_{\rm sys}$ [μb/sr]	$d\sigma/d\Omega$ [μb/sr]	$\Delta_{\rm stat}$ [μb/sr]	$\Delta_{\rm sys}$ [μb/sr]	$d\sigma/d\Omega$ [μb/sr]	$\Delta_{\rm stat}$ [μb/sr]	$\Delta_{\rm sys}$ [μb/sr]
−0.90	1.1643	0.0206	0.0650	1.0963	0.0199	0.0612	1.0354	0.0208	0.0699	1.0807	0.0179	0.0688
−0.70	0.8492	0.0168	0.0274	0.8552	0.0148	0.0262	0.7777	0.0141	0.0370	0.8335	0.0146	0.0279
−0.50	0.6961	0.0148	0.0169	0.6912	0.0144	0.0171	0.6797	0.0125	0.0214	0.7202	0.0136	0.0179
−0.30	0.7734	0.0138	0.0171	0.7118	0.0137	0.0199	0.7373	0.0124	0.0190	0.7490	0.0134	0.0197
−0.10	0.8013	0.0148	0.0216	0.7930	0.0155	0.0254	0.7721	0.0157	0.0188	0.7979	0.0141	0.0202
0.10	0.7450	0.0166	0.0246	0.7868	0.0162	0.0250	0.8419	0.0157	0.0212	0.8029	0.0152	0.0189
0.30	0.6816	0.0149	0.0249	0.7066	0.0155	0.0212	0.7190	0.0143	0.0187	0.7599	0.0150	0.0195
0.50	0.5731	0.0144	0.0214	0.6079	0.0132	0.0182	0.6071	0.0152	0.0215	0.6369	0.0135	0.0246
0.70	0.4989	0.0122	0.0274	0.5146	0.0138	0.0380	0.4386	0.0149	0.0285	0.4831	0.0133	0.0396
0.90	0.2669	0.0255	0.0242	0.3157	0.0271	0.0747	0.4279	0.0275	0.0421	0.2754	0.0261	0.0744

$\cos(\theta^*_{2\pi^0})$	$W=(1688.0\pm4.0)$ MeV			$W=(1696.0\pm4.0)$ MeV			$W=(1704.0\pm4.0)$ MeV			$W=(1712.0\pm4.0)$ MeV		
	$d\sigma/d\Omega$ [μb/sr]	$\Delta_{\rm stat}$ [μb/sr]	$\Delta_{\rm sys}$ [μb/sr]	$d\sigma/d\Omega$ [μb/sr]	$\Delta_{\rm stat}$ [μb/sr]	$\Delta_{\rm sys}$ [μb/sr]	$d\sigma/d\Omega$ [μb/sr]	$\Delta_{\rm stat}$ [μb/sr]	$\Delta_{\rm sys}$ [μb/sr]	$d\sigma/d\Omega$ [μb/sr]	$\Delta_{\rm stat}$ [μb/sr]	$\Delta_{\rm sys}$ [μb/sr]
−0.90	1.0025	0.0199	0.0928	0.9752	0.0177	0.0662	0.9261	0.0196	0.0544	0.8706	0.0185	0.0565
−0.70	0.8487	0.0155	0.0302	0.7810	0.0153	0.0297	0.7418	0.0128	0.0298	0.6479	0.0154	0.0263
−0.50	0.7326	0.0128	0.0199	0.6762	0.0130	0.0202	0.6764	0.0131	0.0207	0.6165	0.0130	0.0180
−0.30	0.7133	0.0131	0.0182	0.7367	0.0122	0.0177	0.7051	0.0110	0.0188	0.6498	0.0109	0.0167
−0.10	0.8237	0.0158	0.0174	0.8178	0.0152	0.0170	0.7594	0.0135	0.0194	0.7470	0.0139	0.0185
0.10	0.8310	0.0152	0.0167	0.8076	0.0148	0.0166	0.7869	0.0137	0.0188	0.7664	0.0146	0.0173
0.30	0.7604	0.0160	0.0180	0.7673	0.0172	0.0173	0.7150	0.0157	0.0150	0.7103	0.0162	0.0153
0.50	0.6191	0.0131	0.0190	0.6285	0.0145	0.0195	0.6322	0.0153	0.0148	0.5750	0.0145	0.0158
0.70	0.5088	0.0143	0.0264	0.5070	0.0141	0.0266	0.4680	0.0133	0.0294	0.4439	0.0121	0.0271
0.90	0.3028	0.0258	0.0368	0.3042	0.0199	0.0327	0.2738	0.0218	0.0470	0.3170	0.0217	0.0418

$\cos(\theta^*_{2\pi^0})$	$W=(1720.0\pm4.0)$ MeV			$W=(1728.0\pm4.0)$ MeV			$W=(1736.0\pm4.0)$ MeV			$W=(1744.0\pm4.0)$ MeV		
	$d\sigma/d\Omega$ [μb/sr]	$\Delta_{\rm stat}$ [μb/sr]	$\Delta_{\rm sys}$ [μb/sr]	$d\sigma/d\Omega$ [μb/sr]	$\Delta_{\rm stat}$ [μb/sr]	$\Delta_{\rm sys}$ [μb/sr]	$d\sigma/d\Omega$ [μb/sr]	$\Delta_{\rm stat}$ [μb/sr]	$\Delta_{\rm sys}$ [μb/sr]	$d\sigma/d\Omega$ [μb/sr]	$\Delta_{\rm stat}$ [μb/sr]	$\Delta_{\rm sys}$ [μb/sr]
−0.90	0.8791	0.0175	0.0637	0.8075	0.0167	0.0475	0.6847	0.0160	0.0460	0.6438	0.0140	0.0562
−0.70	0.6592	0.0129	0.0288	0.6557	0.0109	0.0249	0.5593	0.0110	0.0231	0.5149	0.0103	0.0213
−0.50	0.5956	0.0106	0.0216	0.5871	0.0116	0.0193	0.5459	0.0102	0.0201	0.4922	0.0108	0.0129
−0.30	0.6338	0.0107	0.0165	0.6239	0.0102	0.0169	0.5839	0.0125	0.0186	0.5889	0.0103	0.0130
−0.10	0.7835	0.0144	0.0153	0.7438	0.0127	0.0166	0.7134	0.0132	0.0154	0.6711	0.0139	0.0139
0.10	0.8203	0.0144	0.0160	0.7675	0.0150	0.0153	0.7454	0.0135	0.0134	0.7061	0.0150	0.0148
0.30	0.6881	0.0163	0.0152	0.6803	0.0154	0.0139	0.6257	0.0131	0.0149	0.6245	0.0147	0.0153
0.50	0.5413	0.0134	0.0140	0.5104	0.0105	0.0146	0.5201	0.0141	0.0136	0.5100	0.0124	0.0163
0.70	0.3803	0.0133	0.0203	0.4154	0.0126	0.0216	0.4252	0.0120	0.0231	0.4139	0.0116	0.0276
0.90	0.3462	0.0208	0.0606	0.2835	0.0180	0.0412	0.3041	0.0197	0.0712	0.2579	0.0183	0.0738

$\cos(\theta^*_{2\pi^0})$	$W=(1752.0\pm4.0)$ MeV			$W=(1760.0\pm4.0)$ MeV			$W=(1768.0\pm4.0)$ MeV			$W=(1776.0\pm4.0)$ MeV		
	$d\sigma/d\Omega$ [μb/sr]	$\Delta_{\rm stat}$ [μb/sr]	$\Delta_{\rm sys}$ [μb/sr]	$d\sigma/d\Omega$ [μb/sr]	$\Delta_{\rm stat}$ [μb/sr]	$\Delta_{\rm sys}$ [μb/sr]	$d\sigma/d\Omega$ [μb/sr]	$\Delta_{\rm stat}$ [μb/sr]	$\Delta_{\rm sys}$ [μb/sr]	$d\sigma/d\Omega$ [μb/sr]	$\Delta_{\rm stat}$ [μb/sr]	$\Delta_{\rm sys}$ [μb/sr]
−0.90	0.6170	0.0132	0.0532	0.5504	0.0137	0.0450	0.5906	0.0128	0.0534	0.5286	0.0148	0.0353
−0.70	0.4785	0.0109	0.0202	0.4647	0.0098	0.0199	0.4455	0.0090	0.0196	0.4257	0.0089	0.0165
−0.50	0.4934	0.0101	0.0128	0.4615	0.0100	0.0130	0.4287	0.0100	0.0131	0.3911	0.0089	0.0113
−0.30	0.5866	0.0114	0.0124	0.5189	0.0093	0.0123	0.4820	0.0095	0.0119	0.4761	0.0087	0.0114
−0.10	0.6434	0.0133	0.0139	0.6267	0.0113	0.0139	0.5492	0.0109	0.0122	0.5580	0.0102	0.0132
0.10	0.6547	0.0134	0.0145	0.6227	0.0120	0.0148	0.5606	0.0122	0.0124	0.5606	0.0120	0.0128
0.30	0.6124	0.0132	0.0125	0.5730	0.0118	0.0142	0.5438	0.0128	0.0114	0.5001	0.0108	0.0120
0.50	0.4558	0.0142	0.0107	0.4791	0.0126	0.0144	0.4073	0.0104	0.0128	0.4411	0.0118	0.0125
0.70	0.3872	0.0125	0.0219	0.3853	0.0101	0.0221	0.3501	0.0104	0.0294	0.3115	0.0119	0.0199
0.90	0.2844	0.0257	0.0408	0.2647	0.0246	0.0271	0.1468	0.0217	0.0369	0.3038	0.0205	0.0529

$\cos(\theta^*_{2\pi^0})$	$W=(1784.0\pm4.0)$ MeV			$W=(1792.0\pm4.0)$ MeV			$W=(1800.0\pm4.0)$ MeV			$W=(1808.0\pm4.0)$ MeV		
	$d\sigma/d\Omega$ [μb/sr]	$\Delta_{\rm stat}$ [μb/sr]	$\Delta_{\rm sys}$ [μb/sr]	$d\sigma/d\Omega$ [μb/sr]	$\Delta_{\rm stat}$ [μb/sr]	$\Delta_{\rm sys}$ [μb/sr]	$d\sigma/d\Omega$ [μb/sr]	$\Delta_{\rm stat}$ [μb/sr]	$\Delta_{\rm sys}$ [μb/sr]	$d\sigma/d\Omega$ [μb/sr]	$\Delta_{\rm stat}$ [μb/sr]	$\Delta_{\rm sys}$ [μb/sr]
−0.90	0.4415	0.0141	0.0335	0.4061	0.0125	0.0411	0.3989	0.0135	0.0322	0.4542	0.0134	0.0263
−0.70	0.4197	0.0085	0.0159	0.3897	0.0108	0.0160	0.3622	0.0090	0.0152	0.3747	0.0103	0.0136
−0.50	0.3938	0.0101	0.0113	0.4348	0.0090	0.0132	0.3970	0.0080	0.0130	0.3383	0.0097	0.0127
−0.30	0.4769	0.0091	0.0102	0.4192	0.0088	0.0128	0.4185	0.0086	0.0125	0.4004	0.0086	0.0130
−0.10	0.5675	0.0107	0.0112	0.5191	0.0101	0.0143	0.4965	0.0089	0.0128	0.4357	0.0088	0.0106
0.10	0.5153	0.0107	0.0132	0.4894	0.0094	0.0113	0.5023	0.0111	0.0114	0.4909	0.0087	0.0108
0.30	0.4425	0.0120	0.0115	0.4442	0.0099	0.0102	0.4071	0.0096	0.0098	0.4486	0.0123	0.0114
0.50	0.3574	0.0109	0.0114	0.3543	0.0112	0.0140	0.3729	0.0097	0.0104	0.3611	0.0102	0.0101
0.70	0.3527	0.0127	0.0234	0.3315	0.0123	0.0316	0.3411	0.0111	0.0207	0.2848	0.0109	0.0156
0.90	0.2662	0.0249	0.0557	0.2174	0.0204	0.0645	0.1661	0.0206	0.0316	0.2938	0.0235	0.0583

$\cos(\theta^*_{2\pi^0})$	$W=(1816.0\pm4.0)$ MeV			$W=(1824.0\pm4.0)$ MeV			$W=(1832.0\pm4.0)$ MeV			$W=(1840.0\pm4.0)$ MeV		
	$d\sigma/d\Omega$ [μb/sr]	$\Delta_{\rm stat}$ [μb/sr]	$\Delta_{\rm sys}$ [μb/sr]	$d\sigma/d\Omega$ [μb/sr]	$\Delta_{\rm stat}$ [μb/sr]	$\Delta_{\rm sys}$ [μb/sr]	$d\sigma/d\Omega$ [μb/sr]	$\Delta_{\rm stat}$ [μb/sr]	$\Delta_{\rm sys}$ [μb/sr]	$d\sigma/d\Omega$ [μb/sr]	$\Delta_{\rm stat}$ [μb/sr]	$\Delta_{\rm sys}$ [μb/sr]
−0.90	0.3747	0.0116	0.0388	0.4081	0.0120	0.0298	0.3533	0.0100	0.0306	0.3654	0.0106	0.0350
−0.70	0.3528	0.0080	0.0148	0.3433	0.0096	0.0153	0.3551	0.0089	0.0188	0.3147	0.0084	0.0150
−0.50	0.3432	0.0093	0.0104	0.3111	0.0089	0.0108	0.3049	0.0106	0.0107	0.3242	0.0086	0.0151
−0.30	0.3822	0.0077	0.0130	0.3714	0.0088	0.0103	0.3640	0.0088	0.0103	0.3689	0.0084	0.0123
−0.10	0.4498	0.0083	0.0165	0.4030	0.0094	0.0097	0.4583	0.0097	0.0112	0.4345	0.0085	0.0109
0.10	0.4430	0.0088	0.0154	0.4550	0.0112	0.0122	0.4250	0.0102	0.0117	0.4272	0.0099	0.0106
0.30	0.3863	0.0104	0.0129	0.4466	0.0114	0.0127	0.3713	0.0134	0.0125	0.3785	0.0138	0.0094
0.50	0.3372	0.0109	0.0097	0.3320	0.0128	0.0084	0.3289	0.0119	0.0092	0.3242	0.0134	0.0082
0.70	0.2941	0.0117	0.0223	0.2618	0.0116	0.0294	0.2985	0.0133	0.0247	0.2645	0.0138	0.0233
0.90	0.1853	0.0253	0.0400	0.1835	0.0224	0.0562	0.2002	0.0267	0.1013	0.1532	0.0289	0.0402

$\cos(\theta^*_{2\pi^0})$	$W=(1848.0\pm4.0)$ MeV			$W=(1856.0\pm4.0)$ MeV			$W=(1864.0\pm4.0)$ MeV			$W=(1872.0\pm4.0)$ MeV		
	$d\sigma/d\Omega$ [μb/sr]	$\Delta_{\rm stat}$ [μb/sr]	$\Delta_{\rm sys}$ [μb/sr]	$d\sigma/d\Omega$ [μb/sr]	$\Delta_{\rm stat}$ [μb/sr]	$\Delta_{\rm sys}$ [μb/sr]	$d\sigma/d\Omega$ [μb/sr]	$\Delta_{\rm stat}$ [μb/sr]	$\Delta_{\rm sys}$ [μb/sr]	$d\sigma/d\Omega$ [μb/sr]	$\Delta_{\rm stat}$ [μb/sr]	$\Delta_{\rm sys}$ [μb/sr]
−0.90	0.3666	0.0119	0.0359	0.3004	0.0135	0.0328	0.3565	0.0172	0.0460	0.3124	0.0166	0.0376
−0.70	0.3428	0.0118	0.0162	0.4017	0.0118	0.0173	0.3205	0.0100	0.0162	0.3710	0.0114	0.0363
−0.50	0.3252	0.0090	0.0085	0.2971	0.0086	0.0123	0.3577	0.0101	0.0129	0.3356	0.0113	0.0352
−0.30	0.3807	0.0091	0.0101	0.3206	0.0088	0.0126	0.3438	0.0104	0.0133	0.3371	0.0116	0.0203
−0.10	0.4153	0.0098	0.0147	0.3648	0.0107	0.0109	0.4151	0.0116	0.0143	0.4091	0.0118	0.0144
0.10	0.4121	0.0117	0.0142	0.3991	0.0119	0.0123	0.4146	0.0118	0.0136	0.4043	0.0126	0.0167
0.30	0.4027	0.0125	0.0111	0.3403	0.0102	0.0131	0.3742	0.0109	0.0149	0.2980	0.0146	0.0158
0.50	0.3132	0.0123	0.0123	0.3109	0.0127	0.0162	0.2629	0.0144	0.0155	0.3009	0.0131	0.0294
0.70	0.2751	0.0157	0.0482	0.2641	0.0123	0.0289	0.2412	0.0144	0.0499	0.2540	0.0143	0.0294
0.90	0.1414	0.0334	0.0145	0.1366	0.0304	0.0920	0.0904	0.0344	0.0375	0.1115	0.0377	0.0050

$\cos(\theta^*_{2\pi^0})$	$W=(1880.0\pm4.0)$ MeV			$W=(1888.0\pm4.0)$ MeV			$W=(1896.0\pm4.0)$ MeV		
	$d\sigma/d\Omega$ [μb/sr]	$\Delta_{\rm stat}$ [μb/sr]	$\Delta_{\rm sys}$ [μb/sr]	$d\sigma/d\Omega$ [μb/sr]	$\Delta_{\rm stat}$ [μb/sr]	$\Delta_{\rm sys}$ [μb/sr]	$d\sigma/d\Omega$ [μb/sr]	$\Delta_{\rm stat}$ [μb/sr]	$\Delta_{\rm sys}$ [μb/sr]
−0.90	0.2754	0.0176	0.0316	0.2678	0.0224	0.0269	0.3285	0.0343	0.0414
−0.70	0.3513	0.0134	0.0179	0.2263	0.0153	0.0227	0.3083	0.0178	0.0175
−0.50	0.3500	0.0154	0.0103	0.2742	0.0154	0.0156	0.2372	0.0157	0.0146
−0.30	0.3430	0.0110	0.0098	0.3437	0.0141	0.0145	0.2919	0.0149	0.0278
−0.10	0.3721	0.0114	0.0116	0.4098	0.0168	0.0182	0.3817	0.0188	0.0279
0.10	0.3032	0.0139	0.0148	0.3827	0.0154	0.0123	0.3098	0.0215	0.0363
0.30	0.2957	0.0172	0.0159	0.3276	0.0147	0.0115	0.3023	0.0167	0.0368
0.50	0.3125	0.0191	0.0189	0.2557	0.0139	0.0166	0.3091	0.0176	0.0200
0.70	0.2940	0.0166	0.0506	0.2241	0.0231	0.0434	0.1853	0.0226	0.0336
0.90	0.0411	0.0305	0.0522	0.1448	0.0354	0.1119	0.1606	0.0586	0.0590

E.4 Polarized Results for Double π^0 from the A2 Data

E.4.1 Observables for $\gamma d \to \pi^0\pi^0 p(n)$ as a Function of E_γ

E_γ [MeV]	ΔE_γ [MeV]	E	Δ_{stat}	Δ_{sys}	$\sigma_{1/2}$ [μb]	Δ_{stat} [μb]	Δ_{sys} [μb]	$\sigma_{3/2}$ [μb]	Δ_{stat} [μb]	Δ_{sys} [μb]
420.0	20.0	−1.8019	9.7435	1.8110	−0.0366	0.4469	0.1933	0.1279	0.4469	0.1105
460.0	20.0	1.1518	0.7080	0.1487	0.6496	0.2157	0.0861	−0.0458	0.2157	0.0251
500.0	20.0	−0.0510	0.1519	0.0310	1.1272	0.1824	0.1855	1.2483	0.1824	0.2457
540.0	20.0	−0.3060	0.0731	0.0558	1.9212	0.2043	0.3769	3.6158	0.2043	0.6747
580.0	20.0	−0.3121	0.0639	0.0478	2.5918	0.2424	0.4014	4.9437	0.2424	0.6208
620.0	20.0	−0.4561	0.0462	0.0733	2.8147	0.2419	0.5475	7.5346	0.2419	0.9808
660.0	20.0	−0.3766	0.0311	0.0569	3.9303	0.1994	0.6386	8.6797	0.1994	1.0768
700.0	20.0	−0.2657	0.0291	0.0412	5.1945	0.2084	0.7678	8.9528	0.2084	1.1109
740.0	20.0	−0.3318	0.0277	0.0445	4.9616	0.2098	0.6877	9.8897	0.2098	1.1758
780.0	20.0	−0.1873	0.0296	0.0230	5.4759	0.2014	0.6689	7.9991	0.2014	0.9357
820.0	20.0	−0.1162	0.0300	0.0196	5.3995	0.1856	0.7778	6.8198	0.1856	0.9142
860.0	20.0	0.0085	0.0332	0.0088	5.3833	0.1807	0.6177	5.2930	0.1807	0.5949
900.0	20.0	0.0985	0.0289	0.0130	5.9608	0.1598	0.7839	4.8921	0.1598	0.6401
940.0	20.0	0.0607	0.0267	0.0089	5.9210	0.1521	0.7989	5.2438	0.1521	0.6961
980.0	20.0	0.0900	0.0209	0.0135	6.7619	0.1325	1.0199	5.6454	0.1325	0.8290
1020.0	20.0	0.0506	0.0168	0.0076	7.2559	0.1198	0.9435	6.5568	0.1198	0.8309
1060.0	20.0	0.0918	0.0179	0.0121	7.9298	0.1335	1.0684	6.5961	0.1335	0.8775
1100.0	20.0	0.0958	0.0189	0.0167	8.0383	0.1413	1.0688	6.6327	0.1413	0.8497
1140.0	20.0	0.1432	0.0191	0.0181	8.0180	0.1367	1.0419	6.0094	0.1367	0.7790
1180.0	20.0	0.1702	0.0177	0.0221	7.4518	0.1160	0.9743	5.2843	0.1160	0.6992
1220.0	20.0	0.2056	0.0200	0.0239	6.8635	0.1168	0.7930	4.5223	0.1168	0.5365
1260.0	20.0	0.3273	0.0231	0.0395	6.9190	0.1231	0.7979	3.5068	0.1231	0.4405
1300.0	20.0	0.1642	0.0272	0.0205	5.8415	0.1390	0.7484	4.1938	0.1390	0.5325
1340.0	20.0	0.1949	0.0322	0.0260	5.6119	0.1542	0.7293	3.7810	0.1542	0.5231
1380.0	20.0	0.2207	0.0370	0.0294	5.4948	0.1686	0.6514	3.5081	0.1686	0.4355
1420.0	20.0	0.1055	0.0422	0.2005	4.6305	0.1836	2.9642	3.7468	0.1836	3.7242
1460.0	20.0	0.0000	0.0000	0.3852	0.0000	0.0000	2.8246	0.0000	0.0000	3.0375
1500.0	20.0	0.0000	0.0000	0.0000	0.0000	0.0000	0.0000	0.0000	0.0000	0.0000
1540.0	20.0	0.0000	0.0000	0.0000	0.0000	0.0000	0.0000	0.0000	0.0000	0.0000
1580.0	20.0	0.0000	0.0000	0.0000	0.0000	0.0000	0.0000	0.0000	0.0000	0.0000

E.4.2 Observables for $\gamma d \to \pi^0\pi^0 p(n)$ as a Function of W

W [MeV]	ΔW [MeV]	E	Δ_{stat}	Δ_{sys}	$\sigma_{1/2}$ [μb]	Δ_{stat} [μb]	Δ_{sys} [μb]	$\sigma_{3/2}$ [μb]	Δ_{stat} [μb]	Δ_{sys} [μb]
1310.0	10.0	0.5041	0.5876	0.0751	0.6698	0.2721	0.0949	0.2208	0.2721	0.0445
1330.0	10.0	−0.1145	0.3697	0.0446	0.6629	0.2834	0.0743	0.8343	0.2834	0.1059
1350.0	10.0	−0.1413	0.1423	0.0417	1.4778	0.2533	0.3452	1.9640	0.2533	0.4598
1370.0	10.0	−0.3395	0.0860	0.0447	1.7378	0.2326	0.2441	3.5241	0.2326	0.4299
1390.0	10.0	−0.1692	0.0608	0.0334	3.3304	0.2485	0.6161	4.6873	0.2485	0.8444
1410.0	10.0	−0.4099	0.0552	0.0785	2.8647	0.2716	0.6201	6.8443	0.2716	0.9882
1430.0	10.0	−0.3950	0.0491	0.0638	3.4980	0.2882	0.6662	8.0650	0.2882	1.1527
1450.0	10.0	−0.3320	0.0390	0.0496	4.1852	0.2491	0.6272	8.3446	0.2491	1.0076
1470.0	10.0	−0.2979	0.0332	0.0381	5.2010	0.2505	0.7040	9.6139	0.2505	1.1753
1490.0	10.0	−0.3095	0.0312	0.0473	5.3482	0.2466	0.8259	10.1434	0.2466	1.2743
1510.0	10.0	−0.2977	0.0324	0.0390	5.2355	0.2457	0.6863	9.6745	0.2457	1.1263
1530.0	10.0	−0.2523	0.0334	0.0333	5.0952	0.2311	0.6640	8.5340	0.2311	1.0110
1550.0	10.0	−0.1378	0.0343	0.0218	5.1147	0.2075	0.6725	6.7491	0.2075	0.8139
1570.0	10.0	0.0347	0.0353	0.0095	5.7375	0.2003	0.7627	5.3524	0.2003	0.6744
1590.0	10.0	0.1566	0.0343	0.0225	6.2393	0.1885	0.8740	4.5496	0.1885	0.6636
1610.0	10.0	0.0763	0.0311	0.0112	5.8641	0.1731	0.8676	5.0329	0.1731	0.7393
1630.0	10.0	0.1205	0.0241	0.0197	6.7784	0.1497	1.0485	5.3207	0.1497	0.8521
1650.0	10.0	0.0864	0.0207	0.0112	7.0508	0.1392	0.9282	5.9290	0.1392	0.7818
1670.0	10.0	0.0459	0.0187	0.0077	7.5159	0.1394	1.0228	6.8565	0.1394	0.9051
1690.0	10.0	0.0380	0.0186	0.0080	7.6787	0.1417	0.9576	7.1159	0.1417	0.8636
1710.0	10.0	0.1543	0.0206	0.0184	8.5567	0.1560	1.0458	6.2692	0.1560	0.7812
1730.0	10.0	0.1661	0.0192	0.0202	8.1961	0.1386	1.0047	5.8614	0.1386	0.7253
1750.0	10.0	0.2110	0.0212	0.0250	7.4968	0.1346	0.9062	4.8841	0.1346	0.5933
1770.0	10.0	0.1918	0.0204	0.0264	6.8540	0.1205	0.9274	4.6476	0.1205	0.6572
1790.0	10.0	0.2364	0.0224	0.0372	6.4382	0.1205	0.9846	3.9764	0.1205	0.6489
1810.0	10.0	0.2714	0.0266	0.0322	6.3919	0.1369	0.7425	3.6632	0.1369	0.4476
1830.0	10.0	0.2099	0.0328	0.0237	5.7097	0.1586	0.6636	3.7289	0.1586	0.4308
1850.0	10.0	0.1473	0.0366	0.0165	5.6376	0.1837	0.6406	4.1899	0.1837	0.4771
1870.0	10.0	0.2748	0.0463	0.0318	5.8971	0.2200	0.6776	3.3547	0.2200	0.4065
1890.0	10.0	0.1367	0.0710	0.0270	5.1111	0.3244	1.1020	3.8814	0.3244	0.8827

Angular Distributions

	W=(1310.0±10.0) MeV			W=(1330.0±10.0) MeV			W=(1350.0±10.0) MeV			W=(1370.0±10.0) MeV		
$\cos(\theta^*_{2\pi^0})$	E	Δ_{stat}	Δ_{sys}	E	Δ_{stat}	Δ_{sys}	E	Δ_{stat}	Δ_{sys}	E	Δ_{stat}	Δ_{sys}
−0.80	0.3407	0.5849	0.1568	−0.0180	−0.4004	0.0240	0.8421	0.2036	0.2583	−0.3808	−0.1446	0.0339
−0.40	1.1482	1.1356	0.3585	−0.8776	−0.4226	0.0594	−0.0278	−0.2017	0.0240	−0.4888	−0.1488	0.0862
0.00	2.2253	2.0167	0.1297	0.8154	0.6643	0.1747	−0.3635	−0.2296	0.1011	−0.3270	−0.1534	0.0433
0.40	1.7832	13.0370	2.0748	−2.2252	−3.7517	4.0712	−3.1900	−0.8383	0.0938	−0.0696	−0.4273	0.0475
0.80	13.3872	22.9475	41.3736	414.90[illegible]	[illegible]76.4903	206.1452	−73.458[illegible]	[illegible]78.9293	40.7483	41.3414	29.7194	32.6025

$\cos(\theta^*_{2\pi^0})$	$W=(1390.0\pm10.0)$ MeV			$W=(1410.0\pm10.0)$ MeV			$W=(1430.0\pm10.0)$ MeV			$W=(1450.0\pm10.0)$ MeV		
	E	Δ_{stat}	Δ_{sys}	E	Δ_{stat}	Δ_{sys}	E	Δ_{stat}	Δ_{sys}	E	Δ_{stat}	Δ_{sys}
−0.80	0.2527	0.1035	0.0261	0.1390	0.0973	0.0333	0.2024	0.0711	0.0176	0.1356	0.0653	0.0161
−0.40	−0.1318	−0.1008	0.0254	−0.3591	−0.0764	0.1040	−0.3049	−0.0737	0.0660	−0.2136	−0.0616	0.0332
0.00	−0.3129	−0.1054	0.0476	−0.5685	−0.0976	0.0497	−0.6281	−0.0750	0.1249	−0.5893	−0.0676	0.0858
0.40	−0.3370	−0.2101	0.1255	−1.1935	−0.1755	0.2623	−0.5638	−0.1248	0.0735	−0.3991	−0.0937	0.0533
0.80	0.3494	3.2339	0.4781	0.5535	1.7602	0.2539	−5.1993	−1.9903	10.7976	0.0451	1.9000	0.0442

$\cos(\theta^*_{2\pi^0})$	$W=(1470.0\pm10.0)$ MeV			$W=(1490.0\pm10.0)$ MeV			$W=(1510.0\pm10.0)$ MeV			$W=(1530.0\pm10.0)$ MeV		
	E	Δ_{stat}	Δ_{sys}	E	Δ_{stat}	Δ_{sys}	E	Δ_{stat}	Δ_{sys}	E	Δ_{stat}	Δ_{sys}
−0.80	0.0562	0.0545	0.0090	0.0948	0.0473	0.0134	0.0702	0.0491	0.0154	0.0818	0.0487	0.0091
−0.40	−0.3244	−0.0575	0.0192	−0.3259	−0.0562	0.0299	−0.3821	−0.0641	0.0187	−0.1930	−0.0694	0.0129
0.00	−0.4504	−0.0616	0.0348	−0.5525	−0.0619	0.0550	−0.3958	−0.0624	0.0355	−0.5824	−0.0713	0.0260
0.40	−0.4438	−0.0848	0.0750	−0.4577	−0.0809	0.0426	−0.3985	−0.0743	0.0348	−0.3690	−0.0725	0.0413
0.80	−0.7754	−0.4816	0.4357	−0.4825	−0.4398	0.0469	−0.3618	−0.3318	0.2347	0.6138	0.3042	0.0985

$\cos(\theta^*_{2\pi^0})$	$W=(1550.0\pm10.0)$ MeV			$W=(1570.0\pm10.0)$ MeV			$W=(1590.0\pm10.0)$ MeV			$W=(1610.0\pm10.0)$ MeV		
	E	Δ_{stat}	Δ_{sys}	E	Δ_{stat}	Δ_{sys}	E	Δ_{stat}	Δ_{sys}	E	Δ_{stat}	Δ_{sys}
−0.80	0.0804	0.0513	0.0085	0.1054	0.0498	0.0201	0.3583	0.0544	0.0577	0.2036	0.0518	0.0500
−0.40	−0.2899	−0.0749	0.0019	0.2167	0.0786	0.0032	0.2550	0.0782	0.0026	0.2318	0.0731	0.0090
0.00	−0.1848	−0.0764	0.0226	−0.2760	−0.0801	0.0173	−0.1586	−0.0708	0.0220	−0.1078	−0.0748	0.0083
0.40	−0.2781	−0.0809	0.0279	−0.1568	−0.0766	0.0285	0.0219	0.0716	0.0094	−0.2374	−0.0598	0.0293
0.80	−0.4360	−0.2304	0.1700	0.3156	0.2096	0.0989	0.1391	0.1604	0.0404	0.1003	0.1437	0.0118

$\cos(\theta^*_{2\pi^0})$	$W=(1630.0\pm10.0)$ MeV			$W=(1650.0\pm10.0)$ MeV			$W=(1670.0\pm10.0)$ MeV			$W=(1690.0\pm10.0)$ MeV		
	E	Δ_{stat}	Δ_{sys}	E	Δ_{stat}	Δ_{sys}	E	Δ_{stat}	Δ_{sys}	E	Δ_{stat}	Δ_{sys}
−0.80	0.2953	0.0454	0.0549	0.1769	0.0409	0.0249	0.0835	0.0334	0.0127	0.0122	0.0341	0.0037
−0.40	0.1543	0.0576	0.0115	0.1573	0.0539	0.0192	0.0772	0.0525	0.0128	0.0228	0.0471	0.0181
0.00	0.0696	0.0606	0.0089	0.1343	0.0533	0.0137	0.0339	0.0484	0.0032	0.2986	0.0462	0.0118
0.40	−0.0646	−0.0495	0.0212	−0.0696	−0.0435	0.0089	−0.0627	−0.0382	0.0033	−0.0784	−0.0378	0.0206
0.80	0.0058	0.1115	0.0296	−0.1572	−0.1054	0.0323	−0.1160	−0.0906	0.0251	−0.1945	−0.0938	0.0117

$\cos(\theta^*_{2\pi^0})$	$W=(1710.0\pm10.0)$ MeV			$W=(1730.0\pm10.0)$ MeV			$W=(1750.0\pm10.0)$ MeV			$W=(1770.0\pm10.0)$ MeV		
	E	Δ_{stat}	Δ_{sys}	E	Δ_{stat}	Δ_{sys}	E	Δ_{stat}	Δ_{sys}	E	Δ_{stat}	Δ_{sys}
−0.80	0.1392	0.0381	0.0168	0.1527	0.0420	0.0272	0.1305	0.0441	0.0212	0.2722	0.0477	0.0267
−0.40	0.2829	0.0511	0.0138	0.0681	0.0527	0.0103	0.2178	0.0528	0.0061	0.1120	0.0514	0.0053
0.00	0.3611	0.0461	0.0186	0.2853	0.0464	0.0158	0.2872	0.0482	0.0109	0.2508	0.0467	0.0427
0.40	−0.0741	−0.0441	0.0232	0.1678	0.0417	0.0110	0.2179	0.0487	0.0149	0.1841	0.0479	0.0063
0.80	0.0773	0.0896	0.0160	−0.0908	−0.0765	0.0369	0.1308	0.0824	0.0321	−0.0124	−0.0856	0.0273

$\cos(\theta^*_{2\pi^0})$	$W=(1790.0\pm10.0)$ MeV			$W=(1810.0\pm10.0)$ MeV			$W=(1830.0\pm10.0)$ MeV			$W=(1850.0\pm10.0)$ MeV		
	E	Δ_{stat}	Δ_{sys}	E	Δ_{stat}	Δ_{sys}	E	Δ_{stat}	Δ_{sys}	E	Δ_{stat}	Δ_{sys}
−0.80	0.1657	0.0648	0.0069	0.1886	0.0759	0.0133	0.2750	0.0890	0.0176	−0.2656	−0.1120	0.0215
−0.40	0.2859	0.0577	0.0609	0.1851	0.0725	0.0170	0.2122	0.0751	0.0184	0.2503	0.0943	0.0111
0.00	0.4652	0.0505	0.0956	0.4143	0.0590	0.0103	0.2474	0.0800	0.0108	0.3244	0.0842	0.0050
0.40	0.0219	0.0514	0.0300	0.2871	0.0582	0.0210	0.2745	0.0741	0.0167	0.0779	0.0808	0.0105
0.80	0.0916	0.1053	0.0130	0.2560	0.1267	0.0415	−0.1279	−0.1490	0.0183	0.0537	0.1606	0.0161

$\cos(\theta^*_{2\pi^0})$				$W=(1870.0\pm10.0)$ MeV						$W=(1890.0\pm10.0)$ MeV		
				E	Δ_{stat}	Δ_{sys}				E	Δ_{stat}	Δ_{sys}
−0.80				−0.0226	−0.1143	0.0270				0.0685	0.1508	0.0139
−0.40				0.3415	0.1287	0.0326				0.2139	0.1718	0.0156
0.00				0.4395	0.1160	0.0235				0.1627	0.1455	0.0359
0.40				0.1608	0.1143	0.0167				0.0782	0.1623	0.0302
0.80				0.3511	0.2088	0.0495				0.2810	0.3233	0.0590

$\cos(\theta^*_{2\pi^0})$	$W=(1310.0\pm10.0)$ MeV			$W=(1330.0\pm10.0)$ MeV			$W=(1350.0\pm10.0)$ MeV			$W=(1370.0\pm10.0)$ MeV		
	$d\sigma_{1/2}/d\Omega$ [μb/sr]	Δ_{stat} [μb/sr]	Δ_{sys} [μb/sr]	$d\sigma_{1/2}/d\Omega$ [μb/sr]	Δ_{stat} [μb/sr]	Δ_{sys} [μb/sr]	$d\sigma_{1/2}/d\Omega$ [μb/sr]	Δ_{stat} [μb/sr]	Δ_{sys} [μb/sr]	$d\sigma_{1/2}/d\Omega$ [μb/sr]	Δ_{stat} [μb/sr]	Δ_{sys} [μb/sr]
−0.80	0.0364	0.0160	0.0097	0.0425	0.0174	0.0051	0.1819	0.0204	0.0443	0.0878	0.0208	0.0089
−0.40	0.0699	0.0371	0.0173	0.0097	0.0335	0.0047	0.1783	0.0371	0.0517	0.1310	0.0385	0.0327
0.00	0.1379	0.0865	0.0084	0.1578	0.0579	0.0324	0.1268	0.0460	0.0356	0.1850	0.0425	0.0105
0.40	0.0628	0.2943	0.0468	−0.0671	0.2060	0.2231	−0.3129	0.1219	0.0308	0.2223	0.1023	0.0337
0.80	0.7597	1.3818	1.0759	0.9048	26.3675	0.5655	0.4511	5.0216	0.2852	2.4076	2.2694	1.8573

$\cos(\theta^*_{2\pi^0})$	$W=(1390.0\pm10.0)$ MeV			$W=(1410.0\pm10.0)$ MeV			$W=(1430.0\pm10.0)$ MeV			$W=(1450.0\pm10.0)$ MeV		
	$d\sigma_{1/2}/d\Omega$ [μb/sr]	Δ_{stat} [μb/sr]	Δ_{sys} [μb/sr]	$d\sigma_{1/2}/d\Omega$ [μb/sr]	Δ_{stat} [μb/sr]	Δ_{sys} [μb/sr]	$d\sigma_{1/2}/d\Omega$ [μb/sr]	Δ_{stat} [μb/sr]	Δ_{sys} [μb/sr]	$d\sigma_{1/2}/d\Omega$ [μb/sr]	Δ_{stat} [μb/sr]	Δ_{sys} [μb/sr]
−0.80	0.2865	0.0240	0.0295	0.3390	0.0292	0.0376	0.4687	0.0282	0.0440	0.5245	0.0307	0.0561
−0.40	0.3285	0.0386	0.0549	0.2944	0.0356	0.0771	0.3886	0.0417	0.0783	0.4616	0.0368	0.0612
0.00	0.2707	0.0419	0.0467	0.2005	0.0459	0.0343	0.2146	0.0440	0.0821	0.2536	0.0425	0.0673
0.40	0.2228	0.0710	0.0671	−0.0755	0.0694	0.0709	0.2065	0.0597	0.0511	0.3206	0.0507	0.0533
0.80	0.2163	0.5195	0.1671	0.3150	0.3580	0.0870	−0.7371	0.3850	0.1110	0.1198	0.2198	0.0468

$\cos(\theta^*_{2\pi^0})$	$W=(1470.0\pm10.0)$ MeV			$W=(1490.0\pm10.0)$ MeV			$W=(1510.0\pm10.0)$ MeV			$W=(1530.0\pm10.0)$ MeV		
	$d\sigma_{1/2}/d\Omega$ [μb/sr]	Δ_{stat} [μb/sr]	Δ_{sys} [μb/sr]	$d\sigma_{1/2}/d\Omega$ [μb/sr]	Δ_{stat} [μb/sr]	Δ_{sys} [μb/sr]	$d\sigma_{1/2}/d\Omega$ [μb/sr]	Δ_{stat} [μb/sr]	Δ_{sys} [μb/sr]	$d\sigma_{1/2}/d\Omega$ [μb/sr]	Δ_{stat} [μb/sr]	Δ_{sys} [μb/sr]
−0.80	0.6368	0.0336	0.0664	0.7549	0.0335	0.1033	0.7615	0.0359	0.0927	0.7685	0.0357	0.0817
−0.40	0.4398	0.0382	0.0313	0.4528	0.0386	0.0485	0.3778	0.0401	0.0239	0.4428	0.0388	0.0253
0.00	0.3583	0.0410	0.0432	0.2893	0.0409	0.0509	0.3665	0.0387	0.0306	0.2082	0.0364	0.0176
0.40	0.3189	0.0495	0.0726	0.3154	0.0479	0.0457	0.3490	0.0441	0.0399	0.3248	0.0381	0.0411
0.80	0.0764	0.1673	0.1481	0.1839	0.1590	0.0226	0.2307	0.1222	0.1025	0.5370	0.1038	0.1310

$\cos(\theta^*_{2\pi^0})$	$W=(1550.0\pm10.0)$ MeV			$W=(1570.0\pm10.0)$ MeV			$W=(1590.0\pm10.0)$ MeV			$W=(1610.0\pm10.0)$ MeV		
	$d\sigma_{1/2}/d\Omega$ [μb/sr]	Δ_{stat} [μb/sr]	Δ_{sys} [μb/sr]	$d\sigma_{1/2}/d\Omega$ [μb/sr]	Δ_{stat} [μb/sr]	Δ_{sys} [μb/sr]	$d\sigma_{1/2}/d\Omega$ [μb/sr]	Δ_{stat} [μb/sr]	Δ_{sys} [μb/sr]	$d\sigma_{1/2}/d\Omega$ [μb/sr]	Δ_{stat} [μb/sr]	Δ_{sys} [μb/sr]
−0.80	0.6983	0.0343	0.0662	0.6971	0.0326	0.1038	0.7820	0.0326	0.1059	0.7200	0.0324	0.1369
−0.40	0.3151	0.0341	0.0025	0.4986	0.0330	0.0076	0.4568	0.0293	0.0092	0.4463	0.0271	0.0023
0.00	0.3470	0.0332	0.0317	0.2706	0.0308	0.0194	0.3141	0.0271	0.0290	0.3178	0.0273	0.0247
0.40	0.3159	0.0363	0.0366	0.3634	0.0340	0.0376	0.4369	0.0315	0.0283	0.3420	0.0276	0.0392
0.80	0.2089	0.0883	0.0714	0.4881	0.0818	0.0451	0.4721	0.0688	0.0978	0.4398	0.0607	0.0531

$\cos(\theta^*_{2\pi^0})$	$W=(1630.0\pm10.0)$ MeV			$W=(1650.0\pm10.0)$ MeV			$W=(1670.0\pm10.0)$ MeV			$W=(1690.0\pm10.0)$ MeV		
	$d\sigma_{1/2}/d\Omega$ [μb/sr]	Δ_{stat} [μb/sr]	Δ_{sys} [μb/sr]	$d\sigma_{1/2}/d\Omega$ [μb/sr]	Δ_{stat} [μb/sr]	Δ_{sys} [μb/sr]	$d\sigma_{1/2}/d\Omega$ [μb/sr]	Δ_{stat} [μb/sr]	Δ_{sys} [μb/sr]	$d\sigma_{1/2}/d\Omega$ [μb/sr]	Δ_{stat} [μb/sr]	Δ_{sys} [μb/sr]
−0.80	0.7984	0.0294	0.1160	0.7347	0.0269	0.0954	0.7428	0.0241	0.0982	0.6823	0.0243	0.0758
−0.40	0.4534	0.0234	0.0364	0.4836	0.0232	0.0102	0.5030	0.0251	0.0369	0.4970	0.0235	0.0127
0.00	0.4002	0.0235	0.0306	0.4752	0.0230	0.0277	0.4828	0.0234	0.0271	0.6396	0.0238	0.0288
0.40	0.4942	0.0269	0.0598	0.5456	0.0263	0.0524	0.6120	0.0259	0.0312	0.6366	0.0271	0.0375
0.80	0.5048	0.0585	0.0613	0.4505	0.0604	0.0470	0.5262	0.0581	0.0477	0.4794	0.0587	0.0166

$\cos(\theta^*_{2\pi^0})$	$W=(1710.0\pm10.0)$ MeV			$W=(1730.0\pm10.0)$ MeV			$W=(1750.0\pm10.0)$ MeV			$W=(1770.0\pm10.0)$ MeV		
	$d\sigma_{1/2}/d\Omega$ [μb/sr]	Δ_{stat} [μb/sr]	Δ_{sys} [μb/sr]	$d\sigma_{1/2}/d\Omega$ [μb/sr]	Δ_{stat} [μb/sr]	Δ_{sys} [μb/sr]	$d\sigma_{1/2}/d\Omega$ [μb/sr]	Δ_{stat} [μb/sr]	Δ_{sys} [μb/sr]	$d\sigma_{1/2}/d\Omega$ [μb/sr]	Δ_{stat} [μb/sr]	Δ_{sys} [μb/sr]
−0.80	0.7328	0.0255	0.0754	0.6530	0.0249	0.0747	0.5295	0.0216	0.0507	0.5006	0.0199	0.0517
−0.40	0.6491	0.0264	0.0334	0.5162	0.0259	0.0171	0.4997	0.0222	0.0146	0.4342	0.0207	0.0189
0.00	0.7121	0.0251	0.0141	0.6693	0.0251	0.0346	0.6056	0.0237	0.0128	0.5552	0.0215	0.0428
0.40	0.6522	0.0319	0.0495	0.7949	0.0294	0.0413	0.7341	0.0304	0.0595	0.6762	0.0283	0.0301
0.80	0.6106	0.0534	0.0239	0.5231	0.0468	0.0280	0.5735	0.0442	0.0280	0.4824	0.0437	0.0512

$\cos(\theta^*_{2\pi^0})$	$W=(1790.0\pm10.0)$ MeV			$W=(1810.0\pm10.0)$ MeV			$W=(1830.0\pm10.0)$ MeV			$W=(1850.0\pm10.0)$ MeV		
	$d\sigma_{1/2}/d\Omega$ [μb/sr]	Δ_{stat} [μb/sr]	Δ_{sys} [μb/sr]	$d\sigma_{1/2}/d\Omega$ [μb/sr]	Δ_{stat} [μb/sr]	Δ_{sys} [μb/sr]	$d\sigma_{1/2}/d\Omega$ [μb/sr]	Δ_{stat} [μb/sr]	Δ_{sys} [μb/sr]	$d\sigma_{1/2}/d\Omega$ [μb/sr]	Δ_{stat} [μb/sr]	Δ_{sys} [μb/sr]
−0.80	0.3647	0.0211	0.0165	0.3518	0.0234	0.0303	0.3182	0.0228	0.0133	0.1780	0.0278	0.0081
−0.40	0.4831	0.0223	0.0672	0.4107	0.0256	0.0286	0.4091	0.0260	0.0354	0.4093	0.0316	0.0139
0.00	0.6246	0.0224	0.0938	0.5838	0.0252	0.0064	0.4591	0.0301	0.0216	0.5157	0.0336	0.0078
0.40	0.5556	0.0287	0.0722	0.6923	0.0322	0.0491	0.6498	0.0390	0.0409	0.5785	0.0445	0.0126
0.80	0.4714	0.0482	0.0796	0.4967	0.0516	0.0538	0.3254	0.0586	0.0746	0.4655	0.0733	0.0138

$\cos(\theta^*_{2\pi^0})$	$W=(1870.0\pm10.0)$ MeV			$W=(1890.0\pm10.0)$ MeV		
	$d\sigma_{1/2}/d\Omega$ [μb/sr]	Δ_{stat} [μb/sr]	Δ_{sys} [μb/sr]	$d\sigma_{1/2}/d\Omega$ [μb/sr]	Δ_{stat} [μb/sr]	Δ_{sys} [μb/sr]
−0.80	0.2409	0.0291	0.0256	0.2469	0.0356	0.0177
−0.40	0.3921	0.0383	0.0364	0.3620	0.0523	0.0373
0.00	0.5047	0.0420	0.0260	0.4172	0.0538	0.1183
0.40	0.5943	0.0601	0.0384	0.5721	0.0876	0.1057
0.80	0.5350	0.0865	0.0858	0.4290	0.1113	0.1408

$\cos(\theta^*_{2\pi^0})$	$W=(1310.0\pm10.0)$ MeV			$W=(1330.0\pm10.0)$ MeV			$W=(1350.0\pm10.0)$ MeV			$W=(1370.0\pm10.0)$ MeV		
	$d\sigma_{3/2}/d\Omega$ [μb/sr]	Δ_{stat} [μb/sr]	Δ_{sys} [μb/sr]	$d\sigma_{3/2}/d\Omega$ [μb/sr]	Δ_{stat} [μb/sr]	Δ_{sys} [μb/sr]	$d\sigma_{3/2}/d\Omega$ [μb/sr]	Δ_{stat} [μb/sr]	Δ_{sys} [μb/sr]	$d\sigma_{3/2}/d\Omega$ [μb/sr]	Δ_{stat} [μb/sr]	Δ_{sys} [μb/sr]
−0.80	0.0179	0.0160	0.0063	0.0441	0.0174	0.0037	0.0156	0.0204	0.0255	0.1959	0.0208	0.0098
−0.40	−0.0048	0.0371	0.0099	0.1482	0.0335	0.0061	0.1885	0.0371	0.0550	0.3816	0.0385	0.0465
0.00	−0.0524	0.0865	0.0055	0.0161	0.0579	0.0177	0.2717	0.0460	0.0642	0.3648	0.0425	0.0157
0.40	−0.0177	0.2943	0.0666	0.1768	0.2060	0.2602	0.5987	0.1219	0.0510	0.2555	0.1023	0.0404
0.80	−0.6541	1.3818	1.0029	−0.9004	26.3675	0.4472	−0.4635	5.0216	0.2537	−2.2939	2.2694	1.9315

$\cos(\theta^*_{2\pi^0})$	$W=(1390.0\pm10.0)$ MeV			$W=(1410.0\pm10.0)$ MeV			$W=(1430.0\pm10.0)$ MeV			$W=(1450.0\pm10.0)$ MeV		
	$d\sigma_{3/2}/d\Omega$ [μb/sr]	Δ_{stat} [μb/sr]	Δ_{sys} [μb/sr]	$d\sigma_{3/2}/d\Omega$ [μb/sr]	Δ_{stat} [μb/sr]	Δ_{sys} [μb/sr]	$d\sigma_{3/2}/d\Omega$ [μb/sr]	Δ_{stat} [μb/sr]	Δ_{sys} [μb/sr]	$d\sigma_{3/2}/d\Omega$ [μb/sr]	Δ_{stat} [μb/sr]	Δ_{sys} [μb/sr]
−0.80	0.1709	0.0240	0.0205	0.2562	0.0292	0.0279	0.3109	0.0282	0.0291	0.3993	0.0307	0.0358
−0.40	0.4282	0.0386	0.0797	0.6244	0.0356	0.0897	0.7294	0.0417	0.0964	0.7123	0.0368	0.0674
0.00	0.5172	0.0419	0.0665	0.7290	0.0459	0.0532	0.9395	0.0440	0.1426	0.9812	0.0425	0.1000
0.40	0.4492	0.0710	0.1027	0.8560	0.0694	0.1164	0.7404	0.0597	0.0964	0.7466	0.0507	0.0800
0.80	0.1043	0.5195	0.1828	0.0905	0.3580	0.1677	1.0881	0.3850	0.1352	0.1094	0.2198	0.0602

$\cos(\theta^*_{2\pi^0})$	$W=(1470.0\pm10.0)$ MeV			$W=(1490.0\pm10.0)$ MeV			$W=(1510.0\pm10.0)$ MeV			$W=(1530.0\pm10.0)$ MeV		
	$d\sigma_{3/2}/d\Omega$ [μb/sr]	Δ_{stat} [μb/sr]	Δ_{sys} [μb/sr]	$d\sigma_{3/2}/d\Omega$ [μb/sr]	Δ_{stat} [μb/sr]	Δ_{sys} [μb/sr]	$d\sigma_{3/2}/d\Omega$ [μb/sr]	Δ_{stat} [μb/sr]	Δ_{sys} [μb/sr]	$d\sigma_{3/2}/d\Omega$ [μb/sr]	Δ_{stat} [μb/sr]	Δ_{sys} [μb/sr]
−0.80	0.5690	0.0336	0.0533	0.6242	0.0335	0.0786	0.6615	0.0359	0.0714	0.6523	0.0357	0.0647
−0.40	0.8622	0.0382	0.0368	0.8905	0.0386	0.0598	0.8451	0.0401	0.0261	0.6546	0.0388	0.0307
0.00	0.9455	0.0410	0.0590	1.0036	0.0409	0.0666	0.8466	0.0387	0.0237	0.7891	0.0364	0.0177
0.40	0.8279	0.0495	0.1091	0.8478	0.0479	0.0777	0.8115	0.0441	0.0482	0.7047	0.0381	0.0434
0.80	0.6036	0.1673	0.2708	0.5269	0.1590	0.0064	0.4924	0.1222	0.1565	0.1285	0.1038	0.0472

$\cos(\theta^*_{2\pi^0})$	W=(1550.0±10.0) MeV			W=(1570.0±10.0) MeV			W=(1590.0±10.0) MeV			W=(1610.0±10.0) MeV		
	$d\sigma_{3/2}/d\Omega$ [μb/sr]	$\Delta_{\rm stat}$ [μb/sr]	$\Delta_{\rm sys}$ [μb/sr]	$d\sigma_{3/2}/d\Omega$ [μb/sr]	$\Delta_{\rm stat}$ [μb/sr]	$\Delta_{\rm sys}$ [μb/sr]	$d\sigma_{3/2}/d\Omega$ [μb/sr]	$\Delta_{\rm stat}$ [μb/sr]	$\Delta_{\rm sys}$ [μb/sr]	$d\sigma_{3/2}/d\Omega$ [μb/sr]	$\Delta_{\rm stat}$ [μb/sr]	$\Delta_{\rm sys}$ [μb/sr]
−0.80	0.5943	0.0343	0.0518	0.5641	0.0326	0.0871	0.3694	0.0326	0.0701	0.4764	0.0324	0.0985
−0.40	0.5724	0.0341	0.0061	0.3210	0.0330	0.0063	0.2712	0.0293	0.0065	0.2783	0.0271	0.0054
0.00	0.5043	0.0332	0.0298	0.4770	0.0308	0.0224	0.4325	0.0271	0.0297	0.3946	0.0273	0.0314
0.40	0.5593	0.0363	0.0488	0.4986	0.0340	0.0310	0.4181	0.0315	0.0324	0.5550	0.0276	0.0428
0.80	0.5319	0.0883	0.1074	0.2540	0.0818	0.0566	0.3568	0.0688	0.0762	0.3596	0.0607	0.0391

$\cos(\theta^*_{2\pi^0})$	W=(1630.0±10.0) MeV			W=(1650.0±10.0) MeV			W=(1670.0±10.0) MeV			W=(1690.0±10.0) MeV		
	$d\sigma_{3/2}/d\Omega$ [μb/sr]	$\Delta_{\rm stat}$ [μb/sr]	$\Delta_{\rm sys}$ [μb/sr]	$d\sigma_{3/2}/d\Omega$ [μb/sr]	$\Delta_{\rm stat}$ [μb/sr]	$\Delta_{\rm sys}$ [μb/sr]	$d\sigma_{3/2}/d\Omega$ [μb/sr]	$\Delta_{\rm stat}$ [μb/sr]	$\Delta_{\rm sys}$ [μb/sr]	$d\sigma_{3/2}/d\Omega$ [μb/sr]	$\Delta_{\rm stat}$ [μb/sr]	$\Delta_{\rm sys}$ [μb/sr]
−0.80	0.4344	0.0294	0.0834	0.5138	0.0269	0.0747	0.6284	0.0241	0.0805	0.6658	0.0243	0.0707
−0.40	0.3322	0.0234	0.0273	0.3522	0.0232	0.0143	0.4309	0.0251	0.0252	0.4749	0.0235	0.0122
0.00	0.3482	0.0235	0.0303	0.3627	0.0230	0.0135	0.4512	0.0234	0.0233	0.3455	0.0238	0.0180
0.40	0.5624	0.0269	0.0558	0.6273	0.0263	0.0662	0.6939	0.0259	0.0334	0.7449	0.0271	0.0261
0.80	0.4990	0.0585	0.0466	0.6185	0.0604	0.0372	0.6643	0.0581	0.0494	0.7109	0.0587	0.0378

$\cos(\theta^*_{2\pi^0})$	W=(1710.0±10.0) MeV			W=(1730.0±10.0) MeV			W=(1750.0±10.0) MeV			W=(1770.0±10.0) MeV		
	$d\sigma_{3/2}/d\Omega$ [μb/sr]	$\Delta_{\rm stat}$ [μb/sr]	$\Delta_{\rm sys}$ [μb/sr]	$d\sigma_{3/2}/d\Omega$ [μb/sr]	$\Delta_{\rm stat}$ [μb/sr]	$\Delta_{\rm sys}$ [μb/sr]	$d\sigma_{3/2}/d\Omega$ [μb/sr]	$\Delta_{\rm stat}$ [μb/sr]	$\Delta_{\rm sys}$ [μb/sr]	$d\sigma_{3/2}/d\Omega$ [μb/sr]	$\Delta_{\rm stat}$ [μb/sr]	$\Delta_{\rm sys}$ [μb/sr]
−0.80	0.5537	0.0255	0.0626	0.4800	0.0249	0.0669	0.4072	0.0216	0.0478	0.2864	0.0199	0.0360
−0.40	0.3628	0.0264	0.0206	0.4504	0.0259	0.0099	0.3210	0.0222	0.0121	0.3467	0.0207	0.0168
0.00	0.3342	0.0251	0.0088	0.3721	0.0251	0.0276	0.3354	0.0237	0.0101	0.3325	0.0215	0.0426
0.40	0.7565	0.0319	0.0319	0.5665	0.0294	0.0372	0.4714	0.0304	0.0363	0.4659	0.0283	0.0172
0.80	0.5230	0.0534	0.0291	0.6276	0.0468	0.0207	0.4408	0.0442	0.0084	0.4946	0.0437	0.0377

$\cos(\theta^*_{2\pi^0})$	W=(1790.0±10.0) MeV			W=(1810.0±10.0) MeV			W=(1830.0±10.0) MeV			W=(1850.0±10.0) MeV		
	$d\sigma_{3/2}/d\Omega$ [μb/sr]	$\Delta_{\rm stat}$ [μb/sr]	$\Delta_{\rm sys}$ [μb/sr]	$d\sigma_{3/2}/d\Omega$ [μb/sr]	$\Delta_{\rm stat}$ [μb/sr]	$\Delta_{\rm sys}$ [μb/sr]	$d\sigma_{3/2}/d\Omega$ [μb/sr]	$\Delta_{\rm stat}$ [μb/sr]	$\Delta_{\rm sys}$ [μb/sr]	$d\sigma_{3/2}/d\Omega$ [μb/sr]	$\Delta_{\rm stat}$ [μb/sr]	$\Delta_{\rm sys}$ [μb/sr]
−0.80	0.2610	0.0211	0.0120	0.2402	0.0234	0.0238	0.1809	0.0228	0.0110	0.3068	0.0278	0.0267
−0.40	0.2683	0.0223	0.0505	0.2824	0.0256	0.0187	0.2659	0.0260	0.0250	0.2454	0.0316	0.0133
0.00	0.2280	0.0224	0.0619	0.2418	0.0252	0.0075	0.2770	0.0301	0.0176	0.2631	0.0336	0.0058
0.40	0.5318	0.0287	0.0446	0.3835	0.0322	0.0343	0.3700	0.0390	0.0276	0.4949	0.0445	0.0203
0.80	0.3923	0.0482	0.0667	0.2942	0.0516	0.0445	0.4208	0.0586	0.0845	0.4181	0.0733	0.0121

$\cos(\theta^*_{2\pi^0})$	W=(1870.0±10.0) MeV			W=(1890.0±10.0) MeV		
	$d\sigma_{3/2}/d\Omega$ [μb/sr]	$\Delta_{\rm stat}$ [μb/sr]	$\Delta_{\rm sys}$ [μb/sr]	$d\sigma_{3/2}/d\Omega$ [μb/sr]	$\Delta_{\rm stat}$ [μb/sr]	$\Delta_{\rm sys}$ [μb/sr]
−0.80	0.2521	0.0291	0.0330	0.2152	0.0356	0.0103
−0.40	0.1925	0.0383	0.0149	0.2344	0.0523	0.0305
0.00	0.1966	0.0420	0.0186	0.3004	0.0538	0.1079
0.40	0.4297	0.0601	0.0336	0.4890	0.0876	0.0748
0.80	0.2570	0.0865	0.0739	0.2408	0.1113	0.1210

E.4.3 Observables for $\gamma d \to \pi^0\pi^0 n(p)$ as a Function of E_γ

E_γ [MeV]	ΔE_γ [MeV]	E	$\Delta_{\rm stat}$	$\Delta_{\rm sys}$	$\sigma_{1/2}$ [μb]	$\Delta_{\rm stat}$ [μb]	$\Delta_{\rm sys}$ [μb]	$\sigma_{3/2}$ [μb]	$\Delta_{\rm stat}$ [μb]	$\Delta_{\rm sys}$ [μb]
420.0	20.0	1.1380	3.2302	0.4618	0.4167	0.6309	0.1177	−0.0269	0.6309	0.0865
460.0	20.0	−0.9155	0.9301	0.2155	0.0260	0.2884	0.0970	0.5891	0.2884	0.1230
500.0	20.0	0.5853	0.2747	0.0836	1.4138	0.2478	0.1987	0.3698	0.2478	0.0923
540.0	20.0	−0.0524	0.1075	0.0345	2.0037	0.2298	0.3401	2.2251	0.2298	0.3004
580.0	20.0	−0.3543	0.0961	0.0426	1.9223	0.2882	0.2177	4.0315	0.2882	0.4505
620.0	20.0	−0.5464	0.0767	0.0637	1.9545	0.3333	0.2561	6.6626	0.3333	0.7584
660.0	20.0	−0.4453	0.0535	0.0532	3.1966	0.3121	0.3917	8.3284	0.3121	0.9171
700.0	20.0	−0.4362	0.0458	0.0487	3.8097	0.3142	0.4298	9.7056	0.3142	1.0687
740.0	20.0	−0.2414	0.0431	0.0278	5.8231	0.3353	0.6747	9.5283	0.3353	1.0714
780.0	20.0	−0.1493	0.0446	0.0197	6.6187	0.3509	0.7605	8.9416	0.3509	0.9910
820.0	20.0	−0.1067	0.0437	0.0124	6.5777	0.3255	0.7346	8.1488	0.3255	0.9021
860.0	20.0	−0.1016	0.0487	0.0140	5.9392	0.3294	0.6669	7.2832	0.3294	0.8067
900.0	20.0	−0.1307	0.0418	0.0149	6.0221	0.2937	0.6697	7.8334	0.2937	0.8643
940.0	20.0	−0.0469	0.0398	0.0054	6.8590	0.2907	0.7963	7.5340	0.2907	0.8703
980.0	20.0	−0.1382	0.0362	0.0157	6.4803	0.2766	0.7293	8.5584	0.2766	0.9575
1020.0	20.0	−0.0814	0.0324	0.0142	7.1077	0.2560	0.8224	8.3675	0.2560	0.9617
1060.0	20.0	−0.1658	0.0346	0.0205	6.4529	0.2721	0.7336	9.0173	0.2721	1.0109
1100.0	20.0	−0.2077	0.0387	0.0257	5.5805	0.2772	0.7615	8.5068	0.2772	1.0772
1140.0	20.0	−0.0011	0.0422	0.0023	6.4280	0.2753	0.8554	6.4419	0.2753	0.8569
1180.0	20.0	−0.1864	0.0398	0.0216	4.6884	0.2329	0.5319	6.8369	0.2329	0.7675
1220.0	20.0	−0.1820	0.0451	0.0273	4.0386	0.2272	0.7714	5.8360	0.2272	0.9662
1260.0	20.0	−0.2422	0.0511	0.0305	3.2851	0.2254	0.4705	5.3850	0.2254	0.7071
1300.0	20.0	−0.2720	0.0589	0.0353	3.0066	0.2473	0.3635	5.2527	0.2473	0.6656
1340.0	20.0	−0.2109	0.0652	0.0291	3.0570	0.2573	0.5121	4.6907	0.2573	0.6873
1380.0	20.0	−0.0850	0.0723	0.0159	3.2933	0.2629	0.8625	3.9052	0.2629	0.9338
1420.0	20.0	−0.2172	0.0794	0.4186	2.9044	0.3003	4.0699	4.5164	0.3003	2.8499
1460.0	20.0	0.0000	0.0000	2.0664	0.0000	0.0000	2.9461	0.0000	0.0000	4.5731
1500.0	20.0	0.0000	0.0000	0.0000	0.0000	0.0000	0.0000	0.0000	0.0000	0.0000
1540.0	20.0	0.0000	0.0000	0.0000	0.0000	0.0000	0.0000	0.0000	0.0000	0.0000
1580.0	20.0	0.0000	0.0000	0.0000	0.0000	0.0000	0.0000	0.0000	0.0000	0.0000

E.4.4 Observables for $\gamma d \rightarrow \pi^0\pi^0 n(p)$ as a Function of W

W [MeV]	ΔW [MeV]	E	Δ_{stat}	Δ_{sys}	$\sigma_{1/2}$ [μb]	Δ_{stat} [μb]	Δ_{sys} [μb]	$\sigma_{3/2}$ [μb]	Δ_{stat} [μb]	Δ_{sys} [μb]
1310.0	10.0	1.0126	0.9070	0.2679	0.7138	0.3288	0.1354	−0.0045	0.3288	0.1319
1330.0	10.0	−0.0479	0.7484	0.0190	0.4522	0.3584	0.1417	0.4977	0.3584	0.1751
1350.0	10.0	−0.6136	0.2540	0.0745	0.4854	0.3243	0.0897	2.0273	0.3243	0.2494
1370.0	10.0	0.3139	0.1858	0.0376	2.4355	0.3490	0.2888	1.2718	0.3490	0.1631
1390.0	10.0	−0.4289	0.1282	0.0584	1.5605	0.3541	0.2303	3.9044	0.3541	0.4614
1410.0	10.0	−0.1987	0.0975	0.0220	3.0290	0.3711	0.3504	4.5311	0.3711	0.5284
1430.0	10.0	−0.4302	0.0761	0.0555	2.7320	0.3706	0.3701	6.8580	0.3706	0.7745
1450.0	10.0	−0.4847	0.0638	0.0574	2.9396	0.3681	0.3742	8.4691	0.3681	0.9401
1470.0	10.0	−0.3900	0.0566	0.0430	4.0410	0.3795	0.4490	9.2084	0.3795	1.0233
1490.0	10.0	−0.4028	0.0514	0.0444	4.5764	0.3997	0.5082	10.7492	0.3997	1.1871
1510.0	10.0	−0.2663	0.0487	0.0348	6.0358	0.4068	0.8137	10.4163	0.4068	1.2697
1530.0	10.0	−0.2509	0.0496	0.0310	6.0931	0.4083	0.7216	10.1745	0.4083	1.1418
1550.0	10.0	−0.1305	0.0517	0.0145	6.3894	0.3851	0.7110	8.3068	0.3851	0.9217
1570.0	10.0	−0.0194	0.0489	0.0064	6.9421	0.3515	0.7742	7.2168	0.3515	0.7960
1590.0	10.0	−0.0800	0.0491	0.0088	6.4850	0.3515	0.7199	7.6135	0.3515	0.8444
1610.0	10.0	−0.0666	0.0440	0.0129	6.7656	0.3247	0.8978	7.7307	0.3247	0.9661
1630.0	10.0	−0.1203	0.0403	0.0134	6.5778	0.3066	0.7348	8.3760	0.3066	0.9294
1650.0	10.0	−0.1465	0.0396	0.0197	6.5311	0.3082	0.7674	8.7730	0.3082	1.0165
1670.0	10.0	−0.1648	0.0371	0.0187	6.5204	0.2957	0.7510	9.0933	0.2957	1.0329
1690.0	10.0	−0.1646	0.0370	0.0214	6.6333	0.2993	0.8268	9.2465	0.2993	1.1458
1710.0	10.0	0.0045	0.0411	0.0017	7.0988	0.2956	0.8940	7.0351	0.2956	0.8870
1730.0	10.0	−0.1863	0.0426	0.0228	5.4942	0.2922	0.7028	8.0105	0.2922	0.9757
1750.0	10.0	−0.1122	0.0455	0.0144	5.1805	0.2706	0.6216	6.4906	0.2706	0.7647
1770.0	10.0	−0.1320	0.0451	0.0196	4.3768	0.2322	0.5501	5.7074	0.2322	0.6949
1790.0	10.0	−0.2802	0.0469	0.0333	3.2526	0.2166	0.4208	5.7848	0.2166	0.6944
1810.0	10.0	−0.2367	0.0512	0.0294	3.3622	0.2303	0.4117	5.4476	0.2303	0.6385
1830.0	10.0	−0.1972	0.0636	0.0266	3.1595	0.2553	0.3876	4.7118	0.2553	0.5566
1850.0	10.0	−0.1872	0.0754	0.0245	3.1044	0.2951	0.4660	4.5348	0.2951	0.6199
1870.0	10.0	−0.1272	0.0930	0.0217	3.1146	0.3386	0.6902	4.0222	0.3386	0.7914
1890.0	10.0	−0.0357	0.1278	0.0203	3.1722	0.4267	1.2966	3.4070	0.4267	1.3280

Angular Distributions

$\cos(\theta^*_{2\pi^0})$	$W=(1310.0\pm10.0)$ MeV			$W=(1330.0\pm10.0)$ MeV			$W=(1350.0\pm10.0)$ MeV			$W=(1370.0\pm10.0)$ MeV		
	E	Δ_{stat}	Δ_{sys}	E	Δ_{stat}	Δ_{sys}	E	Δ_{stat}	Δ_{sys}	E	Δ_{stat}	Δ_{sys}
−0.80	1.1348	1.3180	0.3077	−0.4372	−0.7651	0.2301	−0.1552	−0.4445	0.0206	0.4898	0.2807	0.1437
−0.40	1.3064	1.9580	0.4064	0.7163	0.7834	0.4223	−0.2451	−0.3899	0.1436	−0.1472	−0.2477	0.0668
0.00	2.6564	2.2286	2.3046	0.2021	0.9135	0.0510	−0.8779	−0.3831	0.0645	−0.2077	−0.2701	0.0602
0.40	0.5382	2.2468	29.3644	−0.7423	−3.8017	0.3688	−0.2120	−0.7507	0.0719	1.0162	0.5754	0.0840
0.80	6.8396	6.4309	1.3498	6.3572	12.5922	4.3603	0.2727	3.6512	0.2976	26.5213	101.3007	156.0186

$\cos(\theta^*_{2\pi^0})$	$W=(1390.0\pm10.0)$ MeV			$W=(1410.0\pm10.0)$ MeV			$W=(1430.0\pm10.0)$ MeV			$W=(1450.0\pm10.0)$ MeV		
	E	Δ_{stat}	Δ_{sys}	E	Δ_{stat}	Δ_{sys}	E	Δ_{stat}	Δ_{sys}	E	Δ_{stat}	Δ_{sys}
−0.80	0.2504	0.2771	0.0134	0.0574	0.1836	0.0368	−0.1180	−0.1255	0.0279	−0.1039	−0.0972	0.0460
−0.40	−0.2297	−0.2029	0.0334	0.2207	0.1510	0.0266	−0.6090	−0.1241	0.0360	−0.7055	−0.1096	0.0175
0.00	−0.5364	−0.1814	0.0367	−0.2982	−0.1623	0.0306	−0.4800	−0.1409	0.0511	−0.5287	−0.1139	0.0775
0.40	−0.7417	−0.3133	0.0380	−0.8971	−0.2335	0.0346	−0.7661	−0.2045	0.0523	−0.1724	−0.1452	0.0161
0.80	7.1467	13.9382	4.1531	−2.5023	−1.2902	0.4960	−0.5547	−1.3670	0.0810	0.2347	0.5991	0.0350

$\cos(\theta^*_{2\pi^0})$	$W=(1470.0\pm10.0)$ MeV			$W=(1490.0\pm10.0)$ MeV			$W=(1510.0\pm10.0)$ MeV			$W=(1530.0\pm10.0)$ MeV		
	E	Δ_{stat}	Δ_{sys}	E	Δ_{stat}	Δ_{sys}	E	Δ_{stat}	Δ_{sys}	E	Δ_{stat}	Δ_{sys}
−0.80	−0.0085	−0.0825	0.0068	−0.0444	−0.0713	0.0060	−0.0011	−0.0622	0.0029	−0.1228	−0.0660	0.0236
−0.40	−0.4376	−0.1002	0.0091	−0.5721	−0.0954	0.0227	−0.5076	−0.0983	0.0304	−0.4284	−0.1065	0.0224
0.00	−0.4742	−0.1056	0.0429	−0.2373	−0.1014	0.0131	−0.4673	−0.1055	0.0138	−0.2566	−0.1015	0.0323
0.40	−0.5389	−0.1267	0.0515	−0.7140	−0.1350	0.0219	−0.2540	−0.1324	0.0387	−0.3441	−0.1208	0.0469
0.80	−2.5549	−1.9375	0.9788	−1.2325	−0.6066	0.2926	−0.0020	−0.3716	0.0275	0.4504	0.2896	0.0379

$\cos(\theta^*_{2\pi^0})$	$W=(1550.0\pm10.0)$ MeV			$W=(1570.0\pm10.0)$ MeV			$W=(1590.0\pm10.0)$ MeV			$W=(1610.0\pm10.0)$ MeV		
	E	Δ_{stat}	Δ_{sys}	E	Δ_{stat}	Δ_{sys}	E	Δ_{stat}	Δ_{sys}	E	Δ_{stat}	Δ_{sys}
−0.80	0.0056	0.0682	0.0006	0.1173	0.0647	0.0119	0.0369	0.0622	0.0103	−0.0416	−0.0575	0.0237
−0.40	−0.2721	−0.1009	0.0063	−0.0699	−0.1049	0.0039	−0.1247	−0.1050	0.0037	−0.1536	−0.0945	0.0121
0.00	−0.0229	−0.1126	0.0246	−0.4259	−0.1123	0.0183	−0.1783	−0.1116	0.0096	−0.1570	−0.1068	0.0064
0.40	−0.3959	−0.1284	0.0616	−0.2853	−0.1367	0.0418	−0.0852	−0.1282	0.0033	0.1138	0.1183	0.0189
0.80	−0.4189	−0.2927	0.0381	1.4434	0.4323	0.1435	−0.4932	−0.2610	0.0520	−0.3778	−0.2541	0.3156

$\cos(\theta^*_{2\pi^0})$	$W=(1630.0\pm10.0)$ MeV			$W=(1650.0\pm10.0)$ MeV			$W=(1670.0\pm10.0)$ MeV			$W=(1690.0\pm10.0)$ MeV		
	E	Δ_{stat}	Δ_{sys}	E	Δ_{stat}	Δ_{sys}	E	Δ_{stat}	Δ_{sys}	E	Δ_{stat}	Δ_{sys}
−0.80	0.2433	0.0609	0.0373	0.1418	0.0624	0.0149	0.1699	0.0581	0.0127	0.1334	0.0576	0.0275
−0.40	−0.1295	−0.0850	0.0087	−0.2239	−0.0866	0.0116	−0.3258	−0.0704	0.0111	−0.1873	−0.0760	0.0191
0.00	−0.4120	−0.0831	0.0124	−0.5175	−0.0766	0.0188	−0.4080	−0.0718	0.0125	−0.1847	−0.0730	0.0082
0.40	−0.2863	−0.1060	0.0109	−0.1188	−0.0946	0.0065	−0.1323	−0.0884	0.0012	−0.3979	−0.0914	0.0277
0.80	−0.7742	−0.2750	0.0962	−0.2500	−0.2404	0.0659	0.0309	0.1950	0.0223	−0.7597	−0.2775	0.1726

$\cos(\theta^*_{2\pi^0})$	$W=(1710.0\pm10.0)$ MeV			$W=(1730.0\pm10.0)$ MeV			$W=(1750.0\pm10.0)$ MeV			$W=(1770.0\pm10.0)$ MeV		
	E	Δ_{stat}	Δ_{sys}	E	Δ_{stat}	Δ_{sys}	E	Δ_{stat}	Δ_{sys}	E	Δ_{stat}	Δ_{sys}
−0.80	0.2181	0.0670	0.0182	0.1696	0.0709	0.0104	0.1215	0.0761	0.0242	0.0548	0.0796	0.0176
−0.40	−0.1347	−0.0826	0.0046	−0.5584	−0.0769	0.0398	−0.2341	−0.0828	0.0059	−0.3712	−0.0884	0.0292
0.00	−0.1982	−0.0762	0.0042	−0.2099	−0.0797	0.0269	−0.1121	−0.0788	0.0073	−0.1030	−0.0828	0.0090
0.40	−0.0285	−0.0963	0.0213	−0.0954	−0.1131	0.0091	−0.4054	−0.1143	0.0377	−0.1351	−0.1123	0.0132
0.80	0.2643	0.2394	0.0653	−0.2447	−0.2097	0.0751	−0.3926	−0.2296	0.0766	0.2250	0.4031	0.2714

$\cos(\theta^*_{2\pi^0})$	$W=(1790.0\pm10.0)$ MeV			$W=(1810.0\pm10.0)$ MeV			$W=(1830.0\pm10.0)$ MeV			$W=(1850.0\pm10.0)$ MeV		
	E	Δ_{stat}	Δ_{sys}	E	Δ_{stat}	Δ_{sys}	E	Δ_{stat}	Δ_{sys}	E	Δ_{stat}	Δ_{sys}
−0.80	0.0303	0.0961	0.0336	0.2348	0.1004	0.0052	−0.0418	−0.1434	0.0204	0.0282	0.1415	0.0513
−0.40	−0.3897	−0.1066	0.0130	−0.4536	−0.1042	0.0388	−0.3105	−0.1279	0.0588	−0.0173	−0.1329	0.0198
0.00	−0.5123	−0.0911	0.0226	−0.1082	−0.1023	0.0015	−0.7035	−0.1224	0.0785	−0.2413	−0.1551	0.0334
0.40	−0.2287	−0.1362	0.0160	−0.4150	−0.1435	0.0355	0.3951	0.1923	0.0494	−0.5831	−0.2311	0.0949
0.80	0.6020	0.3507	0.0629	−0.4042	−0.2641	2.6474	−1.0265	−0.4952	0.2478	0.1695	0.6115	0.0563

$\cos(\theta^*_{2\pi^0})$				$W=(1870.0\pm10.0)$ MeV						$W=(1890.0\pm10.0)$ MeV		
				E	Δ_{stat}	Δ_{sys}				E	Δ_{stat}	Δ_{sys}
−0.80				−0.4698	−0.1629	0.0119				0.0722	0.2552	0.0080
−0.40				−0.3155	−0.1754	0.0199				0.0530	0.2201	0.0954
0.00				−0.2439	−0.1723	0.0376				−0.1936	−0.2565	0.0161
0.40				0.1757	0.2632	0.0378				0.3688	0.3762	0.1052
0.80				0.7654	1.1381	0.1765				6.0910	2.0326	2.3320

$\cos(\theta^*_{2\pi^0})$	$W=(1310.0\pm10.0)$ MeV			$W=(1330.0\pm10.0)$ MeV			$W=(1350.0\pm10.0)$ MeV			$W=(1370.0\pm10.0)$ MeV		
	$d\sigma_{1/2}/d\Omega$ [μb/sr]	Δ_{stat} [μb/sr]	Δ_{sys} [μb/sr]	$d\sigma_{1/2}/d\Omega$ [μb/sr]	Δ_{stat} [μb/sr]	Δ_{sys} [μb/sr]	$d\sigma_{1/2}/d\Omega$ [μb/sr]	Δ_{stat} [μb/sr]	Δ_{sys} [μb/sr]	$d\sigma_{1/2}/d\Omega$ [μb/sr]	Δ_{stat} [μb/sr]	Δ_{sys} [μb/sr]
−0.80	0.0779	0.0486	0.0051	0.0350	0.0481	0.0246	0.0885	0.0469	0.0085	0.2372	0.0453	0.0523
−0.40	0.0607	0.0518	0.0106	0.1081	0.0495	0.0020	0.0853	0.0444	0.0188	0.1602	0.0468	0.0089
0.00	0.0904	0.0561	0.0281	0.0738	0.0563	0.0078	0.0164	0.0518	0.0090	0.1493	0.0512	0.0125
0.40	0.0464	0.0681	0.6542	0.0051	0.0767	0.0074	0.0749	0.0718	0.0256	0.2492	0.0720	0.0226
0.80	0.4437	0.4355	0.0632	−0.2033	0.4000	0.1102	0.0728	0.2121	0.0130	−0.2787	1.4374	1.5801

$\cos(\theta^*_{2\pi^0})$	$W=(1390.0\pm10.0)$ MeV			$W=(1410.0\pm10.0)$ MeV			$W=(1430.0\pm10.0)$ MeV			$W=(1450.0\pm10.0)$ MeV		
	$d\sigma_{1/2}/d\Omega$ [μb/sr]	Δ_{stat} [μb/sr]	Δ_{sys} [μb/sr]	$d\sigma_{1/2}/d\Omega$ [μb/sr]	Δ_{stat} [μb/sr]	Δ_{sys} [μb/sr]	$d\sigma_{1/2}/d\Omega$ [μb/sr]	Δ_{stat} [μb/sr]	Δ_{sys} [μb/sr]	$d\sigma_{1/2}/d\Omega$ [μb/sr]	Δ_{stat} [μb/sr]	Δ_{sys} [μb/sr]
−0.80	0.2454	0.0551	0.0076	0.3550	0.0622	0.0332	0.3885	0.0561	0.0342	0.5150	0.0570	0.0651
−0.40	0.1969	0.0522	0.0172	0.4120	0.0515	0.0413	0.1758	0.0566	0.0238	0.1462	0.0555	0.0117
0.00	0.1433	0.0567	0.0170	0.2543	0.0596	0.0201	0.2378	0.0654	0.0401	0.2479	0.0612	0.0547
0.40	0.0571	0.0702	0.0102	0.0325	0.0749	0.0113	0.0846	0.0753	0.0219	0.3925	0.0700	0.0374
0.80	−0.1656	0.3612	0.0836	−0.1965	0.1799	0.0649	0.0425	0.1370	0.0192	0.2359	0.1173	0.0404

$\cos(\theta^*_{2\pi^0})$	$W=(1470.0\pm10.0)$ MeV			$W=(1490.0\pm10.0)$ MeV			$W=(1510.0\pm10.0)$ MeV			$W=(1530.0\pm10.0)$ MeV		
	$d\sigma_{1/2}/d\Omega$ [μb/sr]	Δ_{stat} [μb/sr]	Δ_{sys} [μb/sr]	$d\sigma_{1/2}/d\Omega$ [μb/sr]	Δ_{stat} [μb/sr]	Δ_{sys} [μb/sr]	$d\sigma_{1/2}/d\Omega$ [μb/sr]	Δ_{stat} [μb/sr]	Δ_{sys} [μb/sr]	$d\sigma_{1/2}/d\Omega$ [μb/sr]	Δ_{stat} [μb/sr]	Δ_{sys} [μb/sr]
−0.80	0.7038	0.0600	0.0780	0.9179	0.0705	0.0942	1.1444	0.0737	0.1908	1.0795	0.0834	0.1367
−0.40	0.3319	0.0602	0.0141	0.2796	0.0635	0.0255	0.3215	0.0654	0.0338	0.3478	0.0660	0.0234
0.00	0.3142	0.0644	0.0439	0.4910	0.0664	0.0396	0.3253	0.0660	0.0170	0.4330	0.0607	0.0270
0.40	0.2388	0.0671	0.0414	0.1541	0.0747	0.0176	0.4098	0.0742	0.0601	0.3472	0.0654	0.0498
0.80	−0.1045	0.1482	0.1102	−0.0499	0.1402	0.0991	0.3153	0.1218	0.0288	0.5228	0.1082	0.0570

$\cos(\theta^*_{2\pi^0})$	$W=(1550.0\pm10.0)$ MeV			$W=(1570.0\pm10.0)$ MeV			$W=(1590.0\pm10.0)$ MeV			$W=(1610.0\pm10.0)$ MeV		
	$d\sigma_{1/2}/d\Omega$ [μb/sr]	Δ_{stat} [μb/sr]	Δ_{sys} [μb/sr]	$d\sigma_{1/2}/d\Omega$ [μb/sr]	Δ_{stat} [μb/sr]	Δ_{sys} [μb/sr]	$d\sigma_{1/2}/d\Omega$ [μb/sr]	Δ_{stat} [μb/sr]	Δ_{sys} [μb/sr]	$d\sigma_{1/2}/d\Omega$ [μb/sr]	Δ_{stat} [μb/sr]	Δ_{sys} [μb/sr]
−0.80	1.1535	0.0806	0.0995	1.2574	0.0752	0.1216	1.1760	0.0732	0.1450	1.0729	0.0673	0.1528
−0.40	0.4142	0.0585	0.0123	0.4927	0.0568	0.0034	0.4788	0.0586	0.0104	0.4692	0.0536	0.0379
0.00	0.4975	0.0584	0.0209	0.2730	0.0552	0.0137	0.3797	0.0529	0.0197	0.4101	0.0531	0.0218
0.40	0.2842	0.0623	0.0508	0.3212	0.0631	0.0435	0.4099	0.0590	0.0129	0.4924	0.0537	0.0254
0.80	0.1744	0.0928	0.0333	0.5383	0.1065	0.0539	0.1660	0.0904	0.0285	0.2094	0.0898	0.1054

$\cos(\theta^*_{2\pi^0})$	$W=(1630.0\pm10.0)$ MeV			$W=(1650.0\pm10.0)$ MeV			$W=(1670.0\pm10.0)$ MeV			$W=(1690.0\pm10.0)$ MeV		
	$d\sigma_{1/2}/d\Omega$ [μb/sr]	Δ_{stat} [μb/sr]	Δ_{sys} [μb/sr]	$d\sigma_{1/2}/d\Omega$ [μb/sr]	Δ_{stat} [μb/sr]	Δ_{sys} [μb/sr]	$d\sigma_{1/2}/d\Omega$ [μb/sr]	Δ_{stat} [μb/sr]	Δ_{sys} [μb/sr]	$d\sigma_{1/2}/d\Omega$ [μb/sr]	Δ_{stat} [μb/sr]	Δ_{sys} [μb/sr]
−0.80	1.3111	0.0672	0.1631	1.1843	0.0672	0.1068	1.1251	0.0592	0.0890	1.0818	0.0582	0.0813
−0.40	0.5192	0.0519	0.0175	0.4677	0.0533	0.0349	0.4442	0.0479	0.0266	0.5224	0.0503	0.0241
0.00	0.3339	0.0487	0.0105	0.2976	0.0490	0.0140	0.4131	0.0520	0.0210	0.5625	0.0520	0.0327
0.40	0.3532	0.0545	0.0100	0.4515	0.0497	0.0317	0.4715	0.0500	0.0195	0.3372	0.0528	0.0453
0.80	0.0702	0.0908	0.0514	0.2322	0.0784	0.1023	0.3757	0.0748	0.0338	0.0646	0.0800	0.1120

$\cos(\theta^*_{2\pi^0})$	$W=(1710.0\pm10.0)$ MeV			$W=(1730.0\pm10.0)$ MeV			$W=(1750.0\pm10.0)$ MeV			$W=(1770.0\pm10.0)$ MeV		
	$d\sigma_{1/2}/d\Omega$ [μb/sr]	Δ_{stat} [μb/sr]	Δ_{sys} [μb/sr]	$d\sigma_{1/2}/d\Omega$ [μb/sr]	Δ_{stat} [μb/sr]	Δ_{sys} [μb/sr]	$d\sigma_{1/2}/d\Omega$ [μb/sr]	Δ_{stat} [μb/sr]	Δ_{sys} [μb/sr]	$d\sigma_{1/2}/d\Omega$ [μb/sr]	Δ_{stat} [μb/sr]	Δ_{sys} [μb/sr]
−0.80	0.9760	0.0564	0.0851	0.8833	0.0558	0.0149	0.6712	0.0473	0.1184	0.5916	0.0463	0.0702
−0.40	0.5088	0.0496	0.0213	0.2501	0.0448	0.0471	0.3927	0.0437	0.0127	0.2750	0.0398	0.0409
0.00	0.5099	0.0500	0.0127	0.4890	0.0509	0.0396	0.4800	0.0440	0.0119	0.4142	0.0395	0.0166
0.40	0.4961	0.0509	0.0568	0.4153	0.0528	0.0376	0.2381	0.0477	0.0458	0.3115	0.0415	0.0436
0.80	0.3678	0.0726	0.0513	0.2144	0.0623	0.0576	0.1699	0.0697	0.0462	0.1825	0.0642	0.0147

$\cos(\theta^*_{2\pi^0})$	$W=(1790.0\pm10.0)$ MeV			$W=(1810.0\pm10.0)$ MeV			$W=(1830.0\pm10.0)$ MeV			$W=(1850.0\pm10.0)$ MeV		
	$d\sigma_{1/2}/d\Omega$ [μb/sr]	$\Delta_{\rm stat}$ [μb/sr]	$\Delta_{\rm sys}$ [μb/sr]	$d\sigma_{1/2}/d\Omega$ [μb/sr]	$\Delta_{\rm stat}$ [μb/sr]	$\Delta_{\rm sys}$ [μb/sr]	$d\sigma_{1/2}/d\Omega$ [μb/sr]	$\Delta_{\rm stat}$ [μb/sr]	$\Delta_{\rm sys}$ [μb/sr]	$d\sigma_{1/2}/d\Omega$ [μb/sr]	$\Delta_{\rm stat}$ [μb/sr]	$\Delta_{\rm sys}$ [μb/sr]
−0.80	0.4033	0.0395	0.0400	0.5309	0.0451	0.0199	0.3323	0.0507	0.0127	0.3688	0.0521	0.0113
−0.40	0.2290	0.0409	0.0095	0.2020	0.0395	0.0229	0.2279	0.0431	0.0355	0.3349	0.0460	0.0092
0.00	0.2020	0.0388	0.0146	0.3718	0.0433	0.0165	0.1064	0.0452	0.0312	0.2587	0.0538	0.0622
0.40	0.2513	0.0456	0.0227	0.1889	0.0474	0.0228	0.4027	0.0566	0.0668	0.1163	0.0657	0.0673
0.80	0.3463	0.0794	0.0395	0.1649	0.0769	0.4567	−0.0052	0.1044	0.0550	0.1931	0.1084	0.0347

$\cos(\theta^*_{2\pi^0})$	$W=(1870.0\pm10.0)$ MeV			$W=(1890.0\pm10.0)$ MeV		
	$d\sigma_{1/2}/d\Omega$ [μb/sr]	$\Delta_{\rm stat}$ [μb/sr]	$\Delta_{\rm sys}$ [μb/sr]	$d\sigma_{1/2}/d\Omega$ [μb/sr]	$\Delta_{\rm stat}$ [μb/sr]	$\Delta_{\rm sys}$ [μb/sr]
−0.80	0.1727	0.0564	0.0038	0.3035	0.0760	0.0481
−0.40	0.2030	0.0531	0.0167	0.3140	0.0668	0.0194
0.00	0.2587	0.0600	0.0751	0.2691	0.0867	0.0333
0.40	0.3344	0.0759	0.1184	0.3446	0.0958	0.1939
0.80	0.2065	0.1421	0.1176	0.8975	0.3204	0.4780

$\cos(\theta^*_{2\pi^0})$	$W=(1310.0\pm10.0)$ MeV			$W=(1330.0\pm10.0)$ MeV			$W=(1350.0\pm10.0)$ MeV			$W=(1370.0\pm10.0)$ MeV		
	$d\sigma_{3/2}/d\Omega$ [μb/sr]	$\Delta_{\rm stat}$ [μb/sr]	$\Delta_{\rm sys}$ [μb/sr]	$d\sigma_{3/2}/d\Omega$ [μb/sr]	$\Delta_{\rm stat}$ [μb/sr]	$\Delta_{\rm sys}$ [μb/sr]	$d\sigma_{3/2}/d\Omega$ [μb/sr]	$\Delta_{\rm stat}$ [μb/sr]	$\Delta_{\rm sys}$ [μb/sr]	$d\sigma_{3/2}/d\Omega$ [μb/sr]	$\Delta_{\rm stat}$ [μb/sr]	$\Delta_{\rm sys}$ [μb/sr]
−0.80	−0.0049	0.0486	0.0081	0.0894	0.0481	0.0084	0.1210	0.0469	0.0082	0.0812	0.0453	0.0294
−0.40	−0.0081	0.0518	0.0115	0.0179	0.0495	0.0217	0.1407	0.0444	0.0110	0.2155	0.0468	0.0170
0.00	−0.0409	0.0561	0.0230	0.0490	0.0563	0.0112	0.2515	0.0518	0.0075	0.2275	0.0512	0.0242
0.40	0.0139	0.0681	0.6393	0.0348	0.0767	0.0075	0.1151	0.0718	0.0152	−0.0020	0.0720	0.0122
0.80	−0.3305	0.4355	0.0277	0.1481	0.4000	0.1783	0.0416	0.2121	0.0263	0.2585	1.4374	1.5885

$\cos(\theta^*_{2\pi^0})$	$W=(1390.0\pm10.0)$ MeV			$W=(1410.0\pm10.0)$ MeV			$W=(1430.0\pm10.0)$ MeV			$W=(1450.0\pm10.0)$ MeV		
	$d\sigma_{3/2}/d\Omega$ [μb/sr]	$\Delta_{\rm stat}$ [μb/sr]	$\Delta_{\rm sys}$ [μb/sr]	$d\sigma_{3/2}/d\Omega$ [μb/sr]	$\Delta_{\rm stat}$ [μb/sr]	$\Delta_{\rm sys}$ [μb/sr]	$d\sigma_{3/2}/d\Omega$ [μb/sr]	$\Delta_{\rm stat}$ [μb/sr]	$\Delta_{\rm sys}$ [μb/sr]	$d\sigma_{3/2}/d\Omega$ [μb/sr]	$\Delta_{\rm stat}$ [μb/sr]	$\Delta_{\rm sys}$ [μb/sr]
−0.80	0.1471	0.0551	0.0090	0.3165	0.0622	0.0395	0.4924	0.0561	0.0217	0.6345	0.0570	0.0521
−0.40	0.3143	0.0522	0.0407	0.2630	0.0515	0.0232	0.7235	0.0566	0.0421	0.8467	0.0555	0.0261
0.00	0.4748	0.0567	0.0273	0.4705	0.0596	0.0460	0.6770	0.0654	0.0726	0.8042	0.0612	0.0528
0.40	0.3848	0.0702	0.0056	0.5993	0.0749	0.0197	0.6388	0.0753	0.0369	0.5561	0.0700	0.0546
0.80	0.1249	0.3612	0.1753	0.4582	0.1799	0.1079	0.1483	0.1370	0.0301	0.1462	0.1173	0.0147

$\cos(\theta^*_{2\pi^0})$	$W=(1470.0\pm10.0)$ MeV			$W=(1490.0\pm10.0)$ MeV			$W=(1510.0\pm10.0)$ MeV			$W=(1530.0\pm10.0)$ MeV		
	$d\sigma_{3/2}/d\Omega$ [μb/sr]	$\Delta_{\rm stat}$ [μb/sr]	$\Delta_{\rm sys}$ [μb/sr]	$d\sigma_{3/2}/d\Omega$ [μb/sr]	$\Delta_{\rm stat}$ [μb/sr]	$\Delta_{\rm sys}$ [μb/sr]	$d\sigma_{3/2}/d\Omega$ [μb/sr]	$\Delta_{\rm stat}$ [μb/sr]	$\Delta_{\rm sys}$ [μb/sr]	$d\sigma_{3/2}/d\Omega$ [μb/sr]	$\Delta_{\rm stat}$ [μb/sr]	$\Delta_{\rm sys}$ [μb/sr]
−0.80	0.7158	0.0600	0.0724	1.0032	0.0705	0.0979	1.1470	0.0737	0.1872	1.3818	0.0834	0.1479
−0.40	0.8483	0.0602	0.0263	1.0271	0.0635	0.0436	0.9844	0.0654	0.0456	0.8690	0.0660	0.0302
0.00	0.8811	0.0644	0.0557	0.7965	0.0664	0.0546	0.8962	0.0660	0.0330	0.7319	0.0607	0.0113
0.40	0.7970	0.0671	0.0577	0.9232	0.0747	0.0308	0.6888	0.0742	0.0691	0.7113	0.0654	0.0527
0.80	0.2389	0.1482	0.1807	0.4793	0.1402	0.1638	0.3166	0.1218	0.0206	0.1981	0.1082	0.0406

$\cos(\theta^*_{2\pi^0})$	$W=(1550.0\pm10.0)$ MeV			$W=(1570.0\pm10.0)$ MeV			$W=(1590.0\pm10.0)$ MeV			$W=(1610.0\pm10.0)$ MeV		
	$d\sigma_{3/2}/d\Omega$ [μb/sr]	$\Delta_{\rm stat}$ [μb/sr]	$\Delta_{\rm sys}$ [μb/sr]	$d\sigma_{3/2}/d\Omega$ [μb/sr]	$\Delta_{\rm stat}$ [μb/sr]	$\Delta_{\rm sys}$ [μb/sr]	$d\sigma_{3/2}/d\Omega$ [μb/sr]	$\Delta_{\rm stat}$ [μb/sr]	$\Delta_{\rm sys}$ [μb/sr]	$d\sigma_{3/2}/d\Omega$ [μb/sr]	$\Delta_{\rm stat}$ [μb/sr]	$\Delta_{\rm sys}$ [μb/sr]
−0.80	1.1407	0.0806	0.0988	0.9935	0.0752	0.0950	1.0922	0.0732	0.1455	1.1660	0.0673	0.1547
−0.40	0.7240	0.0585	0.0130	0.5667	0.0568	0.0083	0.6153	0.0586	0.0116	0.6395	0.0536	0.0527
0.00	0.5208	0.0584	0.0082	0.6780	0.0552	0.0046	0.5445	0.0529	0.0198	0.5628	0.0531	0.0249
0.40	0.6568	0.0623	0.0455	0.5775	0.0631	0.0421	0.4863	0.0590	0.0120	0.3918	0.0537	0.0325
0.80	0.4258	0.0928	0.0447	−0.0977	0.1065	0.0263	0.4890	0.0904	0.0199	0.4638	0.0898	0.1398

$\cos(\theta^*_{2\pi^0})$	$W=(1630.0\pm10.0)$ MeV			$W=(1650.0\pm10.0)$ MeV			$W=(1670.0\pm10.0)$ MeV			$W=(1690.0\pm10.0)$ MeV		
	$d\sigma_{3/2}/d\Omega$ [μb/sr]	$\Delta_{\rm stat}$ [μb/sr]	$\Delta_{\rm sys}$ [μb/sr]	$d\sigma_{3/2}/d\Omega$ [μb/sr]	$\Delta_{\rm stat}$ [μb/sr]	$\Delta_{\rm sys}$ [μb/sr]	$d\sigma_{3/2}/d\Omega$ [μb/sr]	$\Delta_{\rm stat}$ [μb/sr]	$\Delta_{\rm sys}$ [μb/sr]	$d\sigma_{3/2}/d\Omega$ [μb/sr]	$\Delta_{\rm stat}$ [μb/sr]	$\Delta_{\rm sys}$ [μb/sr]
−0.80	0.7980	0.0672	0.1237	0.8901	0.0672	0.0901	0.7982	0.0592	0.0720	0.8271	0.0582	0.0703
−0.40	0.6737	0.0519	0.0237	0.7375	0.0533	0.0419	0.8735	0.0479	0.0377	0.7631	0.0503	0.0069
0.00	0.8017	0.0487	0.0071	0.9361	0.0490	0.0098	0.9824	0.0520	0.0233	0.8175	0.0520	0.0382
0.40	0.6365	0.0545	0.0035	0.5732	0.0497	0.0351	0.6153	0.0500	0.0242	0.7830	0.0528	0.0608
0.80	0.5514	0.0908	0.0813	0.3870	0.0784	0.0998	0.3532	0.0748	0.0412	0.4729	0.0800	0.1583

$\cos(\theta^*_{2\pi^0})$	$W=(1710.0\pm10.0)$ MeV			$W=(1730.0\pm10.0)$ MeV			$W=(1750.0\pm10.0)$ MeV			$W=(1770.0\pm10.0)$ MeV		
	$d\sigma_{3/2}/d\Omega$ [μb/sr]	$\Delta_{\rm stat}$ [μb/sr]	$\Delta_{\rm sys}$ [μb/sr]	$d\sigma_{3/2}/d\Omega$ [μb/sr]	$\Delta_{\rm stat}$ [μb/sr]	$\Delta_{\rm sys}$ [μb/sr]	$d\sigma_{3/2}/d\Omega$ [μb/sr]	$\Delta_{\rm stat}$ [μb/sr]	$\Delta_{\rm sys}$ [μb/sr]	$d\sigma_{3/2}/d\Omega$ [μb/sr]	$\Delta_{\rm stat}$ [μb/sr]	$\Delta_{\rm sys}$ [μb/sr]
−0.80	0.6264	0.0564	0.0617	0.6272	0.0558	0.0145	0.5258	0.0473	0.0948	0.5301	0.0463	0.0655
−0.40	0.6672	0.0496	0.0240	0.8826	0.0448	0.0697	0.6327	0.0437	0.0156	0.5997	0.0398	0.0640
0.00	0.7620	0.0500	0.0126	0.7488	0.0509	0.0260	0.6011	0.0440	0.0175	0.5093	0.0395	0.0163
0.40	0.5252	0.0509	0.0581	0.5029	0.0528	0.0499	0.5628	0.0477	0.0609	0.4088	0.0415	0.0484
0.80	0.2140	0.0726	0.0332	0.3533	0.0623	0.0270	0.3895	0.0697	0.0230	0.1155	0.0642	0.0514

$\cos(\theta^*_{2\pi^0})$	$W=(1790.0\pm10.0)$ MeV			$W=(1810.0\pm10.0)$ MeV			$W=(1830.0\pm10.0)$ MeV			$W=(1850.0\pm10.0)$ MeV		
	$d\sigma_{3/2}/d\Omega$ [μb/sr]	$\Delta_{\rm stat}$ [μb/sr]	$\Delta_{\rm sys}$ [μb/sr]	$d\sigma_{3/2}/d\Omega$ [μb/sr]	$\Delta_{\rm stat}$ [μb/sr]	$\Delta_{\rm sys}$ [μb/sr]	$d\sigma_{3/2}/d\Omega$ [μb/sr]	$\Delta_{\rm stat}$ [μb/sr]	$\Delta_{\rm sys}$ [μb/sr]	$d\sigma_{3/2}/d\Omega$ [μb/sr]	$\Delta_{\rm stat}$ [μb/sr]	$\Delta_{\rm sys}$ [μb/sr]
−0.80	0.3796	0.0395	0.0276	0.3290	0.0451	0.0139	0.3612	0.0507	0.0129	0.3485	0.0521	0.0349
−0.40	0.5213	0.0409	0.0130	0.5373	0.0395	0.0151	0.4332	0.0431	0.0279	0.3467	0.0460	0.0049
0.00	0.6262	0.0388	0.0163	0.4619	0.0433	0.0197	0.6111	0.0452	0.0307	0.4232	0.0538	0.0701
0.40	0.4002	0.0456	0.0272	0.4569	0.0474	0.0312	0.1746	0.0566	0.0481	0.4416	0.0657	0.0938
0.80	0.0860	0.0794	0.0267	0.3886	0.0769	0.2845	0.3985	0.1044	0.0587	0.1371	0.1084	0.0309

$\cos(\theta^*_{2\pi^0})$	$W=(1870.0\pm10.0)$ MeV			$W=(1890.0\pm10.0)$ MeV		
	$d\sigma_{3/2}/d\Omega$ [μb/sr]	$\Delta_{\rm stat}$ [μb/sr]	$\Delta_{\rm sys}$ [μb/sr]	$d\sigma_{3/2}/d\Omega$ [μb/sr]	$\Delta_{\rm stat}$ [μb/sr]	$\Delta_{\rm sys}$ [μb/sr]
−0.80	0.4787	0.0564	0.0048	0.2627	0.0760	0.0452
−0.40	0.3901	0.0531	0.0195	0.2824	0.0668	0.0624
0.00	0.4256	0.0600	0.0837	0.3983	0.0867	0.0387
0.40	0.2345	0.0759	0.1077	0.1589	0.0958	0.1674
0.80	0.0274	0.1421	0.0716	−0.6444	0.3204	0.2700

E.4.5 Observables for $\gamma p \to \pi^0\pi^0 p$ as a Function of W

W [MeV]	ΔW [MeV]	E	$\Delta_{\rm stat}$	$\Delta_{\rm sys}$	$\sigma_{1/2}$ [μb]	$\Delta_{\rm stat}$ [μb]	$\Delta_{\rm sys}$ [μb]	$\sigma_{3/2}$ [μb]	$\Delta_{\rm stat}$ [μb]	$\Delta_{\rm sys}$ [μb]
1310.0	10.0	0.5041	0.4839	0.0751	0.5634	0.2289	0.0799	0.1858	0.2289	0.0374
1330.0	10.0	−0.1145	0.2694	0.0446	0.6249	0.2672	0.0700	0.7866	0.2672	0.0999
1350.0	10.0	−0.1413	0.1051	0.0417	1.2027	0.2061	0.2809	1.5985	0.2061	0.3742
1370.0	10.0	−0.3395	0.0660	0.0447	2.0083	0.2688	0.2821	4.0727	0.2688	0.4968
1390.0	10.0	−0.1692	0.0445	0.0334	3.6455	0.2721	0.6744	5.1309	0.2721	0.9243
1410.0	10.0	−0.4099	0.0428	0.0785	3.2846	0.3114	0.7110	7.8475	0.3114	1.1331
1430.0	10.0	−0.3950	0.0379	0.0638	4.0250	0.3317	0.7665	9.2802	0.3317	1.3264
1450.0	10.0	−0.3320	0.0296	0.0496	5.1691	0.3077	0.7747	10.3062	0.3077	1.2444
1470.0	10.0	−0.2979	0.0249	0.0381	6.1739	0.2973	0.8357	11.4122	0.2973	1.3951
1490.0	10.0	−0.3095	0.0236	0.0473	6.3792	0.2941	0.9851	12.0988	0.2941	1.5200
1510.0	10.0	−0.2977	0.0243	0.0390	6.2754	0.2945	0.8226	11.5961	0.2945	1.3500
1530.0	10.0	−0.2523	0.0247	0.0333	5.9171	0.2684	0.7711	9.9105	0.2684	1.1741
1550.0	10.0	−0.1378	0.0250	0.0218	5.8774	0.2384	0.7728	7.7556	0.2384	0.9353
1570.0	10.0	0.0347	0.0256	0.0095	6.5604	0.2290	0.8721	6.1200	0.2290	0.7711
1590.0	10.0	0.1566	0.0250	0.0225	6.8362	0.2065	0.9576	4.9849	0.2065	0.7271
1610.0	10.0	0.0763	0.0225	0.0112	6.6216	0.1955	0.9797	5.6831	0.1955	0.8348
1630.0	10.0	0.1205	0.0176	0.0197	7.5968	0.1678	1.1751	5.9631	0.1678	0.9550
1650.0	10.0	0.0864	0.0152	0.0112	8.0967	0.1599	1.0659	6.8085	0.1599	0.8977
1670.0	10.0	0.0459	0.0137	0.0077	9.0038	0.1670	1.2253	8.2138	0.1670	1.0843
1690.0	10.0	0.0380	0.0136	0.0080	9.3784	0.1730	1.1695	8.6910	0.1730	1.0547
1710.0	10.0	0.1543	0.0151	0.0184	10.5695	0.1927	1.2919	7.7439	0.1927	0.9649
1730.0	10.0	0.1661	0.0141	0.0202	9.8316	0.1663	1.2052	7.0311	0.1663	0.8701
1750.0	10.0	0.2110	0.0157	0.0250	8.6188	0.1547	1.0418	5.6151	0.1547	0.6821
1770.0	10.0	0.1918	0.0151	0.0264	7.6171	0.1340	1.0307	5.1651	0.1340	0.7304
1790.0	10.0	0.2364	0.0168	0.0372	7.0502	0.1319	1.0782	4.3544	0.1319	0.7106
1810.0	10.0	0.2714	0.0199	0.0322	7.0766	0.1515	0.8221	4.0556	0.1515	0.4955
1830.0	10.0	0.2099	0.0243	0.0237	6.3112	0.1753	0.7335	4.1218	0.1753	0.4762
1850.0	10.0	0.1473	0.0267	0.0165	6.0315	0.1966	0.6854	4.4827	0.1966	0.5104
1870.0	10.0	0.2748	0.0349	0.0318	6.3826	0.2381	0.7333	3.6309	0.2381	0.4400
1890.0	10.0	0.1367	0.0515	0.0270	5.7721	0.3664	1.2445	4.3833	0.3664	0.9968

Angular Distributions

$\cos(\theta^*_{2\pi^0})$	$W=(1310.0\pm10.0)$ MeV			$W=(1330.0\pm10.0)$ MeV			$W=(1350.0\pm10.0)$ MeV			$W=(1370.0\pm10.0)$ MeV		
	E	$\Delta_{\rm stat}$	$\Delta_{\rm sys}$	E	$\Delta_{\rm stat}$	$\Delta_{\rm sys}$	E	$\Delta_{\rm stat}$	$\Delta_{\rm sys}$	E	$\Delta_{\rm stat}$	$\Delta_{\rm sys}$
−0.80	0.3407	0.4393	0.1568	−0.0180	−0.2848	0.0240	0.8421	0.1913	0.2583	−0.3808	−0.1107	0.0339
−0.40	1.1482	1.2281	0.3585	−0.8776	−0.3999	0.0594	−0.0278	−0.1432	0.0240	−0.4888	−0.1182	0.0862
0.00	2.2253	3.4893	0.1297	0.8154	0.6073	0.1747	−0.3635	−0.1736	0.1011	−0.3270	−0.1149	0.0433
0.40	1.7832	18.8680	2.0748	−2.2252	−6.4833	4.0712	−3.1900	−2.0168	0.0938	−0.0696	−0.3035	0.0475
0.80	13.3872	248.4042	41.3736	[illegible]	[illegible]64.3614	206.1452	−73.4589	[illegible]05.4753	40.7483	41.3411	[illegible]67.0657	32.6025

$\cos(\theta^*_{2\pi^0})$	$W=(1390.0\pm10.0)$ MeV			$W=(1410.0\pm10.0)$ MeV			$W=(1430.0\pm10.0)$ MeV			$W=(1450.0\pm10.0)$ MeV		
	E	$\Delta_{\rm stat}$	$\Delta_{\rm sys}$	E	$\Delta_{\rm stat}$	$\Delta_{\rm sys}$	E	$\Delta_{\rm stat}$	$\Delta_{\rm sys}$	E	$\Delta_{\rm stat}$	$\Delta_{\rm sys}$
−0.80	0.2527	0.0765	0.0261	0.1390	0.0702	0.0333	0.2024	0.0522	0.0176	0.1356	0.0474	0.0161
−0.40	−0.1318	−0.0727	0.0254	−0.3591	−0.0583	0.1040	−0.3049	−0.0551	0.0660	−0.2136	−0.0453	0.0332
0.00	−0.3129	−0.0788	0.0476	−0.5685	−0.0803	0.0497	−0.6281	−0.0636	0.1249	−0.5893	−0.0564	0.0858
0.40	−0.3370	−0.1576	0.1255	−1.1935	−0.1958	0.2623	−0.5638	−0.1024	0.0735	−0.3991	−0.0724	0.0533
0.80	0.3494	2.4275	0.4781	0.5535	1.4270	0.2539	−5.1993	−8.2107	10.7976	0.0451	1.3571	0.0442

$\cos(\theta^*_{2\pi^0})$	$W=(1470.0\pm10.0)$ MeV			$W=(1490.0\pm10.0)$ MeV			$W=(1510.0\pm10.0)$ MeV			$W=(1530.0\pm10.0)$ MeV		
	E	$\Delta_{\rm stat}$	$\Delta_{\rm sys}$	E	$\Delta_{\rm stat}$	$\Delta_{\rm sys}$	E	$\Delta_{\rm stat}$	$\Delta_{\rm sys}$	E	$\Delta_{\rm stat}$	$\Delta_{\rm sys}$
−0.80	0.0562	0.0394	0.0090	0.0948	0.0345	0.0134	0.0702	0.0358	0.0154	0.0818	0.0356	0.0091
−0.40	−0.3244	−0.0436	0.0192	−0.3259	−0.0428	0.0299	−0.3821	−0.0496	0.0187	−0.1930	−0.0510	0.0129
0.00	−0.4504	−0.0487	0.0348	−0.5525	−0.0512	0.0550	−0.3958	−0.0485	0.0355	−0.5824	−0.0598	0.0260
0.40	−0.4438	−0.0668	0.0750	−0.4577	−0.0640	0.0426	−0.3985	−0.0578	0.0348	−0.3690	−0.0559	0.0413
0.80	−0.7754	−0.4404	0.4357	−0.4825	−0.3512	0.0469	−0.3618	−0.2541	0.2347	0.6138	0.2590	0.0985

$\cos(\theta^*_{2\pi^0})$	$W=(1550.0\pm10.0)$ MeV			$W=(1570.0\pm10.0)$ MeV			$W=(1590.0\pm10.0)$ MeV			$W=(1610.0\pm10.0)$ MeV		
	E	$\Delta_{\rm stat}$	$\Delta_{\rm sys}$	E	$\Delta_{\rm stat}$	$\Delta_{\rm sys}$	E	$\Delta_{\rm stat}$	$\Delta_{\rm sys}$	E	$\Delta_{\rm stat}$	$\Delta_{\rm sys}$
−0.80	0.0804	0.0377	0.0085	0.1054	0.0367	0.0201	0.3583	0.0426	0.0577	0.2036	0.0391	0.0500
−0.40	−0.2899	−0.0566	0.0019	0.2167	0.0582	0.0032	0.2550	0.0587	0.0026	0.2318	0.0543	0.0090
0.00	−0.1848	−0.0561	0.0226	−0.2760	−0.0605	0.0173	−0.1586	−0.0521	0.0220	−0.1078	−0.0545	0.0083
0.40	−0.2781	−0.0609	0.0279	−0.1568	−0.0564	0.0285	0.0219	0.0522	0.0094	−0.2374	−0.0448	0.0293
0.80	−0.4360	−0.1839	0.1700	0.3156	0.1634	0.0989	0.1391	0.1184	0.0404	0.1003	0.1079	0.0118

$\cos(\theta^*_{2\pi^0})$	$W=(1630.0\pm10.0)$ MeV			$W=(1650.0\pm10.0)$ MeV			$W=(1670.0\pm10.0)$ MeV			$W=(1690.0\pm10.0)$ MeV		
	E	Δ_{stat}	Δ_{sys}	E	Δ_{stat}	Δ_{sys}	E	Δ_{stat}	Δ_{sys}	E	Δ_{stat}	Δ_{sys}
−0.80	0.2953	0.0352	0.0549	0.1769	0.0309	0.0249	0.0835	0.0250	0.0127	0.0122	0.0255	0.0037
−0.40	0.1543	0.0426	0.0115	0.1573	0.0397	0.0192	0.0772	0.0381	0.0128	0.0228	0.0342	0.0181
0.00	0.0696	0.0445	0.0089	0.1343	0.0392	0.0137	0.0339	0.0355	0.0032	0.2986	0.0356	0.0118
0.40	−0.0646	−0.0361	0.0212	−0.0696	−0.0317	0.0089	−0.0627	−0.0281	0.0033	−0.0784	−0.0278	0.0206
0.80	0.0058	0.0824	0.0296	−0.1572	−0.0809	0.0323	−0.1160	−0.0695	0.0251	−0.1945	−0.0710	0.0117

$\cos(\theta^*_{2\pi^0})$	$W=(1710.0\pm10.0)$ MeV			$W=(1730.0\pm10.0)$ MeV			$W=(1750.0\pm10.0)$ MeV			$W=(1770.0\pm10.0)$ MeV		
	E	Δ_{stat}	Δ_{sys}	E	Δ_{stat}	Δ_{sys}	E	Δ_{stat}	Δ_{sys}	E	Δ_{stat}	Δ_{sys}
−0.80	0.1392	0.0283	0.0168	0.1527	0.0314	0.0272	0.1305	0.0329	0.0212	0.2722	0.0371	0.0267
−0.40	0.2829	0.0384	0.0138	0.0681	0.0380	0.0103	0.2178	0.0391	0.0061	0.1120	0.0376	0.0053
0.00	0.3611	0.0360	0.0186	0.2853	0.0355	0.0158	0.2872	0.0371	0.0109	0.2508	0.0352	0.0427
0.40	−0.0741	−0.0321	0.0232	0.1678	0.0309	0.0110	0.2179	0.0365	0.0149	0.1841	0.0356	0.0063
0.80	0.0773	0.0669	0.0160	−0.0908	−0.0577	0.0369	0.1308	0.0622	0.0321	−0.0124	−0.0633	0.0273

$\cos(\theta^*_{2\pi^0})$	$W=(1790.0\pm10.0)$ MeV			$W=(1810.0\pm10.0)$ MeV			$W=(1830.0\pm10.0)$ MeV			$W=(1850.0\pm10.0)$ MeV		
	E	Δ_{stat}	Δ_{sys}	E	Δ_{stat}	Δ_{sys}	E	Δ_{stat}	Δ_{sys}	E	Δ_{stat}	Δ_{sys}
−0.80	0.1657	0.0482	0.0069	0.1886	0.0568	0.0133	0.2750	0.0671	0.0176	−0.2656	−0.0839	0.0215
−0.40	0.2859	0.0436	0.0609	0.1851	0.0531	0.0170	0.2122	0.0556	0.0184	0.2503	0.0704	0.0111
0.00	0.4652	0.0411	0.0956	0.4143	0.0467	0.0103	0.2474	0.0596	0.0108	0.3244	0.0642	0.0050
0.40	0.0219	0.0373	0.0300	0.2871	0.0441	0.0210	0.2745	0.0561	0.0167	0.0779	0.0588	0.0105
0.80	0.0916	0.0793	0.0130	0.2560	0.0953	0.0415	−0.1279	−0.1120	0.0183	0.0537	0.1175	0.0161

$\cos(\theta^*_{2\pi^0})$	$W=(1870.0\pm10.0)$ MeV			$W=(1890.0\pm10.0)$ MeV		
	E	Δ_{stat}	Δ_{sys}	E	Δ_{stat}	Δ_{sys}
−0.80	−0.0226	−0.0835	0.0270	0.0685	0.1091	0.0139
−0.40	0.3415	0.0978	0.0326	0.2139	0.1268	0.0156
0.00	0.4395	0.0926	0.0235	0.1627	0.1074	0.0359
0.40	0.1608	0.0841	0.0167	0.0782	0.1171	0.0302
0.80	0.3511	0.1637	0.0495	0.2810	0.2440	0.0590

$\cos(\theta^*_{2\pi^0})$	$W=(1310.0\pm10.0)$ MeV			$W=(1330.0\pm10.0)$ MeV			$W=(1350.0\pm10.0)$ MeV			$W=(1370.0\pm10.0)$ MeV		
	$d\sigma_{1/2}/d\Omega$ [μb/sr]	Δ_{stat} [μb/sr]	Δ_{sys} [μb/sr]	$d\sigma_{1/2}/d\Omega$ [μb/sr]	Δ_{stat} [μb/sr]	Δ_{sys} [μb/sr]	$d\sigma_{1/2}/d\Omega$ [μb/sr]	Δ_{stat} [μb/sr]	Δ_{sys} [μb/sr]	$d\sigma_{1/2}/d\Omega$ [μb/sr]	Δ_{stat} [μb/sr]	Δ_{sys} [μb/sr]
−0.80	0.0306	0.0134	0.0081	0.0401	0.0164	0.0048	0.1480	0.0166	0.0360	0.1015	0.0240	0.0103
−0.40	0.0588	0.0312	0.0146	0.0091	0.0316	0.0044	0.1451	0.0302	0.0421	0.1514	0.0445	0.0377
0.00	0.1160	0.0728	0.0070	0.1488	0.0546	0.0305	0.1032	0.0374	0.0290	0.2138	0.0491	0.0122
0.40	0.0528	0.2476	0.0394	−0.0633	0.1942	0.2103	−0.2547	0.0992	0.0251	0.2569	0.1182	0.0390
0.80	0.6391	1.1624	0.9050	0.8530	24.8584	0.5332	0.3671	4.0870	0.2321	2.7824	2.6227	2.1465

$\cos(\theta^*_{2\pi^0})$	$W=(1390.0\pm10.0)$ MeV			$W=(1410.0\pm10.0)$ MeV			$W=(1430.0\pm10.0)$ MeV			$W=(1450.0\pm10.0)$ MeV		
	$d\sigma_{1/2}/d\Omega$ [μb/sr]	Δ_{stat} [μb/sr]	Δ_{sys} [μb/sr]	$d\sigma_{1/2}/d\Omega$ [μb/sr]	Δ_{stat} [μb/sr]	Δ_{sys} [μb/sr]	$d\sigma_{1/2}/d\Omega$ [μb/sr]	Δ_{stat} [μb/sr]	Δ_{sys} [μb/sr]	$d\sigma_{1/2}/d\Omega$ [μb/sr]	Δ_{stat} [μb/sr]	Δ_{sys} [μb/sr]
−0.80	0.3136	0.0263	0.0323	0.3886	0.0335	0.0431	0.5393	0.0325	0.0507	0.6479	0.0379	0.0693
−0.40	0.3595	0.0422	0.0601	0.3376	0.0408	0.0884	0.4471	0.0480	0.0901	0.5701	0.0454	0.0756
0.00	0.2963	0.0458	0.0511	0.2299	0.0526	0.0393	0.2469	0.0506	0.0945	0.3132	0.0524	0.0831
0.40	0.2438	0.0777	0.0735	−0.0866	0.0796	0.0813	0.2376	0.0687	0.0588	0.3960	0.0626	0.0659
0.80	0.2368	0.5687	0.1829	0.3612	0.4105	0.0998	−0.8481	0.4430	0.1277	0.1479	0.2714	0.0578

$\cos(\theta^*_{2\pi^0})$	$W=(1470.0\pm10.0)$ MeV			$W=(1490.0\pm10.0)$ MeV			$W=(1510.0\pm10.0)$ MeV			$W=(1530.0\pm10.0)$ MeV		
	$d\sigma_{1/2}/d\Omega$ [μb/sr]	Δ_{stat} [μb/sr]	Δ_{sys} [μb/sr]	$d\sigma_{1/2}/d\Omega$ [μb/sr]	Δ_{stat} [μb/sr]	Δ_{sys} [μb/sr]	$d\sigma_{1/2}/d\Omega$ [μb/sr]	Δ_{stat} [μb/sr]	Δ_{sys} [μb/sr]	$d\sigma_{1/2}/d\Omega$ [μb/sr]	Δ_{stat} [μb/sr]	Δ_{sys} [μb/sr]
−0.80	0.7559	0.0399	0.0788	0.9004	0.0400	0.1232	0.9127	0.0430	0.1111	0.8925	0.0414	0.0948
−0.40	0.5221	0.0453	0.0371	0.5400	0.0461	0.0578	0.4528	0.0480	0.0286	0.5142	0.0451	0.0294
0.00	0.4253	0.0486	0.0512	0.3450	0.0488	0.0607	0.4393	0.0464	0.0367	0.2418	0.0423	0.0204
0.40	0.3786	0.0588	0.0862	0.3762	0.0571	0.0545	0.4183	0.0528	0.0479	0.3772	0.0443	0.0477
0.80	0.0907	0.1986	0.1758	0.2194	0.1896	0.0269	0.2766	0.1464	0.1228	0.6236	0.1206	0.1521

$\cos(\theta^*_{2\pi^0})$	$W=(1550.0\pm10.0)$ MeV			$W=(1570.0\pm10.0)$ MeV			$W=(1590.0\pm10.0)$ MeV			$W=(1610.0\pm10.0)$ MeV		
	$d\sigma_{1/2}/d\Omega$ [μb/sr]	Δ_{stat} [μb/sr]	Δ_{sys} [μb/sr]	$d\sigma_{1/2}/d\Omega$ [μb/sr]	Δ_{stat} [μb/sr]	Δ_{sys} [μb/sr]	$d\sigma_{1/2}/d\Omega$ [μb/sr]	Δ_{stat} [μb/sr]	Δ_{sys} [μb/sr]	$d\sigma_{1/2}/d\Omega$ [μb/sr]	Δ_{stat} [μb/sr]	Δ_{sys} [μb/sr]
−0.80	0.8024	0.0394	0.0761	0.7970	0.0373	0.1187	0.8569	0.0358	0.1160	0.8130	0.0366	0.1546
−0.40	0.3621	0.0392	0.0029	0.5701	0.0377	0.0087	0.5005	0.0321	0.0100	0.5039	0.0306	0.0027
0.00	0.3987	0.0381	0.0364	0.3094	0.0352	0.0221	0.3442	0.0297	0.0318	0.3589	0.0308	0.0279
0.40	0.3630	0.0417	0.0420	0.4155	0.0389	0.0430	0.4787	0.0345	0.0310	0.3862	0.0312	0.0443
0.80	0.2400	0.1015	0.0821	0.5582	0.0935	0.0516	0.5173	0.0753	0.1071	0.4966	0.0685	0.0599

$\cos(\theta^*_{2\pi^0})$	$W=(1630.0\pm10.0)$ MeV			$W=(1650.0\pm10.0)$ MeV			$W=(1670.0\pm10.0)$ MeV			$W=(1690.0\pm10.0)$ MeV		
	$d\sigma_{1/2}/d\Omega$ [μb/sr]	Δ_{stat} [μb/sr]	Δ_{sys} [μb/sr]	$d\sigma_{1/2}/d\Omega$ [μb/sr]	Δ_{stat} [μb/sr]	Δ_{sys} [μb/sr]	$d\sigma_{1/2}/d\Omega$ [μb/sr]	Δ_{stat} [μb/sr]	Δ_{sys} [μb/sr]	$d\sigma_{1/2}/d\Omega$ [μb/sr]	Δ_{stat} [μb/sr]	Δ_{sys} [μb/sr]
−0.80	0.8948	0.0329	0.1300	0.8437	0.0308	0.1095	0.8899	0.0289	0.1176	0.8333	0.0296	0.0926
−0.40	0.5082	0.0262	0.0408	0.5554	0.0266	0.0117	0.6026	0.0301	0.0442	0.6071	0.0287	0.0155
0.00	0.4486	0.0263	0.0343	0.5457	0.0264	0.0318	0.5784	0.0281	0.0325	0.7812	0.0290	0.0352
0.40	0.5539	0.0302	0.0670	0.6266	0.0301	0.0602	0.7332	0.0310	0.0374	0.7775	0.0331	0.0458
0.80	0.5658	0.0656	0.0687	0.5173	0.0694	0.0540	0.6303	0.0696	0.0572	0.5855	0.0717	0.0203

$\cos(\theta^*_{2\pi^0})$	$W=(1710.0\pm10.0)$ MeV			$W=(1730.0\pm10.0)$ MeV			$W=(1750.0\pm10.0)$ MeV			$W=(1770.0\pm10.0)$ MeV		
	$d\sigma_{1/2}/d\Omega$ [μb/sr]	$\Delta_{\rm stat}$ [μb/sr]	$\Delta_{\rm sys}$ [μb/sr]	$d\sigma_{1/2}/d\Omega$ [μb/sr]	$\Delta_{\rm stat}$ [μb/sr]	$\Delta_{\rm sys}$ [μb/sr]	$d\sigma_{1/2}/d\Omega$ [μb/sr]	$\Delta_{\rm stat}$ [μb/sr]	$\Delta_{\rm sys}$ [μb/sr]	$d\sigma_{1/2}/d\Omega$ [μb/sr]	$\Delta_{\rm stat}$ [μb/sr]	$\Delta_{\rm sys}$ [μb/sr]
−0.80	0.9052	0.0315	0.0932	0.7833	0.0298	0.0896	0.6087	0.0248	0.0583	0.5563	0.0222	0.0575
−0.40	0.8018	0.0326	0.0412	0.6192	0.0311	0.0205	0.5745	0.0255	0.0168	0.4826	0.0230	0.0210
0.00	0.8796	0.0310	0.0174	0.8028	0.0302	0.0415	0.6963	0.0272	0.0148	0.6170	0.0238	0.0475
0.40	0.8056	0.0394	0.0611	0.9536	0.0352	0.0495	0.8440	0.0349	0.0684	0.7515	0.0314	0.0334
0.80	0.7543	0.0660	0.0295	0.6275	0.0561	0.0336	0.6593	0.0509	0.0321	0.5361	0.0486	0.0569

$\cos(\theta^*_{2\pi^0})$	$W=(1790.0\pm10.0)$ MeV			$W=(1810.0\pm10.0)$ MeV			$W=(1830.0\pm10.0)$ MeV			$W=(1850.0\pm10.0)$ MeV		
	$d\sigma_{1/2}/d\Omega$ [μb/sr]	$\Delta_{\rm stat}$ [μb/sr]	$\Delta_{\rm sys}$ [μb/sr]	$d\sigma_{1/2}/d\Omega$ [μb/sr]	$\Delta_{\rm stat}$ [μb/sr]	$\Delta_{\rm sys}$ [μb/sr]	$d\sigma_{1/2}/d\Omega$ [μb/sr]	$\Delta_{\rm stat}$ [μb/sr]	$\Delta_{\rm sys}$ [μb/sr]	$d\sigma_{1/2}/d\Omega$ [μb/sr]	$\Delta_{\rm stat}$ [μb/sr]	$\Delta_{\rm sys}$ [μb/sr]
−0.80	0.3994	0.0231	0.0181	0.3895	0.0259	0.0335	0.3517	0.0252	0.0147	0.1905	0.0297	0.0087
−0.40	0.5291	0.0244	0.0736	0.4547	0.0284	0.0317	0.4522	0.0287	0.0391	0.4379	0.0338	0.0149
0.00	0.6840	0.0246	0.1028	0.6463	0.0279	0.0070	0.5074	0.0333	0.0239	0.5517	0.0360	0.0083
0.40	0.6084	0.0314	0.0791	0.7665	0.0357	0.0544	0.7183	0.0431	0.0452	0.6190	0.0476	0.0134
0.80	0.5162	0.0528	0.0871	0.5499	0.0572	0.0596	0.3597	0.0648	0.0824	0.4981	0.0784	0.0147

$\cos(\theta^*_{2\pi^0})$	$W=(1870.0\pm10.0)$ MeV			$W=(1890.0\pm10.0)$ MeV		
	$d\sigma_{1/2}/d\Omega$ [μb/sr]	$\Delta_{\rm stat}$ [μb/sr]	$\Delta_{\rm sys}$ [μb/sr]	$d\sigma_{1/2}/d\Omega$ [μb/sr]	$\Delta_{\rm stat}$ [μb/sr]	$\Delta_{\rm sys}$ [μb/sr]
−0.80	0.2607	0.0315	0.0277	0.2788	0.0402	0.0200
−0.40	0.4244	0.0414	0.0394	0.4088	0.0590	0.0421
0.00	0.5463	0.0455	0.0281	0.4711	0.0607	0.1335
0.40	0.6432	0.0651	0.0416	0.6460	0.0989	0.1194
0.80	0.5790	0.0936	0.0928	0.4845	0.1257	0.1590

$\cos(\theta^*_{2\pi^0})$	$W=(1310.0\pm10.0)$ MeV			$W=(1330.0\pm10.0)$ MeV			$W=(1350.0\pm10.0)$ MeV			$W=(1370.0\pm10.0)$ MeV		
	$d\sigma_{3/2}/d\Omega$ [μb/sr]	$\Delta_{\rm stat}$ [μb/sr]	$\Delta_{\rm sys}$ [μb/sr]	$d\sigma_{3/2}/d\Omega$ [μb/sr]	$\Delta_{\rm stat}$ [μb/sr]	$\Delta_{\rm sys}$ [μb/sr]	$d\sigma_{3/2}/d\Omega$ [μb/sr]	$\Delta_{\rm stat}$ [μb/sr]	$\Delta_{\rm sys}$ [μb/sr]	$d\sigma_{3/2}/d\Omega$ [μb/sr]	$\Delta_{\rm stat}$ [μb/sr]	$\Delta_{\rm sys}$ [μb/sr]
−0.80	0.0151	0.0134	0.0053	0.0416	0.0164	0.0035	0.0127	0.0166	0.0208	0.2264	0.0240	0.0113
−0.40	−0.0041	0.0312	0.0083	0.1397	0.0316	0.0058	0.1534	0.0302	0.0448	0.4410	0.0445	0.0537
0.00	−0.0441	0.0728	0.0047	0.0151	0.0546	0.0167	0.2211	0.0374	0.0522	0.4216	0.0491	0.0181
0.40	−0.0149	0.2476	0.0560	0.1666	0.1942	0.2453	0.4873	0.0992	0.0415	0.2953	0.1182	0.0467
0.80	−0.5502	1.1624	0.8436	−0.8489	24.8584	0.4216	−0.3772	4.0870	0.2064	−2.6510	2.6227	2.2322

$\cos(\theta^*_{2\pi^0})$	$W=(1390.0\pm10.0)$ MeV			$W=(1410.0\pm10.0)$ MeV			$W=(1430.0\pm10.0)$ MeV			$W=(1450.0\pm10.0)$ MeV		
	$d\sigma_{3/2}/d\Omega$ [μb/sr]	$\Delta_{\rm stat}$ [μb/sr]	$\Delta_{\rm sys}$ [μb/sr]	$d\sigma_{3/2}/d\Omega$ [μb/sr]	$\Delta_{\rm stat}$ [μb/sr]	$\Delta_{\rm sys}$ [μb/sr]	$d\sigma_{3/2}/d\Omega$ [μb/sr]	$\Delta_{\rm stat}$ [μb/sr]	$\Delta_{\rm sys}$ [μb/sr]	$d\sigma_{3/2}/d\Omega$ [μb/sr]	$\Delta_{\rm stat}$ [μb/sr]	$\Delta_{\rm sys}$ [μb/sr]
−0.80	0.1871	0.0263	0.0224	0.2938	0.0335	0.0320	0.3578	0.0325	0.0335	0.4932	0.0379	0.0442
−0.40	0.4687	0.0422	0.0872	0.7159	0.0408	0.1029	0.8393	0.0480	0.1109	0.8797	0.0454	0.0832
0.00	0.5661	0.0458	0.0728	0.8359	0.0526	0.0609	1.0811	0.0506	0.1641	1.2119	0.0524	0.1236
0.40	0.4917	0.0777	0.1124	0.9815	0.0796	0.1335	0.8519	0.0687	0.1109	0.9221	0.0626	0.0988
0.80	0.1142	0.5687	0.2001	0.1038	0.4105	0.1923	1.2521	0.4430	0.1555	0.1352	0.2714	0.0744

$\cos(\theta^*_{2\pi^0})$	$W=(1470.0\pm10.0)$ MeV			$W=(1490.0\pm10.0)$ MeV			$W=(1510.0\pm10.0)$ MeV			$W=(1530.0\pm10.0)$ MeV		
	$d\sigma_{3/2}/d\Omega$ [μb/sr]	$\Delta_{\rm stat}$ [μb/sr]	$\Delta_{\rm sys}$ [μb/sr]	$d\sigma_{3/2}/d\Omega$ [μb/sr]	$\Delta_{\rm stat}$ [μb/sr]	$\Delta_{\rm sys}$ [μb/sr]	$d\sigma_{3/2}/d\Omega$ [μb/sr]	$\Delta_{\rm stat}$ [μb/sr]	$\Delta_{\rm sys}$ [μb/sr]	$d\sigma_{3/2}/d\Omega$ [μb/sr]	$\Delta_{\rm stat}$ [μb/sr]	$\Delta_{\rm sys}$ [μb/sr]
−0.80	0.6755	0.0399	0.0633	0.7445	0.0400	0.0938	0.7929	0.0430	0.0856	0.7576	0.0414	0.0751
−0.40	1.0234	0.0453	0.0437	1.0621	0.0461	0.0713	1.0130	0.0480	0.0313	0.7601	0.0451	0.0356
0.00	1.1223	0.0486	0.0700	1.1971	0.0488	0.0794	1.0147	0.0464	0.0284	0.9164	0.0423	0.0206
0.40	0.9828	0.0588	0.1295	1.0112	0.0571	0.0926	0.9727	0.0528	0.0578	0.8183	0.0443	0.0504
0.80	0.7166	0.1986	0.3215	0.6285	0.1896	0.0077	0.5902	0.1464	0.1876	0.1492	0.1206	0.0549

$\cos(\theta^*_{2\pi^0})$	$W=(1550.0\pm10.0)$ MeV			$W=(1570.0\pm10.0)$ MeV			$W=(1590.0\pm10.0)$ MeV			$W=(1610.0\pm10.0)$ MeV		
	$d\sigma_{3/2}/d\Omega$ [μb/sr]	$\Delta_{\rm stat}$ [μb/sr]	$\Delta_{\rm sys}$ [μb/sr]	$d\sigma_{3/2}/d\Omega$ [μb/sr]	$\Delta_{\rm stat}$ [μb/sr]	$\Delta_{\rm sys}$ [μb/sr]	$d\sigma_{3/2}/d\Omega$ [μb/sr]	$\Delta_{\rm stat}$ [μb/sr]	$\Delta_{\rm sys}$ [μb/sr]	$d\sigma_{3/2}/d\Omega$ [μb/sr]	$\Delta_{\rm stat}$ [μb/sr]	$\Delta_{\rm sys}$ [μb/sr]
−0.80	0.6830	0.0394	0.0595	0.6450	0.0373	0.0996	0.4048	0.0358	0.0768	0.5379	0.0366	0.1112
−0.40	0.6578	0.0392	0.0070	0.3670	0.0377	0.0072	0.2971	0.0321	0.0072	0.3142	0.0306	0.0061
0.00	0.5795	0.0381	0.0343	0.5454	0.0352	0.0256	0.4739	0.0297	0.0326	0.4456	0.0308	0.0355
0.40	0.6427	0.0417	0.0561	0.5701	0.0389	0.0355	0.4581	0.0345	0.0355	0.6267	0.0312	0.0484
0.80	0.6112	0.1015	0.1234	0.2904	0.0935	0.0647	0.3909	0.0753	0.0835	0.4061	0.0685	0.0442

$\cos(\theta^*_{2\pi^0})$	$W=(1630.0\pm10.0)$ MeV			$W=(1650.0\pm10.0)$ MeV			$W=(1670.0\pm10.0)$ MeV			$W=(1690.0\pm10.0)$ MeV		
	$d\sigma_{3/2}/d\Omega$ [μb/sr]	$\Delta_{\rm stat}$ [μb/sr]	$\Delta_{\rm sys}$ [μb/sr]	$d\sigma_{3/2}/d\Omega$ [μb/sr]	$\Delta_{\rm stat}$ [μb/sr]	$\Delta_{\rm sys}$ [μb/sr]	$d\sigma_{3/2}/d\Omega$ [μb/sr]	$\Delta_{\rm stat}$ [μb/sr]	$\Delta_{\rm sys}$ [μb/sr]	$d\sigma_{3/2}/d\Omega$ [μb/sr]	$\Delta_{\rm stat}$ [μb/sr]	$\Delta_{\rm sys}$ [μb/sr]
−0.80	0.4868	0.0329	0.0935	0.5900	0.0308	0.0858	0.7528	0.0289	0.0964	0.8132	0.0296	0.0863
−0.40	0.3723	0.0262	0.0306	0.4044	0.0266	0.0164	0.5163	0.0301	0.0302	0.5800	0.0287	0.0149
0.00	0.3902	0.0263	0.0339	0.4165	0.0264	0.0155	0.5405	0.0281	0.0280	0.4219	0.0290	0.0220
0.40	0.6303	0.0302	0.0625	0.7203	0.0301	0.0761	0.8313	0.0310	0.0400	0.9098	0.0331	0.0319
0.80	0.5593	0.0656	0.0522	0.7103	0.0694	0.0427	0.7958	0.0696	0.0592	0.8682	0.0717	0.0462

$\cos(\theta^*_{2\pi^0})$	$W=(1710.0\pm10.0)$ MeV			$W=(1730.0\pm10.0)$ MeV			$W=(1750.0\pm10.0)$ MeV			$W=(1770.0\pm10.0)$ MeV		
	$d\sigma_{3/2}/d\Omega$ [μb/sr]	$\Delta_{\rm stat}$ [μb/sr]	$\Delta_{\rm sys}$ [μb/sr]	$d\sigma_{3/2}/d\Omega$ [μb/sr]	$\Delta_{\rm stat}$ [μb/sr]	$\Delta_{\rm sys}$ [μb/sr]	$d\sigma_{3/2}/d\Omega$ [μb/sr]	$\Delta_{\rm stat}$ [μb/sr]	$\Delta_{\rm sys}$ [μb/sr]	$d\sigma_{3/2}/d\Omega$ [μb/sr]	$\Delta_{\rm stat}$ [μb/sr]	$\Delta_{\rm sys}$ [μb/sr]
−0.80	0.6840	0.0315	0.0773	0.5758	0.0298	0.0803	0.4682	0.0248	0.0550	0.3183	0.0222	0.0400
−0.40	0.4481	0.0326	0.0255	0.5402	0.0311	0.0119	0.3690	0.0255	0.0139	0.3853	0.0230	0.0187
0.00	0.4129	0.0310	0.0109	0.4464	0.0302	0.0331	0.3855	0.0272	0.0116	0.3696	0.0238	0.0473
0.40	0.9345	0.0394	0.0394	0.6795	0.0352	0.0447	0.5420	0.0349	0.0417	0.5178	0.0314	0.0191
0.80	0.6460	0.0660	0.0360	0.7529	0.0561	0.0249	0.5068	0.0509	0.0097	0.5496	0.0486	0.0419

$\cos(\theta^*_{2\pi^0})$	$W=(1790.0\pm10.0)$ MeV			$W=(1810.0\pm10.0)$ MeV			$W=(1830.0\pm10.0)$ MeV			$W=(1850.0\pm10.0)$ MeV		
	$d\sigma_{3/2}/d\Omega$ [μb/sr]	Δ_{stat} [μb/sr]	Δ_{sys} [μb/sr]	$d\sigma_{3/2}/d\Omega$ [μb/sr]	Δ_{stat} [μb/sr]	Δ_{sys} [μb/sr]	$d\sigma_{3/2}/d\Omega$ [μb/sr]	Δ_{stat} [μb/sr]	Δ_{sys} [μb/sr]	$d\sigma_{3/2}/d\Omega$ [μb/sr]	Δ_{stat} [μb/sr]	Δ_{sys} [μb/sr]
−0.80	0.2858	0.0231	0.0132	0.2659	0.0259	0.0263	0.2000	0.0252	0.0121	0.3283	0.0297	0.0286
−0.40	0.2938	0.0244	0.0553	0.3126	0.0284	0.0207	0.2939	0.0287	0.0276	0.2626	0.0338	0.0143
0.00	0.2496	0.0246	0.0678	0.2676	0.0279	0.0083	0.3062	0.0333	0.0195	0.2814	0.0360	0.0062
0.40	0.5823	0.0314	0.0489	0.4245	0.0357	0.0380	0.4089	0.0431	0.0305	0.5295	0.0476	0.0217
0.80	0.4295	0.0528	0.0730	0.3257	0.0572	0.0493	0.4651	0.0648	0.0934	0.4473	0.0784	0.0129

$\cos(\theta^*_{2\pi^0})$	$W=(1870.0\pm10.0)$ MeV			$W=(1890.0\pm10.0)$ MeV		
	$d\sigma_{3/2}/d\Omega$ [μb/sr]	Δ_{stat} [μb/sr]	Δ_{sys} [μb/sr]	$d\sigma_{3/2}/d\Omega$ [μb/sr]	Δ_{stat} [μb/sr]	Δ_{sys} [μb/sr]
−0.80	0.2728	0.0315	0.0357	0.2431	0.0402	0.0116
−0.40	0.2083	0.0414	0.0161	0.2647	0.0590	0.0345
0.00	0.2127	0.0455	0.0201	0.3393	0.0607	0.1219
0.40	0.4651	0.0651	0.0364	0.5523	0.0989	0.0845
0.80	0.2781	0.0936	0.0800	0.2719	0.1257	0.1367

E.4.6 Observables for $\gamma n \rightarrow \pi^0\pi^0 n$ as a Function of W

W [MeV]	ΔW [MeV]	E	Δ_{stat}	Δ_{sys}	$\sigma_{1/2}$ [μb]	Δ_{stat} [μb]	Δ_{sys} [μb]	$\sigma_{3/2}$ [μb]	Δ_{stat} [μb]	Δ_{sys} [μb]
1310.0	10.0	1.0126	0.9330	0.2679	0.6004	0.2766	0.1139	−0.0038	0.2766	0.1109
1330.0	10.0	−0.0479	0.5341	0.0190	0.4263	0.3378	0.1336	0.4692	0.3378	0.1651
1350.0	10.0	−0.6136	0.2142	0.0745	0.3951	0.2640	0.0730	1.6500	0.2640	0.2030
1370.0	10.0	0.3139	0.1395	0.0376	2.8147	0.4033	0.3338	1.4698	0.4033	0.1884
1390.0	10.0	−0.4289	0.0997	0.0584	1.7082	0.3876	0.2521	4.2738	0.3876	0.5051
1410.0	10.0	−0.1987	0.0708	0.0220	3.4730	0.4255	0.4018	5.1952	0.4255	0.6059
1430.0	10.0	−0.4302	0.0595	0.0555	3.1436	0.4264	0.4259	7.8913	0.4264	0.8912
1450.0	10.0	−0.4847	0.0507	0.0574	3.6306	0.4547	0.4622	10.4600	0.4547	1.1611
1470.0	10.0	−0.3900	0.0435	0.0430	4.7969	0.4505	0.5330	10.9308	0.4505	1.2147
1490.0	10.0	−0.4028	0.0398	0.0444	5.4587	0.4767	0.6062	12.8214	0.4767	1.4160
1510.0	10.0	−0.2663	0.0362	0.0348	7.2347	0.4876	0.9753	12.4853	0.4876	1.5219
1530.0	10.0	−0.2509	0.0366	0.0310	7.0759	0.4742	0.8380	11.8156	0.4742	1.3260
1550.0	10.0	−0.1305	0.0374	0.0145	7.3423	0.4426	0.8170	9.5456	0.4426	1.0591
1570.0	10.0	−0.0194	0.0351	0.0064	7.9378	0.4019	0.8853	8.2518	0.4019	0.9101
1590.0	10.0	−0.0800	0.0354	0.0088	7.1054	0.3852	0.7888	8.3419	0.3852	0.9252
1610.0	10.0	−0.0666	0.0317	0.0129	7.6396	0.3666	1.0137	8.7293	0.3666	1.0909
1630.0	10.0	−0.1203	0.0292	0.0134	7.3720	0.3436	0.8235	9.3873	0.3436	1.0416
1650.0	10.0	−0.1465	0.0288	0.0197	7.4999	0.3539	0.8812	10.0744	0.3539	1.1673
1670.0	10.0	−0.1648	0.0271	0.0187	7.8111	0.3543	0.8997	10.8933	0.3543	1.2373
1690.0	10.0	−0.1646	0.0270	0.0214	8.1015	0.3656	1.0098	11.2933	0.3656	1.3994
1710.0	10.0	0.0045	0.0296	0.0017	8.7686	0.3652	1.1043	8.6899	0.3652	1.0956
1730.0	10.0	−0.1863	0.0311	0.0228	6.5905	0.3505	0.8430	9.6090	0.3505	1.1704
1750.0	10.0	−0.1122	0.0330	0.0144	5.9559	0.3111	0.7146	7.4620	0.3111	0.8792
1770.0	10.0	−0.1320	0.0328	0.0196	4.8641	0.2581	0.6114	6.3429	0.2581	0.7723
1790.0	10.0	−0.2802	0.0352	0.0333	3.5618	0.2372	0.4607	6.3347	0.2372	0.7604
1810.0	10.0	−0.2367	0.0380	0.0294	3.7223	0.2550	0.4559	6.0312	0.2550	0.7069
1830.0	10.0	−0.1972	0.0467	0.0266	3.4923	0.2822	0.4285	5.2082	0.2822	0.6152
1850.0	10.0	−0.1872	0.0556	0.0245	3.3213	0.3157	0.4986	4.8517	0.3157	0.6632
1870.0	10.0	−0.1272	0.0676	0.0217	3.3710	0.3665	0.7470	4.3534	0.3665	0.8566
1890.0	10.0	−0.0357	0.0918	0.0203	3.5824	0.4819	1.4642	3.8476	0.4819	1.4998

Angular Distributions

$\cos(\theta^*_{2\pi^0})$	$W=(1310.0\pm10.0)$ MeV			$W=(1330.0\pm10.0)$ MeV			$W=(1350.0\pm10.0)$ MeV			$W=(1370.0\pm10.0)$ MeV		
	E	Δ_{stat}	Δ_{sys}	E	Δ_{stat}	Δ_{sys}	E	Δ_{stat}	Δ_{sys}	E	Δ_{stat}	Δ_{sys}
−0.80	1.1348	1.4247	0.3077	−0.4372	−0.5966	0.2301	−0.1552	−0.3203	0.0206	0.4898	0.2241	0.1437
−0.40	1.3064	2.2890	0.4064	0.7163	0.6837	0.4223	−0.2451	−0.2860	0.1436	−0.1472	−0.1779	0.0668
0.00	2.6564	4.5520	2.3046	0.2021	0.6611	0.0510	−0.8779	−0.3641	0.0645	−0.2077	−0.1964	0.0602
0.40	0.5382	1.8114	29.3644	−0.7423	−3.3782	0.3688	−0.2120	−0.5461	0.0719	1.0162	0.5877	0.0840
0.80	6.8396	37.6094	1.3498	6.3572	65.8549	4.3603	0.2727	2.7156	0.2976	26.52[illegible]	[illegible]63.5110	156.0186

$\cos(\theta^*_{2\pi^0})$	$W=(1390.0\pm10.0)$ MeV			$W=(1410.0\pm10.0)$ MeV			$W=(1430.0\pm10.0)$ MeV			$W=(1450.0\pm10.0)$ MeV		
	E	Δ_{stat}	Δ_{sys}	E	Δ_{stat}	Δ_{sys}	E	Δ_{stat}	Δ_{sys}	E	Δ_{stat}	Δ_{sys}
−0.80	0.2504	0.2046	0.0134	0.0574	0.1312	0.0368	−0.1180	−0.0907	0.0279	−0.1039	−0.0705	0.0460
−0.40	−0.2297	−0.1482	0.0334	0.2207	0.1104	0.0266	−0.6090	−0.1043	0.0360	−0.7055	−0.0968	0.0175
0.00	−0.5364	−0.1471	0.0367	−0.2982	−0.1213	0.0306	−0.4800	−0.1121	0.0511	−0.5287	−0.0930	0.0775
0.40	−0.7417	−0.2798	0.0380	−0.8971	−0.2253	0.0346	−0.7661	−0.1853	0.0523	−0.1724	−0.1059	0.0161
0.80	7.1467	90.6729	4.1531	−2.5023	−2.6200	0.4960	−0.5547	−1.1617	0.0810	0.2347	0.4460	0.0350

$\cos(\theta^*_{2\pi^0})$	$W=(1470.0\pm10.0)$ MeV			$W=(1490.0\pm10.0)$ MeV			$W=(1510.0\pm10.0)$ MeV			$W=(1530.0\pm10.0)$ MeV		
	E	Δ_{stat}	Δ_{sys}	E	Δ_{stat}	Δ_{sys}	E	Δ_{stat}	Δ_{sys}	E	Δ_{stat}	Δ_{sys}
−0.80	−0.0085	−0.0598	0.0068	−0.0444	−0.0520	0.0060	−0.0011	−0.0455	0.0029	−0.1228	−0.0483	0.0236
−0.40	−0.4376	−0.0787	0.0091	−0.5721	−0.0791	0.0227	−0.5076	−0.0794	0.0304	−0.4284	−0.0834	0.0224
0.00	−0.4742	−0.0844	0.0429	−0.2373	−0.0749	0.0131	−0.4673	−0.0843	0.0138	−0.2566	−0.0760	0.0323
0.40	−0.5389	−0.1041	0.0515	−0.7140	−0.1206	0.0219	−0.2540	−0.0986	0.0387	−0.3441	−0.0924	0.0469
0.80	−2.5549	−4.2763	0.9788	−1.2325	−0.7327	0.2926	−0.0020	−0.2725	0.0275	0.4504	0.2327	0.0379

$\cos(\theta^*_{2\pi^0})$	$W=(1550.0\pm10.0)$ MeV			$W=(1570.0\pm10.0)$ MeV			$W=(1590.0\pm10.0)$ MeV			$W=(1610.0\pm10.0)$ MeV		
	E	Δ_{stat}	Δ_{sys}	E	Δ_{stat}	Δ_{sys}	E	Δ_{stat}	Δ_{sys}	E	Δ_{stat}	Δ_{sys}
−0.80	0.0056	0.0497	0.0006	0.1173	0.0476	0.0119	0.0369	0.0457	0.0103	−0.0416	−0.0425	0.0237
−0.40	−0.2721	−0.0753	0.0063	−0.0699	−0.0761	0.0039	−0.1247	−0.0764	0.0037	−0.1536	−0.0691	0.0121
0.00	−0.0229	−0.0812	0.0246	−0.4259	−0.0892	0.0183	−0.1783	−0.0822	0.0096	−0.1570	−0.0782	0.0064
0.40	−0.3959	−0.1007	0.0616	−0.2853	−0.1033	0.0418	−0.0852	−0.0934	0.0033	0.1138	0.0864	0.0189
0.80	−0.4189	−0.2372	0.0381	1.4434	0.6005	0.1435	−0.4932	−0.2175	0.0520	−0.3778	−0.2016	0.3156

$\cos(\theta^*_{2\pi^0})$	$W=(1630.0\pm10.0)$ MeV			$W=(1650.0\pm10.0)$ MeV			$W=(1670.0\pm10.0)$ MeV			$W=(1690.0\pm10.0)$ MeV		
	E	Δ_{stat}	Δ_{sys}	E	Δ_{stat}	Δ_{sys}	E	Δ_{stat}	Δ_{sys}	E	Δ_{stat}	Δ_{sys}
−0.80	0.2433	0.0463	0.0373	0.1418	0.0463	0.0149	0.1699	0.0442	0.0127	0.1334	0.0435	0.0275
−0.40	−0.1295	−0.0620	0.0087	−0.2239	−0.0640	0.0116	−0.3258	−0.0540	0.0111	−0.1873	−0.0563	0.0191
0.00	−0.4120	−0.0657	0.0124	−0.5175	−0.0633	0.0188	−0.4080	−0.0569	0.0125	−0.1847	−0.0542	0.0082
0.40	−0.2863	−0.0811	0.0109	−0.1188	−0.0690	0.0065	−0.1323	−0.0656	0.0012	−0.3979	−0.0717	0.0277
0.80	−0.7742	−0.2612	0.0962	−0.2500	−0.1846	0.0659	0.0309	0.1453	0.0223	−0.7597	−0.2642	0.1726

$\cos(\theta^*_{2\pi^0})$	$W=(1710.0\pm10.0)$ MeV			$W=(1730.0\pm10.0)$ MeV			$W=(1750.0\pm10.0)$ MeV			$W=(1770.0\pm10.0)$ MeV		
	E	Δ_{stat}	Δ_{sys}	E	Δ_{stat}	Δ_{sys}	E	Δ_{stat}	Δ_{sys}	E	Δ_{stat}	Δ_{sys}
−0.80	0.2181	0.0510	0.0182	0.1696	0.0530	0.0104	0.1215	0.0563	0.0242	0.0548	0.0584	0.0176
−0.40	−0.1347	−0.0602	0.0046	−0.5584	−0.0641	0.0398	−0.2341	−0.0618	0.0059	−0.3712	−0.0686	0.0292
0.00	−0.1982	−0.0567	0.0042	−0.2099	−0.0594	0.0269	−0.1121	−0.0579	0.0073	−0.1030	−0.0609	0.0090
0.40	−0.0285	−0.0705	0.0213	−0.0954	−0.0817	0.0091	−0.4054	−0.0909	0.0377	−0.1351	−0.0822	0.0132
0.80	0.2643	0.1826	0.0653	−0.2447	−0.1599	0.0751	−0.3926	−0.1894	0.0766	0.2250	0.3122	0.2714

$\cos(\theta^*_{2\pi^0})$	$W=(1790.0\pm10.0)$ MeV			$W=(1810.0\pm10.0)$ MeV			$W=(1830.0\pm10.0)$ MeV			$W=(1850.0\pm10.0)$ MeV		
	E	Δ_{stat}	Δ_{sys}	E	Δ_{stat}	Δ_{sys}	E	Δ_{stat}	Δ_{sys}	E	Δ_{stat}	Δ_{sys}
−0.80	0.0303	0.0713	0.0336	0.2348	0.0762	0.0052	−0.0418	−0.1035	0.0204	0.0282	0.1027	0.0513
−0.40	−0.3897	−0.0827	0.0130	−0.4536	−0.0830	0.0388	−0.3105	−0.0965	0.0588	−0.0173	−0.0955	0.0198
0.00	−0.5123	−0.0744	0.0226	−0.1082	−0.0739	0.0015	−0.7035	−0.1088	0.0785	−0.2413	−0.1148	0.0334
0.40	−0.2287	−0.1016	0.0160	−0.4150	−0.1123	0.0355	0.3951	0.1492	0.0494	−0.5831	−0.1928	0.0949
0.80	0.6020	0.3033	0.0629	−0.4042	−0.2119	2.6474	−1.0265	−0.5378	0.2478	0.1695	0.4709	0.0563

$\cos(\theta^*_{2\pi^0})$				$W=(1870.0\pm10.0)$ MeV						$W=(1890.0\pm10.0)$ MeV		
				E	Δ_{stat}	Δ_{sys}				E	Δ_{stat}	Δ_{sys}
−0.80				−0.4698	−0.1353	0.0119				0.0722	0.1904	0.0080
−0.40				−0.3155	−0.1328	0.0199				0.0530	0.1585	0.0954
0.00				−0.2439	−0.1276	0.0376				−0.1936	−0.1871	0.0161
0.40				0.1757	0.1916	0.0378				0.3688	0.2869	0.1052
0.80				0.7654	1.0819	0.1765				6.0910	11.0475	2.3320

$\cos(\theta^*_{2\pi^0})$	$W=(1310.0\pm10.0)$ MeV			$W=(1330.0\pm10.0)$ MeV			$W=(1350.0\pm10.0)$ MeV			$W=(1370.0\pm10.0)$ MeV		
	$d\sigma_{1/2}/d\Omega$ [μb/sr]	Δ_{stat} [μb/sr]	Δ_{sys} [μb/sr]	$d\sigma_{1/2}/d\Omega$ [μb/sr]	Δ_{stat} [μb/sr]	Δ_{sys} [μb/sr]	$d\sigma_{1/2}/d\Omega$ [μb/sr]	Δ_{stat} [μb/sr]	Δ_{sys} [μb/sr]	$d\sigma_{1/2}/d\Omega$ [μb/sr]	Δ_{stat} [μb/sr]	Δ_{sys} [μb/sr]
−0.80	0.0655	0.0409	0.0043	0.0330	0.0453	0.0232	0.0720	0.0382	0.0070	0.2741	0.0524	0.0605
−0.40	0.0511	0.0436	0.0089	0.1019	0.0467	0.0019	0.0694	0.0361	0.0153	0.1851	0.0540	0.0103
0.00	0.0760	0.0472	0.0236	0.0696	0.0530	0.0074	0.0133	0.0422	0.0073	0.1725	0.0592	0.0145
0.40	0.0391	0.0573	0.5503	0.0049	0.0723	0.0070	0.0609	0.0584	0.0208	0.2880	0.0833	0.0261
0.80	0.3732	0.3663	0.0532	−0.1917	0.3771	0.1039	0.0593	0.1726	0.0106	−0.3221	1.6612	1.8261

$\cos(\theta^*_{2\pi^0})$	$W=(1390.0\pm10.0)$ MeV			$W=(1410.0\pm10.0)$ MeV			$W=(1430.0\pm10.0)$ MeV			$W=(1450.0\pm10.0)$ MeV		
	$d\sigma_{1/2}/d\Omega$ [μb/sr]	Δ_{stat} [μb/sr]	Δ_{sys} [μb/sr]	$d\sigma_{1/2}/d\Omega$ [μb/sr]	Δ_{stat} [μb/sr]	Δ_{sys} [μb/sr]	$d\sigma_{1/2}/d\Omega$ [μb/sr]	Δ_{stat} [μb/sr]	Δ_{sys} [μb/sr]	$d\sigma_{1/2}/d\Omega$ [μb/sr]	Δ_{stat} [μb/sr]	Δ_{sys} [μb/sr]
−0.80	0.2686	0.0603	0.0083	0.4070	0.0713	0.0380	0.4471	0.0645	0.0393	0.6361	0.0704	0.0805
−0.40	0.2155	0.0572	0.0189	0.4724	0.0590	0.0473	0.2023	0.0652	0.0274	0.1806	0.0686	0.0145
0.00	0.1568	0.0620	0.0186	0.2916	0.0683	0.0230	0.2737	0.0752	0.0462	0.3062	0.0755	0.0676
0.40	0.0625	0.0769	0.0112	0.0373	0.0859	0.0130	0.0974	0.0866	0.0252	0.4848	0.0864	0.0462
0.80	−0.1813	0.3954	0.0915	−0.2253	0.2062	0.0744	0.0489	0.1577	0.0221	0.2914	0.1449	0.0499

$\cos(\theta^*_{2\pi^0})$	$W=(1470.0\pm10.0)$ MeV			$W=(1490.0\pm10.0)$ MeV			$W=(1510.0\pm10.0)$ MeV			$W=(1530.0\pm10.0)$ MeV		
	$d\sigma_{1/2}/d\Omega$ [μb/sr]	Δ_{stat} [μb/sr]	Δ_{sys} [μb/sr]	$d\sigma_{1/2}/d\Omega$ [μb/sr]	Δ_{stat} [μb/sr]	Δ_{sys} [μb/sr]	$d\sigma_{1/2}/d\Omega$ [μb/sr]	Δ_{stat} [μb/sr]	Δ_{sys} [μb/sr]	$d\sigma_{1/2}/d\Omega$ [μb/sr]	Δ_{stat} [μb/sr]	Δ_{sys} [μb/sr]
−0.80	0.8354	0.0712	0.0926	1.0949	0.0841	0.1124	1.3717	0.0884	0.2287	1.2537	0.0969	0.1588
−0.40	0.3939	0.0714	0.0168	0.3335	0.0757	0.0304	0.3854	0.0783	0.0406	0.4038	0.0766	0.0272
0.00	0.3730	0.0765	0.0521	0.5857	0.0791	0.0473	0.3899	0.0791	0.0204	0.5029	0.0704	0.0313
0.40	0.2835	0.0797	0.0491	0.1837	0.0892	0.0210	0.4912	0.0890	0.0720	0.4032	0.0760	0.0578
0.80	−0.1241	0.1759	0.1308	−0.0595	0.1672	0.1182	0.3779	0.1460	0.0345	0.6072	0.1256	0.0662

$\cos(\theta^*_{2\pi^0})$	$W=(1550.0\pm10.0)$ MeV			$W=(1570.0\pm10.0)$ MeV			$W=(1590.0\pm10.0)$ MeV			$W=(1610.0\pm10.0)$ MeV		
	$d\sigma_{1/2}/d\Omega$ [μb/sr]	Δ_{stat} [μb/sr]	Δ_{sys} [μb/sr]	$d\sigma_{1/2}/d\Omega$ [μb/sr]	Δ_{stat} [μb/sr]	Δ_{sys} [μb/sr]	$d\sigma_{1/2}/d\Omega$ [μb/sr]	Δ_{stat} [μb/sr]	Δ_{sys} [μb/sr]	$d\sigma_{1/2}/d\Omega$ [μb/sr]	Δ_{stat} [μb/sr]	Δ_{sys} [μb/sr]
−0.80	1.3255	0.0926	0.1144	1.4378	0.0860	0.1391	1.2885	0.0802	0.1588	1.2115	0.0759	0.1725
−0.40	0.4760	0.0672	0.0141	0.5634	0.0650	0.0039	0.5247	0.0642	0.0114	0.5298	0.0605	0.0427
0.00	0.5716	0.0672	0.0240	0.3121	0.0631	0.0157	0.4161	0.0580	0.0216	0.4630	0.0600	0.0246
0.40	0.3266	0.0716	0.0583	0.3672	0.0722	0.0497	0.4491	0.0646	0.0141	0.5560	0.0606	0.0287
0.80	0.2004	0.1067	0.0383	0.6155	0.1218	0.0616	0.1818	0.0990	0.0312	0.2365	0.1014	0.1190

$\cos(\theta^*_{2\pi^0})$	$W=(1630.0\pm10.0)$ MeV			$W=(1650.0\pm10.0)$ MeV			$W=(1670.0\pm10.0)$ MeV			$W=(1690.0\pm10.0)$ MeV		
	$d\sigma_{1/2}/d\Omega$ [μb/sr]	Δ_{stat} [μb/sr]	Δ_{sys} [μb/sr]	$d\sigma_{1/2}/d\Omega$ [μb/sr]	Δ_{stat} [μb/sr]	Δ_{sys} [μb/sr]	$d\sigma_{1/2}/d\Omega$ [μb/sr]	Δ_{stat} [μb/sr]	Δ_{sys} [μb/sr]	$d\sigma_{1/2}/d\Omega$ [μb/sr]	Δ_{stat} [μb/sr]	Δ_{sys} [μb/sr]
−0.80	1.4694	0.0753	0.1828	1.3600	0.0772	0.1227	1.3478	0.0709	0.1066	1.3212	0.0711	0.0993
−0.40	0.5819	0.0581	0.0196	0.5371	0.0612	0.0401	0.5321	0.0573	0.0318	0.6380	0.0614	0.0295
0.00	0.3742	0.0546	0.0117	0.3417	0.0563	0.0161	0.4948	0.0623	0.0251	0.6871	0.0635	0.0399
0.40	0.3958	0.0611	0.0112	0.5184	0.0570	0.0364	0.5649	0.0599	0.0233	0.4119	0.0645	0.0553
0.80	0.0786	0.1017	0.0576	0.2667	0.0901	0.1175	0.4501	0.0897	0.0405	0.0789	0.0976	0.1367

$\cos(\theta^*_{2\pi^0})$	$W=(1710.0\pm10.0)$ MeV			$W=(1730.0\pm10.0)$ MeV			$W=(1750.0\pm10.0)$ MeV			$W=(1770.0\pm10.0)$ MeV		
	$d\sigma_{1/2}/d\Omega$ [μb/sr]	Δ_{stat} [μb/sr]	Δ_{sys} [μb/sr]	$d\sigma_{1/2}/d\Omega$ [μb/sr]	Δ_{stat} [μb/sr]	Δ_{sys} [μb/sr]	$d\sigma_{1/2}/d\Omega$ [μb/sr]	Δ_{stat} [μb/sr]	Δ_{sys} [μb/sr]	$d\sigma_{1/2}/d\Omega$ [μb/sr]	Δ_{stat} [μb/sr]	Δ_{sys} [μb/sr]
−0.80	1.2056	0.0697	0.1051	1.0596	0.0670	0.0179	0.7717	0.0544	0.1361	0.6574	0.0514	0.0780
−0.40	0.6284	0.0612	0.0263	0.3000	0.0537	0.0565	0.4515	0.0502	0.0146	0.3056	0.0442	0.0454
0.00	0.6299	0.0618	0.0157	0.5866	0.0610	0.0476	0.5518	0.0506	0.0137	0.4603	0.0439	0.0185
0.40	0.6128	0.0628	0.0702	0.4981	0.0633	0.0451	0.2737	0.0548	0.0527	0.3462	0.0461	0.0485
0.80	0.4544	0.0897	0.0634	0.2572	0.0748	0.0691	0.1953	0.0802	0.0531	0.2028	0.0713	0.0164

$\cos(\theta^*_{2\pi^0})$	$W=(1790.0\pm10.0)$ MeV			$W=(1810.0\pm10.0)$ MeV			$W=(1830.0\pm10.0)$ MeV			$W=(1850.0\pm10.0)$ MeV		
	$d\sigma_{1/2}/d\Omega$ [μb/sr]	Δ_{stat} [μb/sr]	Δ_{sys} [μb/sr]	$d\sigma_{1/2}/d\Omega$ [μb/sr]	Δ_{stat} [μb/sr]	Δ_{sys} [μb/sr]	$d\sigma_{1/2}/d\Omega$ [μb/sr]	Δ_{stat} [μb/sr]	Δ_{sys} [μb/sr]	$d\sigma_{1/2}/d\Omega$ [μb/sr]	Δ_{stat} [μb/sr]	Δ_{sys} [μb/sr]
−0.80	0.4416	0.0432	0.0439	0.5878	0.0499	0.0220	0.3673	0.0560	0.0140	0.3946	0.0557	0.0121
−0.40	0.2507	0.0447	0.0104	0.2236	0.0437	0.0253	0.2519	0.0476	0.0392	0.3583	0.0492	0.0098
0.00	0.2212	0.0425	0.0159	0.4116	0.0479	0.0183	0.1176	0.0499	0.0345	0.2768	0.0576	0.0665
0.40	0.2752	0.0500	0.0248	0.2091	0.0524	0.0253	0.4451	0.0626	0.0738	0.1244	0.0703	0.0720
0.80	0.3792	0.0870	0.0433	0.1825	0.0851	0.5057	−0.0058	0.1154	0.0608	0.2065	0.1160	0.0372

$\cos(\theta^*_{2\pi^0})$				$W=(1870.0\pm10.0)$ MeV						$W=(1890.0\pm10.0)$ MeV		
				$d\sigma_{1/2}/d\Omega$ [μb/sr]	Δ_{stat} [μb/sr]	Δ_{sys} [μb/sr]				$d\sigma_{1/2}/d\Omega$ [μb/sr]	Δ_{stat} [μb/sr]	Δ_{sys} [μb/sr]
−0.80				0.1869	0.0611	0.0041				0.3428	0.0859	0.0543
−0.40				0.2197	0.0575	0.0181				0.3546	0.0754	0.0219
0.00				0.2800	0.0649	0.0813				0.3039	0.0979	0.0376
0.40				0.3619	0.0822	0.1282				0.3892	0.1082	0.2190
0.80				0.2235	0.1538	0.1273				1.0136	0.3618	0.5399

$\cos(\theta^*_{2\pi^0})$	$W=(1310.0\pm10.0)$ MeV			$W=(1330.0\pm10.0)$ MeV			$W=(1350.0\pm10.0)$ MeV			$W=(1370.0\pm10.0)$ MeV		
	$d\sigma_{3/2}/d\Omega$ [μb/sr]	Δ_{stat} [μb/sr]	Δ_{sys} [μb/sr]	$d\sigma_{3/2}/d\Omega$ [μb/sr]	Δ_{stat} [μb/sr]	Δ_{sys} [μb/sr]	$d\sigma_{3/2}/d\Omega$ [μb/sr]	Δ_{stat} [μb/sr]	Δ_{sys} [μb/sr]	$d\sigma_{3/2}/d\Omega$ [μb/sr]	Δ_{stat} [μb/sr]	Δ_{sys} [μb/sr]
−0.80	−0.0041	0.0409	0.0068	0.0843	0.0453	0.0080	0.0985	0.0382	0.0066	0.0939	0.0524	0.0340
−0.40	−0.0068	0.0436	0.0097	0.0168	0.0467	0.0205	0.1145	0.0361	0.0089	0.2490	0.0540	0.0197
0.00	−0.0344	0.0472	0.0193	0.0462	0.0530	0.0106	0.2047	0.0422	0.0061	0.2630	0.0592	0.0280
0.40	0.0117	0.0573	0.5378	0.0328	0.0723	0.0071	0.0937	0.0584	0.0124	−0.0023	0.0833	0.0141
0.80	−0.2780	0.3663	0.0233	0.1396	0.3771	0.1681	0.0339	0.1726	0.0214	0.2987	1.6612	1.8358

$\cos(\theta^*_{2\pi^0})$	$W=(1390.0\pm10.0)$ MeV			$W=(1410.0\pm10.0)$ MeV			$W=(1430.0\pm10.0)$ MeV			$W=(1450.0\pm10.0)$ MeV		
	$d\sigma_{3/2}/d\Omega$ [μb/sr]	Δ_{stat} [μb/sr]	Δ_{sys} [μb/sr]	$d\sigma_{3/2}/d\Omega$ [μb/sr]	Δ_{stat} [μb/sr]	Δ_{sys} [μb/sr]	$d\sigma_{3/2}/d\Omega$ [μb/sr]	Δ_{stat} [μb/sr]	Δ_{sys} [μb/sr]	$d\sigma_{3/2}/d\Omega$ [μb/sr]	Δ_{stat} [μb/sr]	Δ_{sys} [μb/sr]
−0.80	0.1610	0.0603	0.0099	0.3629	0.0713	0.0452	0.5666	0.0645	0.0249	0.7836	0.0704	0.0644
−0.40	0.3441	0.0572	0.0446	0.3016	0.0590	0.0266	0.8325	0.0652	0.0484	1.0457	0.0686	0.0322
0.00	0.5197	0.0620	0.0299	0.5394	0.0683	0.0527	0.7790	0.0752	0.0835	0.9933	0.0755	0.0652
0.40	0.4212	0.0769	0.0062	0.6871	0.0859	0.0226	0.7351	0.0866	0.0425	0.6868	0.0864	0.0675
0.80	0.1368	0.3954	0.1919	0.5253	0.2062	0.1237	0.1707	0.1577	0.0346	0.1806	0.1449	0.0182

$\cos(\theta^*_{2\pi^0})$	$W=(1470.0\pm10.0)$ MeV			$W=(1490.0\pm10.0)$ MeV			$W=(1510.0\pm10.0)$ MeV			$W=(1530.0\pm10.0)$ MeV		
	$d\sigma_{3/2}/d\Omega$ [μb/sr]	Δ_{stat} [μb/sr]	Δ_{sys} [μb/sr]	$d\sigma_{3/2}/d\Omega$ [μb/sr]	Δ_{stat} [μb/sr]	Δ_{sys} [μb/sr]	$d\sigma_{3/2}/d\Omega$ [μb/sr]	Δ_{stat} [μb/sr]	Δ_{sys} [μb/sr]	$d\sigma_{3/2}/d\Omega$ [μb/sr]	Δ_{stat} [μb/sr]	Δ_{sys} [μb/sr]
−0.80	0.8497	0.0712	0.0859	1.1966	0.0841	0.1167	1.3748	0.0884	0.2243	1.6047	0.0969	0.1718
−0.40	1.0069	0.0714	0.0313	1.2251	0.0757	0.0519	1.1799	0.0783	0.0547	1.0092	0.0766	0.0351
0.00	1.0459	0.0765	0.0661	0.9500	0.0791	0.0651	1.0742	0.0791	0.0396	0.8499	0.0704	0.0131
0.40	0.9461	0.0797	0.0684	1.1012	0.0892	0.0368	0.8257	0.0890	0.0828	0.8261	0.0760	0.0612
0.80	0.2836	0.1759	0.2145	0.5717	0.1672	0.1953	0.3795	0.1460	0.0247	0.2301	0.1256	0.0471

$\cos(\theta^*_{2\pi^0})$	$W=(1550.0\pm10.0)$ MeV			$W=(1570.0\pm10.0)$ MeV			$W=(1590.0\pm10.0)$ MeV			$W=(1610.0\pm10.0)$ MeV		
	$d\sigma_{3/2}/d\Omega$ [μb/sr]	Δ_{stat} [μb/sr]	Δ_{sys} [μb/sr]	$d\sigma_{3/2}/d\Omega$ [μb/sr]	Δ_{stat} [μb/sr]	Δ_{sys} [μb/sr]	$d\sigma_{3/2}/d\Omega$ [μb/sr]	Δ_{stat} [μb/sr]	Δ_{sys} [μb/sr]	$d\sigma_{3/2}/d\Omega$ [μb/sr]	Δ_{stat} [μb/sr]	Δ_{sys} [μb/sr]
−0.80	1.3108	0.0926	0.1136	1.1360	0.0860	0.1086	1.1967	0.0802	0.1594	1.3166	0.0759	0.1747
−0.40	0.8320	0.0672	0.0149	0.6480	0.0650	0.0095	0.6741	0.0642	0.0127	0.7221	0.0605	0.0595
0.00	0.5985	0.0672	0.0094	0.7752	0.0631	0.0052	0.5966	0.0580	0.0217	0.6355	0.0600	0.0281
0.40	0.7547	0.0716	0.0523	0.6604	0.0722	0.0481	0.5328	0.0646	0.0132	0.4424	0.0606	0.0366
0.80	0.4892	0.1067	0.0514	−0.1117	0.1218	0.0300	0.5358	0.0990	0.0218	0.5237	0.1014	0.1578

$\cos(\theta^*_{2\pi^0})$	$W=(1630.0\pm10.0)$ MeV			$W=(1650.0\pm10.0)$ MeV			$W=(1670.0\pm10.0)$ MeV			$W=(1690.0\pm10.0)$ MeV		
	$d\sigma_{3/2}/d\Omega$ [μb/sr]	Δ_{stat} [μb/sr]	Δ_{sys} [μb/sr]	$d\sigma_{3/2}/d\Omega$ [μb/sr]	Δ_{stat} [μb/sr]	Δ_{sys} [μb/sr]	$d\sigma_{3/2}/d\Omega$ [μb/sr]	Δ_{stat} [μb/sr]	Δ_{sys} [μb/sr]	$d\sigma_{3/2}/d\Omega$ [μb/sr]	Δ_{stat} [μb/sr]	Δ_{sys} [μb/sr]
−0.80	0.8943	0.0753	0.1387	1.0221	0.0772	0.1035	0.9563	0.0709	0.0863	1.0102	0.0711	0.0859
−0.40	0.7551	0.0581	0.0266	0.8469	0.0612	0.0481	1.0464	0.0573	0.0452	0.9320	0.0614	0.0084
0.00	0.8985	0.0546	0.0079	1.0749	0.0563	0.0113	1.1768	0.0623	0.0279	0.9984	0.0635	0.0466
0.40	0.7134	0.0611	0.0039	0.6582	0.0570	0.0403	0.7371	0.0599	0.0290	0.9563	0.0645	0.0743
0.80	0.6180	0.1017	0.0911	0.4444	0.0901	0.1146	0.4232	0.0897	0.0494	0.5776	0.0976	0.1934

$\cos(\theta^*_{2\pi^0})$	W=(1710.0±10.0) MeV			W=(1730.0±10.0) MeV			W=(1750.0±10.0) MeV			W=(1770.0±10.0) MeV		
	$d\sigma_{3/2}/d\Omega$ [μb/sr]	Δ_{stat} [μb/sr]	Δ_{sys} [μb/sr]	$d\sigma_{3/2}/d\Omega$ [μb/sr]	Δ_{stat} [μb/sr]	Δ_{sys} [μb/sr]	$d\sigma_{3/2}/d\Omega$ [μb/sr]	Δ_{stat} [μb/sr]	Δ_{sys} [μb/sr]	$d\sigma_{3/2}/d\Omega$ [μb/sr]	Δ_{stat} [μb/sr]	Δ_{sys} [μb/sr]
−0.80	0.7738	0.0697	0.0762	0.7523	0.0670	0.0174	0.6045	0.0544	0.1090	0.5891	0.0514	0.0728
−0.40	0.8242	0.0612	0.0296	1.0587	0.0537	0.0836	0.7274	0.0502	0.0179	0.6664	0.0442	0.0711
0.00	0.9412	0.0618	0.0156	0.8982	0.0610	0.0312	0.6911	0.0506	0.0201	0.5660	0.0439	0.0181
0.40	0.6487	0.0628	0.0718	0.6033	0.0633	0.0598	0.6470	0.0548	0.0700	0.4543	0.0461	0.0538
0.80	0.2644	0.0897	0.0411	0.4238	0.0748	0.0324	0.4478	0.0802	0.0265	0.1283	0.0713	0.0571

$\cos(\theta^*_{2\pi^0})$	W=(1790.0±10.0) MeV			W=(1810.0±10.0) MeV			W=(1830.0±10.0) MeV			W=(1850.0±10.0) MeV		
	$d\sigma_{3/2}/d\Omega$ [μb/sr]	Δ_{stat} [μb/sr]	Δ_{sys} [μb/sr]	$d\sigma_{3/2}/d\Omega$ [μb/sr]	Δ_{stat} [μb/sr]	Δ_{sys} [μb/sr]	$d\sigma_{3/2}/d\Omega$ [μb/sr]	Δ_{stat} [μb/sr]	Δ_{sys} [μb/sr]	$d\sigma_{3/2}/d\Omega$ [μb/sr]	Δ_{stat} [μb/sr]	Δ_{sys} [μb/sr]
−0.80	0.4156	0.0432	0.0303	0.3642	0.0499	0.0154	0.3993	0.0560	0.0142	0.3729	0.0557	0.0374
−0.40	0.5709	0.0447	0.0142	0.5949	0.0437	0.0167	0.4788	0.0476	0.0308	0.3709	0.0492	0.0053
0.00	0.6858	0.0425	0.0178	0.5114	0.0479	0.0218	0.6755	0.0499	0.0339	0.4528	0.0576	0.0750
0.40	0.4383	0.0500	0.0298	0.5058	0.0524	0.0345	0.1930	0.0626	0.0532	0.4725	0.0703	0.1003
0.80	0.0942	0.0870	0.0292	0.4302	0.0851	0.3150	0.4405	0.1154	0.0649	0.1467	0.1160	0.0331

$\cos(\theta^*_{2\pi^0})$	W=(1870.0±10.0) MeV			W=(1890.0±10.0) MeV		
	$d\sigma_{3/2}/d\Omega$ [μb/sr]	Δ_{stat} [μb/sr]	Δ_{sys} [μb/sr]	$d\sigma_{3/2}/d\Omega$ [μb/sr]	Δ_{stat} [μb/sr]	Δ_{sys} [μb/sr]
−0.80	0.5181	0.0611	0.0052	0.2966	0.0859	0.0511
−0.40	0.4223	0.0575	0.0211	0.3189	0.0754	0.0705
0.00	0.4607	0.0649	0.0905	0.4498	0.0979	0.0437
0.40	0.2538	0.0822	0.1165	0.1795	0.1082	0.1891
0.80	0.0297	0.1538	0.0775	−0.7277	0.3618	0.3049

E.5 Unpol. Results for $\pi^0\pi^0$ from CBELSA/TAPS Data

E.5.1 Total Cross Sections as a Function of E_γ

E_γ [MeV]	ΔE_γ [MeV]	σ_{qf-inc} [μb]	Δ_{stat} [μb]	Δ_{sys} [μb]	σ_p [μb]	Δ_{stat} [μb]	Δ_{sys} [μb]	σ_n [μb]	Δ_{stat} [μb]	Δ_{sys} [μb]
420.0	20.0	0.4639	0.0336	0.0231	0.2530	0.0995	0.1918	0.1825	0.0997	0.1072
460.0	20.0	0.7661	0.5589	0.1906	0.8204	0.3801	0.5101	0.7268	0.2308	0.3876
500.0	20.0	2.7814	0.1067	0.0239	1.4200	0.2877	0.2966	0.7148	0.2069	0.1297
540.0	20.0	4.6164	0.1313	0.0558	2.0541	0.1978	0.1412	2.1141	0.2710	0.1430
580.0	20.0	7.2666	0.1580	0.0769	3.8767	0.2262	0.2595	3.9904	0.3031	0.3011
620.0	20.0	9.8945	0.1620	0.0789	5.4781	0.2181	0.2152	5.2059	0.2960	0.2038
660.0	20.0	12.7948	0.2100	0.1406	5.6811	0.3093	0.4837	6.1573	0.6190	1.2398
700.0	20.0	13.7666	0.1894	0.0716	7.4633	0.2213	0.3295	7.4847	0.3720	0.5221
740.0	20.0	15.2691	0.1598	0.0509	7.5428	0.1798	0.4087	8.3322	0.4155	0.8059
780.0	20.0	15.0008	0.1747	0.0963	7.4137	0.1894	0.4917	7.7962	0.4872	0.9378
820.0	20.0	14.2456	0.1843	0.0615	6.4246	0.1758	0.5578	7.9791	0.4828	0.8491
860.0	20.0	13.7823	0.1884	0.0622	5.9067	0.1733	0.4315	7.5409	0.3367	0.9740
900.0	20.0	12.6988	0.1842	0.0547	5.3074	0.1715	0.4633	7.4164	0.3303	0.7780
940.0	20.0	13.2107	0.1809	0.0494	5.6299	0.1625	0.3571	7.3880	0.3198	0.7389
980.0	20.0	14.1183	0.1252	0.0476	6.1671	0.1726	0.5169	7.4155	0.3310	0.6425
1020.0	20.0	15.1408	0.0863	0.0675	7.0456	0.1601	0.4740	7.6648	0.3257	0.8423
1060.0	20.0	14.3386	0.0963	0.1094	7.4249	0.1973	0.5458	8.2112	0.1394	0.4273
1100.0	20.0	13.7661	0.0922	0.0363	6.9958	0.1802	0.4204	7.1288	0.1376	0.2474
1140.0	20.0	13.1779	0.0824	0.0444	7.1859	0.1600	0.3776	6.6241	0.1173	0.2172
1180.0	20.0	10.0048	0.0743	0.0219	6.7256	0.0560	0.6177	5.2183	0.1019	0.4777
1220.0	20.0	9.0863	0.0843	0.0411	6.1455	0.0583	0.4290	4.3845	0.0981	0.2987
1260.0	20.0	7.8944	0.0740	0.1081	5.2770	0.0521	0.3734	3.8578	0.0749	0.2707
1300.0	20.0	8.2189	0.0688	0.1267	5.4679	0.0481	0.3737	4.0387	0.0690	0.2828
1340.0	20.0	8.4525	0.0696	0.0869	5.4666	0.0495	0.3098	3.9431	0.0788	0.2154
1380.0	20.0	7.3360	0.0745	0.0596	4.7334	0.0516	0.2691	3.5139	0.0888	0.1942
1420.0	20.0	7.3963	0.0740	0.1168	4.7210	0.0503	0.2644	3.5463	0.0858	0.2198
1460.0	20.0	7.4921	0.0695	0.1218	4.7307	0.0468	0.3229	3.6449	0.0772	0.2498
1500.0	20.0	7.5110	0.0680	0.0711	4.6461	0.0438	0.2261	3.5330	0.0785	0.1927
1540.0	20.0	7.1090	0.0757	0.0472	4.4255	0.0513	0.2482	3.4844	0.0826	0.1941
1580.0	20.0	7.0311	0.0774	0.0650	4.2191	0.0486	0.1944	3.2230	0.0827	0.1545
1620.0	20.0	6.9713	0.0706	0.1861	3.9285	0.0418	0.1122	3.5347	0.0841	0.1003
1660.0	20.0	6.5982	0.0716	0.0690	3.9958	0.0448	0.1275	3.1252	0.0690	0.1011
1700.0	20.0	5.9787	0.0687	0.0808	3.5747	0.0420	0.1632	2.9577	0.0716	0.1408
1740.0	20.0	6.2212	0.0645	0.0575	3.6435	0.0392	0.1103	2.8211	0.0629	0.0872
1780.0	20.0	5.9448	0.0678	0.0664	3.5369	0.0403	0.1338	2.7550	0.0656	0.1068
1820.0	20.0	5.9043	0.0657	0.0601	3.4663	0.0404	0.1401	2.6929	0.0668	0.1090
1860.0	20.0	5.6686	0.0670	0.0932	3.1881	0.0393	0.0710	2.6071	0.0685	0.0749
1900.0	20.0	5.7063	0.0648	0.1817	3.2869	0.0364	0.0867	2.7102	0.0648	0.0780
1940.0	20.0	5.3663	0.0784	0.1988	3.1633	0.0450	0.0966	2.6080	0.0844	0.0846
1980.0	20.0	5.1480	0.0618	0.0377	2.9755	0.0353	0.1424	2.3591	0.0637	0.1177
2020.0	20.0	5.4129	0.0620	0.0647	3.1325	0.0350	0.1184	2.3731	0.0644	0.0745
2060.0	20.0	5.6539	0.0702	0.0703	3.3610	0.0406	0.0647	2.5691	0.0779	0.0554
2100.0	20.0	5.3301	0.0616	0.0649	3.0916	0.0361	0.1482	2.3184	0.0587	0.0958
2140.0	20.0	5.3652	0.0729	0.0689	3.2016	0.0446	0.1172	2.5108	0.0727	0.1016
2180.0	20.0	5.2215	0.0718	0.1853	3.1796	0.0438	0.0977	2.3321	0.0759	0.0845
2220.0	20.0	5.1484	0.0772	0.0558	3.0823	0.0507	0.1181	2.2837	0.0796	0.0958
2260.0	20.0	4.9551	0.0814	0.0769	3.0435	0.0521	0.0958	2.1272	0.0807	0.0788
2300.0	20.0	4.6964	0.2067	0.1721	2.9494	0.1323	0.2745	1.6433	0.1884	0.1795
2340.0	20.0	0.0000	0.0000	0.0000	0.0000	0.0000	0.0000	0.0000	0.0000	0.0000
2380.0	20.0	0.0000	0.0000	0.0000	0.0000	0.0000	0.0000	0.0000	0.0000	0.0000

E.5.2 Total Cross Sections as a Function of W

W [MeV]	ΔW [MeV]	σ_{qfp} [μb]	Δ_{stat} [μb]	Δ_{sys} [μb]	σ_{qfn} [μb]	Δ_{stat} [μb]	Δ_{sys} [μb]
1310.0	10.0	0.5280	0.4866	0.0329	0.3857	0.1561	0.0045
1330.0	10.0	0.4990	0.3751	0.3426	−0.0001	0.1701	0.2187
1350.0	10.0	1.9180	0.3677	0.3179	0.8010	0.1779	0.1222
1370.0	10.0	4.1200	0.3638	0.5526	1.7200	0.2010	0.1536
1390.0	10.0	5.6077	0.5060	0.7204	3.0412	0.2606	0.2627
1410.0	10.0	6.9658	0.3541	0.9077	3.8681	0.3001	0.3216
1430.0	10.0	6.9605	0.3079	0.5492	4.2163	0.3095	0.3639
1450.0	10.0	6.9478	0.4137	0.7037	5.1105	0.5040	0.5792
1470.0	10.0	7.8028	0.2741	0.7727	7.3781	0.4515	0.4755
1490.0	10.0	7.9524	0.2361	0.3179	8.3325	0.3420	0.7420
1510.0	10.0	7.5957	0.2131	0.4162	8.4282	0.3529	0.7383
1530.0	10.0	6.9739	0.2125	0.4793	8.4410	0.3878	0.9804
1550.0	10.0	6.3517	0.1934	0.5843	7.8324	0.4989	0.8036
1570.0	10.0	5.7406	0.1823	0.4840	7.6511	0.4245	0.8203
1590.0	10.0	5.4611	0.2504	0.4601	6.8179	0.3466	0.9895
1610.0	10.0	5.2043	0.1838	0.4388	7.8101	0.3234	1.0421
1630.0	10.0	5.8514	0.1756	0.4380	7.5938	0.2954	0.6003
1650.0	10.0	6.6316	0.1848	0.4826	8.3069	0.3124	0.6762
1670.0	10.0	7.0859	0.1808	0.6057	7.9627	0.3285	0.6413
1690.0	10.0	7.6418	0.1846	0.6372	8.4826	0.1450	0.4281
1710.0	10.0	7.6040	0.1942	0.4066	7.4740	0.1406	0.2552
1730.0	10.0	6.7143	0.1927	0.3586	6.4012	0.1329	0.2089
1750.0	10.0	6.6275	0.0949	0.6164	5.4169	0.1154	0.4945
1770.0	10.0	6.0917	0.0899	0.4806	4.7774	0.1045	0.4343
1790.0	10.0	5.8581	0.0538	0.4086	4.1966	0.0872	0.2866
1810.0	10.0	5.3857	0.0483	0.3854	3.8831	0.0756	0.2747
1830.0	10.0	5.0510	0.0496	0.3509	3.5583	0.0704	0.2424
1850.0	10.0	5.1224	0.0535	0.2934	3.5897	0.0854	0.2029
1870.0	10.0	4.8958	0.0501	0.2804	3.8149	0.0818	0.2147
1890.0	10.0	4.7072	0.0481	0.2581	3.4832	0.0835	0.2011
1910.0	10.0	4.4617	0.0463	0.2989	3.5012	0.0766	0.2301
1930.0	10.0	4.3887	0.0452	0.2101	3.4852	0.0856	0.1812
1950.0	10.0	4.3044	0.0445	0.2317	3.6079	0.0794	0.1938
1970.0	10.0	4.1077	0.0443	0.1831	3.2623	0.0771	0.1482
1990.0	10.0	3.7560	0.0418	0.1187	3.3791	0.0787	0.1036
2010.0	10.0	3.6814	0.0399	0.1636	2.7785	0.0675	0.1303
2030.0	10.0	3.5041	0.0408	0.1086	2.8279	0.0670	0.0917
2050.0	10.0	3.3690	0.0383	0.1300	2.8356	0.0652	0.1098
2070.0	10.0	3.2766	0.0379	0.1302	2.7946	0.0674	0.1129
2090.0	10.0	3.3362	0.0374	0.0686	2.6827	0.0711	0.0634
2110.0	10.0	3.2080	0.0387	0.0860	2.6674	0.0618	0.1335
2130.0	10.0	3.1543	0.0355	0.0920	2.3811	0.0685	0.0938
2150.0	10.0	3.0262	0.0358	0.1446	2.5661	0.0637	0.1281
2170.0	10.0	3.0111	0.0397	0.0389	2.2609	0.0633	0.0620
2190.0	10.0	3.0121	0.0373	0.1309	2.4562	0.0671	0.1067
2210.0	10.0	3.0520	0.0423	0.1113	2.4915	0.0790	0.1017
2230.0	10.0	3.1702	0.0481	0.0850	2.4637	0.0881	0.0760
2250.0	10.0	3.3326	0.0537	0.1078	2.4511	0.0973	0.0824
2270.0	10.0	3.6172	0.0901	0.1154	2.9283	0.1402	0.1177
2290.0	10.0	4.3231	0.1146	0.0701	2.7669	0.1761	0.0790

W [MeV]	ΔW [MeV]	σ_p [μb]	Δ_{stat} [μb]	Δ_{sys} [μb]	σ_n [μb]	Δ_{stat} [μb]	Δ_{sys} [μb]
1286.2	9.0	0.0169	0.0123	2.3412	0.4901	0.1984	0.2057
1304.4	8.9	9.3447	2.7296	2.3412	−0.0005	0.2144	0.2797
1322.2	8.8	6.2078	2.1425	0.0032	1.0014	0.2224	0.1274
1339.8	8.7	5.8729	2.1082	2.2391	2.1340	0.2493	0.1981
1357.2	8.6	0.1751	1.3987	2.2391	4.0909	0.4008	0.2667
1374.4	8.5	5.5232	0.7775	0.1929	5.0021	0.4295	0.3238
1391.4	8.4	3.6877	0.4249	0.3610	5.3213	0.4062	0.3120
1408.1	8.3	5.4408	0.2853	0.3610	7.0308	0.7650	0.5083
1424.7	8.2	5.4286	0.2649	0.4054	9.2938	0.6073	0.4782
1441.1	8.1	7.0800	0.2759	0.4054	9.6442	0.4006	0.5274
1457.2	8.0	6.6260	0.1289	0.5594	10.7303	0.5213	0.7072
1473.3	8.0	8.7651	0.2114	0.6690	9.7660	0.4892	0.8400
1489.1	7.9	8.8411	0.1257	0.6690	9.4777	0.7310	0.9096
1504.8	7.8	9.4467	0.1374	0.4790	8.9425	0.5259	0.7218
1520.3	7.7	8.4960	0.1352	0.4437	8.2422	0.4912	0.6661
1535.6	7.6	8.4450	0.1295	0.4437	9.2947	0.3932	0.8012
1550.8	7.6	7.3792	0.1352	0.3872	8.9239	0.3636	0.6663
1565.9	7.5	7.3586	0.1287	0.3872	9.3920	0.3636	0.8898
1580.8	7.4	6.7086	0.1212	0.3706	9.1249	0.3807	0.6845
1595.6	7.3	6.3071	0.1131	0.4217	9.9771	0.1681	0.7145
1610.2	7.2	7.2996	0.1221	0.4217	8.4256	0.1593	0.5150
1624.7	7.2	6.2526	0.1091	0.3856	7.7561	0.1642	0.4363
1639.1	7.2	7.2531	0.1212	0.3347	5.8683	0.1215	0.6301
1653.3	7.2	8.9749	0.1372	0.3347	5.1677	0.1105	0.5512
1667.4	7.1	9.3480	0.1242	0.3501	4.6198	0.0943	0.3988
1681.4	7.0	9.2262	0.1187	0.3500	4.2454	0.0832	0.3748
1695.3	6.9	8.9949	0.1195	0.3627	3.9676	0.0773	0.3363
1709.1	6.9	10.5885	0.1782	0.3193	4.0581	0.0988	0.3009
1722.8	6.8	9.7503	0.1115	0.3193	4.1791	0.0898	0.3114
1736.4	6.8	9.2093	0.1200	0.2652	3.7595	0.0892	0.2911
1749.8	6.7	7.3520	0.0962	0.3264	3.8763	0.0857	0.3134
1763.2	6.7	7.4746	0.1081	0.3264	3.7558	0.0920	0.2724
1776.4	6.7	6.6237	0.1258	0.2318	3.8575	0.0847	0.2818
1789.6	6.6	5.9339	0.0973	0.2318	3.5186	0.0838	0.2408
1802.6	6.6	6.4976	0.0866	0.3657	3.4977	0.0786	0.2146
1815.6	6.5	5.5598	0.0758	0.8038	2.9878	0.0723	0.2058
1828.5	6.4	5.5629	0.0853	0.8038	2.9757	0.0691	0.1829
1841.3	6.3	5.5755	0.0770	0.1986	2.9624	0.0673	0.1963
1854.0	6.3	5.8149	0.0878	0.2088	2.8652	0.0667	0.1914
1866.6	6.3	4.9713	0.1055	0.2088	2.8214	0.0747	0.1558
1879.1	6.3	5.2478	0.0891	0.1684	2.8615	0.0665	0.1399
1891.5	6.2	4.7529	0.0725	0.1684	2.4640	0.0705	0.1438
1903.9	6.2	5.3713	0.0798	0.1415	2.6136	0.0643	0.2118
1916.2	6.1	4.7036	0.0722	0.1151	2.4322	0.0693	0.1386
1928.4	6.1	4.7585	0.0792	0.1151	2.5706	0.0727	0.1663
1940.5	6.1	4.9446	0.0954	0.1118	2.6569	0.0880	0.1704
1952.6	6.0	4.6321	0.0829	0.1525	2.6499	0.0941	0.1467
1964.5	6.0	4.2369	0.0919	0.1525	2.4764	0.0988	0.1542
1976.4	5.9	4.4748	0.0766	0.1528	2.9779	0.1491	0.1825
1988.3	5.9	4.1532	0.0776	0.1528	2.6090	0.1921	0.1396

E.5.3 $\gamma d \rightarrow \pi^0\pi^0 p(n)$ as a Function of W

Angular Distributions

$\cos(\theta^*_{2\pi^0})$	W=(1310.0±10.0) MeV			W=(1330.0±10.0) MeV			W=(1350.0±10.0) MeV			W=(1370.0±10.0) MeV		
	$d\sigma/d\Omega$ [μb/sr]	Δ_{stat} [μb/sr]	Δ_{sys} [μb/sr]	$d\sigma/d\Omega$ [μb/sr]	Δ_{stat} [μb/sr]	Δ_{sys} [μb/sr]	$d\sigma/d\Omega$ [μb/sr]	Δ_{stat} [μb/sr]	Δ_{sys} [μb/sr]	$d\sigma/d\Omega$ [μb/sr]	Δ_{stat} [μb/sr]	Δ_{sys} [μb/sr]
−0.80	0.0287	0.0097	0.0048	0.0769	0.0157	0.0094	0.1204	0.0193	0.0202	0.1479	0.0222	0.0128
−0.40	0.0405	0.0129	0.0145	0.0545	0.0125	0.0178	0.1422	0.0192	0.0130	0.2211	0.0182	0.0062
0.00	0.0407	0.0229	0.0227	0.0914	0.0214	0.0470	0.1241	0.0220	0.0155	0.2127	0.0245	0.0063
0.40	−0.0457	0.0694	−0.0246	0.0053	0.0476	−0.0199	0.0798	0.0280	0.0144	0.2734	0.0300	0.0247
0.80	0.0897	0.1562	−0.0042	−0.0659	0.1191	0.0820	0.2568	0.1160	0.0634	0.7349	0.1130	0.1699

$\cos(\theta^*_{2\pi^0})$	W=(1390.0±10.0) MeV			W=(1410.0±10.0) MeV			W=(1430.0±10.0) MeV			W=(1450.0±10.0) MeV		
	$d\sigma/d\Omega$ [μb/sr]	Δ_{stat} [μb/sr]	Δ_{sys} [μb/sr]	$d\sigma/d\Omega$ [μb/sr]	Δ_{stat} [μb/sr]	Δ_{sys} [μb/sr]	$d\sigma/d\Omega$ [μb/sr]	Δ_{stat} [μb/sr]	Δ_{sys} [μb/sr]	$d\sigma/d\Omega$ [μb/sr]	Δ_{stat} [μb/sr]	Δ_{sys} [μb/sr]
−0.80	0.1789	0.0226	0.0120	0.3046	0.0258	0.0156	0.3008	0.0463	0.0342	0.4968	0.0419	0.0621
−0.40	0.2557	0.0170	0.0051	0.2808	0.0189	0.0038	0.3844	0.0381	0.0613	0.5092	0.0387	0.0443
0.00	0.2278	0.0209	0.0062	0.3536	0.0188	0.0100	0.3833	0.0352	0.0467	0.5380	0.0341	0.0328
0.40	0.3809	0.0281	0.0440	0.4281	0.0305	0.0492	0.5475	0.0264	0.0240	0.6569	0.0199	0.0440
0.80	1.1260	0.1640	0.2195	1.2428	0.1111	0.2825	1.1203	0.0738	0.0524	0.6087	0.1206	0.0967

$\cos(\theta^*_{2\pi^0})$	W=(1470.0±10.0) MeV			W=(1490.0±10.0) MeV			W=(1510.0±10.0) MeV			W=(1530.0±10.0) MeV		
	$d\sigma/d\Omega$ [μb/sr]	Δ_{stat} [μb/sr]	Δ_{sys} [μb/sr]	$d\sigma/d\Omega$ [μb/sr]	Δ_{stat} [μb/sr]	Δ_{sys} [μb/sr]	$d\sigma/d\Omega$ [μb/sr]	Δ_{stat} [μb/sr]	Δ_{sys} [μb/sr]	$d\sigma/d\Omega$ [μb/sr]	Δ_{stat} [μb/sr]	Δ_{sys} [μb/sr]
−0.80	0.7706	0.0382	0.1041	0.8122	0.0381	0.0242	0.8269	0.0363	0.0237	0.7764	0.0359	0.0337
−0.40	0.6831	0.0645	0.0911	0.7407	0.0568	0.0383	0.6567	0.0490	0.0577	0.4952	0.0457	0.0505
0.00	0.5306	0.0497	0.0694	0.6544	0.0430	0.0360	0.5991	0.0386	0.0436	0.5570	0.0389	0.0578
0.40	0.6767	0.0142	0.0226	0.6156	0.0100	0.0131	0.6184	0.0090	0.0201	0.5439	0.0081	0.0291
0.80	0.5604	0.0323	0.0201	0.3889	0.0188	0.0149	0.3658	0.0146	0.0204	0.3563	0.0147	0.0196

$\cos(\theta^*_{2\pi^0})$	W=(1550.0±10.0) MeV			W=(1570.0±10.0) MeV			W=(1590.0±10.0) MeV			W=(1610.0±10.0) MeV		
	$d\sigma/d\Omega$ [μb/sr]	$\Delta_{\rm stat}$ [μb/sr]	$\Delta_{\rm sys}$ [μb/sr]	$d\sigma/d\Omega$ [μb/sr]	$\Delta_{\rm stat}$ [μb/sr]	$\Delta_{\rm sys}$ [μb/sr]	$d\sigma/d\Omega$ [μb/sr]	$\Delta_{\rm stat}$ [μb/sr]	$\Delta_{\rm sys}$ [μb/sr]	$d\sigma/d\Omega$ [μb/sr]	$\Delta_{\rm stat}$ [μb/sr]	$\Delta_{\rm sys}$ [μb/sr]
−0.80	0.7087	0.0389	0.0244	0.6708	0.0355	0.0674	0.5517	0.0667	0.0756	0.6094	0.0412	0.0302
−0.40	0.5922	0.0529	0.0926	0.4509	0.0441	0.0416	0.4044	0.0432	0.0309	0.3828	0.0426	0.0349
0.00	0.4446	0.0316	0.0576	0.3759	0.0311	0.0363	0.3909	0.0318	0.0297	0.2504	0.0284	0.0335
0.40	0.5067	0.0078	0.0306	0.4766	0.0075	0.0259	0.4589	0.0072	0.0238	0.5085	0.0070	0.0374
0.80	0.3592	0.0112	0.0274	0.3560	0.0098	0.0214	0.3834	0.0101	0.0230	0.4355	0.0091	0.0387

$\cos(\theta^*_{2\pi^0})$	W=(1630.0±10.0) MeV			W=(1650.0±10.0) MeV			W=(1670.0±10.0) MeV			W=(1690.0±10.0) MeV		
	$d\sigma/d\Omega$ [μb/sr]	$\Delta_{\rm stat}$ [μb/sr]	$\Delta_{\rm sys}$ [μb/sr]	$d\sigma/d\Omega$ [μb/sr]	$\Delta_{\rm stat}$ [μb/sr]	$\Delta_{\rm sys}$ [μb/sr]	$d\sigma/d\Omega$ [μb/sr]	$\Delta_{\rm stat}$ [μb/sr]	$\Delta_{\rm sys}$ [μb/sr]	$d\sigma/d\Omega$ [μb/sr]	$\Delta_{\rm stat}$ [μb/sr]	$\Delta_{\rm sys}$ [μb/sr]
−0.80	0.6114	0.0368	0.0362	0.6459	0.0378	0.0299	0.6761	0.0295	0.0496	0.6970	0.0280	0.1067
−0.40	0.4478	0.0451	0.0492	0.4347	0.0352	0.0484	0.4830	0.0342	0.0632	0.4944	0.0417	0.0513
0.00	0.3289	0.0282	0.0267	0.3960	0.0313	0.0449	0.4103	0.0342	0.0609	0.4627	0.0352	0.0461
0.40	0.5600	0.0068	0.0242	0.6289	0.0066	0.0415	0.6983	0.0073	0.0467	0.7382	0.0075	0.0403
0.80	0.4919	0.0094	0.0380	0.5993	0.0099	0.0274	0.6566	0.0101	0.0206	0.7259	0.0108	0.0092

$\cos(\theta^*_{2\pi^0})$	W=(1710.0±10.0) MeV			W=(1730.0±10.0) MeV			W=(1750.0±10.0) MeV			W=(1770.0±10.0) MeV		
	$d\sigma/d\Omega$ [μb/sr]	$\Delta_{\rm stat}$ [μb/sr]	$\Delta_{\rm sys}$ [μb/sr]	$d\sigma/d\Omega$ [μb/sr]	$\Delta_{\rm stat}$ [μb/sr]	$\Delta_{\rm sys}$ [μb/sr]	$d\sigma/d\Omega$ [μb/sr]	$\Delta_{\rm stat}$ [μb/sr]	$\Delta_{\rm sys}$ [μb/sr]	$d\sigma/d\Omega$ [μb/sr]	$\Delta_{\rm stat}$ [μb/sr]	$\Delta_{\rm sys}$ [μb/sr]
−0.80	0.6797	0.0298	0.0559	0.5290	0.0280	0.0237	0.4460	0.0251	0.0567	0.4046	0.0239	0.0355
−0.40	0.4008	0.0398	0.0114	0.4150	0.0328	0.0366	0.3951	0.0304	0.0337	0.3990	0.0269	0.0314
0.00	0.4708	0.0371	0.0163	0.4029	0.0380	0.0177	0.5276	0.0080	0.0461	0.4741	0.0077	0.0297
0.40	0.7573	0.0087	0.0464	0.6849	0.0080	0.0318	0.6188	0.0072	0.0579	0.5745	0.0070	0.0435
0.80	0.7458	0.0118	0.0317	0.7203	0.0104	0.0329	0.6234	0.0102	0.0510	0.5791	0.0100	0.0512

$\cos(\theta^*_{2\pi^0})$	W=(1790.0±10.0) MeV			W=(1810.0±10.0) MeV			W=(1830.0±10.0) MeV			W=(1850.0±10.0) MeV		
	$d\sigma/d\Omega$ [μb/sr]	$\Delta_{\rm stat}$ [μb/sr]	$\Delta_{\rm sys}$ [μb/sr]	$d\sigma/d\Omega$ [μb/sr]	$\Delta_{\rm stat}$ [μb/sr]	$\Delta_{\rm sys}$ [μb/sr]	$d\sigma/d\Omega$ [μb/sr]	$\Delta_{\rm stat}$ [μb/sr]	$\Delta_{\rm sys}$ [μb/sr]	$d\sigma/d\Omega$ [μb/sr]	$\Delta_{\rm stat}$ [μb/sr]	$\Delta_{\rm sys}$ [μb/sr]
−0.80	0.4113	0.0111	0.0275	0.3621	0.0087	0.0173	0.3505	0.0101	0.0220	0.3738	0.0111	0.0171
−0.40	0.4406	0.0095	0.0225	0.3931	0.0078	0.0285	0.3764	0.0082	0.0253	0.4080	0.0085	0.0219
0.00	0.4485	0.0076	0.0265	0.4169	0.0070	0.0288	0.3792	0.0068	0.0259	0.3650	0.0069	0.0218
0.40	0.5154	0.0060	0.0388	0.4766	0.0063	0.0320	0.4747	0.0067	0.0304	0.4782	0.0064	0.0295
0.80	0.5382	0.0078	0.0472	0.5076	0.0080	0.0468	0.4695	0.0076	0.0361	0.4779	0.0088	0.0265

$\cos(\theta^*_{2\pi^0})$	W=(1870.0±10.0) MeV			W=(1890.0±10.0) MeV			W=(1910.0±10.0) MeV			W=(1930.0±10.0) MeV		
	$d\sigma/d\Omega$ [μb/sr]	$\Delta_{\rm stat}$ [μb/sr]	$\Delta_{\rm sys}$ [μb/sr]	$d\sigma/d\Omega$ [μb/sr]	$\Delta_{\rm stat}$ [μb/sr]	$\Delta_{\rm sys}$ [μb/sr]	$d\sigma/d\Omega$ [μb/sr]	$\Delta_{\rm stat}$ [μb/sr]	$\Delta_{\rm sys}$ [μb/sr]	$d\sigma/d\Omega$ [μb/sr]	$\Delta_{\rm stat}$ [μb/sr]	$\Delta_{\rm sys}$ [μb/sr]
−0.80	0.3392	0.0100	0.0149	0.3385	0.0096	0.0145	0.3090	0.0090	0.0236	0.3114	0.0093	0.0131
−0.40	0.3706	0.0082	0.0200	0.3480	0.0076	0.0202	0.3309	0.0072	0.0214	0.3372	0.0070	0.0189
0.00	0.3583	0.0064	0.0229	0.3404	0.0061	0.0260	0.3181	0.0058	0.0204	0.3013	0.0055	0.0220
0.40	0.4647	0.0067	0.0291	0.4460	0.0066	0.0308	0.4271	0.0062	0.0273	0.4027	0.0062	0.0232
0.80	0.4653	0.0087	0.0246	0.4444	0.0085	0.0112	0.4377	0.0086	0.0263	0.4420	0.0080	0.0063

$\cos(\theta^*_{2\pi^0})$	W=(1950.0±10.0) MeV			W=(1970.0±10.0) MeV			W=(1990.0±10.0) MeV			W=(2010.0±10.0) MeV		
	$d\sigma/d\Omega$ [μb/sr]	$\Delta_{\rm stat}$ [μb/sr]	$\Delta_{\rm sys}$ [μb/sr]	$d\sigma/d\Omega$ [μb/sr]	$\Delta_{\rm stat}$ [μb/sr]	$\Delta_{\rm sys}$ [μb/sr]	$d\sigma/d\Omega$ [μb/sr]	$\Delta_{\rm stat}$ [μb/sr]	$\Delta_{\rm sys}$ [μb/sr]	$d\sigma/d\Omega$ [μb/sr]	$\Delta_{\rm stat}$ [μb/sr]	$\Delta_{\rm sys}$ [μb/sr]
−0.80	0.3127	0.0094	0.0125	0.2965	0.0091	0.0122	0.2880	0.0089	0.0136	0.2650	0.0084	0.0173
−0.40	0.3410	0.0067	0.0177	0.3283	0.0068	0.0158	0.2854	0.0062	0.0075	0.2859	0.0060	0.0138
0.00	0.3078	0.0053	0.0211	0.2843	0.0056	0.0149	0.2569	0.0050	0.0087	0.2516	0.0048	0.0101
0.40	0.3808	0.0060	0.0249	0.3654	0.0055	0.0186	0.3295	0.0053	0.0134	0.3287	0.0050	0.0130
0.80	0.4099	0.0078	0.0159	0.4050	0.0076	0.0113	0.3649	0.0072	0.0040	0.3709	0.0069	0.0109

$\cos(\theta^*_{2\pi^0})$	W=(2030.0±10.0) MeV			W=(2050.0±10.0) MeV			W=(2070.0±10.0) MeV			W=(2090.0±10.0) MeV		
	$d\sigma/d\Omega$ [μb/sr]	$\Delta_{\rm stat}$ [μb/sr]	$\Delta_{\rm sys}$ [μb/sr]	$d\sigma/d\Omega$ [μb/sr]	$\Delta_{\rm stat}$ [μb/sr]	$\Delta_{\rm sys}$ [μb/sr]	$d\sigma/d\Omega$ [μb/sr]	$\Delta_{\rm stat}$ [μb/sr]	$\Delta_{\rm sys}$ [μb/sr]	$d\sigma/d\Omega$ [μb/sr]	$\Delta_{\rm stat}$ [μb/sr]	$\Delta_{\rm sys}$ [μb/sr]
−0.80	0.2743	0.0089	0.0085	0.2815	0.0077	0.0090	0.2583	0.0082	0.0109	0.2704	0.0083	0.0052
−0.40	0.2646	0.0058	0.0080	0.2524	0.0055	0.0111	0.2231	0.0058	0.0069	0.2286	0.0056	0.0064
0.00	0.2272	0.0049	0.0078	0.2153	0.0052	0.0098	0.2125	0.0046	0.0075	0.2180	0.0045	0.0052
0.40	0.3070	0.0050	0.0104	0.3096	0.0050	0.0123	0.3015	0.0047	0.0134	0.2984	0.0044	0.0043
0.80	0.3538	0.0067	0.0086	0.3226	0.0063	0.0096	0.3325	0.0063	0.0132	0.3315	0.0060	0.0062

$\cos(\theta^*_{2\pi^0})$	W=(2110.0±10.0) MeV			W=(2130.0±10.0) MeV			W=(2150.0±10.0) MeV			W=(2170.0±10.0) MeV		
	$d\sigma/d\Omega$ [μb/sr]	$\Delta_{\rm stat}$ [μb/sr]	$\Delta_{\rm sys}$ [μb/sr]	$d\sigma/d\Omega$ [μb/sr]	$\Delta_{\rm stat}$ [μb/sr]	$\Delta_{\rm sys}$ [μb/sr]	$d\sigma/d\Omega$ [μb/sr]	$\Delta_{\rm stat}$ [μb/sr]	$\Delta_{\rm sys}$ [μb/sr]	$d\sigma/d\Omega$ [μb/sr]	$\Delta_{\rm stat}$ [μb/sr]	$\Delta_{\rm sys}$ [μb/sr]
−0.80	0.2514	0.0088	0.0038	0.2662	0.0076	0.0058	0.2205	0.0076	0.0315	0.2332	0.0073	0.0014
−0.40	0.2478	0.0057	0.0067	0.2103	0.0055	0.0065	0.2037	0.0052	0.0096	0.1980	0.0054	0.0043
0.00	0.1962	0.0045	0.0082	0.1989	0.0045	0.0070	0.2050	0.0046	0.0042	0.1849	0.0060	0.0037
0.40	0.3000	0.0045	0.0102	0.2801	0.0048	0.0085	0.2824	0.0045	0.0070	0.3016	0.0048	0.0038
0.80	0.3320	0.0063	0.0052	0.3163	0.0057	0.0088	0.3118	0.0057	0.0052	0.3186	0.0062	0.0023

$\cos(\theta^*_{2\pi^0})$	W=(2190.0±10.0) MeV			W=(2210.0±10.0) MeV			W=(2230.0±10.0) MeV			W=(2250.0±10.0) MeV		
	$d\sigma/d\Omega$ [μb/sr]	$\Delta_{\rm stat}$ [μb/sr]	$\Delta_{\rm sys}$ [μb/sr]	$d\sigma/d\Omega$ [μb/sr]	$\Delta_{\rm stat}$ [μb/sr]	$\Delta_{\rm sys}$ [μb/sr]	$d\sigma/d\Omega$ [μb/sr]	$\Delta_{\rm stat}$ [μb/sr]	$\Delta_{\rm sys}$ [μb/sr]	$d\sigma/d\Omega$ [μb/sr]	$\Delta_{\rm stat}$ [μb/sr]	$\Delta_{\rm sys}$ [μb/sr]
−0.80	0.2184	0.0077	0.0220	0.2033	0.0087	0.0168	0.2033	0.0083	0.0042	0.2086	0.0097	0.0157
−0.40	0.1999	0.0059	0.0076	0.1870	0.0067	0.0075	0.2024	0.0087	0.0077	0.2046	0.0080	0.0068
0.00	0.1710	0.0046	0.0021	0.1963	0.0056	0.0054	0.2031	0.0071	0.0096	0.2179	0.0075	0.0051
0.40	0.2962	0.0051	0.0059	0.3151	0.0057	0.0078	0.3016	0.0068	0.0086	0.3121	0.0086	0.0087
0.80	0.3553	0.0064	0.0145	0.3446	0.0068	0.0068	0.3733	0.0081	0.0037	0.3960	0.0095	0.0067

$\cos(\theta^*_{2\pi^0})$	$W=(2270.0\pm10.0)$ MeV $d\sigma/d\Omega$ [μb/sr]	Δ_{stat} [μb/sr]	Δ_{sys} [μb/sr]	$W=(2290.0\pm10.0)$ MeV $d\sigma/d\Omega$ [μb/sr]	Δ_{stat} [μb/sr]	Δ_{sys} [μb/sr]
−0.80	0.2317	0.0143	0.0171	0.2238	0.0170	0.0053
−0.40	0.2165	0.0131	0.0045	0.2558	0.0182	0.0047
0.00	0.2168	0.0152	0.0022	0.3043	0.0154	0.0018
0.40	0.3306	0.0101	0.0079	0.3396	0.0151	0.0017
0.80	0.4582	0.0130	0.0142	0.5560	0.0243	0.0144

Decomposed Total Cross Sections

W [MeV]	ΔW [MeV]	$\sigma_{PhaseSpace}$ [μb]	Δ_{stat} [μb]	$\sigma_{\Delta(1232)}$ [μb]	Δ_{stat} [μb]	$\sigma_{N(1520)}$ [μb]	Δ_{stat} [μb]
1320.0	20.0	0.0800	0.2505	0.1206	0.0219	0.1964	0.0518
1360.0	20.0	0.5672	0.0687	0.8985	0.0767	0.5642	0.0704
1400.0	20.0	0.0057	0.0004	4.9665	0.2418	1.0655	0.0510
1440.0	20.0	0.0024	0.0002	6.0759	0.2014	0.8367	0.0603
1480.0	20.0	0.1793	0.0075	7.7133	0.1584	0.1279	0.0044
1520.0	20.0	0.1907	0.0059	7.0269	0.1296	0.0000	0.0000
1560.0	20.0	0.3440	0.0086	5.7872	0.1233	0.0000	0.0000
1600.0	20.0	0.3202	0.0070	4.9651	0.1324	0.0000	0.0000
1640.0	20.0	1.1829	0.0214	4.8716	0.1095	0.1581	0.0063
1680.0	20.0	1.9909	0.0238	5.0837	0.1016	0.4230	0.0208
1720.0	20.0	0.8890	0.0118	5.0441	0.0977	0.9587	0.0358
1760.0	20.0	1.1730	0.0374	3.9550	0.0515	1.1215	0.0309
1800.0	20.0	0.9334	0.0141	2.9275	0.0241	1.6235	0.0140
1840.0	20.0	1.4480	0.0189	2.6693	0.0228	1.0658	0.0136
1880.0	20.0	1.3852	0.0160	3.2324	0.0270	0.2951	0.0036
1920.0	20.0	1.2431	0.0133	2.9166	0.0258	0.3752	0.0048
1960.0	20.0	1.3310	0.0145	2.4510	0.0230	0.4734	0.0059
2000.0	20.0	1.1454	0.0135	2.0947	0.0209	0.5296	0.0066
2040.0	20.0	1.0441	0.0113	1.7642	0.0193	0.5427	0.0073
2080.0	20.0	1.3432	0.0168	1.3923	0.0153	0.5809	0.0068
2120.0	20.0	1.2329	0.0148	1.1590	0.0138	0.7180	0.0096
2160.0	20.0	1.1696	0.0153	1.0210	0.0130	0.8227	0.0104
2200.0	20.0	1.0624	0.0148	0.8156	0.0116	1.1396	0.0152
2240.0	20.0	1.4014	0.0221	0.7396	0.0159	1.1065	0.0174
2280.0	20.0	1.7068	0.0415	0.7401	0.0232	1.2259	0.0339

E.5.4 $\gamma d \to \pi^0\pi^0 n(p)$ as a Function of W

Angular Distributions

$\cos(\theta^*_{2\pi^0})$	$W=(1310.0\pm10.0)$ MeV $d\sigma/d\Omega$ [μb/sr]	Δ_{stat} [μb/sr]	Δ_{sys} [μb/sr]	$W=(1330.0\pm10.0)$ MeV $d\sigma/d\Omega$ [μb/sr]	Δ_{stat} [μb/sr]	Δ_{sys} [μb/sr]	$W=(1350.0\pm10.0)$ MeV $d\sigma/d\Omega$ [μb/sr]	Δ_{stat} [μb/sr]	Δ_{sys} [μb/sr]	$W=(1370.0\pm10.0)$ MeV $d\sigma/d\Omega$ [μb/sr]	Δ_{stat} [μb/sr]	Δ_{sys} [μb/sr]
−0.80	0.0757	0.0309	0.0086	0.0559	0.0296	0.0093	0.0317	0.0228	0.0055	0.0965	0.0285	0.0083
−0.40	0.0296	0.0236	0.0109	0.0650	0.0336	0.0244	0.0904	0.0327	0.0083	0.2388	0.0421	0.0068
0.00	0.0314	0.0220	0.0196	0.0480	0.0267	0.0269	0.1163	0.0333	0.0136	0.1716	0.0288	0.0042
0.40	−0.0040	0.0166	−0.0043	0.0455	0.0245	0.0296	0.0578	0.0225	0.0159	0.0969	0.0282	0.0098
0.80	−0.0024	0.0231	−0.0330	−0.0143	0.0244	−0.0033	0.0115	0.0206	0.0053	0.1039	0.0395	0.0320

$\cos(\theta^*_{2\pi^0})$	$W=(1390.0\pm10.0)$ MeV $d\sigma/d\Omega$ [μb/sr]	Δ_{stat} [μb/sr]	Δ_{sys} [μb/sr]	$W=(1410.0\pm10.0)$ MeV $d\sigma/d\Omega$ [μb/sr]	Δ_{stat} [μb/sr]	Δ_{sys} [μb/sr]	$W=(1430.0\pm10.0)$ MeV $d\sigma/d\Omega$ [μb/sr]	Δ_{stat} [μb/sr]	Δ_{sys} [μb/sr]	$W=(1450.0\pm10.0)$ MeV $d\sigma/d\Omega$ [μb/sr]	Δ_{stat} [μb/sr]	Δ_{sys} [μb/sr]
−0.80	0.2009	0.0511	0.0166	0.2529	0.0528	0.0144	0.3004	0.0590	0.0610	0.4564	0.0671	0.0618
−0.40	0.2785	0.0496	0.0064	0.2955	0.0438	0.0072	0.3714	0.0451	0.0163	0.4644	0.1263	0.0470
0.00	0.2657	0.0320	0.0055	0.3921	0.0466	0.0152	0.4035	0.0428	0.0142	0.4812	0.0962	0.0536
0.40	0.2654	0.0335	0.0266	0.2671	0.0307	0.0314	0.3312	0.0446	0.0348	0.4966	0.0349	0.0449
0.80	0.2268	0.0477	0.0495	0.2587	0.0470	0.0598	0.2598	0.0521	0.0185	0.1943	0.0410	0.0232

$\cos(\theta^*_{2\pi^0})$	$W=(1470.0\pm10.0)$ MeV $d\sigma/d\Omega$ [μb/sr]	Δ_{stat} [μb/sr]	Δ_{sys} [μb/sr]	$W=(1490.0\pm10.0)$ MeV $d\sigma/d\Omega$ [μb/sr]	Δ_{stat} [μb/sr]	Δ_{sys} [μb/sr]	$W=(1510.0\pm10.0)$ MeV $d\sigma/d\Omega$ [μb/sr]	Δ_{stat} [μb/sr]	Δ_{sys} [μb/sr]	$W=(1530.0\pm10.0)$ MeV $d\sigma/d\Omega$ [μb/sr]	Δ_{stat} [μb/sr]	Δ_{sys} [μb/sr]
−0.80	0.6970	0.0656	0.0323	1.0044	0.0564	0.1625	1.0045	0.0551	0.0735	1.0242	0.0768	0.1524
−0.40	0.6358	0.0734	0.0758	0.7215	0.0443	0.0456	0.6850	0.0761	0.0807	0.6140	0.0800	0.0922
0.00	0.6560	0.0879	0.0510	0.6621	0.0652	0.0436	0.6567	0.0666	0.0816	0.6384	0.0663	0.0879
0.40	0.5760	0.0283	0.0149	0.6077	0.0221	0.0233	0.6472	0.0206	0.0369	0.6155	0.0207	0.0349
0.80	0.3630	0.0318	0.0152	0.3221	0.0201	0.0201	0.3607	0.0225	0.0211	0.4093	0.0228	0.0226

$\cos(\theta^*_{2\pi^0})$	$W=(1550.0\pm10.0)$ MeV $d\sigma/d\Omega$ [μb/sr]	Δ_{stat} [μb/sr]	Δ_{sys} [μb/sr]	$W=(1570.0\pm10.0)$ MeV $d\sigma/d\Omega$ [μb/sr]	Δ_{stat} [μb/sr]	Δ_{sys} [μb/sr]	$W=(1590.0\pm10.0)$ MeV $d\sigma/d\Omega$ [μb/sr]	Δ_{stat} [μb/sr]	Δ_{sys} [μb/sr]	$W=(1610.0\pm10.0)$ MeV $d\sigma/d\Omega$ [μb/sr]	Δ_{stat} [μb/sr]	Δ_{sys} [μb/sr]
−0.80	0.9409	0.0576	0.0497	0.9396	0.1059	0.1123	0.8325	0.0640	0.1531	0.8868	0.0815	0.0793
−0.40	0.5890	0.1209	0.1134	0.5879	0.1070	0.0858	0.6819	0.1156	0.1022	0.6395	0.1139	0.1766
0.00	0.5821	0.1011	0.0899	0.5410	0.0564	0.0686	0.4165	0.0573	0.0796	0.5970	0.0361	0.0828
0.40	0.5446	0.0196	0.0355	0.5500	0.0195	0.0340	0.4926	0.0307	0.0324	0.5086	0.0176	0.0375
0.80	0.4069	0.0224	0.0314	0.4063	0.0213	0.0257	0.4044	0.0189	0.0264	0.4266	0.0207	0.0385

$\cos(\theta^*_{2\pi^0})$	$W=(1630.0\pm10.0)$ MeV			$W=(1650.0\pm10.0)$ MeV			$W=(1670.0\pm10.0)$ MeV			$W=(1690.0\pm10.0)$ MeV		
	$d\sigma/d\Omega$ [μb/sr]	Δ_{stat} [μb/sr]	Δ_{sys} [μb/sr]	$d\sigma/d\Omega$ [μb/sr]	Δ_{stat} [μb/sr]	Δ_{sys} [μb/sr]	$d\sigma/d\Omega$ [μb/sr]	Δ_{stat} [μb/sr]	Δ_{sys} [μb/sr]	$d\sigma/d\Omega$ [μb/sr]	Δ_{stat} [μb/sr]	Δ_{sys} [μb/sr]
−0.80	0.9249	0.0692	0.0804	0.9635	0.0718	0.0465	0.7436	0.0597	0.0539	0.7654	0.0313	0.1074
−0.40	0.6703	0.0655	0.0596	0.6728	0.0786	0.0863	0.6096	0.0741	0.0707	0.7208	0.0246	0.0235
0.00	0.5176	0.0426	0.0392	0.5953	0.0459	0.0748	0.7167	0.0584	0.0761	0.7220	0.0190	0.0115
0.40	0.5969	0.0176	0.0266	0.6172	0.0180	0.0403	0.5796	0.0183	0.0381	0.6573	0.0185	0.0227
0.80	0.3890	0.0203	0.0331	0.4663	0.0181	0.0212	0.4307	0.0189	0.0163	0.5059	0.0213	0.0053

$\cos(\theta^*_{2\pi^0})$	$W=(1710.0\pm10.0)$ MeV			$W=(1730.0\pm10.0)$ MeV			$W=(1750.0\pm10.0)$ MeV			$W=(1770.0\pm10.0)$ MeV		
	$d\sigma/d\Omega$ [μb/sr]	Δ_{stat} [μb/sr]	Δ_{sys} [μb/sr]	$d\sigma/d\Omega$ [μb/sr]	Δ_{stat} [μb/sr]	Δ_{sys} [μb/sr]	$d\sigma/d\Omega$ [μb/sr]	Δ_{stat} [μb/sr]	Δ_{sys} [μb/sr]	$d\sigma/d\Omega$ [μb/sr]	Δ_{stat} [μb/sr]	Δ_{sys} [μb/sr]
−0.80	0.6233	0.0279	0.0158	0.4970	0.0298	0.0055	0.3644	0.0213	0.0410	0.3055	0.0203	0.0351
−0.40	0.6430	0.0235	0.0058	0.4968	0.0221	0.0122	0.4384	0.0187	0.0364	0.3962	0.0166	0.0330
0.00	0.6829	0.0226	0.0240	0.6157	0.0192	0.0233	0.5017	0.0178	0.0433	0.4649	0.0159	0.0405
0.40	0.5903	0.0181	0.0375	0.5229	0.0147	0.0245	0.4494	0.0143	0.0432	0.3826	0.0127	0.0365
0.80	0.4214	0.0146	0.0185	0.3661	0.0140	0.0176	0.3852	0.0165	0.0329	0.3243	0.0143	0.0278

$\cos(\theta^*_{2\pi^0})$	$W=(1790.0\pm10.0)$ MeV			$W=(1810.0\pm10.0)$ MeV			$W=(1830.0\pm10.0)$ MeV			$W=(1850.0\pm10.0)$ MeV		
	$d\sigma/d\Omega$ [μb/sr]	Δ_{stat} [μb/sr]	Δ_{sys} [μb/sr]	$d\sigma/d\Omega$ [μb/sr]	Δ_{stat} [μb/sr]	Δ_{sys} [μb/sr]	$d\sigma/d\Omega$ [μb/sr]	Δ_{stat} [μb/sr]	Δ_{sys} [μb/sr]	$d\sigma/d\Omega$ [μb/sr]	Δ_{stat} [μb/sr]	Δ_{sys} [μb/sr]
−0.80	0.2499	0.0150	0.0169	0.2561	0.0115	0.0124	0.2284	0.0133	0.0140	0.2528	0.0136	0.0114
−0.40	0.3206	0.0158	0.0174	0.3400	0.0138	0.0256	0.2914	0.0125	0.0217	0.2931	0.0129	0.0168
0.00	0.4050	0.0133	0.0244	0.3734	0.0113	0.0262	0.3564	0.0102	0.0245	0.3414	0.0147	0.0207
0.40	0.3635	0.0113	0.0276	0.2958	0.0087	0.0201	0.2730	0.0089	0.0179	0.2891	0.0103	0.0179
0.80	0.3082	0.0139	0.0278	0.2613	0.0140	0.0251	0.2316	0.0110	0.0184	0.2331	0.0115	0.0139

$\cos(\theta^*_{2\pi^0})$	$W=(1870.0\pm10.0)$ MeV			$W=(1890.0\pm10.0)$ MeV			$W=(1910.0\pm10.0)$ MeV			$W=(1930.0\pm10.0)$ MeV		
	$d\sigma/d\Omega$ [μb/sr]	Δ_{stat} [μb/sr]	Δ_{sys} [μb/sr]	$d\sigma/d\Omega$ [μb/sr]	Δ_{stat} [μb/sr]	Δ_{sys} [μb/sr]	$d\sigma/d\Omega$ [μb/sr]	Δ_{stat} [μb/sr]	Δ_{sys} [μb/sr]	$d\sigma/d\Omega$ [μb/sr]	Δ_{stat} [μb/sr]	Δ_{sys} [μb/sr]
−0.80	0.2939	0.0142	0.0141	0.2489	0.0152	0.0112	0.2894	0.0144	0.0223	0.2737	0.0159	0.0124
−0.40	0.3261	0.0130	0.0186	0.2857	0.0137	0.0176	0.2923	0.0125	0.0192	0.2924	0.0142	0.0176
0.00	0.3565	0.0131	0.0232	0.3547	0.0132	0.0273	0.3121	0.0120	0.0202	0.3247	0.0131	0.0243
0.40	0.2636	0.0096	0.0163	0.2618	0.0097	0.0186	0.2436	0.0085	0.0156	0.2419	0.0090	0.0147
0.80	0.2422	0.0119	0.0132	0.1947	0.0117	0.0054	0.2266	0.0102	0.0143	0.2191	0.0126	0.0031

$\cos(\theta^*_{2\pi^0})$	$W=(1950.0\pm10.0)$ MeV			$W=(1970.0\pm10.0)$ MeV			$W=(1990.0\pm10.0)$ MeV			$W=(2010.0\pm10.0)$ MeV		
	$d\sigma/d\Omega$ [μb/sr]	Δ_{stat} [μb/sr]	Δ_{sys} [μb/sr]	$d\sigma/d\Omega$ [μb/sr]	Δ_{stat} [μb/sr]	Δ_{sys} [μb/sr]	$d\sigma/d\Omega$ [μb/sr]	Δ_{stat} [μb/sr]	Δ_{sys} [μb/sr]	$d\sigma/d\Omega$ [μb/sr]	Δ_{stat} [μb/sr]	Δ_{sys} [μb/sr]
−0.80	0.3026	0.0140	0.0136	0.2429	0.0131	0.0102	0.2867	0.0163	0.0080	0.2139	0.0124	0.0152
−0.40	0.2805	0.0126	0.0151	0.2805	0.0123	0.0136	0.2770	0.0114	0.0094	0.2399	0.0115	0.0117
0.00	0.3209	0.0132	0.0221	0.2968	0.0128	0.0160	0.2845	0.0110	0.0119	0.2345	0.0099	0.0099
0.40	0.2503	0.0100	0.0164	0.2373	0.0091	0.0125	0.2353	0.0089	0.0086	0.2259	0.0083	0.0093
0.80	0.2381	0.0100	0.0099	0.2225	0.0103	0.0067	0.2375	0.0118	0.0033	0.2002	0.0109	0.0057

$\cos(\theta^*_{2\pi^0})$	$W=(2030.0\pm10.0)$ MeV			$W=(2050.0\pm10.0)$ MeV			$W=(2070.0\pm10.0)$ MeV			$W=(2090.0\pm10.0)$ MeV		
	$d\sigma/d\Omega$ [μb/sr]	Δ_{stat} [μb/sr]	Δ_{sys} [μb/sr]	$d\sigma/d\Omega$ [μb/sr]	Δ_{stat} [μb/sr]	Δ_{sys} [μb/sr]	$d\sigma/d\Omega$ [μb/sr]	Δ_{stat} [μb/sr]	Δ_{sys} [μb/sr]	$d\sigma/d\Omega$ [μb/sr]	Δ_{stat} [μb/sr]	Δ_{sys} [μb/sr]
−0.80	0.2146	0.0127	0.0060	0.2133	0.0112	0.0068	0.2111	0.0131	0.0101	0.1875	0.0105	0.0048
−0.40	0.2314	0.0106	0.0068	0.2169	0.0096	0.0095	0.2375	0.0104	0.0073	0.1653	0.0094	0.0052
0.00	0.2299	0.0090	0.0078	0.2249	0.0098	0.0104	0.2191	0.0094	0.0078	0.2109	0.0109	0.0052
0.40	0.2352	0.0088	0.0082	0.2397	0.0086	0.0096	0.2108	0.0076	0.0099	0.2257	0.0102	0.0035
0.80	0.2224	0.0118	0.0077	0.2371	0.0110	0.0075	0.2371	0.0112	0.0099	0.2564	0.0131	0.0065

$\cos(\theta^*_{2\pi^0})$	$W=(2110.0\pm10.0)$ MeV			$W=(2130.0\pm10.0)$ MeV			$W=(2150.0\pm10.0)$ MeV			$W=(2170.0\pm10.0)$ MeV		
	$d\sigma/d\Omega$ [μb/sr]	Δ_{stat} [μb/sr]	Δ_{sys} [μb/sr]	$d\sigma/d\Omega$ [μb/sr]	Δ_{stat} [μb/sr]	Δ_{sys} [μb/sr]	$d\sigma/d\Omega$ [μb/sr]	Δ_{stat} [μb/sr]	Δ_{sys} [μb/sr]	$d\sigma/d\Omega$ [μb/sr]	Δ_{stat} [μb/sr]	Δ_{sys} [μb/sr]
−0.80	0.2157	0.0105	0.0118	0.1565	0.0103	0.0046	0.2019	0.0102	0.0295	0.1655	0.0109	0.0053
−0.40	0.1665	0.0097	0.0092	0.1644	0.0097	0.0078	0.1469	0.0076	0.0070	0.1467	0.0096	0.0046
0.00	0.1801	0.0081	0.0158	0.1751	0.0108	0.0091	0.1624	0.0099	0.0041	0.1559	0.0088	0.0039
0.40	0.2226	0.0072	0.0127	0.1992	0.0074	0.0068	0.2187	0.0081	0.0055	0.2358	0.0103	0.0051
0.80	0.2688	0.0124	0.0036	0.2492	0.0121	0.0090	0.2832	0.0110	0.0048	0.2212	0.0116	0.0057

$\cos(\theta^*_{2\pi^0})$	$W=(2190.0\pm10.0)$ MeV			$W=(2210.0\pm10.0)$ MeV			$W=(2230.0\pm10.0)$ MeV			$W=(2250.0\pm10.0)$ MeV		
	$d\sigma/d\Omega$ [μb/sr]	Δ_{stat} [μb/sr]	Δ_{sys} [μb/sr]	$d\sigma/d\Omega$ [μb/sr]	Δ_{stat} [μb/sr]	Δ_{sys} [μb/sr]	$d\sigma/d\Omega$ [μb/sr]	Δ_{stat} [μb/sr]	Δ_{sys} [μb/sr]	$d\sigma/d\Omega$ [μb/sr]	Δ_{stat} [μb/sr]	Δ_{sys} [μb/sr]
−0.80	0.1714	0.0118	0.0168	0.1896	0.0145	0.0157	0.1634	0.0163	0.0061	0.2131	0.0157	0.0134
−0.40	0.1456	0.0108	0.0063	0.1192	0.0109	0.0053	0.1373	0.0097	0.0058	0.0956	0.0097	0.0039
0.00	0.1696	0.0095	0.0028	0.1586	0.0115	0.0067	0.1512	0.0108	0.0070	0.1298	0.0156	0.0040
0.40	0.1851	0.0076	0.0038	0.2187	0.0085	0.0068	0.1822	0.0105	0.0053	0.2476	0.0113	0.0074
0.80	0.2792	0.0121	0.0128	0.2863	0.0133	0.0060	0.3208	0.0179	0.0061	0.2895	0.0160	0.0042

$\cos(\theta^*_{2\pi^0})$				$W=(2270.0\pm10.0)$ MeV						$W=(2290.0\pm10.0)$ MeV		
				$d\sigma/d\Omega$ [μb/sr]	Δ_{stat} [μb/sr]	Δ_{sys} [μb/sr]				$d\sigma/d\Omega$ [μb/sr]	Δ_{stat} [μb/sr]	Δ_{sys} [μb/sr]
−0.80				0.2300	0.0257	0.0184				0.1989	0.0364	0.0128
−0.40				0.1715	0.0188	0.0061				0.1369	0.0256	0.0029
0.00				0.1654	0.0189	0.0033				0.1693	0.0221	0.0034
0.40				0.2151	0.0160	0.0049				0.2125	0.0172	0.0039
0.80				0.3637	0.0261	0.0140				0.3489	0.0309	0.0084

Decomposed Total Cross Sections

W [MeV]	ΔW [MeV]	$\sigma_{PhaseSpace}$ [μb]	Δ_{stat} [μb]	$\sigma_{\Delta(1232)}$ [μb]	Δ_{stat} [μb]	$\sigma_{N(1520)}$ [μb]	Δ_{stat} [μb]
1320.0	20.0	0.0812	0.0562	0.1568	0.0520	0.0592	0.0512
1360.0	20.0	0.3341	0.0570	0.1233	0.0493	0.4134	0.0608
1400.0	20.0	0.1274	0.0131	2.4907	0.1572	0.5029	0.0543
1440.0	20.0	0.7219	0.0875	3.3443	0.2146	0.3608	0.0341
1480.0	20.0	0.8711	0.0399	7.0707	0.2000	0.0002	0.0000
1520.0	20.0	0.2114	0.0144	7.9179	0.2218	0.0000	0.0000
1560.0	20.0	0.2253	0.0121	7.3094	0.2959	0.0000	0.0000
1600.0	20.0	0.5628	0.0253	6.7946	0.2614	0.0000	0.0000
1640.0	20.0	0.8328	0.0220	7.2057	0.1992	0.0000	0.0000
1680.0	20.0	0.8556	0.0204	6.9643	0.1174	0.3731	0.0098
1720.0	20.0	0.5255	0.0105	5.7541	0.0829	0.4650	0.0111
1760.0	20.0	0.3842	0.0087	3.4595	0.0606	0.6009	0.0141
1800.0	20.0	0.7617	0.0164	2.1074	0.0399	0.8112	0.0220
1840.0	20.0	0.9725	0.0227	1.7809	0.0357	0.2130	0.0066
1880.0	20.0	1.0384	0.0273	2.1316	0.0395	0.1973	0.0092
1920.0	20.0	0.8240	0.0204	2.0777	0.0401	0.1512	0.0049
1960.0	20.0	1.1250	0.0259	1.9140	0.0378	0.2571	0.0082
2000.0	20.0	0.7346	0.0203	1.6925	0.0343	0.1574	0.0061
2040.0	20.0	1.1676	0.0244	1.5576	0.0328	0.0827	0.0027
2080.0	20.0	1.2572	0.0277	1.0626	0.0267	0.1308	0.0044
2120.0	20.0	1.1868	0.0291	0.9803	0.0242	0.3326	0.0111
2160.0	20.0	1.1695	0.0282	0.8032	0.0229	0.3593	0.0115
2200.0	20.0	1.0906	0.0335	0.6465	0.0213	0.5978	0.0172
2240.0	20.0	1.3133	0.0449	0.5555	0.0204	0.3906	0.0156
2280.0	20.0	1.0434	0.0606	0.6565	0.0400	0.6868	0.0394

E.5.5 $\gamma p \to \pi^0\pi^0 p$ as a Function of W

Angular Distributions

	W=(1304.4±9.0) MeV			W=(1322.2±8.9) MeV			W=(1339.8±8.8) MeV			W=(1357.2±8.6) MeV		
$\cos(\theta^*_{2\pi^0})$	$d\sigma/d\Omega$ [μb/sr]	Δ_{stat} [μb/sr]	Δ_{sys} [μb/sr]	$d\sigma/d\Omega$ [μb/sr]	Δ_{stat} [μb/sr]	Δ_{sys} [μb/sr]	$d\sigma/d\Omega$ [μb/sr]	Δ_{stat} [μb/sr]	Δ_{sys} [μb/sr]	$d\sigma/d\Omega$ [μb/sr]	Δ_{stat} [μb/sr]	Δ_{sys} [μb/sr]
−0.90	0.0201	0.0054	0.0087	0.0683	0.0067	0.0117	0.1230	0.0137	0.0235	0.1415	0.0131	0.0235
−0.70	0.0287	0.0060	0.0087	0.0589	0.0077	0.0117	0.1034	0.0107	0.0235	0.1310	0.0106	0.0235
−0.50	0.0138	0.0041	−0.0022	0.0454	0.0049	0.0074	0.1375	0.0112	0.0051	0.1696	0.0137	0.0051
−0.30	0.0062	0.0086	−0.0022	0.0318	0.0057	0.0074	0.1001	0.0099	0.0051	0.1802	0.0102	0.0051
−0.10	−0.0080	0.0335	0.1504	0.0285	0.0095	0.0119	0.0982	0.0120	0.0513	0.1481	0.0104	0.0513
0.10	0.1488	0.1728	0.1504	0.1278	0.0694	0.0119	0.1287	0.0311	0.0513	0.1296	0.0213	0.0513
0.30	0.0553	0.3650	6.3810	0.8933	0.4798	−0.1896	0.8695	0.3338	1.6810	0.3477	0.1103	1.6810
0.50	0.3744	0.5568	6.3810	0.5414	0.4587	−0.1896	0.2289	0.4876	1.6810	0.6062	0.2472	1.6810
0.70	−0.6023	1.0372	−3.9097	1.5003	1.1659	−0.0261	0.7576	0.7755	−1.1734	−0.1698	0.6446	−1.1734
0.90	6.2682	2.5716	−3.9097	1.7487	1.2425	−0.0261	1.7189	1.7198	−1.1734	−2.2176	1.1281	−1.1734

	W=(1374.4±8.5) MeV			W=(1391.4±8.4) MeV			W=(1408.1±8.3) MeV			W=(1424.7±8.2) MeV		
$\cos(\theta^*_{2\pi^0})$	$d\sigma/d\Omega$ [μb/sr]	Δ_{stat} [μb/sr]	Δ_{sys} [μb/sr]	$d\sigma/d\Omega$ [μb/sr]	Δ_{stat} [μb/sr]	Δ_{sys} [μb/sr]	$d\sigma/d\Omega$ [μb/sr]	Δ_{stat} [μb/sr]	Δ_{sys} [μb/sr]	$d\sigma/d\Omega$ [μb/sr]	Δ_{stat} [μb/sr]	Δ_{sys} [μb/sr]
−0.90	0.2648	0.0258	0.0166	0.3217	0.0186	0.0142	0.4112	0.0246	0.0142	0.4891	0.0251	0.0347
−0.70	0.3254	0.0217	0.0166	0.2963	0.0163	0.0142	0.3981	0.0208	0.0142	0.4105	0.0161	0.0347
−0.50	0.2673	0.0144	0.0194	0.3683	0.0189	0.0238	0.4803	0.0202	0.0238	0.4981	0.0162	0.0332
−0.30	0.3444	0.0157	0.0194	0.3882	0.0154	0.0238	0.5920	0.0290	0.0238	0.5910	0.0211	0.0332
−0.10	0.3049	0.0178	0.0397	0.3472	0.0191	0.0200	0.5504	0.0263	0.0200	0.5368	0.0189	0.0369
0.10	0.2396	0.0232	0.0397	0.3327	0.0206	0.0200	0.4250	0.0231	0.0200	0.4951	0.0182	0.0369
0.30	0.1263	0.0445	0.0699	0.2668	0.0327	0.0595	0.3074	0.0278	0.0595	0.3522	0.0186	0.0353
0.50	0.3869	0.1685	0.0699	0.6276	0.1212	0.0595	0.8542	0.1994	0.0595	0.2968	0.0514	0.0353
0.70	1.0008	0.4877	−0.0143	0.2221	0.2304	0.0450	0.2833	0.1117	0.0450	0.2258	0.0722	0.0226
0.90	−0.2440	0.4591	−0.0143	−0.0471	0.2347	0.0450	0.2958	0.1567	0.0450	0.3910	0.2134	0.0226

	W=(1441.1±8.1) MeV			W=(1457.2±8.0) MeV			W=(1473.3±8.0) MeV			W=(1489.1±7.9) MeV		
$\cos(\theta^*_{2\pi^0})$	$d\sigma/d\Omega$ [μb/sr]	Δ_{stat} [μb/sr]	Δ_{sys} [μb/sr]	$d\sigma/d\Omega$ [μb/sr]	Δ_{stat} [μb/sr]	Δ_{sys} [μb/sr]	$d\sigma/d\Omega$ [μb/sr]	Δ_{stat} [μb/sr]	Δ_{sys} [μb/sr]	$d\sigma/d\Omega$ [μb/sr]	Δ_{stat} [μb/sr]	Δ_{sys} [μb/sr]
−0.90	0.6366	0.0388	0.0347	0.7323	0.0390	0.0420	0.9062	0.0521	0.0404	0.9992	0.0512	0.0404
−0.70	0.6086	0.0300	0.0347	0.5911	0.0270	0.0420	0.7330	0.0356	0.0404	0.8428	0.0320	0.0404
−0.50	0.6155	0.0226	0.0332	0.6408	0.0261	0.0405	0.8640	0.0359	0.0476	0.7812	0.0300	0.0476
−0.30	0.7307	0.0268	0.0332	0.6578	0.0213	0.0405	0.9461	0.0338	0.0476	0.9283	0.0291	0.0476
−0.10	0.7416	0.0239	0.0369	0.6982	0.0224	0.0401	0.8543	0.0282	0.0390	0.8583	0.0244	0.0390
0.10	0.6846	0.0216	0.0369	0.6897	0.0208	0.0401	0.8925	0.0259	0.0390	0.8968	0.0224	0.0390
0.30	0.4803	0.0197	0.0353	0.5469	0.0188	0.0411	0.7227	0.0227	0.0364	0.7803	0.0197	0.0364
0.50	0.3109	0.0356	0.0353	0.2960	0.0255	0.0411	0.4075	0.0271	0.0364	0.4805	0.0218	0.0364
0.70	0.1661	0.0665	0.0226	0.3504	0.0628	0.0605	0.2911	0.0482	0.1198	0.3875	0.0349	0.1198
0.90	0.6322	0.2502	0.0226	0.1018	0.0509	0.0605	0.3852	0.1370	0.1198	0.1616	0.0380	0.1198

$\cos(\theta^*_{2\pi^0})$	$W=(1504.8\pm7.8)$ MeV			$W=(1520.3\pm7.7)$ MeV			$W=(1535.6\pm7.6)$ MeV			$W=(1550.8\pm7.6)$ MeV		
	$d\sigma/d\Omega$ [μb/sr]	Δ_{stat} [μb/sr]	Δ_{sys} [μb/sr]	$d\sigma/d\Omega$ [μb/sr]	Δ_{stat} [μb/sr]	Δ_{sys} [μb/sr]	$d\sigma/d\Omega$ [μb/sr]	Δ_{stat} [μb/sr]	Δ_{sys} [μb/sr]	$d\sigma/d\Omega$ [μb/sr]	Δ_{stat} [μb/sr]	Δ_{sys} [μb/sr]
−0.90	0.9444	0.0443	0.0313	0.9848	0.0502	0.0161	0.9833	0.0565	0.0161	0.8668	0.0452	0.0227
−0.70	0.9202	0.0376	0.0313	0.7640	0.0361	0.0161	0.8565	0.0398	0.0161	0.7124	0.0388	0.0227
−0.50	0.9311	0.0345	0.0448	0.8354	0.0317	0.0412	0.8443	0.0331	0.0412	0.7455	0.0332	0.0323
−0.30	0.9618	0.0311	0.0448	0.8551	0.0282	0.0412	0.8283	0.0286	0.0412	0.7337	0.0283	0.0323
−0.10	0.9255	0.0265	0.0246	0.8116	0.0239	0.0273	0.7824	0.0242	0.0273	0.6481	0.0232	0.0177
0.10	0.9533	0.0239	0.0246	0.7973	0.0207	0.0273	0.7557	0.0207	0.0273	0.5560	0.0187	0.0177
0.30	0.7877	0.0202	0.0480	0.6969	0.0179	0.0295	0.6702	0.0180	0.0295	0.5912	0.0177	0.0306
0.50	0.5267	0.0212	0.0480	0.4621	0.0173	0.0295	0.5256	0.0178	0.0295	0.4821	0.0172	0.0306
0.70	0.2418	0.0340	0.0526	0.3158	0.0292	0.0795	0.3859	0.0279	0.0795	0.2584	0.0222	0.0593
0.90	0.2892	0.0526	0.0526	0.2885	0.0546	0.0795	0.1362	0.0354	0.0795	0.3107	0.0688	0.0593

$\cos(\theta^*_{2\pi^0})$	$W=(1565.9\pm7.5)$ MeV			$W=(1580.8\pm7.4)$ MeV			$W=(1595.6\pm7.4)$ MeV			$W=(1610.2\pm7.3)$ MeV		
	$d\sigma/d\Omega$ [μb/sr]	Δ_{stat} [μb/sr]	Δ_{sys} [μb/sr]	$d\sigma/d\Omega$ [μb/sr]	Δ_{stat} [μb/sr]	Δ_{sys} [μb/sr]	$d\sigma/d\Omega$ [μb/sr]	Δ_{stat} [μb/sr]	Δ_{sys} [μb/sr]	$d\sigma/d\Omega$ [μb/sr]	Δ_{stat} [μb/sr]	Δ_{sys} [μb/sr]
−0.90	0.8610	0.0542	0.0227	0.7697	0.0544	0.0174	0.6630	0.0503	0.0276	0.8815	0.0588	0.0276
−0.70	0.7690	0.0418	0.0227	0.6737	0.0376	0.0174	0.6160	0.0365	0.0276	0.7443	0.0400	0.0276
−0.50	0.6848	0.0326	0.0323	0.6328	0.0301	0.0351	0.5779	0.0293	0.0260	0.5912	0.0299	0.0260
−0.30	0.6382	0.0271	0.0323	0.5768	0.0249	0.0351	0.5563	0.0249	0.0260	0.6276	0.0266	0.0260
−0.10	0.6489	0.0238	0.0177	0.5584	0.0212	0.0196	0.5208	0.0209	0.0205	0.5296	0.0210	0.0205
0.10	0.6229	0.0201	0.0177	0.5243	0.0178	0.0196	0.5015	0.0178	0.0205	0.5582	0.0188	0.0205
0.30	0.6047	0.0183	0.0306	0.5457	0.0167	0.0263	0.5317	0.0168	0.0343	0.5738	0.0174	0.0343
0.50	0.4980	0.0173	0.0306	0.4911	0.0161	0.0263	0.5327	0.0151	0.0343	0.6280	0.0138	0.0343
0.70	0.3273	0.0246	0.0593	0.2895	0.0198	0.0623	0.3637	0.0210	0.0635	0.4627	0.0191	0.0635
0.90	0.1780	0.0380	0.0593	0.2502	0.0366	0.0623	0.1638	0.0285	0.0635	0.2182	0.0284	0.0635

$\cos(\theta^*_{2\pi^0})$	$W=(1624.7\pm7.2)$ MeV			$W=(1639.1\pm7.2)$ MeV			$W=(1653.3\pm7.1)$ MeV			$W=(1667.4\pm7.0)$ MeV		
	$d\sigma/d\Omega$ [μb/sr]	Δ_{stat} [μb/sr]	Δ_{sys} [μb/sr]	$d\sigma/d\Omega$ [μb/sr]	Δ_{stat} [μb/sr]	Δ_{sys} [μb/sr]	$d\sigma/d\Omega$ [μb/sr]	Δ_{stat} [μb/sr]	Δ_{sys} [μb/sr]	$d\sigma/d\Omega$ [μb/sr]	Δ_{stat} [μb/sr]	Δ_{sys} [μb/sr]
−0.90	0.6878	0.0507	0.0191	0.6663	0.0454	0.0075	0.9505	0.0619	0.0075	0.9461	0.0557	0.0209
−0.70	0.6169	0.0360	0.0191	0.6032	0.0336	0.0075	0.7887	0.0410	0.0075	0.7743	0.0307	0.0209
−0.50	0.4930	0.0262	0.0249	0.6491	0.0273	0.0331	0.7735	0.0308	0.0331	0.6267	0.0224	0.0357
−0.30	0.4943	0.0203	0.0249	0.5022	0.0218	0.0331	0.6479	0.0272	0.0331	0.6647	0.0205	0.0357
−0.10	0.4150	0.0174	0.0261	0.5045	0.0195	0.0250	0.5958	0.0186	0.0250	0.6372	0.0211	0.0355
0.10	0.4634	0.0171	0.0261	0.4804	0.0171	0.0250	0.6177	0.0195	0.0250	0.6180	0.0173	0.0355
0.30	0.5285	0.0154	0.0377	0.5514	0.0154	0.0374	0.7238	0.0186	0.0374	0.7376	0.0157	0.0400
0.50	0.5426	0.0143	0.0377	0.6544	0.0171	0.0374	0.8917	0.0162	0.0374	0.8618	0.0157	0.0400
0.70	0.4960	0.0169	0.0473	0.5388	0.0169	0.0433	0.7710	0.0202	0.0433	0.8432	0.0206	0.0144
0.90	0.2599	0.0307	0.0473	0.6885	0.0663	0.0433	0.5304	0.0519	0.0433	0.7418	0.0518	0.0144

$\cos(\theta^*_{2\pi^0})$	$W=(1681.4\pm7.0)$ MeV			$W=(1695.3\pm6.9)$ MeV			$W=(1709.1\pm6.9)$ MeV			$W=(1722.8\pm6.8)$ MeV		
	$d\sigma/d\Omega$ [μb/sr]	Δ_{stat} [μb/sr]	Δ_{sys} [μb/sr]	$d\sigma/d\Omega$ [μb/sr]	Δ_{stat} [μb/sr]	Δ_{sys} [μb/sr]	$d\sigma/d\Omega$ [μb/sr]	Δ_{stat} [μb/sr]	Δ_{sys} [μb/sr]	$d\sigma/d\Omega$ [μb/sr]	Δ_{stat} [μb/sr]	Δ_{sys} [μb/sr]
−0.90	0.9102	0.0534	0.0209	0.7907	0.0439	0.0406	1.1194	0.0918	0.0225	0.8392	0.0381	0.0225
−0.70	0.7852	0.0283	0.0209	0.6989	0.0320	0.0406	0.8512	0.0377	0.0225	0.8188	0.0424	0.0225
−0.50	0.6631	0.0256	0.0357	0.6073	0.0229	0.0275	0.7414	0.0299	0.0313	0.6892	0.0240	0.0313
−0.30	0.6531	0.0209	0.0357	0.6950	0.0215	0.0275	0.6736	0.0302	0.0313	0.6785	0.0191	0.0313
−0.10	0.6083	0.0206	0.0355	0.6335	0.0213	0.0262	0.7541	0.0296	0.0298	0.6725	0.0189	0.0298
0.10	0.6202	0.0162	0.0355	0.6197	0.0205	0.0262	0.8449	0.0274	0.0298	0.6809	0.0185	0.0298
0.30	0.7631	0.0178	0.0400	0.7460	0.0213	0.0416	0.9129	0.0220	0.0377	0.8192	0.0186	0.0377
0.50	0.9200	0.0162	0.0400	0.9432	0.0193	0.0416	1.0875	0.0280	0.0377	0.9720	0.0201	0.0377
0.70	0.8884	0.0208	0.0144	0.8895	0.0224	0.0189	0.9624	0.0321	0.0138	0.8874	0.0194	0.0138
0.90	0.5591	0.0470	0.0144	0.5505	0.0518	0.0189	0.4782	0.0649	0.0138	0.7840	0.0509	0.0138

$\cos(\theta^*_{2\pi^0})$	$W=(1736.4\pm6.8)$ MeV			$W=(1749.8\pm6.7)$ MeV			$W=(1763.2\pm6.7)$ MeV			$W=(1776.4\pm6.6)$ MeV		
	$d\sigma/d\Omega$ [μb/sr]	Δ_{stat} [μb/sr]	Δ_{sys} [μb/sr]	$d\sigma/d\Omega$ [μb/sr]	Δ_{stat} [μb/sr]	Δ_{sys} [μb/sr]	$d\sigma/d\Omega$ [μb/sr]	Δ_{stat} [μb/sr]	Δ_{sys} [μb/sr]	$d\sigma/d\Omega$ [μb/sr]	Δ_{stat} [μb/sr]	Δ_{sys} [μb/sr]
−0.90	0.7108	0.0372	0.0245	0.4862	0.0329	0.0090	0.4716	0.0378	0.0090	0.3929	0.0369	0.0089
−0.70	0.5911	0.0263	0.0245	0.4825	0.0260	0.0090	0.4796	0.0216	0.0090	0.4611	0.0287	0.0089
−0.50	0.6382	0.0198	0.0206	0.5083	0.0228	0.0234	0.4453	0.0271	0.0234	0.4606	0.0231	0.0247
−0.30	0.6438	0.0185	0.0206	0.5167	0.0166	0.0234	0.5428	0.0172	0.0234	0.4614	0.0333	0.0247
−0.10	0.6709	0.0202	0.0350	0.6055	0.0181	0.0294	0.5663	0.0181	0.0294	0.5455	0.0222	0.0213
0.10	0.6990	0.0192	0.0350	0.6249	0.0173	0.0294	0.6160	0.0168	0.0294	0.5470	0.0222	0.0213
0.30	0.8051	0.0196	0.0393	0.6781	0.0170	0.0356	0.6752	0.0155	0.0356	0.6669	0.0242	0.0244
0.50	0.8988	0.0188	0.0393	0.8555	0.0153	0.0356	0.7565	0.0222	0.0356	0.6802	0.0203	0.0244
0.70	0.8414	0.0219	0.0038	0.7389	0.0177	0.0347	0.7216	0.0191	0.0347	0.6618	0.0231	0.0179
0.90	0.8586	0.0716	0.0038	0.3995	0.0432	0.0347	0.6623	0.0588	0.0347	0.4097	0.0648	0.0179

$\cos(\theta^*_{2\pi^0})$	$W=(1789.6\pm6.6)$ MeV			$W=(1802.6\pm6.5)$ MeV			$W=(1815.6\pm6.5)$ MeV			$W=(1828.5\pm6.4)$ MeV		
	$d\sigma/d\Omega$ [μb/sr]	Δ_{stat} [μb/sr]	Δ_{sys} [μb/sr]	$d\sigma/d\Omega$ [μb/sr]	Δ_{stat} [μb/sr]	Δ_{sys} [μb/sr]	$d\sigma/d\Omega$ [μb/sr]	Δ_{stat} [μb/sr]	Δ_{sys} [μb/sr]	$d\sigma/d\Omega$ [μb/sr]	Δ_{stat} [μb/sr]	Δ_{sys} [μb/sr]
−0.90	0.3130	0.0311	0.0089	0.3835	0.0317	0.0144	0.2953	0.0255	0.0274	0.3054	0.0301	0.0274
−0.70	0.4405	0.0329	0.0089	0.4140	0.0257	0.0144	0.3880	0.0185	0.0274	0.3866	0.0241	0.0274
−0.50	0.3805	0.0238	0.0247	0.4256	0.0202	0.0103	0.3764	0.0157	0.0143	0.4171	0.0237	0.0143
−0.30	0.4352	0.0239	0.0247	0.4410	0.0168	0.0103	0.4241	0.0198	0.0143	0.4081	0.0201	0.0143
−0.10	0.4637	0.0168	0.0213	0.4851	0.0156	0.0156	0.4247	0.0167	0.0228	0.4323	0.0145	0.0228
0.10	0.5169	0.0205	0.0213	0.5197	0.0186	0.0156	0.4460	0.0151	0.0228	0.5127	0.0220	0.0228
0.30	0.5646	0.0171	0.0244	0.5592	0.0155	0.0356	0.5211	0.0184	0.0686	0.5600	0.0170	0.0686
0.50	0.6499	0.0193	0.0244	0.7199	0.0146	0.0356	0.6080	0.0153	0.0686	0.6293	0.0133	0.0686
0.70	0.6312	0.0177	0.0179	0.6603	0.0148	0.0773	0.5594	0.0161	0.2252	0.5457	0.0153	0.2252
0.90	0.3187	0.0368	0.0179	0.5438	0.0332	0.0773	0.3518	0.0251	0.2252	0.2422	0.0293	0.2252

$\cos(\theta^*_{2\pi^0})$	$W=(1841.3\pm6.4)$ MeV			$W=(1854.0\pm6.3)$ MeV			$W=(1866.6\pm6.3)$ MeV			$W=(1879.1\pm6.2)$ MeV		
	$d\sigma/d\Omega$ [μb/sr]	Δ_{stat} [μb/sr]	Δ_{sys} [μb/sr]	$d\sigma/d\Omega$ [μb/sr]	Δ_{stat} [μb/sr]	Δ_{sys} [μb/sr]	$d\sigma/d\Omega$ [μb/sr]	Δ_{stat} [μb/sr]	Δ_{sys} [μb/sr]	$d\sigma/d\Omega$ [μb/sr]	Δ_{stat} [μb/sr]	Δ_{sys} [μb/sr]
−0.90	0.3445	0.0255	0.0088	0.3494	0.0274	0.0096	0.2672	0.0397	0.0096	0.2844	0.0271	0.0089
−0.70	0.3514	0.0210	0.0088	0.4955	0.0281	0.0096	0.3900	0.0316	0.0096	0.3190	0.0318	0.0089
−0.50	0.3846	0.0220	0.0152	0.3627	0.0205	0.0246	0.3695	0.0230	0.0246	0.3632	0.0257	0.0090
−0.30	0.3927	0.0159	0.0152	0.3819	0.0236	0.0246	0.3348	0.0277	0.0246	0.4115	0.0181	0.0090
−0.10	0.4124	0.0180	0.0213	0.3877	0.0142	0.0182	0.3581	0.0193	0.0182	0.3719	0.0170	0.0114
0.10	0.5059	0.0158	0.0213	0.4639	0.0184	0.0182	0.3915	0.0184	0.0182	0.4227	0.0188	0.0114
0.30	0.5865	0.0170	0.0253	0.5375	0.0176	0.0207	0.4571	0.0181	0.0207	0.5425	0.0174	0.0187
0.50	0.5797	0.0147	0.0253	0.6271	0.0170	0.0207	0.5785	0.0178	0.0207	0.5881	0.0187	0.0187
0.70	0.5315	0.0121	0.0120	0.5751	0.0188	0.0158	0.5177	0.0249	0.0158	0.6137	0.0186	0.0196
0.90	0.3766	0.0279	0.0120	0.4049	0.0322	0.0158	0.3158	0.0335	0.0158	0.2996	0.0291	0.0196

$\cos(\theta^*_{2\pi^0})$	$W=(1891.5\pm6.2)$ MeV			$W=(1903.9\pm6.2)$ MeV			$W=(1916.2\pm6.1)$ MeV			$W=(1928.4\pm6.1)$ MeV		
	$d\sigma/d\Omega$ [μb/sr]	Δ_{stat} [μb/sr]	Δ_{sys} [μb/sr]	$d\sigma/d\Omega$ [μb/sr]	Δ_{stat} [μb/sr]	Δ_{sys} [μb/sr]	$d\sigma/d\Omega$ [μb/sr]	Δ_{stat} [μb/sr]	Δ_{sys} [μb/sr]	$d\sigma/d\Omega$ [μb/sr]	Δ_{stat} [μb/sr]	Δ_{sys} [μb/sr]
−0.90	0.2870	0.0229	0.0089	0.3405	0.0293	0.0057	0.3018	0.0267	0.0037	0.2626	0.0291	0.0037
−0.70	0.3540	0.0213	0.0089	0.3781	0.0228	0.0057	0.3729	0.0218	0.0037	0.3730	0.0226	0.0037
−0.50	0.2909	0.0183	0.0090	0.3664	0.0199	0.0095	0.3676	0.0227	0.0074	0.3824	0.0181	0.0074
−0.30	0.3624	0.0153	0.0090	0.4164	0.0189	0.0095	0.3042	0.0160	0.0074	0.3439	0.0161	0.0074
−0.10	0.3881	0.0173	0.0114	0.3882	0.0167	0.0188	0.3320	0.0123	0.0127	0.3775	0.0143	0.0127
0.10	0.3745	0.0144	0.0114	0.4254	0.0159	0.0188	0.3662	0.0132	0.0127	0.3328	0.0184	0.0127
0.30	0.4456	0.0169	0.0187	0.5039	0.0166	0.0175	0.4504	0.0159	0.0170	0.4430	0.0161	0.0170
0.50	0.5544	0.0143	0.0187	0.5503	0.0152	0.0175	0.4908	0.0141	0.0170	0.5053	0.0149	0.0170
0.70	0.4885	0.0134	0.0196	0.5428	0.0161	0.0084	0.5240	0.0159	0.0082	0.5074	0.0143	0.0082
0.90	0.2664	0.0250	0.0196	0.3177	0.0228	0.0084	0.2450	0.0190	0.0082	0.2895	0.0272	0.0082

$\cos(\theta^*_{2\pi^0})$	$W=(1940.5\pm6.0)$ MeV			$W=(1952.6\pm6.0)$ MeV			$W=(1964.5\pm6.0)$ MeV			$W=(1976.4\pm5.9)$ MeV		
	$d\sigma/d\Omega$ [μb/sr]	Δ_{stat} [μb/sr]	Δ_{sys} [μb/sr]	$d\sigma/d\Omega$ [μb/sr]	Δ_{stat} [μb/sr]	Δ_{sys} [μb/sr]	$d\sigma/d\Omega$ [μb/sr]	Δ_{stat} [μb/sr]	Δ_{sys} [μb/sr]	$d\sigma/d\Omega$ [μb/sr]	Δ_{stat} [μb/sr]	Δ_{sys} [μb/sr]
−0.90	0.3246	0.0327	0.0121	0.3217	0.0278	0.0185	0.2606	0.0386	0.0185	0.3214	0.0354	0.0127
−0.70	0.3591	0.0350	0.0121	0.3196	0.0273	0.0185	0.3349	0.0223	0.0185	0.3423	0.0198	0.0127
−0.50	0.4398	0.0260	0.0075	0.3463	0.0235	0.0133	0.3009	0.0208	0.0133	0.3805	0.0196	0.0150
−0.30	0.3633	0.0307	0.0075	0.3086	0.0174	0.0133	0.3859	0.0197	0.0133	0.3190	0.0190	0.0150
−0.10	0.3328	0.0151	0.0091	0.3032	0.0170	0.0094	0.2917	0.0188	0.0094	0.3104	0.0131	0.0152
0.10	0.3774	0.0170	0.0091	0.3402	0.0159	0.0094	0.3405	0.0160	0.0094	0.3172	0.0115	0.0152
0.30	0.4175	0.0191	0.0101	0.4185	0.0158	0.0086	0.3815	0.0148	0.0086	0.3723	0.0146	0.0140
0.50	0.5276	0.0184	0.0101	0.5248	0.0173	0.0086	0.4267	0.0136	0.0086	0.4217	0.0152	0.0140
0.70	0.4860	0.0194	0.0068	0.4753	0.0168	0.0115	0.4344	0.0178	0.0115	0.4832	0.0163	0.0053
0.90	0.3168	0.0246	0.0068	0.3371	0.0251	0.0115	0.2653	0.0315	0.0115	0.2952	0.0202	0.0053

$\cos(\theta^*_{2\pi^0})$	$W=(1988.3\pm5.9)$ MeV			$W=(2000.0\pm5.9)$ MeV			$W=(2011.7\pm5.8)$ MeV			$W=(2023.3\pm5.8)$ MeV		
	$d\sigma/d\Omega$ [μb/sr]	Δ_{stat} [μb/sr]	Δ_{sys} [μb/sr]	$d\sigma/d\Omega$ [μb/sr]	Δ_{stat} [μb/sr]	Δ_{sys} [μb/sr]	$d\sigma/d\Omega$ [μb/sr]	Δ_{stat} [μb/sr]	Δ_{sys} [μb/sr]	$d\sigma/d\Omega$ [μb/sr]	Δ_{stat} [μb/sr]	Δ_{sys} [μb/sr]
−0.90	0.3352	0.0347	0.0127	0.3316	0.0357	0.0138	0.1980	0.0201	0.0153	0.2164	0.0211	0.0153
−0.70	0.3070	0.0315	0.0127	0.3603	0.0266	0.0138	0.2664	0.0225	0.0153	0.2775	0.0219	0.0153
−0.50	0.3046	0.0167	0.0150	0.3667	0.0248	0.0168	0.2987	0.0210	0.0089	0.2715	0.0189	0.0089
−0.30	0.2968	0.0181	0.0150	0.3790	0.0189	0.0168	0.2102	0.0160	0.0089	0.2573	0.0234	0.0089
−0.10	0.2981	0.0136	0.0152	0.3345	0.0166	0.0116	0.2348	0.0155	0.0109	0.2300	0.0148	0.0109
0.10	0.2940	0.0112	0.0152	0.3026	0.0159	0.0116	0.2260	0.0120	0.0109	0.2541	0.0119	0.0109
0.30	0.3455	0.0122	0.0140	0.3876	0.0163	0.0121	0.2816	0.0152	0.0090	0.3498	0.0123	0.0090
0.50	0.4331	0.0119	0.0140	0.4438	0.0161	0.0121	0.3500	0.0169	0.0090	0.3792	0.0134	0.0090
0.70	0.4266	0.0123	0.0053	0.4973	0.0176	0.0036	0.3447	0.0128	0.0088	0.3739	0.0123	0.0088
0.90	0.2770	0.0175	0.0053	0.3218	0.0223	0.0036	0.2617	0.0207	0.0088	0.3165	0.0196	0.0088

$\cos(\theta^*_{2\pi^0})$	$W=(2034.9\pm5.8)$ MeV			$W=(2046.4\pm5.7)$ MeV			$W=(2057.8\pm5.7)$ MeV			$W=(2069.2\pm5.7)$ MeV		
	$d\sigma/d\Omega$ [μb/sr]	Δ_{stat} [μb/sr]	Δ_{sys} [μb/sr]	$d\sigma/d\Omega$ [μb/sr]	Δ_{stat} [μb/sr]	Δ_{sys} [μb/sr]	$d\sigma/d\Omega$ [μb/sr]	Δ_{stat} [μb/sr]	Δ_{sys} [μb/sr]	$d\sigma/d\Omega$ [μb/sr]	Δ_{stat} [μb/sr]	Δ_{sys} [μb/sr]
−0.90	0.2003	0.0184	0.0106	0.2980	0.0248	0.0088	0.4585	0.0390	0.0088	0.3158	0.0359	0.0250
−0.70	0.2669	0.0173	0.0106	0.2099	0.0192	0.0088	0.2346	0.0314	0.0088	0.2481	0.0196	0.0250
−0.50	0.2921	0.0184	0.0093	0.2175	0.0164	0.0158	0.2612	0.0244	0.0158	0.2715	0.0242	0.0186
−0.30	0.2875	0.0153	0.0093	0.2356	0.0158	0.0158	0.2632	0.0189	0.0158	0.2379	0.0179	0.0186
−0.10	0.2743	0.0145	0.0061	0.2430	0.0128	0.0081	0.2473	0.0150	0.0081	0.2477	0.0124	0.0136
0.10	0.2202	0.0120	0.0061	0.2327	0.0174	0.0081	0.2336	0.0117	0.0081	0.2396	0.0112	0.0136
0.30	0.3285	0.0116	0.0098	0.3231	0.0139	0.0103	0.3339	0.0118	0.0103	0.2983	0.0124	0.0161
0.50	0.3825	0.0127	0.0098	0.3877	0.0126	0.0103	0.3619	0.0134	0.0103	0.3486	0.0151	0.0161
0.70	0.3874	0.0135	0.0135	0.3214	0.0132	0.0168	0.3787	0.0147	0.0168	0.3681	0.0144	0.0205
0.90	0.2784	0.0186	0.0135	0.2383	0.0168	0.0168	0.2784	0.0184	0.0168	0.2550	0.0172	0.0205

$\cos(\theta^*_{2\pi^0})$	$W=(2080.5\pm5.6)$ MeV			$W=(2091.7\pm5.6)$ MeV			$W=(2102.9\pm5.6)$ MeV			$W=(2114.1\pm5.5)$ MeV		
	$d\sigma/d\Omega$ [μb/sr]	Δ_{stat} [μb/sr]	Δ_{sys} [μb/sr]	$d\sigma/d\Omega$ [μb/sr]	Δ_{stat} [μb/sr]	Δ_{sys} [μb/sr]	$d\sigma/d\Omega$ [μb/sr]	Δ_{stat} [μb/sr]	Δ_{sys} [μb/sr]	$d\sigma/d\Omega$ [μb/sr]	Δ_{stat} [μb/sr]	Δ_{sys} [μb/sr]
−0.90	0.3360	0.0369	0.0250	0.3021	0.0380	0.0124	0.3400	0.0337	0.0073	0.3547	0.0298	0.0073
−0.70	0.2705	0.0219	0.0250	0.2901	0.0262	0.0124	0.3186	0.0231	0.0073	0.2820	0.0220	0.0073
−0.50	0.2568	0.0170	0.0186	0.2655	0.0276	0.0147	0.2804	0.0168	0.0077	0.2407	0.0197	0.0077
−0.30	0.2642	0.0191	0.0186	0.2584	0.0145	0.0147	0.1766	0.0186	0.0077	0.2234	0.0138	0.0077
−0.10	0.2389	0.0143	0.0136	0.2351	0.0205	0.0126	0.1902	0.0131	0.0067	0.2031	0.0133	0.0067
0.10	0.2372	0.0106	0.0136	0.2320	0.0163	0.0126	0.2506	0.0128	0.0067	0.2167	0.0103	0.0067
0.30	0.3151	0.0135	0.0161	0.3119	0.0125	0.0102	0.3041	0.0115	0.0090	0.3096	0.0112	0.0090
0.50	0.4036	0.0146	0.0161	0.3739	0.0147	0.0102	0.3445	0.0150	0.0090	0.3618	0.0117	0.0090
0.70	0.3330	0.0133	0.0205	0.3738	0.0145	0.0159	0.3361	0.0132	0.0185	0.3934	0.0134	0.0185
0.90	0.2295	0.0167	0.0205	0.2458	0.0154	0.0159	0.2674	0.0171	0.0185	0.2642	0.0180	0.0185

$\cos(\theta^*_{2\pi^0})$	W=(2125.1±5.5) MeV			W=(2136.1±5.5) MeV			W=(2147.1±5.5) MeV			W=(2158.0±5.4) MeV		
	$d\sigma/d\Omega$ [μb/sr]	Δ_{stat} [μb/sr]	Δ_{sys} [μb/sr]	$d\sigma/d\Omega$ [μb/sr]	Δ_{stat} [μb/sr]	Δ_{sys} [μb/sr]	$d\sigma/d\Omega$ [μb/sr]	Δ_{stat} [μb/sr]	Δ_{sys} [μb/sr]	$d\sigma/d\Omega$ [μb/sr]	Δ_{stat} [μb/sr]	Δ_{sys} [μb/sr]
−0.90	0.2425	0.0299	0.0134	0.2013	0.0251	0.0226	0.4004	0.0310	0.0226	0.2317	0.0197	0.0118
−0.70	0.2309	0.0215	0.0134	0.2369	0.0279	0.0226	0.3309	0.0216	0.0226	0.2680	0.0192	0.0118
−0.50	0.1869	0.0186	0.0161	0.1656	0.0168	0.0194	0.2635	0.0233	0.0194	0.2331	0.0164	0.0064
−0.30	0.2006	0.0139	0.0161	0.1848	0.0176	0.0194	0.2407	0.0261	0.0194	0.2288	0.0116	0.0064
−0.10	0.2105	0.0138	0.0097	0.1750	0.0192	0.0095	0.2872	0.0203	0.0095	0.2211	0.0117	0.0066
0.10	0.2199	0.0201	0.0097	0.1770	0.0110	0.0095	0.2592	0.0178	0.0095	0.2173	0.0146	0.0066
0.30	0.2610	0.0115	0.0095	0.2343	0.0115	0.0099	0.3675	0.0157	0.0099	0.2784	0.0167	0.0096
0.50	0.3013	0.0117	0.0095	0.2207	0.0108	0.0099	0.4230	0.0168	0.0099	0.3635	0.0110	0.0096
0.70	0.3201	0.0120	0.0244	0.2460	0.0133	0.0177	0.4054	0.0152	0.0177	0.3846	0.0107	0.0137
0.90	0.2865	0.0172	0.0244	0.1879	0.0160	0.0177	0.3279	0.0211	0.0177	0.2646	0.0149	0.0137

$\cos(\theta^*_{2\pi^0})$	W=(2168.8±5.4) MeV			W=(2179.6±5.4) MeV			W=(2190.4±5.4) MeV			W=(2201.0±5.3) MeV		
	$d\sigma/d\Omega$ [μb/sr]	Δ_{stat} [μb/sr]	Δ_{sys} [μb/sr]	$d\sigma/d\Omega$ [μb/sr]	Δ_{stat} [μb/sr]	Δ_{sys} [μb/sr]	$d\sigma/d\Omega$ [μb/sr]	Δ_{stat} [μb/sr]	Δ_{sys} [μb/sr]	$d\sigma/d\Omega$ [μb/sr]	Δ_{stat} [μb/sr]	Δ_{sys} [μb/sr]
−0.90	0.2906	0.0227	0.0118	0.2886	0.0405	0.0139	0.2132	0.0184	0.0211	0.2080	0.0236	0.0211
−0.70	0.2992	0.0334	0.0118	0.2502	0.0266	0.0139	0.2220	0.0179	0.0211	0.3265	0.0296	0.0211
−0.50	0.2158	0.0171	0.0064	0.2826	0.0219	0.0041	0.2594	0.0160	0.0146	0.2563	0.0239	0.0146
−0.30	0.1510	0.0126	0.0064	0.2264	0.0177	0.0041	0.1945	0.0116	0.0146	0.1941	0.0145	0.0146
−0.10	0.1804	0.0127	0.0066	0.2059	0.0141	0.0062	0.1907	0.0109	0.0167	0.2263	0.0163	0.0167
0.10	0.2411	0.0137	0.0066	0.2738	0.0149	0.0062	0.2047	0.0107	0.0167	0.2119	0.0163	0.0167
0.30	0.2994	0.0133	0.0096	0.3116	0.0158	0.0190	0.2979	0.0129	0.0165	0.3298	0.0230	0.0165
0.50	0.3381	0.0122	0.0096	0.3405	0.0219	0.0190	0.3299	0.0137	0.0165	0.3426	0.0149	0.0165
0.70	0.3313	0.0141	0.0137	0.3791	0.0151	0.0251	0.3082	0.0152	0.0164	0.3769	0.0145	0.0164
0.90	0.3218	0.0190	0.0137	0.3406	0.0207	0.0251	0.2802	0.0163	0.0164	0.3328	0.0200	0.0164

$\cos(\theta^*_{2\pi^0})$	W=(2211.7±5.3) MeV			W=(2222.2±5.3) MeV			W=(2232.8±5.3) MeV			W=(2243.3±5.2) MeV		
	$d\sigma/d\Omega$ [μb/sr]	Δ_{stat} [μb/sr]	Δ_{sys} [μb/sr]	$d\sigma/d\Omega$ [μb/sr]	Δ_{stat} [μb/sr]	Δ_{sys} [μb/sr]	$d\sigma/d\Omega$ [μb/sr]	Δ_{stat} [μb/sr]	Δ_{sys} [μb/sr]	$d\sigma/d\Omega$ [μb/sr]	Δ_{stat} [μb/sr]	Δ_{sys} [μb/sr]
−0.90	0.3543	0.0342	0.0244	0.2846	0.0429	0.0190	0.2225	0.0224	0.0190	0.3732	0.0512	0.0170
−0.70	0.2439	0.0218	0.0244	0.1686	0.0209	0.0190	0.1565	0.0192	0.0190	0.1928	0.0263	0.0170
−0.50	0.1720	0.0161	0.0111	0.2733	0.0268	0.0091	0.1886	0.0162	0.0091	0.1689	0.0202	0.0199
−0.30	0.1626	0.0161	0.0111	0.1912	0.0251	0.0091	0.1645	0.0131	0.0091	0.1813	0.0175	0.0199
−0.10	0.1826	0.0119	0.0074	0.2133	0.0267	0.0099	0.1749	0.0149	0.0099	0.1450	0.0143	0.0131
0.10	0.2240	0.0185	0.0074	0.2507	0.0177	0.0099	0.2425	0.0133	0.0099	0.1959	0.0205	0.0131
0.30	0.2533	0.0136	0.0092	0.2917	0.0170	0.0148	0.2316	0.0203	0.0148	0.2782	0.0144	0.0094
0.50	0.3097	0.0176	0.0092	0.3637	0.0161	0.0148	0.3151	0.0150	0.0148	0.3013	0.0186	0.0094
0.70	0.3398	0.0123	0.0176	0.4138	0.0291	0.0175	0.3440	0.0157	0.0175	0.3148	0.0248	0.0164
0.90	0.3042	0.0153	0.0176	0.3347	0.0261	0.0175	0.3224	0.0186	0.0175	0.3105	0.0217	0.0164

$\cos(\theta^*_{2\pi^0})$	W=(2253.7±5.2) MeV			W=(2264.1±5.2) MeV		
	$d\sigma/d\Omega$ [μb/sr]	Δ_{stat} [μb/sr]	Δ_{sys} [μb/sr]	$d\sigma/d\Omega$ [μb/sr]	Δ_{stat} [μb/sr]	Δ_{sys} [μb/sr]
−0.90	0.1609	0.0196	0.0170	0.2613	0.0384	0.0319
−0.70	0.2759	0.0302	0.0170	0.2601	0.0324	0.0319
−0.50	0.2291	0.0240	0.0199	0.2464	0.0215	0.0160
−0.30	0.2636	0.0283	0.0199	0.1743	0.0245	0.0160
−0.10	0.2319	0.0212	0.0131	0.2236	0.0203	0.0150
0.10	0.2759	0.0200	0.0131	0.2166	0.0165	0.0150
0.30	0.3499	0.0172	0.0094	0.3101	0.0267	0.0096
0.50	0.3714	0.0281	0.0094	0.3409	0.0277	0.0096
0.70	0.4034	0.0171	0.0164	0.3579	0.0208	0.0125
0.90	0.3421	0.0208	0.0164	0.3063	0.0230	0.0125

E.5.6 $\gamma n \to \pi^0\pi^0 n$ as a Function of W

Angular Distributions

$\cos(\theta^*_{2\pi^0})$	W=(1310.0±10.0) MeV			W=(1330.0±10.0) MeV			W=(1350.0±10.0) MeV			W=(1370.0±10.0) MeV		
	$d\sigma/d\Omega$ [μb/sr]	Δ_{stat} [μb/sr]	Δ_{sys} [μb/sr]	$d\sigma/d\Omega$ [μb/sr]	Δ_{stat} [μb/sr]	Δ_{sys} [μb/sr]	$d\sigma/d\Omega$ [μb/sr]	Δ_{stat} [μb/sr]	Δ_{sys} [μb/sr]	$d\sigma/d\Omega$ [μb/sr]	Δ_{stat} [μb/sr]	Δ_{sys} [μb/sr]
−0.80	0.0961	0.0393	0.0118	0.0705	0.0373	0.0083	0.0396	0.0285	0.0070	0.1197	0.0354	0.0112
−0.40	0.0376	0.0300	0.0140	0.0819	0.0424	0.0300	0.1130	0.0409	0.0115	0.2963	0.0522	0.0157
0.00	0.0400	0.0279	0.0223	0.0605	0.0336	0.0340	0.1453	0.0416	0.0183	0.2129	0.0358	0.0109
0.40	−0.0050	0.0211	0.0033	0.0573	0.0308	0.0360	0.0722	0.0282	0.0131	0.1202	0.0349	0.0119
0.80	−0.0030	0.0294	0.0305	−0.0180	0.0308	0.0030	0.0144	0.0258	0.0008	0.1290	0.0490	0.0290

$\cos(\theta^*_{2\pi^0})$	W=(1390.0±10.0) MeV			W=(1410.0±10.0) MeV			W=(1430.0±10.0) MeV			W=(1450.0±10.0) MeV		
	$d\sigma/d\Omega$ [μb/sr]	Δ_{stat} [μb/sr]	Δ_{sys} [μb/sr]	$d\sigma/d\Omega$ [μb/sr]	Δ_{stat} [μb/sr]	Δ_{sys} [μb/sr]	$d\sigma/d\Omega$ [μb/sr]	Δ_{stat} [μb/sr]	Δ_{sys} [μb/sr]	$d\sigma/d\Omega$ [μb/sr]	Δ_{stat} [μb/sr]	Δ_{sys} [μb/sr]
−0.80	0.3772	0.0960	0.0326	0.3953	0.0824	0.0266	0.4404	0.0864	0.0329	0.7347	0.1080	0.0761
−0.40	0.4562	0.0812	0.0218	0.5881	0.0871	0.0257	0.7044	0.0856	0.0349	0.6526	0.1775	0.0408
0.00	0.4974	0.0599	0.0220	0.6459	0.0767	0.0362	0.5744	0.0610	0.0287	0.7541	0.1508	0.0351
0.40	0.1648	0.0208	0.0187	0.2019	0.0232	0.0267	0.2293	0.0309	0.0165	0.4444	0.0312	0.0357
0.80	0.0336	0.0071	0.0110	0.0408	0.0074	0.0136	0.1543	0.0309	0.0111	0.1078	0.0227	0.0146

$\cos(\theta^*_{2\pi^0})$	$W=(1470.0\pm10.0)$ MeV			$W=(1490.0\pm10.0)$ MeV			$W=(1510.0\pm10.0)$ MeV			$W=(1530.0\pm10.0)$ MeV		
	$d\sigma/d\Omega$	Δ_{stat}	Δ_{sys}	$d\sigma/d\Omega$	Δ_{stat}	Δ_{sys}	$d\sigma/d\Omega$	Δ_{stat}	Δ_{sys}	$d\sigma/d\Omega$	Δ_{stat}	Δ_{sys}
	[μb/sr]	[μb/sr]	[μb/sr]	[μb/sr]	[μb/sr]	[μb/sr]	[μb/sr]	[μb/sr]	[μb/sr]	[μb/sr]	[μb/sr]	[μb/sr]
−0.80	0.8460	0.0796	0.0544	1.0148	0.0569	0.0597	1.2648	0.0694	0.0632	1.0046	0.0753	0.0544
−0.40	0.7790	0.0899	0.0406	0.7979	0.0490	0.0434	1.0385	0.1153	0.0830	0.9225	0.1203	0.1094
0.00	0.9141	0.1226	0.0386	0.7960	0.0784	0.0451	1.0335	0.1048	0.0742	0.8830	0.0917	0.0953
0.40	0.5693	0.0279	0.0312	0.6207	0.0226	0.0333	0.7389	0.0235	0.0436	0.6711	0.0226	0.0456
0.80	0.4256	0.0373	0.0256	0.5207	0.0324	0.0283	0.1551	0.0097	0.0173	0.3806	0.0212	0.0294

$\cos(\theta^*_{2\pi^0})$	$W=(1550.0\pm10.0)$ MeV			$W=(1570.0\pm10.0)$ MeV			$W=(1590.0\pm10.0)$ MeV			$W=(1610.0\pm10.0)$ MeV		
	$d\sigma/d\Omega$	Δ_{stat}	Δ_{sys}	$d\sigma/d\Omega$	Δ_{stat}	Δ_{sys}	$d\sigma/d\Omega$	Δ_{stat}	Δ_{sys}	$d\sigma/d\Omega$	Δ_{stat}	Δ_{sys}
	[μb/sr]	[μb/sr]	[μb/sr]	[μb/sr]	[μb/sr]	[μb/sr]	[μb/sr]	[μb/sr]	[μb/sr]	[μb/sr]	[μb/sr]	[μb/sr]
−0.80	1.0597	0.0648	0.0594	0.9407	0.1061	0.0682	1.0105	0.0777	0.0849	0.8493	0.0781	0.0452
−0.40	0.7393	0.1518	0.1059	0.8213	0.1495	0.0779	0.8675	0.1471	0.0470	0.9187	0.1636	0.0879
0.00	0.8730	0.1517	0.1144	0.8190	0.0853	0.0703	0.6606	0.0908	0.0675	0.9632	0.0583	0.1052
0.40	0.6462	0.0232	0.0516	0.6174	0.0219	0.0433	0.5234	0.0326	0.0408	0.5081	0.0175	0.0455
0.80	0.3198	0.0176	0.0306	0.3200	0.0167	0.0275	0.2657	0.0124	0.0249	0.3223	0.0157	0.0350

$\cos(\theta^*_{2\pi^0})$	$W=(1630.0\pm10.0)$ MeV			$W=(1650.0\pm10.0)$ MeV			$W=(1670.0\pm10.0)$ MeV			$W=(1690.0\pm10.0)$ MeV		
	$d\sigma/d\Omega$	Δ_{stat}	Δ_{sys}	$d\sigma/d\Omega$	Δ_{stat}	Δ_{sys}	$d\sigma/d\Omega$	Δ_{stat}	Δ_{sys}	$d\sigma/d\Omega$	Δ_{stat}	Δ_{sys}
	[μb/sr]	[μb/sr]	[μb/sr]	[μb/sr]	[μb/sr]	[μb/sr]	[μb/sr]	[μb/sr]	[μb/sr]	[μb/sr]	[μb/sr]	[μb/sr]
−0.80	0.9912	0.0742	0.0510	1.0037	0.0748	0.0614	0.8247	0.0663	0.0519	0.7499	0.0307	0.1128
−0.40	0.8103	0.0792	0.0734	0.9061	0.1059	0.1061	0.7246	0.0880	0.0671	0.8442	0.0288	0.0501
0.00	0.7390	0.0609	0.0621	0.7562	0.0583	0.0993	0.8464	0.0690	0.0776	1.0225	0.0270	0.0500
0.40	0.6229	0.0183	0.0416	0.6707	0.0195	0.0557	0.6113	0.0193	0.0476	0.6945	0.0196	0.0433
0.80	0.3822	0.0199	0.0369	0.4483	0.0174	0.0315	0.4942	0.0217	0.0283	0.5218	0.0220	0.0281

$\cos(\theta^*_{2\pi^0})$	$W=(1710.0\pm10.0)$ MeV			$W=(1730.0\pm10.0)$ MeV			$W=(1750.0\pm10.0)$ MeV			$W=(1770.0\pm10.0)$ MeV		
	$d\sigma/d\Omega$	Δ_{stat}	Δ_{sys}	$d\sigma/d\Omega$	Δ_{stat}	Δ_{sys}	$d\sigma/d\Omega$	Δ_{stat}	Δ_{sys}	$d\sigma/d\Omega$	Δ_{stat}	Δ_{sys}
	[μb/sr]	[μb/sr]	[μb/sr]	[μb/sr]	[μb/sr]	[μb/sr]	[μb/sr]	[μb/sr]	[μb/sr]	[μb/sr]	[μb/sr]	[μb/sr]
−0.80	0.5983	0.0268	0.0336	0.5296	0.0317	0.0269	0.3410	0.0200	0.0428	0.3106	0.0206	0.0390
−0.40	0.9329	0.0341	0.0432	0.5935	0.0264	0.0323	0.5857	0.0250	0.0559	0.4949	0.0207	0.0475
0.00	0.8569	0.0283	0.0510	0.9098	0.0284	0.0538	0.5460	0.0194	0.0548	0.5017	0.0172	0.0508
0.40	0.5987	0.0184	0.0492	0.5175	0.0145	0.0369	0.5119	0.0163	0.0555	0.4553	0.0151	0.0489
0.80	0.4009	0.0139	0.0280	0.3221	0.0123	0.0238	0.4180	0.0179	0.0417	0.3332	0.0147	0.0331

$\cos(\theta^*_{2\pi^0})$	$W=(1790.0\pm10.0)$ MeV			$W=(1810.0\pm10.0)$ MeV			$W=(1830.0\pm10.0)$ MeV			$W=(1850.0\pm10.0)$ MeV		
	$d\sigma/d\Omega$	Δ_{stat}	Δ_{sys}	$d\sigma/d\Omega$	Δ_{stat}	Δ_{sys}	$d\sigma/d\Omega$	Δ_{stat}	Δ_{sys}	$d\sigma/d\Omega$	Δ_{stat}	Δ_{sys}
	[μb/sr]	[μb/sr]	[μb/sr]	[μb/sr]	[μb/sr]	[μb/sr]	[μb/sr]	[μb/sr]	[μb/sr]	[μb/sr]	[μb/sr]	[μb/sr]
−0.80	0.2470	0.0148	0.0212	0.2556	0.0115	0.0182	0.2324	0.0135	0.0186	0.2513	0.0135	0.0176
−0.40	0.3363	0.0165	0.0254	0.3387	0.0138	0.0315	0.3583	0.0153	0.0319	0.2637	0.0116	0.0211
0.00	0.4539	0.0149	0.0357	0.4026	0.0122	0.0349	0.4681	0.0134	0.0392	0.4215	0.0181	0.0326
0.40	0.4695	0.0146	0.0418	0.3690	0.0108	0.0306	0.3583	0.0117	0.0286	0.3593	0.0128	0.0281
0.80	0.3364	0.0152	0.0345	0.3137	0.0167	0.0340	0.1454	0.0069	0.0155	0.2588	0.0127	0.0202

$\cos(\theta^*_{2\pi^0})$	$W=(1870.0\pm10.0)$ MeV			$W=(1890.0\pm10.0)$ MeV			$W=(1910.0\pm10.0)$ MeV			$W=(1930.0\pm10.0)$ MeV		
	$d\sigma/d\Omega$	Δ_{stat}	Δ_{sys}	$d\sigma/d\Omega$	Δ_{stat}	Δ_{sys}	$d\sigma/d\Omega$	Δ_{stat}	Δ_{sys}	$d\sigma/d\Omega$	Δ_{stat}	Δ_{sys}
	[μb/sr]	[μb/sr]	[μb/sr]	[μb/sr]	[μb/sr]	[μb/sr]	[μb/sr]	[μb/sr]	[μb/sr]	[μb/sr]	[μb/sr]	[μb/sr]
−0.80	0.3069	0.0148	0.0221	0.2453	0.0150	0.0167	0.2817	0.0141	0.0263	0.2952	0.0171	0.0187
−0.40	0.3271	0.0131	0.0250	0.2944	0.0141	0.0236	0.3036	0.0130	0.0253	0.2989	0.0145	0.0234
0.00	0.3996	0.0147	0.0323	0.3878	0.0144	0.0358	0.3864	0.0149	0.0312	0.3546	0.0143	0.0318
0.40	0.3111	0.0114	0.0244	0.3175	0.0118	0.0274	0.2792	0.0098	0.0227	0.2880	0.0107	0.0222
0.80	0.2699	0.0132	0.0200	0.2186	0.0131	0.0124	0.2337	0.0105	0.0192	0.2250	0.0129	0.0123

$\cos(\theta^*_{2\pi^0})$	$W=(1950.0\pm10.0)$ MeV			$W=(1970.0\pm10.0)$ MeV			$W=(1990.0\pm10.0)$ MeV			$W=(2010.0\pm10.0)$ MeV		
	$d\sigma/d\Omega$	Δ_{stat}	Δ_{sys}	$d\sigma/d\Omega$	Δ_{stat}	Δ_{sys}	$d\sigma/d\Omega$	Δ_{stat}	Δ_{sys}	$d\sigma/d\Omega$	Δ_{stat}	Δ_{sys}
	[μb/sr]	[μb/sr]	[μb/sr]	[μb/sr]	[μb/sr]	[μb/sr]	[μb/sr]	[μb/sr]	[μb/sr]	[μb/sr]	[μb/sr]	[μb/sr]
−0.80	0.3084	0.0143	0.0198	0.2408	0.0130	0.0164	0.2425	0.0138	0.0151	0.2055	0.0119	0.0176
−0.40	0.2932	0.0132	0.0217	0.2929	0.0128	0.0207	0.3339	0.0137	0.0200	0.2465	0.0118	0.0176
0.00	0.3495	0.0143	0.0299	0.3423	0.0148	0.0250	0.3062	0.0118	0.0202	0.2716	0.0114	0.0176
0.40	0.2950	0.0118	0.0241	0.2818	0.0108	0.0200	0.2732	0.0104	0.0167	0.2617	0.0097	0.0167
0.80	0.2526	0.0107	0.0167	0.2228	0.0103	0.0137	0.2551	0.0127	0.0134	0.2087	0.0114	0.0125

$\cos(\theta^*_{2\pi^0})$	$W=(2030.0\pm10.0)$ MeV			$W=(2050.0\pm10.0)$ MeV			$W=(2070.0\pm10.0)$ MeV			$W=(2090.0\pm10.0)$ MeV		
	$d\sigma/d\Omega$	Δ_{stat}	Δ_{sys}	$d\sigma/d\Omega$	Δ_{stat}	Δ_{sys}	$d\sigma/d\Omega$	Δ_{stat}	Δ_{sys}	$d\sigma/d\Omega$	Δ_{stat}	Δ_{sys}
	[μb/sr]	[μb/sr]	[μb/sr]	[μb/sr]	[μb/sr]	[μb/sr]	[μb/sr]	[μb/sr]	[μb/sr]	[μb/sr]	[μb/sr]	[μb/sr]
−0.80	0.2009	0.0119	0.0127	0.2084	0.0110	0.0131	0.1675	0.0104	0.0125	0.1962	0.0110	0.0112
−0.40	0.2500	0.0115	0.0147	0.2271	0.0100	0.0154	0.2874	0.0126	0.0161	0.1778	0.0102	0.0106
0.00	0.2535	0.0100	0.0155	0.2352	0.0102	0.0164	0.2482	0.0106	0.0151	0.2287	0.0118	0.0128
0.40	0.2794	0.0105	0.0167	0.2886	0.0103	0.0183	0.2548	0.0092	0.0171	0.2450	0.0110	0.0131
0.80	0.2281	0.0121	0.0132	0.2478	0.0115	0.0150	0.2277	0.0107	0.0154	0.2563	0.0131	0.0143

$\cos(\theta^*_{2\pi^0})$	$W=(2110.0\pm10.0)$ MeV			$W=(2130.0\pm10.0)$ MeV			$W=(2150.0\pm10.0)$ MeV			$W=(2170.0\pm10.0)$ MeV		
	$d\sigma/d\Omega$	Δ_{stat}	Δ_{sys}	$d\sigma/d\Omega$	Δ_{stat}	Δ_{sys}	$d\sigma/d\Omega$	Δ_{stat}	Δ_{sys}	$d\sigma/d\Omega$	Δ_{stat}	Δ_{sys}
	[μb/sr]	[μb/sr]	[μb/sr]	[μb/sr]	[μb/sr]	[μb/sr]	[μb/sr]	[μb/sr]	[μb/sr]	[μb/sr]	[μb/sr]	[μb/sr]
−0.80	0.2363	0.0115	0.0100	0.1518	0.0100	0.0091	0.2354	0.0119	0.0362	0.1717	0.0113	0.0110
−0.40	0.1539	0.0089	0.0080	0.1889	0.0112	0.0102	0.1647	0.0085	0.0110	0.1514	0.0099	0.0081
0.00	0.2011	0.0090	0.0110	0.1840	0.0114	0.0110	0.1570	0.0095	0.0087	0.1818	0.0103	0.0095
0.40	0.2465	0.0080	0.0127	0.2146	0.0080	0.0123	0.2363	0.0087	0.0133	0.2187	0.0096	0.0129
0.80	0.2781	0.0129	0.0140	0.2539	0.0123	0.0145	0.2605	0.0101	0.0150	0.2388	0.0125	0.0137

$\cos(\theta^*_{2\pi^0})$	W=(2190.0±10.0) MeV			W=(2210.0±10.0) MeV			W=(2230.0±10.0) MeV			W=(2250.0±10.0) MeV		
	$d\sigma/d\Omega$ [μb/sr]	Δ_{stat} [μb/sr]	Δ_{sys} [μb/sr]	$d\sigma/d\Omega$ [μb/sr]	Δ_{stat} [μb/sr]	Δ_{sys} [μb/sr]	$d\sigma/d\Omega$ [μb/sr]	Δ_{stat} [μb/sr]	Δ_{sys} [μb/sr]	$d\sigma/d\Omega$ [μb/sr]	Δ_{stat} [μb/sr]	Δ_{sys} [μb/sr]
−0.80	0.1544	0.0106	0.0172	0.2400	0.0184	0.0227	0.1412	0.0141	0.0083	0.2142	0.0157	0.0170
−0.40	0.1583	0.0117	0.0100	0.1118	0.0102	0.0072	0.1310	0.0093	0.0086	0.0981	0.0100	0.0059
0.00	0.2223	0.0124	0.0109	0.1737	0.0125	0.0098	0.1799	0.0128	0.0118	0.1365	0.0164	0.0073
0.40	0.1916	0.0078	0.0106	0.2101	0.0082	0.0124	0.1961	0.0113	0.0114	0.2927	0.0133	0.0159
0.80	0.2503	0.0109	0.0174	0.2748	0.0128	0.0157	0.3602	0.0201	0.0183	0.2696	0.0149	0.0152

$\cos(\theta^*_{2\pi^0})$	W=(2270.0±10.0) MeV			W=(2290.0±10.0) MeV		
	$d\sigma/d\Omega$ [μb/sr]	Δ_{stat} [μb/sr]	Δ_{sys} [μb/sr]	$d\sigma/d\Omega$ [μb/sr]	Δ_{stat} [μb/sr]	Δ_{sys} [μb/sr]
−0.80	0.1875	0.0210	0.0184	0.2692	0.0493	0.0121
−0.40	0.1748	0.0191	0.0101	0.1703	0.0319	0.0081
0.00	0.2231	0.0254	0.0108	0.1803	0.0235	0.0094
0.40	0.2362	0.0175	0.0126	0.1983	0.0161	0.0107
0.80	0.3296	0.0237	0.0207	0.2029	0.0180	0.0153

E.6 Pol. Results for $\pi^0\pi^0$ from CBELSA/TAPS Data

E.6.1 Observables for $\gamma d \to \pi^0\pi^0 p(n)$ as a Function of E_γ

E_γ [MeV]	ΔE_γ [MeV]	E	Δ_{stat}	Δ_{sys}	$\sigma_{1/2}$ [μb]	Δ_{stat} [μb]	Δ_{sys} [μb]	$\sigma_{3/2}$ [μb]	Δ_{stat} [μb]	Δ_{sys} [μb]
440.0	40.0	−6.1453	357.2814	3.0219	−1.6507	114.6205	6.5600	2.2923	114.6205	7.6868
520.0	40.0	−0.4584	1.5296	0.1291	0.7007	1.9987	0.7895	1.8867	1.9987	0.9572
600.0	40.0	−0.3657	0.1970	0.0364	2.4236	0.7820	0.1844	5.2177	0.7820	0.3557
680.0	40.0	−0.3630	0.1392	0.0349	3.6307	0.8316	0.2702	7.7678	0.8316	0.5374
760.0	40.0	−0.4127	0.0805	0.0489	4.4263	0.6307	0.5023	10.6470	0.6307	0.7101
840.0	40.0	−0.2212	0.0846	0.0333	5.0531	0.5729	0.4705	7.9242	0.5729	0.5513
920.0	40.0	−0.2033	0.0836	0.0242	4.3756	0.4858	0.2887	6.6090	0.4858	0.4760
1000.0	40.0	−0.1530	0.0756	0.0244	5.4003	0.5065	0.4740	7.3515	0.5065	0.7077
1080.0	40.0	0.2145	0.0667	0.0236	9.2111	0.5335	0.5975	5.9569	0.5335	0.4704
1160.0	40.0	0.1731	0.0584	0.0196	8.5762	0.4451	0.5328	6.0456	0.4451	0.3825
1240.0	40.0	0.1684	0.0702	0.0152	7.2736	0.4402	0.4449	5.1769	0.4402	0.3184
1320.0	40.0	0.1625	0.0636	0.0181	6.3843	0.3519	0.4831	4.5996	0.3519	0.3317
1400.0	40.0	0.2035	0.0728	0.0205	5.8300	0.3557	0.3612	3.8581	0.3557	0.2448
1480.0	40.0	0.0114	0.0625	0.0136	4.9091	0.3062	0.3289	4.7984	0.3062	0.2993
1560.0	40.0	0.0810	0.0676	0.0086	4.9022	0.3101	0.3790	4.1676	0.3101	0.3157
1640.0	40.0	0.0698	0.0670	0.0140	4.3746	0.2767	0.4982	3.8041	0.2767	0.4169
1720.0	40.0	0.1162	0.0724	0.0172	4.1131	0.2695	0.3632	3.2569	0.2695	0.2724
1800.0	40.0	0.1027	0.0712	0.0095	3.9666	0.2586	0.3576	3.2277	0.2586	0.2947
1880.0	40.0	0.2399	0.0762	0.0167	4.0583	0.2519	0.2459	2.4878	0.2519	0.1518
1960.0	40.0	0.0875	0.0824	0.0129	3.5060	0.2688	0.2618	2.9416	0.2688	0.2079
2040.0	40.0	0.1845	0.0742	0.0148	3.7880	0.2394	0.3009	2.6081	0.2394	0.2101
2120.0	40.0	0.1378	0.0779	0.0165	3.5972	0.2484	0.2691	2.7260	0.2484	0.1935
2200.0	40.0	0.3148	0.0838	0.0319	4.3149	0.2785	0.4440	2.2487	0.2785	0.2666
2280.0	40.0	0.1261	0.1331	0.0159	3.4787	0.4140	0.2502	2.6997	0.4140	0.2240
2360.0	40.0	0.0000	0.0000	0.0000	0.0000	0.0000	0.0000	0.0000	0.0000	0.0000

E.6.2 Observables for $\gamma d \to \pi^0\pi^0 p(n)$ as a Function of W

W [MeV]	ΔW [MeV]	E	Δ_{stat}	Δ_{sys}	$\sigma_{1/2}$ [μb]	Δ_{stat} [μb]	Δ_{sys} [μb]	$\sigma_{3/2}$ [μb]	Δ_{stat} [μb]	Δ_{sys} [μb]
1320.0	20.0	8.8832	20.0958	3.6291	3.8213	8.6906	1.6743	−3.0480	8.6906	1.2183
1360.0	20.0	−0.3021	1.1155	0.0604	1.2687	2.0539	0.5660	2.3670	2.0539	0.7624
1400.0	20.0	−0.4565	0.1720	0.1375	2.9633	1.0487	0.9808	7.9408	1.0487	1.4732
1440.0	20.0	−0.3223	0.1276	0.0744	4.6603	0.9201	0.9232	9.0939	0.9201	1.1549
1480.0	20.0	−0.1543	0.1021	0.0478	6.8473	0.8622	0.9459	9.3456	0.8622	0.9307
1520.0	20.0	−0.4524	0.0882	0.0449	4.2205	0.7096	0.4708	11.1949	0.7096	0.7711
1560.0	20.0	−0.2831	0.0891	0.0501	4.7051	0.6157	0.6451	8.4207	0.6157	0.7666
1600.0	20.0	−0.1019	0.0905	0.0206	4.9417	0.5436	0.3161	6.0630	0.5436	0.3910
1640.0	20.0	−0.1518	0.0801	0.0200	5.2015	0.5190	0.3417	7.0637	0.5190	0.5044
1680.0	20.0	0.0113	0.0722	0.0178	7.4327	0.5500	0.5141	7.2671	0.5500	0.5849
1720.0	20.0	0.1812	0.0657	0.0199	9.0679	0.5297	0.5683	6.2855	0.5297	0.4509
1760.0	20.0	0.1208	0.0681	0.0234	7.3547	0.4595	0.4930	5.7690	0.4595	0.4771
1800.0	20.0	0.2632	0.0664	0.0245	7.4732	0.3958	0.5272	4.3594	0.3958	0.2942
1840.0	20.0	0.1536	0.0687	0.0168	5.9442	0.3570	0.3625	4.3615	0.3570	0.2883
1880.0	20.0	0.0511	0.0653	0.0196	5.2782	0.3310	0.3981	4.7654	0.3310	0.3192
1920.0	20.0	0.1166	0.0655	0.0155	5.1151	0.3032	0.3334	4.0472	0.3032	0.2505
1960.0	20.0	0.0228	0.0638	0.0149	4.5040	0.2838	0.4018	4.3029	0.2838	0.3478
2000.0	20.0	0.0220	0.0683	0.0065	3.9165	0.2643	0.3353	3.7477	0.2643	0.3092
2040.0	20.0	0.1964	0.0689	0.0210	4.2908	0.2500	0.3696	2.8818	0.2500	0.2436
2080.0	20.0	0.2182	0.0716	0.0155	4.0658	0.2416	0.2535	2.6095	0.2416	0.1603
2120.0	20.0	0.1190	0.0706	0.0093	3.7332	0.2381	0.2733	2.9390	0.2381	0.2253
2160.0	20.0	0.2030	0.0751	0.0177	3.6989	0.2331	0.3270	2.4508	0.2331	0.2271
2200.0	20.0	0.0652	0.0807	0.0067	3.3218	0.2539	0.2000	2.9152	0.2539	0.1778
2240.0	20.0	0.3958	0.1025	0.0311	4.5034	0.3342	0.3547	1.9492	0.3342	0.1668
2280.0	20.0	0.3476	0.1625	0.0427	4.9238	0.5988	0.5226	2.3839	0.5988	0.4043

Angular Distributions

$\cos(\theta^*_{2\pi^0})$	$W=(1320.0\pm20.0)$ MeV			$W=(1360.0\pm20.0)$ MeV			$W=(1400.0\pm20.0)$ MeV			$W=(1440.0\pm20.0)$ MeV		
	E	Δ_{stat}	Δ_{sys}	E	Δ_{stat}	Δ_{sys}	E	Δ_{stat}	Δ_{sys}	E	Δ_{stat}	Δ_{sys}
−0.80	−14.6627	−10.4248	4.8994	2.2852	1.6252	0.8234	0.8592	0.6109	0.2551	−0.2396	−0.4041	0.0942
−0.40	3.0002	12.4185	1.2574	−3.0156	−1.4665	0.9340	−1.4779	−0.3405	0.2269	−0.7466	−0.3170	0.1395
0.00	−6.9690	−34.9721	3.3814	3.3059	2.1718	1.1521	−0.7173	−0.5167	0.1072	−0.7427	−0.2981	0.0446
0.40	−163.3718	−869.2353	82.6349	−0.7878	−9.2757	0.3643	−0.6005	−0.5847	0.0904	−0.5642	−0.2725	0.1117
0.80	−86.2754	−499.5066	42.8534	−0.3445	10.1190	0.2085	−0.6602	−0.5805	0.0817	0.1988	0.5726	0.0549

$\cos(\theta^*_{2\pi^0})$	$W=(1480.0\pm20.0)$ MeV			$W=(1520.0\pm20.0)$ MeV			$W=(1560.0\pm20.0)$ MeV			$W=(1600.0\pm20.0)$ MeV		
	E	Δ_{stat}	Δ_{sys}	E	Δ_{stat}	Δ_{sys}	E	Δ_{stat}	Δ_{sys}	E	Δ_{stat}	Δ_{sys}
−0.80	−0.1524	−0.2044	0.0707	−0.0183	−0.1928	0.0226	−0.2065	−0.2139	0.0300	−0.2058	−0.2247	0.0639
−0.40	0.2140	0.1942	0.0191	−0.9444	−0.2010	0.2198	−0.2366	−0.1878	0.0097	−0.3263	−0.2297	0.0362
0.00	−0.5472	−0.2145	0.0554	−0.6277	−0.1629	0.0668	−0.5410	−0.1907	0.0490	0.2069	0.1724	0.0547
0.40	−0.2153	−0.1730	0.1031	−0.5274	−0.1386	0.1156	−0.1260	−0.1368	0.0698	−0.1837	−0.1284	0.0490
0.80	−0.3032	−0.6852	0.1955	−0.2434	−0.6515	0.0809	0.0928	0.5430	0.3351	−0.2596	−0.3033	0.0128

$\cos(\theta^*_{2\pi^0})$	$W=(1640.0\pm20.0)$ MeV			$W=(1680.0\pm20.0)$ MeV			$W=(1720.0\pm20.0)$ MeV			$W=(1760.0\pm20.0)$ MeV		
	E	Δ_{stat}	Δ_{sys}	E	Δ_{stat}	Δ_{sys}	E	Δ_{stat}	Δ_{sys}	E	Δ_{stat}	Δ_{sys}
−0.80	0.0847	0.1836	0.0099	−0.3739	−0.1435	0.0462	0.0589	0.1348	0.0107	−0.3824	−0.1965	0.0565
−0.40	0.2400	0.1505	0.0127	0.0751	0.1309	0.0139	0.0723	0.1551	0.0210	−0.0667	−0.1266	0.0263
0.00	−0.1162	−0.1668	0.0153	0.2857	0.1598	0.0489	0.7248	0.1399	0.0751	0.4132	0.1016	0.1096
0.40	−0.3317	−0.0860	0.0150	−0.0159	−0.0753	0.0133	0.1180	0.0753	0.0224	0.2013	0.0744	0.0267
0.80	−0.1370	−0.2188	0.0092	−0.0350	−0.1528	0.0145	0.0732	0.1492	0.0262	0.1144	0.0966	0.0429

$\cos(\theta^*_{2\pi^0})$	$W=(1800.0\pm20.0)$ MeV			$W=(1840.0\pm20.0)$ MeV			$W=(1880.0\pm20.0)$ MeV			$W=(1920.0\pm20.0)$ MeV		
	E	Δ_{stat}	Δ_{sys}	E	Δ_{stat}	Δ_{sys}	E	Δ_{stat}	Δ_{sys}	E	Δ_{stat}	Δ_{sys}
−0.80	−0.0590	−0.1708	0.0058	−0.1648	−0.1914	0.0528	−0.1265	−0.1813	0.0084	−1.2314	−0.1560	0.3446
−0.40	0.0271	0.1045	0.1144	−0.2393	−0.1069	0.0410	−0.2640	−0.1143	0.0607	0.1368	0.1174	0.0423
0.00	0.5932	0.1161	0.1045	0.3762	0.1244	0.0189	0.2747	0.1164	0.0235	0.1677	0.1131	0.0107
0.40	0.1970	0.0927	0.0284	0.3119	0.0920	0.0161	0.1628	0.0871	0.0182	0.3113	0.0859	0.0224
0.80	0.2306	0.1041	0.0401	−0.0101	−0.1076	0.0015	−0.1016	−0.1104	0.0223	−0.0040	−0.1005	0.0009

$\cos(\theta^*_{2\pi^0})$	$W=(1960.0\pm20.0)$ MeV			$W=(2000.0\pm20.0)$ MeV			$W=(2040.0\pm20.0)$ MeV			$W=(2080.0\pm20.0)$ MeV		
	E	Δ_{stat}	Δ_{sys}	E	Δ_{stat}	Δ_{sys}	E	Δ_{stat}	Δ_{sys}	E	Δ_{stat}	Δ_{sys}
−0.80	−0.2648	−0.1387	0.0290	−0.2852	−0.1254	0.0797	−0.1121	−0.1205	0.0823	0.3623	0.1222	0.0964
−0.40	0.0648	0.1007	0.0143	−0.3353	−0.1068	0.0492	−0.1146	−0.1064	0.0828	−0.1473	−0.1118	0.0129
0.00	0.1297	0.1019	0.0398	0.2298	0.1032	0.0643	−0.1173	−0.1139	0.0311	0.1992	0.1063	0.0470
0.40	0.0262	0.0843	0.0422	0.0807	0.0831	0.0178	0.5815	0.0788	0.0568	0.4096	0.0787	0.0388
0.80	−0.0481	−0.1046	0.0076	0.0773	0.1034	0.0139	0.2952	0.1003	0.0515	0.1223	0.1032	0.0199

$\cos(\theta^*_{2\pi^0})$	$W=(2120.0\pm20.0)$ MeV			$W=(2160.0\pm20.0)$ MeV			$W=(2200.0\pm20.0)$ MeV			$W=(2240.0\pm20.0)$ MeV		
	E	Δ_{stat}	Δ_{sys}	E	Δ_{stat}	Δ_{sys}	E	Δ_{stat}	Δ_{sys}	E	Δ_{stat}	Δ_{sys}
−0.80	0.2684	0.1232	0.0234	−0.1193	−0.1260	0.0393	0.0582	0.1334	0.0392	−0.3883	−0.1742	0.2187
−0.40	−0.0754	−0.1182	0.0203	0.3412	0.1092	0.0519	0.0998	0.1370	0.0324	−0.0594	−0.1465	0.0219
0.00	0.0400	0.1356	0.0368	0.3682	0.1443	0.1127	−0.1940	−0.1461	0.0139	0.0364	0.1856	0.0352
0.40	0.0180	0.0839	0.0147	0.2649	0.0803	0.0410	0.1168	0.0872	0.0302	0.4846	0.1268	0.0811
0.80	0.2050	0.0964	0.0336	0.0761	0.0935	0.0188	0.1138	0.0954	0.0157	0.5913	0.1232	0.0912

$\cos(\theta^*_{2\pi^0})$	$W=(2280.0\pm20.0)$ MeV		
	E	Δ_{stat}	Δ_{sys}
−0.80	0.4711	0.2498	0.0459
−0.40	0.1081	0.2663	0.0310
0.00	0.1582	0.2560	0.0267
0.40	0.6510	0.2379	0.1060
0.80	0.2567	0.1879	0.0525

$\cos(\theta^*_{2\pi^0})$	$W=(1320.0\pm20.0)$ MeV			$W=(1360.0\pm20.0)$ MeV			$W=(1400.0\pm20.0)$ MeV			$W=(1440.0\pm20.0)$ MeV		
	$d\sigma_{1/2}/d\Omega$ [μb/sr]	Δ_{stat} [μb/sr]	Δ_{sys} [μb/sr]	$d\sigma_{1/2}/d\Omega$ [μb/sr]	Δ_{stat} [μb/sr]	Δ_{sys} [μb/sr]	$d\sigma_{1/2}/d\Omega$ [μb/sr]	Δ_{stat} [μb/sr]	Δ_{sys} [μb/sr]	$d\sigma_{1/2}/d\Omega$ [μb/sr]	Δ_{stat} [μb/sr]	Δ_{sys} [μb/sr]
−0.80	−0.3916	0.3310	0.1374	0.3956	0.2016	0.2090	0.3326	0.1133	0.1520	0.2287	0.1305	0.1728
−0.40	0.1619	0.5041	0.1595	−0.2867	0.2173	0.1328	−0.1222	0.0922	0.0580	0.0974	0.1308	0.0701
0.00	−0.2432	1.4340	0.5639	0.5345	0.2801	0.2229	0.0644	0.1205	0.0486	0.0986	0.1224	0.0262
0.40	7.4241	16.7393	5.7691	0.0169	0.7409	0.4916	0.1522	0.2251	0.0387	0.2386	0.1522	0.0753
0.80	−7.6493	22.4053	6.7604	0.1683	2.6012	1.3761	0.3826	0.6825	0.1852	1.3429	0.6459	0.0978

$\cos(\theta^*_{2\pi^0})$	$W=(1480.0\pm20.0)$ MeV			$W=(1520.0\pm20.0)$ MeV			$W=(1560.0\pm20.0)$ MeV			$W=(1600.0\pm20.0)$ MeV		
	$d\sigma_{1/2}/d\Omega$ [μb/sr]	Δ_{stat} [μb/sr]	Δ_{sys} [μb/sr]	$d\sigma_{1/2}/d\Omega$ [μb/sr]	Δ_{stat} [μb/sr]	Δ_{sys} [μb/sr]	$d\sigma_{1/2}/d\Omega$ [μb/sr]	Δ_{stat} [μb/sr]	Δ_{sys} [μb/sr]	$d\sigma_{1/2}/d\Omega$ [μb/sr]	Δ_{stat} [μb/sr]	Δ_{sys} [μb/sr]
−0.80	0.6531	0.1622	0.0836	0.8118	0.1635	0.0948	0.5623	0.1567	0.1154	0.4382	0.1415	0.1718
−0.40	0.8293	0.1482	0.0363	0.0365	0.1482	0.1485	0.4521	0.1238	0.0076	0.2724	0.1034	0.0571
0.00	0.2402	0.1271	0.0319	0.2230	0.1077	0.0484	0.2041	0.0921	0.0229	0.4718	0.0748	0.0240
0.40	0.5311	0.1180	0.1347	0.2922	0.0863	0.0911	0.4428	0.0697	0.0808	0.3746	0.0594	0.0438
0.80	0.3905	0.3855	0.4442	0.2768	0.2388	0.1736	0.3926	0.1954	0.1112	0.2839	0.1168	0.0185

$\cos(\theta^*_{2\pi^0})$	$W=(1640.0\pm20.0)$ MeV			$W=(1680.0\pm20.0)$ MeV			$W=(1720.0\pm20.0)$ MeV			$W=(1760.0\pm20.0)$ MeV		
	$d\sigma_{1/2}/d\Omega$ [μb/sr]	$\Delta_{\rm stat}$ [μb/sr]	$\Delta_{\rm sys}$ [μb/sr]	$d\sigma_{1/2}/d\Omega$ [μb/sr]	$\Delta_{\rm stat}$ [μb/sr]	$\Delta_{\rm sys}$ [μb/sr]	$d\sigma_{1/2}/d\Omega$ [μb/sr]	$\Delta_{\rm stat}$ [μb/sr]	$\Delta_{\rm sys}$ [μb/sr]	$d\sigma_{1/2}/d\Omega$ [μb/sr]	$\Delta_{\rm stat}$ [μb/sr]	$\Delta_{\rm sys}$ [μb/sr]
−0.80	0.6632	0.1182	0.0993	0.4233	0.1020	0.0930	0.7198	0.0964	0.0165	0.2755	0.0917	0.0935
−0.40	0.5553	0.0818	0.0261	0.5193	0.0720	0.0307	0.4298	0.0739	0.0655	0.3688	0.0586	0.0102
0.00	0.2907	0.0618	0.0590	0.5275	0.0746	0.0433	0.8120	0.0803	0.0282	0.7456	0.0543	0.0623
0.40	0.3742	0.0487	0.0174	0.6872	0.0531	0.0164	0.8467	0.0577	0.0614	0.7433	0.0466	0.0168
0.80	0.4246	0.1081	0.0499	0.6337	0.1009	0.0795	0.8004	0.1119	0.0468	0.6947	0.0611	0.0625

$\cos(\theta^*_{2\pi^0})$	$W=(1800.0\pm20.0)$ MeV			$W=(1840.0\pm20.0)$ MeV			$W=(1880.0\pm20.0)$ MeV			$W=(1920.0\pm20.0)$ MeV		
	$d\sigma_{1/2}/d\Omega$ [μb/sr]	$\Delta_{\rm stat}$ [μb/sr]	$\Delta_{\rm sys}$ [μb/sr]	$d\sigma_{1/2}/d\Omega$ [μb/sr]	$\Delta_{\rm stat}$ [μb/sr]	$\Delta_{\rm sys}$ [μb/sr]	$d\sigma_{1/2}/d\Omega$ [μb/sr]	$\Delta_{\rm stat}$ [μb/sr]	$\Delta_{\rm sys}$ [μb/sr]	$d\sigma_{1/2}/d\Omega$ [μb/sr]	$\Delta_{\rm stat}$ [μb/sr]	$\Delta_{\rm sys}$ [μb/sr]
−0.80	0.3871	0.0711	0.0025	0.2928	0.0679	0.0329	0.2962	0.0623	0.0125	−0.0715	0.0503	0.1293
−0.40	0.4525	0.0470	0.0929	0.2863	0.0411	0.0380	0.2728	0.0432	0.0488	0.3761	0.0395	0.0669
0.00	0.7146	0.0528	0.1049	0.5218	0.0477	0.0285	0.4568	0.0422	0.0389	0.3715	0.0365	0.0192
0.40	0.6169	0.0482	0.0152	0.6227	0.0442	0.0198	0.5403	0.0410	0.0289	0.5601	0.0373	0.0070
0.80	0.6623	0.0566	0.0193	0.4648	0.0511	0.0579	0.4181	0.0521	0.0220	0.4359	0.0448	0.0458

$\cos(\theta^*_{2\pi^0})$	$W=(1960.0\pm20.0)$ MeV			$W=(2000.0\pm20.0)$ MeV			$W=(2040.0\pm20.0)$ MeV			$W=(2080.0\pm20.0)$ MeV		
	$d\sigma_{1/2}/d\Omega$ [μb/sr]	$\Delta_{\rm stat}$ [μb/sr]	$\Delta_{\rm sys}$ [μb/sr]	$d\sigma_{1/2}/d\Omega$ [μb/sr]	$\Delta_{\rm stat}$ [μb/sr]	$\Delta_{\rm sys}$ [μb/sr]	$d\sigma_{1/2}/d\Omega$ [μb/sr]	$\Delta_{\rm stat}$ [μb/sr]	$\Delta_{\rm sys}$ [μb/sr]	$d\sigma_{1/2}/d\Omega$ [μb/sr]	$\Delta_{\rm stat}$ [μb/sr]	$\Delta_{\rm sys}$ [μb/sr]
−0.80	0.2299	0.0444	0.0215	0.2059	0.0373	0.0516	0.2436	0.0342	0.0221	0.3519	0.0327	0.0142
−0.40	0.3631	0.0350	0.0692	0.1897	0.0312	0.0324	0.2343	0.0288	0.0592	0.1902	0.0256	0.0193
0.00	0.3477	0.0318	0.0611	0.3160	0.0270	0.0643	0.2006	0.0263	0.0134	0.2549	0.0231	0.0441
0.40	0.3908	0.0326	0.0371	0.3561	0.0279	0.0146	0.4855	0.0249	0.0583	0.4251	0.0243	0.0173
0.80	0.3901	0.0436	0.0541	0.3931	0.0384	0.0592	0.4582	0.0362	0.0704	0.3732	0.0349	0.0330

$\cos(\theta^*_{2\pi^0})$	$W=(2120.0\pm20.0)$ MeV			$W=(2160.0\pm20.0)$ MeV			$W=(2200.0\pm20.0)$ MeV			$W=(2240.0\pm20.0)$ MeV		
	$d\sigma_{1/2}/d\Omega$ [μb/sr]	$\Delta_{\rm stat}$ [μb/sr]	$\Delta_{\rm sys}$ [μb/sr]	$d\sigma_{1/2}/d\Omega$ [μb/sr]	$\Delta_{\rm stat}$ [μb/sr]	$\Delta_{\rm sys}$ [μb/sr]	$d\sigma_{1/2}/d\Omega$ [μb/sr]	$\Delta_{\rm stat}$ [μb/sr]	$\Delta_{\rm sys}$ [μb/sr]	$d\sigma_{1/2}/d\Omega$ [μb/sr]	$\Delta_{\rm stat}$ [μb/sr]	$\Delta_{\rm sys}$ [μb/sr]
−0.80	0.3188	0.0323	0.0050	0.1942	0.0288	0.0140	0.2311	0.0302	0.0151	0.1244	0.0365	0.0478
−0.40	0.2291	0.0298	0.0371	0.2731	0.0229	0.0396	0.2199	0.0280	0.0177	0.1904	0.0309	0.0121
0.00	0.2041	0.0270	0.0278	0.2805	0.0300	0.0620	0.1379	0.0254	0.0107	0.2105	0.0384	0.0526
0.40	0.3054	0.0256	0.0140	0.3572	0.0231	0.0233	0.3307	0.0263	0.0349	0.4478	0.0390	0.0623
0.80	0.4000	0.0326	0.0743	0.3355	0.0297	0.0556	0.3957	0.0345	0.0704	0.5941	0.0469	0.0859

$\cos(\theta^*_{2\pi^0})$	$W=(2280.0\pm20.0)$ MeV		
	$d\sigma_{1/2}/d\Omega$ [μb/sr]	$\Delta_{\rm stat}$ [μb/sr]	$\Delta_{\rm sys}$ [μb/sr]
−0.80	0.3408	0.0600	0.0295
−0.40	0.2399	0.0591	0.0078
0.00	0.2511	0.0576	0.0086
0.40	0.5457	0.0795	0.0495
0.80	0.5759	0.0872	0.1825

$\cos(\theta^*_{2\pi^0})$	$W=(1320.0\pm20.0)$ MeV			$W=(1360.0\pm20.0)$ MeV			$W=(1400.0\pm20.0)$ MeV			$W=(1440.0\pm20.0)$ MeV		
	$d\sigma_{3/2}/d\Omega$ [μb/sr]	$\Delta_{\rm stat}$ [μb/sr]	$\Delta_{\rm sys}$ [μb/sr]	$d\sigma_{3/2}/d\Omega$ [μb/sr]	$\Delta_{\rm stat}$ [μb/sr]	$\Delta_{\rm sys}$ [μb/sr]	$d\sigma_{3/2}/d\Omega$ [μb/sr]	$\Delta_{\rm stat}$ [μb/sr]	$\Delta_{\rm sys}$ [μb/sr]	$d\sigma_{3/2}/d\Omega$ [μb/sr]	$\Delta_{\rm stat}$ [μb/sr]	$\Delta_{\rm sys}$ [μb/sr]
−0.80	0.4489	0.3310	0.1644	−0.1548	0.2016	0.1456	0.0252	0.1133	0.1147	0.3729	0.1305	0.1877
−0.40	−0.0809	0.5041	0.1048	0.5711	0.2173	0.2565	0.6337	0.0922	0.1147	0.6715	0.1308	0.0610
0.00	0.3247	1.4340	0.6737	−0.2862	0.2801	0.1428	0.3913	0.1205	0.0908	0.6681	0.1224	0.0602
0.40	−7.5156	16.7393	3.7783	0.1426	0.7409	0.5990	0.6096	0.2251	0.0355	0.8563	0.1522	0.1185
0.80	7.8287	22.4053	10.6044	0.3452	2.6012	1.7357	1.8694	0.6825	0.2772	0.8976	0.6459	0.0602

$\cos(\theta^*_{2\pi^0})$	$W=(1480.0\pm20.0)$ MeV			$W=(1520.0\pm20.0)$ MeV			$W=(1560.0\pm20.0)$ MeV			$W=(1600.0\pm20.0)$ MeV		
	$d\sigma_{3/2}/d\Omega$ [μb/sr]	$\Delta_{\rm stat}$ [μb/sr]	$\Delta_{\rm sys}$ [μb/sr]	$d\sigma_{3/2}/d\Omega$ [μb/sr]	$\Delta_{\rm stat}$ [μb/sr]	$\Delta_{\rm sys}$ [μb/sr]	$d\sigma_{3/2}/d\Omega$ [μb/sr]	$\Delta_{\rm stat}$ [μb/sr]	$\Delta_{\rm sys}$ [μb/sr]	$d\sigma_{3/2}/d\Omega$ [μb/sr]	$\Delta_{\rm stat}$ [μb/sr]	$\Delta_{\rm sys}$ [μb/sr]
−0.80	0.8881	0.1622	0.0640	0.8420	0.1635	0.0962	0.8550	0.1567	0.1334	0.6653	0.1415	0.1936
−0.40	0.5370	0.1482	0.0171	1.2768	0.1482	0.1603	0.7323	0.1238	0.0058	0.5363	0.1034	0.0717
0.00	0.8209	0.1271	0.0249	0.9751	0.1077	0.0603	0.6851	0.0921	0.0203	0.3101	0.0748	0.0231
0.40	0.8224	0.1180	0.1498	0.9445	0.0863	0.1390	0.5705	0.0697	0.0726	0.5431	0.0594	0.0377
0.80	0.7304	0.3855	0.2641	0.4549	0.2388	0.1589	0.3259	0.1954	0.1601	0.4829	0.1168	0.0406

$\cos(\theta^*_{2\pi^0})$	$W=(1640.0\pm20.0)$ MeV			$W=(1680.0\pm20.0)$ MeV			$W=(1720.0\pm20.0)$ MeV			$W=(1760.0\pm20.0)$ MeV		
	$d\sigma_{3/2}/d\Omega$ [μb/sr]	$\Delta_{\rm stat}$ [μb/sr]	$\Delta_{\rm sys}$ [μb/sr]	$d\sigma_{3/2}/d\Omega$ [μb/sr]	$\Delta_{\rm stat}$ [μb/sr]	$\Delta_{\rm sys}$ [μb/sr]	$d\sigma_{3/2}/d\Omega$ [μb/sr]	$\Delta_{\rm stat}$ [μb/sr]	$\Delta_{\rm sys}$ [μb/sr]	$d\sigma_{3/2}/d\Omega$ [μb/sr]	$\Delta_{\rm stat}$ [μb/sr]	$\Delta_{\rm sys}$ [μb/sr]
−0.80	0.5596	0.1182	0.0932	0.9290	0.1020	0.1122	0.6396	0.0964	0.0083	0.6165	0.0917	0.1228
−0.40	0.3404	0.0818	0.0214	0.4467	0.0720	0.0311	0.3719	0.0739	0.0659	0.4215	0.0586	0.0144
0.00	0.3671	0.0618	0.0760	0.2931	0.0746	0.0523	0.1296	0.0803	0.0456	0.3096	0.0543	0.0687
0.40	0.7457	0.0487	0.0208	0.7094	0.0531	0.0102	0.6679	0.0577	0.0422	0.4943	0.0466	0.0174
0.80	0.5593	0.1081	0.0651	0.6796	0.1009	0.1023	0.6912	0.1119	0.0767	0.5520	0.0611	0.0912

$\cos(\theta^*_{2\pi^0})$	$W=(1800.0\pm20.0)$ MeV			$W=(1840.0\pm20.0)$ MeV			$W=(1880.0\pm20.0)$ MeV			$W=(1920.0\pm20.0)$ MeV		
	$d\sigma_{3/2}/d\Omega$ [μb/sr]	$\Delta_{\rm stat}$ [μb/sr]	$\Delta_{\rm sys}$ [μb/sr]	$d\sigma_{3/2}/d\Omega$ [μb/sr]	$\Delta_{\rm stat}$ [μb/sr]	$\Delta_{\rm sys}$ [μb/sr]	$d\sigma_{3/2}/d\Omega$ [μb/sr]	$\Delta_{\rm stat}$ [μb/sr]	$\Delta_{\rm sys}$ [μb/sr]	$d\sigma_{3/2}/d\Omega$ [μb/sr]	$\Delta_{\rm stat}$ [μb/sr]	$\Delta_{\rm sys}$ [μb/sr]
−0.80	0.4356	0.0711	0.0034	0.4083	0.0679	0.0634	0.3821	0.0623	0.0092	0.6895	0.0503	0.0320
−0.40	0.4286	0.0470	0.0541	0.4665	0.0411	0.0504	0.4685	0.0432	0.0562	0.2856	0.0395	0.0591
0.00	0.1825	0.0528	0.0418	0.2365	0.0477	0.0173	0.2599	0.0422	0.0262	0.2648	0.0365	0.0162
0.40	0.4138	0.0482	0.0185	0.3266	0.0442	0.0200	0.3890	0.0410	0.0189	0.2942	0.0373	0.0125
0.80	0.4141	0.0566	0.0252	0.4742	0.0511	0.0578	0.5126	0.0521	0.0329	0.4394	0.0448	0.0469

$\cos(\theta^*_{2\pi^0})$	W=(1960.0±20.0) MeV			W=(2000.0±20.0) MeV			W=(2040.0±20.0) MeV			W=(2080.0±20.0) MeV		
	$d\sigma_{3/2}/d\Omega$ [μb/sr]	$\Delta_{\rm stat}$ [μb/sr]	$\Delta_{\rm sys}$ [μb/sr]	$d\sigma_{3/2}/d\Omega$ [μb/sr]	$\Delta_{\rm stat}$ [μb/sr]	$\Delta_{\rm sys}$ [μb/sr]	$d\sigma_{3/2}/d\Omega$ [μb/sr]	$\Delta_{\rm stat}$ [μb/sr]	$\Delta_{\rm sys}$ [μb/sr]	$d\sigma_{3/2}/d\Omega$ [μb/sr]	$\Delta_{\rm stat}$ [μb/sr]	$\Delta_{\rm sys}$ [μb/sr]
−0.80	0.3955	0.0444	0.0121	0.3702	0.0373	0.0746	0.3051	0.0342	0.0331	0.1647	0.0327	0.0434
−0.40	0.3189	0.0350	0.0577	0.3811	0.0312	0.0540	0.2950	0.0288	0.0509	0.2560	0.0256	0.0229
0.00	0.2678	0.0318	0.0505	0.1979	0.0270	0.0461	0.2539	0.0263	0.0128	0.1702	0.0231	0.0341
0.40	0.3708	0.0326	0.0255	0.3029	0.0279	0.0064	0.1285	0.0249	0.0251	0.1780	0.0243	0.0230
0.80	0.4296	0.0436	0.0607	0.3367	0.0384	0.0604	0.2493	0.0362	0.0668	0.2919	0.0349	0.0376

$\cos(\theta^*_{2\pi^0})$	W=(2120.0±20.0) MeV			W=(2160.0±20.0) MeV			W=(2200.0±20.0) MeV			W=(2240.0±20.0) MeV		
	$d\sigma_{3/2}/d\Omega$ [μb/sr]	$\Delta_{\rm stat}$ [μb/sr]	$\Delta_{\rm sys}$ [μb/sr]	$d\sigma_{3/2}/d\Omega$ [μb/sr]	$\Delta_{\rm stat}$ [μb/sr]	$\Delta_{\rm sys}$ [μb/sr]	$d\sigma_{3/2}/d\Omega$ [μb/sr]	$\Delta_{\rm stat}$ [μb/sr]	$\Delta_{\rm sys}$ [μb/sr]	$d\sigma_{3/2}/d\Omega$ [μb/sr]	$\Delta_{\rm stat}$ [μb/sr]	$\Delta_{\rm sys}$ [μb/sr]
−0.80	0.1839	0.0323	0.0122	0.2468	0.0288	0.0088	0.2057	0.0302	0.0098	0.2823	0.0365	0.0442
−0.40	0.2665	0.0298	0.0391	0.1342	0.0229	0.0238	0.1800	0.0280	0.0070	0.2144	0.0309	0.0052
0.00	0.1884	0.0270	0.0264	0.1295	0.0300	0.0389	0.2042	0.0254	0.0131	0.1957	0.0384	0.0492
0.40	0.2946	0.0256	0.0058	0.2076	0.0231	0.0129	0.2616	0.0263	0.0256	0.1554	0.0390	0.0378
0.80	0.2639	0.0326	0.0675	0.2881	0.0297	0.0559	0.3149	0.0345	0.0655	0.1526	0.0469	0.0703

$\cos(\theta^*_{2\pi^0})$	W=(2280.0±20.0) MeV		
	$d\sigma_{3/2}/d\Omega$ [μb/sr]	$\Delta_{\rm stat}$ [μb/sr]	$\Delta_{\rm sys}$ [μb/sr]
−0.80	0.1226	0.0600	0.0189
−0.40	0.1931	0.0591	0.0169
0.00	0.1825	0.0576	0.0167
0.40	0.1154	0.0795	0.0386
0.80	0.3406	0.0872	0.1585

E.6.3 Observables for $\gamma d \to \pi^0\pi^0 n(p)$ as a Function of E_γ

E_γ [MeV]	ΔE_γ [MeV]	E	$\Delta_{\rm stat}$	$\Delta_{\rm sys}$	$\sigma_{1/2}$ [μb]	$\Delta_{\rm stat}$ [μb]	$\Delta_{\rm sys}$ [μb]	$\sigma_{3/2}$ [μb]	$\Delta_{\rm stat}$ [μb]	$\Delta_{\rm sys}$ [μb]
440.0	40.0	−121.1573	970.0198	60.4378	−23.0229	186.1669	11.5789	23.4061	186.1669	23.0788
520.0	40.0	−2.8362	3.1744	0.5842	−1.4060	2.4793	0.4362	2.9374	2.4793	0.7468
600.0	40.0	0.0270	0.2921	0.0568	3.9336	1.1527	0.6244	3.7271	1.1527	0.4512
680.0	40.0	−0.9402	0.2423	0.1639	0.3508	1.6015	0.8729	11.3812	1.6015	1.7192
760.0	40.0	−0.3394	0.1330	0.0833	5.5142	1.1539	1.2821	11.1806	1.1539	1.7873
840.0	40.0	−0.2629	0.1374	0.0732	5.7764	1.1485	1.1349	9.8970	1.1485	1.3143
920.0	40.0	−0.0927	0.1191	0.0343	6.8666	0.9699	1.1166	8.2689	0.9699	1.1568
1000.0	40.0	0.1370	0.1176	0.0302	8.6645	0.9468	1.3317	6.5770	0.9468	0.9791
1080.0	40.0	−0.2367	0.1061	0.0948	6.1833	0.8691	1.6862	10.0191	0.8691	2.2089
1160.0	40.0	−0.1970	0.1048	0.0956	5.1738	0.6833	1.4195	7.7126	0.6833	1.7340
1240.0	40.0	−0.2335	0.1537	0.0931	3.2911	0.6661	0.8532	5.2967	0.6661	1.0625
1320.0	40.0	−0.4928	0.1278	0.1184	2.0399	0.5189	0.6425	6.0041	0.5189	1.1034
1400.0	40.0	−0.5100	0.1480	0.1554	1.6929	0.5186	0.6426	5.2175	0.5186	1.0806
1480.0	40.0	−0.0576	0.1248	0.0262	3.3483	0.4481	0.5959	3.7575	0.4481	0.6125
1560.0	40.0	−0.2929	0.1306	0.1269	2.4352	0.4564	0.7648	4.4528	0.4564	1.0747
1640.0	40.0	−0.1280	0.1170	0.0497	2.9814	0.4064	0.6455	3.8568	0.4064	0.7357
1720.0	40.0	−0.3717	0.1277	0.1711	1.8698	0.3857	0.7024	4.0818	0.3857	1.1113
1800.0	40.0	−0.1992	0.1336	0.1066	2.2290	0.3768	0.6721	3.3376	0.3768	0.8627
1880.0	40.0	−0.1645	0.1371	0.0624	2.1674	0.3608	0.4785	3.0208	0.3608	0.5552
1960.0	40.0	−0.1000	0.1457	0.0333	2.3408	0.3859	0.4770	2.8610	0.3859	0.5396
2040.0	40.0	0.0501	0.1386	0.0331	2.5197	0.3374	0.4689	2.2790	0.3374	0.3876
2120.0	40.0	−0.1498	0.1466	0.0401	1.9550	0.3412	0.3471	2.6441	0.3412	0.4020
2200.0	40.0	−0.2717	0.1618	0.0534	1.6518	0.3729	0.2516	2.8844	0.3729	0.3002
2280.0	40.0	−0.0560	0.2441	0.0326	2.0578	0.5370	0.3816	2.3019	0.5370	0.3827
2360.0	40.0	0.0000	0.0000	0.0000	0.0000	0.0000	0.0000	0.0000	0.0000	0.0000

E.6.4 Observables for $\gamma d \to \pi^0\pi^0 n(p)$ as a Function of W

W [MeV]	ΔW [MeV]	E	Δ_{stat}	Δ_{sys}	$\sigma_{1/2}$ [μb]	Δ_{stat} [μb]	Δ_{sys} [μb]	$\sigma_{3/2}$ [μb]	Δ_{stat} [μb]	Δ_{sys} [μb]
1320.0	20.0	28.8251	19.5655	19.0701	9.7749	7.4748	6.2518	−9.1194	7.4748	6.9256
1360.0	20.0	−0.2465	3.0030	0.0613	0.5826	2.3270	0.3624	0.9637	2.3270	0.4125
1400.0	20.0	−0.2980	0.4234	0.0872	2.1828	1.3410	0.3508	4.0362	1.3410	0.3221
1440.0	20.0	−0.4052	0.3332	0.0789	2.4912	1.4267	0.4676	5.8849	1.4267	0.5527
1480.0	20.0	−0.5945	0.1959	0.1444	2.9836	1.4976	1.1909	11.7328	1.4976	2.4652
1520.0	20.0	−0.4093	0.1491	0.1224	4.9791	1.2975	1.4925	11.8803	1.2975	2.1670
1560.0	20.0	−0.1897	0.1530	0.0463	6.2390	1.2559	0.9193	9.1601	1.2559	1.0076
1600.0	20.0	−0.1138	0.1422	0.0319	6.2981	1.0783	0.9010	7.9163	1.0783	0.9539
1640.0	20.0	−0.0601	0.1225	0.0254	7.3201	0.9917	1.1796	8.2563	0.9917	1.1996
1680.0	20.0	−0.0990	0.1218	0.0433	6.9751	0.9862	1.1512	8.5078	0.9862	1.1461
1720.0	20.0	−0.0746	0.1108	0.0466	6.8862	0.8339	1.6397	7.9971	0.8339	1.7445
1760.0	20.0	−0.3733	0.1278	0.1564	3.3690	0.6953	1.1519	7.3829	0.6953	1.5653
1800.0	20.0	−0.3930	0.1447	0.1068	2.5130	0.6049	0.6728	5.7670	0.6049	0.9333
1840.0	20.0	−0.5876	0.1467	0.2111	1.4311	0.5145	0.7274	5.5094	0.5145	1.4899
1880.0	20.0	−0.3713	0.1284	0.0860	2.3424	0.4842	0.5519	5.1086	0.4842	0.7898
1920.0	20.0	−0.1387	0.1282	0.0569	2.9528	0.4445	0.6090	3.9036	0.4445	0.6665
1960.0	20.0	−0.0038	0.1190	0.0169	3.4859	0.4218	0.8049	3.5124	0.4218	0.7801
2000.0	20.0	−0.1631	0.1166	0.0741	2.7788	0.3933	0.7054	3.8617	0.3933	0.8424
2040.0	20.0	−0.3192	0.1267	0.0855	1.9394	0.3664	0.4917	3.7577	0.3664	0.7258
2080.0	20.0	−0.3383	0.1246	0.0997	1.8552	0.3548	0.5052	3.7526	0.3548	0.7433
2120.0	20.0	−0.1346	0.1295	0.0638	2.2915	0.3473	0.5478	3.0044	0.3473	0.6225
2160.0	20.0	−0.2063	0.1287	0.0457	2.0208	0.3323	0.3448	3.0716	0.3323	0.4215
2200.0	20.0	−0.0665	0.1461	0.0356	2.2308	0.3540	0.4488	2.5489	0.3540	0.4642
2240.0	20.0	0.0101	0.1818	0.0227	2.4238	0.4427	0.3673	2.3754	0.4427	0.3252
2280.0	20.0	−0.3268	0.2546	0.0992	1.9387	0.7440	0.5184	3.8208	0.7440	0.7351

Angular Distributions

	$W=(1320.0\pm20.0)$ MeV			$W=(1360.0\pm20.0)$ MeV			$W=(1400.0\pm20.0)$ MeV			$W=(1440.0\pm20.0)$ MeV		
$\cos(\theta^*_{2\pi^0})$	E	Δ_{stat}	Δ_{sys}	E	Δ_{stat}	Δ_{sys}	E	Δ_{stat}	Δ_{sys}	E	Δ_{stat}	Δ_{sys}
−0.80	15.6084	9.8968	36.3508	8.4424	14.0718	3.8937	−0.0600	−1.0190	0.1845	0.8017	0.8655	0.1371
−0.40	18.1516	39.9245	341.2424	−0.2693	−4.4000	0.1414	−1.6123	−0.7239	0.8692	0.3334	0.5737	0.2931
0.00	41.6946	40.6351	16.9113	−5.8236	−3.8469	0.9130	0.8017	0.7957	0.0771	−0.1616	−0.5528	0.2983
0.40	−53.3069	−288.2668	26.0672	0.4692	5.7995	0.3122	−0.7803	−0.7366	0.1043	−1.5506	−0.5797	0.3464
0.80	−612.17[illegible]	[illegible]801.7320	311.2408	23.1579	63.0489	11.2862	−0.8689	−1.1369	0.2220	−0.5001	−1.0845	0.2242

	$W=(1480.0\pm20.0)$ MeV			$W=(1520.0\pm20.0)$ MeV			$W=(1560.0\pm20.0)$ MeV			$W=(1600.0\pm20.0)$ MeV		
$\cos(\theta^*_{2\pi^0})$	E	Δ_{stat}	Δ_{sys}	E	Δ_{stat}	Δ_{sys}	E	Δ_{stat}	Δ_{sys}	E	Δ_{stat}	Δ_{sys}
−0.80	−0.1184	−0.3785	0.0391	−0.3726	−0.3271	0.0212	0.3633	0.2895	0.0565	0.8337	0.3070	0.2151
−0.40	−0.6157	−0.3997	0.0849	−1.0374	−0.3500	0.2694	−0.2335	−0.3693	0.0726	−0.3183	−0.2658	0.0416
0.00	−0.9375	−0.3732	0.2081	−0.7411	−0.3395	0.0917	−0.7320	−0.3580	0.1645	−0.0763	−0.3382	0.0744
0.40	−0.6120	−0.3596	0.1606	−0.4056	−0.2738	0.1264	−0.0839	−0.3083	0.2180	−0.3809	−0.2742	0.1389
0.80	−1.0295	−0.7854	0.3812	−0.4658	−0.6314	0.0109	0.1092	0.4854	0.0549	−0.0682	−0.3762	0.0256

	$W=(1640.0\pm20.0)$ MeV			$W=(1680.0\pm20.0)$ MeV			$W=(1720.0\pm20.0)$ MeV			$W=(1760.0\pm20.0)$ MeV		
$\cos(\theta^*_{2\pi^0})$	E	Δ_{stat}	Δ_{sys}	E	Δ_{stat}	Δ_{sys}	E	Δ_{stat}	Δ_{sys}	E	Δ_{stat}	Δ_{sys}
−0.80	−0.0394	−0.2207	0.0480	0.3590	0.2505	0.0181	−0.6135	−0.2517	0.0770	−0.0124	−0.2587	0.0162
−0.40	0.1013	0.2177	0.0334	0.0285	0.2470	0.0258	−0.3388	−0.1594	0.1803	−0.6038	−0.2243	0.2818
0.00	−0.0345	−0.2632	0.0249	−0.3492	−0.1735	0.1153	0.0290	0.1752	0.0113	−0.3372	−0.1842	0.4281
0.40	−0.4748	−0.1995	0.1185	−0.1750	−0.1936	0.0675	−0.0000	−0.1727	0.0112	−0.0914	−0.1675	0.1001
0.80	0.6499	0.3580	0.0180	0.1448	0.3053	0.0212	0.5252	0.3348	0.0555	−0.7518	−0.2588	0.1146

	$W=(1800.0\pm20.0)$ MeV			$W=(1840.0\pm20.0)$ MeV			$W=(1880.0\pm20.0)$ MeV			$W=(1920.0\pm20.0)$ MeV		
$\cos(\theta^*_{2\pi^0})$	E	Δ_{stat}	Δ_{sys}	E	Δ_{stat}	Δ_{sys}	E	Δ_{stat}	Δ_{sys}	E	Δ_{stat}	Δ_{sys}
−0.80	−0.0111	−0.3140	0.0121	−0.0985	−0.3081	0.0219	0.6316	0.2399	0.2027	0.0136	0.2579	0.1620
−0.40	−0.1822	−0.2216	0.2225	−0.3946	−0.2485	0.3514	−0.7004	−0.2177	0.3531	−0.1664	−0.1818	0.0214
0.00	−0.3855	−0.1916	0.3968	−0.7858	−0.2075	2.8542	−0.2174	−0.1773	0.1110	0.0709	0.1910	0.0549
0.40	−0.7156	−0.1953	0.1708	−0.2490	−0.1982	0.0849	−0.5210	−0.2210	0.0633	−0.3344	−0.1978	0.0602
0.80	−0.1850	−0.3579	0.0182	−1.1889	−0.3223	0.1183	−0.0112	−0.3011	0.0156	0.3361	0.2914	0.0697

	$W=(1960.0\pm20.0)$ MeV			$W=(2000.0\pm20.0)$ MeV			$W=(2040.0\pm20.0)$ MeV			$W=(2080.0\pm20.0)$ MeV		
$\cos(\theta^*_{2\pi^0})$	E	Δ_{stat}	Δ_{sys}	E	Δ_{stat}	Δ_{sys}	E	Δ_{stat}	Δ_{sys}	E	Δ_{stat}	Δ_{sys}
−0.80	0.3619	0.2375	0.1252	−0.1351	−0.1820	0.0148	−0.1089	−0.2077	0.0856	0.3493	0.2941	0.2022
−0.40	−0.1612	−0.1921	0.1782	−0.0989	−0.1731	0.0963	−0.2052	−0.1735	37.5059	−0.2429	−0.2023	0.4619
0.00	−0.1119	−0.1644	0.1675	−0.3329	−0.1588	0.1672	−0.8103	−0.1946	0.2573	−0.2431	−0.1772	0.2013
0.40	0.3122	0.1843	0.1798	−0.0208	−0.1612	0.0074	−0.1338	−0.1501	0.0361	−0.1812	−0.1778	0.0226
0.80	−0.1782	−0.2818	0.0638	−0.5325	−0.2216	0.0812	0.0999	0.2672	0.0333	−0.4124	−0.2582	0.0683

	$W=(2120.0\pm20.0)$ MeV			$W=(2160.0\pm20.0)$ MeV			$W=(2200.0\pm20.0)$ MeV			$W=(2240.0\pm20.0)$ MeV		
$\cos(\theta^*_{2\pi^0})$	E	Δ_{stat}	Δ_{sys}	E	Δ_{stat}	Δ_{sys}	E	Δ_{stat}	Δ_{sys}	E	Δ_{stat}	Δ_{sys}
−0.80	0.2949	0.1893	0.0362	−0.9019	−0.2679	0.2959	0.0018	0.2154	0.2180	−0.0369	−0.3567	0.0528
−0.40	−0.4298	−0.2194	0.1180	−0.3582	−0.2599	0.1787	−0.2252	−0.2125	0.0370	0.1480	0.4383	0.0475
0.00	0.2858	0.2096	0.1141	−0.4353	−0.2625	0.1528	−0.3560	−0.2376	0.6056	0.0703	0.2684	0.0236
0.40	−0.4667	−0.1546	0.3752	0.0072	0.1951	0.0143	−0.6922	−0.1847	0.0355	−0.1056	−0.2489	0.0220
0.80	0.1093	0.1963	0.0135	−0.3340	−0.2161	0.0087	0.5651	0.2288	0.1074	−0.2589	−0.2402	0.0384

$\cos(\theta^*_{2\pi^0})$	$W=(2280.0\pm20.0)$ MeV		
	E	Δ_{stat}	Δ_{sys}
−0.80	0.4648	0.4109	0.1215
−0.40	−1.2616	−0.4397	5.5104
0.00	−0.0088	−0.5441	0.0917
0.40	−0.2432	−0.3595	0.7748
0.80	−0.5160	−0.4329	0.1527

$\cos(\theta^*_{2\pi^0})$	$W=(1320.0\pm20.0)$ MeV			$W=(1360.0\pm20.0)$ MeV			$W=(1400.0\pm20.0)$ MeV			$W=(1440.0\pm20.0)$ MeV		
	$d\sigma_{1/2}/d\Omega$ [μb/sr]	Δ_{stat} [μb/sr]	Δ_{sys} [μb/sr]	$d\sigma_{1/2}/d\Omega$ [μb/sr]	Δ_{stat} [μb/sr]	Δ_{sys} [μb/sr]	$d\sigma_{1/2}/d\Omega$ [μb/sr]	Δ_{stat} [μb/sr]	Δ_{sys} [μb/sr]	$d\sigma_{1/2}/d\Omega$ [μb/sr]	Δ_{stat} [μb/sr]	Δ_{sys} [μb/sr]
−0.80	1.2567	0.8916	0.6584	0.2994	0.4864	0.2919	0.1888	0.2110	0.0359	0.5412	0.2708	0.1563
−0.40	0.5673	1.2580	0.4217	0.0661	0.3992	0.0369	−0.1705	0.2225	0.1730	0.4953	0.2184	0.2087
0.00	1.3427	1.5727	0.5932	−0.5608	0.4885	0.0656	0.4786	0.2153	0.0710	0.3383	0.2272	0.1337
0.40	0.2071	1.4445	0.1032	0.0849	0.3359	0.0892	0.0583	0.2001	0.0278	−0.1824	0.2089	0.0746
0.80	1.4507	20.0833	0.8149	0.2776	0.8681	0.3512	0.0297	0.2655	0.0433	0.1299	0.2877	0.0586

$\cos(\theta^*_{2\pi^0})$	$W=(1480.0\pm20.0)$ MeV			$W=(1520.0\pm20.0)$ MeV			$W=(1560.0\pm20.0)$ MeV			$W=(1600.0\pm20.0)$ MeV		
	$d\sigma_{1/2}/d\Omega$ [μb/sr]	Δ_{stat} [μb/sr]	Δ_{sys} [μb/sr]	$d\sigma_{1/2}/d\Omega$ [μb/sr]	Δ_{stat} [μb/sr]	Δ_{sys} [μb/sr]	$d\sigma_{1/2}/d\Omega$ [μb/sr]	Δ_{stat} [μb/sr]	Δ_{sys} [μb/sr]	$d\sigma_{1/2}/d\Omega$ [μb/sr]	Δ_{stat} [μb/sr]	Δ_{sys} [μb/sr]
−0.80	0.6144	0.2720	0.0194	0.6302	0.3338	0.0644	1.2828	0.2792	0.0724	1.5265	0.2688	0.1789
−0.40	0.2443	0.2683	0.0543	−0.0256	0.2636	0.1572	0.4515	0.2505	0.0822	0.4648	0.2181	0.0340
0.00	0.0410	0.2729	0.1236	0.1700	0.2379	0.0648	0.1560	0.2431	0.0927	0.3847	0.1521	0.0413
0.40	0.2235	0.2098	0.0991	0.3847	0.1786	0.1216	0.4990	0.1691	0.1593	0.3050	0.1390	0.0910
0.80	−0.0107	0.2887	0.0960	0.1927	0.2291	0.0043	0.4514	0.1988	0.0234	0.3768	0.1533	0.0788

$\cos(\theta^*_{2\pi^0})$	$W=(1640.0\pm20.0)$ MeV			$W=(1680.0\pm20.0)$ MeV			$W=(1720.0\pm20.0)$ MeV			$W=(1760.0\pm20.0)$ MeV		
	$d\sigma_{1/2}/d\Omega$ [μb/sr]	Δ_{stat} [μb/sr]	Δ_{sys} [μb/sr]	$d\sigma_{1/2}/d\Omega$ [μb/sr]	Δ_{stat} [μb/sr]	Δ_{sys} [μb/sr]	$d\sigma_{1/2}/d\Omega$ [μb/sr]	Δ_{stat} [μb/sr]	Δ_{sys} [μb/sr]	$d\sigma_{1/2}/d\Omega$ [μb/sr]	Δ_{stat} [μb/sr]	Δ_{sys} [μb/sr]
−0.80	0.8885	0.2155	0.0128	1.0106	0.1968	0.0562	0.2409	0.1603	0.0626	0.3599	0.0966	0.0382
−0.40	0.7383	0.1601	0.0905	0.6270	0.1678	0.0812	0.4252	0.1055	0.1659	0.1737	0.1007	0.1074
0.00	0.4998	0.1428	0.0469	0.4665	0.1389	0.1263	0.7028	0.1218	0.1602	0.3325	0.0943	0.1875
0.40	0.3135	0.1206	0.0994	0.4782	0.1137	0.0909	0.5903	0.1036	0.1274	0.4083	0.0766	0.1119
0.80	0.6418	0.1414	0.0202	0.4930	0.1329	0.0199	0.6428	0.1420	0.0240	0.0956	0.1018	0.0448

$\cos(\theta^*_{2\pi^0})$	$W=(1800.0\pm20.0)$ MeV			$W=(1840.0\pm20.0)$ MeV			$W=(1880.0\pm20.0)$ MeV			$W=(1920.0\pm20.0)$ MeV		
	$d\sigma_{1/2}/d\Omega$ [μb/sr]	Δ_{stat} [μb/sr]	Δ_{sys} [μb/sr]	$d\sigma_{1/2}/d\Omega$ [μb/sr]	Δ_{stat} [μb/sr]	Δ_{sys} [μb/sr]	$d\sigma_{1/2}/d\Omega$ [μb/sr]	Δ_{stat} [μb/sr]	Δ_{sys} [μb/sr]	$d\sigma_{1/2}/d\Omega$ [μb/sr]	Δ_{stat} [μb/sr]	Δ_{sys} [μb/sr]
−0.80	0.2472	0.0799	0.0062	0.2059	0.0716	0.0053	0.4795	0.0725	0.0741	0.2933	0.0760	0.0845
−0.40	0.2622	0.0728	0.0986	0.1764	0.0737	0.1024	0.0977	0.0728	0.1143	0.2436	0.0546	0.0299
0.00	0.2489	0.0789	0.1396	0.0763	0.0751	1.0173	0.2790	0.0646	0.0901	0.3342	0.0608	0.1008
0.40	0.1034	0.0724	0.0621	0.2050	0.0549	0.0554	0.1263	0.0593	0.0258	0.1622	0.0490	0.0238
0.80	0.2512	0.1112	0.0096	−0.0437	0.0766	0.0287	0.2395	0.0739	0.0245	0.3028	0.0669	0.0564

$\cos(\theta^*_{2\pi^0})$	$W=(1960.0\pm20.0)$ MeV			$W=(2000.0\pm20.0)$ MeV			$W=(2040.0\pm20.0)$ MeV			$W=(2080.0\pm20.0)$ MeV		
	$d\sigma_{1/2}/d\Omega$ [μb/sr]	Δ_{stat} [μb/sr]	Δ_{sys} [μb/sr]	$d\sigma_{1/2}/d\Omega$ [μb/sr]	Δ_{stat} [μb/sr]	Δ_{sys} [μb/sr]	$d\sigma_{1/2}/d\Omega$ [μb/sr]	Δ_{stat} [μb/sr]	Δ_{sys} [μb/sr]	$d\sigma_{1/2}/d\Omega$ [μb/sr]	Δ_{stat} [μb/sr]	Δ_{sys} [μb/sr]
−0.80	0.4121	0.0734	0.0933	0.2480	0.0547	0.0252	0.1912	0.0463	0.0308	0.2849	0.0636	0.0336
−0.40	0.2353	0.0554	0.0904	0.2496	0.0493	0.0837	0.1839	0.0416	1.2719	0.1798	0.0492	0.0964
0.00	0.2849	0.0544	0.1202	0.1898	0.0466	0.0704	0.0436	0.0462	0.0523	0.1659	0.0400	0.0675
0.40	0.3284	0.0473	0.1017	0.2304	0.0390	0.0449	0.2037	0.0364	0.0256	0.1726	0.0383	0.0156
0.80	0.1956	0.0679	0.0360	0.1111	0.0543	0.0267	0.2446	0.0606	0.0128	0.1393	0.0624	0.0520

$\cos(\theta^*_{2\pi^0})$	$W=(2120.0\pm20.0)$ MeV			$W=(2160.0\pm20.0)$ MeV			$W=(2200.0\pm20.0)$ MeV			$W=(2240.0\pm20.0)$ MeV		
	$d\sigma_{1/2}/d\Omega$ [μb/sr]	Δ_{stat} [μb/sr]	Δ_{sys} [μb/sr]	$d\sigma_{1/2}/d\Omega$ [μb/sr]	Δ_{stat} [μb/sr]	Δ_{sys} [μb/sr]	$d\sigma_{1/2}/d\Omega$ [μb/sr]	Δ_{stat} [μb/sr]	Δ_{sys} [μb/sr]	$d\sigma_{1/2}/d\Omega$ [μb/sr]	Δ_{stat} [μb/sr]	Δ_{sys} [μb/sr]
−0.80	0.2794	0.0423	0.0415	0.0198	0.0558	0.0592	0.1717	0.0388	0.0565	0.1574	0.0605	0.0132
−0.40	0.0949	0.0380	0.0269	0.0943	0.0390	0.0367	0.1128	0.0329	0.0181	0.1576	0.0609	0.0354
0.00	0.2315	0.0387	0.0449	0.0917	0.0439	0.0335	0.1092	0.0415	0.0865	0.1618	0.0420	0.0280
0.40	0.1187	0.0353	0.0835	0.2203	0.0434	0.0117	0.0570	0.0354	0.0059	0.1630	0.0465	0.0314
0.80	0.2982	0.0542	0.0207	0.1886	0.0623	0.0057	0.4369	0.0654	0.0647	0.2377	0.0793	0.0273

$\cos(\theta^*_{2\pi^0})$	$W=(2280.0\pm20.0)$ MeV		
	$d\sigma_{1/2}/d\Omega$ [μb/sr]	Δ_{stat} [μb/sr]	Δ_{sys} [μb/sr]
−0.80	0.3369	0.0987	0.0268
−0.40	−0.0449	0.0812	0.9451
0.00	0.1640	0.0920	0.0229
0.40	0.1628	0.0791	0.1667
0.80	0.1760	0.1602	0.2063

$\cos(\theta^*_{2\pi^0})$	$W=(1320.0\pm20.0)$ MeV			$W=(1360.0\pm20.0)$ MeV			$W=(1400.0\pm20.0)$ MeV			$W=(1440.0\pm20.0)$ MeV		
	$d\sigma_{3/2}/d\Omega$ [μb/sr]	Δ_{stat} [μb/sr]	Δ_{sys} [μb/sr]	$d\sigma_{3/2}/d\Omega$ [μb/sr]	Δ_{stat} [μb/sr]	Δ_{sys} [μb/sr]	$d\sigma_{3/2}/d\Omega$ [μb/sr]	Δ_{stat} [μb/sr]	Δ_{sys} [μb/sr]	$d\sigma_{3/2}/d\Omega$ [μb/sr]	Δ_{stat} [μb/sr]	Δ_{sys} [μb/sr]
−0.80	−1.1054	0.8916	0.5824	−0.2360	0.4864	0.1819	0.2129	0.2110	0.0570	0.0596	0.2708	0.0781
−0.40	−0.5081	1.2580	0.4625	0.1147	0.3992	0.0660	0.7275	0.2225	0.2336	0.2476	0.2184	0.0906
0.00	−1.2798	1.5727	0.5281	0.7933	0.4885	0.0751	0.0527	0.2153	0.0214	0.4687	0.2272	0.0781
0.40	−0.2150	1.4445	0.1912	0.0307	0.3359	0.0940	0.4725	0.2001	0.0200	0.8448	0.2089	0.1119
0.80	−1.4554	20.0833	0.7387	−0.2546	0.8681	0.2215	0.4239	0.2655	0.0294	0.3897	0.2877	0.0517

$\cos(\theta^*_{2\pi^0})$	$W=(1480.0\pm20.0)$ MeV			$W=(1520.0\pm20.0)$ MeV			$W=(1560.0\pm20.0)$ MeV			$W=(1600.0\pm20.0)$ MeV		
	$d\sigma_{3/2}/d\Omega$ [μb/sr]	Δ_{stat} [μb/sr]	Δ_{sys} [μb/sr]	$d\sigma_{3/2}/d\Omega$ [μb/sr]	Δ_{stat} [μb/sr]	Δ_{sys} [μb/sr]	$d\sigma_{3/2}/d\Omega$ [μb/sr]	Δ_{stat} [μb/sr]	Δ_{sys} [μb/sr]	$d\sigma_{3/2}/d\Omega$ [μb/sr]	Δ_{stat} [μb/sr]	Δ_{sys} [μb/sr]
−0.80	0.7795	0.2720	0.0691	1.3787	0.3338	0.0857	0.5991	0.2792	0.0815	0.1384	0.2688	0.1956
−0.40	1.0272	0.2683	0.1399	1.3957	0.2636	0.3615	0.7265	0.2505	0.0655	0.8989	0.2181	0.0171
0.00	1.2709	0.2729	0.2176	1.1434	0.2379	0.1161	1.0081	0.2431	0.1068	0.4483	0.1521	0.0285
0.40	0.9285	0.2098	0.1916	0.9096	0.1786	0.1908	0.5903	0.1691	0.1098	0.6803	0.1390	0.1006
0.80	0.7368	0.2887	0.0963	0.5288	0.2291	0.0032	0.3625	0.1988	0.0355	0.4320	0.1533	0.0977

$\cos(\theta^*_{2\pi^0})$	$W=(1640.0\pm20.0)$ MeV			$W=(1680.0\pm20.0)$ MeV			$W=(1720.0\pm20.0)$ MeV			$W=(1760.0\pm20.0)$ MeV		
	$d\sigma_{3/2}/d\Omega$ [μb/sr]	Δ_{stat} [μb/sr]	Δ_{sys} [μb/sr]	$d\sigma_{3/2}/d\Omega$ [μb/sr]	Δ_{stat} [μb/sr]	Δ_{sys} [μb/sr]	$d\sigma_{3/2}/d\Omega$ [μb/sr]	Δ_{stat} [μb/sr]	Δ_{sys} [μb/sr]	$d\sigma_{3/2}/d\Omega$ [μb/sr]	Δ_{stat} [μb/sr]	Δ_{sys} [μb/sr]
−0.80	0.9614	0.2155	0.0834	0.4766	0.1968	0.0417	1.0057	0.1603	0.1084	0.3689	0.0966	0.0315
−0.40	0.6024	0.1601	0.0937	0.5923	0.1678	0.0634	0.8608	0.1055	0.2693	0.7031	0.1007	0.2018
0.00	0.5355	0.1428	0.0595	0.9669	0.1389	0.1520	0.6631	0.1218	0.1496	0.6709	0.0943	0.2620
0.40	0.8803	0.1206	0.1789	0.6810	0.1137	0.0950	0.5904	0.1036	0.1237	0.4905	0.0766	0.1069
0.80	0.1362	0.1414	0.0070	0.3683	0.1329	0.0129	0.2001	0.1420	0.0296	0.6747	0.1018	0.0671

$\cos(\theta^*_{2\pi^0})$	$W=(1800.0\pm20.0)$ MeV			$W=(1840.0\pm20.0)$ MeV			$W=(1880.0\pm20.0)$ MeV			$W=(1920.0\pm20.0)$ MeV		
	$d\sigma_{3/2}/d\Omega$ [μb/sr]	Δ_{stat} [μb/sr]	Δ_{sys} [μb/sr]	$d\sigma_{3/2}/d\Omega$ [μb/sr]	Δ_{stat} [μb/sr]	Δ_{sys} [μb/sr]	$d\sigma_{3/2}/d\Omega$ [μb/sr]	Δ_{stat} [μb/sr]	Δ_{sys} [μb/sr]	$d\sigma_{3/2}/d\Omega$ [μb/sr]	Δ_{stat} [μb/sr]	Δ_{sys} [μb/sr]
−0.80	0.2527	0.0799	0.0020	0.2509	0.0716	0.0184	0.1083	0.0725	0.0584	0.2855	0.0760	0.0554
−0.40	0.3790	0.0728	0.1085	0.4064	0.0737	0.1957	0.5545	0.0728	0.1958	0.3409	0.0546	0.0361
0.00	0.5612	0.0789	0.2436	0.6365	0.0751	1.1794	0.4341	0.0646	0.1440	0.2900	0.0608	0.0811
0.40	0.6236	0.0724	0.1273	0.3410	0.0549	0.0831	0.4010	0.0593	0.0563	0.3251	0.0490	0.0217
0.80	0.3652	0.1112	0.0008	0.5069	0.0766	0.0519	0.2449	0.0739	0.0173	0.1504	0.0669	0.0332

$\cos(\theta^*_{2\pi^0})$	$W=(1960.0\pm20.0)$ MeV			$W=(2000.0\pm20.0)$ MeV			$W=(2040.0\pm20.0)$ MeV			$W=(2080.0\pm20.0)$ MeV		
	$d\sigma_{3/2}/d\Omega$ [μb/sr]	Δ_{stat} [μb/sr]	Δ_{sys} [μb/sr]	$d\sigma_{3/2}/d\Omega$ [μb/sr]	Δ_{stat} [μb/sr]	Δ_{sys} [μb/sr]	$d\sigma_{3/2}/d\Omega$ [μb/sr]	Δ_{stat} [μb/sr]	Δ_{sys} [μb/sr]	$d\sigma_{3/2}/d\Omega$ [μb/sr]	Δ_{stat} [μb/sr]	Δ_{sys} [μb/sr]
−0.80	0.1931	0.0734	0.0580	0.3255	0.0547	0.0294	0.2379	0.0463	0.0129	0.1374	0.0636	0.0590
−0.40	0.3257	0.0554	0.1192	0.3044	0.0493	0.0989	0.2788	0.0416	1.3855	0.2952	0.0492	0.1420
0.00	0.3568	0.0544	0.1844	0.3792	0.0466	0.1140	0.4163	0.0462	0.0936	0.2724	0.0400	0.1075
0.40	0.1721	0.0473	0.0649	0.2402	0.0390	0.0468	0.2666	0.0364	0.0209	0.2490	0.0383	0.0173
0.80	0.2805	0.0679	0.0229	0.3640	0.0543	0.0415	0.2002	0.0606	0.0189	0.3349	0.0624	0.0637

$\cos(\theta^*_{2\pi^0})$	$W=(2120.0\pm20.0)$ MeV			$W=(2160.0\pm20.0)$ MeV			$W=(2200.0\pm20.0)$ MeV			$W=(2240.0\pm20.0)$ MeV		
	$d\sigma_{3/2}/d\Omega$ [μb/sr]	Δ_{stat} [μb/sr]	Δ_{sys} [μb/sr]	$d\sigma_{3/2}/d\Omega$ [μb/sr]	Δ_{stat} [μb/sr]	Δ_{sys} [μb/sr]	$d\sigma_{3/2}/d\Omega$ [μb/sr]	Δ_{stat} [μb/sr]	Δ_{sys} [μb/sr]	$d\sigma_{3/2}/d\Omega$ [μb/sr]	Δ_{stat} [μb/sr]	Δ_{sys} [μb/sr]
−0.80	0.1521	0.0423	0.0229	0.3841	0.0558	0.0612	0.1711	0.0388	0.0698	0.1694	0.0605	0.0151
−0.40	0.2380	0.0380	0.0360	0.1996	0.0390	0.0784	0.1784	0.0329	0.0218	0.1169	0.0609	0.0268
0.00	0.1286	0.0387	0.0353	0.2330	0.0439	0.0583	0.2300	0.0415	0.1494	0.1405	0.0420	0.0238
0.40	0.3264	0.0353	0.1534	0.2171	0.0434	0.0134	0.3131	0.0354	0.0226	0.2014	0.0465	0.0293
0.80	0.2394	0.0542	0.0173	0.3777	0.0623	0.0064	0.1214	0.0654	0.0256	0.4039	0.0793	0.0320

$\cos(\theta^*_{2\pi^0})$	$W=(2280.0\pm20.0)$ MeV		
	$d\sigma_{3/2}/d\Omega$ [μb/sr]	Δ_{stat} [μb/sr]	Δ_{sys} [μb/sr]
−0.80	0.1231	0.0987	0.0504
−0.40	0.3879	0.0812	1.0321
0.00	0.1669	0.0920	0.0317
0.40	0.2674	0.0791	0.2707
0.80	0.5514	0.1602	0.2435

E.6.5 Observables for $\gamma p \to \pi^0\pi^0 p$ as a Function of W

W [MeV]	ΔW [MeV]	E	Δ_{stat}	Δ_{sys}	$\sigma_{1/2}$ [μb]	Δ_{stat} [μb]	Δ_{sys} [μb]	$\sigma_{3/2}$ [μb]	Δ_{stat} [μb]	Δ_{sys} [μb]
1320.0	20.0	0.6612	17.5555	0.3503	0.8128	10.1326	7.9284	0.1658	10.1326	7.9743
1360.0	20.0	−0.1978	0.7940	0.0720	1.8162	2.4940	2.8899	2.7119	2.4940	3.2239
1400.0	20.0	−0.4131	0.1354	0.0607	3.9265	1.1841	0.5452	9.4546	1.1841	0.6737
1440.0	20.0	−0.3946	0.0964	0.0483	5.0397	1.0559	0.5891	11.6083	1.0559	0.8156
1480.0	20.0	−0.1444	0.0740	0.0349	8.2780	1.0016	0.7780	11.0719	1.0016	0.7749
1520.0	20.0	−0.4545	0.0717	0.0364	4.9648	0.8400	0.3936	13.2366	0.8400	0.8149
1560.0	20.0	−0.2910	0.0678	0.0366	5.4330	0.7051	0.5013	9.8924	0.7051	0.6551
1600.0	20.0	−0.1024	0.0663	0.0216	5.7063	0.5926	0.3714	7.0086	0.5926	0.5137
1640.0	20.0	−0.1341	0.0481	0.0179	6.0756	0.4735	0.4637	7.9570	0.4735	0.6440
1680.0	20.0	0.0063	0.0388	0.0189	8.3846	0.4567	0.6376	8.2793	0.4567	0.7504
1720.0	20.0	0.2025	0.0406	0.0275	10.3746	0.4857	0.6661	6.8799	0.4857	0.5632
1760.0	20.0	0.1555	0.0346	0.0408	8.4520	0.3539	0.5966	6.1774	0.3539	0.7048
1800.0	20.0	0.2939	0.0360	0.0411	8.4683	0.3196	0.6742	4.6209	0.3196	0.3855
1840.0	20.0	0.2630	0.0403	0.0602	7.1476	0.3117	0.4932	4.1706	0.3117	0.5412
1880.0	20.0	0.0478	0.0368	0.0203	5.7397	0.2846	0.4778	5.2156	0.2846	0.3799
1920.0	20.0	0.1041	0.0354	0.0130	5.4817	0.2473	0.3380	4.4482	0.2473	0.2726
1960.0	20.0	0.0177	0.0330	0.0142	4.8273	0.2210	0.4251	4.6595	0.2210	0.3745
2000.0	20.0	0.0199	0.0335	0.0080	4.1857	0.1947	0.3135	4.0227	0.1947	0.2890
2040.0	20.0	0.1860	0.0343	0.0194	4.5306	0.1822	0.3535	3.1095	0.1822	0.2362
2080.0	20.0	0.1988	0.0331	0.0157	4.2402	0.1626	0.2594	2.8336	0.1626	0.1843
2120.0	20.0	0.1127	0.0326	0.0069	3.9144	0.1613	0.2414	3.1215	0.1613	0.1915
2160.0	20.0	0.1850	0.0331	0.0128	3.8244	0.1486	0.2304	2.6304	0.1486	0.1605
2200.0	20.0	0.0492	0.0352	0.0106	3.4190	0.1620	0.2287	3.0986	0.1620	0.2335
2240.0	20.0	0.3992	0.0528	0.0358	4.6975	0.2329	0.2879	2.0170	0.2329	0.1636
2280.0	20.0	0.3823	0.0865	0.0466	5.2345	0.4327	0.5742	2.3394	0.4327	0.4472

Angular Distributions

$\cos(\theta^*_{2\pi^0})$	$W=(1320.0\pm20.0)$ MeV			$W=(1360.0\pm20.0)$ MeV			$W=(1400.0\pm20.0)$ MeV			$W=(1440.0\pm20.0)$ MeV		
	E	Δ_{stat}	Δ_{sys}	E	Δ_{stat}	Δ_{sys}	E	Δ_{stat}	Δ_{sys}	E	Δ_{stat}	Δ_{sys}
−0.80	−14.6627	−120.0099	4.8994	2.2852	2.9525	0.8234	0.8592	0.5902	0.2551	−0.2396	−0.3155	0.0942
−0.40	3.0002	27.8618	1.2574	−3.0156	−3.4331	0.9340	−1.4779	−0.4549	0.2269	−0.7466	−0.3003	0.1395
0.00	−6.9690	−175.2176	3.3814	3.3059	5.5117	1.1521	−0.7173	−0.4602	0.1072	−0.7427	−0.2813	0.0446
0.40	−163.3[illegible]	[illegible]93.4537	82.6349	−0.7878	−8.3592	0.3643	−0.6005	−0.4875	0.0904	−0.5642	−0.2258	0.1117
0.80	−86.2[illegible]	[illegible]38.9551	42.8534	−0.3445	−7.5763	0.2085	−0.6602	−0.5136	0.0817	0.1988	0.4157	0.0549

$\cos(\theta^*_{2\pi^0})$	$W=(1480.0\pm20.0)$ MeV			$W=(1520.0\pm20.0)$ MeV			$W=(1560.0\pm20.0)$ MeV			$W=(1600.0\pm20.0)$ MeV		
	E	Δ_{stat}	Δ_{sys}	E	Δ_{stat}	Δ_{sys}	E	Δ_{stat}	Δ_{sys}	E	Δ_{stat}	Δ_{sys}
−0.80	−0.1524	−0.1505	0.0707	−0.0183	−0.1398	0.0226	−0.2065	−0.1597	0.0300	−0.2058	−0.1851	0.0639
−0.40	0.2140	0.1568	0.0191	−0.9444	−0.2194	0.2198	−0.2366	−0.1519	0.0097	−0.3263	−0.1902	0.0362
0.00	−0.5472	−0.1931	0.0554	−0.6277	−0.1501	0.0668	−0.5410	−0.1665	0.0490	0.2069	0.1382	0.0547
0.40	−0.2153	−0.1261	0.1031	−0.5274	−0.1116	0.1156	−0.1260	−0.0981	0.0698	−0.1837	−0.0930	0.0490
0.80	−0.3032	−0.5082	0.1955	−0.2434	−0.4751	0.0809	0.0928	0.3862	0.3351	−0.2596	−0.2225	0.0128

$\cos(\theta^*_{2\pi^0})$	$W=(1640.0\pm20.0)$ MeV			$W=(1680.0\pm20.0)$ MeV			$W=(1720.0\pm20.0)$ MeV			$W=(1760.0\pm20.0)$ MeV		
	E	Δ_{stat}	Δ_{sys}	E	Δ_{stat}	Δ_{sys}	E	Δ_{stat}	Δ_{sys}	E	Δ_{stat}	Δ_{sys}
−0.80	0.0847	0.1372	0.0099	−0.3739	−0.1139	0.0462	0.0589	0.1004	0.0107	−0.3824	−0.1556	0.0565
−0.40	0.2400	0.1328	0.0127	0.0751	0.1056	0.0139	0.0723	0.1307	0.0210	−0.0667	−0.1050	0.0263
0.00	−0.1162	−0.1337	0.0153	0.2857	0.1337	0.0489	0.7248	0.1489	0.0751	0.4132	0.0787	0.1096
0.40	−0.3317	−0.0648	0.0150	−0.0159	−0.0538	0.0133	0.1180	0.0543	0.0224	0.2013	0.0543	0.0267
0.80	−0.1370	−0.1568	0.0092	−0.0350	−0.1087	0.0145	0.0732	0.1064	0.0262	0.1144	0.0698	0.0429

$\cos(\theta^*_{2\pi^0})$	$W=(1800.0\pm20.0)$ MeV			$W=(1840.0\pm20.0)$ MeV			$W=(1880.0\pm20.0)$ MeV			$W=(1920.0\pm20.0)$ MeV		
	E	Δ_{stat}	Δ_{sys}	E	Δ_{stat}	Δ_{sys}	E	Δ_{stat}	Δ_{sys}	E	Δ_{stat}	Δ_{sys}
−0.80	−0.0590	−0.1225	0.0058	−0.1648	−0.1387	0.0528	−0.1265	−0.1310	0.0084	−1.2314	−0.1826	0.3446
−0.40	0.0271	0.0755	0.1144	−0.2393	−0.0795	0.0410	−0.2640	−0.0852	0.0607	0.1368	0.0853	0.0423
0.00	0.5932	0.0968	0.1045	0.3762	0.0951	0.0189	0.2747	0.0864	0.0235	0.1677	0.0822	0.0107
0.40	0.1970	0.0673	0.0284	0.3119	0.0690	0.0161	0.1628	0.0633	0.0182	0.3113	0.0646	0.0224
0.80	0.2306	0.0763	0.0401	−0.0101	−0.0769	0.0015	−0.1016	−0.0796	0.0223	−0.0040	−0.0724	0.0009

$\cos(\theta^*_{2\pi^0})$	$W=(1960.0\pm20.0)$ MeV			$W=(2000.0\pm20.0)$ MeV			$W=(2040.0\pm20.0)$ MeV			$W=(2080.0\pm20.0)$ MeV		
	E	Δ_{stat}	Δ_{sys}	E	Δ_{stat}	Δ_{sys}	E	Δ_{stat}	Δ_{sys}	E	Δ_{stat}	Δ_{sys}
−0.80	−0.2648	−0.1040	0.0290	−0.2852	−0.0952	0.0797	−0.1121	−0.0888	0.0823	0.3623	0.0953	0.0964
−0.40	0.0648	0.0727	0.0143	−0.3353	−0.0815	0.0492	−0.1146	−0.0773	0.0828	−0.1473	−0.0820	0.0129
0.00	0.1297	0.0737	0.0398	0.2298	0.0763	0.0643	−0.1173	−0.0825	0.0311	0.1992	0.0783	0.0470
0.40	0.0262	0.0606	0.0422	0.0807	0.0600	0.0178	0.5815	0.0663	0.0568	0.4096	0.0615	0.0388
0.80	−0.0481	−0.0753	0.0076	0.0773	0.0746	0.0139	0.2952	0.0754	0.0515	0.1223	0.0748	0.0199

$\cos(\theta^*_{2\pi^0})$	$W=(2120.0\pm20.0)$ MeV			$W=(2160.0\pm20.0)$ MeV			$W=(2200.0\pm20.0)$ MeV			$W=(2240.0\pm20.0)$ MeV		
	E	Δ_{stat}	Δ_{sys}	E	Δ_{stat}	Δ_{sys}	E	Δ_{stat}	Δ_{sys}	E	Δ_{stat}	Δ_{sys}
−0.80	0.2684	0.0940	0.0234	−0.1193	−0.0931	0.0393	0.0582	0.0978	0.0392	−0.3883	−0.1362	0.2187
−0.40	−0.0754	−0.0854	0.0203	0.3412	0.0841	0.0519	0.0998	0.0996	0.0324	−0.0594	−0.1082	0.0219
0.00	0.0400	0.0973	0.0368	0.3682	0.1102	0.1127	−0.1940	−0.1071	0.0139	0.0364	0.1337	0.0352
0.40	0.0180	0.0603	0.0147	0.2649	0.0599	0.0410	0.1168	0.0633	0.0302	0.4846	0.1016	0.0811
0.80	0.2050	0.0709	0.0336	0.0761	0.0676	0.0188	0.1138	0.0691	0.0157	0.5913	0.1033	0.0912

$\cos(\theta^*_{2\pi^0})$	$W=(2280.0\pm20.0)$ MeV		
	E	Δ_{stat}	Δ_{sys}
−0.80	0.4711	0.2024	0.0459
−0.40	0.1081	0.1942	0.0310
0.00	0.1582	0.1902	0.0267
0.40	0.6510	0.2030	0.1060
0.80	0.2567	0.1388	0.0525

$\cos(\theta^*_{2\pi^0})$	$W=(1320.0\pm20.0)$ MeV			$W=(1360.0\pm20.0)$ MeV			$W=(1400.0\pm20.0)$ MeV			$W=(1440.0\pm20.0)$ MeV		
	$d\sigma_{1/2}/d\Omega$ [μb/sr]	Δ_{stat} [μb/sr]	Δ_{sys} [μb/sr]	$d\sigma_{1/2}/d\Omega$ [μb/sr]	Δ_{stat} [μb/sr]	Δ_{sys} [μb/sr]	$d\sigma_{1/2}/d\Omega$ [μb/sr]	Δ_{stat} [μb/sr]	Δ_{sys} [μb/sr]	$d\sigma_{1/2}/d\Omega$ [μb/sr]	Δ_{stat} [μb/sr]	Δ_{sys} [μb/sr]
−0.80	−0.4955	0.4188	0.1738	0.4927	0.2510	0.2603	0.4081	0.1390	0.1865	0.2769	0.1580	0.2092
−0.40	0.2048	0.6379	0.2018	−0.3570	0.2707	0.1654	−0.1500	0.1131	0.0712	0.1179	0.1583	0.0849
0.00	−0.3078	1.8146	0.7136	0.6657	0.3489	0.2776	0.0791	0.1479	0.0596	0.1194	0.1482	0.0317
0.40	9.3946	21.1821	7.3003	0.0211	0.9227	0.6123	0.1867	0.2763	0.0475	0.2888	0.1843	0.0912
0.80	−9.6795	28.3519	8.5547	0.2096	3.2396	1.7139	0.4695	0.8376	0.2272	1.6255	0.7818	0.1184

$\cos(\theta^*_{2\pi^0})$	$W=(1480.0\pm20.0)$ MeV			$W=(1520.0\pm20.0)$ MeV			$W=(1560.0\pm20.0)$ MeV			$W=(1600.0\pm20.0)$ MeV		
	$d\sigma_{1/2}/d\Omega$ [μb/sr]	Δ_{stat} [μb/sr]	Δ_{sys} [μb/sr]	$d\sigma_{1/2}/d\Omega$ [μb/sr]	Δ_{stat} [μb/sr]	Δ_{sys} [μb/sr]	$d\sigma_{1/2}/d\Omega$ [μb/sr]	Δ_{stat} [μb/sr]	Δ_{sys} [μb/sr]	$d\sigma_{1/2}/d\Omega$ [μb/sr]	Δ_{stat} [μb/sr]	Δ_{sys} [μb/sr]
−0.80	0.7805	0.1938	0.0999	0.9585	0.1931	0.1119	0.6565	0.1830	0.1348	0.5063	0.1634	0.1985
−0.40	0.9910	0.1770	0.0434	0.0431	0.1749	0.1753	0.5278	0.1445	0.0088	0.3148	0.1195	0.0660
0.00	0.2871	0.1519	0.0382	0.2633	0.1272	0.0572	0.2383	0.1075	0.0267	0.5451	0.0864	0.0277
0.40	0.6346	0.1410	0.1610	0.3451	0.1019	0.1075	0.5170	0.0814	0.0943	0.4328	0.0686	0.0507
0.80	0.4666	0.4606	0.5308	0.3268	0.2820	0.2050	0.4584	0.2281	0.1298	0.3280	0.1349	0.0214

$\cos(\theta^*_{2\pi^0})$	$W=(1640.0\pm20.0)$ MeV			$W=(1680.0\pm20.0)$ MeV			$W=(1720.0\pm20.0)$ MeV			$W=(1760.0\pm20.0)$ MeV		
	$d\sigma_{1/2}/d\Omega$ [μb/sr]	Δ_{stat} [μb/sr]	Δ_{sys} [μb/sr]	$d\sigma_{1/2}/d\Omega$ [μb/sr]	Δ_{stat} [μb/sr]	Δ_{sys} [μb/sr]	$d\sigma_{1/2}/d\Omega$ [μb/sr]	Δ_{stat} [μb/sr]	Δ_{sys} [μb/sr]	$d\sigma_{1/2}/d\Omega$ [μb/sr]	Δ_{stat} [μb/sr]	Δ_{sys} [μb/sr]
−0.80	0.7588	0.1352	0.1136	0.4799	0.1156	0.1054	0.8089	0.1083	0.0185	0.3071	0.1022	0.1042
−0.40	0.6353	0.0936	0.0299	0.5887	0.0816	0.0348	0.4831	0.0830	0.0736	0.4111	0.0653	0.0113
0.00	0.3325	0.0707	0.0675	0.5980	0.0845	0.0490	0.9125	0.0902	0.0317	0.8311	0.0605	0.0694
0.40	0.4282	0.0557	0.0199	0.7791	0.0602	0.0186	0.9516	0.0649	0.0690	0.8286	0.0520	0.0187
0.80	0.4857	0.1237	0.0571	0.7183	0.1143	0.0902	0.8995	0.1258	0.0526	0.7744	0.0681	0.0696

$\cos(\theta^*_{2\pi^0})$	$W=(1800.0\pm20.0)$ MeV			$W=(1840.0\pm20.0)$ MeV			$W=(1880.0\pm20.0)$ MeV			$W=(1920.0\pm20.0)$ MeV		
	$d\sigma_{1/2}/d\Omega$ [μb/sr]	Δ_{stat} [μb/sr]	Δ_{sys} [μb/sr]	$d\sigma_{1/2}/d\Omega$ [μb/sr]	Δ_{stat} [μb/sr]	Δ_{sys} [μb/sr]	$d\sigma_{1/2}/d\Omega$ [μb/sr]	Δ_{stat} [μb/sr]	Δ_{sys} [μb/sr]	$d\sigma_{1/2}/d\Omega$ [μb/sr]	Δ_{stat} [μb/sr]	Δ_{sys} [μb/sr]
−0.80	0.4282	0.0787	0.0028	0.3215	0.0745	0.0361	0.3231	0.0680	0.0136	−0.0775	0.0545	0.1402
−0.40	0.5006	0.0520	0.1028	0.3144	0.0452	0.0417	0.2975	0.0471	0.0532	0.4076	0.0428	0.0725
0.00	0.7905	0.0584	0.1161	0.5730	0.0524	0.0313	0.4982	0.0461	0.0424	0.4026	0.0395	0.0208
0.40	0.6824	0.0533	0.0168	0.6839	0.0486	0.0217	0.5894	0.0448	0.0315	0.6070	0.0404	0.0076
0.80	0.7327	0.0626	0.0214	0.5104	0.0561	0.0636	0.4560	0.0568	0.0240	0.4724	0.0486	0.0497

$\cos(\theta^*_{2\pi^0})$	$W=(1960.0\pm20.0)$ MeV			$W=(2000.0\pm20.0)$ MeV			$W=(2040.0\pm20.0)$ MeV			$W=(2080.0\pm20.0)$ MeV		
	$d\sigma_{1/2}/d\Omega$ [μb/sr]	Δ_{stat} [μb/sr]	Δ_{sys} [μb/sr]	$d\sigma_{1/2}/d\Omega$ [μb/sr]	Δ_{stat} [μb/sr]	Δ_{sys} [μb/sr]	$d\sigma_{1/2}/d\Omega$ [μb/sr]	Δ_{stat} [μb/sr]	Δ_{sys} [μb/sr]	$d\sigma_{1/2}/d\Omega$ [μb/sr]	Δ_{stat} [μb/sr]	Δ_{sys} [μb/sr]
−0.80	0.2476	0.0479	0.0232	0.2205	0.0399	0.0553	0.2595	0.0365	0.0235	0.3729	0.0347	0.0151
−0.40	0.3911	0.0377	0.0745	0.2032	0.0334	0.0347	0.2496	0.0306	0.0630	0.2016	0.0271	0.0204
0.00	0.3745	0.0343	0.0659	0.3384	0.0289	0.0688	0.2136	0.0281	0.0142	0.2701	0.0245	0.0467
0.40	0.4209	0.0352	0.0400	0.3814	0.0299	0.0157	0.5171	0.0265	0.0621	0.4504	0.0257	0.0184
0.80	0.4203	0.0469	0.0583	0.4210	0.0411	0.0634	0.4880	0.0385	0.0750	0.3955	0.0370	0.0350

$\cos(\theta^*_{2\pi^0})$	$W=(2120.0\pm20.0)$ MeV			$W=(2160.0\pm20.0)$ MeV			$W=(2200.0\pm20.0)$ MeV			$W=(2240.0\pm20.0)$ MeV		
	$d\sigma_{1/2}/d\Omega$ [μb/sr]	Δ_{stat} [μb/sr]	Δ_{sys} [μb/sr]	$d\sigma_{1/2}/d\Omega$ [μb/sr]	Δ_{stat} [μb/sr]	Δ_{sys} [μb/sr]	$d\sigma_{1/2}/d\Omega$ [μb/sr]	Δ_{stat} [μb/sr]	Δ_{sys} [μb/sr]	$d\sigma_{1/2}/d\Omega$ [μb/sr]	Δ_{stat} [μb/sr]	Δ_{sys} [μb/sr]
−0.80	0.3362	0.0341	0.0053	0.2039	0.0303	0.0147	0.2415	0.0315	0.0157	0.1294	0.0380	0.0498
−0.40	0.2416	0.0315	0.0391	0.2867	0.0241	0.0416	0.2298	0.0293	0.0185	0.1981	0.0322	0.0126
0.00	0.2152	0.0285	0.0293	0.2944	0.0315	0.0651	0.1441	0.0266	0.0112	0.2191	0.0399	0.0548
0.40	0.3220	0.0270	0.0148	0.3749	0.0243	0.0245	0.3456	0.0275	0.0364	0.4659	0.0406	0.0648
0.80	0.4218	0.0344	0.0784	0.3522	0.0312	0.0584	0.4135	0.0361	0.0736	0.6182	0.0488	0.0894

$\cos(\theta^*_{2\pi^0})$	$W=(2280.0\pm20.0)$ MeV		
	$d\sigma_{1/2}/d\Omega$ [μb/sr]	Δ_{stat} [μb/sr]	Δ_{sys} [μb/sr]
−0.80	0.3533	0.0622	0.0306
−0.40	0.2487	0.0613	0.0081
0.00	0.2603	0.0597	0.0090
0.40	0.5656	0.0824	0.0513
0.80	0.5968	0.0903	0.1892

$\cos(\theta^*_{2\pi^0})$	$W=(1320.0\pm20.0)$ MeV			$W=(1360.0\pm20.0)$ MeV			$W=(1400.0\pm20.0)$ MeV			$W=(1440.0\pm20.0)$ MeV		
	$d\sigma_{3/2}/d\Omega$ [μb/sr]	Δ_{stat} [μb/sr]	Δ_{sys} [μb/sr]	$d\sigma_{3/2}/d\Omega$ [μb/sr]	Δ_{stat} [μb/sr]	Δ_{sys} [μb/sr]	$d\sigma_{3/2}/d\Omega$ [μb/sr]	Δ_{stat} [μb/sr]	Δ_{sys} [μb/sr]	$d\sigma_{3/2}/d\Omega$ [μb/sr]	Δ_{stat} [μb/sr]	Δ_{sys} [μb/sr]
−0.80	0.5680	0.4188	0.2081	−0.1927	0.2510	0.1813	0.0309	0.1390	0.1407	0.4513	0.1580	0.2272
−0.40	−0.1024	0.6379	0.1326	0.7113	0.2707	0.3195	0.7776	0.1131	0.1407	0.8128	0.1583	0.0738
0.00	0.4109	1.8146	0.8525	−0.3565	0.3489	0.1779	0.4801	0.1479	0.1115	0.8086	0.1482	0.0729
0.40	−9.5103	21.1821	4.7811	0.1776	0.9227	0.7460	0.7481	0.2763	0.0436	1.0365	0.1843	0.1435
0.80	9.9065	28.3519	13.4189	0.4300	3.2396	2.1617	2.2940	0.8376	0.3401	1.0864	0.7818	0.0729

$\cos(\theta^*_{2\pi^0})$	$W=(1480.0\pm20.0)$ MeV			$W=(1520.0\pm20.0)$ MeV			$W=(1560.0\pm20.0)$ MeV			$W=(1600.0\pm20.0)$ MeV		
	$d\sigma_{3/2}/d\Omega$ [μb/sr]	$\Delta_{\rm stat}$ [μb/sr]	$\Delta_{\rm sys}$ [μb/sr]	$d\sigma_{3/2}/d\Omega$ [μb/sr]	$\Delta_{\rm stat}$ [μb/sr]	$\Delta_{\rm sys}$ [μb/sr]	$d\sigma_{3/2}/d\Omega$ [μb/sr]	$\Delta_{\rm stat}$ [μb/sr]	$\Delta_{\rm sys}$ [μb/sr]	$d\sigma_{3/2}/d\Omega$ [μb/sr]	$\Delta_{\rm stat}$ [μb/sr]	$\Delta_{\rm sys}$ [μb/sr]
−0.80	1.0612	0.1938	0.0764	0.9941	0.1931	0.1135	0.9983	0.1830	0.1557	0.7687	0.1634	0.2237
−0.40	0.6416	0.1770	0.0204	1.5075	0.1749	0.1893	0.8550	0.1445	0.0068	0.6197	0.1195	0.0828
0.00	0.9809	0.1519	0.0297	1.1514	0.1272	0.0712	0.7999	0.1075	0.0237	0.3582	0.0864	0.0267
0.40	0.9828	0.1410	0.1790	1.1152	0.1019	0.1641	0.6661	0.0814	0.0848	0.6275	0.0686	0.0435
0.80	0.8728	0.4606	0.3156	0.5371	0.2820	0.1876	0.3805	0.2281	0.1869	0.5579	0.1349	0.0469

$\cos(\theta^*_{2\pi^0})$	$W=(1640.0\pm20.0)$ MeV			$W=(1680.0\pm20.0)$ MeV			$W=(1720.0\pm20.0)$ MeV			$W=(1760.0\pm20.0)$ MeV		
	$d\sigma_{3/2}/d\Omega$ [μb/sr]	$\Delta_{\rm stat}$ [μb/sr]	$\Delta_{\rm sys}$ [μb/sr]	$d\sigma_{3/2}/d\Omega$ [μb/sr]	$\Delta_{\rm stat}$ [μb/sr]	$\Delta_{\rm sys}$ [μb/sr]	$d\sigma_{3/2}/d\Omega$ [μb/sr]	$\Delta_{\rm stat}$ [μb/sr]	$\Delta_{\rm sys}$ [μb/sr]	$d\sigma_{3/2}/d\Omega$ [μb/sr]	$\Delta_{\rm stat}$ [μb/sr]	$\Delta_{\rm sys}$ [μb/sr]
−0.80	0.6403	0.1352	0.1067	1.0531	0.1156	0.1272	0.7189	0.1083	0.0094	0.6873	0.1022	0.1369
−0.40	0.3894	0.0936	0.0245	0.5064	0.0816	0.0352	0.4179	0.0830	0.0741	0.4699	0.0653	0.0160
0.00	0.4200	0.0707	0.0869	0.3322	0.0845	0.0593	0.1456	0.0902	0.0513	0.3451	0.0605	0.0766
0.40	0.8532	0.0557	0.0238	0.8042	0.0602	0.0115	0.7507	0.0649	0.0474	0.5510	0.0520	0.0194
0.80	0.6399	0.1237	0.0745	0.7704	0.1143	0.1160	0.7768	0.1258	0.0862	0.6154	0.0681	0.1016

$\cos(\theta^*_{2\pi^0})$	$W=(1800.0\pm20.0)$ MeV			$W=(1840.0\pm20.0)$ MeV			$W=(1880.0\pm20.0)$ MeV			$W=(1920.0\pm20.0)$ MeV		
	$d\sigma_{3/2}/d\Omega$ [μb/sr]	$\Delta_{\rm stat}$ [μb/sr]	$\Delta_{\rm sys}$ [μb/sr]	$d\sigma_{3/2}/d\Omega$ [μb/sr]	$\Delta_{\rm stat}$ [μb/sr]	$\Delta_{\rm sys}$ [μb/sr]	$d\sigma_{3/2}/d\Omega$ [μb/sr]	$\Delta_{\rm stat}$ [μb/sr]	$\Delta_{\rm sys}$ [μb/sr]	$d\sigma_{3/2}/d\Omega$ [μb/sr]	$\Delta_{\rm stat}$ [μb/sr]	$\Delta_{\rm sys}$ [μb/sr]
−0.80	0.4819	0.0787	0.0038	0.4484	0.0745	0.0697	0.4167	0.0680	0.0100	0.7472	0.0545	0.0347
−0.40	0.4741	0.0520	0.0598	0.5123	0.0452	0.0554	0.5110	0.0471	0.0613	0.3095	0.0428	0.0641
0.00	0.2018	0.0584	0.0462	0.2598	0.0524	0.0190	0.2835	0.0461	0.0285	0.2870	0.0395	0.0176
0.40	0.4578	0.0533	0.0205	0.3587	0.0486	0.0220	0.4243	0.0448	0.0206	0.3188	0.0404	0.0136
0.80	0.4581	0.0626	0.0279	0.5208	0.0561	0.0635	0.5591	0.0568	0.0359	0.4763	0.0486	0.0508

$\cos(\theta^*_{2\pi^0})$	$W=(1960.0\pm20.0)$ MeV			$W=(2000.0\pm20.0)$ MeV			$W=(2040.0\pm20.0)$ MeV			$W=(2080.0\pm20.0)$ MeV		
	$d\sigma_{3/2}/d\Omega$ [μb/sr]	$\Delta_{\rm stat}$ [μb/sr]	$\Delta_{\rm sys}$ [μb/sr]	$d\sigma_{3/2}/d\Omega$ [μb/sr]	$\Delta_{\rm stat}$ [μb/sr]	$\Delta_{\rm sys}$ [μb/sr]	$d\sigma_{3/2}/d\Omega$ [μb/sr]	$\Delta_{\rm stat}$ [μb/sr]	$\Delta_{\rm sys}$ [μb/sr]	$d\sigma_{3/2}/d\Omega$ [μb/sr]	$\Delta_{\rm stat}$ [μb/sr]	$\Delta_{\rm sys}$ [μb/sr]
−0.80	0.4260	0.0479	0.0131	0.3964	0.0399	0.0799	0.3250	0.0365	0.0352	0.1746	0.0347	0.0460
−0.40	0.3435	0.0377	0.0622	0.4081	0.0334	0.0578	0.3142	0.0306	0.0542	0.2713	0.0271	0.0243
0.00	0.2885	0.0343	0.0544	0.2119	0.0289	0.0494	0.2704	0.0281	0.0137	0.1803	0.0245	0.0361
0.40	0.3995	0.0352	0.0275	0.3244	0.0299	0.0069	0.1368	0.0265	0.0267	0.1887	0.0257	0.0244
0.80	0.4628	0.0469	0.0654	0.3606	0.0411	0.0647	0.2656	0.0385	0.0712	0.3093	0.0370	0.0399

$\cos(\theta^*_{2\pi^0})$	$W=(2120.0\pm20.0)$ MeV			$W=(2160.0\pm20.0)$ MeV			$W=(2200.0\pm20.0)$ MeV			$W=(2240.0\pm20.0)$ MeV		
	$d\sigma_{3/2}/d\Omega$ [μb/sr]	$\Delta_{\rm stat}$ [μb/sr]	$\Delta_{\rm sys}$ [μb/sr]	$d\sigma_{3/2}/d\Omega$ [μb/sr]	$\Delta_{\rm stat}$ [μb/sr]	$\Delta_{\rm sys}$ [μb/sr]	$d\sigma_{3/2}/d\Omega$ [μb/sr]	$\Delta_{\rm stat}$ [μb/sr]	$\Delta_{\rm sys}$ [μb/sr]	$d\sigma_{3/2}/d\Omega$ [μb/sr]	$\Delta_{\rm stat}$ [μb/sr]	$\Delta_{\rm sys}$ [μb/sr]
−0.80	0.1939	0.0341	0.0129	0.2591	0.0303	0.0093	0.2149	0.0315	0.0102	0.2937	0.0380	0.0460
−0.40	0.2810	0.0315	0.0412	0.1408	0.0241	0.0249	0.1881	0.0293	0.0073	0.2231	0.0322	0.0054
0.00	0.1986	0.0285	0.0278	0.1360	0.0315	0.0409	0.2134	0.0266	0.0136	0.2037	0.0399	0.0512
0.40	0.3106	0.0270	0.0061	0.2179	0.0243	0.0136	0.2733	0.0275	0.0267	0.1617	0.0406	0.0393
0.80	0.2783	0.0344	0.0712	0.3023	0.0312	0.0587	0.3291	0.0361	0.0685	0.1588	0.0488	0.0731

$\cos(\theta^*_{2\pi^0})$	$W=(2280.0\pm20.0)$ MeV		
	$d\sigma_{3/2}/d\Omega$ [μb/sr]	$\Delta_{\rm stat}$ [μb/sr]	$\Delta_{\rm sys}$ [μb/sr]
−0.80	0.1270	0.0622	0.0196
−0.40	0.2001	0.0613	0.0175
0.00	0.1891	0.0597	0.0173
0.40	0.1196	0.0824	0.0400
0.80	0.3530	0.0903	0.1642

E.6.6 Observables for $\gamma n \to \pi^0\pi^0 n$ as a Function of W

W [MeV]	ΔW [MeV]	E	$\Delta_{\rm stat}$	$\Delta_{\rm sys}$	$\sigma_{1/2}$ [μb]	$\Delta_{\rm stat}$ [μb]	$\Delta_{\rm sys}$ [μb]	$\sigma_{3/2}$ [μb]	$\Delta_{\rm stat}$ [μb]	$\Delta_{\rm sys}$ [μb]
1320.0	20.0	31.3456	482.4190	107.7236	13.4146	9.0220	31.9378	−12.5851	9.0220	32.1968
1360.0	20.0	−1.2752	3.7831	0.4692	−0.2650	3.1789	1.2758	2.1908	3.1789	1.7265
1400.0	20.0	−0.4866	0.3167	0.1471	1.9590	1.5369	0.6126	5.6728	1.5369	0.5057
1440.0	20.0	−0.3615	0.2219	0.0904	3.2369	1.4959	0.6726	6.9014	1.4959	0.7111
1480.0	20.0	−0.7308	0.1772	0.1252	2.3673	1.7792	1.0779	15.2182	1.7792	2.6072
1520.0	20.0	−0.4906	0.1254	0.0843	5.0697	1.5840	1.1727	14.8367	1.5840	1.7957
1560.0	20.0	−0.4882	0.1301	0.0968	4.6011	1.4861	0.6413	13.3786	1.4861	2.0476
1600.0	20.0	−0.1210	0.1031	0.0221	7.2179	1.1889	0.6212	9.2055	1.1889	0.6314
1640.0	20.0	−0.0617	0.0776	0.0168	8.3609	0.9765	1.1614	9.4601	0.9765	1.1845
1680.0	20.0	−0.1046	0.0839	0.0361	7.8581	1.0352	1.0483	9.6934	1.0352	1.0390
1720.0	20.0	−0.0760	0.0645	0.0357	7.7277	0.7607	1.6832	8.9986	0.7607	1.7745
1760.0	20.0	−0.3842	0.0763	0.1785	3.6902	0.6037	1.3854	8.2952	0.6037	1.9521
1800.0	20.0	−0.3812	0.0760	0.1368	2.8338	0.4602	0.9035	6.3257	0.4602	1.2981
1840.0	20.0	−0.5872	0.0893	0.2753	1.5732	0.4150	1.0448	6.0490	0.4150	2.0215
1880.0	20.0	−0.3579	0.0765	0.1071	2.6094	0.4141	0.7360	5.5179	0.4141	1.0771
1920.0	20.0	−0.0978	0.0678	0.0447	3.3519	0.3544	0.6679	4.0788	0.3544	0.7028
1960.0	20.0	−0.0380	0.0619	0.0271	3.6262	0.3297	0.9341	3.9123	0.3297	0.9834
2000.0	20.0	−0.1628	0.0606	0.0701	2.9769	0.3006	0.7223	4.1351	0.3006	0.8557
2040.0	20.0	−0.2824	0.0669	0.0780	2.1774	0.2763	0.5270	3.8910	0.2763	0.7460
2080.0	20.0	−0.2588	0.0659	0.0726	2.2022	0.2680	0.4752	3.7404	0.2680	0.5977
2120.0	20.0	−0.0863	0.0646	0.0454	2.5514	0.2542	0.5193	3.0332	0.2542	0.5255
2160.0	20.0	−0.1957	0.0656	0.0373	2.1495	0.2435	0.3410	3.1956	0.2435	0.4029
2200.0	20.0	−0.1208	0.0647	0.0260	2.1955	0.2268	0.3692	2.7991	0.2268	0.4242
2240.0	20.0	−0.0333	0.1010	0.0198	2.4140	0.3565	0.2100	2.5800	0.3565	0.1850
2280.0	20.0	−0.2293	0.1136	0.0319	2.3004	0.4675	0.2759	3.6689	0.4675	0.3325

Angular Distributions

	W=(1320.0±20.0) MeV			W=(1360.0±20.0) MeV			W=(1400.0±20.0) MeV			W=(1440.0±20.0) MeV		
$\cos(\theta^*_{2\pi^0})$	E	$\Delta_{\rm stat}$	$\Delta_{\rm sys}$	E	$\Delta_{\rm stat}$	$\Delta_{\rm sys}$	E	$\Delta_{\rm stat}$	$\Delta_{\rm sys}$	E	$\Delta_{\rm stat}$	$\Delta_{\rm sys}$
−0.80	15.6084	130.3153	36.3508	8.4424	92.2041	3.8937	−0.0600	−0.7441	0.1845	0.8017	0.8169	0.1371
−0.40	18.1516	545.9338	341.2424	−0.2693	−3.2337	0.1414	−1.6123	−1.0716	0.8692	0.3334	0.4382	0.2931
0.00	41.6946	474.8239	16.9113	−5.8236	617.5565	0.9130	0.8017	0.7346	0.0771	−0.1616	−0.4034	0.2983
0.40	[illegible]	[illegible]	26.0672	0.4692	4.5423	0.3122	−0.7803	−0.6761	0.1043	−1.5506	−0.8230	0.3464
0.80	[illegible]	[illegible]	311.2408	23.1579	1238.1382	11.2862	−0.8689	−1.0965	0.2220	−0.5001	−0.8755	0.2242

	W=(1480.0±20.0) MeV			W=(1520.0±20.0) MeV			W=(1560.0±20.0) MeV			W=(1600.0±20.0) MeV		
$\cos(\theta^*_{2\pi^0})$	E	$\Delta_{\rm stat}$	$\Delta_{\rm sys}$	E	$\Delta_{\rm stat}$	$\Delta_{\rm sys}$	E	$\Delta_{\rm stat}$	$\Delta_{\rm sys}$	E	$\Delta_{\rm stat}$	$\Delta_{\rm sys}$
−0.80	−0.1184	−0.2778	0.0391	−0.3726	−0.2507	0.0212	0.3633	0.2232	0.0565	0.8337	0.2972	0.2151
−0.40	−0.6157	−0.3505	0.0849	−1.0374	−0.3921	0.2694	−0.2335	−0.3088	0.0726	−0.3183	−0.2374	0.0416
0.00	−0.9375	−0.4032	0.2081	−0.7411	−0.3188	0.0917	−0.7320	−0.3661	0.1645	−0.0763	−0.2590	0.0744
0.40	−0.6120	−0.3019	0.1606	−0.4056	−0.2106	0.1264	−0.0839	−0.2203	0.2180	−0.3809	−0.2135	0.1389
0.80	−1.0295	−0.8072	0.3812	−0.4658	−0.4954	0.0109	0.1092	0.3475	0.0549	−0.0682	−0.2687	0.0256

	W=(1640.0±20.0) MeV			W=(1680.0±20.0) MeV			W=(1720.0±20.0) MeV			W=(1760.0±20.0) MeV		
$\cos(\theta^*_{2\pi^0})$	E	$\Delta_{\rm stat}$	$\Delta_{\rm sys}$	E	$\Delta_{\rm stat}$	$\Delta_{\rm sys}$	E	$\Delta_{\rm stat}$	$\Delta_{\rm sys}$	E	$\Delta_{\rm stat}$	$\Delta_{\rm sys}$
−0.80	−0.0394	−0.1649	0.0480	0.3590	0.1988	0.0181	−0.6135	−0.2133	0.0770	−0.0124	−0.1875	0.0162
−0.40	0.1013	0.1698	0.0334	0.0285	0.1948	0.0258	−0.3388	−0.1224	0.1803	−0.6038	−0.1898	0.2818
0.00	−0.0345	−0.1952	0.0249	−0.3492	−0.1451	0.1153	0.0290	0.1261	0.0113	−0.3372	−0.1403	0.4281
0.40	−0.4748	−0.1582	0.1185	−0.1750	−0.1409	0.0675	−0.0000	−0.1240	0.0112	−0.0914	−0.1211	0.1001
0.80	0.6499	0.3064	0.0180	0.1448	0.2204	0.0212	0.5252	0.2692	0.0555	−0.7518	−0.2338	0.1146

	W=(1800.0±20.0) MeV			W=(1840.0±20.0) MeV			W=(1880.0±20.0) MeV			W=(1920.0±20.0) MeV		
$\cos(\theta^*_{2\pi^0})$	E	$\Delta_{\rm stat}$	$\Delta_{\rm sys}$	E	$\Delta_{\rm stat}$	$\Delta_{\rm sys}$	E	$\Delta_{\rm stat}$	$\Delta_{\rm sys}$	E	$\Delta_{\rm stat}$	$\Delta_{\rm sys}$
−0.80	−0.0111	−0.2261	0.0121	−0.0985	−0.2228	0.0219	0.6316	0.2062	0.2027	0.0136	0.1857	0.1620
−0.40	−0.1822	−0.1633	0.2225	−0.3946	−0.1921	0.3514	−0.7004	−0.1926	0.3531	−0.1664	−0.1340	0.0214
0.00	−0.3855	−0.1476	0.3968	−0.7858	−0.1895	2.8542	−0.2174	−0.1311	0.1110	0.0709	0.1382	0.0549
0.40	−0.7156	−0.1731	0.1708	−0.2490	−0.1465	0.0849	−0.5210	−0.1792	0.0633	−0.3344	−0.1500	0.0602
0.80	−0.1850	−0.2595	0.0182	−1.1889	−0.3632	0.1183	−0.0112	−0.2157	0.0156	0.3361	0.2202	0.0697

	W=(1960.0±20.0) MeV			W=(2000.0±20.0) MeV			W=(2040.0±20.0) MeV			W=(2080.0±20.0) MeV		
$\cos(\theta^*_{2\pi^0})$	E	$\Delta_{\rm stat}$	$\Delta_{\rm sys}$	E	$\Delta_{\rm stat}$	$\Delta_{\rm sys}$	E	$\Delta_{\rm stat}$	$\Delta_{\rm sys}$	E	$\Delta_{\rm stat}$	$\Delta_{\rm sys}$
−0.80	0.3619	0.1824	0.1252	−0.1351	−0.1361	0.0148	−0.1089	−0.1536	0.0856	0.3493	0.2257	0.2022
−0.40	−0.1612	−0.1414	0.1782	−0.0989	−0.1264	0.0963	−0.2052	−0.1297	37.5059	−0.2429	−0.1508	0.4619
0.00	−0.1119	−0.1206	0.1675	−0.3329	−0.1222	0.1672	−0.8103	−0.1830	0.2573	−0.2431	−0.1329	0.2013
0.40	0.3122	0.1400	0.1798	−0.0208	−0.1171	0.0074	−0.1338	−0.1104	0.0361	−0.1812	−0.1304	0.0226
0.80	−0.1782	−0.2047	0.0638	−0.5325	−0.1831	0.0812	0.0999	0.1936	0.0333	−0.4124	−0.2013	0.0683

	W=(2120.0±20.0) MeV			W=(2160.0±20.0) MeV			W=(2200.0±20.0) MeV			W=(2240.0±20.0) MeV		
$\cos(\theta^*_{2\pi^0})$	E	$\Delta_{\rm stat}$	$\Delta_{\rm sys}$	E	$\Delta_{\rm stat}$	$\Delta_{\rm sys}$	E	$\Delta_{\rm stat}$	$\Delta_{\rm sys}$	E	$\Delta_{\rm stat}$	$\Delta_{\rm sys}$
−0.80	0.2949	0.1445	0.0362	−0.9019	−0.2632	0.2959	0.0018	0.1599	0.2180	−0.0369	−0.2621	0.0528
−0.40	−0.4298	−0.1757	0.1180	−0.3582	−0.1995	0.1787	−0.2252	−0.1635	0.0370	0.1480	0.3174	0.0475
0.00	0.2858	0.1579	0.1141	−0.4353	−0.2088	0.1528	−0.3560	−0.1838	0.6056	0.0703	0.1969	0.0236
0.40	−0.4667	−0.1238	0.3752	0.0072	0.1404	0.0143	−0.6922	−0.1645	0.0355	−0.1056	−0.1817	0.0220
0.80	0.1093	0.1435	0.0135	−0.3340	−0.1640	0.0087	0.5651	0.1902	0.1074	−0.2589	−0.1805	0.0384

$\cos(\theta^*_{2\pi^0})$	$W=(2280.0\pm20.0)$ MeV		
	E	Δ_{stat}	Δ_{sys}
−0.80	0.4648	0.3345	0.1215
−0.40	−1.2616	−0.5392	5.5104
0.00	−0.0088	−0.3931	0.0917
0.40	−0.2432	−0.2675	0.7748
0.80	−0.5160	−0.3504	0.1527

$\cos(\theta^*_{2\pi^0})$	$W=(1320.0\pm20.0)$ MeV			$W=(1360.0\pm20.0)$ MeV			$W=(1400.0\pm20.0)$ MeV			$W=(1440.0\pm20.0)$ MeV		
	$d\sigma_{1/2}/d\Omega$ [μb/sr]	Δ_{stat} [μb/sr]	Δ_{sys} [μb/sr]	$d\sigma_{1/2}/d\Omega$ [μb/sr]	Δ_{stat} [μb/sr]	Δ_{sys} [μb/sr]	$d\sigma_{1/2}/d\Omega$ [μb/sr]	Δ_{stat} [μb/sr]	Δ_{sys} [μb/sr]	$d\sigma_{1/2}/d\Omega$ [μb/sr]	Δ_{stat} [μb/sr]	Δ_{sys} [μb/sr]
−0.80	1.5902	1.1282	0.8331	0.3729	0.6058	0.3635	0.2317	0.2589	0.0441	0.6551	0.3278	0.1892
−0.40	0.7179	1.5919	0.5336	0.0823	0.4972	0.0459	−0.2093	0.2730	0.2123	0.5995	0.2643	0.2527
0.00	1.6990	1.9901	0.7506	−0.6984	0.6084	0.0817	0.5874	0.2642	0.0872	0.4094	0.2750	0.1619
0.40	0.2620	1.8279	0.1306	0.1057	0.4184	0.1110	0.0716	0.2455	0.0341	−0.2207	0.2529	0.0903
0.80	1.8357	25.4137	1.0312	0.3458	1.0812	0.4374	0.0365	0.3258	0.0532	0.1572	0.3483	0.0709

$\cos(\theta^*_{2\pi^0})$	$W=(1480.0\pm20.0)$ MeV			$W=(1520.0\pm20.0)$ MeV			$W=(1560.0\pm20.0)$ MeV			$W=(1600.0\pm20.0)$ MeV		
	$d\sigma_{1/2}/d\Omega$ [μb/sr]	Δ_{stat} [μb/sr]	Δ_{sys} [μb/sr]	$d\sigma_{1/2}/d\Omega$ [μb/sr]	Δ_{stat} [μb/sr]	Δ_{sys} [μb/sr]	$d\sigma_{1/2}/d\Omega$ [μb/sr]	Δ_{stat} [μb/sr]	Δ_{sys} [μb/sr]	$d\sigma_{1/2}/d\Omega$ [μb/sr]	Δ_{stat} [μb/sr]	Δ_{sys} [μb/sr]
−0.80	0.7342	0.3250	0.0231	0.7441	0.3941	0.0761	1.4978	0.3260	0.0845	1.7638	0.3106	0.2066
−0.40	0.2920	0.3206	0.0649	−0.0303	0.3112	0.1857	0.5271	0.2924	0.0960	0.5370	0.2520	0.0393
0.00	0.0490	0.3261	0.1477	0.2008	0.2809	0.0765	0.1821	0.2839	0.1082	0.4445	0.1757	0.0477
0.40	0.2670	0.2507	0.1184	0.4542	0.2109	0.1435	0.5826	0.1974	0.1860	0.3524	0.1606	0.1052
0.80	−0.0128	0.3450	0.1147	0.2275	0.2705	0.0050	0.5270	0.2321	0.0273	0.4354	0.1771	0.0910

$\cos(\theta^*_{2\pi^0})$	$W=(1640.0\pm20.0)$ MeV			$W=(1680.0\pm20.0)$ MeV			$W=(1720.0\pm20.0)$ MeV			$W=(1760.0\pm20.0)$ MeV		
	$d\sigma_{1/2}/d\Omega$ [μb/sr]	Δ_{stat} [μb/sr]	Δ_{sys} [μb/sr]	$d\sigma_{1/2}/d\Omega$ [μb/sr]	Δ_{stat} [μb/sr]	Δ_{sys} [μb/sr]	$d\sigma_{1/2}/d\Omega$ [μb/sr]	Δ_{stat} [μb/sr]	Δ_{sys} [μb/sr]	$d\sigma_{1/2}/d\Omega$ [μb/sr]	Δ_{stat} [μb/sr]	Δ_{sys} [μb/sr]
−0.80	1.0166	0.2466	0.0147	1.1457	0.2231	0.0637	0.2707	0.1801	0.0703	0.4011	0.1077	0.0426
−0.40	0.8446	0.1832	0.1035	0.7107	0.1903	0.0920	0.4778	0.1185	0.1864	0.1936	0.1123	0.1197
0.00	0.5718	0.1634	0.0537	0.5288	0.1574	0.1432	0.7898	0.1369	0.1800	0.3707	0.1052	0.2090
0.40	0.3586	0.1380	0.1137	0.5421	0.1289	0.1030	0.6634	0.1164	0.1432	0.4551	0.0854	0.1248
0.80	0.7343	0.1617	0.0231	0.5589	0.1506	0.0226	0.7224	0.1596	0.0270	0.1066	0.1135	0.0499

$\cos(\theta^*_{2\pi^0})$	$W=(1800.0\pm20.0)$ MeV			$W=(1840.0\pm20.0)$ MeV			$W=(1880.0\pm20.0)$ MeV			$W=(1920.0\pm20.0)$ MeV		
	$d\sigma_{1/2}/d\Omega$ [μb/sr]	Δ_{stat} [μb/sr]	Δ_{sys} [μb/sr]	$d\sigma_{1/2}/d\Omega$ [μb/sr]	Δ_{stat} [μb/sr]	Δ_{sys} [μb/sr]	$d\sigma_{1/2}/d\Omega$ [μb/sr]	Δ_{stat} [μb/sr]	Δ_{sys} [μb/sr]	$d\sigma_{1/2}/d\Omega$ [μb/sr]	Δ_{stat} [μb/sr]	Δ_{sys} [μb/sr]
−0.80	0.2734	0.0884	0.0068	0.2261	0.0787	0.0058	0.5230	0.0791	0.0808	0.3179	0.0824	0.0915
−0.40	0.2900	0.0806	0.1091	0.1937	0.0809	0.1124	0.1066	0.0794	0.1246	0.2641	0.0592	0.0324
0.00	0.2753	0.0873	0.1544	0.0838	0.0825	1.1172	0.3044	0.0705	0.0982	0.3622	0.0659	0.1093
0.40	0.1144	0.0800	0.0687	0.2252	0.0603	0.0608	0.1378	0.0646	0.0281	0.1758	0.0531	0.0258
0.80	0.2778	0.1230	0.0106	−0.0480	0.0841	0.0315	0.2612	0.0806	0.0268	0.3281	0.0725	0.0611

$\cos(\theta^*_{2\pi^0})$	$W=(1960.0\pm20.0)$ MeV			$W=(2000.0\pm20.0)$ MeV			$W=(2040.0\pm20.0)$ MeV			$W=(2080.0\pm20.0)$ MeV		
	$d\sigma_{1/2}/d\Omega$ [μb/sr]	Δ_{stat} [μb/sr]	Δ_{sys} [μb/sr]	$d\sigma_{1/2}/d\Omega$ [μb/sr]	Δ_{stat} [μb/sr]	Δ_{sys} [μb/sr]	$d\sigma_{1/2}/d\Omega$ [μb/sr]	Δ_{stat} [μb/sr]	Δ_{sys} [μb/sr]	$d\sigma_{1/2}/d\Omega$ [μb/sr]	Δ_{stat} [μb/sr]	Δ_{sys} [μb/sr]
−0.80	0.4439	0.0791	0.1005	0.2656	0.0586	0.0270	0.2037	0.0494	0.0328	0.3019	0.0674	0.0356
−0.40	0.2534	0.0596	0.0973	0.2673	0.0528	0.0897	0.1959	0.0443	1.3548	0.1905	0.0522	0.1022
0.00	0.3069	0.0586	0.1295	0.2033	0.0499	0.0754	0.0465	0.0492	0.0557	0.1758	0.0424	0.0715
0.40	0.3537	0.0510	0.1096	0.2468	0.0417	0.0481	0.2170	0.0388	0.0273	0.1829	0.0405	0.0165
0.80	0.2107	0.0731	0.0388	0.1189	0.0582	0.0286	0.2605	0.0645	0.0136	0.1477	0.0661	0.0551

$\cos(\theta^*_{2\pi^0})$	$W=(2120.0\pm20.0)$ MeV			$W=(2160.0\pm20.0)$ MeV			$W=(2200.0\pm20.0)$ MeV			$W=(2240.0\pm20.0)$ MeV		
	$d\sigma_{1/2}/d\Omega$ [μb/sr]	Δ_{stat} [μb/sr]	Δ_{sys} [μb/sr]	$d\sigma_{1/2}/d\Omega$ [μb/sr]	Δ_{stat} [μb/sr]	Δ_{sys} [μb/sr]	$d\sigma_{1/2}/d\Omega$ [μb/sr]	Δ_{stat} [μb/sr]	Δ_{sys} [μb/sr]	$d\sigma_{1/2}/d\Omega$ [μb/sr]	Δ_{stat} [μb/sr]	Δ_{sys} [μb/sr]
−0.80	0.2946	0.0446	0.0438	0.0208	0.0586	0.0621	0.1794	0.0405	0.0590	0.1637	0.0630	0.0137
−0.40	0.1001	0.0401	0.0284	0.0990	0.0410	0.0385	0.1179	0.0343	0.0189	0.1640	0.0634	0.0369
0.00	0.2441	0.0408	0.0473	0.0962	0.0461	0.0351	0.1142	0.0434	0.0904	0.1684	0.0437	0.0292
0.40	0.1252	0.0372	0.0881	0.2312	0.0456	0.0123	0.0595	0.0370	0.0062	0.1696	0.0484	0.0326
0.80	0.3144	0.0572	0.0218	0.1980	0.0654	0.0060	0.4566	0.0683	0.0676	0.2474	0.0825	0.0284

$\cos(\theta^*_{2\pi^0})$	$W=(2280.0\pm20.0)$ MeV		
	$d\sigma_{1/2}/d\Omega$ [μb/sr]	Δ_{stat} [μb/sr]	Δ_{sys} [μb/sr]
−0.80	0.3492	0.1023	0.0278
−0.40	−0.0465	0.0842	0.9796
0.00	0.1700	0.0953	0.0237
0.40	0.1688	0.0820	0.1728
0.80	0.1824	0.1660	0.2138

$\cos(\theta^*_{2\pi^0})$	$W=(1320.0\pm20.0)$ MeV			$W=(1360.0\pm20.0)$ MeV			$W=(1400.0\pm20.0)$ MeV			$W=(1440.0\pm20.0)$ MeV		
	$d\sigma_{3/2}/d\Omega$ [μb/sr]	Δ_{stat} [μb/sr]	Δ_{sys} [μb/sr]	$d\sigma_{3/2}/d\Omega$ [μb/sr]	Δ_{stat} [μb/sr]	Δ_{sys} [μb/sr]	$d\sigma_{3/2}/d\Omega$ [μb/sr]	Δ_{stat} [μb/sr]	Δ_{sys} [μb/sr]	$d\sigma_{3/2}/d\Omega$ [μb/sr]	Δ_{stat} [μb/sr]	Δ_{sys} [μb/sr]
−0.80	−1.3987	1.1282	0.7370	−0.2940	0.6058	0.2266	0.2613	0.2589	0.0699	0.0721	0.3278	0.0945
−0.40	−0.6429	1.5919	0.5853	0.1429	0.4972	0.0822	0.8928	0.2730	0.2867	0.2997	0.2643	0.1097
0.00	−1.6194	1.9901	0.6682	0.9880	0.6084	0.0935	0.0647	0.2642	0.0263	0.5673	0.2750	0.0946
0.40	−0.2720	1.8279	0.2419	0.0382	0.4184	0.1171	0.5798	0.2455	0.0246	1.0226	0.2529	0.1354
0.80	−1.8417	25.4137	0.9348	−0.3171	1.0812	0.2759	0.5201	0.3258	0.0361	0.4717	0.3483	0.0626

$\cos(\theta^*_{2\pi^0})$	$W=(1480.0\pm20.0)$ MeV			$W=(1520.0\pm20.0)$ MeV			$W=(1560.0\pm20.0)$ MeV			$W=(1600.0\pm20.0)$ MeV		
	$d\sigma_{3/2}/d\Omega$ [μb/sr]	Δ_{stat} [μb/sr]	Δ_{sys} [μb/sr]	$d\sigma_{3/2}/d\Omega$ [μb/sr]	Δ_{stat} [μb/sr]	Δ_{sys} [μb/sr]	$d\sigma_{3/2}/d\Omega$ [μb/sr]	Δ_{stat} [μb/sr]	Δ_{sys} [μb/sr]	$d\sigma_{3/2}/d\Omega$ [μb/sr]	Δ_{stat} [μb/sr]	Δ_{sys} [μb/sr]
−0.80	0.9315	0.3250	0.0826	1.6278	0.3941	0.1012	0.6995	0.3260	0.0952	0.1599	0.3106	0.2260
−0.40	1.2275	0.3206	0.1671	1.6479	0.3112	0.4269	0.8483	0.2924	0.0765	1.0386	0.2520	0.0197
0.00	1.5187	0.3261	0.2601	1.3501	0.2809	0.1371	1.1771	0.2839	0.1248	0.5179	0.1757	0.0329
0.40	1.1095	0.2507	0.2290	1.0740	0.2109	0.2252	0.6892	0.1974	0.1282	0.7860	0.1606	0.1162
0.80	0.8804	0.3450	0.1151	0.6243	0.2705	0.0038	0.4233	0.2321	0.0415	0.4991	0.1771	0.1129

$\cos(\theta^*_{2\pi^0})$	$W=(1640.0\pm20.0)$ MeV			$W=(1680.0\pm20.0)$ MeV			$W=(1720.0\pm20.0)$ MeV			$W=(1760.0\pm20.0)$ MeV		
	$d\sigma_{3/2}/d\Omega$ [μb/sr]	Δ_{stat} [μb/sr]	Δ_{sys} [μb/sr]	$d\sigma_{3/2}/d\Omega$ [μb/sr]	Δ_{stat} [μb/sr]	Δ_{sys} [μb/sr]	$d\sigma_{3/2}/d\Omega$ [μb/sr]	Δ_{stat} [μb/sr]	Δ_{sys} [μb/sr]	$d\sigma_{3/2}/d\Omega$ [μb/sr]	Δ_{stat} [μb/sr]	Δ_{sys} [μb/sr]
−0.80	1.0999	0.2466	0.0954	0.5403	0.2231	0.0472	1.1302	0.1801	0.1218	0.4112	0.1077	0.0351
−0.40	0.6892	0.1832	0.1073	0.6714	0.1903	0.0719	0.9674	0.1185	0.3026	0.7838	0.1123	0.2250
0.00	0.6127	0.1634	0.0681	1.0961	0.1574	0.1723	0.7453	0.1369	0.1681	0.7479	0.1052	0.2921
0.40	1.0072	0.1380	0.2047	0.7720	0.1289	0.1077	0.6635	0.1164	0.1390	0.5467	0.0854	0.1192
0.80	0.1558	0.1617	0.0080	0.4175	0.1506	0.0146	0.2249	0.1596	0.0333	0.7522	0.1135	0.0748

$\cos(\theta^*_{2\pi^0})$	$W=(1800.0\pm20.0)$ MeV			$W=(1840.0\pm20.0)$ MeV			$W=(1880.0\pm20.0)$ MeV			$W=(1920.0\pm20.0)$ MeV		
	$d\sigma_{3/2}/d\Omega$ [μb/sr]	Δ_{stat} [μb/sr]	Δ_{sys} [μb/sr]	$d\sigma_{3/2}/d\Omega$ [μb/sr]	Δ_{stat} [μb/sr]	Δ_{sys} [μb/sr]	$d\sigma_{3/2}/d\Omega$ [μb/sr]	Δ_{stat} [μb/sr]	Δ_{sys} [μb/sr]	$d\sigma_{3/2}/d\Omega$ [μb/sr]	Δ_{stat} [μb/sr]	Δ_{sys} [μb/sr]
−0.80	0.2796	0.0884	0.0022	0.2755	0.0787	0.0203	0.1181	0.0791	0.0637	0.3094	0.0824	0.0600
−0.40	0.4193	0.0806	0.1200	0.4463	0.0809	0.2149	0.6048	0.0794	0.2136	0.3695	0.0592	0.0391
0.00	0.6208	0.0873	0.2695	0.6990	0.0825	1.2953	0.4735	0.0705	0.1571	0.3143	0.0659	0.0879
0.40	0.6898	0.0800	0.1408	0.3745	0.0603	0.0913	0.4374	0.0646	0.0614	0.3524	0.0531	0.0235
0.80	0.4040	0.1230	0.0009	0.5567	0.0841	0.0570	0.2671	0.0806	0.0189	0.1630	0.0725	0.0360

$\cos(\theta^*_{2\pi^0})$	$W=(1960.0\pm20.0)$ MeV			$W=(2000.0\pm20.0)$ MeV			$W=(2040.0\pm20.0)$ MeV			$W=(2080.0\pm20.0)$ MeV		
	$d\sigma_{3/2}/d\Omega$ [μb/sr]	Δ_{stat} [μb/sr]	Δ_{sys} [μb/sr]	$d\sigma_{3/2}/d\Omega$ [μb/sr]	Δ_{stat} [μb/sr]	Δ_{sys} [μb/sr]	$d\sigma_{3/2}/d\Omega$ [μb/sr]	Δ_{stat} [μb/sr]	Δ_{sys} [μb/sr]	$d\sigma_{3/2}/d\Omega$ [μb/sr]	Δ_{stat} [μb/sr]	Δ_{sys} [μb/sr]
−0.80	0.2080	0.0791	0.0624	0.3486	0.0586	0.0315	0.2534	0.0494	0.0138	0.1456	0.0674	0.0625
−0.40	0.3508	0.0596	0.1284	0.3260	0.0528	0.1060	0.2970	0.0443	1.4758	0.3128	0.0522	0.1505
0.00	0.3843	0.0586	0.1986	0.4062	0.0499	0.1221	0.4434	0.0492	0.0997	0.2887	0.0424	0.1139
0.40	0.1854	0.0510	0.0699	0.2573	0.0417	0.0501	0.2840	0.0388	0.0223	0.2638	0.0405	0.0183
0.80	0.3022	0.0731	0.0247	0.3899	0.0582	0.0444	0.2132	0.0645	0.0201	0.3549	0.0661	0.0675

$\cos(\theta^*_{2\pi^0})$	$W=(2120.0\pm20.0)$ MeV			$W=(2160.0\pm20.0)$ MeV			$W=(2200.0\pm20.0)$ MeV			$W=(2240.0\pm20.0)$ MeV		
	$d\sigma_{3/2}/d\Omega$ [μb/sr]	Δ_{stat} [μb/sr]	Δ_{sys} [μb/sr]	$d\sigma_{3/2}/d\Omega$ [μb/sr]	Δ_{stat} [μb/sr]	Δ_{sys} [μb/sr]	$d\sigma_{3/2}/d\Omega$ [μb/sr]	Δ_{stat} [μb/sr]	Δ_{sys} [μb/sr]	$d\sigma_{3/2}/d\Omega$ [μb/sr]	Δ_{stat} [μb/sr]	Δ_{sys} [μb/sr]
−0.80	0.1604	0.0446	0.0241	0.4031	0.0586	0.0642	0.1788	0.0405	0.0729	0.1763	0.0630	0.0157
−0.40	0.2510	0.0401	0.0380	0.2095	0.0410	0.0823	0.1864	0.0343	0.0228	0.1217	0.0634	0.0279
0.00	0.1356	0.0408	0.0372	0.2446	0.0461	0.0612	0.2404	0.0434	0.1561	0.1462	0.0437	0.0247
0.40	0.3442	0.0372	0.1618	0.2279	0.0456	0.0141	0.3272	0.0370	0.0236	0.2096	0.0484	0.0305
0.80	0.2524	0.0572	0.0182	0.3965	0.0654	0.0067	0.1269	0.0683	0.0267	0.4202	0.0825	0.0333

$\cos(\theta^*_{2\pi^0})$	$W=(2280.0\pm20.0)$ MeV		
	$d\sigma_{3/2}/d\Omega$ [μb/sr]	Δ_{stat} [μb/sr]	Δ_{sys} [μb/sr]
−0.80	0.1276	0.1023	0.0522
−0.40	0.4020	0.0842	1.0697
0.00	0.1730	0.0953	0.0329
0.40	0.2772	0.0820	0.2806
0.80	0.5715	0.1660	0.2523

References

[1] J. Dalton, "On the Absorption of Gases by Water and other Liquids", 15–24 (1805) 10.1080/14786440608563325.

[2] P. Curie, M. P. Curie, and G. Bémont, "Sur une nouvelle substance fortement radio-active, contenue dans la pechblende", Comptes rendus de l'Académie des Sciences, Paris **127**, 1215–1217 (1898).

[3] *Standard Model of Elementary Particles*, https://commons.wikimedia.org/wiki/File:Standard_Model_of_Elementary_Particles.svg (visited on 11/06/2015).

[4] M. Gell-Mann, "A Schematic Model of Baryons and Mesons", Phys.Lett. **8**, 214–215 (1964).

[5] R. P. Feynman, *Lectures on gravitation*, California Institute of Technology, Pasadena, CA, USA, 1971.

[6] B. Povh et al., *Teilchen und Kerne*, 9th ed. (Teilchen und Kerne: Eine Einführung in die physikalischen Konzepte, Jan. 2014).

[7] R. Frisch and O. Stern, "Über die magnetische Ablenkung von Wasserstoffmolekülen und das magnetische Moment des Protons. I", Zeitschrift für Physik **85**, 4–16, ISSN: 0044-3328 (1933) 10.1007/BF01330773, http://dx.doi.org/10.1007/BF01330773.

[8] *CODATA internationally recommended values of the fundamental physics constants*, http://physics.nist.gov/constants (visited on 11/09/2015).

[9] S. Bethke, "The 2009 world average of α_s", The European Physical Journal C **64**, 689–703 (2009).

[10] W. Bartel, Physics Letters B **28**, 148–151 (1968).

[11] U. Löring et al., "Relativistic quark models of baryons with instantaneous forces . Theoretical background", The European Physical Journal A **10**, 309–346 (2001).

[12] U. Löring, B. C. Metsch, and H. R. Petry, "The light-baryon spectrum in a relativistic quark model with instanton-induced quark forces . The non-strange-baryon spectrum and ground states", The European Physical Journal A **10**, 395–446 (2001).

[13] S. Schadmand, "Double Pion Photoproduction", in Proceedings to the sixth Workshop on Electromagnetic Induced Two-Hadron Emission, Pavia, 2004 (2004), ISBN: 88-85159-20-6.

[14] B. Krusche, "Photoproduction of mesons off nuclei", The European Physical Journal Special Topics **198**, 199–238 (2011).

[15] S. Boffi et al., *Electromagnetic Response of Atomic Nuclei* (Carlendon Press, Oxford, 1996).

[16] D. Drechsel and L. Tiator, "Threshold pion photoproduction on nucleons", Journal of Physics G: Nuclear and Particle Physics **18**, 449–497 (1992).

[17] G. F. Chew et al., "Relativistic Dispersion Relation Approach to Photomeson Production", Physical Review **106**, 1345–1355 (1957).

[18] B. Krusche and S. Schadmand, "Study of Non-Strange Baryon Resonances with Meson Photoproduction", Prog.Part.Nucl.Phys. **nucl-ex**, 399–485 (2003).

[19] D. E. Groom et al., "Review of particle physics. Particle Data Group", Eur. Phys. J. **C15**, 1–878 (2000).

[20] K. M. Watson, "The Hypothesis of Charge Independence for Nuclear Phenomena", Physical Review **85**, 852–857 (1952).

[21] I. S. Barker, A. Donnachie, and J. K. Storrow, "Complete experiments in pseudoscalar photoproduction", Nuclear Physics **95**, 347–356 (1975).

[22] A. M. Sandorfi et al., "Determining pseudoscalar meson photoproduction amplitudes from complete experiments", Journal of Physics G: Nuclear and Particle Physics **38**, 053001 (2011).

[23] R. L. Walker, "Phenomenological Analysis of Single-Pion Photoproduction", Physical Review **182**, 1729–1748 (1969).

[24] G. Keaton and R. Workman, "Amplitude ambiguities in pseudoscalar meson photoproduction", Physical Review C (Nuclear Physics) **53**, 1434–1436 (1996).

[25] W.-T. Chiang and F. Tabakin, "Completeness rules for spin observables in pseudoscalar meson photoproduction", Physical Review C (Nuclear Physics) **55**, 2054–2066 (1997).

[26] Y. Wunderlich, R. Beck, and L. Tiator, "The complete-experiment problem of photoproduction of pseudoscalar mesons in a truncated partial-wave analysis", Phys. Rev. C **89**, 055203–14 (2014).

[27] O. Bartholomy et al., "Neutral-Pion Photoproduction off Protons in the Energy Range 0.3 GeV $< E_\gamma <$ 3 GeV", Physical Review Letters **94**, 012003 (2005).

[28] O. Bartalini et al., “Measurement of π^0 photoproduction on the proton from 550 to 1500 MeV at GRAAL”, Eur. Phys. J. A **26**, 399–419 (2006).

[29] The CB-ELSA Collaboration et al., “Photoproduction of π^0-mesons off protons from the $\Delta(1232)$ region to $E_\gamma = 3$ GeV”, Eur. Phys. J. A **31**, 61–77 (2007).

[30] M. Dugger et al., “π^0 photoproduction on the proton for photon energies from 0.675 to 2.875 GeV”, Phys. Rev. C **76**, 025211–16 (2007).

[31] The CBELSA/TAPS Collaboration et al., “Linearly polarised photon beams at ELSA and measurement of the beam asymmetry in π^0 photoproduction off the proton”, Eur. Phys. J. A **39**, 373–381 (2009).

[32] N. Sparks et al., “Measurement of the beam asymmetry Σ in the forward direction for $\vec{\gamma}p \to p\pi^0$”, Phys. Rev. C **81**, 065210–10 (2010).

[33] V. Crede et al., “Photoproduction of neutral pions off protons”, Phys. Rev. C **84**, 055203–11 (2011).

[34] A. Thiel et al., “Well-Established Nucleon Resonances Revisited by Double-Polarization Measurements”, Physical Review Letters **109**, 102001 (2012).

[35] M. Gottschall et al., “ First Measurement of the Helicity Asymmetry for $\gamma p \to \pi^0 p$ in the Resonance Region ”, Physical Review Letters **112**, 012003 (2014).

[36] M. H. Sikora et al., “Measurement of the ${}^1H(\vec{\gamma}, \vec{p})\pi^0$ Reaction Using a Novel Nucleon Spin Polarimeter”, Physical Review Letters **112**, 022501–5 (2014).

[37] K. A. Olive and P. D. Group, “Review of Particle Physics”, Chinese Physics C **38**, 090001 (2014).

[38] A. V. Anisovich et al., “Properties of baryon resonances from a multichannel partial wave analysis”, The European Physical Journal A **48**, 15 (2012).

[39] R. L. Workman et al., “Unified Chew-Mandelstam SAID analysis of pion photoproduction data”, Physical Review C **86**, 015202 (2012).

[40] D. Drechsel et al., “A unitary isobar model for pion photo- and electroproduction on the proton up to 1 GeV”, Nucl. Phys. A **645**, 145–174. 32 p (1998).

[41] R. L. Workman et al., “Updated SAID analysis of pion photoproduction data”, Physical Review C **85**, 025201 (2012).

[42] K. Wijesooriya et al., “Polarization measurements in neutral pion photoproduction”, Phys. Rev. C **66**, 034614–14 (2002).

[43] E. Gutz et al., “High statistics study of the reaction $\gamma p \to p\pi^0\eta$”, The European Physical Journal A **50**, 74 (2014).

[44] C. Bacci et al., “Angular distributions for single neutral pion photoproduction from neutrons at 450-800 MeV”, Phys.Lett. **B39**, 559–562 (1972).

[45] Y. Hemmi et al., “Photoproduction of neutral pions off neutrons in the energy region between 500 MeV and 900 MeV”, Nucl. Phys. **B55**, 333–362 (1973).

[46] R. Di Salvo et al., "Measurement of Σ beam asymmetry in π^0 photoproduction off the neutron in the second and third resonances region", The European Physical Journal A **42**, 151–157 (2009).

[47] A. Braghieri et al., "Total cross section measurement for the three double pion photoproduction channels on the proton", Physics Letters B **363**, 46–50 (1995).

[48] J. Ahrens et al., "Intermediate resonance excitation in the $\gamma p \rightarrow p\pi^0\pi^0$ reaction", Physics Letters B **624**, 173–180 (2005).

[49] F. Härter et al., "Two neutral pion photoproduction off the proton between threshold and 800 MeV", Physics Letters B **401**, 229–233 (1997).

[50] M. Wolf et al., "Photoproduction of neutral pion pairs from the proton", The European Physical Journal A **9**, 5–8 (2000).

[51] A. V. Sarantsev et al., "New results on the Roper resonance and the P_{11} partial wave", Physics Letters B **659**, 94–100 (2008).

[52] F. Zehr et al., "Photoproduction of $\pi^0\pi^0$ - and $\pi^0\pi^+$ -pairs off the proton from threshold to the second resonance region", Eur. Phys. J. A **48**, 98–19 (2012).

[53] M. Kotulla et al., "Double π^0 photoproduction off the proton at threshold", Physics Letters B **578**, 63–68 (2004).

[54] D. Krambrich et al., "Beam-Helicity Asymmetries in Double-Pion Photoproduction off the Proton", Physical Review Letters **103**, 052002 (2009).

[55] V. L. Kashevarov et al., "Experimental study of the $\gamma p \rightarrow \pi^0\pi^0 p$ reaction with the Crystal Ball/TAPS detector system at the Mainz Microtron", Phys. Rev. C **85**, 064610–11 (2012).

[56] M. Oberle et al., "Measurement of the beam-helicity asymmetry $I^{\odot}$ in the photoproduction of π^0-pairs off the proton and off the neutron", Physics Letters B **721**, 237–243 (2013).

[57] Y. Assafiri et al., "Double π^0 Photoproduction on the Proton at GRAAL", Physical Review Letters **90**, 222001–4 (2003).

[58] A. Thiel et al., "Three-Body Nature of N^* and Δ^* Resonances from Sequential Decay Chains", Physical Review Letters **114**, 091803–5 (2015).

[59] U. Thoma et al., "N^* and Δ^* decays into $N\pi^0\pi^0$", Physics Letters B **659**, 87–93 (2008).

[60] V. Sokhoyan et al., "Data on I^s and I^c in $\vec{\gamma} p \rightarrow p\pi^0\pi^0$ reveal cascade decays of $N(1900)$ via $N(1520)\pi$", Physics Letters B **746**, 127–131 (2015).

[61] V. Sokhoyan et al., "High-statistics study of the reaction $\gamma p \rightarrow p2\pi^0$", Eur. Phys. J. A **51**, 95–29 (2015).

[62] A. Fix and H. Arenhövel, "Double-pion photoproduction on nucleon and deuteron", Eur. Phys. J. A **A25**, 115–135 (2005).

[63] L. Murphy and J. Laget, *CEA Report No. DAPNIA 96-10, Saclay*, 1996.

[64] J. A. Gómez Tejedor and E. Oset, "Double pion photoproduction on the nucleon: study of the isospin channels", Nuclear Physics **600**, 413–435 (1996).

[65] J. C. Nacher et al., "The Role of $\Delta(1700)$ excitation and ρ production in double pion photoproduction", arXiv.org **A695**, 295–327 (2001).

[66] J. C. Nacher and E. Oset, "Study of polarization observables in double-pion photoproduction on the proton", Nuclear Physics **697**, 372–387 (2002).

[67] M. Hirata, N. Katagiri, and T. Takaki, "πNN coupling and two-pion photoproduction on the nucleon", Phys. Rev. C **67**, 034601–16 (2003).

[68] J. Ajaka et al., "Double π^0 photoproduction on the neutron at GRAAL", Physics Letters B **651**, 108–113 (2007).

[69] B. Krusche et al., "Single and double pion photoproduction from the deuteron", Eur. Phys. J. A **6**, 309–324 (1999).

[70] V. Kleber et al., "Double-π^0 photoproduction from the deuteron", Eur. Phys. J. A **9**, 1–4 (2000).

[71] R. A. Arndt et al., "Extended partial-wave analysis of πNscattering data", Phys. Rev. C **74**, 045205–14 (2006).

[72] *SAID - INS Data Analysis Center*, http://gwdac.phys.gwu.edu/.

[73] *Maid - photo- and electroproduction of pions, etas and kaons on the nucleon*, http://portal.kph.uni-mainz.de/MAID/.

[74] D. Drechsel, S. S. Kamalov, and L. Tiator, "Unitary isobar model –MAID2007", Eur. Phys. J. A **34**, 69–97 (2007).

[75] *Bonn-gatchina partial wave analysis*, http://pwa.hiskp.uni-bonn.de/.

[76] A. V. Anisovich et al., "Photoproduction of pions and properties of baryon resonances from a Bonn-Gatchina partial-wave analysis", Eur. Phys. J. A **44**, 203–220 (2010).

[77] V. E. Tarasov et al., "Extracting the photoproduction cross sections off the neutron, via the $\gamma n \to \pi^- p$ reaction, from deuteron data with final-state interaction effects", Phys. Rev. C **84**, 035203–14 (2011).

[78] M. I. Levchuk, V. A. Petrun′kin, and M. Schumacher, "π^0 photoproduction on quasi-free neutrons in the reaction $\gamma d \to \pi^0 np$ in the Δ region", Zeitschrift für Physik A: Hadrons and Nuclei **355**, 317–326 (1996).

[79] H. Arenhövel and A. Fix, "Incoherent pion photoproduction on the deuteron with polarization observables. I. Formal expressions", Phys. Rev. C **72**, 064004–9 (2005).

[80] A. Fix and H. Arenhövel, "Incoherent pion photoproduction on the deuteron with polarization observables. II. Influence of final state rescattering", Phys. Rev. C **72**, 064005–21 (2005).

[81] M. I. Levchuk et al., "Incoherent pion photoproduction on the deuteron in the first resonance region", Phys. Rev. C **74**, 014004–20 (2006).

[82] V. E. Tarasov et al., "On the Extraction of Cross Sections for π^0 and η Photoproduction off Neutrons from Deuteron Data", arXiv.org, 6671 (2015).

[83] G. F. Chew and M. L. Goldberger, "The Scattering of Elementary Particles by Complex Nuclei-A Generalization of the Impulse Approximation", Physical Review **87**, 778–782 (1952).

[84] *Thomas Jefferson National Accelerator Facility*, https://www.jlab.org (visited on 08/27/2015).

[85] *Mainzer Mikrotron MAMI*, http://www.kph.uni-mainz.de/eng/108.php (visited on 08/27/2015).

[86] *Elektronen Stretcher Anlage ELSA*, https://www-elsa.physik.uni-bonn.de (visited on 08/27/2015).

[87] M. Dehn et al., "The MAMI C accelerator", The European Physical Journal Special Topics **198**, 19–47 (2011).

[88] H. Euteneuer et al., "The Injector Linac for the Mainz Microtron", (1989).

[89] K. H. Kaiser et al., "Four Years of Operation of the 180 MeV CW Electron Accelerator MAMI A", (1989).

[90] H. Euteneuer et al., "Experience with the 855-MeV RTM-Cascade MAMI", Conf. Proc. **C920324**, 418–420 (1992).

[91] U. Ludwig-Mertin et al., "Three dimensional design of the bending magnets for a 1.5-GeV double sided microtron", in Particle accelerator. proceedings, 6th european conference, epac'98, stockholm, sweden, june 22-26, 1998. vol. 1-3 (1998), pp. 1931–1933.

[92] A. Thomas et al., "Design and Status of the 250t-Bending Magnets for the 1.5 GeV Harmonic Double Sided Microtron for MAMI", 1–3 (2002).

[93] A. Jankowiak et al., "Design and status of the 1.5-GeV harmonic double sided microtron for MAMI", 1085–1087–3 (2002).

[94] A. Jankowiak et al., "Experiences in Fabrication and Testing the Prototype of the 4.90 GHz Accelerating Sections for MAMI C", (2004).

[95] K. H. Kaiser et al., "The 1.5GeV harmonic double-sided microtron at Mainz University", Nuclear Instruments and Methods in Physics Research Section A: Accelerators, Spectrometers, Detectors and Associated Equipment **593**, 159–170 (2008).

[96] K. Aulenbacher et al., "The MAMI source of polarized electrons", Nuclear Instruments and Methods in Physics Research Section A: Accelerators, Spectrometers, Detectors and Associated Equipment **391**, 498–506 (1997).

[97] H. G. Andresen et al., "Operational experience with the MAMI-source of polarized electrons", Conf. Proc. **C960610**, 1502–1504 (1996).

[98] H. Herminghaus, "Continuous Beam Electron Accelerators", (1989).

[99] T. Walcher, "Highlights and Perspectives of the Mainz Microtron MAMI", Progress in Particle and Nuclear Physics **50**, 503–522 (2003).

[100] D. Werthmüller, “Experimental study of nucleon resonance contributions to η-photoproduction on the neutron”, PhD thesis (Universität Basel, 2014).

[101] H. W. Koch and J. W. Motz, “Bremsstrahlung Cross-Section Formulas and Related Data”, Rev. Mod. Phys. **31**, 920–955 (1959).

[102] J. C. McGeorge et al., “Upgrade of the Glasgow photon tagging spectrometer for Mainz MAMI-C”, The European Physical Journal A **37**, 129–137 (2008).

[103] S. J. Hall et al., “A focal plane system for the 855 MeV tagged photon spectrometer at MAMI-B”, Nuclear Instruments and Methods in Physics Research Section A: Accelerators, Spectrometers, Detectors and Associated Equipment **368**, 698–708 (1996).

[104] M. J. Oreglia, “A study of the reactions ψ'meson $\rightarrow \gamma, \gamma, \psi$”, PhD thesis (Stanford University, Aug. 2015).

[105] A. Starostin et al., “Measurement of $K^-p \rightarrow \eta\Lambda$ near threshold”, Physical Review C (Nuclear Physics) **64**, 55205 (2001).

[106] R. Novotny, *The BaF_2 Photon Spectrometer TAPS* (IEEE, 1990).

[107] A. R. Gabler et al., “Response of TAPS to monochromatic photons with energies between 45 and 790 MeV”, Nuclear Instruments and Methods in Physics Research Section A: Accelerators, Spectrometers, Detectors and Associated Equipment **346**, 168–176 (1994).

[108] R. Novotny, “Performance of the BaF_2-calorimeter TAPS”, in Nuclear physics b (proceedings supplements) (II. Physics Institute, University Giessen, Heinrich-Buff-Ring 16, D-35392 Giessen, Germany, Feb. 1998), pp. 137–142.

[109] P.-B. Otte, “Erste Messung der π^0-Photoproduktion an transversal polarisierten Protonen nahe der Schwelle”, PhD thesis (Johannes Gutenberg Universität Mainz, Apr. 2015).

[110] *Data Acquisition Wikipedia of the A2-Collaboration*, https://wwwa2.kph.uni-mainz.de/intern/daqwiki/ (visited on 09/03/2015).

[111] K. H. Althoff et al., “The 2.5 GeV electron synchrotron of the University of Bonn”, Nuclear Instruments and Methods **61**, 1–30 (1968).

[112] K. H. Althoff et al., “ELSA, a Proposed Stretcher and Post Accelerator for the Bonn 2.5 GeV Electron Synchrotron”, in *11th international conference on high-energy accelerators* (Birkhäuser Basel, Basel, 1980), pp. 196–200.

[113] D. Husmann, “ELSA, A Stretcher and Post-accelerator for the Bonn 2.5-GeV Electron Synchrotron”, IEEE Trans. Nucl. Sci. **30**, 3252–3256 (1983).

[114] D. Husmann, “The ELSA stretcher ring”, in *Electron and photon interactions at intermediate energies* (Springer Berlin Heidelberg, Berlin, Heidelberg, 1985), pp. 379–391.

[115] W. Hillert, “The Bonn Electron Stretcher Accelerator ELSA: Past and future”, The European Physical Journal A **28**, 139–148 (2006).

[116] S. Friedrich, "Experimental constraints on the real part of the ω-nucleus optical potential", PhD thesis (Justus-Liebig-Universität Giessen, June 2014).

[117] K. Fornet-Ponse, "Die Photonenmarkierungsanlage für das Crystal-Barrel/TAPS-Experiment an ELSA", PhD thesis (Rheinische Friedrich-Wilhelms-Universität Bonn, Dec. 2009).

[118] J. Hartmann, "Zeitkalibrierung und Photonenflussbestimmung für das Crystal-Barrel-Experiment an ELSA", MA thesis (Rheinische Friedrich-Wilhelms-Universität Bonn, Dec. 2008).

[119] H. Koch et al., *The crystal barrel: meson spectroscopy at LEAR with a 4π neutral and charged detector*, tech. rep. (Geneva, 1985).

[120] W. Leo, *Techniques for Nuclear and Particle Physics Experiments* (Springer-Verlag, Würzburg, Germany, 1994).

[121] C. Wendel, "Design und Aufbau eines Szintillationsdetektors zur Identifizierung geladener Teilchen im Crystal-Barrel-Vorwärtsdetektor", PhD thesis (Rheinische Friedrich-Wilhelms-Universität Bonn, July 2008).

[122] C. Funke, "Analyse der Triggerfähigkeiten zur Selektion hadronischer Ereignisse und Entwicklung eines Hochgeschwindigkeits-Triggers für den Vorwärtskonus des Crystal-Barrel-Detektors", PhD thesis (Rheinische Friedrich-Wilhelms-Universität Bonn, Sept. 2008).

[123] A. Foesel, "Entwicklung und Bau des Innendetektors für das Crystal Barrel Experiment an ELSA/Bonn", PhD thesis (Rheinische Friedrich-Wilhelms-Universität Bonn, Sept. 2015).

[124] *Webpage of the CBELSA/TAPS Collaboration at ELSA*, http://www1.cb.uni-bonn.de/fileadmin/user_upload/internal/MiniTAPS/geometry/minitaps-front.pdf (visited on 09/05/2015).

[125] D. Kaiser, "Aufbau und Test des Gas-Čerenkov-Detektors für den Crystal-Barrel-Aufbau an ELSA", MA thesis (Rheinische Friedrich-Wilhelms-Universität Bonn, Apr. 2007).

[126] J. Dielmann, "Entwicklung, Aufbau und Test eines Detektors zur Bestimmung des Photonenflusses an der Bonner Photonenmarkierungsanlage", MA thesis (Rheinische Friedrich-Wilhelms-Universität Bonn, Oct. 2008).

[127] H. Flemming, "Entwurf und Aufbau eines Zellularlogik-Triggers für das Crystal-Barrel-Experiment an der Elektronenbeschleunigeranlage ELSA", PhD thesis (Rheinische Friedrich-Wilhelms-Universität Bonn, Sept. 2001).

[128] P. Hoffmeister, "Konzipierung der Analogsignalverarbeitung für den Crystal Barrel Vorwärtsdetektor", MA thesis (Rheinische Friedrich-Wilhelms-Universität Bonn, Dec. 2004).

[129] D. Lohmann et al., "Linearly polarized photons at MAMI (Mainz)", Nuclear Instruments and Methods in Physics Research Section A **343**, 494–507 (1994).

[130] T. Maruyama et al., "Systematic study of polarized electron emission from strained GaAs/GaAsP superlattice photocathodes", Applied Physics Letters **85**, 2640–3 (2004).

[131] W. Hillert, "The 50 kV inverted source of polarized electrons at ELSA", in The fourteenth international spin physics symposium, spin2000 (June 2001), pp. 961–964.

[132] R. H. Pratt, "Transfer of Helicity in Radiation and Absorption of High-Energy Photons", Physical Review **123**, 1508–1510 (1961).

[133] H. Olsen and L. C. Maximon, "Photon and Electron Polarization in High-Energy Bremsstrahlung and Pair Production with Screening", Physical Review **114**, 887–904 (1959).

[134] V. Tioukine, K. Aulenbacher, and E. Riehn, "A Mott polarimeter operating at MeV electron beam energies", Review of Scientific Instruments **82**, 033303–9 (2011).

[135] *Manual of the Møller Polarimeter*, http://wwwa2.kph.uni-mainz.de/images/internal/detectors%20and%20setup/Moeller/HowToDoMoellerMeasurement.pdf (visited on 08/31/2015).

[136] P.-B. Otte, "Aufbau und Test eines Møllerpolarimeters für das Crystal-Ball-Experiment an MAMI-C", MA thesis (Johannes Gutenberg Universität Mainz, Apr. 2010).

[137] H. Eberhardt, "Messung der Targetpolarisation und Detektorstudie für das Møllerpolarimeter des Crystal-Barrel-Aufbaus an ELSA", MA thesis (Rheinische Friedrich-Wilhelms-Universität Bonn, Dec. 2006).

[138] S. Kammer, "Strahlpolarimetrie am CBELSA/TAPS Experiment", PhD thesis (Rheinische Friedrich-Wilhelms-Universität Bonn, Mar. 2010).

[139] A. Thomas, *Crystal Ball Hydrogen (Deuterium) Target manual* (May 2013).

[140] A. Thomas, "Polarised targets for 4π detectors at MAMI", Eur. Phys. J. ST **198**, 171–180 (2011).

[141] C. Bradtke et al., "A new frozen-spin target for 4π particle detection", Nuclear Instruments and Methods in Physics Research Section A: Accelerators, Spectrometers, Detectors and Associated Equipment **436**, 430–442 (1999).

[142] T. O. Niinikoski and J. M. Rieubland, "Dynamic Nuclear Polarization in Irradiated Ammonia Below 0.5-K", Phys.Lett. **A72**, 141–144 (1979).

[143] U. Härtel et al., "Experience with NH_3 as Target Material for Polarized Proton Targets at the Bonn 2.5 GEV Electron Synchrotron", in *High-energy physics with polarized beams and polarized targets* (Birkhäuser Basel, Basel, 1981), pp. 447–450.

[144] W. Meyer et al., "Irradiated ammonia (NH_3) as target material for polarized proton targets", Nuclear Instruments and Methods in Physics Research **215**, 65–69 (1983).

[145] W. Meyer et al., "Dynamic Deuteron Polarization in Irradiated D Ammonia (ND_3) and Its First Use in a High-energy Photon Beam", Nucl. Instrum. Meth. **A227**, 35–44 (1984).

[146] J. Ball, "Thirty years of research with lithium compounds in Saclay", Nucl. Instrum. Meth. **A526**, 7–11 (2004).

[147] S. Mango, "Early target material research with chemical dopants", Nucl. Instrum. Meth. **A526**, 1–6 (2004).

[148] H. Dutz et al., "The new Bonn frozen spin target for experiments with real photons", Nuclear Instruments and Methods in Physics Research Section A **340**, 272–277 (1994).

[149] H. Dutz, "Highlights of polarized solid state target instrumentation", Nuclear Instruments and Methods in Physics Research Section A: Accelerators, Spectrometers, Detectors and Associated Equipment **526**, 117–125 (2003).

[150] A. Thomas, "Review on the last developments on polarized targets at Mainz", in Annual meeting of the gdr ph-qcd, saclay 2013 (Universitaet Mainz, Nov. 2013), pp. 1–40.

[151] M. Schiemann, "Polarisationsmessungen an mit Trityl-Radikalen dotiertem D-Butanol", MA thesis (Ruhr-Universität Bochum, Sept. 2006).

[152] S. T. Goertz et al., "Highest polarizations in deuterated compounds", Nuclear Instruments and Methods in Physics Research Section A: Accelerators, Spectrometers, Detectors and Associated Equipment **526**, 43–52 (2004).

[153] S. T. Goertz, "The dynamic nuclear polarization process", Nuclear Instruments and Methods in Physics Research Section A: Accelerators, Spectrometers, Detectors and Associated Equipment **526**, 28–42 (2003).

[154] M. Plückthun et al., "Polarization measurements of TEMPO-doped butanol targets", Nuclear Inst. and Methods in Physics Research **400**, 133–136 (1997).

[155] A. Thomas, private communication, 2013.

[156] A. Thomas, "Frozen Spin Target", in A2 collaboration meeting (Mar. 2015), pp. 1–31.

[157] O. V. Lounasmaa and R. D. Parks, "Experimental Principles and Methods Below 1 K", Physics Today **28**, 74–75 (2008).

[158] E. Rickert, "Untersuchung der Ortsabhängigkeit der Polarisation des Mainzer Frozen-Spin-Targets", PhD thesis (Johannes Gutenberg Universität Mainz, June 2015).

[159] R. Brun and F. Rademakers, "ROOT — An object oriented data analysis framework", Nuclear Inst. and Methods in Physics Research **389**, 81–86 (1997).

[160] I. Antcheva et al., "ROOT — A C++ framework for petabyte data storage, statistical analysis and visualization", Computer Physics Communications **180**, 2499–2512 (2008).

[161] *ROOT, a Modular Scientific Software Toolkit*, https://root.cern.ch/ (visited on 09/05/2015).

[162] *Homepage of CERN, The European Organization for Nuclear Research*, http://www.cern.ch/ (visited on 09/05/2015).

[163] J. R. M. Annand, *Data Analysi within an AcquRoot Framework* (Sept. 2015).

[164] D. Glazier, "A Geant4 simulation for the CrystalBall@MAMI Setup", 1–14 (2012).

[165] C. Schmidt, "Entwicklung eines neuen Datenakquisitionssystems für das CB-ELSA-Experiment", PhD thesis (Rheinische Friedrich-Wilhelms-Universität Bonn, Aug. 2004).

[166] D. Piontek, "Entwicklung eines Online-Monitors für das Crystal-Barrel-Experiment an ELSA", MA thesis (Rheinische Friedrich-Wilhelms-Universität Bonn, Mar. 2007).

[167] *CBGEANT 1.08/01* (2001).

[168] S. Agostinelli et al., "GEANT4: A Simulation toolkit", Nucl. Instrum. Meth. **A506**, 250–303 (2003).

[169] J. Allison et al., "Geant4 developments and applications", IEEE Transactions on Nuclear Science **53**, 270–278 (2006).

[170] R. Brun et al., "Geant steps into the future", in 7th international conference on computing in high-energy and nuclear physics (chep 1994) san francisco, california, april 21-27, 1994 (1994).

[171] I. Froehlich et al., "Pluto: A Monte Carlo Simulation Tool for Hadronic Physics", arXiv.org, 2382 (2007).

[172] I. Froehlich et al., "Design of the Pluto Event Generator", arXiv.org, 032039 (2009).

[173] L. Witthauer, "Measurement of Cross Sections and Polarisation Observables in η Photoproduction from Neutrons and Protons Bound in Light Nuclei", PhD thesis (Universität Basel, Oct. 2015).

[174] *Webpage of the A2 Collaboration at MAMI*, https://wwwa2.kph.uni-mainz.de/intern/daqwiki/ (visited on 09/03/2015).

[175] *Reference Physics Lists of Geant4*, http://geant4.web.cern.ch/geant4/support/proc_mod_catalog/physics_lists/referencePL.shtml (visited on 09/10/2015).

[176] D. H. Wright et al., "Low and High Energy Modeling in Geant4", in Hadronic shower simulation workshop. proceedings held at batavia (Stanford Linear Accelerator Center, Menlo Park, California, Mar. 2007), pp. 11–20.

[177] J. Linturi, private communication, 2013.

[178] R. Brun, F. Carminati, and S. Giani, "GEANT Detector Description and Simulation Tool", (1994).

[179] T. A. Gabriel, J. D. Amburgey, and B. L. Bishop, *CALOR: A Monte Carlo Program Package for the Design and Analysis of Calorimeter Systems.* Oak Ridge National Laboratory (ORNL), Oak Ridge, TN (United States) (Apr. 1977).

[180] *Webpage of the HADES Collaboration*, https://www-hades.gsi.de/ (visited on 09/05/2015).

[181] M. Lacombe et al., “Parametrization of the deuteron wave function of the Paris N-N potential”, Phys.Lett. **B101**, 139–140 (1981).

[182] J. S. Mccarthy, I. Sick, and R. R. Whitney, “Electromagnetic Structure of the Helium Isotopes”, Phys.Rev. **C15**, 1396–1414 (1977).

[183] K. Nakamura et al., “The reactions ^{6,7}Li, ^{9}Be, ^{10}B(e, e'p) at 700 MeV and DWIA analysis”, Nuclear Physics A **296**, 431–443 (1978).

[184] K. Nakamura et al., “The reaction ^{12}C(e, e'p) at 700 MeV and DWIA analysis”, Nuclear Physics A **268**, 381–407 (1976).

[185] M. Roebig-Landau, “Photoproduktion von η-Mesonen an komplexen Kernen”, PhD thesis (Justus-Liebig-Universität Giessen).

[186] *Pluto, a Monte Carlo Simulation Tool for Hadronic Physics*, https://www-hades.gsi.de/?q=pluto (visited on 09/05/2015).

[187] F. M. Marques et al., “Identification of photons and particles in the segmented electromagnetic calorimeter TAPS”, Nucl. Instrum. Meth. **A365**, 392–409 (1995).

[188] V. Hejny, “Photoproduktion von η-Mesonen an Helium 4”, PhD thesis (Justus-Liebig-Universität Giessen, Sept. 2002).

[189] T. C. Awes et al., “A Simple method of shower localization and identification in laterally segmented calorimeters”, Nucl. Instrum. Meth. **A311**, 130–138 (1992).

[190] A. Thiel, “Bestimmung der Doppelpolarisationsobservablen G in π^0-Photoproduktion”, PhD thesis (Rheinische Friedrich-Wilhelms-Universität Bonn, July 2012).

[191] T. Seifen, “Verbesserung der Rekonstruktion und Entwicklung eines First-Level-Triggerschemas für das Crystal-Barrel-Kalorimeter”, MA thesis (Rheinische Friedrich-Wilhelms-Universität Bonn, Sept. 2009).

[192] J. Müller, “Bestimmung einer Energiekorrekturfunktion für das Kalorimeter des Crystal-Barrel-Experiments an ELSA”, MA thesis (Rheinische Friedrich-Wilhelms-Universität Bonn, Mar. 2007).

[193] J. Junkersfeld, “Kalibration des Crystal-Barrel-ELSA Detektors mit Hilfe der Reaktion $\gamma p \to p\pi^0$”, MA thesis (Rheinische Friedrich-Wilhelms-Universität Bonn, Nov. 2015).

[194] T. Dahlke, “Bestimmung einer winkelabhängigen Energiekorrekturfunktion für das TAPS-Kalorimeter des Crystal-Barrel/TAPS-Experimentes an ELSA”, MA thesis (Rheinische Friedrich-Wilhelms-Universität Bonn, Dec. 2008).

[195] *Helmholtz-Institut für Strahlen- und Kernphysik*, http://www.hiskp.uni-bonn.de/ (visited on 09/16/2015).

[196] M. Unverzagt, "Energie-Eichung des Crystal Ball-Detektors am MAMI", MA thesis (Johannes Gutenberg Universität Mainz, 2004).

[197] S. Schumann, "Strahlungsbegleitete π^0-Photoproduktion am Proton", PhD thesis (Rheinische Friedrich-Wilhelms-Universität Bonn, Jan. 2008).

[198] S. Böse, "Modifikation und Test des Lichtpulsersystems für den Crystal Barrel Aufbau an ELSA", MA thesis (Rheinische Friedrich-Wilhelms-Universität Bonn, June 2006).

[199] E. F. McNicoll et al., "Experimental study of the $\gamma p \to \eta p$ reaction with the Crystal Ball detector at the Mainz Microtron (MAMI-C)", Phys. Rev. C **82**, 035208 (2010).

[200] E. Aker et al., "The Crystal Barrel spectrometer at LEAR", Nucl. Instrum. Methods Phys. Res., A **321**, 69–108. 80 p (1992).

[201] *Atomic and Nuclear Properties of Materials*, http://pdg.lbl.gov/2009/AtomicNuclearProperties/ (visited on 09/02/2015).

[202] *The Review of Particle Physics*, http://pdg.lbl.gov/ (visited on 09/25/2015).

[203] R. O. Owens, "Statistical treatment of tagged photon experiments", Nucl. Instrum. Meth. **A288**, 574–584 (1990).

[204] M. Unverzagt, "Bestimmung des Dalitz-Plot-Parameters α für den Zerfall $\eta \to 3\pi^0$ mit dem Crystal Ball am MAMI", PhD thesis (Rheinische Friedrich-Wilhelms-Universität Bonn, Aug. 2008).

[205] T. C. Jude, "Strangeness Photoproduction off the Proton at Threshold Energies", PhD thesis (University of Edinburgh, Jan. 2009).

[206] H. Holvoet, "Study of the helicity dependence of double pion photoproduction on the proton", PhD thesis (Universiteit Gent, May 2001).

[207] D. Werthmuller et al., "Narrow Structure in the Excitation Function of η Photoproduction off the Neutron", Physical Review Letters **111**, 232001 (2013).

[208] L. Witthauer et al., "Quasi-free photoproduction of η-mesons off ^{3}He nuclei", The European Physical Journal A **49**, 154–18 (2013).

[209] H. Dutz, private communication, 2011.

[210] H. Rochholz, "Entwicklungsarbeiten fuer einen Freie-Elektronen- Laser auf der Basis des Smith-Purcell-Effektes im infraroten Spektralbereich", MA thesis (Johannes Gutenberg Universität Mainz).

[211] A. Thomas, private communication, 2015.

[212] R. L. Workman et al., "Unified Chew-Mandelstam SAID analysis of pion photoproduction data", arXiv.org, 015202 (2012).

[213] B. Krusche et al., "Photoproduction of π^0-mesons from nuclei", The European Physical Journal A **22**, 277–291 (2004).

[214] D. Werthmuller et al., “Quasifree photoproduction of η mesons off protons and neutrons”, Phys. Rev. C **90**, 015205–24 (2014).

[215] *Mott polarimeter at MAMI* (Sept. 2009).

[216] H. Dutz, private communication, 2015.

[217] U. Siodlaczek et al., “Coherent and incoherent π^0 photoproduction from the deuteron”, Eur.Phys.J. **A10**, 365–371 (2001).

[218] A. Sarantsev, private communication, 2013.

[219] M. Dieterle et al., “Photoproduction of π^0-pairs off protons and off neutrons”, Eur. Phys. J. A **51**, 142–18 (2015).

[220] A. Käser et al., “The isospin structure of photoproduction of $\pi\eta$ pairs from the nucleon in the threshold region”, Physics Letters B **748**, 244–250 (2015).

[221] M. Dieterle et al., “Photoproduction of π^0 Mesons off Neutrons in the Nucleon Resonance Region”, Physical Review Letters **112**, 142001–6 (2014).

[222] M. Egorov and A. Fix, “Coherent $\pi^0\pi^0$ photoproduction on lightest nuclei”, Nuclear Physics A **933**, 104–113 (2015).

[223] R. G. Moorhouse, “Photoproduction of N^* Resonances in the Quark Model”, Physical Review Letters **16**, 772–774 (1966).

[224] J. Hartmann et al., “$N(1520)3/2^-$ Helicity Amplitudes from an Energy-Independent Multipole Analysis Based on New Polarization Data on Photoproduction of Neutral Pions”, Physical Review Letters **113**, 062001–5 (2014).

[225] S. Brandt, *Datenanalyse*, 4. Auflage (Spektrum Akademischer Verlag, Heidelberg, Berlin, Germany, 1999).